PROCEEDINGS OF THE FOURTEENTH WORKSHOP ON GENERAL RELATIVITY AND GRAVITATION in JAPAN

KYOTO UNIVERSITY, KYOTO, JAPAN
NOVEMBER 29 - DECEMBER 3, 2004

Edited by

Wataru Hikida, Misao Sasaki,
Takahiro Tanaka, Takashi Nakamura

Table of Contents

Preface iii

Invited talks

1. **Gamma Ray Bursts and Their Afterglows**
Re'em Sari 1
2. **Relativistic SPH Calculations of Compact Binary Mergers**
Frederic Rasio 21
3. **Large-Scale Cryogenic Gravitational-Wave Telescope: LCGT**
Masaki Ando 33
4. **Binary Compact Object Inspiral: Rate Expectations**
Vassiliki Kalogera 43
5. **Gravity Probe B - Experiment and Mission**
Paul Shestople 53
6. **Statistical isotropy of CMB anisotropy from WMAP**
Tarun Souradeep 62
7. **Inflation from String Theory**
James M. Cline 82
8. **Quantum Computation, Information and Relativity**
Akio Hosoya .....
9. **Vacuum energy: Screened, self-adjusted or finely-tuned?**
Jaume Garriga .....
10. **Cosmological Surprises from Brane-world models of Dark Energy**
Varun Sahni 95
11. **Mass and angular momenta of Kerr-anti-de Sitter spacetimes**
Nathalie Deruelle 115
12. **Strings in Cosmology?**
Edmund J. Copeland 123

Oral Presentation

1. **Anisotropic scalar field emission from TeV scale black hole**
Seong Chan Park 134
2. **Universal area spectrum in single-horizon black holes**
Takashi Tamaki 138
3. **Leading order corrections to the cosmological evolution of tensor perturbations in braneworld**
Tsutomu Kobayashi 142
4. **Renormalization Group approach to Cosmology**
Sanjay Jhingan 146

5. **Initial Data for Dynamical Evolutions of Binary Black Holes in Quasicircular Orbit**
Hwei-Jang Yo 151
6. **Gravitational Radiation from Magnetorotational Core-Collapse of Massive Stars**
Kei Kotake 155
7. **Particle production in a two-brane collision and Reheating of the Universe**
Yuichi Takamizu 159
8. **Gravitational Waves from a spinning particle with time domain approach**
Kenta Kiuchi 163
9. **Generalized cosmological scaling solutions**
Shuntaro Mizuno 167
10. **BPS pp-wave brane Cosmology Solution in String Theory**
Makoto Tanabe 171
11. **Domain-Wall Induced Entropy Production**
Fuminobu Takahashi 175
12. **Casimir Dark Energy**
Je-An Gu 179
13. **Probing Strong-Field Scalar-Tensor Gravity with Gravitational Wave Asteroseismology**
Hajime Sotani 183
14. **The disinformation problem for black holes**
Sean A. Hayward 187
15. **Cosmological term by deforming the Friedmann equation**
Erico Tanaka 191
16. **Stability of wormhole**
Sung-Won Kim .....
17. **The stability of smeared black branes and the Gubser-Mitra conjecture**
Gungwon Kang .....
18. **Structure of Magnetic field in a Black Hole–Disk System**
Masaaki Takahashi .....
19. **Secular Stability and Rotational Limit of Strange Stars**
Shigeyuki Karino 195
20. **Mass Deficit in Cylindrically Symmetric System**
Yasunari Kurita 199
21. **Chaotic dynamics in preheating after inflation**
Jin Yoshida 203
22. **Solving gravitino problem by a brane world effect**
Osamu Seto 207
23. **String theory on curved spacetime**
Makoto Natsuume 211
24. **Large-scale magnetic fields in dilaton electromagnetism in noncommutative inflation-**

ary cosmology
Kazuharu Bamba 215
25. **Ghost Condensation and Gravity in Higgs Phase**
Shinji Mukohyama 219
26. **Generation of New Axisymmetric stationary Solutions in five-dimensional asymptotically flat spacetimes**
Takashi Mishima 223
27. **Deciphering imprints of CDM substructure:Current Status and Future Prospects**
Kaiki Taro Inoue 227
28. **Radiation Drag Effects on GRB Internal Shocks**
Ryo Takagi 231
29. **Axisymmertic collapse simulations of rotating stellar cores in full GR: Numerical study for prompt black hole formation**
Yuichiro Sekiguchi 235
30. **Functional Determinant of the Laplacian on the Spherical Suspension**
Antonino Flachi 239
31. **Radiated Net Angular Momentum from Numerical Evolution of Black Hole Spacetimes**
Ryoji Takahashi 244
32. **KK gravitons are negative energy dust in brane cosmology**
Masato Minamitsuji 248
33. **Comments on a Factorizable Metric Ansatz in String Cosmology**
Sugumi Kanno 252
34. **Constraining Neutrino Masses by CMB Experiments Alone**
Ichikawa Kazuhide .....
35. **Infrared divergences in the inflationary brane world**
Oriol Pujolas 256
36. **A Possible Origin of Bimodal Distribution of Gamma-Ray Bursts**
Kenji Toma 260
37. **Reconstructing the Primordial Spectrum with CMB Temperature and Polarization**
Noriyuki Kogo 264
38. **A Unified Model of Short and Long Gamma-Ray Bursts, X-Ray Rich Gamma-Ray Bursts, and X-Ray Flashes**
Ryo Yamazaki 268
39. **Self-force on a particle orbiting a Schwarzschild black hole – Case of a scalar-charged particle –**
Wataru Hikida 272
40. **Partially ionizing the universe by decaying particles and CMB**
Shinta Kasuya 276
41. **Three-dimensional simulations of stellar core collapse in full general relativity: Non-**

axisymmetric dynamical instabilties
Masaru Shibata 280
42. **New Numerical Methods to Evaluate Homogeneous Solutions of the Teukolsky Equation**
Ryuichi Fujita 281
43. **Supergravity Description of the open string tachyon in the D/anti D-brane system**
Shinpei Kobayashi 285
44. **The Condition on Black Hole Formation in Five-Dimensional Spacetimes**
Chul-Moon Yoo 289
45. **Quantization of scalar perturbations in brane-world inflation**
Hiroyuki Yoshiguchi 293
46. **Evolution of gravitational waves in the high-energy regime of brane-world cosmology**
Takashi Hiramatsu 293
47. **Current status of the joint LIGO-TAMA inspiral analysis**
Hirotaka Takahashi .....
48. **Cohomogeneity One Cosmic String in Maximally Symmetric Spacetime**
Hiroshi Kozaki 297
49. **Positivity Bounds for the Y-ADM Mass Density**
Shinya Tomizawa 301

Poster Presentation

1. **May gravitons be super-strong interacting particles?**
Michael A. Ivanov 305
2. **The Accelerating Universe with Spinor Fields**
Tomoki Watanabe 309
3. **Junction conditions of cosmological perturbations**
Kenji Tomita 313
4. **Formula for determining parameters of an astrometric binary**
Hideki Asada 317
5. **Energy Extraction from five dimensional black holes and Catastrophe theory**
Masato Nozawa 321
6. **Second order gauge invariant perturbation thoery**
Kouji Nakamura 325
7. **Does nonlinear backreaction accelerate the cosmic expansion?**
Masumi Kasai .....
8. **Gravitational radiation from stationary cosmic strings**
Kouji Ogawa .....
9. **Spherically symmetric perfect fluid in area-radial coordinate**
Hideo Iguchi 329
10. **Correspondence between the adhesion model and the velocity dispersion for the cos-**

mological fluid
Takayuki Tatekawa 333
11. Electromagnetic radiation from naked singularity in self-similar gravitational collapse: spectral decomposition approach
Eiji Mitsuda 337
12. Field Evolution of the Black Hole Bomb model
Hironobu Furuhashi 341
13. Brane cosmology with curvature corrections
Takashi Torii 345
14. Non-Gaussianity from inflation with stochastic approach
Takeshi Hattori 349
15. Large-scale spectrums after inflation -nonminimal coupling scalar field case-
Yohei Araki 353
16. Information entropy of an inhomogeneous universe
Masaaki Morita .....
17. Approach to the Cosmological Constant Problem with a Diluting Mechanism by Extra-Dimensions
Satsuki Shimono 357
18. BH Evaporation and Nonequilibrium Thermodynamics for a Radiation Field
Hiromi Saida 361
19. Collective Quantisation of a Gravitating Skyrmion
Noriko Shiiki 365
20. Quasinormal Ringing for Acoustic Black Holes in Low Temperature
Hiroyuki Nakano 369
21. Wavelet-Based Method to Search for Gravitational Wave Bursts
Kazuhiro Hayama 373
22. Quantum Fluctuations in de Sitter brane world
Wade Naylor 377
23. Wave Optics In Gravitational Lensing Without Thin Lens Approximation
Teruaki Suyama 381
24. Gravitational Radiation from Inhomogeneous Core-collapse
Tomoya Takiwaki 385
25. Deformed horizon and singularity in 5-dim. charged black hole
Ken Matsuno 389
26. Extended Self-Similar Solutions of the Einstein-Scalar Field System
Makoto Yoshikawa 393
27. Gravitational wave from stellar core collapse:Odd parity perturbation of Tolman-Bondi space time
Aya Sekido 397
28. Scattering of Gravitational Waves by the Weak Gravitational Potential of Lens Ob-

jects
Ryuichi Takahashi 401
29. **S-branes from multi-black holes**
Kenji Sakamoto 405
30. **A New Formula for the Spectrum of Curvature Perturbation Produced from Inflation**
Shuichiro Yokoyama 409
31. **Gravitational Radiation from Coalesce of Binary Neutron Stars – Gauge-Invariant Wave Form Extraction –**
Mari Kawamura 413
32. **Probing gravitational-wave backgrounds with a space-based interferometer I**
Hideaki Kudoh 418
33. **Probing gravitational-wave backgrounds with a space-based interferometer II**
Atsushi Taruya 422
34. **Dark energy reflections in the redshift-space quadrupole**
Kazuhiro Yamamoto 426
35. **The gravitational self-force effect on a particle orbiting a Schwarzschild black hole**
Norichika Sago 430
36. **Asymptotically AdS spacetimes and conserved quantities in higher curvature gravitational theories**
Naoya Okuyama 434
37. **Scalar field perturbation on six-dimensional ultra-spinning black holes**
Yoshiyuki Morisawa 438
38. **Improved analysis of black hole formation in high-energy particle collision**
Hirotaka Yoshino 442
39. **Kink instability and stabilization of the Friedmann universe**
Hideki Maeda 446
40. **Structure and Stability of Transition Layer Between Interstellar Cloud and Intercloud Gas**
Tsuyoshi Inoue .....
41. **Geometrical Pinning in Supercondutor**
Izumi Tanaka 450
42. **CMB temperature and polarization anisotropies produced by the primordial magnetic fields**
Hiroyuki Tashiro 454
43. **Dynamical bar instability in collapsing stars**
Motoyuki Saijo 458
44. **Constant of motions for spinning particles**
Ewa Czuchry .....
45. **Stochastic Gravitational Wave Background in Brane World Cosmology**
Kiyotomo Ichiki 462

Gamma Ray Bursts and Their Afterglows

Re'em Sari[1],

[1] *Theoretical Astrophysics, Caltech 130-33, Pasadena, CA 91125*

Abstract

Gamma-Ray Bursts, are extreme astrophysical events, which emit the bulk of their energy as photons in the $0.1 - 1.0$ MeV range, and whose durations span milliseconds to tens of minutes. They are formed in extreme relativistic outflows. The breakthrough in their understanding came in early 1997, when BeppoSAX allowed rapid and accurate localization of GRBs. Follow-up on these positions resulted in the discovery of X-ray, optical and radio afterglows. These observations revealed that GRBs come from 'cosmological' distances, and that they are by far the most luminous photon sources in the Universe, with peak luminosities in γ rays up to 10^{52} erg/s, and total energy budgets up to several times 10^{53-54} erg, if assumed to be isotropic. However, GRB outflows are collimated in the form of jets and when corrected for the geometry the energies of GRBs appear to cluster around 5×10^{50} ergs- very comparable to that of supernovae. Evidence in the last several years shows that a significant fraction of long GRBs may be related to a peculiar type of supernova explosions. These supernovae most likely mark the birth events of stellar mass black holes as the final products of the evolution of very massive stars.

1 γ-ray burst - The generic picture

The Burst And Transient Source Experiment (BATSE) on board the Compton Gamma-Ray Observatory observed about one GRB a day over the nineties. BATSE provides a wealth of information on GRB light curves and spectra [1]. Some of the key properties are listed below:

- GRBs have durations ranging from milliseconds to $\sim 10^3$ s. The distribution of burst durations is bimodal and separates GRBs into two classes, the short events (<2s) and the longer ones (>2s) [2]. The duration appears to be anticorrelated with spectral hardness: short bursts are predominantly harder than long ones.

- Some GRBs show rapid variability, on time scales of order of a a millisecond [3, 4]. It is therefore generally believed that GRBs originate from compact objects, such as neutron stars (NS) or black holes (BH).

- The distribution of the burst over the sky is uniform to a large degree. Nevertheless, the number of bursts above a flux s falls less steeply that $s^{-3/2}$, which is the expectation from a uniform distribution in euclidean space.

- High-energy emission is a unique feature of GRBs. Spectral measurements extend from a few keV to $\sim$ GeV. The continuum spectra of GRBs are very broad and hard; most of the power is emitted above 50 keV. GRB spectra are well described by an empirical function, the so called Band function [5]. This function consists of a low- and high-energy power law, smoothly joined by an exponential turnover. It has four parameters, the peak energy, the low- and high-energy photon index, and an overall normliozation. The high energy photon index is close to -2, i.e. roughly equall amount of energy in each decade of photon energy.

On scales of Gpc or more, all objects are distributed roughly isotropically and uniformly. Moreover, a cosmological distribution of sources would reveal a natural deficiency of weaker bursts by relativistic effects that affect the weaker (on average at greater distances) bursts [6, 7, 8]. Therefore, it is already in

[1] E-mail:sari@tapir.caltech.edu

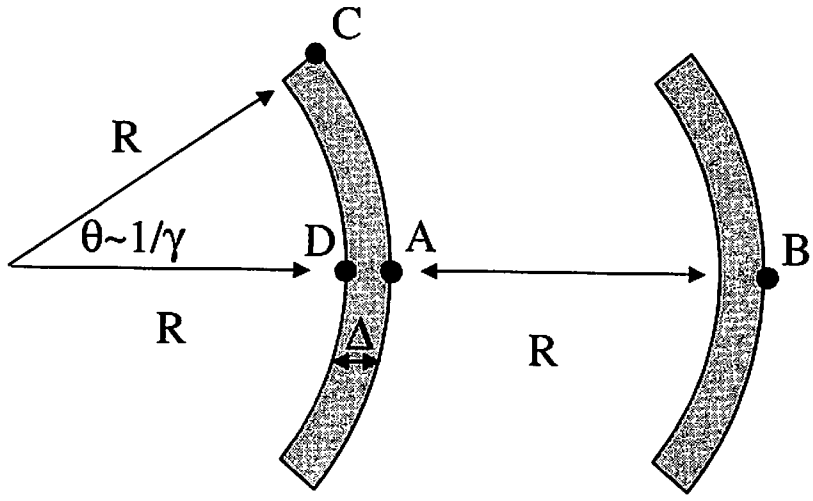


Figure 1: *Timescales from an expanding relativistic fireball. The gray area represents the observed section of the fireball that can be seen by an observer located far to the right. The angular opening of that section is $1/\gamma$ due to relativistic beaming. Consider the 4 photons emitted at points A, B, C, and D. Photons A, C and D where emitted simultaneously, but photon A will arrive at the observer first, since it is closer to the observer. The arrival-time delay of photons C and D with respect to photon A is simply given by the extra distance they have to travel. Therefore $\delta T_{C-A} = R(1-\cos\theta)/c = R/2\gamma^2 c$, and $\delta T_{D-A} = \Delta/c \sim R/\gamma^2 c$, where we have used the fact that relativistic dynamics of fireballs imply $\Delta \sim R/\gamma^2$. Finally, photon B was emitted long after photon A (about a time R/c later than photon A), however, it is much closer to the observer, resulting in $\delta T_{B-A} = R/2\gamma^2 c$. All three timescales lead to the expression $R/\gamma^2 c$. A short observed variability time scale can therefore be obtained even for large radius, if the Lorentz factor is sufficiently high. The naive estimate of $R \leq c\delta T$ is, therefore, to be replaced by $R \leq \gamma^2 c\delta T$.*

the BATSE days that cosmological distances seems the most plausible. The energy implied is of order 10^{51} erg

The observed spectra, energies and timescales of GRBs have lead to a generic model, the so called fireball shock model that is almost independent of the 'inner engine'.

The extreme characteristics of GRBs, i.e. the observed large energies and short timescales, lead to a paradox, the so called 'compactness problem'. An energy of 10^{52}erg is released within a variability time $\delta T \sim 0.1$s in the form of photons of about 1 MeV. This translates into a huge number of $N = 10^{56}$ photons. If we now assume that the energy is released in a small volume of linear dimensions $R \leq c\delta T \sim 10^9$cm (which is naively required by the variability timescale), then the optical depth to pair creation would be the number of photons per unit area, multiplied by the Thomson cross section σ_T or

$$\tau \sim \sigma_T \frac{N}{4\pi R^2} \sim 3 \times 10^{11} \gg 1.$$

But, if that were true, such a large optical depth implies that all the photons will have created pairs and thermalized. However, the observed spectrum of GRBs is highly non-thermal!

The only known solution to the 'compactness problem' is relativistic motion [6, 9]. These effects were considered in detail in [10, 11, 12]. A critical review of these as well as some new limits are given by Lithwick and Sari [13]. If the emission site is moving relativistically, with a Lorentz factor γ, toward the observer, then the optical depth is reduced, compared to the stationary estimate, due to two effects. First, the size of the source can be larger by a factor of γ^2. This will still produce variability over a short time scale given by $\delta T = R/\gamma^2 c$ since not all of the source is seen as the radiation for a relativistically moving object is beamed (see figure 1). Second, the photons in the local frame are softer by a factor of γ, and therefore only a small fraction of them, the ones at the high-energy tail of the GRB spectrum, have enough energy to create pairs. The combination of these two effects reduces the optical depth by a factor of $\sim \gamma^{6.5}$, where the exact power depends on the GRB spectrum (see [13]). Therefore, the optical depth is reduced below unity, and the 'compactness problem' is solved, if the Lorentz factor is larger than about a hundred.

This solution to the compactness problem led to a three stage generic scenario for GRBs. First, a compact source releases about 10^{52} erg, in a small volume of space and on a short time scale. This large concentration of energy expands due to its own pressure. If the rest mass that contaminates the site is not too large, $\leq 10^{-5} M_{\odot}$, this will result in relativistic expansion with $\gamma > 100$. Finally, at a large enough radius, the kinetic energy (bulk motion) of the expanding material is converted to internal energy and radiated, mainly in γ-rays. At this stage the system is optically thin and high energy photons can escape. We now discuss this third stage in some detail.

1.1 Internal vs. external shocks

Assume a flow carrying 10^{52} erg as kinetic energy. In order for this to produce photons, the kinetic energy must be converted back into internal energy and radiated away. The flow must therefore, at least partially, slow down. Two scenarios were proposed for this deceleration: external shocks [14] and internal shocks [15, 16]. In the external shocks scenario, the relativistic material is running into some (external) ambient medium, possibly the interstellar medium (ISM) or a stellar wind that was emitted earlier by the progenitor. In the internal-shocks scenario the inner engine is assumed to emit an irregular flow, that consists of many shells, that travel with a variety of Lorentz factors and therefore collide with one another and thermalize part of their kinetic energy.

The property that proved to be very useful in constraining these two possibilities is the variability observed in many of the bursts. In the external-shocks scenario, this variability is attributed to irregularities in the surrounding medium, e.g., clouds. Each time the ejecta runs into a higher density environment, it produces a peak in the emission. In the internal shocks scenario, the source has to emit many shells, and when two of them collide a peak in the emission is produced. External shocks thus require a complicated surrounding with a relatively simple source that explodes once, while internal shocks require a more complicated source that will explode many times to produce several shells. Due to these very different requirements on the source, the question of internal or external shocks is of a fundamental importance in understanding the nature of the phenomenon.

The size of the clouds that the ejecta runs into, in the external-shocks scenario, has to be very small in order to produce peaks that are narrower than the duration of the burst [17]. Sari & Piran [18] gave the following argument. The size of the clouds has to be smaller than $R/N\gamma$ to produce peaks that are narrower by a factor of N than the duration of the burst. The number of clouds should be smaller than N otherwise pulses arriving from different clouds will overlap and the amplitude of the variability will be reduced. Finally, the observable area of the ejecta, due to relativistic beaming is $(R/\gamma)^2$. The maximal efficiency of the external shocks scenario is therefore given by

$$\frac{\text{cloud area} \times \text{number of clouds}}{\text{observed shell area}} \leq \frac{1}{N} \sim 1\%. \qquad (1)$$

Since in many bursts $N > 100$, external shocks have a severe efficiency problem in producing highly variable bursts. Also other predictions of external shocks are inconsistent with the observed temporal profile [19]. Moreover, the density ratio between the clouds and the surroundings has to be huge, of the order of $\gamma N^2 \sim 10^6$, in order for the ejecta to be slowed down mainly by the dense clouds rather than by the low density medium that they are embedded in.

Internal shocks do not suffer from these problems. Detailed calculations show that the observed temporal structure from internal shocks, closely follows the operation of the inner engine that generated the shells [20]. In this scenario, the source must be variable on time scales shorter than a second and last for as long as 100 seconds, just as the bursts themselves.

The efficiency of internal shocks is largely determined by the ratio of Lorentz factors between different shells which are colliding with each other. The larger the ratio, the larger the efficiency. A simple scenario that demonstrates this is the case of two equal mass shells with Lorentz factor $\gamma_1 \gg \gamma_2 \gg 1$. Conservation of energy and momentum in a collision between the shells leads to a Lorentz factor which is the geometric mean of the initial ones $\sqrt{\gamma_1 \gamma_2}$. Therefore, the energy left in the system as non thermal is a small fraction $\sqrt{\gamma_2/\gamma_1}$ of the initial energy. Beloboradov [21] has argued that if large Lorentz factor ratios are allowed, the internal shock efficiency is only limited by the fraction of energy in the shock given to the radiating electrons. Kobayashi and Sari [22] have then shown that multiple collisions between shocks may result in

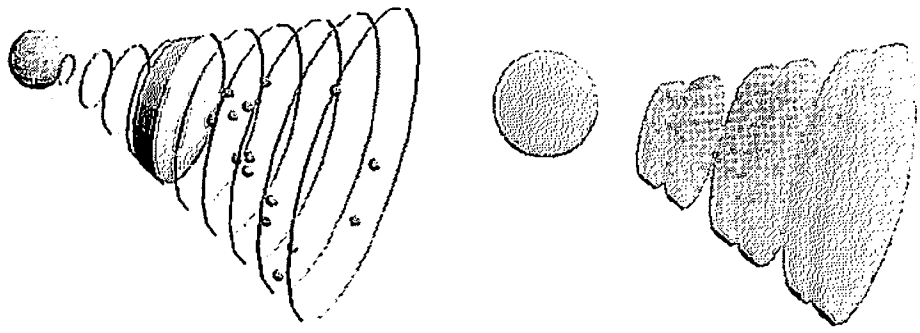


Figure 2: *Producing variability by external shocks (left) or internal shocks (right). In the external shocks scenario, the variability is produced by irregularities in the surrounding. If the surrounding consists of a low density medium that contains high density clouds, then whenever the shell hits one of the clouds a peak in the emission is produced. The number of clouds, within the observable cone (of angular size $1/\gamma$ due to relativistic beaming) should therefore roughly be the number of observed peaks. The source itself, in this model, needs to produce only a single shell in a single (simple) explosion. However, the external shocks scenario has low efficiency, due to the small total surface area of the clouds when compared to the area of the shell. In the internal-shocks case, the temporal structure arises from the source, i.e. the source produces a more complex explosion. There is no efficiency problem, provided that the relative Lorentz factor between shells is large.*

'ultra efficient' internal shocks, in the sense that even more than the fraction of energy given to electrons can be radiated away.

The mechanism by which the thermal energy produced by internal shocks is converted to radiation is almost certainly synchrotron and inverse Compton, since these are the dominant radiation mechanisms at the low densities involved. While both mechanisms probably take place, it is actually not very clear which of the two produces the observed radiation. Synchrotron emission is for several reasons preferred [23, 24] and inverse Compton probably produces a higher energy component.

2 The afterglow: theory and observations

After the internal shocks produced the GRB, the shell interacts with the surrounding medium and decelerates. Again it emits radiation by synchrotron and inverse Compton. As the flow decelerates, the emission shifts to lower and lower frequencies. This emission, the afterglow, may last on detectable levels for years after the GRB event!

Afterglow was predicted well before it was observed [25, 26, 27, 28]. The afterglow theory is relatively simple. It deals with the emission on timescales much longer than that of the GRB. The details of the complex initial conditions are therefore forgotten and the condition of the GRB remnant can be described by a self similar solution with a small number of parameters, such as the total energy and the external density. It is assumed that the electrons are accelerated by the shock into a power-law distribution (index p) of electron Lorentz factors $N(\gamma_e) \propto \gamma_e^{-p}$ for $\gamma_e > \gamma_m$. The lower cutoff, γ_m, of this distribution is set by the assumption that the electrons acquire a fixed fraction, ϵ_e, of the thermal energy (assumption of equipartition). It is also assumed that a considerable magnetic field is built behind the shock, which is again characterized by a certain fraction ϵ_B of equipartition. The energy density behind a relativistic shock is given by $4\gamma^2 n_1 m_p c^2$, where n_1 is the proton density ahead of the shock in units of cm^{-3}, γ is the Lorentz factor of the fluid behind the shock, and m_p is the proton mass. These equipartition assumptions then result in

$$\gamma_m = \frac{p-2}{p-1}\frac{m_p}{m_e}\epsilon_e\gamma \cong 630\epsilon_e\gamma \qquad (2)$$

$$B = 0.4\sqrt{\epsilon_B n_1}\gamma \text{ Gauss}, \tag{3}$$

where B is the magnetic field, and m_e is the electron mass. The relativistic electrons then emit synchrotron radiation which produces the observed afterglow. The broad band spectrum of such afterglow emission was given by Sari, Piran & Narayan [29].

The afterglow synchrotron spectrum can fully be described by the electron energy index p, the peak flux F_m and three characteristic frequencies (ν_m, ν_c, ν_a):

(I) ν_m is the synchrotron frequency of the minimal energy electron, with Lorentz factor γ_m. From synchrotron theory $\nu_m \cong (eB/2\pi m_e c)\gamma_m^2$ in the local frame of the fluid; here e is the electron charge. Transforming this to the observer frame (blue shifted by the Lorentz factor and redshifted by a factor of $[1+z]$) and using equations 2 and 3 we obtain

$$\nu_m = 1.4 \times 10^{13}\text{Hz}\,(1+z)^{-1}\left(\frac{\epsilon_e}{0.1}\right)^2\left(\frac{\epsilon_B}{0.1}\right)^{1/2}(\frac{\gamma}{10})^4 n_1^{1/2}. \tag{4}$$

(II) The cooling time of an electron is inversely proportional to its Lorentz factor γ_e. Therefore, electrons with a Lorentz factor higher than a critical Lorentz factor $\gamma_e > \gamma_c$ cool on the dynamical timescale of the system. This characteristic Lorentz factor is given by the condition $\sigma_T c\gamma^2\gamma_c^2 B^2 t\gamma/6\pi(1+z) = \gamma_c m_e c^2$, and corresponds to the 'cooling frequency'

$$\nu_c = 1.2 \times 10^{13}\text{Hz}\,(1+z)\left(\frac{\epsilon_B}{0.1}\right)^{-3/2}\left(\frac{\gamma}{10}\right)^{-4} n_1^{-3/2} t_{days}^{-2}, \tag{5}$$

where t_{days} is the observer time in days. Here we had also to take into account that time is redshifted.
(III) Below some critical frequency ν_a the flux is self absorbed and is given by the Rayleigh-Jeans portion

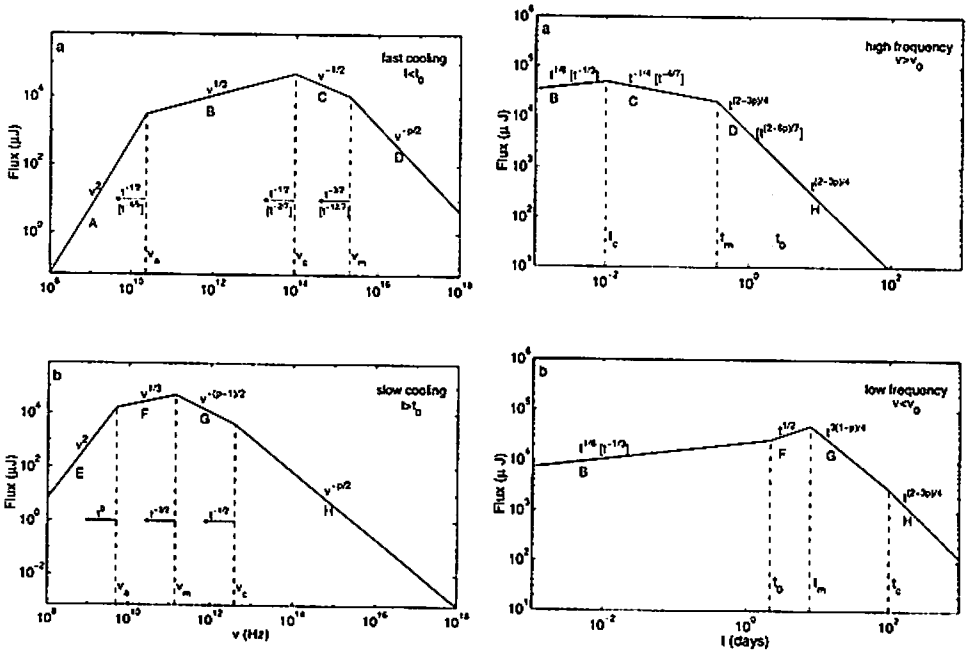


Figure 3: *Theoretical spectra (left) and light curves (right) of synchrotron emission from a powerlaw distribution of electrons for the case of a constant density ambient medium and a spherical explosion. For most cases $p = 2.2 - 2.5$ fits well the observed spectra and lightcurves.*

of a black body spectrum[2]. The self-absorption frequency is given by

$$\nu_{sa} = 93\,\mathrm{GHz}\,(1+z)^{-13/5}\left(\frac{\epsilon_B}{0.1}\right)^{6/5}\left(\frac{\gamma}{10}\right)^{28/5} n_1^{9/5} t_{days}^{8/5}, \tag{6}$$

if $\nu_c < \nu_m$, and by

$$\nu_{sa} = 87\,\mathrm{GHz}\,(1+z)^{-8/5}\left(\frac{\epsilon_e}{0.1}\right)^{-1}\left(\frac{\epsilon_B}{0.1}\right)^{1/5}\left(\frac{\gamma}{10}\right)^{8/5} n_1^{4/5} t_{days}^{3/5}, \tag{7}$$

if $\nu_c > \nu_m$.

(IV) The normalization of the spectrum is given by the total number of radiating electrons $4\pi R^3 n_1/3$ times the peak flux from a single electron, resulting in

$$F_m = 220\,\mathrm{mJy}(1+z)^{-2} d_{L,28}^{-2}\left(\frac{\epsilon_B}{0.1}\right)^{1/2}\left(\frac{\gamma}{10}\right)^{8} n_1^{3/2} t_{days}^{3}, \tag{8}$$

where $d_{L,28}$ is the luminosity distance in units of 10^{28}cm.

The broad band spectrum of the well studied GRB 970508 [31] is in very good agreement with the theoretical picture. Note that the derivation above is quite general. It does not depend neither on the surrounding density profile nor on the geometry of the event. Both these effects are hidden in the evolution of the fluid Lorentz factor γ, and the particle density n_1 as a function of time.

The evolution of this spectrum as a function of time depends on the hydrodynamics. The simplest, which describes the observations in some cases quite well, is the adiabatic model with a constant density surrounding medium. The rest mass collected by the shock at radius R is about $R^3\rho$, where ρ is the mass density. On average, the particles move with a Lorentz factor of γ^2 in the observer frame (one factor of γ is the bulk motion and the other is the random thermal motion). Therefore, the total energy is given by $E \propto \gamma^2 R^3 \rho c^2$. Assuming that the radiated energy is negligible compared to the energy of the flow, we obtain that $\gamma \propto R^{-3/2}$ or in terms of the observer time, $t = R/\gamma^2 c$, we get $\gamma \propto t^{-3/8}$.

$$\nu_m = 6\times 10^{15}\,\mathrm{Hz}\,(1+z)^{1/2} E_{52}^{1/2} \epsilon_e^2 \epsilon_B^{1/2} t_{\mathrm{days}}^{-3/2}$$

$$\nu_c = 9\times 10^{12}\,\mathrm{Hz}\,(1+z)^{-1/2} \epsilon_B^{-3/2} n_1^{-1} E_{52}^{-1/2} t_{\mathrm{days}}^{-1/2}$$

$$\nu_{sa} = 2\times 10^{9}\,\mathrm{Hz}\,(1+z)^{-1} \epsilon_e^{-1} \epsilon_B^{1/5} n_1^{3/5} E_{52}^{1/5}$$

$$F_m = 20\,\mathrm{mJy}\,(1+z)\epsilon_B^{1/2} n_1^{1/2} E_{52} d_{L28}^{-2}$$

These simple scalings, for the case of a constant density ambient medium, lead to the spectral evolution as given in Figure 3. The derivations above use a very simple description of the flow. It represents the fluid as if it has a single magnetic field strength and a single Lorentz factor γ and all of the material is moving directly towards the observer. Also, a very approximate description of the synchrotron emission was used. In reality, of course, the situation is more complicated. There are two effects that must be taken into account. The most dramatic one is the fact that matter slightly off the line of sight does not move directly towards the observer [32, 33, 34]. The amount of Lorentz boost from that matter is reduced. Secondly, fluid elements at different distances from the shock have somewhat different Lorentz factors, magnetic fields and electron energies. These variations can be estimated using the self-similar solution of Blandford and McKee [35]. The outcome of these more detailed calculations are the same scaling laws, but with a more accurate coefficient for the break frequencies as well as an estimate of the shape of the spectrum around each break frequency [36, 37, 38, 39]. The equations given above already take these effects into account, and the coefficients given are accurate for $p = 2.2$.

[2]Granot, Piran & Sari [30] have found that if $\nu_c < \nu_m$, then the self absorption frequency actually splits into two: ν_{ac} and ν_{sa}, where an optical depth of unity is produced by non-cooled electrons and all electrons, respectively. In between these two frequencies the spectral slope is $\nu^{11/8}$.

Given the above hydrodynamic evolution, one can construct light curves at any given frequency. These will also consist of power laws, changing from one power law to the other once the break frequencies pass through the observed band. These predicted power law lightcurves and spectra are in fair agreement with afterglow observations.

The observational breakthrough came in early 1997, when the Wide-Field Cameras (WFCs; [40]) onboard the Italian-Dutch satellite BeppoSAX [41] obtained their first quickly available (within hours) accurate positions of GRBs (several arcminutes). This allowed rapid follow-up observations which led to the discoveries of X-ray [42], optical [43], millimeter [44] and radio [45] counterparts of GRBs. These observations quickly settled the distance controversy. The first transient optical counterpart, of GRB 970228, is in a faint galaxy with $\sim 0.8''$ diameter [46]. And, detection of absorption features in the OT's spectrum of GRB 970508 [47] established that this event was at a redshift greater than $z = 0.835$. GRBs come from 'cosmological' distances and are thus extremely powerful events. They are by far the most luminous photon sources in the Universe, with (isotropic) peak luminosities in γ rays up to 10^{52} erg/s, and total energy budgets up to several 10^{53-54} erg [48, 49]. Within the first day, the optical emission is usually brighter than 20th magnitude (some 10 mag brighter [absolute] than the brightest supernovae) and therefore small telescopes can play an important role in measuring the lightcurve. Nowadays, a large worldwide collaboration is observing these events and the data are submitted to a Global-Coordinate-Network in real time, allowing other observatories to react rapidly.

A stringent test of the relativistic blast-wave model came with the discovery of X-ray [42] and optical afterglow following GRB 970228 [43, 50]. The X-ray and optical afterglows of GRB 970228, show a power-law temporal decay; this is a trend observed in all subsequent X-ray and optical afterglows, with power-law exponents in the range 1 to 2.

Let us first concentrate on the forward shock and assume slow cooling (the bulk of the electrons do not radiate a significant fraction of their own energy and the evolution is adiabatic); this appears applicable to some observed GRB afterglows at late times ($t > 1$ hr). The simplest assumption is that of spherical symmetry and a constant ambient density. As both the afterglow's spectrum and the temporal evolution of the break frequencies ν_a, ν_m, ν_c are, in the relativistic blast-wave model, power laws, the evolution of the flux is also a power law in time. For example, for $\nu_m \leq \nu \leq \nu_c$, the decay of the flux is $F_\nu \propto t_{obs}^{-3(p-1)/4}$, and the power law spectral slope α relates to the spectral slope β as $\alpha = -3/2\beta$. Several authors [51, 52, 53] showed that to first order this model describes the X-ray and optical afterglow of GRB 970228 very well.

GRB 970508 was the first GRB with a radio counterpart [45]. The radio light curves (8.5 and 4.9 GHz) show large variations on time scales of less than a day, but these damp out after one month. This finds a viable explanation in interstellar scintillation (irregular plasma refraction by the interstellar medium between the source and the observer). The damping of the fluctuations can then be understood as the effect of source expansion on the diffractive interstellar scintillation. Thus a source size of roughly 10^{17} cm was derived (at 3 weeks), corresponding to a mildly relativistic expansion of the shell [45].

GRB 970508 remains one of the best observed afterglows: the radio afterglow was visible at least 400 days [54], and the optical afterglow up to $\sim$ 450 days (e.g. [55, 56, 57]). In addition millimeter [44], infrared and X-ray [58] counterparts were detected, and it is the first GRB for which a spectral transition in the optical/near IR range was found [31, 56]; this transition is interpreted as the effect of the passage of the cooling frequency through the optical/near IR passbands. These multiwavelength observations allowed the reconstruction of the broad radio to X-ray spectrum for this GRB [31] (see Fig. 4). Galama et. al. [31] found that the 'standard' model provides a successful and consistent description of the afterglow observations over nine decades in frequency, ranging in time from the event until several months later. The synchrotron afterglow spectrum of this GRB allows measurement of the electron energy spectrum p, the three break frequencies (ν_a, ν_m and ν_c), and the flux at the peak, F_m. For GRB 970508 the redshift, z, is also known, and all blast wave parameters could be deduced: the total energy (per unit solid angle) $E = 3.5 \times 10^{52}$ erg, the ambient (nucleon) density $n_1 = 0.030$, the fraction of the energy in electrons $\epsilon_e = 0.12$ and that of the magnetic field $\epsilon_B = 0.089$ [59]. The numbers themselves are uncertain by an order of magnitude (see e.g., [38]), but the result shows that the 'standard' model fits the expectations very well. Following these first attempts at modeling the broad-band afterglow more detailed modeling efforts have been made on other well studied afterglows [60, 61, 62, 63, 64, 65, 66, 67].

All knowledge derived from afterglow detections to date (distance scale, progenitor distribution,

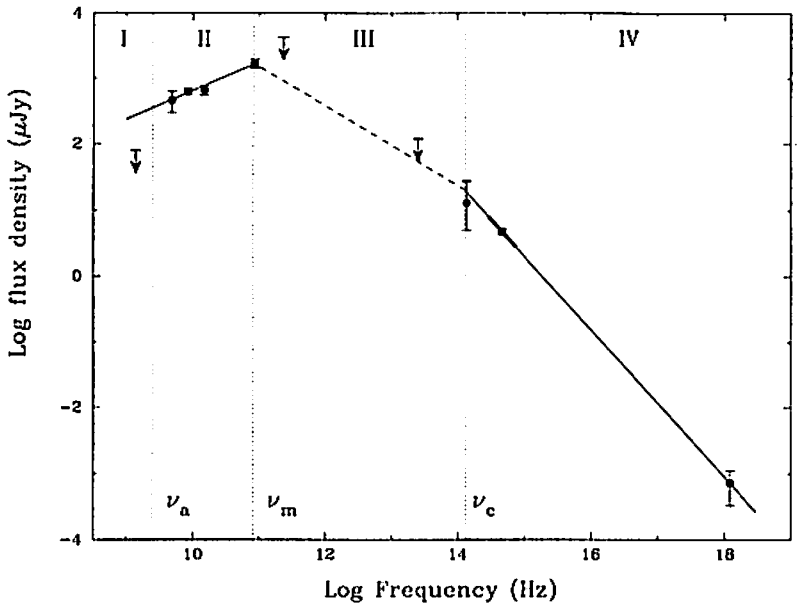


Figure 4: *The X-ray to radio spectrum of GRB 970508 on May 21.0 UT (12.1 days after the event). The location of the break frequencies ν_a, ν_m and ν_c, inferred from transitions in the light curves and from spectra of the afterglow, are indicated (from [31]).*

etc.) applies only to long-duration ($t > 2$ s) GRBs, as short-duration GRBs have never been precisely localized, quickly. There is good evidence that the short GRBs comprise a distinct population in terms of their γ-ray properties, and it is therefore likely that GRBs derive from multiple progenitor types. It is possible that short GRBs may result from mergers, and, residing in low-density regions, have very faint afterglows [68].

3 Collimated outflow - jets

The hydrodynamic evolution described in Sect. 2, assumed spherical symmetry. However, many astrophysical phenomena, especially those involving extreme energetics are not spherical but in the form of jets. This is most probably the case also for GRBs.

Jets have been discussed extensively in the context of GRBs. First, the similarity between some of the observed features of blazars and AGNs led to the speculation that jets also appear in GRBs [69]. Second, the regions emitting the GRBs as well as the afterglow must be moving relativistically. The emitted radiation is strongly beamed, and we can observe only a region with an opening angle $1/\gamma$ off the line of sight. Emission outside of this very narrow cone is not observed. These considerations have lead to numerous speculations on the existence of jets and to attempts to search for the observational signature of jets both during the GRB phase [70] and in the context of the afterglow [71, 72, 73]. Finally, jets appear naturally in the context of several leading scenarios for the 'inner engine'.

We begin by clarifying some of the confusing terminology. There are two distinct, but related, effects. The first, *'jets'*, describes scenarios in which the relativistic flow emitted from the source is not isotropic but collimated towards a finite solid angle. The term jet refers to the geometrical shape of the relativistic flow emitted from the inner engine. The second effect is that of *'relativistic beaming'*. The radiation from any object that is radiating isotropically in its own rest frame, but moving with a large Lorentz factor γ in the observer frame, is beamed into a small angle $1/\gamma$ around its direction of motion. This is an effect of special relativity. It has nothing to do with the ejecta's geometry (spherical or jet) but only with the

fact that the ejecta is moving relativistically. The effect of relativistic beaming allows an observer to see only a small angular extent, of size $1/\gamma$ centered around the line of sight. Since we know the flow is ultra-relativistic (initially $\gamma > 100$), there is no question that the relativistic beaming effect is always relevant for GRBs. The question we are interested in is that of the existence of 'jets'.

The idealized description of a jet is a flow that occupies only a conical volume with half opening angle θ_0. In fact, the relativistic dynamics is such that the width of the material in the direction of its propagation is much smaller than its distance from the source by a factor of $1/\gamma^2$. The flow, therefore, does not fill the whole cone. Instead it occupies only a thin disk at its base, looking more like a flying pancake [74] (see Figure 2). If the 'inner engine' emits two such jets in opposite directions then the total solid angle towards which the flow is emitted is $\Omega = 2\pi\theta_0^2$. Whether the relativistic flow is in the form of a jet or a sphere has two important implications.

The Total Emitted Energy. Optical observations of afterglows enabled redshift determination, and therefore a reasonably accurate estimate of the distance, D, to these events (the uncertainty is now in the cosmological parameters of the Universe). The so called 'isotropic energy' can then be inferred from the fluence F (the total observed energy per unit area at earth) as $E_{iso} = 4\pi D^2 F$ (taking cosmological corrections into account, $D = d_L/\sqrt{1+z}$ where d_L is the luminosity distance and z is the redshift). The numbers obtained in this way range from 10^{51} erg to 10^{54} erg with the record of 3×10^{54} erg held by the famous GRB 990123. These huge numbers approach the equivalent energy of a solar mass, all emitted in a few tens of seconds! If instead the emission is confined to some solid angle Ω then the true energy is $E = \Omega D^2 F$.

The Event Rate. BATSE's detection rate of about one burst per day, combined with several redshift measurements, translates to about 10^{-7} bursts per year per galaxy or 0.5 bursts/Gpc^{-3}/year [75, 76, 77]. However, if the emission is collimated to $\Omega \ll 4\pi$ then we do not see most of the events. The true event rate is then larger than that measured by BATSE by a factor of $4\pi/\Omega$ (see, however, [77]).

3.1 The jet-break

As the afterglow evolves, γ decreases and it will eventually fall below the initial inverse opening angle of the jet. The observer will notice that some of the sphere is missing from the fact that less radiation is observed. This effect alone, will produce a significant break, steepening the lightcurve decay by a factor of $\gamma^2 \propto t^{-3/4}$ even if the dynamics of each fluid element has not changed. The transition should occur at the time t_{jet} when $1/\gamma \cong \theta_0$. Observing this time can therefore provide an estimate of the jet's opening angle according to

$$t_{\rm jet} \approx 6.2{\rm hr}(1+z)(E_{52}/n_1)^{1/3}(\theta_0/0.1)^{8/3}. \quad (9)$$

Additionally, Rhoads [72] has shown that at about the same time (see however [78, 79, 80, 81]), the jet will begin to spread laterally so that its opening angle $\theta(t) \sim 1/\gamma$. The ejecta now encounters more surrounding matter and decelerates faster than in the spherical case. The Lorentz factor then decays exponentially with the radius and as $\gamma \propto t^{-1/2}$ with observed time. Taking this into account, the observed break is even more significant. The slow cooling spectrum given in Figure 3 evolves with decreasing peak flux $F_m \propto t^{-1}$ and the break frequencies evolve as $\nu_m \propto t^{-2}$, $\nu_c \propto t^0$ and $\nu_a \propto t^{-1/5}$. This translates to a temporal decay in a given frequency as listed in Table 1. The jet break is an hydrodynamic one. It should therefore appear at the same time at all frequencies - an achromatic break[3].

The theory of jets evolution and of the resulting light curves has been worked out before evidence for jets was obtained. In fact, Rhoads [72], has used this theory to constrain the amount of collimation in GRB 970508, which did not show any significant steepening of the afterglow lightcurve. He concluded that the opening angle of a jet, if it exists, must be more than 30 degrees.

The first claims for narrow jets came from GRB 990123 [49, 83, 84] and from analysies of a few fast decaying afterglows [85]. The latter noted that the observed decays in GRB afterglows that do not show a break are either of a shallow slope $F_\nu \propto t^{-1/2}$ or a very steep slope $F_\nu \propto t^{-2}$. They argued that the rapidly decaying bursts are those in which the ejecta was a narrow jet and the break in the light curve was

[3]Sari 1997 [82], argued that there may be about a factor of two difference in the effective transition time between the four different spectral regimes (e.g. below or above ν_m) due to the fact that the emission in these different regimes weighs differently contributions from various emission radii.

	spectral index β, $F_\nu \propto \nu^{-\beta}$	light curve index α, $F_\nu \propto t^{-\alpha}$ sphere	jet
$\nu < \nu_a$	$\beta = -2$	$\alpha = -1/2$	$\alpha = 0$
$\nu_a < \nu < \nu_m$	$\beta = -1/3$	$\alpha = -1/2$	$\alpha = 1/3$
$\nu_m < \nu < \nu_c$	$(p-1)/2 \cong 0.7$	$\alpha = 3(p-1)/4 \cong 1.05$ $\alpha = 3\beta/2$	$\alpha = p \cong 2.4$ $\alpha = 2\beta + 1$
$\nu > \nu_c$	$p/2 \cong 1.2$	$\alpha = (3p-2)/4 \cong 1.3$ $\alpha = 3\beta/2 - 1/2$	$\alpha = p \cong 2.4$ $\alpha = 2\beta$

Table 1: *The spectral index β and the temporal index α as function of p for a spherical and a jet-like evolution. Typical values are quoted using $p = 2.4$. The parameter free relation between α and β is given for each case (eliminating p). The difference in α between a jet and a sphere is always substantial at all frequencies.*

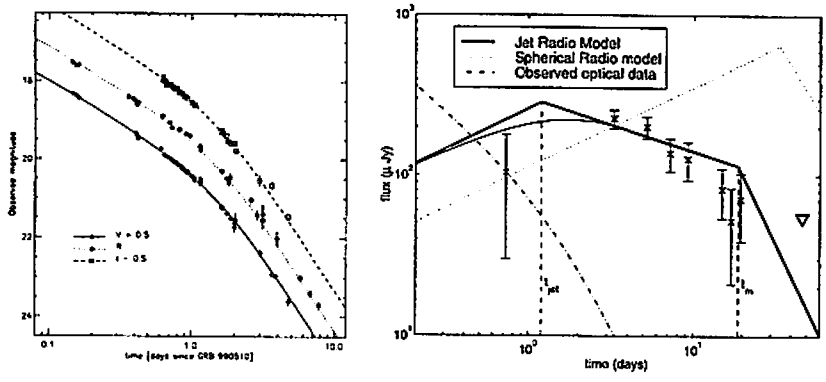


Figure 5: *GRB 990510, the 'classical' case for a 'jet': an achromatic break in optical and radio at $t_{\rm jet} = 1.2$ days implying a jet-opening angle $\theta_0 = 0.08$. The temporal slope before and after the break agree well with the theory if $p = 2.2$. For this burst the isotropic gamma-ray energy $E_{\rm iso} = 2.9 \times 10^{53}$ erg but the 'true' total energy is only $E = 10^{51}$ erg. From [86].*

before the first observations. Interestingly, evidence for jets are found when the inferred energy (without taking jets into account) is the largest. This implies that the jets account for a considerable fraction of the wide luminosity distribution seen in GRBs, and the true energy distribution is less wide than it seems to be.

The predicted light-curve transition (from a regular to a fast decay caused by a jet) has been observed in the optical afterglow of GRB 990123 [49, 83, 84]. However, no evidence for such an increase of the decay rate was found in near-infrared K-band observations [49]. A similar transition was better sampled in afterglow data of GRB 990510; optical observations of GRB 990510, show a clear steepening of the rate of decay of the light simultaneously in all optical bands between ~ 3 hours and several days [86, 87] to roughly $F_\nu(t) \propto t^{-2.2}$. Together with radio observations, which also reveal a transition, it is found that the transition is very much frequency-independent; this virtually excludes explanations in terms of the passage of the cooling frequency, but is what is expected in case of beaming. Harrison et al.[86] derive a jet opening angle (from the jet-break time) of $\theta_0 \cong 0.08$, which for this burst would reduce the total energy in γ rays to $\sim 10^{51}$ erg.

Frail et al. [88] have determined the jet-break times for a sample of GRBs with known redshifts. From these, a wide range of jet-opening angles is inferred in GRBs: from 3° to more than 25°, with a strong concentration near 4°. This relatively narrow collimation implies that the observed GRB rate has to be corrected for the fact that conical fireballs are visible to only a fraction of observers. Frail et al. find that the 'true' GRB rate is ~ 500 times larger than the observed GRB rate. Although the isotropic

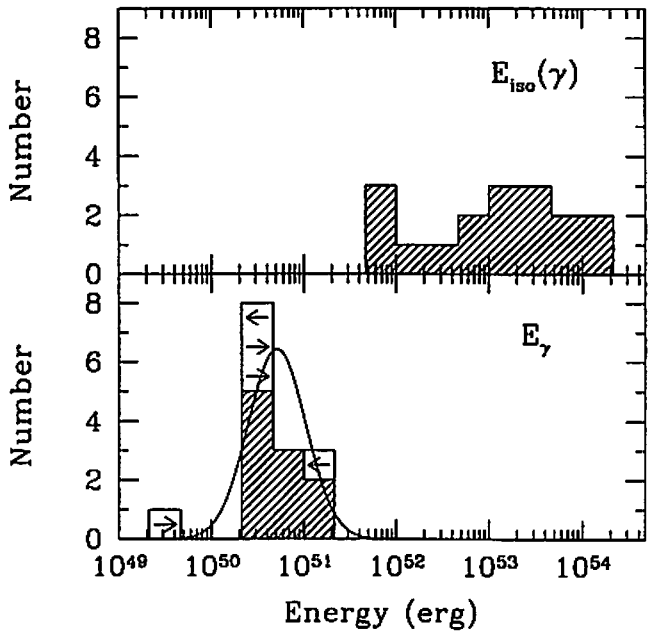


Figure 6: *The distribution of the apparent isotropic γ-ray burst energy of GRBs with known redshifts (top) versus the geometry-corrected energy (bottom). While the isotropic energy E_{iso} spans three orders of magnitudes, the geometrically corrected energy, $E_\gamma = E_{iso}\theta^2/2$, is very narrowly distributed. This implies that the sources of GRBs produce roughly the same amount of energy, about 5×10^{50}erg, but that energy is distributed over a variety of angles resulting in a wide distribution of isotropic energies. From [88].*

equivalent energies of GRBs range from about 5×10^{51} to 1.4×10^{54} erg, when one corrects the observed γ-ray energies for the geometry of the outflow, GRB energies appear narrowly clustered around 5×10^{50} ergs (see Fig. 6).

The central engines of GRBs thus produce approximately a similar amount of energy, and the broad range of fluence and luminosity observed for GRBs appears largely the result of a wide variation of opening angles. The reason for why this range in angles exists is currently not understood. It is interesting to note that before the redshift era, most models assumed that the events were standard candles with energies of about 10^{51} erg. As more and more redshifts are determined, the energy record increased steadily up to 10^{54} erg. The standard-candle hypothesis was abandoned. It is remarkable, that now, when more detailed understanding allows us to infer the beaming angles of these explosions, the true energy budget is back at $\sim 10^{51}$ erg, and the explosions are once again standard candles (though not in the same sense as before). Berger et. al. [89] suggested that the energy in the gamma-ray part of the spectrum may fall below the Frail et. al. relation, however, the total energy emitted (some of which may be in more mildly relativistic ejecta) is still constant, and reveals itself during the afterglow stage.

[90, 91, 92] pointed out that another interpretation is possible for the Frail et. al result. Instead of a variaty of jets with different opening angles, a standard jet can be invoked with energy density per unit solid angle falling away from the axis as θ^{-2}, the differences in the aparent opening angle comes from variation in the orientation of the observer relative to the jet's axis. [77] showed that the distribution of the observed opening angles is consistant with this assumption, adding credance to the universal jet model (see however, [93]). If this model is correct, the rate of GRBs is much lower as it should not be corrected by the factor of 500 of Frail et. al., however, the energy is still low, of order 10^{51} ergs. Clearly, additional complication may exist, and the ejecta may be non uniform on smaller scales, so called patchy shell model [94] or minijets [95].

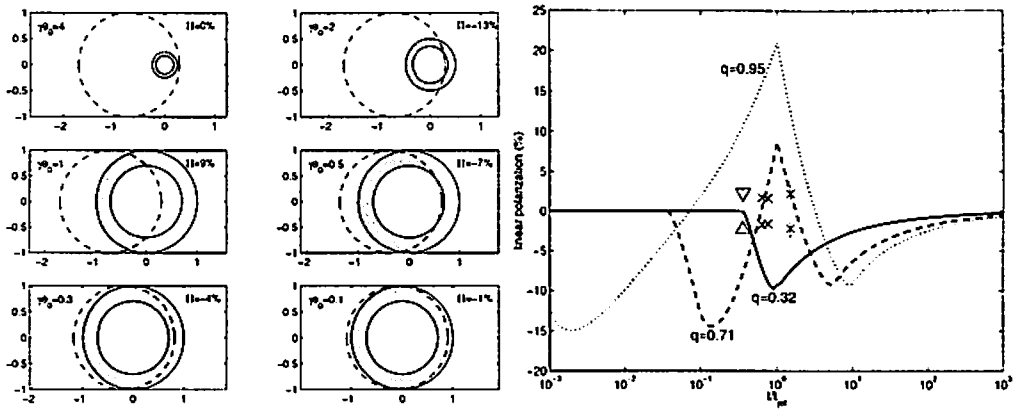


Figure 7: *Left: Shape of the emitting region. The dashed line marks the physical extent of the jet, and solid lines give the viewable region $1/\gamma$. The observed radiation arises from the gray-shaded region. In each frame, the percentage of polarization is given at the top right and the initial size of the jet relative to $1/\gamma$ is given on the left. The frames are scaled so that the size of the jet is unity. Right: Observed and theoretical polarization lightcurves for three possible offsets of the observer relative to the jet axis Observational data for GRB 990510 is marked by crosses (x), assuming $t_{jet} = 1.2$ days. The upper limit for GRB 990123 is given by a triangle, assuming $t_{jet} = 2.1$ days.*

4 Polarization - A promising tool

An exciting possibility to further constrain the models and obtain a more direct proof of the geometrical picture of 'jets' is to measure linear polarization. Varying polarization at optical wavelengths has been observed in GRB afterglows at the level of a few percent [96, 97].

High levels of linear polarization are usually the smoking gun of synchrotron radiation. The direction of the polarization is perpendicular to the magnetic field and can be as high as 70%. Gruzinov and Waxman [37] and Medvedev and Loeb [98] considered the emission from spherical ejecta which by symmetry should produce no polarization on the average, except for fluctuations of order a few percent. Polarization is more natural if the ejecta is a 'jet' and the line of sight to the observer is within the jet but does not coincide with its axis. In this case, the spherical symmetry is broken [99, 100, 101], and the polarization produced by synchrotron radiation will not vanish. For simplicity, lets assume that the magnetic field behind the shock is directed along the shock's plane (the results hold more generally, as long as the magnetic field has a preferred direction). The synchrotron polarization from each part of the shock front, which is perpendicular to the magnetic field, is therefore directed radially.

As long as the relativistic beaming angle $1/\gamma$ is narrower than the physical size of the jet θ_0, one is able to see a full ring and therefore the radial polarization averages out (the first frame, with $\gamma\theta_0 = 4$ of the left plot in Figure 7). As the flow decelerates, the relativistic beaming angle $1/\gamma$ becomes comparable to θ_0 and only a part of the ring is visible; net polarization is then observed. Note that due to the radial direction of the polarization from each fluid element, the total polarization is maximal when a quarter ($\gamma\theta_0 = 2$ in Figure 7) or when three quarters ($\gamma\theta_0 = 1$ in Figure 7) of the ring are missing (or radiate less efficiently) and vanishes for a full and for half ring. The polarization, when more than half of the ring is missing, is perpendicular to the polarization direction when less than half of it is missing.

At late stages the jet expands sideways and since the offset of the observer from the physical center of the jet is constant, spherical symmetry is regained. The vanishing and re-occurrence of significant parts of the ring results in a unique prediction: there should be three peaks of polarization, with the polarization position angle during the central peak rotated by 90° with respect to the other two peaks. In case the observer is very close to the center, more than half of the ring is always observed, and therefore only a single direction of polarization is expected. A few possible polarization light curves are presented in Figure 7.

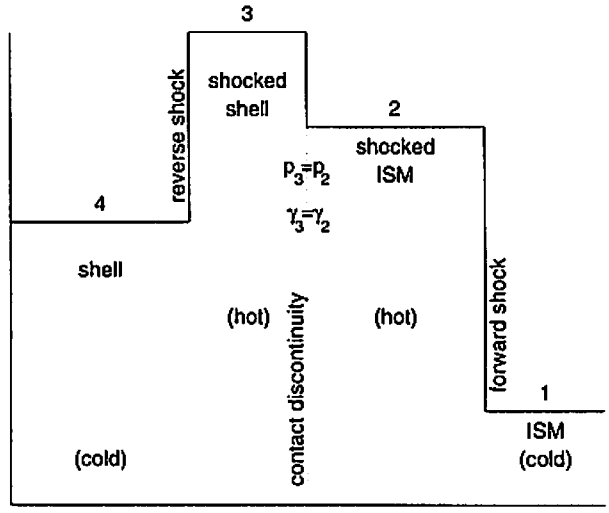


Figure 8: *Schematic representation of the four zones that are present when a relativistic fireball starts to interact with the interstellar medium (ISM). The solid line indicates the density as a function of radius. The undisturbed ISM is zone 1 at large radius, and the unshocked shell material is zone 4 at small radii. The shocked zones, 2 and 3, are the result of the forward and reverse shocks and are separated by a contact discontinuity (based on Sari & Piran 1995).*

Excellent polarization data is available for the bright afterglow of GRB 030329 [102]. Unfortunately, this bursts shows considerable variability in its afterglow, that suggest a complex jet structure, and does not allow for a straight forward comparison with the theory. Yet, a few conclusions seems generic. First, the variations of the magnitude of polarization without change in the position angle favor geometrical effect (e.g. [99, 100, 101]) rather than that of random magnetic field cells (e.g. [37, 98]). Second, the low level of polarization suggest that the magnetic field is quite entangled with the components in the two directions differing by about 10%. Third, the erratic polarization behaviour seems to support the complex jet structure deduced from the fluctuating optical light curve.

5 The Reverse Shock Emission: Theory and Observations

The previous sections discussed the theory and the observations of the 'late' afterglow, hours or more after the burst. During that time, most of the energy of the system was already given to the shocked surroundings, and it is that region that dominates the emission. However, during the first few tens of seconds, the evolution of the Lorentz factor as a function of time is not self similar. There are two shocks: a forward shock going into the surrounding medium and a reverse shock going into the expanding ejecta (see Figure 8). The hydrodynamic details were discussed in [103].

During the initial stages, the internal energy stored behind the shocked-surrounding matter and the energy of the shocked ejecta are comparable. However, the temperature of the shocked ejecta is much lower, typically by a factor of $\gamma \sim 10^2$. This results in an additional emission component with a typical frequency lower by a factor of $\gamma^2 \sim 10^4$, which, for typical parameters, is near the optical passband. Contrary to the 'standard' late afterglow, this emission is very sensitive to the initial Lorentz factor. Theoretical predictions for such a flash were given in detail by Sari & Piran [104, 105] and were earlier suggested as a possibility by Mészáros & Rees [106]. Figure 9 is a sketch of the predicted optical lightcurve combining the reverse shock, the forward shock, the jet break and the transition to subrelativistic velocities.

One of the most exciting events in the field of afterglow studies, was the detection of an extremely bright (9th magnitude) optical emission simultaneous with GRB 990123 by the ROTSE team [107]. The

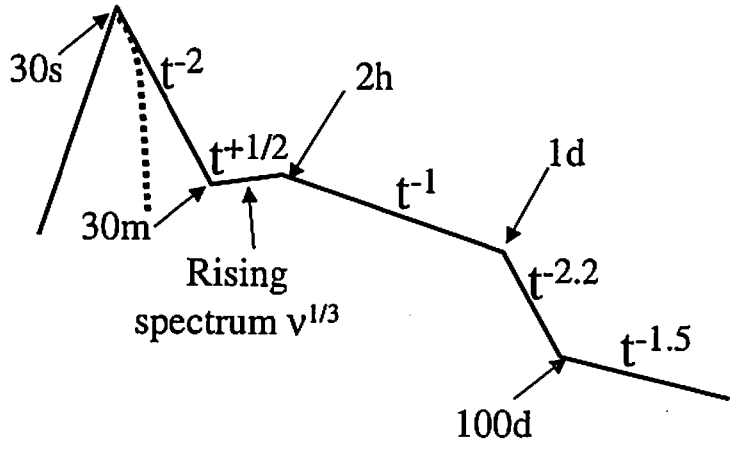


Figure 9: *Predicted optical afterglow-light curve over more than six orders of magnitude in time (from a few seconds up to a about year). Sequentially from left to right: a rapid rise to maximum emission from the reverse shock, followed by a rapid decay $F \propto t^{-2}$ as the reverse-shock heated ejecta cool down. When the emission from the forward shock takes over, the flux is expected to rise slowly as $F \propto t^{+1/2}$ up to a second peak when the frequency ν_m of the forward shock passes the optical passband. During that rise, a positive spectral slope is expected, which has not yet been observed. The subsequent decay of roughly $F \propto t^{-1}$ is steepened to about $F \propto t^{-2.2}$ due to the jet break. The final transition is to the non-relativistic phase.*

ROTSE telescope obtained its first images only 22 seconds after the start of GRB 990123 (i.e. during the GRB), following a notification received from the BATSE aboard the Compton-satellite. The ROTSE observations show that the optical light curve peaked at $m_V \sim 9$ magnitudes some 60 seconds after the event [107]. After maximum a fast decay followed for at least 15 minutes. The late-time afterglow observations show a more gradual decline [108, 49, 83, 84, 109] (see Fig. 10).

The redshift $z = 1.6$, inferred from absorption features in the OT's spectrum, implies that the optical flash would have been as bright as the full moon had the GRB occurred in the nearby galaxy M31 (Andromeda). A different way to put this in perspective is that the flash was some 18 mag brighter (absolute) than the brightest supernovae. Galama et al. [108] have shown, that if one assumes that the emission detected by ROTSE comes from a non-relativistic source of size ct, that then the observed brightness temperature $T_b > 10^{17}$ K of the optical flash exceeds the Compton limit of 10^{12} K. This confirms the highly relativistic nature of the GRB source.

The observed optical properties of this event are well described by emission from the reverse shock that initially decelerates the ejecta, provided that the initial Lorentz factor is about 200 [109, 111]. It takes tens of seconds for the reverse shock to sweep through the ejecta and produce the bright flash. Later, the shocked hot matter expands adiabatically and the emission quickly shifts to lower frequencies and considerably weakens.

The ROTSE observations show that the prompt optical and γ-ray light curves do not track each other [107]. In addition, detailed comparison of the prompt optical emission with the BATSE spectra of GRB 990123 (at three epochs for which both optical and gamma-ray information is available) shows that the ROTSE emission is not a simple extrapolation of the GRB spectrum to much lower energies [108, 110].

If this interpretation is correct, GRB 990123 would be the first burst in which all three emitting regions have been seen: internal shocks causing the GRB, the reverse shock causing the prompt optical flash, and the forward shock causing the afterglow. The emissions thus arise from three different emitting regions, explaining the lack of correlation between the GRB, the prompt optical and the late-time optical emission [108] (but see [112]).

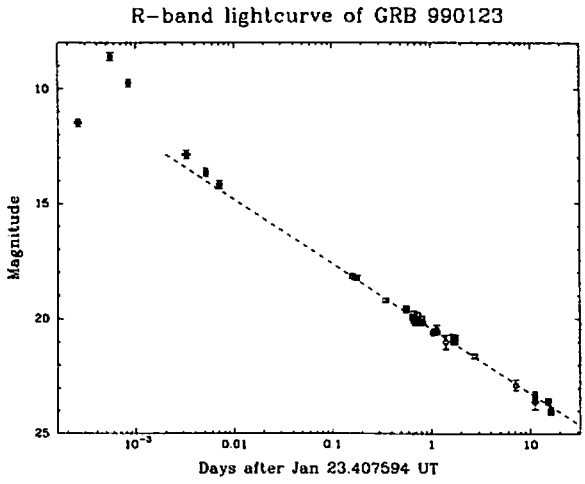


Figure 10: *R-band light curve of the afterglow of GRB 990123. The ROTSE data show that the optical light curve peaked at* $m_V \sim 9$ *[107]. The dashed line indicates a power law fit to the light curve (for* $t > 0.1$ *days), which has exponent* -1.12 ± 0.03 *(from [108]).*

Another new ingredient that was found in GRB 990123 is a radio flare [113]. Contrary to all other afterglows, where the radio peaks around a few weeks and then decays slowly, this burst had a fast rising flare, peaking around a day and then decaying quickly. This can be interpreted as emission from the cooling ejecta that was earlier on heated by the reverse shock. Using the Blandford and McKee [35] self-similar solution to derive the evolution of the ejecta and its emission properties one finds that the typical frequency scales as $\nu_m^r \propto t^{-73/48}$ and the flux at that frequency scales as $F_m^r \propto t^{-47/48}$ [105] (see [22] for revised scalings when the temperature of the ejecta is non relativistic). Therefore, within a day the emission from the adiabatically cooling ejecta that produced the 60s optical flash in GRB 990123 is expected to shift to radio frequencies [109]. Using the observed optical flash, and the above scalings, a good fit to the radio data is obtained. The optical flash and the radio flare may therefore be related.

Given the above interpretation of the reverse shock emission, it is important to ask whether GRB 990123 is an exception, or whether the phenomena of radio flares and optical flashes is more common. Radio flares appear to exist in other cases [88]. However, since early radio data is usually sparse, and these events did not have an early optical observation to find the associated optical flash, the interpretation in terms of emission from the reverse shock is less secure than in the case of GRB 990123. In the optical, from robotic optical experiments such as ROTSE and LOTIS, strong upper limits exists for several bursts. The upper limits show that the optical flash does not scale with the fluence of the event [114, 115]. However, with reasonably small changes in the density or the initial Lorentz factor, those events could have escaped detection [116]. More detailed work argues that the reverse shock emission was overestimated and suggested more observational tests [117, 118, 119]. Once satellites provide accurate positioning on timescales of seconds, strong constraints on the generality of optical flashes and radio flares will be possible to obtain.

Finally, we mention the possibility of a source operating on an afterglow timescale. In this case the reverse shock continues for a long time, newly shock-heated electrons are continuously created, and the emission in a significant part of the spectrum, especially in the sub-mm regime [120, 121], will be dominated by the reverse shock. A similar situation will occur if the source has emitted a slower, but energetic shell, which later catches up with the decelerating ejecta. The relation between the reverse and forward shock spectrum in such a case was given in [121].

6 Progenitors and the GRB/Supernova connection

Observationally it is hard to distinguish between models of progenitors for GRBs. The GRB and the afterglow are produced when relativistic ejecta are slowed down, and no observable radiation emerges directly from the 'hidden engine' that powers the GRB. Thus, in spite of all discoveries the origin of GRBs has remained rather mysterious. Popular models for the origin of GRBs that (in principle) can provide the required energies, come in two classes: (i) compact object mergers such as the neutron star-neutron star (e.g., [125]) and neutron star-black hole mergers [15, 126, 127], and (ii) the core collapses of very massive stars (termed collapsars, 'failed' supernovae or hypernovae or collaprsar [128, 129, 130]).

The first observational evidence for a possible GRB/SN connection was provided by the discovery of SN 1998bw in the error box of GRB 980425 [131]. The temporal and spatial coincidence of SN 1998bw with GRB 980425 suggest that the two phenomena are related [131, 132]. But, the clearest indication that SN 1998bw may be related to GRB 980425 comes from the fact that the radio emitting shell in SN 1998bw must be expanding at relativistic velocities, $\gamma > 2$ [132]. This had thusfar never been observed in a SN. From minimum energy arguments, it was estimated that this relativistic shock carried 5×10^{49} erg, and could well have produced the GRB at early time [122]. Further, detailed analysis of the radio light curve [123] showed additional energy injection one month after the SN event – highly suggestive of a central engine (i.e. black hole versus neutron star formation) rather than a purely impulsive explosion.

However, the redshift of SN 1998bw is 0.0085 and the corresponding γ-ray peak luminosity of GRB 980425 and its total γ-ray energy budget are about a factor of $\sim 10^5$ smaller than those of 'normal' GRBs [131]. Such SN-GRBs may well be the most frequently occurring GRBs in the Universe. But they do not dominate the observed GRB population due to their faintness.

Evidence for a possible supernova connection for the 'normal' high-luminosity GRBs comes from the late-time red spectrum and the late-time rebrightnening of their afterglow light curves. GRB 980326 shows possible evidence that at late times the emission is dominated by an underlying supernova [133]. A template supernova light curve, provided by the well-studied type $I_{b/c}$ SN 1998bw provides an adequate description of the observations (see Figure 11).

Similarly, the optical afterglow of GRB 970228 showed indications that the standard model was not sufficient to describe the observations in detail [50]. The early-time decay of the optical emission is faster than that at later times and, as the source faded, it showed an unexpected reddening [50]. It was not until supernova-like emission accompanying GRB 980326 was found that the behavior of GRB 970228 was better understood. Also for GRB 970228 the late-time light curve and reddening of the transient can be well explained by an initial power-law decay modified at late times by SN 1998bw-like emission [134, 135].

Theoretical work [136, 137] has shown that these SNe most likely mark the birth events of stellar mass black holes as the final products of the evolution of very massive stars.

At the time, the relation between distant GRBs like GRB 980326 and GRB 980425/SN 1998bw was unclear. Is SN 1998bw a different phenomenon or a more local and lower energy equivalent? Attempts have been made to unify the GRB 980425/SN 1998bw phenomenon with the more distant GRBs. It has been argued that the result may be solely due to a difference in viewing angle [138, 139]. And, are all afterglows consistent with such a phenomenon? Claims have been made for the existence of SN signatures in other afterglow lightcurves, but for a number of reasons, such as the presence of contaminating host galaxy light or the brightness of the regular afterglow itself, the evidence for other cases than 970228 and 980326 is less strong.

The ultimate evidence for the GRB/SN connection came with observation of GRB 030329. This burst was relatively nearby allowing accurate spectra at the time of the expected SN peak. Indeed, as the afterglow decayed, a spectrum remarkably close to that of SN1998bw was revealed [140, 141, 143, 144]. Large observational campaign of this bright nearby event [142, 145, 146, 147, 148, 149, 150, 151] allowed direct measure of it afterglow size [152] in agreement with theoretical models [152, 153]. Given this identification, it is now clear that the interpretation of red bumps in several afterglows as signals of SN was justified. It remains unclear weather or not all long GRBs are accompanied by SN, and what is the source of short GRBs.

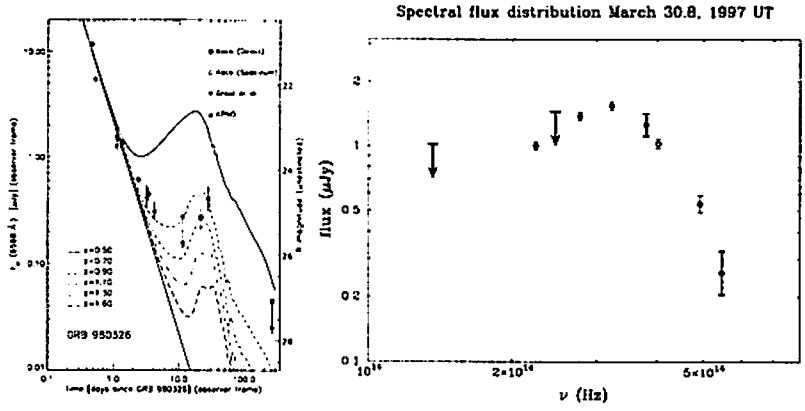


Figure 11: *Left: R-band light curve of GRB 980326 and the sum of an initial power-law decay plus Ic supernova light curve for redshifts ranging from $z = 0.50$ to $z = 1.60$ (from [133]). Right: The broad-band spectrum of the OT of GRB 970228 at March 30.8, 1997 UT (• and upper-limit arrow). Also shown is the spectral flux distribution of SN 1998bw (o) redshifted to the redshift of GRB 970228 ($z = 0.695$). The similarity of the spectral flux distributions is remarkable (from [135]).*

References

[1] Fishman, G.J. & Meegan, C.A. 1995, ARA&A 33, 415

[2] Kouveliotou, C. et al. 1993, ApJL 413, L101

[3] Bhat, P.N. et al. 1992, Nature 359, 217

[4] Schaefer, B.E. & Walker, K.C. 1999, ApJL 511, L89

[5] Band, D. et al., 1993, ApJ 413, 281

[6] Paczyński, B. 1986, ApJ 308, L43

[7] Paczyński, B. 1992, Nature 355, 521

[8] Mao, S. & Paczyński, B. 1992a, ApJL 388, L45

[9] Goodman, J. 1986, ApJL 308, 46

[10] Krolik, J. H. & Pier, E. A. 1991, ApJ 373, 277

[11] Fenimore, E. E., Epstein, R. I., & Ho, C. 1993, A&AS 97, 59

[12] Baring, M. G. & Harding, A. K. 1997, ApJ 491, 663

[13] Lithwick, Y., & Sari, R. 2001, ApJ 555, 540

[14] Mészáros, P. & Rees, M. J. 1993, ApJ 405, 278

[15] Narayan, R. & Paczyński, B. & Piran, T. 1992, ApJL 395, L83

[16] Rees, M. J. & Mészáros, P. 1994, ApJL 403, L93

[17] Fenimore, E. E., Madras C. D. & Nayakchin, S. 1996, ApJ 473, 998

[18] Sari, R., & Piran T. 1997, ApJ, 485, 270

[19] Ramirez-Ruiz, E., & Fenimore, E. E. 1999, A&A, 138, 521

[20] Kobayashi, S., Piran, T., & Sari, R. 1997, ApJ, 490, 92

[21] Beloborodov A. 2000 ApJ 539, 25

[22] Kobayashi, S. & Sari, R. 2001, ApJ 551, 934

[23] Sari, R., Narayan, R. & Piran, T. 1996, ApJ 473, 204

[24] Sari, R., & Piran T. 1997, MNRAS 287, 110

[25] Paczyński, B. & Rhoads, J. 1993, ApJ 418, L5

[26] Katz, J. I., 1994, ApJ 422, 248
[27] Vietri, M. 1997, ApJ 478, L9
[28] Mészáros, P., & Rees M. J. 1997, ApJ 476, 232
[29] Sari, R., Piran, T. & Narayan, R. 1998, ApJL 497, L17
[30] Granot, J., Piran, T. & Sari, R. 2000, ApJ 534, L163
[31] Galama, T.J. et al. 1998, ApJL 501, L97
[32] Waxman, E. 1997, ApJL 491, L19
[33] Panaitescu A., Mészáros, P. 1998, ApJL 493, L31
[34] Sari, R. 1998, ApJL 494, L17
[35] Blandford, R. & Mc Kee, C.F. 1976, Phys. Fluids 19, 1130
[36] Granot, J., Piran, T. & Sari, R. 2000, ApJ 513, 679
[37] Gruzinov A., & Waxman E., 1999, ApJ, 511, 852
[38] Granot, J., Piran, T. & Sari, R. 1999, ApJL 527, 236
[39] Granot, J. & Sari, R. 2002, ApJ, 568, 820.
[40] Jager, R. et al. 1993, Adv. Space Res. 13, 12, 315
[41] Piro, L., Scarsi, L. & Butler, R.C. 1995, Proc. SPIE 2517, 169
[42] Costa, E. et al. 1997, Nature 387, 783
[43] Van Paradijs, J. et al. 1997, Nature 386, 686
[44] Bremer, M. et al. 1998, A&A 332, L13
[45] Frail, D.A. et al. 1997, Nature 389, 261
[46] Sahu, K.C. et al. 1997, Nature 387, 476
[47] Metzger, M.R. et al. 1997, Nature 387, 879
[48] Kulkarni, S.R. et al. 1998, Nature 393, 35
[49] Kulkarni, S.R. et al. 1999, Nature 398, 389
[50] Galama, T.J. et al. 1997, Nature 387, 479
[51] Wijers, R.A.M.J., Rees, M.J. & Mészáros, P. 1997, MNRAS 288, L51
[52] Reichart, D.E. 1997, ApJL 485, L57
[53] Waxman, E. 1997, ApJL 485, L5
[54] Frail, D.A., Waxman, E. & Kulkarni, S.R. 2000, ApJ, 537, 191
[55] Fruchter, A. et al. 2000, ApJ 545, 664
[56] Galama, T.J. et al. 1998, ApJL 497, L13
[57] Castro-Tirado, A. et al. 1998, Science 279, 1011
[58] Piro, L. et al. 1998, A&A 331, L41
[59] Wijers, R.A.M.J. & Galama, T.J 1999, ApJ 523, 177
[60] Berger, E. et al. 2000, ApJ 545, 56
[61] Panaitescu, A. & Kumar, P. 2001, ApJ 554, 667.
[62] Panaitescu, A. & Kumar, P. 2002, ApJ 571, 779.
[63] Panaitescu, A. 2001, ApJ, 556, 1002.
[64] Harrison, F.A. et al. 2001, ApJ, 559, 123.
[65] Yost, S. A., et al. 2002, ApJ, 577, 155.
[66] Frail, et al. 2003, ApJ, 590, 992.
[67] Yost, S. A., et al. 2003, ApJ, 597, 459.
[68] Li, L. & Paczyński, B. 1998, ApJL 507, L59
[69] Paczyński, B. 1993, Ann. NY Acad Sci. 688, 321

[70] Mao, S. & Yi, I. 1994, ApJ 424, L131
[71] Rhoads, J.E. 1997, ApJL 478, L1
[72] Rhoads, J. E. 1999, ApJ, 525, 737
[73] Mszros, P. Rees, M. & Wijers, R.A.M.J. 1998, ApJ 499, 301
[74] Piran, T. 1999, in the proceedings of the Gräftåvallen workshop 'Gamma Ray Bursts: The First Three Minutes', Ed. Juri Poutanen.
[75] Schmidt, M. 1999, ApJ 523, L117
[76] Schmidt, M. 2001, ApJ 552, 36
[77] Perna, R., Sari, R. & Frail, D.A. 2003, ApJ, 594, 379.
[78] Panaitescu, A. & Mészáros, P., 1999, ApJ, 503, 314
[79] Mészáros, P., & Rees M. J. 1999, MNRAS, 299, L10
[80] Moderski, R., Sikora, M., Bulik, T. 2000, ApJ 529, 151.
[81] Granot et al. 2001, Proc. of the rome workshop, Edt. E. Costa, F. Frontera, J. Hjorth, Springer.
[82] Sari, R. 1997, ApJL 489, L37
[83] Castro-Tirado, A. et al. 1999, Science 283, 2069
[84] Fruchter, A.S. et al. 1999, ApJL 519, L13
[85] Sari, R., Piran, T. & Halpern, J. 1999, ApJ 519, L17
[86] Harrison, F.A. et al. 1999, ApJL 523, L121
[87] Stanek, K.Z. et al. 1999, ApJL 522, L39
[88] Frail, D.A. et al. 2001, in preparation
[89] Berger E. et al. 2003, Nature, 426, 154.
[90] Postnov, K. A., Prokhorov, M. E., Lipunov, V. M. 2001, Astronomy Report, 45, 236
[91] Rossi, E., Lazzati, D. & Rees, M. J. 2002, MNRAS, 332, 945
[92] Zhang, B. & Meszaros, P. 2002, ApJ, 571, 876
[93] Nakar, E., Granot, Y. & Gucta, D. 2004, ApJ, 606, 37.
[94] Kumar, P. & Piran, T. 2000, ApJ, 535, 152.
[95] Yamazaki, R., Ioka, K. & Nakamura, T. 2004, ApJL, 607, 106.
[96] Wijers, R.A.M.J. et al. 1999, ApJL 523, L33
[97] Rol, E. et al. 2000, ApJ 544, 707
[98] Medvedev, M. V., & Loeb A., 1999, ApJ 526, 697
[99] Gruzinov A. 1999, ApJ, 525, L29
[100] Ghisellini, G., & Lazzati, D., 1999, MNRAS, 309, L7
[101] Sari, R. 1999, ApJ, 524, L43
[102] Greiner, J. et al. 2003, Nature, 426, 157.
[103] Sari, R., & Piran T. 1995, ApJ, 455, L143
[104] Sari, R., & Piran, T. 1999, A&A 138, 537.
[105] Sari, R. & Piran, T. 1999, ApJ 520, 641
[106] Mészáros, P. & Rees, M.J. 1997, ApJ 476, 232
[107] Akerlof, C. et al. 1999, Nature 398, 400
[108] Galama, T.J. et al. 1999, Nature 398, 394
[109] Sari, R. & Piran, T. 1999, ApJL 517, L109
[110] Briggs, M.S. et al. 1999, ApJ 524, 82
[111] Mészáros, P. & Rees, M. J. 1999, MNRAS 306, L39
[112] Liang, E.P. et al. 1999, ApJL 519, L21
[113] Kulkarni, S. R., et al. 1999, ApJ 522, L97

[114] Akerlof, C. et al. 2000, ApJL 532, L25
[115] Kehoe, R. et al. 2001, ApJ 554, L159
[116] Kobayashi, S. 2000, ApJ 545, 807
[117] Nakar, E. & Piran, T. 2004, MNRAS, 53, 647.
[118] Panaitescu, A. & Kumra, P. MNRAS, 353, 511.
[119] Nakar, E. & Piran, T. 2005, ApJL, 619 147.
[120] Kumar, P., & Piran, T. 2000, ApJ 532, 286
[121] Sari, R., & Mészáros, P. 2000, ApJ 535, L33
[122] Tan, J. C., Matzner, C. D. & McKee, C. F. 2001, ApJ 551, 946
[123] Chevalier, R.A. & Li, Z. 1999, ApJL 520, L29
[124] Chevalier, R.A. & Li, Z. 2000, ApJ 536, 195
[125] Eichler, D. et al. 1989, Nature 340, 126
[126] Mochkovitch, R. et al. 1993, Nature 361, 236
[127] Lattimer, J.M. & Schramm, D.N. 1974, ApJL 192, L145
[128] Woosley, S.E. 1993, ApJ 405, 273
[129] Paczyński, B. 1998, ApJL 494, L45
[130] MacFadyen, A. I., Woosley, S. E. 1999, ApJ, 524, 262.
[131] Galama, T.J. et al. 1998, Nature 395, 670
[132] Kulkarni, S.R. et al. 1998, Nature 395, 663
[133] Bloom, J.S. et al. 1999, Nature 401, 453
[134] Reichart, D.E. 1999, ApJL 521, 111
[135] Galama, T.J. et al. 2000, ApJ 536, 185
[136] Iwamoto, K. et al. 1998, Nature 395, 672
[137] Woosley, S.E., Eastman, R.G. & Schmidt, B.P. 1999, ApJ 516, 788
[138] Salmonson, J. 2001, ApJL 546, L29
[139] Ioka, K. & Nakamura, T. 2001, ApJL, 554, 163.
[140] Stanek, K. et al. 2003, ApJL, 591, 17.
[141] Kawabata, k. et al. 2003, ApJL, 593, 19.
[142] Sheth, k. et al. 2003, ApJL, 595, 33.
[143] Matheson, T. et al. 2003, ApJ 599, 394.
[144] Mazzali, P. A. et al. 2003, ApJL, 599 95.
[145] Burenin, R. A. et al. 2003, AsL, 29, 573.
[146] Tiengo, A. et al. 2003, A&A, 409, 983.
[147] Smith, D. A. et al. 2003, ApJL, 596, 151.
[148] Torii et. al. 2003, ApJL 597, L101.
[149] Urata et. al. 2004, ApJL, 601, 17.
[150] Lipkin, Y. M. et al. 2004, ApJL, 606, 381.
[151] Frail, D. A. et al. 2005, ApJ, 619, 994.
[152] Taylor et al. 2004, ApJL, 609, 1.
[153] Granot et al. 2005, ApJ, 618, 413.

Relativistic SPH Calculations of Compact Binary Mergers

Frederic Rasio[1], Joshua Faber[2], Shiho Kobayashi[3], and Pablo Laguna[4]

[1]*Department of Physics and Astronomy, Northwestern University, Evanston, IL 60208, USA*
[2]*Department of Physics, University of Illinois, Urbana, IL 61801, USA*
[3]*Center for Gravitational Wave Physics, Pennsylvania State University, University Park, PA 16802, USA*
[4]*Department of Astronomy and Astrophysics and Department of Physics, Pennsylvania State University, University Park, PA 16802, USA*

Abstract

We review recent progress in understanding the hydrodynamics of compact binary mergers using relativistic smoothed particle hydrodynamics (SPH) codes. Recent results are discussed for both double neutron stars and black hole - neutron star binaries. The gravitational wave signals from these mergers contain a lot of information about the masses and radii of the stars and the equation of state of the neutron star fluid. For black hole - neutron star mergers, the final fate of the fluid and the gravitational wave emission depend strongly on the mass ratio and the black hole spin.

1 Introduction

Coalescing compact binaries containing neutron star (NS) or black hole (BH) components are the leading candidates to become the first observed sources of gravitational waves (GW). With LIGO, GEO, and TAMA all taking scientific data, and VIRGO in the commissioning stage, it is now more important than ever to develop quantitatively accurate predictions of the GW signals we expect to observe from the binary merger process. These GW signals contain crucial information about the masses, NS radii, and NS equation of state (EOS).

Calculations of binary NS coalescence have been performed for many years, beginning almost 20 years ago with studies in Newtonian gravity (see, e.g., Nakamura 1994; Rasio & Shapiro 1999; for reviews of early work). It was recognized all along, however, that general relativity (GR) must play an important role, given the strong gravitational fields and relativistic velocities involved, particularly near the end of the merging process. As a result, increasingly sophisticated gravitational formalisms have been used in combination with 3-D hydrodynamic calculations, starting with post-Newtonian (PN) treatments (Oohara & Nakamura 1992; Shibata 1997; Lombardi, Rasio, & Shapiro 1997; Faber & Rasio 2000, 2002; Ayal et al. 2001). Several recent studies were based on the PN hydrodynamics formalism developed by Blanchet, Damour & Schäfer (1990), which includes all lowest-order 1PN effects as well as the lowest-order dissipative effects from gravitational radiation reaction. Most recently, calculations have been performed in full GR, using the techniques of 3-D numerical relativity (Shibata & Uryu 2000, 2001; Shibata, Taniguchi, & Uryu 2003; Miller, Gressman, & Suen 2004). These are plagued by numerical difficulties, but allow one to address fundamentally new and important questions, such as the stability of the final merger remnant to gravitational collapse.

Unfortunately, while considerably easier to implement numerically, the PN approximation breaks down during the merger when higher-order relativistic effects grow significant. A middle ground is provided by the conformally flat (CF) approximation to GR, developed originally by Wilson and collaborators (see, e.g., Wilson, Mathews & Marronetti 1996). This approximation is used in essentially all quasi-equilibrium calculations of initial data for compact binary mergers (NS–NS, BH–NS, and BH–BH; see, e.g., Faber et al. 2002; Grandclément, Gourgoulhon, & Bonazzola 2002). It has also been used more recently for

[1]Email: rasio@northwestern.edu
[2]Email: jfaber@uiuc.edu
[3]Email: shiho@gravity.psu.edu
[4]Email: pablo@astro.psu.edu

full hydrodynamic merger calculations (Oechslin, Rosswog, & Thielemann 2002; Faber, Grandclément, & Rasio 2004). An overview of the latest results from Faber et al. (2004) is given in Sec. 3. The CF approximation includes much of the non-linearities inherent in GR, but reduces the Einstein field equations to a set of coupled, non-linear, elliptic equations, which can be solved numerically using well-understood, robust techniques. While this approach cannot reproduce the exact GR solution for a general 3-D matter configuration, it is exact for spherically symmetric systems, and, in practice, yields solutions that often agree closely with those calculated using full GR (Mathews, Marronetti, & Wilson 1998; Shibata & Sekiguchi 2004). Most remarkably, CF solutions for BH–BH binaries in quasi-equilibrium agree extremely well with those obtained from the most accurate, high-order PN treatment (Damour, Gourgoulhon, & Grandclément 2002).

In contrast to NS–NS merger calculations, relatively little work has been done on BH–NS mergers. Newtonian hydrodynamic calculations for a polytrope around a point mass (e.g., Lee 2001) are of limited applicability to the highly relativistic BH–NS systems. Relativistic quasi-equilibrium calculations of BH–NS binaries near the Roche limit have been performed recently by several groups (Baumgarte, Skoge, & Shapiro 2004; Ishii, Shibata, & Mino 2005). Some initial results from our own relativistic hydrodynamic study of BH–NS mergers are presented in Sec. 4. In spite of the great astrophysical importance of BH–NS binaries, our theoretical understanding of these systems lags behind that of NS–NS binaries by at least 10 years. One key question concerns the timescale of the tidal disruption and whether quasi-stable mass transfer from a NS to a BH can ever occur. This has important consequences for the detectability of the GW signal associated with the tidal disruption. This signal carries information about the NS EOS, and could be easier to detect with broadband interferometers than NS–NS merger signals (Vallisneri 2000).

A systematic study of BH–NS binary mergers will require exploration of a parameter space much larger than for NS–NS binaries. In particular, a wide range of mass ratios should be considered, $q = M_{\rm h}/M_{\rm ns} \simeq 1 - 20$, since BH masses are not expected to be concentrated in a narrow range (observations of BH X-ray binaries suggest $M_{\rm h} \simeq 5 - 15\,M_\odot$, but this may be biased by observational selection effects). Newtonian results suggest that for very low-mass BH ($q \simeq 1$) the NS is quickly disrupted after the system reaches the ISCO, while for more massive BH ($q \gtrsim 5$) the behavior is more erratic and complete tidal disruption of the NS may only occur after a large number of orbital periods and repeated brief episodes of mass transfer (Davies, Levan, & King 2005). In most cases, roughly one third of the NS mass is left in a thick torus around the BH while the rest is quickly accreted. While these results may be (at best) qualitatively correct, it is clear that relativistic effects must play an important role in the evolution. For a massive BH in particular, the tidal disruption of the NS takes place entirely in a strong field region (see Sec. 4).

Although this paper will focus on the GW aspects of the binary coalescence problem, the astrophysical motivation for the study of this problem is much broader. The ejection of nuclear matter during mergers has been discussed as a possibly major source of heavy "r-process" elements in galaxies (Lattimer & Schramm 1974; Rosswog, Freiburghaus, & Thielemann 2001). Many theoretical models of gamma-ray bursts (GRBs) have also relied on coalescing compact binaries to provide the energy of GRBs at cosmological distances (e.g., Eichler et al. 1989; Narayan, Paczyński, & Piran 1992; Mészáros & Rees 1992). Currently these models all assume that the coalescence leads to the formation of a rapidly rotating Kerr BH surrounded by a torus of debris (e.g., van Putten & Levinson 2002). Energy can then be extracted either from the rotation of the BH or from the material in the torus so that, with sufficient beaming, the gamma-ray fluxes observed from even the most distant GRBs could be explained. Here also, it is important to understand the hydrodynamic processes taking place during the final coalescence before making assumptions about its outcome. For example, contrary to widespread belief, it is not clear that the coalescence of two $1.4\,M_\odot$ NS will form an object that must collapse to a BH (Sec. 3).

2 Smoothed Particle Hydrodynamics

The hydrodynamic calculations of compact binary coalescence described below in Sec. 3 and 4 were done using two different relativistic smoothed particle hydrodynamics (SPH) codes, which we will refer to as the "Northwestern code" and the "Penn State code." SPH is a Lagrangian, particle-based method ideally suited to calculations involving self-gravitating fluids moving freely in 3D.

Because of its Lagrangian nature, SPH presents some clear advantages over more traditional grid-based methods for calculations of stellar interactions. Most importantly, fluid advection, even for stars with a sharply defined surface such as NSs, is accomplished without difficulty in SPH, since the particles simply follow their trajectories in the flow. In contrast, to track accurately the orbital motion of two stars across a large 3-D grid can be very difficult, and sharp stellar surfaces often require a special treatment (to avoid "bleeding"). SPH is also very computationally efficient, since it concentrates the numerical elements (particles) where the fluid is at all times, not wasting any resources on empty regions of space. For this reason, with given computational resources, SPH can provide higher averaged spatial resolution than grid-based calculations, although Godunov-type schemes such as PPM typically provide better resolution of shock fronts. This is certainly not a decisive advantage for binary coalescence calculations, where no strong shocks ever develop. SPH also makes it easy to track the hydrodynamic ejection of matter to large distances from the central dense regions. Sophisticated nested-grid algorithms are necessary to accomplish the same with grid-based methods.

The first relativistic version of the Northwestern code (using PN gravity) was developed by Faber & Rasio (2000, 2002). For a detailed description of the purely hydrodynamic aspects of this code, including the results of many test calculations, see Lombardi et al. (1999). In addition to binary coalescence problems this code has also been used extensively in Newtonian gravity to study many problems related to stellar collisions in dense star clusters (e.g., Sills et al. 2001). Our current relativistic version of the code is based on the CF approximation to full GR (Faber et al. 2004). We solve the elliptic field equations using spectral methods. Specifically, our SPH code was coupled to the software developed by the Meudon group, which is publicly available as part of the C++ LORENE library (`www.lorene.obspm.fr`). In contrast to finite-difference schemes, the fields are represented in terms of expansions over analytic basis functions. The effects of all operators, such as derivatives, are then represented by matrix multiplication on the coefficients of the expansion. In LORENE, the tensorial basis of decomposition is Cartesian, but each component is given in terms of spherical coordinates. In the current version, the usual basis of decomposition contains trigonometric polynomials or spherical harmonics for the dependence on the angles and Chebyshev polynomials for the dependence on the radial coordinate (Bonazzola et al. 1999).

The original version of the Penn State code is described by Laguna, Miller, & Zurek (1993). This code models relativistic fluid flow in a *fixed* curved spacetime geometry assuming that (a) the background spacetime is static (e.g., Schwarzschild or Kerr BH), and (b) the density of mass-energy of the fluid is sufficiently small that a Newtonian model of the fluid's self-gravity is an adequate approximation. The code was calibrated with several 1-D benchmarks (Laguna et al. 1993) such as relativistic shock tubes, dust infall onto a BH, and Bondi collapse. It has been used recently to study the tidal disruption of main sequence stars by a supermassive BH (Laguna et al. 1993b; Kobayashi et al. 2004). For our BH–NS merger calculations we use the Kerr-Schild form of the Kerr (or Schwarzschild) metric to describe a fixed background. The coordinates smoothly penetrate the horizon of the holes, and they are suitable for studying the evolution of stars orbiting closely around the horizon or even falling into it. An absorbing boundary is set up well inside the horizon, and SPH particles crossing this boundary are removed from the calculation before they hit the BH singularity. This ensures a long-term, stable numerical evolution of the system. For obvious reasons this code should apply most accurately to BH–NS binaries in which the BH mass is much larger than the NS mass.

3 Neutron Star Binaries

A typical NS–NS binary merger, calculated with the Northwestern SPH code in CF gravity, is illustrated in Fig. 1 (from Faber et al. 2004). The initial phase of the evolution corresponds to the end of the binary inspiral, but with finite-size effects becoming important. In particular, a significant "tidal lag" (misalignment of the stellar long axes with respect to the binary axis) develops before contact. When physical merging begins, the two stars come together in an off-axis manner, with a very small amount of mass running along the surface interface before being spun off the newly forming remnant. This small amount of ejected matter, representing less than 1% of the total system mass in this particular calculation, remains gravitationally bound, forming a tenuous halo around the rapidly and differentially rotating remnant, which is stable to gravitational collapse.

We calculate the GW signal produced during the merger in the lowest-order quadrupole limit, finding

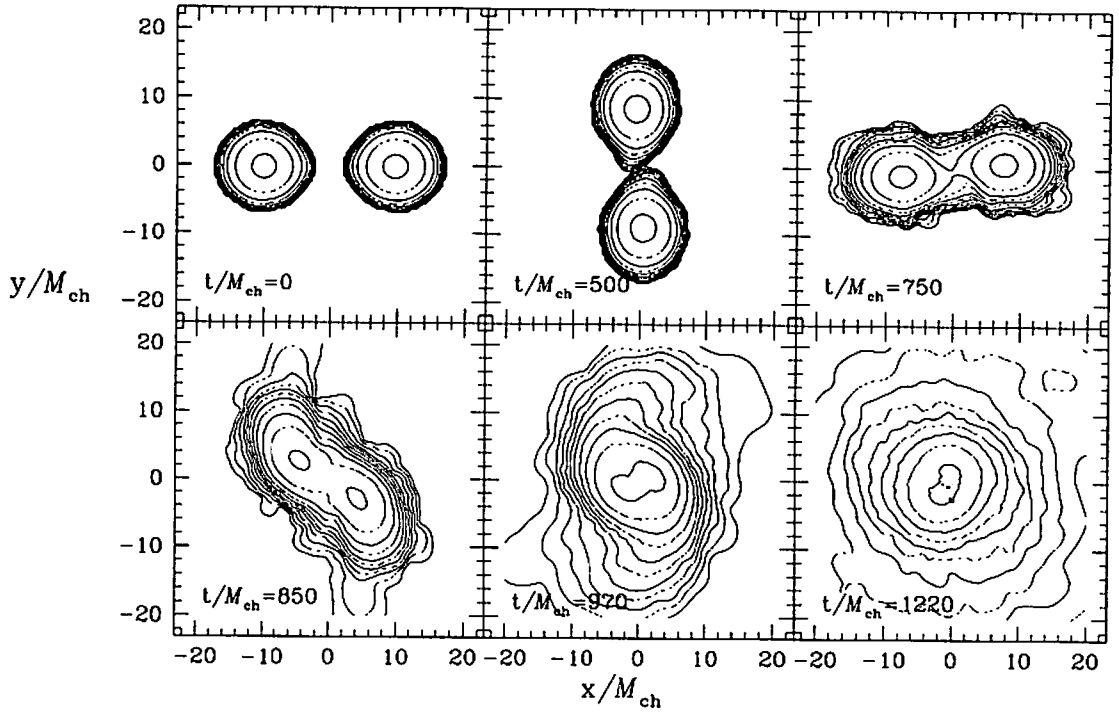


Figure 1: Final merger of a NS–NS binary. Units are defined such that $G = c = 1$, and $M_{\rm ch}$ is the chirp mass of the system. Density contours are shown in the equatorial $(x - y)$ plane of the system, logarithmically spaced with two contours per decade. We first see the development of significant tidal lag, followed by an "off-center collision" that leads to the formation of a vortex sheet at the interface between the two stars and a small amount of matter ejection. The final configuration is a very rapidly and differentially rotating, spheroidal NS, which is stable against gravitational collapse. This calculation was performed using 10^5 SPH particles in the CF approximation of GR. The initial condition consists of two identical, non-spinning (irrotational) NSs with a $\Gamma = 2$ polytropic EOS, in a quasi-equilibrium circular orbit outside the ISCO. The orbital rotation is in the counter-clockwise direction.

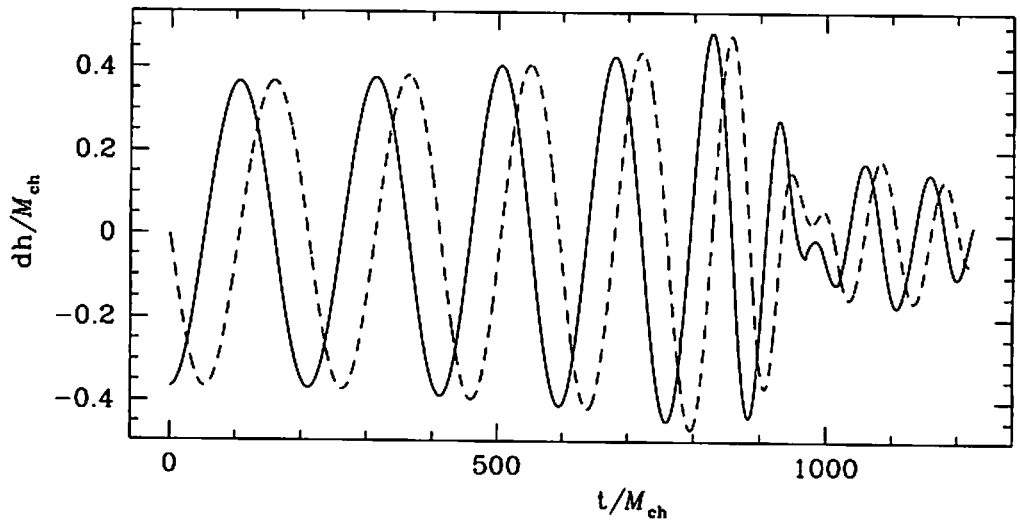


Figure 2: Gravitational wave signal in the h_+ (solid line) and $h_\times$ (dashed line) polarizations, for an observer located a distance d from the system along the rotation axis. Units are as in Fig. 1. We see the end of the inspiral chirp signal, followed by a lower-amplitude, modulated burst of high-frequency emission during the final merger.

good agreement with other recent relativistic calculations (Faber et al. 2004). Prior to final merger, we observe a "chirp" signal, as the frequency and amplitude both increase while the two NSs approach each other. After the merger, there is a period of strong, modulated high-frequency emission, which damps away as the remnant relaxes toward a spheroidal shape.

While the time-dependence of the GW signal is important, it is more useful in practice to look at the frequency dependence of the signal, and, in particular, the energy spectrum $dE_{\rm GW}/df$. Indeed, one can show (Faber et al. 2002) that the changes in the total energy along quasi-equilibrium binary configurations for NS models with different compactness values M/R should leave an imprint in the energy spectrum in the form of a "break," where the spectrum plunges rapidly below the power-law extrapolation of the low-frequency, slow inspiral spectrum ($dE_{\rm GW}/df \propto f^{-1/3}$). This corresponds to the sudden acceleration of the orbital decay as the NS binary approaches the point of onset of dynamical instability along a quasi-equilibrium sequence (Lai, Rasio, & Shapiro 1994; Lombardi et al. 1997). This is potentially detectable by narrow-band detectors in advanced interferometers. Using a parameterized model of these "break frequencies," Hughes (2002) showed that the NS radius could be determined to within a few percent with at most ~ 50 Advanced LIGO observations of NS mergers, and perhaps far fewer for optimal parameter values.

Since our calculation was started from a proper quasi-equilibrium initial condition, we can easily attach the inspiral waveform onto our calculated merger waveform at the point where the binary reaches the correct infall velocity. We note, however, that the exact point where the crossover is made has virtually no effect on the resulting spectrum. In Fig. 3, we show (as the solid line) a complete and *self-consistent* relativistic spectrum for a binary NS merger. At low frequencies, the primary contribution is from the inspiral signal, and at high frequencies, from the calculated merger waveform. The short-dashed line shows the Newtonian power-law result for two point masses, and the long-dashed curve shows the fit we find from our quasi-equilibrium sequence data (following Faber et al. 2002). We see excellent agreement up until the peak at frequencies around $M_{\rm ch} f_{\rm GW} \simeq 0.007 - 0.009$. This peak represents the "piling up" of energy corresponding to the moment when the stars make contact and the radial infall rate slows down in response to pressure building up. The second peak, at $M_{\rm ch} f_{\rm GW} \simeq 0.010 - 0.011$, represents emission from the ringdown of the merger remnant. It is likely that we underestimate the true height of this second peak somewhat, since we assume that the GW signal after our calculation ends continues to damp away exponentially, but the detection of this high-frequency peak will be quite challenging anyway.

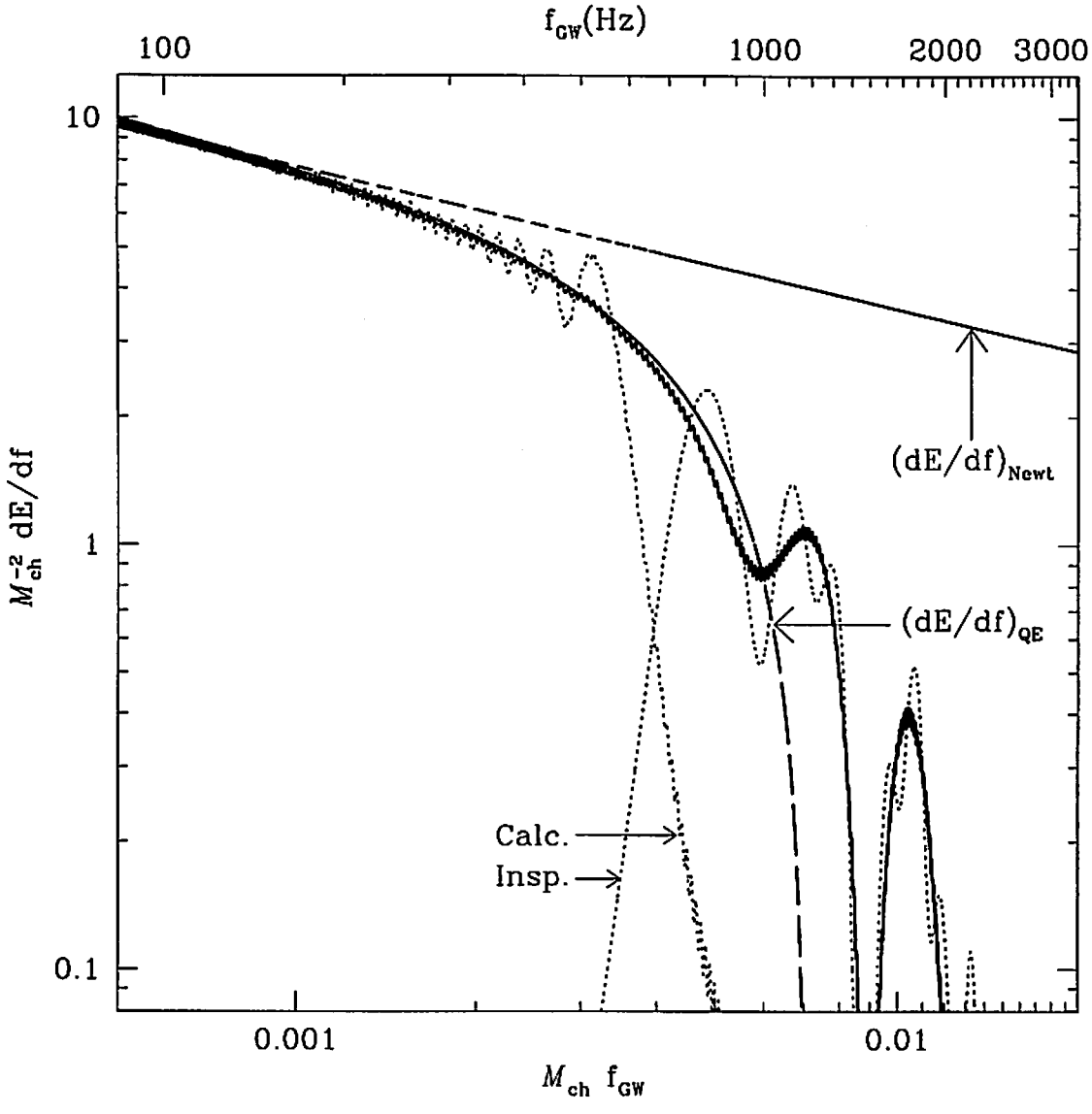


Figure 3: Gravitational wave energy spectrum, dE/df, as a function of GW frequency, f_{GW}. Units are defined such that $G = c = 1$, and M_{ch} is the chirp mass of the system. The dotted lines at high and low frequencies show the components contributed by our calculated signal and the quasi-equilibrium inspiral component, respectively. Also shown are the Newtonian point-mass energy spectrum (short-dashed line), and the semi-analytic result derived from a quasi-equilibrium binary NS sequence (long dashed line; Faber et al. 2002). On the upper horizontal axis, we also show the corresponding frequencies in Hz assuming that each NS has a mass of $1.4\,M_\odot$. We see that the "break frequency" occurs well below ~ 1 kHz, where ground-based interferometers retain good sensitivity (above ~ 1 kHz laser shot noise leads to a rapid loss of sensitivity).

The final fate of a NS–NS merger depends crucially on the NS EOS, and on the extraction of angular momentum from the system during the final merger. For a stiff NS EOS, it is by no means certain that the core of the final merged configuration would collapse on a dynamical timescale to form a BH. One reason is that the Kerr parameter a/M of the core may exceed unity for an extremely stiff EOS (Baumgarte et al. 1998), although recent hydrodynamic calculations suggest that this is never the case (see, e.g., Faber & Rasio 2000). More importantly, the rapidly rotating core may in fact be dynamically stable. Take the obvious example of a system containing two identical $1.4\,M_\odot$ NSs. The total baryonic mass of the system for a stiff NS EOS is then about $3\,M_\odot$. Most modern (stiff) nuclear EOS allow stable, maximally rotating NS with baryonic masses exceeding $3\,M_\odot$ (Cook, Shapiro, & Teukolsky 1994), i.e., above the mass of the final merger core, even if we entirely neglect fluid ejection. *Differential* rotation can further increase this maximum stable mass very significantly (Baumgarte, Shapiro, & Shibata 2000). Using realistic nuclear EOS, Morrison, Baumgarte, & Shapiro (2004) show that the merger remnants of all NS binaries observed in our Galaxy as binary pulsars could be supported stably against prompt collapse by rapid differential rotation. Recent full GR calculations of NS binary mergers in 3-D numerical relativity have also suggested that at least some merger remnants with stiff EOS are stable to collapse (Shibata, Taniguchi, & Uryu (2003).

However, for slowly rotating stars, the same EOS give maximum stable baryonic masses in the range $2.5 - 3\,M_\odot$. Thus the final fate of the merger depends critically on its rotational profile and total angular momentum. Many processes such as electromagnetic radiation, neutrino emission, or the development of various secular instabilities (e.g., r-modes), which may also lead to angular momentum losses, take place on timescales much longer than the dynamical timescale (see, e.g., Baumgarte & Shapiro 1998, who show that neutrino emission is probably negligible). These processes are therefore decoupled from the hydrodynamics of the merger. Unfortunately their study is plagued by many fundamental uncertainties in the microphysics. Duez et al. (2004) have demonstrated for the first time in full GR how viscosity and magnetic fields can drive a differentially rotating, "hypermassive" NS merger remnant toward uniform rotation, possibly leading to delayed collapse to a BH. This delayed collapse would be accompanied by a secondary burst of GW.

The question of the final fate of the merger also depends crucially on the evolution of the fluid vorticity during the coalescence. Close NS binaries are likely to be *nonsynchronized*. Indeed, the tidal synchronization time is almost certainly much longer than the orbital decay time (Kochanek 1992; Bildsten & Cutler 1992). For NS binaries that are far from synchronized, the final coalescence involves complex hydrodynamic processes (Rasio & Shapiro 1999). In the simple case of an irrotational system (containing stars that are non-spinning at large separation), the two sides appear to be counter-spinning in the corotating frame of the binary. At the moment of first contact, a *vortex sheet* is formed. Such a vortex sheet is Kelvin-Helmholtz unstable on all wavelengths and the hydrodynamics is therefore very challenging to model accurately given the limited spatial resolution of 3-D calculations (see Faber & Rasio 2002 for a high-resolution SPH calculation using 10^6 particles and focusing on this aspect of the problem).

The final fate of the merger could depend crucially on the evolution of this shear flow inside the merging stars. In particular, if the shear persists and can support a highly triaxial shape for the remnant, a much larger fraction of the total angular momentum of the system could be radiated away through GW emission. In this case the final merged core may resemble a Dedekind ellipsoid, i.e., it will have a triaxial shape supported entirely by internal fluid motions, but with a stationary shape in the inertial frame (so that it no longer radiates GWs). The stability of such a configuration to gravitational collapse has never been studied. In contrast, in all 3-D numerical simulations performed to date, the shear is quickly dissipated, so that GW emission never gets a chance to extract more than a small fraction ($\sim 10\%$) of the angular momentum, and the final core appears to be nearly axisymmetric. However, this behavior could be an artefact of the spurious shear viscosity present in all 3-D simulations.

4 Black Hole – Neutron Star Mergers

We now turn to BH–NS binaries, summarizing some recent (and rather preliminary) results we have obtained with the Penn State SPH code. Fig. 4 shows why the final merger of a BH–NS binary (for a typical stellar-mass BH) is particularly interesting but also particularly difficult to compute: the tidal (Roche) limit is typically right around the ISCO and the BH horizon. On the one hand, this implies

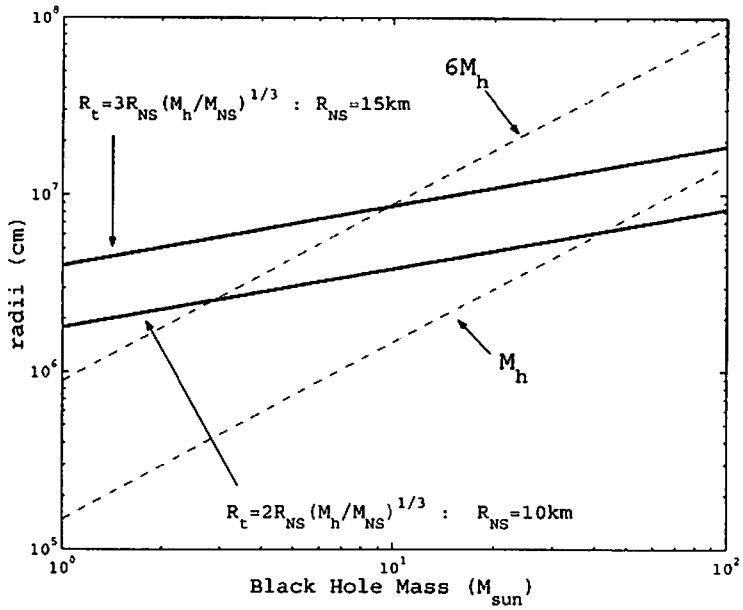


Figure 4: Tidal disruption limits for a 1.4 $M_\odot$ NS in circular orbit around a BH of mass M_h. The radius of the innermost stable circular orbit (ISCO) is also shown for the Schwarzschild and maximally corotating Kerr cases (dashed lines). The two solid lines bracket the Roche limit for NS with different spins and radii.

that careful, fully relativistic calculations are needed. On the other hand, it also means that the fluid behavior and the GW signals could depend sensitively (and carry rich information) on both the masses and spins of the stars, and on the NS EOS. How much information is carried about the fluid depends on where exactly the tidal disruption of the NS occurs: for a sufficiently massive BH, the horizon will always be encountered well outside the tidal limit, in which case the NS behavior remains point-like throughout the merger.

We set up initial conditions for BH–NS binaries near the Roche limit using the Penn State SPH code and a relaxation technique similar to those used for previous SPH studies of close binaries (e.g., Rasio & Shapiro 1995). First we construct hydrostatic equilibrium NS models for a simple gamma-law EOS by solving the Lane-Emden equation. When the NS with this hydrostatic profile is placed in orbit near a BH, spurious motions could result as the fluid responds dynamically to the sudden appearance of a strong tidal force. Instead, the initial conditions for our dynamical calculations are obtained by relaxing the NS in the presence of a BH in the corotating frame of the binary. For *synchronized* configurations (assumed here), the relaxation is done by adding an artificial friction term to the Euler equation of motion in the corotation frame. This forces the system to relax to a minimum-energy state. We numerically determine the angular velocity Ω corresponding to a circular orbit at a given r as part of the relaxation process. The advantage of using SPH itself for setting up equilibrium solution is that the dynamical stability of these solutions can then be tested immediately by using them as initial conditions for dynamical calculations.

We illustrate our results from two simulations using 10^4 SPH particles to represent a NS with a $\Gamma = 2$ polytropic EOS. The only difference between these two simulations is in the assumed spin of the BH: maximally corotating (Kerr parameter $a/M_h = 1$ and corotating NS in the equatorial plane) in one case; non-rotating (Schwarzschild BH) for the other. Snapshots of the SPH particles near the end of these simulations are shown in Figs. 5 and 6. Around the maximally rotating BH, the fluid forms a stable ring just outside the BH horizon, while for the non-spinning BH the entire mass of the NS disappears into the horizon and is accreted by the BH on a dynamical timescale. There are many obvious implications of these results for models of gamma-ray bursts, which depend crucially on the presence of an accretion disk or torus around the BH. We note also that, so far, we have never observed the behavior seen in Newtonian simulations, where "stable mass transfer" from the NS onto the BH can persist for many

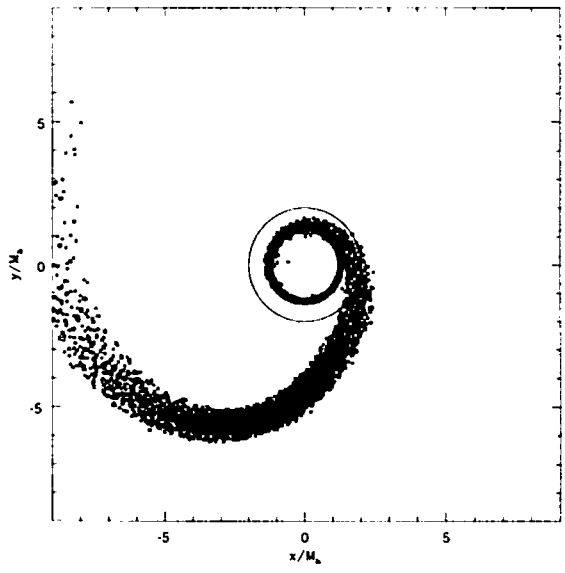


Figure 5: Tidal disruption of a $1.4\,M_\odot$ NS by a maximally corotating Kerr BH of mass $M_{\rm h} = 10\,M_\odot$. The NS was initially placed just outside the Roche limit ($r \simeq 6.5\,M_{\rm h}$ for this NS of radius $R \simeq 15\,$km with a $\Gamma = 2$ polytropic EOS). In this snapshot near the end of the simulation all SPH particles are shown projected onto the equatorial plane of the system. The NS has been completely disrupted, and a ring of material has formed just outside the BH horizon (at $r = M_{\rm h}$; the circle drawn for reference corresponds to $r = 2\,M_{\rm h}$).

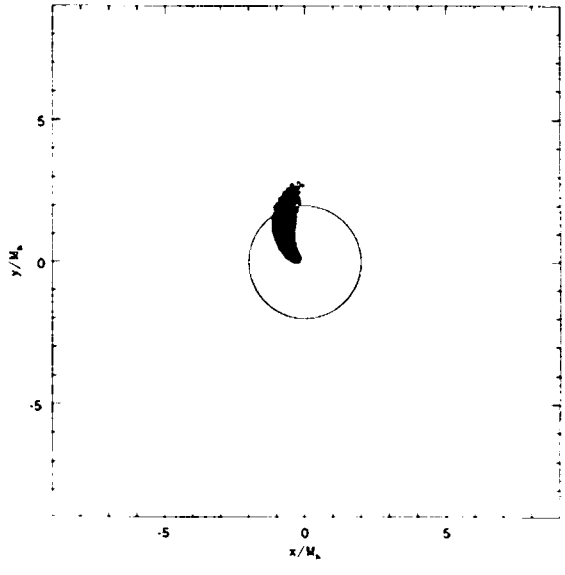


Figure 6: Same as in Fig. 5 but for a nonrotating (Schwarzschild) BH. Here again the NS has been completely disrupted, but the NS fluid is disappearing into the BH horizon (at $r = 2\,M_{\rm h}$, indicated by circle) and a stable ring of matter cannot form around the BH. Note that our inner absorbing boundary is located at $r = 0.2\,M_{\rm h}$, well inside the horizon.

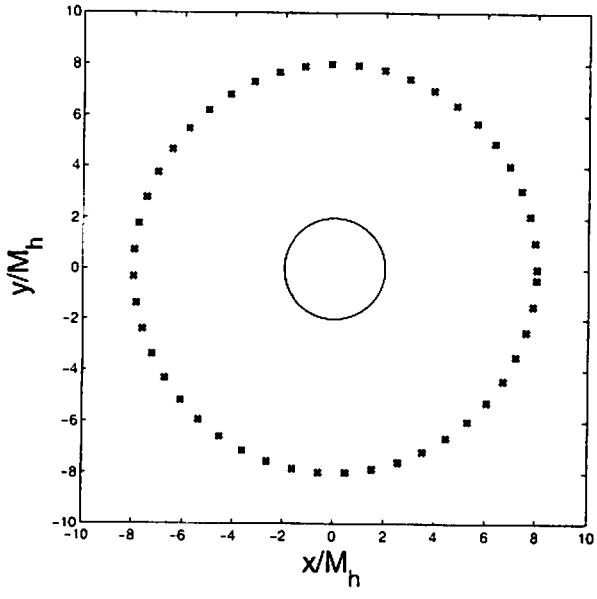


Figure 7: Test calculation for a WD orbiting a much more massive BH at $r = 8\,M_{\rm h}$. The mass ratio in this case is $q \simeq 4 \times 10^5$. The constant radius of this circular orbit is maintained by our code to within better than 10^{-3} over one full period. Here each cross indicates the position of the WD (center of mass of all SPH particles) at a different time along the orbit (counter-clockwise).

orbits. Although our calculations so far have been for initial circular orbits in the equatorial plane of a Kerr BH, this is probably not realistic for most BH–NS binaries, where the NS is formed second, with a kick that would have likely tilted the plane of the orbit with respect to the BH spin (Kalogera 2000).

We have also performed several test calculations for white dwarfs (WDs) orbiting stably around a much more massive BH near their Roche limits. In this case the mass ratio is extreme, and our approximation (moving the fluid on a fixed background metric) should be nearly exact. For example, if we place a $0.6\,M_\odot$ WD in orbit around a Schwarzschild BH with $M_{\rm h} = 2 \times 10^5\,M_\odot$, we find that we can maintain a circular orbit at $r = 8\,M_{\rm h}$ to within $|\Delta r|/r < 10^{-3}$ over one full orbital period. This is illustrated in Fig. 7.

Acknowledgements

This work was supported by NSF Grant PHY-0245028 at Northwestern University. SK and PL acknowledge support from the Eberly Research Funds of Pennsylvania State University, the Center for Gravitational Wave Physics, funded under NSF cooperative agreement PHY-0114375, and a NASA Swift Cycle 1 GI program. FR also thanks the Center for Gravitational Wave Physics for hospitality and support. JF is supported by an NSF Postdoctoral Fellowship in Astronomy and Astrophysics at UIUC.

References

[1] Ayal, S., Piran, T., Oechslin, R., Davies, M.B., Rosswog, S. 2001, ApJ, 550, 846

[2] Baumgarte, T.W., & Shapiro, S.L. 1998, ApJ, 504, 431

[3] Baumgarte, T.W., Cook, G.B., Scheel, M.A., Shapiro, S.L., & Teukolsky, S.A. 1998, PRD 57, 7299

[4] Baumgarte, T.W., Shapiro, S.L., & Shibata, M. 2000, ApJ, 528, L29

[5] Baumgarte,T.W., Skoge,M.L., & Shapiro,S.L. 2004, PRD, 70, 064040

[6] Bildsten, L., & Cutler, C. 1992, ApJ, 400, 175

[7] Blanchet, L., Damour, & Schäfer, G. 1990, MNRAS, 242, 289

[8] Bonazzola, S., Gourgoulhon, E., & Marck, J.-A. 1999, J. Comp. Appl. Math., 109, 433

[9] Cook, G.B., Shapiro, S.L., & Teukolsky, S.A. 1994, ApJ, 424, 823

[10] Damour, T., Gourgoulhon, E., & Grandclément, P. 2002, PRD, 66, 024007

[11] Davies,M.B., Levan,A.J., & King,A.R. 2005, MNRAS, 356, 54

[12] Duez, M.D., Liu, Y.T., Shapiro, S.L., Stephens,B.C. 2004, PRD, 69, 104030

[13] Eichler, D., Livio, M., Piran, T., & Schramm, D.N. 1989, Nature, 340, 126

[14] Faber, J.A., & Rasio, F.A. 2000, PRD, 62, 064012

[15] Faber, J.A., & Rasio, F.A. 2002, PRD, 65, 084042

[16] Faber, J.A., Grandclément, P., Rasio, F.A., & Taniguchi, K. 2002, PRL, 89, 231102

[17] Faber, J.A., Grandclément, P., & Rasio, F.A. 2004, PRD, 69, 124036

[18] Grandclément,P., Gourgoulhon,E., & Bonazzola,S. 2002, PRD, 65, 044021

[19] Hughes, S.A. 2002, PRD, 66, 102001

[20] Ishii,M., Shibata,M., & Mino,Y. 2005, PRD, 71, 044017

[21] Kalogera, V. 2000, ApJ, 541, 319

[22] Kobayashi, S, Laguna, P., Phinney, E.S., & Meszaros, P. 2004, ApJ, 615, 855

[23] Kochanek, C.S. 1992, ApJ, 398, 234

[24] Laguna, P., Miller, W.A. & Zurek, W.H. 1993a, ApJ, 404, 678

[25] Laguna, P., Miller, W.A., Zurek, W.H. & Davies, M.B. 1993b, ApJ, 410, L83

[26] Lai, D., Rasio, F.A., & Shapiro, S.L.1994, ApJ, 420, 811

[27] Lattimer, J.M., & Schramm, D.N. 1974, ApJ, 192, L145

[28] Lee, W.H. 2001, MNRAS, 328, 583

[29] Lombardi, J.C., Rasio, F.A., & Shapiro, S.L. 1997, PRD, 56, 3416

[30] Lombardi, J.C., Sills, A., Rasio, F.A., & Shapiro, S.L. 1999, J. Comp. Phys., 152, 687

[31] Mathews, G.J., Marronetti, P., & Wilson, J.R. 1998, PRD, 58, 043003

[32] Mészáros, P., & Rees, M.J. 1992, ApJ, 397, 570

[33] Miller,M., Gressman,P., & Suen,W. 2004, PRD, 69, 064026

[34] Morrison,I.A., Baumgarte,T.W., & Shapiro,S.L. 2004, ApJ, 610, 941

[35] Nakamura, T. 1994, in Relativistic Cosmology, ed. M. Sasaki (Universal Academy Press), 155

[36] Narayan, R., Paczyński, B., & Piran, T. 1992, ApJ, 395, L83

[37] Oechslin,R., Rosswog,S., Thielemann,F. 2002, PRD 65, 103005

[38] Oohara, K., & Nakamura, T. 1992, Prog. Th. Phys., 88, 307

[39] Rasio, F.A., & Shapiro, S.L. 1995, ApJ, 438, 887

[40] Rasio, F.A., & Shapiro, S.L. 1999, CQG, 16, 1

[41] Rosswog, S., Freiburghaus, C., & Thielemann, F.-K. 2001, Nucl. Phys. A, 688, 344

[42] Shibata, M. 1997, PRD, 55, 6019

[43] Shibata, M., & Uryu, K. 2000, PRD, 61, 064001

[44] Shibata, M., & Uryu, K. 2001, PRD, 64, 104017

[45] Shibata, M., & Sekiguchi, Y. 2004, 69, 084024

[46] Shibata,M., Taniguchi,K., & Uryu,K. 2003, PRD, 68, 084020

[47] Sills, A., Faber, J.A., Lombardi, J.C., Rasio, F.A., & Warren, A. 2001, ApJ, 548, 323

[48] Vallisneri, M. 2000, PRL, 84, 3519

[49] van Putten, M.H.P.M., & Levinson, A. 2002, Science, 295, 1874

[50] Wilson, J.R., Mathews, G.J., & Marronetti, P. 1996, PRD, 54, 1317

Large-scale Cryogenic Gravitational-wave Telescope: LCGT

Masaki Ando[1] and the LCGT collaboration

Department of Physics, University of Tokyo, 7-3-1 Hongo, Bunkyo-ku, Tokyo 113-0033, Japan

Abstract

Large-scale Cryogenic Gravitational-wave Telescope (LCGT) is a gravitational detector to be constructed at the Kamioka underground site. The detector is comprised of two independent interferometers with 3km baseline lengths. These two interferometers are required to reject fake events effectively, and to increase the confidence of the detection of gravitational waves. Each interferometer will have an observable range of 170 Mpc for $1.4M_{\odot}$ neutron star inspiral events, with a strain sensitivity of $4\times10^{-24}/\sqrt{\mathrm{Hz}}$. In order to achieve a high sensitivity, several advanced techniques are used in LCGT: cryogenic mirrors to reduce thermal noises, an optical configuration of a resonant-sideband extraction to optimize the optical readout noise, a high-power laser source, and a high-performance seismic attenuation system, an so on. In this article, we present a conceptual design of LCGT, and the current status of research and development efforts for LCGT.

1 Introduction

We will obtain a new probe to investigate astrophysical and cosmological phenomena by observing gravitational waves (GWs). Since GWs are emitted by the violent motion of matter, and are hardly absorbed or scattered, they have a potential to carry astrophysical and cosmological information different from that by electromagnetic waves [1]. However, no GW has yet been detected directly because of its weakness. In order to create a new field of GW astronomy, several GW detectors were constructed and observation data have been accumulated. Currently, five resonant detectors (EXPLOLER, ALLEGRO, NIOBE, NAUTILUS, and AURIGA [2]) and four interferometric GW detectors (LIGO [3], VIRGO [4] and GEO [5], and TAMA [6, 7]) are under operation (or become operational in near future). However, no clear evidence of a GW signal has been found in these data to date, though some of these detectors have sufficient sensitivity to observe a GW event in our Galaxy. This is because the GW event rate in our Galaxy is very small: about $10^{-4}-10^{-5}$ event/yr for the coalescence of binary neutron stars [8], and about 10^{-2} event/yr for supernova explosions, and because GW signals from distant galaxies are too faint for the current detectors.

In order to detect GWs with a much higher rate, and to obtain astrophysical and cosmological information from GW signals, we need more sensitive GW detectors that can observe GW events at distant galaxies. Since the number of detectable events is proportional to the volume within the detectable range, the detectable event rate increases as the cube of the observable distance in a rough estimation. Thus, several next-generation detectors, such as Advanced LIGO [9], LCGT [10] (Large-scale Cryogenic Gravitational-wave Telescope), and EGO [11], are being proposed. These future detectors will have a detectable distance of 200-300 Mpc for the inspiral of neutron star binaries. With this detectable distance, an event rate of over 10 events/year is expected. Besides the chirp GW signals from binary inspirals, these detectors will have a potential to detect ringdown GW waves from new-born or perturbed black holes. In addition, they will have sufficient sensitivity for burst GW signals from stellar-core collapses (supernova explosions) and continuous GW signals from spinning neutron stars (pulsars) in our Galaxy. These detectors will also provide us cosmological information by looking for stochastic background GWs.

In this article, we present the conceptual design and current status of the research and development tasks for LCGT.

[1] E-mail: ando@granite.phys.s.u-tokyo.ac.jp

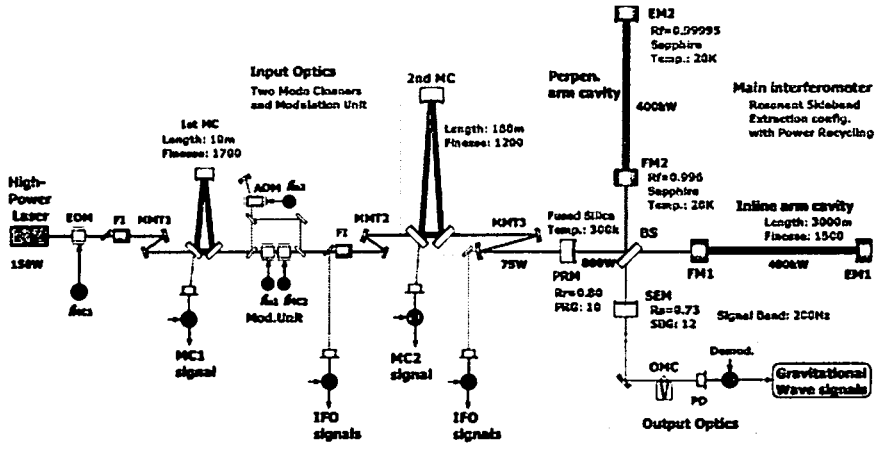


Figure 1: Optical configuration of LCGT. The laser source is a Nd:YAG laser with an output power of 150 W. The beam from the laser source passes through two mode cleaners to reject useless higher-order mode beams. After passing through the mode cleaner, the beam is introduced to the main interferometer. The interferometer has an optical configuration of resonant-sideband extraction (RSE).

2 LCGT conceptual design

2.1 Overview

LCGT is a project to construct two interferometric detectors with baseline lengths of 3 km at the Kamioka underground site. This site is about 1000 m underground below the top of a mountain, and provides a very stable seismic and temperature environment. LCGT has a characteristic feature that the interferometers are comprised of cryogenic sapphire mirrors suspended by cryogenic pendulums in order to reduce the thermal noises of the mirror and suspension system. In order to reduce and to optimize the optical-readout noise, a high-power laser source and a resonant-sideband extraction configuration are used in LCGT.

Figure 1 shows the optical configuration of a LCGT interferometer. The laser source is a Nd:YAG laser with an output power of 150 W [12]. In this laser, the beam from a 2-W master laser source is amplified by injection-locking with a slave laser, and further amplified by power amplifiers. The beam from the laser source passes through two mode cleaners to reject useless higher-order mode beams. These mode cleaners are also used to stabilize the laser frequency. After passing through the mode cleaner, the beam is introduced to the main interferometer. The interferometer has an optical configuration of resonant-sideband extraction (RSE) [13] and power recycling [14]. With this configuration, the optical power is mainly stored in the arm cavities, while the laser beams that contain the GW information are effectively extracted to an output port where the main photo-detector is placed.

The two interferometers of LCGT are placed nearby at the same Kamioka site. Since the separation between the two interferometers is 50 m at most, and since the directions of these interferometers are aligned, they have almost the same response to GW signals. On the other hand, these interferometers are built so as to be independent as possible to have different responses to various kind of noises. With this design, these two interferometers are used to reject fake events by checking the consistency of the output of the two detectors. With a naive estimation, the fake rate will be reduced by a factor about 10^{-6}, which corresponds to the GW traveling time (seconds) between the interferometers.

Figure 2 shows the designed sensitivity of each interferometer of LCGT. The strain sensitivity is $4 \times 10^{-24}/\sqrt{\mathrm{Hz}}$ at around 100 Hz. The sensitivity curve is dominated by the optical readout noise (shot noise and radiation-pressure noise) at most of the frequency band. Thermal noise, which is one of fundamental noise sources in the other detectors, does not limit the LCGT sensitivity, thanks to the cryogenic interferometer design. The observation band is limited by the seismic noise at a low frequency

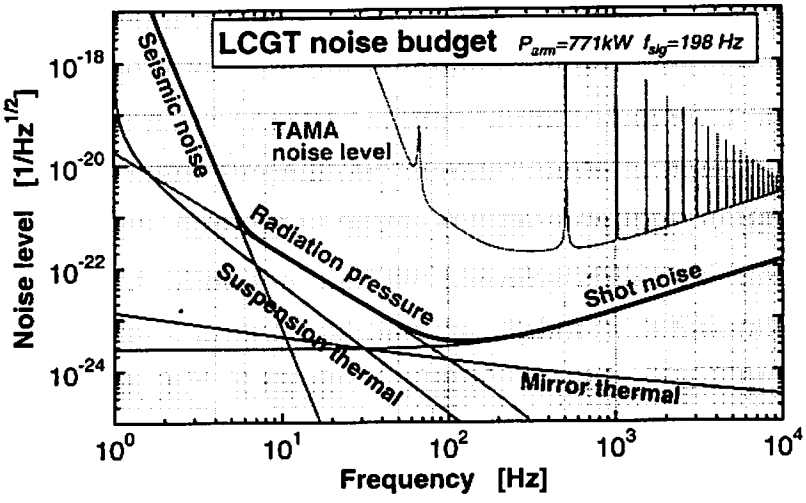


Figure 2: Design sensitivity of LCGT. The floor level is $4 \times 10^{-24}/\sqrt{\text{Hz}}$ at around 100 Hz. The sensitivity is dominated by optical readout noise (shot noise and radiation-pressure noise) at most of the frequency band. The observation band is limited by seismic noise at a low-frequency band below 10 Hz. Thermal noise does not limit the LCGT sensitivity, thanks to the cryogenic interferometer design.

band below 10 Hz. In the following parts, we describe the LCGT design to reduce these noises (optical readout noise, thermal noise, and seismic noise).

2.2 Optical readout noise

The LCGT sensitivity is mostly limited by the optical readout noise because the other noises, such as the thermal noises of the mirror and the suspension, are sufficiently suppressed. The optical readout noise, which originates in the quantum behavior of the laser beam, is a fundamental noise source in an interferometric detector. Optical readout noise contains two types of noise: shot noise and radiation-pressure noise. Shot noise is understood to be photon-counting noise at the photo detector, and the noise level is inverse-proportional to the square-root of the laser power. On the other hand, radiation-pressure noise is caused by fluctuation of the photon number reflected by the mirror. The radiation-pressure noise level is proportional to the square-root of the laser power. As shown in Fig. 2, the LCGT design noise sensitivity is dominated by the shot noise in the high-frequency region and by the radiation-pressure noise in the low-frequency region. Since these two noises have an opposite dependence to the laser power, the detector is designed to optimized the total optical readout noise.

In LCGT, the interferometer has a optical configuration of resonant-sideband extraction (RSE). Originally, the RSE scheme was adopted in LCGT because it is indispensable to realize a cryogenic and high-power interferometer. In the RSE configuration, the optical power is mainly stored in the high-finesse arm cavities, and the power-recycling gain is designed to be moderate. With this configuration, heat absorbed in the mirror substrates can be reduced to a sufficiently small amount to keep the mirror at a low temperature.

The optical parameters of LCGT are designed so that the optical readout noise would be optimal for the observation of neutron binary inspirals (Fig. 3). The finesse of the arm cavities are designed to be 1500. The power-recycling gain and the signal-band gain are designed to be 10 and 15, respectively. With this design, about 800 kW laser power is stored in the arm cavities, and a 200 Hz signal bandwidth is realized for GW signals.

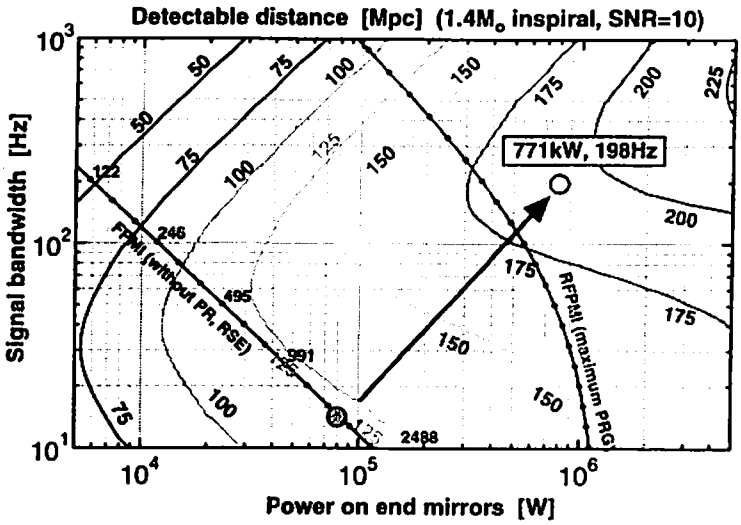


Figure 3: Contour of the detectable range for $1.4M_\odot$ neutron star inspiral; the range is shown as a function of the laser power in the arm cavities (horizontal axis) and the signal bandwidth (vertical axis) of the detector. This figure is used to determine of the optical parameters. The line at the left-bottom region represents the realized power-bandwidth relationship without power recycling and RSE, which is drawn by changing the finesse of the arm cavity. Power recycling increases the power in the arm cavities without changing the signal bandwidth. On the contrary, RSE increases the signal bandwidth without changing the power in the arm cavities. In LCGT, the finesse of the arm cavities, power-recycling gain, and the signal-band gain are designed to be 1500, 10 and 15, respectively. With this design, about 800 kW laser power is stored in the arm cavities, and a 200 Hz signal bandwidth is realized for GW signals.

2.3 Thermal fluctuation

Thermal noise, which originates in the thermal fluctuation of mirrors and suspension systems, is also one of the fundamental noises in an interferometric detector [16]. The thermal noise level is proportional to the square-root of the temperature and is inversely proportional to the Q-factors of the components (mirrors and suspensions). Thus, in order to reduce the thermal noise, it is important to reduce the temperature and to use high-Q (low mechanical-loss) materials.

In LCGT, the main mirrors, which form the 3 km arm cavities, are made of sapphire and are cooled down to 20 K. Sapphire is selected because of its good behavior at cryogenic temperature: a high Q-value of about 3×10^8 and a high thermal conductivity [17]. The wires that suspend the sapphire main mirrors are also made of sapphire. This sapphire fiber is used as a heat link between the main mirror and the upper mass [18]. Thanks to the high Q-value of sapphire and the low temperature, the thermal noise of the mirrors and suspensions do not affect the sensitivity of LCGT.

Although it is clear that thermal noise can be reduced by cooling the components that form the interferometer, it is not simple to design a cryogenic interferometer in practice because of the constraint from the cooling system (Fig. 4). One of the difficulties concerning a cryogenic interferometer is vibration of the cryocooler; vibration may pass through heat links and may be introduced to the mirror. Thus, we use a low-vibration pulse-tube-type cryocooler, which enables continuous detector operation without frequent refill of liquid helium and nitrogen, and flexible heat links to reduce the excitation from the cryocooler [19] .

A cryostat for the mirror housing has two radiation shields (8 K and 80 K), which are cooled by a cryocooler by thermal conductivity. The heat link between them is comprised of pure aluminum wires. The upper mass of the mirror suspension is flexibly connected to the radiation shield, also with pure aluminum wires. In addition to using a low-vibration cryocooler and vibration isolation by flexible heat

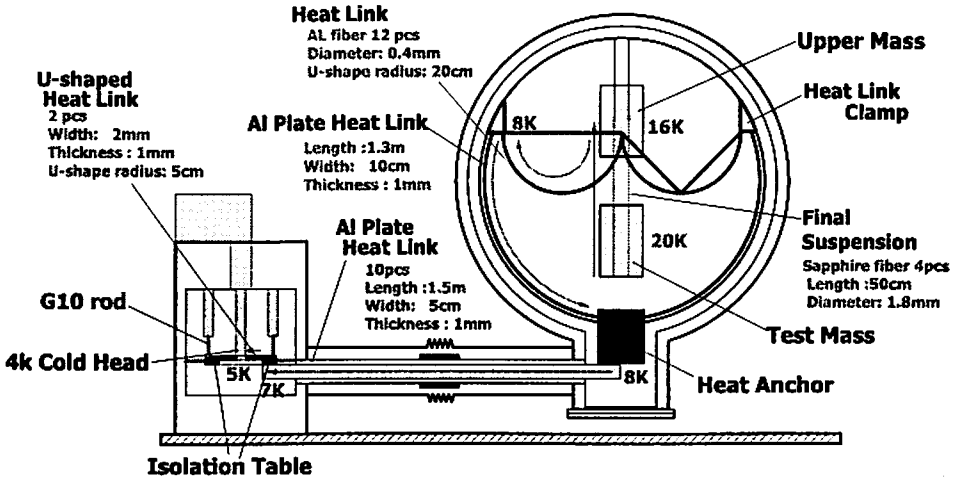


Figure 4: Schematic drawing for the mirror cooling system. The mirror for the main interferometer is housed in a cryostat with two-layer radiation shields (8 K and 80 K) and is suspended from the upper mass by sapphire fibers. These fibers have a role of a heat link to pump the heat of the main mirror by conduction. The upper mass is connected to an inner radiation shield located inside of the vacuum tank with heat links made of pure aluminum. The cryocooler is connected to a heat anchor at the bottom of the radiation shield with aluminum heat links. In order to keep the vibration of the cryocooler from exciting the mirror motion, flexible heat links are used. In addition, we use a low-vibration pulse tube cryocooler, in which the vibration of the cold head is almost below the seismic motion level of the Kamioka underground site.

links, a full-scale (3 km baseline length) interferometer, called a suspension point interferometer (SPI), is formed by the upper masses in order to suppress the vibration introduced from the cryocooler [15]. By detecting the relative motion of the upper masses by the SPI, and feeding it back to the upper mass, the relative motion caused by the vibration of heat links is actively suppressed.

2.4 Seismic disturbances

Since an interferometric detector placed on the earth is very sensitive to seismic disturbance, the isolation of seismic excitation is important both for long-term stable operation of the detector and for high detector sensitivity. In current ground-based interferometers, the detector sensitivity is limited by the seismic noise in a low frequency band below 10-100 Hz. In LCGT, the detector is placed at the Kamioka underground site, which has a much lower seismic environment than sites on the ground [20]. In addition, a low-frequency seismic attenuation system (SAS) [21], and a suspension-point interferometer [15] are adopted in LCGT so as to reduce the seismic noise and to expand the detector observation band to a lower frequency.

The LCGT detector is placed at a Kamioka underground site of the Institute of Cosmic Ray Research, which is 37 km away from Nippon Ocean and 358 m above sea level. The site used to be an abandoned mine, and 1000 m underground from the top of the mountain. Figure 5 shows the seismic fluctuation levels at the LCGT site and at several sites for a comparison. The bold curves represent the displacement spectrum at the LCGT site (Kamioka underground site in Gifu) and at the TAMA300 site (Mitaka campus of the National Astronomical Observatory Japan in Tokyo). The LCGT site is quieter than that of the TAMA site by a factor of 10^2-10^3 in the 1-10 Hz frequency range. In addition, since the detector is fixed on the hard and large bedrock of Hida gneiss, we can expect a common-mode rejection of seismic motion.

Figure 6 shows a diagram of the suspension system for LCGT. This system is comprised of a low-

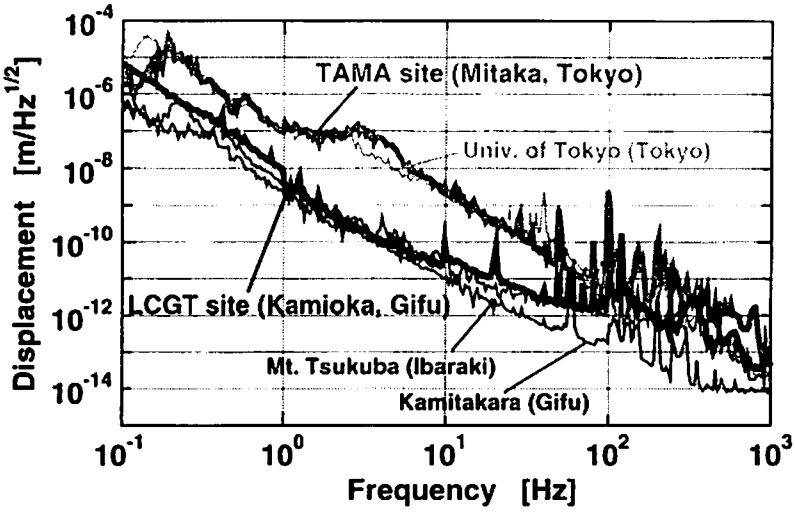


Figure 5: Displacement spectrum of the seismic fluctuation at several sites. The bold curves represent the spectrum at the TAMA300 site (National Astronomical Observatory Japan, Tokyo) and the LCGT site (Kamioka underground site of Institute of Cosmic Ray Research, Gifu). The LCGT site is quieter than that of the TAMA site by a factor of 10^2-10^3 in the 1-10 Hz frequency range.

frequency seismic-isolation system, called SAS (Seismic Attenuation System), at room temperature, and a double suspension system at cryogenic temperature. The SAS is formed by inverted pendulums (IP) for horizontal seismic isolation, and geometric anti-springs (GAS) filters for vertical seismic isolation. Their resonant frequencies are designed to be low so as to realize high seismic attenuation performance: about 30 mHz for IP and about 500 mHz for the GAS. The cryogenic suspension is a double pendulum with recoil masses to control the mirror position. The wires for the final pendulum to suspend the main mirror of the interferometer are made of sapphire. The heat generated at the mirror by light absorption is pumped up through these sapphire fibers. The upper mass is also made of sapphire. Heat links to a cryocooler are connected to this upper mass. SPI plays an important role to improve the stability and sensitivity of the main interferometer by suppressing the differential motion of the mirrors caused by seismic fluctuation, and by suppressing the noise of the mirror actuator, as well as by suppressing the vibration from the heat links.

3 Research and development efforts

There are many research and development tasks required to construct the LCGT detector. In this section, we describe two large topics, CLIO and TAMA, among these efforts.

3.1 Cryogenic prototype interferometer

CLIO (Cryogenic Laser Interferometer Observatory) is a cryogenic interferometer with a 100 m baseline length, which is being constructed at the Kamioka underground site [22]. This interferometer has been developed to show the feasibility of a cryogenic laser interferometer with sapphire mirrors, cryocoolers and flexible heat links. In addition, since this interferometer is constructed at the same site as the LCGT, it has a role of a prototype to test the environment and to prepare the equipment of the facility. The target of CLIO is to realize a displacement noise level of 1×10^{-19} m/$\sqrt{\text{Hz}}$ (1×10^{-21} /$\sqrt{\text{Hz}}$ in a strain noise level) and to see a reduction of the thermal noise as expected in cryogenic temperature.

CLIO has an optical configuration of a locked Fabry-Perot; differential length changes in two orthogo-

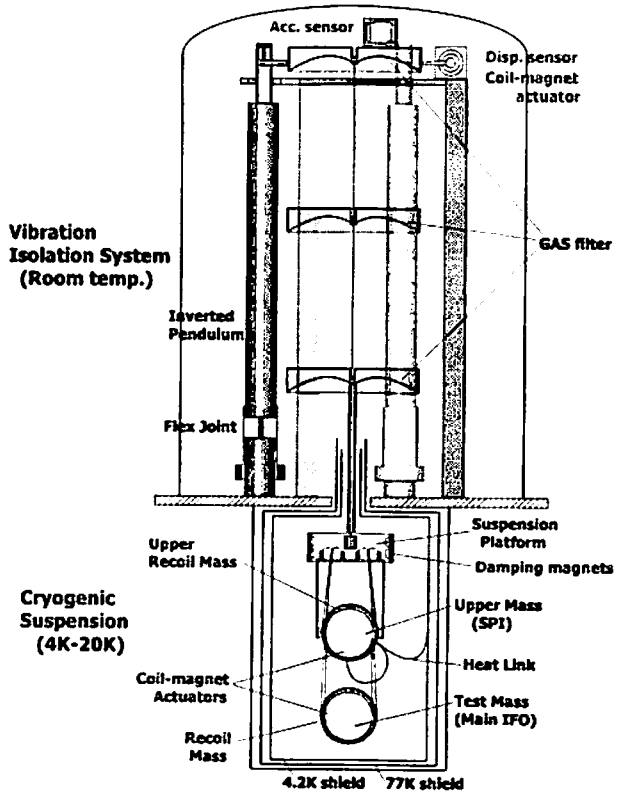


Figure 6: Seismic isolation and suspension system of LCGT. The main mirror is suspended as a double pendulum from a suspension platform at cryogenic temperature. The suspension platform is suspended from a seismic isolation system set at room temperature by a wire with low heat conductivity. The seismic isolation system at room temperature is comprised of a inverted pendulum (IP) for horizontal vibration isolation and monolithic anti-springs (MGASs) for vertical isolation.

nal Fabry-Perot cavities are measured as gravitational-wave signal channel. As a laser source, a Nd:YAG laser with an output power of 2 W is used. The beam from the laser source passes though a 10-m mode cleaner to reject any unnecessary higher-order mode light before being introduced to the main 100-m arm cavities. The mirrors for the main arm cavities are suspended by sapphire fibers and placed in cryogenic chambers. The mirror substrates are made of sapphire, and the mirror surfaces are coated by dielectric multilayer films of SiO_2 and Ta_2O_5.

The cooling system is based on the design of LCGT. A low-vibration pulse-tube cryocooler is placed in a separated vacuum tank, and connected to the radiation shield of the chamber for the main mirror by flexible heat links made of pure aluminum. The main mirrors are suspended by sapphire fibers from the upper mass, and pure aluminum heat links are connected to the upper mass.

The construction of the facility, such as digging of the tunnel and building clean booths, has been completed, and the laser source and the 10 m mode cleaner are operational to date. Currently, we are in a construction and shakedown phase of the low-vibration cryocoolers and the vacuum system. The suspension system and some part of the interferometer will be operated in one year, and the CLIO interferometer will be operated with the full configuration in two years.

Table 1: Summary of long data-taking runs by TAMA300. The noise level and total observation data amount are described. The last column (D.C.) represents the duty cycle throughout the data-taking run.

	Term	Noise level [$Hz^{-1/2}$]	Data [hours]	D.C.
DT6	Summer 2001	5×10^{-21}	1038	87%
DT8	Spring 2003	3×10^{-21}	1157	81%
DT9	Winter 2004	2×10^{-21}	558	54%

3.2 Research with TAMA300

The other topic is a research using TAMA300: data-analysis efforts, and tests of the seismic attenuation system (TAMA-SAS). TAMA is a Japanese project to construct and operate an interferometric gravitational-wave detector at the Mitaka campus of National Astronomical Observatory in Tokyo (35°40′N, 139°32′E) [6, 7]. The aim of this project is to develop techniques necessary for future large-scale interferometers and, moreover, to detect gravitational waves (GWs) generated within our local group of galaxies. The target strain sensitivity of TAMA is $h_{\rm rms} \sim 3 \times 10^{-21}$ at 300 Hz with a bandwidth of 300 Hz, which corresponds to $h \sim 2 \times 10^{-22}$ $/\sqrt{\rm Hz}$. With this sensitivity, the TAMA detector would be able to detect GWs from supernova explosions, or the coalescence of compact binary systems within our local group of galaxies.

In TAMA, nine observation runs have been carried out so far since the first observation run in 1999, and over 2700 hours of data have been collected. Among them, we obtained a large amount of data in the sixth, eighth, and ninth data-taking runs (DT6, DT8, and DT9, respectively, Table 1). We obtained over 1000 hours of data in each of DT6 and DT8, operating the detector stably and with a good duty cycle. In DT9, most of the day time was spent to adjust and measure of the detector during the first half term. On the other hand, we obtained data with uniform quality with a high duty cycle in the second half; the duty cycle was 96% in this quiet term of DT9. Typical noise spectra in these observation runs are shown in Fig. 2. The noise level has gradually been improved by detector investigations between these runs. The floor level is $2 \times 10^{-21}\,{\rm Hz}^{-1/2}$ in DT9 at around 1 kHz.

The data collected by TAMA300 are being used to search for GW signals with several kinds of waveforms. Though we have not obtained any clear evidence of a GW signal yet, we developed data-analysis schemes and set upper limits on the GW signals. For chirp GW signals from binary inspirals, we developed a data analysis scheme using matched filtering for extracting event candidates, and a χ^2-test for rejecting fake events. As a result, we found that the TAMA 300 detector has a high detection efficiency of 60% for Galactic events. Moreover, we set an upper limit of 29 events/day on the event rate in our Galaxy with a confidence level of 90%, using the DT8 data [23]. As for burst GW signals, several analysis schemes, called burst filters, have been developed. In addition, fake reduction schemes are being developed using a time-scale selection of event candidates and using auxiliary monitor signals of the interferometer obtained during data-taking runs. As a result, we set an upper limit of 5×10^3 events/sec on the event rate of GW signals from stellar-core collapse in our Galaxy with a confidence level of 90% [24]. On a ringdown GW signals from quasi-normal-mode oscillation of new-born blackholes, an analysis scheme based on a matched filtering has been developed. The data-analysis result will be published soon [25]. We are also analyzing the TAMA data for continuous GW signals from rotating neutron stars (pulsars). In a continuous-wave analysis, we use an analysis scheme based on a matched filtering with a correction of a pulsar spin down, a Doppler effect caused by the relative motion between the pulsar and the Earth, and so on. As a result of a analysis using the TAMA DT9 data, we set a preliminary upper limit of $h_{\rm UL} = 4 \times 10^{-23}$ for the strain amplitude of GW from a reported pulsar in the 1987A remnant [26]. As well as investigations only with the TAMA300 data described above, coincidence analyses with the other detectors are underway [27]. These schemes developed for the analysis of the TAMA data will also be used for LCGT.

Another important topic on the research efforts for LCGT using the TAMA detector is the development of a high-performance seismic isolation system, called TAMA-SAS. This isolation system will be used as the room-temperature part of a LCGT seismic isolation system. TAMA-SAS has been devel-

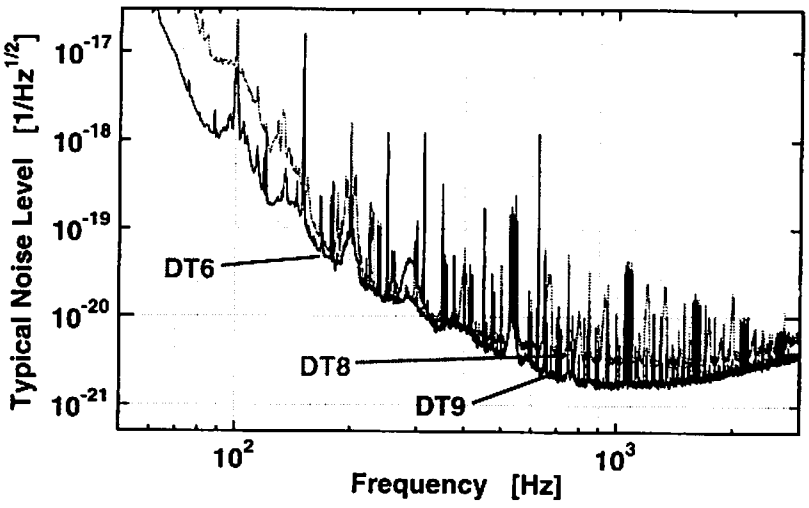


Figure 7: Typical noise spectra of the TAMA300 detector during data-taking runs. The noise level has gradually been improved by detector investigations between these runs. The floor level is 2×10^{-21} [$\mathrm{Hz}^{-1/2}$] in DT9 at around 1 kHz.

oped and tested using a prototype interferometer with a 3-m Fabry-Perot cavity. In this experiment, the obtained isolation ratio was as good as we had expected: a better isolation ratio than that of the current TAMA isolation system by a factor of 10^3 around 4 Hz [28]. Currently, we are assembling four TAMA-SASs for four main mirrors of Fabry-Perot arm cavities; they will be installed to TAMA in a few month, and TAMA will be operated with them by the end of 2005.

4 Conclusion

LCGT will have high sensitivity to observe gravitational-wave (GW) signals with realistic detection rates, and will provide astronomical and cosmological information that will be complementary with that by observations by electromagnetic waves. LCGT will detect GW signals from binary inspirals at a rate of about one per month. In addition, LCGT is formed by two independent interferometers. By combining the outputs of these two detectors, we can effectively reject fake events, and increase the confidence when we detect GW signals. The feasibility of LCGT is being studied both in detailed designs and in experiments, such as TAMA, CLIO, prototype interferometers, and table-top experiments. We are hoping that LCGT will soon be funded, and will start observations in several years.

References

[1] K. S. Thorne, in: *Three hundred years of gravitation*, eds: S. Hawking and W. Israel (Cambridge University Press) p. 330-458 (1987).

[2] P. Astone *et al.*, Phys. Rev. D **68** 022001 (2003).

[3] A. Abramovici *et al.*, Science **256** 325 (1992).

[4] The VIRGO collaboration, *VIRGO Final Design Report* VIR-TRE-1000-13 (1997), C. Bradaschia, *et al.*, Nucl. Instrum. Meth. A **289** 518 (1990).

[5] K. Danzmann *et al.*, *Proposal for a 600m Laser-Interferometric Gravitational Wave Antenna* (Max-Planck-Institut für Quantenoptik Report) 190 (1994).

[6] K. Tsubono, *Gravitational Wave Experiments*, eds: E. Coccia, G. Pizzella, and F. Ronga (World Scientific) p. 112 (1995), K. Kuroda et al., *Gravitational Waves: Sources and Detectors*, eds: I. Ciufolini and F. Fidecaro (World Scientific) p. 100 (1997).

[7] M. Ando *et al.*, Phys. Rev. Lett. **86** 3950 (2001).

[8] V. Kalogera *et al.*, ApJ **601** L179 (2004), V. Kalogera *et al.*, ApJ **614** L137 (2004).

[9] P. Fritschel, 'Second generation instruments for the Laser Interferometer Gravitational Wave Observatory (LIGO)' in: Proceedings of the SPIE meeting 'Gravitational-Wave Detection' (4856-39), eds: P. Saulson and M. Cruise, pp. 282-291 (Waikoloa, Hawaii, 2002).

[10] K. Kuroda *et al.*, Int. J. Mod. Phys. D **8** 557-579 (1999), K. Kuroda *et al.*, Class. Quantum Grav. **20** S871 (2003), T. Uchiyama *et al.*, Class. Quantum Grav. **21** S1161 (2004).

[11] A. Giazotto and G. Cella Class. Quantum Grav. **21** S1183 (2004).

[12] K. Takeno *et al.*, Class. Quantum Grav. **21** S881 (2004).

[13] J. Mizuno *et al.*, Phys. Lett. A **175** 273 (1993).

[14] R. W. P. Drever, Fabry-Perot cavity gravity-wave detectors, *The detection of gravitational waves*, ed. D. G. Blair, Cambridge University Press (1991) p. 306-328.

[15] R. W. P. Drever and S. J. Augst Class. Quantum Grav. **19** 2005 (2002), Y. Aso *et al.* Phys. Lett. A **327** 1 (2004).

[16] P. R. Saulson, Phys. Rev. D **42** 2437 (1990).

[17] T. Uchiyama *et al.*, Phys. Lett. A **261** (1999) 5.

[18] T. Tomaru *et al.*, Phys. Lett. A **301** 215 (2002).

[19] T. Tomaru *et al.*, Class. Quantum Grav. **21** S1005 (2004).

[20] S. Sato *et al.*, Phys. Rev. D **69** 102005 (2004).

[21] S. Marka *et al.*, Class. Quantum Grav. **19** 1605 (2002), A. Takamori *et al.*, Class. Quantum Grav. **19** 1615 (2002).

[22] M. Ohashi *et al.*, Class. Quantum Grav. **20** S599 (2003). S. Miyoki *et al.*, Class. Quantum Grav. **21** S1173 (2004).

[23] H. Tagoshi *et al.*, Phys. Rev. D **63** 062001 (2001), H. Takahashi and H. Tagoshi, Class. Quantum Grav. **21** S697 (2004).

[24] M. Ando *et al.*, Class. Quantum Grav. **21** S735 (2004). M. Ando *et al.*, submitted to Phys. Rev. D.

[25] Y. Tsunesada, Class. Quantum Grav. **21** S703 (2004). H. Nakano *et al.*, Progress of Theoretical Physics **111** 781 (2004).

[26] K. Soida *et al.*, Class. Quantum Grav. **20** S645 (2003), T. Masumura, Master thesis, the University of Tokyo (2005).

[27] P. J. Sutton *et al.*, Class. Quantum Grav. **21** S1801 (2004), H. Takahashi and S. Fairhurst, *'Current status of the joint LIGO-TAMA inspiral analysis'*, talk at the 9th Gravitational data analysis workshop (Dec. 16, 2004 Annecy, France).

[28] A. Takamori, Ph.D thesis, the University of Tokyo (2002).

Binary Compact Object Inspiral: Rate Expectations

Vassiliki Kalogera[1], Chunglee Kim[2], Richard O'Shaughnessy[3], and Krzysztof Belczynski[4]

[1,2,3] *Theoretical Astrophysics Group, Department of Physics & Astronomy, Northwestern University, Evanston, IL 60208, USA*

[4] *Tombaugh Fellow; Department of Astronomy, New Mexico State University, 1320 Frenger Mall, Las Cruces, NM 8800, USA; and Nicolaus Copernicus Astronomical Center, Bartycka 18, 00-716 Warszawa, Poland*

Abstract

We summarize our results on the Galactic merger rate of double neutron stars (NS-NS) in view of the discovery of PSR J0737–3039. We also present results for the *global* probability distribution of merger rate values that incorporate the presently known systematics from the radio pulsar luminosity function. The most likely value obtained from the global distribution is only $\simeq 15\,\mathrm{Myr}^{-1}$, but a re-analysis of the current pulsar sample and radio luminosities is needed for a reliable assessment of the best fitting distribution. Next, we use our theoretical understanding of NS-NS formation to calculate a possible upper limit on the NS-NS merger rate from current Type Ib/c supernova rate estimates.

In the second part of our paper we use the observed sample of NS-NS binaries and its implication for inspiral rates to constrain population synthesis models of NS-NS formation. We select from an extremely broad family of possible population synthesis models those few (about 2%) which are consistent with the observed sample of NS-NS binaries. To further sharpen the constraints the observed NS-NS population places upon our understanding of compact-object formation processes, we separate the observed NS-NS population into two channels:, (i) merging NS-NS binaries, which will inspiral and merge through the action of gravitational waves within 15 Gyr, and (ii) wide NS-NS binaries, consisting of all the rest. With the subset of astrophysically consistent models, we explore the implications for the rates at which double black hole (BH-BH), black hole-neutron star (BH-NS), and NS-NS binaries will merge through the emission of gravitational waves.

1 Introduction

Soon after the discovery of the highly relativistic pulsar J0737−3039 (Burgay et al. 2004) we applied our analysis method for pulsar populations and calculated the updated merger rate estimates for the current sample of Galactic merging NS-NS (Kalogera et al. 2004). Our main conclusion was that this new, remarkably relativistic system is very significant for these estimates and leads to a rate increase by a factor of $6-7$. This implies a correspondingly significant increase in NS-NS inspiral event rates for gravitational-wave (GW) interferometers like LIGO. In what follows, we summarize our recent results and also present results on (i) how a *global* probability distribution of rate estimates can be calculated with the systematic uncertainties, and (ii) the possible upper limits that could be imposed on the NS-NS merger rate if we adopt

[1]E-mail:vicky@northwestern.edu
[2]E-mail:c-kim1@northwestern.edu
[3]E-mail:oshaughn@northwestern.edu
[4]E-mail:kbelczyn@nmsu.edu

the theoretically expected relationship between NS-NS merger rates and Type Ib/c supernova (SN) rates.

With the notable exception of NS-NS binaries the merger rates for double compact objects (DCO) with black holes have not been constrained empirically, since none have been detected yet. The only route to rate estimates for double black hole (BH-BH) and black hole-neutron star (BH-NS) binaries is through population synthesis – that is, through a Monte Carlo exploration of the likely life histories of binary stars, given statistics governing the initial conditions for binaries and a method for following the behavior of single and binary stars (see e.g., Belczynski, Kalogera, & Bulik 2002). Unfortunately, our understanding of the evolution of single and binary stars is incomplete, and we parameterize that uncertainty with a great many parameters (~ 30), many of which can cause the predicted merger rates to vary by more than an order of magnitude when varied independently through their plausible range. To arrive at more definitive answers for DCO merger rates, we must substantially reduce our uncertainty in the parameters that enter into population synthesis calculations through comparison with observations. However, the simplest and most direct way to constrain the parameters of a given population synthesis code is to compare several of its many predictions against observations. Specifically the empirically estimated formation rates derived based on the known Galactic NS-NS binaries – 3 of which have been studied already and are tight enough to merge through the emission of gravitational waves within 10 Gyr – should be reproduced by any physically reasonable combination of model parameters for population synthesis. In the second part of this paper, we describe the constraints the observed NS-NS population places upon the most significant parameters that enter into one population synthesis code, *StarTrack* (Belczynski, Kalogera, & Bulik 2002). Furthermore, we use the set of models consistent with this observational constraint to revise our population-synthesis-based expectations for various DCO merger rates.

2 The Revised Galactic NS-NS Merger Rate

In Kim, Kalogera, & Lorimer (2003; hereafter KKL), we introduced a statistical method to calculate the probability density function (PDF) of the rate estimates for Galactic merging NS-NS. After the discovery of PSR J0737–3039, we derived a combined $P(\mathcal{R})$ considering the three known merging NS-NS systems in the Galactic disk (for details see Appendix A of Kim et al. 2004).

To calculate the merger rate of NS-NS systems in our Galaxy, we need to estimate (i) the number $N_{\rm tot}$ of Galactic pulsars with pulse and orbital characteristics *similar* to those in the observed sample, (ii) the lifetime $\tau_{\rm life}$ of each observed system, and (iii) an upward correction factor $f_{\rm b}$ for pulsar beaming.

We calculate $N_{\rm tot}$ by modeling in detail the pulsar-survey selection effects for a number of pulsar population models described in KKL. The model assumptions for the pulsar luminosity function dominate the systematic uncertainties of our overall calculation.

The lifetime of the system is defined by $\tau_{\rm life} \equiv \tau_{\rm sd} + \tau_{\rm mrg}$, where $\tau_{\rm sd}$ is a spin-down age of a recycled pulsar (Arzoumanian, Cordes, & Wasserman 1999) and $\tau_{\rm mrg}$ is the remaining lifetime until the two neutron stars merge (Peters & Mathews 1963). We note that the lifetime of J0737–3039 is estimated to be 185 Myr, which is the shortest among the observed systems.

The beaming correction factor $f_{\rm b}$ is defined as the inverse of the fractional solid angle subtended by the pulsar beam. Its calculation requires detailed geometrical information on the beam. Following Kalogera et al. (2001), we adopt $f_{\rm b} = 5.72$ for PSR B1913+16 (Hulse & Taylor 1975) and 6.45 for PSR B1534+12 (Wolszczan 1991). Without good knowledge of the geometry of J0737–3039A, we adopt the average value of the other two systems ($\simeq 6.1$).

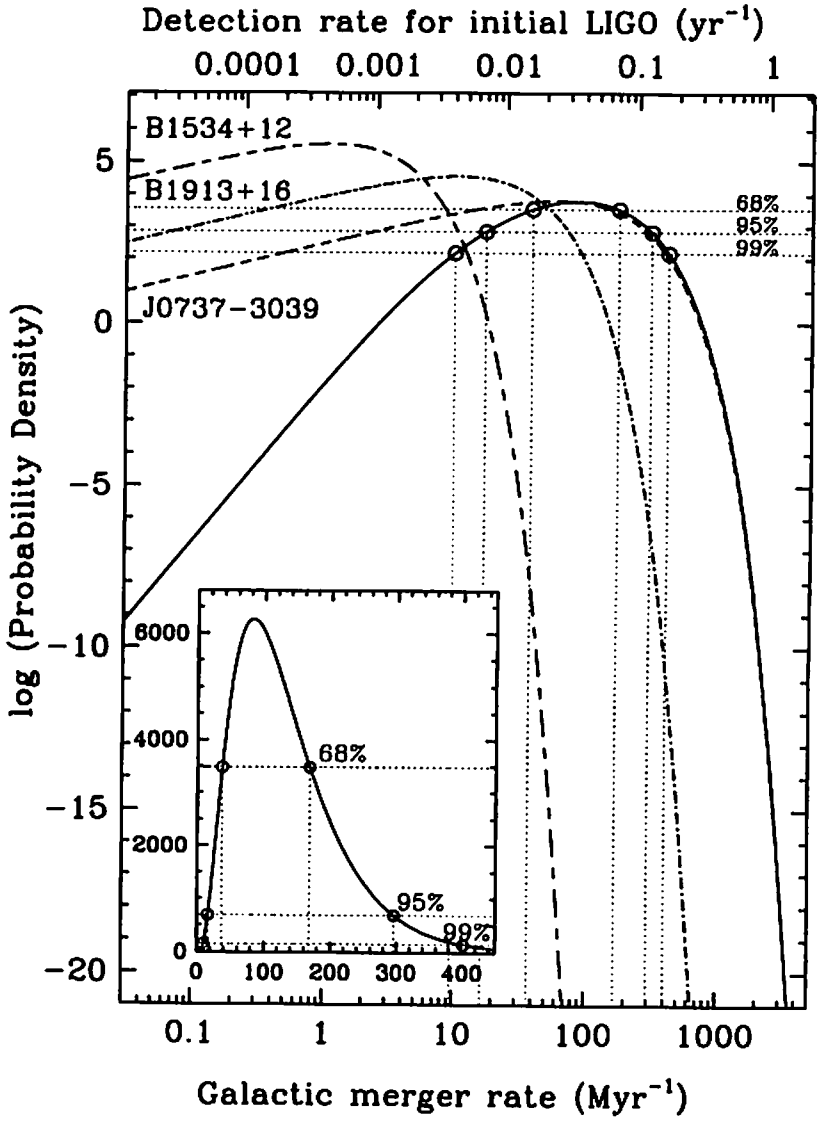


Figure 1: The NS-NS merger rate probability $P(\mathcal{R})$ is shown on a log scale. The thick solid line is the total Galactic rate estimate overlapped with results for individual observed systems (dashed lines). Dotted lines indicate confidence intervals for the rate estimates. The same results are shown on a linear scale in the small inset. All results shown are for our reference model.

In Figure 1, we show $P(\mathcal{R})$ for our chosen reference model that allows for a low minimum pulsar luminosity (Model 6 in KKL). The most likely value of $\mathcal{R}$ turns out to be $\simeq 83\,\mathrm{Myr}^{-1}$, larger by a factor of 6 – 7 than the rate estimated before the discovery of J0737–3039. We find the same increase factor for all pulsar population models examined. This revised merger rate implies an increase in the detection rate of NS-NS inspirals for ground-based GW interferometers such as LIGO (Abramovici et al. 1992). Using the standard extrapolation of our reference model out to extragalactic distances (see Kalogera et al. 2001), we find that the most probable event rates for our reference model are 1 per 29 yr and 1 per 2 days, for initial and advanced LIGO, respectively. At the 95% confidence interval, the most optimistic predictions for the reference model are 1 event per 8 yr and 2 events per day for initial and advanced LIGO, respectively. For more details see Kalogera et al. (2004).

The revised NS-NS merger rate is dominated by PSR J0737–3039. Therefore, if the estimated lifetime of this system is revised in the future, it will directly affect our rate estimation. Lorimer et al. (2004) calculated the spin-down age of the system with various spin-down models and suggested an age in the range 30–70 Myr, which is shorter than the value we adopted for our calculation ($\tau_{\rm sd}$ =100 Myr). The edges of this range give us rate estimates of $\mathcal{R} \simeq 90 - 115\,\mathrm{Myr}^{-1}$.

3 Global Probability Distribution of the Rate Estimates

In KKL, we showed that estimated Galactic NS-NS merger rates are strongly dependent on the assumed luminosity distribution function for pulsars. Most commonly, we have reported results for each set of population model assumptions. Here we describe how we can incorporate the systematic uncertainties from these models and calculate a *global* PDF of rate estimates. However, we stress that the information needed for such a calculation is currently not up to date; therefore the specific quantitative results could change when constraints on the luminosity function are derived from the current pulsar sample.

We calculate the global PDF of $\mathcal{R}$ using the prior distributions of the two model parameters for the pulsar luminosity function: the cut-off luminosity $L_{\rm min}$ and power-index p. We calculate these priors by fitting the marginal PDFs of $L_{\rm min}$ and p presented by Cordes & Chernoff (1997). We obtain the following analytic formulae for $f(L_{\rm min})$ and $g(p)$: $f(L_{\rm min}) = \alpha_0 + \alpha_1 L_{\rm min} + \alpha_2 L_{\rm min}^2$ and $g(p) = 10^{\beta_0 + \beta_1 p + \beta_2 p^2}$, where $\alpha_{\rm i}$ and $\beta_{\rm i}$ (i = 0, 1, 2) are coefficients we obtain from the least-square fits and the functions are defined over the intervals $L_{\rm min}$ = [0.0, 1.7] mJy kpc^2 and p = [1.4, 2.6]. We note that, although Cordes and Chernoff (1997) obtained $f(L_{\rm min})$ over $L_{\rm min} \simeq$ [0.3, 2] mJy kpc^2 centered at 1.1 mJy kpc^2, we consider $f(L_{\rm min})$ with a peak at $\sim$ 0.8 mJy kpc^2 considering the discoveries of faint pulsars with L_{1400} below 1 mJy kpc^2 (Camilo 2003).

We use the above priors to calculate $P_{global}(\mathcal{R})$:

$$P_{global}(\mathcal{R}) = \int_p dp \int_{L_{\rm min}} dL_{\rm min} P(R) f(L_{\rm min}) g(p) \; . \qquad (1)$$

In Figure 2, we show the distributions of p and $L_{\rm min}$ adopted (top panels) and the resulting global distribution of Galactic NS-NS merger rate estimates (bottom panel). We find that the global $P(\mathcal{R})$ is strongly peaked at *only* around $15\,\mathrm{Myr}^{-1}$. We note that this is a factor $\simeq 5.5$ smaller than the revised rate from the reference model ($\mathcal{R} = 83\,\mathrm{Myr}^{-1}$). At the 95% confidence interval, we find that the Galactic NS-NS merger rates lie in the range $\sim$ 1–170 Myr^{-1}. These imply LIGO event rates in the range $\sim (0.4 - 70) \times 10^{-3}\,\mathrm{yr}^{-1}$ (initial) and $\sim (2 - 380)\,\mathrm{yr}^{-1}$ (advanced). Given these implications, it is clear that up-to-date constraints on $L_{\rm min}$ and p and their PDFs (a follow-up on Cordes & Chernoff 1997) are urgently needed.

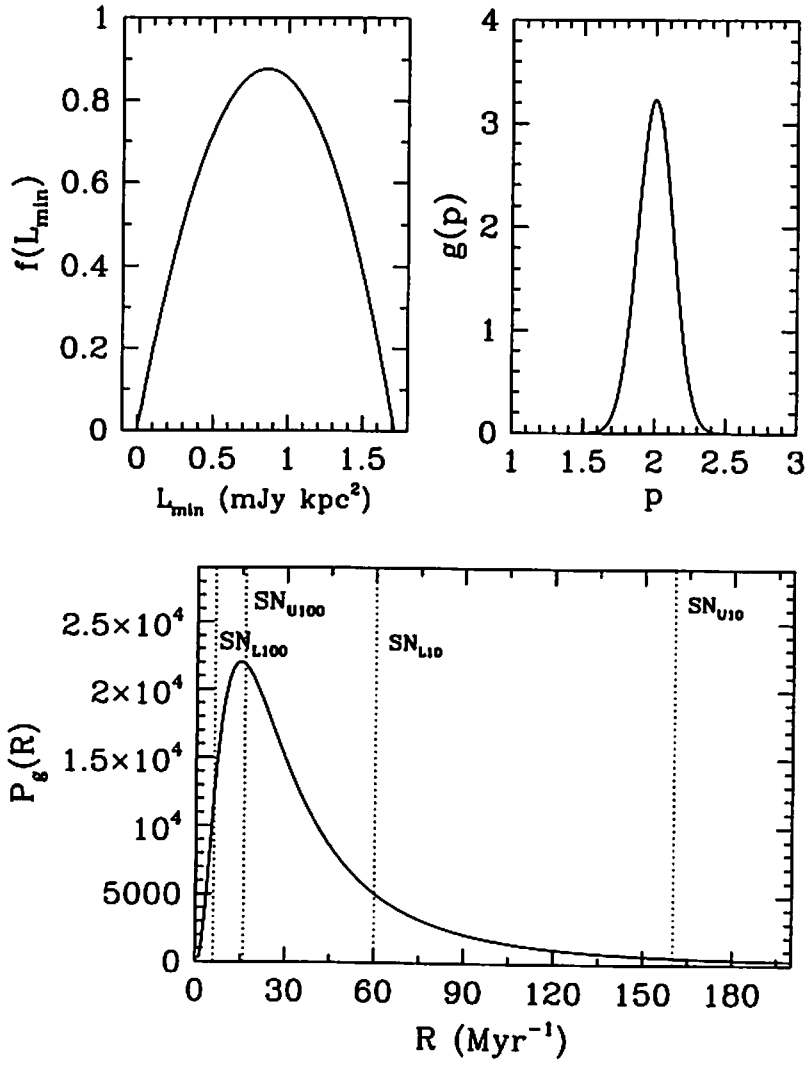


Figure 2: The global $P(\mathcal{R})$ on a linear scale (lower panel) and the assumed intrinsic distributions for $L_{\rm min}$ and p (upper panels). Dotted lines represent the lower ($SN_{\rm L}$) and upper ($SN_{\rm U}$) bounds on the observed SN Ib/c rate scaled by 1/10 and 1/100 (see text). The empirical SN Ib/c rates range over $\sim 600 - 1600\,{\rm Myr}^{-1}$ (Cappellaro, Evans, & Turatto 1999), beyond the range shown here.

4 Rate Constraints from Type Ib/c Supernovae and Binary Evolution Models

Based on our current understanding of NS-NS formation, the progenitor of the second neutron star is expected to form during a Type Ib/c supernova. Therefore, the empirical estimates for the Type Ib/c SN rate in our Galaxy can be used to provide upper limits on the NS-NS merger rate estimates. From Cappellaro, Evans, & Turatto (1999) we adopt $\mathcal{R}_{\rm SN\,Ib/c} \simeq (0.11\pm0.05)\times10^{-2}\,{\rm yr}^{-1}$ (for Sbc–Sd galaxies and $H_0 = 71$ km/s/Mpc).

In order to find the fraction of SN Ib/c actually involved in the formation of NS-NS, we have examined population synthesis models calculated with the code `StarTrack` (Belczynski, Kalogera, & Bulik 2002; Belczynski et al. 2005) and find very low rate ratios between NS-NS and SN Ib/c: $\gamma \sim 0.001 - 0.005$. Several models with He-star winds consistent with current observations (weaker than previously thought) lead to $\gamma \simeq 0.005$. We note that systematic overestimation of $\mathcal{R}_{\rm SN\,Ib/c}$ relative to SN II rates has already been pointed out (Belczynski, Kalogera, & Bulik 2002; this is related to the assumption of *complete* removal of H-rich envelopes). However, we find that this discrepancy would raise the value of γ by just a factor of a few. As an approximate constraint, we adopt the empirical $\mathcal{R}_{\rm SN\,Ib/c}$ and scale it by 1/10 and 1/100, reflecting the results from population synthesis calculations. We overlay the scaled values onto the result for our global $P(\mathcal{R})$ (Fig. 2; dotted lines in the bottom panel).

We note that the empirical $\mathcal{R}_{\rm SN\,Ib/c} \sim 1100\,{\rm Myr}^{-1}$ is comparable to our estimated NS-NS merger rate for the most optimistic NS-NS model (Model 15 in KKL), ($\mathcal{R} = 224^{+594}_{-181}\,{\rm Myr}^{-1}$ at a 95% confidence interval). Here, we assume $L_{\rm B,gal} = 9\times10^9\,L_{\rm B,sun}$. Considering the uncertainty in the blue luminosity of our Galaxy (a factor of a few), it is safe to consider our NS-NS merger rates consistent with the observed SN Ib/c rate. However, if the true number of SN Ib/c relevant to NS-NS formation is smaller than the total observed rate by a factor 100, we have $\mathcal{R} \leq 15\,{\rm Myr}^{-1}$, which is a fairly strong constraint on the rate estimates.

5 Empirical rate constraints from Wide NS-NS Binaries

As mentioned in the Introduction we use the observed sample of NS-NS binaries (both merging and wide) to constrain population synthesis models and predictions for black-hole merger rates. Following the same general technique as outlined in KKL we extracted estimates for the formation rates of NS-NS binaries similar to each of the observed wide NS-NS binaries. In the absence of any observations to constrain the beaming angle in these binaries, we have made conservative assumptions in a manner consistent with the observed beaming angles in the merging NS-NS binaries and we adopt a beaming factor of 5. For simplicity, we adopt the results for only the preferred luminosity model (Model 6 in KKL). For more details see O'Shaughnessy, Kalogera, & Belczynski (2005; hereafter OKB).

6 Merger Rates from Population Synthesis Models

We estimated formation and merger rates for several classes of double compact objects using the *StarTrack* code first developed by Belczynski, Kalogera, & Bulik (2002) and recently significantly updated and tested as described in detail in Belczynski et al. (2005). In this code, seven parameters strongly influence compact object merger rates: the supernova kick distribution (3 parameters), the solar wind strength (1), the common-envelope energy transfer efficiency (1), the fraction of angular momentum lost to infinity in phases of non-conservative mass transfer

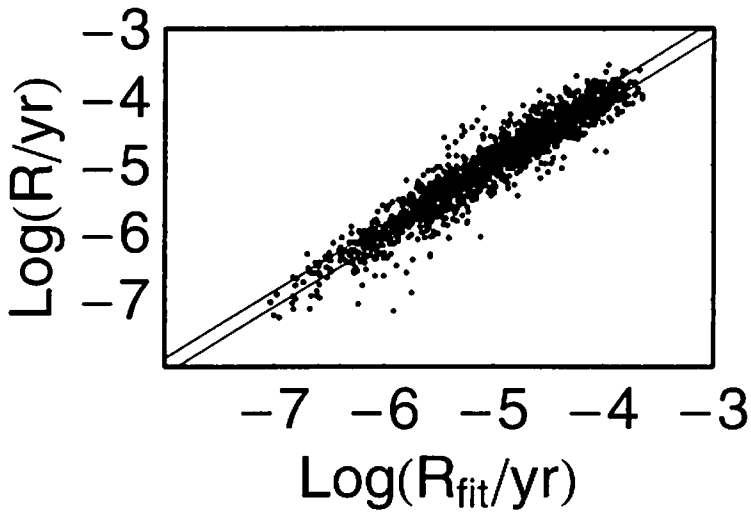


Figure 3: This plot of the $\log_{10}$ of the rate versus our fit to the rate, shown for all three BH-BH, BH-NS, and NS-NS sample points. The shaded region is offset by a factor $1 \pm 1/\sqrt{10}$. This region estimates the error expected due to random fluctuations in the number of binary merger events seen in a given sample.

(1), and the relative distribution of masses in the binary (1). To allow for an extremely broad range of possible models, we used the specific parameter ranges quoted in OKB.

We proceeded to randomly choose model parameters in this space and evaluate their implications, by progressively examining the evolution of binary after binary. We then extracted from our simulations predictions for several DCO formation rates (BH-BH, BH-NS, and NS-NS) by scaling up the ratio of DCO formation events we observed in each simulation (n) to the total number of binaries studied in the simulation (N) by a factor proportional to the expected ratio between N and the number of stars in the Milky Way, as described in the Appendix of OKB.

Extracting predictions for the visible NS-NS formation rates: To compare the predictions of population synthesis calculations against what is observed – that is, against detections of spun up pulsars in NS-NS binaries – we additionally determined the formation rate of the "visible" NS-NS binaries: those binaries similar enough to the observed spun-up pulsar systems. These systems will consist of all binaries in which one NS is spun up through a mass transfer episode (Roche-lobe overflow or common-envelope).

OKB first demonstrated that, even using sparse data in a high-dimensional space of population synthesis parameters, an effective fit could be found for formation rates of DCOs (cf. OKB Fig. 2 and their Section 4). We constructed separate polynomial (cubic) least-squares fits to each of the five rate functions. Figure 3 demonstrates that the fit is good: the errors are on the limiting scale we would expect, given the uncertainties in the input. The fits are sufficiently good that for our purposes we can replace population synthesis calculations with evaluations of our fits. In particular and by way of example, in Figure 4 we generate a histogram for various DCO formation rates predicted by population synthesis, using (i) the actual outputs deduced from the population synthesis code, sampled at random Monte Carlo points, and (ii) the outputs obtained from fits to the previous dataset, sampled at a much larger number of data points (to insure smoothness). The two methods produce strikingly similar histograms, demonstrating

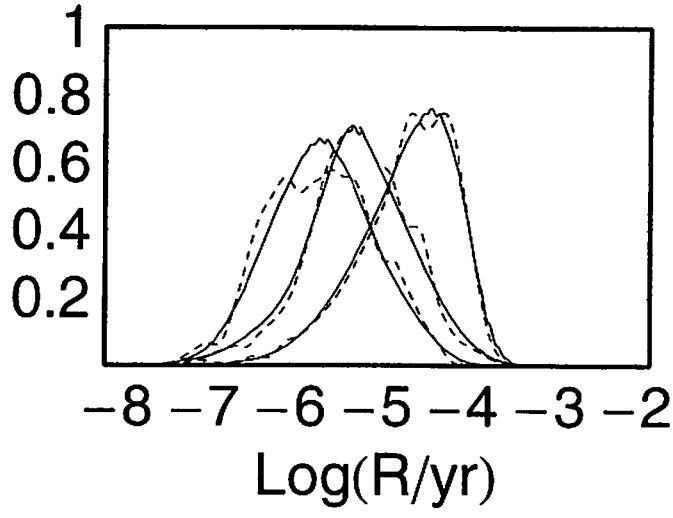


Figure 4: A plot of the a priori probability distribution for the BH-BH (leftmost set of curves), BH-NS (middle), and NS-NS (rightmost) merger rates, versus the $\log_{10}$ of the rate. These distributions were generated from the population synthesis code (solid) and fits (dashed) assuming all parameters in the population synthesis code were chosen at random in the allowed region.

that the fit will be adequate for our purposes.

7 Constraints from NS-NS observations

We have so far constructed two straightforward empirical constraints (i.e., confidence intervals for the formation rate of visible merging and wide NS-NS binaries) we could impose on the output of population synthesis calculations. In this section, we apply these two constraints, both separately and together, and determine their effect on concrete predictions of population synthesis calculations.

Bounding merging NS-NS rate: If we limit attention only to those population synthesis models which predict a "visible" (i.e., having a mass-transfer episode onto one NS) NS-NS merger rate to be consistent with the confidence interval 95%, then we exclude 76% of all models we initially considered plausible. When this single constraint is applied, we see the NS-NS and BH-NS merger rates go up substantially (a factor of 2.84, 2.55, respectively) and the BH-BH rate drops slightly.

Bounding wide NS-NS rate: On the other hand, if we consider only parameter combinations which produce a visible wide NS-NS formation rate consistent with that rate's empirical confidence interval (95%), we exclude 70% of a priori plausible models. Moreover, using only models which satisfy this second constraint, we find compact object merger rates have dropped relative to our a priori predictions: the average BH-BH rate drops by a factor of about 0.6, and the NS-NS and BH-NS rates drop by a factor of about 0.3.

Both constraints simultaneously: Very few population synthesis models (less than 2%) satisfy both constraints simultaneously. Since the set of consistent models is much smaller than initially permitted a priori, we have much less uncertainty in our predictions: the standard deviation in the log of the merger rates has dropped from our initial a priori uncertainty of 0.60, 0.55, and

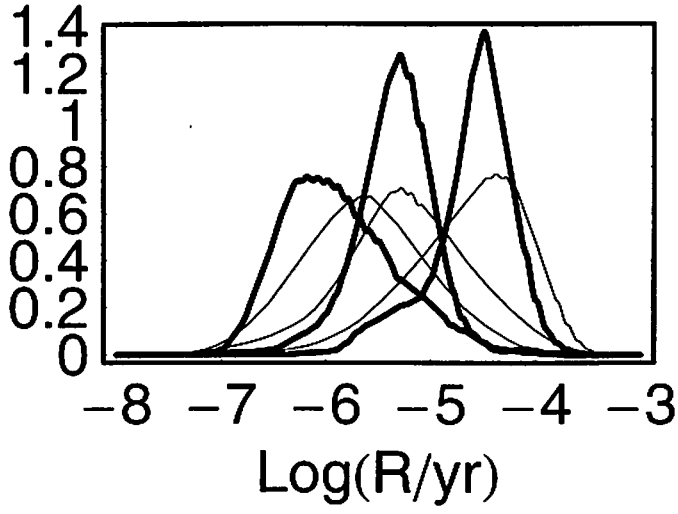


Figure 5: A plot of the probability distributions for the BH-BH (leftmost), BH-NS (middle), and NS-NS (rightmost) merger rates, versus the $\log_{10}$ of the rate without (thin) and with (thick) our two constraints.

0.63 (i.e., plus or minus a factor of 4, 3.5, and 4.3) for BH-BH, NS-NS, and BH-NS mergers, respectively, to 0.51, 0.38, and 0.37 (i.e., plus or minus a factor of 3.3, 2.4, and 2.3). However, the mean values have changed little from their prior expectations: the average predicted merger rates are 1.4/Myr [BH-BH], 4.7/Myr [BH-NS], and 25/Myr [NS-NS]. Results are shown in Figure 5 and it is clear that the constrained probability functions are tighter than those derived directly from population synthesis models.

8 Summary of Constrained Population Models

In the context of matching theory with observations of the binary NS population, we have described how to constrain the parameters that enter into population synthesis codes such as *StarTrack* by using multiple observational constraints. We find that to be consistent with the statistics of the observed NS-NS population, we must exclude at least 98% of all the models we think a priori likely. We have not, however, explicitly described the seven-dimensional region of StarTrack model parameters consistent with our constraints, both because (i) we lack a compact way to describe a seven-dimensional region and (ii) our region has meaning specifically for the StarTrack code. Other codes will have different parameterizations of the same physical phenomena, leading to potentially quite different representations of the same constraint region.

Instead, to extract a representation-invariant prediction about the effect of imposing constraints, we have described how these constraints have improved our understanding of DCO merger rates for BH-BH, BH-NS, and NS-NS binaries.

Acknowledgments: We would like to thank Kip Thorne for suggesting incorporating the systematics into a single PDF, Takashi Nakamura and Steinn Sigurdsson for raising the question of Ib/c SN rates. We also thank Tassos Fragkos and Mia Ihm for help in the caluclations

presented here. This research is partially supported by NSF Grant 0353111, a Packard Foundation Fellowship in Science and Engineering and a Cottrell Scholar Award by the Research Corporation to VK. KB also acknowledges support from grant PBZ-KBN-054/p03/2001.

References

[1] Abramovici, A., et al. 1992, Science, 256, 325

[2] Arzoumanian, Z., Cordes, J.M., & Wasserman, I. 1999, ApJ, 520, 696

[3] Belczynski, K., Kalogera, V., & Bulik, T. 2002, ApJ, 572, 407

[4] Belczynski, K., Kalogera, V., Rasio, F.A., & Taam, R.E. 2005, ApJ, submitted

[5] Burgay, M., et al. 2004, Nature, 426, 531

[6] Camilo, F. 2003, in Radio Pulsars, ed. M. Bailes,D.J. Nice, & S.E. Thorsett (ASP Conf. Series, Vol. 302), 145

[7] Cappellaro, E., Evans, R., & Turatto, M. 1999, ApJ, 351, 459

[8] Cordes, J.M., & Chernoff, D.F. 1997, ApJ, 482, 971

[9] Hulse R.A., & Taylor J.H. 1975, ApJ, 195, L51

[10] Kalogera, V., et al. 2001, ApJ, 556, 340

[11] Kalogera, V., Kim, C., & Lorimer, D.R. 2003, in Radio Pulsars, ed. M. Bailes, D.J. Nice, & S.E. Thorsett (ASP Conf. Series, Vol. 302), 299

[12] Kalogera, V., et al. 2004, ApJ, 601, L179

[13] Kim, C., Kalogera, V., & Lorimer, D.R. 2003, ApJ, 584, 985 [KKL]

[14] Kim, C., et al. 2004, ApJ, 616, 1109

[15] Lorimer, D.R., et al. 2005, in Radio Pulsars, ed. F.A. Rasio & I.H. Stairs, (ASP Conf. Series, Vol. 328), in print

[16] O'Shaughnessy, R., Kalogera, V., & Belczynski, K. 2005, ApJ, 620, 385

[17] Peters, P.C., & Mathews, J. 1963, Phys. Rev., 131, 435

[18] Wolszczan, A. 1991, Nature, 350, 688

GRAVITY PROBE B: Experiment and Mission

Paul Shestople[1], M.E. Adams, W.J. Bencze, K. Bower, R.W. Brumley, S. Buchman, B. Clarke, D. DeBra, M. Dolphin, C.W.F. Everitt, C. Gray, G. Green, M.I. Heifetz, D.N. Hipkins, T. Holmes, B.T. Jones, G.M. Keiser, T. Langenstein, M. Lemieux, J. Li, J. Lockhart*, P.M.C. McGown, H.D. Meriwether, J. Mester, B. Muhlfelder, D. Murray, J.R. Newquist, Y. Ohshima, B.D. Owens, B.W. Parkinson, S. Patterson, C.C. Perry, G.V. Picard, M. Salomon, D.I. Santiago, R.J. Sharbaugh, A.S. Silbergleit, V. Solomonik, J Spencer, K.A. Stahl, B.A. Stroozas, M.A. Taber, B. Tham, J.P. Turneaure, J. Wade, C.E. Westblom, S.M. Young

W.W. Hansen Experimental Physics Laboratories, Stanford University, Stanford, CA 94305-4085

**Also at Department of Physics and Astronomy, San Francisco State University, 1600 Holloway Ave, San Francisco, CA 94132-4163*

Abstract

The Gravity Probe B satellite was launched on April 20th, 2004, at 17:57:24 UTC. The science data collection phase of the mission began on August 28th, at 00:08:32. Prior to that, the satellite was in the Initialization and On-orbit Checkout (IOC) phase. During the nineteen weeks of IOC, all payload subsystems were thoroughly tested and calibrated, science gyroscopes were spun up and aligned towards the guide star. Many additional activities occurred. This paper will give background on the Gravity Probe B experiment, discuss payload subsystems, highlight IOC activities, and present the current mission status, as of January 6, 2005. The paper will conclude with an outline of future planned activities.

1 Introduction

Two years after the launch of Sputnik 1 by the Soviet Union, George Pugh[1] (1959) and Leonard Schiff[2,3] (1960) independently realized that an orbiting gyroscope could be used to test general relativity. Specifically, two effects could be observed by monitoring the drift of the spin axis of an orbiting gyroscope: The Frame Dragging effect and the Geodetic effect. Frame dragging, also called the Lense-Thirring effect, is the notion that a rotating mass will drag local inertial frame. This effect is also called gravitomagnetism, in analogy with classical electrodynamics. The Geodetic effect is a relativistic warping of local space time caused by a massive object. The Gravity Probe B (GP-B) experiment is designed to measure these effects to an accuracy of better than 0.5 mas/yr (milli-arc-sec/year).

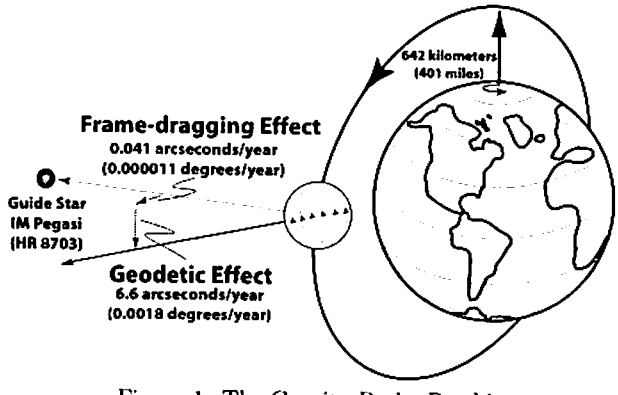


Figure 1: The Gravity Probe B orbit

[1]E-mail: shestopl@relgyro.stanford.edu

The experimental concept is deceptively simple. Merely observe the spin axis orientation of a spinning mechanical gyroscope in an inertial frame isolated from Newtonian torques. In practice, four gyros are mounted inside the Gravity Probe B satellite, which is in a low Earth, polar orbit, at an altitude of 642 km. An inertial frame is established by pointing the satellite towards a single guide star, IM Pegasi, in the constellation Pegasus. The two effects are orthogonal in a polar orbit (see figure 1). The predicted magnitude of the frame-dragging effect is 41 mas/yr at GP-B's altitude. The predicted magnitude of the Geodetic effect at GP-B's altitude is 6.6 as/yr (arc-sec/year). More precise values will be computed based on on-orbit data[4]. For a more rigorous background regarding the Gravity Probe B experiment, please see reference 5.

2 Payload Subsystems

GP-B is perhaps the most sophisticated satellite ever flown. The complexity arises from the motivation to minimize classical torques and noise sources. Those goals require the large number of payload subsystems, all of which must work in harmony to achieve the desired measurement. At the core of the experiment are the four gyroscopes, contained within the gyroscope housings. The housings are rigidly mounted inside a fused quartz block. The quartz block is mated to a Cassegrain telescope such that the spin axis of the gyroscope is precisely aligned with the boresight of the telescope. The quartz block, telescope and gyroscopes are referred to as the Science Instrument Assembly (SIA). The SIA is attached to a cryogenic probe, enclosed in a vacuum can, and then inserted into the flight Dewar while maintained at low temperature. The residual gas pressure inside the vacuum can is less than 10^{-11} torr. At the time of launch, the Dewar contains 2317 liters of superfluid liquid helium at 1.8 K, a quantity sufficient to keep the experiment at cryogenic temperatures for the duration of the mission. The satellite structure is built around the Dewar, and subsystem electronics boxes are fastened to the structure.

Significant integration testing was conducted prior to launch to verify proper functionality. In this section, the Gyroscope Suspension, Superconducting QUantum Interference Device (SQUID) Readout Electronics, Attitude and Translation Control, Telescope Readout Electronics, Experimental Control Unit, and Global Positioning System subsystems are discussed.

The Gyroscope Suspension System (GSS) has several essential functions. During launch the gyroscopes were not spinning, and were, in fact, resting inside their housings. Once on orbit, each gyroscope must be electrostatically levitated, and spun up to the desired spin speed using helium gas at 6 K, accomplished in a series of steps. Once levitated and spun up, each gyroscope must be aligned towards the guide star, as will be discussed further. Finally, the GSS must ensure that a spinning gyroscope never touches the housing; the rotational energy of a spinning gyroscope is sufficient to catastrophically damage the gyroscopes and the housing, effectively destroying that gyroscope. To accomplish these tasks the GSS has four controllers: a digital controller for normal operations, and three analog controllers used during auxiliary operations and as backups. While the digital controller offers the least amount of control authority, and therefore exerts the least amount of electrostatic torque on a gyroscope, it cannot provide sufficient stiffness to ensure gyroscope safety in the event of, say, a micrometeoroid strike. The analog controllers therefore take control if the gyroscope exceeds preset radius limits. The analog controllers exert considerably more electrostatic torque on the gyroscope, undesirable for normal operations, but required during the auxiliary operations of spin-up and spin axis orientation.

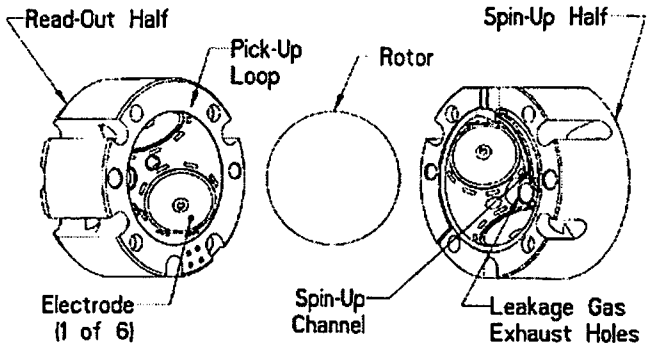


Figure 2: Gyroscope and Housing. Note the electrodes, gas spin-up channel and SQUID pickup loop position.

Figure 2 shows the gyroscope and housing. Several features merit comment. The gyroscope, or gyro, is fabricated from quartz and coated with niobium. The gyros are perhaps the most spherical objects ever manufactured - if increased to the same diameter as the Earth, the largest deviation from perfect sphericity would be less than 3 meters. The niobium coating allows the gyros to be electrostatically manipulated by three orthogonal pairs of electrodes. Each gyro is spun up by flowing helium gas through the spin-up channel, tangential to the gyro. The leakage gas exhaust holes are used to evacuate the gyro housing during and after the spin-up operation, since the pressure in the housing directly effects the spin-down rate of the rotating gyroscope. Also shown in figure 2 is the location of a four turn, superconducting pick-up loop, used by the SQUID readout electronics (SRE) discussed in the next paragraph. Additional information about the GSS subsystem can be found in reference 6.

The instrument is designed such that the gyro spin axis is nearly in the plane of the niobium pick-up loop. Recall that niobium is a superconductor. A spinning superconductor generates a magnetic field aligned with its instantaneous spin axis, called the London magnetic dipole moment. The London moment can be detected by the pick-up loop, provided the loop is attached to a sufficiently sensitive detector. GP-B uses a SQUID as the detector, sensitive enough to resolve an angle of 1 mas (milli-arc-second) in 5 hours. The SRE also contains a precision oven controlled crystal oscillator, which oscillates at 16.368 MHz, from which all satellite time is derived.

A brief digression regarding GP-B's orbit. Since the guide star is, on average, in the orbital plane of the satellite, the Earth eclipses the guide star during roughly half of every orbit. GP-B has a telescope mounted such that the spin axis of the gyroscopes is precisely aligned with the boresight of the telescope. When the guide star is not eclipsed, GP-B's telescope is used to track the relative position of the optical center of the guide star. Because GP-B collects valid data only while the guide star is within the linear range of the telescope, it is important that the telescope begin tracking the guide star as quickly as possible after the end of every eclipse period.

The Telescope Readout Electronics subsystem (TRE) works with the Attitude and Translation Control subsystem (ATC) to ensure that the telescope is pointed to within 200 mas of the guide star's optical centroid when the guide star is in view. The ATC keeps the satellite pointed towards the known position of the guide star during the eclipse periods. The TRE's Cassegrain telescope contains roof prisms, located at the image of the star, which divide the focused image into separate beams, and four sets of redundant silicon photodiodes, two sets each for the telescope's X and Y axes. When the relative photocurrent of each set of photodiodes is equal (after calibration), the optical center of the guide star is in the center of the telescope's field of view. The ATC's sixteen micro-thrusters, which use boil-off gas from the liquid helium Dewar as a propellant, enable precision adjustment of the satellite's attitude to keep the guide star in the center of the field of view. The thrusters also enable drag-free operation, as will be discussed below. The ATC also has star sensors and rate gyroscopes which allow the ATC to point towards the last

known position of the guide star during eclipse periods. The star sensors, rate gyroscopes and thrusters enable smooth rotation of the satellite about the telescope axis, averaging body-fixed torques towards zero.

GP-B is heavily instrumented with operational sensors, e.g. thermometers, whose data must be telemetered to the ground. The Experiment Control Unit (ECU) provides access to that data, and also provides other key functions. Primary among these functions is control of the Gas Management Assembly (GMA), used to spin up the gyros at the start of the mission. A Proton Detector, and a set of four three-axis Magnetometers are used to track the radiation and magnetic environment of the satellite, and are also controlled through the ECU. Ionizing radiation increases the gyro potential by about 0.1 mV per day; an ultraviolet lamp controlled through the ECU is used to discharge the accumulated charge.

Finally, GP-B is outfitted with a redundant pair of Global Positioning System (GPS) receivers. The GPS subsystem provides relatively coarse orbit position and velocity data. Ground processing uses that data to calculate precise satellite ephemeris, augmented by laser ranging position solutions. The GPS subsystem is retrofit with electronics which output a pulse per second (PPS), on the GPS second. That pulse is fed into the SRE, and allows reconciliation of satellite time with Coordinated Universal Time (UTC).

Before moving on to IOC activities, it is worth noting that every effort has been made to remove single-point failures from the GP-B mission. For example, only one science gyroscopes are needed, yet four are flown. Similarly, most of the electronics subsystems described above have built-in redundancy, and many of the electronic subsystems have a fully functional backup on-board. In this way, the satellite has, in effect, two quasi-independent sides, both of which are capable of achieving mission goals. While the mission is designed to operate on side A, catastrophic failure of any subsystem results in an automatic switch to side B.

3 Initialization and On-orbit Checkout activities

The spin-up of gyroscopes is but one of literally thousands of activities which occurred during the IOC phase of the mission. Stanford maintains a complete listing of the activities, which fills several large filing cabinets. The activities can be categorized into three areas: 1) Verification and optimization of satellite performance, 2) verification and optimization of payload performance, and 3) verification and optimization of the science mission setup. What follows is a highlight of activities broken down by week, and is meant only to provide the flavor of IOC operations, as well as additional details regarding the complexity of the mission.

On the first day of the mission the satellite was vaulted into space atop a Boeing Delta II 7920-10 expendable launch satellite. Because the GP-B target orbit is highly constrained, significant pre-launch effort had been dedicated towards correcting any possible initial orbital error. Happily, none was needed, as Boeing placed the satellite into an orbit which can only be described as a bull's eye. Shortly thereafter, and for the next several days, the various subsystems were turned on and self tested to verify on-orbit functionality. Towards the end of the first week one of the sixteen ATC micro-thrusters was turned off, as it had developed a leak.

The gyroscopes were successfully suspended in digital mode for the first time during the second week of the mission. Two radiation induced multi-bit memory upsets occurred within one second in the main flight computer, automatically switching the satellite to the B side. Only one such multi-bit error (MBE) is predicted during the course of the mission; it was quite surprising that two MBEs should occur during week two. While the single bit error (SBE) rate agrees with pre-launch predictions, GP-B has shown a higher than anticipated susceptibility to MBEs. The increased susceptibility is under investigation. While the mission could have continued to operate on the B side, the decision was made to return to the A side. The return to the A side was a significant and complicated effort which took the rest of the week,

but went very well.

During the third week, mission operators practiced a low temperature bake-out. The low temperature bake-out reduces the residual gas pressure in the gyro housing, thereby reducing the spin down rate of the gyroscope. The operation did result in the partial spin-up of the gyroscopes to about 5 mHz. As will become clear, typical operational mode for the IOC phase is to first practice high risk operations in a low risk scenario, in some cases several times. This is done because the complexity of the GP-B satellite leaves little margin for error.

To best reduce classical torques on the gyroscopes, the satellite is flown drag-free about one of the gyroscopes, meaning that one gyroscope is essentially in free fall, with the satellite flying around it. During week 4 a position based method for flying drag-free was achieved for the first time. ATC star sensors were used to roughly align the science telescope with the guide star, and a series of small maneuvers were started to locate the guide star.

Because determination of gyro spin axis orientation is based upon the London moment, the experiment requires a very low background magnetic field. The magnetic properties of each component were carefully measured prior to assembly, but without a clever exploitation of superconducting properties the Earth's magnetic field would have dominated the magnetic field within the Dewar. A lead bag was cooled below its superconducting transition temperature, then expanded, leaving a significantly lower field within. By using a series of lead bags during the Dewar preparation process, GP-B was able to achieve a background magnetic level of 10^{-7} gauss, prior to insertion of the Science Instrument Assembly. Additional magnetic fields, however, are generated and trapped in the gyro rotors by the launch environment, and in week five a magnetic flux reduction procedure was completed, reducing the trapped flux to acceptable limits.

A second micro-thruster was turned off during week five. Although the loss of the second thruster does not adversely affected the satellite's ability to fly drag-free, the additional loss of any one of several key micro-thrusters would have. For that reason, it was decided to develop a new thruster control algorithm. As will be seen, the development would take several weeks.

During week six, mission specialists performed a low flow spin-up procedure, flowing just 2 sccm (standard cubic centimeters per minute) past the gyros for 90 seconds, to practice the process of spinning up the gyroscopes and verify functionality of all subsystems required for the full spin-up. The practice spin-up resulted in a gyro spin speed of approximately 0.3 Hz. Note that the helium gas used for gyro spin-up comes from a reservoir of gas within the GMA, not from boil-off of the liquid helium used to cool the experiment.

The guide star was acquired with the science telescope during week seven. The satellite was then maneuvered so as to point the science telescope towards a series of adjacent stars.

A brief digression concerning the guide star is in order. HR 8703 is a variable star in a binary system in the Pegasus constellation. The star's position relative to extragalactic reference sources was first measured by the Very Long Base Interferometer (VLBI) in December of 1991, and has been measured at least 29 times since 1991[7]. The star's position relative to extragalactic reference sources is perhaps the best known in the catalogue. The periodicity of the variable star is also well documented, allowing additional calibration of the science telescope. Such detailed understanding is essential for the mission, as was the maneuver towards the two adjacent stars to confirm that the guide star being used was indeed IM Pegasi.

A series of practice calibration tests involving the application of asymmetric science gyro suspension voltages were started during week seven and continued through week ten. The tests were designed to exert a well understood torque on the gyroscopes. The actual tests will be run on the fully spinning gyroscope at the end of the mission, during the post-science calibration phase.

Also during weeks seven and eight, mission operators successfully demonstrated the ability to discharge the science gyroscopes to specification (< 15 mV) and successfully tested a control-effort based method of flying drag-free for one orbit. The control-effort drag-free mode minimizes the GSS control efforts on the gyroscope, while the position drag-free mode applies no control effort to the gyroscope. Both modes are sufficient to meet mission requirements, but the control-effort drag-free mode turned out to be more robust, and was therefore chosen as the mission baseline drag-free mode.

During weeks nine and ten the roll rate of the satellite was increased from 0.1 rpm to 0.9 rpm for several reasons. The mass of the satellite must be properly balanced to allow the satellite to roll precisely about the telescope boresight. Gravity Probe B has five mass balance mechanisms, each essentially a weight on an motorized, threaded rod, which allow sub-millimeter adjustments to the center of mass and cross products of moments of inertia. Additionally, increasing the satellite's roll rate increases the likelihood of wrapping the gaseous helium bubble about the well of the Dewar (which houses the cryogenic probe and SIA). Furthermore, a higher roll rate places the science signal in a more quiet region of the SQUID noise spectrum, and decreases thermally induced bias errors. The desire for a higher roll rate is balanced against the ATC and GPS subsystems decreasing performance at a higher roll rate.

Also during week ten, the GSS team applied 120 percent of the expected gyro spin-up voltages as a stress/health test in preparation for gyro spin-up; all gyroscopes worked perfectly. Mission programmers completed the reworked ATC control algorithm in week ten; the new code was uploaded in week eleven. Implementing the new code required rebooting the flight computer. As planned, during the four minute reboot process the satellite was completely out of contact with the ground. The procedure was perfectly executed.

During week twelve all four science gyroscopes were successfully spun up to approximately 3 Hz. The spin-up process required the maximum flow rate of 700 sccm for 90 seconds. Calibration testing of the gyros took the remainder of the week. Additionally, the satellite roll rate was reduced to 0.5 rpm. During week thirteen gyro 4 was successfully spun up to 106 Hz. The full spin-up used the maximum flow rate for several hours. Gyroscopes 2, 3, and 1 were spun up during week fourteen. As anticipated, because all four gyroscopes are in the same vacuum probe, the spin-up of one gyro causes spin down of the other gyros. The final spin speed for the four gyros was 79.4, 61.8, 82.1, and 64.9 Hz.

Weeks fifteen through nineteen were devoted primarily to spin axis alignment, a process of applying torques to the gyros in order to align the spin axis with the guide star. Alignment rates were significantly lower than predicted, suggesting that gyro sphericity is much better than required, and electrostatic interaction between the gyroscopes and the GSS is also lower than anticipated. Since electrostatic torques are the largest torques on the gyroscopes, the lower than predicted alignment rates were very welcome news, although it did require the spin axis alignment process to take longer than anticipated. The final alignment of the gyroscope spin axis was completed for gyros 1, 2 and 3 on August 28, and on September 14 for gyro 4. The satellite's roll rate was set to 0.77419 rpm (a 77.5 second period) for the science mission, a good balance between science and engineering needs.

4 Current Status

As of January 6, 2005, day 261 of the mission, the Gravity Probe B satellite and all subsystems are performing nominally.

The gyroscopes continue to operate as required. As previously mentioned, the sphericity of the gyroscopes is better than pre-launch estimations: The distance between the geometric center of each gyroscope and center of mass has been calculated to be on the order of five nanometers for all four gyros. The gyroscopes are experiencing a polhode motion[8], as predicted prior to launch. Not predicted was that the period of the polhode motion would change, decreasing towards an asymptotic value.

Current spin speeds and spin down rates of the gyroscopes are given in table 1. For a gyroscope spinning at 60 Hz, a spin down rate of 0.50 μHz/Hr corresponds to an exponential spin down time constant of almost 14,000 years.

Table 1: Spin Speeds and Spin Down Rates as of January 6, 2005

Gyroscope	Spin Speed (Hz)	Spin Down Rate (μHz/Hr)
1	79.3879	0.61
2	61.8181	0.51
3	82.0930	1.35
4	64.8506	0.32

Guide star acquisitions by the ATC occur typically one minute after the guide star comes within view; the guide star remains within the linear range of telescope better than ninety percent of the approximately fifty minute guide star valid period.

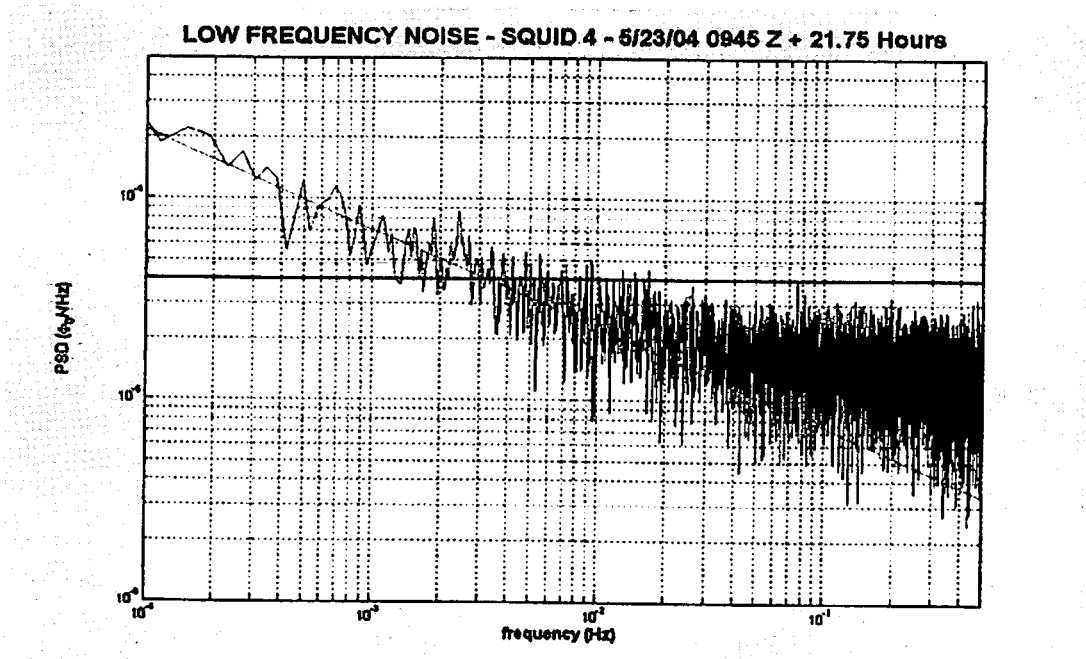


Figure 3: SQUID Readout Electronics Noise. The heavy line is the noise requirement. The science signal occurs at the roll frequency of 12.9 mHz.

The SRE is performing very well; the SQUID noise is lower than specifications, as seen in figure 3.

The GPS subsystem is performing extremely well. The subsystem maintains a lock with the GPS constellation better than 98 percent of the time at the current roll rate of 0.77419 rpm.

Orbit Determination is performing exceptionally. GP-B uses a commercial software package to calculate post-processed orbits. Based on overlapping post fit residuals between consecutive datasets, on-orbit cross-track position accuracy is less than 10 meters, while cross-track velocity accuracy is less than 8 mm/s.

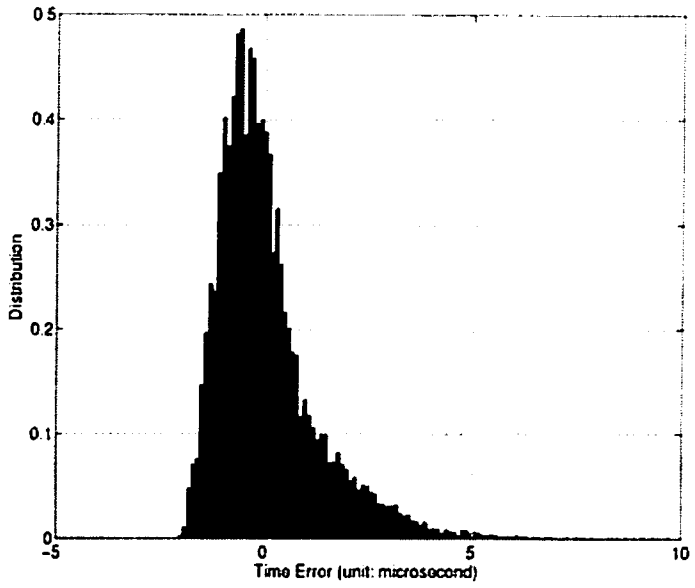


Figure 4: Time Transfer.

Time transfer has also been successful. Daily analysis includes calculating the time difference of Pulse Per Second (PPS) to integer GPS second. Differences are typically less than 2 microseconds, as shown in figure 4. The difference arises because the PPS circuitry within the GPS receiver only calculates a time, position, and velocity solution every 1.7 seconds, whereas the PPS signal is output every second. The receiver determines the time of the GPS second between consecutive solutions based on an internal 1.023 MHz oscillator.

5 Future Work

During the IOC phase of the mission a variety of calibrations were completed to characterize GP-B performance, primarily torques. These calibrations included measurements of the telescope and SQUID noise (see figure 3), measurements of thermal sensitivity of payload electronics, and of telescope and gyro readout scale factors. Post science phase calibrations will be started several weeks prior to running out of liquid helium. In addition to redoing many of the IOC phase calibrations in order to understand how the calibrations vary with time, new calibrations are planned which will place tight constraints on potential systematic errors.

For example, a number of calibrations involve applying enhanced torques to the science gyroscopes are planned. These calibrations were practiced from week seven through ten of IOC, when the gyroscopes were spinning at just 3 Hz. The satellite will also be maneuvered towards the adjacent stars, as was done during week seven of IOC. This maneuver will further calibrate the telescope, since the photocurrent can be compared to the earlier values. Dark currents can be measured by closing the telescope shutter. Other potential calibrations include applying a fixed acceleration to the satellite to understand how induced torques affect the gyros.

6 Conclusion

The Gravity Probe B satellite has completed the Initialization and On-orbit Checkout Phase and as of this writing has been collecting science data for eighteen weeks. All satellite and science subsystems required for completion of the mission are nominal. The Dewar liquid helium depletion rate is small enough to provide adequate time to complete the science phase and post-science calibrations.

With almost half of the science phase behind us, and post science phase calibrations before us, there are no known reasons why Gravity Probe B will not out perform its science mission requirement of 0.5 mas/yr.

7 Acknowledgements

Over the past forty years, many people have made significant contributions to the Gravity Probe B mission, without which the satellite would simply not be on-orbit today. A complete list of the contributors and their contributions would require an entire volume, but the authors would like to acknowledge the following partial list: J. Aguinaldo, N. Bennett, R. Demars, P. Dulgov, K. Burns, T. Cahoon, R.A. Campo, O. Chan, R. Farley, R. Fontecha, T. Gill, R. Miller, B. Jacobsen, M. Johnston, J. Kirshenbaum, S.E. Larsen, J. Lay, T. Mcginnis, F, Mendoza, R. Miller, P. Rittmuller, S. Shehata, R. Schultz, M. Simon, and D.M. Spencer of Lockheed Martin Missile and Space Corporation, and E. Ingraham, K. Galal, J. Goebel, J. Kolodziejczak, M.A. Smith, and K. Nevitt of NASA. Additional thanks to J. Bower, J. Conklin, H. Matthews, J. Qiu, S. Wang and P. Worden of Stanford University. The authors would also like to thank both NASA and Lockheed Martin Missiles and Space for technical support and facilities.

Gravity Probe B has been accomplished under NASA funding, Contract No. NAS8-39225. Additional support for this paper was accomplished under funding from the 14th Workshop for General Relativity and Gravitation, YITP-W-04-13.

References

[1] G.E. Pugh, *Proposal for a Satellite Test of the Coriolis Prediction of General Relativity*, WSEG Research Memorandum No.11, 1959. This paper was published for the first time in "Nonlinear Gravitodynamics, The Lense-Thirring Effect," (ed R.J. Ruffini, C. Sigismondi), p. 414. World Scientific, Singapore, 2003.

[2] L.I. Schiff, Proceedings of the National Academy of Science 46, p. 871, 1960.

[3] L.I. Schiff, Physics Review Letters 4, p. 215, 1960.

[4] R.J. Adler, A.S. Silbergleit, International Journal of Theoretical Physics, 39, p. 1291, 2000.

[5] S. Buchman, *et al.*, "The Gravity Probe B Relativity Mission," Adv Space Res 25(6), p. 1177, 2000.

[6] W.J. Bencze, *et al.*, in *SICE Annual Conference 2003*, 480. Fukui (Japan).

[7] M.I. Ratner, *et al.*, in *Proceedings of the Seventh Marcel Grossman Meeting on General Relativity* (ed R.T. Jantzen, G.M. Keiser), p. 1553. World Scientific, Singapore, 1996.

[8] H. Goldstein, "Classical Mechanics, Second Edition." p. 207. Addison Wesley, 1980.

[9] G.M. Keiser, *et al.*, "Gravity Probe B: Launch and Initialization" in *Proceedings of ICPT 2004*, to be published. 2004.

Statistical isotropy of CMB anisotropy from WMAP

Tarun Souradeep [1] and Amir Hajian [2]

Inter-University Centre for Astronomy and Astrophysics,
Post Bag 4, Ganeshkhind, Pune 411007, India

Abstract

The statistical expectation values of the temperature fluctuations of cosmic microwave background (CMB) are assumed to be preserved under rotations of the sky. We investigate the statistical isotropy of the CMB anisotropy maps recently measured by the Wilkinson Microwave Anisotropy Probe (WMAP) using bipolar spherical harmonic power spectrum proposed in Hajian & Souradeep 2003. The Bipolar Power Spectrum (BiPS) is estimated for the full sky CMB anisotropy maps of the first year WMAP data. The method allows us to isolate regions in multipole space and study each region independently. This search shows that there is no evidence for violation of statistical isotropy in the first-year WMAP data on angular scales larger than that corresponding to $l \approx 60$.

1 Introduction

In standard cosmology, CMB anisotropy signal is expected to be statistically isotropic, i.e., statistical expectation values of the temperature fluctuations $\Delta T(\hat{q})$ are preserved under rotations of the sky. In particular, the angular correlation function $C(\hat{q}, \hat{q}') \equiv \langle \Delta T(\hat{q}) \Delta T(\hat{q}') \rangle$ is rotationally invariant for Gaussian fields. In spherical harmonic space, where $\Delta T(\hat{q}) = \sum_{lm} a_{lm} Y_{lm}(\hat{q})$ the condition of *statistical isotropy* (SI) translates to a diagonal $\langle a_{lm} a^*_{l'm'} \rangle = C_l \delta_{ll'} \delta_{mm'}$ where C_l, the widely used angular power spectrum of CMB anisotropy. SI CMB sky is essential for C_l to be a complete description of (Gaussian) CMB anisotropy and hence an adequate measure for comparing with models. Hence, it is crucial to be able to determine from the observed CMB sky whether it is a realization of a statistically isotropic process, or not. The detection of statistical isotropy (SI) violations in the CMB signal can have exciting and far-reaching implication for cosmology. For example, a generic consequence of cosmic topology is the breaking of statistical isotropy in characteristic patterns determined by the photon geodesic structure of the manifold as probed by the CMB photons traveling to us from the surface of last scattering over a distance comparable to the cosmic horizon, R_H. On the other hand, SI violation could also arise from foreground contamination, non-cosmological signals and be artifacts of observational technique.

The first-year *Wilkinson Microwave Anisotropy Probe* (*WMAP*) observations are consistent with predictions of the concordance ΛCDM model with scale-invariant and adiabatic fluctuations which have been generated during the inflationary epoch [Hinshaw et al. 2003, Kogut et al. 2003, Spergel et al. 2003, Page et al. 2003, Peiris et al., 2003]. After the first year of *WMAP* data, the SI of the CMB anisotropy (*i.e.* rotational invariance of n-point correlations) has attracted considerable attention. Tantalizing evidence of SI breakdown (albeit, in very different guises) has mounted in the *WMAP* first year sky maps, using a variety of different statistics. It was pointed out that the suppression of power in the quadrupole and octopole are aligned [Tegmark et al. 2004]. Further "multipole-vector" directions associated with these multipoles (and some other low multipoles as well) appear to be anomalously correlated [Copi et al. 2004, Schwarz et al. 2004]. There are indications of asymmetry in the power spectrum at low multipoles in opposite hemispheres [Eriksen et al. 2004a, Hansen et al. 2004, Naselsky et al. 2004]. Possibly related, are the results of tests of Gaussianity that show asymmetry in the amplitude of the measured genus amplitude (at about 2 to 3σ significance) between the north and south galactic hemispheres [Park 2004, Eriksen et al. 2004b, Eriksen et al. 2004c]. Analysis of the distribution of extrema in *WMAP* sky maps has indicated non-gaussianity, and to some extent, violation of SI [Larson & Wandelt 2004].

[1] E-mail:tarun@iucaa.ernet.in
[2] E-mail:amir@iucaa.ernet.in

However, what is missing is a common, well defined, mathematical language to quantify SI (as distinct from non Gaussianity) and the ability to ascribe statistical significance to the anomalies unambiguously.

Since the observed CMB sky is a single realization of the underlying correlation, the detection of SI violation or correlation patterns pose a great observational challenge. For statistically isotropic CMB sky, the correlation function

$$C(\hat{n}_1, \hat{n}_2) \equiv C(\hat{n}_1 \cdot \hat{n}_2) = \frac{1}{8\pi^2} \int dR C(\mathcal{R}\hat{n}_1, \mathcal{R}\hat{n}_2), \tag{1}$$

where $\mathcal{R}\hat{n}$ denotes the direction obtained under the action of a rotation $\mathcal{R}$ on $\hat{n}$, and dR is a volume element of the three-dimensional rotation group. The invariance of the underlying statistics under rotation allows the estimation of $C(\hat{n}_1 \cdot \hat{n}_2)$ using the average of the temperature product $\widetilde{\Delta T}(\hat{n})\widetilde{\Delta T}(\hat{n}')$ between all pairs of pixels with the angular separation θ. In the absence of statistical isotropy, $C(\hat{n}, \hat{n}')$ is estimated by a single product $\widetilde{\Delta T}(\hat{n})\widetilde{\Delta T}(\hat{n}')$ and hence is poorly determined from a single realization. Although it is not possible to estimate each element of the full correlation function $C(\hat{n}, \hat{n}')$, some measures of statistical anisotropy of the CMB map can be estimated through suitably weighted angular averages of $\widetilde{\Delta T}(\hat{n})\widetilde{\Delta T}(\hat{n}')$. The angular averaging procedure should be such that the measure involves averaging over sufficient number of independent 'measurements', but should ensure that the averaging does not erase all the signature of statistical anisotropy (as would happen in eq. (1) or eq. (21)). Recently, we proposed the Bipolar Power spectrum (BiPS) κ_ℓ ($\ell = 1, 2, 3, \ldots$) of the CMB map as a statistical tool of detecting and measuring departure from SI [Hajian & Souradeep 2003b, Souradeep & Hajian 2003] and reviewed in this article in sec. 3. The non-zero value of the BiPS spectrum imply the break down of statistical isotropy

$$\text{STATISTICAL ISOTROPY} \quad \Longrightarrow \quad \kappa_\ell = 0 \quad \forall \ell \neq 0. \tag{2}$$

The BiPS is sensitive to structures and patterns in the underlying total two-point correlation function [Hajian & Souradeep 2003b, Souradeep & Hajian 2003]. The BiPS is particularly sensitive to real space correlation patterns (preferred directions, etc.) on characteristic angular scales. In harmonic space, the BiPS at multipole ℓ sums power in off-diagonal elements of the covariance matrix, $\langle a_{lm} a_{l'm'} \rangle$, in the same way that the 'angular momentum' addition of states lm, $l'm'$ have non-zero overlap with a state with angular momentum $|l - l'| < \ell < l + l'$. Signatures, like a_{lm} and a_{l+nm} being correlated over a significant range l are ideal targets for BiPS. These are typical of SI violation due to cosmic topology and the predicted BiPS in these models have a strong spectral signature in the bipolar multipole ℓ space [Hajian & Souradeep 2003a]. The orientation independence of BiPS is an advantage since one can obtain constraints on cosmic topology that do not depend on the unknown specific orientation of the pattern (*e.g.*, preferred directions).

The results of WMAP are a milestone in CMB anisotropy measurements since it combines high angular resolution, high sensitivity, with 'full' sky coverage allowed by a space mission. The frequency coverage allows for WMAP CMB sky maps to be foreground cleaned up to $l \sim 100$ [Tegmark et al. 2004]. The CMB anisotropy map based on the WMAP data are ideal for testing for statistical isotropy.

2 Sources of Statistical Isotropy violation

An observed map of CMB anisotropy, ΔT_i^{obs}, contains the true CMB temperature fluctuations, ΔT_i, convolved with the beam and buried into noise and foreground contaminations. The observed map ΔT is related to the true map through this relation

$$\Delta T_i^{obs} = \sum_j B_{ij} \Delta T_j + N_i, \tag{3}$$

in which B is a matrix that contains the information about the beam smoothing effect and n is the contribution from instrumental noise and foreground contamination. Hence, the observed map is a realization of a Gaussian process with covariance $C = C^T + C^N + C^{res}$ where C^T is the theoretical covariance of the CMB temperature fluctuations, C^N is the noise covariance matrix and C^{res} is the covariance of residuals of foregrounds. Breakdown of statistical isotropy $C(\hat{n}, \hat{n}') \neq C(\hat{n} \cdot \hat{n}')$ can occur in any of these parts of the correlation function. Broadly, these effects may be divided into two kinds:

- Theoretical signals: These effects are theoretically motivated and are intrinsic to the true CMB sky, ΔT. We discuss two examples of these effects, *i.e.* non-trivial cosmic topology and primordial magnetic fields, in the next subsections.

- Observational artifacts: In an ideally cleaned CMB map, the true CMB temperature fluctuations are completely extracted from the observed map. But this is not always true. Sometimes there are some artifacts (related to B or N) left in the cleaned map which may in principle violate the SI. These effects are explained in section 2.3.

2.1 Cosmic Topology & Ultra-large scale structure

The cosmic microwave background anisotropy is currently the most promising observational probe of the global spatial structure of the universe on length scales near to and even somewhat beyond the 'horizon' scale ($\sim cH_0^{-1}$). Figure 1 depicts a prevalent view within the concept of inflation, that this relatively smooth Hubble volume that we observe is perhaps a tiny patch of an extremely inhomogeneous and complex spatial manifold. The complexity could involve non-trivial topology (multiple connectivity) on these ultra-large scales. Within a general program to address the observability of such a diverse global structure, a more well defined and tractable path would be to restrict oneself to spaces of uniform curvature (locally homogeneous and isotropic FRW models) but with non-trivial topology; in particular, compact spaces which have additional theoretical.

The question of size and the shape of our universe are very old problems studied earlier [Ellis 1971, Sokolov & Shvartsman 1974, 1, Lachieze-Rey & Luminet 1995]. With remarkable improvements in cosmological observations, in particular the CMB anisotropy measurements, these questions have received considerable attention over the past few years [de Oliveira-Costa et al. 1996, Starkman 1998, Levin et al. 1998, Bond,Pogosyan & Souradeep 1998,2000, de Oliveira-Costa et al. 2003, Dineen et al. 2004, Copi et al. 2004]. Although a multiply connected universe sounds non-trivial, but there are theoretical motivations [Linde 2004, Levin 2002] to favor a spatially compact universe. One possibility to have a compact flat universe is the consideration of multiply connected (topologically nontrivial) spaces. The oldest way of searching for global structure of the universe is by identifying ghost images of local galaxies and clusters or quasars at higher redshifts [Lachieze-Rey & Luminet 1995]. This method can probe the topology of the universe only on scales substantially smaller than the apparent radius of the observable universe. Another method to search for the shape of the universe is through the effect on the cosmic density perturbation fields. For compact topologies, the two main effects on the CMB are: (1) the breaking of statistical isotropy in characteristic patterns determined by the photon geodesic structure of the manifold and (2) an infrared cutoff in the power spectrum of perturbations imposed by the finite spatial extent. More generally, in a universe with non-trivial global spatial topology, the multiple connectivity of the space could lead to observable characteristic angular correlation patterns in the CMB anisotropy.

Over the past few years, many independent methods have been proposed to search for evidence of a finite universe in CMB maps. These methods can be classified in three main groups.

- Using the angular power spectrum of CMB anisotropies to probe the topology of the Universe. The angular power spectrum, however, is inadequate to characterize the peculiar form of the anisotropy manifest in small universes of this type. Since nontrivial topology breaks down SI, there is more information in a map of temperature fluctuations than just the angular power spectrum [Levin et al. 1998, Bond,Pogosyan & Souradeep 1998,2000, Hajian & Souradeep 2003a].

- The second class of methods are direct methods that rely on multiple imaging (or strong correlation features) of the CMB sky. The most well known methods among these methods are S-map statistics [de Oliveira-Costa et al. 1996, de Oliveira-Costa et al. 2003] and the search for circles-in-the-sky [Cornish,Spergel & Starkman 1998].

- Third class of methods are indirect probes which deal with the correlation patterns of the CMB anisotropy field by using an appropriate combination of coefficients of the harmonic expansion of the field [Dineen et al. 2004, Donoghue et al. 2004, Hajian & Souradeep 2003a, Copi et al. 2004]. The Bipolar power spectrum (BiPS) method is one of the strategies in this class.

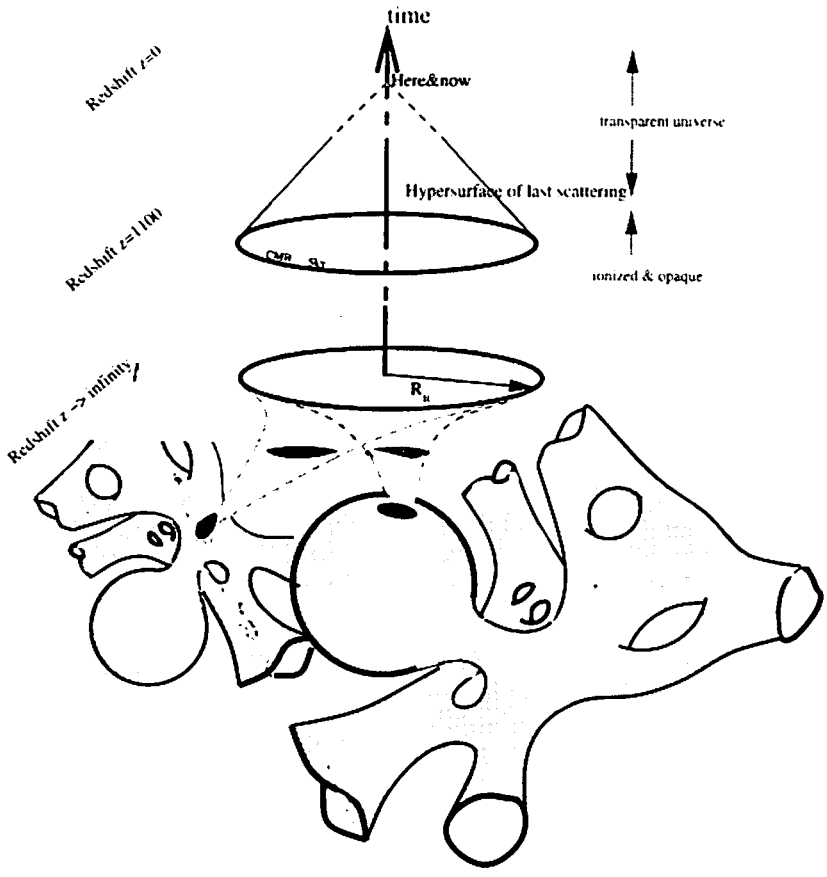


Figure 1: A cartoon depicting a prevalent view within the inflationary paradigm. The observable universe corresponds to a small patch of a very complicated manifold that has been blown to cosmological scales during an inflationary epoch. Ultra-large scale structure could be observable if the the size of this patch is not much smaller that the scales of inhomogeneity and non-trivial topology.

The correlation patterns in CMB that lead to violation of SI implies that imply $\langle \hat{a}_{lm}\hat{a}^*_{lm}\rangle$ has off-diagonal elements. Figure 2 taken from [Bond,Pogosyan & Souradeep 1998.2000] shows the off-diagonal elements in the CMB correlation for two compact universe models. BiPS gathers together the power in the off-diagonal elements of $\langle \hat{a}_{lm}\hat{a}^*_{lm}\rangle$ as shown in Fig. 3.

Using the fact that statistical isotropy is violated in compact spaces one could use the bipolar power spectrum as a probe to detect the topology of the universe. A simple example of is the BiPS signature of a non-trivial topology can be given for a T^3 universe, where the correlation function is given by

$$C(\hat{q}.\hat{q}') = L^{-3}\sum_{\mathbf{n}} P_\Phi(k_{\mathbf{n}})\ \mathrm{e}^{-\imath\pi(\epsilon_q \mathbf{n}\cdot\hat{q} - \epsilon_{q'}\mathbf{n}\cdot\hat{q}')}. \qquad (4)$$

in which, $\mathbf{n}$ is 3-tuple of integers (in order to avoid confusion, we use $\hat{q}$ to represent the direction instead of $\hat{n}$), the small parameter $\epsilon_q \leq 1$ is the physical distance to the SLS along $\hat{q}$ in units of $L/2$ (more generally, $\bar{L}/2$ where $\bar{L} = (L_1L_2L_3)^{1/3}$) and L is the size of the Dirichlet domain (DD). When ϵ is a small constant, the leading order terms in the correlation function eq. (4) can be readily obtained in power

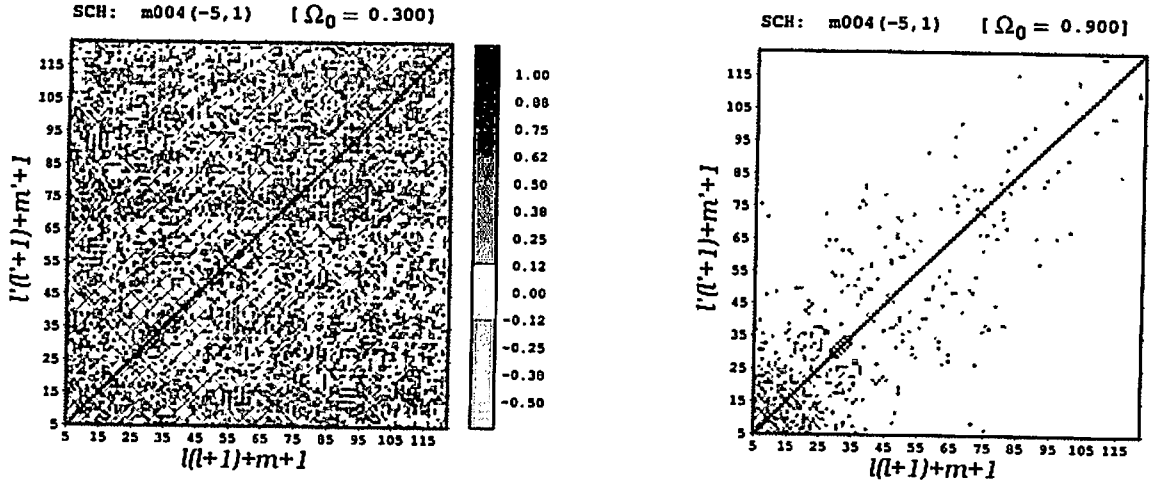


Figure 2: The figure taken from [Bond,Pogosyan & Souradeep 1998,2000] illustrates the non-diagonal nature of the expectation values of $a_{\ell m}$ pair products when the CMB anisotropy violates SI in two model compact universe. The radical violation in the model on the left corresponds to a small compact universe where CMB photons have traversed across multiple times. The model on the left with mild violation of SI corresponds to a universe of size comparable to the observable horizon. For more details, see [Bond,Pogosyan & Souradeep 1998,2000]

series expansion in powers of ϵ. For the lowest wave numbers $|\mathbf{n}|^2 = 1$ in a cuboid torus

$$\begin{aligned} C(\hat{q},\hat{q}') &\approx 2\sum_i P_\Phi(2\pi/L_i)\cos(\pi\epsilon\beta_i\Delta q_i) \\ &\approx C_0\left[1-\epsilon^2|\Delta q|^2+3\,\epsilon^4\sum_{i=1}^{3}(\Delta q_i)^4\right], \end{aligned} \tag{5}$$

where Δq_i are the components of $\Delta q = \hat{q} - \hat{q}'$ along the three axes of the torus and $\beta_i = \bar{L}/L_i$. From this, the non-zero κ_ℓ can be analytically computed to be

$$\begin{aligned} \frac{\kappa_0}{C_0^2} &= \pi^2(1-4\epsilon^2+\frac{368}{15}\epsilon^4-\frac{288}{5}\epsilon^6+\frac{20736}{125}\epsilon^8) \\ \frac{\kappa_4}{C_0^2} &= \frac{12288\pi^2}{875}\epsilon^8 \end{aligned} \tag{6}$$

κ_4 has the information of the relative size of the Dirichlet domain and one can use it to constrain the topology of the universe. A detailed study of the BiPS signature of cosmic topology is given in [Hajian & Souradeep 2003a]. These prediction allow us to constrain cosmic topology using the BiPS measured in the observed CMB maps [Hajian et al. 2004].

2.2 Primordial Magnetic Fields

Cosmological magnetic field, generated during an early epoch of inflation [Ratra 1992, Bamba et al. 2004], can generate CMB anisotropies [Durrer et al. 1998]. The presence of a preferred direction due to a homogeneous magnetic field background leads to non-zero off-diagonal elements in the covariance matrix [Chen et al. 2004]. This induces correlations between $a_{l+1,m}$ and $a_{l-1,m}$ multipole coefficients of the CMB temperature anisotropy field in the following manner

$$\langle a_{lm}a^*_{l'm'}\rangle = \delta_{m,m'}[\delta_{l,l'}C_l + (\delta_{l+1,l'-1}+\delta_{l-1,l'+1}D_l)], \tag{7}$$

where D_l is the power spectrum of off-diagonal elements of the covariance matrix. For a Harrison-Peebles-Yu-Zel'dovich scale-invariant spectrum, D_l behaves as l^{-2}. More precisely, it is given by

$$D_l = 4 \times 10^{-16} l^{-2} (\frac{B}{1nG})^4. \tag{8}$$

This clearly violates the statistical isotropy and gives rise to a non-zero BiPS predictions for magnetic fields. This open the way to use BiPS analysis on CMB maps to constrain or measure primordial cosmic magnetic fields [Hajian et al. 2004b].

2.3 Observational Artifacts

Foregrounds and observational artifacts (such as non-circular beam, incomplete/non-uniform sky coverage and anisotropic noise) would also manifest themselves as violations of SI.

- Anisotropic noise : The CMB temperature measured by an instrument is a linear sum of the cosmological signal as well as instrumental noise. The two point correlation function then has two parts, one part comes from the signal and the other one comes from the noise

$$C(\hat{n}_1, \hat{n}_2) = C^S(\hat{n}_1, \hat{n}_2) + C^N(\hat{n}_1, \hat{n}_2). \tag{9}$$

  Both signal and noise should be statistically isotropic to have a statistically isotropic CMB map. So even for a statistically isotropic signal, if the noise fails to be statistically isotropic the resultant map will turn out to be anisotropic. The noise matrix can fail to be statistically isotropic due to non-uniform coverage. Also if the noise is correlated between different pixels the noise matrix could be statistically anisotropic. A simple example of this is the diagonal (but anisotropic) noise given by the following correlation

$$C^N(\hat{n}, \hat{n}') = \sigma^2(\hat{n}) \delta_{\hat{n}\hat{n}'}. \tag{10}$$

  This noise clearly violates the SI and will lead to a non-zero BiPS given by

$$\kappa_\ell = \sum_{m=-\ell}^{\ell} |f_{\ell m}|^2, \tag{11}$$

  where $f_{\ell m}$ are spherical harmonic transform of the noise, $f_{\ell m} = \int \mathrm{d}\Omega_{\hat{n}} Y^*_{\ell m}(\hat{n}) \sigma^2(\hat{n})$.

- The effect of non-circular beam : In practice when we deal with data, it is necessary to take into account the *instrumental response*. The instrumental response is nothing but the beams width and the form of the beam and can be taken into account by defining a beam profile function $B(\hat{n}, \hat{n}')$. Here $\hat{n}$ denotes the direction to the center of the beam and $\hat{n}'$ denotes the direction of the incoming photon. The temperature measured by the instrument is given by

$$\Delta\tilde{T}(\hat{n}) = \int \Delta T(\hat{n}') B(\hat{n}, \hat{n}') d\Omega_{\hat{n}'}. \tag{12}$$

  Using this relation to calculate the correlation function $\tilde{C}(\hat{n}_1, \hat{n}_2) = \langle \Delta\tilde{T}(\hat{n}_1) \Delta\tilde{T}(\hat{n}_2) \rangle$ one would get

$$\begin{aligned} \tilde{C}(\hat{n}_1, \hat{n}_2) &= \int d\Omega_{\hat{n}'} \int d\Omega_{\hat{n}''} \langle \Delta T(\hat{n}') \Delta T(\hat{n}'') \rangle B(\hat{n}_1, \hat{n}') B(\hat{n}_2, \hat{n}'') \\ &= \int d\Omega_{\hat{n}'} \int d\Omega_{\hat{n}''} C(\hat{n}', \hat{n}'') B(\hat{n}_1, \hat{n}') B(\hat{n}_2, \hat{n}''). \end{aligned} \tag{13}$$

  Only for a circular beam where $B(\hat{n}, \hat{n}') \equiv B(\hat{n} \cdot \hat{n}')$, the correlation function is statistically isotropic, $\tilde{C}(\hat{n}_1, \hat{n}_2) \equiv \tilde{C}(\hat{n}_1 \cdot \hat{n}_2)$. Breakdown of SI is obvious since even C_l get mixed for a non-circular beam, $\tilde{C}_l = \sum_{l'} A_{ll'} C_{l'}$ [Mitra et al. 2004]. Non-circularity of the beam in CMB anisotropy experiments is becoming increasingly important as experiments go for higher resolution measurements at higher sensitivity.

- Mask effects : Many experiments map only a part of the sky. Even in the best case, contamination by galactic foreground residuals make parts of the sky unusable. The incomplete sky or mask effect is another source of breakdown of SI. But, this effect can be readily modeled out. The effect of a general mask on the temperature field is as follows

$$\Delta T^{masked}(\hat{n}) = \Delta T(\hat{n}) W(\hat{n}), \tag{14}$$

where $W(\hat{n})$ is the mask function. One can cut different parts of the sky by choosing appropriate mask functions. Masked a_{lm} coefficients can be computed from the masked temperature field,

$$\begin{aligned} a_{lm}^{masked} &= \int \Delta T^{masked}(\hat{n}) Y^*_{lm}(\hat{n}) d\Omega_{\hat{n}} \\ &= \sum_{l_1 m_1} a_{l_1 m_1} \int Y_{l_1 m_1}(\hat{n}) Y^*_{lm}(\hat{n}) W(\hat{n}) d\Omega_{\hat{n}}. \end{aligned} \tag{15}$$

Where $a_{l_1 m_1}$ are spherical harmonic transforms of the original temperature field. We can expand $W(\hat{n})$ in spherical harmonics as well

$$W(\hat{n}) = \sum_{lm} w_{lm} Y_{lm}(\hat{n}), \tag{16}$$

and after substituting this into eq. (15) it is seen that the masked a_{lm} is given by the effect of a kernel $K^{l_1 m_1}_{lm}$ on original a_{lm} [Prunet et al. 2004]

$$a_{lm}^{masked} = \sum_{l_1 m_1} a_{l_1 m_1} K^{l_1 m_1}_{lm}. \tag{17}$$

The kernel contains the information of our mask function and is defined by

$$\begin{aligned} K^{l_1 m_1}_{lm} &= \sum_{l_2 m_2} w_{l_2 m_2} \int Y_{l_1 m_1}(\hat{n}) Y_{l_2 m_2}(\hat{n}) Y^*_{lm}(\hat{n}) d\Omega_{\hat{n}} \\ &= \sum_{l_2 m_2} w_{l_2 m_2} \sqrt{\frac{(2l_1+1)(2l_2+1)}{4\pi(2l+1)}} C^{l0}_{l_1 0 l_2 0} C^{lm}_{l_1 m_1 l_2 m_2}. \end{aligned} \tag{18}$$

The covariance matrix of a masked sky will no longer have the diagonal form because of the action of the kernel

$$\begin{aligned} \langle a_{lm}^{masked} a_{l'm'}^{masked\,*} \rangle &= \langle a_{l_1 m_1} a^*_{l'_1 m'_1} \rangle K^{l_1 m_1}_{lm} K^{l'_1 m'_1}_{l'm'} \\ &= C_{l_1} \delta_{l_1 l'_1} \delta_{m_1 m'_1} K^{l_1 m_1}_{lm} K^{l'_1 m'_1}_{l'm'} \\ &= \sum_{l_1, m_1} C_{l_1} K^{l_1 m_1}_{lm} K^{l_1 m_1}_{l'm'}. \end{aligned} \tag{19}$$

This clearly violates the SI and results a non-zero BiPS for masked CMB skies. In the next section we apply a galactic mask to ILC map and show that signature of this mask on BiPS is a rising tail at low ℓ, ($\ell < 20$).

- Residuals from foreground removal : Besides the cosmological signal and instrumental noise, a CMB map also contains foreground emission such as galactic emission, etc. The foreground is usually modeled out using spectral information. However, residuals from foreground subtractions in the CMB map will violate SI. Interestingly, BiPS does sense the difference between maps with grossly different emphasis on the galactic foreground. As shown in [Hajian & Souradeep 2005b] the BiPS of a Wiener filtered map shows a signal very similar to that of a galactic cut sky. This can be understood if one writes the effect of the Wiener filter as a weight on the 'contaminated' galactic regions of the map.

$$\Delta T^W(\hat{n}) = \Delta T(\hat{n})(1 + W(\hat{n})). \tag{20}$$

This explains the similarity between a cut sky and a Wiener filtered map. The effect of foregrounds on BiPS still needs to be studied more carefully.

3 The Bipolar Power Spectrum (BiPS)

Two point correlation of the CMB anisotropy is given by ensemble average, but there is only one observable CMB sky. Hence, the ensemble average is meaningless unless the CMB sky is SI, when the two point correlation function $C(\theta)$ can be well estimated as in eq. (21) by the average product of temperature fluctuations over all pairs of directions $\hat{n}_1$ and $\hat{n}_2$ whose angular separation is θ. In particular, for CMB temperature map $\widetilde{\Delta T}(\hat{n}_i)$ defined on a discrete set of points on celestial sphere (pixels) $\hat{n}_i$ $(i = 1, \ldots, N_p)$

$$\hat{C}(\theta) = \sum_{i,j=1}^{N_p} \widetilde{\Delta T}(\hat{n}_i)\widetilde{\Delta T}(\hat{n}_j)\delta(\cos\theta - \hat{n}_i \cdot \hat{n}_j), \tag{21}$$

is an estimator of the correlation function $C(\theta)$ of an underlying SI statistics. If the statistical isotropy is violated the estimate of the correlation function from a sky map given by a single temperature product

$$\hat{C}(\hat{n}_1, \hat{n}_2) = \Delta T(\hat{n}_1)\Delta T(\hat{n}_2) \tag{22}$$

is poorly determined.

Although it is not possible to estimate each element of the full correlation function $C(\hat{n}_1, \hat{n}_2)$, some measures of statistical isotropy of the CMB map can be estimated through suitably weighted angular averages of $\Delta T(\hat{n}_1)\Delta T(\hat{n}_2)$. The angular averaging procedure should be such that the measure involves averaging over sufficient number of independent measurements , but should ensure that the averaging does not erase all the signature of statistical anisotropy. Another important desirable property is that measure be independent of the overall orientation of the sky. Based on these considerations, we have proposed a set of measures of statistical isotropy [Hajian & Souradeep 2003b]

$$\kappa^\ell = (2l+1)^2 \int d\Omega_{n_1} \int d\Omega_{n_2} [\frac{1}{8\pi^2} \int d\mathcal{R} \chi^\ell(\mathcal{R}) C(\mathcal{R}\hat{n}_1, \mathcal{R}\hat{n}_2)]^2. \tag{23}$$

In the above expression, $C(\mathcal{R}\hat{n}_1, \mathcal{R}\hat{n}_2)$ is the two point correlation at $\mathcal{R}\hat{n}_1$ and $\mathcal{R}\hat{n}_2$ which are the coordinates of the two pixels $\hat{n}_1$ and $\hat{n}_2$ after rotating the coordinate system through an angle ω where $(0 \le \omega \le \pi)$ about the axis $\mathbf{n}(\Theta, \Phi)$. The direction of this rotation axis $\mathbf{n}$ is defined by the polar angles Θ where $(0 \le \Theta \le \pi)$ and Φ, where $(0 \le \Phi \le 2\pi)$. χ^ℓ is the trace of the finite rotation matrix in the ℓM-representation

$$\chi^\ell(\mathcal{R}) = \sum_{M=-\ell}^{\ell} D^\ell_{MM}(\mathcal{R}), \tag{24}$$

which is called the *characteristic function*, or the character of the irreducible representation of rank ℓ. It is invariant under rotations of the coordinate systems. Explicit forms of $\chi^\ell(\mathcal{R})$ are simple when $\mathcal{R}$ is specified by ω, Θ, Φ, then $\chi^\ell(\mathcal{R})$ is completely determined by the rotation angle ω and it is independent of the rotation axis $\mathbf{n}(\Theta, \Phi)$,

$$\begin{aligned} \chi^\ell(\mathcal{R}) &= \chi^\ell(\omega) \\ &= \frac{\sin[(2\ell+1)\omega/2]}{\sin[\omega/2]} . \end{aligned} \tag{25}$$

And finally $d\mathcal{R}$ in eq.(23) is the volume element of the three-dimensional rotation group and is given by

$$d\mathcal{R} = 4\sin^2\frac{\omega}{2}\, d\omega \sin\Theta\, d\Theta\, d\Phi . \tag{26}$$

For a statistically isotropic model $C(\hat{n}_1, \hat{n}_2)$ is invariant under rotation, and therefore $C(\mathcal{R}\hat{n}_1, \mathcal{R}\hat{n}_2) = C(\hat{n}_1, \hat{n}_2)$ and the orthonormality of $\chi^\ell(\omega)$, we will recover the condition for SI.

$$\kappa^\ell = \kappa^0 \delta_{\ell 0}. \tag{27}$$

Real-space representation of BiPS is very suitable for analytical computation of BiPS for theoretical models where we know the analytical expression for the two point correlation of the model, such as

theoretical models in [Hajian & Souradeep 2003a]. On the other hand, the harmonic representation of BiPS that we describe next allows computationally rapid methods for BiPS estimation from a given CMB map.

Two point correlation of CMB anisotropies, $C(\hat{n}_1, \hat{n}_2)$, is a two point function on $S^2 \times S^2$, and hence can be expanded as

$$C(\hat{n}_1, \hat{n}_2) = \sum_{l_1, l_2, L, M} A^{\ell M}_{l_1 l_2} \{Y_{l_1}(\hat{n}_1) \otimes Y_{l_2}(\hat{n}_2)\}_{\ell M}, \tag{28}$$

where $A^{\ell M}_{l_1 l_2}$ are coefficients of the expansion (here after BipoSH coefficients) and $\{Y_{l_1}(\hat{n}_1) \otimes Y_{l_2}(\hat{n}_2)\}_{\ell M}$ are the bipolar spherical harmonics which transform as a spherical harmonic with ℓ, M with respect to rotations [Varshalovich et al. 1988] given by

$$\{Y_{l_1}(\hat{n}_1) \otimes Y_{l_2}(\hat{n}_2)\}_{\ell M} = \sum_{m_1 m_2} C^{\ell M}_{l_1 m_1 l_2 m_2} Y_{l_1 m_1}(\hat{n}_2) Y_{l_2 m_2}(\hat{n}_2), \tag{29}$$

in which $C^{\ell M}_{l_1 m_1 l_2 m_2}$ are Clebsch-Gordan coefficients. We can inverse-transform $C(\hat{n}_1, \hat{n}_2)$ to get the $A^{\ell M}_{l_1 l_2}$ by multiplying both sides of eq.(28) by $\{Y_{l'_1}(\hat{n}_1) \otimes Y_{l'_2}(\hat{n}_2)\}^*_{\ell' M'}$ and integrating over all angles, then the orthonormality of bipolar harmonics implies that

$$A^{\ell M}_{l_1 l_2} = \int d\Omega_{\hat{n}_1} \int d\Omega_{\hat{n}_2}\, C(\hat{n}_1, \hat{n}_2)\, \{Y_{l_1}(\hat{n}_1) \otimes Y_{l_2}(\hat{n}_2)\}^*_{\ell M}. \tag{30}$$

The above expression and the fact that $C(\hat{n}_1, \hat{n}_2)$ is symmetric under the exchange of $\hat{n}_1$ and $\hat{n}_2$ lead to the following symmetries of $A^{\ell M}_{l_1 l_2}$

$$\begin{aligned} A^{\ell M}_{l_2 l_1} &= (-1)^{(l_1 + l_2 - L)} A^{\ell M}_{l_1 l_2}, \\ A^{\ell M}_{ll} &= A^{\ell M}_{ll}\, \delta_{\ell, 2k+1}, \qquad k = 0, 1, 2, \cdots. \end{aligned} \tag{31}$$

The Bipolar Spherical Harmonic (BipoSH) coefficients, $A^{\ell M}_{l_1 l_2}$, are linear combinations of off-diagonal elements of the covariance matrix,

$$A^{\ell M}_{l_1 l_2} = \sum_{m_1 m_2} (a_{l_1 m_1} a^*_{l_2 m_2})(-1)^{m_2} C^{\ell M}_{l_1 m_1 l_2 - m_2}. \tag{32}$$

This means that $A^{\ell M}_{l_1 l_2}$ completely represent the information of the covariance matrix. Fig. 3 shows how $A^{2M}_{l_1 l_2}$ and $A^{4M}_{l_1 l_2}$ combine the elements of the covariance matrix. When SI holds, the covariance matrix is diagonal and hence

$$\begin{aligned} A^{\ell M}_{ll'} &= (-1)^l C_l (2l+1)^{1/2}\, \delta_{ll'}\, \delta_{\ell 0}\, \delta_{M 0}, \\ A^{00}_{l_1 l_2} &= (-1)^{l_1} \sqrt{2l_1 + 1}\, C_{l_1}\, \delta_{l_1 l_2}. \end{aligned} \tag{33}$$

BipoSH expansion is the most general representation of the two point correlation functions of CMB anisotropy. The well known angular power spectrum, C_l is a subspace of BipoSH coefficients corresponding to the A^{00}_{ll} that represent the statistically isotropic part of a general correlation function. When SI holds, A^{00}_{ll} or equivalently C_l have all the information of the field. But if the SI breaks down, A^{00}_{ll} are not adequate for describing the field, and one needs to take the other terms into account. This simply means that the And when the statistical isotropy holds, these coefficients will reduce to the well-known angular power spectrum of CMB anisotropy.

It is impossible to measure all $A^{\ell M}_{l_1 l_2}$ individually because of cosmic variance. Combining BipoSH coefficients into Bipolar Power Spectrum reduces the cosmic variance[3]. BiPS of CMB anisotropy is defined as a convenient contraction of the BipoSH coefficients

$$\kappa_\ell = \sum_{l, l', M} |A^{\ell M}_{ll'}|^2 \geq 0. \tag{34}$$

[3]This is similar to combining a_{lm} to construct the angular power spectrum, $C_l = \frac{1}{2l+1} \sum_m |a_{lm}|^2$, to reduce the cosmic variance

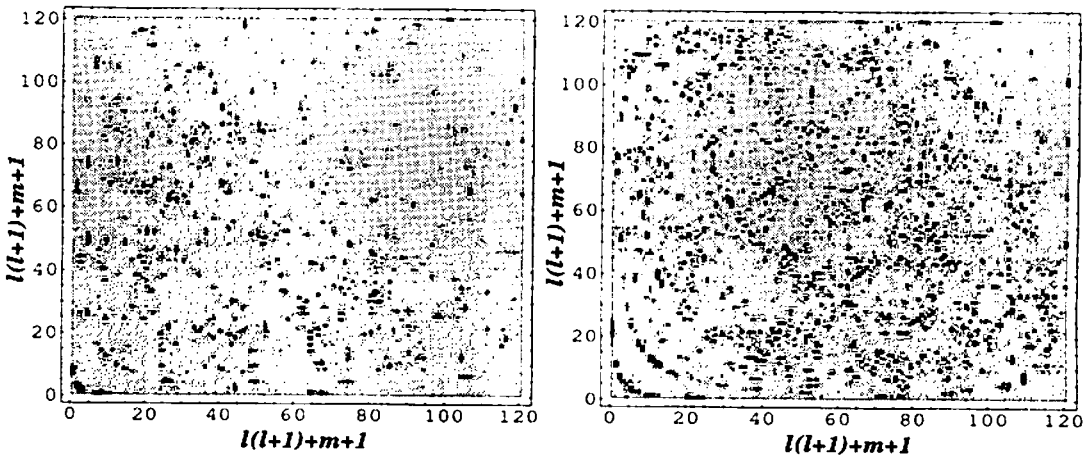


Figure 3: BipoSH coefficients are linear combinations of elements of the covariance matrix. Here $A^{2M}_{ll'}$ (*left*) and $A^{4M}_{ll'}$ (*right*) are plotted to show how BiPS covers the off-diagonal elements of the covariance matrix in harmonic space.

The BiPS, which can be shown that is equivalent to the one in eq.(23), has interesting properties. It is orientation independent and is invariant under rotations of the sky. For models in which statistical isotropy is valid, BipoSH coefficients are given by eq. (33). And results in a null BiPS, i.e. $\kappa_\ell = 0$ for every positive ℓ,

$$\kappa_\ell = \kappa_0 \delta_{\ell 0}. \tag{35}$$

3.1 Unbiased Estimator of BiPS

An estimator for measuring BipoSH coefficients from a given CMB map is

$$\tilde{A}^{\ell M}_{ll'} = \sum_{mm'} \sqrt{W_l W_{l'}}\, a_{lm} a_{l'm'}\, C^{\ell M}_{lml'm'} \quad , \tag{36}$$

where W_l is the Legendre transform of the window function. The above estimator is a linear combination of C_l and hence is unbiased. An unbiased estimator of BiPS is given by

$$\tilde{\kappa}_\ell = \sum_{ll'M} \left| \tilde{A}^{\ell M}_{ll'} \right|^2 - \mathfrak{B}_\ell \,, \tag{37}$$

where the bias for the BiPS is defined as $\mathfrak{B}_\ell = \langle \tilde{\kappa}_\ell \rangle - \kappa_\ell$ is equal to

$$\mathfrak{B}_\ell = \sum_{l_1 l_2} W_{l_1} W_{l_2} \sum_{m_1, m_1'} \sum_{m_2, m_2'} \left[\langle a^*_{l_1 m_1} a_{l_1 m_1'} \rangle \langle a^*_{l_2 m_2} a_{l_2 m_2'} \rangle + \langle a^*_{l_1 m_1} a_{l_2 m_2'} \rangle \langle a^*_{l_2 m_2} a_{l_1 m_1'} \rangle \right] \times \sum_M C^{\ell M}_{l_1 m_1 l_2 m_2} C^{\ell M}_{l_1 m_1' l_2 m_2'} \,. \tag{38}$$

The above expression for $\mathfrak{B}_\ell$ is obtained by assuming Gaussian statistics of the temperature fluctuations. The procedure is very similar to computing cosmic variance (which is discussed in the next section), but much simpler. However, we can not measure the ensemble average in the above expression and as a result, elements of the covariance matrix (obtained from a single map) are poorly determined due to the cosmic variance. The best we can do is to compute the bias for the SI component of a map

$$\mathfrak{B}_\ell \equiv \langle \tilde{\kappa}^B_\ell \rangle_{SI} = (2\ell + 1) \sum_{l_1} \sum_{l_2 = |\ell - l_1|}^{\ell + l_1} C_{l_1} C_{l_2} W_{l_1} W_{l_2} \left[1 + (-1)^\ell \delta_{l_1 l_2} \right] . \tag{39}$$

Note , the estimator $\tilde{\kappa}_\ell$ is unbiased, only for SI correlation,i.e., $\langle \tilde{\kappa}_\ell \rangle = 0$. Consequently, for SI correlation, the measured $\tilde{\kappa}_\ell$ will be consistent with zero within the error bars given by σ_{SI} [Hajian & Souradeep 2003b]. We simulated 1000 SI CMB maps and computed BiPS for them using different filters. The average BiPS of SI maps is an estimation of the bias which can be compared to our analytical estimation. The left panel of Fig. 4 shows that the theoretical bias (computed from average C_l) match the numerical estimations of average κ_ℓ of the 1000 realizations of the SI maps.

It is important to note that bias cannot be correctly subtracted for non-SI maps. Non-zero $\tilde{\kappa}_\ell$ estimated from a non-SI map will have contribution from the non-SI terms in full bias given in eq. (38). It is not inconceivable that for strong SI violation, $\mathfrak{B}_\ell$ over-corrects for the bias leading to negative values of $\tilde{\kappa}_\ell$. *What is important is whether measured $\tilde{\kappa}_\ell$ differs from zero at a statistically significant level.*

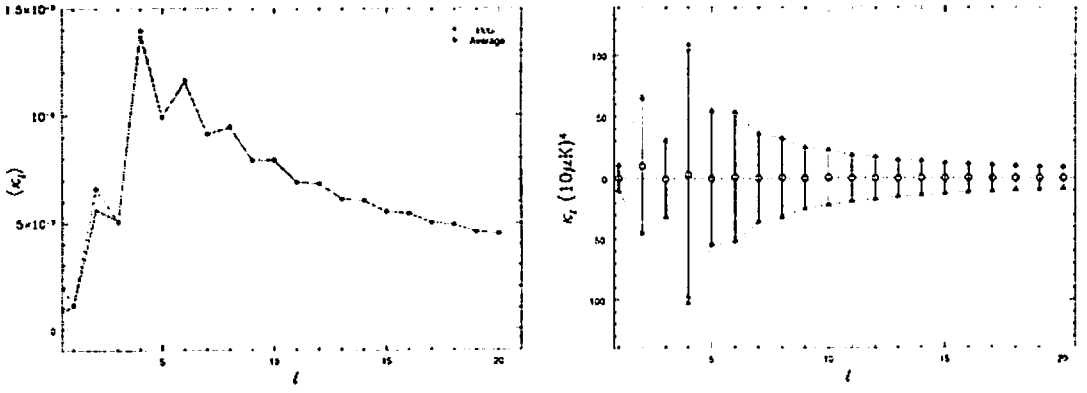


Figure 4: **Left:** Analytical bias for a Gaussian window function with $W_l^G(40)$ computed from the average C_l from 1000 realizations of a SI CMB map compared with $\langle \kappa_l^{realization} \rangle$ (the average κ_l from 1000 realizations). This shows that the theoretical bias is a very good estimation of the bias for a statistically isotropic map. **Right:** The cosmic error, $\sigma(\kappa_\ell)$, obtained using 1000 independent realizations of CMB (full) sky map matches the analytical results shown by dotted curve with triangles . This shows a much better fit to the theoretical cosmic variance compared to what was obtained for 100 realizations [Hajian & Souradeep 2003b]

3.2 Cosmic Variance of BiPS

A crucial point is how well one can hope to estimate the BiPS given the single observed sky. This is limited by the Cosmic variance of the BiPS estimator defined as

$$\sigma^2 = < \tilde{\kappa}_\ell^2 > - < \tilde{\kappa}_\ell >^2 \tag{40}$$

It is possible to obtain an analytic expression variance of $\tilde{\kappa}^\ell$ using the Gaussianity of ΔT. Looking back at the eq.(23) we can see, we will have to calculate the eighth moment of the field

$$\langle \Delta T(\hat{n}_1)\Delta T(\hat{n}_2)\Delta T(\hat{n}_3)\Delta T(\hat{n}_4)\Delta T(\hat{n}_5)\Delta T(\hat{n}_6)\Delta T(\hat{n}_7)\Delta T(\hat{n}_8)\rangle. \tag{41}$$

Assuming Gaussianity of the field we can rewrite the eight point correlation in terms of two point correlations. One can write a simple code to do that[4]. This will give us $(8-1)!! = 7 \times 5 \times 3 = 105$ terms. These 105 terms consist of terms like:

$$\langle \Delta T(\hat{n}_1)\Delta T(\hat{n}_2)\rangle\langle \Delta T(\hat{n}_3)\Delta T(\hat{n}_4)\rangle\langle \Delta T(\hat{n}_5)\Delta T(\hat{n}_6)\rangle\langle \Delta T(\hat{n}_7)\Delta T(\hat{n}_8)\rangle, \tag{42}$$

and all other permutations of them. On the other hand $\langle \tilde{\kappa}_\ell \rangle$ has a 4 point correlation in it which can also be expanded versus two point correlation functions. If we form $\langle \tilde{\kappa}_\ell^2 \rangle - \langle \tilde{\kappa}_\ell \rangle^2$, only 96 terms will be

[4]F90 software implementing this is available from the authors upon request

left which are in the following form

$$(\frac{2\ell+1}{8\pi^2})^2 \int d\Omega_1 \cdots d\Omega_4 \int dR \int dR' \chi_\ell(R)\chi_\ell(R')C(\hat{n}_1, R'\hat{n}_4)C(\hat{n}_2, R'\hat{n}_3)C(R\hat{n}_1, \hat{n}_4)C(R\hat{n}_2, \hat{n}_3) \quad (43)$$

and all other permutations. As described in detail in our paper [Hajian & Souradeep 2005b], it is possible to simplify and group together the 96 terms and obtain a compact expression as

$$\begin{aligned}
\sigma^2_{\rm SI}(\tilde{\kappa}_\ell) &= \sum_{l:2l\geq\ell} 4\, C_l^4 W_l^4 \left[2\frac{(2\ell+1)^2}{2l+1} + (-1)^\ell(2\ell+1) + (1+2(-1)^\ell)F^\ell_{ll}\right] \\
&+ \sum_{l_1} \sum_{l_2=|\ell-l_1|}^{\ell+l_1} 4\, C^2_{l_1} C^2_{l_2} W^2_{l_1} W^2_{l_2} \left[(2\ell+1) + F^\ell_{l_1 l_2}\right] \\
&+ 8 \sum_{l_1} \frac{(2\ell+1)^2}{2l_1+1} C^2_{l_1} W^2_{l_1} \left[\sum_{l_2=|\ell-l_1|}^{\ell+l_1} C_{l_2} W_{l_2}\right]^2 \\
&+ 16(-1)^\ell \sum_{l_1\, 2l_1\geq\ell} \frac{(2\ell+1)^2}{2l_1+1} \sum_{l_2=|\ell-l_1|}^{\ell+l_1} C^3_{l_1} C_{l_2} W^3_{l_1} W_{l_2}.
\end{aligned} \quad (44)$$

Numerical computation of $\sigma^2_{\rm SI}$ is fast. But the challenge is to compute Clebsch-Gordan coefficients for large quantum numbers. We use drc3j subroutine of netlib[5] in order to compute the Clebsch-Gordan coefficients in our codes. Again we can check the accuracy of our analytical estimation of cosmic variance by comparing it against the standard deviation of BiPS of 1000 simulations of SI CMB sky. The result is shown the right panel of in Fig. 4 and shows a very good agreement between the two.

4 Results of BiPS analysis of WMAP CMB maps

We carry out measurement of the BiPS, on the following CMB anisotropy maps

A) a foreground cleaned map (denoted as 'TOH') [Tegmark et al. 2004],

B) the Internal Linear Combination map (denoted as 'ILC' in the figures) [Bennett et al. 2003], and

C) a customized linear combination of the QVW maps of WMAP with a galactic cut (denoted as 'CSSK').

Also for comparison, we measure the BiPS of

D) a Wiener filtered map of WMAP data (denoted as 'Wiener') [Tegmark et al. 2004], and

E) the ILC map with a 10° cut around the equator (denoted as 'Gal. cut.').

Angular power spectra of these maps are shown in Fig. 5. The best fit theoretical power spectrum from the WMAP analysis [6] [Spergel et al. 2003] is plotted on the same figure. C_l from observed maps are consistent with the theoretical curve, C_l^T (except for the lowest multipoles). The bias and cosmic variance of BiPS depend on the total SI angular power spectrum of the signal and noise $C_l = C_l^S + C_l^N$. However, we have restricted our analysis to $l \lesssim 60$ where the errors in the WMAP power spectrum is dominated by cosmic variance. It is conceivable that the SI violation is limited to particular range of angular scales. Hence, multipole space windows that weigh down the contribution from the SI region of multipole space will enhance the signal relative to cosmic error, $\sigma_{\rm SI}$. We use simple filter functions in l space to isolate different ranges of angular scales; a low pass, Gaussian filter

$$W_l^G(l_s) = \exp(-(l+1/2)^2/(l_s+1/2)^2) \quad (45)$$

[5] http://www.netlib.org/slatec/src/

[6] Based on an LCDM model with a scale-dependent (running) spectral index which best fits the dataset comprised of WMAP, CBI and ACBAR CMB data combined with 2dF and Ly-α data

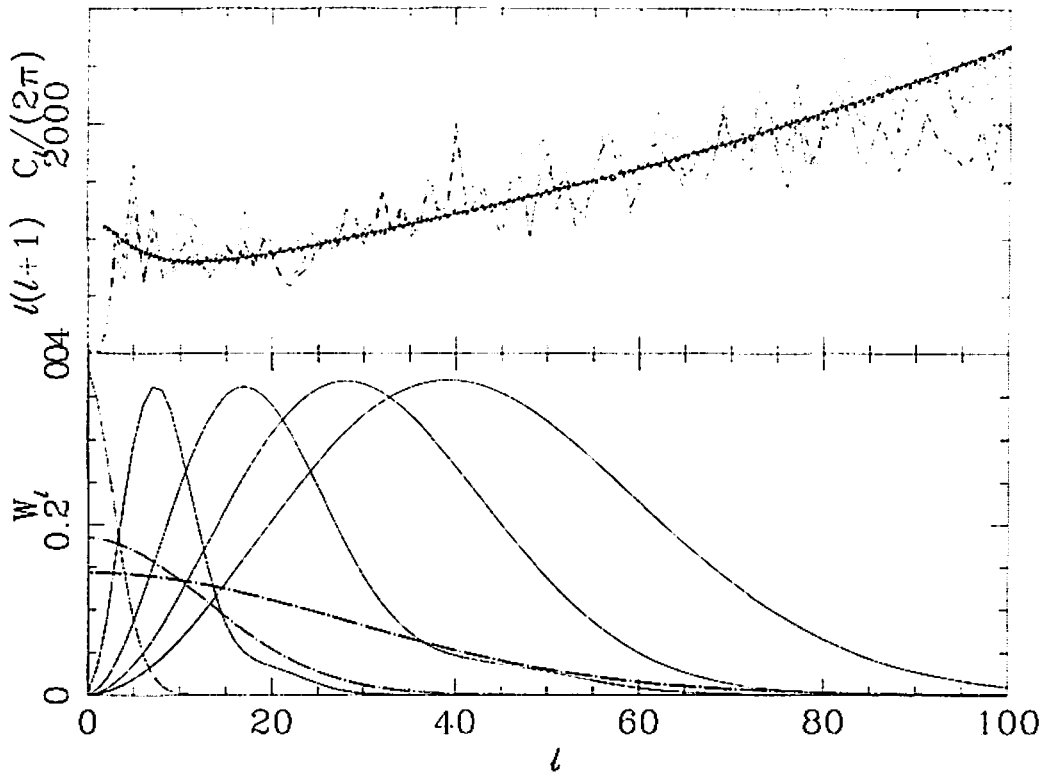


Figure 5: *Top:* C_ℓ of the two WMAP CMB anisotropy maps. The red, magenta and green curves correspond to map A, B and C, respectively. The black line is a 'best fit' WMAP theoretical C_ℓ used for simulating SI maps. Blue dots are the average C_l recovered from 1000 realizations. *Bottom:* These plots show the window functions used. The dashed curves with increasing l coverage are 'low-pass' filter, $W_l^G(l_s)$, with $l_s = 4, 18, 40$, respectively. The solid lines are 'band-pass' filter $W_l^S(l_t, l_s)$ with $(l_s, l_t) = (13, 2), (30, 5), (30, 20), (45, 20)$, respectively.

that cuts off power on small angular scales ($\lesssim 1/l_s$) and a band pass filter,

$$W_l^S(l_t, l_s) = [2(1 - J_0((l + 1/2)/(l_t + 1/2)))] \exp(-(l + 1/2)^2/(l_s + 1/2)^2) \quad (46)$$

that retains power within a range of multipoles set by l_t and l_s. The windows are normalized such that $\sum_l (l + 1/2)/(l(l + 1))W_l = 1$, i.e., unit *rms* for unit flat band power $C_l = 1/(l(l + 1))$. The window functions used in our work are plotted in figure 5. We use the C_l^T to generate 1000 simulations of the SI CMB maps. a_{lm}'s are generated up to an l_{max} of 1024 (corresponding to HEALPix resolution $N_{side} = 512$). These are then multiplied by the window functions $W_l^G(l_s)$ and $W_l^S(l_t, l_s)$. We compute the BiPS for each realization. Fig.5 shows that the average power spectrum obtained from the simulation matches the theoretical power spectrum, C_l^T, used to generate the realizations. We use C_l^T to analytically compute bias and cosmic variance estimation for κ_ℓ. This allows us to rapidly compute BiPS with 1σ error bars for different theoretical C_l^T.

We use the estimator given in eq.(36) to measure BiPS for the given CMB maps. We compute the BiPS for all window functions shown in Fig 5. Results for one these windows are plotted in Figs. 6. In the low-l regime, where we have kept the low multipoles, BiPS for all three given maps are consistent with zero. But in the intermediate-l regime (Fig. 6), although BiPS of ILC and TOH maps are well consistent with zero, the CSSK map shows a rising tail in BiPS due to the galactic mask. To confirm

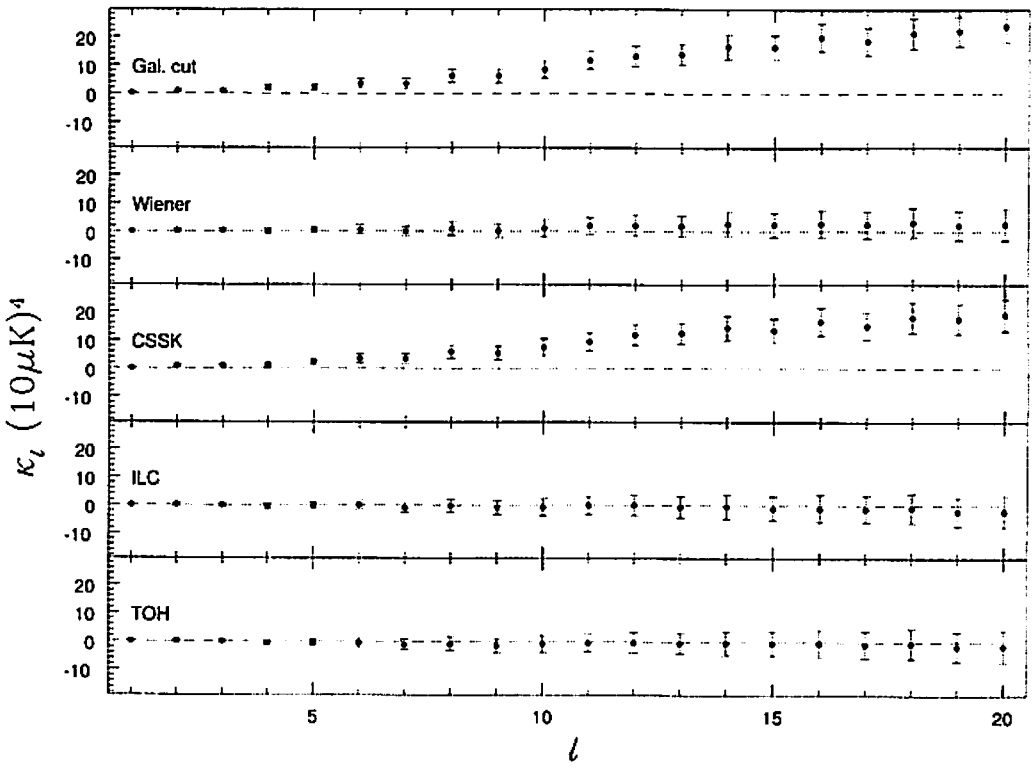


Figure 6: Measured BiPS for maps A, B and C filtered with a window with $l_s = 30$, $l_t = 20$. This is to check the statistical isotropy of the WMAP in the modest $20 < l < 40$ range in the multipole space where certain anomalies have been reported. ILC with a 10-degree-cut (top) has the same BiPS as map C ($l_s = 30$, $l_t = 20$) which explains that the raising tail of CSSK map is because of the mask.

it, we compute the BiPS for the ILC map with a 10-degree cut around the galactic plane (filtered with the same window function). The result is shown on the top panel of Fig. 6. Another interesting effect is seen when we apply a $W_l^S(20,45)$ filter, where Wiener filtered map has a non zero BiPS very similar to that of CSSK but weaker. The reason is that Wiener filter takes out more modes from regions with more foregrounds since these are inconsistent with the theoretical model. As a result, a Wiener filtered map at $W_l^s(20,45)$ filter has a BiPS similar to a cut sky map. The fact that Wiener map has less power at the Galactic plane can even be seen by eye! Hence using different filters allows us to uncover different types of violation of SI in a CMB map. In our analysis we have used a set of filters which enables us to probe SI breakdown on angular scales $l \lesssim 60$.

The BiPS measured from 1000 simulated SI realizations of C_l^T is used to estimate the probability distribution functions (PDF), $p(\tilde{\kappa}_\ell)$. A sample of the PDF for two windows is shown in Fig. 7. Measured values of BiPS for ILC, TOH and CSSK maps are plotted on the same plot. BiPS for ILC and TOH maps are located very close to the peak of the PDF. We compute the individual probabilities of the map being SI for each of the measured $\tilde{\kappa}_\ell$. This probability is obtained by integrating the PDF beyond the measured $\tilde{\kappa}_\ell$. To be precise, we compute

$$P(\tilde{\kappa}_\ell|C_l^T) \;=\; P(\kappa_\ell > \tilde{\kappa}_\ell) = \int_{\tilde{\kappa}_\ell}^{\infty} d\kappa_\ell\, p(\kappa_\ell), \quad \tilde{\kappa}_\ell > 0, \tag{47}$$

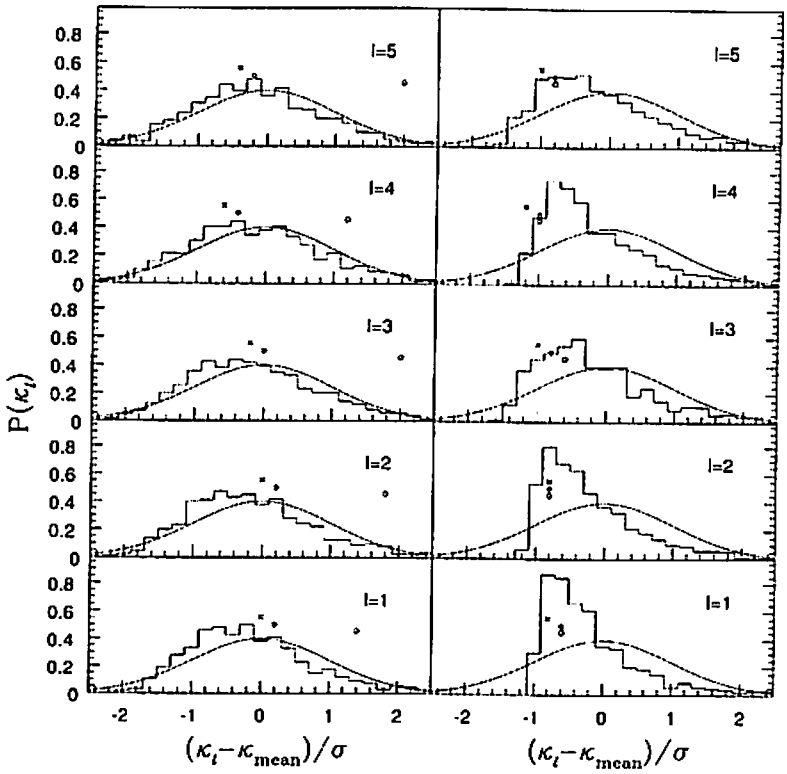


Figure 7: Probability distribution function for κ_1 to κ_5 constructed from 1000 realizations. The left panel shows the PDF for the maps filtered with $W_l^S(20,30)$ (left panel) and $W_l^G(l_s = 40)$ (right panel). The latter is more skewed, which explains the apparent $\sim 1\sigma$ shift in the κ_ℓ values for $W_l^G(l_s = 40)$ at low ℓ. The green, magenta and red (circular, pentagonal and rectangular) points represent ILC, CSSK and TOH maps, respectively. The smooth solid curves are Gaussian approximations.

$$= \quad P(\kappa_\ell < \tilde{\kappa}_\ell) = \int_{-\infty}^{\tilde{\kappa}_\ell} d\kappa_\ell \, p(\kappa_\ell), \quad \tilde{\kappa}_\ell < 0.$$

The probabilities obtained are shown in Figs. 4 and 4 for $W^S(20,30), W_l^G(40)$ and $W_l^G(4)$. The probabilities for the $W_l^S(20,30)$ window function are greater than 0.25 and the minimum probability at ~ 0.05 occurs at κ_4 for $W^G(40)$. The reason for systematically lower SI probabilities for $W_l{}^S(20,30)$ as compared to $W_l{}^G(40)$ is simply due to lower cosmic variance of the former. The contribution to the cosmic variance of BiPS is dominated by the low spherical harmonic multipoles. Filters that suppress the a_{lm} at low multipoles have a lower cosmic variance.

It is important to note that the above probability is a conditional probability of measured $\tilde{\kappa}_\ell$ being SI given the theoretical spectrum C_l^T (used to estimate the bias). A final probability emerges as the Bayesian chain product with the probability of the theoretical C_l^T used given data. Hence, small difference in these conditional probabilities for the two maps are perhaps not necessarily significant. Since the BiPS is close to zero, the computation of a probability marginalized over the C_l^T may be possible using Gaussian (or, improved) approximation to the PDF of κ_ℓ.

The important role played by the choice of the theoretical model for the BiPS measurement is shown for a W_l that retains power in the lowest multipoles, $l = 2$ and $l = 3$. Assuming C_l^T, there are hints of non-

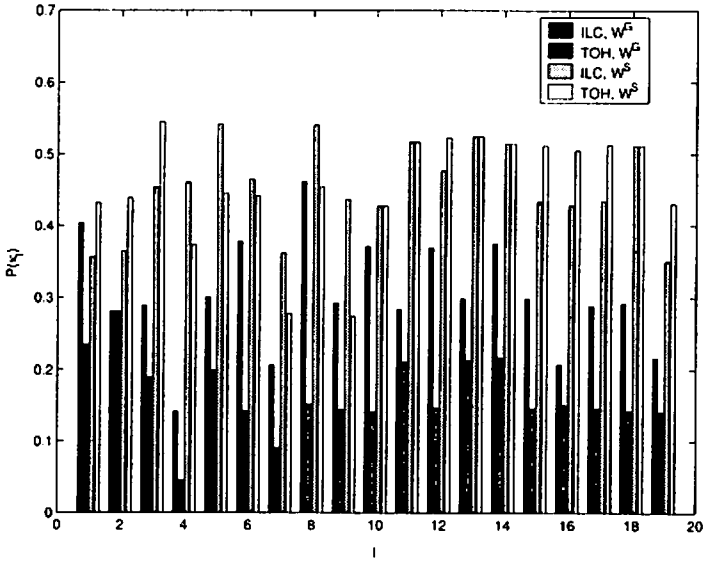


Figure 8: The probability of two of the *WMAP* based CMB maps being SI when filtered by $W_l^S(20,30)$ and a Gaussian filter $W_l^G(40)$.

SI detections in the low ℓ's (top-left panel of Fig. 9). We also compute the BiPS using a C_l^T for a model that accounts for suppressed quadrupole and octopole in the WMAP data [Shafieloo & Souradeep 2004]. The mild detections of a non zero BiPS vanish for this case (top-right panel of Fig. 9). The corresponding SI probabilities for the two choices of C_l^T are shown in the lower panels.

5 Discussion and Conclusion

The SI of the CMB anisotropy has been under scrutiny after the release of the first year of WMAP data. We use the BiPS which is sensitive to structures and patterns in the underlying total two-point correlation function as a statistical tool of searching for departures from SI. We carry out a BiPS analysis of WMAP full sky maps. We find no strong evidence for SI violation in the WMAP CMB anisotropy maps considered here. We have verified that our null results are consistent with measurements on simulated SI maps. The BiPS measurement reported here is a Bayesian estimate of the conditional probability of SI (for each κ_ℓ of the BiPS) given an underlying theoretical spectrum C_l^T. We point out that the excess power in the C_l^T with respect to the measured C_l from WMAP at the lowest multipoles tends to indicate mild deviations from SI. BiPS measurements are shown to be consistent with SI assuming an alternate model C_l^T that is consistent with suppressed power on low multipoles. Note that it is possible to band together κ_ℓ measurements to tighten the error bars further. The full sky maps and the restriction to low $l < 60$ (where instrumental noise is sub-dominant) permits the use of our analytical bias subtraction and error estimates. The excellent match with the results from numerical simulations is a strong verification of the numerical technique. This is an important check before using Monte-Carlo simulations in future work for computing BiPS from CMB anisotropy sky maps with a galactic mask and non uniform noise matrix.

There are strong theoretical motivations for hunting for SI violation in the CMB anisotropy. The possibility of non-trivial cosmic topology is a theoretically well motivated possibility that has also been observationally targeted [Ellis 1971, Lachieze-Rey & Luminet 1995, Levin 2002, Linde 2004]. The breakdown of statistical homogeneity and isotropy of cosmic perturbations is a generic feature of ultra large scale structure of the cosmos, in particular, of non trivial cosmic topology [Bond,Pogosyan & Souradeep 1998,2000].

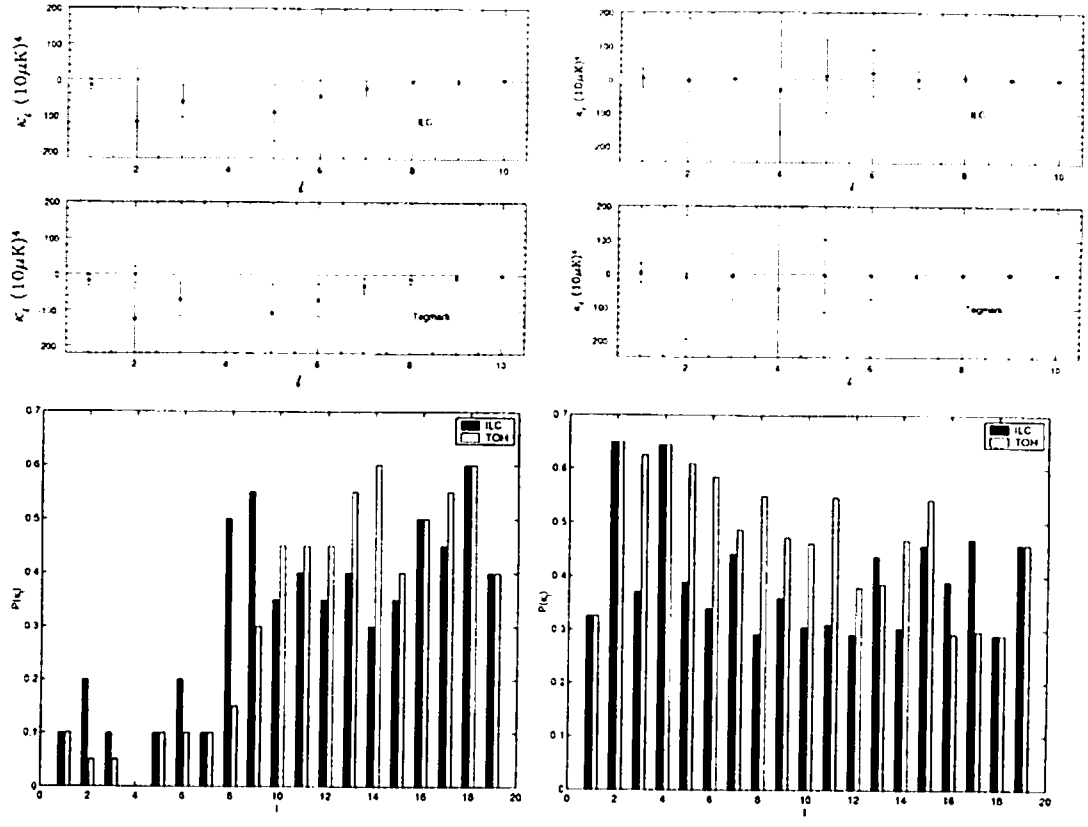


Figure 9: **Top;** Figure compares the measured values of κ_ℓ for maps A and B filtered to retain power only on the lowest multipoles, $l = 2$ and $l = 3$ assuming the WMAP theoretical spectrum WMAPbf (*left*) and a model spectrum that matches the suppressed power at the lowest multipoles [Shafieloo & Souradeep 2004]. The non zero κ_ℓ 'detections' assuming the WMAP theoretical spectrum become consistent with zero for a C_l^T that has power suppressed at low multipoles. **Bottom:** The corresponding SI probability assuming the WMAP theoretical spectrum, C_l^T (*left*) and a model spectrum that matches the suppressed power at the lowest multipoles (*right*).

The underlying correlation patterns in the CMB anisotropy in a multiply connected universe is related to the symmetry of the Dirichlet domain. The BiPS expected in flat, toroidal models of the universe has been computed and shown to be related to the principle directions in the Dirichlet domain [Hajian & Souradeep 2003a]. As a tool for constraining cosmic topology, the BiPS has the advantage of being independent of the overall orientation of the Dirichlet domain with respect to the sky. Hence, the null result of BiPS can have important implication for cosmic topology. This approach complements direct search for signature of cosmic topology [Cornish,Spergel & Starkman 1998, de Oliveira-Costa et al. 1996] and our results are consistent with the absence of the matched circles and the null S-map test of the WMAP CMB maps [Cornish et al. 2003, de Oliveira-Costa et al. 2003]. Full Bayesian likelihood comparison to the data of specific cosmic topology models is another approach that has applied to COBE-DMR data [Bond,Pogosyan & Souradeep 1998,2000]. Work is in progress to carry out similar analysis on the large angle WMAP data. We defer to future publication, detailed analyzes and constraints on cosmic topology using null BiPS measurements, and the comparison to the results from complementary approaches. There are also other theoretical scenarios that predict breakdown of SI that can be probed using BiPS, e.g., primordial cosmological magnetic fields [Durrer et al. 1998, Chen et al. 2004].

The null BiPS results also has implications for the observation and data analysis techniques used to create the CMB anisotropy maps. Observational artifacts such as non-circular beam, inhomogeneous noise correlation, residual stripping patterns, etc. are potential sources of SI breakdown. Our null BiPS results confirm that these artifacts do not significantly contribute to the maps studied here. Foreground residuals can also be sources of SI breakdown. The extent to which BiPS probes foreground residuals is yet to be fully studied and explored. We do not see any significant effect of the residual foregrounds in ILC and the TOH maps as it was mentioned by [Eriksen et al. 2004c]. This can not be necessarily called a discrepancy between the two results unless we know what should have been seen in the BiPS. The question is if the signal is strong enough and whether the effect smeared out in bipolar multipole space within our angular l-space window. On the other hand, the very fact that BiPS does show a strong signal for the Wiener filtered map, mean that at some level BiPS is sensitive to galactic residuals.

In summary, we study the Bipolar power spectrum (BiPS) of CMB which is a promising measure of SI. We find null measurements of the BiPS for a selection of full sky CMB anisotropy maps based on the first year of WMAP data. Our results rule out radical violation of statistical isotropy in the CMB anisotropy measured by WMAP.

References

[Bamba et al. 2004] Bamba, K., Yokoyama, J., Phys.Rev. D69 (2004) 043507.

[Bardeen et al. 1983] Bardeen, J. M., Steinhardt, P. J. & Turner, M. S. 1983, Phys. Rev. D 28, 679.

[Bartolo et al. 2004] Bartolo, N., Komatsu, E., Matarrese, S., Riotto, A., *preprint* (astro-ph/0406398)

[Bennett et al. 2003] Bennett, C. L., et.al., 2003, Astrophys. J. Suppl., **148**, 1.

[Bond 2004] Bond, J. R. et al. 2004, Int. J. Theor. Phys. 2004, ed. Verdaguer, E., "The Early Universe: Confronting theory with observations" (June 21-27, 2003) (astro-ph/0406195).

[Bond,Pogosyan & Souradeep 1998,2000] Bond, J. R., Pogosyan, D. & Souradeep,T. 1998, Class. Quant. Grav. **15**, 2671; *ibid.* 2000, Phys. Rev. **D 62**,043005;2000, Phys. Rev. **D 62**,043006.

[Chen et al. 2004] Chen, G., Mukherjee, P., Kahniashvili, T., Ratra, B., Wang, Y., Astrophys.J. 611 (2004) 655.

[Coles 2003] Coles, P. et al. 2003, *preprint* (astro-ph/0310252).

[Copi et al. 2004] Copi, C. J., Huterer, D. & Starkman, G. D. 2004, Phys. Rev. D. *in press*, (astro-ph/0310511).

[Cornish,Spergel & Starkman 1998] Cornish, N.J., Spergel, D.N. & Starkman, G. D. 1998, Class. Quantum Grav., **15**, 2657

[Cornish et al. 2003] Cornish, N. J., Spergel, D., Starkman, G. , Komatsu, E., 2004, Phys.Rev.Lett. 92, 201302.

[Cruz et al. 2004] Cruz, M., Martinez-Gonzalez, E., Vielva, P., Cayon, L., *preprint* (astro-ph/0405341).

[de Oliveira-Costa et al. 2003] de Oliveira-Costa, A., Tegmark, M., Zaldarriaga, M. & Hamilton, A. 2004, Phys. Rev.**D69**, 063516.

[de Oliveira-Costa et al. 1996] de Oliveira-Costa, A. Smoot, G. F., Starobinsky, A. A., 1996, ApJ **468**, 457.

[Dineen et al. 2004] Dineen, P. , Rocha, G., Coles, P, *preprint* (astro-ph/0404356).

[Donoghue et al. 2004] Donoghue, E. P., and Donoghue, J. F., *preprint* (astro-ph/0411237).

[Durrer et al. 1998] Durrer, R., Kahniashvili, T. and Yates, A., 1998, Phys. Rev. **D 58**, 3004.

[Ellis 1971] Ellis, G. F. R. 1971, Gen. Rel. Grav. **2**, 7.

[Eriksen et al. 2004a] Eriksen, H. K. et al., 2004, Astrophys. J **605**, 14.

[Eriksen et al. 2004b] Eriksen, H. K. et al., 2004, Astrophys. J. **612**, 64.

[Eriksen et al. 2004c] Eriksen, H. K. et al., 2004, Astrophys. J. **612**, 633.

[Gaztanaga & Wagg 2003] Gaztanaga, E. & Wagg, J. 2003, Phys. Rev. D68 021302.

[Górski,Hivon & Wandelt 1999] Górski,K. M., Hivon, E., Wandelt, B. D. 1999, in "Evolution of Large-Scale Structure", eds. A.J. Banday, R.S. Sheth and L. Da Costa, PrintPartners Ipskamp, NL, pp. 37-42 (also astro-ph/9812350).

[1] J. R. Gott 1980. Mon. Not. R. Astr. Soc. **193**, 153.

[Guth & Pi 1982] Guth, A. H. & Pi, S.-Y. 1982, Phys. Rev. Lett., 49, 1110.

[Hajian & Souradeep 2003a] Hajian, A. & Souradeep, T., 2003 *preprint* (astro-ph/0301590).

[Hajian & Souradeep 2003b] Hajian, A. and Souradeep, T., 2003b, ApJ 597, L5 (2003).

[Hajian & Souradeep 2005a] Hajian, A. & Souradeep, T., 2005, ApJ 618, L63.

[Hajian & Souradeep 2005b] Hajian, A. & Souradeep, 2005, *preprint* (astro-ph/0501001)

[Hajian et al. 2004] Hajian, A., Pogosyan, D. Souradeep, T., Contaldi, C., Bond, R., 2004 *in preparation*; Proc. 20th IAP Colloquium on Cosmic Microwave Background physics and observation, 2004.

[Hajian et al. 2004b] Hajian, A., Chen, G., Souradeep, T., Kahniashvilli, T., Ratra, B., 2004 *in preparation.*

[Hansen et al. 2004] Hansen, F. K., Banday, A. J. & Gorski, K. M. 2004, *preprint.* (astro-ph/0404206)

[Hinshaw et al. 2003] G. Hinshaw, Astrophys. J. Suppl.,(2003) ,**148**, 135.

[Komatsu et al. 2003] Komatsu, E. et.al., 2003, ApJS, **148**, 119.

[Kogut et al. 2003] Kogut A. et al., 2003, Astrophys. J. Suppl.,**148**, 161.

[Lachieze-Rey & Luminet 1995] Lachieze-Rey, M. and Luminet,J. -P. 1995, Phys. Rep. **25**, 136.

[Larson & Wandelt 2004] Larson, D. L. & Wandelt, B. D. 2004, *preprint*, (astro-ph/0404037).

[Levin 2002] Levin, J. 2002, Phys. Rep. **365**, 251.

[Levin et al. 1998] Levin J., Scannapieco E., Silk J., (1998), Class.Quant.Grav. 15, 2689.

[Linde 2004] Linde, A., (2004), JCAP 0410, 004, (astro-ph/0408164).

[Luminet et al. 2003] Luminet, J.-P. et al. 2003, Nature 425 593.

[Ma & Bertschinger 1995] Ma, C.-P., & Bertschinger, E. 1995, ApJ, 455, 7

[Mitra et al. 2004] Mitra, S., Sengupta, A., S., Souradeep, T.,*preprint* astro-ph/0405406

[Munshi et al. 1995] Munshi, D., Souradeep, T., and Starobinsky, A. A., (1995), Astrophys. J., 454, 552.

[Page et al. 2003] Page L. et al., 2003, Astrophys. J. Suppl.,**148**, 233.

[Naselsky et al. 2004] Naselsky et al, 2004, *preprint*, (astro-ph/0405523); *ibid* (astro-ph/0405181), 2003; ApJ,599,L53 and references therein.

[Park 2004] Park, C., 2004, Mon. Not. Roy. Astron. Soc. **349**, 313.

[Peiris et al., 2003] Peiris H.V. et al., 2003, Astrophys. J. Suppl.,148, 213.

[Prunet et al. 2004] Prunet, S., Uzan, J., Bernardeau, F., Brunier, T., 2004, *preprint* (astro-ph/0406364).

[Ratra 1992] Ratra, B., (1992), Astrophys.J. 391, L1.

[Sachs and Wolfe, 1967] Sachs, R. K., and Wolfe, A. M. 1967, ApJ, 147, 73.

[Schwarz et al. 2004] Schwarz, D. J. et al., 2004, *preprint* (astro-ph/0403353).

[Shafieloo & Souradeep 2004] Shafieloo, A. & Souradeep, T., 2004, Phys. Rev. D, *in press*, (astro-ph/0312174).

[Sokolov & Shvartsman 1974] D. D. Sokolov and V. F. Shvartsman (1974) Zh. Eksp. Theor. Fiz. **66**, 412 [JETP, **39**, 196 (1974)].

[Souradeep 2000] Souradeep,T. 2000, in 'The Universe', eds. Dadhich, N. & Kembhavi, A., Kluwer.

[Souradeep & Hajian 2003] Souradeep, T. and Hajian, A., 2004, Pramana, **62**, 793.

[Spergel et al. 2003] Spergel, D. et al., 2003, Astrophys. J. Suppl., **148**, 175.

[Spergel et al. 1999] Spergel, D., and Goldberg, D. M., (1999), Phys.Rev. D59, 103001.

[Starkman 1998] Starkman, G. Class. 1998, Quantum Grav. **15**, 2529.

[Starobinsky 1982] Starobinsky, A. A. 1982, Phys. Lett, 117B, 175.

[Tegmark et al. 2004] Tegmark, M., de Oliveira-Costa, A. & Hamilton, A., 2004, Phys.Rev. **D68** 123523.

[Varshalovich et al. 1988] Varshalovich, D. A., Moskalev, A. N., Khersonskii, V. K., 1988 *Quantum Theory of Angular Momentum* (World Scientific).

[Vielva et al. 2003] Vielva, P., Martinez-Gonzalez, E., Barreiro, R. B., Sanz, J. L., Cayon, L., 2003, *preprint* (astro-ph/0310273).

[Zaldarriaga et al. 1998] Zaldarriaga, M., Seljak, U., Bertschinger, E., 1998, Astrophys. J., 494, 491.

Inflation from String Theory

James M. Cline[1]

Department of Physics, McGill University, 3600 University St., Montréal, Qc H3A 2T8 Canada

Abstract

I review some aspects of obtaining inflation from string theory, in particular brane-antibrane inflation within the framework of KKLMMT, and racetrack inflation. Further, I discuss recent work on the problem of reheating after brane-antibrane annihilation, and possible distinctive features of production of cosmic string and brane defects at this time.

1 Introduction

Many experiments are now yielding exciting, high-precision results about the universe, concerning the cosmic microwave background, large scale structure through galaxy surveys, Lyman α forest observations and weak gravitational lensing, and the dark energy via distant type Ia supernovae. Particle physics experiments, on the other hand, are presently quite limited in what they can tell us about physics at the most fundamental level, for which string theory is a very attractive candidate theory. For these reasons many string theorists have turned to the early universe as a possible laboratory for testing the theory.

In this talk I will focus on string theory as a source of inflation, various aspects of which have been investigated in references [1]-[5]. I will start by reviewing the KKLT [6] and KKLMMT [7] picture, then describe our attempt to embed this in a more realistic theory including the standard model [1], as well as a variant dubbed "racetrack inflation" [2]. Following the discussion of these inflationary models, I will then turn to the issues surrounding the end of inflation, namely how reheating may be realized [3], the production of cosmic superstring defects [4], and the question of whether our universe itself could be a 3-brane defect created at the end of inflation [5].

2 Brane-antibrane inflation in flux compactifications

Intuitively it is quite appealing to imagine that inflation could have been driven by the potential energy which gives rise to the attractive force between a brane and antibrane in the early universe [8, 9], and that reheating results from their mutual annihilation. However it was initially not easy to get this simple idea to work in detail. First, the potential was not automatically flat enough to get inflation, so it was necessary to look for means to get around this problem [10, 11]. Even then, there remained a serious shortcoming: various moduli parametrizing the size and shape of the compact dimensions were considered to be fixed without specifying the mechanism. It was not clear whether an actual stabilization mechanism would preserve whatever degree of flatness one had managed to achieve for the inflaton potential.

The problem of modulus stabilization received a big boost within the context of type IIB string theory through reference [12] (GKP), where the paradigm of stabilization by fluxes of NS-NS and R-R gauge fields in 3-cycles of the Calabi-Yau manifold appeared (figure 1). A nice feature of this approach is that a warped throat with an exponentially large hierarchy could be generated from a small hierarchies in the ratio of the fluxes. Such throats provide a way of solving the hierarchy problem [13] for an observer living on a brane in the bottom of the throat. In this compactification the dilaton and complex structure (shape) moduli are stabilized, but not the overall volume (Kähler) modulus.

[1] E-mail:jcline@physics.mcgill.ca

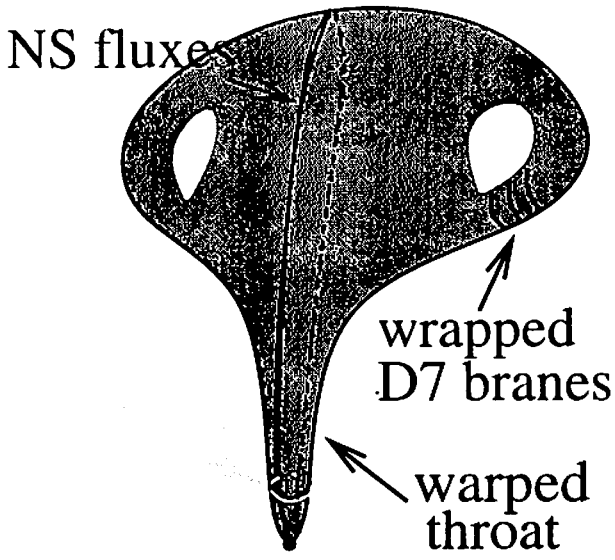


Fig. 1: stabilization by fluxes

The GKP idea was put into a cosmological context in reference [6], where nonperturbative effects like gaugino condensation were invoked to generate a superpotential for the Kähler modulus, T,

$$W = W_0 + Ae^{-aT} \tag{1}$$

where the constant piece W_0 was already arising within GKP. This gives rise to a supergravity F-term potential

$$V_F = e^K \left(K^{ab} D_a W \overline{D_b W} - 3|W|^2 \right) \tag{2}$$

with a supersymmetric AdS (negative energy) minimum, where T is stabilized. For cosmological purposes one would like to raise this minimum to a positive value to obtain deSitter space. KKLT realized that this could be achieved by putting an anti-D3 brane, which breaks SUSY, into the throat. The antibrane gives an additional contribution to the potential,

$$V_{\overline{D3}} = \frac{k}{T^2} \tag{3}$$

which can raise the minimum of the potential to a positive value. The resulting minimum was only metastable, with the decompactified theory at $T \to \infty$ being the true minimum, but it was shown that the lifetime of the deSitter vacuum could easily be cosmologically long.

The step from eternal deSitter space to inflation was made in [7] (KKLMMT) by adding to this picture a mobile D3 brane which would fall down the throat due to its attraction to the antibrane. (Note that there should actually be more than one antibrane in the throat since we want inflation to end with Minkowski space, not AdS, which would result from the annihilation of the antibrane if there was only one of them.) This was the first example of brane-antibrane inflation where the problem of modulus stabilization was addressed in a rigorous way. The idea would have worked perfectly, in that the effect of warping in the throat was to make the potential of the inflaton (the brane-antibrane separation) naturally small and thus flat:

$$V_{inf} = \frac{k'}{T^2 |\psi - \psi_0|^4} \tag{4}$$

Here ψ and ψ_0 are the positions of the brane and antibrane respectively, and the coefficient k' is suppressed by exponentially small warp factors. However, this nice picture was spoiled by a crucial technicality. Namely, the brane can only be consistently introduced if the volume modulus appearing in the Kähler

function K and in the $1/T^2$ factors in (3,4) becomes $T - f(|\psi|^2)$ instead of just T. The function f can be expanded as $|\psi|^2 + O(\psi^3)$ near $\psi = 0$. Thus the inflaton gets a large additional contribution to its mass^2 which is of order the total potential, $V/M_p^2 \sim H^2$, ruining the slow-roll condition. To counteract this, it was necessary to imagine some source of ψ-dependence in the superpotential, which would be fine-tuned to cancel the unwanted contributions [7, 14, 15].

3 Realistic brane-antibrane inflation

One might also wonder where the standard model (SM) is living in this picture. In [1] we considered a construction in which the SM brane is at a singular fixed point of a 4-torus in the bottom of the throat, which has been orbifolded under a Z_N symmetry (figure 2). These singularities have the advantage of admitting chiral gauge theories and are thus good candidates for placing the SM. Each singularity (of which there are many) bring with it a new a modulus, a blowing-up mode described by a chiral field B_i. We were interested to see if these modes could have a significant effect on inflation. To investigate this, we simplified the problem by keeping only one of these modes.

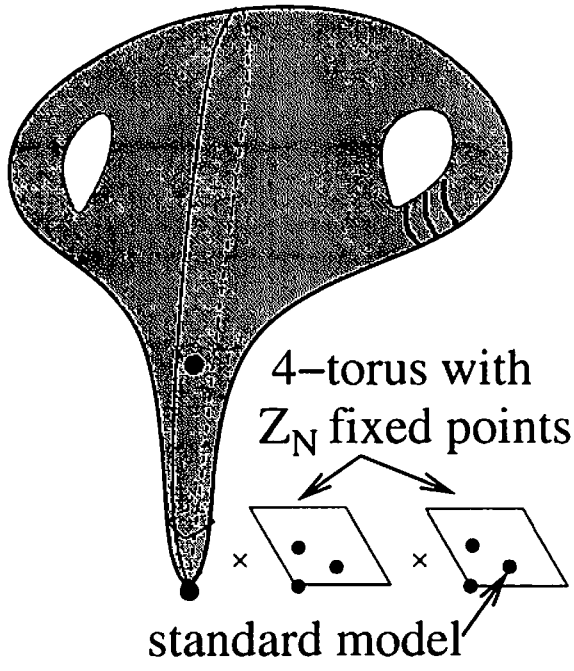


Fig. 2: the KKLMMT construction with the Standard Model

The resulting potential is complicated, and depends on three complex fields, the brane position $\psi + i\phi$, the Kähler modulus $T = \sigma + i\tau$ and the blowing-up mode $B + i\beta$:

$$\begin{aligned} V &= \frac{e^{2B^2}}{r^3}\left(2\frac{AC(ra+4B^2-2cB)\cos(\tau-\beta)}{e^{a\sigma/2}e^{cB}} + 2\frac{AW_0(ra+4B^2)\cos\tau}{e^{a\sigma/2}}\right. \\ &+ \left. 4\frac{BCW_0(2B-c)\cos\beta}{e^{cB}} + \frac{A^2(12B^2+6ra+r\sigma a^2)}{3e^{a\sigma}} + \frac{C^2(2B-c)^2}{(e^{cB})^2} + 4B^2{W_0}^2\right) \\ &+ 2\frac{B^2}{f_0^2} + \frac{k}{r^2} + \frac{k'}{r^2|\psi-\psi_0|^4} \end{aligned} \tag{5}$$

where $r = \sigma - \psi^2$. The kinetic energy is also complicated. However one finds that most of the fields are heavy and can be integrated out, with the exception of σ and ψ. In principle the σ field could also be

integrated out, but since its nontrivial minimum is a delicate feature, we keep track of its dynamics. In the right regime of parameters, the potential looks like figure 3, with a trough in the ψ direction at the value of σ where it is stabilized.

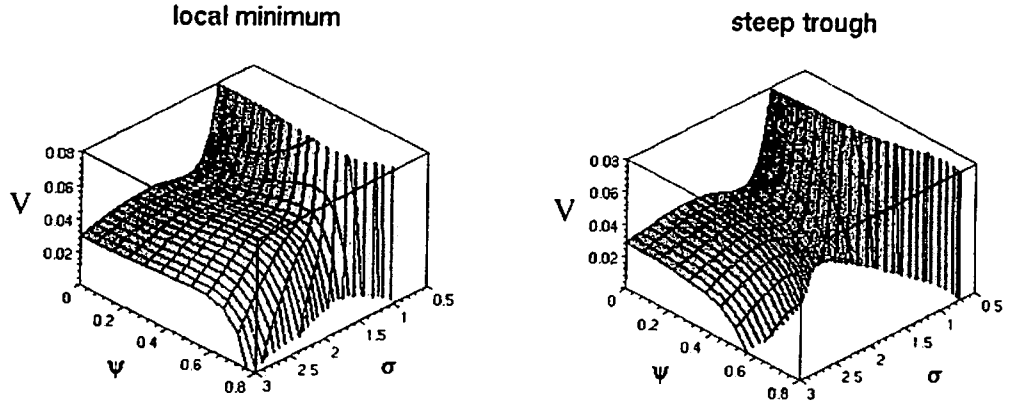


Fig. 3: Inflaton potential not yet tuned to be sufficiently flat. There is a local minimum (left) leading to eternal deSitter space, or else it rolls too quickly to give enough inflation (right).

We found that it is possible to tune parameters so that the trough is sufficiently flat, without introducing any new source of ψ dependence such as in the superpotential. Hence this is in way a simpler realization than was suggested in KKLMMT. Detailed study of the inflaton dynamics shows that the degree of fine-tuning needed is rather severe however. Figure 4 shows that the value of k needed to get a given number of e-foldings of inflation, for some fixed values of the other parameters, must be tuned to a part in 1000 to get 60 e-foldings.

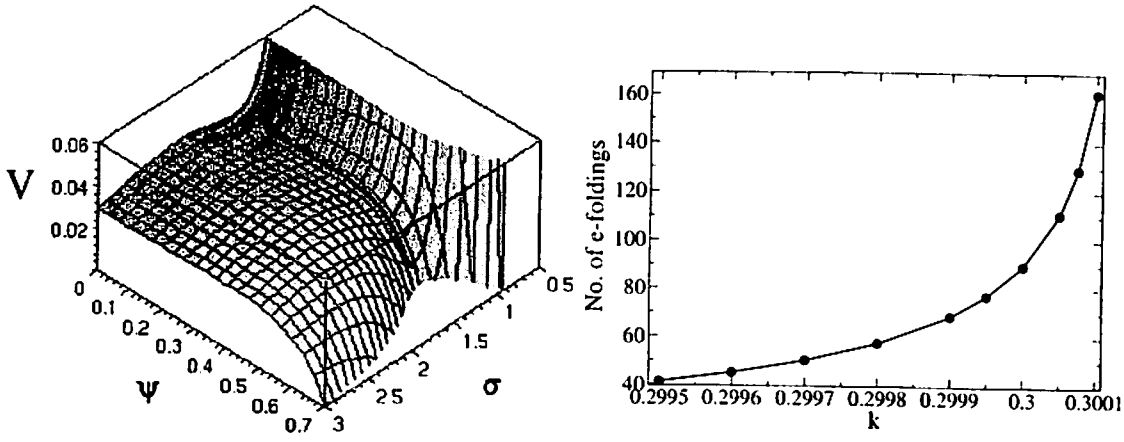


Fig. 4: To obtain a flat trough (left), strong tuning of parameters is required (right).

Nevertheless, other models of inflation also require tuning to get a flat potential, so it is worthwhile to reserve judgment and consider whether the theory has any distinctive predictions. One prediction is that the scalar spectral index may have significant deviations from $n = 1$ and some level of negative running, $dn/d\ln k < 0$, as illustrated in figure 5, for a model where the COBE fluctuations are produced between 30 and 40 e-foldings after the beginning of inflation.

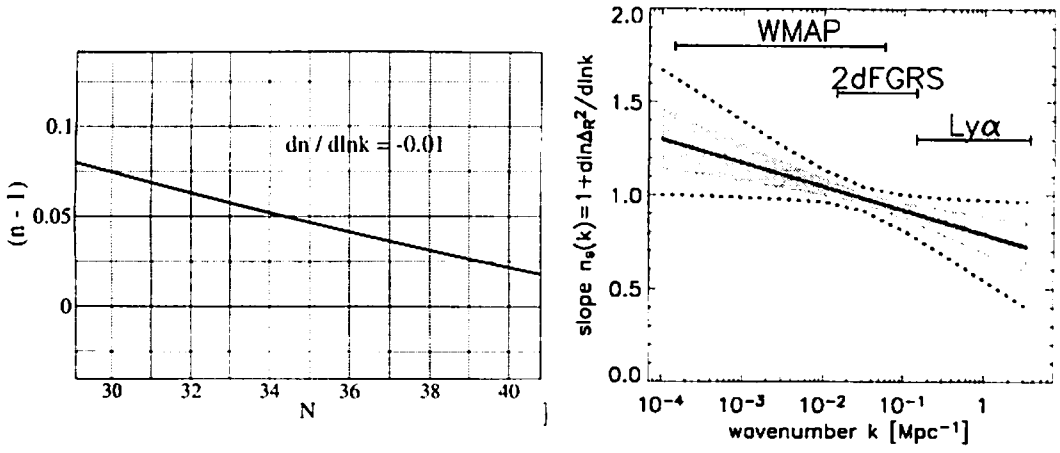


Fig. 5: Left: deviation of scalar spectral index from 1 as a function of $N \sim \ln k$, over the range visible in the CMB for a particular choice of model parameters. Right: WMAP, 2DF galaxy redshift survey and Lyman alpha combined constraints.

Unfortunately such predictions are only indicative and not robust, since one can always tune the potential to be even more flat, to further suppress the deviations from $n = 1$. However the fact that more tuning would be required encourages one to believe that the most natural situation is one in which inflation lasted for only a short time (the minimal canonical 60 e-foldings), which leads to the largest deviations from $n = 1$ which are not yet ruled out. Interestingly the constraints are becoming stronger with the combination of Lyman alpha forest data from the Sloan Digital Sky Survey with WMAP data [16], claiming a determination of $n = 0.98 \pm 0.02$.

It is also interesting that one can find more exotic inflaton trajectories in which the Kähler modulus plays a role, by opening up a gap in the trough through which σ can escape, as shown in figure 6. (To be realistic, these would require additional metastable minima at larger values of σ to prevent decompactification of the extra dimensions.) Such complications could give rise to isocurvature fluctuations, and to bumpy features in the scalar spectrum as shown in figure 7. Although there is not yet evidence of such features, we can hope they will appear in future data, giving a valuable fingerprint that will help to identify which inflationary model is correct.

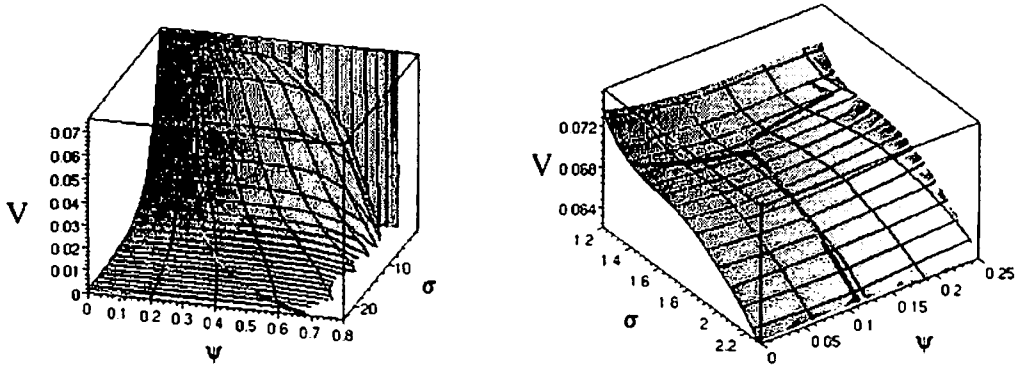


Fig. 6: Examples of inflation with combined motion of brane and Kähler moduli.

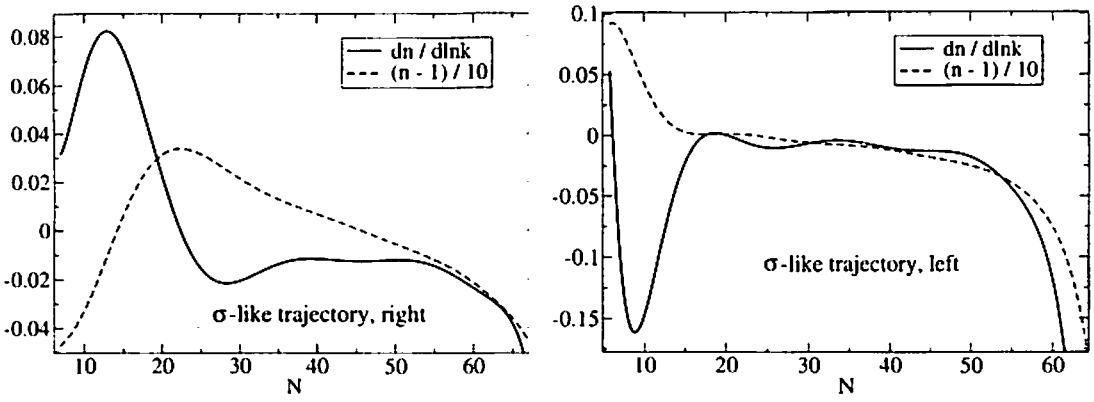


Fig. 7: Features in the power spectrum arising from the twisted inflaton trajectories of fig. 6, right.

4 Racetrack inflation

In [2] we considered a variant of the KKLMMT model which is simpler, in that no mobile D3 brane is required. Instead we enlarge the gauge group in which the gauginos are condensing to be a product, SU(N)×SU(M), which generalizes the superpotential to

$$W = W_0 + Ae^{-aT} + Be^{-bT} \tag{6}$$

where $a = 2\pi/N$ and $b = 2\pi/M$. Remarkably, this sufficient to obtain inflation from the Kähler field itself, which marks perhaps the first time where string moduli have been successfully used for inflation in a rigorous setting. The potential is simply the F-term (2) and the antibrane term (3). The former by itself would be the conventional racetrack potential which has been previously studied for modulus stabilization.

Writing $T = X + iY$, the potential can be viewed as in figure 8. Since it has two degenerate minima, it provides an example of topological inflation: there will be separated domains of the universe in different minima, and between them inflating domain walls which guarantee the existence of regions in the universe where the initial conditions are correct for inflation to take place.

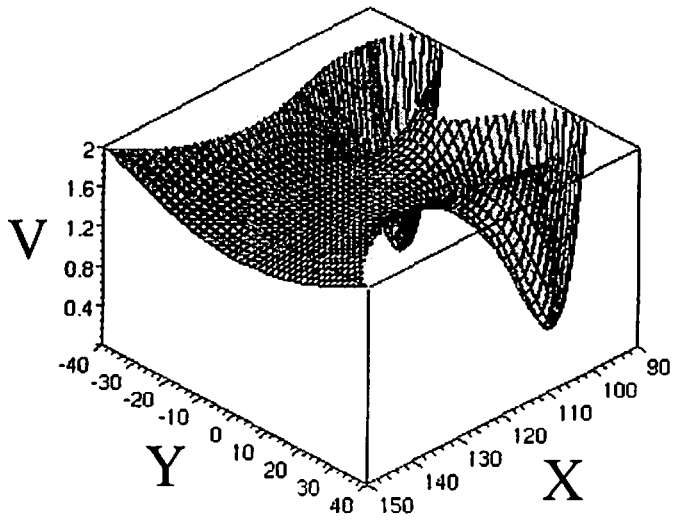


Fig. 8: The racetrack inflation potential

Unfortunately this model is just as fine tuned as the previous one. For sample values of the parameters given by $A = \frac{20}{1000}$, $B = -\frac{3\cdot1}{1000}$, $a = \frac{2\pi}{100}$, $b = \frac{2\pi}{90}$, the term W_0 must lie in the narrow range $-\frac{1}{20389} \leq W_0 \leq -\frac{1}{20400}$, constituting a 1 part in 2000 tuning. On the positive side, the predictions of this model are more robust than in the previous one. We find that regardless of how long inflation lasts, the spectral index 60 e-foldings before the end of inflation is always near $n = 0.95$, as shown in figure 9. It is interesting that such values may already be starting to feel pressure from the observational constraints.

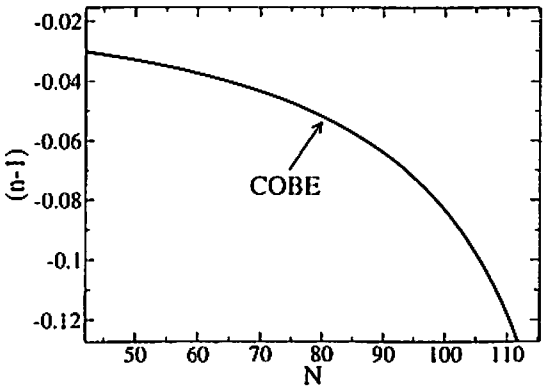


Fig. 9: spectral index of the racetrack model

5 The reheating problem in brane-antibrane inflation

It is not as obvious how reheating will work in brane-antibrane inflation as in conventional inflation models. The brane-antibrane case is almost like hybrid inflation, but there is an important difference, illustrated in figure 10. In both cases, the end of inflation is signaled by a field orthogonal to the inflaton becoming tachyonic. In the hybrid case this second field rolls to a stable minimum, oscillates around it, and causes conventional reheating (or preheating). In the string-theory case, the tachyonic field is described by Sen's effective action (for a review see [17]),

$$S = -\int d^{p+1}x\, e^{-|T|^2/a^2}\left(\sqrt{1-|\partial T|^2}\right) \tag{7}$$

Here a is the string length scale, and T now stands for the mode of the open string between a brane and antibrane which becomes tachyonic when their distance becomes smaller than some critical value. The potential is minimized only as $T \to \infty$, with no oscillations that can give reheating in the usual way. In fact the whole action vanishes in this limit. At zero string coupling, the coherent tachyon condensate would persist forever, with the equation of state of cold dark matter, and the universe would never reheat. At nonzero string coupling, the tachyon fluid quickly decays into closed strings. There is a danger that these closed string states will naturally decay into the ground state of the closed string, namely gravitons. If this is the whole story, then there is still no reheating, since the gravitons are not visible radiation.

In [3] we have pointed out a very simple solution to this problem, namely that inflation should take place in a separate throat from that where the SM is living, as depicted in figure 11(a). This is already a very natural assumption to make from the standpoint of the hierarchy problem, since large warping in the SM model throat is needed to explain the smallness of the Higgs mass, whereas we need a larger energy scale hence smaller warping in the inflation throat to get the right level of density fluctuations.

To see why two throats help solve the reheating problem, notice that the geometry of the throats is like that of the Randall-Sundrum model [13]:

$$ds^2 = a^2(y)\,dx^2 + dy^2 + y^2 d\Omega_5^2 \tag{8}$$

where y represents distance along the throat and Ω_5 are the orthogonal directions of the 6D Calabi-Yau space. The warp factor is an exponential, $a(y) = e^{-ky}$. The idea is that the closed string states which result from the decay of the tachyon condensate have the right quantum numbers to decay into Kaluza-Klein graviton excitations. Consider then the wave functions of these KK states along the y direction. Schematically they have the form shown in figure 12: they are exponentially enhanced inside the throats, relative to outside. Because of this exponential enhancement, the KK gravitons decay with the largest branching fraction into particles on branes in the most strongly warped throats. The KK gravitons couple to SM model like ordinary gravity, but with a suppression of the TeV scale rather than the Planck scale. Thus efficient reheating of the SM brane is guaranteed so long as it lives in the deepest throat.

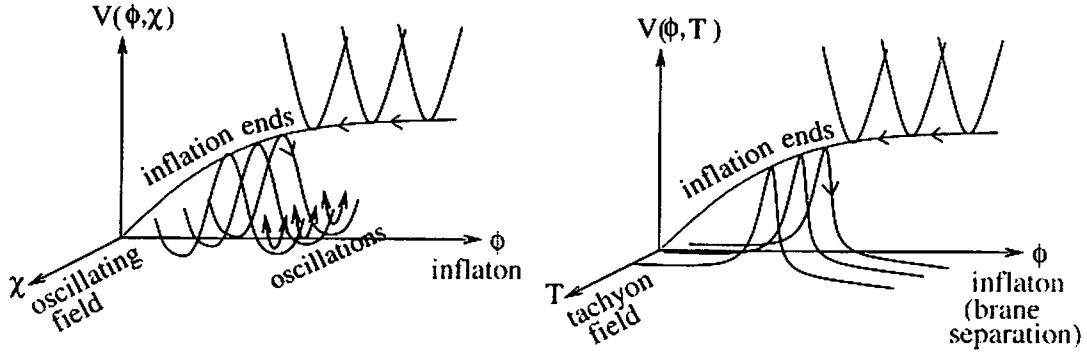


Fig. 10: potentials for hybrid inflation (left) and brane-antibrane inflation (right).

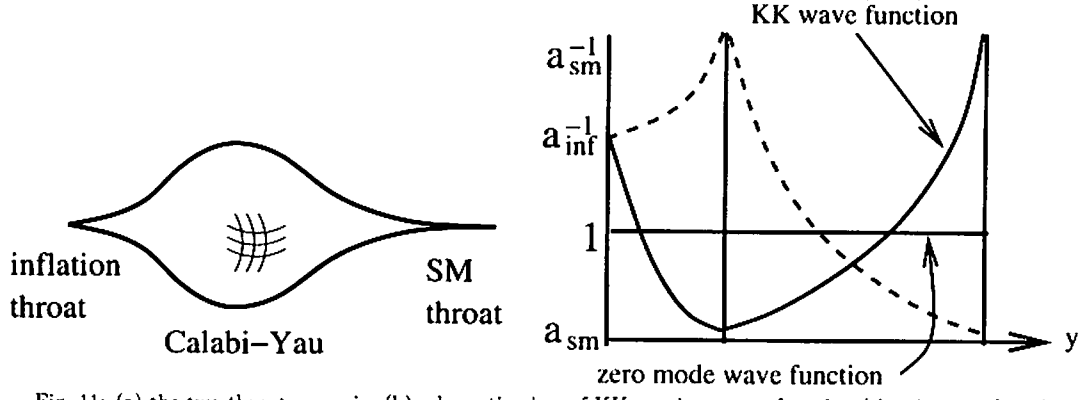


Fig. 11: (a) the two-throat scenario; (b) schematic view of KK graviton wave function (showing envelope but not oscillations) in the two-throat model, with a fictitious Planck brane between the throats.

There is another reason why this scenario for reheating is attractive. Recently there has been intense interest in the possibility that superstrings survive as cosmological remnants [18, 19]. Although they cannot be the dominant source of density fluctuations, a small contribution could be detectable in the CMB. The gravity waves created by kinks and cusps on such strings could also be observable in future pulsar timing measurements, and especially the LIGO gravitational wave interferometer experiment [20]. It is very exciting that cosmic superstrings could provide the strongest signal for LIGO, if the string tension μ is sufficiently low. The warp factor of the inflationary throat provided by the flux compactification scenario gives the dial needed for adjusting μ to low enough scales. However the stability of relic superstrings requires that the SM brane (and other branes) be separated from the remnant strings within the extra dimensions—otherwise the strings can reconnect to branes and break up. The two-throat picture we propose for reheating is just what is needed to also allow for the survival of string relics.

6 Overproduction of cosmic superstrings?

At the end of brane-antibrane inflation, the fate of the false vacuum energy in the tension of the annihilating branes is determined by the dynamics of the tachyon field in (7). Because it is a complex field, it is possible for defects of codimension two to form. These are topological defects, where the phase of the field winds around the core of the defect. On annihilating 3-branes, they would be cosmic D-strings, as illustrated in figure 12. It has been rigorously established that the defects which form from unstable branes or annihilating branes are actually consistent with being D-branes themselves, of smaller dimensionality [17].

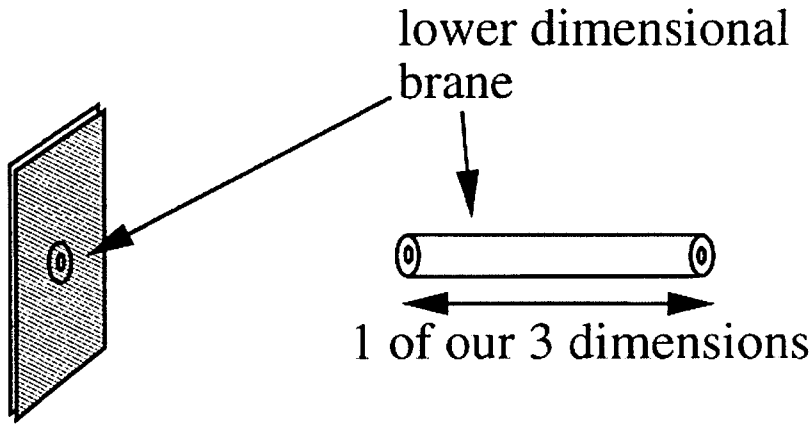


Fig. 12: formation of a cosmic string defect from annihilating 3-branes.

In the conventional formation of string defects, as in a GUT phase transition, the initial density of would-be defects is set by a microphysical scale, the inverse mass of the fields forming the defect. But in these theories the large initial gradient energy can be minimized by unwinding of the phase. This occurs through the annihilation of nearby defects with opposite winding number. Such unwinding can occur between defects that are in causal contact, but in an expanding universe, strings in different Hubble volumes cannot interact. This is the basis for the Kibble mechanism, guaranteeing at least of order 1 defect surviving per Hubble volume during the initial stages of defect formation. It is worth noting however that this is only a lower bound. If the defects were less efficient in annihilating, many more could survive this initial stage of unwinding.

The unusual form of the action (7) leads to precisely to such an expectation for cosmic superstrings, that their initial density will be much higher than the minimum dictated by Kibble's argument. This is because of the exponential suppression factor $e^{-|T|^2/a^2}$ which multiplies the kinetic term as well as the potential. Because of this, the restoring force which would normally attract defects to antidefects quickly becomes negligible as the tachyon field rolls from its unstable maximum. As a result, we observe a high density of initial defects forming from the vacuum quantum fluctuations of the T field, as shown in figure 13.

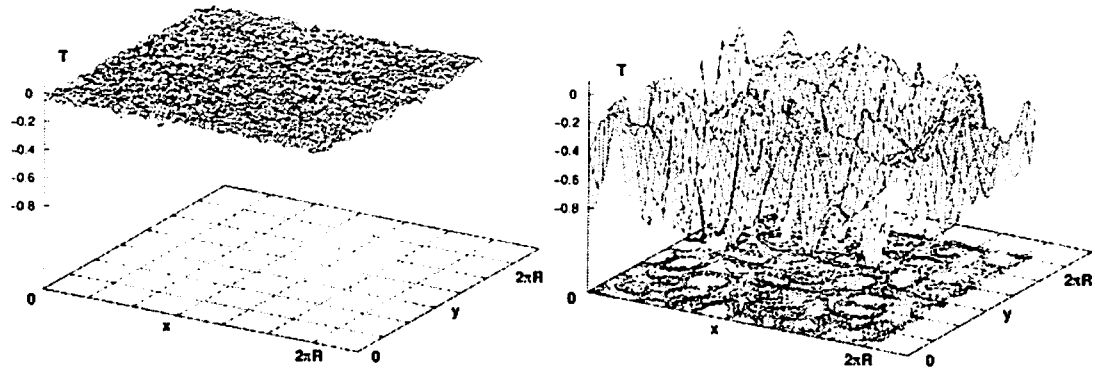


Fig. 13: Growth of defects from initial fluctuations for the open string tachyon field. Distances are in units of the string length scale.

Even though this initial string density is many orders of magnitude greater than the Kibble argument lower bound, there appear to be no observational consequences, thanks to the scaling property of string networks. In the subsequent evolution, long strings start to self-intersect, chopping off small loops which decay away by gravitational radiation. The steady-state solution is one where the energy density in strings scales with that of radiation. We have investigated the approach to the scaling solution and found that scaling sets in after a few Hubble times, regardless of how overdense the initial network was. This is illustrated in figure 14(a).

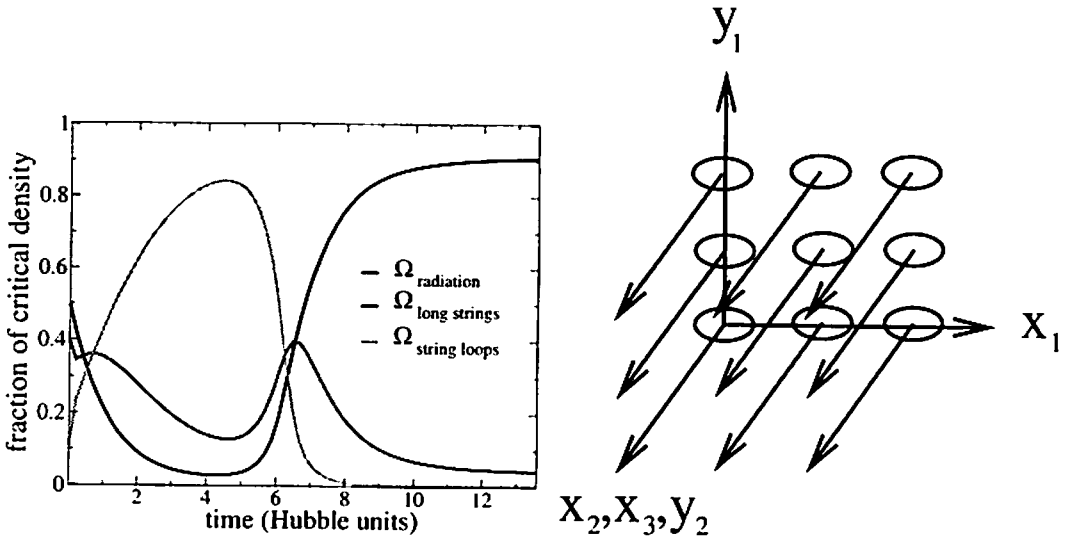


Fig. 14: (a) Evolution of different components of the energy density in a string network, starting from equal parts of energy in strings and radiation. Not shown is the gravitational radiation component. (b) Schematic illustration of domain walls forming in large dimensions x_2, x_3

However, there is one kind of situation where the initial overdensity can make an important difference. This is when the original annihilating branes were higher than 3-dimensional. For example, in the annihilation of 5-branes, the resulting defects will be 3-branes. However, the original 5-branes had to wrap two compact dimensions, so the defects may appear to a 3D observer to be strings, domain walls, or 3-branes, depending on how they are oriented with respect to the compact directions. This is illustrated in fig. 14(b) for the case of domain wall production. Domain walls are highly constrained relics since they quickly come to dominate the energy density of the universe. Unlike strings, they do not generically shed their energy by self-intersections (which would pinch off a closed surface that could decay through gravitational radiation). Therefore the defect overproduction problem would at first sight appear to rule

out inflation driven by higher-dimensional branes. One might question this conclusion based on the fact that the defects in question are always close to each other in one of the small compact directions. Would this not cause them to annihilate efficiently? But they can be separated from each other widely in the large transverse direction, which is growing with the Hubble expansion. We therefore consider it an open question, subject to more detailed simulations of domain wall network evolution in the case where one of the dimensions tranverse to the walls is compact and small.

7 Could our universe be a defect?

The previous discussion also has implications for another idea for reheating at the end of brane-antibrane inflation. It was suggested in [21], and more convincingly argued in [5], that our universe could have arisen just as described above: a 3-brane defect created at the end of 5-brane annihilation. In this case the directions transverse to the defect are all compact ones, so it should be easier for defects to annihilate within this compact space. One can imagine getting around this objection within a multi-throat picture, where defects and antidefects fell into different throats and were thus preserved from annihilating each other. And in the previous section we overcame another argument against the idea, namely the prejudice that defects can only form in regions larger than the Hubble radius, whereas the compact dimensions are smaller than H^{-1}. The previous analysis shows that in fact many such defects can initially form within the small dimensions, provided they are at least a few string lengths in extent.

The main motivation for this picture was that radiation within one of the final state branes would be very efficiently produced by its coupling to the time-dependent background tachyon field. This can be seen by looking at Sen's action in the presence of U(1) gauge fields originally living on the brane or antibrane:

$$S = -\int d^{p+1}x\, e^{-|T|^2/a^2} \left(\sqrt{-\det M^{(1)}} + \sqrt{-\det M^{(2)}} \right)$$

where

$$M^{(i)}_{MN} = g_{MN} + F^{(i)}_{MN} + \frac{1}{2}\left(D_M T\, D_N T^* + \text{c.c.}\right)$$

$$D_M = \partial_M - iA^{(1)}_M + iA^{(2)}_M$$

Here the combination $A^{(1)} - A^{(2)}$ gets a VEV, which is part of the defect, and the orthogonal combination $A^{(1)} + A^{(2)}$ plays the role of a massless photon. We find that there is strong production of $A^{(1)} + A^{(2)}$ due to its coupling to the violently changing background $T(t,x)$. Thus reheating would not be a problem in such models. But we are left with the question of why only 3-branes or cosmic strings would be produced by 5-brane annihilation, since the domain walls should appear with equal likelihood, and overclose the universe. Unless there is a mechanism to suppress domain walls, we must conclude that it is unlikely our universe arose as a defect itself, which was created at the end of inflation.

8 Conclusions

I find it encouraging that we now have string inflation models which are starting to come under pressure from the data. Although not all of the predictions are hard, some such as those of the racetrack model are. At last, a fasifiable prediction coming from string theory!

I would find models of stringy inflation more compelling if they were able to address the fine tuning problem (for recent progress see [15, 23]). On the other hand, the tuning problem tells us that the most natural situation, which is least fine-tuned, is the one with the minimal amount of inflation needed to explain what is observed. This opens the door for us to expect nongeneric features in the power spectrum: departures from flatness, running of the spectral index, isocurvature fluctuations, bumps and wiggles in the spectrum... Such features would obviously make the interaction between theory and observation more interesting, and I hope the observers will find them soon.

In this talk I have argued that two-throat models of brane-antibrane inflation naturally solve the problem of reheating, explaining the hierarchy between the inflation scale and the TeV scale of the standard model, and they help to preserve possible cosmic superstring defects. It is a very exciting

prospect that gravitational waves observed by LIGO could be first signal of string theory in the laboratory. Although it may be challenging to distinguish cosmic superstrings from conventional cosmic strings, in principle this is a good counterexample to the the naysayers of string theory's testability.

9 Acknowledgements

I warmly thank Jiro Soda, Misao Sasaki, Takahiro Tanaka and the other organizers of JGRG14 for their kind hospitality during the conference.

References

[1] C. P. Burgess, J. M. Cline, H. Stoica and F. Quevedo, "Inflation in realistic D-brane models," JHEP **0409**, 033 (2004) [arXiv:hep-th/0403119].

[2] J. J. Blanco-Pillado *et al.*, "Racetrack inflation," JHEP **0411**, 063 (2004) [arXiv:hep-th/0406230].

[3] N. Barnaby, C. P. Burgess and J. M. Cline, "Warped reheating in brane-antibrane inflation," arXiv:hep-th/0412040.

[4] N. Barnaby, A. Berndsen, J. M. Cline and H. Stoica, "Overproduction of cosmic superstrings," arXiv:hep-th/0412095.

[5] N. Barnaby and J. M. Cline, "Creating the universe from brane-antibrane annihilation," Phys. Rev. D **70**, 023506 (2004) [arXiv:hep-th/0403223].

[6] S. Kachru, R. Kallosh, A. Linde and S. P. Trivedi, "De Sitter vacua in string theory," Phys. Rev. D **68**, 046005 (2003) [arXiv:hep-th/0301240].

[7] S. Kachru, R. Kallosh, A. Linde, J. Maldacena, L. McAllister and S. P. Trivedi, "Towards inflation in string theory," JCAP **0310**, 013 (2003) [arXiv:hep-th/0308055].

[8] G. R. Dvali and S. H. H. Tye, "Brane inflation," Phys. Lett. B **450**, 72 (1999) [arXiv:hep-ph/9812483].

[9] C. P. Burgess, M. Majumdar, D. Nolte, F. Quevedo, G. Rajesh and R. J. Zhang, "The inflationary brane-antibrane universe," JHEP **0107**, 047 (2001) [arXiv:hep-th/0105204].

[10] C. P. Burgess, P. Martineau, F. Quevedo, G. Rajesh and R. J. Zhang, "Brane antibrane inflation in orbifold and orientifold models," JHEP **0203**, 052 (2002) [arXiv:hep-th/0111025].

[11] N. Jones, H. Stoica and S. H. H. Tye, JHEP **0207**, 051 (2002) [arXiv:hep-th/0203163].

[12] S. B. Giddings, S. Kachru and J. Polchinski, "Hierarchies from fluxes in string compactifications," Phys. Rev. D **66**, 106006 (2002) [arXiv:hep-th/0105097].

[13] L. Randall and R. Sundrum, "A large mass hierarchy from a small extra dimension," Phys. Rev. Lett. **83**, 3370 (1999) [arXiv:hep-ph/9905221].

[14] M. Berg, M. Haack and B. Kors, "On the moduli dependence of nonperturbative superpotentials in brane arXiv:hep-th/0409282; "Loop corrections to volume moduli and inflation in string theory," Phys. Rev. D **71**, 026005 (2005) [arXiv:hep-th/0404087].

[15] H. Firouzjahi and S. H. H. Tye, "Closer towards inflation in string theory," Phys. Lett. B **584**, 147 (2004) [arXiv:hep-th/0312020].

[16] U. Seljak *et al.*, "Cosmological parameter analysis including SDSS Ly-alpha forest and galaxy bias: Constraints on the primordial spectrum of fluctuations, neutrino mass, and dark energy," arXiv:astro-ph/0407372.

[17] A. Sen, "Tachyon dynamics in open string theory," arXiv:hep-th/0410103.

[18] S. Sarangi and S. H. H. Tye, "Cosmic string production towards the end of brane inflation," Phys. Lett. B **536**, 185 (2002) [arXiv:hep-th/0204074].

[19] E. J. Copeland, R. C. Myers and J. Polchinski, "Cosmic F- and D-strings," JHEP **0406**, 013 (2004) [arXiv:hep-th/0312067].

[20] T. Damour and A. Vilenkin, "Gravitational radiation from cosmic (super)strings: Bursts, stochastic background, and observational windows," arXiv:hep-th/0410222.

[21] J. M. Cline, H. Firouzjahi and P. Martineau, "Reheating from tachyon condensation," JHEP **0211**, 041 (2002) [arXiv:hep-th/0207156].

[22] H. Firouzjahi and S. H. Tye, "Brane Inflation and Cosmic String Tension in Superstring Theory," arXiv:hep-th/0501099.

[23] C. P. Burgess, R. Easther, A. Mazumdar, D. F. Mota and T. Multamaki, "Multiple Inflation, Cosmic String Networks and the String Landscape," arXiv:hep-th/0501125.

Cosmological Surprises from Braneworld models of Dark Energy

Varun Sahni[1]

Inter-University Centre for Astronomy and Astrophysics, Pune 411 007, India

Abstract

Properties of Braneworld models of dark energy are reviewed. Braneworld models admit the following interesting possibilities: (i) The effective equation of state can be $w \leq -1$ as well as $w \geq -1$. In the former case the expansion of the universe is well behaved at all times and the universe does not run into a future 'Big Rip' singularity which is usually encountered by Phantom models. (ii) For a class of Braneworld models the acceleration of the universe can be a *transient* phenomenon. In this case the current acceleration of the universe is sandwiched between two matter dominated epochs. Such a braneworld does not have a horizon in contrast to LCDM and most Quintessence models. (iii) For a specific set of parameter values the universe can either originate from, or end its existence in a *Quiescent* singularity, at which the density, pressure and Hubble parameter *remain finite*, while the deceleration parameter and all invariants of the Riemann tensor diverge to infinity within a finite interval of cosmic time. (iv) Braneworld models of dark energy can *loiter* at high redshifts: $6 \lesssim z \lesssim 40$. The Hubble parameter *decreases* during the loitering epoch relative to its value in LCDM. As a result the age of the universe at loitering dramatically increases and this is expected to boost the formation of high redshift gravitationally bound systems such as $10^9 M_\odot$ black holes at $z \sim 6$ and lower-mass black holes and/or Population III stars at $z > 10$, whose existence could be problematic within the LCDM scenario. (v) Braneworld models with a time-like extra dimension bounce at early times thereby avoiding the initial 'Big Bang singularity'. (vi) Both Inflation and Dark Energy can be successfully unified within a single scheme (Quintessential Inflation).

1 Introduction

One of the most remarkable discoveries of the past decade is that the universe is accelerating. Evidence for an accelerating universe comes from observations of high redshift type Ia supernovae treated as standardized candles [1] and, more indirectly, by observations of the cosmic microwave background and galaxy clustering [2, 3]. Perhaps the simplest explanation for acceleration is the presence of vacuum energy exhibiting itself as a small cosmological constant with equation of state $p = -\rho =$ constant. However, its un-evolving nature implies that the cosmological constant must be set to an extremely small value in order to dominate the expansion dynamics of the universe at precisely the present epoch and this gives rise (according to one's perspective) either to an initial 'fine-tuning' problem or to a 'cosmic coincidence' problem. As a result several radically different alternative methods of generating 'dark energy' at a sufficiently late cosmological epoch have been suggested (see [4, 5, 6, 7, 8] for reviews on this subject). In this talk I will focus on one such approach which rests on the notion that space-time is higher-dimensional, and that our observable universe is a (3+1)-dimensional 'brane' which is embedded in a (4+1)-dimensional 'bulk' space-time. As we shall see, higher-dimensional braneworld models allow the expansion dynamics to be radically different from that predicted by conventional Einstein gravity in 3+1 dimensions. Some cosmological 'surpises' which spring from Braneworld models include:

- Both early and late time acceleration can be successfully unified within a single scheme (Quintessential Inflation) in which the very same scalar field which drives Inflation at early times becomes Quintessence at late times.
- The (effective) equation of state of dark energy in the braneworld scenario can be 'phantom-like' ($w < -1$) or 'Quintessence-like' ($w > -1$). (These two possibilities are essentially related to the two distinct ways in which the brane can be embedded in the bulk.)

[1] E-mail:varun@iucaa.ernet.in

- The acceleration of the universe can be a *transient* phenomenon: braneworld models accelerate during the present epoch but return to matter-dominated expansion at late times.
- A class of braneworld models encounter a *Quiescent future singularity*, at which $\dot{a} \to$ constant, but $\ddot{a} \to -\infty$. The surprising feature of this singularity is that while the Hubble parameter, density and pressure remain finite, the deceleration parameter and all curvature invariants *diverge* as the singularity is approached.
- A spatially flat Braneworld can *mimick* a closed universe and *loiter* at large redshifts.
- A braneworld embedded in a five-dimensional space in which the extra (bulk) dimension is time-like can *bounce at early times*, thereby generically avoiding the big bang singularity. Cyclic models of the universe with successive expansion-contraction cycles can be constructed based on such a bouncing braneworld.

Let us now dwell a little on each of these cosmological properties ('surprises').

2 Quintessential Inflation on the Brane

An intriguing issue in cosmology is that the universe appears to accelerate twice: once at the very beginning during Inflation and again about 10 billion years later, during the present epoch. Although most theoretical models assume that there is no real connection between the two epochs and that Inflation and Dark energy are distinct physical entities, it might well be that the two phenomena are in fact related, and that the same scalar field which initially drives inflation, later, when its density has been considerably reduced, plays the role of Quintessence. This notion of Quintessential Inflation was first explored in the context of the Einstein gravity in 3+1 dimensions by Peebles and Vilenkin [11]. The possibility that Braneworld models could provide a more efficient realisation of this scenario was suggested by Copeland, Liddle and Lidsey [12] and subsequently discussed in greater detail by several authors [13, 14, 15, 16, 17].

The main line of reasoning behind this approach is simple. In the Randall–Sundrum model [9] the modified Einstein equations on the brane contain high-energy corrections as well as the projection of the Weyl tensor from the bulk on to the brane. The Friedmann equation on the brane in this case becomes [10]

$$H^2 + \frac{\kappa}{a^2} = \frac{\Lambda_b}{6} + \frac{C}{a^4} + \frac{(\rho+\sigma)^2}{9M^6} . \tag{1}$$

where $\kappa = 0, \pm 1$, σ is the brane tension, Λ_b is the value of the cosmological constant in the five-dimensional 'bulk' and C/a^4 is the 'dark radiation' term which describes the projected five-dimensional degrees of freedom onto the brane. It is easy to see from (1) that

$$H^2(a \to \infty) = \frac{\Lambda_{RS}}{3} , \tag{2}$$

where

$$\Lambda_{RS} = \frac{\Lambda_b}{2} + \frac{\sigma^2}{3M^6} \tag{3}$$

is the effective four dimensional cosmological constant in the Randall–Sundrum model.

During Inflation the expansion of the universe is driven by a scalar field propagating on the brane with energy density and pressure given by

$$\rho_\phi = \frac{\dot{\phi}^2}{2} + V(\phi), \quad p_\phi = \frac{\dot{\phi}^2}{2} - V(\phi) , \tag{4}$$

while the evolution equation for the scalar field is

$$\ddot{\phi}(t) + 3H\dot{\phi}(t) + V_{,\phi} = 0 . \tag{5}$$

Braneworld models add an interesting new dimension to the scalar-field dynamics. As demonstrated by (1), for $\rho \gg \sigma$ a quadratic density term appears in the modified Friedmann equation on the brane. This

radically alters the expansion dynamics at early epochs by speeding up the rate of expansion and the value of the Hubble parameter, which now becomes $H \propto \rho$ instead of the more conventional $H \propto \sqrt{\rho}$. Since the value of H affects the motion of ϕ through the damping term '$3H\dot{\phi}$' in (5), the scalar field experiences significantly greater damping in braneworld cosmology than in conventional GR. Consequently, inflation on the brane can be realized by very steep potentials – precisely those that are used to describe Quintessence. The braneworld scenario therefore provides us with the opportunity to unify inflation and dark energy through the notion of quintessential inflation [11, 21, 12, 13, 14, 15, 17]. An example of quintessential inflation is shown in Figure 1.

An important property of Quintessential Inflation on the brane is that once the inflationary regime is over and braneworld corrections cease to play an important role, the extreme steepness of the potential causes the scalar field to plunge down its potential resulting in a 'kinetic regime' prior to reheating during which $p_\phi \simeq \rho_\phi$. It is well known that the spectrum of relic gravity waves created quantum mechanicaly during Inflation is sensitive to and bears an imprint of the post-inflationary equation of state [18, 19]. The effect of the kinetic regime is to create a 'blue' gravity wave spectrum on short wavelength scales which is an important observational signature of Quintessential Inflation on the brane [14, 17]; see also [20].

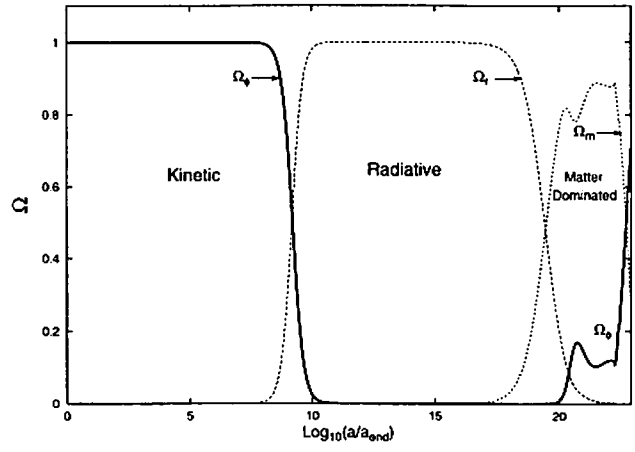


Figure 1: The post-inflationary density parameter Ω is plotted for the scalar field (solid line), radiation (dashed line), and cold dark matter (dotted line) in the quintessential-inflationary model described by the potential [22] $V(\phi) = V_0[\cosh \lambda\phi - 1]^p$ with $p = 0.2$. Late-time oscillations of the scalar field ensure that the mean equation of state turns negative $\langle w_\phi \rangle \simeq -2/3$, giving rise to the current epoch of cosmic acceleration with $a(t) \propto t^2$ and present-day values $\Omega_{0\phi} \simeq 0.7$, $\Omega_{0m} \simeq 0.3$. Note the existence of two epochs, early and late, when the scalar field dominates the matter density of the universe. Figure courtesy of [17].

3 Braneworld models of Dark Energy with $w \leq -1$ and $w \geq -1$

A radically different way of making the universe accelerate was suggested in [23, 27]. The braneworld model which I now discuss presents a successful synthesis of the higher-dimensional ansatzes proposed by Randall and Sundrum [9] and Dvali, Gabadadze, and Porrati [23], and is described by the action [24]

$$S = M^3 \left[\int_{\rm bulk} (\mathcal{R} - 2\Lambda_{\rm b}) - 2 \int_{\rm brane} K \right] + \int_{\rm brane} \left(m^2 R - 2\sigma \right) + \int_{\rm brane} L(h_{ab}, \phi) \,. \qquad (6)$$

Here, $\mathcal{R}$ is the scalar curvature of the five-dimensional metric g_{ab} in the bulk, and R is the scalar curvature of the induced metric $h_{ab} = g_{ab} - n_a n_b$ on the brane, where n^a is the vector field of the inner unit normal to the brane. The quantity $K = K_{ab}h^{ab}$ is the trace of the symmetric tensor of extrinsic curvature $K_{ab} = h^c{}_a \nabla_c n_b$ of the brane, and $L(h_{ab}, \phi)$ denotes the Lagrangian density of the four-dimensional

matter fields ϕ whose dynamics is restricted to the brane (the notation and conventions are those of [25]). Integrations over the bulk and brane are taken with the natural volume elements $\sqrt{-g}d^5x$ and $\sqrt{-h}d^4x$, respectively. The constants M and m denote, respectively, the five-dimensional and four-dimensional Planck masses, Λ_b is the five-dimensional (bulk) cosmological constant, and σ is the brane tension.

An important difference between the action (6) and that describing the Randall-Sundrum cosmology is the presence of the term $m^2 \int Rd^4x$ in (6). This term can be thought of as resulting from the backreaction of quantum fluctuations of matter fields residing on the brane, and this mechanism of generating the gravitational part of the action was proposed by Sakharov in a seminal paper in 1967 [26]. The effect of including such a term in the braneworld action was explored in [24, 23, 27].

Action (6) leads to the following expression for the Hubble parameter on the brane for a *spatially flat* universe [27]:

$$H^2(a) = \frac{A}{a^3} + B + \frac{2}{\ell^2}\left[1 \pm \sqrt{1 + \ell^2\left(\frac{A}{a^3} + B - \frac{\Lambda_b}{6} - \frac{C}{a^4}\right)}\right], \tag{7}$$

where

$$A = \frac{\rho_0 a_0^3}{3m^2}, \quad B = \frac{\sigma}{3m^2}, \quad \ell = \frac{2m^2}{M^3}. \tag{8}$$

Note that the four-dimensional Planck mass m is related to the effective Newton's constant on the brane as $m = 1/\sqrt{8\pi G}$. The two Planck masses M and m define a new length scale $\ell = 2m^2/M^3 \sim cH_0^{-1}$ in a braneworld which begins to accelerate at the current epoch [23, 27]. (Other applications of braneworlds to the late-time acceleration of the universe are discussed in [29, 36, 30, 31, 33, 34, 35, 28].)

The two signs in (7) correspond to two branches of braneworld models and are related to the two different ways in which the brane can be embedded in the bulk. As shown in [27], the '+' sign in (7) corresponds to late time acceleration of the universe driven by dark energy with an 'effective' equation of state $w \geq -1$ (we call this model BRANE2) whereas the '−' sign is associated with phantom-like behaviour $w \leq -1$ (this model is called BRANE1).

Some limiting cases of (7) will be of interest to the reader:

1. For $m = 0$ equation (7) reduces to a Randall-Sundrum universe [10] described earlier in (1).

2. In the other extreme case when $M = 0$, extra-dimensional effects become unimportant, and (7) reduces to the LCDM model
$$H^2(a) = \frac{A}{a^3} + B. \tag{9}$$

3. Finally, when $\Lambda_b = 0$ and $\sigma = 0$, (7) reduces to the DGP braneworld [23].

Consider now the Braneworld with the '−' sign on the right-hand side of (7), *i.e.* BRANE1. In this case the Hubble parameter on the brane can be rewritten as:

$$H^2(a) = \frac{A}{a^3} + \Lambda_{\rm eff}.$$

The term $\Lambda_{\rm eff}$ is composed of two terms, namely, a constant Λ-term and a 'screening term':

$$\Lambda_{\rm eff} = \underbrace{\left(B + \frac{2}{\ell^2}\right)}_{\Downarrow} - \underbrace{\frac{2}{\ell^2}\sqrt{1 + \ell^2\left(\frac{A}{a^3} + B\right)}}_{\Downarrow} \tag{10}$$

$$\Lambda \qquad \text{Screening term} \tag{11}$$

Since the screening term decreases with time, the value of the **effective cosmological constant** $\Lambda_{\rm eff}$ **increases.** Therefore the Braneworld behaves just like a Phantom model ($w < -1$) but without Phantom's problems: no violation of the weak energy condition and no future singularity. Indeed, from (10) its clear that the universe evolves to ΛCDM in the future (see also [36, 40, 37, 38, 39, 41, 42, 43] [44, 45, 46, 47, 48, 49, 50] for discussions of related issues).

The fact that the Braneworld model (7) can give rise to Phantom-like behaviour can also be seen if we rewrite (7) in terms of the cosmological redshift 'z' so that [27]

$$\frac{H^2(z)}{H_0^2} = \Omega_{\rm m}(1+z)^3 + \Omega_\sigma + 2\Omega_\ell \pm 2\sqrt{\Omega_\ell}\,\sqrt{\Omega_{\rm m}(1+z)^3 + \Omega_\sigma + \Omega_\ell + \Omega_{\Lambda_{\rm b}}}\,, \tag{12}$$

where we have set the dark radiation term in (7) to zero ($C = 0$) and

$$\Omega_\ell = \frac{1}{\ell^2 H_0^2}\,,\ \Omega_{\rm m} = \frac{\rho_{0m}}{3m^2H_0^2}\,,\ \Omega_\sigma = \frac{\sigma}{3m^2H_0^2}\,,\ \Omega_{\Lambda_{\rm b}} = -\frac{\Lambda_{\rm b}}{6H_0^2}\,. \tag{13}$$

The quantities Ω_i satisfy the constraint equation

$$\Omega_{\rm m} + \Omega_\kappa + \Omega_\sigma \pm 2\sqrt{\Omega_\ell}\,\sqrt{1 - \Omega_\kappa + \Omega_\Lambda} = 1\,, \tag{14}$$

where the $\pm$ sign in (14) is commensurate with that in (12). For future reference we also note the cosmological density associated with the four-dimensional cosmological constant (3) in Randall-Sundram cosmology

$$\Omega_{\rm RS} = \frac{\Lambda_{\rm RS}}{3H_0^2} = \frac{\Omega_\sigma^2}{4\Omega_\ell} - \Omega_{\Lambda_{\rm b}}\,. \tag{15}$$

The expression for the current value of the effective equation of state is

$$w_0 = \frac{2q_0 - 1}{3(1 - \Omega_{\rm m})} = -1 \pm \frac{\Omega_{\rm m}}{1 - \Omega_{\rm m}}\sqrt{\frac{\Omega_\ell}{\Omega_{\rm m} + \Omega_\sigma + \Omega_\ell + \Omega_{\Lambda_{\rm b}}}}\,, \tag{16}$$

and we immediately find that $w_0 \leq -1$ when we take the lower sign in (16), which corresponds to choosing one of two possible embeddings of this braneworld in the higher dimensional bulk (this is BRANE1). (The second choice of embedding (BRANE2) gives $w_0 \geq -1$.) It is important to note that all BRANE1 models have $w_0 \leq -1$ and $w(z) \simeq -0.5$ at $z \gg 1$. They therefore successfully cross the 'great divide' at $w = -1$ (see page 26 of [27] for a discussion of this issue).

4 Transient Dark Energy

Braneworld cosmology has the interesting property that it allows the acceleration of the universe to be a transient phenomenon. (In [27] these models were referred to as 'Disappearing Dark Energy' (DDE).) Indeed, by setting the effective four dimensional cosmological constant (3) to zero so that $\Omega_{\rm RS} = 0$ in (15) we get

$$\Omega_\sigma = \pm 2\sqrt{\Omega_\ell \Omega_{\Lambda_{\rm b}}}\,. \tag{17}$$

Selecting the lower sign in (17) and substituting $\Omega_\sigma = -2\sqrt{\Omega_\ell\Omega_{\Lambda_{\rm b}}}$ in (12) we find that[2]

$$\left[\frac{H(z=-1)}{H_0}\right]^2 = 2\sqrt{\Omega_\ell}\left(\sqrt{\Omega_\ell} - \sqrt{\Omega_{\Lambda_{\rm b}}} \pm \left|\sqrt{\Omega_\ell} - \sqrt{\Omega_{\Lambda_{\rm b}}}\right|\right)\,. \tag{18}$$

which *vanishes* for the upper sign when $\Omega_\ell \leq \Omega_{\Lambda_{\rm b}}$. This implies that, since the effective four dimensional cosmological constant vanishes, the universe reverts to matter dominated expansion in the future: $H^2(z \to -1) \simeq \Omega_m(1+z)^3 \to 0$. The current acceleration of the universe is therefore a transient phase in this model, as illustrated in figure 2.

It is well known that an eternally accelerating universe is endowed with a cosmological event horizon which prevents the construction of a conventional S-matrix describing particle interactions within the framework of string or M-theory [51]. A transiently accelerating braneworld may therefore help reconcile string/M-theory with accelerating cosmology, which is an attractive feature of this braneworld cosmology.

[2]Note that the case $\Omega_\sigma = 2\sqrt{\Omega_\ell\Omega_{\Lambda_{\rm b}}}$ leads to transient acceleration with $\Omega_m > 1$ which is unrealistic [27].

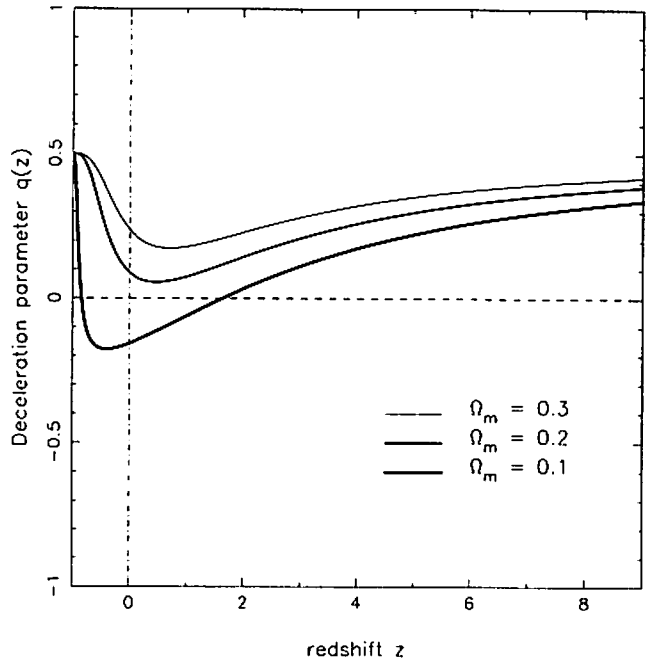


Figure 2: The deceleration parameter $q = -\ddot{a}/aH^2$ is plotted as a function of redshift for the BRANE2 model with the Randall-Sundrum constraint $\Omega_\sigma = -2\sqrt{\Omega_\ell \Omega_{\Lambda_b}}$. The vertical (dot-dashed) line at $z = 0$ marks the present epoch, while the horizontal (dashed) line at $q = 0$ corresponds to a Milne universe [$a(t) \propto t$] which neither accelerates nor decelerates. The case $q = 0.5$ corresponds to matter dominated expansion. Note that the universe ceases to accelerate and becomes matter dominated in the past *as well as in the future*. Figure courtesy of [27].

5 Quiescent Future Singularity

As remarked earlier, an interesting property of the Braneworld (7) is that the late-time expansion of the universe can culminate in a 'Quiescent' singularity at which the density, pressure and Hubble parameter remain finite while the deceleration parameter and geometrical invariants constructed from the Riemann tensor diverge [52].

In order to appreciate the origin of such unusual future singularities in the braneworld, consider again the expansion law (12). For simplicity, we shall only discuss the solution corresponding to the '+' sign in (12) (called BRANE2 in [27]).

A necessary and sufficient condition for the existence of a Quiescent singularity is for the inequality

$$\Omega_\sigma + \Omega_\ell + \Omega_\Lambda < 0\,, \tag{19}$$

to be satisfied [52]. In this case the expression under the square root of (12) becomes zero at a suitably late time, and the cosmological solution *cannot be extended beyond this time.* It can be shown that the scale factor $a(t)$ and its first time derivative remain finite, while all the higher time derivatives of $a(t)$ *tend to infinity* as the singularity is approached.

The limiting redshift, $z_s = a_0/a(z_s) - 1$, at which the braneworld becomes singular is given by

$$z_s = \left(-\frac{\Omega_\sigma + \Omega_\ell + \Omega_\Lambda}{\Omega_{\rm m}}\right)^{1/3} - 1\,. \tag{20}$$

The time of occurance of the singularity (measured from the present moment) can easily be determined from

$$T_s = t(z = z_s) - t(z = 0) = \int_{z_s}^{0} \frac{dz}{(1+z)H(z)}, \tag{21}$$

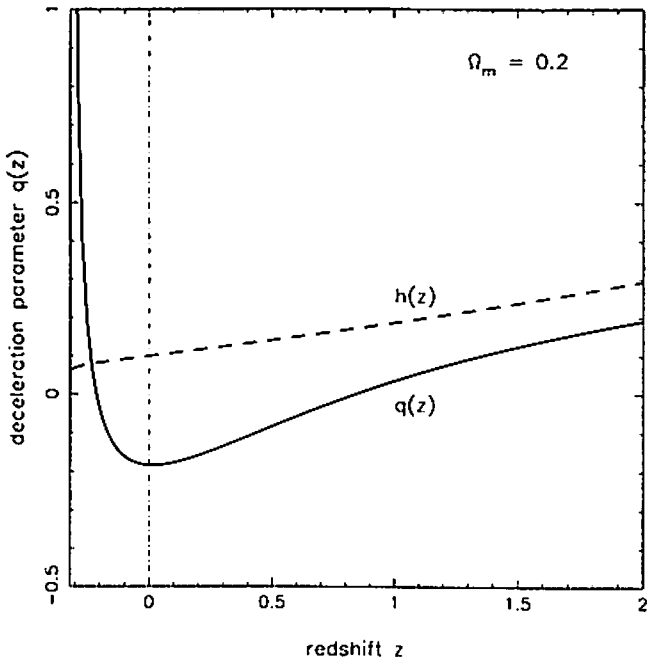


Figure 3: The deceleration parameter (solid line) is shown for a braneworld model with $\Omega_m = 0.2$, $\Omega_\ell = 0.4$, $\Omega_\Lambda = \Omega_\kappa = 0$, and Ω_σ determined from (14). We find that $q(z) \to 0.5$ for $z \gg 1$ while $q(z) \to \infty$ as $z \to -0.312779...$ Currently $q_0 < 0$, which indicates that the universe is accelerating. Also shown is the dimensionless Hubble parameter $h(z) = 0.1 \times H(z)/H_0$ (dashed line) which remains finite in this model. The vertical line at $z = 0$ shows the present epoch. Figure courtesy of [52].

where $H(z)$ is given by (12). In Fig. 3 we show a specific braneworld model having $\Omega_m = 0.2$, $\Omega_\ell = 0.4$, $\Omega_\Lambda = \Omega_\kappa = 0$. In keeping with observations of high redshift supernovae our model universe is currently accelerating [1], but will become singular at $z_s \simeq -0.3 \Rightarrow a(z_s) \simeq 1.4 \times a_0$, i.e. after $T_s \simeq 4.5\ h_{100}^{-1}$ Gyr ($h_{100} = H_0/100$ km/sec/Mpc). Figure 3 demonstrates that the deceleration parameter becomes singular as z_s is approached:

$$q = -\frac{\ddot{a}}{aH^2} \equiv \frac{H'}{H}(1+z) - 1\,; \quad \lim_{z \to z_s} q(z) \to \infty\,, \tag{22}$$

while the Hubble parameter remains finite:

$$\frac{H^2(z_s)}{H_0^2} = \Omega_\ell - \Omega_\Lambda\,. \tag{23}$$

The possible presence of such 'Quiescent' singularity in Braneworld theory can also be seen from the following consideration. As shown in [27], the action (6) leads to the bulk being described by the usual Einstein equation with cosmological constant:

$$\mathcal{G}_{ab} + \Lambda_b g_{ab} = 0\,, \tag{24}$$

while the field equation on the brane is

$$m^2 G_{ab} + \sigma h_{ab} = \tau_{ab} + \underline{\epsilon M^3 (K_{ab} - h_{ab} K)}\,. \tag{25}$$

Here, τ_{ab} is the stress-energy tensor on the brane. A divergent form for the extrinsic curvature (underlined term) caused by a singular embedding of the brane in the bulk will, through (25), lead to a singular value for the Einstein tensor G_{ab} even though all components of the stress-energy tensor on the brane remain finite!

More generally it is well known that Quiescent singularites occur when the original equations of motion are non-linear with respect to the highest derivative. They have earlier been discussed in the context of

Einstein gravity with the conformal anomaly [53]. (This result is not surprising in view of the formal similarity between braneworld theory and GR-based models with the conformal anomaly, discussed in [27].) 'Determinant singularities' having a similar structure and properties are known to arise in the anisotropic Bianchi I model containing a dilaton coupled to a Gauss–Bonnet term in the action [54] and also in other cosmological models [55, 56]. For instance [55] refer to singularities in which the deceleration parameter tends to infinity as the 'Big Brake' while in [56] they are called 'sudden' singularities.

We should also emphasise that both the past and future quiescent singularities occur for a wide range in parameter space and might provide an interesting alternative to the 'big bang'/'big crunch' singularities of general relativity.

6 Loitering Braneworld Models

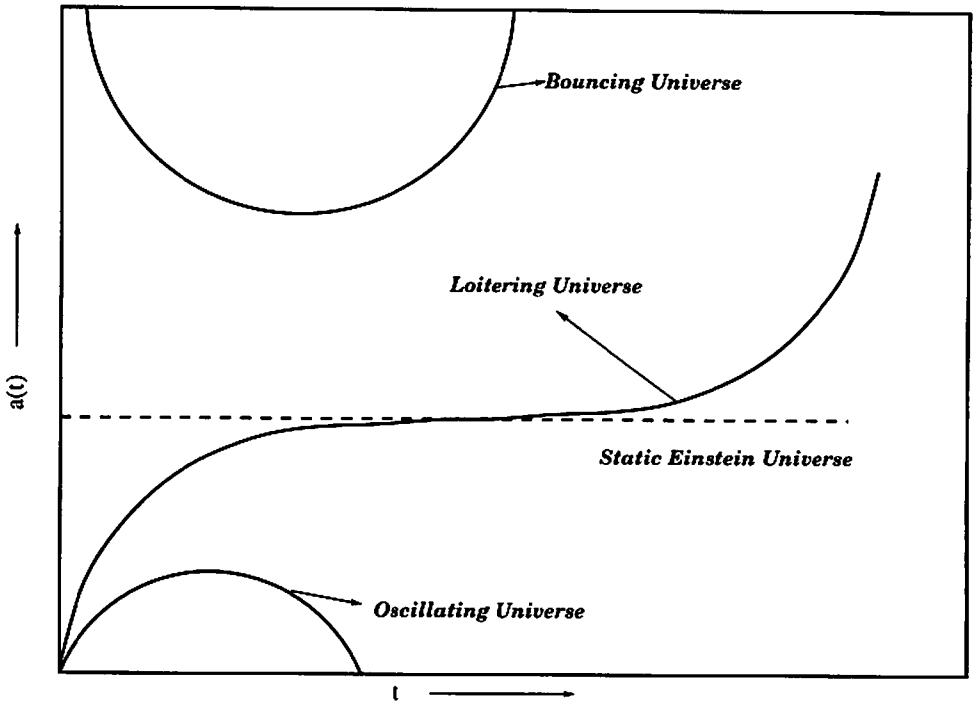


Figure 4: Dynamical possibilities in a closed FRW universe are essentially the same as in the *spatially flat brane* (26) and are summarised above. Figure courtesy of [4].

An interesting aspect of the Braneworld models (7) is that they allow for the existence of an early *loitering* epoch [57]. Loitering is characterized by the fact that the Hubble parameter dips in value over a narrow redshift range referred to as the 'loitering epoch'. During loitering density perturbations are expected to grow rapidly. In addition, since the expansion of the universe slows down, its age near loitering dramatically increases. An early epoch of loitering is expected to boost the formation of high redshift gravitationally bound systems such as $10^9 M_\odot$ black holes at $z \sim 6$ and lower-mass black holes and/or Population III stars at $z > 10$, whose existence could be problematic within the LCDM scenario.

To demonstrate the possibility of loitering note that for large values of the 'dark radiation' term C/a^4, when $C < 0$ and $\ell^2|C|/a^4 \gg 1$, equation (7) acquires the form

$$H^2(a) \approx \frac{A}{a^3} + B \pm \frac{2\sqrt{-C}}{\ell a^2}. \tag{26}$$

Equation (26) bears a formal resemblance to the Hubble parameter in standard GR

$$H^2 = \frac{8\pi G}{3}\frac{\rho_0 a_0^3}{a^3} + \frac{\Lambda}{3} - \frac{\kappa}{a^2}. \tag{27}$$

Remarkably, the role of the spatial curvature in (27) is played by the dark-radiation term in (26); consequently, a spatially open universe is mimicked by the BRANE2 model whereas a closed universe is mimicked by BRANE1.

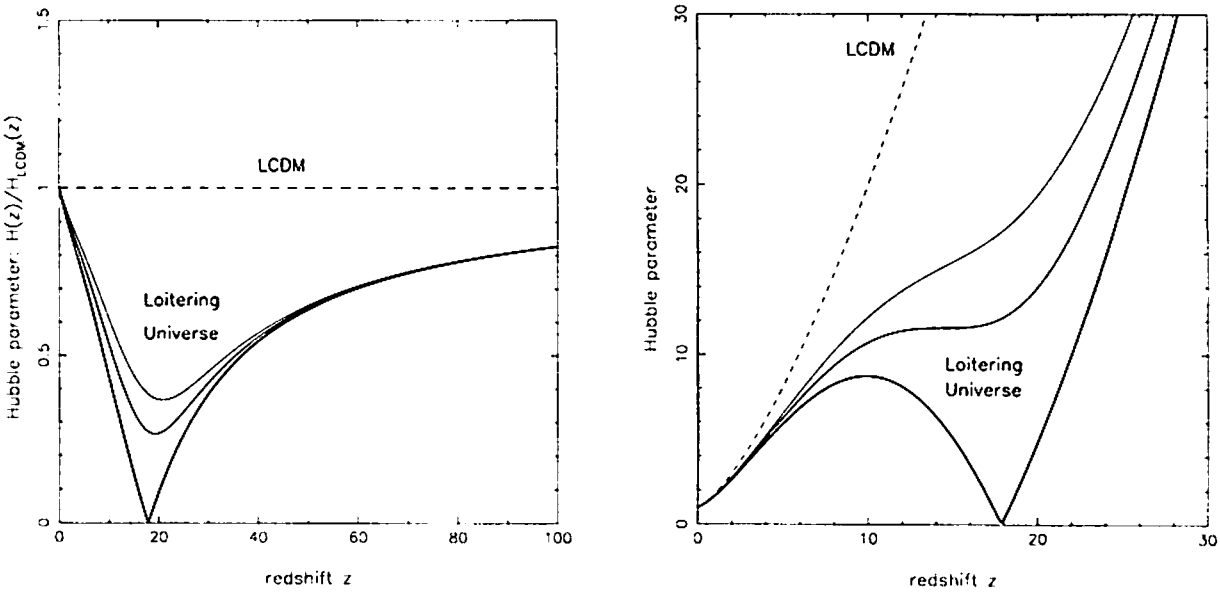


Figure 5: The Hubble parameter for three different universes all of which loiter at $z_{\rm loit} \simeq 18$. Parameter values are $\Omega_{\rm m} = 0.3$, $\Omega_C = 8.0$, $\Omega_\ell = 3.0$, and $\Omega_{\Lambda_b}/10^5 = 6, 4.5, 3.4$ (solid lines, from top to bottom). The left panel shows the Hubble parameter with respect to the LCDM value while, in the right panel, the LCDM (dashed) and loitering (solid) Hubble parameters are shown separately. Figure courtesy of [57].

Loitering solutions in standard cosmology were first found for a closed FRW model with a cosmological constant in [58]. Loitering in more general situations was discussed in [59, 60, 57]. An intriguing aspect of braneworld models is that, since a spatially flat braneworld can behave dynamically just like a closed universe, loitering may be realised within a spatially flat setting and therefore be consistent both with Inflationary cosmology and recent CMB results [2]. Indeed, loitering solutions to (7) & (26) can easily be found by requiring that the loitering condition $dH/dz = 0$ is satisfied. This allows us to determine the 'loitering redshift' [57]

$$1 + z_{\rm loit} \simeq \frac{4}{3} \frac{\sqrt{\Omega_C \Omega_\ell}}{\Omega_{\rm m}} . \tag{28}$$

From this expression we find that the universe will loiter at a large redshift $z_{\rm loit} \gg 1$ provided $\Omega_C \Omega_\ell \gg \Omega_{\rm m}^2$. Since $\Omega_{\rm m}^2 \ll 1$, loitering at large redshifts is not difficult to achieve.

One should note here that a closed FRW universe with a cosmological constant can loiter only at rather small redshifts: $z_{\rm loit} \leq 2$ for $\Omega_{\rm m} \geq 0.1$ [59]. Therefore Braneworld cosmology is endowed with two fundamentally new attributes: (i) it permits loitering in a spatially flat universe and (ii) it allows the loitering redshift to be large. Neither of these possibilities is allowed in standard Einsteinian cosmology.

The Hubble parameter at loitering is given by the approximate expression [57]

$$\frac{H^2(z_{\rm loit})}{H_0^2} \simeq \Omega_\sigma - \frac{32}{27} \frac{(\Omega_C \Omega_\ell)^{3/2}}{\Omega_{\rm m}^2} . \tag{29}$$

Examples of a loitering model are shown in Fig. 5, where the Hubble parameter of a universe which loitered at $z \simeq 18$ is plotted against the redshift. The right hand panel of figure 5 illustrates the fact that the loitering universe can show a variety of interesting behaviour: (i) top curve, $H(z)$ is monotonically increasing and $H'(z) \simeq$ constant in the loitering interval; (ii) middle curve, $H(z)$ appears to have an

inflexion point ($H' \simeq 0, H'' \simeq 0$) during loitering; (iii) lower curve, $H(z)$ has both a maximum and a mininimum, the latter occuring in the loitering regime.

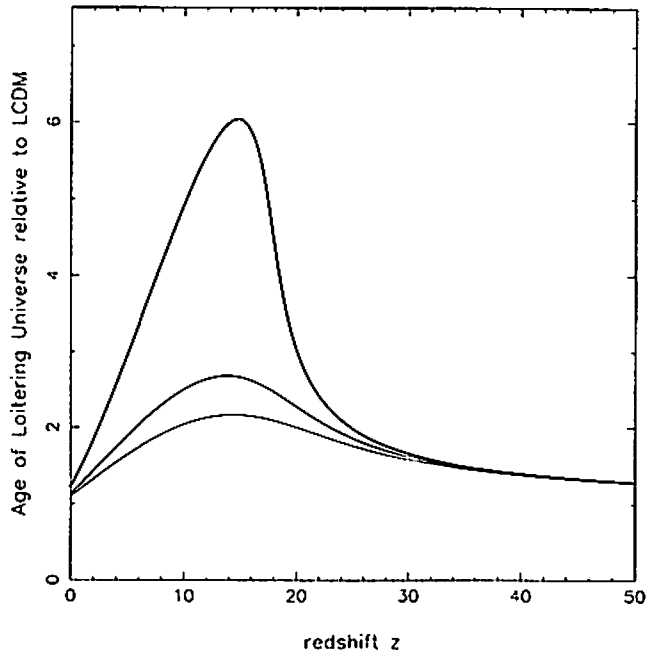


Figure 6: The age of three loitering models is shown relative to the age in LCDM (model parameters are the same as in Fig. 5). Note that the age of the universe near loitering ($z_{\rm loit} \sim 18$) is significantly greater than that in LCDM although, at the present epoch, the difference in ages between the two models is relatively small. Figure courtesy of [57].

A loitering universe could have several important cosmological consequences, one of them being that the age of the universe during loitering *increases*, as shown in Fig. 6. The reason for the age increase rests in the expression

$$t(z) = \int_z^\infty \frac{dz'}{(1+z')H(z')}. \tag{30}$$

which shows that a lower value of $H(z)$ close to loitering will boost the age of the universe at that epoch. An important consequence of having a larger age of the universe at $z \sim 20$ (or so) is that astrophysical processes at these redshifts have more time in which to develop. This is especially important for gravitational instability which forms gravitationally bound systems from the extremely tiny fluctuations existing at the epoch of last scattering. Thus, an early loitering epoch may be conducive to the formation of Population III stars and low-mass black holes at $z \sim 17$ and also of $\sim 10^9 M_\odot$ black holes at lower redshifts ($z \sim 6$) whose existence could be problematic within the LCDM scenario [61]. (Note that age of a LCDM universe at $z \gg 1$ is $t(z) \simeq (2/3H_0\sqrt{\Omega_{\rm m}})(1+z)^{-3/2} = 5.38 \times 10^8 (1+z/10)^{-3/2}$ years for $\Omega_{\rm m} = 0.3, h = 0.7$.)

6.1 The effective equation of state in a loitering Braneworld.

The deceleration parameter q and the effective equation of state w in our loitering model are given by the expressions

$$\begin{aligned} q(z) &= \frac{H'(z)}{H(z)}(1+z) - 1, \\ w(z) &= \frac{2q(z)-1}{3\left[1-\Omega_{\rm m}(z)\right]}, \end{aligned} \tag{31}$$

where $H(z)$ is determined from (12). The current values of these quantities are

$$q_0 = \frac{3}{2}\Omega_{\rm m}\left[1 - \frac{\sqrt{\Omega_\ell}}{\sqrt{\sum_i \Omega_i}}\left(1 + \frac{4}{3}\frac{\Omega_C}{\Omega_{\rm m}}\right)\right] - 1\,,$$
$$w_0 = -1 - \frac{\Omega_{\rm m}}{(1-\Omega_{\rm m})}\frac{\sqrt{\Omega_\ell}}{\sqrt{\sum_i \Omega_i}}\left(1 + \frac{4}{3}\frac{\Omega_C}{\Omega_{\rm m}}\right)\,, \qquad (32)$$

where $\sum_i \Omega_i = \Omega_{\rm m} + \Omega_C + \Omega_\ell + \Omega_\sigma + \Omega_{\Lambda_{\rm b}} = \left(\sqrt{\Omega_\ell} + \sqrt{1 + \Omega_{\Lambda_{\rm b}} + \Omega_C}\right)^2$. From Eq. (32) we find that $w_0 < -1$ if $\Omega_C \geq 0$; in other words, our loitering universe has a phantom-like effective equation of state (EOS). (In particular, for the loitering models shown in Fig. 5, we have $w_0 = -1.035\,, -1.04\,, -1.047$ (top to bottom), all of which are in excellent agreement with recent observations [62, 63].)

An interesting consequence of the loitering braneworld is that the matter density $\Omega_{\rm m} = 8\pi G\rho_{\rm m}/3H^2$ *exceeds* unity at some time in the past. This follows immediately from the fact that, since the value of $H(z)$ in the loitering braneworld model is *smaller* than its counterpart in LCDM, the value of $\Omega_{\rm m}(z)$ is larger than its counterpart in LCDM. One important consequence of this behaviour is that, as expected from (32), the effective equation of state (EOS) blows up precisely when $\Omega_{\rm m} = 1$.

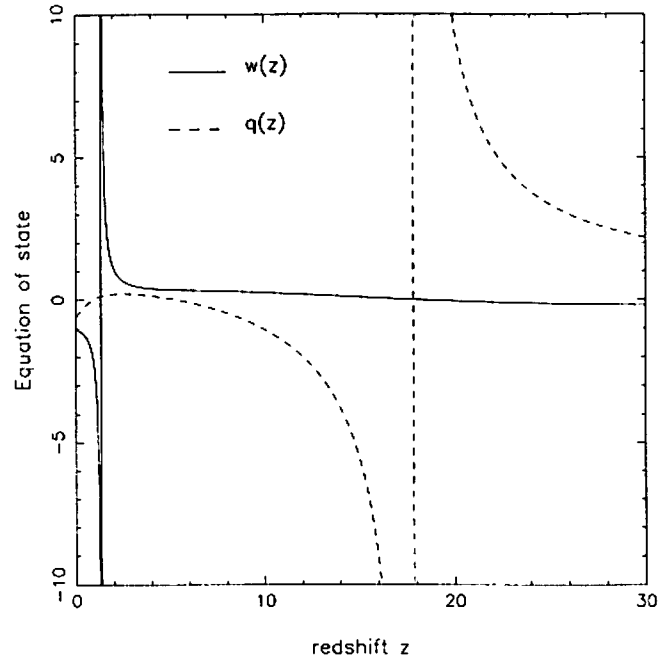


Figure 7: The effective equation of state of dark energy (solid) and the deceleration parameter (dashed) are shown for a universe which loitered at $z \simeq 18$. Note that the effective equation of state of dark energy becomes infinite at low redshifts when $\Omega_{\rm m}(z) = 1$. However, this behaviour is not reflected in the deceleration parameter, which becomes large only near the loitering redshift when $H \simeq 0$. Figure courtesy of [57].

In Fig. 7, we show that, in contrast to the singular behaviour of the EOS, the deceleration parameter remains finite and well behaved even as $w \to \infty$. Note that the *finite behaviour* of $q(z)$ when $\Omega_{\rm m}(z) = 1$ reflects the fact that the EOS for the braneworld is an *effective* quantity and not a real physical property of the theory. This is an important point with broader ramifications since it concerns dark energy models constructed from modifications to the 'gravity sector' of the theory of which Braneworld models are but one example (others being: scalar-tensor gravity, Cardassian approximation, $R + f(R)$ gravity, k-essence, to name but a few). Let me therefore dwell on this point in some more detail.

Within the framework of general relativity the rate of expansion of a FRW universe and its acceleration

are described by the pair of equations

$$H^2 = \frac{8\pi G}{3}\sum_i \rho_i - \frac{k}{a^2}\,,$$
$$\frac{\ddot{a}}{a} = -\frac{4\pi G}{3}\sum_i(\rho_i + 3p_i), \tag{33}$$

where the summation is over all matter fields contributing to the dynamics of the universe. Within this framework, and in the absence of spatial curvature, the energy density and pressure of dark energy can be defined as:

$$\rho_{\rm DE} = \rho_{\rm critical} - \rho_{\rm m} = \frac{3H^2}{8\pi G}\left(1 - \Omega_{\rm m}\right)\,,$$
$$p_{\rm DE} = \frac{H^2}{4\pi G}\left(q - \frac{1}{2}\right)\,, \tag{34}$$

where $\rho_{\rm critical} = 3H^2/8\pi G$ is the critical density associated with a FRW universe and $q = -\ddot{a}/aH^2$ is the deceleration parameter. An important consequence of using (33) & (34) is that the ratio $w_{DE} \equiv p_{DE}/\rho_{DE}$ can be expressed in terms of the deceleration parameter

$$w_{\rm eff}(x) = \frac{2q(x) - 1}{3\left(1 - \Omega_{\rm m}(x)\right)} \equiv \frac{(2x/3)\; d\,\ln H \;/\; dx - 1}{1 \;-\; (H_0/H)^2\Omega_m\; x^3}\quad,\quad x = 1 + z\,. \tag{35}$$

i.e. we recover equation (31) which had earlier been used to determine the equation of state in a loitering universe. Since this derivation of $w_{\rm eff}(z)$ uses the general relativistic formulation it can be expected to recover standard results for GR-based dark energy models such as LCDM and quintessence. However the same cannot be said of braneworld models since the Hubble parameter for the latter contains interaction terms between matter and dark energy (see for instance equation (12)) and therefore does not subscribe to the general relativistic format (33). "One can however extend the above definition of $w_{\rm eff}$ to non-Einsteinian theories by *defining* dark energy density to be the remainder term after one subtracts the matter density from the critical density in the Einstein equations. It should be emphasised that, according to this prescription all interaction terms between matter and dark energy (such terms arise in scalar-tensor and brane models) are attributed *solely* to dark energy. Therefore $w_{\rm eff}(z)$ defined according to (35) is an *effective equation of state* in these models and not a fundamental physical entity (as it is in LCDM, for instance)" [64]. The fact that the EOS is indeed an effective equation of state and not a fundamental physical quantity is illustrated by figure 7 which shows that $w_{\rm eff}(z)$ *diverges* when $\Omega_m(z) \simeq 1$ and that this divergence is not reflected in other characteristics of expansion such as the deceleration parameter. [3]

6.2 The Statefinder diagnostic and Dark Energy

As demonstrated above, the equation of state is not a fundamental physical quantity for dark energy models based either on non-Einsteinian gravity (scalar-tensor theories, Cardassian approximation, k-essence, R + f(R) gravity, etc.) or on Einstein gravity in more than 3+1 dimensions, or indeed in cosmological models with explicit interaction terms between dark matter and dark energy. In all these cases it is useful to supplement the effective equation of state by other geometrical variables, which are 'model independent', in the sense that they do not depend upon an underlying theory of gravity in an explicit way, but can be constructed solely from the expansion factor and its derivatives, and therefore would be expected to apply to all metric theories of gravity defined on a space-time manifold. In all such theories the universe can be expected to be characterised by the following general form for the expansion factor:

$$a(t) = a(t_0) + \dot{a}\big|_0(t - t_0) + \frac{\ddot{a}\big|_0}{2}(t - t_0)^2 + \frac{\dddot{a}\,\big|_0}{6}(t - t_0)^3 + \ldots\,. \tag{36}$$

[3] It should also be stressed that the propagation velocity of small inhomogeneities in dark energy is generically neither $\sqrt{w_{DE}}$, nor $\sqrt{dp_{DE}/d\rho_{DE}}$. Therefore although $w(z)$ is an important physical quantity it does not provide us with an exhaustive description of dark energy and its use as a diagnostic should be treated with some caution, as emphasised in [64].

Usually dark energy models such as quiessence, quintessence, k-essence, braneworld models, Chaplygin gas etc. give rise to families of curves $a(t)$ having quite different properties. Since we know that the acceleration of the universe is a fairly recent phenomenon we can, in principle, confine our attention to small values of $|t - t_0|$ in (36).

Accordingly, as dicussed in [65, 64], a new diagnostic of dark energy called 'statefinder' can be constructed using both the second and third derivatives of the expansion factor (see also [67, 68, 69]). The statefinder pair $\{r, s\}$, defines two new cosmological parameters (in addition to H and q):

$$r \equiv \frac{\dddot{a}}{aH^3} = 1 + \frac{9w}{2}\Omega_X(1+w) - \frac{3}{2}\Omega_X\frac{\dot{w}}{H}\,, \tag{37}$$

$$s \equiv \frac{r-1}{3(q-1/2)} = 1 + w - \frac{1}{3}\frac{\dot{w}}{wH}\,. \tag{38}$$

In figure 8 we show the statefinder pair for several dark energy models including LCDM, quintessence and the Chaplygin gas. For the sake of completeness we say a few words about each of these models below. (Note that the ensuing discussion is largely based on [65, 64] and the reader should refer to these papers for more details.)

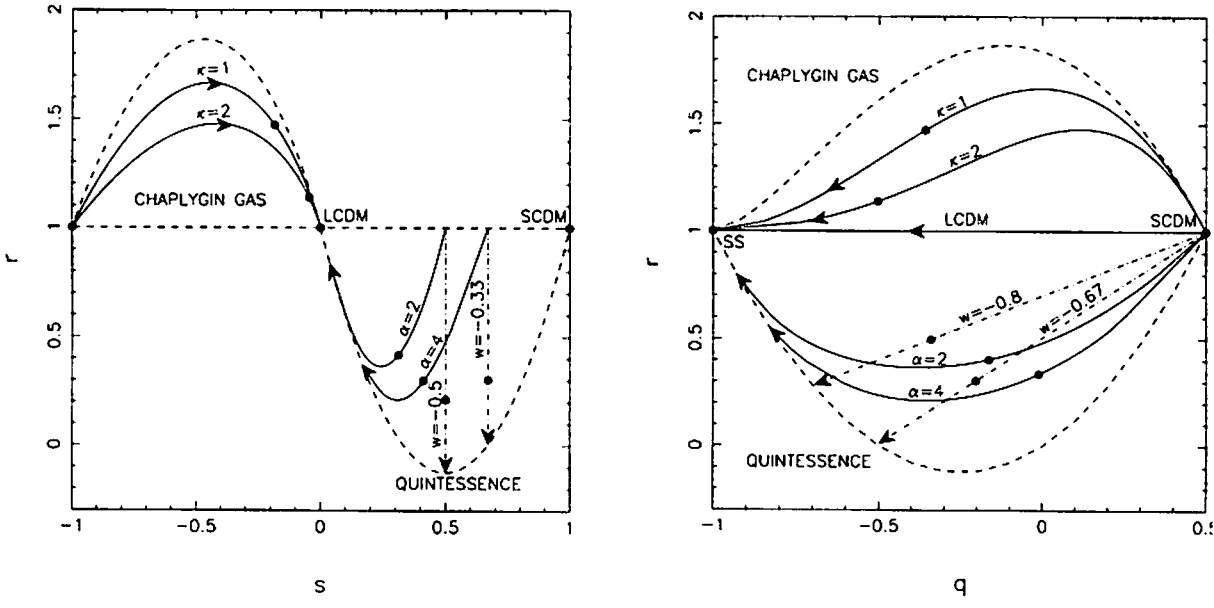


Figure 8: The left panel (a) shows the time evolution of the statefinder pair $\{r, s\}$ for quintessence models and the Chaplygin gas. Quintessence models lie to the right of the LCDM fixed point ($r = 1, s = 0$) (solid lines represent tracker potentials $V = V_0/\phi^\alpha$, dot-dashed lines representing quiessence with constant equation of state w). For quiessence models, s remains constant at $1 + w$ while r declines asymptotically to $1 + \frac{9}{2}w(1 + w)$. For tracker models, s monotonically decreases to zero whereas r first decreases from unity to a minimum value, then rises to unity. These models tend to approach the LCDM fixed point ($r = 1, s = 0$) from the right at $t \to \infty$. Chaplygin gas models (solid lines) lie to the left of the LCDM fixed point. The right panel (b) shows the time evolution of the pair $\{r, q\}$, where q is the deceleration parameter. The solid line, which corresponds to the time evolution of the LCDM model, divides the $r - q$ plane into two halves. The upper half is occupied by Chaplygin gas models, while the lower half contains quintessence models. All models diverge at the same point in the past ($r = 1, q = 0.5$) which corresponds to a matter dominated universe (SCDM), and converge to the same point in the future ($r = 1, q = -1$) which corresponds to the steady state model (SS) - the de Sitter expansion (LCDM $\to$ SS as $t \to \infty$ and $\Omega_m \to 0$). The dark dots on the curves show current values $\{r_0, s_0\}$ (left) and $\{r_0, q_0\}$ (right) for different dark energy models. In all models, $\Omega_m = 0.3$ at the current epoch. In both panels quiessence is shown as dot-dashed while dashed lines mark envelopes for Chaplygin gas (upper) and quintessence (lower). Figure courtesy of [64].

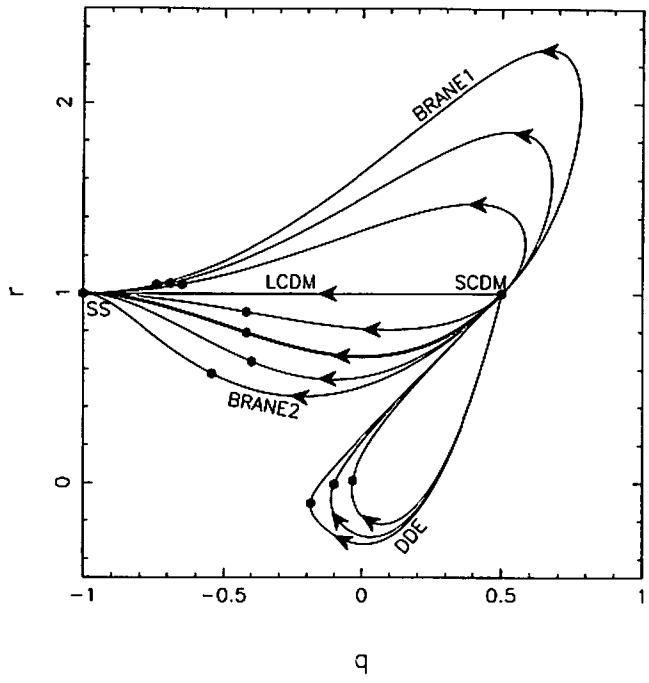


Figure 9: Trajectories in the statefinder plane $\{r, q\}$ for the **Braneworld models** discussed in (12). BRANE1 models have $w \leq -1$ generically, whereas BRANE2 models have $w \geq -1$. The closed loop represents 'Disappearing Dark Energy' (DDE) (discussed in section 4) for which the acceleration of the universe is a transient phenomenon. The thick solid curve in BRANE2 corresponds to the DGP model [23]. Dark dots indicate the current value of $\{r, q\}$ for the models. All models are in reasonable agreement with current supernova data. One can see that the statefinder plane $\{r, q\}$ easily helps distinguish the three Braneworld models from each other. Figure courtesy of [64].

- In **Quiessence** the equation of state of dark energy is a constant so that

$$H(z) = H_0 \left[\Omega_m (1+z)^3 + \Omega_X (1+z)^{3(1+w)}\right]^{1/2} . \tag{39}$$

where w = constant. Important examples of quiessence include: LCDM ($w = -1$), a network of non-interacting cosmic strings ($w = -1/3$), domain walls ($w = -2/3$) and phantom models ($w < -1$). Quiessence in a FRW universe can also be produced by a scalar field (quintessence) which has the potential $V(\phi) \propto \sinh^{\frac{-2(1+w)}{w}}(C\phi + D)$, with appropriately chosen values of C and D [4, 66, 65].

- The density and pressure of **Quintessence** are given by

$$\rho_\phi = \frac{1}{2}\dot{\phi}^2 + V(\phi), \quad p_\phi = \frac{1}{2}\dot{\phi}^2 - V(\phi) , \tag{40}$$

while evolution of the Quintessence field ϕ is governed by the equation of motion

$$\ddot{\phi} + 3H\dot{\phi} + \frac{dV}{d\phi} = 0 , \tag{41}$$

where

$$H^2 = \frac{8\pi G}{3}\left[\rho_{0m}(1+z)^3 + \frac{1}{2}\dot{\phi}^2 + V(\phi)\right] . \tag{42}$$

It is clear from (40) that $w < -1/3$ provided $\dot{\phi}^2 < V(\phi)$. Models with this property can lead to an accelerating universe at late times. An important subclass of Quintessence models displays

the so-called 'tracker' behaviour during which the ratio of the scalar field energy density to that of the matter/radiation background changes very slowly over a substantial period of time. Models belonging to this class satisfy $V''V/(V')^2 \geq 1$ and approach a common evolutionary 'tracker path' from a wide range of initial conditions.

- An interesting alternative form of dark energy is provided by the **Chaplygin gas** [70, 71] which obeys the equation of state

$$p_c = -A/\rho_c \,. \tag{43}$$

The energy density of the Chaplygin gas evolves according to

$$\rho_c = \sqrt{A + B(1+z)^6} \,, \tag{44}$$

from where we see that $\rho_c \to \sqrt{A}$ as $z \to -1$ and $\rho_c \to \sqrt{B}(1+z)^3$ as $z \gg 1$. Thus, the Chaplygin gas behaves like pressureless dust at early times and like a cosmological constant during very late times.

The Hubble parameter for a universe containing cold dark matter and the Chaplygin gas is given by

$$H(z) = H_0 \left[\Omega_m (1+z)^3 + \frac{\Omega_m}{\kappa} \sqrt{\frac{A}{B} + (1+z)^6} \right]^{1/2} \,, \tag{45}$$

where $\kappa = \rho_{0m}/\sqrt{B}$. It is easy to see from (45) that

$$\kappa = \frac{\rho_{0m}}{\rho_c} (z \to \infty) \,. \tag{46}$$

Thus, κ defines the ratio between CDM and the Chaplygin gas energy densities at the commencement of the matter-dominated stage.

For all of the above models the statefinders r and s can be easily expressed in terms of the Hubble parameter $H(z)$ and its derivatives as follows:

$$\begin{aligned} r(x) &= 1 - 2\frac{H'}{H}x + \left\{ \frac{H''}{H} + \left(\frac{H'}{H}\right)^2 \right\} x^2, \\ s(x) &= \frac{r(x) - 1}{3(q(x) - 1/2)} \,, \end{aligned} \tag{47}$$

where $x = 1 + z$ and H is given by (39), (42), (45), (12) for the different dark energy models. The results, shown in figures 8 & 9, demonstrate that the Statefinder diagnostic can successfully differentiate between dark energy models as diverse as LCDM, Quintessence, the Chaplgyn Gas and Braneworlds (see [72] for other recent applications of the Statefinder diagnostic).

7 Bouncing Braneworlds

A remarkable feature of Braneworld cosmology is that the expansion dynamics of the early universe can be *non-singular*. Indeed, as shown in [73] bouncing Braneworld models can be constructed, based upon a Randall–Sundrum type action, but in which the extra dimension is *time-like*. In this case one starts from the action [73]

$$S = M^3 \left[\int_{\rm bulk} (\mathcal{R} - 2\Lambda) - 2\epsilon \int_{\rm brane} K \right] - \int_{\rm brane} 2\sigma + \int_{\rm brane} L(h_{ab}, \phi) \,. \tag{48}$$

where the parameter $\epsilon = 1$ if the signature of the bulk space is Lorentzian, so that the extra dimension is spacelike, and $\epsilon = -1$ if the signature is $(-,-,+,+,+)$, so that the extra dimension is timelike. The evolution equations resulting from (48) have the form [73]

$$H^2 + \frac{\kappa}{a^2} = \frac{\Lambda_{\rm eff}}{3} + \frac{8\pi G_{\rm N}\rho}{3} + \frac{\epsilon\rho^2}{9M^6} + \frac{C}{a^4} \,. \tag{49}$$

Where $G_N = \epsilon\sigma/12\pi M^6$ is the effective gravitational constant, and $\Lambda_{\rm eff} = \Lambda/2 + \epsilon\sigma^2/3M^6$ is the effective cosmological constant on the brane. For $\epsilon = 1$, Eq. (49) reduces to the well-known Randall-Sundrum form (we ignore $\kappa/a^2, \Lambda_{\rm eff}$ and C/a^4 which are unimportant for our purposes)

$$H^2 = \frac{8\pi G_N}{3}\rho\left(1 + \frac{\rho}{2\sigma}\right) . \tag{50}$$

On the other hand if $\epsilon = -1$ then we obtain

$$H^2 = \frac{8\pi G_N}{3}\rho\left(1 - \frac{\rho}{2|\sigma|}\right) , \tag{51}$$

where the brane tension $\sigma < 0$. (The two braneworld models (50) and (51) are dual, as demonstrated in [74].) Equation (51) clearly demonstrates that $H \simeq 0$ when $\rho_{\rm bounce} = 2|\sigma|$ *i.e.* the universe *bounces* when the energy density of matter becomes sufficiently large. It is important to note that the singularity-free nature of the early universe is a generic outcome of this theory and does not depend upon whether or not matter violates the energy conditions. An example of a bouncing braneworld universe is shown in figure (10) below.

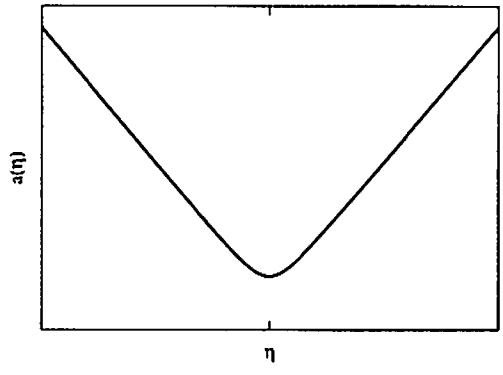


Figure 10: A bouncing radiation-dominated braneworld ($\eta = \int dt/a$ is the conformal time). Figure courtesy of [73].

An early time bounce, such as (51), can be used to construct cyclic models of the universe [75, 76, 77, 78]. Consider for instance the mechanism proposed in [75] in which Phantom dark energy is presumed to exist in addition to matter and radiation so that

$$\rho = \rho_r + \rho_m + \rho_P \tag{52}$$

where $\rho_r \propto a^{-4}$, $\rho_m \propto a^{-3}$, $\rho_P \propto a^{-3(1+w)}$ and $w < -1$ in the case of Phantom leading to

$$\rho = \frac{A}{a^4} + \frac{B}{a^3} + Ca^{3(|1+w|)} . \tag{53}$$

It is clear from (53) that ρ grows at small *as well as* large values of $a(t)$. Indeed within one cycle the value of H will pass through zero twice: (i) at early times when the bounce in (51) is brought about due to large values of the radiation density and (ii) during late times, when the large value of the Phantom energy leads to $H = 0$ in (51) and initiates the universe's recollapse.

Similarly, it is easy to show that a bouncing spatially closed universe with matter satisfying $\rho + 3p > 0$ will also be 'cyclic' in the sense that it will pass through an infinite number of nonsingular expanding-collapsing epochs [76, 77]. As demonstrated in [76, 77], a massive scalar field in such a universe usually leads to an increase in the amplitude of consecutive expansion cycles and to a gradual amelioration of the flatness problem; see figure 11.

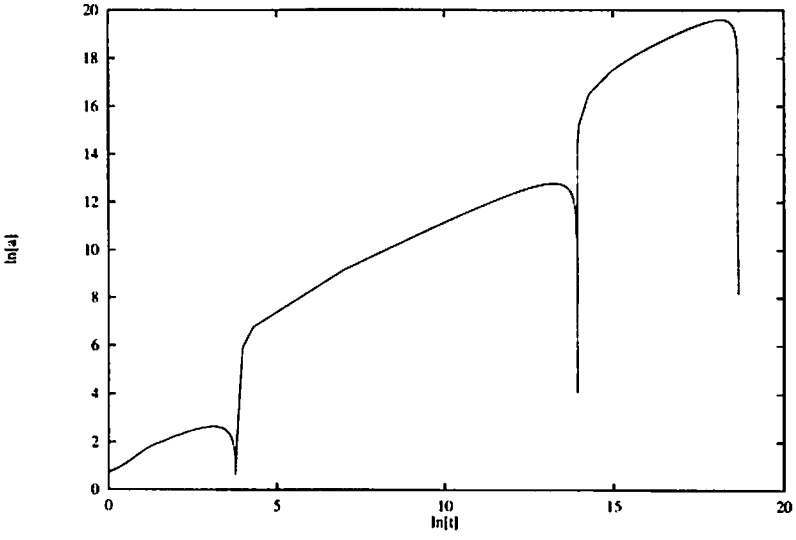


Figure 11: A cyclic universe with ever-increasing successive expansion maxima. Figure courtesy of [76].

8 Conclusions

Braneworld models hold interesting consequences both for the early as well as the late-time evolution of the universe. At early times, the *increased rate of expansion* in RSII type braneworlds allows scalar fields with steep potentials to play the dual role of being the inflaton as well as Quintessence.

Braneworld models in which the RSII action is supplemented by an induced gravity term on the brane have important consequences for the *late-time* evolution of the universe. For instance: (i) The effective equation of state of dark energy in this scenario can be $w \leq -1$ as well as $w \geq -1$. (ii) The current acceleration of the universe can be a *transient* phenomenon. (iii) The braneworld universe can end its existence in a *Quiescent* singularity at which the density, pressure and Hubble parameter *remain finite*, while the deceleration parameter and all invariants of the Riemann tensor diverge. (iv) Braneworld models of dark energy can *loiter* at high redshifts: $6 \lesssim z \lesssim 40$. The Hubble parameter *decreases* during the loitering epoch relative to its value in LCDM. As a result the age of the universe at loitering dramatically increases and this is expected to boost the formation of high redshift gravitationally bound systems such as $10^9 M_\odot$ black holes at $z \sim 6$ and lower-mass black holes and/or Population III stars at $z > 10$, whose existence could be problematic within the LCDM scenario. (v) In addition to the above, an RSII type Braneworld in which the extra dimension is time-like (instead of space-like) avoids the initial Big Bang singularity by bouncing at early times. This property (which holds even if matter satisfies all the energy conditions) has been used to construct cyclic models of a singularity free universe.

9 Acknowldgements

It is a pleasure to thank Yuri Shtanov who collaborated with me on most of the projects discussed in this paper.

References

[1] S.J. Perlmutter *et al.*, Astroph. J. **517**, 565 (1999) [astro-ph/9812133]; A. Riess *et al.*, Astron. J. **116**, 1009 (1998) [astro-ph/9805201]. A.G. Riess, et al., Astroph. J. **607**, 665 (2004) [astro-ph/0402512]

[2] D.N. Spergel, et al., Phys. Rev. D 69, 103501 (2004) [astro-ph/0302209].

[3] M. Tegmark, et al., astro-ph/0310723.

[4] V. Sahni and A.A. Starobinsky, IJMP D 9, 373 (2000) [astro-ph/9904398].

[5] S.M. Carroll, Living Rev.Rel. 4 1 (2001) [astro-ph/0004075].

[6] P.J.E. Peebles and B. Ratra, Rev.Mod.Phys. 75, 559 (2002) [astro-ph/0207347].

[7] T. Padmanabhan, Phys. Rep. 380, 235 (2003) [hep-th/0212290].

[8] V. Sahni, *Dark Matter and Dark Energy*, Lectures given at the 2nd Aegean Summer School on the Early Universe, Ermoupoli, Island of Syros, Greece, astro-ph/0403324 .

[9] L. Randall and R. Sundrum, Phys. Rev. Lett. 83, 3370 (1999), [hep-ph/9905221]; L. Randall and R. Sundrum, Phys. Rev. Lett. 83, 4690 (1999), [hep-th/9906064].

[10] P. Binétruy, C. Deffayet, and D. Langlois, Nucl. Phys. B 565, 269 (2000), [hep-th/9905012]; C. Csáki, M. Graesser, C. Kolda, and J. Terning, Phys. Lett. B 462, 34 (1999), [hep-ph/9906513]; J. M. Cline, C. Grojean, and G. Servant, Phys. Rev. Lett. 83, 4245 (1999), [hep-ph/9906523]; P. Binétruy, C. Deffayet, U. Ellwanger, and D. Langlois, Phys. Lett. B 477, 285 (2000), [hep-th/9910219]. T. Shiromizu, K. Maeda, and M. Sasaki, Phys. Rev. D 62, 024012 (2001), [hep-th/9910076].

[11] P. J. Peebles and A. Vilenkin, Phys. Rev. D 59, 063505 (1999).

[12] E.J. Copeland, A. R. Liddle and J. E. Lidsey, Phys. Rev. D 64, 023509 (2001) [astro-ph/0006421].

[13] G. Huey and Lidsey, Phys. Lett. B 514, 217 (2001).

[14] V. Sahni, M. Sami and T. Souradeep, Phys. Rev. D65, 023518 (2002).

[15] A. S. Majumdar, Phys.Rev. D64, 083503 (2001).

[16] S. Nojiri and S. D. Odintsov, Phys. Rev. D 68, 123512 (2003); Phys. Lett. B 599, 137 (2004).

[17] M. Sami and V. Sahni, Phys.Rev. D70, 083513 (2004).

[18] A. A. Starobinsky, JETP Lett., 30, 682 (1979).

[19] V. Sahni, Phys. Rev. D 42, 453 (1990).

[20] M. Giovannini, Phys. Rev. D 58, 083504 (1998); Phys. Rev. D 60, 123511 (1999).

[21] R. Maartens, D. Wands, B.A. Bassett and I.P.C. heard, Phys. Rev. D 62, 041301(R) (2000)

[22] V. Sahni, and L. Wang, Phys. Rev. D 62, 103517 (2000).

[23] G. Dvali, G. Gabadadze, and M. Porrati, Phys. Lett. B 485, 208 (2000), [hep-th/0005016].

[24] H. Collins and B. Holdom, Phys. Rev. D 62, 105009 (2000), hep-ph/0003173; Yu. V. Shtanov, *On Brane World Cosmology*, hep-th/0005193; C. Deffayet, Phys. Lett. B 502, 199 (2001), hep-th/0010186.

[25] R. M. Wald, *General Relativity*, University of Chicago Press, Chicago (1984).

[26] A. D. Sakharov, Dokl. Akad. Nauk SSSR. Ser. Fiz. 177, 70 (1967) [Sov. Phys. Dokl. 12, 1040 (1968)]; reprinted in: Usp. Fiz. Nauk 161, 64 (1991) [Sov. Phys. Usp. 34, 394 (1991)]; Gen. Rel. Grav. 32, 365 (2000).

[27] V. Sahni and Yu. V. Shtanov, JCAP 0311, 014 (2003), [astro-ph/0202346]; IJMP D 11, 1515 (2002), [gr-qc/0205111]; U. Alam and V. Sahni, *Supernova Constraints on Braneworld Dark Energy*, astro-ph/0209443.

[28] J.S. Alcaniz, D. Jain, A. Dev Phys. Rev. D **66**, 067301 (2002) [astro-ph/0206448]; D. Jain, A. Dev, J.S. Alcaniz Phys. Rev. D **66**, 083511 (2002) [astro-ph/0206224]

[29] K. Maeda, S. Mizuno, T. Torii Phys. Rev. D **68**, 024033 (2003) [gr-qc/0303039].

[30] R. Maartens Living Rev.Rel. **7**, 7 (2004) [gr-qc/0312059].

[31] P. Brax, C. van de Bruck, A-C. Davis, Rept.Prog.Phys. **67**, 2183 (2004) [hep-th/0404011].

[32] J.A.S. Lima, Braz.J.Phys. **34**, 194 (2004) [astro-ph/0402109].

[33] R. G. Vishwakarma and P. Singh, Class.Quant.Grav. **20**, 2033 (2003) [astro-ph/0211285].

[34] J.A. Alcaniz and N. Pires, Phys. Rev. D **70**, 047303 (2004) [astro-ph/0404146].

[35] A. Padilla, *Infra-red modification of gravity from asymmetric branes*, hep-th/0410033; A. Padilla, *Cosmic acceleration from asymmetric branes*, hep-th/0406157.

[36] A. Lue and G.D. Starkmann, Phys. Rev. D **D70**, 101501 (2004) [astro-ph/0408246].

[37] R. R. Caldwell, Phys. Lett. B **545**, 23 (2002) [astro-ph/9908168].

[38] J.M. Cline, S. Jeon and G.D. Moore, Phys. Rev. D **70**, 043543 (2004) [hep-ph/0311312].

[39] A.A. Starobinsky, JETP Lett. **68**, 757 (1998).

[40] T. Chiba, T. Okabe, T. and M. Yamaguchi, Phys. Rev. D **62**, 023511 (2000).

[41] B. McInnes, JHEP **0208**, 029 (2002) [hep-th/0112066].

[42] R.R. Caldwell, M. Kamionkowski and N.N. Weinberg, Phys.Rev.Lett. **91**, 071301 (2003) [astro-ph/0302506].

[43] S.M. Carroll, M. Hoffman and M. Trodden, Phys. Rev. D **68**, 023509 (2003) [astro-ph/0301273].

[44] P. Frampton, Phys. Lett. B **555**, 139 (2003).

[45] P. Frampton and T. Takahashi, Phys. Lett. B **557**, 135 (2003).

[46] P. Singh, M. Sami and N.K. Dadhich Phys. Rev. D **68**, 023522 (2003) [hep-th/0305110].

[47] V.B. Johri, Phys. Rev. D **70**, 041303 (2004) [astro-ph/0311293].

[48] M. P. Dabrowski, T. Stachowiak, M. Szydlowski, Phys. Rev. D **68**, 103519 (2003) [hep-th/0307128];

[49] S. Nojiri and S. D. Odintsov, Phys. Lett. B **595**, 1 (2004), hep-th/0405078; S. Nojiri and S. D. Odintsov, *The final state and thermodynamics of dark energy universe*, hep-th/0408170; M. C. B. Abdalla, S. Nojiri, and S. D. Odintsov, *Consistent modified gravity: dark energy, acceleration and the absence of cosmic doomsday*, hep-th/0409177.

[50] S. Nesseris, L. Perivolaropoulos Phys. Rev. D **70**, 123529 (2004) [astro-ph/0410309].

[51] W. Fischler, A. Kashani-Poor, R. McNees, and S. Paban, JHEP **0107**, 3 (2001) [hep-th/0104181]; J. Ellis, N. E. Mavromatos, and D. V. Nanopoulos, *String theory and an accelerating universe*, hep-th/0105206; J. M. Cline, JHEP **0108**, 35 (2001) [hep-ph/0105251]; X.-G. He, *Accelerating universe and event horizon*, astro-ph/0105005.

[52] Yu. Shtanov and V. Sahni, Class.Quant.Grav. **19**, L101 (2002) [gr-qc/0204040].

[53] R. M. Wald, Ann. Phys. **110**, 472 (1978); M. V. Fischetti, J. B. Hartle, and B. L. Hu, Phys. Rev. D **20**, 1757 (1979).

[54] S. Alexeyev, A. Toporensky, and V. Ustiansky, Phys. Let. B **509**, 151 (2001); A. Toporensky and S. Tsujikawa, Phys. Rev. D **65**, 123509, (2002), [gr-qc/0202067].

[55] V. Gorini, A. Yu. Kamenshchik, U. Moschella, V. Pasquier, Phys. Rev. D 69, 123512 (2004).

[56] J.D. Barrow, Class.Quant.Grav. 21, L79 (2004).

[57] V. Sahni and Yu. Shtanov, astro-ph/0410221.

[58] A. G. Lemaître, MNRAS 91, 483 (1931).

[59] V. Sahni, H. Feldman and A. Stebbins, Astrophys. J. 385, 1 (1992).

[60] S. Alexander, R. Brandenberger, D. Easson, Phys. Rev. D 62, 103509 (2000); R. Brandenberger, D. Easson, D. Kimberley, Nuc. Phys. B623, 421 (2002).

[61] G. T. Richards et al., Astron. J. 127, 1305 (2004) [astro-ph/0309274]; Z. Haiman and E. Quataert, *The Formation and Evolution of the First Massive Black Holes*, astro-ph/0403225; D. N. Spergel, *et al.*, Astrophys. J. Suppl. 148, 175 (2003) [astro-ph/0302209]; R. Barkana and A. Loeb, *In the Beginning: The First Sources of Light and the Reionization of the Universe*, astro-ph/0010468; B. Ciardi and A. Ferrara, *The First Cosmic Structures and their Effects*, astro-ph/0409018.

[62] U. Alam, V. Sahni, and A. A. Starobinsky, JCAP 06, 008 (2004), [astro-ph/0403687].

[63] U. Seljak *et al.*, *Cosmological parameter analysis including SDSS Ly-alpha forest and galaxy bias: constraints on the primordial spectrum of fluctuations, neutrino mass, and dark energy*, astro-ph/0407372.

[64] U. Alam, V. Sahni, T. D. Saini and A. A. Starobinsky, MNRAS 344, 1057 (2003), [astro-ph/0303009].

[65] V. Sahni, T.D. Saini, A.A. Starobinsky, and U. Alam, JETP Lett. 77 201 (2003) [astro-ph/0201498].

[66] L.A. Urena-Lopez, T. Matos, Phys. Rev. D 62, 081302, (2000) [astro-ph/0003364].

[67] T. Chiba and N. Nakamura, Prog. Theor. Phys. 100, 1077 (1998).

[68] M. Visser, Class.Quant.Grav. 21, 2603 (2004) [gr-qc/0309109].

[69] E. Linder, astro-ph/0404032.

[70] A. Kamenshchik, U. Moschella, and V. Pasquier, Phys. Lett. B 511 265 (2001).

[71] M.C. Bento, O. Bertolami, A.A. Sen, Phys. Rev. D D66, 043507 (2002) [gr-qc/0202064]; N. Bilic, G.B. Tupper and R. Viollier Phys. Lett. B 535, 17 (2002). J.S. Fabris, S.V. Goncalves and P.E. de Souza, astro-ph/0207430; V. Gorini, A. Kamenshchikand U. Moschella, Phys. Rev. D 67 063509 (2003) [astro-ph/0209395]; J.S. Alcaniz, D. Jain and A. Dev Phys. Rev. D 67, 043514 (2003) [astro-ph/0210476]; C. Avelino, L.M.G. Beca, J.P.M. de Carvalho, C.J.A.P. Martins, and P. Pinto, Phys. Rev. D 67, 023511 (2003) [astro-ph/0208528]; O. Bertolami, A.A. Sen, S. Sen and P.T. Silva, MNRAS 353, 329 (2004) [astro-ph/0402387].

[72] W. Zimdahl and D. Pavon, Gen.Rel.Grav. 36, 1483 (2004) [gr-qc/0311067]; A.K.D. Evans, I.K. Wehus, O. Gron, O. Elgaroy astro-ph/0406407.

[73] Yu. Shtanov and V. Sahni, Phys.Lett.B 557, 1 (2003) [gr-qc/0208047]

[74] E. J. Copeland, S-J. Lee, J. E. Lidsey, S. Mizuno, astro-ph/0410110

[75] M. G. Brown, K. Freese, W. H. Kinney, astro-ph/0405353

[76] N. Kanekar, V. Sahni and Yu. Shtanov, Phys. Rev. D 63, 083520 (2001) [astro-ph/0101448].

[77] Y-S. Piao, gr-qc/0407027

[78] Y-S. Piao, Phys. Rev. D 70, 101302, (2004) [hep-th/0407258].

Mass and angular momenta of Kerr-anti-de Sitter spacetimes

Nathalie Deruelle[1]

Institut des Hautes Etudes Scientifiques, 35 Route de Chartres, 91440, Bures-sur-Yvette, France

Abstract

We briefly review how to compute the mass and angular momenta of rotating, asymptotically anti-de Sitter spacetimes in Einstein-Gauss-Bonnet theory of gravity using superpotentials derived from standard Nœther identities. The calculations depend on the asymptotic form of the metrics only and hence take no account of the source of the curvature. When the source of curvature is a black hole, the results can be checked using the first law of black hole thermodynamics.

1 Introduction

Consider Kerr-AdS$_4$ spacetime ($\mathcal{M}$) in Boyer-Lindquist coordinates [1]

$$ds^2 = -\frac{\Delta}{\rho^2}\left(dt - \frac{a\sin^2\theta}{\Xi}d\phi\right)^2 + \frac{\rho^2}{\Delta}dr^2 + \frac{\rho^2}{\Delta_\theta}d\theta^2 + \frac{\Delta_\theta \sin^2\theta}{\rho^2}\left(a\,dt - \frac{r^2+a^2}{\Xi}d\phi\right)^2$$

where $\Delta \equiv (r^2+a^2)(1+r^2/l^2) - 2mr$, $\rho^2 \equiv r^2 + a^2\cos^2\theta$, $\Delta_\theta \equiv 1 - (a^2/l^2)\cos^2\theta$ and $\Xi \equiv 1 - a^2/l^2$. It solves the Einstein equations with cosmological constant, $R^\mu_\nu = -(12/l^2)\delta^\mu_\nu$, and depends on two integration constants, the "mass" and "rotation" parameters m and a. $\mathcal{M}$ is asymptotically anti-de Sitter but, as noticed in [2], the Boyer-Lindquist frame is rotating with angular velocity $\Omega_{BL} = a/l^2$ with respect to the standard, static, AdS$_4$ frame.

$\mathcal{M}$ describes a black hole. Its horizon r_+, which can be defined as the surface where signals from infalling test particles are measured at infinity with infinite redshift by static observers, is located at

$$\Delta(r_+) = 0 \quad \Longleftrightarrow \quad m = \frac{(r_+^2+a^2)(1+r_+^2/l^2)}{2r_+}.$$

Its angular velocity can be defined as the angular velocity of photons orbiting the horizon, as measured at infinity with respect to the static AdS$_4$ frame, and is

$$\Omega = \frac{a(1+r_+^2/l^2)}{r_+^2+a^2}.$$

A Bekenstein entropy can be associated to this black hole, as well as a Hawking black body temperature, respectively related to the area A of the horizon and its surface gravity κ by

$$S = \frac{1}{4}A = \frac{\pi(r_+^2+a^2)}{\Xi} \quad , \quad T = \frac{\kappa}{2\pi} = \frac{4\pi(r_+^2+a^2)}{r_+(1+a^2/l^2+3r_+^2/l^2-a^2/r_+^2)}.$$

Since $\mathcal{M}$ is stationary and axially symmetric, it possesses two Killing vectors. Hence there exists global conserved charges that can be interpreted as the mass M and angular momentum J of the black hole. There are various ways to construct them. As reviewed in [2] there is general agreement in the literature on the definition of J but not on the definition of M. The "right" results are

$$M = \frac{m}{\Xi^2} \quad , \quad J = \frac{ma}{\Xi^2}$$

where the mass is associated with the Killing vector describing time translations in a locally free falling *non rotating* inertial frame in AdS$_4$. In the rotating Boyer-Linquist frame its components are $(1,0,0,-a/l^2)$.

[1] deruelle@ihes.fr

The reason why one can speak of the "right" results for M and J is that, as emphasized in [2], the first law of thermodynamics must hold, that is, one must have

$$T\,dS = dM - \Omega\,dJ\,.$$

Now, T, S, Ω, M, J are known functions of the two parameters m and a (or, computationally more simply, of r_+ and a). Therefore the two equalities

$$T\frac{\partial S}{\partial r_+} = \frac{\partial M}{\partial r_+} - \Omega\frac{\partial J}{\partial r_+} \quad , \quad T\frac{\partial S}{\partial a} = \frac{\partial M}{\partial a} - \Omega\frac{\partial J}{\partial a}$$

must hold and, if they do, provide a consistency check of the interpretation of the Kerr-AdS$_4$ metric as representing a radiating black hole spacetime, and in particular a check of the pertinence of the definition of its mass.

The object of this contribution is, first, to review in section 2 a method based on standard Nœther identities which defines conserved charges associated to a spacetime $\mathcal{M}$ with respect to its asymptotic background $\overline{\mathcal{M}}$ in Einstein-Gauss-Bonnet (EGB) theory [3], irrespective of the source of curvature, that is whether it is a "star" or a black hole.

In Einstein's theory, when applied to the recently discovered D-Dimensional Kerr-anti-de Sitter Einstein black holes [4], that method yields the right mass, that is, for which the first law holds, as shown in [5] and reviewed in Section 4.

In Einstein-Gauss-Bonnet's theory the rotating Kerr-like solution is not known. However, on one hand, only the asymptotic form of the metric is required to define the conserved charges and, on the other hand, the Einstein and Einstein-Gauss-Bonnet vacuum equations are the same when linearized on a maximally symmetric background (see section 3) : hence the D-dimensional Kerr-anti-de Sitter solutions to the Einstein field equations found in [4] are also asymptotic solutions to the Einstein-*Gauss-Bonnet* equations. Those two remarks were used in [6] to give an explicit expression for the mass and angular momenta of Kerr-AdS spacetimes in EGB theory, which is reviewed in section 4. When the full geometry of the Kerr-like rotating EGB black holes is eventually obtained, a test of the proposed definitions will be to see if the first law of EGB black hole thermodynamics is satisfied.

2 Nœther superpotential and charges in EGB theory

There are various ways to associate conserved charges to a D-dimensional spacetime $\mathcal{M}$. We shall review here the approach advocated in [7] and [8] and applied to Einstein-Gauss-Bonnet theory of gravity in [3].

Consider the lagrangian

$$\mathcal{L} = L + D_\mu k^\mu \tag{2.1}$$

where L is some function of curvature invariants, functional of the metric $g_{\mu\nu}(x^\rho)$, its first and second derivatives with respect to the coordinates x^ρ and where k^μ is a vector to be appropriatly chosen (see below). The variation of the scalar density $\hat{\mathcal{L}}$ with respect to the metric can be written as

$$\delta\hat{\mathcal{L}} = -\hat{\sigma}^{\mu\nu}\delta g_{\mu\nu} + \partial_\mu(\hat{V}^\mu + \delta\hat{k}^\mu)\,. \tag{2.2}$$

(A hat denotes multiplication by $\sqrt{-g}$ where g is the determinant of the metric.) The tensor $\sigma^{\mu\nu}$ is the variational derivative of $\hat{\mathcal{L}}$ and the field equations are $\sigma^{\mu\nu} = 0$, whatever the vector k^μ. As for the vector V^μ it can be written under the form

$$V^\mu = \alpha^{\mu\nu\rho}\,\delta g_{\nu\rho} + \beta^{\mu\nu\rho}{}_\sigma\,\delta\Gamma^\sigma_{\nu\rho} \tag{2.3}$$

where $\Gamma^\sigma_{\nu\rho}$ are the Christoffel symbols, where $\delta\Gamma^\sigma_{\nu\rho} = \frac{1}{2}g^{\sigma\lambda}(D_\nu\delta g_{\rho\lambda} + D_\rho\delta g_{\nu\lambda} - D_\lambda\delta g_{\nu\rho})$ and where the tensors $\alpha^{\mu\nu\rho}$ and $\beta^{\mu\nu\rho}{}_\sigma$ depend on the precise dependence of L on the metric and its derivatives.

If the variation $\delta g_{\mu\nu}$ is due to a mere change of coordinates $x^\mu \to \tilde{x}^\mu = x^\mu - \xi^\mu$ with ξ^μ an infinitesimal vector (so that $\delta\hat{\mathcal{L}} = \partial_\mu(\hat{\mathcal{L}}\xi^\mu)$ and $\delta g_{\mu\nu} = 2D_{(\mu}\xi_{\nu)}$, parentheses denoting symmetrisation), then the variation (2) of the Lagrangian density can be cast in the form :

$$\partial_\mu\hat{j}^\mu = D_\mu\hat{j}^\mu = 0 \qquad \text{with} \qquad \hat{j}^\mu \equiv (2\hat{\sigma}^{\mu\nu} + g^{\mu\nu}\hat{L})\xi_\nu - \hat{V}^\mu + 2D_\nu(\xi^{[\mu}\hat{k}^{\nu]}) \tag{2.4}$$

thanks to the (generalized) Bianchi identities. (Brackets stand for anti-symmetrization : $f_{[\mu\nu]} \equiv \frac{1}{2}(f_{\mu\nu} - f_{\nu\mu})$.)

The conservation of j^μ implies that there exists an antisymmetric tensor $j^{[\mu\nu]}$ such that

$$\hat{j}^\mu \equiv D_\nu \hat{j}^{[\mu\nu]} = \partial_\nu \hat{j}^{[\mu\nu]} . \tag{2.5}$$

If we look for an expression of the form

$$j^{[\mu\nu]} = \mathcal{A}^{[\mu\nu]\rho}\xi_\rho + \mathcal{B}^{[\mu\nu]\rho\sigma} D_\rho \xi_\sigma + 2\xi^{[\mu} k^{\nu]} \tag{2.6}$$

then $\mathcal{A}^{[\mu\nu]\rho}$ and $\mathcal{B}^{[\mu\nu]\rho\sigma}$ are obtained in terms of $\alpha^{\mu\nu\rho}$ and $\beta^{\mu\nu\rho}{}_\sigma$ from (4) and (5) by identification.

We obtain similarly $\overline{\hat{j}^\mu}$ and $\overline{\hat{j}^{[\mu\nu]}}$ for the background $\overline{\mathcal{M}}$ (an overline means that the quantity is evaluated on the background spacetime with metric $\overline{g}_{\mu\nu}(x^\rho)$). In practice the only demand on $\overline{\mathcal{M}}$ is that it asymptotes $\mathcal{M}$. The KBL superpotential density [7] [8] is then defined as

$$j^{[\mu\nu]} = -\frac{1}{16\pi}\left(\hat{j}^{[\mu\nu]} - \overline{\hat{j}^{[\mu\nu]}}\right) . \tag{2.7}$$

We now integrate (7) over a region $\mathcal{M}$ of spacetime bounded by $\partial\mathcal{M} = \partial\overline{\mathcal{M}}$, a timelike hypercylinder limited by two spacelike hypersurfaces $x^0 = t_0$ and $x^0 = t_1$. We apply Stokes' theorem and obtain that the "charge"

$$Q = \int_S d^{D-2}x \; n_i \hat{j}^{[0i]} \tag{2.8}$$

is independent of time if $\int_S d^{D-2}x \; n_i(\hat{j}^i - \overline{\hat{j}^i}) = 0$ where S is the $(D-2)$-dimensional sphere at infinity, with n^i its unit normal vector pointing towards infinity.

In practice we shall restrict our attention to stationary spacetimes and choose ξ^μ to be a Killing vector, so that Q will indeed be time-independent. When that Killing vector is associated with time translations with respect to a non rotating frame at infinity the associated conserved charge is the mass M of $\mathcal{M}$. If the Killing vector is associated with rotations then the associated charges are the angular momenta J_i.

As for the vector k^μ it is chosen according to circumstances (that is, according to L) in order to cancel as many normal derivatives of the metric variations as possible in the divergence in (2). If they all cancel, the field equations are obtained by keeping only the metric and its tangential derivatives fixed at the boundary, leaving their normal derivatives free, and the variational problem falls within the scope of ordinary Lagrangian field theory.

Let us now specialize to Einstein-Gauss-Bonnet's theory of gravity. The Lagrangian is (see e.g. [9] for a review of its properties)

$$L \equiv -2\Lambda + R + \alpha\, R^{\mu\nu\rho\sigma} P_{\mu\nu\rho\sigma} \quad \text{with} \quad P_{\mu\nu\rho\sigma} \equiv R_{\mu\nu\rho\sigma} - 2(R_{\mu[\rho}g_{\sigma]\nu} - R_{\nu[\rho}g_{\sigma]\mu}) + R\, g_{\mu[\rho}g_{\sigma]\nu} \tag{2.9}$$

(so that $R^{\mu\nu\rho\sigma}P_{\mu\nu\rho\sigma} = R^{\mu\nu\rho\sigma}R_{\mu\nu\rho\sigma} - 4R^{\mu\nu}R_{\mu\nu} + R^2$). Λ is a (negative) cosmological constant, α a coupling constant which is zero in Einstein's theory, and $R_{\mu\nu\rho\sigma}$, $R_{\mu\nu}$ and R are the Riemann tensor, Ricci tensor and curvature scalar of the metric $g_{\mu\nu}$.

The equations of motion derived from that Lagrangian are

$$\sigma^{\mu\nu} \equiv \sigma_E^{\mu\nu} + \alpha\sigma_{GB}^{\mu\nu} = 0 \tag{2.10}$$

with

$$\sigma_E^{\mu\nu} \equiv \Lambda g^{\mu\nu} + R^{\mu\nu} - \frac{1}{2}R\, g^{\mu\nu} \tag{2.11}$$

and

$$\sigma_{GB}^{\mu\nu} \equiv 2R^{\mu\lambda\rho\sigma}P^{\nu}{}_{\lambda\rho\sigma} - \frac{1}{2}g^{\mu\nu}R^{\alpha\beta\rho\sigma}P_{\alpha\beta\rho\sigma} . \tag{2.12}$$

The explicit form of the vector V^μ appearing in (2) (3) is

$$V^\mu \equiv V_E^\mu + \alpha V_{GB}^\mu \tag{2.13}$$

with

$$V_E^\mu = -\left(g^{\mu\nu}\delta\Gamma^\rho_{\nu\rho} - g^{\nu\rho}\delta\Gamma^\mu_{\nu\rho}\right) \tag{2.14}$$

and

$$V_{GB}^\mu = 4D^{(\mu}\sigma_E^{\nu)\rho}\delta g_{\nu\rho} - 4\left(P^{\mu\alpha\beta}{}_\gamma - Q^{\mu\alpha\beta}{}_\gamma\right)\delta\Gamma^\gamma_{\alpha\beta} \tag{2.15}$$

where the tensor $P_{\mu\nu\rho\sigma}$ is defined in (9) and where $Q_{\mu\nu\rho\sigma} \equiv 2(R_{\rho[\mu}g_{\nu]\sigma} + R_{\sigma[\mu}g_{\nu]\rho})$. The tensors $\mathcal{A}^{[\mu\nu]\rho}$ and $\mathcal{B}^{[\mu\nu]\rho\sigma}$ in (6) are then easily calculated and yield the following expression for the EGB superpotential

$$\hat{J}^{[\mu\nu]} \equiv \hat{J}_E^{[\mu\nu]} + \alpha\,\hat{J}_{GB}^{[\mu\nu]} \tag{2.16}$$

where the Einstein contribution is given by, see [7-8]

$$-8\pi\hat{J}_E^{[\mu\nu]} \equiv D^{[\mu}\hat{\xi}^{\nu]} - \overline{D^{[\mu}\hat{\xi}^{\nu]}} + \hat{\xi}^{[\mu}k_E^{\nu]}\,. \tag{2.17}$$

As for the Gauss-Bonnet contribution $\hat{J}_{GB}^{[\mu\nu]}$ it is, when ξ^μ is a Killing vector [3]

$$-8\pi\hat{J}_{GB}^{[\mu\nu]} \equiv 2\left[P^{\mu\nu\alpha\beta}D_{[\alpha}\hat{\xi}_{\beta]} - \overline{P^{\mu\nu\alpha\beta}D_{[\alpha}\hat{\xi}_{\beta]}}\right] + \hat{\xi}^{[\mu}k_{GB}^{\nu]}\,. \tag{2.18}$$

The last step is to choose the vectors k_E^μ and k_{GB}^μ. The choice made in [7] and [8], that is

$$k_E^\nu = g^{\mu\nu}\Delta^\rho_{\nu\rho} - g^{\nu\rho}\Delta^\mu_{\nu\rho} \quad \text{with} \quad \Delta^\mu_{\nu\rho} \equiv \Gamma^\mu_{\nu\rho} - \overline{\Gamma^\mu_{\nu\rho}} \tag{2.19}$$

has passed all tests with flying colours (see e.g. [10]). The following proposal was made in [3] for the Gauss-Bonnet contribution

$$k_{GB}^\mu = 4\left(P^{\mu\alpha\beta}{}_\gamma - Q^{\mu\alpha\beta}{}_\gamma\right)\Delta^\gamma_{\alpha\beta} \tag{2.20}$$

where it was shown that such a definition yielded the correct formula for the mass of the static EGB-Schwarzschild-like spacetimes, that is, which is consistent with the first law of EGB black hole thermodynamics.

More generally, when the vector ξ_t^μ is the Killing vector of time translations with respect to a non rotating frame at infinity the associated conserved charge is the mass M. If the vector ξ_i^μ is a Killing vector for rotations with respect to the i-axis then the associated charges is the angular momentum J_i :

$$M = \int_S d^{D-2}x\hat{J}_t^{[01]} \quad , \quad J_i = \int_S d^{D-2}x\hat{J}_i^{[01]}\,. \tag{2.21}$$

Equipped with those formulae it is then a matter of straightforward calculation to obtain the mass M and angular momenta J_i for a given metric which solves the field equations (10-12). It is important to note that only the asymptotic form of the metric is needed and that the mass and angular momenta thus obtained do not depend on the source of curvature, which can be a "star" or a black hole.

3 The asymptotic Kerr-AdS solutions of the EGB equations

The Einstein-Gauss-Bonnet equations of motion were given in the previous section, equations (2.10-2.12). In order to compute the mass and angular momenta of stationary and axi-symmetric spacetimes which solve those field equations, only the aymptotic form of the metric is required. We therefore linearize the EGB equations, that is, we set

$$g_{\mu\nu} = \overline{g}_{\mu\nu} + h_{\mu\nu}\,. \tag{3.1}$$

We choose the background $\overline{g}_{\mu\nu}$ to be the metric of a maximally symmetric spacetime $\overline{\mathcal{M}}$ solving the EGB equations. Since they are quadratic in the Riemann tensor there are two solutions, defined by

$$\overline{R}_{\mu\nu\rho\sigma} = -\frac{1}{\mathcal{L}^2}(\overline{g}_{\mu\rho}\overline{g}_{\nu\sigma} - \overline{g}_{\mu\sigma}\overline{g}_{\nu\rho}) \quad \text{where} \quad \frac{1}{\mathcal{L}^2} \equiv \frac{1}{2\tilde{\alpha}}\left(1 \pm \sqrt{1 - \frac{4\tilde{\alpha}}{l^2}}\right) \tag{3.2}$$

with $\tilde{\alpha} \equiv (D-3)(D-4)\alpha$ and $l^2 \equiv -\frac{(D-1)(D-2)}{2\Lambda}$, D being the dimension of spacetime. We shall choose the lower sign for $\mathcal{L}^2$ so that the limit when $\alpha = 0$ solves the Einstein equations. (When Λ and α are such that $\sqrt{1-4\tilde{\alpha}/l^2} = 0$ the two roots coalesce into a single double root.)

Using the fact that

$$R^{\mu}{}_{\nu\rho\sigma} = \overline{R^{\mu}{}_{\nu\rho\sigma}} + \frac{1}{2}\overline{D}_{\rho}(\overline{D}_{\nu}h^{\mu}_{\sigma} + \overline{D}_{\sigma}h^{\mu}_{\nu} - \overline{D}^{\mu}h_{\sigma\nu}) - \frac{1}{2}\overline{D}_{\sigma}(\overline{D}_{\nu}h^{\mu}_{\rho} + \overline{D}_{\rho}h^{\mu}_{\nu} - \overline{D}^{\mu}h_{\rho\nu}) + \mathcal{O}(h^2) \tag{3.3}$$

($\overline{D}_{\mu}$ being the covariant derivative associated to $\overline{g}_{\mu\nu}$) it is an exercise to compute $R^{\mu\lambda\rho\sigma}P_{\nu\lambda\rho\sigma}$ at linear order and see that the EGB equations read (a result first obtained in [11] for $\Lambda = 0$)

$$\sqrt{1-\frac{4\tilde{\alpha}}{l^2}}\left[R^{\mu}_{\nu} - \frac{1}{2}\delta^{\mu}_{\nu}R + \delta^{\mu}_{\nu}\Lambda\frac{l^2}{\mathcal{L}^2}\right] = \mathcal{O}(h^2) \tag{3.4}$$

where

$$R^{\mu}_{\nu} = -\frac{(D-1)}{\mathcal{L}^2}(\delta^{\mu}_{\nu} - h^{\mu}_{\nu}) + \frac{1}{2}\left[\overline{D}_{\alpha}(\overline{D}_{\nu}h^{\alpha\mu} + \overline{D}^{\mu}h^{\alpha}_{\nu} - \overline{D}^{\alpha}h^{\mu}_{\nu}) - \overline{D}^{\mu}\overline{D}_{\nu}h^{\rho}_{\rho}\right] + \mathcal{O}(h^2) \tag{3.5}$$

is the linearized Ricci tensor on $\overline{\mathcal{M}}$.

Hence, when linearized on a maximally symmetric background, the Einstein-Gauss-Bonnet equations are the same as the linearized pure Einstein equations ($\alpha = 0$) with effective cosmological constant $\Lambda_e \equiv \Lambda\frac{l^2}{\mathcal{L}^2}$, and up to the overall factor $\sqrt{1-4\tilde{\alpha}/l^2}$ that we shall assume not to be zero.

Now, in [4] Gibbons, Lu, Page and Pope found D-dimensional Kerr-anti-de Sitter exact solutions of Einstein's equations. Since the linearized Einstein-Gauss-Bonnet equations are the same as the linearized pure Einstein equations, those solutions also solve the Einstein-Gauss-Bonnet equations at linear order.

We shall write them in Kerr-Schild coordinates. In odd dimensions $D = 2n+1$ for instance, the line element reads

$$ds^2 = g_{\mu\nu}dx^{\mu}dx^{\nu} = d\bar{s}^2 + \frac{2m}{U}(h_{\mu}dx^{\mu})^2 \qquad \text{with} \quad \mu = \{0, 1, \mu_i, \phi_i\} \quad (i = 1, ..., n) \tag{3.6}$$

where $d\bar{s}^2$ is the metric of the anti-de Sitter background and where the coordinates μ_i are subject to the constraint $\sum_{i=1}^{i=n}\mu_i^2 = 1$. The mass parameter m is an integration constant, h_{μ} is some null vector (denoted k_{μ} in [2] [4]) depending on n rotation parameters a_i and U is a scalar function. Explicit forms of those functions can be found in Section 2 of ref [4].

As an example, the 5-dimensional AdS line element in Kerr-Schild ellipsoidal coordinates $x^{\mu} = (t, r, \theta, \phi, \psi)$ reads :

$$d\bar{s}^2 = -\frac{(1+r^2/\mathcal{L}^2)\Delta_{\theta}}{\Xi_a\Xi_b}dt^2 + \frac{r^2\rho^2}{(1+r^2/\mathcal{L}^2)(r^2+a^2)(r^2+b^2)}dr^2 + \frac{\rho^2}{\Delta_{\theta}}d\theta^2 +$$
$$+\frac{r^2+a^2}{\Xi_a}\sin^2\theta\, d\phi^2 + \frac{r^2+b^2}{\Xi_b}\cos^2\theta\, d\psi^2 \tag{3.7}$$

where $\Delta_{\theta} \equiv \Xi_a\cos^2\theta + \Xi_b\sin^2\theta$, where $\rho^2 \equiv r^2 + \mathcal{L}^2(1-\Delta_{\theta})$, and where Ξ_a and Ξ_b are related to the rotation parameters a and b by $\Xi_a \equiv 1 - a^2/\mathcal{L}^2$, $\Xi_b \equiv 1 - b^2/\mathcal{L}^2$. As for the function U and the null vector h_{μ} they are given by $U = \rho^2$ and

$$h_{\mu}dx^{\mu} = \frac{\Delta_{\theta}}{\Xi_a\Xi_b}dt + \frac{r^2\rho^2}{(1+r^2/\mathcal{L}^2)(r^2+a^2)(r^2+b^2)}dr + \frac{a\sin^2\theta}{\Xi_a}d\phi + \frac{b\cos^2\theta}{\Xi_b}d\psi\,. \tag{3.8}$$

Note that we shall only need their asymptotic behaviours at leading order. Note also that the full Ricci tensor of the Kerr-Schild metric (6-8) is linear in $h_{\mu\nu} = \frac{2m}{U}h_{\mu}h_{\nu}$ and hence exactly given by (5), see e.g. [4].

The background admits a timelike Killing vector $\xi = \xi_t$ and n plane rotation Killing vectors $\xi = \xi_i$ associated with one parameter displacements, say τ. ξ_t is normalized in such a way that $\xi_t^{\mu}\delta\tau$ is an infinitesimal time translation in a locally free falling *non rotating* inertial frame in the background. Thus

for the background metric in its conventional static form when $D = 2n + 1$ for instance (equations (2.11) and (2.12) of Ref [4])

$$d\bar{s}^2 = -\left(1 + \frac{y^2}{l^2}\right) dt^2 + \frac{dy^2}{1 + y^2/l^2} + y^2 d\sigma^2_{(D-2)} \qquad \text{where} \quad d\sigma^2_{(D-2)} = \sum_{i=1}^{i=n} (d\tilde{\mu}_i^2 + \tilde{\mu}_i^2 d\phi_i^2), \tag{3.9}$$

with $\Sigma_i \tilde{\mu}_i^2 = 1$, the components of the timelike Killing vector ξ_t corresponding to time translations are $(1, 0, 0, 0, ...)$. In Kerr-Schild ellipsoidal coordinates ξ_t has the same components. If the vector ξ_i^μ is the Killing vector associated with rotations, for example with respect to the ϕ (resp. ψ) axis in five dimensions, that is $\xi_a^\mu = (0, 0, 0, 1, 0)$ (resp. $\xi_b^\mu = (0, 0, 0, 0, 1)$), then the associated charges are the angular momenta.

4 Kerr-AdS masses and angular momenta in EGB theory

To obtain the mass and angular momenta of the 5D-Kerr-like solution of EGB theory we inserted the metric (3.6-3.8) of section 3 in the definitions (2.16-2.21) of section 2 and took the large r limit (using *Maple* and *GR tensor*). The result was found to be [6]

$$M_{(5)} = \sqrt{1 - \frac{4\tilde{\alpha}}{l^2}} \left[\frac{m\pi}{4(\Xi_a \Xi_b)^2} (2\Xi_a + 2\Xi_b - \Xi_a \Xi_b) \right] \ , \ J_{(5)a} = \sqrt{1 - \frac{4\tilde{\alpha}}{l^2}} \left[\frac{\pi m a}{2\Xi_a^2 \Xi_b} \right] . \tag{4.1}$$

We calculated similarly the mass and angular momentum in $D = 6, 7, 8$ dimensions in the case when there is only one non zero rotation parameter. The results could be cast under the form ($D = 5, 6, 7, 8$) [6]

$$M_D = \sqrt{1 - \frac{4\tilde{\alpha}}{l^2}} \frac{m\mathcal{V}_{D-2}}{4\pi\Xi_a^2} \left[1 + \frac{(D-4)}{2} \Xi_a \right] \quad , \quad J_D = \sqrt{1 - \frac{4\tilde{\alpha}}{l^2}} \frac{ma\mathcal{V}_{D-2}}{4\pi\Xi_a^2} \tag{4.2}$$

where $\mathcal{V}_{D-2}$ is the volume of the $(D-2)$-unit sphere. Finally, we extrapolated to all dimensions the asymptotic expressions for the Kerr-AdS Riemann tensor obtained with *Maple* and *GR tensor* in $D = 5, 6, 7, 8$ dimensions, and found (by hand) the mass and angular momenta of the general D-dimensional Kerr-like solutions of Einstein-Gauss-Bonnet theory as [6]

$$M_{2n} = \sqrt{1 - \frac{4\tilde{\alpha}}{l^2}} \left[\frac{m\mathcal{V}_{2n-2}}{4\pi\Xi} \sum_{i=1}^{i=n-1} \frac{1}{\Xi_i} \right] \quad , \quad M_{2n+1} = \sqrt{1 - \frac{4\tilde{\alpha}}{l^2}} \left[\frac{m\mathcal{V}_{2n-1}}{4\pi\Xi} \left(\sum_{i=1}^{i=n} \frac{1}{\Xi_i} - \frac{1}{2} \right) \right]$$

$$J_{(D)i} = \sqrt{1 - \frac{4\tilde{\alpha}}{l^2}} \left[\frac{m\mathcal{V}_{D-2}}{4\pi\Xi} \frac{a_i}{\Xi_i} \right] , \tag{4.3}$$

where $\Xi = \Pi_{i=1}^{i=(n-1)} \Xi_i$ for $D = 2n$ and $\Xi = \Pi_{i=1}^{i=n} \Xi_i$ for $D = 2n + 1$.

Let us fill up some details of the calculation.

We worked in Kerr-Schild coordinates in which the metric is given for example by (3.6-3.8). Some useful properties are that the metric coefficients do not depend on x^0 and ϕ_i; the $g_{\mu_i \mu}$, coefficients do not depend on m; the other off-diagonal components are linear in m and hence do not enter the calculation. The fact that the vector h^μ is null further simplifies the calculation since $\sqrt{-g} = \sqrt{-\bar{g}}$. Using those informations one thus arrives for example at

$$D^{[0}\hat{\xi}_t^{1]} - \overline{D^{[0}\hat{\xi}_t^{1]}} = \overline{D^{[0}\hat{\xi}_t^{1]}} \left(\frac{\delta g'_{tt}}{\bar{g}'_{tt}} - \frac{\delta g_{tt}}{\bar{g}_{tt}} - \frac{\delta g_{rr}}{\bar{g}_{rr}} \right) + \mathcal{O}(m^2) \quad \text{with} \quad \overline{D^{[0}\hat{\xi}_t^{1]}} = -\frac{\sqrt{-\bar{g}}\ \bar{g}'_{tt}}{2\bar{g}_{tt}\bar{g}_{rr}} \tag{4.4}$$

where $\xi_t^\mu = (1, 0, ..., 0)$, where $\delta g_{\mu\nu} \equiv g_{\mu\nu} - \bar{g}_{\mu\nu}$ and where a prime denotes differentiation with respect to r. A similar expression is obtained for $\hat{\xi}_t^{[0} k_E^{1]}$ with k_E^μ given by equation (2.19) of section 2.

Using then the asymptotic form of the D-dimensional Kerr-AdS metric found in [4] at leading order in r one then arrives for example at

$$\hat{\xi}_t^{[0} k_E^{1]} = -\frac{m}{\Xi} \sqrt{g_{(D-2)}} + \mathcal{O}\left(\frac{m^2}{r}\right) , \tag{4.5}$$

and

$$\hat{J}^{[01]}_{E\,t} = \frac{m}{8\pi\Xi}\left[(D-1)W-1\right]\sqrt{g_{(D-2)}} + \mathcal{O}\left(\frac{m^2}{r}\right) \quad \text{with} \quad W \equiv \sum_{i=1}^{i=n}\frac{\mu_i^2}{\Xi_i} \tag{4.6}$$

where $g_{(D-2)}$ is the determinant of the metric $d\sigma^2_{(D-2)}$ in (3.9) with tildes dropped and with $a_n = 0$ in even dimensions $D = 2n$.

The calculation of $\hat{\xi}^{[0}_t k^{1]}_{GB}$ is straightforward since

$$k^{\mu}_{GB} = -\frac{2}{\mathcal{L}^2}(D-2)(D-3)\,k^{\mu}_{E} + \mathcal{O}(m^2)\,. \tag{4.7}$$

The calculation of $-4\pi\hat{J}^{[01]}_{P,t} \equiv (P^{01\alpha\beta}D_{[\alpha}\hat{\xi}_{t\,\beta]} - \overline{P^{01\alpha\beta}D_{[\alpha}\hat{\xi}_{t\,\beta]}})$ at leading order yields in a first step

$$-4\pi\hat{J}^{[01]}_{P,t} = \frac{\sqrt{g_{(D-2)}}}{\Xi\mathcal{L}^2}\left[-\frac{2}{\mathcal{L}^2}\lim_{r\to\infty} r^{D+1}\delta R^0{}_{101} + mW(D-1)(D-2)(D-3) - 2m(D^2-5D+8)\right] \tag{4.8}$$

and requires the knowledge of the asymptotic form of the Riemann tensor. The structure of the relevant component for the calculation of the mass is easily guessed and depends on two constants only :

$$\delta R^0{}_{101} \equiv \lim_{r\to\infty}(R^0{}_{101} - \overline{R^0{}_{101}}) = \frac{m\mathcal{L}^2}{r^{D+1}}(D-1)[c_1(D-3)W - c_2] \tag{4.9}$$

where, recall, $W \equiv \sum_{i=1}^{i=[D/2]}\frac{\mu_i^2}{\Xi_i}$, with $\sum_{i=1}^{i=[D/2]}\mu_i^2 = 1$ and $\Xi_{D/2} = 1$ if D is even. The *Maple* and *GRtensor* calculations in $D = 5$ determine the constants c_1 and c_2 to be one, similar calculations in $D = 6, 7, 8$ confirm them, so that the results can confidently be extended to any D.

After gathering all the previous information the remaining task is to integrate the superpotential on the sphere at infinity. While the "multi-cylindrical" pairs of coordinates (μ_i, ϕ_i) were convenient in [4] to find the Kerr-anti-de Sitter metric as well as in our previous calculations, the explicit integrations are more easily performed in spherical coordinates, say, φ_k with $(k = 1, 2, \cdots, D-2)$.

The final results are given above, formulae (3).

The calculation of the angular momenta proceeds along similar lines. Note that neither the background nor the vectors k^{μ}_{E} and k^{μ}_{GB} enter the calculations. However, in Einstein-Gauss-Bonnet theory, they are not given simply by Komar's integrals because the first term in (2.18) (that is $\hat{J}^{[01]}_{P,i}$) is not zero.

5 Conclusion

Formulae (4.3) for the mass and angular momenta of Kerr-AdS spacetimes in Einstein-Gauss-Bonnet theory have the right limits. When $\alpha = 0$ (Einstein's theory) they reduce to the results obtained in [2] and [5] and, as shown in [2], they are consistent with the first law of Einstein black hole thermodynamics.

When there is no rotation ($a_i = 0, \Xi_i = 1$) the masses (4.3) reduce to the result obtained in [12-13] and [3] (noting that the coefficients of the metric (3.6) then tend to $g_{tt} \simeq 1/g_{rr} \simeq r^2/\mathcal{L}^2 - 2m/r^{D-3}$) and are also consistent with the first law of Einstein-Gauss-Bonnet black hole thermodynamics (where the entropy is no longer proportional to the surface area of the horizon, see e.g. [12-13]).

Since the overall factor in (4.3) is the same as the one which appears in (3.4) one may conjecture that in the general Lovelock theory in D dimensions (whose Lagrangian is the sum of the first $[D/2]$ dimensionally continued Euler forms) the expressions for the masses and angular momenta will also be proportional to their values in Einstein's theory with an overall coefficient which is zero when the equation for the maximally symmetric space curvature has one single root of maximal multiplicity $[D/2]$.

Finally, the decisive check of formulae (4.3), that is of the pertinence of the proposal (2.20) made in [3] for the vector k^{μ}_{GB}, will be possible when the full geometry of the Kerr-like rotating *black holes* is known, by seeing if, with such definitions, the first law of thermodynamics is still satisfied.

6 Acknowledgements

Most of the work summarized here is the result of greatly enjoyable collaborations with Joseph Katz, Yoshiyuki Morisawa and Sachiko Ogushi.

References

[1] B. Carter, *Hamilton-Jacobi and Schrödinger separable solutions of Einstein's equations*, Comm. Math. Phys. **10** (1968) 280

[2] G.W. Gibbons, M.J. Perry and C.N. Pope, *The First Law of Thermodynamics for Kerr-de Sitter Metrics*, hep-th/0408217

[3] N. Deruelle, J. Katz and S. Ogushi, *Conserved Charges in Einstein- Gauss-Bonnet theory*, Class. Quantum Grav., **21** (2004) 1971, gr-qc/0310098

[4] G.W. Gibbons, H. Lu, Don N. Page and C.N. Pope, *The General Kerr-de Sitter Metrics in All Dimensions*, hep-th/0404008

[5] N. Deruelle and J.Katz, *On the mass of a Kerr-anti-de Sitter spacetime in D dimensions*, Class. Quantum Grav. **22** (2005) 421-424, gr-qc/0411035

[6] N. Deruelle and Y. Morisawa, *Mass and angular momenta of Kerr-anti-de Sitter spacetimes in Einstein-Gauss-Bonnet theory*, accepted by Class. and Quant. Grav, gr-qc/0411135

[7] J. Katz, *A note on Komar's anomalous factor*, Class. Quantum Grav., **2** (1985) 423

[8] J. Katz, J. Bičák, D. Lynden-Bell, *Relativistic conservation laws and integral constraints for large cosmological perturbations*, Phys. Rev. **D55** (1997) 5759

[9] N. Deruelle and J. Madore, *On the quasi-linearity of the Einstein "Gauss-Bonnet" gravity field equations*, in "Progress in General Relativity and Quantum Cosmology", gr-qc/0305004

[10] B. Julia and S. Silva, *Currents and superpotentials in classical gauge theories : II. Global aspects and the extension of affine gravity, Class. Quan. Grav.*, **17** (2000) 4733, gr-qc/0005127

[11] D.G. Boulware and S. Deser, *String generated gravity models*, Phys. Rev. Lett. **55** (1985) 2656

[12] Rong-Gen Cai, *Gauss-Bonnet Black Holes in AdS Spaces*, Phys.Rev. **D65** (2002) 084014, hep-th/0109133

[13] I. Neupane, *Black hole entropy in string-generated gravity models*, Phys.Rev.**D67** (2003) 061501, hep-th/0212092

Strings in Cosmology?

Ed Copeland[1]

School of Physics and Astronomy,
University of Nottingham,
University Park,
Nottingham, NG1 2RD, UK

Robert C. Myers[2]

Perimeter Institute for Theoretical Physics,
Waterloo,
Ontario N2J 2W9 Canada
and
Department of Physics
University of Waterloo
Waterloo, Ontario N2L 3G1 Canada

Joseph Polchinski[3]

Kavli Institute for Theoretical Physics
University of California
Santa Barbara, CA 93106-4030, USA

Abstract

We review the possibility of testing string theory through cosmology. In particular we describe recent efforts to show how macroscopic fundamental strings may be found through their distinctive signatures arising from the production of gravitational waves, their approach to scaling networks and the new types of macroscopic meta-stable strings that can form.

1 Introduction

In the mid 1980's just as string theory was taking off, another type of string theory was also enjoying a boom period. Cosmic strings, topological defects associated with phase transitions in the early universe were proving to be exciting objects for cosmologists trying to understand the nature of the primordial density fluctuations. Over the course of the following decade or so, a great deal of effort went into exploring both fields. For cosmic strings the observational consequences of these objects were investigated in detail, but unfortunately the outcome appeared to be one of disappointment for those of us who had placed so much effort into understanding them. The investigation of Fundamental strings carried on at a pace, with breakthroughs being made in our understanding of the underlying properties of the theory, but this generally did not include the cosmological implications of the theory. However, over the past few years this has changed and there at last appears to be a real move towards linking string theory and cosmology.

In this lecture we will attempt to describe some of the excitement there is concerning the possibility that we may be able to use cosmology as a way of directly testing for fundamental strings. Introducing the original cosmic strings in section 2, we will describe the existence of scaling solutions in the string

[1]E-mail:ed.copeland@nottingham.ac.uk
[2]E-mail:rmyers@perimeterinstitute.ca
[3]E-mail:joep@kitp.ucsb.edu

network, as a way of motivating the equivalent properties of cosmic superstrings. In section 3 we will describe why it is that cosmic F and D strings could be of interest for cosmology, primarily because of the possibility that they can be macroscopic and metastable. This will be extended in section 4 to show why they may be observed in future astronomical observations, perhaps through the anisotropies in microwave background radiation, but more likely through gravitational lensing events or gravitational wave detectors. Finally we will conclude in section 5.

2 Brief review of cosmic string properties

The original cosmic strings can be thought of arising in any field theory with a spontaneously broken U(1) symmetry (for a detailed review see [1]). For Abelian gauge field theories, they correspond to magnetic flux tube solutions (Nielsen-Oleson vortices) [2]. The potential of the Higgs-field associated with the flux tube, is the famous Mexican hat potential, circling the string in real space corresponds to the Higgs field circling the minimum of its potential. It was Kibble, in a pioneering paper, who realised that these objects could have significant consequences for cosmology [3]. He showed that should there be phase transitions in the early universe where a U(1) symmetry becomes broken, this would necessarily lead to formation of network of such flux tubes, as the Higgs field roles down the potential in different directions in different regions. A crucial number that emerges is the dimensionless coupling of the string mass per unit length or tension μ, to gravity, given by $G\mu$, where G is Newton's constant. What sparked our imaginations back in the 1980's, was the fact that the natural scale associated with a Grand Unified Scale phase transition was $G\mu \sim 10^{-6}$, a small but not insignificant number, and expected to parameterise the scale of the microwave anisotropies in the early universe. Here it described the size of string induced metric perturbations.

The initial distribution of a network of strings is comprised of a combination of infinite strings that stretch across the universe and a scale invariant distribution of loops of string. Roughly 80% of the string is initially infinite in length and 20% is in loops. There exist a series of characteristic length scales on the network. One, ξ, corresponds to the typical separation between strings, and is given in terms to the volume V and total length L of strings by $\xi^2 = V/L$. Another scale, $\bar{\xi}$ corresponds to the typical curvature scale on the strings, the persistence length of the long strings. Finally, ζ, corresponds to the small scale structure on the string network. As the universe expands, the network evolves and the characteristic length scales change with time as well. There are a number of physical processes that occur allowing the network to lose energy. The long strings can cross themselves forming loops which are chopped off the long strings, strings oscillate and because they are so massive they radiate energy through gravitational radiation. Meanwhile the long strings are stretched by the expansion, which increases the energy stored in the network. Hence there are competing effects which act against each other. Determining precisely how such a network evolves is a challenge that has proved difficult to solve exactly. The equations of motion are non-linear and the requirement of keeping track of the whole network in case new loops are formed from string intersections, requires considerable computing power. Alternate approaches include analytic attempts, but these too have their restrictions, as we can not solve the Nambu equations exactly for a network of strings. Here we will briefly describe an attempt one of us was involved in with Kibble and Austin in which we used a probabilistic approach to describe the network properties [4]. In particular the approach was to take a random segment of string of length l and extension r. We then wrote down evolution equations for the probability distribution p[r(l)] of finding a segment of extension r and length l, due to various physical processes. Heuristically this can be written as

$$\frac{\partial p}{\partial t} = \left(\frac{\partial p}{\partial t}\right)_{\rm str} + \left(\frac{\partial p}{\partial t}\right)_{\rm GR} + \left(\frac{\partial p}{\partial t}\right)_{\rm LSI} + \left(\frac{\partial p}{\partial t}\right)_{\rm loops} \qquad (1)$$

where the acronyms stand for stretching, Gravitational radiation, long string intercommuting and loop formation respectively. The total length L of the network changes with time,

$$\frac{\partial L}{\partial t} = \left(\frac{\partial L}{\partial t}\right)_{\rm str} + \left(\frac{\partial L}{\partial t}\right)_{\rm GR} + \left(\frac{\partial L}{\partial t}\right)_{\rm loops} \qquad (2)$$

The key assumption we had to make was the form of the ansatz for the probability. We chose a Gaussian ansatz given by

$$p[\mathrm{r}(l)] = \left(\frac{3}{2\pi K(l)}\right)^{3/2} \exp\left(-\frac{3}{2}\frac{\mathrm{r}^2}{K(l)}\right) \tag{3}$$

where $K(l)$ is the variance. Such an ansatz then allows us to determine the characteristic length scales on the network in terms of $K(l)$. In particular $\bar{\xi}$ is related to the large distance behaviour where the strings look Brownian,

$$K(l) \sim 2\bar{\xi}l \qquad l \gg t \tag{4}$$

where as the small scale structure scale ζ naturally arises in the limit $l \ll t$ as

$$K(l) \sim l^2 - \frac{l^3}{3\zeta} \tag{5}$$

Recall, we still have the definition of the string density in terms of $\xi^2 = V/L$. Based on the ansatz and evolution equations for p[r(l)] it is possible to write down rate equations for the length scales. What was intriguing was that it was possible to find stable solutions where the scales evolved with the Hubble parameter. These scaling solutions depended on the details of the model and assumptions but basically they satisfied $\xi \sim \bar{\xi} \sim 0.1H^{-1}$, and $\zeta \sim G\mu H^{-1}$. Thus we were in interesting territory. Given that these single string networks evolve with the Nambu-Goto action, decaying primarily by forming loops through intercommutaion and emitting gravitational radiation, whenever they crossed each other, (gauge theory simulations had shown they must always intercommute or exchange partners, hence form loops), the string network would enter an attractor regime where the energy density in the strings reached a constant fraction of the background energy density. This is easy to see. Given that the energy density in a typical length of string, ρ_{strings} is given by $\rho_{\mathrm{strings}} = \frac{\mu\xi}{\xi^3} \propto \frac{\mu}{t^2}$, where t is the cosmic time, and that the background radiation or matter scales as $\rho_{\mathrm{bgd}} \propto \frac{1}{Gt^2}$, it follows that at scaling the ratio is given by $\frac{\rho_{\mathrm{strings}}}{\rho_{\mathrm{bgd}}} \propto G\mu$. Typically we find $\frac{\rho_{\mathrm{strings}}}{\rho_{\mathrm{rad}}} \propto 400G\mu$ and $\frac{\rho_{\mathrm{strings}}}{\rho_{\mathrm{matter}}} \propto 60G\mu$. Of note for later in the talk, the scaling density of strings decreases as the intercommuting probability decreases because it takes longer for the network to lose energy to loops. Of course the goal of cosmic strings was to provide a better explanation for the formation of structure than the Inflationary universe could. Unfortunately as more precise numerical calculations later showed, it simply could not provide the detailed features that are now recognised as being present in the beautiful maps which are the cosmic microwave anisotropies. These maps show a number of acoustic peaks, and it appears to be the case that whereas this is trivial for your average inflation model to reproduce (in fact too easy in some sense), when the strings are normalised to COBE to obtain their tension, they then fail to produce sufficient acoustic peak structure. The basic reason is that Inflation models have temporal coherence built into them, such coherence leads to peaks and troughs as in waves interacting. Cosmic strings are all higgledy piggledy across the universe and tend to cancel out peaks rather than reinforce them. This of course simply means that strings by themselves are ruled out as the primary seeds for structure formation. It does not rule them out as contributors. Many cosmologists balk at the idea of mixing strings and other objects, but it is well worth investigating and as we shall shortly see, strings can occur very easily with inflation, forming at or near the end of a period of inflation. In that case, they can contribute. Recent work on this approach suggests that strings can contribute of order no more than 13% of the scalar perturbations to the cmb anisotropies, which means that $G\mu < 10^{-6}$ [5, 6].

Another significant bound which becomes tighter year by year arises from the fact that strings are massive objects, emitting gravitational waves as they oscillate. The incredibly demanding pulsar bounds on any source of gravitational waves produced in the relevant frequency range (0.1 inverse year) can be used to constrain the allowed energy stored in the stochastic gravitational wave background arising from the string network, hence to bound the combination $G\mu$. The energy density stored in stochastic gravitational waves per logarithmic frequency range has been constrained to be $\Omega_{\mathrm{GW}} < 1.2 \times 10^{-7}$ [8]. Vilenkin and Shellard present the estimate of the associated energy density arising from a string network as $\Omega_{\mathrm{GW}} < 0.04G\mu$, giving $G\mu < 10^{-5.5}$ [1]. We will discuss further constraints emerging from gravitational lensing later in the lecture.

3 The new generation of strings for cosmology – Cosmic Superstrings

As we mentioned earlier, around the same time we were getting very excited about cosmic strings for cosmology, the first superstring revolution was taking off in a really big way. Needless to say it crossed peoples minds very early in this revolution of string theory, that fundamental strings could be cosmic strings, responsible for the primordial density perturbations. It was Witten who ruled it out in a beautiful short letter [9]. The first problem was that unification of the gauge coupling constants in Heterotic string theory required $G\mu = \frac{\alpha_{GUT}}{16\pi} \geq 10^{-3}$, whereas the constraints emerging from the cmb anisotropies on large scales implied $G\mu \leq 10^{-6}$! Consequently, people felt that cosmic strings would have to be magnetic or electric flux tubes arising in low energy theory. Inflation was already having a dramatic impact on cosmology and would have diluted any fundamental (as well as cosmic) strings which were around before the inflationary period began, implying there would be very few (if any) macroscopic fundamental strings. On top of that, Witten also showed that there were unlikely to be any macroscopic fundamental strings because they decayed. As can be seen in Fig. 1, Type I strings would break up into ordinary quanta on a string time scale (in fact this is because they are ending on spacetime filling D9 branes). The other types of string also had their own favourite decay modes, a long Heterotic string would bound an axion domain wall whose tension would make it shrink and disappear, and a similar fate would befall a Type II string where in that case a Neveu Schwarz five-brane instanton would produce an axion potential, again leading to domain walls.

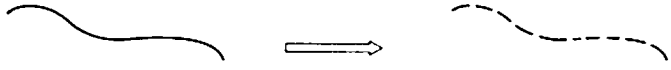


Fig. 1: The decay of an open Type I string

The second superstring revolution began in the mid 1990's with the introduction of new higher dimensional objects, branes. These included new one-dimensional strings, Dirichilet (D) strings, or higher dimensional D-, Neveu Schwarz-, or M- branes partly wrapped on compact cycles with only one non-compact dimension left. On top of that, new solutions began to emerge in these models where Branes were playing an integral part. One class of particular interest have large compact dimensions or large warp factors which as we will see allow for much lower string tensions, hence provide a 'get out' clause to one of the initial objections raised by Witten. Given these new possibilities it leads to the natural question of what they imply for cosmic strings? At the turn of the Millenium, in a series of papers, physicists began to investigate how in these brane models strings could survive inflation by forming at the end of the inflationary period [10, 11]. The basic idea of inflation in brane worlds was first developed in [10] and involved inflation arising from the separation of brane-antibrane pairs in the early universe. Inflation itself was induced by the energy density of branes with the inflaton being the brane-antibrane separation. Initially the branes experienced a weak attraction at long distance giving rise to a flat potential, which only steepened as the branes came together. In the models that were investigated the D-branes/antibrane system possessed a U(1)×U(1) symmetry, which disappeared when the branes annihilated with each other. During this period, reheating of the Universe would occur, leading, where appropriate to the production of strings just as in the case of ordinary field theory. One U(1) symmetry would tend to lead to the production of Dirichlet strings [11, 12, 13] whereas the other U(1) lead to the production of fundamental strings [14].

Tye and colleagues in particular showed how D-brane-antibrane inflation leads to the formation of D1 branes in our non-compact space, and crucially for cosmology they showed that although strings formed, domain walls or monopoles would not form [11]. In general they argued that the allowed range of string tensions in these models lived in the range $10^{-11} \leq G\mu \leq 10^{-6}$, well within the observational limits referred to earlier. However, in general for cosmic strings to be cosmologically interesting today we require that they are not too massive (from CMB constraints), are produced after inflation (or survive inflation) and are stable enough to survive until today. In many ways these methods of producing strings at the end of a period of inflation are like a version of hybrid inflation involving two coupled scalar fields, such that the as the inflation period ends, it causes the defect field to become unstable are fall down to its true minima leading to strings forming. Having seen that strings can form with a much reduced tension at the end of a period of inflation in these brane/anti-brane collisions, an important question is whether they

are stable enough to survive until today so that they could have been stretched to cosmological scales? This was addressed in [14] and here we will just refer briefly to the main conclusions. As mentioned earlier, all of these strings naturally have decay routes. We need to suppress them. Type I strings decay on a short timescale, which we can interpret as the end points attaching to space filling D9 branes. Type II (F) strings can end on any Dp brane, so can decay on any brane that fills the non-compact dimensions ($p \geq 3$). However if p < 9, the brane does not fill the compact dimensions, and breaking could be suppressed due to the transverse separation between the string and the D-brane, thereby allowing the possibility of metastable strings. Both D1 and F1 strings can break on D3 branes as shown in Fig. 2. Where they end, the endpoints are magnetic or electric sources on the brane, hence they are connected by flux lines in the brane. in that sense the string has dissolved and flux lines spread out lowering its energy. So, D1 and F1 strings break on D3 branes, however, not all such connections lead to a breakage. A D1 string ending on a D5 or D7 brane can not lower its energy by having the flux spreading out[14]. In other words it must maintain a non-zero energy per unit length. In summary: stability requires there are no space filling branes, branes filling the noncompact dimensions, on which the string can end, or that decay is suppressed by transverse separation.

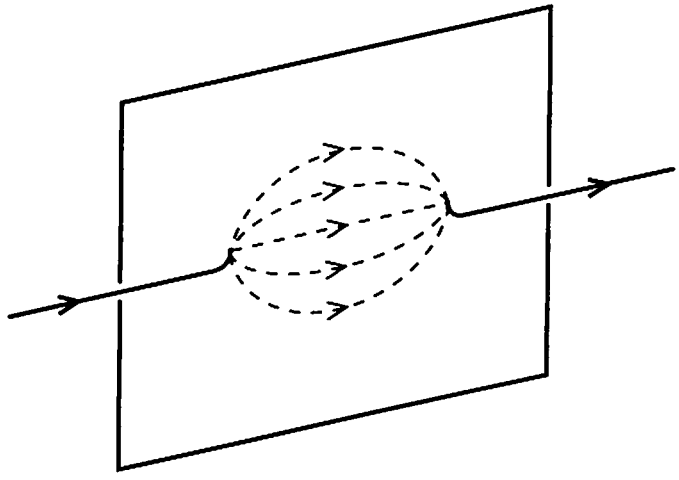


Fig. 2: String ending on a brane, the flux lines spread out in the brane but are still connected to the endpoints.

For the case of decay by formation of domain walls which then collapse, they tend to form in the first place because the BPS string couples to a form field which is a four dimensional axion. The axion acquires a potential from instanton effects, causing the string to bound the axion wall with the wall tension causing the string loop to collapse unless the tension is very small. In order to avoid this decay route we would have to form non-BPS strings in the first case. In the inflationary model we have just mentioned, typically such nonBPS branes can be thought of as bound states of a brane and antibrane, which are then prone to decay through a tachyonic mode.. This tachyon is an open string stretching between the D-Dbar pair. Therefore to suppress this decay we need to introduce a transverse separation between the D-brane and the anti D-brane.

One of the more enterprising models of string driven inflation was introduced by Kachru et al [16], using a framework where all the moduli had been stabilised [15]. They considered Type IIB string theory compactified on a Calabi Yau manifold, which was orientifolded by a $\mathbf{Z}_2$ symmetry with isolated fixed points, which become O3 planes, as shown in Fig. 3.

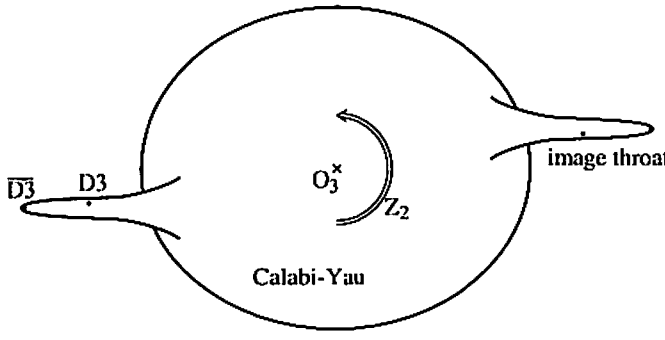


Fig. 3: The geometry of [15]: a warped Calabi-Yau manifold with throats, identified under a Z_2 orientifold

The corresponding warped metric was given by

$$ds^2 = e^{2A(x_\perp)}\eta_{\mu\nu}dx^\mu dx^\nu + ds_\perp^2 \ , \tag{6}$$

where $ds_\perp^2$ represents the metric on the internal space, and the warp factor $e^{A(x_\perp)} << 1$ in the throats of the Calabi Yau space, where inflation occurs due to the separation of D3 and anti D3 branes in the throat. Annihilation of the branes then occurs in a region of large gravitational redshift. This redshift in the throat is very important. The Inflation scale and string tension, as measured by a 10 dimensional inertial observer, are set by string physics, hence are close to the four-dimensional Planck scale. However, the corresponding energy scales as measured by a 4 dimensional observer are suppressed by a factor of $e^A << 1$ deep in the throat. In other words the effective tension, μ, we would measure any strings as having is much below the ten dimensional string tension $\bar{\mu}$, the two being related by $\mu = e^{2A(x_\perp)}\bar{\mu}$. What sort of strings might we expect to see? There would be strings in the non-compact dimensions where reheating will occur. These would be F1-branes (fundamental IIB string) and D1 branes localised in the throat. D1 branes - defects arising in the in tachyon field describing D3-anti D3 annihilation, would be produced by the usual Kibble mechanism and these strings created at end of inflation at bottom of inflationary throat are likely to remain there because of the depth of the potential well. Another type of string could well form, which if detected would provide a good indicator for the scenario. F1 and D1 branes can combine to give what are known as (p,q) strings for relatively prime integers p and q, and which are interpreted as bound states of p F1-branes and q D1-branes [17, 18, 19]. We will return to these composite type of strings shortly, the key point about them is that in general they will not intercommute, and so open up the possibility of forming a more complicated network.

In their paper, Kachru et al were able to use the normalisation to COBE of the density fluctuations arising during the inflationary period to constrain the allowed energy scale of inflation, hence the tensions of the F and D strings that are formed at the end of the inflationary period [16]. They showed that the density fluctuation δ_H on COBE scales, the number of e-foldings N_e, before the end of inflation when the observed fluctuation left the Hubble radius are related to the model parameters through

$$\frac{G^2 e^{4A_0}}{(2\pi\alpha')^2 g_s} = \frac{\delta_H^3}{32\pi C_1^3 N_e^{5/2}} \ , \tag{7}$$

where α' is the string tension, g_s is the string coupling and $C_1 \sim O(1)$. Inserting the specific parameters, $\delta_H = 1.9 \times 10^{-5}$, $C_1 = 0.39$, and $N_e = 60$ the right hand side becomes 4×10^{-20} (Note in [20], they claim a typographical error in [16] leading to the right hand side becoming 16×10^{-20}). The left-hand side is the product of the values of $G\mu$ for the F-string and the D-string under certain simplifying assumptions. In other words

$$\sqrt{G\mu_F\, G\mu_D} \sim 2 \times 10^{-10} \ , \qquad \frac{\mu_D}{\mu_F} = \frac{1}{g_s} \ . \tag{8}$$

Now, the value of g_s is likely in the range 0.1 to 1 so we find $G\mu$ for both strings is in the range 10^{-10} to 10^{-9}.

Having established that strings may form in such warped models, how stable are they? We are interested in branes located in, or intersecting the throat of the compactified space. First of all, if no

branes are present in the throat (i.e. assuming the standard model and moduli stabilising branes are located outside the throat), any F1 and D1 branes formed would be non-BPS, because the orientifold projection removes from the massless spectrum the forms $B_{\mu\nu}$ and $C_{\mu\nu}$ that couple to F1 and D1 branes. The orientifold projection also has the effect of turning a D1 brane into an anti D1 brane, it reverses its orientation. Hence the four dimensional D-string is a bound state of the D1-anti D1 system. This is a potentially unstable configuration , but the D1 is confined to the tip of the inflationary potential. The image anti D1 is in the image throat. The length of each throat is large in string units, so D1-anti D1 strings are stretched and non-tachyonic. Although they could annihilate the anti D1 string by a D1 fluctuating into the image well, to do that it must first tunnel out of warped throat, something that is heavily suppressed compared to the natural string scale because of the warping of the compact space – hence the strings are essentially stable[14]. Similar arguments apply to the decay of F strings and other (p,q) strings. These are also stabilised because they involve world-sheets that stretch from one throat to its image, through an unwarped region. That was the case where there were no branes present in the inflationary throat. Life gets more difficult when branes are present, as they provide decay routes for the strings that are formed. For example stabilising anti D3 branes, standard model D3 and anti D3 branes all destabilise any strings formed in the throat. Generally we want to avoid this situation if the strings are to survive until today– put the branes outside the throat where they are harmless as far as the strings are concerned.

4 Smoking guns and observational features of Cosmic Superstrings

Two clear routes have opened up for distinguishing these new strings. The first involves the intercommuting properties of the strings. For the original gauged strings, the intercommuting probability was shown to be very close to unity always. In other words when two pieces of string cross each other, they reconnect. This is not the case for superstrings, where Polchinski and his collaborators have shown it to be a model dependent probability, the results depend on the type of string, the string coupling, and the details of the compactification [21]. For example in the model of Kachru at al [16], they obtained probabilities for F-F string reconnection ranging from $10^{-3} - 1$, and for D-D string reconnection it ranged from $10^{-1} - 1$. If the probability turns out to be at the lower end of these ranges it could have significant impact on the dynamics of the network and we need to see how these fit into the simulations. Such a task is already under way, for recent attempts see [22, 23, 24].

The second possibility involves the existence of new hybrid networks of F and D strings which could have different scaling properties. These (p,q) string networks offer an exciting prospect. When two strings of different type cross, they can not intercommute in general, instead they produce a pair of trilinear vertices connected by a new segment of string as shown in Fig. 4. For example, the crossing of a (p, q) string and a (p', q') string can produce a $(p + p', q + q')$ string or a $(p - p', q - q')$ string.

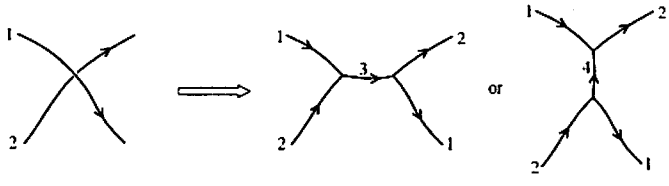


Fig. 4: Crossing of strings of different types.

What happens to such a network in an expanding background? Does it scale or freeze out in a local minimum of its potential energy as shown by Sen for static networks [25]? If the latter it could lead to a frustrated network scaling as w=-1/3. Solving for genuine (p,q) strings has yet to be done. A possible starting point is to consider the evolution of a network of non-abelian strings because reconnection is forbidden in that case for most crossing events. The (p,q) string networks can be mimicked with non-abelian field theory. Under a symmetry breaking G → K , where the original simple group G is broken to a sub-group K which contains a discrete subgroup, defects can form. The non-abelian case of $K = Z_N$ was investigated in [26], where they showed the existence of self-similar or scaling behaviour for the

monopole-string system. The case of $K = S_3$ [27, 28] appears to indicate that these systems scale rather than freeze, but with some enhanced density of strings. Simulations of $K = S_8$ [27] show an energy density that grows relative to the scaling solution and appears to indicate freezing behaviour, but it is ambiguous as to what is really happening. Recently, with Saffin, Copeland has revisited this question and they appear to find evidence of scaling even for the case of large N. Figure 5 shows how the correlation length $\xi(t)$ approaches scaling for both different values of N, and as a function of time t. At scaling $\xi(t) \propto t$, and we have plotted $\xi(N,t) = \xi(N)_0 + \alpha(N)t$. As can be seen, for large N, $\alpha(N)$ appears to head to a constant independent of N.

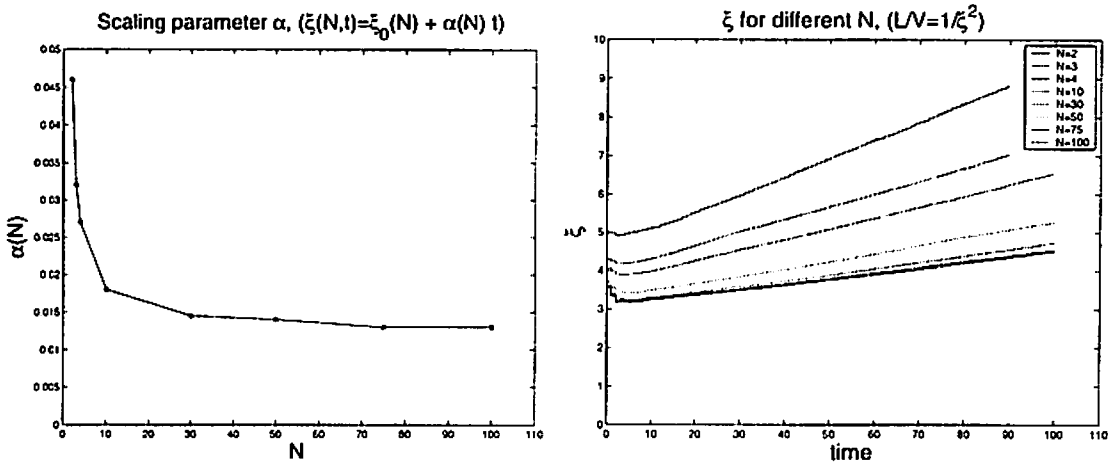


Fig. 5: The approach to scaling for the network as a function of N [29]

These interesting results deserve further investigation but do appear to suggest that non-abelian networks can also reach scaling solutions.

We have already mentioned the observable bounds on a network of strings arising from the tight pulsar bounds. Assuming a network reaches scaling, there are also tight CMB constraints which constrains the allowed tension [30, 5], namely $G\mu \leq 0.7 \times 10^{-6}$. How on earth though can we expect to be able to see evidence of strings with a tension as low as $G\mu \leq 10^{-10} - 10^{-11}$? Damour and Vilenkin in a couple of wonderful papers have opened up the distinct possibility that gravitational wave detection could provide the smoking gun for string detection [31, 32]. Strings are massive, and move rapidly oscillating with velocities approaching the speed of light. In doing so, they emit copious amounts of gravitational waves. Damour and Vilenkin have pointed out that the strong non-gaussian nature of stochastic gravitational wave emission from loops which contain kinks and cusps could provide the tell tale sign, claiming that in a loop network, if only 10% of loops have cusps, bursts of gravitational waves above the 'confusion gravitational wave noise could be detected by LIGO and LISA for $G\mu \sim 10^{-12}$, for bursts emitted by cusps in the LIGO frequency range of order 150Hz ! Similar conclusions hold for LISA, in that case the bursts being in the frequency range of order 4 mHz. The presence of cusps and kinks on the network are vital for these estimates, as are our understanding of the network itself. For those cosmic stringers – the old questions are back including how to estimate the fraction of loops that have cusps on them, the impact of varying intercommutation probabilities on the string network.

Finally, let us end on a positive but speculative note. Perhaps, we have already seen string out in the universe! Sazhin et al have claimed evidence from Gravitational lensing events of two images of a giant elliptical galaxy with a large number of lens candidates in its vicinity [33, 34] If this is the case it would imply $G\mu \geq 4 \times 10^{-7}$, which would of course be too high for the strings coming from warped compactifications described earlier, but are still compatible with observation. Time and more detailed observations of these lensing candidates will help determine how significant a result this is. Just to remind the reader, the interest here is not in the single lensing event but in the fact there may be many events nearby, something one would expect of an extended object such as a string. Schild et al have also made an interesting claim [35]. They may have seen the effect of an oscillating loop, determined through brightness fluctuations in the gravitational lens system Q0957+561. Using the fact that the two quasars separated are by 6 would imply for the cosmic string loop. a radius $R \sim 0.02pc$, with the distance to

the loop of $D_{\rm loop} \sim 3kpc$ they find a string tension of $G\mu \geq 6 \times 10^{-7}$. Of course all of these approaches both in the observations and their interpretations have large uncertainties associated with them – but it is fun!

5 Conclusions

We have discussed the fascinating possibility of having cosmic superstrings oscillating in our Universe, a true relic of the early Universe. Although there are plenty of ways not to have F and D strings of cosmic length today because there are many decay mechanisms open to the strings, if we are lucky with inflation in string theory, they may be metastable and survive long enough to be of interest. If they do, then we should be working out how they would evolve and how we might see them as they might just show up. We may just have a new window on string theory through cosmology!

6 Acknowledgements

EJC would like to thank Jiro Soda, Misao Sasaki, Takahiro Tanaka and the other organizers of JGRG14 for their kind hospitality during this very enjoyable conference.

References

[1] M. B. Hindmarsh and T. W. Kibble, "Cosmic strings," Rept. Prog. Phys. **58**, 477 (1995) [arXiv:hep-ph/9411342];

A. Vilenkin and E.P.S. Shellard, *Cosmic strings and other topological defects*, Cambridge Univ. Press (Cambridge 1994).

[2] H. B. Nielsen and P. Olesen, "Vortex-Line Models For Dual Strings," Nucl. Phys. B **61**, 45 (1973).

[3] T.W.B. Kibble, "Topology of cosmic domains and strings" J. Phys A **9**, 1387 (1976)

[4] D. Austin, E. J. Copeland and T. W. B. Kibble, "Evolution of cosmic string configurations," Phys. Rev. D **48**, 5594 (1993) [arXiv:hep-ph/9307325].

[5] L. Pogosian, S. H. H. Tye, I. Wasserman and M. Wyman, "Observational constraints on cosmic string production during brane inflation," Phys. Rev. D **68**, 023506 (2003) [arXiv:hep-th/0304188].

[6] N. Bevis, M. Hindmarsh and M. Kunz, "WMAP constraints on inflationary models with global defects," Phys. Rev. D **70**, 043508 (2004) [arXiv:astro-ph/0403029].

[7] J. Rocher and M. Sakellariadou, "D-term inflation, cosmic strings, and consistency with cosmic microwave background measurement," Phys. Rev. Lett. **94**, 011303 (2005) [arXiv:hep-ph/0412143].

[8] V.M. Kaspi, J.H. Taylor and M.F. Ryba, Astrophys. J. **428**, 713 (1994)

[9] E. Witten, "Cosmic superstrings," Phys. Lett. B **153**, 243 (1985).

[10] G. R. Dvali and S. H. H. Tye, "Brane inflation," Phys. Lett. B **450**, 72 (1999) [arXiv:hep-ph/9812483];

S. H. S. Alexander, "Inflation from D - anti-D brane annihilation," Phys. Rev. D **65**, 023507 (2002) [arXiv:hep-th/0105032];

C. P. Burgess, M. Majumdar, D. Nolte, F. Quevedo, G. Rajesh and R. J. Zhang, "The inflationary brane-antibrane universe," JHEP **0107**, 047 (2001) [arXiv:hep-th/0105204];

G. R. Dvali, Q. Shafi and S. Solganik, "D-brane inflation," arXiv:hep-th/0105203.

[11] N. Jones, H. Stoica and S. H. Tye, "Brane interaction as the origin of inflation," JHEP **0207**, 051 (2002) [arXiv:hep-th/0203163];

S. Sarangi and S. H. Tye, "Cosmic string production towards the end of brane inflation," Phys. Lett. B **536**, 185 (2002) [arXiv:hep-th/0204074];

N. T. Jones, H. Stoica and S. H. Tye, "The production, spectrum and evolution of cosmic strings in brane inflation," Phys. Lett. B **563**, 6 (2003) [arXiv:hep-th/0303269].

[12] G. Dvali, R. Kallosh and A. Van Proeyen, "D-term strings," JHEP **0401**, 035 (2004) [arXiv:hep-th/0312005].

[13] G. Dvali and A. Vilenkin, "Formation and evolution of cosmic D-strings," JCAP **0403**, 010 (2004) [arXiv:hep-th/0312007].

[14] E. J. Copeland, R. C. Myers and J. Polchinski, "Cosmic F- and D-strings," JHEP **0406**, 013 (2004) [arXiv:hep-th/0312067].

[15] S. Kachru, R. Kallosh, A. Linde and S. P. Trivedi, "De Sitter vacua in string theory," Phys. Rev. D **68**, 046005 (2003) [arXiv:hep-th/0301240].

[16] S. Kachru, R. Kallosh, A. Linde, J. Maldacena, L. McAllister and S. P. Trivedi, "Towards inflation in string theory," JCAP **0310**, 013 (2003) [arXiv:hep-th/0308055].

[17] J. A. Harvey and A. Strominger, "The heterotic string is a soliton," Nucl. Phys. B **449**, 535 (1995) [Erratum-ibid. B **458**, 456 (1996)] [arXiv:hep-th/9504047];

J. H. Schwarz, "An SL(2,Z) multiplet of type IIB superstrings," Phys. Lett. B **360**, 13 (1995) [Erratum-ibid. B **364**, 252 (1995)] [arXiv:hep-th/9508143].

[18] J. Polchinski, "Dirichlet-branes and Ramond-Ramond charges," Phys. Rev. Lett. **75**, 4724 (1995) [arXiv:hep-th/9510017].

[19] E. Witten, "Bound states of strings and p-branes," Nucl. Phys. B **460**, 335 (1996) [arXiv:hep-th/9510135].

[20] H. Firouzjahi and S. H. Tye, arXiv:hep-th/0501099.

[21] M.G. Jackson, N.T. Jones and J. Polchinski, arXiv:hep-th/0405229.

[22] M. Sakellariadou, "A note on the evolution of cosmic string / superstring networks," arXiv:hep-th/0410234.

[23] C. J. A. Martins, "Scaling laws for non-intercommuting cosmic string networks," Phys. Rev. D **70**, 107302 (2004) [arXiv:hep-ph/0410326].

[24] A. Avgoustidis and E. P. S. Shellard, "Cosmic string evolution in higher dimensions," arXiv:hep-ph/0410349.

[25] A. Sen, "String network," JHEP **9803**, 005 (1998) [arXiv:hep-th/9711130].

[26] T. Vachaspati and A. Vilenkin "Evolution of cosmic networks," Phys. Rev. D35, 1131 (1987)

[27] D. Spergel and U. L. Pen, "Cosmology in a string-dominated universe," Astrophys. J. **491**, L67 (1997) [arXiv:astro-ph/9611198].

[28] P. McGraw, "Evolution of a non-Abelian cosmic string network," Phys. Rev. D **57**, 3317 (1998) [arXiv:astro-ph/9706182].

[29] E.J. Copeland and P.M. Saffin (In preparation-2005)

[30] M. Landriau and E. P. S. Shellard, "Large angle CMB fluctuations from cosmic strings with a comsological constant," [arXiv:astro-ph/0302166].

[31] T. Damour and A. Vilenkin, "Gravitational wave bursts from cusps and kinks on cosmic strings," Phys. Rev. D **64**, 064008 (2001) [arXiv:gr-qc/0104026].

[32] T. Damour and A. Vilenkin, "Gravitational radiation from cosmic (super)strings: Bursts, stochastic background, and observational windows," arXiv:hep-th/0410222.

[33] M.V. Sazhin et al, Mon. Not. Roy. Astron. Soc. **343**, 353 (2003) [arXiv:astro-ph/0302547].

[34] M.V. Sazhin et al, [arXiv:astro-ph/0406516].

[35] R.E. Schild et al, [arXiv:astro-ph/0406434].

Anisotropic scalar field emission from TeV scale black hole

Daisuke Ida[1]

Department of Physics, Gakushuin University, Tokyo 171-8588, Japan

Kin-ya Oda[2]

Physikalisches Institut der Universität Bonn, Nussallee 12, Bonn 53115, Germany

Seong Chan Park[3]

School of Physics, Korea Institute for Advanced Study (KIAS), Seoul 207-43, Korea

Abstract

Black holes are predicted to be copiously produced at the CERN Large Hadron Collider in the scenarios of TeV scale gravity. We report recent progress in studying decay of such a higher dimensional black hole in $D = 4 + n$ dimensions through the Hawking radiation into brane localized fields taking into account its angular momentum which is indispensable for realistic simulations. Presented is the greybody factors for a scalar field emission, which confirms our previous results in low energy approximation: (i) the existence of super-radiance modes and (ii) the non-trivial angular distribution of radiated scalar field. Phenomenological implications and future plans are discussed.

1 Introduction

Black hole is one of the most important key objects in theoretical physics. Its quantum behavior and thermodynamic property have played great roles in the path to understand yet unknown quantum theory of gravity but a direct experimental test has been believed almost impossible. Recently, the scenarios of large and warped extra dimension(s) have led to an amazing possibility of producing black holes at the CERN Large hadron Collider (LHC) with distinct signals [1, 2]. When the center-of-mass energy of a collision exceeds the Planck scale, which is of the order of TeV here, the cross section is dominated by a black hole production [3]. In this trans-Planckian energy domain, the larger the center-of-mass energy is, the larger the mass of the resulting black hole, and hence the better its decay is treated semi-classically via Hawking radiation. Main purpose of this talk is to discuss such decay signals.

In previous publications, we have pointed out that the production cross section of a black hole *increases* with its angular momentum, so that the produced black holes are highly rotating [4, 5]. (See also Ref. [6] for an earlier attempt.) The form factor for the production cross section, taking this rotation into account [4], is larger than unity and increases with the number of extra dimensions n. (The result is in good agreement with an independent numerical simulation of a classical gravitational collision of two massless point particles [7].) We note that this form factor is hardly interpretative without considering the angular momentum. It is essential to take into account the angular momentum of the black hole when we perform a realistic calculation of its production and evaporation.

Black holes radiate mainly into the standard model fields that are localized on the brane [8]. The master equation for brane field perturbation on the Myers-Perry higher dimensional rotating black hole background has been derived [4] for general fields with spin zero, one half and one (that is, for all the standard model fields). In the paper [4], we have shown analytic expressions for the greybody factor of $D = 5$ (Randall-Sundrum) black hole by solving the master equation under the low energy approximation of radiating field. In this talk we present a generalized result to higher dimensional black hole in $D > 5$ for brane localized scalar field without relying on the low energy approximation and discuss its physical implications.

[1]E-mail: daisuke.ida@gakushuin.ac.jp
[2]E-mail: odakin@th.physik.uni-bonn.de
[3]E-mail: spark@kias.re.kr

2 Master equation for Brane field perturbation

The Teukolsky equation for spin s brane field in $D = 4+n$ dimensional Myers-Perry black hole background has been derived and the resultant equation is shown to be separable into the angular and the radial parts in our previous paper [4]. The angular function S, the spin weighted spheroidal harmonics, is a regular function on $[0, \pi]$ which satisfies the equation

$$0 = \frac{1}{\sin\vartheta}\frac{d}{d\vartheta}\left(\sin\vartheta\frac{dS}{d\vartheta}\right) + \left[(s - a\omega\cos\vartheta)^2 - \left(\frac{s}{\tan\vartheta} + \frac{m}{\sin\vartheta}\right)^2 + E - 2s^2\right]S, \tag{1}$$

with the eigenvalue E for a given angular mode (l, m). This angular equation is exactly the same as the usual four dimensional Kerr black hole. The radial function R satisfies the equation

$$0 = \Delta^{-s}\frac{d}{dr}\left(\Delta^{s+1}\frac{dR}{dr}\right) + \left[\frac{K^2 - isK\Delta_{,r}}{\Delta} - \lambda_s + 4isr\omega + s(\Delta_{,rr} - 2)\right]R, \tag{2}$$

where $\Delta = r^2 + a^2 - (r_H^2 + a^2)\,(r/r_H)^{-(n-1)}$, $K = (r^2 + a^2)\omega - ma$ and $\lambda_s = E - s(s+1) - 2ma\omega + (a\omega)^2$ with r_H and a being the horizon radius and the rescaled dimensionless angular momentum of the black hole. The ω is the frequency of the radiated field that was assumed to be small in the derivation of the greybody factors in Ref. [4]. If the number of extra dimensions n is put to be zero, the radial equation reduces to the usual Teukolsky equation in four dimensions.

3 Greybody factor for Brane scalar field emission

Evolution of the mass and the angular momentum of a black hole can be determined by emissions via Hawking radiation up to the final Planck phase where a semi-classical description breaks down

$$-\frac{d}{dt}\begin{pmatrix} M \\ J \end{pmatrix} = \frac{1}{2\pi}\sum_{s,l,m} g_s \int d\omega \frac{\Gamma_{s,l,m}(\omega)}{e^{\omega - m\Omega/T} \mp 1}\begin{pmatrix} \omega \\ m \end{pmatrix}, \tag{3}$$

where g_s is the effective degrees of freedom for spin s field, Ω is the surface angular velocity of the rotating hole, T is Hawking Temperature and $\Gamma_{s,l,m}$ is the greybody factor for a given angular mode (l, m). The analytic expression for $\Gamma_{s,l,m}$ for five dimensional black hole has been obtained in Ref. [4].

One immediate observation is that the Hawking radiation of $m > 0$ mode dominates over that of $m < 0$ mode when $\Omega \to \infty$, i.e. when the hole is highly rotating. In this limit, the modes with $m > 0$ show super-radiance with negative greybody factor $\Gamma_{s,l,m} < 0$, namely Hawking *absorption*. This can in principle result in the initial *increase* of the area and entropy for a highly rotating black hole [10].

The numerical results of the greybody factors for the $D = 5$ black hole is in good agreement with the analytic expression in [4]. As an example for $D > 5$ case, we present a result of $l = 1, m = 1$ mode, where the effects of rotation and the existence of super-radiance (negative greybody factor) can be clearly seen. Complete results for $D \geq 4$ will be shown in [9]. We plot for a $D = 10$ non-rotating hole $a = 0$ (the thin line) and for rotating one $a = 1$ (the thick line) in Figure 1. A super-radiance does not exist in negative mode $m = -1$ which is not presented here. When black hole is highly rotating, i.e. having large a, the difference between $m = 1$ and $m = -1$ modes leads to the non-trivial angular distribution of Hawking radiation even for a scalar field emission. This is a clear signature of the *rotating* black hole. According to the analytic expression for the $D = 5$ dimensional black hole [4], the criteria of super-radiance in $l = 1$ mode is: $\omega - m\Omega < 0$ since $\Gamma \propto \omega - m\Omega$. The numerical result is consistent with this: for $a = 1.0$ which is denoted as the thick line in the figure, we obtain the super-radiance mode when $\omega \lesssim \Omega$. Further results of the general $D = 4 + n$ dimensional black holes with varying angular momentum for the general angular modes (l, m) will be presented elsewhere [9].

4 Discussion

Here we have explained the importance of the angular momentum when one considers TeV scale black hole production and evaporation. New numerical results are reported: greybody factor for the brane scalar

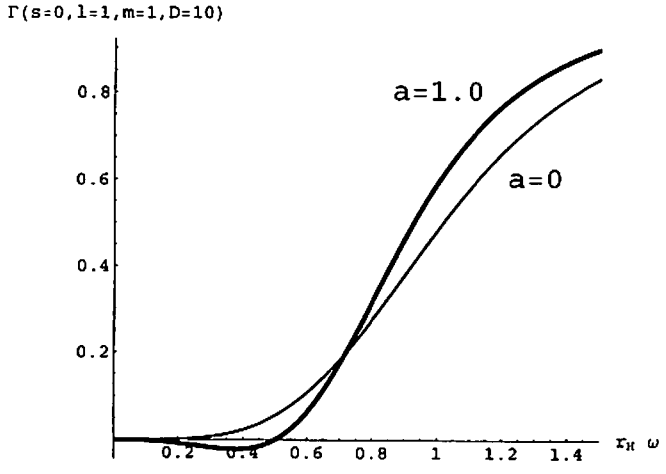


Figure 1: Greybody factor for $D = 10$, $(l, m) = (1, 1)$ mode. The thin and thick curves denote non-rotating $a = 0$ and rotating $a = 1.0$, respectively. Super-radiance in the small energy region can be observed for the latter.

emission from a general $D = 4 + n$ dimensional rotating black hole without relying on the low frequency expansions. We observe super-radiance in $m > 0$ modes for $\Omega > 0$. The existence of super-radiance mode is crucially important new feature of the rotating black hole. Nontrivial angular dependence of the emission is observed even for the scalar field, which will be a signature of *rotating* black hole.

To understand the actual evolution of a black hole and to predict the collider signature, we need further investigations. It is important to determine the greybody factors for spinor and vector fields [4, 11]. The evolution of the angular momentum and the mass is determined by integrating Eq. (3), once all the greybody factors are determined. In particular, the spin-down phase, which has been simply neglected so far, can be precisely described. One can in principle determine the angular momentum of the produced black hole from the nontrivial angular distribution of the signals. The super-radiance mode is a unique feature of rotating black hole and its phenomenological implications should be clarified. Detailed simulations of black hole evaporation at LHC are to be done. Some of these points will be presented soon [9].

References

[1] S. B. Giddings and S. Thomas, Phys. Rev. D **65**, 056010 (2002) [arXiv:hep-ph/0106219].

[2] S. Dimopoulos and G. Landsberg, Phys. Rev. Lett. **87**, 161602 (2001) [arXiv:hep-ph/0106295].

[3] G. 't Hooft, Phys. Lett. B **198**, 61 (1987).

[4] D. Ida, K. Oda and S. C. Park, Phys. Rev. D**67**, 064025 (2003) [Erratum-ibid. D **69**, 049901 (2004)] [arXiv:hep-th/0212108].

[5] D. Ida, K. Oda and S. C. Park, Proceedings of 2nd ICFP [arXiv:hep-ph/0311297]; ibid. Proceedings of 10th Marcell-Grossmann meeting [arXiv:hep-ph/0312061]; ibid. Proceedings of 6th RESCEU international symposium [arXiv:hep-ph/0312385]; S. C. Park, J. Korean Phys. Soc. **45**, 208 (2004).

[6] S. C. Park and H. S. Song, J. Korean Phys. Soc. **43**, 30 (2003) [arXiv:hep-ph/0111069].

[7] H. Yoshino and Y. Nambu, Phys. Rev. D **67**, 024009 (2003) [arXiv:gr-qc/0209003]; H. Yoshino, in this proceedings.

[8] R. Emparan, G. T. Horowitz and R. C. Myers, Phys. Rev. Lett. **85**, 499 (2000) [arXiv:hep-th/0003118].

[9] D. Ida, K. Oda and S. C. Park, in preperation.

[10] D. N. Page, Phys. Rev. D **14** (1976) 3260.

[11] P. Kanti and J. March-Russell, Phys. Rev. D **67**, 104019 (2003) [arXiv:hep-ph/0212199] ,ibid. **66**, 024023 (2002) [arXiv:hep-ph/0203223],C. M. Harris and P. Kanti, JHEP **0310**, 014 (2003) [arXiv:hep-ph/0309054].

Universal area spectrum in single-horizon black holes

Takashi Tamaki[1], Hidefumi Nomura[2]

[1] *Department of Physics, Kyoto University, 606-8501, Japan*
[2] *Department of Physics, Waseda University, Ohkubo, Shinjuku, Tokyo 169-8555, Japan*

Abstract

We investigate highly damped quasinormal mode of single-horizon black holes motivated by its relation to the loop quantum gravity. Using the WKB approximation, we show that the real part of the frequency approaches the value $T_{\rm H} \ln 3$ for dilatonic black hole. It is surprising since the area specrtum of the black hole completely agrees with that of Schwarzschild black hole. We discuss its generality.

1 Introduction

Progress in the loop quantum gravity (LQG) has been remarkable particularly after the introduction of the spin network formalism [1]. The area spectrum A is obtained in this formalism as [2, 3]

$$A = 8\pi\gamma \sum \sqrt{j(j+1)}\,, \tag{1}$$

where γ is the Immirzi parameter. The sum is added up all intersections between a surface and a spin network carrying a label $j = 0,\ 1/2,\ 1,\ 3/2,\ \ldots$ reflecting the SU(2) nature of the gauge group. The statistical origin of the black hole entropy S is also derived using this formalism[4, 5].

$$S = \frac{A \ln(2j_{\rm min}+1)}{8\pi\gamma\sqrt{j_{\rm min}(j_{\rm min}+1)}}\,, \tag{2}$$

where $j_{\rm min}$ is the lowest nontrivial representation.

Recently, quite a new encounter to the LQG and the quasinormal mode was considered in Ref. [6]. We apply the first law of black hole thermodynamics, $dA = \frac{4}{T_{\rm H}} dM$. We identify minimum change dM as the real part of the highly damped quasinormal mode ${\rm Re}(\omega)$ [7]. For Schwarzschild black hole [8, 9],

$$\omega = T_{\rm H} \ln 3 - 2\pi T_{\rm H} i \left(n + \frac{1}{2}\right). \tag{3}$$

In this case, we obtain $dA = 4 \ln 3$. Then, we identify this with the minimum in (1), i.e.,

$$dA = 4 \ln 3 = 8\pi\gamma\sqrt{j_{\rm min}(j_{\rm min}+1)}\,. \tag{4}$$

By substituting this formula to (2), we obtain $j_{\rm min} = 1$ to produce $S = A/4$. This consideration calls various arguments such as modification of the gauge group SU(2) to SO(3) and so on.

We must also suspect that only Schwarzschild black hole has the relation (4). We should notice that the formulae (1) and (2) in the LQG do not depend on matter fields since their symplectic structures do not have a contribution for the horizon surface term [5]. Thus, it is important to investigate these properties in other black holes in determining whether or not the discussion above is related to the LQG.

The analysis for Reissner-Nordström black hole in Ref. [8, 9] shows that existence of the inner horizon disturbs the imaginary part to be periodic. The strategy we take here is to investigate whether or not the formula (3) holds for the single-horizon black holes. From this view point, we examine the WKB analysis following Ref. [9] by exemplifying the case for dilatonic black hole [10]. Surprisingly, the answer is in the affirmative. Notice that dilatonic black hole is a charged black hole with single-horizon. Thus, considering this model provides the evidence that the essential thing that determines whether or not (3) holds is *not* the electromagnetic charge *but* the space-time structure. We also consider this direction and thier meaning in the LQG.

[1] E-mail:tamaki@tap.scphys.kyoto-u.ac.jp
[2] E-mail:nomura@gravity.phys.waseda.ac.jp

2 The WKB Analysis for single-horizon black holes.

As a background, we consider the static and spherically symmetric metric as

$$ds^2 = -f(r)e^{-2\delta(r)}dt^2 + f(r)^{-1}dr^2 + r^2d\Omega^2, \tag{5}$$

where $f(r) := 1 - 2m(r)/r$. We define $g(r) = e^{-\delta}f(r)$. Notice that

$$g'(r_{\rm H}) = 4\pi T_{\rm H} \ , \tag{6}$$

where $' := d/dr$ and $r_{\rm H}$ is the event horizon. Our basic equation for black hole perturbations are $\frac{d^2\psi}{dr_*^2} + [\omega^2 - V(r)]\psi = 0$ where the time dependence of the perturbations are assumed to be $e^{-i\omega t}$. The tortoise coordinate r_* is defined as $\frac{dr_*}{dr} = \frac{1}{g(r)}$. The potential $V(r)$ for the general case (5) is written as

$$V(r) = g\left[\frac{l(l+1)}{r^2}e^{-\delta} + (1-k^2)\frac{2m}{r^3}e^{-\delta} + (1-k)(\frac{g'}{r} - \frac{2m}{r^3}e^{-\delta})\right] \ . \tag{7}$$

For $k = 0$, 1 and 2, $V(r)$ corresponds to the case for the scalar, electromagnetic and the odd parity gravitational perturbations, respectively. We concentrate on the odd parity gravitational perturbations, i.e., $k = 2$. We also define $\Psi = g^{1/2}\psi$. Our basic equation can be rewritten as

$$\Psi'' + R(r)\Psi = 0 \ , \tag{8}$$

where $R(r) := g^{-2}[\omega^2 - V + (g')^2/4 - gg''/2]$. Then, we consider the WKB analysis combined with the complex-integration technique which is a good approximation in the limit $\mathrm{Im}(\omega) \to -\infty$.

First, we summarize the analysis for Schwarzschild black hole and consider in the complex r-plane below. Two WKB solutions in (8) can be written as

$$\Psi^{(s)}_{1,2}(r) = Q^{-1/2}\exp\left[\pm i\int_s^r Q(x)dx\right] \ , \tag{9}$$

where $Q^2 = R$+extra term. Here, the extra term is chosen for Ψ to bahave near the origin appropriately. From (8), $\Psi(r) \sim r^{1/2\pm 2}$ at $r \to 0$. Since $R \sim -15/4r^2$ at $r \to 0$ in Schwarzschild black hole, we should choose $Q^2 := R - 1/(4r^2)$ for the WKB solution (9) to behave correctly.

We should consider the problem concerning the "Stokes phenomenon" related to the zeros and poles of Q^2 [11], which are written in Fig. 1 in the limit $\mathrm{Im}(\omega) \to -\infty$. One of the important points are that the zeros of Q^2 approach the origin in the limit $\mathrm{Im}(\omega) \to -\infty$. Near the origin, we can write as

$$Q^2 = g^{-2}\left[\omega^2 - \frac{4g^2}{r^2}\right] \ . \tag{10}$$

Since $g \to -2M/r$ for $r \to 0$ where M is the mass of Schwarzschild black hole, Q^2 has four zeros. When we start the outgoing solution at the point a as $\Psi_a = \Psi_1^{(r_1)}$, and proceeds along anti-Stokes lines and encircles the pole at the horizon clockwise, and turns back to a, we investigate what conditions are imposed to reproduce the original solution. We should account for the Stokes phenomenon associated with the zeros r_1, r_2 and r_3. For example, if we proceeds the point a to b passing the Stokes line, we have the solution $\Psi_b = e^{-iI}\Psi_1^{(r_3)} - ie^{iI}\Psi_2^{(r_3)}$, where $I = \int_{r_3}^{r_1} Qdr$. The final condition to be imposed is

$$e^{2i\Gamma} = -1 - 2\cos 2I \ , \tag{11}$$

where $\Gamma = \oint Qdr$. We should also perform for the ingoing solution near $r_{\rm H}$. The result is same as (11). We can evaluate Γ in the limit $\mathrm{Im}(\omega) \to -\infty$ (Remember, (6).) as

$$\Gamma = -2\pi i \lim_{r\to r_{\rm H}} \frac{r - r_{\rm H}}{g}\omega = -2\pi i \lim_{r\to r_{\rm H}} \frac{r - r_{\rm H}}{g'(r - r_{\rm H})}\omega = -i\frac{\omega}{2T_{\rm H}} \ . \tag{12}$$

Notice that this result does not depend on species of black holes.

To integrate I, we define $y = \frac{\omega r^2}{4M}$. From (10), we can perform the integral I as

$$I = -\int_{-1}^{1} \sqrt{1 - \frac{1}{y^2}} dy = \pi \ . \tag{13}$$

By substituting (12) and (13) into (11), we have (3) as derived in previous papers.

Next, we consider the case in dilatonic black hole which is [10]

$$ds^2 = -\lambda^2(\rho)dt^2 + \frac{1}{\lambda^2}d\rho^2 + r^2(\rho)d\Omega^2 \ , \tag{14}$$

$$\lambda^2 = \left(1 - \frac{\rho_+}{\rho}\right)\left(1 - \frac{\rho_-}{\rho}\right)^{(1-\alpha^2)/(1+\alpha^2)} \ , \quad r = \rho\left(1 - \frac{\rho_-}{\rho}\right)^{\alpha^2/(1+\alpha^2)} \tag{15}$$

ρ_+, ρ_- and α are the event horizon, the "inner horizon", and the dilaton coupling, respectively. We see from (15) that ρ_- corresponds to the origin in the area radius. By comparing (14) and (5), we obtain

$$g(r) = \left(1 - \frac{\rho_+}{\rho}\right)\left(1 - \frac{\rho_-}{\rho}\right)^{1/(1+\alpha^2)}\left(1 + \frac{\alpha^2}{1+\alpha^2}\frac{\rho_-}{\rho - \rho_-}\right) \ , \tag{16}$$

$$e^{-\delta} = \left(1 - \frac{\rho_-}{\rho}\right)^{-\alpha^2/(1+\alpha^2)}\left(1 + \frac{\alpha^2}{1+\alpha^2}\frac{\rho_-}{\rho - \rho_-}\right)^{-1} \tag{17}$$

We can find from (16) and (17) that $e^{-\delta}$ and $g(r)$ do not show singular behavior for $r \neq 0$, r_H ($\rho \neq \rho_-$, ρ_+). Thus, zeros approaches the origin as in the Schwarzschild case. We evaluate $g(r)$ in this limit as

$$g(r) \simeq \frac{\alpha^2}{1+\alpha^2}\frac{\rho_- - \rho_+}{r} \ . \tag{18}$$

Using this asymptotic relation, we have $Q^2(r) = R - 1/(4r^2)$ again for Ψ to behave near the origin appropriately. Then, we have the form (10) near the origin and using the fact that dilatonic black hole has one horizon, we find that $Q^2(r)$ have four zeros and two second order poles as in Schwarzschild black hole. Therefore, the WKB condition is written as (11). As we noted above, the expression (12) is not also changed in dilatonic black hole. The nontrivial factor is I. However, if we define

$$y = \frac{\omega r^2}{\frac{2\alpha^2}{1+\alpha^2}(\rho_+ - \rho_-)} \ , \tag{19}$$

we can also perform the integral I as (13). Thus, we obtain (3) again.

3 Conclusion and discussion.

We investigated the highly damped quasinormal mode of dilatonic black hole and considered its generality. Then, what we think about the confrontation in determining γ and the case in multi-horizon black holes ? We should mention that there was a mistake in the entropy calculation in the original paper [12]. However, if we take into account the symmetry around black holes, the original result (2) is recovered [13]. In our opinion, we still need to discuss more carefully about entropy calculation. The discussion in the quasinormal modes is like the old quantum theory and its description is within the general relativity. Thus, the above confrontation and the appearent discrepancy for multi-horizon black holes may be caused by this temporal description. If we can appropriately consider the problem corresponding to the quasinormal modes in the LQG, these may be solved. It is one of the directions we are seeking for.

References

[1] C. Rovelli and L. Smolin, Phys. Rev. D **52**, 5743 (1995).

[2] C. Rovelli and L. Smolin, Nucl. Phys. B **442**, 593 (1995); Erratum, *ibid.*, **456**, 753 (1995).

[3] A. Ashtekar and J. Lewandowski, Class. Quantum Grav. **14**, A55 (1997).

[4] A. Ashtekar, A. Corichi, and K. Krasnov, Adv. Theor. Math. Phys. **3**, 418 (1999).

[5] A. Ashtekar, J. Baez, A. Corichi, and K. Krasnov, Phys. Rev. Lett. **80**, 904 (1998).

[6] O. Dreyer, Phys. Rev. Lett. **90**, 081301 (2003).

[7] S. Hod, Phys. Rev. Lett. **81**, 4293 (1998).

[8] L. Motl, Adv. Theor. Math. Phys. **6**, 1135 (2003); L. Motl and A. Neitzke, *ibid.*, **7**, 307 (2003).

[9] N. Andersson and C. J. Howls, Class. Quantum Grav. **21**, 1623 (2004).

[10] G. W. Gibbons and K. Maeda, Nucl. Phys. B **298**, 741 (1988); D. Garfinkle, G. T. Horowitz and A. Strominger, Phys. Rev. D **43**, 3140 (1991).

[11] M. V. Berry, Proc. Roy. Soc. A **422**, 7 (1989).

[12] M. Domagala and J. Lewandowski, Class. Quantum Grav. **21**, 5233 (2004). ; K. A. Meissner, *ibid.*, 5245 (2004).

[13] O. Dreyer, F. Markopoulou, and L. Smolin, hep-th/0409056.

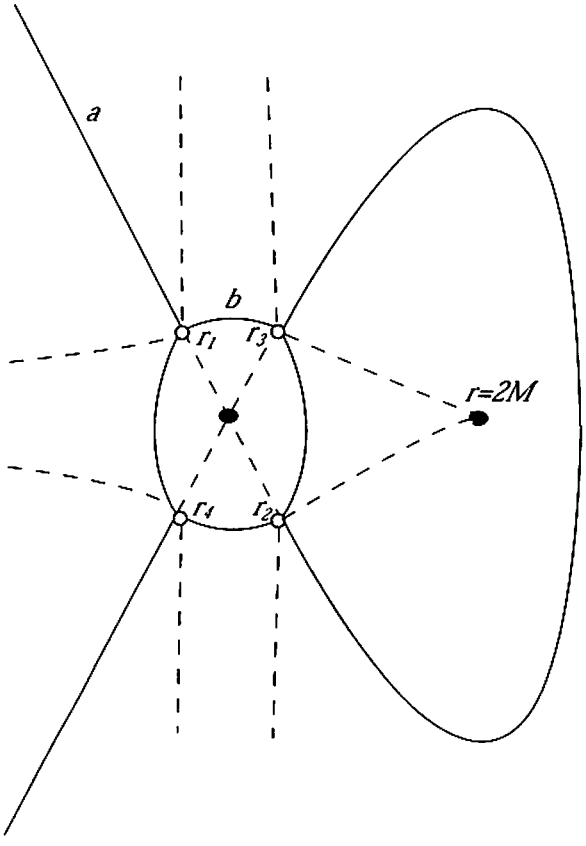


Figure 1: Zeros and poles of $Q^2(r)$ for Schwarzschild black hole. The related Stokes and anti-Stokes lines are witten by dashed lines and solid lines, respectively.

Leading order corrections to the cosmological evolution of tensor perturbations in braneworld

Tsutomu Kobayashi[1] and Takahiro Tanaka[2]

Theoretical Astrophysics Group, Department of Physics, Kyoto University, Kyoto 606-8502, Japan

Abstract

Tensor perturbations in an expanding braneworld of the Randall Sundrum type are investigated. We consider a model composed of a slow-roll inflation phase and the succeeding radiation phase. The effect of the presence of an extra dimension through the transition to the radiation phase is studied, giving an analytic formula for leading order corrections.

1 Introduction

In recent years there has been much interest in braneworld scenarios [1]. Among various models, the second Randall-Sundrum model (RS II) [2] with one brane in an anti de Sitter (AdS) bulk is particularly interesting in the point that, despite an infinite extra dimension, four dimensional general relativity (4D GR) can be recovered at low energies/long distances on the brane. Then, what is leading order corrections to the conventional gravitational theory? It was shown that the Newtonian potential in the RS II braneworld, including the correction due to the bulk gravitational effects with a precise numerical factor, is given by [3]

$$V(r) \simeq -\frac{Gmm'}{r}\left(1+\frac{2\ell^2}{3r^2}\right).$$

Here ℓ is the curvature length of the AdS space and is experimentally constrained to be $\ell \lesssim 0.1$ mm. It is natural to ask next what are leading order corrections to the evolution of cosmological perturbations.

Great efforts have been paid for the problem of calculating cosmological perturbations in braneworld scenarios. In order to correctly evaluate perturbations on the brane, we need to solve bulk perturbations, which reduces to a problem of solving partial differential equations with appropriate boundary conditions. There is another difficulty concerned with a physical, fundamental aspect of the problem; we do not know how to specify appropriate initial conditions for perturbations with bulk degrees of freedom. Hence it is not as easy as in the standard four dimensional cosmology.

In this short article, we investigate cosmological tensor perturbations in the RS II braneworld, and evaluate leading order corrections to the 4D GR result analytically. For this purpose, we make use of the reduction scheme to a four dimensional effective equation which iteratively takes into account the effects of the bulk gravitational fields [4]. As a first step, we concentrate on perturbations which is initially at super-horizon scales. A detailed discussion is done in a much longer paper [5].

2 Tensor perturbations on a Friedmann brane

Background model: The background spacetime that we consider is composed of a five dimensional AdS bulk, whose metric is given in Poincaré coordinates as $ds^2 = (\ell/z)^2\left(dz^2 - dt^2 + \delta_{ij}dx^i dx^j\right)$, with a Friedmann brane at $z = z(t)$. The induced metric on $z = z(t)$ is $ds^2 = a^2(t)\left[-(1-\dot{z}^2)dt^2 + \delta_{ij}dx^i dx^j\right]$, where $a(t) = \ell/z(t)$ and the overdot denotes ∂_t. From this we see that the conformal time on the brane is given by $d\eta = \sqrt{1-\dot{z}^2}dt$. The brane motion is related to the energy density of matter localized on the brane by the modified Friedmann equation as

$$\mathcal{H}^2 = \frac{8\pi G}{3}a^2\left(\rho + \frac{\rho^2}{2\sigma}\right), \quad \mathcal{H} = -\dot{z}/(z\sqrt{1-\dot{z}^2}), \tag{1}$$

[1]E-mail:tsutomu@tap.scphys.kyoto-u.ac.jp
[2]E-mail:tama@scphys.kyoto-u.ac.jp

where $\sigma = 3/4\pi G\ell^2$ is a tension of the brane. The quadratic term in ρ in the Friedmann equation modifies the standard cosmological expansion law. As a background Friedmann brane model, we consider slow-roll inflation at low energies, characterized by a small slow-roll parameter, $\epsilon := 1 - \partial_\eta \mathcal{H}/\mathcal{H}^2 \ll 1$, followed by a radiation dominant phase, where $a \propto \eta + \mathcal{O}(\ell^2)$.

Tensor perturbations on the brane: We use the method to reduce the five dimensional equation for tensor perturbations in a Friedmann braneworld at low energies to a four dimensional effective equation of motion, derived in Ref. [4]. Tensor perturbations on a Friedmann brane are given by $ds^2 = (\ell/z)^2 \left[dz^2 - dt^2 + (\delta_{ij} + h_{ij})dx^i dx^j\right]$. We expand the perturbations by using $Y^k_{ij}(x)$, a transverse traceless tensor harmonics with comoving wave number k, as $h_{ij} = \sum_k Y^k_{ij}(x)\Phi_k(t,z)$. Then the equation of motion for the tensor perturbations in the bulk is given by

$$\left(-\partial_z^2 + \frac{3}{z}\partial_z + \partial_t^2 + k^2\right)\Phi_k = 0, \tag{2}$$

Hereafter we will discuss each Fourier mode separately, and we will abbreviate the subscript k. The general solution of this equation is $\Phi = \int d\omega \tilde{\Psi}(\omega) e^{-i\omega t} 2(pz)^2 K_2(pz)$ where $p^2 = -\omega^2 + k^2$. We have chosen the branch cut of the modified Bessel function K_2 so that there is no incoming wave from past null infinity in the bulk. The coefficients $\tilde{\Psi}(\omega)$ are to be determined by the boundary condition on the brane $n^\mu \partial_\mu \Phi|_{z=z(t)} = 0$, where n^μ is an unit normal to the brane, or, equivalently, by the effective Einstein equations on the brane [6],

$$^{(4)}G_{\mu\nu} = 8\pi G\, T_{\mu\nu} + (8\pi G_5)^2 \pi_{\mu\nu} - E_{\mu\nu}. \tag{3}$$

A projected Weyl tensor $E_{\mu\nu} := C_{\alpha\mu\beta\nu} n^\alpha n^\beta$ represents the effects of the bulk gravitational fields, giving rise to corrections to four dimensional Einstein gravity in a fairly nontrivial way. In the present case, this can be written explicitly. After some manipulation the effective four dimensional equation reduces to

$$\left(\partial_\eta^2 + 2\overset{(0)}{\mathcal{H}}\partial_\eta + k^2\right)\phi \simeq \frac{\ell^2}{\overset{(0)}{a}{}^2}\left(\mathcal{S}_0[\phi] + \mathcal{S}_1[\phi] + \mathcal{S}_2[\phi]\right), \tag{4}$$

where

$$\mathcal{S}_0[\phi] = -\frac{2\overset{(0)}{a}{}^2}{\ell^2}\delta\mathcal{H}\phi',\ \mathcal{S}_1[\phi] = (3\overset{(0)}{\mathcal{H}}{}^3 - 2\overset{(0)}{\mathcal{H}}\overset{(0)}{\mathcal{H}}{}')\phi' + k^2\overset{(0)}{\mathcal{H}}{}^2,\ \mathcal{S}_2[\phi] = -\frac{1}{2}\int d\omega p^4 \tilde{\phi} e^{-i\omega\eta}\left[\ln\left(\frac{p\ell}{2a}\right) + \gamma\right], \tag{5}$$

and the prime denotes ∂_η. This is our basic equation. The cosmic expansion rate at zeroth order is described by $\overset{(0)}{\mathcal{H}}$ and $\overset{(0)}{a}$, and can be obtained by dropping the quadratic term in ρ in Eq. (1). The first term $\mathcal{S}_0$ arises due to the non-standard cosmic expansion included in $\mathcal{H}$, while the other two terms are the corrections from the bulk effects $E_{\mu\nu}$. We can see that all terms are suppressed by ℓ^2 (or $\ell^2 \ln \ell$). $\mathcal{S}_2$ is essentially nonlocal because of the presence of the log term.

3 Leading order corrections

The perturbation equation (4) can be solved iteratively by taking ℓ^2 as a small parameter. We write $\phi = \overset{(0)}{\phi}\, e^{F(\eta)} = \overset{(0)}{\phi}\, \exp\left[\int^\eta f(\eta')d\eta'\right]$, and a zeroth order solution $\overset{(0)}{\phi}$ by definition satisfies the equation obtained by dropping the source terms on the right hand side. Then f obeys $\partial_\eta f + 2(\partial_\eta \overset{(0)}{\phi}/\overset{(0)}{\phi} + \overset{(0)}{\mathcal{H}})f = \ell^2 \mathcal{S}[\overset{(0)}{\phi}]/\overset{(0)}{a}{}^2\overset{(0)}{\phi}$, which can be integrated immediately to give $f(\eta) = (\ell/\overset{(0)}{a}\overset{(0)}{\phi})^2 \int^\eta d\eta' \overset{(0)}{\phi}\mathcal{S}[\overset{(0)}{\phi}]$. Here $\mathcal{S} = \mathcal{S}_0 + \mathcal{S}_1 + \mathcal{S}_2$. Integrating this expression, we obtain the first order correction F. We hereafter denote the corrections f and F coming from $\mathcal{S}_i$ as f_i and F_i, respectively.

During slow-roll inflation and the earlier stage of the radiation dominated phase, the perturbation modes are well outside the horizon and thus we can use the long wavelength approximation, which simplifies the calculation. In the long wavelength approximation, the zeroth order solution can be explicitly written as $\overset{(0)}{\phi} \simeq A_k\left[1 - k^2\int^\eta d\eta' I(\eta')\right]$, where A_k is an amplitude of the perturbation which can depend on k, and $I(\eta) := \overset{(0)}{a}{}^{-2}(\eta)\int_{-\infty}^\eta \overset{(0)}{a}{}^2(\eta')d\eta'$. We simply keep the terms up to $\mathcal{O}(k^2)$.

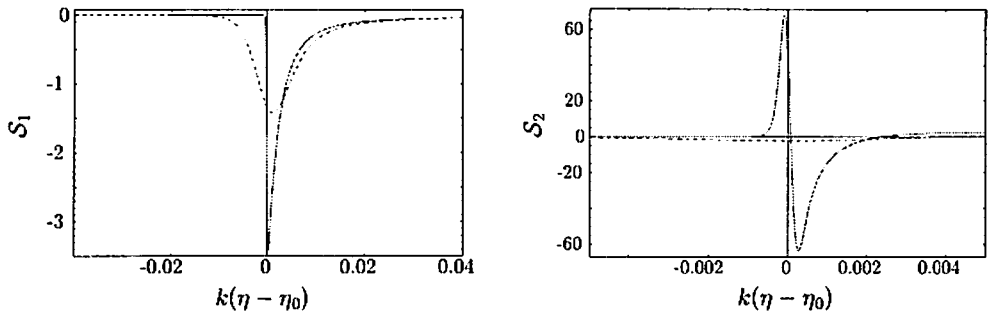


Figure 1: Behavior of the source terms of corrections $\mathcal{S}_1$ and $\mathcal{S}_2$ around the transition time with the vertical axis in an arbitrary unit. Solid line shows the case of a sharp transition with $s = 0.02\eta_0$, while dashed line represents the case of a smooth transition with $s = 0.5\eta_0$. The wavelength of the mode is chosen to be $k\eta_0 = 0.01$.

Slow-roll inflation: Let us consider slow-roll inflation on the brane. In this case $\mathcal{S}_0$ vanishes, since $\delta\mathcal{H} = 0$ by construction. Besides, $\hat{p}^4 \overset{(0)}{\phi}$ is shown to vanish at first order in the slow-roll parameters during inflation. Consequently, the only relevant term in the present situation is $\mathcal{S}_1 \simeq -A_k k^2 \overset{(0)}{\mathcal{H}}{}^2 \epsilon$. Integrating twice, we obtain

$$F(\eta) \approx \frac{k^2\ell^2}{2\overset{(0)}{a}{}^2}\epsilon. \tag{6}$$

Here we chose the integration constant so that F vanishes in $a \to \infty$ limit. We see that the correction arising during inflation is very tiny, suppressed by the slow-roll parameter ϵ in addition to the factor $k^2\ell^2/\overset{(0)}{a}{}^2$. For pure de Sitter inflation there is no correction, as is expected.

Transition from inflation to the radiation stage: Now we investigate the effects of the transition from the inflation stage to the radiation stage. First, just for the illustrative purpose, we plot the behavior of $\mathcal{S}_1$ and $\mathcal{S}_2$ for the modes well outside the horizon in the neighborhood of the transition time η_0 in Fig. 1. These plots are for ϵ given by $\epsilon(\eta) = \tanh[(\eta - \eta_0)/s] + 1$, where the parameter s controls the smoothness of the transition. From the figures it can be seen that the corrections from $E_{\mu\nu}$, $\mathcal{S}_1$ and $\mathcal{S}_2$, become significant only around the transition time.

Let us consider the limiting case where ϵ is given by $\epsilon(\eta) = 2\theta(\eta - \eta_0)$. We neglect the tiny effect of the non vanishing slow-roll parameter during inflation. In this case, by an elaborate calculation we can analytically obtain the corrections from the source term $\mathcal{S}_1$ and $\mathcal{S}_2$. They become time independent long time after the transition, and are given by

$$\lim_{\eta\to\infty} F_1(\eta) = -\frac{k^2\ell^2}{a_0^2}, \quad \lim_{\eta\to\infty} F_2(\eta) = \frac{2k^2\ell^2}{a_0^2}\left\{\frac{37}{75} - \frac{2}{15}\left[\gamma + \ln\left(\frac{k}{a_0 H_0}\right)\right] + \frac{1}{5}\ln\left(\frac{\ell H_0}{2}\right)\right\}. \tag{7}$$

Corrections due to the unconventional cosmic expansion: It might be possible that further corrections arise after the mode re-enters the horizon. However, we can show that such corrections are highly suppressed. A basic observation supporting this conclusion is that the contributions from $E_{\mu\nu}$ term in the right hand side of Eq. (4) become significantly large only at the transition time. It decreases in powers of $a(\eta)$ after the transition, and will be negligible when the long wavelength approximation brakes down. Hence, the long wavelength approximation suffices for our purpose to obtain the corrections from $E_{\mu\nu}$.

Now we compute the correction due to the unconventional cosmic expansion. In the radiation stage, $u(\eta) := a(\eta)\phi(\eta)$, is a convenient variable. In terms of this new variable, we can rewrite the equation of

motion (4) as

$$u'' + k^2 u = \frac{\ell^2}{a}\left(\bar{\mathcal{S}}_0 + \mathcal{S}_1 + \mathcal{S}_2\right), \tag{8}$$

with $\bar{\mathcal{S}}_0 = (a''/\ell^2)u$. If we neglect the deviation of the expansion law from the standard one, we have $a \propto \eta$ in the radiation stage and so $a'' = 0$. This means that, just as $\mathcal{S}_0$, the first term on the right hand side gives a contribution of $\mathcal{O}(\ell^2)$ from the modification of the expansion law. Thus, all the terms collected on the right hand side are of $O(\ell^2)$, and at zeroth order u behaves like a harmonic oscillator. We define "energy" of the harmonic oscillator as $\mathcal{E} := |u'|^2/2 + k^2|u|^2/2$. At the zeroth order this energy is conserved, but taking into account the correction of $\mathcal{O}(\ell^2)$ it varies with time due to the "external force" $\bar{\mathcal{S}}_0$. The variation of the energy, $\Delta\mathcal{E}_0 = \int^\infty \mathcal{E}_0' d\eta = \int^\infty [\ell^2 (u')^* \bar{\mathcal{S}}_0/2a + \text{ c.c.}] d\eta$, is related to that of the amplitude of the oscillator, i.e., the amplitude of the tensor perturbations, via $\lim_{\eta\to\infty}\{\Re[F_0] + \delta a/\overset{(0)}{a}\} = \Delta\mathcal{E}_0/(2\overset{(0)}{\mathcal{E}})$. Using this formula it is easy to obtain the correction arising due to the modification of the expansion law:

$$\lim_{\eta\to\infty} \Re[F_0(\eta)] = \frac{1}{10}\frac{k^2\ell^2}{a_0^2}. \tag{9}$$

4 Summary

We have investigated leading order corrections to tensor perturbations in the RS II braneworld cosmology by using the perturbative expansion scheme of Ref. [4]. We have studied a model composed of slow-roll inflation on the brane, followed by a radiation dominant era. In our expansion scheme the asymptotic boundary conditions in the bulk are imposed by choosing outgoing solutions of bulk perturbations, whose general expression is known in the Poincaré coordinate system. Hence, the issue of bulk boundary conditions is handled without introducing an artificial regulator brane. This is one of the notable advantages of the present scheme.

Combining the results obtained in Eqs. (7) and (9), we find that the amplitude of a fluctuation with comoving wave number k is modified by a factor $e^{\Re[F]}$ due to the effect of an extra dimension with

$$\lim_{\eta\to\infty} \Re[F(\eta)] = \frac{k^2\ell^2}{a_0^2}\left\{\frac{13}{150} - \frac{4}{15}\left[\gamma + \ln\left(\frac{k}{a_0 H_0}\right)\right] + \frac{2}{5}\ln\left(\frac{\ell H_0}{2}\right)\right\}, \tag{10}$$

where a_0 and H_0 are the scale factor and the Hubble parameter at the transition time, and γ is the Euler's constant. Leading corrections are proportional to $k^2\ell^2/a_0^2$ or $k^2\ell^2/a_0^2 \log k$, as is expected from the dimensional analysis. However, our calculation here determined the precise numerical factors analytically.

References

[1] R. Maartens, Living Rev. Rel. **7**, 1 (2004).

[2] L. Randall and R. Sundrum, Phys. Rev. Lett. **83**, 4690 (1999).

[3] J. Garriga and T. Tanaka, Phys. Rev. Lett. **84**, 2778 (2000).

[4] T. Tanaka, arXiv:gr-qc/0402068.

[5] T. Kobayashi and T. Tanaka, JCAP **0410**, 015 (2004).

[6] T. Shiromizu, K. i. Maeda and M. Sasaki, Phys. Rev. D **62**, 024012 (2000).

Renormalization Group approach to Inhomogeneous Cosmology

Sanjay Jhingan[1] and J. Ibáñez [2]

Departamento de Física Teórica, Universidad del País Vasco, Apartado 644, 48080, Bilbao, Spain

Abstract

Soliton solutions are recovered as scale-invariant asymptotic states of vacuum inhomogeneous cosmologies using renormalization group method. The stability analysis of these states is also given.

1 Introduction

In this paper we have studied the asymptotic evolution of vacuum G_2 metrics using a different approach than that used in earlier studies [1] : we have applied renormalization group (RG) tools to study the structurally stable characteristics of the inhomogeneous metrics. Recently, RG techniques have been exhibited as a powerful implement to study the asymptotic behavior of partial differential equations [2]. The RG method has been applied to study homogeneous and isotropic universe, spherically symmetric dust collapse [3], critical phenomena related with gravitational collapse [4], Newtonian cosmology [5], homogeneous flat causal bulk viscous cosmological models [6] and the theory of perturbations of isotropic universe with dynamically evolving Newton constant and cosmological constant [7], analyzing the Cosmological term by deforming the Friedmann equation [8].

The plan of this article is the following: in Section 2 we illustrate the RG method. In Section 3 we apply the RG technique to the vacuum, diagonal, G_2 metric. We find the fixed-points and analyze their stability as well. We conclude with a short discussion in the last section.

2 The RG method

It is well known that the asymptotics of partial differential equations can often be found from the consideration of scaling solutions (the equivalence of RG theory and the theory of intermediate asymptotics was shown by Goldenfeld et. al. [9]). Though it is a usual practice to find the similarity variable to analyze scaling solutions from a combination of variables using dimensional arguments, however, there is a large class of problems where this cannot be done [10]. RG provides a systematic approach for finding the scaling variables as well as the asymptotics of partial differential equations. The general (RG) method adapted to partial differential equations is well known [2] and we only give a quick review here.

We define a indexed variable $u_i(t)$, the index signifies a set of physical variables corresponding to $i = 1, 2, 3, 4 \ldots$, which characterize the system. $u_i(t)$ satisfy certain evolution equations, partial or ordinary differential equations, which are also known. Our interest is in the asymptotics of solution of the form

$$\lim_{t\to\infty} u_i(t) = t^{-\alpha_i} u_i^*(1) \,, \tag{1}$$

where argument "1" signifies initial value of the quantity. It is convenient to fix initial time as $t = 1$. Now we will illustrate how RG method gives a systematic procedure to fix α_i and determine the scaling function $u_i^*(1)$ as fixed-points of RG equations (in a inhomogeneous case the argument of u_i^* will not be a constant but will depend on a combination of time and spatial variable, the scaling variable).

Let us consider transformations of the form

$$t \longrightarrow Lt, \quad u_i(t) \longrightarrow U_i(t) = L^{\alpha_i} u_i(Lt) \,. \tag{2}$$

We use a number $L > 1$ as a parameter of scale transformation. Note that unlike in the application of RG method to quantum field theories or statistical mechanics, there is no natural way to choose a scale

[1] E-mail:wtpsaxxj@lg.ehu.es
[2] E-mail:wtpibmcj@lg.ehu.es

L here. Moreover, L never appears explicitly in the equations. Requirement that scale transformations (2) leave the evolution equations of u_i invariant, i.e., if $u_i(t)$ is a solution so is $U_i(t)$, fixes α_i.

Now, defining $L = \exp(\tau)$, and using Eq. (2) we get a new set of evolution equations:

$$\frac{dU_i}{d\tau} = \alpha_i U_i + \frac{\partial U_i}{\partial t} . \tag{3}$$

The procedure of defining τ is, in a sense, analogous to summing over all degrees of freedom corresponding to fluctuations of scale less than L and then re-scaling everything by L^{-1}. This new set of evolution equations define the RG transformations. Scale-invariant solutions emerge now from the fixed-point structure of the RG map, which is defined by

$$\frac{dU_i^*}{d\tau} = 0 , \tag{4}$$

with U_i^* being the fixed-points. The linearized stability of the system can be studied by analyzing RG flow in the neighbourhood of the fixed-points.

3 Inhomogeneous Case

We begin with a family of metrics which have been a very useful tool for studying inhomogeneous cosmological models, known as the generalized Einstein-Rosen spacetimes (see for example, [11, 12]). The line element for this spacetime can be written in the form

$$ds^2 = f^2(dz^2 - dt^2) + t(h^2 dx^2 + h^{-2} dy^2) , \tag{5}$$

where f and h are functions of t and z only. These metrics admit an Abelian G_2 group of isometries with 2 spacelike commuting killing vectors ∂_x and ∂_y. The set of Einstein field equations in the vacuum case reduces to

$$h_{,t} = \frac{1}{2t}\frac{f_{,z}}{f}\frac{h^2}{h_{,z}}, \qquad f_{,t} = -\frac{1}{4t}f + tf\left(\frac{h_{,z}}{h}\right)^2 + \frac{1}{4t}\frac{(f_{,z})^2}{f}\left(\frac{h}{h_{,z}}\right)^2 . \tag{6}$$

From Eqn. set (6) we have the evolution equations for h and f, respectively, and it is easy to check that the remaining field equations are identically satisfied. We now follow the prescription given in the previous section to recover the exact scaling solutions.

Let us consider the following scale transformation

$$z \longrightarrow Lz \, , t \longrightarrow L^\epsilon t \, , h(t,z) \longrightarrow \phi(t,z) = L^\alpha h(L^\epsilon t, Lz) \, , f(t,z) \longrightarrow \psi(t,z) = L^\beta f(L^\epsilon t, Lz) . \tag{7}$$

Here ϕ and ψ are the scaled quantities. Since scaled quantities should satisfy the original equations, this fixes

$$\epsilon = 1 . \tag{8}$$

The scaling relations (7) along with (8) and successive transformations, first $t \to 1$ and then $L \to t$, gives scale invariant solution of the form

$$h(t,z) = t^{-\alpha}\phi(1, z/t) \qquad f(t,z) = t^{-\beta}\psi(1, z/t) . \tag{9}$$

The equations above express arbitrary solution in terms of initial data (at $t = 1$). As stated earlier we work with $t = 1$ as our initial time and evolution is in sense of scaled time Lt with $L > 1$.

From simple dimensional analysis we would have $\beta = 0$ and $\alpha = \pm 1/2$ (introducing a dimensional constant multiplying either dx or dy). However, as we will see later this would lead to a trivial solution: the homogeneous Kasner metric. The fact that we recover Kasner solution as a fixed point of a general inhomogeneous G2 metric though is non-trivial and it elucidates the appearance of this solution in earlier studies; it is used as a seed metric in different solution generating techniques, and more importantly, is known to describe "generic" cosmological singularity in the analysis of Belinskii et al. [13]. In order to get a non-trivial structure in fix-point analysis we need to analyze the anomalous dimensions for both the functions f and h. It is well known [14] that the anomalous dimensions $\alpha \neq \pm 1/2$ and $\beta \neq 0$ are fixed

by initial or boundary conditions. In our case, cosmological vacuum solutions, initial condition refers to geometry at $t = 0$. Since, metrics of the type (5) are singular at $t = 0$, there is not strict functional constraint on the system described by (6). Nevertheless, interpreting a posteriori the fixed points we can give some hints to understand the role of anomalous dimensions α and β.

Denoting $L = \exp(\tau)$ the RG equations are

$$\frac{d\phi}{d\tau} = \alpha\phi + \phi' z + \frac{1}{2}\left(\frac{\psi'}{\psi}\right)\left(\frac{\phi^2}{\phi'}\right), \quad \frac{d\psi}{d\tau} = \left(\beta - \frac{1}{4}\right)\psi + \psi' z + \psi\left(\frac{\phi'}{\phi}\right)^2 + \frac{1}{4}\frac{(\psi')^2}{\psi}\left(\frac{\phi}{\phi'}\right)^2 . \tag{10}$$

We now investigate the fix-point structure of the equation set above, i.e., $d\phi^*/d\tau = 0$ and $d\psi^*/d\tau = 0$. The system of equations decouple and the fixed-points are

$$\phi^* = (z + \sqrt{z^2-1})^{\pm\sqrt{\Delta}}, \qquad \psi^* = c_f (z + \sqrt{z^2-1})^{\mp 2\alpha\sqrt{\Delta}} (z^2-1)^{-\Delta}, \tag{11}$$

were c_f is an integration constant and $\Delta = \alpha^2 + \beta - 1/4$. The real solutions correspond to $\Delta > 0$ for $z^2 > 1$ and $\Delta < 0$ for $z^2 < 1$. We have dropped the constant of integration from ψ^* since this can be absorbed simply by scaling of x and y. Also, we note here that the new parameter Δ relates our spacetime metric with Kasner metric; $\Delta = 0$ case corresponds to the Kasner models. When $\Delta > 0$ ($z^2 > t^2$) the critical solution is:

$$h(t,z) = t^{-\alpha\mp\sqrt{\Delta}}(z+\sqrt{z^2-t^2})^{\sqrt{\Delta}}, \quad f(t,z) = c_f t^{(\alpha\pm\sqrt{\Delta}+1/2)(\alpha\pm\sqrt{\Delta}-1/2)} (z+\sqrt{z^2-t^2})^{\mp 2\alpha\sqrt{\Delta}} (z^2-t^2)^{-\Delta}. \tag{12}$$

and when $\Delta < 0$ ($z^2 < t^2$) the critical solution is:

$$h(t,z) = t^{-\alpha}\exp(\mp\sqrt{-\Delta}\arccos\frac{z}{t}), \quad f(t,z) = c'_f t^{\alpha^2+\Delta-1/4}(t^2-z^2)^{-\Delta}\exp(\pm 2\alpha\sqrt{-\Delta}\arccos\frac{z}{t}). \tag{13}$$

The spacetime is split into two regions separated by the light-cone $z = t$. In each region the solution takes one of the forms given by the expressions above. For $\Delta = 0$ we have the Kasner metric. We would like to stress here that the solutions which we have obtained are actually the future asymptotic states, i.e., to which spacetime "prefers" to settle down. This makes this analysis very powerful since not only we recover in a very simple fashion a whole class of scale invariant solutions but also, due to "universality", these solutions actually are the preferred asymptotic states.

We will consider now the linear stability analysis. Since these solutions emerge as fixed-points of the RG map, the stability of these solutions is the stability of these fix-points. Let us define

$$\phi = \phi^*(1+\delta\phi), \qquad \psi = \psi^*(1+\delta\psi), \tag{14}$$

where $\delta\phi \ll 1$ and $\delta\psi \ll 1$. The above form of perturbations is chosen to facilitate the analysis since both unperturbed functions ϕ^* and ψ^* can diverge at $z = \pm 1$ and $z = \pm\infty$.

The perturbation equations take the form

$$\frac{d\delta\phi}{d\tau} = \left(\frac{\phi^*}{\phi^{*\prime}}\right)\left[\left(\alpha + 2z\frac{\phi^{*\prime}}{\phi^*}\right)\frac{d\delta\phi}{dz} + \frac{1}{2}\frac{d\delta\psi}{dz}\right], \quad \frac{d\delta\psi}{d\tau} = -\left(\frac{\phi^*}{\phi^{*\prime}}\right)\left[2\left(\alpha^2 + \Delta + 2\alpha z\frac{\phi^{*\prime}}{\phi^*}\right)\frac{d\delta\phi}{dz} + \alpha\frac{d\delta\psi}{dz}\right]. \tag{15}$$

We shall compute normal modes assuming the following form for the perturbations:

$$\delta\phi = e^{\omega\tau}\rho(z), \qquad \delta\psi = e^{\omega\tau}\sigma(z), \tag{16}$$

where ω is a constant. The perturbation equations (15) can be written as:

$$\omega\sigma = -2\sqrt{\Delta}\sqrt{z^2-1}\rho' - 2\alpha\omega\rho, \tag{17}$$

$$0 = \rho'' + \frac{z}{z^2-1}(1-2\omega)\rho' + \frac{\omega^2}{z^2-1}\rho. \tag{18}$$

Thus, the problem of solving linear perturbations around the fixed-points has been reduced to finding solutions of (18) equation, and (17) completes the solution. The general solution of (18) is given by:

$$\rho(z) = (z^2-1)^{\omega/2+1/4}\left(c_1 P^{\omega+1/2}_{-1/2}(z) + c_2 Q^{\omega+1/2}_{-1/2}(z)\right), \tag{19}$$

where P^{μ}_{ν} and Q^{μ}_{ν} are Legendre functions of first and second kind, respectively, and c_1 and c_2 are arbitrary constants. From (17) the solution for σ can be easily obtained:

$$\begin{aligned}\sigma(z) = \quad & -2\sqrt{\Delta}(z^2-1)^{\omega/2-1/4}\left[c_1\left(zP^{\omega+1/2}_{-1/2}(z) - P^{\omega+1/2}_{1/2}(z)\right) + c_2\left(zQ^{\omega+1/2}_{-1/2}(z) - Q^{\omega+1/2}_{1/2}(z)\right)\right] \\ & -2\alpha(z^2-1)^{\omega/2+1/4}\left(c_1 P^{\omega+1/2}_{-1/2}(z) + c_2 Q^{\omega+1/2}_{-1/2}(z)\right) . \end{aligned} \tag{20}$$

We require that the perturbations be regular for all z. Since the differential equation (18) has four regular singular points at $z = \pm 1, \pm\infty$ we must consider three different regions: $1 < z < \infty$, $-\infty < z < -1$ and $-1 < z < 1$. The first and the second region are equivalent. Let's first analyze the behavior in the first region. It is easy to see that the leading terms of the two linearly independent solutions ρ_1 and ρ_2 of (18) in the neighborhood of $z = \infty$ are respectively $\rho_1 \approx z^{\omega} + O(z^{\omega-2})$ and $\rho_2 \approx \rho_1 \ln z + O(z^{\omega-2})$. Both solutions are regular if $\omega \leq 0$. Furthermore, from (17), σ is also regular provided that $\omega \leq 0$. At $z = 1$ the leading terms of the two linearly independent solutions for ρ are: $(z-1)^{\omega+1/2} + O((z-1)^{\omega+3/2})$ and $constant + O((z-1))$. For σ the leading terms are: $(z-1)^{\omega}$ and $constant + O((z-1))$. Since ω is negative the first independent solution must be neglected so that we have regular solutions. For instance, tacking $c_2 = 0$ in (19) the solution is regular.

Making the scale transformation given by (7)-(9) we get the the behavior of the solution near the fixed-point :

$$\delta\phi = t^{\omega}\rho(z/t) , \qquad \delta\psi = t^{\omega}\sigma(z/t) , \tag{21}$$

with $\omega \leq 0$ and $z > t$. Since the solution above is valid in the region $z > t$, taking limit $t \to \infty$ means $z \to \infty$ as well. We can therefore distinguish two different situations. First, when we approach infinity in such a way that we encounter the light-cone $z = t$ without crossing it. In this case asymptotically $z/t = 1$ and, bearing in mind the behavior of the regular solutions of (18) close to the point $z = 1$, the above perturbations behave as:

$$\delta\phi \approx \delta\psi \approx constant \times t^{\omega} . \tag{22}$$

In the second situation we approach infinity through a path that does not encounter the light-cone. In this case z/t tends to a constant greater than 1, and the perturbations behave in a similar way that that given by the above expressions. So, in both cases the perturbations tend to zero when $t \to \infty$ which means that the fixed solution outside the light-cone is stable. A similar analysis in the region $-1 < z < 1$ (cosoliton) shows that solution there is unstable.

4 Discussion

In this paper we have shown how the RG method can be used to obtain the asymptotic regime of cosmological solutions. We have first illustrated the method and then applied to the diagonal, vacuum inhomogeneous G_2 metric. In this case, the system reduces to a set of coupled partial differential equations whose analysis using the RG method is not difficult. The fixed-points are exact solutions depending on two parameters and belongs to a class of soliton solutions [11]. In particular, one of the found fixed-point is a soliton solution with real poles with origin at $z = 0$, whose "seed" metric is the Kasner metric (soliton origin marks the origin of the light-cone $z^2 = t^2$). Since the metric (5) is invariant under a z translation the fact that the origin is at $z = 0$ is not important. It is interesting to note that, generically, the solution doesn't homogenize, let alone isotropize, for the final state is inhomogeneous. There is, however, a few particular cases for which the metric tends to a homogeneous solution: when $\Delta = 0$ the solution is the Bianchi type I Kasner metric, and for a particular value of the parameters α and Δ the solution is Ellis and McCallum family of vacuum Bianchi models [15]. Finally, we would like to note that the fixed-points recovered in the RG technique gives all the scale-invariant exact solutions of vacuum G_2 cosmologies.

The RG method allows us to study the linear perturbations around the fixed-points as well. We have shown that the solution out-side the light-cone, which corresponds to the soliton solution with real poles, is stable against bounded perturbations, contrary to the solution inside the light-cone (cosoliton solution) which we find to be unstable.

There remain a few open questions that we hope to deal-with in future works. It would be interesting to extend the analysis performed in this paper to general inhomogeneous non-vacuum metrics. Solutions

with a scalar field are of particular interest in order to investigate issues like isotropization, scaling solutions, etc.. Finally, this technique can be used to analyze long time behavior of spacetimes with more that four dimensions, for example, brane-world scenarios. For a more detailed discussion on this article see [16].

Acknowledgements

We thank Takahiro Tanaka and Akio Hosoya for discussions and encouragement. Authors acknowledge financial support under CICYT grant FIS2004-01626. S.J. acknowledges support under a Basque Govt. postdoctoral fellowship.

References

[1] See, chapter 12 in *Dynamical Systems in Cosmology*, Ed. J. Wainwright and G. F. R. Ellis (Cambridge University Press, 1997), and references therein; J. Ibáñez and I. Olasagasti, J. Math. Phys. **37** (1996) 6238; J. Carot and M. M. Collinge, Class. Quant. Grav. **18** (2001) 5441.

[2] J. Bricmont, A. Kupiainen and G. Lin, Commun. Pure and Appl. Math. **XLVII** (1994) 893; J. Bricmont and A. Kupiainen, *Renormalizing Partial Differential Equations*, in Constructive Physics, (ed. V. Rivasseau, Springer, 1995) [chao-dyn/9411015]; L. Y. Chen, N. Goldenfeld and Y. Oono, Phys. Rev. Lett. **73** (1994) 1311; L. Y. Chen, N. Goldenfeld and Y. Oono, Phys. Rev. E, **54** (1996) 376.

[3] O. Iguchi, A. Hosoya and T. Koike, Phys. Rev. D **57** (1998) 3340.

[4] T. Koike, T. Hara and S. Adachi, Phys. Rev. Lett. **74** (1995) 5170.

[5] Y. Sota, T. Kobayashi, K. Maeda, T. Kurokawa, M. Morikawa and A. Nakamichi, gr-qc/9801083.

[6] J. A. Belinchón, T. Harko and M. K. Mak, Class. Quant. Grav. **19** (2002) 3003.

[7] A. Bonnano and M. Reuter, Phys. Lett. B **527** (2002) 9; I. L. Shapiro, J. Sola, C. Espana-Bonet and P. Ruiz-Lapuente Phys. Lett. B **574** (2003) 149; M. Reuter and H. Weyer, Phys. Rev. D **69** (2004) 104022; A. Bonnano and M. Reuter, Int. J. Mod. Phys. D **13** (2004) 107.

[8] E. Tanaka et al., *Cosmological term by deforming the Friedmann equation*, see PRE-15 in these proceedings .

[9] N. Goldenfeld, O. Martin and Y. Oono, J. Sci. Comput. 4 (1989) 355.

[10] G. I. Barenblatt, *Similarity, Self-Similarity and Intermediate Asymptotics*, (Consultants Bureau, New York, 1989).

[11] E. Verdaguer, Phys. Rep. **229** (1993) 1.

[12] M. Carmeli, Ch. Charach and S. Malin, Phys. Rep. **76** (1981) 79.

[13] V. A. Belinskii, E. M. Lifshitz and I. M. Khalatnikov, Sov. Phys. Uspechi **13** (1971) 745.

[14] N. Goldenfeld, *Lectures on Phase Transitions and the Renormalization Group*, Frontiers in Physics Series **85** (Addison-Wesley publishing company, 1985).

[15] G. F. R. Ellis and M. A. H. MacCallum, Commun. Math. Phys. **12** (1969) 108.

[16] J. Ibáñez and S. Jhingan, Phys. Rev. D **70** (2004) 063507.

Initial Data for Dynamical Evolutions of Binary Black Holes in Quasicircular Orbit

Hwei-Jang Yo[1], James N. Cook[2], Stuart L. Shapiro[3], and Thomas W. Baumgarte[4]

[1] *Department of Physics, National Cheng-Kung University, Tainan 701, Taiwan, ROC*
[2] *Department of Physics, University of Illinois at Urbana-Champaign, Urbana IL61801*
[3] *Departments of Physics & Astronomy, University of Illinois at Urbana-Champaign, Urbana IL61801*
[4] *Department of Physics and Astronomy, Bowdoin College, Brunswick, ME 04011*

Abstract

We present a formalism for constructing quasi-equilibrium binary black hole initial data suitable for numerical evolution. We construct quasi-equilibrium models by imposing an approximate helical Killing symmetry appropriate for quasi-circular orbits. We adopt a superposition of two Kerr-Schild metrics as our background metric, thereby improving on conformally flat backgrounds that do not accommodate rotating black holes and providing a horizon-penetrating lapse, convenient for implementing black hole excision. We construct inner boundary conditions that incorporate the quasi-equilibrium condition and that recover the solution for isolated black holes in the limit of large separation. We use our formalism both to generate initial data for binary black hole evolutions and to construct a crude quasi-equilibrium, inspiral sequence for binary black holes of fixed irreducible mass.

Constructing numerical models of the binary inspiral typically proceeds in two steps (see, e.g. [1] for a recent review). In the first step, initial data are constructed by solving the constraint equations of general relativity. These initial data, which provide a snapshot of the gravitational fields at a certain instant of time, are not unique, and certain freely specifiable functions have to be chosen in accordance with the astrophysical situation at hand (see also the review [2]). In the second step, the initial data are evolved dynamically forward in time, which provides the subsequent binary evolution and with it the emitted gravitational wave signal.

To date neither one of these two steps has been solved completely satisfactorily. A number of groups have constructed initial data describing binary black holes in nearly circular orbit [3, 4, 5, 6, 7], and there have been several attempts at dynamical simulations of binary black holes [8, 9]. While this effort has made significant progress, the numerical modeling of binary black hole inspiral remains an unsolved theoretical problem.

Building on the success of the BSSN formulation of the evolution equations of general relativity [10, 11], we have recently developed a code that can stably evolve single, rotating black holes for arbitrary long times [12]. This code adopts a simple excision scheme [13] to remove the black hole deep interior and its singularities from the numerical grid. Implementation of such a scheme requires a coordinate system that smoothly extends into the black hole interior ("horizon-penetrating coordinates"), as for example Kerr-Schild coordinates. Our goal is to use this code for dynamical simulations of binary black hole systems in corotating coordinates. This requires initial data that describe binary black holes in quasi-circular orbit in horizon-penetrating coordinates.

The conformal thin-sandwich approach [14, 2, 5] seems appealing for the construction of quasi-equilibrium initial data, since it allows for the explicit specification of the time derivatives of the conformally related metric and the trace of the extrinsic curvature. In addition, this approach automatically provides a coordinate system that reflects quasi-equilibrium.

We borrow various ideas and approaches from previous investigators to construct initial data that are suitable for evolution with our dynamical evolution code. In particular, we adopt the thin-sandwich decomposition of the constraint equations together with Kerr-Schild background data. We set the time

[1] E-mail:hjyo@phys.ncku.edu.tw
[2] E-mail:jncook@uiuc.edu
[3] E-mail:shapiro@astro.physics.uiuc.edu
[4] E-mail:tbaumgar@bowdoin.edu

derivative of the trace of the extrinsic curvature to zero, as one would expect for equilibrium data. On the excision surface we impose a boundary condition that is derived from requiring that the time derivative of the conformal factor vanish there. We impose circular orbits by setting the ADM mass equal to the Komar mass, which is equivalent to imposing a relativistic virial theorem [5] (see also [7, 15].) For full details, see [16].

The thin-sandwich formalism provides three equations for the three unknowns α, β^i and ψ, from which the tracefree part of the extrinsic curvature can be constructed. The freely specifiable quantities are the background metric $\tilde{\gamma}_{ij}$ and mean curvature K as well as their time derivatives. As discussed above we set the latter to zero, and identify the former with a superposition of two single Kerr-Schild black holes. On the outer boundaries of our computational grid we assume the following fall-off conditions

$$\psi - 1 \sim \frac{1}{r}, \quad \beta^x - \bar{\beta}^x \sim \frac{y}{r^3}, \quad \beta^y - \bar{\beta}^y \sim \frac{x}{r^3}, \quad \beta^z - \bar{\beta}^z \sim \frac{z}{r^4}, \quad \alpha - 1 \sim \frac{1}{r}. \tag{1}$$

Here the boundary condition for the shift vector consists of an analytic part, $\bar{\beta}^i$, and a higher-order part. The former is the sum of the analytic shifts from each non-spinning black hole ($a = 0$) plus $(\vec{\Omega} \times \vec{r})^i$, which accounts for all shift terms except for terms due to the orbital rotation (frame-dragging) as identified above. For the inner boundary conditions we assume

$$\alpha = \alpha_A \alpha_B, \quad \beta^i = \alpha_A \beta^i_B + \alpha_B \beta^i_A, \quad 6\beta^i \partial_i \psi = -\psi \beta^i (\tilde{\Gamma}^j{}_{ji} + \partial_i \ln \alpha) \tag{2}$$

In the limit of infinite separation each black hole reduces to an isolated Kerr-Schild black hole, which satisfies the above conditions. For details, see [16].

The binding energy of an equal mass binary can be defined as $E_b = M_{\rm ADM} - 2M_{\rm irr}$[3]. A simultaneous turning point in the binding energy and the angular momentum locates the ISCO. In Fig. 2 we show both the binding energy and the angular momentum. We show numerical results obtained with a resolution of $\Delta x = M_0/4$ and with the outer boundary at $30M_0$. We also compare our results with the numerical results of: Cook [17], for an Eddington-Finkelstein slicing and $d\alpha\psi/dr = 0$ inner boundary condition ([17]a), an Eddington-Finkelstein slicing and $\alpha\psi = 1/2$ inner boundary condition ([17]b), and a maximal slicing and $d\alpha\psi/dr = \alpha\psi/2r$ inner boundary condition ([17]c); with the binary initial data in [5]; with the second-order, post-Newtonian sequence in [3]; and with the third-order, post-Newtonian sequence in [18].

Our results for the binding energy agree fairly well with those of [17]b, while our results for the angular momentum do not. Note that we find a turning point in the binding energy, but not in the angular momentum. There are several possible reasons for these findings. Solving the constraints in the thin-sandwich decomposition leads to configurations that are in approximate equilibrium, but lacking dynamical evolutions, it is difficult to determine just how good this approximation is for this scenario. Another potential reason for our findings are the inner boundary conditions (2), which may lead to undesirable deviations from quasi-equilibrium. Probably more important, however, is the limited numerical accuracy of our finite-difference, Cartesian code. We estimate that the accuracy of our values for the masses and angular momenta is of the order of a percent or so. The binding energy is computed as the difference between two masses, and is of the order of about 10 % of each of those masses (see Fig. 2). The relative error in this smaller difference is therefore significantly larger than the error in each of the terms separately, and may be as large as 10 % or more. Such an error is large enough to spoil the accuracy of an inspiral sequence. However, if taken at face value, the orbital parameters at the turning point of the binding energy agree fairly well with recent results for the binary black hole ISCO[16].

To summarize, we solve the constraint equations in a conformal thin-sandwich decomposition (e.g. [16]), and impose quasi-circular orbits by imposing that the ADM mass of the binary be equal to its Komar mass (compare [5]). We adopt a superposition of two Schwarzschild black holes in Kerr-Schild coordinates as the conformal background solution. This background choice leads to horizon-penetrating coordinates, which are needed for dynamical evolutions, and may produce less spurious gravitational radiation than conformally flat data, at least for rotating black holes. We present a new set of simple inner boundary conditions, which we hope leads to reasonable approximation to equilibrium (compare [19, 17, 20]). We construct an approximate inspiral sequence. Our numerical accuracy may not be sufficient to track the binding energy to high precision, since it is computed as the small difference between two significantly larger numbers. However, we do expect that our solutions provide adequate initial data for current

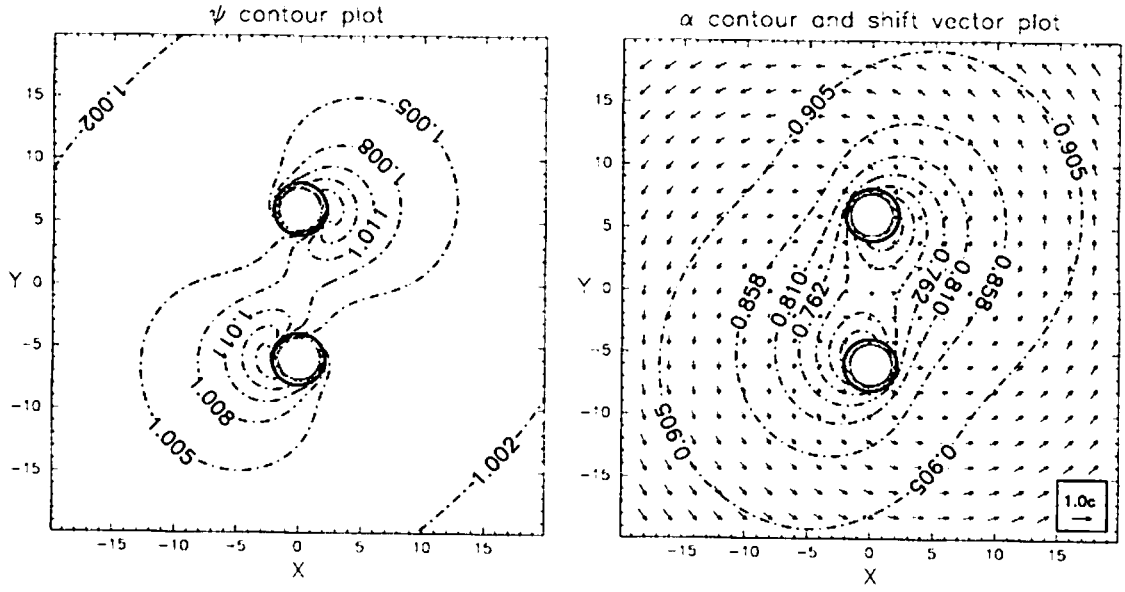


Figure 1: Contour plots of binary initial data with coordinate separation $12M_0$ and corresponding orbital velocity $2\Omega M_{\rm irr} = 0.0788$. The left panel shows contours of the conformal factor ψ; the right panel shows contours of the lapse function α as well as errors denoting the shift vector in the equatorial plane. The excision radius is at $1.6M_0$. The two thick circles in the plots are the apparent horizons. The numerical value of the lapse α on the apparent horizons exceeds 0.5 and is therefore positive, as required for horizon-penetrating coordinates. It is evident from the plots that the solutions do not satisfy octant symmetry.

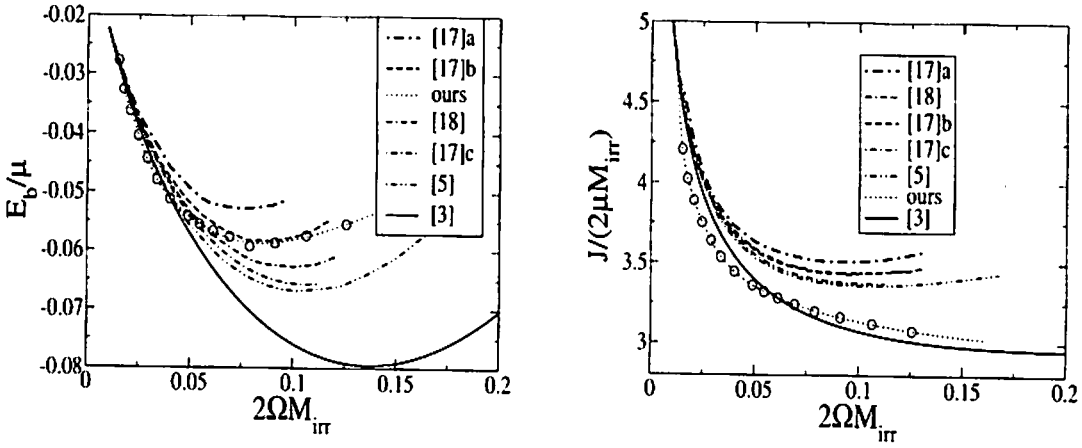


Figure 2: The binding energy E_b and angular momentum J as a function of orbital angular velocity. The dotted lines are least square fits to our numerical results, marked by open circles. We compare with thin-sandwich results in [17] for an Eddington-Finkelstein slicing and $d\alpha\psi/dr = 0$ inner boundary condition ([17]a), an Eddington-Finkelstein slicing and $\alpha\psi = 1/2$ inner boundary condition ([17]b), , and a maximal slicing and $d\alpha\psi/dr = \alpha\psi/2r$ inner boundary condition ([17]c), with the binary initial data in [5], with the second-order, post-Newtonian sequence in [3], and with the third-order, post-Newtonian sequence in [18]. Here μ is the reduced mass ($M_{\rm irr}/2$) and $M_{\rm irr}$ is the irreducible mass for one black hole.

finite-difference evolution codes. We also expect that when our formalism is implemented with higher resolution and/or more accurate numerical schemes, the inspiral sequence may provide a more reliable estimate of the ISCO parameters.

Acknowledgments

This paper was supported in part by NSF Grants PHY-0090310 and PHY-0345151 and NASA Grant NNG04GK54G at the University of Illinois at Urbana-Champaign (UIUC) and by NSF Grant PHY-0139907 at Bowdoin College, and by the National Science Council of the ROC under grant number NSC93-2112-M-006-024. Numerical calculations were carried out at the National Center for Supercomputing Applications at UIUC.

References

[1] T. W. Baumgarte & S. L. Shapiro, Phys. Rep. 376 41 (2003).

[2] G. B. Cook, Living Reviews in Relativity **3**, 2000-5 (2000) (http://www.livingreviews.org/).

[3] G. B. Cook, Phys. Rev. D **50**, 5025 (1994).

[4] T. W. Baumgarte, Phys. Rev. D **62**, 024018 (2000).

[5] P. Grandclement, E. Gourgoulhon, & S. Bonazzola, Phys. Rev. D **65**, 044021 (2002).

[6] H. P. Pfeiffer, S. A. Teukolsky, & G. B. Cook, Phys. Rev. D **62** 104018 (2000).

[7] W. Tichy & Bernd Brügmann, Phys.Rev. D **69**, 024006 (2004).

[8] B. Brügmann, W. Tichy & N. Jansen, Phys. Rev. Lett. **92** 211101 (2004).

[9] M. Alcubierre *et al*, gr-qc/0411149.

[10] M. Shibata & T. Nakamura, Phys. Rev. D **52**, 5428 (1995).

[11] T.W. Baumgarte & S.L. Shapiro, Phys. Rev. D **59**, 024007 (1999).

[12] H.J. Yo, T.W. Baumgarte, & S.L. Shapiro, Phys. Rev. D**66**, 084026 (2002).

[13] M. Alcubierre & B. Brügmann, Phys.Rev. D **63** 104006 (2001).

[14] J. W. York, Jr., Phys. Rev. Lett. **82**, 1350 (1999).

[15] M. L. Skoge and T. W. Baumgarte, Phys. Rev. D **66**, 107501 (2002).

[16] H.J. Yo, J.N. Cook, S.L. Shapiro, and T.W. Baumgarte, Phys.Rev. D **70** 084033 (2004).

[17] G.B. Cook, talk presentation in ITP, Santa Barbara, http://online.kitp.ucsb.edu/online/gravity_c03 (2003). See also G.B. Cook and H.P. Pfeiffer, Phys. Rev. D **70**, 104016 (2004).

[18] T. Damour, E. Gourgoulhon, and P. Grandclément, Phys. Rev. D **66** 024007 (2002).

[19] G.B. Cook, Phys. Rev. D **65** 084003 (2002).

[20] J.L. Jaramillo, E. Gourgoulhon, and G. A. Mean Marugán, Phys. Rev. D **70**, 124036 (2004).

Gravitational Radiation from Magnetorotational Core-Collapse of Massive Stars

Kei Kotake[1], Shoichi Yamada[2], and Katsuhiko Sato[3]

[1]*Department of Physics, School of Science, The University of Tokyo, 7-3-1 Hongo, Bunkyo-ku, Tokyo 113-0033, Japan, email: kkotake@utap.phys.s.u-tokyo.ac.jp*
[2]*Science & Engineering, Waseda University, 3-4-1 Okubo, Shinjuku, Tokyo, 169-8555, Japan*
[3]*Research Center for the Early Universe (RESCEU), School of Science, The University of Tokyo, 7-3-1 Hongo, Bunkyo-ku, Tokyo 113-0033, Japan*

Abstract

We perform a series of two-dimensional hydrodynamic simulations of the rotational core collapse of a supernova core and calculate the gravitational waveforms from the anisotropic neutrino radiation induced by rotation. In order to calculate the waveforms, we derive a closed form of the formula obtained by our analytical integration of a conventional formula. Since the angular momentum distribution of the massive stars are still uncertain, we systematically change the degree of differential rotation and the rotational profiles to construct the initial conditions. As for the microphysics, we employ a realistic equation of state and take into account electron capture and neutrino transport in an approximate method. With these computations, we find that the waveforms of the gravitational waves due to the anisotropic neutrino are mainly determined by the neutronization, which occurs twice and anisotropically in the rotating core. At the first neutronization, the wave amplitude shows a rise, on the other hand, the wave amplitude shows a fall at the second one, which predominantly depends on the degree of the differential rotation, and thus, determines the waveforms. After the second neutronization, the wave amplitudes from the neutrinos are found to rise much larger with time for the strongly differential rotation models than for the weakly differential rotation models. This feature is regardless of the initial rotational profiles. The difference is determined by the competition between the degree of the anisotropic neutrino radiation depending on the initial degree of the differential rotation and the weight function obtained by our analytical formula. By the analysis of the gravitational wave spectra, it is found that the gravitational waves from the neutrinos dominate over those from the matter motions below the frequency of $\sim$ 60 Hz. We point out that the corresponding amplitudes are well within the detection limits of laser interferometers in the next generation such as LCGT and advanced LIGO for a supernova in our Galactic center.

1 Introduction

The gravitational astronomy is becoming a reality. In fact, the ground-based laser interferometers such as TAMA300, the first LIGO and GEO600 are beginning to take data at sensitivities where astrophysical events are predicted. For the detectors, core collapse supernovae especially in our Galaxy, have been supposed to be the most plausible sources of gravitational waves. The detection of gravitational waves is important not only for themselves but also for the understanding of core collapse supernovae itself.

So far, most of the theoretical predictions of the gravitational waves in core collapse supernovae have focussed on the bounce signal (for a review, see *eg.*, [1]). In such cases, the gravitational waves are emitted as bursts in which the wave amplitude rises from zero at core bounce, oscillates for several cycles and then approaches to zero. This reflects the hydrodynamic motions of the central core near core bounce. In addition, there is another class of gravitational wave, that is, bursts with memory, in which the wave amplitude rises from zero and then after the neutrino bursts settles into a non-zero final value. As the source of such gravitational waves, the anisotropic neutrino radiation has been pointed out to be an important ingredient [2]. In this study, we pay particular attention to how the anisotropic neutrino radiation induced by rapid rotation affects the gravitational wave signals (see, [3] for the gravitational

waves from neutrinos induced by convection). In order to calculate the neutrino emissions, we employ a realistic EOS and treat the approximated neutrino transport and the relevant microphysics. Here it is noted that the anisotropic neutrino radiation induced by rotation is likely to produce an asymmetric explosion [4] as suggested by the observation of SN 1987A. In this sense, it should be important to detect the gravitational waves from the neutrinos for the understanding of the explosion mechanism of the core-collapse supernovae. Thus, we discuss whether the gravitational waves from the neutrinos can be detected or not by the currently running and future detectors.

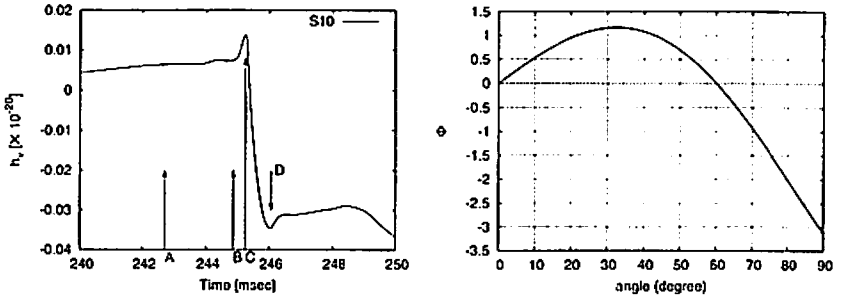


Figure 1: Left panel is the waveform due to the anisotropic neutrino radiation for model S10. In the panel, points A, B, C, and D represents the epoch of core bounce (t = 242.7 ms), the onset of the first neutronization (t = 244.8 ms), the peak of the neutronization, which corresponds to the onset of the second neutronization (t = 245.3 ms), and the offset of the second neutronization (t = 246.1 ms), respectively. Right panel represents the angular dependence of Φ in Eq. (1). Note that the angle is measured from the rotational axis.

2 Numerical Results

2.1 Properties of waveforms from anisotropic neutrino radiation

We first show the properties of waveforms due to the anisotropic neutrino radiation. First of all, we take model S10 as an example model, because the model is based on the recent stellar evolution calculation [5]. The waveform for the model near core bounce is given in the left panel of Figure 1. About 2.1 ms after core bounce at point A in the panel, the amplitude begins to rise more steeply than before (see point B in the figure). This epoch corresponds to the so-called neutronization, which occurs when the shock wave goes over the neutrino sphere. At this moment, the trapped electron neutrinos inside the neutrino sphere decouple from the matter and propagate ahead of the shock waves. Here it should be noted that the neutronization occurs anisotropically in our rotating models. Due to the non-sphericity of the shapes of the shock wave and the neutrino sphere, the neutronization can occur more than once while it occurs only once for spherical models. In which direction the neutronization occurs is determined by the shapes of the deformed neutrino sphere and the anisotropically propagating shock wave. The first neutronization (at point B in the panel) occurs near the pole at the radius of $\sim$ 20 km along the rotational axis. The shape of the shock wave formed by core bounce is prolate initially because the bounce occurs near the rotational axis. This prolate shock wave crosses the neutrino sphere, whose shape is deformed to be oblate due to rotation. Since the area of surface, where the first neutronization occurs, is small, the neutrino luminosity is relatively low at this epoch ($L_\nu \sim 10^{52}$ erg s^{-1}). About 0.5 ms after the first neutronization at point B in the left panel of Figure 1, the amplitude shows sudden fall from t = 245.3 ms (point C) to t = 246.1 ms (point D). After the first neutronization occurs at the pole, the shock wave in the polar region is weakened by the neutrino energy loss and ram pressure of the infalling material. Then, the subsequent shock wave is formed in the vicinity of the equatorial plane and begins to move rather parallel to the plane. Since the first shock wave almost stalls along the rotational axis during a several millisecond after the first neutronization, the shape of the shock wave becomes rather oblate due

to the propagation of the second shock wave rather parallel to the equatorial plane. As this oblate shock wave propagates along the equatorial plane, it crosses the oblate neutrino sphere. At this moment, the second neutronization occurs, where its luminosity becomes maximum, whose value reaches as high as $\lesssim 10^{54}$ erg s^{-1}. In the following, we mention what makes the difference between the signatures of the gravitational waves from the neutrinos at the two epochs of the neutronization.

At the first neutronization, the neutrino emissions are concentrated near the rotational axis. Note that the gravitational waves generated by the anisotropic neutrino radiations can be expressed as

$$h_{\nu}^{\rm TT} = \frac{8G}{c^4 R} \int_{-\infty}^{t-R/c} dt' \int_0^{\pi/2} d\theta' \, \Phi(\theta') \, \frac{dL_{\nu}(\theta', t')}{d\Omega'}, \tag{1}$$

where $\Phi(\theta)$ is the latitudinal angle dependent function (see the right panel of Figure 1) and $dL_{\nu}(\theta, t)/d\Omega$ is the latitudinal angle dependent neutrino luminosity. Thus the enhancement of the neutrino radiation near the rotational axis does not work sufficiently to change the amplitude although the amplitude shows a rise at the first neutronization due to the non-zero contributions of Φ and the neutrino luminosity near the rotational axis (see from point B to C in Figure 1). On the other hand, at the second neutronization, the neutrino emissions are concentrated in the vicinity of the equatorial plane. The value of the function Φ is negative ($\theta = \pi/2$) and its absolute value is large compared to the value near the rotational axis ($\theta \sim 0$) (see the right panel of Figure 1). In addition, the neutrino luminosity is much larger at the second neutronization. This is because the area of the surface at the second neutronization is quite larger than that at the first neutronization near the pole, since the oblate shock wave crosses the oblate neutrino sphere. As a result, the amplitude of the gravitational waves from the neutrinos shows a steep fall at the second neutronization.

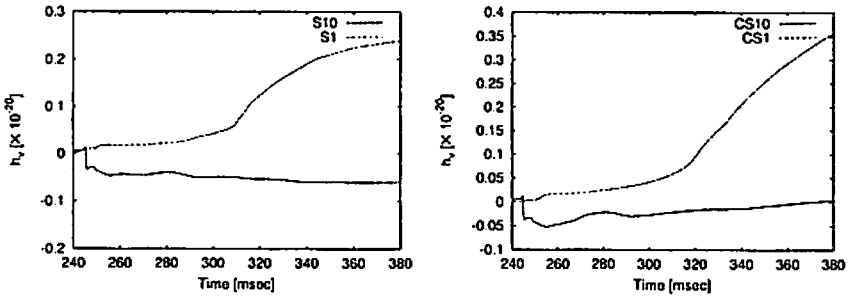


Figure 2: Waveforms due to the anisotropic neutrino radiations for some representative models with the shell-type (left panel) and the cylindrical rotation (right panel) profiles. Note that the source is assumed to be located at the distance of 10 kpc.

2.2 Effect of differential rotation

Next, we show the effect of the differential rotation on the properties of waveforms due to the anisotropic neutrino radiation. In Figure 2, the waveforms h_{ν} from near core bounce up to the final time of our simulation are presented for the representative models with the shell-type (left panel) and cylindrical rotation profiles (right panel), respectively. It can be seen from the figures that the amplitude due to the neutrinos in the later times becomes much larger for the models with the stronger differential rotation (compare S10 (weakest differential rotation) with S1 (strongest differential rotation), CS10 (weakest one) with CS1 (strongest one), respectively). Simultaneously, it is found that this feature is regardless of the rotational profiles (compare the left (shell-type rotation) with the right panels (cylindrical rotation) in Figure 2). As the differential rotation becomes stronger, the shape of the shock wave becomes more prolate, which makes the neutrino emission more stronger in the vicinity of the rotational axis. This makes the gravitational amplitudes from the neutrinos more larger (please see [6] for the more detailed explanations).

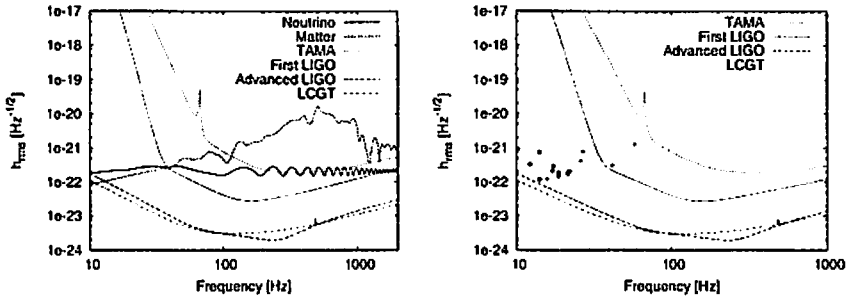


Figure 3: Detection limits of TAMA, first LIGO, advanced LIGO, and Large-scale Cryogenic Gravitational wave Telescope (LCGT) with the expected gravitational wave spectrum obtained from the numerical simulations. The left panel shows the model with the weak differential rotation (model S10) and the strong differential rotation (model S1), respectively. In the right panel, the open circles and the pluses represent the amplitudes of $h_{\nu,\mathrm{eq}}$ with the characteristic frequencies of ν_{eq} for the models with the cylindrical and the shell-type rotation profiles, respectively. Under the frequency of ν_{eq}, the gravitational waves from the neutrinos dominate over those from the matter contributions. Note that the source is assumed to be located at the distance of 10 kpc.

2.3 Detectability

In the left panel of Figures 3, the root mean square (rms) sensitivity curves with the rms gravitational wave spectra for the standard model is given. From the panel, it can be seen that the gravitational waves due to the anisotropic neutrino radiation dominate over those due to the mass motions at the frequency lower than several 10 Hz. In the 21 models we computed, it is found that the values of ν_{eq} ranges from 8 to 58.1 Hz with the rms amplitude ranging from 7.28×10^{-23} to 1.28×10^{-21} and that the values of $h_{\nu,\mathrm{eq}}$ generally become larger for the stronger differential rotation models. Here ν_{eq} represents a characteristic frequency, below which the gravitational waves from the neutrinos dominate over those from the mass motions, and the corresponding rms gravitational wave amplitude is named as $h_{\nu,\mathrm{eq}}$. In the right panel of Figure 3, the values of $h_{\nu,\mathrm{eq}}$ with ν_{eq} for all the models are plotted with the sensitivity curves of laser interferometers. It can be seen that the gravitational waves from the neutrinos are the detection limits of the detectors in the next generation such as LCGT and advanced LIGO. Thus, we conclude that the detection of the gravitational wave at the low frequency range ($\lesssim 100$ Hz) becomes more hopeful due to the contributions from the anisotropic neutrino radiation.

References

[1] K.C.B. New, Living Reviews in Relativity. **6**, 2 (2003), see also GWs in Magnetorotational core-collapse, K. Kotake, S. Yamada, K. Sato, K. Sumiyoshi, H. Ono, and H. Suzuki, Phys. Rev. D., **69**, 124004, (2004).

[2] R. Eptein, Astrophys. J. **223**, 1037 (1978), V.B. Braginsky and K.S. Thorne, Nature, **327**, 14 (1987).

[3] A. Burrows and J. Hayes, Phys. Rev. Lett., **76**, 352 (1996), C.L. Fryer, D.E. Holz and S.A Hughes, Astrophys. J. in press (2004), E. Müller, M. Rampp, R. Buras, H.-T. Janka, and D.H. Shoemaker, Astrophys. J. **603**, 221 (2004).

[4] K. Kotake, S. Yamada, and K. Sato, Astrophys. J. **595**, 304 (2003). K. Kotake, H. Sawai, S. Yamada, and K. Sato, Astrophys. J. **608**, 391 (2004).

[5] A. Heger, N. Langer and S. E. Woosley, Astrophys. J. **528**, 368 (2000).

[6] K. Kotake, S. Yamada, and K. Sato, submitted to Phys. Rev. D.

Particle production in a two-brane collision and Reheating of the Brane Universe

Yu-ichi Takamizu [a, 1], Kei-ichi Maeda [a,b,c, 2]

[a] *Department of Physics, Waseda University, Okubo 3-4-1, Shinjuku, Tokyo 169-8555, Japan*
[b] *Advanced Research Institute for Science and Engineering, Waseda University, Okubo 3-4-1, Shinjuku, Tokyo 169-8555, Japan*
[c] *Waseda Institute for Astrophysics, Waseda University, Okubo 3-4-1, Shinjuku, Tokyo 169-8555, Japan*

Abstract

We study particle production at the collision of two domain walls in 5-D Minkowski spacetime. This may provide the reheating mechanism of an ekpyrotic brane universe. We evaluate a production rate of particles confined to the domain wall. The energy density of created particles is given as $\rho \approx 20\bar{g}^4 N_b\, m_\eta^4$ where $\bar{g}$ is a coupling constant of particles to a domain-wall scalar field, N_b is the number of bounces at the collision and m_η is the fundamental mass scale of the domain wall. It does not depend on the width d of the domain wall, although the typical energy scale of created particles is given by $\omega \sim 1/d$. The reheating temperature is evaluated as $T_{\rm R} \approx 0.88\, \bar{g}\, N_b^{1/4}$. In order to have the baryogenesis at the electro-weak energy scale, the fundamental mass scale is constrained as $m_\eta \gtrsim 1.1 \times 10^7$ GeV for $\bar{g} \sim 10^{-5}$.

1 Introduction

Inflation not only gives some picture of the earlier stage of the universe before the big bang but also it seems to be supported by some recent observational data on CMB. While, it is still unclear what the origin of inflaton is. So far, there is no convincing link with fundamental unified theories such as string/M-theory.

On the other hand, recently a new paradigm on the early universe has been proposed, the so-called brane world. Based on such a new world picture, many cosmological scenarios have been studied. In such a brane world scenario, for resolving the key theoretical problems in the big bang theory, a new idea of the early universe has been proposed, which is called the ekpyrotic scenario [1]. It is based on a collision of two cold branes. This scenario is that the two branes approach each other and then collide. The energy is dissipated on the brane and the big bang universe starts. Since this scenario is not only motivated by the fundamental unified theory but also may resolve the key theoretical problems, it would be very attractive. There has been much discussion about density perturbations to see whether this scenario is really a reliable scenario. On the other hand, even though there are some works, the reheating process itself in this scenario has not been so far investigated in detail. Hence, we study how we can recover the hot big bang universe after the collision of the branes. Here we investigate quantum creation of particles, which are confined to the brane, at the collision of two branes [3]. It may be difficult to deal properly with the collision of two branes in basic string theory. So we adopt a domain wall constructed by some scalar field as a brane, and analyze the collision of two domain walls in a 5-D bulk spacetime. In order to analyze particle creation at the brane collision, we consider the simplest situation, that is we discuss the collision of two domain walls collide in 5-D Minkowski spacetime.

2 Collision of two domain walls

We study the collision of two domain walls in 5-D Minkowski spacetime. To construct a domain wall structure, we adopt a real scalar field Φ with a double-well potential. The equation of motion for Φ in

[1] E-mail:takamizu@gravity.phys.waseda.ac.jp
[2] E-mail:maeda@gravity.phys.waseda.ac.jp

5-D is given by

$$\ddot{\Phi} - \Phi'' + \lambda\Phi(\Phi^2 - 1) = 0\,, \tag{1}$$

where $\dot{}$ and $'$ denote $\partial/\partial t$ and $\partial/\partial y$ (y: 5-th direction), respectively.

Eq. (1) has a static kink solution (K) , called a domain wall, which is described by

$$\Phi_K(y) = \tanh\left[\frac{y}{d}\right]\,, \tag{2}$$

where $d = \sqrt{2/\lambda}$ is the thickness of the wall. We also find another solution, that is, the antikink solution, which is obtained from Eq. (2) by reflecting the spatial coordinate y. When a domain wall moves with constant speed v in the y direction, we obtain correspoding solution by boosting Eq. (2) as $\Phi_v(y,t)$.

In order to discuss the collision of two domain walls, we first have to set up the initial data. We can construct such an initial data as follows. Provide a kink solution at $y = -y_0$ and an antikink solution at $y = y_0$, which are separated by a large distance and approaching each other with the same speed v. We then obtain the following explicit profile;

$$\Phi(y,0) = \Phi_v(y + y_0, 0) - \Phi_{-v}(y - y_0, 0) - 1\,. \tag{3}$$

The initial value of $\dot{\Phi}$ is also given by the above equation. Using these initial values, we solve the dynamical equation (1) numerically. We have two free parameters in our simulation of the two-wall collision, i.e. a wall thickness $d = \sqrt{2/\lambda}$ and an initial wall velocity v. The collision of two walls has been discussed in 4-D Minkowski space[2]. Although we discuss the domain wall collision in 5-D Minkowski space, our basic equations are exactly the same as the cited case, and we find the same results as there.

Let us show the numerical results for typical initial velocities, $v = 0.4, 0.2$. Here we show the latter case. The evolution of Φ is depicted in Fig. 1, while that of the energy density is shown in Fig. 2. From Figs. 2, we find some peaks in the energy density, by which we define the positions of moving walls ($y = \pm y_W(t)$). Where the initial velocity $v = 0.2$, the collision occurs twice, while where $v = 0.4$, the collision occurs once. In particular, the results are very sensitive to the initial velocity v.

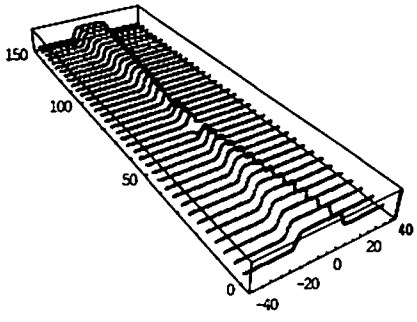


Figure. 1

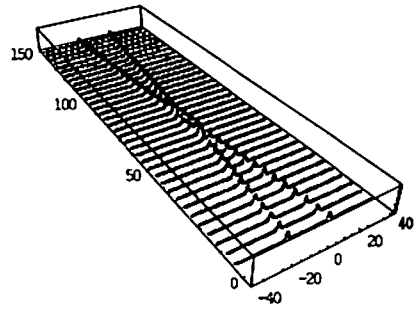


Figure. 2

Figure 1: Collision of two domain walls where the initial velocity $v = 0.2$. The time evolution of the scalar field Φ is shown from $t = 0$ to 150. We find that collision occurs twice, at $t \approx 58$ and 77. We set $\lambda = 1.0$.

Figure 2: The time evolution of scalar field energy density in the case of Fig. 1. From this figure, we find clearly that collision occurs twice.

3 Particle production on a moving domain wall

Once we find the solution of colliding domain walls, we can evaluate the time evolution of a scalar field on the domain wall. Since we assume that we are living on one domain wall, we are interested in production of a particle confined to the domain wall. We assume that there is some coupling between a 5-D scalar

field Φ that is responsible for the domain wall and a particle on the domain wall. Because the value of the scalar field changes with time, we expect quantum particle production to occur. This may be important to a reheating mechanism for the colliding domain walls.

Hence we have to know the value of the scalar field Φ on the domain wall, i.e. $\Phi_{\rm W}(\tau) = \Phi(t, y_{\rm W}(t))$. Since the wall is moving in a 5-D Minkowski space, we have to use the proper time τ of the wall, which is given by

$$\tau = \int_0^t dt \sqrt{1 - \dot{y}_{\rm W}^2(t)} \ , \tag{4}$$

when we estimate the particle production in our 4-D domain wall. Let us consider a particle on the domain wall described by a 4-D scalar field ψ. Although the confined scalar field may also be extended in the 5-th direction because the domain wall has a finite width, we assume here that this scalar field is 4-D, which means that it has the value only at the position of the domain wall ($y = y_W(t)$). This ansatz may be justified [3]. Assuming an interaction with the scalar field Φ as $\sim \bar{g}^2 \Phi_{\rm W}^2 \psi^2$, where $\bar{g}$ is a coupling constant, we find the dynamical equation for ψ, given by the 4-D equation as

$$\frac{\partial^2 \psi}{\partial \tau^2} - \nabla^2 \psi + \bar{g}^2 \, \Phi_{\rm W}^2(\tau) \, \psi = 0 \ , \tag{5}$$

where $\Phi_{\rm W}$ gives the potential term in ψ field.

Once we find the basic equation as Eq. (5), it is easy to quantize the scalar field ψ because our background spacetime is 4-D Minkowski space. Approaching a usual canonical quantization scheme, as a result, the number density of produced particles is given by

$$n = \int |\beta_k|^2 d^3\boldsymbol{k} \ , \tag{6}$$

where β is the Bogolubov coefficient. Now we estimate the particle production by the domain wall collision numerically.

We can summarize our numerical results by the following empirical formula

$$n \approx 25 d \bar{g}^4 N_b \ , \tag{7}$$

$$\rho \approx 20 \bar{g}^4 N_b \ , \tag{8}$$

where N_b denotes the number of bounces, i.e., if $v = 0.2$, $N_b = 2$. If the energy of the particles is thermalized by interaction, we can estimate the reheating temperature by

$$\rho = \frac{\pi^2}{30} g_{\rm eff} T_{\rm R}^4 \ , \tag{9}$$

where $g_{\rm eff}$ is the effective number of degrees of freedom of particles. Hence we find the reheating temperature by the domain wall collision as

$$T_{\rm R} = \left(\frac{\pi^2}{30}\right)^{-1/4} g_{\rm eff}^{-1/4} \rho^{1/4} \approx 0.88 \times \left(\frac{g_{\rm eff}}{100}\right)^{-1/4} \bar{g} \, N_b^{1/4} .$$

In order to see more details, we show a spectrum of the produced particles of number density n, i.e.

$$n = \int_0^\infty dk \ n_k \quad \text{with} \quad n_k = 4\pi |\beta_k|^2 k^2 \ . \tag{10}$$

The spectrum n_k is well fitted as a Gaussian distribution as

$$n_k \approx 4\pi A e^{-\frac{k^2}{2k_0^2}} \ , \tag{11}$$

where $k_0 = 0.73$ and $A = 3.12 \times 10^{-8}$. These parameters can be described by physical quantities as $k_0 \approx 1/d$ and $A \approx \Phi_0 d^2 \bar{g}^4$. The reason is well understood. $k_0 \approx 1/d$ means that the typical wave number

is given by the width of the scalar field when domain walls collide. As for β, it corresponds to the " reflection " coefficient of the " potential " given by Φ_W. It will be proportional to the coupling constant $\bar{g}^2$, and the reflection rate ($|\beta|^2$) will be related to the potential depth Φ_0 and the square of the width d^2. Integrating the fitting spectrum (11), we obtain

$$n = \int_0^\infty n_k dk = (2\pi)^{3/2}\Phi_0 d\bar{g}^4 \approx 25 d\bar{g}^4 , \tag{12}$$

$$\rho = \int_0^\infty n_k \omega_k dk = 4\pi\Phi_0\bar{g}^4 \approx 20\bar{g}^4 , \tag{13}$$

whose values are exactly the same as those obtained by numerical integration in the case with one bounce (see Eqs. (7) and (8)). We expect that they are enhanced by the factor N_b when we find N_b bounces at the collision. Therefore, although we obtain particle creation numerically, the result is easily understood and summarized by a simple formula.

4 Conclusion

We have studied particle production at the collision of two domain walls in 5-D Minkowski spacetime. This may provide the reheating mechanism of an ekpyrotic brane universe. We evaluated the production rate for particles confined to the domain wall. The energy density of created particles was approximated as $\rho \approx 4\pi\Phi_0\bar{g}^4 N_b$ where Φ_0 is the maximum amplitude of Φ_W, N_b is the number of bounces at the collision, and $\bar{g}$ is a coupling constant of a particle to the scalar field of a domain wall. If this energy is converted into standard matter fields, we find the reheating temperature as $T_R \approx 0.88 \times \bar{g}\, N_b^{1/4} (g_{\rm eff}/100)^{-1/4}$. We find that the particle creation is affected more greatly by the coupling constant $\bar{g}$ than the other two parameters v and λ. The initial velocity changes the collision process, that is, the number of bounces at the collision, but this is less sensitive to the temperature. The thickness of a domain wall d (or a self-coupling constant λ) changes the width of potential $\Phi_w^2(\tau)$ of a particle field ψ, and it changes the typical energy scale of created particles, which is estimated as $\omega \sim 1/d$.

In order to produce a successful reheating, a reheating temperature must be higher than 10^2 GeV, because we wish to explain the baryon number generation at the electro-weak energy scale. Since Eq. (10) is written in the following form;

$$\begin{aligned} m_\eta &\approx 1.1 N_b^{-1/4}\bar{g}^{-1} T_R \\ &\approx 1.1 \times 10^7 [\mathrm{GeV}]\; N_b^{-1/4} \left(\frac{\bar{g}}{10^{-5}}\right)^{-1} \left(\frac{T_R}{10^2 \mathrm{GeV}}\right) , \end{aligned} \tag{14}$$

we find a constraint on the fundamental energy scale m_η as $m_\eta \gtrsim 1.1 \times 10^7$ GeV for $\bar{g} = 10^{-5}$ and $m_\eta \gtrsim 1.1 \times 10^4$ GeV for $\bar{g} = 10^{-2}$, which are slightly larger than TeV scale. Here we assume $g_{\rm eff} = 100$. We showed that particle production at the two-wall collision may provide a successful mechanism for reheating in the ekpyrotic universe. Here, we have not taken account of effects from background spacetime. We are planning to study how such a generalization affects the present results about particle creation at the collision.

References

[1] J. Khoury, B. A. Ovrut, P. J. Steinhardt and N. Turok, Phys. Rev. D 64, 123522 (2001).

[2] P. Anninos, S. Oliveira and R. A. Matzner, Phys. Rev. D 44, 1147 (1991).

[3] Y. i. Takamizu and K. i. Maeda, D 70, 123514 (2004) [arXiv:hep-th/0406235].

Gravitational Waves from a spinning particle with time domain approach

Kenta Kiuchi[a,1], Kei-ichi Maeda[a,b,c,2]

[a] *Department of Physics, Waseda University, 3-4-1 Okubo, Shinjuku-ku, Tokyo 169-8555, Japan*
[b] *Advanced Research Institute for Science and Engineering, Waseda University, Shinjuku, Tokyo 169-8555, Japan*
[c] *Waseda Institute for Astrophysics, Waseda University, Shinjuku, Tokyo 169-8555, Japan*

Abstract

To investigate how chaos affects gravitational waves, we study the gravitational waves from a spinning test particle moving around the Schwarzschild black hole, which is a typical chaotic system. We estimate the emitted gravitational waves by the Regge-Wheeler-Zerilli equation. As a result, We find a striking difference in the energy spectra of the gravitational waves. The spectrum for a strongly chaotic orbit of a spinning particle, contains various frequencies, while some characteristic frequencies appear in a weakly chaotic case.

1 Introduction

For a future gravitational wave astronomy, it is very important to make theoretical templates of gravitational waves from any kinds of relativistic dynamical system. Here, we focus on gravitational waves from a chaotic dynamical system. It is motivated as follows. Chaos appears universally in nature and it is expected to explain various nonlinear phenomena. Because chaos indicates unpredictability of motion of objects, it comes into a question whether or not that it is possible to extract useful information from a chaotic system. Therefore, we believe that it is necessary to study chaos in general relativity. Because chaos will occur in a realistic strong gravitational field described by general relativity.

As a concrete example, we adopt a spinning test particle orbiting around a non-rotating black hole. The orbits of the spinning particle can be chaotic. To solve the perturbation equation, that is the Regge-Wheeler-Zerilli equation, we use the time domain approach with the narrow Gaussian approximation [1]. We analyze an energy flux, a wave form and an energy spectrum of a gravitational wave.

2 Perturbation Equation

In our previous work [2], we use the multipole expansion of the gravitational field, in which the two approximation, the weak field approximation and the slow motion approximation, are contained. But in the system we set up, which is a spinning test particle orbiting around a black hole, the gravitational field is strong because of the existence of the black hole and the particle moves very fast $v \approx 0.1c$. Therefore, we have to use the black hole perturbation theory to estimate a gravitational wave from such a system more precisely.

2.1 Regge-Wheeler-Zerilli equation in time domain

In this work, we solve the Regge-Wheeler-Zerilli equation with the time domain approach. The form of this equation is as follows.

$$\left[-\frac{\partial^2}{\partial t^2}+\frac{\partial^2}{\partial r_*^2}-V_l^{(\pm)}(r)\right]\psi_{lm}^{(\pm)}(t,r)=S_{lm}^{(\pm)}(t,r), \tag{1}$$

[1] E-mail:kiuchi@gravity.phys.waseda.ac.jp
[2] E-mail:maeda@gravity.phys.waseda.ac.jp

	TD	FD	Error
Total	2.03×10^{-4}	2.03×10^{-4}	0.2%

Table 1: The energy flux up to $l = 5$ for a circular orbit, calculated using our time domain (TD) code, are compared with fluxes calculated by using the frequency approach (FD). Here we chose $r_{circular} = 7.9456M$. The energy fluxes are in the units of $(M/\mu)^2$.

where (-) and (+) means the odd and even parity, respectively and $V_l^{(\pm)}(r)$ is the Regge-Wheeler-Zerilli potential defined as

$$V_l^{(-)}(r) = \frac{r-2M}{r}\left(\frac{2(\lambda+1)}{r^2} - \frac{6M}{r^3}\right), \tag{2}$$

$$V_l^{(+)}(r) = \left(1-\frac{2M}{r}\right)\frac{2\lambda^2(\lambda+1)r^3 + 6\lambda^2 M r^2 + 18\lambda M^2 r + 18M^3}{r^3(\lambda r + 3M)^2}, \tag{3}$$

where $\lambda = (l+2)(l-1)/2$.

2.2 Boundary condition and initial condition

To solve Eq. (1) numerically, we impose the pure outgoing boundary condition at the infinity and the pure ingoing one at the event horizon. We also set the initial conditions as

$$\psi(0,r) = 0, \tag{4}$$

$$\left.\frac{\partial\psi}{\partial t}\right|_{t=0} = 0. \tag{5}$$

Note that because these boundary conditions and initial conditions are not perfect, errors due to the reflection from these boundaries bounce back into the computational domain and an artificial burst of radiation is generated. To avoid these problems, we make the computational domain large enough that any numerical reflections will note take it back to the point where we compute the waveforms and the energy flux, typically $r_*^{E.H.} = -40M$ and $r_*^{\infty} = 5000M$.

2.3 Narrow Gaussian approximation

The source term of Eq. (1) contains the delta function because of the presence of the test particle. To avoid the divergence, we approximate the delta function with the narrow Gaussian function,

$$\delta(x - x(t)) \approx \frac{1}{\sqrt{2\pi}\sigma}\exp\left(-\frac{(x-x(t))^2}{2\sigma^2}\right) \qquad \text{for } \sigma \text{ small.} \tag{6}$$

3 Code Check

To check the accuracy of our code, we compute an energy flux from a spinless test particle in a circular orbit and compare the result to that of the previous work by Poisson with the frequency domain approach. The energy flux for each mode is calculated by

$$\frac{dE_{lm}}{dt} = \frac{1}{64\pi}\frac{(l+2)!}{(l-2)!}\left[\left|\frac{\partial\psi^{(+)}}{\partial t}\right|^2 + 4|\psi^{(-)}|^2\right]. \tag{7}$$

We chose a circular orbit radius as $7.456M$ and an observer position as $r_*^{obs} = 1500M$. The result is shown in the Table 1. The relative error is less than 1 %. Therefore, we confirm our code works well.

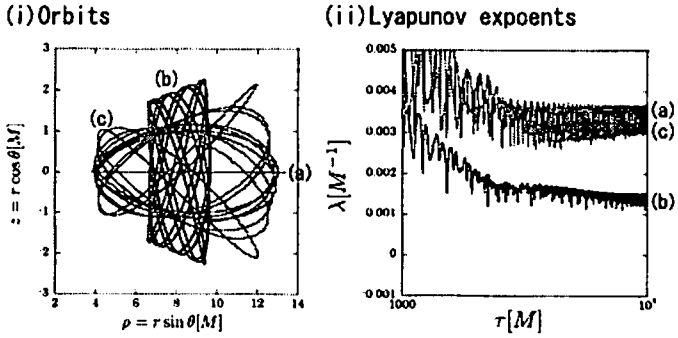


Figure 1: (i) Three kinds of trajectory. We set the parameters as $(E, J_z, S) = (0.947\mu, 4.0\mu M, 1.0\mu M)$ and initial conditions as $(r_a, \eta_a) = (7.0M, 0.5\pi)$, $(r_b, \eta_b) = (7.0M, 0.25\pi)$ and $(r_c, \eta_c) = (3.9M, 0.43\pi)$, respectively, where η represents an initial direction of the spin. (ii) Lyapunov exponents for each orbits. This figure shows that the orbit (a) is strongly chaotic. On the other hand, the orbit(b) is weakly chaotic.

l	(a)	(b)	(c)
2	1.01×10^{-3}	1.68×10^{-4}	7.98×10^{-4}
3	2.22×10^{-4}	2.95×10^{-5}	1.78×10^{-4}
4	6.16×10^{-5}	6.37×10^{-6}	5.56×10^{-5}
5	1.53×10^{-5}	1.03×10^{-6}	1.49×10^{-5}
total	1.31×10^{-3}	2.05×10^{-4}	1.05×10^{-3}

Table 2: The energy fluxes for orbit (a), (b) and (c). The energy fluxes are in the units of $(M/\mu)^2$. From these values, we find that the more chaotic the orbit is, the more the gravitational wave emits.

4 Gravitational wave from a spinning particle

Subsequently, we estimate gravitational waves from a spinning particle with our time domain code.

As equations of motion of a spinning particle, we adopt the Papapetrou-Dixon equations. From the analysis by Suzuki and Maeda [3], we chose three kinds of trajectories shown in Fig. 1 (i). We also calculate Lyapunov exponents for each orbits and show in Fig. 1 (ii). Comparing the values of the Lyapunov exponents, we find that the orbit (a) is strongly chaotic and the orbit (b) is weakly chaotic. The energy momentum tensor of spinning particle in tetrad frame is given by

$$T^{ab} = \int d\tau \Big\{ [p^{(a}v^{b)} + \omega_{dc}{}^{(a}v^{b)}S^{dc} - \omega_{dc}{}^{(a}S^{b)d}v^{c}] \frac{\delta^{(4)}(x - z(\tau))}{\sqrt{-g}} - \frac{1}{\sqrt{-g}} \partial_\mu [S^{\mu(a}v^{b)}\delta^{(4)}(x - z(\tau))] \Big\}, \quad (8)$$

where $z(\tau)$ express the position of the particle and $\omega_{ab}{}^{c}$ is the Ricci rotation. Using this tensor, we calculate the expansion coefficients of the tensor harmonics and construct the source term of Eq. (1). Here, we omit the explicit forms of the source term.

We actually perform the numerical integration of Eq. (1) and estimate the energy fluxes, wave forms and energy spectra for the each orbits. In Table 2, we show the energy fluxes and find that the amounts of the energy flux correspond to the values of the Lyapunov exponents ($dE_a/dt > dE_c/dt > dE_b/dt \leftrightarrow \lambda_a > \lambda_c > \lambda_b$) We also show wave forms for each orbits in Fig. 2 (I). These figures show that there are no differences between the wave forms. From the date of the wave forms, we estimate the energy spectra and show the results in the Fig. 2 (II). From these figures, we find there are clear differences in the energy spectra.

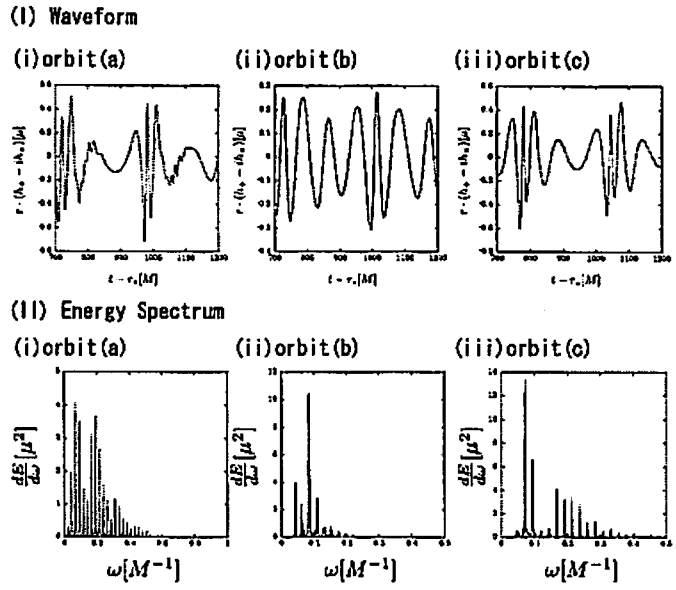


Figure 2: (I) Wave forms from orbit (a), (b) and (c). In these wave forms, we cannot find clear differences. (II) Energy spectra for each orbits. These energy spectra show a feature, which is the more chaotic the orbit is, the more frequencies the energy spectrum contains.

5 Conclusion

At last, we summarize our works. We estimate the gravitational waves from a spinning test particle traveling around the Schwarzschild black hole. To estimate the gravitational waves, we solve the Regge-Wheeler-Zerilli equation by using the time domain approach. We actually calculate the energy fluxes, the wave forms and the energy spectrum. As a result, we find three interesting points. One is that the more chaotic the particle orbit is, the more the gravitational wave emits. Another is gravitational wave forms do not contain the clear difference. From the wave forms, we cannot distinguish which one is chaotic. The other point is the energy spectrum shows the clear difference. For the strongly chaotic case, we find a continuous energy spectrum with several peaks. While, in the case of weakly chaotic case, the spectrum contains the discrete characteristic frequencies. This result consist our previous work [2].

When the gravitational waves are detected and the energy spectrum is determined by observation, not only the astrophysical parameters ,e.g., the mass, the angular momentum, and the spin are determined but also some fundamental physics such as relativistic nonlinear dynamics could be discussed.

References

[1] G. Khanna, gr-qc/0309107 (2003)

[2] K. Kiuchi and K. Maeda, Phys. Rev. D **70**, 064036 (2004)

[3] S. Suzuki and K. Maeda, Phys. Rev. D **55**, 4848 (1997)

Generalized cosmological scaling solutions

Shuntaro Mizuno[a] [1], Edmund J. Copeland[b] [2], Seung-Joo Lee[b] [3], James E. Lidsey[c] [4]

[a] *Department of Physics, Waseda University, Okubo 3-4-1, Shinjuku, Tokyo 169-8555, Japan*
[b] *Department of Physics and Astronomy, University of Sussex, Falmer, Brighton BN1 9QJ, UK*
[c] *Astronomy Unit, School of Mathematical Sciences, Queen Mary, University of London, Mile End Road, London, E1 4NS, UK*

Abstract

Motivated by the recent interest in cosmologies arising out of energy density modifications to the the Friedmann equation, we analyse the scaling behaviour for a broad class of these cosmologies comprising of scalar fields and background fluid sources. In particular we determine the corresponding scalar field potentials which leads to attractor scaling solutions. We show how a number of recent proposals can be thought of as being dual to one another, and determine the conditions under which solutions can be considered as being dual.

1 Introduction

The Friedmann equation is one of the cornerstones of modern cosmology relating the expansion of the Universe to the total energy density within it. It forms the starting point for almost all investigations in cosmology. However, over the past few years possible corrections to the Friedmann equation have been derived in a number of contexts, generally inspired by braneworld investigations. These corrections are often of a form that involves the total energy density ρ, and are such that they tend to play a role early in the history of the Universe, fading away as we enter the late, post-nucleosynthesis universe (although that is not always the case as we shall see). Up to now, the different models have been presented in the literature without any attempt to relate them. In this paper, by introducing a generalised form for the correction, we will provide a formalism which allows us to relate a large class of such modified Friedmann cosmologies. Assuming the total energy density is comprised of a canonical scalar field ϕ with potential $V(\phi)$ and some form of background radiation we will demonstrate how the existence of scaling solutions determines the form of $V(\phi)$, and in doing so we will establish a direct relation between the form of the potential and the functional form of the modification of the Friedmann equation.

2 Equations of motion

We consider spatially flat Friedmann-Robertson-Walker (FRW) cosmologies such that the dynamics is determined by an effective Friedmann equation of the form

$$H^2 = \frac{8\pi}{3m_4^2}\rho L^2(\rho). \tag{1}$$

Modifications to standard relativistic cosmology are parametrized by the function $L(\rho)$ and this is assumed to be positive-definite without loss of generality.

We will investigate models where the universe is sourced by a self-interacting scalar field ϕ with potential $V(\phi)$ together with a barotropic fluid with equation of state $P_\gamma = (\gamma - 1)\rho_\gamma$.

In standard cosmology the stability of scaling solutions is analyzed by introducing the variables [1]:

$$X_{\rm CLW} \equiv \sqrt{\frac{4\pi}{3m_4^2}}\frac{\dot{\phi}}{H}, \quad Y_{\rm CLW} \equiv \sqrt{\frac{8\pi}{3m_4^2}}\frac{\sqrt{V}}{H}, \tag{2}$$

[1] E-mail:shuntaro@gravity.phys.waseda.ac.jp
[2] E-mail:E.J.Copeland@sussex.ac.uk
[3] E-mail:S.J.Lee@sussex.ac.uk
[4] E-mail:j.e.lidsey@qmul.ac.uk

and rewriting the field equations as an autonomous system. Following [2, 3], we define the new pair:

$$X \equiv \frac{\dot{\phi}}{\sqrt{2\rho}}, \quad Y \equiv \frac{\sqrt{V}}{\sqrt{\rho}}, \tag{3}$$

that are related to those of Eq. (2) by $\frac{X}{X_{CLW}} = \frac{Y}{Y_{CLW}} = \epsilon L$, where $\epsilon = \pm 1$ for expanding and contracting universes, respectively. In what follows, we consider expanding models unless otherwise stated.

When expressed in terms of the new variables, the equations of motion can be written in the form:

$$X' = -3X + \epsilon\lambda\sqrt{\frac{3}{2}}Y^2 + \frac{3}{2}X[2X^2 + \gamma(1 - X^2 - Y^2)], \tag{4}$$

$$Y' = -\epsilon\lambda\sqrt{\frac{3}{2}}XY + \frac{3}{2}Y[2X^2 + \gamma(1 - X^2 - Y^2)], \tag{5}$$

$$\lambda' = -\epsilon\sqrt{6}\lambda^2(\Gamma - 1)X + 3\lambda[2X^2 + \gamma(1 - X^2 - Y^2)]\rho\frac{d}{d\rho}[\ln L(\rho)], \tag{6}$$

where $\lambda \equiv -\frac{1}{L}\frac{m_4}{\sqrt{8\pi}}\frac{dV/d\phi}{V}$, $\Gamma \equiv V\frac{d^2V/d\phi^2}{(dV/d\phi)^2}$, and a prime denotes differentiation with respect to $N \equiv \ln a$. As in Ref. [6] Eqs. λ and Γ generalize the expressions introduced in Refs. [1, 3, 4, 5]. In particular, λ is related to the parameter $\lambda_{CLW} \equiv -\frac{m_4}{\sqrt{8\pi}}\frac{dV/d\phi}{V}$ introduced in Ref. [1] such that $\frac{\lambda}{\lambda_{CLW}} = \frac{1}{L}$.

Eqs. (4-6) exhibit an important property. For the case where λ is constant, they have an identical form to that of the plane-autonomous system of standard relativistic cosmology that is formulated in terms of the variables $\{X_{CLW}, Y_{CLW}, \lambda_{CLW}\}$. This duality immediately implies that the system (4-5) admits an identical set of critical points to that of the standard scenario when these solutions are expressed in terms of the variables $\{X, Y, \lambda\}$.

A further consequence of such a duality is that the stability of each fixed point solution can be determined directly from the stability analysis of Ref. [1]. In total, there are five critical solutions to Eqs. (4) and (5) where the variables $\{X, Y, \lambda\} = \{X_c, Y_c, \lambda_c\}$ are constants. Three of these represent the unstable solutions $(X_c = 1,\ Y_c = 0)$,$(X_c = -1,\ Y_c = 0)$, $(X_c = 0,\ Y_c = 0)$ for all values of λ and γ. The value of λ determines the nature of the other two points. For $\lambda^2 > 3\gamma$, there exists an attractor solution $(X_c = \sqrt{\frac{3}{2}}\frac{\gamma}{\lambda},\ Y_c = \sqrt{\frac{3(2-\gamma)\gamma}{2\lambda^2}})$, where the effective adiabatic index of the scalar field, defined by $\gamma_\phi \equiv 2X^2/(X^2 + Y^2)$ satisfies the condition $\gamma_\phi = \gamma$. For this late-time attractor solution, the relative contribution of the scalar field's energy density to the total energy density of the universe is constant, $\Omega_{\phi c} \equiv X^2 + Y^2 = 3\gamma/\lambda^2$, and consequently, the energy densities of the scalar field and fluid redshift at the same rate as the universe expands. The fifth critical point arises if $\lambda^2 < 6$ and is given by $(X_c = \frac{\lambda}{\sqrt{6}},\ Y_c = \sqrt{1 - \frac{\lambda^2}{6}})$. This corresponds to the case where the scalar field dominates the fluid and has an effective adiabatic index $\gamma_\phi = \lambda^2/3$. The solution is stable if $\gamma_\phi < \gamma$, i.e., $\lambda^2 < 3\gamma$.

3 General Conditions for Scaling Solutions

Since the relation between the standard and modified FRW cosmologies involves the correction function $L(\rho)$, the scalar field potential that gives rise to the fixed point attractor solutions in a given generalized scenario will depend on the specific form of this function. In particular, the potential will differ from the purely exponential form that leads to scaling solutions in the conventional FRW model. It is important, therefore, to establish the correspondence between the modified Friedmann equation and the scaling potential.

It can be shown by direct substitution that both sets of critical points represent solutions to the field equations (4)-(6) of the form $X' = Y' = \lambda' = 0$ if the relation $\Gamma = 1 + \rho\frac{d}{d\rho}[\ln L(\rho)]$ is satisfied.

We find that a necessary and sufficient condition on the scalar field potential if the solution is to represent a scaling solution for a given choice of correction function $L(\rho)$,

$$\int \frac{d\rho}{\rho L} = -\frac{\sqrt{8\pi}\lambda}{m_4}\phi, \tag{7}$$

where one of the integration constants has been set to zero without loss of generality by performing a linear shift in the value of the scalar field and the constant of proportionality on the right-hand side follows by requiring consistency with λ. Once $\rho(\phi)$ is obtained for scaling solutions, $V(\phi)$ can be lead immediately.

It is also of interest to determine the evolution of the scale factor for a given class of scaling solutions. Since X_c is a non-zero constant for these solutions, Eq. (3) implies that the scalar field is a monotonically varying function of proper time ($\dot{\phi} \neq 0$). It is natural, therefore, to view the value of the field as the dynamical variable of the system and to express all time-dependent parameters in terms of this variable. In general, the definition of the Hubble parameter can be expressed in the form,

$$3H^2 = -\frac{1}{a}\frac{da}{d\phi}\frac{d\rho_\phi}{d\phi}, \tag{8}$$

and substituting Eq. (8) into Eq. (1) implies that the Friedmann equation can be expressed in the form $\frac{da}{d\phi}\frac{d\rho}{d\phi} = -\frac{8\pi}{\Omega_\phi m_4^2} a\rho L^2(\rho)$. Defining a new variable $b(\phi) \equiv \exp\left[\Omega_\phi \int^\rho d\rho \frac{1}{\rho L^2(\rho)}\right]$ then simplifies the above to $\frac{da}{d\phi}\frac{db}{d\phi} = -\frac{8\pi}{m_4^2} ab$ and the scale factor is then determined up to a single quadrature:

$$a(\phi) = \exp\left[-\frac{8\pi}{m_4^2}\int^\phi d\phi b(\phi)\left(\frac{db}{d\phi}\right)^{-1}\right]. \tag{9}$$

Thus, for a given cosmological scenario characterized by the correction function $L(\rho)$, the potential (and equivalently the total energy density) yielding the scaling solution is determined by integrating Eq. (7). Integration then yields the dependence of $b(\phi)$ on the scalar field and the evolution of the scale factor follows after integration of Eq. (9). Finally, the time-dependence of the scale factor can in principle be deduced:

$$t = -\frac{\sqrt{24\pi}}{\Omega_\phi m_4}\int^\phi d\phi L(\phi)\rho^{1/2}(\phi)\left(\frac{d\rho}{d\phi}\right)^{-1}, \tag{10}$$

and inverting the result.

4 Duality between Scaling Solutions

$\frac{da}{d\phi}\frac{db}{d\phi} = -\frac{8\pi}{m_4^2} ab$ is invariant under the simultaneous interchange $a(\phi) \rightarrow b^p(\phi)$, $b(\phi) \rightarrow a^{1/p}(\phi)$, where p is an arbitrary constant. This symmetry implies that a given scaling solution may be employed as a seed to generate a new scaling cosmology for a different Friedmann equation and associated scalar field potential. To be specific, let us consider the scaling solution parametrized by the functions $\{a_+(\phi), b_+(\phi), \rho_+(\phi)\}$ that arises for a specific choice of correction function $L_+(\rho)$. We now denote the 'dual' scaling solution as $\{a_-(\phi), b_-(\phi), \rho_-(\phi)\}$ and assume an *ansatz* of the form $b_-(\phi) = [a_+(\phi)]^{1/p}$. The new scale factor is then determined from Eq. (9):

$$a_-(\phi) = \exp\left[-\frac{8\pi p}{m_4^2}\int d\phi a_+(\phi)\left(\frac{da_+}{d\phi}\right)^{-1}\right]. \tag{11}$$

However, since the function $a_+(\phi)$ is itself a solution to the Friedmann equation, Eq. (11) simplifies after integration to $a_-(\phi) = [b_+(\phi)]^p$ modulo an arbitrary (constant) prefactor.

We may now determine the condition that the dual correction function $L_-(\rho)$ must satisfy for the above solution to also represent a scaling solution satisfying Eq. (7). If we assume that the two solutions $a_\pm(\phi)$ represent scaling solutions characterized by $\lambda_\pm$, respectively, Eq. (7) implies that $\frac{1}{\lambda_+\rho_+ L_+}\frac{d\rho_+}{d\phi} = \frac{1}{\lambda_-\rho_- L_-}\frac{d\rho_-}{d\phi}$. After some calculations, the condition $\frac{1}{\rho_+^2 L_+^2}\left(\frac{d\rho_+}{d\phi}\right)^2 = -\frac{8\pi}{\Omega_\phi^2 m_4^2}\frac{\lambda_+}{\lambda_- p} L_- L_+$ is obtained. Consistency with Eq. (7) therefore implies that a necessary and sufficient condition for the dual cosmology $\{a_-(\phi), L_-(\phi)\}$ to represent a scaling solution is that *the correction functions arising in the respective Friedmann equations must be proportional to the inverse of each other when both are expressed as functions of the scalar field:* $L_+(\phi)L_-(\phi) = -p\lambda_+\lambda_-\Omega_\phi^2$. It is interesting that when $p\Omega_\phi^2\lambda_+\lambda_- = -1$, the standard relativistic cosmology ($L = 1$) is the self-dual model.

5 Summary

In this paper we have brought together a number of recent approaches to cosmology which involve modifications of the Friedmann equation. By introducing the general function $L(\rho)$ as the way of parametrising the modification, we have been able to establish the conditions under which the new system enters scaling solutions. Considering the case where the energy density is comprised of a scalar field and background barotropic fluid, we have obtained the general relationship that would have to be satisfied between the evolving scalar field and $L(\rho)$. This has allowed us to relate solutions which would otherwise appear quite distinct, including those involving collapsing and expanding cosmologies.

Moreover, the duality can directly relate singular and non-singular cosmologies. To illustrate this property, consider a particular scaling solution $a_+(\phi)$ that is singular in the sense that the scale factor vanishes at $a_+(0) = 0$. (The value of the scalar field can be chosen to be $\phi = 0$ without loss of generality). Suppose, however, that the logarithmic derivative of the scale factor with respect to the field is non-zero at this point, $d\ln a_+/d\phi|_0 \neq 0$, and furthermore, that the scale factor is a monotonic function with a finite first derivative for all physical (non-zero) values of the field.

The qualitative behaviour of the dual solution, $a_-(\phi)$, is then determined from Eq. (11). If we define a new parameter $\epsilon(\phi) \equiv [d\ln a/d\phi]^{-1}$, the value of the scale factor is simply given by the area under the curve $\epsilon_+(\phi)$, where the field evolves from zero to some value ϕ. (We are assuming implicitly that $\dot{\phi} > 0$ and $p < 0$ again without loss of generality). However, due to the exponential nature of Eq. (11) the initial value of the dual scale factor is *non-zero* and this results in a non-singular background.

For the concrete applications and further discussions about this article, please see Ref. []

Acknowledgments

SM would like to thank Kei-ichi Maeda for continuous encouragement and is grateful to the University of Sussex for their hospitality during a period when this work was initiated.

References

[1] E. J. Copeland, A. R. Liddle and D. Wands, Phys. Rev. D **57**, 4686 (1998).

[2] G. Huey and J. E. Lidsey, Phys. Lett. B **514**, 217 (2001).

[3] G. Huey and R. K. Tavakol, Phys. Rev. D **65**, 043504 (2002).

[4] A. de la Macorra and G. Piccinelli, Phys. Rev. D **61**, 123503 (2000).

[5] R. R. Caldwell, R. Dave and P. J. Steinhardt, Phys. Rev. Lett. **80** (1998) 1582; I. Zlatev, L. M. Wang and P. J. Steinhardt, Phys. Rev. Lett. **82**, 896 (1999); P. J. Steinhardt, L. M. Wang and I. Zlatev, Phys. Rev. D **59**, 123504 (1999).

[6] S. C. C. Ng, N. J. Nunes and F. Rosati, Phys. Rev. D **64**, 083510 (2001).

[7] Mizuno, S. J. Lee and E. J. Copeland, Phys. Rev. D **70**, 043525 (2004); E. J. Copeland, S. J. Lee, J. E. Lidsey and S. Mizuno, arXiv:astro-ph/0410110.

General Relativity and Gravitation
—BPS pp-wave brane Cosmological Solutions in String Theory —

Makoto Tanabe[1], Shuntaro Mizuno[2]

[1]*Department of Physics Waseda University Maeda Laboratory, Okubo 3-4-1, Shinjuku-ku Tokyo 169 Japan*

[2]*Department of Physics Waseda University Maeda Laboratory, Okubo 3-4-1, Shinjuku-ku Tokyo 169 Japan*

Abstract

We construct time dependent BPS pp-wave solutions in the context of M-theory and type II supergravity. It is found that the solutions satisfy that the crossing rule and 1/8 sueprsymmetry. We found an inflationary solution with consistency of the four-dimensional inflationary solution. The extra dimensions are dynamically compactified in natural. We also discuss the cosmological scenario with this solution.

1 Introduction

Low energy effective actions of string or M-theories are known to admit various kinds of time dependent solutions. These solutions are interesting from the cosmological point of view and are believed to shed light on the dS/CFT correspondence. One particular class of solutions which might be useful in this context were assumed in the literature to have the symmetry $ISO(p+1) \times SO(D-p-2,1)$ of the metric in D space-time dimensions and can be regarded as those of magnetically charged Euclidean or Space-like branes (S-brane). These are the non-BPS solutions with S-brane, which mean that these solutions don't remain the supersymmetry anymore. However supersymmetric cosmological solutions with landscape of superstring theory are recently given by [13]. It is obtain the inflationary solutions with dS compactificaion [?].

PP-wave background provides an example of exact string theory background. It has been known for some time that pp-wave spacetime yields exact classical backgrounds for string theory, with all α' corrections vanishing. Also it has been shown that these backgrounds are exactly solvable in the light cone gauge. Many of these backgrounds are obtained in the Penrose limit of $AdS_d \times S^p$ type of geometry and preserve at least the same amount of supersymmetry as that of parent background. PP-wave background have also proven as interesting place to test the ideas of holography. It was conjectured that the type IIB string theory in $AdS_5 \times S^5$ background is dual to the $\mathcal{N}=4$ super Yang-Mills theory on the boundary of AdS_5.

2 Cosmological Solution

We obtain $d=4$ case with the BPS pp-wave solutions uniquely as follow,

$$\begin{aligned} ds_{11}^2 &= H_2^{1/3} H_5^{2/3} [(H_2 H_5)^{-1} 2du(dv + fdu) \\ &\quad + (H_2 H_5)^{-1} dy_2^2 + H_5^{-1}(dy_3^2 + \cdots + dy_6^2) + H_2^{-1} dy_7^2 + dx_1^2 + dx_2^2 + dx_3^2], \end{aligned} \tag{1}$$

where H_A is a harmonic function on $\{u, v\}$ satisfying

$$\partial_u \partial_v H_A = \partial_v^2 H_A = 0, \tag{2}$$

in which NM2-brane occupies the u, y^2 and y^7 directions and NM5-brane occupies the $u, y^2 \ldots, y^6$ directions.

[1]E-mail:tanabe@gravity.phys.waseda.ac.jp
[2]E-mail:shuntaro@gravity.phys.waseda.ac.jp

After compactifying the y_α ($\alpha = 2, \cdots, p$) coordinates and conformally transforming into the (d+1)-dimensional Einstein frame, the original Einstein-Hilbert action in the D-dimensional theory can be given by

$$\sqrt{-g_D}R_D \propto \Omega^{d+1}\sqrt{-g_{d+1}}\prod_A H_A^{-q_A\frac{D-q_A-3}{\Delta_A}+(p-q_A-1)\frac{q_A+1}{\Delta_A}}\Omega^{-2}R_{d+1}, \tag{3}$$

where g_{d+1} and R_{d+1} are the determinant and the scalar curvature with respect to (d+1)-dimensional metric in the Einstein frame $g^{(d+1)}_{\mu\nu}$. Ω is the conformal factor which relates $g^{(d+1)}_{\mu\nu}$ and the metric directly obtained by the compactification $g^{*(d+1)}_{\mu\nu}$ as $g^{*(d+1)}_{\mu\nu} = \Omega^2 g^{(d+1)}_{\mu\nu}$. We omit the term from the volume of the compactified y_α coordinates.

Since in the (d+1)-dimensional Einstein frame, this term should also scale as $\sqrt{-g_{d+1}}R_{d+1}$, Ω can be determined as

$$\Omega = \prod_A H_A^{-\frac{D-q_A-3-(q_A+1)(d-2)}{(d-1)\Delta_A}}. \tag{4}$$

Therefore the (d+1)-dimensional metric after compactifying the y_α coordinates can be written as

$$\begin{aligned} ds^2 &= \Xi^{d-2}2du(dv+fdu)+\Xi^{-1}\sum_{i=1}^{d-1}dx_i^2, \\ \Xi &= \prod_A H_A^{-\frac{2(D-2)}{(d-1)\Delta_A}}. \end{aligned} \tag{5}$$

Furthermore, in order to obtain the cosmological solutions, that is, time-dependent ones, we now compactify the $y_1 = (u+v)/\sqrt{2}$ coordinates on S^1, by which the fucntions H_2, H_5 and f come to depend only t and the resulting d-dimensional metric can be written by

$$\begin{aligned} ds_d^2 &= -\Upsilon^{d-3}dt^2+\Upsilon^{-1}\sum_{i=1}^{d-1}dx_i^2, \\ \Upsilon &= (1+f)^{-\frac{1}{d-2}}\prod_A H_A^{-\frac{2(D-2)}{(d-2)\Delta_A}}. \end{aligned} \tag{6}$$

In 4-dimensional case, in which we consider the intersecting NM2-brane and NM5-brane especially, the metric can be written as

$$\begin{aligned} ds^2 &= -((1+f)H_2H_5)^{-1/2}dt^2+((1+f)H_2H_5)^{1/2}\sum_{i=1}^{3}dx_i^2 \\ &= -d\tau^2+a(\tau)^2\sum_{i=1}^{3}dx_i^2, \end{aligned} \tag{7}$$

where τ is the cosmic time and $a(\tau) = dt/d\tau$ is the scale factor of our universe. In this model, the evolution of the scale factor depends on the form of $H_2(t)$, $H_5(t)$ and $f(t)$. One interesting question about the early stage of the universe is whether the inflationary solutions are consistent with supersymmetry. We find if $((1+f)H_2H_5) \propto t^4$, the exponentialy expanding universe $a(\tau) \propto e^\tau$ is realized. One example satisying the BPS conditions is H_2, H_5, $f \propto t^{4/3}$. We can also show if $((1+f)H_2H_5) \propto t^{4(p-1)/p}$, the power law inflationary solutions in which $a(\tau) \propto \tau^{p-1}$ are obtained. It can be easily seen that the solution such as H_2, H_5, $f \propto t^{4(p-1)/3p}$ satisfies the BPS conditions.

In the above, we construct the inflationary solution from the view point of our 4-dimensional spacetime by compactifying the y_1 coordinate first. However, we can show the compactification of that coordinate realizes dynamically for the examples considered above. 5-dimensional metric with y_1 direction is given

by

$$
\begin{aligned}
ds^2 &= (H_2H_5)^{-2/3}2du(dv + fdu) + (H_2H_5)^{1/3}\sum_{i=1}^{3} dx_i^2 \\
&= \Omega^2(-d\tau^2 + a(\tau)^2\sum_{i=1}^{3} dx_i^2 + b(\tau)^2 dy^2), \qquad (8)
\end{aligned}
$$

where

$$
dy = dy_1 - \frac{f}{1+f}dt, \quad b(\tau, y_1)^2 = \sqrt{\frac{(1+f)^3}{H_2H_5}}, \qquad (9)
$$

$$
\Omega^2 = (1+f)^{-1/2}(H_2H_5)^{-1/6}. \qquad (10)
$$

The ratio of scale factor is given as $a/b \propto (H_2H_5/1+f)^{1/2}$, thus we choose the case which all functions are the same contributions as mentioned above, for the exponentialy inflation case we find $a/b \propto e^{2\tau/3}$, and for the power law inflation case we find $a/b \propto \tau^{\frac{2(p-1)}{3}}$, which means that for these cases, the compactification of the y coordinate happens dynamically.

It is worthwhile to relate the above cosmological solution with other solutions based on other types of string theory. When it comes to $y_2, \ldots, y_7$ coordinates, which are compactified in the above analysis, following to the similar idea, it can be shown that the volume element of y_2 coordinate shrinks more rapidly than that of $y_3, \ldots, y_7$ coordinates. If we comapctify only y_2 coordinate in 11-dimensional M-theory, we can find the $D2$ and $NS5$-brane's bound state in type IIA string theory. Furthermore, using the T-duality transformation on y^3 direction, the $D3$- and $NS5$-brane's bound state is obtained. It is shown that the $D3$-brane is rolling in"throat geometry" on the $NS5$ background [17], and the corresponding cosmological solutions are already provided by [18], which is related to rolling tachyon given by [?], from the point of view of the string theory.

3 Conclusion

In this paper we have examined a system where $D = d + p$ dimensional gravity was coupled to a scalar field and arbitrary rank form gauge fields. The ansatz employed here was to take the metric as pp-wave spacetime, and the $n = q + 2$ gauge field to have a composite electric q-brane form and magnetic $D - p - d - 2$-brane form. All ansatz functions depended only on the null coordinate (u, v). Under these conditions we have constructed intersection BPS brane solutions with pp-wave. These pp-wave brane solutions satisfied crossing rule and the harmonic function rule, thus by dimensional reduction and applying S and T-duality trasformations, one can also obtain all standard intersecting BPS brane solutions with pp-wave. Under another dimensional reduction for y^1 direction, we can obtain usual S-brane solutions in type II superstring theory [7].

As the scale factor $a(t)$ increasing in the inflational phase, the energy scale is decreasing. Thus at the critical energy, the supersymmetry must be breaking and the inflation will be ended at that time. In M-theory, the supersymmetry breaking mean that we must calculate the Einstein equations directly. If we choose the $\zeta_\alpha = \text{const}$, then we find $\xi = \text{const}, \eta = \text{const}$ and $f/H_A = \text{const}$. In this case only we found $H_A = H_A(u) = f(u)$, and we can also have a radiational solutions in four dimension. The supersymmetry breaking makes latent heat, and it gives reheating processes. After the supersymmetry braking baryongenesis can be occurred and the dark energy and dark matter may be explained by some model of symmetry breaking [15], however we doesn't mention about it, because our main purpose is to make a general cosmological solutions in string theory.

The fundamental problem about these solutions is the question of their stability. Still they have preserve supersymmetry, the solutions dive into the future singularity in four dimension. However using the AdS/CFT correpondence the Big crunch singularity are not

singularity in CFT point of view by [16]. The supersymmetrical inflationary solutions in de Sitter solutions are stable too [?]. Therefore the presence of a singularity is not so bad only for inflationary solutions, but it is still open problems. Our solutions in the view point of string theory doesn't understand despite they have preserve supersymmetry at all, thus we must make a dynamical state in type II string theory, and compare to the solutions to the state of the string.

Acknowledgment

The work M.T. was supported by a 21COE at Waseda university "Holistic Research and Education Center for Physics of Self-organization System". M.T. would like to thank Amanda and Cliff Burgess for nice comment at Cosmo-04 in Toronto. We thank Kei-ichi Maeda and Takashi Torii for useful discussions.

References

[1] C. Chen, D. V. Gal'tsov, and M. Gutperle, *Phys.Rev.* D66 (2002) 024043, [hep-th/0204071].

[2] N. S. Deger and A. Kaya, *JHEP* 0207 (2002) 038, [hep-th/0206057].

[3] S. Bhattacharya, S. Mukherji and S. Roy, *Phys.Lett.* B584 (2004) 163, [hep-th/0308069].

[4] M. Gutperle and A. Strominger, *JHEP* 0204 (2002) 018, [hep-th/0202210].

[5] A. Strominger, JHEP 0110, 034 (2001) [arXiv:hep-th/0106113].

[6] C. Martínez-Prieto, P. Pbregón and J. Socorro, [hep-th/0406087].

[7] N. Ohta, *Phys.Lett.* B558 (2003) 213, [hep-th/0301095].

[8] S. Bhattacharya and S. Roy, *JHEP* 0312 (2003) 015, [hep-th/0309202].

[9] K. Hashimoto, P. Ho and J. E. Wang, *Phys.Rev.Lett.* 90 (2003) 141601, [hep-th/0211090].

[10] G. Jones, A. Maloney and A. Strominger, *Phys.Rev.* D69 (2004) 126008, [hep-th/0403050].

[11] G. Tasinato, I. Zavala, C. P. Burgess and F. Quevedo, *JHEP* 0404 (2004) 038, [hep-th/0403156].

[12] E. Witten, *Nucl. Phys.* B443 (1995) 85, [hep-th/9503124].

[13] K. Dasgupta, J. P. Hsu, R. Kallosh, A. Linde, and M. Zagermann, *JHEP* 0408 (2004) 030, [hep-th/0405247].

[14] J. D. Edelstein, L. Tataru and R. Tatar, *JHEP* 9806 (1998) 003, [hep-th/9801049].

[15] J. Boer, K. Hori, H. Ooguri and Y. Oz *Nucl. Phys.* B522 (1998) 20-68, [hep-th/9801060].

[16] T. Hertog and G. T. Horowitz, *JHEP* 0407 (2004) 073, [hep-th/0406134].

[17] Y. Nakayama, K. L. Panigrahi, S. Rey and H. Takayanagi, [hep-th/0412038].

[18] H. Yavartanoo, [hep-th/0407079].

Domain-Wall Induced Entropy Production

Masahiro Kawasaki[1], Fuminobu Takahashi[2 3]

Institute for Cosmic Ray Research, University of Tokyo, Kashiwa 277-8582, Japan

Abstract

It is shown that late-time decay of domain walls can dilute unwanted relics such as moduli, if the universe was dominated by frustrated domain walls with tension $\sigma = (1 \sim 100\,\mathrm{TeV})^3$. Since energy density of the frustrated domain walls decreases as slow as the inverse of the scale factor, an overclosure limit on the axion decay constant f_a is also considerably relaxed. In fact f_a can be as large as the Planck scale, which may enable us to naturally implement the QCD axion in the string scheme. Furthermore, in contrast to thermal inflation models, the Affleck-Dine baryogenesis can generate enough asymmetry to explain the present baryon abundance, even in the presence of late-time entropy production.

1 Introduction

Particle physics beyond the standard model predicts a number of new particles, some of which have long lifetimes and decay at cosmological time scales. If such long-lived particles are substantially produced in the early universe, they may give crucial effects on cosmology and spoil success of the standard big-bang model.

One well-known example of such dangerous relic particles is gravitino in supergravity theories. Gravitinos are produced during reheating after inflation and the abundance of the produced gravitino is proportional to the reheating temperature. The gravitino with mass $\sim 0.1 - 10$ TeV decays during or after the big-bang nucleosynthesis (BBN) and may destroy the light elements synthesized in BBN. Thus, in order to keep success of BBN the reheating temperature should be sufficiently low (for recent works, see [1, 2, 3, 4]).

Another class of dangerous relics are light scalar fields called moduli which appear in superstring theories [5, 6, 7]. The moduli fields are expected to acquire masses of the order of the gravitino mass from nonperturbative effects of the SUSY breaking and have long lifetimes since they have only the gravitationally suppressed interactions. During inflation the field value of moduli generally deviates from the vacuum value due to extra SUSY breaking by the cosmic density. The deviation is of the order of the Planck scale $M_G (= 2.4 \times 10^{18}$ GeV) since no other mass scale exists. Then, when the Hubble becomes less than the modulus mass, the modulus field starts to osciilate with amplitude $\sim M_G$. Because the modulus denity is comparable to the cosmic density at onset of the oscillation, it soon dominates the density of the universe and causes the serious cosmological problem (moduli problem). Since the abundance of the moduli is independent of the reheating temperature, the moduli problem is much more serious than the gravitino problem. To solve the moduli problem (as well as the gravitino problem) it is necessary to dilute the oscillating moduli by huge entropy production. So far the most successful model to produce such large entropy is thermal inflation proposed by Lyth and Stewart [8, 9]. The thermal inflation is mini-inflation with the number of e-folds ~ 10 which takes place at the weak scale. A comprehensive study of the thermal inflation was done in Ref. [10] and it was shown that for modulus mass between 10 eV and 10 TeV the thermal inflation solves the cosmological moduli problem. However, the thermal inflation also dilute the baryon number of the universe and hence we need an efficient baryogenesis mechanism. In Refs. [11, 10] it was pointed out that the Affleck-Dine mechanism does that job. But later it was shown that Q-ball formation obstructs the baryogenesis [12].

In this paper we propose an alternative model to dilute the dangerous cosmological relics based on Ref. [13]. In our model domain walls, which are usually considered as cosmological disaster, play an

[1]E-mail:kawasaki@icrr.u-tokyo.ac.jp
[2]E-mail:fumi@icrr.u-tokyo.ac.jp
[3]Talk given by F. Takahashi.

important role. The domain walls are produced when some discrete symmetry is spontaneously broken. The domain wall network in the universe become very complicated if there are many discrete vacua. The density of such domain wall network decreases very slowly and quickly dominates the universe. In extreme case, the domain walls become frustrated and their density ρ_{DW} decreases as $\rho_{DW} \propto a^{-1}$ (a: the scale factor) which is slower than the scaling evolution $\rho_{DW} \propto a^{-3/2}$ in matter-dominated universe. Furthermore, if the scalar potential has a tiny term which explicitly breaks the discrete symmetry, the vacua separated by domain walls have slightly different energies and hence the domain wall network is no longer stable and decays producing large entropy. It will be shown that the entropy production by the decay of domain wall is enough to dilute the moduli density. Moreover, because the density of domain wall decreases much more slowly than the matter density, the cosmic axion density is also diluted. As a result, the axion decay constant f_a as large as M_G is allowed, which might enable us to implement the axion into the string framework. In addition, the Affleck-Dine baryogenesis is compatible with our model. Therefore, the domain walls provide more efficient and consistent dilution mechanism than the thermal inflation.

2 Basic Scenario

First we present our scenario that the decay of domain walls generates large entropy to dilute unwanted relics such as moduli and gravitinos, and derive constraints on tension of the domain walls. In contrast to the other candidates for late-time entropy production, domain walls have an advantage that the energy density decreases relatively slowly, which ensures huge entropy production. To be specific, an equation-of-state w equals to $-2/3$ if the domain walls are completely frustrated, that is, the structure of the domain wall network remains unchanged as the universe expands. Throughout this paper, we assume this is the case.

Let us consider the evolution of the energy density of domain walls, which eventually dominate the universe. The energy density of the domain walls at the formation is estimated as

$$\rho_{DW,i} \sim \sigma H_i, \tag{1}$$

where σ is the tension of the wall, H_i the Hubble parameter at the phase transition. We have assumed that there are only a few domain walls per one horizon when they are formed. Here and in what follows we neglect $O(1)$ numerical factors. If the domain walls are fully frustrated, the energy density falls off as the inverse of the scale factor: $\rho_{DW} \propto a^{-1}$. For definite discussion, we assume that the universe is dominated by either the inflaton or modulus fields when the domain walls are formed. Noting that the energy density of an oscillating massive scalar field decreases as $\propto a^{-3}$, the domain walls dominate the universe when the Hubble parameter becomes equal to

$$H_{eq} \sim \sigma^{\frac{3}{4}} H_i^{\frac{1}{4}} M_G^{-\frac{3}{4}}. \tag{2}$$

If the reheating occurs earlier than $H = H_{eq}$, the radiation-dominated epoch might last for a while, which makes it easy for the domain walls to dominate the unverse. Thus, for conservative discussion, we assume that the universe is dominated by nonrelativistic particles until the domain walls dominate the universe.

The decay of domain walls can proceed if there is a tiny bias between vacua, $\delta\rho$. When this energy difference becomes comparable to the energy of the domain walls, the decay occurs and the universe is reheated. Since the universe was dominated by the domain walls in our scenario, $\delta\rho$ is simply related to the decay temperature as $\delta\rho \sim T_d^4$. In order to have both large enough entropy production and the successful BBN, we take the decay temperature as low as 10MeV. It is the smallness of $\delta\rho$ that enables domain walls to be long-lived. Let us note that, when the domain walls decay, at least several domain walls must be present inside one horizon, otherwise the old inflation occurs somewhere leading to unacceptably inhomogeneous universe. This requires that the decay temperature T_d satisfy the following inequality: $T_d^4 > \sigma H_d$, where $H_d \sim T_d^2/M_G$ is the Hubble parameter when the domain walls decay. Thus the tension is bounded above:

$$\sigma < T_d^2 M_G \sim (100\,\mathrm{TeV})^3 \left(\frac{T_d}{10\,\mathrm{MeV}}\right)^2. \tag{3}$$

On the other hand, the tension should be large enough to dominate the universe before the decay: $H_{eq} > H_d$. That is,

$$\sigma > \left(\frac{T_d^8 M_G^2}{H_i}\right)^{\frac{1}{3}} \sim (100\,\mathrm{GeV})^3 \left(\frac{T_d}{10\,\mathrm{MeV}}\right)^{\frac{8}{3}} \left(\frac{H_i}{1\,\mathrm{TeV}}\right)^{-\frac{1}{3}}. \tag{4}$$

Now let us estimate the the abundance of the modulus field after decay of the domain walls. For domain walls with the tension satisfying (3) and (4), H_{eq} is much smaller than the modulus mass. Since the modulus field dominates the universe as soon as it starts oscillating, it is reasonable to assume that the universe was dominated by the modulus field when $H = H_{eq}$. Then the modulus-to-entropy ratio is given by

$$\frac{\rho_{mod}}{s} \sim T_d \left(\frac{H_d}{H_{eq}}\right)^4 \sim \frac{T_d^9 M_G^2}{\sigma^3 H_i}, \tag{5}$$

where we have used the fact that the Hubble parameter falls off as $\propto a^{-1/2}$ while the domain walls dominate the universe, and Eq. (2) is substituted in the last equation. This must satisfy the observational bound:

$$\frac{\rho_{mod}}{s} < \kappa \frac{\rho_c}{s} = 3.6 \times 10^{-9} \kappa h^2\,\mathrm{GeV}, \tag{6}$$

where ρ_c is the critical density, κ varies from 10^{-10} to 0.2 depending on the modulus mass [10], and h is the Hubble constant in units of 100 km/sec/Mpc. Thus the tension is further constrained as

$$\sigma > \kappa^{-\frac{1}{3}} (500\,\mathrm{GeV})^3 \left(\frac{T_d}{10\,\mathrm{MeV}}\right)^3 \left(\frac{H_i}{1\,\mathrm{TeV}}\right)^{-\frac{1}{3}}. \tag{7}$$

To sum up, the domain walls with the tension $\sigma = (1 \sim 100\,\mathrm{TeV})^3$, which decay just before the BBN starts, can dilute the moduli to the observationally allowed level.

3 Conclusion

In this paper we have investigated the dilution of unwanted cosmological relics such as moduli by entropy production of the domain wall network. It has been shown that the frustrated domain walls quickly dominates the density of the universe and their decay produces entropy large enough to dilute the dangerous moduli. A concrete model which leads to frustrated network of domain walls is given in Ref. [13]. Moreover, we have found that the late-time decay of the domain walls greatly relaxes the constraint on the axion model and the axion decay constant f_a as large as the Planck scale is allowed.

Up to here, we have assumed fully frustrated domain walls, however, this assumption can be weaken to some extent. Similar arguments show that domain walls whose energy evolves as $\rho_{DW} \propto a^{-1-\gamma}$ with $\gamma \lesssim 0.2(0.1)$ for $\kappa = 0.2(10^{-10})$ works as well. Finally we make a comment on baryon number generation in the present model. The domain-wall decay also dilute pre-existing baryon number. Therefore, there should be large baryon asymmetry before the entropy production or baryon number should be generated after the decay of the domain wall. Since the decay temperature is expected to be low ($\sim$ 10 MeV), it is unlikely to produce the baryon number after the decay. Then the most promising candidate for baryogenesis is the Affleck-Dine mechanism. In order to produce sufficient baryon asymmetry the gravitino mass should be relatively small, $m_{3/2} \lesssim 10$ MeV [10]. In the case of the thermal inflation, the Affleck-Dine mechanism does not work due to Q-balls formation [12]. The crucial point is that the thermal inflation requires large messenger scale, which leads to large Q-balls and small baryon number in the background universe. However, our model given in Ref. [13] allows relatively small messenger scale, since v_2 is much smaller than the vev of the flaton. Thus the Affleck-Dine baryogenesis does work in the present scenario.

References

[1] M. Kawasaki, K. Kohri and T. Moroi, Phys. Rev. D **63**, 103502 (2001).

[2] K. Jedamzik, Phys. Rev. Lett. **84**, 3248 (2000).

[3] R. H. Cyburt, J. R. Ellis, B. D. Fields and K. A. Olive, Phys. Rev. D **67**, 103521 (2003).

[4] M. Kawasaki, K. Kohri and T. Moroi, arXiv:astro-ph/0408426.

[5] G. D. Coughlan, W. Fischler, E. W. Kolb, S. Raby and G. G. Ross, Phys. Lett. B **131**, 59 (1983).

[6] T. Banks, D. B. Kaplan and A. E. Nelson, Phys. Rev. D **49**, 779 (1994) [arXiv:hep-ph/9308292].

[7] B. de Carlos, J. A. Casas, F. Quevedo and E. Roulet, Phys. Lett. B **318**, 447 (1993) [arXiv:hep-ph/9308325].

[8] D. H. Lyth and E. D. Stewart, Phys. Rev. Lett. **75**, 201 (1995) [arXiv:hep-ph/9502417].

[9] D. H. Lyth and E. D. Stewart, Phys. Rev. D **53**, 1784 (1996) [arXiv:hep-ph/9510204].

[10] T. Asaka and M. Kawasaki, Phys. Rev. D **60**, 123509 (1999) [arXiv:hep-ph/9905467].

[11] A. de Gouvea, T. Moroi and H. Murayama, Phys. Rev. D **56**, 1281 (1997) [arXiv:hep-ph/9701244].

[12] S. Kasuya, M. Kawasaki and F. Takahashi, Phys. Rev. D **65**, 063509 (2002) [arXiv:hep-ph/0108171].

[13] M. Kawasaki and F. Takahashi, arXiv:hep-ph/0410158.

Casimir Dark Energy

Je-An Gu[1], Pisin Chen[2]

[1] *Department of Physics, National Taiwan University, Taipei 106, Taiwan, R.O.C.*
[2] *Stanford Linear Accelerator Center, Stanford University, Stanford, CA 94309, USA*

Abstract

In dark energy models the smallness of the energy density has been recognized as the most crucial difficulty. Recently we proposed in arXiv:astro-ph/0409238 a new dark energy model in which the smallness of the cosmological constant is easily achieved by invoking the Casimir energy in a supersymmetry-breaking brane-world. In this paper we introduce the basic elements of this model. Various implications, subtleties, and perspectives of this model are briefly discussed.

1 Introduction

The accelerating expansion of the present universe was first indicated by the type Ia supernova (SN Ia) data in 1998 [1, 2]. It is recently reinforced by new SN Ia data [3, 4] obtained using the Hubble Space Telescope. For explaining this mysterious phenomena, cosmologists first resorted to energy sources which entail strongly negative pressure and thereby provide anti-gravity (i.e. repulsive gravitational force), e.g. a positive cosmological constant [5] and quintessence [6, 7]. It is in this viewpoint to use the designation "dark energy" for the origin of the accelerating expansion.

In addition to dark energy that can be regarded as a modification of the right-hand side (i.e. the energy part) of the Einstein equations, recently people started to consider modifications of the left-hand side (i.e. the geometry part) of the Einstein equations as a new scenario of understanding the accelerating universe [8, 9, 10, 11, 12, 13, 14, 15]. It is natural to designate this new category of explanations of the accelerating expansion "dark geometry" [10, 11, 15].

Among these possible origins of accelerating expansion, a positive cosmological constant is the simplest. Although the cosmological constant hitherto can explain all the observational results, it suffers a fine-tuning problem, especially when facing a possible huge contribution from quantum vacuum energy. That is, it is hard to satisfactorily explain the smallness of the cosmological constant required by observations.

Recently we proposed in arXiv:astro-ph/0409238 a new dark energy model in which the smallness of the cosmological constant is easily achieved by invoking the Casimir energy in a supersymmetry-breaking brane-world. In the following section we will introduce the basic elements of this model, then investigate its implications and subtleties in Sec. 3, and briefly discuss possible perspectives in Sec. 4.

2 Casimir Dark Energy in a Supersymmetry-Breaking Brane-World

The possibility that the Casimir energy in extra dimensions can play the role of dark energy has been explored by Milton [16]. Note that the reason of employing extra dimensions is that in general a positive Casimir energy in ordinary dimensions cannot entail negative pressure and anti-gravity, while the Casimir energy in extra dimensions on the contrary behaves like a cosmological constant. Its sign depends on the geometry, the boundary condition, and the field contents in the extra space. If all extra dimensions have the same size a, the value of the Casimir energy density measured by a 3-dimensional observer is in general proportional to a^{-4}. Naively it should not be larger than the energy density of the universe that is very close to the critical density ρ_c as required by CMB data [17], accordingly providing a lower limit to

[1] E-mail:jagu@phys.ntu.edu.tw
[2] E-mail:chen@SLAC.Stanford.EDU

the extra-dimension size. From this requirement Milton obtained a stringent constraint that the number of extra dimensions cannot exceed two and the extra-dimension size should be larger than microns [16]. This constraint on the extra-dimension size is not far from the current experimental upper limit around 100 microns [18].

Stringent constraints and fine tuning are common features in many dark energy/dark geometry models. Generally speaking, it is very difficult to achieve the smallness of the dark energy density if the energy scale corresponding to dark energy/dark geometry is not a natural scale required by some principle or symmetry. In our recently proposed dark energy model invoking the Casimir effect in a supersymmetry-breaking brane-world, this difficulty is solved [19].

In our model we consider a $(3+n+1)$-dimensional space-time with n compact extra dimensions, in which the standard model fields and their superpartners are confined on a 3-brane while the gravity (graviton-gravitino) sector resides in the (higher-dimensional) bulk. We assume supersymmetry is preserved in the bulk and only broken around the 3-brane with a breaking scale $M_{\rm SUSY}$ and an extra-dimensional width δ for the broken region. Accordingly there is a nonzero residual Casimir energy — induced by the supersymmetry breaking — around the brane, while the vacuum energy (also the Casimir energy) contributed from supersymmetry fields in the bulk region away from the brane is perfectly cancelled.

As an example for demonstration, here we present the result of the case in which extra dimensions are toroidal and only graviton and gravitino reside in the bulk. As a result of our supersymmetry-breaking setting, gravitino acquires a mass m only around the brane and graviton remains massless everywhere. The resultant net Casimir energy density measured by a 3-dimensional observer is

$$\delta\rho_{\rm g}^{(4)} \cong \alpha_n \cdot m^2\, a^{-2} \cdot \left(\frac{V_\delta}{V_a}\right), \tag{1}$$

where $V_\delta \propto \delta^n$, is the extra-dimensional volume of the supersymmetry-broken region, $V_a \propto a^n$, is the total extra-dimensional volume, and α_n is a constant factor depending on the number of extra dimensions n and the boundary conditions in extra dimensions. It is natural to have the situation that $V_\delta \ll V_a$. Consequently the ratio V_δ/V_a provides a strong suppression factor in the above formula of the Casimir energy density. This suppression is indeed a manifestation of the sharp contrast between the volume of the supersymmetry-broken region around the brane and that of the supersymmetry-preserved bulk. It is the very key to achieving the smallness of the cosmological constant/dark energy in our model.

The quantities a, δ, and m involved in the above expression of the Casimir energy density can be related to several fundamental energy scales: the fundamental gravity scale $M_{\rm G}$, the string scale $M_{\rm S}$, the supersymmetry-breaking scale $M_{\rm SUSY}$, and the Planck scale $M_{\rm pl}$, as follows.

$$a \sim \left(M_{\rm pl}/M_{\rm G}\right)^{2/n} M_{\rm G}^{-1}, \tag{2}$$

$$\delta \sim l_{\rm S}\ (\text{string length}) = M_{\rm S}^{-1}, \tag{3}$$

$$m \sim M_{\rm SUSY}^2/M_{\rm pl}. \tag{4}$$

The Casimir energy expression can then be rewritten in terms of these fundamental scales:

$$\delta\rho_{\rm g}^{(4)} \sim \alpha_n\, M_{\rm G}^{(n+2)^2/n} M_{\rm S}^{-n} M_{\rm SUSY}^4 M_{\rm pl}^{-4-4/n}. \tag{5}$$

Insisting $\rho_{\rm g}^{(4)}$ as the dark energy density $\sim 3\times 10^{-11}\,{\rm eV}^4$, we arrive at the following constraint among these fundamental scales:

$$\left(\frac{M_{\rm G}}{M_{\rm pl}}\right)^{(n+2)^2/n} \left(\frac{M_{\rm S}}{M_{\rm pl}}\right)^{-n} \left(\frac{M_{\rm SUSY}}{M_{\rm pl}}\right)^4 \sim 10^{123}\,\alpha_n^{-1}. \tag{6}$$

This constraint is quite loose, i.e., it can be satisfied by a wide range of $M_{\rm G}$, $M_{\rm S}$ and $M_{\rm SUSY}$. For example, if the allowed range of $M_{\rm S}$ and $M_{\rm SUSY}$ is from 1 TeV to $M_{\rm pl}$, $M_{\rm G}$ will be barely constrained within the same range and correspondingly the extra-dimension size a can be as large as atomic scales (for small n) or as small as the Planck length. The looseness of this constraint indicates that the smallness of dark energy can be easily achieved in our model.

3 Behind the Scene

In this model the role of dark energy is played by the Casimir energy (in extra dimensions) that is a vacuum energy difference. The legitimacy of choosing vacuum energy difference while ignoring absolute vacuum energy should to be further investigated.

In Einstein's general relativity naively all forms of energies are on an equal footing regarding the ability of curving the space-time. Under the requirement of energy conservation and allowing energy transfer among different energy forms, it is hard to imagine the possibility that some part of energies cannot gravitate. In this regard, our disregard for absolute vacuum energy needs explanation. This problem is indeed related to the "old" part of the cosmological constant problem before the discovery of the accelerating expansion (pre-dark-energy): how to make the cosmological constant vanish [20]. The involvement of absolute energies in the Einstein equations is the key origin of the pre-dark-energy cosmological constant problem. In all gauge theories excluding gravity, it is the energy difference, but not the absolute energy, that is physically meaningful. By comparison, general relativity involving absolute energies is distinctive and mysterious.

Nevertheless, general relativity may not be the very fundamental theory of gravity, but could be an effective theory working well in scales such as that of the solar system. That is, general relativity may need to be significantly modified in the cosmic and the microscopic scales. In this regard, the naive and brute-force incorporation of the absolute vacuum energy (into the Einstein equations) stemming from microscopic quantum fluctuations is doubtful. In contrast, it is generally believed that the energy difference is physically meaningful. It will be wonderful if quantum gravity or the final theory can possess the feature that it is the energy difference that is relevant to all the interactions including gravity. It is possible that in a successful quantum gravity theory the absolute vacuum energy will be renormalized away or cancelled by modifications of the gravity action accompanying the RG running.

From a more conservative angle our model invoking Casimir energy can be regarded as a solution to the "new" part of the cosmological constant problem emerging from the discovery of the accelerating expansion (post-dark-energy): how to make the cosmological constant slightly deviate from zero (i.e. tackling the smallness). The smallness, as mentioned in the introduction, is one of the crucial difficulties in dark energy models. In our model this difficulty is solved by invoking the sharp contrast between two volumes: the volume of the supersymmetry-broken region and that of the supersymmetry-preserved region.

4 Perspectives

When invoking the vacuum energy difference, the energy reference needs to be specified. The energy reference corresponding to general relativity, which is regarded as an effective theory of gravity, is unknown. Insisting Casimir energy as dark energy in our model implies the energy-reference assumption that the higher-dimensional space-time is Minkowskian when there are no boundary condition, no particles, and no other energy forms. The experimental test of this energy reference choice could provide a crucial way to verify or falsify our model.

The possibility of the evolution of the extra-dimension size is an important issue yet to be studied. The extra-dimension size could be fixed by some stabilization mechanism. In this case the Casimir energy in our model is exactly a cosmological constant in our 3-dimensional world. On the contrary, it is possible that at some epochs the stabilization mechanism was not strong enough or did not function at all so that extra dimensions could evolve. In this case the Casimir energy in our model may behave like quintessence. This possibility of a time-varying dark energy is worthy of further investigation.

In this model the configuration of extra dimensions is ADD-like [21]. It is important to explore our scenario invoking Casimir energy and the sharp contrast between two extra-dimensional volumes under the RS configuration [22]. The ADD and the RS models were devised to explain the weakness of gravity. It is interesting to note that all these three models (ADD, RS, and ours) for tackling the smallness or the hierarchy involve extra dimensions. In particular our model suggests that the observed dark energy may be another evidence of the existence of the extra dimensions and the supersymmetry-breaking brane-world.

Acknowledgements

This work is supported by the Ministry of Education (MoE 89-N-FA01-1-4) and the National Science Council (NSC 93-2811-M-002-033; NSC 93-2112-M-002-047) of Taiwan, R.O.C., and in part by the US Department of Energy under Contract No. DE-AC03-76SF00515.

References

[1] A. G. Riess *et al.* [Supernova Search Team Collaboration], Astron. J. **116**, 1009 (1998).

[2] S. Perlmutter *et al.* [Supernova Cosmology Project Collaboration], Astrophys. J. **517**, 565 (1999).

[3] A. G. Riess *et al.* [Supernova Search Team Collaboration], Astrophys. J. **607**, 665 (2004).

[4] B. J. Barris *et al.*, Astrophys. J. **602**, 571 (2004); R. A. Knop *et al.*, Astrophys. J. **598**, 102 (2003); J. L. Tonry *et al.* [Supernova Search Team Collaboration], Astrophys. J. **594**, 1 (2003).

[5] L. M. Krauss and M. S. Turner, Gen. Rel. Grav. **27**, 1137 (1995); J. P. Ostriker and P. J. Steinhardt, Nature **377**, 600 (1995); A. R. Liddle, D. H. Lyth, P. T. Viana and M. White, Mon. Not. Roy. Astron. Soc. **282**, 281 (1996).

[6] R. R. Caldwell, R. Dave and P. J. Steinhardt, Phys. Rev. Lett. **80**, 1582 (1998).

[7] Je-An Gu and W-Y. P. Hwang, Phys. Lett. B **517**, 1 (2001); L. A. Boyle, R. R. Caldwell and M. Kamionkowski, Phys. Lett. B **545**, 17 (2002).

[8] C. Deffayet, G. Dvali and G. Gabadadze, Phys. Rev. D **65**, 044023 (2002).

[9] Je-An Gu and W-Y. P. Hwang, Phys. Rev. D **66**, 024003 (2002).

[10] Je-An Gu, "A way to the dark side of the universe through extra dimensions," in *Proceedings of CosPA 2002 Symposium*, Taiwan, 2002 (World Scientific, 2003), p.125-133 [astro-ph/0209223].

[11] Je-An Gu, W-Y. Hwang and J.-W. Tsai, Nucl. Phys. B **700**, 313 (2004).

[12] S. M. Carroll, V. Duvvuri, M. Trodden and M. S. Turner, Phys. Rev. D **70**, 043528 (2004).

[13] A. Lue, R. Scoccimarro and G. Starkman, Phys. Rev. D **69**, 044005 (2004).

[14] N. Arkani-Hamed, H. C. Cheng, M. A. Luty and S. Mukohyama, JHEP **0405**, 074 (2004).

[15] Je-An Gu, "Dark Geometry — an alternative to Dark Energy," in the Cosmo-04 workshop, Toronto, Canada, 2004.

[16] K. A. Milton, Grav. Cosmol. **9**, 66 (2003).

[17] C. L. Bennett *et al.*, Astrophys. J. Suppl. **148**, 1 (2003); D. N. Spergel *et al.*, Astrophys. J. Suppl. **148**, 175 (2003).

[18] J. C. Long, H. W. Chan, A. B. Churnside, E. A. Gulbis, M. C. M. Varney and J. C. Price, Nature **421**, 922 (2003).

[19] Pisin Chen and Je-An Gu, arXiv:astro-ph/0409238.

[20] S. Weinberg, Rev. Mod. Phys. **61**, 1 (1989).

[21] N. Arkani-Hamed, S. Dimopoulos and G. Dvali, Phys. Lett. B **429**, 263 (1998); I. Antoniadis, N. Arkani-Hamed, S. Dimopoulos and G. R. Dvali, Phys. Lett. B **436**, 257 (1998).

[22] L. Randall and R. Sundrum, Phys. Rev. Lett. **83**, 3370 (1999); **83**, 4690 (1999).

Probing Strong-Field Scalar-Tensor Gravity with Gravitational Wave Asteroseismology

Hajime Sotani[1], Kostas D. Kokkotas[2]

[1]*Research Institute for Science and Engineering, Waseda University, Okubo 3-4-1, Shinjuku, Tokyo 169-8555, Japan*
[2]*Department of Physics, Aristotle University of Thessaloniki, Thessaloniki 54124, Greece*

Abstract

We present an alternative way of tracing the existence of a scalar field based on the analysis of the gravitational wave spectrum of a vibrating neutron star. The detection of gravitational waves from neutron stars can set constraints on the existence and the strength of scalar fields. We show that the oscillation spectrum is dramatically affected by the presence of a scalar field, and can provide unique confirmation of its existence.

1 Introduction

A natural alternative/generalisation to general relativity is the scalar-tensor theory in which gravity is mediated by long-range scalar fields in addition to the usual tensor field present in Einstein's theory [1]. Scalar-tensor theories of gravity can be obtained from the low-energy limit of string theory or/and other gauge theories. Still it is not clear how the scalar fields couple to gravity, a basic assumption is that the scalar and gravitational fields φ and $g_{\mu\nu}$ are coupled to matter via an "effective metric" $\tilde{g}_{\mu\nu} = A^2(\varphi)g_{\mu\nu}$. The existence of the scalar field has not yet been verified while a number of experiments in the weak field limit of general relativity disproved or set severe limits in the existence and the strength of the scalar fields [1].

Recently, DeDeo and Psaltis [2] suggested that the effects of the scalar fields might be apparent in the observed redshifted lines of the X-rays and γ-rays observed by Chandra and XMM-Newton. Testing strong gravity via electromagnetic observations is a really novel idea, which have been recently extended, by the same authors [3], in suggesting tests via the quasi-periodic oscillations (QPOs). To that end, we examine whether gravitational wave observations of the oscillation spectra of neutron stars can provide an alternative way of testing scalar-tensor theories. The aforementioned results [2, 4, 5] show that for a specific range of values of the coupling constant β, which are not constrained by the current experimental limits in the weak-field regime, neutron stars can have significantly larger masses and radii. This immediately suggests that the natural oscillation frequencies of the neutron stars will be altered accordingly and a possible detection of gravitational waves from such oscillations will not only probe the existence of the scalar field but might provide a way of estimating its strength.

The estimation of the stellar parameters (mass, radius and equation of state) via their oscillation properties is not a new idea. In the late '90s it was suggested [6] that the oscillation spectra of neutron stars can reveal in a unique way their properties. The radius, the mass and the equation of state can be easily deduced by an analysis of the oscillation spectrum of the f, p and w-modes [7]. Moreover, the rotation period of a neutron star can be revealed by the r-mode oscillations since their frequency is proportional to the rotation rate ($\omega_{r-\mathrm{mode}} \sim 4\Omega/3$). The oscillations of a neutron star in the scalar-tensor theory will produce not only gravitational but also scalar waves. Detectable scalar waves will be a unique probe for the theory, but this might not be the case if the radiated energy is small. Still, we show that there is no need for direct observation of scalar waves, the presence of the scalar field will be apparent in the gravitational wave spectrum, since the spectra will be shifted according to the strength of the scalar field.

This article is organized as follows. In the next section we present the basic equations for the construction of the unperturbed spherically symmetric stellar models and the perturbation equations which will

[1]E-mail:sotani@gravity.phys.waseda.ac.jp
[2]E-mail:kokkotas@auth.gr

be used for the numerical estimation of the oscillation frequencies. In Section 3, we show the numerical results. Finally, in Section 4 we discuss the results in connection to gravitational wave asteroseismology. Note that the present study will be based on two equations of state, which have been used earlier [4, 5]. Our aim is to demonstrate the effect of the scalar field in the neutron star oscillation spectra, while more detailed analysis for a wide range of EOS is underway.

2 Basic Equations

The metrics in scalar-tensor fram $\tilde{g}_{\mu\nu}$ and in Einstein fram $g_{*\mu\nu}$ are related via the conformal transformation, which is $\tilde{g}_{\mu\nu} = A^2(\varphi) g_{*\mu\nu}$. Hereafter, we relate all tilded quantities with "physical frame" and those with asterisk with the "Einstein frame". The scalar field is coupled with the matter through the variable $\alpha(\varphi)$ defined by $\alpha(\varphi) = d\ln A(\varphi)/d\varphi$ and for $\alpha(\varphi) = 0$ the theory reduces to general relativity. In this study, we adopt the same form of conformal factor $A(\varphi)$ as in Damour and Esposito-Farèse[4], which is $A(\varphi) = \exp(\beta\varphi^2/2)$ i.e. $\alpha(\varphi) = \beta\varphi$ where β is a real number.

We will model the neutron stars as self-gravitating perfect fluids, made out of degenerate matter at equilibrium and admitting cold equation of state. Then the metric describing an unperturbed, non-rotating, spherically symmetric neutron star can be written as

$$ds_*^2 = g_{*\mu\nu}dx^\mu dx^\nu = -e^{2\Phi}dt^2 + e^{2\Lambda}dr^2 + r^2(d\theta^2 + \sin^2\theta d\phi^2) \tag{1}$$

where $\exp(-2\Lambda) = 1 - 2\mu(r)/r$, while the "potential" function $\Phi(r)$ will be calculated later. The stellar matter is assumed to be a perfect fluid such as $\tilde{T}_{\mu\nu} = \left(\tilde{\rho} + \tilde{P}\right)\tilde{U}_\mu\tilde{U}_\nu + \tilde{P}\tilde{g}_{\mu\nu}$, where $\tilde{U}_\mu$ is the four-velocity of the fluid, $\tilde{\rho}$ is the total energy density in the fluid frame, and $\tilde{P}$ is the pressure. Spherical symmetry simplifies significantly the procedure of constructing stellar models. The equations for background configuration are deduced in [4, 5],

$$\frac{d\mu}{dr} = 4\pi G_* r^2 A^4\tilde{\rho} + \frac{1}{2}r(r-2\mu)\Psi^2, \tag{2}$$

$$\frac{d\Phi}{dr} = 4\pi G_* \frac{r^2A^4\tilde{P}}{r-2\mu} + \frac{1}{2}r\Psi^2 + \frac{\mu}{r(r-2\mu)}, \tag{3}$$

$$\frac{d\varphi}{dr} = \Psi, \tag{4}$$

$$\frac{d\Psi}{dr} = 4\pi G_* \frac{rA^4}{r-2\mu}\left[\alpha(\tilde{\rho}-3\tilde{P}) + r(\tilde{\rho}-\tilde{P})\Psi\right] - \frac{2(r-\mu)}{r(r-2\mu)}\Psi, \tag{5}$$

$$\frac{d\tilde{P}}{dr} = -\left(\tilde{\rho}+\tilde{P}\right)\left[\frac{d\Phi}{dr} + \alpha\Psi\right] = -\left(\tilde{\rho}+\tilde{P}\right)\left[4\pi G_* \frac{r^2A^4\tilde{P}}{r-2\mu} + \frac{1}{2}r\Psi^2 + \frac{\mu}{r(r-2\mu)} + \alpha\Psi\right] \tag{6}$$

On the other hand, in this study we adopt Cowling approximation, which means that the fluid is perturbed on a fixed background. The fluid perturbations will be described by the Lagrangian displacement vector $\tilde{\xi}^i = (\tilde{\xi}^r, \tilde{\xi}^\theta, \tilde{\xi}^\phi) = \left(\exp(-\Lambda)W, -V\partial/\partial\theta, -V/\sin^2\theta \times \partial/\partial\phi\right) r^{-2}Y_{lm}$, where W and V are functions with of t and r. With Cowling approximation, we can get the perturbation equations from $\delta\left(\tilde{\nabla}_\nu\tilde{T}_\mu{}^\nu\right) = 0$ as follows,

$$\frac{d\bar{W}}{dr} = \frac{d\tilde{\rho}}{d\tilde{P}}\left[\omega^2 e^{\Lambda-2\Phi}r\bar{V} + \left(\frac{d\Phi}{dr} + \alpha\Psi\right)\bar{W}\right] - \frac{l(l+1)}{r}e^{\Lambda}\bar{V} - \left(\frac{l+1}{r} + 3\alpha\Psi\right)\bar{W}, \tag{7}$$

$$\frac{d\bar{V}}{dr} = \left(2\frac{d\Phi}{dr} - \frac{l}{r}\right)\bar{V} - e^{\Lambda}\frac{\bar{W}}{r}, \tag{8}$$

with following boundary conditions at the center and the surface of neutron star

$$\bar{W} = -l\bar{V} \quad (\text{at } r = 0), \tag{9}$$

$$\omega^2 e^{-2\Phi}r\bar{V} + e^{-\Lambda}\left(\frac{d\Phi}{dr} + \alpha\Psi\right)\bar{W} = 0 \quad (\text{at } r = R). \tag{10}$$

Equations (7), (8), (9) and (10) form a well posed eigenvalue problem for the real eigenfrequency ω^2. Using shooting method we can get in a quite simple way the eigenvalues i.e. the characteristic frequencies of the oscillations. It should notice that the above system of perturbation equations and boundary conditions has been derived for an arbitrary form of the scalar function $\alpha(\varphi)$, later in the numerical calculations we will fix its functional form to the one of equation $\alpha(\varphi)$.

3 Numerical Results

First, we will examine the effect of the scalar factor β on the frequency and especially whether the "spontaneous scalarization" can be traced in the spectrum. A discontinuous change in a system, as one varies its parameters, signals a catastrophic behavior and the so called "spontaneous scalarization"[4] is related to it. Harada [5] shown that in the scalar-tensor theory the value $\beta = -4.35$ is the critical one for the "spontaneous scalarization". DeDeo and Psaltis [2] verified that the effects of the scalar field on the line redshifts of neutron stars become pronounced for values $\beta \lesssim -4.35$. We show here that the spontaneous scalarization is also present in the oscillation spectra of neutron stars. In order to study this effect we fixed the asymptotic value of the scalar field to $\varphi_0 = 0.0$ and we constructed a sequence of stellar models with $M = 1.4 M_\odot$ by varying β. In the left panel of Figure 1 the effect of varying β on the frequencies of the fluid becomes immediately apparent. For values $\beta \lesssim -4.35$ the frequency gets a sharp change and increases linearly with decreasing β signaling the "spontaneous scalarization". The effect becomes more pronounced for the higher p-modes as $\partial\omega/\partial(-\beta)$ increases with the order of the mode showing the dramatic impact of the "spontaneous scalarization" on the spectrum. By studying the first thirty modes for each equation of state we have actually found that $\partial\omega_n/\partial(-\beta) \approx n/4$ for $\beta \lesssim -4.35$, where ω_n is the frequency of the nth mode. This relation seems to be independent of the equation of state and suggests that a possible tracing (via electromagnetic or gravitational observations) of the higher p-modes will signal the existence of a scalar field even for small deviations from general relativity.

The idea of a gravitational wave asteroseismology [6, 7] was based on empirical relations that can be drawn for the relation of the stellar parameters to the eigenfrequencies of an oscillating neutron star. These empirical relations were derived by taking into account data for a dozen or more EOS, and it was shown that through these relations one can extract the stellar parameters by analyzing the gravitational wave signal of an oscillating neutron star. The easiest relation to be understood on intuitive physical grounds is the one between the fundamental oscillation mode the f-mode and the average density. This relation emerges naturally by combining the time that a perturbation needs to propagate across the star and the sound speed, this boils down to a linear relation between the period of oscillation and the average density of the star or better $\omega^2 \sim M/R^3$. This was the reason that we have normalized the frequencies in the left panel of Figure 1 with the average density. According to [6] the empirical relation between the f-mode frequency and the average density of typical neutron stars is $f_{f-\mathrm{mode}}(\mathrm{kHz}) \approx 0.78 + 1.63\,(M/1.4M_\odot)^{1/2}\,(R/10\mathrm{km})^{-3/2}$ Almost, all EOS follow this empirical relation (including the two EOS used in this article). This observation suggests a unique way in estimating the average density of a star via its f-mode frequency, and it can be a very good observational test for the neutron stars in scalar-tensor theories. In the right panel of Figure 1 we draw the frequency as function of the averaged density. The actual relations of the frequency of the f-mode as functions of the average density for general relativistic neutron stars are shown as thick solid lines in right panels of Figure 1. Solid lines correspond to normal neutron stars with $\beta = 0$ and follow the above empirical relation with quite small error. The introduction of a scalar field even in moderate central densities alters completely the behavior of the f-mode for EOS A. The frequencies grow considerably faster as functions of the average density, for $\beta \lesssim -4.35$, and the three examples that we have chosen ($\beta = -6.0$, -7.0 and -8.0) show exactly this behavior. The change is quite dramatic even for typical neutron stars with average density. Depending on the value of the parameter β they become $30 - 50\%$ larger than those of a general relativistic neutron star. This can be an observable effect, since the detection of frequencies are higher than those expected from a typical neutron star, would signal in a unique way the presence of a scalar field.

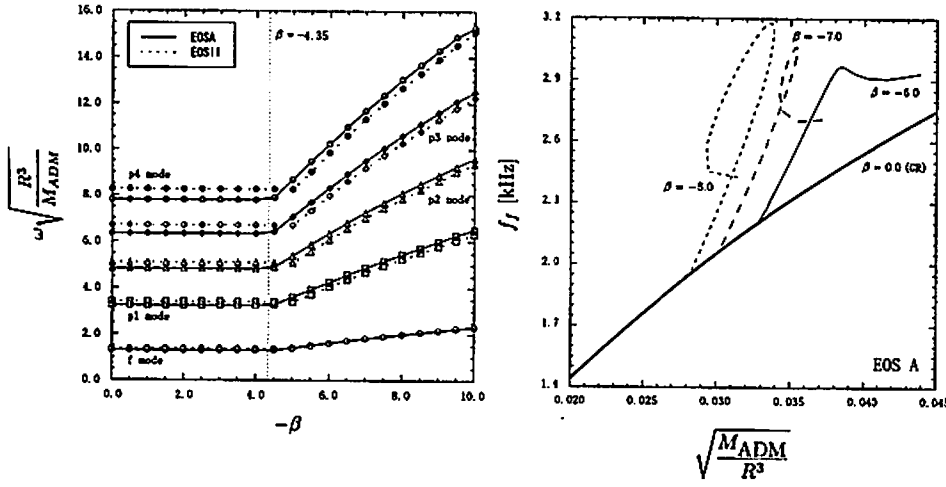


Figure 1: The left panel is that the normalized eigenvalues ω for the first few modes (f, p_1, p_2, p_3 and p_4) are shown as functions the parameter β for the equations of state EOS A (solid line) and EOS II (dashed line) with $\varphi_0 = 0.0$ and $M_{ADM} = 1.4M_\odot$. The right panel is that the frequency of the f-mode as function of the averaged density $(M_{\rm ADM}/R^3)^{1/2}$ of the star with EOS A and $\varphi_0 = 0.0$ (notice that $f_f = \omega_f/2\pi$). The thick solid line corresponds to the values of the mode for $\beta = 0.0$ (GR) while we also show the effect of the scalar field for three values of the scalar parameter β (-8.0, -7.0 and -6.0).

4 Conclusions

We have discussed the effect of the scalar-tensor theories on the oscillation spectra of neutron stars. The presence of a scalar field in the the strong-field regime has already been constrained by weak field experiments and here we provide an additional way of testing/constraining their existence via the gravitational wave asteroseismology. We show that the oscillation frequencies of neutron stars carry very "clean" imprints of the presence of the scalar field. An observation of the neutron star oscillation spectrum via gravitational waves or via electromagnetic signals emanating from or around the surface of a neutron star will not only probe the existence of the scalar field but it might also provide a measurement of its asymptotic value. In this study we have used the Cowling approximation which, although a restricted way of studying stellar oscillation, has proven to be a very accurate and useful tool in asteroseismology. Still, more detailed study is needed for proper modeling of the effect. The inclusion of metric and scalar field perturbations will result to additional information in the gravitational wave spectrum. The combination of this extra information should provide more accurate constraints on the existence of the scalar field.

References

[1] C.M.Will Living Rev. Relativ. 4 (2001), (http://www.livingreviews.org/Articles/Volume4/2001-4).

[2] S. DeDeo and D. Psaltis, Phys. Rev. Lett. **90**, 141101 (2003).

[3] S. DeDeo and D. Psaltis, astro-ph/0405067.

[4] T. Damour and G. Esposito-Farèse, Phys. Rev. Lett. **70**, 2220 (1993).

[5] T. Harada, Phys. Rev. D **57**, 4802 (1998).

[6] N. Andersson, K.D. Kokkotas, MNRAS, **299**, 1059 (1998).

[7] K. D. Kokkotas, T. A. Apostolatos and N. Andersson, MNRAS, **320** , 307 (2001)

The disinformation problem for black holes

Sean A. Hayward

Department of Physics, National Central University, Jhongli, Taoyuan 320, Taiwan

No escape?

1966: "*event horizon*... is the boundary of the region from which particles or photons can escape to infinity... a *black hole* is a region... from which particles or photons cannot escape"

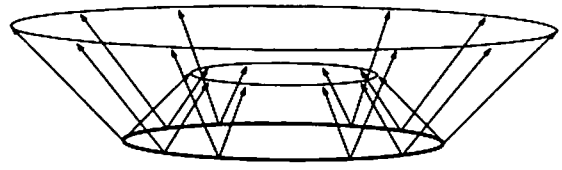
1976: "Because part of the information about the state of the system is lost down the hole, the final situation is represented by a density matrix rather than a pure quantum state"

1997: "Whereas Stephen Hawking and Kip Thorne firmly believe that information swallowed by a black hole is forever hidden from the outside universe, and can never be revealed even as the black hole evaporates and completely disappears..."

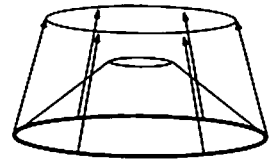
2004: "Thus the total path integral is unitary and information is not lost in the formation and evaporation of black holes. The way the information gets out seems to be that a true event horizon never forms, just an apparent horizon"

[Hawking quotes]

How should black holes be defined? Event and apparent horizons are too indirectly defined.
Assume spherical symmetry for simplicity (everything generalizes).
Area A, null coordinates $x^\pm$: $g^{-1}(dx^\pm, dx^\pm) = 0$, future-pointing, unique up to $x^\pm \mapsto \tilde{x}^\pm(x^\pm)$.
Null expansions $\theta_\pm = \partial_\pm A/A$, $\partial_\pm = \partial/\partial x^\pm$.
Normally, outgoing light rays diverge, $\theta_+ > 0$,
ingoing light rays converge, $\theta_- < 0$;
outgoing wavefront expands,
ingoing wavefront contracts:

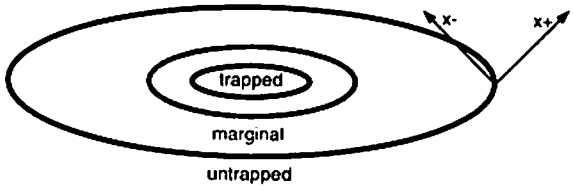


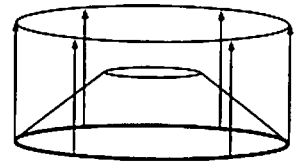
But if there is a massive source inside the surface,
its gravitational field has an attractive or converging effect.
Close enough to a massive enough source,
the outgoing light rays may also be converging, $\theta_+ < 0$; a trapped surface:



Everything inside is trapped within a shrinking area.
Nothing can escape, not even light.

In between, there will be a marginal surface (marginally trapped surface), $\theta_+ = 0$,
where the outgoing light rays are instantaneously parallel:





This is a black hole: its surface is located by the marginal surface, where outgoing light rays are instantaneously parallel, $\theta_+ = 0$, ingoing light rays are converging, $\theta_- < 0$, and outgoing light rays are diverging just outside and converging just inside, $\partial_- \theta_+ < 0$. As time develops, the marginal surfaces generate a hypersurface in space-time.

Gravity traps

$$\text{A surface is } \left\{\begin{matrix}\text{untrapped}\\ \text{marginal}\\ \text{trapped}\end{matrix}\right\} \text{ if } \theta_+\theta_- \left\{\begin{matrix}<0\\ =0\\ >0\end{matrix}\right\},$$

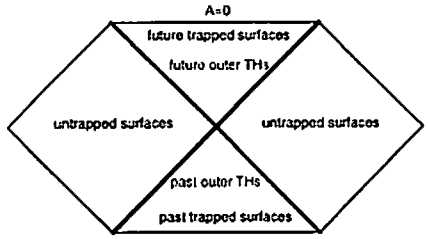
$$\left\{\begin{matrix}\text{future}\\ \text{past}\end{matrix}\right\} \text{trapped if } \theta_\pm \left\{\begin{matrix}<0\\ >0\end{matrix}\right\}, \left\{\begin{matrix}\text{future}\\ \text{past}\end{matrix}\right\} \text{marginal if } \theta_- \left\{\begin{matrix}<0\\ >0\end{matrix}\right\} \text{(for } \theta_+ = 0).$$

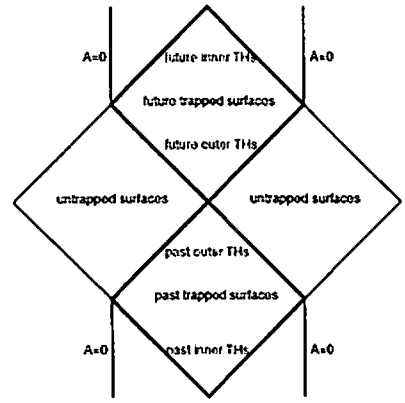
Trapping horizon: a hypersurface foliated by marginal surfaces,

$$\left\{\begin{matrix}\text{outer}\\ \text{degenerate}\\ \text{inner}\end{matrix}\right\} \text{ if } \partial_-\theta_+ \left\{\begin{matrix}<0\\ =0\\ >0\end{matrix}\right\} \text{(for } \theta_+ = 0).$$

$$\text{A } \left\{\begin{matrix}\text{future}\\ \text{past}\end{matrix}\right\} \text{outer trapping horizon can be taken as the local definition of a } \left\{\begin{matrix}\text{black}\\ \text{white}\end{matrix}\right\} \text{hole.}$$

e.g. Schwarzschild and Reissner-Nordström black holes:





Signature law:

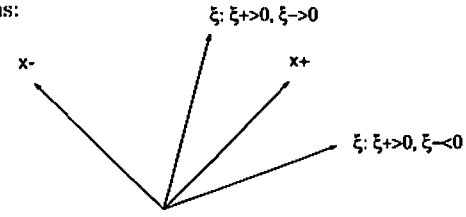
$$\text{NEC (null energy condition)} \Rightarrow \left\{\begin{matrix}\text{outer}\\ \text{inner}\end{matrix}\right\} \text{trapping horizons are } \left\{\begin{matrix}\text{spatial or null}\\ \text{temporal or null}\end{matrix}\right\},$$

and null if and only if the ingoing energy density vanishes.

Proof. Take the case $\theta_+ \cong 0$ (evaluation on the horizon),
write the horizon-generating vector $\xi = \xi^+\partial_+ + \xi^-\partial_-$,
then $0 \cong \xi \cdot d\theta_+ = \xi^+\partial_+\theta_+ + \xi^-\partial_-\theta_+$ relates three signs:

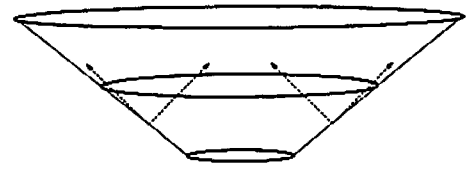
$$\frac{\xi^-}{\xi^+} \left\{\begin{matrix}<0\\ =0\\ >0\end{matrix}\right\} \text{ for a } \left\{\begin{matrix}\text{spatial}\\ \text{null}\\ \text{temporal}\end{matrix}\right\} \text{ trapping horizon;}$$

$$\partial_-\theta_+ \left\{\begin{matrix}<0\\ >0\end{matrix}\right\} \text{ for an } \left\{\begin{matrix}\text{outer}\\ \text{inner}\end{matrix}\right\} \text{ trapping horizon;}$$



$\partial_+\theta_+ \cong -8\pi G T_{++}$ (null focusing equation, from Einstein equation),
$T_{\pm\pm} = T(\partial_\pm, \partial_\pm)$ (energy tensor), NEC $\Rightarrow T_{\pm\pm} \geq 0$.

$\Rightarrow$ Black hole horizons are one-way traversable;
one can fall into a black hole but not escape:



Area law: NEC $\Rightarrow$

$$\left\{\begin{array}{l}\text{future outer or past inner}\\ \text{past outer or future inner}\end{array}\right\}\text{trapping horizons have}\left\{\begin{array}{l}\text{non-decreasing}\\ \text{non-increasing}\end{array}\right\}\text{area,}\left\{\begin{array}{l}A'\geq 0\\ A'\leq 0\end{array}\right\},$$

instantaneously constant ($A'=0$) if and only if the horizon is null.

Proof. $A'=\xi\cdot dA=A(\xi^+\theta_+ +\xi^-\theta_-)\cong A\xi^-\theta_-$. Fixing orientation $\xi^+>0$,

$$\xi^-\left\{\begin{array}{ll}\leq 0 & \text{for outer horizons}\\ \geq 0 & \text{for inner horizons}\\ =0 & \text{for null horizons}\end{array}\right\}\text{as above; }\theta_-\left\{\begin{array}{l}<0\\ >0\end{array}\right\}\text{for}\left\{\begin{array}{l}\text{future}\\ \text{past}\end{array}\right\}\text{horizons.}$$

$\Rightarrow$ Black holes grow if they absorb any matter, and otherwise remain the same size.

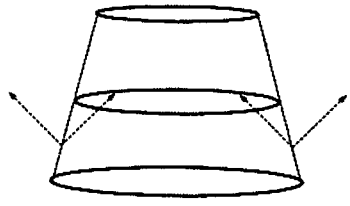
(Actually general results, not restricted to spherical symmetry).

Evaporating black holes: Hawking radiation is based on pair production of
positive-energy outgoing radiation, $T_{--}>0$,
and negative-energy ingoing radiation, $T_{++}<0$.
$\Rightarrow$ area and signature properties reverse:

$$\text{ingoing energy density negative}\Rightarrow\left\{\begin{array}{l}\text{outer}\\ \text{inner}\end{array}\right\}\text{trapping horizons are}\left\{\begin{array}{l}\text{temporal}\\ \text{spatial}\end{array}\right\},$$

$$\left\{\begin{array}{l}\text{future outer or past inner}\\ \text{future inner or past outer}\end{array}\right\}\text{trapping horizons have}\left\{\begin{array}{l}\text{decreasing}\\ \text{increasing}\end{array}\right\}\text{area,}\left\{\begin{array}{l}A'<0\\ A'>0\end{array}\right\}.$$

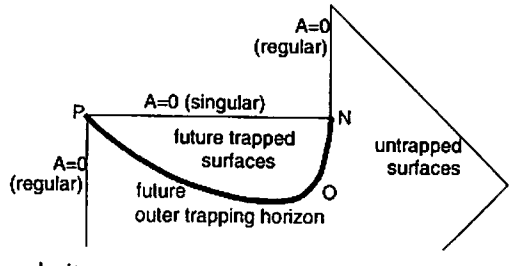
The black-hole horizon is shrinking and two-way traversable:
Matter and information clearly will escape.



Losing it?

No reason to expect a purely thermal spectrum for an evaporating black hole;
Hawking's thermal spectrum holds only for a stationary black hole,
ignoring the back-reaction of the radiation on the black hole, which is not evaporating.

Endpoint of evaporation? Usual picture:

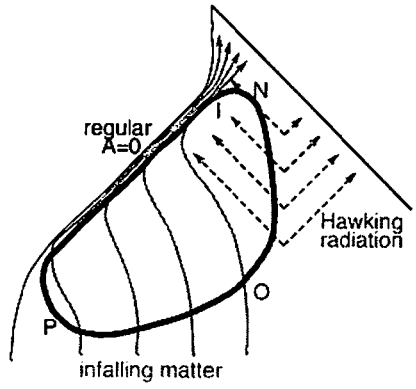


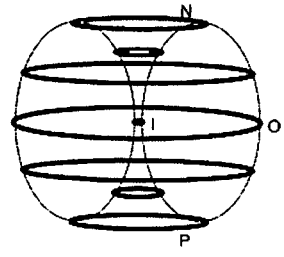
PO: $T_{++}>0$, outer $\Rightarrow$ spatial, growing.
ON: $T_{++}<0$, outer $\Rightarrow$ temporal, shrinking.
The horizon shrinks to zero size, intersecting the singularity.
Some of the matter (and information) escapes, some is lost in the singularity.
However, this is a semi-classical approximation, valid only away from the singularity.
In full quantum gravity, is the singularity resolved?

The great escape

Assume that the centre never becomes singular.
Regular centre ⇒ ∃ untrapped neighbourhood
⇒ ∃ inner (future) trapping horizon.
Inner horizon and centre approach, become almost null,
matter becomes almost pure outgoing radiation:
(∃ exact Einstein-Klein-Gordon solution).
During black-hole formation:
PO: $T_{++} > 0$, outer ⇒ spatial, growing.
PI: $T_{++} > 0$, inner ⇒ temporal, shrinking.
During black-hole evaporation:
ON: $T_{++} < 0$, outer ⇒ temporal, shrinking.
IN: $T_{++} < 0$, inner ⇒ spatial, growing.
The outer and inner sections eventually meet,
marking the endpoint of evaporation.
Metric C^2 ⇒ inner and outer sections join smoothly.
⇒ ∃ single trapping horizon of $S^2 \times S^1$ topology,
enclosing a compact region of trapped surfaces.

The black hole has evaporated completely,
with all its contents re-emerging, albeit mangled.





No information loss: no event horizon. Obtained by (at least) three independent methods:
- Euclidean quantum gravity [Hawking, unpublished];
- loop quantum gravity [Ashtekar & Bojowald, unpublished];
- this qualitative classical analysis with minimal assumptions about "correct" quantum gravity,
that a singularity never forms
and that the ingoing radiation has negative energy density during the entire evaporation phase.

Orthodox paradox

- Logically there are no true paradoxes, just misunderstandings, usually simple but fundamental.
The *disinformation problem* for black holes: defining them by event horizons as regions of no escape.
- Understanding black holes locally by trapping horizons, the supposed paradox disappears.

Cosmological term by deforming the Friedmann equation

Erico Tanaka[1], Takayoshi Ootsuka[2]

[1] *Astrophysics and Cosmology Group, Department of Physics, Ochanomizu University, Tokyo 112-8610, Japan*

Abstract

We show that by considering the indifferentiability of the space-time structure, a term corresponding to cosmological term could be produced in the Friedmann equation. The origin of this indifferentiability could be traced back to the fractal or highly complex distribution of the matter, though this distribution is assumed to be almost homogeneous at the large scale of the universe. Dimakis and Müller-Hoissen's non-commutative differential geometry is used to deal with the indifferentiable variables in the theory.

1 Introduction

We would like to introduce a way of describing the cosmological term as an "apparent" effect of ignoring the small inhomogeneity of the matter distribution and approximating the universe by isotropic and homogenous model. We assume there are small fluctuations on the matter density which are extremely crumpled, but the amplitude of the fluctuation depends on the scale we consider. That is, when we select the size of the system and the size of the object we are interested in, we can change the characteristic length scale which denotes the minimum interval l between the crumples. We may assume that when taking the system size large and size of the object small, so that l gets near to 0, the fluctuation amplitude gets small and therefore reduces to the homogeneous case. In this way we introduce inhomogeneity as indifferentiability, and since the usual differential scheme does not hold, we incorporate non-commutative differential geometry as a tool for handling indifferentiable functions. In section 2 we introduce briefly the method of non-commutative differential geometry constructed by Dimakis and Müller-Hoissen. In section 3 we review the Einstein-Cartan gravity and applies the method defined in section 2. We summarize our results in section 4.

2 Non-commutative geometry

We first think of nearly homogeneous and isotropic matter distribution ρ, which in fact is described by indifferentiable function, though its inhomogeneity is only noticed for sufficiently large l. When we attribute this indifferentiablity to fractal like matter distribution, the space-time construction also would be affected by indifferentiablity through Einstein equation. So, the matter density ρ and scale factor a depends on spatial coordinates as well, and we denote its difference by an operator Δ_i, which in the limit of $l \to 0$ becomes the usual spatial derivative $\frac{\partial}{\partial x^i}$. Here we introduce the non-commutative differential geometry, by Dimakis and Müller-Hoissen. Their method holds the manifold structure, and by keeping the conditions defined bellow, the usual techniques of differential geometry are applicable. The rule is,

1. to define exterior derivative as:

$$\mathrm{d} = \mathrm{d}t \wedge \frac{\partial}{\partial t} + \mathrm{d}x^i \wedge \Delta_i, \tag{1}$$

2. and keep Lebnitz rule:

$$\mathrm{d}(fg) = \mathrm{d}f\, g + f\, \mathrm{d}g. \tag{2}$$

[1] E-mail:erico@cosmos.phys.ocha.ac.jp
[2] E-mail:ootsuka@cosmos.phys.ocha.ac.jp

Usual partial derivative is taken for time component. The form of taking the difference operation is arbitrary. For example, if we define

$$\Delta f(x) = \frac{f(x+l) - f(x)}{l}, \tag{3}$$

the 2nd condition requires the relation, $f(x)\mathrm{d}x = \mathrm{d}x f(x+l)$. Another example is what is referred to as q-derivative,

$$\Delta f(x) = \frac{f(qx) - f(x)}{(q-1)x}, \tag{4}$$

and in this case, $f(x)\mathrm{d}x = \mathrm{d}x f(qx)$. l and q could be regarded as a deformation parameter, which indicates the scale of crumpiness. The non-commutativity of the function and differential forms are the essential part of our story. What we need to do is to recast the Friedmann equation to a Δ-difference taking fashion, observing the above conditions and considering finite spatial differences, ex. $\Delta_i a \neq 0$. Since these methods are expressed in words of differential forms and functions, we apply the Cartan's scheme of treating gravity, which is compatible to above conditions and has less ambiguity of ordering forms and functions, compared to usual metric approach.

3 Einstein-Cartan theory and deformation

The equation of motion of Einstein-Cartan theory is given as:

$$[*F \wedge \theta] = \kappa T, \tag{5}$$

$$D\theta = 0, \tag{6}$$

where, $F = \mathrm{d}A + \frac{1}{2}[A \wedge A]$ is the $SO(3,1)$ curvature, and A the $SO(3,1)$ connection $A = \frac{1}{2}A^{ij}{}_{\mu}\theta^{\mu} \otimes M_{ij}$, $\theta = \theta^{\mu} \otimes P_{\mu}$ the cotetrad, and $T = \frac{1}{3!}T^{i}{}_{\mu\nu\rho}\theta^{\mu} \wedge \theta^{\nu} \wedge \theta^{\rho} \otimes P_i$ is the energy-momentum described by a 3-form. (M_{ij}, P_i) are the generators of Poincare algebra. To derive the Friedmann equation, we set the following ansatz to the tetrad,

$$\theta = \mathrm{d}t \otimes P_0 + \sigma^i a \otimes P_i, \tag{7}$$

$$\begin{cases} k = +1 & \cdots & \mathrm{d}\sigma^i = \epsilon^i{}_{jk}\sigma^j \wedge \sigma^k \\ k = 0 & \cdots & \mathrm{d}\sigma^i = 0 \\ k = +1 & \cdots & \mathrm{d}\sigma^1 = \sigma^1 \wedge \sigma^3,\ \mathrm{d}\sigma^2 = \sigma^2 \wedge \sigma^3,\ \mathrm{d}\sigma^3 = 0 \end{cases} \tag{8}$$

where a is the scale factor, σ^i the triad on a 3-dimensional hypersurface. Then from the torsionless condition (6), one can solve for the connection A, by which curvature F could be constructed. The energy-momentum in the rhs of the Einstein equation (5) could be expressed as,

$$T = \langle u, e \rangle \cdot \rho u. \tag{9}$$

The vector u is the P-valued four-velocity, and e is the tetrad, dual of θ. The matter density ρ is described by a 4-form, $\rho = \rho_{\mu\nu\rho\sigma}\theta^{\mu} \wedge \theta^{\nu} \wedge \theta^{\rho} \wedge \theta^{\sigma}$. Then we obtain the usual Friedmann equation,

$$\frac{3}{a^2}((\dot{a})^2 + k) = \kappa \rho_{0123} \tag{10}$$

$$\frac{2\ddot{a}}{a} + \frac{(\dot{a})^2 + k}{a^2} = 0. \tag{11}$$

The non-commutativity could be implied by introducing spatial dependence on the matter ρ and scale factor a, and replacing the spatial part of partial derivative with difference operator, Δ. For simplicity, we only calculated for the $k = 0$ flat case, which the cotriad σ^i becomes $\mathrm{d}x^i$, and makes the problem much easier to handle. We also would need to adjust the time-like vector, for the anisotropy and inhomogeneity of the space-time. This modification is denoted by the lapse function N and shift vector N,

$$\theta = \mathrm{d}tN \otimes P_0 + (\mathrm{d}x^i a + \mathrm{d}t\mathrm{N}^i) \otimes P_i, \tag{12}$$

and when we take the deformation parameter as l, we assume that N becomes 1 and N^i becomes 0 in the $l \to 0$ limit. The order of differential form and function are defined always such that differential form should come first. When these order are exchanged during the calculation, the spatial term in the function are shifted. We denote this shift by, $\mathrm{d}x^i f(x^i) = f(x^i)_{-x^i}\mathrm{d}x^i$ or $f(x^i)\mathrm{d}x^i = \mathrm{d}x^i f(x^i)_{+x^i}$. Solving the torsionless condition, we can get the modified connection ${}^l\!A$ in the following form,

$$ {}^l\!A = {}^l\!A^{0i}(a, N, N^j) \otimes M_{0i} + \frac{1}{2}{}^l\!A^{ij}(a, N^k) \otimes M_{ij}, \tag{13} $$

and each components are shown bellow:

$$ \begin{aligned} {}^l\!A^{0i}{}_0 &= -(\Delta_i N)_{-x^i}(a^{-1})_{-x^i} + \frac{1}{2}(\Delta_i \mathrm{N}^j + \Delta_j \mathrm{N}^i)_{-x^i}\mathrm{N}^j{}_{-x^i}N^{-1}_{-x^i}(a^{-1})_{-x^i} \\ {}^l\!A^{0i}{}_j &= \frac{1}{2}(\Delta_i \mathrm{N}^j + \Delta_j \mathrm{N}^i)N^{-1}_{-x^i},\ {}^l\!A^{0i}{}_i = (-\dot{a} + \Delta_i \mathrm{N}^i + (\Delta a)_{-x^i}(a^{-1})_{-x^i})N^{-1} \\ {}^l\!A^{ij}{}_0 &= \frac{1}{2}(\Delta_i \mathrm{N}^j - \Delta_j \mathrm{N}^i)_{-x^i}a^{-1}_{-x^i},\ {}^l\!A^{ij}{}_j = (\Delta a)_{-x^i}(a^{-1})_{-x^i},\ {}^l\!A^{ij}{}_k = 0. \end{aligned} \tag{14} $$

The script with a bar means no summation. Curvature ${}^l\!F$ could be calculated from this connection, and the energy-momentum is given by,

$$ \begin{aligned} T &= \mathrm{d}x^1\wedge\mathrm{d}x^2\wedge\mathrm{d}x^3(u^0)^2\tilde{\rho}a_{++}a_+a \otimes P_0 \\ &+ \left(\mathrm{d}t\wedge\mathrm{d}x^2\wedge\mathrm{d}x^3 + \mathrm{d}t\wedge\mathrm{d}x^3\wedge\mathrm{d}x^1 + \mathrm{d}t\wedge\mathrm{d}x^1\wedge\mathrm{d}x^2\right)\left(\mathrm{N}u^0 - N\bar{u}\right)u^0\tilde{\rho}a_+a \otimes P_0 \\ &+ \mathrm{d}x^1\wedge\mathrm{d}x^2\wedge\mathrm{d}x^3 u^0\bar{u}^i\tilde{\rho}a_{++}a_+a \otimes P_i \\ &+ \left(\mathrm{d}t\wedge\mathrm{d}x^2\wedge\mathrm{d}x^3 + \mathrm{d}t\wedge\mathrm{d}x^3\wedge\mathrm{d}x^1 + \mathrm{d}t\wedge\mathrm{d}x^1\wedge\mathrm{d}x^2\right)\left(\mathrm{N}u^0 - N\bar{u}\right)u^i\tilde{\rho}a_+a \otimes P_i. \end{aligned} \tag{15} $$

Here, we assumed $\mathrm{N}^1 = \mathrm{N}^2 = \mathrm{N}^3 \equiv \mathrm{N}$ for simplicity. The matter should satisfy the geodesic equation $D_{(u,e)}u = 0$ and conservation law, $\mathrm{d}\left((u,e)\cdot\rho\right) = 0$. The former gives condition for the 4-vector u,

$$ \begin{aligned} &N^{-1}\left(u^0\dot{u}^0 - \mathrm{N}u^0a^{-1}\dot{a}(u^1+u^2+u^3) - \mathrm{N}u^0a^{-1}\Delta u^0 + a^{-1}\right) \\ &+a^{-1}\Delta u^0(u^1+u^2+u^3) + a_+\dot{a}(-1+(u^0)^2)) = 0 \qquad (16) \\ &N^{-1}\left(u^0\dot{u}^i - \mathrm{N}u^0a^{-1}(3\Delta u^i + \dot{a}u^0)\right) + a^{-1}(u^1+u^2+u^3)\Delta u^i \\ &+a^{-1}u^i\left(\dot{a}u^0 + fa_+(u^1+u^2+u^3)\right) - fa_+a^{-1}(-1+(u^0)^2) = 0 \qquad (17) \\ & \qquad (18) \end{aligned} $$

and the latter becomes

$$ \frac{\partial}{\partial t}\left(a_{++}a_+a\right)\tilde{\rho} + a_{++}a_+a\Delta\tilde{\rho} - 6\left(\Delta\left(\mathrm{N}a_+a\right)\tilde{\rho} + \mathrm{N}a_+a\Delta\tilde{\rho}\right) = 0. \tag{19} $$

First term corresponds to the normal conservation law.

4 Deformed Einstein equation

We could now obtain the modified Einstein equations. For simplicity, we assumed the isotropy of fluctuations so that $\Delta_1 a = \Delta_2 a = \Delta_3 a \equiv \Delta a$, and also set $\mathrm{N}^1 = \mathrm{N}^2 = \mathrm{N}^3 \equiv \mathrm{N}$. We also set $\Delta N = 0$ and $\Delta\mathrm{N} = 0$ for calculation ability, though it should be considered for further evaluation. Using the assumptions, the modified Einstein equations become,

$$ \begin{aligned} &1.\ N\left(2\Delta A_2 - A_{1+}A_1 + A_{2+}A_2\right) + 2a\dot{A}_{1+} + 2\mathrm{N}\left(-\Delta A_1 + \frac{1}{2}\left(A_{1+}A_2 + A_1A_{2+}\right)\right) = 0, \\ &2.\ 3a\left(2\left(\Delta A_2\right)_+ - A_{1++}A_{1+} + A_{2++}A_{2+}\right) = -\frac{8\pi G}{c^4}\tilde{\rho}(u^0)^2a_{++}a_+a, \\ &3.\ N(-\Delta A_2 + A_{2+}A_2) = 0, \\ &4.\ -2\dot{A}_{2+}a + \mathrm{N}(2\Delta A_1 - 2\Delta A_2 - A_1A_{1+} + 3A_2A_{2+}) = 0 \\ &5.\ -2a\left(-\Delta A_{1+} + \frac{1}{2}\left(A_{1++}A_{2+} + A_{1+}A_{2++}\right)\right) = -\frac{8\pi G}{c^4}\tilde{\rho}u^0\bar{u}a_{++}a_+a, \end{aligned} \tag{20} $$

and the variable A_1 and A_2 represents

$$A_1 = (-\dot{a} + 3(\Delta a)_-(a^{-1})_-\mathrm{N})N^{-1}$$
$$A_2 = (\Delta a)_-(a^{-1})_-. \tag{21}$$

The first and second equation corresponds to the usual Friedmann equations, while the rest appears as conditions for the increased degrees of freedom. The solution must obey these 5 equations and further, the equation for matter conservation. While obtaining the exact solution should be hard (if not impossible), we can easily compare the terms in these equation to the original Friedmann equation. Before doing this, we put our attention on equation 3., which looks most favourable out of the five. Indeed, we can determine our difference of the scale factor Δa up to function, using this equation. Setting $\Delta a = f a a_+$, where f is either a constant or an arbitrary function of t, one can easily confirm the lhs of eq.3 becomes exactly 0. We may use this property for evaluating other equations. Combining 1st and 5th will delete the term which includes $\Delta\dot{a}$. This term is not defined, but is rather derived from the 5th condition. The 1st and 2nd Friedmann equation becomes,

$$1.\ 3\left(\dot{a}a_+ - 3f\frac{\partial}{\partial t}(aa_+)\mathrm{N}\right) - 9f^2N^2\left(1 - \frac{3\mathrm{N}^2}{N^2}\right)aa_+ = \frac{8\pi G}{c^4}\tilde{\rho}_-(u^0)^2N^2aa_+,$$
$$2.\ -2\ddot{a}_+a - \dot{a}\dot{a}_+ + 3\left(2a\frac{\partial}{\partial t}(fa_+) + f\frac{\partial}{\partial t}(aa_+)\right)\mathrm{N} + 3f^2N^2\left(1 - \frac{3\mathrm{N}^2}{N^2}\right)aa_+ + \frac{8\pi G}{c^4}\tilde{\rho}_-u^0\bar{u}N\mathrm{N}aa_+ = 0. \tag{22}$$

For the limit $l \to 0$, values such as a_+, becomes a value without a shift. It is clear from its definition, $a_+ = a + l\Delta a$. f should also disappear, since we assumed isotropy and homogeneity to recover in this limit, and therefore $\Delta a \to \frac{\partial a}{\partial x} = 0$. Then one can see that this equation reduces to the ordinary Friedmann equations, as expected. However, if one preserve finite f in the limit, the term proportional to f^2 remains in both equation. This term is usually referred to as the cosmological term. In our case, the coefficient differs from the usual Friedmann equation, and $\Lambda \sim 9f^2$ in the case of equation 1., and $\Lambda \sim 3f^2$ in the case of equation 2. Therefore Λ in our method is positive. There are some remarks; when one suppose a separable scale function $a(t,x,y,z) = X(t)Y(x,y,z)$, so that the function X corresponds naturally to the scale factor without inhomogeneity, conflicts emerges from certain conditions in (20). For instance, the lhs of equation 5 becomes 0, while the rhs $\neq 0$ for general value of N. This conflict can be dissolved by non-separable scale function, since in this case the non-commutativity of taking the difference in space D and time t occurs, and lhs of the equation 4 also becomes non-zero. The sign of $\ddot{a}$ can be discussed properly after deciding the specific form of f and ρ. For the meanwhile, we can evaluate it using the 4th of (20) and (22).

$$\ddot{a} = -\frac{4\pi G}{3c^4}N^2\tilde{\rho}_-(u^0)^2a_+. \tag{23}$$

So, only deceleration is implemented in this case. However, when anisotropy and spatial dependence of N, N and u are considered, correction term appears in rhs of (23), and this may change the situation.

5 Acknowledgements

We greatly appreciate the opportunity of joining the JGRG and be given useful comments and questions. We especially thank Hiroyuki Nakano, and Sanjay Jhingan for helpful discussion. We also thank conference staffs of Yukawa Institute for Theoretical Physics.

References

[1] A Dimakis, F Müller-Hoissen and T Striker, "Non-commutative differential calculus and lattice gauge theory", J. Phys. A:Math. Gen.**26** (1993) 1927-49.

Secular Stability and Rotational Limit of Strange Stars

Shigeyuki Karino[1]

SISSA, International School for Advanced Studies, via Beirut 2/4, Trieste 34014, Italy

Abstract

The stability of rotating strange stars for the gravitational-wave-driven secular instability is considered. Linearized perturbed fluid equations are solved by imposing conditions that the perturbed quantities can be expanded as proportional to $\exp[im\varphi - i\sigma t]$. We found that low mass strange stars are stable for the $m = 2$ f-mode, even the rotation rates are significantly large. As a result, strange stars may rotate with extremely high frequencies.

1 Introduction

The existence of strange stars has been suggested on the hypothesis that the ground state strange quark matters may be extremely stable [1]. Following this suggestion, the structure and stability of strange quark stars have been studied for two decades. If strange stars really exist, they will be observed with the same techniques used to observe normal neutron stars (NSs). And If the masses and radii can be measured from pulsar observations, we may be able to distinguish strange stars from normal NSs, because strange stars may have much different mass-radius relation from NSs [2]. Alternatively, if we could detect gravitational waves emitted from oscillating strange stars, also we can confirm the existences of strange stars [3] [4].

One of the other possibilities to find strange stars is to measure the compact stellar rotations which are limited by several different mechanisms. In particular, gravitational radiation driven (secular) instabilities for the f- and r-modes have attracted attention not only as a plausible mechanism to restrict the rotation rates of compact stars, but also as a powerful source of gravitational waves (GW). Such rotational secular instabilities have been called Chandrasekhar-Friedman-Schutz (CFS) mechanism [5] [6]. On the other hand, in the case of strange stars, the mass shedding limits will appear associated with extremely rapid rotations, because they will be bounded by not only the self-gravity but also tight self-bounding force [7]. It is therefore natural to consider that non-axisymmetric instabilities may limit the rotation rates of strange stars. Within this context, Colpi & Miller (1992) have studied the maximum rotation rates of strange stars approximately [8]. They conclude that in strange stars, secular instabilities caused by $m = 3$ or 2 modes will be dominant and the estimated minimum rotational periods of strange stars can achieve to $P_{\rm min} \lesssim 1$ms. NSs cannot achieve such a high spin rate. However, it is not clear whether the properties of oscillation modes in such self-bounded systems are the same as those with ordinary NSs. For instance, in the spherical strange star model, the response of the oscillation frequencies to the compactness becomes quite different from that in NS models [3]. Hence, it is important to consider the response of the oscillation modes to the rotation correctly.

In view of this, we perform a linear stability analysis of rotating strange stars, in which we calculate the eigenfrequencies of the $m = 2$ non-axisymmetric acoustic mode (bar-mode), and estimate the stability of the CFS mechanism. For simplicity, we consider only in Newtonian theory of gravity, while we take into account the effect of rotation precisely. Our results show that self-bounded systems as like strange stars are stable against GW-driven secular instability.

2 Numerical Method

The procedure for the linear stability analysis is the same as introduced in Karino & Eriguchi (2002), which was used to study the stability of NSs for the f-mode secular instability [9]. The only important

[1] E-mail:karino@sissa.it

difference is that we have used the so-called MIT-Bag equation of state (EOS) described as

$$p = \frac{1}{3}(\rho - 4B), \tag{1}$$

where B is the Bag constant [1] [10]. Although the real value is unknown, usually, we chose the value of B as $B^{1/4} \approx 145$ MeV. It is clear from Equation (1), a stellar model constructed with the Bag-model EOS has a surface with finite density, $\rho_s = 4B$. Using this EOS, we compute the two-dimensional equilibrium configurations of rotating strange stars [11]. We assume the stars to rotate rigidly allowing also for very rapid rotation. Although strange stars are considered as compact objects, in this paper we consider the problem in Newtonian theory of gravity. Therfore, strictly speaking it is necessary to consider the problem in the framework of general relativity, if the strange star mass is higher than the solar mass.

Once the background model is constructed, we solve the linearized perturbed fluid equations iteratively, assuming that we can expand the perturbed quantities as $\delta f = \sum_m f_m \exp[-i\sigma t + im\varphi]$, where δf denotes the Euler perturbation of the quantity f, σ and m denote the eigenfrequency and azimuthal wave number of the considered mode, respectively. Also we assume that the perturbation is adiabatic. Here, we focus only on the polar mode with $m = 2$ (bar-mode). The numerical computation of the system of perturbed fluid equations were carried out by the modified version of the code used in [9].

3 Results

In our computation, the stellar models are parameterized by two parameters: the axis ratio ($r_p = r_{ax}/r_{eq}$) and the ratio between the Bag constant and the central density, $4B/\rho_c$. Though it is said that the typical value of the Bag constant is near $(145\text{MeV})^4$, we do not know the accurate value of B, hence, in this study we use $4B/\rho_c$ as the parameter instead of B. Instead of the rotational parameter r_p, some results will be shown as the functions of $T/|W|$, since historically this parameter has been used for a long time in order to denote the stellar stability limits. For example, the secular stability limit of Maclaurin spheroid for bar-mode oscillation can be shown as $T/|W| = 0.14$. Here, T and W are defined as $T = \frac{1}{2}\int \rho(r\sin\theta)^2\Omega^2 dV$ and $W = \frac{1}{2}\int \rho\phi dV$, respectively. Here, ϕ denotes the gravitational potential. Along the sequence of $4B/\rho_c$ = constant, we compute eigenvalues and eigenfunctions by changing the values of r_p from the spherical limits.

We show the eigenfrequencies of the bar-mode in Figure 1. The curves correspond to $4B/\rho_c = 0.1, 0.3, 0.5, 0.7$ and 0.9, downward from the top, respectively. In this figure, the eigenfrequencies are normalized by $(4\pi G\rho_c)^{1/2}$. Along these curves, $4B/\rho_c$ is conserved, and consequently, the mass of the star is not the same. Because of the freedom of the normalization, the absolute values of these curves do not have significant meanings, since these values will change if we induce other normalization factors as like the mass of the star. The important point is that, however, the location of the neutral point (zero-eigenfrequency point) is not changed by any normalizations.

From Figure 1, it is shown that eigenfrequencies in low mass (i.e. larger $4B/\rho_c$) strange stars do not have neutral points, at least in the computed regime. This result indicates that strange stars will be stable even if they have sufficiently high rotation rate, and the classical stability limit $T/|W| \gtrsim 0.14$, cannot be applied. We conclude that the GW driven CFS instability for $m = 2$ f-mode will not occur in strange stars.

4 Discussion

4.1 Cause of the Stability

We must consider now why strange stars are secularly stable for non-axisymmetric perturbations (bar-mode). Here, we propose several effects which may make strange stars stable.

High density? The eigenfrequency of the f-mode oscillation must reflect the timescale of the sound wave. In general, strange stars with large Bag constant usually have higher mean density. Therefore, it is quite natural to consider that the absolute value of the eigenfrequency for the large $4B/\rho_c$ star will be larger than that for models with smaller $4B/\rho_c$. Now, since the branch of the f-mode has minus sign, the

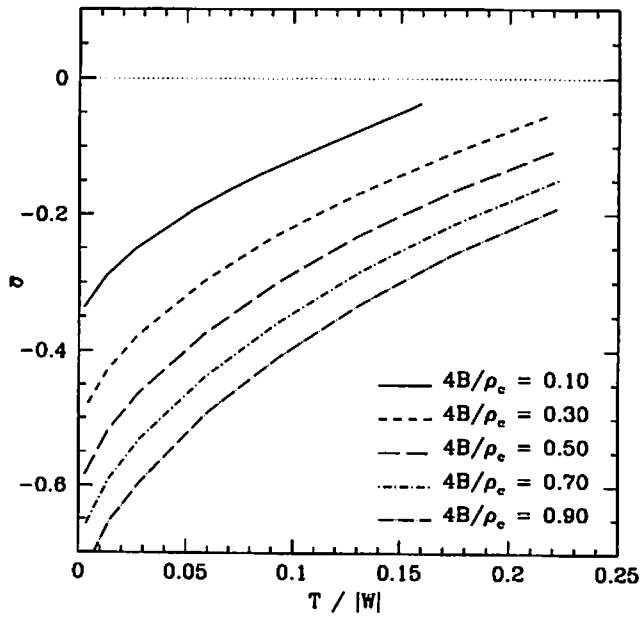


Figure 1: Eigenfrequencies of the bar-mode, $\tilde{\sigma}$. Each eigenfrequency curves are normalized by $(4\pi G\rho_c)^{1/2}$. The five curves correspond to $4B/\rho_c$ = 0.1, 0.3, 0.5, 0.7 and 0.9, in descending order from the top, respectively. The curve with $4B/\rho_c = 0.1$ terminated at the end-point of the equilibrium sequences.

eigenfrequency for the low mass (i.e. large $4B/\rho_c$) strange stars will locate lower in Fig. 1. It is clear from this figure that the downward-shift of the eigenfrequency contributes to make the star stable.

Weak gravity? Another insight about the stability of strange stars is deduced from the weakness of the self-gravity of strange stars. As we mentioned, strange stellar matter is bounded not only by the self-gravitational force, but also by the self-bounding force via Bag constant. Therefore, in this system, the self-gravitational force will be relatively less important, comparing with normal stars bounded by only their self-gravity forces. Here, it is important to recall that, the eigenfrequencies of acoustic modes strongly depends on the effects of the gravitational force. In this sense, the property that gravity force plays less important role may change the eigenfrequency of acoustic modes significantly.

Gravitational energy? Also another possibility deduced from the weakness of the self-gravity of strange stars will appear on the definition of the "rotation rate" used here, and will affect the scale of the horizontal axis in Figure 1. If the gravitation is less important in the system, the gravitational energy may be reduced effectively [7]. In this case, the parameter $T/|W|$ may be over-estimated. This modification of rotation rate will rescale the horizontal axis in Fig. 1.

4.2 Fate of strange star rotation

In this paper, we have shown that CFS instability caused by $m = 2$ f-mode oscillation does not limit the rotation rates of strange stars. Also mass shedding does not tend to restrict their rotations. Then, can strange stars really achieve extremely rapid rotations? If not, what kind of mechanism will stop the infinite acceleration of strange star rotations? Even if bar-mode instability cannot play an important role to limit the rotation rate of the strange stars, other mechanisms will restrict the rotation of those stars. For instance, r-mode instability or f-mode instability with large m may work even in strange stars. Also magnetic effect may be able to limit the rotation rate. In order to make it clear, further investigations are needed.

5 summary

In this study, we have performed the linear stability analysis of strange stars for gravitational wave driven secular instability due to bar-mode. The stellar models have been constructed by using Bag model EOS. The stability of the stars has been studied via the neutral point search. Effects of viscosity, magnetic field, and general relativity are neglected.

As the result, the bar-mode eigenfrequencies in strange stars with large $4B/\rho_c$ ratio do not have neutral points even the deformation become significant due to the rapid rotation. This implies that low-mass strange stars are significantly stable against CFS instability and may be able to rotate extremely rapidly. In order to understand the spin evolutions of strange stars, it is necessary to investigate other instability mechanisms and dumping mechanism of oscillations.

References

[1] E. Witten, Phys. Rev. D **30**, 272 (1984)

[2] C. Alcock, E. Farhi, and A. Olinto, Astrophys. J. **310**, 261 (1986)

[3] Y. Kojima, and K. Sakata, Prog. Th. Phys. **108**, 801 (2002)

[4] H. Sotani, and T. Harada, Phys. Rev. D **68**, 024019 (2003)

[5] S. Chandrasekhar, Phys. Rev. Lett. **24**, 611 (1970)

[6] J. L. Friedman, and B. Schutz, Astrophys. J. **222**, 281 (1978)

[7] E. Gourgoulhon, P. Haensel, R. Livine, et al., Astron. and Astrophys. **349**, 851 (1999)

[8] M. Colpi, and J. C. Miller, Astrophys. J. **388**, 513 (1992)

[9] S. Karino, and Y. Eriguchi, Astrophys. J. **578**, 413 (2002)

[10] A. Chodos, R. L. Jaffe, K. Johnson, et al. Phys. Rev. D **9**, 3471 (1974)

[11] Y. Eriguchi, and E. Müller, Astron. and Astrophys. **146**, 260 (1985)

Mass Deficit in Cylindrically Symmetric System

Yasunari Kurita[3,1], Yoshiyuki Morisawa[2] and Ken-ichi Nakao[3]

[1] *Department of Earth and Space Science, Graduate School of Science, Osaka University, Osaka, Toyonaka 560-0043, Japan*
[2] *Yukawa Institute for Theoretical Physics, Kyoto University, Kyoto 606-8502, Japan*
[3] *Department of Physics, Graduate School of Science, Osaka City University, Osaka 558-8585, Japan*

Abstract

We consider static equilibrium states in a thin cylindrically symmetric shell model, made of pressure-free counter-rotating dust. Using C-energy of the shell, we evaluate mass deficit of the shell's static equilibrium states. As a result, we find a strange state that has large mass deficit and large proper radius.

1 Introduction

Gravitational collapses is one of the most important problems in general relativity. However, in general cases, we have to face with the difficulties of non-linear nature of gravity and complexity of gravitational wave emissions. Usually, some symmetry is imposed on the system under consideration; for example, spherically symmetric systems are well studied. Although there is no gravitational waves in those systems, the collapses of various matters are complicated enough and represent rich gravitational physics. In contrast to spherical collapses, other symmetric systems are not so investigated; for example, cylindrically symmetric systems.

The cylindrically symmetric systems include gravitational waves known as Einstein-Rosen gravitational waves [1] and are expected to have different physical properties from those of the spherical ones. In fact, there is no black string solution in four-dimensional Einstein gravity and the final state of the collapses can not be black objects. Although cylindrical systems are not realistic in astrophysical context, it is important to investigate them because it will reveal some aspect of gravitational physics, in particular, their interaction with gravitational waves and will be a simplified model of axially symmetric collapse such as the collapse of the non-rotating dust spheroid [2].

In this article, we consider a thin cylindrically symmetric shell originally constructed by Apostolatos and Thorne [3]. Under general initial conditions, the shell will evolve dynamically; for examples, collapsing to form a naked singularity, or oscillating radially with gravitational wave emissions to finally settle down at some fixed radius, or bouncing to expand in the radial direction infinitely. Our main interest is in its static final states, and we restrict our attention to them. One of physical quantities characterizing them is mass deficit; usually, large mass deficit means that it is a strongly bound state. If the final state has large mass deficit and is localized in a compact small region, then we may effectively call it a singularity. Thus, our main questions here are: "how much energy can be extracted from the shell?" and "how large is the size of the final state?"

For the purpose of defining mass deficit of the cylindrical shell, there is a useful energetic quantity in cylindrically symmetric spacetime called cylindrical energy or "C-energy", which is originally introduced by Thorne [4]. After giving a brief review of the thin cylindrical model in the next section, we define mass deficit of the equilibrium state of the shell and evaluate it in two particular limits. One of them, we find a strange state that is strongly bound, having large proper radius. In section 4, we summarize and discuss about remaining problems.

In this article, we set Newton's gravitational constant and the speed of light to unity.

[1] E-mail:kurita@sci.osaka-cu.ac.jp
[2] E-mail:morisawa@yukawa.kyoto-u.ac.jp
[3] E-mail:knakao@sci.osaka-cu.ac.jp

2 Cylindrical shell of counter-rotating dust particles

In this section, we briefly review a thin cylindrical shell made of counter-rotating dust, originally constructed in [3]. Here, the term "counter-rotating" indicates that the situation in which the half of the dust particles orbit around the symmetric axis in the opposite direction to the other half of particles.

In the vacuum interior and exterior of the shell, the metric can be expressed as follows:

$$ds^2 = e^{2(\gamma-\psi)}(-dt^2 + dr^2) + e^{2\psi}dz^2 + r^2e^{-2\psi}d\phi^2, \tag{1}$$

where $\gamma = \gamma(t,r)$ and $\psi = \psi(t,r)$. The metric function ψ obeys a wave equation and represents the distortions of the geometry. Thus, it is sometimes referred as the gravitational-wave field. $\partial/\partial z$ and $\partial/\partial\phi$ are Killing vectors which generate translations along the cylinder and rotations around the symmetry axis, respectively.

The shell is characterized by the following parameters: (1) the angular momentum per unit rest mass of the dust particles, $\pm\alpha$; (2) its coordinate radius R; (3) the value ψ_s of ψ on the shell; (4) $\mathcal{R} = Re^{-\psi_s}$ (circumference radius of the shell); (5) $u = \alpha/\mathcal{R}$ (the dust particle's linear momentum per unit rest mass as measured by an observer who rides on the shell and orbit neither rightward nor leftward.); (6) λ (shell's total rest mass per unit Killing length); (7) $\Lambda = \lambda e^{-\psi_s}$ (shell's total rest mass per unit proper length). Of these parameters, the conserved quantities are only α and λ in the dynamical evolution of the shell: other parameters generally change. The conservation of λ is due to the dust particles number conservation and that of α is based on the fact that the gravitational field ψ can not extract angular momentum from the shell.

Then, the shell's proper mass per unit proper area as measured by the rest observer on it can be expressed as

$$\sigma = \frac{\lambda\sqrt{1+u^2}}{2\pi R}, \tag{2}$$

and the proper mass of the shell per unit Killing length is

$$\mu = 2\pi R\sigma = \lambda\sqrt{1+u^2}. \tag{3}$$

In this article, we are interested in the configuration in which the shell is in static equilibrium, and thus, we shall consider the static (means vanishing radial velocity of the shell) and radiation-free configuration. Then, in the vacuum exterior of the shell, the spacetime region is given by the Levi-Civita solution to the Einstein equations [5]:

$$\psi = \psi_s - \kappa\ln(r/R), \quad \gamma = \gamma_+ + \kappa^2\ln(r/R), \tag{4}$$

where ψ_s and γ_+ are the values of the field ψ and γ at the shell respectively, and κ is a constant. In the vacuum interior, the Einstein equations and the regularity at the symmetric axis require vanishing γ and constant ψ, (thus $\psi = \psi_s$), and thus, the interior region of the shell is flat.

The dynamical evolution of the shell is determined by Israel's junction condition [6]. Together with the Einstein equations, it implies

$$\kappa = \frac{2\Lambda}{(1-4\Lambda\sqrt{1+u^2})\sqrt{1+u^2}}, \quad \gamma_+ = -\ln(1-4\Lambda\sqrt{1+u^2}). \tag{5}$$

The dynamics of the shell is characterized by $R(\tau)$, where τ is the proper time of an observer on the shell, but not rotating with the shell's particles. The Israel's condition also gives the equation of motion for the shell:

$$\frac{d^2R}{d\tau^2} = \frac{(1+2u^2)^2}{R(1+u^2)^{3/2}}e^{2\psi_s}\left(\Lambda_{eq}(u) - \Lambda\right), \tag{6}$$

where $\Lambda_{eq}(u) := u^2\sqrt{1+u^2}/(1+2u^2)^2$. Thus, in static equilibrium, the right hand side of eq.(6) should vanish and the shell's total rest mass per unit proper length will take the value:

$$\Lambda = \frac{u^2\sqrt{1+u^2}}{(1+2u^2)^2}. \tag{7}$$

For cylindrically symmetric spacetimes, there is a useful energetic quantity, called cylindrical energy or "C-energy" which is originally introduced by Thorne [4]. In this system, C-energy of the region $r \leq r_0$ per unit Killing length z is

$$C = \frac{1}{8}\left(1 - e^{-2\gamma(t,r_0)}\right). \tag{8}$$

This is interpreted as the total energy of the spacetime region $r \leq r_0$ per unit (translational) Killing length. If $r_0 \to \infty$, then the metric function γ goes to zero and the C-energy C becomes 1/8. Thus, the C-energy of the whole cylindrical spacetime is 1/8. If $r_0 < R$, i.e., inside the shell, then the C-energy inside the radius r_0 equals zero. Thus, C-energy at the shell ($r_0 = R$) is equivalent to the total energy of the shell. It should be noted that the C-energy includes not only rest mass but also gravitational energy. In static equilibrium configurations, C-energy at the shell is

$$C_{shell} = \frac{1}{8}\left(1 - e^{-2\gamma_+}\right) = \frac{u^2(1+u^2)(1+2u^2+2u^4)}{(1+2u^2)^4}. \tag{9}$$

Apostolatos and Thorne [3] showed that C-energy minimum at some momentarily static and radiation free configuration (MSRF) corresponds to a static equilibrium of the shell, which might imply that the C-energy plays a role as a potential function in Newtonian theory. However, the linear momentum of dust particles u will not be a conserved quantity in the shell's dynamical evolution and the C-energy minimum will also change. Thus one can not say about the final equilibrium state of some dynamical evolution only from the C-energy argument.

3 Mass deficit in a thin shell model

In order to study some physical properties of the final equilibrium state, let us consider mass deficit in this cylindrical system.

The mass deficit in the static equilibrium configuration can be defined as

$$\Delta\mu = \mu - C_{shell} = \lambda\sqrt{1+u^2} - \frac{u^2(1+u^2)(1+2u^2+2u^4)}{(1+2u^2)^4}. \tag{10}$$

In the following, we consider two limits having large mass deficit.

The first limit is the $u \to \infty$ limit. In this limit, the mass deficit of the equilibrium state becomes

$$\Delta\mu \;\to\; \lambda|u| - \frac{1}{8} \;\simeq\; \lambda|u| \;\simeq\; \mu. \tag{11}$$

Thus, $\Delta\mu/\mu \simeq 1$, meaning that the shell is in a strongly bound state. In this limit, because of the relation $u = \alpha/\mathcal{R}$ and the conservation of α, the shell's circumference radius $\mathcal{R}$ goes to zero. This means that the strongly bound shell is localized in a small compact cylindrical region. This state might be thought of as a singularity, however, C_{shell} is nearly equal to 1/8 which is the energy of the whole cylindrical spacetime. Hence, in order to construct such a state, the whole energy have to be accumulated at the shell. However, in general gravitational collapse, gravitational waves will propagate and carry C-energy to spatial infinity, and therefore, it would not be the final state of the shell's dynamical evolution under some reasonable initial condition.

As the next limit, let us consider the situation that $|u| \ll 1$ and $\psi_s \gg 1$. The value ψ_s is not conserved in the dynamical evolution and there seems to be no apriori reason to forbid large ψ_s. In this case, the shell's total rest mass per unit proper length in static equilibrium Λ_{eq} is

$$\Lambda_{eq} = \lambda e^{-\psi_s} \simeq u^2, \tag{12}$$

and mass deficit is

$$\Delta\mu \;\simeq\; \lambda - u^2 + \mathcal{O}(u^4) \;\simeq\; \lambda - \lambda e^{-\psi_s} + \mathcal{O}(u^4) \tag{13}$$

$$\simeq\; \lambda + \mathcal{O}(u^4). \tag{14}$$

The proper mass of the shell per unit Killing length is

$$\mu = \lambda\sqrt{1+u^2} \simeq \lambda, \tag{15}$$

and thus the ratio of mass deficit to the proper mass is

$$\frac{\Delta\mu}{\mu} \simeq \frac{\lambda}{\lambda} = 1, \tag{16}$$

which means that the shell has large mass deficit. On the other hand, the C-energy at the shell $C_{shell} \simeq u^2 \ll 1$, and thus almost all energy is extracted from the shell. Furthermore, small momenta is equivalent to large circumference or proper radius, i.e.,

$$|u| \ll 1 \;\Leftrightarrow\; \alpha \ll \mathcal{R} = Re^{-\psi_0}. \tag{17}$$

Here, it should be noted that the angular momentum α is conserved quantity. This is quite strange: the shell has large mass deficit and large radius. Is it really strongly bound state?

4 Discussion

In this article, we have investigated the mass deficit of the thin cylindrical shell in particular two limits. In both limits, the shell' mass deficit is large; however, the shell's C-energy is quite different. In the first limit, the shell has the C-energy of the whole cylindrical spacetime, and thus, it seems to be impossible to construct such a shell in a gravitational collapse. On the other hand, in the second limit, the C-energy is almost zero: almost all energy is extracted from the shell in the collapse. In general, gravitational waves carry C-energy away, and we could suspect that, in the second limit, the C-energy is transported from the shell by gravitational waves.

We have shown that, in the second limit, the shell has large mass deficit and also has large circumference or proper radius. Is it possible that, after the final some dynamical evolutions the shell settles down in such a strange state? If it is possible, why do we feel something so strange? It means how we do not understand the cylindrically symmetric gravitational physics. On the other hand, if it is not possible, there should be some unknown mechanics forbidding the strange state. One possibility is that it is dynamically unstable under some perturbation and cannot be realized. If so, there should be some upper limit of energy extraction from the shell. Then, what physics does determine the limit? It might imply that there exists some unknown physics in cylindrical gravitational system. Anyway, we think these investigations give some clue to reveal some strange aspects of cylindrical gravitational systems. We leave these issues for future investigations.

References

[1] A. Einstein and N. Rosen, J. Franklin Inst. **223** 43 (1937)

[2] S. L. Shapiro and S. A. Teukolsky, Phys. Rev. Lett. **66**, 994 (1991)

[3] T. A. Apostolatos and K. S. Thorne, Phys. Rev. D **46** 2435 (1992)

[4] K. S. Thorne, Phys. Rev. **138** B251 (1965)

[5] T. Levi-Civita, Rend. Acc.Lincei **28**, 101 (1919)

[6] W. Israel, Nuovo Cimento **44B**, 1 (1966); **48B**,463 (1967)

Chaotic dynamics in preheating after inflation

Yoshida Jin[1], Shinji Tsujikawa[2]

[1]*Department of Physics, Waseda University, Tokyo 169-8555, Japan*
[2]*Department of Physics, Gunma National College of Technology, Gunma 371-8530, Japan*

Abstract

We study chaotic dynamics in preheating after inflation in which an inflaton ϕ is coupled to another scalar field χ through an interaction $(1/2)g^2\phi^2\chi^2$. First, we estimate the amplitude of the quasi-homogeneous field χ at the end of inflation for large-field inflaton potentials $V(\phi) = V_0\phi^n$ using a Fokker-Planck approach. Unlike the case of standard linear analysis the quasi-homogeneous field χ is not strongly suppressed during inflation, which can give rise to chaos between two dynamical scalar fields. For the quartic potential ($n = 4$, $V_0 = \lambda/4$) chaos actually occurs for $g^2/\lambda \lesssim 70$ in a linear regime before which the backreaction of created particles becomes important. This analysis is supported by several different criteria for the existence of chaos. For the quadratic potential ($n = 2$, $V_0 = m^2/2$) the signature of chaos is not found by the time at which the backreaction begins to work.

1 Introduction

Typically the contribution of the dynamical background field χ is neglected in standard analysis of particle creations in preheating. This may be justified in linear perturbation theory, since super-Hubble perturbations in χ are exponentially suppressed during inflation for the coupling g required for preheating. However if we account for the effect of quantum diffusion using a Fokker-Planck approach [1, 2], the probability distribution of the field χ has a variance that does not exhibit an exponential suppression [3]. This implies that the quasi-homogeneous field χ can play an important role for the dynamics of preheating. In fact Podolsky and Starobinsky [3] pointed out that chaos may occur for the self-coupling potential $V(\phi) = (1/4)\lambda\phi^4$ when the coupling g^2/λ is not too much larger than of order unity. Since it is not obvious whether chaos actually occurs or not in this model only by analytic estimations, we shall perform detailed numerical investigation with/without the backreaction effect of created particles. We will use several different methods to judge the existence of chaos– such as the Toda-Brumer test, Lyapunov exponents and a fractal map.

It was already found that chaos appears for hybrid-type inflation models [4]. The presence of mixing terms between two fields leads to a new instability of perturbations in addition to tachyonic/resonance instabilities. This new type of instability is clearly associated with the presence of chaos.

In this work, which is based on [5], we shall investigate the existence of chaos for large-field potentials $V(\phi) = V_0\phi^n$ with an interaction $(1/2)g^2\phi^2\chi^2$. Our main interest is to find the signature of chaos and the parameter range of the coupling g in which chaos can be seen before the backreaction effect of created particles becomes important. Since chaos can alter the standard picture of preheating by parametric resonance, it is of interest to clarify the situation in which chaos appears.

2 The quasi-homogeneous field χ at the end of inflation

In order to estimate the field variance of χ at the end of inflation, we use the stochastic inflation approach developed by Starobinsky [1]. The Fokker-Planck equation in a de-Sitter background is given by [1, 2]:

$$\frac{\partial P(\chi,t)}{\partial t} = \frac{H^3}{8\pi^2}\frac{\partial^2}{\partial\chi^2}P(\chi,t) + \frac{1}{3H}\frac{\partial}{\partial\chi}\left[\frac{\partial V}{\partial\chi}P(\chi,t)\right], \qquad (1)$$

[1]E-mail:jin@gravity.phys.waseda.ac.jp
[2]E-mail:shinji@nat.gunma-ct.ac.jp

where H is the Hubble rate and $P(\chi,t)$ is the probability of observing the field χ at cosmic time t. When the probability distribution is a Gaussian, it is easy to get the following equation of motion

$$\frac{d}{dt}\sigma^2 = \frac{H^3}{4\pi^2} - \frac{2m_\chi^2(t)}{3H}\sigma^2, \tag{2}$$

where $m_\chi^2 \equiv V_{\chi\chi}$. The variance σ characterizes a typical size of the quasi-homogeneous field χ. The first term on the r.h.s. of Eq. (2) newly appears in the context of stochastic inflation because of the effect of quantum diffusion. In the absence of this term, σ exhibits exponential suppression for $m_\chi^2 \gg H^2$.

Eq. (2) can be integrated using slow roll condition. We find that σ_f, the value of σ at the end of inflation, is

$$\sigma_f \simeq \frac{1}{\sqrt{6\pi}}\frac{m^2}{gm_p} \quad (n=2), \qquad \sigma_f \simeq \frac{1}{\sqrt{6\pi^3}}\frac{\lambda}{g}m_p \quad (n=4), \tag{3}$$

where m_p is the Planck mass.

3 Chaotic dynamics for the quartic potential

The equations for field perturbations in Fourier space may be written as [3]

$$\delta\ddot{\phi}_k + 3H\delta\dot{\phi}_k + \left[\frac{k^2}{a^2} + n(n-1)V_0\phi^{n-2} + g^2\chi^2\right]\delta\phi_k = -2g^2\phi\chi\delta\chi_k, \tag{4}$$

$$\delta\ddot{\chi}_k + 3H\delta\dot{\chi}_k + \left(\frac{k^2}{a^2} + g^2\phi^2\right)\delta\chi_k = -2g^2\phi\chi\delta\phi_k, \tag{5}$$

where k is a comoving wavenumber. The terms on the r.h.s. of Eqs. (4) and (5) are not usually taken into account in standard analysis of preheating, since the field χ was supposed to be dynamically unimportant. If we account for the effect of quantum diffusion, the quasi-homogeneous field χ is not exponentially suppressed during inflation, thereby giving non-negligible contributions to the r.h.s. of Eqs. (4) and (5).

The Toda-Brumer test that is used to judge the existence of chaos is $V_{\phi\phi}V_{\chi\chi} - V_{\phi\chi}^2 < 0$. This corresponds to

$$\chi > \frac{m}{\sqrt{3}g} \quad (n=2), \qquad \chi > \sqrt{\frac{\lambda}{g^2}}\phi \quad (n=4). \tag{6}$$

For the quadratic potential the initial value of χ is $m/m_p \sim 10^{-6}$ times smaller than the value which leads to chaotic instability, see Eqs. (3) and (6). Therefore the system is expected to enter a chaotic phase after the field is amplified more than 10^6 times. For the quartic potential the condition for chaos is not so severe compared to the quadratic potential, since the r.h.s. of Eq. (6) decreases with time.

When $g^2/\lambda = 2$ the Toda-Brumer test gives the condition $\tilde{\chi}/m_p \gtrsim 0.5$ for the existence of chaos, which corresponds to the time $x \equiv \sqrt{\lambda}\phi_I\eta \gtrsim 45$ (see Fig. 1), where $\tilde{\chi}$ and $\tilde{\phi}$ are conformal variables, $\tilde{\chi} \equiv a\chi$, $\tilde{\phi} \equiv a\phi$, and ϕ_I is the initial value of ϕ. We find that the fluctuations $\langle\delta\tilde{\chi}^2\rangle$ and $\langle\delta\tilde{\phi}^2\rangle$ exhibit rapid increase with a similar growth rate after the field χ satisfies the Toda-Brumer test. It is expected that this is associated with the presence of chaos rather than parametric excitation of the χ fluctuation. The quasi-homogeneous field χ is amplified by parametric resonance for $x \lesssim 45$ but stops growing after that. This comes from the fact that the resonance does not occur once the homogeneous oscillation of ϕ is broken by the growth of χ. The $g^2\phi^2$ term on the l.h.s. of Eq. (5) also becomes ineffective at this stage, but the presence of the mixing term on the r.h.s. leads to a new type of instability associated with chaos. The rapid growth of $\langle\delta\tilde{\phi}^2\rangle$ seen in Fig. 1 also comes from the mixing term on the r.h.s. of Eq. (4) rather than from the parametric excitation of the modes with $3/2 < k^2/(\lambda\phi_I^2) < \sqrt{3}$.

In order to check the existence of chaos, we calculate the evolution of the maximal Lyapunov exponent h for several different values of g. The system eventually approaches a phase with a positive constant h, which shows the existence of chaos. The growth of the maximal Lyapunov exponent is regarded as a signature of chaos, since this behavior can not be seen in the absence of chaos. We also use fractal map.

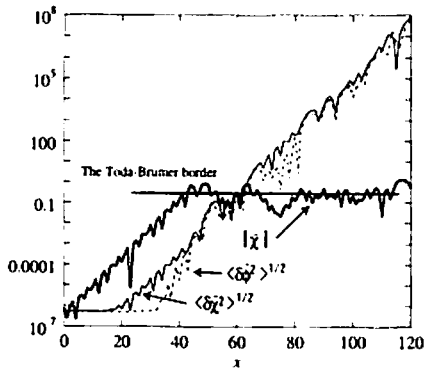


Figure 1: Evolution of $\tilde{\chi}$, $\langle\delta\tilde{\chi}^2\rangle^{1/2}$ and $\langle\delta\tilde{\phi}^2\rangle^{1/2}$ (normalized by m_p) as a function of $x \equiv \sqrt{\lambda}\phi_I\eta$ for $g^2/\lambda = 2$ when the backreaction effect of created particles is neglected. The horizontal line shows the border of the Toda-Brumer test. The perturbations in ϕ and χ exhibit instabilities associated with chaos once the field χ is sufficiently amplified.

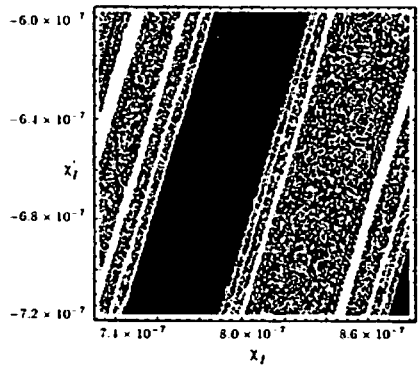


Figure 2: A fractal map for $g^2/\lambda = 2$. We show the map of initial conditions χ_I and χ_I' with exit pockets characterized by $|\tilde{\chi}| \geq 1.2$. The white color corresponds to orbits which give $\tilde{\chi} \geq 1.2$, whereas the black one to orbits which give $\tilde{\chi} \leq -1.2$. The upper panel corresponds to the change of initial conditions by 0.1%. This figure exhibits fractal structures, which result from sensitivity to initial conditions.

Figure 2 shows that the map of initial conditions is fractal. This means that orbits are sensitive to initial data, thereby showing the existence of chaos.

The above discussion neglects the backreaction effect of created particles. By Eq. (4) the backreaction becomes important when

$$\sqrt{\langle\delta\tilde{\chi}^2\rangle} \gtrsim \sqrt{\frac{3\lambda}{g^2}}\,\tilde{\phi}. \tag{7}$$

This is similar to the necessary condition for chaos for the background field χ, see Eq. (6). By implementing the backreaction as a Hartree approximation, we find that this typically tends to work to suppress the growth of field fluctuations. As illustrated in Fig. 3 the fluctuations do not exhibit rapid growth after the backreaction begins to work ($x \gtrsim 60$). Nevertheless we need to caution that linear perturbation theory is no longer valid at this stage. For completeness it is required to account for the mode-mode coupling (rescattering) between the fluctuations. In fact we found a numerical instability for $x \gtrsim 80$ in the simulation of Fig. 3, which signals the limitation of the Hartree approximation.

When $g^2/\lambda = 2$ one can find out the existence of chaos during a short period before the backreaction begins to work. We are interested in the values of g^2/λ in which chaos can be seen by the time at which the backreaction becomes important. For the coupling that belongs to these resonance bands, we find that chaos occurs for

$$g^2/\lambda \lesssim 70, \tag{8}$$

before the backreaction begins to work. When $g^2/\lambda \gtrsim 70$ the field fluctuation $\langle\delta\tilde{\chi}^2\rangle$ satisfies the condition (7) prior to the time at which the necessary condition for chaos is fulfilled. In this case inclusion of nonlinear effects like rescattering is essentially important to understand the evolution of the two-field system and the presence of chaos.

4 Conclusions

In order to estimate the size of the quasi-homogeneous field χ at the beginning of preheating, we made use of the Fokker-Planck approach. The variance of the probability distribution of χ grows during inflation. We derived analytic forms of the variance σ_f at the end of inflation.

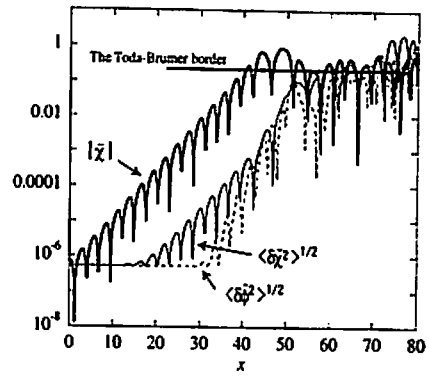


Figure 3: Evolution of $\bar{\chi}$, $\langle\delta\tilde{\chi}^2\rangle^{1/2}$ and $\langle\delta\tilde{\phi}^2\rangle^{1/2}$ (normalized by m_p) for $g^2/\lambda = 2$ when the backreaction effect is taken into account. The horizontal line corresponds to the Toda-Brumer border.

For a quartic potential parametric resonance can occur for the coupling g^2/λ of order unity. In this case the quasi-homogeneous field χ satisfies the Toda-Brumer test (6) before the backreaction effect of created particles becomes important. Since this is only the necessary condition for chaos, we also evaluated Lyapunov exponents in order to confirm the presence of chaos. We find that the maximal Lyapunov exponent shows the existence of chaos. Our analysis using a Fractal map also implies that the system exhibits chaotic behavior. For larger g^2/λ, the backreaction of field fluctuations on sub-Hubble scales works earlier than the time at which the Toda-Brumer test is satisfied for the background field χ. We find signatures of chaos for $g^2/\lambda \lesssim 70$ at the linear regime before the backreaction begins to work.

For a quadratic potential, using the same analysis in quartic potential, we find that chaos can not be observed at least at the linear stage of preheating before the backreaction sets in.

In this work we did not study a nonlinear dynamics of the system during which the mode-mode coupling between perturbations plays an important role. It is of interest to investigate whether the chaotic behavior we found persists in the nonlinear regime. This can give rise to an additional instability of perturbations whose behavior is important toward complete understanding of reheating. It will be of interest to study a non-Gaussian signature on CMB that may result from the presence of chaos in order to have a possibility to rule out this model from observations.

It is a pleasure to thank Kei-ichi Maeda and Alexei Starobinsky for useful discussions. This work was partially supported by a Grant for The 21st Century COE Program at Waseda University.

References

[1] A. A. Starobinsky, in Field Theory, Quantum Gravity, and Strings, proceedings of the Seminar, Meudon and Paris, France, 1984-1985, edited by H. T. de Vega and N. Sanchez, Lecture Notes in Physics, Vol. 246 (Springer-Verlag, New York, 1986), p 107.

[2] K. i. Nakao, Y. Nambu and M. Sasaki, Prog. Theor. Phys. **80**, 1041 (1988); D. S. Salopek and J. R. Bond, Phys. Rev. D **43**, 1005 (1991).

[3] D. I. Podolsky and A. A. Starobinsky, Grav. Cosmol. Suppl. **8N1**, 13 (2002) [arXiv:astro-ph/0204327].

[4] R. Easther and K. i. Maeda, Class. Quant. Grav. **16**, 1637 (1999) [arXiv:gr-qc/9711035]; J. Garcia-Bellido and A. D. Linde, Phys. Rev. D **57**, 6075 (1998) [arXiv:hep-ph/9711360]; M. Bastero-Gil, S. F. King and J. Sanderson, Phys. Rev. D **60**, 103517 (1999) [arXiv:hep-ph/9904315]; J. P. Zibin, arXiv:hep-ph/0108008.

[5] Y. Jin and S. Tsujikawa, submitted to Phys. Rev. D [arXiv:hep-ph/0411164].

Solving gravitino problem by a brane world effect

Nobuchika Okada [1]

Theory Division, KEK, Oho 1-1, Tsukuba, Ibaraki 305-0801, Japan

Osamu Seto [2]

Department of Physics and Astronomy, University of Sussex, Brighton BN1 9QJ, United Kingdom

Abstract

We investigate the thermal production of gravitinos in brane world cosmology. Since the expansion law is modified from that in the standard cosmology, the Boltzmann equation for the gravitino production is also changed. We find that the late-time gravitino abundance is proportional to the "transition temperature", at which the modified expansion law in the brane world cosmology is connecting with the standard one, rather than the reheating temperature after inflation as in the standard cosmology. This means that, even though the reheating temperature is very high, we can avoid the overproduction of gravitinos by taking the transition temperature low enough.

1 Introduction

Several particles which only gravitationally couple to the ordinary matters appear in supergravity models. Their lifetime is quite long as estimated to be

$$\tau \simeq \frac{M_{Pl}^2}{m^3} \simeq 10^5 \left(\frac{1\text{TeV}}{m}\right)^3 \text{sec}, \tag{1}$$

where m is the mass of the particles, and $M_{Pl} \simeq 1.2 \times 10^{19}$ GeV is the Planck mass, because their couplings are Planck suppressed. It is normally assumed that the scale of m is of order of the electroweak scale which is obtained through supersymmetry breaking in supergravity models. These particles with such a long lifetime often cause a serious problem in cosmology. The so-called "gravitino problem" is a famous example [1]. If the gravitino is unstable, they would decay after big bang nucleosynthesis (BBN). Their energetic daughters would destroy the light nuclei by photo-dissociation and, as a result, upset the successful prediction of BBN. As is well known, to avoid this problem the upper bound on the reheating temperature after inflation is imposed.

Gravitinos have been produced by thermal scatterings in plasma at the reheating stage after inflation. The Boltzmann equation relevant to this gravitino production process is given by

$$\frac{dn_{3/2}}{dt} + 3Hn_{3/2} = \langle \sigma_{tot} v \rangle n_{rad}^2, \tag{2}$$

where H is the Hubble parameter, $n_{3/2}$ and n_{rad} are the number densities of gravitino and relativistic species in thermal bath, respectively, and $\langle \sigma_{tot} v \rangle$ denotes the thermal average of the total gravitino production cross section times the relative velocity. In the standard cosmology, the Hubble parameter obeys the Friedmann equation,

$$H^2 = \frac{8\pi G}{3}\rho, \tag{3}$$

[1] E-mail:okadan@post.kek.jp
[2] E-mail:O.Seto@sussex.ac.uk

with the energy density $\rho = \frac{\pi^2}{30} g_* T^4$ in the radiation dominated universe. Here, G is the Newton's gravitational constant, and $g_*(T)$ is the total number of the massless degrees of freedom. It is useful to rewrite Eq. (2) as

$$\frac{dY_{3/2}}{dT} = -\frac{s\langle\sigma_{tot}v\rangle}{HT} Y_{rad}^2, \tag{4}$$

where $Y_{3/2} \equiv n_{3/2}/s$ and $Y_{rad} \equiv n_{rad}/s$ with s being the entropy density. Note that the r.h.s. of this equation is almost independent of temperature T, since $\langle\sigma_{tot}v\rangle \simeq M_{Pl}^{-2}$, $H \propto T^2$, $s \propto T^3$. Thus, the late-time gravitino abundance is proportional to the reheating temperature T_R and approximately described as [2],

$$Y_{3/2} \simeq 10^{-11} \left(\frac{T_R}{10^{10}\mathrm{GeV}}\right). \tag{5}$$

This abundance should be small in order for the gravitino decay products not to destroy the light elements successfully synthesized during BBN, thus we obtain the upper bound on the reheating temperature such as [3, 4]

$$T_R \leq 10^6 - 10^7 \mathrm{GeV}, \tag{6}$$

for the gravitino mass $m_{3/2} = \mathcal{O}(10^2\mathrm{GeV})$. According to a recent analysis, the upper bound depends on not only the gravitino mass but also the efficiency of the hadronic processes [4].

This stringent constraint is problematic in the inflationary cosmology. The reheating temperature provided by typical inflation models such as the chaotic inflation or the hybrid inflation is estimated to be much larger than the upper bound of Eq. (6) [5]. Therefore there exists a gap between the natural reheating temperature for the inflation models and its upper bound of Eq. (6). It seems not so easy to construct an inflation model which can, simultaneously, provide a reheating temperature low enough to satisfy this upper bound and be consistent with the present cosmological observations, the density fluctuations, etc.

Recently, the brane world models have been attracting a lot of attention as a novel higher dimensional theory. In these models, it is assumed that the standard model particles are confined on a "3-brane" while gravity resides in the whole higher dimensional spacetime. The model proposed by Randall and Sundrum [6], the so-called "RS II" model, is a simple and interesting one, and its cosmological evolution have been intensively investigated [7]. In the model, our 4-dimensional universe is realized on the 3-brane with a positive tension located at the ultraviolet (UV) boundary of a five dimensional Anti de-Sitter spacetime. In this setup, the Friedmann equation for a spatially flat spacetime is found to be

$$H^2 = \frac{8\pi G}{3}\rho\left(1 + \frac{\rho}{\rho_0}\right) \tag{7}$$

where

$$\rho_0 = 96\pi G M_5^6, \tag{8}$$

with M_5 being the five dimensional Planck mass, and the four dimensional cosmological constant has been tuned to be zero. Here we have omitted the term so-called "dark radiation", since this term is severely constrained by BBN [8]. The second term proportional to ρ^2 is a new ingredient in the brane world cosmology and lead to a non-standard expansion law.

Note that according to Eq. (7) the evolution of the early universe can be divided into two eras. At the era where $\rho/\rho_0 \gg 1$ the second term dominates and the expansion law is non-standard (brane world cosmology era), while at the era $\rho/\rho_0 \ll 1$ the first term dominates and the expansion of the universe obeys the standard expansion law (standard cosmology era). In the following, we call a temperature defined as $\rho(T_t)/\rho_0 = 1$ "transition temperature", at which the evolution of the early universe changes from the brane world cosmology era into the standard one. Using the transition temperature, we rewrite Eq. (7) into the form

$$H^2 = \frac{8\pi G}{3}\rho\left[1 + \left(\frac{T}{T_t}\right)^4\right] = H_{st}^2\left[1 + \left(\frac{T}{T_t}\right)^4\right], \tag{9}$$

where H_{st} is the Hubble parameter in the standard cosmology (Eq. (3)).

This modification of the expansion law at a high temperature ($T > T_t$) leads some drastic changes for several cosmological issues. In fact, for example, an enhancement of the thermal relic abundance of dark matter has been recently pointed out [9]. Here, we investigate the brane cosmological effect for the gravitino production process. Since the Friedmann equation is modified into Eq. (9), the solution of the Boltzmann equation of Eq. (4) can be modified, which leads us to a different consequence for the gravitino problem [10].

2 Gravitino abundance in brane world cosmology

Now let us analyze the thermal production of the gravitino in the brane world cosmology. Notice that the model we consider is, to be precise, the supersymmetric extended RS II model [11]. But, the cosmological solution of this extended model is the same as that in the non-supersymmetric model, since the Einstein's equation belongs to the bosonic part. Suppose that the SUSY is broken on the brane.

The Boltzmann equation for the gravitino production takes the form of

$$\frac{dY_{3/2}}{dT} = -\frac{s\langle\sigma_{tot}v\rangle}{H_{st}T}Y_{rad}^2 \times \frac{1}{\sqrt{1+\left(\frac{T}{T_t}\right)^4}}. \tag{10}$$

The pre-factor in the r.h.s. is the same as the one in the standard cosmology. Suppose that the reheating temperature after inflation is much higher than the transition temperature. Then we integrate the Boltzmann equation from the reheating temperature $T_R(\gg T_t)$ in the brane world cosmology era to a low temperature $T_{low}(\ll T_t)$ in the standard cosmology era;

$$-\int_{T_R}^{T_{low}} \frac{dT}{\sqrt{1+\left(\frac{T}{T_t}\right)^4}} \sim \int_{T_t}^{T_R} dT \left(\frac{T_t}{T}\right)^2 + \int_{T_{low}}^{T_t} dT \sim 2T_t. \tag{11}$$

Note that the reheating temperature T_R in the formula of the gravitino abundance in the standard cosmology (see Eq. (5)) is replaced by the transition temperature, namely, $T_R \to 2T_t$. Therefore we can avoid overproduction of gravitinos by

$$T_t \leq 10^6 - 10^7 \mathrm{GeV} \tag{12}$$

independently of the reheating temperature. Needless to say, if $T_t \gg T_R$ we can reproduce the result in the standard cosmology.

3 Summary

We have found that the late-time gravitino abundance is proportional to the transition temperature independently of the reheating temperature, if the reheating temperature is higher than the transition temperature. Therefore the gravitino problem disappears by assigning a transition temperature low enough.

A necessary condition to solve the gravitino problem by this manner is that inflation must occur in the brane world cosmology era as we have assumed. In order to verify our strategy toward a solution of the gravitino problem, it is important to explore whether the inflation can take place during the brane world cosmology era [12]. The detailed study of density perturbation generated from inflation models in the brane world cosmology is a key issue [13, 14]. Furthermore, here, we have concentrated on only the zero mode of gravitino. But, gravitino is a bulk field and KK modes also exist. It would be important to investigate the KK gravitino production.

Acknowledgments

The work of N.O. is supported in part by the Grant-in-Aid for Scientific Research (#15740164). The work of O.S. is supported by PPARC and the National Science Council of Taiwan under the grant No. NSC 92-2811-M-009-018.

References

[1] M. Y. Khlopov and A. D. Linde, Phys. Lett. B **138**, 265 (1984); J. R. Ellis, J. E. Kim and D. V. Nanopoulos, Phys. Lett. B **145**, 181 (1984).

[2] M. Kawasaki and T. Moroi, Prog. Theor. Phys. **93**, 879 (1995).

[3] R. H. Cyburt, J. R. Ellis, B. D. Fields and K. A. Olive, Phys. Rev. D **67**, 103521 (2003).

[4] M. Kawasaki, K. Kohri and T. Moroi, astro-ph/0402490.

[5] For a review of inflation, see, e.g. A. D. Linde, *Particle Physics and Inflationary Cosmology* (Harwood, Chur, Switzerland, 1990); K. A. Olive, Phys. Rept. **190**, 307 (1990); D. H. Lyth and A. Riotto, Phys. Rept. **314**, 1 (1999)

[6] L. Randall and R. Sundrum, Phys. Rev. Lett. **83**, 4690 (1999).

[7] For a review, see, e.g., D. Langlois, Prog. Theor. Phys. Suppl. **148**, 181 (2003).

[8] K. Ichiki, M. Yahiro, T. Kajino, M. Orito and G. J. Mathews, Phys. Rev. D **66**, 043521 (2002).

[9] N. Okada and O. Seto, Phys. Rev. D **70**, 083531, (2004).

[10] N. Okada and O. Seto, to appear in Phys. Rev. D, hep-ph/0407235.

[11] T. Gherghetta and A. Pomarol, Nucl. Phys. B **586**, 141 (2000); R. Altendorfer, J. Bagger and D. Nemeschansky, Phys. Rev. D **63**, 125025 (2001); A. Falkowski, Z. Lalak and S. Pokorski, Phys. Lett. B **491**, 172 (2000); M. Zucker, Phys. Rev. D **64**, 024024 (2001); T. Kugo and K. Ohashi, Prog. Theor. Phys. **108**, 203 (2002).

[12] R. Maartens, D. Wands, B. A. Bassett and I. Heard, Phys. Rev. D **62**, 041301 (2000).

[13] H. Kodama, A. Ishibashi and O. Seto, Phys. Rev. D **62**, 064022 (2000); S. Mukohyama, Phys. Rev. D **62**, 084015 (2000); C. van de Bruck, M. Dorca, R. H. Brandenberger and A. Lukas, Phys. Rev. D **62**, 123515 (2000); K. Koyama and J. Soda, Phys. Rev. D **62**, 123502 (2000).

[14] D. Langlois, R. Maartens and D. Wands, Phys. Lett. B **489**, 259 (2000); S. Tsujikawa and A. R. Liddle, JCAP **0403**, 001 (2004).

String theory on curved spacetime [1]

Makoto Natsuume[2]

Theory Division
Institute of Particle and Nuclear Studies
KEK, High Energy Accelerator Research Organization
Tsukuba, Ibaraki, 305-0801 Japan

Abstract

Even though string theory on curved spacetime has been widely discussed since the last decade or so, rigorous discussion is still very difficult. This is due to the lack of string theory on curved spacetime. The point is that the consistency of string theory, especially the no-ghost theorem, is rarely verified for curved spacetime. We review our works on the no-ghost theorem. Our technique applies more generally than standard proofs. Some examples are the backgrounds when only the timelike direction is flat and AdS_3.

1 Introduction

In this talk, I would like to talk about one of our long-term projects [1, 2, 3, 4]. The problem is very old, but is very important. Many people go back to the problem from time to time, and so do I. The work itself is rather technical, so I would rather want to motivate you since probably many of you never heard of the problem.

Strings on curved spacetime have been widely discussed in the last decade or so. One motivation of such works is that string might resolve the unsolved issues in general relativity, unsolved issues related to black holes (such as the information paradox and the singularity problem) and to cosmological spacetime.

Some recent examples are AdS/CFT dualities, string on pp-wave backgrounds, and time-dependent orbifolds. However, most discussion is limited to backgrounds with light-cone directions (*e.g.*, string on pp-wave backgrounds and time-dependent orbifolds). Otherwise, the technology is limited to supergravities (*e.g.*, AdS/CFT dualities). Rigorous discussion for generic spacetime is still difficult.

Why? This is due to the **lack of the string theory on curved spacetime**. This is an important point, so let me rephrase it: string theory on curved spacetime does not really exist. What this means is the following. A physical theory must satisfy consistency conditions such as unitarity. However, it is not clear that such a condition is really satisfied for string theory on curved spacetime.

One very important consistency condition is the **no-ghost theorem**. The theorem states that norm of physical states is positive-definite. Negative-norm states are called ghosts. As an example, consider QED. The equal-time commutator for the gauge field is given by

$$[a^\mu(k), a^{\nu\dagger}(k')] = \eta^{\mu\nu} 2k^0 (2\pi)^3 \delta^3(\vec{k} - \vec{k'}), \tag{1}$$

where $a^{\mu\dagger}(k)$ is the creation operator for the photon. Because the commutator involves the Minkowski metric $\eta_{\mu\nu}$, the timelike photon is a ghost. The longitudinal photon is also problematic. So, a covariant theory generally contains ghosts.

This is not a problem in QED because ghosts do not appear as physical states. In the BRST quantization (I use this scheme throughout the talk), there is a very important operator, the BRST operator Q_{BRST}, which generates a "gauge transformation." And a physical state satisfies two conditions:

$$Q_{BRST}|\text{phys}\rangle = 0, \tag{2}$$

$$|\text{phys}\rangle \neq Q_{BRST}|\chi\rangle. \tag{3}$$

[1] To appear in the Proceedings of the workshop "The 14th workshop on general relativity and gravitation" (YITP-W-04-13).

[2] E-mail:makoto.natsuume@kek.jp

Step 1:	The vanishing theorem
	Introduce a simplified BRST operator (filtration)
	Show the theorem using the simplified operator
	the simplified operator in the standard proofs: reason why light-cone directions
	↓
	Use a different simplified operator (á la FGZ)
	⇓
Step 2:	The no-ghost theorem

Table 1: The outline of the proof.

The first condition states that a physical state is gauge invariant, and the second condition states that a physical state is not in pure gauge. This is the two set of conditions and these remove the timelike and the longitudinal modes. String theory is more complicated than gauge theory due to the infinite number of states, but the story is similar. Thus, the no-ghost theorem is well-established for flat spacetime.

When spacetime is curved, the status is not clear though. And the progress in this direction is very slow. For example, people have spent more than 10 years to make sense of string theory on AdS_3. You might think that what we are doing is just checking the conditions which certainly hold, but this is not the case. One problem for AdS_3 is that ghosts remain as physical states if one naively quantizes string. AdS_3 is one of the simplest curved spacetime, but even AdS_3 is very hard. So, consistency of string theory is not generally known for curved spacetime.

Viewing the situation, I would like to ask the converse question, namely "How general can the no-ghost theorem definitely apply?" This is essentially the same as saying that "What is the most general consistent (perturbative) string theory?"

The answer is partly known from the literature. Most proofs of the no-ghost theorem are stated for flat spacetime, but they are easily extended even if some of spacelike directions are curved. So, the standard proof applies to $\mathbb{R}^{1,d-1} \times K$, where $\mathbb{R}^{1,d-1}$ is the d-dimensional Minkowski spacetime and K corresponds to a "curved space" (Strictly speaking, K must be a unitary CFT.)

But all standard proofs require at least two directions be flat (*i.e.*, $d \geq 2$). Roughly speaking, the standard proofs apply to spacetime of the form

$$ds^2 = -dt^2 + dz^2 + h_{ab}(x^a)dx^a dx^b \tag{4}$$

$$= -dx^+ dx^- + \cdots \tag{5}$$

This is because it is necessary to define light-cone directions in those proofs. Note that h_{ab} is independent of t and z .

Now, our claim is that we prove the no-ghost theorem when only the timelike direction is flat (*i.e.*, $d \geq 1$). Again roughly speaking, our theorem apply to spacetime of the form

$$ds^2 = -dt^2 + h_{ij}(x^i)dx^i dx^j. \tag{6}$$

You might think that this is not a big improvement, but our theorem actually works more generally. It can be extended to completely curved spacetime, and one example is AdS_3. For technically-oriented audience, our technology itself is not new, but we use the old technology by Frenkel, Garland, and Zuckerman back to 1986 (FGZ) [5].

2 Outline of the proof

Table 1 is the outline of our proof. The goal is the no-ghost theorem, but first it is convenient to show a theorem called the **vanishing theorem**. The proof of the theorem itself is rather hard. Fortunately, one can introduce a simplified BRST operator (using a technology called **filtration**), and it is enough to show the theorem using the simplified BRST operator. However, the simplified operator in the standard proof is the reason why light-cone directions are necessary. So, we use the different simplified operator

(á la FGZ) and show the theorem. Then, the proof of the no-ghost theorem is straightforward. (It is simple calculations of the so-called index and signature, and very similar calculation as string partition function.)

So what is the vanishing theorem? The theorem states that "Physical states have zero Faddeev-Popov ghost number." Recall that Faddeev-Popov (FP) ghosts arise from the gauge fixing in the BRST quantization. Please do not confuse the FP-ghosts with the ghosts, which are negative-norm states. As an example, again consider QED. The full specturm is as follows:

- the timelike and longitudinal photons A^0 and A^1
- the transverse photons A^i $(i = 2, 3)$
- the FP-ghost c and the anti-ghost $\bar{c}$

If the vanishing theorem is true, it immediately removes the ghost c and the anti-ghost $\bar{c}$ from the physical spectrum since they have FP-ghost number +1 and -1, respectively. But it does not remove the ghosts in the photon sector (the timelike and longitudinal photons), so the theorem itself is not enough as the no-ghost theorem. But the proof of the no-ghost theorem becomes much easier once one establishes the vanishing theorem. However, the string BRST operator Q_{BRST} is very complicated. It is cubic in oscillators (for QED, it is quadratic in oscillators.) So, the strategy is to show the theorem using a simplified BRST operator.

However, in standard proofs, the simplified operator is written in terms of light-cone oscillators. Explicitly, it is given by

$$Q_0 \sim \sum_m c_m \alpha^-_{-m}. \tag{7}$$

Here, c_m is a FP-ghost and α^-_{-m} represents the string oscillation in a light-cone direction. Thus, spacetime must have light-cone directions.

On the other hand, in our approach, the simplified operator involves only the timelike oscillators, so does not require light-cone directions. Actually, the operator is written only in terms of a $c = 1$ nonunitary Virasoro generator $L_m^{(c=1)}$. This means that even the timelike direction need not be flat, and that it can be replaced by *any* $c = 1$ nonunitary CFT:

$$\begin{array}{c} \mathbb{R}^{1,0} \times K \\ \downarrow \\ (c = 1 \text{ nonunitary CFT}) \times K \end{array} \tag{8}$$

One example is AdS_3. AdS_3 is described by the $SU(1,1)$ group manifold. The group $SU(1,1)$ is the non-compact version of $SU(2)$ and it has a $U(1)$ subgroup. This $U(1)$ is a $c = 1$ nonunitary CFT, and the rest ($SU(1,1)/U(1)$ coset) is known to be a unitary CFT.

For completeness, let me give you the most general no-ghost theorem:

Theorem 2.1 (The no-ghost theorem for string theory) *The observable Hilbert space $\hat{\mathcal{H}}_{\rm obs}$ is a positive definite space under the following conditions:*

- *Let $\mathcal{V}(c,h)$ be a Verma module with highest weight h and central charge c. The matter part of the Hilbert space $\mathcal{H}$ can be decomposed as a sum of the following two Verma modules:*

$$\mathcal{H}_{h^0,h^K} = \mathcal{V}(c^0 = 1, h^0 < 0) \otimes \mathcal{V}(c^K = 25, h^K > 0). \tag{9}$$

- *The Virasoro primaries $|h^0\rangle$ used to construct the $c = 1$ Verma module are positive-definite.*

Our biggest assumption is that the spacetime has the product structure. But note that if you look at AdS_3 metric itself, it has no clear separation. So, hopefully this won't be a big limitation.

3 Consistency of string

Let me go back to the consistency conditions of string theory. The basic physical consistency conditions for a string theory are not many. In general, as a sensible physical theory, we must require

(i). Lorentz invariance (for flat spacetime)

(ii). Unitarity

There are few in number, but it is hard to reconcile these two even in flat spacetime as you know. These in turn imply various consistency conditions such as

1. Vanishing beta-functions
2. The no-ghost theorem
3. Unitarity of S-matrix (decoupling of ghosts)
4. Modular invariance
5. ...

So, the no-ghost theorem alone is not enough for consistency of string theory.

It does not sound an easy job for a string theory to satisfy all these requirements. However, for string theory on flat spacetime, no new condition appears once the no-ghost theorem is established. So, a common belief is that string theory is likely to be automatically consistent once the no-ghost theorem is established. This is the reason why we concentrate on the no-ghost theorem, but checking the other conditions are also important.

I would like to thank M. Asano and M. Kato for collaboration. I would also like to thank the organizers of JGRG14 for the opportunity to present this work.

References

[1] M. Asano and M. Natsuume, "The no-ghost theorem for string theory in curved backgrounds with a flat timelike direction," Nucl. Phys. **B588** (2000) 453 [arXiv:hep-th/0005002].

[2] M. Asano and M. Natsuume, "The no-ghost theorem in curved backgrounds with a timelike u(1): NSR string," Nucl. Phys. B **672** (2003) 39 [arXiv:hep-th/0303051].

[3] M. Asano and M. Natsuume, "The BRST quantization and the no-ghost theorem for AdS_3," JHEP **0309** (2003) 018 [arXiv:hep-th/0304254].

[4] M. Asano, M. Kato, and M. Natsuume, in preparation.

[5] I. B. Frenkel, H. Garland and G. J. Zuckerman, "Semiinfinite cohomology and string theory," Proc. Nat. Acad. Sci. **83**, 8442 (1986).

Large-scale magnetic fields in dilaton electromagnetism in noncommutative inflationary cosmology

Kazuharu Bamba, J. Yokoyama

Department of Earth and Space Science, Graduate School of Science, Osaka University, Toyonaka 560-0043, Japan

Abstract

The generation of large-scale magnetic fields is studied in dilaton electromagnetism in noncommutative inflationary cosmology, taking into account the effects of the spacetime uncertainty principle motivated by string theory. We show that it is possible to generate large-scale magnetic fields with sufficient strength to account for the observed fields in galaxies and clusters of galaxies through only adiabatic compression without dynamo amplification mechanism in models of power-law inflation based on spacetime noncommutativity without introducing a huge hierarchy between the dilaton's potential and its coupling to the electromagnetic fields.

1 Introduction

It is well established that magnetic fields with the field strength $\sim 10^{-6}$G and coherent scale $1-10$kpc exist in our galaxy and other galaxies. Furthermore, in recent years magnetic fields in clusters of galaxies have been observed by means of the Faraday rotation measurements (RMs) of polarized electromagnetic radiation passing through an ionized medium. In general, the strength and the coherent scale are estimated as $10^{-7}-10^{-6}$G and 10kpc$-$1Mpc, respectively. It is very interesting that magnetic fields in clusters of galaxies are as strong as galactic ones and that the coherence scale may be as large as $\sim$Mpc. The most natural origin of such a large-scale magnetic field would be electromagnetic quantum fluctuations generated in the inflationary stage [1]. This is because inflation naturally produces effects on very large scales, larger than Hubble horizon, starting from microphysical processes operating on a causally connected volume. However, there is the following obstacle on the way of this nice scenario. The Friedmann-Robertson-Walker (FRW) metric usually considered is conformally flat. Therefore cosmic expansion does not induce particle production if the underlying theory is conformally invariant. The classical electrodynamics is conformally invariant. Hence large-scale electromagnetic fluctuations could not be generated in cosmological background. If the origin of large-scale magnetic fields in clusters of galaxies is electromagnetic quantum fluctuations generated and stretched in the inflationary stage, the conformal invariance must have been broken at that time. Several breaking mechanisms therefore have been proposed.

Recently we have studied the following model of the dilaton electromagnetism [2]. In addition to the inflaton field ϕ we assumed the existence of the dilaton field Φ with a potential $V[\Phi] = \bar{V}\exp(-\tilde{\lambda}\kappa\Phi)$, where $\bar{V}$ is a constant, and introduced the following coupling in the electromagnetic part of the model Lagrangian,

$$\mathcal{L}_{\rm EM} = -\frac{1}{4}f(\Phi)F_{\mu\nu}F^{\mu\nu}, \quad f(\Phi) = \exp(\lambda\kappa\Phi), \tag{1}$$

where $F_{\mu\nu} = \partial_\mu A_\nu - \partial_\nu A_\mu$ is the electromagnetic field-strength tensor, λ and $\tilde{\lambda}$ are dimensionless constants, and $\kappa^2 \equiv 8\pi/{M_{\rm Pl}}^2$ with $M_{\rm Pl} = G^{-1/2} = 1.2\times10^{19}$GeV being the Planck mass. We use units in which $k_{\rm B} = c = \hbar = 1$ and adopt Heaviside-Lorentz units of electromagnetism. Such coupling is reasonable in the light of indications in higher-dimensional theories including string theory. The coupling was first analyzed by Ratra [3]. In his model, however, the inflaton and the dilaton were identified and only the case the dilaton freezes at the end of inflation was considered. We therefore considered a more realistic situation that the dilaton continues its evolution along with the exponential potential even after reheating but is finally stabilized when it feels other contributions to its potential, say, from gaugino

condensation that generates a potential minimum. As it reaches there, the dilaton starts oscillation with mass m and finally decays into radiation with or without significant entropy production. As a result we have shown magnetic fields with the current strength as large as 10^{-10}G on cluster scale or even larger scale could be generated, but for this to be the case we had to introduce a huge hierarchy between the coupling constant of the dilaton to the electromagnetic field λ and the coupling one $\tilde{\lambda}$ of the dilaton potential, $\lambda/\tilde{\lambda} \approx 400$. Note that the existence of the dilaton under discussion is motivated by higher dimensional theories including string theory. The purpose of the present paper is to argue that if we take another prediction of string theory, namely spacetime uncertainty relation, we can solve the above huge hierarchy problem as well [4]. The stringy spacetime uncertainty relation (SSUR) is *not* a modification of the ordinary energy-time uncertainty relation in the framework of quantum mechanics, but simply a *reinterpretation* in terms of strings [5]. It is therefore natural and important to take into account both of the two consequences of string theory, the dilaton and the SSUR, simultaneously to the problem of the generation of primordial magnetic fields in the high energy regime of the early Universe.

2 Model

From (1), through the canonical quantization, the equation of motion for the Fourier modes $A_i(t,k)$ for U(1) gauge field A_μ in the Coulomb gauge, $A_0(t,\boldsymbol{x}) = 0$ and $\partial_j A^j(t,\boldsymbol{x}) = 0$, reads

$$\ddot{A}_i(t,k) + \left(H + \frac{\dot{f}}{f}\right)\dot{A}_i(t,k) + \frac{k^2}{a^2}A_i(t,k) = 0, \tag{2}$$

in the spatially flat Robertson-Walker Universe $ds^2 = -dt^2 + a^2(t)d\boldsymbol{x}^2$, where H is the Hubble parameter and a is the cosmic scale factor. Here $\boldsymbol{k}$ is comoving wave number, and k denotes its amplitude $|\boldsymbol{k}|$. For convenience in finding the solutions of Eq. (2), we introduce the following approximate form as the expression of f. $f(\Phi) = f[\Phi(t)] = f[\Phi(a(t))] \equiv \bar{f}a^{\beta-1}$, where $\bar{f}$ is a constant and β is a parameter.

In slow-roll exponential inflation models with $a(t) \propto e^{H_{\rm inf}t}$, the model parameter β is given by $\beta \approx 1 + \tilde{\lambda}^2 w X$, $X \equiv \lambda/\tilde{\lambda}$, $w \equiv V[\Phi]/\rho_\phi$, where $\rho_\phi \cong$ const is the energy density of the inflaton ϕ and $w \ll 1$ because we have assumed that during slow-roll inflation the cosmic energy density is dominated by the inflaton potential and the energy density of the dilaton is negligible. Even if the dilaton was rapidly evolving at the onset, its kinetic energy would soon be dissipated, and it is frozen to a value satisfying $V''[\Phi] \lesssim {H_{\rm inf}}^2$. Thus β takes a practically constant value. Consequently, the solution of Eq. (2) with $H = H_{\rm inf}$ is given by

$$A_i(k,a) = \sqrt{\frac{\pi}{4H_{\rm inf}af(a)}}H^{(1)}_{\beta/2}\left(\frac{k}{aH_{\rm inf}}\right)e^{i(\beta+1)\pi/4}, \tag{3}$$

where we have determined the constants of integration in the general solution of Eq. (2) by requiring that the vacuum reduces to the one in Minkowski spacetime at the short-wavelength limit.

The energy density of the large-scale magnetic fields can evaluated using (3) if we specify cosmic evolution after inflation. Here we adopt the scenario as argued in Introduction. The energy density of the magnetic field on a comoving scale $L = 2\pi/k$ at the present time is given by

$$\rho_B(L,t_0) = \frac{2^{|\beta|-3}}{\pi^3}\Gamma^2\left(\frac{|\beta|}{2}\right)H_{\rm inf}{}^4\left(\frac{a_{\rm R}}{a_0}\right)^4\left(\frac{k}{a_{\rm R}H_{\rm inf}}\right)^{-|\beta|+5}\exp\left(-\tilde{\lambda}\kappa\Phi_{\rm R}X\right)(\Delta S)^{-4/3}, \tag{4}$$

$$\Delta S \approx \left(\frac{\bar{V}}{\rho_\phi}\right)\left(\frac{2H_{\rm inf}}{m}\right)^2\left(\frac{M_{\rm Pl}}{m}\right), \tag{5}$$

where $\Phi_{\rm R}$ is the dilaton field amplitude at the end of inflation and ΔS is the entropy ratio after and before dilaton decay. Here the suffixes 'R' and '0' represent the quantities at the end of inflation $t_{\rm R}$ and the present time t_0, respectively. From Eq. (4) we see that the large-scale magnetic fields have a scale-invariant spectrum when $|\beta| = 5$ [2]. The serious problem is that the model parameters should be so chosen that the spectrum of generated magnetic field should not be too blue but close to the

scale-invariant or the red one, which is realized only if a huge hierarchy exists between λ and $\tilde{\lambda}$, namely, $X = \lambda/\tilde{\lambda}$ should be extremely larger than unity. For example, if we take $w = 0.01$ and $\tilde{\lambda} \sim \mathcal{O}(1)$, we must have $X \equiv \lambda/\tilde{\lambda}$ as large as ≈ 400 so that the amplitude of the generated large-scale magnetic field could be sufficiently large.

On the other hand, if we adopt power-law inflation models instead of exponential inflation with the following exponential inflaton potential, $U[\phi] = \tilde{U}\exp(-\zeta\kappa\phi)$, we can relax the constraint on X to a limited extent. Here $\tilde{U}$ is a constant and ζ is a dimensionless constant, the spectral index of curvature perturbation n_s is given by

$$n_s - 1 = -6\epsilon_U + 2\eta_U = -\zeta^2, \quad \epsilon_U \equiv \frac{1}{2\kappa^2}\left(\frac{U'}{U}\right)^2, \quad \eta_U \equiv \frac{1}{\kappa^2}\left(\frac{U''}{U}\right), \tag{6}$$

where primes denote derivatives with respect to the inflaton field ϕ. According to the first year Wilkinson Microwave Anisotropy Probe (WMAP) data [6], $n_s \geq 0.93$, and hence $\zeta \leq 0.26$. In this case the scale factor in the inflationary stage is given by $a(t) \propto t^p$, where $p = 2/\zeta^2 \geq 29$. In this background, if power-law inflation lasts for a sufficiently long time, the dilaton will settle to the scaling solution where $U''[\phi] \approx H^2$ with $H = p/t$. Hence the solution of the dilaton in this regime is given by $\Phi = 2(\tilde{\lambda}\kappa)^{-1}\ln(\sqrt{\tilde{V}}\tilde{\lambda}\kappa t/p)$. Then we find β is constant given by $\beta = (2X/p) + 1$. In this case, the solution of Eq. (2) is given by

$$A_i(k,a) = \sqrt{\frac{p\pi}{4(p-1)Haf(a)}}H^{(1)}_{\tilde{\beta}/2}\left(\frac{pk}{(p-1)aH}\right)e^{i(\tilde{\beta}+1)\pi/4}, \tag{7}$$

$$\tilde{\beta} \equiv 1 + \frac{p}{p-1}(\beta - 1) = 1 + \frac{2X}{p-1}. \tag{8}$$

The energy density of the large-scale magnetic fields on a comoving scale $L = 2\pi/k$ at the present time in the above power-law inflation models, $\tilde{\rho_B}(L,t_0)$, is given by

$$\tilde{\rho_B}(L,t_0) = \frac{2^{|\tilde{\beta}|-3}}{\pi^3}\Gamma^2\left(\frac{|\tilde{\beta}|}{2}\right)\left(\frac{p-1}{p}\right)^{|\tilde{\beta}|-1}H_{\rm R}{}^4\left(\frac{a_{\rm R}}{a_0}\right)^4\left(\frac{k}{a_{\rm R}H_{\rm R}}\right)^{-|\tilde{\beta}|+5}\exp\left(-\tilde{\lambda}\kappa\Phi_{\rm R}X\right)\left(\Delta\tilde{S}\right)^{-4/3}, \tag{9}$$

$$\Delta\tilde{S} \approx \left(\frac{\tilde{V}}{\rho_\phi}\right)\left(\frac{2H_{\rm R}}{m}\right)^2\left(\frac{M_{\rm Pl}}{m}\right), \tag{10}$$

where $H_{\rm R}$ is the Hubble parameter at the end of inflation. Since $p \gg 1$ as noted above, we find from Eqs. (4), (5), and (8)–(10) that $\tilde{\beta} \approx \beta$, which means $\tilde{\rho_B}(L,t_0) \approx \rho_B(L,t_0)$ by identifying $H_{\rm R}$ with $H_{\rm inf}$. Therefore, if $\beta \approx 5$, we find $X \approx 2p \geq 58$ [2]. Consequently, although some progress has been made to lower the required value of X by adopting power-law inflation, it is far from sufficient because X should still be much larger than unity in order that the amplitude of the generated magnetic fields could be sufficiently large at the present time. This is because power-law inflation models are hardly distinguishable from exponential inflation under the constraint imposed by WMAP data as far as the evolution of the dilaton is concerned. Because we cannot expect in realistic high energy theories that a huge hierarchy exists between λ and $\tilde{\lambda}$, this is a serious problem of our previous model to be solved.

3 Effects of the stringy spacetime uncertainty relation

Next, we consider a possible solution to the above huge hierarchy between λ and $\tilde{\lambda}$ in our model. In recent years the effect of the stringy spacetime uncertainty relation (SSUR) [5]

$$\Delta t\Delta x_{\rm phys} \geq L_s^2, \tag{11}$$

on metric perturbations in the early Universe have been investigated [7, 8], where t and $x_{\rm phys}$ are the physical spacetime coordinates and L_s is the string scale. Brandenberger and Ho have first studied the modified action for the cosmological perturbations in noncommutative spacetime, where they have assumed that matter is dominated by a single scalar field [7]. Spacetime noncommutativity at high

energies in the early Universe leads to the following two effects. The first is a coupling between the fluctuation mode and the background which is nonlocal in time. The second is the appearance of a critical time for each mode at which the SSUR is saturated, and which is taken to be the time when the mode is generated in the vacuum state in the absence of cosmological expansion. In a background spacetime with power-law inflation, these two effects lead to a suppression of power for large-wavelength modes, compared to that in standard general relativity. This is because these modes undergo a shorter period of squeezing than they do in the standard calculations in the commutative geometry, that is, large-scale modes, which correspond to higher energies earlier in inflation, are generated outside the Hubble radius owing to stringy effects, and hence experience less growth than the small-scale modes, which are generated inside the Hubble radius at lower energies, and evolve as in the standard case. There is a critical wavenumber $k_{\rm crit}$ such that for $k < k_{\rm crit}$ the mode is generated on super-Hubble scales, and hence undergoes less squeezing during the subsequent evolution than it does in commutative spacetime, on the other hand, for $k > k_{\rm crit}$ the mode is generated on scales inside the Hubble radius.

The spectrum of cosmic microwave background (CMB) anisotropies predicted by the model in [7] has recently been calculated, and thus the prediction of loss of power for infrared modes has been quantified [8]. In addition, Tsujikawa et al. [8] have performed a likelihood analysis at various angular scales to find the best-fit values to the WMAP data of the cosmological parameters, including the power-law exponent p which gives the time dependence on the scale factor, and the critical wavenumber when stringy effects become important. As a result they have shown that high energy stringy effects could account for some loss of power on the largest scales that may be indicated by recent WMAP data. Furthermore, according to their calculation, even a power exponent as small as $p \approx 5$ is consistent within the current errors. One may wonder if electromagnetic quantum fluctuations generated in the inflationary stage are also influenced by spacetime noncommutativity, so that the power for the long-wavelength modes should be suppressed. However, the megaparsec scale, in which we are particularly interested, is smaller than the above critical scale $2\pi/k_{\rm crit}$. In fact, according to Tsujikawa et al. [8], the best-fit value for the crossover scale of the power spectrum of density fluctuation, k_*, which satisfies $k_* \gg k_{\rm crit}$, has been found to be $2\pi/k_* \approx 2.7 \times 10^2$Mpc. Furthermore, we have confirmed that the SSUR has no significant effect on the megaparsec scale fluctuations at the present time and that the amplitude of the generated magnetic field on 1Mpc scale is the same as that in the case of commutative spacetime [4].

4 Conclusion

From Eq. (8) and, say, $p \approx 5$, which is in the allowed range now, we find $\tilde{\beta} = 1 + X/2$. Hence we can generate magnetic fields as strong as $B \sim 10^{-10}$G on 1Mpc scale even if the two coupling constants of the dilaton, λ and $\tilde{\lambda}$, are of the same order of magnitude, $X = \lambda/\tilde{\lambda} \approx 8$. For example, we find $B(1{\rm Mpc}, t_0) = 1.0 \times 10^{-10}$G for $X = 8.1$, $H_{\rm R} = 10^8$GeV, and $\Delta\tilde{S} = 7.0 \times 10^6$. Moreover, we find similarly that a sufficient magnitude of magnetic fields on 1Mpc scale at the present time for the galactic dynamo scenario, $B \sim 10^{-22}$G, could be generated even in the case $X = \lambda/\tilde{\lambda} \approx 6$.

References

[1] M.S. Turner and L.M. Widrow, Phys. Rev. **D37**, 2743 (1988).

[2] K. Bamba and J. Yokoyama, Phys. Rev. **D69**, 043507 (2004).

[3] B. Ratra, Astrophys. J. **391**, L1 (1992); Report No. GRP-287/CALT-68-1751.

[4] K. Bamba and J. Yokoyama, Phys. Rev. **D70**, 083508 (2004).

[5] T. Yoneya, Mod. Phys. Lett **A 4**, 1587 (1989); Prog. Theor. Phys. **103**, 1081 (2000).

[6] H.V. Peiris *et al.*, Astrophys. J., Suppl. Ser. **148**, 213 (2003).

[7] R. Brandenberger and P.-M. Ho, Phys. Rev. **D66**, 023517 (2002).

[8] S. Tsujikawa, R. Maartens, and R. Brandenberger, Phys. Lett. B **574**, 141 (2003).

Ghost Condensation and Gravity in Higgs Phase

Shinji Mukohyama[1]

Department of Physics, The University of Tokyo, Tokyo 113-0033, Japan

Abstract

A tachyon is considered to be sick in the context of particle mechanics, but in field theory just indicates instability of a background. We consider a similar possibility that a ghost in field theory might be just an indication of instability of a background and that it can condense to form a different background around which there is no ghost. We construct a low energy effective field theory based on the derivative expansion around the stable background. Possible applications are discussed, including dark energy, dark matter, inflation and black hole.

1 Introduction

Gravity at long distances shows us many interesting and mysterious phenomena: flattening galaxy rotation curves, dimming supernovae, and so on. These phenomena have been a strong motivation for the paradigm of dark matter and dark energy, i.e. unknown components of the universe which show up only gravitationally. As we essentially do not know what the dark matter and the dark energy are, however, it seems a healthy attitude to consider the possibility that gravity at long distances might be different from what we think we know.

This kind of consideration has been a motivation for attempts for IR modification of gravity, e.g. massive gravity [1] and DGP brane model [2]. However, they are known to have a macroscopic UV scale at around 1000km, where effective field theories break down [3, 4]. This does not necessarily mean that these theories cannot describe the real world, but implies that we need non-trivial assumptions about the unknown UV completion. The recent proposal of ghost condensation [5] evades at least this problem and can be thought to be a step towards a consistent theory of IR modification of general relativity.

In general, if we have scalar fields then there are many things we can play with them. In cosmology, inflation can be driven by the potential part of a scalar field. It is also possible to drive inflation by the kinetic part of a scalar field [6]. On the other hand, scalar fields play important roles also in particle physics. A scalar field is used for spontaneous symmetry breaking and to change force laws in the Higgs mechanism. This is usually achieved by using a potential whose global minimum is charged under the gauge symmetry. The basic idea of ghost condensation is to break a symmetry and change a force law by the kinetic part of a scalar field. In this sense the ghost condensation can be considered as an analogue of Higgs mechanism.

2 Tachyons and Ghosts

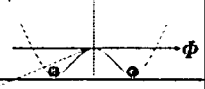
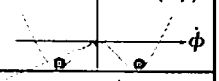
A tachyon in particle mechanics is defined as a particle whose speed exceeds the speed of light. It violates causality and, thus, a theory with tachyons is considered to be sick in the context of particle mechanics. However, this is not necessarily true in field theory. In field theory a tachyon is an excitation around a top of a potential. In this case a tachyon just indicates an instability of the background around which the theory is expanded. If the potential has minima at other field values then the theory can be expanded around any one of them and the low energy effective theory is healthy even in the context of particle mechanics. One important point is that we cannot talk about evolution from the unstable background with tachyons to the stable background without tachyons within the context of particle mechanics. In order to describe such an evolution, we need a framework more general than particle mechanics, namely field theory.

[1]E-mail: mukoyama@phys.s.u-tokyo.ac.jp

A ghost in field theory can be defined as a field with a wrong sign kinetic term. This is equivalent to say that a ghost is a field with a negative norm. Because of this, a field theory with ghosts is thought to be sick. Indeed, aside from the negative norm, the existence of a ghost indicates instability since the energy associated with the ghost excitation is not bounded from below at least perturbatively in the context of field theory. This situation for ghosts in field theory is somehow similar to that for tachyons in particle mechanics. Hence, it seems natural to expect that a more general, perhaps not-yet-known framework should be able to describe a ghost as just an indication of instability of the background around which the theory is expanded. If this is the case, the general framework should be able to describe the dynamics from a background with ghosts to another background without ghosts. What is important here is that, even without such a framework, we can construct a low energy effective field theory (EFT) around the latter background, which we call ghost condensate. For this reason, we do assume the existence of the more general framework, or a UV completion, but do not need to assume any properties of the UV completion to describe low energy excitations of ghost condensate.

3 Ghost Condensation

The ghost condensation can be pedagogically explained by comparison with the usual Higgs mechanism as in the table shown below. First, the order parameter for ghost condensation is the vacuum expectation value (vev) of the derivative $\partial_\mu\phi$ of a scalar field ϕ, while the order parameter for Higgs mechanism is the vev of a scalar field Φ itself. Second, both have instabilities in their symmetric phases: a tachyonic instability around $\Phi = 0$ for Higgs mechanism and a ghost instability around $\partial_\mu\phi = 0$ for ghost condensation. In both cases, because of the instabilities, the system should deviate from the symmetric phase and the order parameter should obtain a non-vanishing vev. Third, there are stable point where small fluctuations do not contain tachyons nor ghosts. For Higgs mechanism, such a point is characterized by the vev of the order parameter satisfying $V' = 0$ and $V'' > 0$. On the other hand, for ghost condensation a stable point is characterized by $P' = 0$ and $P'' > 0$. Fourth, while the usual Higgs mechanism breaks usual gauge symmetry and changes gauge force law, the ghost condensation spontaneously breaks a part of Lorentz symmetry (the time translation symmetry) and changes linearized gravity force law even in Minkowski background. Finally, generated corrections to the standard Gauss-law potential is Yukawa-type for Higgs mechanism but oscillating for ghost condensation.

	Higgs Mechanism	***Ghost Condensation***
Order Parameter	$\langle\Phi\rangle$ 	$\langle\partial_\mu\phi\rangle$ 
Instability	Tachyon $-m^2\Phi^2$	Ghost $-\dot{\phi}^2$
Condensate	V'=0, V''>0	P'=0, P''>0
Spontaneous breaking	Gauge symmetry	Lorents symmetry (Time translation)
Modifying	Gauge force	Gravitational force (in flat background)
New potential	Yukawa-type	Oscillating

For simplicity let us consider a Lagrangian $L_\phi = P(-(\partial\phi)^2)$ in the expanding FRW background with P of the form shown in the upper right part of the table. We assume the shift symmetry, the symmetry under the constant shift $\phi \to \phi + c$ of the scalar field. This symmetry prevents potential terms of ϕ from being generated. The equation of motion for ϕ is simply $\partial_t[a^3P'\dot{\phi}] = 0$, where a is the scale factor of the

universe. This means that $a^3 P'\dot{\phi}$ is constant and that

$$P'\dot{\phi} \propto a^{-3} \to 0 \quad (a \to \infty) \tag{1}$$

as the universe expands. We have two choices: $P' = 0$ or $\dot{\phi} = 0$, namely one of the two bottoms of the function P or the top of the hill between them. Obviously, we cannot take the latter choice since it is a ghosty background and anyway unstable. Thus, we are automatically driven to $P' = 0$ by the expansion of the universe. In this sense the background with $P' = 0$ is an attractor. Thus, if there were inflation(s) (irrespective of whether it is the usual potentially driven inflation, k-inflation or ghost inflation) in the early universe then P' is set to an extremely small value.

Now let us consider a small fluctuation around the background with $P' = 0$. For $\phi = M^2 t + \pi$, the quadratic action for π coming from the Lagrangian P is $\int d^4x[(P'(M^4) + M^4 P''(M^4))\dot{\pi}^2 - P'(M^4)(\nabla\pi)^2]$. By setting $P'(M^4) = 0$ we obtain the time kinetic term $M^4 P''(M^4)\dot{\pi}^2$ with the correct sign. Unless the function P is fine-tuned, P'' is non-zero at $P' = 0$. This means that the coefficient of the time kinetic term is non-vanishing and, thus, we do not have the strong coupling issue which the massive gravity and the DGP brane model are facing with. On the other hand, the coefficient of $(\nabla\pi)^2$ vanishes at $P' = 0$ and the simple Lagrangian P does not give us a spatial kinetic term for π. However, this does not mean that there is no spatial kinetic term in the low energy EFT for π. This just says that the leading spatial kinetic term is not contained in P and that we should look for the leading term in different parts. Indeed, other terms like $\tilde{P}((\partial\phi)^2)Q(\Box\phi)$ do contain spatial kinetic terms for π but the spatial-derivative expansion starts with the fourth derivative: $(\nabla^2\pi)^2 + \cdots$. If there is a non-vanishing second-order spatial kinetic term $(\nabla\pi)^2$ then it can be included in P by redefinition and the redefined P' goes to zero by the expansion of the universe as shown above. Namely, the expansion of the universe ensures that the spatial-derivative expansion starts from $(\nabla^2\pi)^2 + \cdots$. Combining this spatial kinetic term with the previously obtained time kinetic term and properly normalizing π, we obtain the low energy effective action of the form

$$\int d^4x \left[\frac{1}{2}\dot{\pi}^2 - \frac{\alpha}{M^2}(\nabla^2\pi)^2 + \cdots\right], \tag{2}$$

where α is a dimensionless parameter of order unity. One might worry that other (nonlinear) terms in effective theory such as $\dot{\pi}(\nabla\pi)^2$ might mess up the effective action. In fact, it turns out that all such terms are irrelevant at low energy [5]. An important fact to show this is that the scaling dimension of π is not the same as its mass dimension 1 but is 1/4, reflecting the situation that the Lorentz symmetry is broken spontaneously. Moreover, it is also straightforward to show that all spurious modes associates with higher time derivative terms such as $(\ddot{\phi})^2$ have frequency above the cutoff M and, thus, should be ignored. In this sense, we are assuming the existence of a UV completion but not assuming any properties of it. Finally, it must be noted that the effective action of the form (2) is stable against radiative corrections. Indeed, the only would-be more relevant term in the effective theory is the usual spatial kinetic term $(\nabla\pi)^2$, but its coefficient P' is driven to an extremely small value by the expansion of the universe even if it is radiatively generated.

The effective action (2) would imply the low energy dispersion relation for π is $\omega^2 \simeq \alpha k^4/M^2$. However, since the background spontaneously breaks Lorentz invariance, π couples to gravity in the linearized level even in Minkowski or de Sitter background. Hence, mixing with gravity introduces an order M^2/M_{pl}^2 correction to the dispersion relation. As a result the dispersion relation in the presence of gravity is $\omega^2 \simeq \alpha k^4/M^2 - \alpha M^2 k^2/2M_{pl}^2$. This dispersion relation leads to IR modification of gravity due to Jean's instability. Note that there is no ghost around the stable background $P' = 0$ and the Jeans's instability is nothing to do with a ghost.

As stated in the end of Sec. 2, we actually do not need to specify a concrete way of the spontaneous symmetry breaking in order to construct the EFT around the stable background. In this sense, the ghost around $\dot{\phi} = 0$ has nothing to do with the construction of the EFT around $P' = 0$. Indeed, it is suffice to assume the symmetry breaking pattern, namely from the full $4D$ Lorentz symmetry to the $3D$ spatial diffeomorphism [5].

Note that the ghost condensate provides the second most symmetric class of backgrounds for the system of field theory plus gravity. The most symmetric class is of course maximally symmetric solutions: Minkowski, de Sitter and anti-de Sitter. The ghost condensate minimally breaks the maximal symmetry and introduces only one Nambu-Goldstone boson.

4 Possible Applications

Dark energy: In the usual Higgs mechanism, the cosmological constant (cc) would be negative in the broken phase if it is zero in the symmetric phase. Therefore, it seems difficult to imagine how the Higgs mechanism provides a source of dark energy. On the other hand, the situation is opposite with the ghost condensation: the cc would be positive in the broken phase if it is zero in the symmetric phase. Hence, while this by itself does not solve the cc problem, this can be a source of dark energy.

Dark matter: If we consider a small, positive deviation of P' from zero then the homogeneous part of the energy density is proportional to a^{-3} and behaves like dark matter. Inhomogeneous linear perturbations around the homogeneous deviation also behaves like dark matter. However, at this moment it is not clear whether we can replace dark matter with ghost condensate. We need to see if it clumps properly. Ref. [8] can be thought to be a step towards this direction.

Inflation: We can also consider inflation within the regime of the validity of the EFT with ghost condensation. In the very early universe where H is higher than the cutoff M, we do not have a good EFT describing the sector of ghost condensation. However, the contribution of this sector to the total energy density ρ_{tot} is naturally expected to be negligible: $\rho_{ghost} \sim M^4 \ll M_p^2 H^2 \simeq \rho_{tot}$. As the Hubble expansion rate decreases, the sector of ghost condensation enters the regime of validity of the EFT and the Hubble friction drives P' to zero. If we take into account quantum fluctuations then P' is not quite zero but is $\sim (H/M)^{5/2} \sim (\delta\rho/\rho)^2 \sim 10^{-10}$ in the end of ghost inflation. In this way, we have a consistent story, starting from the outside the regime of validity of the EFT and dynamically entering the regime of validity. All predictions of the ghost inflation are derived within the validity of the EFT, including the relatively low-H de Sitter phase, the scale invariant spectrum and the large non-Gaussianity [7].

Black hole: In ref. [9] we consider the question "what happens near a black hole?" A ghost condensate defines a hypersurface-orthogonal congruence of timelike curves, each of which has the tangent vector $u^\mu = -g^{\mu\nu}\partial_\nu\phi$. It is argued that the ghost condensate in this picture approximately corresponds to a congruence of geodesics and the accretion rate of the ghost condensate into a black hole should be negligible for a sufficiently large black hole. This argument is confirmed by a detailed calculation based on the perturbative expansion w.r.t. the higher spatial kinetic term. The essential reason for the smallness of the accretion rate is the same as that for the smallness of the tidal force acted on an extended object freely falling into a large black hole.

Acknowledgements

The author would like to thank Nima Arkani-Hamed, Hsin-Chia Cheng, Paolo Creminelli, Markus Luty, Jesse Thaler, Toby Wiseman and Matias Zaldarriaga for collaboration on the subject.

References

[1] M. Fierz and W. Pauli, Proc. Roy. Soc. Lond. **A173**, 211 (1939).

[2] G. R. Dvali, G. Gabadadze and M. Porrati, Phys. Lett. **B485**, 208 (2000).

[3] N. Arkani-Hamed, H. Georgi and M. D. Schwartz, Annals Phys. **305**, 96 (2003).

[4] M. A. Luty, M. Porrati and R. Rattazzi, JHEP **0309**, 029 (2003).

[5] N. Arkani-Hamed, H.-C. Cheng, M. A. Luty and S. Mukohyama, JHEP **0405**, 074 (2004).

[6] C. Armendariz-Picon, T. Damour and V. Mukhanov, Phys. Lett. **B458**, 209 (1999).

[7] N. Arkani-Hamed, P. Creminelli, S. Mukohyama and M. Zaldarriaga, JCAP **0404**, 001 (2004).

[8] N. Arkani-Hamed, H.-C. Cheng, M. A. Luty, S. Mukohyama, and T. Wiseman, in preparation.

[9] in preparation.

Generation of New Axisymmetric stationary Solutions in five-dimensional asymptotically flat spacetimes

Takashi Mishima[1], Hideo Iguchi[2]

Laboratory of Physics, College of Science and Technology, Nihon University, Narashinodai, Funabashi, Chiba 274-8501, Japan

Abstract

New Axisymmetric stationary solutions of the vacuum Einstein equations in five-dimensional asymptotically flat spacetimes are given by solitonic solution-generating techniques. It is shown that the four-dimensional multi-solitonic solutions derived from particular class of four-dimensional Weyl solutions as seed are equivalent to non-trivial new solutions corresponding to some five-dimensional asymptotically flat vacuum spacetimes. The solutions constructed here include one rotational black rings, which is different from the ones obtained by Emparan and Reall previously.

1 Introduction

Inspired by the recent development of fundamental theories including brane world models, the studies of the spacetime structures in higher dimensional general relativity have been vigorously done and have revealed the rich structure of higher dimensional spacetimes. For example, some qualitative features concerning in the topology of event horizons have been clarified to a certain extent [1]. And also several exact solutions involving black holes have been obtained and the richness of the phase structure of black holes have been discussed. In five dimensions particularly, since the remarkable discovery of a rotating black ring solution by Emparan and Reall [2], numerous investigations have been concentrated on the five-dimensional case. Several authors have obtained other important solutions including supersymmetric black rings [3] and also the solutions under the influence of external fields [4].

Despite of these great advance in the higher dimensional general relativity, the construction of new solutions in higher dimensions than four have not been done fully in comparison with four dimensional case. In particular for the non-supersymmetric spacetimes with asymptotic flatness, available solutions are not so many. From '70s to '80s, in the case of four dimensions solitonic solution-generation techniques were greatly developed and used to construct new series of axisymmetric stationary solutions extensively [5]. Since the discovery of Tomimatsu-Sato solutions [6], the solutions corresponding to spacetimes with asymptotic flatness were derived systematically, which include the famous multi-Kerr solutions by Kramer and Neugebauer [7].

So far it seems that similar techniques like the above ones have not been applied to the higher dimensional general relativity effectively, except Kaluza-Klein theories [8]. If these techniques are available to the higher dimensional cases, we can expect that the investigation of the rich structure of higher dimensional spacetimes will go further. We shall therefore try to construct new solutions of vacuum Einstein equations with asymptotic flatness especially in the case of five dimensions, employing the well-developed solution-generating techniques in four dimensions.

Here we concentrate on the spacetimes which satisfy the following conditions: (1) five dimensions, (2) asymptotically flat spacetimes, (3) the solutions of vacuum Einstein equations, (4) having three commuting Killing vectors including a time symmetric one and (5) one non-zero angular momentum component. Based on these conditions, we first show that the five dimensional solitonic solution-generating problems can be considered some four dimensional problems. Owing to this correspondence we can generate new solutions by adding some solitons to seed solutions which correspond to known five-dimensional spacetimes. Then we apply the above approach to the simple case in which the Minkowski spacetime is taken as a seed. As a result, a new series of solutions which corresponds to the spacetimes asymptoting to

[1]E-mail:tmishima@phys.ge.cst.nihon-u.ac.jp
[2]E-mail:iguchi.h@phys.ge.cst.nihon-u.ac.jp

five-dimensional Minkowski spacetimes is derived. This series has four parameters to characterize the corresponding spacetime structure. It is too complicated to investigate the spacetime structure corresponding to the new solution by the use of only analytic methods. Using numerical analysis together, we can however show that the existence of a sub-sequence of the solutions derived here can corresponds to the sequence of one rotational black rings, which differently rotate from the ones obtained by Emparan and Reall, although the spacetimes generally have some singular objects like closed timelike curves and curvature singularities.

2 Basic equations

Under the conditions assumed in the previous section, the following Weyl-Papapetrou metric form can be adopted as a starting point,

$$ds^2 = -e^{3U_0}(dx^0 - \omega d\phi)^2 + e^{2U_1}\rho^2(d\phi)^2 + e^{2U_2}(d\psi)^2 + e^{2(\gamma+U_1)}\left(d\rho^2 + dz^2\right) \tag{1}$$

where U_0, U_1, U_2, ω and γ are functions of ρ and z. New functions $S := 2U_0 + U_2$ and $T := U_2$ are introduced further, with which the metric form (1) is rewritten into

$$ds^2 = -e^{-T}\left[e^S(dx^0 - \omega d\phi)^2 + e^{-S}\rho^2(d\phi)^2 + e^{2(\gamma-S)}\left(d\rho^2 + dz^2\right)\right] + e^{2T}(d\psi)^2. \tag{2}$$

Then the Einstein equations are reduced to the following set of equations,

$$\begin{aligned}
&\text{(i)} \quad \nabla^2 T = 0 \\
&\text{(ii)} \quad \begin{cases} \partial_\rho \gamma_T = \frac{3}{4}\rho\left[(\partial_\rho T)^2 - (\partial_z T)^2\right], \\ \partial_z \gamma_T = \frac{3}{2}\rho\left[\partial_\rho T\, \partial_z T\right] \end{cases} \\
&\text{(iii)} \quad \nabla^2 \mathcal{E}_S = \frac{1}{\mathrm{Re}\,\mathcal{E}_S}\nabla\mathcal{E}_S \cdot \nabla\mathcal{E}_S \\
&\text{(iv)} \quad \begin{cases} \partial_\rho \gamma_S = \frac{\rho}{2(\mathcal{E}_S+\bar{\mathcal{E}}_S)}\left(\partial_\rho\mathcal{E}_S\partial_\rho\bar{\mathcal{E}}_S - \partial_z\mathcal{E}_S\partial_z\bar{\mathcal{E}}_S\right) \\ \partial_z \gamma_S = \frac{\rho}{2(\mathcal{E}_S+\bar{\mathcal{E}}_S)}\left(\partial_\rho\mathcal{E}_S\partial_z\bar{\mathcal{E}}_S + \partial_\rho\bar{\mathcal{E}}_S\partial_z\mathcal{E}_S\right) \end{cases} \\
&\text{(v)} \quad (\partial_\rho\Phi,\, \partial_z\Phi) = \rho^{-1}e^{2S}\left(-\partial_z w,\, \partial_\rho w\right) \\
&\text{(vi)} \quad \gamma = \gamma_S + \gamma_T
\end{aligned}$$

where Φ is defined through the equation (v) and the function $\mathcal{E}_S$ is defined by $\mathcal{E}_S := e^S + i\Phi$. The equaiton (iii) is exactly the same as the Ernst equation, so that we can consider $\mathcal{E}_S$ Ernst potential. The most crucial point to obtain new metric forms is to solve the equation (iii) because of it's non-linearity. To overcome this difficulty we can however use the methods already established in four-dimensional case. In this place we shall use the method similar to the Neugebauer's Bäckrund transformation or HKX transformation, whose essential idea is that new solutions are generated by adding solitons to seed spacetimes. For the actual analysis in the following sections, we take the five-dimensional Minkowski spacetime as a seed spacetime and use the formulas shown in the paper by Amend and Manko, in which they originally discussed the deformation of a Kerr black hole under the influence of external gravitational field [8].

3 Generation of new solutions

Here we start from the following form of the five-dimensional Minkowski spacetime metric as a seed solution,

$$\begin{aligned}
ds^2 \;=\; & -(dx^0)^2 + \left(\sqrt{\rho^2 + (z+\lambda\sigma)^2} - (z+\lambda\sigma)\right)d\phi^2 \\
& + \left(\sqrt{\rho^2 + (z+\lambda\sigma)^2} + (z+\lambda\sigma)\right)d\psi^2 + \frac{1}{2\sqrt{\rho^2 + (z+\lambda\sigma)^2}}(d\rho^2 + dz^2)
\end{aligned} \tag{3}$$

where λ and σ are arbitrary real constants. From this, we can read the form of the functions S and T as seed functions,

$$S^{(0)} = T^{(0)} = \frac{1}{2}\ln\left[\sqrt{\rho^2 + (z+\lambda\sigma)^2} + (z+\lambda\sigma)\right] \tag{4}$$

where the superscript (0) means the quantity for the seed spacetime. Because the seed functions are no-trivial, the problem can be considered as the four-dimensional problem that new solutions are generated from the seed spacetime with some gravitational field. Using the formulas in the paper by Amend and Manko, we derive the new solution from the above seed metric finally.

After the introduction of the prolate spheroidal coordinates: $\rho = \sigma\sqrt{x^2-1}\sqrt{1-y^2}$, $z = \sigma xy$, the full metric and the Ernst potential are expressed as

$$\begin{aligned} ds^2 = &-\frac{B}{A}\left[dx^0 - \left(2\sigma e^{-S^{(0)}}\frac{C}{A} + C_1\right)d\phi\right]^2 + \frac{A}{B}e^{-2S^{(0)}}\rho^2(d\phi)^2 + e^{2S^{(0)}}(d\psi)^2 \\ &+ C_2 B\left(\frac{x-1}{x+1}\cdot\frac{Y_{-\sigma,-\lambda\sigma}}{Y_{\sigma,-\lambda\sigma}\left[x^2+y^2+2\lambda xy+(\lambda^2-1)\right]},\right)^{1/2}\left(\frac{dx^2}{x^2-1}+\frac{dz^2}{1-y^2}\right) \end{aligned} \tag{5}$$

$$\left(Y_{\pm\sigma,-\lambda\sigma} = \sigma^2\left[(x\mp y)\sqrt{x^2+y^2+2\lambda xy+(\lambda^2-1)} + x^2+y^2+(\lambda\mp 1)xy \mp \lambda\right] \right)$$

$$\mathcal{E}_S = e^{S^{(0)}}\frac{x(1+ab)+iy(b-a)-(1-ia)(1-ib)}{x(1+ab)+iy(b-a)+(1-ia)(1-ib)}. \tag{6}$$

Here the functions a and b are given by

$$a = \alpha\frac{(x-y+1+\lambda)+\sqrt{x^2+y^2+2\lambda xy+(\lambda^2-1)}}{2\left[(xy+\lambda)+\sqrt{x^2+y^2+2\lambda xy+(\lambda^2-1)}\right]^{1/2}} \tag{7}$$

$$b = \beta\frac{2\left[(xy+\lambda)+\sqrt{x^2+y^2+2\lambda xy+(\lambda^2-1)}\right]^{1/2}}{(x+y-1+\lambda)+\sqrt{x^2+y^2+2\lambda xy+(\lambda^2-1)}}, \tag{8}$$

and the quantities A, B and C are defined with a and b as

$$\begin{aligned} A &:= (x^2-1)(1+ab)^2 - (1-y^2)(b-a)^2, \\ B &:= [(x+1)+(x-1)ab]^2 + [(1+y)a+(1-y)b]^2, \\ C &:= (x^2-1)(1+ab)[b-a-y(a+b)] + (1-y^2)(b-a)[1+ab+x(1-ab)]. \end{aligned}$$

From the metric form (5), we know that the sequence of new solutions have four parameters: λ, σ, α and β.

4 Results and Discussion

At present our analysis of the spacetime structure corresponding to the new solutions is far from accomplishment. As mentioned in the Introduction, it is a difficult problem to perform the analysis of the spacetime structure in analytic way. So we comment on a few properties of the spacetimes clarified so far in this place. First we can say that the spacetimes generally hold asymptotic flatness from the form of the asymptotic expansion of the metric or Ernst potential $\mathcal{E}_S$ easily,

$$\begin{aligned} \mathcal{E} = &\; r\cos\theta\left\{1 - \frac{4\sigma}{r^2}\frac{1+\alpha^2-\alpha^2\beta^2}{(1+\alpha\beta)^2}\cdots\right\} \\ &+2i\sigma^{1/2}\left\{\frac{\alpha}{1+\alpha\beta} - \frac{4\sigma\cos^2\theta}{r^2}\frac{\alpha(\alpha^2+1)-\beta(2\alpha\beta+1)(\alpha^2+1)-\alpha^2\beta^3}{(1+\alpha\beta)^3}\cdots\right\}. \end{aligned} \tag{9}$$

The spacetimes however have some local gravitational objects which are generally singular. Figure 1 shows the schematic diagram of the local gravitational object. At a glance it seems like a black ring. We

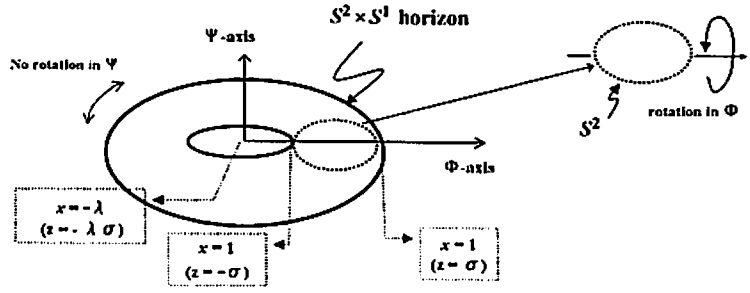


Figure 1: Schematic diagram of a local ring-like object which resides in the spacetimes. Generally some singular behavior appears near the point $(x, z) = (1, -\sigma)$. The parameter λ control the size of the hole of the ring-like object.

must however suspect that the local objects generally have some singular structure like closed timelike curves(CTCs) and curvature singularities near the point $(x, z) = (1, -\sigma)$. As an exceptional case, we expect that the following special combination of parameters,

$$\beta = -\frac{2 + \alpha^2(\lambda + 1) - \sqrt{\alpha^4(\lambda + 1)^2 - 4\alpha^2(\lambda - 3) + 4}}{4\alpha} \tag{10}$$

make the singular structure of the spacetimes fairly mild. For example, considering the behavior of the ϕ-ϕ component of the metric, the CTC-region near the point mentioned above seems to disappear completely in this case. Hence we think that this sub-sequence corresponds to one rotational black rings, which differently rotate from the ones obtained by Emparan and Reall, as depicted in Figure 1. It should be noticed however that a certain kind of strut is always needed to sustain the ring obtained here. The parameter λ controls the size of the disk-strut put on the hole of the ring. As an interesting case, if one sets the parameter λ to 1 as holding the relation (10), the corresponding spacetime becomes the one rotational spherical black hole spacetime with a regular horizon which corresponds to one of the solutions found by Myers and Perry. Finally we comment on the four parameters; λ and σ characterize the size and mass of the local object which resides in the spacetimes; α and β can be considered as the similar parameters to the Kerr-parameter and NUT-parameter in four-dimensional case.

More detailed and systematic treatments of the methods and the new solutions introduced here will be appeared in near future [9].

References

[1] M. I. Cai and G. J. Galloway, Class. Quant. Grav. **18**, 2707(2001); G. W. Gibbons, D. Ida, and T. Shiromizu, Phys. Rev. Lett. **89**, 041101(2002); Y. Morisawa and D. Ida, Phys. Rev. D **69**, 124005(2004).

[2] R. Emparan and H. S. Reall, Phys. Rev. Lett. **88**, 101101(2002).

[3] H. Elvang, R. Emparan, D. Mateos and H. S. Reall, Phys. Rev. Lett. **93**, 211302(2002).

[4] D. Ida and Y. Uchida, Phys. Rev. D **68**, 104014(2003).

[5] D. Kramer *et al*, *Exact Solutions of Einstein's Field Equations, 2nd ed.* (Cambridge University Press, Cambridge, 2003).

[6] A. Tomimatsu and H. Sato, Phys. Rev. Lett. **29**, 1344(1972).

[7] D. Kramer and G. Neugebauer, Phys. Lett. A **75**, 259(1980)

[8] J. Castejon-Amendo and V.S. Manko, Phys. Rev. D **41**, 2018(1990).

[9] T. Mishima and H. Iguchi, to be appeared.

Deciphering Imprints of CDM Substructure
- Current Status and Future Prospects -

Kaiki Taro Inoue [1]

Department of Science and Engineering, Kinki University, Higashi-Osaka, 577-8502, Japan

Abstract

The Cold Dark Matter (CDM) structure formation model predicts that about 5-10 percent of a typical galactic halo mass $\sim 10^{12} M_{\odot}$is in substructures with a mass $\lesssim 10^{8} M_{\odot}$. Recent studies of four-imaged QSO-galaxy lens systems showing flux anomaly suggest existence of localized perturbers along the line-of-sight to multiple images. However, the subhalo location along the line-of-sight remain uncertain owing to degeneracy between the subhalo mass and the distance. I show that a mapping between the spatial distribution of surface brightness of an observed extended image with that of an unperturbed macrolensed image will break degeneracy between the subhalo mass and the distance provided that macrolensing parameters are determined from position and fluxes of multiple images.

1 Introduction

Recent high-resolution N-body simulations of the Cold Dark Matter (CDM) structure formation model show an excess in the number of subhalos ("substructures") in a galaxy-sized halo in comparison with the number of Milky Way or M31 satellites (Klypin et al. 1999; Moore et al. 1999). If the CDM-based structure formation model is the correct one, then we expect a large number of invisible satellites inside a halo of galaxies.

Currently, gravitational lensing is the only probe that can test the abundance of these invisible satellites or equivalently, substructures in a galaxy-sized halo. In fact, gravitationally multiply lensed QSOs have recently been used for putting a limit on the surface density and the mass of such invisible substructures (Mao & Schneider 1998; Metcalf & Madau 2001; Chiba 2002; Metcalf & Zhao 2002; Dalal & Kochanek 2002; Bradac et al. 2002). Statistical analyses on these quadruply imaged QSO-galaxy lensing systems that show anormalous flux ratios imply presence of substructures along the line of sight to the multiple images (Keeton, Gaudi, & Petters 2002; Evans & Witt 2003).

However, locations of substructures along the line-of-sight to multiple images are not constrained at all. In fact, extragalactic substructures other than those associated with primary lensing halos can also contribute significantly to QSO-galaxy lens systems. Using N-body simulations, Wambsganss, Bode, & Ostriker (2004) showed that the fraction of cases for which more than one lens plane contributes significantly to a multiply imaged system is very large for a source at high redshift $z \gtrsim 3$. Metcalf (2004) showed that all the cusp caustic lens anomalies can also be explained by extragalactic ΛCDM halos with a mass range of $10^{8-9} M_{\odot}$.

In order to determine the distances to these substructures, I propose to observe multiply lensed extended sources using an interferometer array with high angular resolution (Inoue & Chiba 2003, Inoue & Chiba 2005). Then we can carry out "astrometry" of a set of points in these substructures in one image relative to a corresponding set of points in an unperturbed macrolensed image (Inoue & Chiba 2004). This method is especially useful for systems in which the macrolensing parameters have been determined from position and fluxes of multiple images which are not significantly affected by perturbers.

2 Observational Method

For mapping $10^{8-9} M_{\odot}$ CDM subhalos, I propose to observe dust continuum emission from a strongly lensed QSO-host galaxy using a large submillimeter interferometer array with a high angular resolution

[1] E-mail:kinoue@phys.kindai.ac.jp

$\sim$ 0.01arcsec such as the planned Atacama Large Submillimeter Array (*ALMA*). It has been argued that about 30% of the QSO-host galaxies are infrared luminous implying that a large amount of energy emitted by stars and AGNs in QSO-host galaxy has been absorbed by dust grains and then re-radiated at longer wavelengths. The dust is heated to temperatures of 20-50K and radiates as a modified blackbody at far-infrared wavelengths. At redshift $z = 3 \sim 4$, the corresponding energy peak is at submillimeter wavelengths $\sim$ 0.1mm. The dust has a typical scale of 10^2pc to a few kpc. Therefore, the extended source effects can be easily observed. Inhomogeneous dust temperature distribution owing to a starbust or an AGN produces inhomogeneous emissivity distribution. Therefore, we have a non-vanishing surface brightness gradient in the source. Furthermore, radiation at submillimeter wavelengths is free from dust extinction or absorption owing to hot plasma along the line-of-sight to the macrolensed image, which is crucial for measuring the distance between macrolens and the perturber. Thus submillimeter mapping of a QSO-galaxy system will give us an ideal opportunity to directly map a CDM substructure not only in the tangential direction but also in the radial direction along the line-of-sight to the macrolensed image.

3 Systematic Distortion

In this section, systematic distortion of extended sources in singular isothermal sphere (SIS) lens with an external background shear and convergence relevant to substructure lensing (Finch et al. 2002; Keeton 2003) is studied. If the mass scale of a substructure is sufficiently smaller than that of a macrolens, this model provides a good approximation in representing the local property of lensing along the line-of-sight to a substructure. For simplicity, we study a circular top-hat source centered at the SIS lens center.

The lens equation for an SIS lens with an external convergence κ and shear $\gamma > 0$ in terms of normalized coordinates, $\mathbf{x} = \theta_x/\theta_E$ and $\mathbf{y} = \theta_y/\theta_E$, the lens equation can be reduced to

$$\mathbf{y} = (1 - \Gamma)\mathbf{x} - \frac{\mathbf{x}}{|\mathbf{x}|}. \tag{1}$$

where

$$\Gamma = \begin{pmatrix} \kappa + \gamma & 0 \\ 0 & \kappa - \gamma \end{pmatrix} \tag{2}$$

and θ_E is the Einstein radius of a SIS lens.

Let us consider an elliptic top-hat source E with semi-major axis $L_1 > 1$ and semi-minor axis $L_2 > 1$ with constant surface brightness. As long as we concern with the neighborhood of the boundary ∂E of the source E, the lens equation can be approximated by a linear equation, which yields the follwing three types of distortion patterns classified by the sign of the eigenvalues of $1 - \Gamma$, $\xi_1 \equiv 1 - (\kappa + \gamma)$ and $\xi_2 \equiv 1 - (\kappa - \gamma)$:(I) $\xi_1 > 0, \xi_2 > 0$ positive parity, (II) $\xi_1 < 0, \xi_2 > 0$ negative parity, (III) $\xi_1 < 0, \xi_2 < 0$ doubly-negative parity[2]. In the positive parity case, both a semi-major axis x_1 and a semi-minor axis x_2 of an image extend by $\Delta x_1 = \xi_1^{-1}$ and $\Delta x_2 = \xi_2^{-1}$ in comparison with an unperturbed lensed image (background shear and convergence only). In the negative parity case, the semi-major axis x_1 shrinks by $|\Delta x_1 < 0| = |\xi_1^{-1}|$ whereas x_2 extends by $\Delta x_2 = \xi_2^{-1}$. In the doubly-negative parity case, both axes shrink, i.e. $\Delta x_1 < 0, \Delta x_2 < 0$. These features are shown in Figures 1.

4 Measurement of Distance

In this section, we study how one can break the degeneracy between the lensing effects of the perturber mass and that of a perturber distance along the line-of-sight. Suppose a halo at redshift $z = z_h$ and a clump (substructure) at redshift $z = z_c$. Let D_s, D_{ch},D_{cs}, and D_h be distance to the source, between clump and halo, between clump and source, and distance to the halo, respcetively. As a function of convergence κ and shear γ in the unperturbed macrolens, the effective convergence and shear for a perturbed lens can be expressed as

$$\kappa_{\rm eff} = \frac{(1-\beta)(\kappa - \beta(\kappa^2 - \gamma^2))}{(1-\beta\kappa)^2 - \beta^2\gamma^2}, \gamma_{\rm eff} = \frac{(1-\beta)\gamma}{(1-\beta\kappa)^2 - \beta^2\gamma^2}, \tag{3}$$

[2]These parities correspond to a maximum (positive), a saddle (negative) and a minimum (doubly-negative) point in the arrival time surface.

where

$$\beta = \frac{D_{ch} D_s}{D_{cs} D_h} \tag{4}$$

encodes information of a distance between a halo and a clump (Keeton 2003). Suppose a source E has a constant surface brightness having an elliptic shape with semi-major axis L and semi-minor axis ϵL. As long as we concern with the boundary ∂E of the source E, the lens equation can be approximated by a linear equation where approximated effective convergence and shear are (Inoue & Chiba 2004)

$$\begin{aligned} \kappa_a &= \kappa_{\rm eff} - \frac{1}{2}\left(\frac{1}{L(1-\kappa_{\rm eff}-\gamma_{\rm eff})} + \frac{1}{\epsilon L(1-\kappa_{\rm eff}+\gamma_{\rm eff})} \right), \\ \gamma_a &= \gamma_{\rm eff} - \frac{1}{2}\left(\frac{1}{L(1-\kappa_{\rm eff}-\gamma_{\rm eff})} - \frac{1}{\epsilon L(1-\kappa_{\rm eff}+\gamma_{\rm eff})} \right). \end{aligned} \tag{5}$$

From equation (5), one can see that the distance ratio β, and the linear source size L in unit of the Einstein radius of the perturber can be determined from observed values of κ_a and γ_a provided that parameters κ, γ, ϵ are determined from the best-fit macrolens model. Furthermore, if the macrolens parameters such as D_s, D_h, D_{hs} and the Einstein radius θ_E (or equivalently, velocity dispersion) are known, then one can measure the distance between the perturber and the macrolens from distance ratio β and the velocity dispersion of the SIS perturber from θ_E.

References

[1] Bradac, M., Schneider, P., Steinmetz, M., Lombardi, M., & King, L. J., 2002, A&A, 388, 373

[2] Chiba, M. 2002, ApJ, 565, 17

[3] Dalal, N.& Kochanek, C. S. 2002, ApJ, 572, 25

[4] Evans, N. W. & Witt, H. J. 2003, MNRAS, 345 1351

[5] Finch, T., Carlivati, L. P., Winn, J. N. & Schechter, P. L. 2002, ApJ, 577, 51

[6] Inoue, K. T. & Chiba, M. 2003, ApJL, 591, L83

[7] Inoue, K. T. & Chiba, M. 2004, astro-ph/0411168

[8] Inoue, K. T. & Chiba, M. 2005, (in preparation)

[9] Keeton, C. R., Gaudi, B.S., & Petters, A. O., 2003, ApJ, 598, 138

[10] Keeton, C. R., 2003, ApJ, 584, 664

[11] Klypin, A., Kravtsov, A. V., Valenzuela, O., & Prada, F. 1999, ApJ, 522, 82

[12] Mao, S. & Schneider, P. 1998, MNRAS, 295, 587

[13] Metcalf, R. B., & Madau, P. 2001, ApJ, 563, 9

[14] Metcalf, R. B. & Zhao, H. 2002, ApJ, 567, L5

[15] Metcalf, R. B. 2004, astro-ph/0412538

[16] Moore, B., Ghigna, S., Governato, F., Lake, G., Quinn, T., & Stadel, J. 1999, ApJ, 524, L19

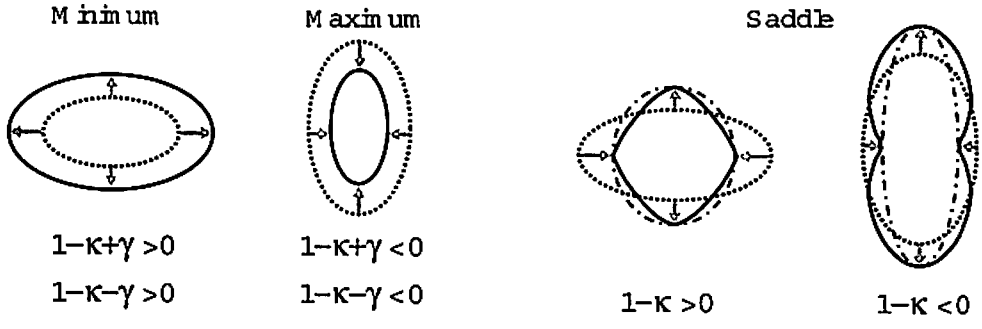


Figure 1: Systematic distortion by an SIS perturber at the center of a top-hat circular source with radius $L \gg 1$ in an external constant shear γ and convergence κ. The dotted and solid closed curves show boundaries of an unperturbed and a perturbed macrolensed image, respectively. The dashed-dotted closed curves denote ellipses with a semi-major axis $a = (L_1 - 1)\xi_1^{-1}$ and a semi-minor axis $b = (L_2 + 1)\xi_2^{-1}$.

Radiation Drag Effects on GRB Internal Shocks

Ryo Takagi[1], Shiho Kobayashi[2,3]

[1] *Department of Physics, Tokyo Institute of Technology, Meguro, Tokyo 152-8551, Japan*
[2] *Center for Gravitational Wave Physics, Pennsylvania State University, University Park, PA 16802*
[3] *Department of Astronomy and Astrophysics, Pennsylvania State University, University Park, PA 16802*

Abstract

We investigate the role of the bulk Compton-scattering process in the internal shock model. We numerically show that the radiation field created by internal shocks does not affect the efficiency of the energy conversion in the shocks even if fireball outflows have highly nonuniform velocity distributions. However, the bulk Compton-scattering produces an additional high energy component especially when variability in the outflows arises because of a modulation of the mass injected into a constant energy flow. We show that an isotropic energy of 10^{50-51} ergs could be radiated in the range of 100MeV-GeV through the scattering process, provided that the shell's Lorentz factor varies between 10 and 10^4.

1 Introduction

Gamma-ray bursts (GRBs) and afterglows are well described by the relativistic fireball model, in which an explosive flow of relativistic matter is released from a compact central engine (e.g. a massive stellar collapse or a compact stellar merger). The kinetic energy of the flow is converted into internal energy by shocks, and it is radiated via synchrotron process. These shocks can be due to collision with the ambient medium (external shocks) or shocks inside the flow itself due to nonuniform velocity (internal shocks). The highly variable temporal structure observed in most of bursts indicates that internal shocks are responsible for the production of GRBs. As internal shocks do not dissipate all the kinetic energy, the remaining energy is dissipated later by external shocks and produces an afterglow.

Since the energy radiated in the afterglow phase is comparable or even smaller than that in the prompt gamma-ray phase (Kumar & Piran 2000; Freedman & Waxman 2001; Lloyd-Ronning & Zhang 2004), GRB outflows should be highly irregular. If we represent the irregular flow by a succession of relativistic shells with random Lorentz factors (Kobayashi, Piran & Sari 1997; Daigne & Mochkovitch 1998; Guetta, Spada & Waxman 2001), the distribution of the Lorentz factors should have a large dispersion to achieve a high conversion efficiency in the internal shocks (Beloborodov 2000; Kobayashi & Sari 2001).

Recently, Lazzati, Ghisellini and Celotti (1999) pointed out that, if the Lorentz factor distribution is very broad, the radiation drag process could affect the conversion efficiency and spectrum of the internal shock emission (see also Gruzinov & Mészáros 2000; Ghisellini 2003). When the Lorentz factors of shells are distributed in a large interval, fast shells would move in the radiation field produced by the previous collisions, and thus Compton-scatter these photons (bulk Compton-scattering). The fast shells could be decelerated before colliding into other shells. This is of significant interest, because high energy γ-rays could be produced as a consequence of the internal shock model. Observations of high energy radiation will provide valuable information about GRB outflows and their central engines. In this Letter, we study the bulk Compton process by using a numerical random shell model. We discuss the implication to the Gamma-Ray Large Area Space Telescope (GLAST).

2 Bulk Compton-Scattering

In the internal shock model, central engines are assumed to produce many relativistic expanding shells with a random distribution of Lorentz factors. A collision of two shells is the elementary process to

[1] E-mail:rtakagi@th.phys.titech.ac.jp

dissipate the kinetic energy of the shells (e.g. Kobayashi et al. 1997). A rapid shell catches up with a slower one and the two merge to form a single one. Electrons are heated by shocks, and the internal energy is then radiated via synchrotron emission.

Consider such a merged shell with a Lorentz factor γ, emitting an internal energy E. When a fast shell with a Lorentz factor $\Gamma \gg \gamma$ collides into the merged shell, the fast shell scatters the photons emitted from the merged shell. In the comoving frame of the merged shell, the internal energy $E' \sim E/\gamma$ is emitted isotropically. Then, the fast shell is moving with the relative Lorentz factor $\Gamma' \sim \Gamma/2\gamma$ into the photon field, scattering a fraction $\sim \min(1,\tau)$ of these photons to energies higher by a factor of Γ'^2 where τ is the optical depth of the fast shell. Using the mass of the fast shell M, we can estimate the energy extracted from the fast shell as

$$Mc^2 d\Gamma \sim -\min(1,\tau)\left(\frac{\Gamma}{2\gamma}\right)^2 dE. \tag{1}$$

The fast shell should have a smaller Lorentz factor Γ_{dec} when it catches up to the merged shell. It is given by

$$\Gamma_{dec} \sim \Gamma\left(1+\frac{\min(1,\tau)\Gamma E}{4\gamma^2 Mc^2}\right)^{-1}. \tag{2}$$

A fraction of the kinetic energy $\sim Mc^2(\Gamma - \Gamma_{dec})$ is radiated away through the scattering process.

3 Numerical Shell Model

We perform Monte Carlo simulations, and discuss how the bulk Compton-scattering affects the evolution of multiple shells. We estimate the conversion efficiency from the kinetic energy of shells to high energy radiation in the bulk Compton-scattering.

We consider a flow consisting of N shells. Each shell is characterized by four variables: a Lorentz factor γ_i, a mass m_i, a width l_i and a position R_i. We assume that the initial Lorentz factor of each shell is distributed uniformly in logarithmic space between $\log\gamma_{min}$ and $\log\gamma_{max}$. The initial masses are assumed to be correlated with the Lorentz factors as $m \propto \gamma^s$. For $s = -1$ and 0, the shells initially have equal energy and equal mass respectively, and for $s = 1$ the shells initially have equal density under an assumption of the equal shell width. We assume a constant value l for the initial widths and the initial separations between the shells. Then, the initial positions of the shells are $R_i = 2(i-1)l$.

The evolution of the shell system in time is basically the same as in Kobayashi et al (1997), but the radiation drag effect is taken into account (see Takagi & Kobayashi 2004) .

For $N = 300$ shells, $\gamma_{min} = 10$, $\Gamma_{max} = 10000$ $l/c = 1$ sec and the initial kinetic energy $E_{kin,iso} = \sum m_i^{(i)} c^2 \gamma_i^{(i)} = 10^{53}$ erg, we have evaluated the conversion efficiencies of internal shocks and the bulk Compton-scattering. The mean efficiencies and their standard deviations for 100 realizations are listed in Table 1. In the third column, "No Scattering" indicates the internal shock efficiencies obtained without the scattering process. We can see that the efficiencies of the internal shocks are not influenced by the radiation drag effect significantly even when the velocity dispersion is large $\gamma_{max}/\gamma_{min} \gg 1$.

Mass Distribution	Internal Shock (No Scattering)	Bulk Compton	Total Efficiency
Equal Energy	10.7±0.4 % (10.9±0.4 %)	1.2±0.3 %	11.9±0.5 %
Equal Mass	24.0±1.4 % (24.0±1.4 %)	$(2 \pm 1) \times 10^{-2}$ %	24.0±1.4 %
Equal Density	14.5±1.4 % (14.5±1.4 %)	$(3 \pm 2) \times 10^{-5}$ %	14.5±1.4 %

Table 1: Efficiency

While the internal shock process is most efficient in the equal mass cases, the bulk Compton-scattering is most efficient in the equal energy cases. Recently Nakar and Piran (2002) studied time scales in GRB temporal profiles. Their results imply that the variability in wind's Lorentz factors arises because of a modulation of the mass injected into a constant energy flow (equal energy case). If this is the case, a

significant amount of energy, corresponding to 1 – 10% of the prompt gamma-ray energy (GRB energy), might be radiated as high energy γ-rays through the bulk Compton-scattering.

A large number of collisions $\sim N$ happen during the evolution of the multiple shells. The first collisions occur between the slowest shells $\sim \gamma_{min}$ and fast shells $\gg \gamma_{min}$ around $R \sim \gamma_{min}^2 l$. In equal energy cases, the Lorentz factors of the merged shells produced by the first collisions are comparable to that of the slowest shells $\sim \gamma_{min}$ (eq. (1) in Kobayashi et al. 1997). This property allows other fast shells to catch up with the merged shells at small radii $\sim \gamma_{min}^2 l$. Since the fast shells still have larger optical depth $\propto R^{-2}$ at the small collision radii, and the relative Lorentz factors are larger, the photons emitted from the first mergers are efficiently scattered into high energies.

In equal density cases, the Lorentz factors of the first mergers are close to $\sim \gamma_{max}$. It is difficult for other shells to catch up to the mergers. Since such collisions happen at large radii and the relative velocities are small, the bulk Compton-scattering is expected to be inefficient. In equal mass cases, the Lorentz factors of the first mergers take intermediate values $\sim (\gamma_{min}\gamma_{max})^{1/2}$. The efficiency of the scattering process is also expected to be intermediate.

We classify shell collisions occurring in the optically thin region into four cases: (I) Collisions happen between two shells, both of which have never experienced collisions. Since we are interested in the radiation drag effect, we count only collisions in the optically thin region. Even if a shell has collided with another shell in the optically thick region, we regard the merger as an unexperienced shell. (II) While the outer slow shell went through collisions at least once, this is the first collision for the inner rapid shell. (III) The outer slow shell has never interact with other shells, and the inner rapid shell has experienced collisions at least once. (IV) The other cases. Assuming the same parameters as in Table 1 and $\gamma_{max} = 10^4$, we have performed numerical simulations for the three mass distributions, and we have analyzed all shell collisions in the optically thin region. We summarize the results for 100 realizations in Table 2. The radiation drag effect is expected to be most significant in type II collisions. Actually, in the equal energy case, for which the bulk Compton-scattering is most efficient, about 50% of collisions are classified into the type II. On the other hand, the fraction of type III collisions is larger than that of the type II in the equal density case. These results are consistent with the above discussion.

Mass Distribution	Type I	Type II	Type III	Type IV
Equal Energy	23.8±1.4 %	50.2±2.8 %	4.0±1.3 %	22.0±1.5 %
Equal Mass	32.1±1.3 %	24.4±2.3 %	13.3±2.1 %	30.2±1.4 %
Equal Density	33.8±1.4 %	16.4±2.2 %	17.9±2.5 %	31.9±1.5 %

Table 2: The basic types of two shell collisions

The spectra of the high energy radiation produced by the bulk Compton-scattering are shown in fig 1 for two example cases. Assuming that all the primary photons produced by shell collisions have the typical GRB frequency of 100 keV, we have integrated up-scattered photons to construct the spectra. Bursts of high energy emission are expected to occur at the same time with the prompt γ-rays (GRBs). The duration should be comparable to that of the associate GRB. If the Lorentz factors of shells are distributed between 10 and 10^4, the typical frequency of the bulk Compton emission is about 100MeV-GeV. We have taken into account the Klein-Nishina effect, which suppressed high energy emission above a few GeV. Since the primary photons are scattered to frequencies higher by a factor of $\sim (\Gamma/\gamma)^2$ where Γ and γ are respectively the Lorentz factors of the scatter and emitter shells, when $\gamma_{max} = 10^3$ is assumed, the typical frequency of the bulk Compton emission is lower, and the emission peaks around 10-100 MeV.

4 Discussion

We have studied the bulk Compton-scattering in the internal shock model by using Monte Carlo simulations. We have shown that the radiation drag does not affect the conversion efficiency in the internal shocks even if fireballs have a very large velocity irregularity. The bulk Compton-scattering is most efficient when an inner engine produces shells with comparable energy but very different Lorentz factors. Such equal energy cases are favored in a recent study on GRB temporal profiles (Nakar & Piran 2002).

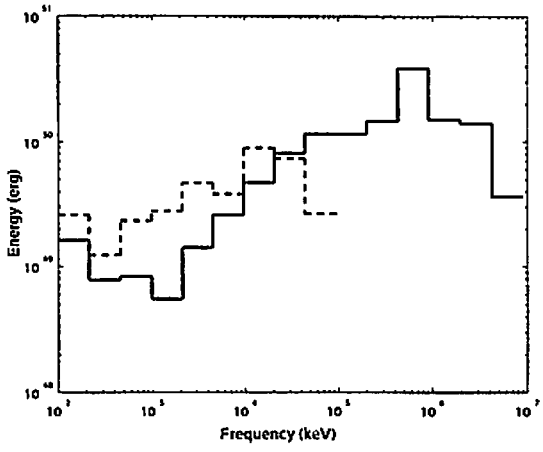


Figure 1: Spectra of bulk Compton emission. $\gamma_{max} = 10^3$ (dashed line) or $\gamma_{max} = 10^4$ (solid line). The other parameters are $E_{kin,iso} = 10^{53}$ ergs, 300 equal energy shells, $\gamma_{min} = 10$ and $l/c = 1$ sec. The cutoff of the solid line around a few GeV is due to the Klein-Nishina effect.

We have obtained about a few % conversion efficiency of the bulk Compton-scattering, provided that the shell's Lorentz factor varies between 10 and 10^4. This implies that $E_{iso} \sim 10^{50-51}$ ergs might be radiated as 100MeV-GeV γ-rays.

The next generation Gamma-Ray Large Area Space Telescope (GLAST), scheduled for launch in 2007, will provide unprecedented sensitivity in the energy range of about 20 MeV to about 300 GeV. GLAST should be able to detect the high energy emission produced by the bulk Compton-scattering if it is associated with GRBs. GLAST observations will provide a variable clue to understand the nature of GRB outflows and the central engines.

References

[1] Beloborodov, A. M. 2000, ApJ, 539, L25

[2] Daigne, F. & Mochkovitch, R. 1998, MNRAS, 296, 275

[3] Freedman, D. L. & Waxman, E. 2001, ApJ, 547, 922

[4] Frontera, F. et al. 2000, ApJS, 127, 59

[5] Ghisellini, G. 2003, "*Gamma Ray Bursts in the Afterglow Era - Third Workshop*" (astro-ph/0301256)

[6] Gruzinov, A. & Mészáros, P. 2000, ApJ, 539, L21

[7] Guetta, D., Spada, M. & Waxman, E. 2001, ApJ, 557, 399

[8] Kobayashi, S., Piran, T. & Sari, R. 1997, ApJ, 490, 92

[9] Kobayashi, S. & Sari, R. 2001, ApJ, 551, 934

[10] Kumar, P. & Piran, T. 2000, ApJ, 535, 152

[11] Lazzati, D., Ghisellini, G. & Celotti, A. 1999, MNRAS, 309, L13

[12] Lloyd-Ronning, N. M. & Zhang, B. 2004, ApJ, 613, L477

[13] Nakar, E. & Piran, T. 2002, ApJ, 572, L139

[14] Takagi, R. & Kobayashi, S. 2004, astro-ph/0412672

Axisymmetric collapse simulations of rotating massive iron cores in full general relativity: Numerical study for prompt black hole formation

Yu-ichirou Sekiguchi[1], Masaru Shibata

[1] *Graduate School of Arts and Sciences, University of Tokyo, Tokyo, 153-8902, Japan*

Abstract

We perform axisymmetric simulations for gravitational collapse of a massive iron core to a black hole in full general relativity. Simulations are performed for a wide variety of initial conditions changing the mass (≈ 2.0-$3.0 M_\odot$), the angular momentum, the rotational velocity profile of the iron core, and the parameters of the equations of state which are chosen so that the maximum mass of the cold spherical polytrope is $\approx 1.6 M_\odot$. Then, the criterion for the prompt black hole formation is clarified in terms of the mass and the angular momentum for several rotational velocity profile of the iron core and equations of state. It is found that (i) with the increase of the thermal energy generated by shocks, the threshold mass for the prompt black hole formation is increased by 20-40%, (ii) the rotational centrifugal force increases the threshold mass by $\lesssim 25\%$, (iii) with the increase of the degree of differential rotation, the threshold mass is also increased, and (iv) the amplification factors shown in the results (i)-(iii) depend sensitively on the equation of state. We also find that the collapse dynamics and the structure of the shock formed at the bounce depend strongly on the stiffness of the adopted equation of state. In particular, as a new feature, a strong bipolar explosion is observed for the collapse of rapidly rotating iron cores with an equation of state which is stiff in subnuclear density and soft in supranuclear density.

1 Parameters

During dynamical evolution, a parametric equation of state is adopted following Müller and his collaborators. In this equation of state, one assumes that the pressure consists of the sum of polytropic and thermal parts as $P = P_{\rm P} + P_{\rm th}$. $P_{\rm P}$ denotes the cold (zero temperature) nuclear equation of state and is given by $P_{\rm P} = K_{\rm P}(\rho)\rho^{\Gamma(\rho)}$ where $K_{\rm P}$ and Γ are functions of ρ. For the density smaller than the nuclear density, $\rho_{\rm nuc}$, we set $\Gamma = \Gamma_1 < 4/3$, and for $\rho \geq \rho_{\rm nuc}$, $\Gamma = \Gamma_2 > 2$. Namely,

$$P_{\rm P} = \begin{cases} K_1 \rho^{\Gamma_1}, & \rho \leq \rho_{\rm nuc}, \\ K_2 \rho^{\Gamma_2}, & \rho \geq \rho_{\rm nuc}, \end{cases} \tag{1}$$

where K_1 and K_2 are constants. Since $P_{\rm P}$ should be continuous at $\rho = \rho_{\rm nuc}$, the relation, $K_2 = K_1 \rho_{\rm nuc}^{\Gamma_1 - \Gamma_2}$, is required. The value of K_1 is fixed to be 5×10^{14} cgs. $P_{\rm th}$ is related to the thermal energy density, $\varepsilon_{\rm th} \equiv \varepsilon - \varepsilon_{\rm P}$, as $P_{\rm th} = (\Gamma_{\rm th} - 1)\rho\varepsilon_{\rm th}$. The parameter sets adopted in this paper are $(\Gamma_1, \Gamma_2, \rho_{14}) = (1.32, 2.25, 2.0)$, $(1.30, 2.50, 2.0)$, $(1.30, 2.22, 1.0)$, and $(1.28, 2.75, 2.0)$ which are referred to as equations of state 'a', 'b', 'c', and 'd', respectively. In this paper, we set $\Gamma_{\rm th} = \Gamma_1$ for simplicity.

The velocity profiles of equilibrium rotating iron cores are given according to a popular relation

$$u^t u_\varphi = \varpi_d^2 (\Omega_a - \Omega), \tag{2}$$

where Ω_a denotes the angular velocity along the rotational axis, and ϖ_d controls the steepness of differential rotation. In this paper, we pick up mainly the rigidly rotating models in which $\varpi_d \to \infty$. For illustration of the effect of differential rotation, we select differentially rotating models with $A \equiv \varpi_d / R_e = 1.0$ and 0.5.

Initial model	$M_{\rm ADM}(M_\odot)$	q	Adopted equations of state			
			a	b	c	d
B0	2.163	0.0	BH	BH	no BH	BH
B1	2.163	0.217	no BH	no BH	no BH	no BH
C0	2.286	0.0	BH	BH	BH	—
C1	2.289	0.221	BH	BH	no BH	—
C15	2.298	0.487	BH	BH	no BH	—
C2	2.310	0.675	BH	no BH	no BH	—
C25	2.321	0.807	no BH	no BH	no BH	—
D15	2.425	0.478	BH	BH	BH	BH
D2	2.438	0.663	BH	BH	no BH	BH
D25	2.449	0.792	BH	BH	no BH	BH
D3	2.459	0.888	BH	no BH	no BH	no BH
D4	2.472	1.006	no BH	no BH	no BH	no BH
D5	2.476	1.045	no BH	no BH	no BH	no BH
E2	2.568	0.652	BH	BH	BH	—
E25	2.580	0.780	BH	BH	no BH	—
E3	2.590	0.873	BH	BH	no BH	—
E4	2.604	0.989	BH	no BH	no BH	—
E5	2.608	1.03	BH	no BH	no BH	—
F3	2.723	0.858	BH	BH	BH	BH
F4	2.738	0.972	BH	BH	no BH	BH
F5	2.742	1.010	BH	BH	no BH	BH
G5	2.879	0.993	BH	BH	BH	—
H5	3.016	0.978	BH	BH	BH	BH

Table 1: Summary of the outcome in the iron core collapse with rigidly rotating initial models. The adopted equations of state are discriminated by a single alphabet: 'a' for $(\Gamma_1, \Gamma_2, \rho_{14}) = (1.32, 2.25, 2.0)$, 'b' for $(1.3, 2.50, 2.0)$, 'c' for $(1.3, 2.22, 1.0)$, and 'd' for $(1.28, 2.75, 2.0)$. "BH" implies that a black hole is formed in a dynamical time scale of the collapse. "no BH" implies that a black hole is not formed promptly. "—" in the last column implies that we did not perform simulations for such models.

model	A	$M_{\rm ADM}/M_\odot$	q	outcome
D20d1b	1.0	2.437	0.647	BH
D22d1b	1.0	2.441	0.698	BH
D23d1b	1.0	2.445	0.746	no BH
D25d1b	1.0	2.450	0.791	no BH
D15d05b	0.5	2.424	0.440	BH
D17d05b	0.5	2.430	0.541	BH
D20d05b	0.5	2.437	0.626	no BH
D25d05b	0.5	2.444	0.702	no BH
H5d1	1.0	3.019	0.978	BH
H5d05	0.5	3.020	0.941	no BH

Table 2: Summary of the final outcome in the iron core collapse with differentially rotating initial models. The adopted equation of state is type 'b' for all the cases; i.e., $(\Gamma_1, \Gamma_2, \rho_{14}) = (1.3, 2.5, 2.0)$.

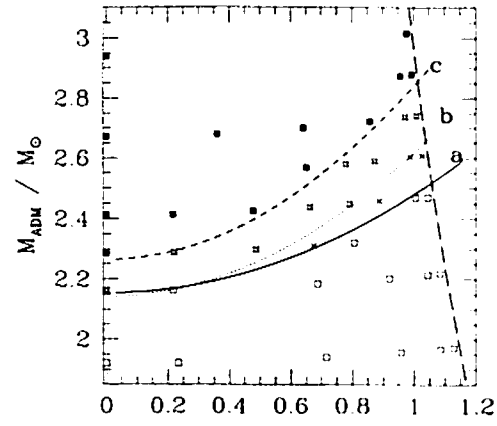


Figure 1: The distribution map of the outcome in the iron core collapse for rigidly rotating initial models. The horizontal and vertical axes denote the spin parameter q and $M_{\rm ADM}$. The filled squares denote the models whose final outcome is a black hole irrespective of the equations of state. The open stars denote the models whose final outcome is a black hole for the equations of state of 'a' and 'b', and a neutron star for the equation of state 'c'. The crosses denote the models whose final outcome is a black hole only for the equations of state 'a'. The open squares indicate no black hole formation irrespective of the equations of state. The solid, dotted, and dashed curves indicate the threshold mass above which a black hole is formed as a result of the collapse for the equations of state 'a', 'b', and 'c', respectively. The long dashed curve denotes the mass-shedding limit for rigidly rotating initial models.

2 Criterion for prompt black hole formation

The dependence of the threshold mass on the these elements can be summarized as follows: (i) The thermal pressure generated by shocks increases the threshold mass by 20–40%. The magnitude of this factor depends on the adopted equation of state: (ii) With the increase of the spin parameter q, the threshold mass increased by $\sim 25q^2$ % for the case that the progenitor is rigidly rotating: (iii) Effect of differential rotation further increases the threshold mass, since the centrifugal force around the central region can be efficiently increased: (iv) The threshold mass depends sensitively on the equations of state since the dynamics of the collapse does. For the smaller value of $|\Gamma_1 - 4/3|$ and for the larger value of $\rho_{\rm nuc}$, prompt black hole formation becomes more liable since the mass of the inner core at the bounce is larger for such equations of state.

About the dynamics of the collapse, we have found the following features: (i) if Γ_1 is close to 4/3, the collapse proceeds in an approximately homologous manner. This implies that the mass of the inner core formed at the bounce is larger for the smaller value of $|\Gamma_1 - 4/3|$, that helps prompt black hole formation (see Fig. 2(a)). Furthermore, the inner core shrinks more significantly resulting in a larger degree of the aspherical deformation and in a significant spin-up. Consequently, the shape of the shock is highly aspherical and the explosion proceeds in a strongly bipolar manner if the progenitor is rapidly rotating as $T_{\rm rot}/W \approx 0.009$ (see Fig. 2(c)): (ii) For $\Gamma_1 \lesssim 1.3$, the collapse does not proceed in the homologous manner. Instead, only the central region rapidly collapses and forms the inner core of a small mass at the bounce (see Fig. 2(b)). As a result, prompt black hole formation is less liable. For the cases of protoneutron star formation, the aspherical deformation of the inner core is not very remarkable since its mass at the bounce is not sufficiently large. The shape of the shock is only sightly aspherical even when the progenitor is rapidly rotating (see Fig. 2(d)).

References

[1] For more details, see paper by authors which is submitted to PRD.

[1] E-mail:sekig@provence.c.u-tokyo.ac.jp

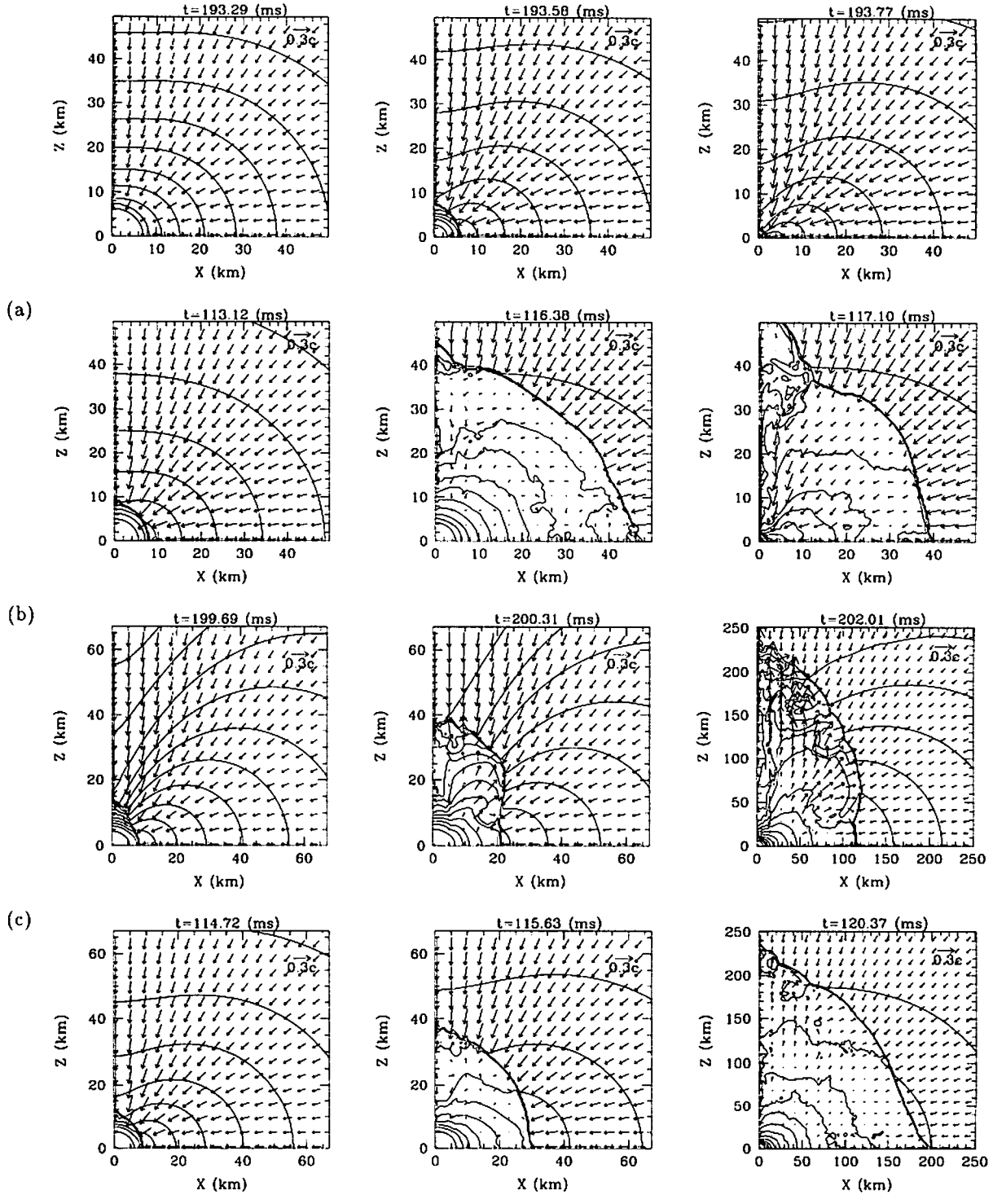


Figure 2: Snapshots of the density contour curves and velocity vectors in the x-z plane for model D2 (a) with the equation of state 'a' and (b) 'b' in which the black hole is formed promptly and for model D5 (c) with the equation of state 'a' and (d) 'b' in which the black hole is not formed promptly.

Functional Determinant of the Laplacian on the Spherical Suspension

Antonino Flachi[1], Misao Sasaki[2]

Yukawa Institute for Theoretical Physics, Kyoto University, Kyoto 606-8502, Japan

Abstract

We study the zeta function associated with the Laplacian on a spherical suspension and obtain formal expressions for $\zeta(0)$ and $\zeta'(0)$. As an application we consider the particular case of a slice of five dimensional de Sitter space, which provides the effective potential of a massless, minimally coupled bulk scalar field in a brane world model where the bulk de Sitter space is bounded by a de Sitter brane.

Physical systems where boundaries or finite size effects are important can be conveniently studied by analyzing suitable functions of the spectrum. A nice account on the use of spectral functions in both mathematics and physics can be found in the recent book by Kirsten [1].

Typically, a positive, second order, elliptic, differential operator $\mathcal{D}$ on a compact manifold is considered and the quantity of physical interest is the functional determinant of $\mathcal{D}$, which can be defined as

$$\ln \det \mathcal{D} = -\zeta'(0) \ , \tag{1}$$

where $\zeta'(0)$ refers to the derivative of the zeta function associated with the spectrum $\{\lambda_i\}$ of the operator $\mathcal{D}$, analytically continued to $s = 0$. The function $\zeta(s)$ is defined as

$$\zeta(s) = \sum_i \lambda_i^{-s} \ . \tag{2}$$

The evaluation of the zeta function is, in most cases, a non-trivial task and the difficulties in evaluating it depend on various features, which boil down to finding the eigenvalues and properly analytically continuing the spectral sum. A direct approach is possible only in few situations, nevertheless, as shown in [2, 3], the explicit knowledge of the eigenvalues is not necessary. For brevity, we refer the reader to the original references, and stress here that although the technique of [2, 3] is very powerful, in some cases it requires some refinements. For instance, when the manifold is a cap of a four sphere, Ref. [4] develops a method which is employed to evaluate the functional determinant, and we have adopted such technique to compute the vacuum energy of a quantum field in the de Sitter brane world model [5].

In this brief note we elaborate slightly more on the subject and apply the method of [4] to the case of a spherical suspension. We obtain a formal result, which is then specified to the case of a sector of five dimensional de Sitter space.

The manifold we consider is described as the $(D+1)$−dimensional space $\mathcal{M} = \Omega \times \mathcal{N}$ with the following line element

$$ds^2 = d\theta^2 + \sin^2\theta ds^2_{\mathcal{N}} \ , \tag{3}$$

where the angular coordinate is restricted to the interval $\Omega \equiv [0, \theta_0]$ and $ds^2_{\mathcal{N}}$ represents the line element of the base manifold $\mathcal{N}$, parametrized by the coordinate X. The eigenvalue equation is

$$-\Delta_{\mathcal{M}} \psi_{n,\mathbf{k}}(\theta, X) = \alpha^2_{n,\mathbf{k}} \psi_{n,\mathbf{k}}(\theta, X) \ , \tag{4}$$

and can be solved by separation of variables

$$\psi_{n,\mathbf{k}}(\theta, X) = \varphi_{n,\mathbf{k}}(\theta) Y_{\mathbf{k}}(X) \ , \tag{5}$$

[1]E-mail:flachi@yukawa.kyoto-u.ac.jp
[2]E-mail:misao@yukawa.kyoto-u.ac.jp

where $Y_{\mathbf{k}}(X)$ are the harmonics on $\mathcal{N}$ with degeneracy $d(\mathbf{k})$ satisfying

$$\Delta_{\mathcal{N}} Y_{\mathbf{k}}(X) = -\lambda_{\mathbf{k}}^2 Y_{\mathbf{k}}(X) \ . \tag{6}$$

We find the eigenmodes to be

$$\psi_{n,\mathbf{k}}(\theta, X) = \sin^q \theta P^{-\mu_{\mathbf{k}}}_{\nu_{n,\mathbf{k}}}(\cos\theta) Y_{\mathbf{k}}(X) \ , \tag{7}$$

where

$$\begin{aligned} q &= (1-D)/2 \\ \mu_{\mathbf{k}} &= \sqrt{q^2 + \lambda_{\mathbf{k}}^2} \ , \\ \nu_{n,\mathbf{k}} &= -\frac{1}{2} \pm i\sqrt{\alpha_{n,\mathbf{k}}^2 - D^2/4} \equiv -\frac{1}{2} \pm i\omega_{n,\mathbf{k}} \ . \end{aligned}$$

We have required the solutions to be regular at $\theta = 0$ and uniquely specified by choosing the generalised Legendre function of Ferrers type, which are analytic in the complex $x(=\cos\theta)$−plane with two cuts lying on the real axis for $x \geq 1$ and $x \leq -1$. For definiteness, we consider Dirichlet boundary conditions:

$$\Phi^d_{\mathbf{k}}(\omega_{n,\mathbf{k}}) \equiv P^{-\mu_{\mathbf{k}}}_{-\frac{1}{2}+i\omega_{n,\mathbf{k}}}(\cos\theta_0) \quad = \quad 0 \ . \tag{8}$$

The previous equation determines the eigenvalues $\alpha_{n,\mathbf{k}}$.

The aim is to compute the zeta-function on $\mathcal{M}$,

$$\zeta_{\mathcal{M}}(s) = \sum_{n,\mathbf{k}} d(\mathbf{k}) \alpha_{n,\mathbf{k}}^{-2s} \tag{9}$$

in terms of the following auxiliary zeta function defined on the manifold $\mathcal{N}$:

$$\zeta_{\mathcal{N}}(s) = \sum_{\mathbf{k}} d(\mathbf{k}) \mu_{\mathbf{k}}^{-2s} \ . \tag{10}$$

The starting point, common to most examples, is a contour integral representation for the zeta function. The residue theorem allows one to write

$$\zeta_{\mathcal{M}}(s) = \frac{1}{2\pi i} \oint_\gamma dz \ (z^2 + a^2)^{-s} \frac{\partial}{\partial z} \sum_{\mathbf{k}} d(\mathbf{k}) \ln \Phi^d_{\mathbf{k}}(z) \ , \tag{11}$$

where the circuit γ in the complex z−plane encloses all the solutions of (8). Here we defined $a^2 = D^2/4$. An appropriate choice of the contour allows us to write the integral (11) as

$$\zeta_{\mathcal{M}}(s) = \frac{\sin \pi s}{\pi} \int_0^\infty dw \ w^{-2s} \frac{\partial}{\partial w} I(w, s) \ , \tag{12}$$

where

$$I(w^2, s) = \sum_{\mathbf{k}} d(\mathbf{k}) \mu_{\mathbf{k}}^{-2s} \ln \Phi^d_{\mathbf{k}}(-i(\mu_{\mathbf{k}}^2 w^2 + a^2)^{1/2}) \ .$$

We have now to perform the analytical continuation to $s = 0$. To see that (12) is convergent for large values of s we use the large $\mu_{\mathbf{k}}$ expansion of $I(w, s)$ [6, 5]:

$$\ln \Phi^d_{\mathbf{k}}(-i(\mu_{\mathbf{k}}^2 w^2 + a^2)^{1/2}) \sim \ln\left(\sqrt{\frac{t}{2\pi\mu_{\mathbf{k}}}} e^{\mu_{\mathbf{k}}\tau} \rho^{\mu_{\mathbf{k}}}\right) + \ln\left(\sum_{n=0}^\infty a_n(w) \mu_{\mathbf{k}}^{-n}\right) \ , \tag{13}$$

$$\rho \equiv \rho(w) \quad = \quad w\sqrt{w + \frac{a^2}{w^2 \mu_{\mathbf{k}}^2}} \ , \qquad t \equiv t(w) = \frac{1}{\sqrt{1 + (\rho/\mu_{\mathbf{k}})^2 \sin^2\theta_0}} \ ,$$

$$\tau \equiv \tau(w) \quad = \quad 1 + \ln\left(\frac{(\rho/\mu_{\mathbf{k}})\sin\theta_0}{\sqrt{1 + (\rho/\mu_{\mathbf{k}})^2 \sin^2\theta_0} + \cos\theta_0}\right) - (\rho/\mu_{\mathbf{k}}) \left[\mathrm{tg}^{-1}(1/(\rho/\mu_{\mathbf{k}})) - \mathrm{tg}^{-1}\left(\frac{\tan\theta_0}{(\rho/\mu_{\mathbf{k}}) t \sin\theta_0}\right)\right] \ .$$

The previous expansion is valid throughout the range of variation of w and the coefficients a_n are bounded functions in the variable w. Thus we obtain

$$I(w^2,s) \sim \sum_{\mathrm{k}} d(\mathrm{k})\mu_{\mathrm{k}}^{-2s}\left(\ln t + \mu_{\mathrm{k}} + \mu_{\mathrm{k}}\ln\rho + \mu_{\mathrm{k}}\tau + \ln(\sum a_n(w)\mu_{\mathrm{k}}^{-n})\right) . \tag{14}$$

Assuming that the spectral sum (10) is convergent for large s, and using the boundedness property of the asymptotic expansion, one easily understands that (12) converges for large values of s. We now need to analytically continue our expression to $s = 0$. To do this we will make use of the following result [4]. Consider a function $f(x)$ which is analytic at $x = \epsilon$, for some small ϵ, and has the following general asymptotic behavior, when $x \to \infty$,

$$f(x) = \sum_{k=1}^{\rho_k<N} \left(f_k + \hat{f}_k \ln x\right) x^{\rho_k} + [f]_{\log}\ln x + [f]_{\mathrm{reg}} + O(x^{-1}) , \qquad \rho_k > 0 , \tag{15}$$

where the subscripts log and reg refer to the solely logarithmic and regular (non-singular) parts of $f(x)$ in the large x limit. Then, there exists the analytic continuation of the integral

$$\int_\epsilon^\infty \frac{dx}{x^s}\frac{d}{dx}f(x) = \frac{[f]_{\log}}{s} + [f]_\epsilon^\infty + O(s) , \tag{16}$$

where $[f]_\epsilon^\infty \equiv [f]_{\mathrm{reg}} - f(\epsilon)$.

We have now to apply the previous machinery to our case. First of all, we note that in the process of analytic continuation the function $I(w^2,s)$ may develop a pole at $s = 0$, thus we define

$$I(w^2,s) = \frac{1}{s}I_p(w^2) + I_f(w^2) + O(s) , \tag{17}$$

the actual calculation will establish what $I_p(w^2)$ and $I_f(w^2)$ are. An application of the previous lemma leads to

$$\zeta_{\mathcal{M}}(s) = \frac{1}{s}[I_p]_{\log} + [I_p]_\epsilon^\infty + [I_f]_{\log} + s\left([I_f]_\epsilon^\infty - \int_0^\infty dw^2 \ln w^2 \frac{\partial}{\partial w^2} I_p(w^2)\right) \tag{18}$$

and the task is thus reduced to calculate the various pieces of the expansion. For brevity, we only sketch their evaluation in the following.

We first consider $I_p(w^2)$. To find the polar term we use the previous expansion for the Legendre functions valid in the whole range of w. By further expanding each term of the expansion (13) in terms of inverse powers of μ_{k} allows one to express the full zeta function in terms of the base zeta function. For example the term proportional to $\ln t$ in (14) will give rise to the following expression:

$$\mathcal{PP}\sum_{\mathrm{k}} d(\mathrm{k})\mu_{\mathrm{k}}^{-2s}\ln t = \mathcal{PP}\frac{1}{2}\sum_{j=1}^{\infty}\left(\frac{a^2\sin^2\theta_0}{1+w^2\sin^2\theta_0}\right)^j \zeta_{\mathcal{N}}(s+j) , \tag{19}$$

where $\mathcal{PP}$ stands for pole part. The Mittag-Leffler expansion for $\zeta_{\mathcal{N}}(s)$,

$$\zeta_{\mathcal{N}}(s) = \frac{1}{\Gamma(s)}\sum_p \frac{C_p}{s - D/2 + p} + f(s) ,$$

where the sum runs over the positive half-integers, the coefficients C_p are the integrated heat-kernel coefficients associated with the Laplacian on the manifold $\mathcal{N}$ and the function $f(s)$ is an entire function, allows us to explicitly extract the pole term:

$$\mathcal{PP}\sum_{\mathrm{k}} d(\mathrm{k})\mu_{\mathrm{k}}^{-2s}\ln t = \frac{1}{2}\sum_{j=1}^{[D/2]}\left(\frac{a^2\sin^2\theta_0}{1+w^2\sin^2\theta_0}\right)^j \frac{C_{D/2-j}}{\Gamma(j)} . \tag{20}$$

By applying the same procedure term by term to the expression (14) we end up with a series whose coefficients depend on the geometry of $\mathcal{N}$. This determines the pole part of $I(w)$ which contribute to both the zeta function and its derivative at zero.

$$I_p(w) = \sum_{l=0}^{\frac{D+1}{2}} \alpha_l(w) C_l \ , \tag{21}$$

where the sum runs over half-integers and the coefficients $\alpha_l(w)$ are determined in the way described above and their evaluation can be implemented in an automatic way by using a symbolic manipulation program, although it becomes quite prohibitive already for $D = 5$. For notational convenience we also define the integrated coefficients

$$\sigma_l = \int_0^\infty dw^2 \ln w^2 \frac{\partial}{\partial w^2} \alpha_l(w) \ . \tag{22}$$

The remaining coefficients, $[I_l]_{\log}$ and $[I_l]_{\rm reg}$, needed for the evaluation of the zeta function can be evaluated using the large$-w$ asymptotic expansion of the Legendre functions [7, 4], whereas the Abel-Plana summation formula can be used to compute $I_l(0)$. Combining all the ingredients, one obtains some formulæ for the zeta function and its derivative:

$$\begin{aligned}
\zeta_{\mathcal{M}}(0) &= -\frac{1}{4}\zeta_{\mathcal{N}}(0) - \frac{1}{2}\zeta_{\mathcal{N}}(-1/2) - \sum_{l=0}^{\frac{D+1}{2}} \alpha_l(0) C_l \\
\zeta'_{\mathcal{M}}(0) &= -\frac{1}{2}\log(2\pi \sin\theta_0)\zeta_{\mathcal{N}}(0) - \sum_{l=0}^{\frac{D+1}{2}} \sigma_l C_l - \mathcal{PF}\int_0^\infty \mathrm{G}(x)\mu_x^{-2s} dx \\
&- \left(i\int_0^\infty \frac{\mathrm{G}(ix) - \mathrm{G}(-ix)}{e^{2\pi x} - 1} dx + \mathrm{CC} \right) - \frac{1}{2}\mathrm{G}(0) \ ,
\end{aligned} \tag{23}$$

where

$$\mathrm{G}(x) = d(x) \ln \left[P^{-\mu_x}_{-\frac{1}{2}+a}(\cos\theta_0) \right] \ ,$$

and $\mathcal{PF}$ means that we have to extract the finite part; the other integral piece is convergent due to the exponential factor. The previous expressions are formal, however explicit results are obtained once the manifold $\mathcal{N}$ is specified. Here, we consider $\mathcal{N} = S^D$ and, for definiteness, we take $D = 4$. In this case the Laplacian $\Delta_{\mathcal{N}}$ is just the Laplacian on a 4$-$sphere and

$$\zeta_{\mathcal{N}}(s) = \frac{1}{3}\zeta_H(s - 3/2, 3, 2) - \frac{1}{12}\zeta_H(s - 1/2, 3, 2) \ .$$

All the coefficients in (23) can be determined and some of algebra leads us to the following result:

$$\zeta_{\mathcal{M}}(0) = \frac{1}{6}\frac{17}{1920} + \frac{5}{128}(-7 + \cos 2\theta_0)\sin^2\theta_0 \ . \tag{24}$$

The derivative is more involved to compute and we find

$$\begin{aligned}
\zeta'_{\mathcal{M}}(0) &= \frac{1}{6}\frac{17}{960}\ln\sin\theta_0 - \frac{1}{64}\zeta'(0,1/2) + \frac{1}{24}\zeta'(-1,1/2) + \frac{1}{24}\zeta'(-2,1/2) - \frac{1}{6}\zeta'(-3,1/2) + \frac{1}{12}\zeta'(-4,1/2) \\
&+ \frac{47}{9216} + \frac{599}{1536}\sin^2\theta_0 + \frac{15}{128}\sin^2\theta_0 \ln\sin^2\theta_0 + \frac{709}{3072}\sin^4\theta_0 - \frac{15}{256}\sin^4\theta_0 \ln\sin^4\theta_0 \\
&- \frac{137}{7200}\frac{d^5\phi}{dx^5}\Big|_{x=0} + \frac{1}{120}\int_0^\infty dx \ln x \frac{d^6\phi}{dx^6} + \int_{2/3}^\infty x^{-6}\phi(x)\, dx - \frac{1}{2}\ln[Z(3/2)] \\
&- i\int_0^\infty dx \frac{(ix + 3/2)^3/3 - (ix + 3/2)/12}{e^{2\pi x} - 1} \ln|Z(ix + 3/2)| - \mathrm{CC} \ ,
\end{aligned} \tag{25}$$

where

$$\phi(x) \equiv \frac{1}{3}\left(x - \frac{1}{3}x^3 \right) \ln Z(1/x) \ , \qquad Z(x) \equiv 2^x \Gamma(1 + x) P^{-x}_{3/2}(\cos\theta_0) \ . \tag{26}$$

The effective potential of a massless, minimally coupled scalar field in five dimensions is then given by $\zeta'_{\mathcal{M}}(0)/2$. A check on the previous result is obtained when θ_0 is small and the ball result has to be recovered, as some calculations, indeed, show.

To conclude, we considered here the functional determinant of the Laplacian on the spherical suspension and specialised the results to the case of a sector of five dimensional de Sitter space bounded by a de Sitter brane, in which case our result provides the effective potential for a massless, minimally coupled scalar field on the above mentioned background spacetime.

Acknowledgments. A.F. is supported by the JSPS under contract No. P04724. M.S. is supported in part by Monbukagakusho Grant-in-Aid for Scientific Research(S) No. 14102004. We have benefited from discussions with A. Knapman, W. Naylor and O. Pujolas.

References

[1] K. Kirsten, "*Spectral Functions in Mathematics and Physics*", Chapman & Hall/Boca Raton, FL, 2001.

[2] M. Bordag, E. Elizalde, B. Geyer, K. Kirsten, Commun. Math. Phys. **179** (1996) 215.

[3] M. Bordag, K. Kirsten, S. Dowker, Commun. Math. Phys. **182** (1996) 371.

[4] A. O. Barvinsky, A. Yu. Kamenshchik and I. P. Karmazin, Annals Phys. **219** (1992) 201.

[5] A. Flachi, A. Knapman, W. Naylor, M. Sasaki, Phys. Rev. **D70** (2004) 124011.

[6] N. R. Khusnutdinov, J. Math. Phys. **44** (2003) 1445.

[7] R. C. Thorne, Phil. Trans. Roy. Soc. London **249** (1957) 597.

Radiated Net Angular Momentum from Numerical Evolution of Black Hole Spacetimes

Ryoji Takahashi[1]

[1] *Center for Computation and Technology, Louisiana State University, 3rd floor Jonston Hall, Baton Rouge, LA 70803, U.S.A*

Abstract

We demonstrate the conservation of net angular momentum in numerical evolutions of single, rotation black hole spactimes. In full 3D numerical evolutions, we show that there is no net angular momentum radiated from axisymmetric data. We also show that net angular momentum radiated in gravitational waves from non-axisymmetric data is consistent with measurements from horizon oscillations. From those results, we may address the question to the current mathematical construction of binary black initial data of an inner stable circular orbit.

1 Introduction

In gravitational wave astronomy, close binary black holes (BBHs) are most promising radiation sources of gravitational wave detectors such as LIGO/GEO/TAMA. Numerical relativity should play an important role for the analysis of sources such as BBHs. For a useful template of such an analysis, we need to evolve for more than one hundred BBH orbits.

The first models of such orbiting BBHs were proposed by Cook and used an effective potential method [1] (it was applied to puncture data in Ref [2]), and they found the sequences of innermost stable circular orbits (ISCO). By assuming a "helical Killing vector" and solving the thin sandwich equations, recent work [3, 4] showed the different from the former ISCO results which is at a further distance. Due to the failure of the combination of the thin-sandwich decomposition with the puncture method [5], the puncture method was solved assuming a helical Killing vector [6, 7]. This calculation showed that the location of the ISCO was similar to the one found using the effective potential method.

Although there are more appealing methods for the construction of quasiequilibruim initial data, our current evolutions of such initial data sets do not show any indication of orbits [10, 11], except indication of timescales of one orbit [9]. Furthermore Ref [11] showed that roughly 20 % or less of total angular momentum is lost in the merger process of the ISCO which is calculated by Cook. To our knowledge, there has never been a systematic study of radiated angular momentum. Here, we present such a study by using single distorted rotating axisymmetic and non-axisymmetric BHs.

2 Formulations

Initial Data: For single rotating, distorted black holes data, we use Bowen-York data [12] such that the conformal flat metric is $\hat{\gamma}_{ij} = \delta_{ij}$, and the conformal extrinsic curvature is defined as

$$\hat{K}_{ij} = \begin{pmatrix} 0 & 0 & 3J\sin^2\theta \\ 0 & 0 & 0 \\ 3J\sin^2\theta & 0 & 0 \end{pmatrix}. \tag{1}$$

For non-axisymmetic data, we extend as

$$\hat{K}_{ij} = m\sin(m\phi)\begin{pmatrix} h_0 & h_1 & 0 \\ h_1 & h_x - h_0 & 0 \\ 0 & 0 & -h_x\sin^2\theta \end{pmatrix}$$

[1] E-mail:ryoji@cct.lsu.edu

$$+\begin{pmatrix} 0 & 0 & \hat{K}_{\eta\phi} \\ 0 & 0 & \hat{K}_{\theta\phi} \\ \hat{K}_{\eta\phi} & \hat{K}_{\theta\phi} & 0 \end{pmatrix}, \tag{2}$$

$$\hat{K}_{\eta\phi} = \sin^2\theta[3J + \cos(m\phi)\frac{1}{\sin^3\theta}\partial_\theta(\sin^4\theta g)], \tag{3}$$

$$\hat{K}_{\theta\phi} = \cos(m\phi)\sin\theta(m^2 v - \sin^2\theta\partial_\eta g), \tag{4}$$

where J is the total angular momentum of spacetimes and m is azimuthal quantum number. When combined with maximal slicing and conformal flatness, the above extrinsic curvatures satisfy the momentum constraints, and only the Hamiltonian constraint needs to be solve numerically. In Ref [13], we describe detailed calculations and parameter studies for those initial data.

Evolutions: As an evolution system, we use the modified version of the Baumgarte-Shapiro-Shibata-Nakamura (BSSN) system that is described in detail in [14]. At the outer boundary we impose a radiative boundary condition [14]. The black holes are handled by introducing a time independent excision boundary according to the "simple excision" method described in [15], with a generalization from cubical to spherical excision regions.

As coordinate conditions we use the dynamic gauge conditions that proved to be successful for single black hole runs with and without excision [15, 8, 14] and for head-on collisions [14]. For the lapse we choose "1+log" slicing without explicit shift dependence, and for the shift we use a particular version of the "Gamma driver" condition:

$$\partial_t\alpha = -2\alpha K\psi^m, \tag{5}$$

$$\partial_t\beta^i = \frac{3}{4}\alpha^p\psi^{-n}B^i, \qquad \partial_t B^i = \partial_t\tilde{\Gamma}^i - \eta B^i, \tag{6}$$

where α is the lapse, β^i is the shift, B^i is its first derivative, K is the trace of the extrinsic curvature, $\tilde{\Gamma}^i$ is the contracted conformal Christoffel symbol of BSSN, and ψ is the time independent conformal factor of Bowen-York data. After some experimentation we settled for our binary runs on $m = 0, 4$ (we use $m = 0$ for all calculations) which helps mimic the singularity avoidance of maximal slicing for puncture runs, and for the shift we set $n = 2$, $p = 1$, and $\eta = 1/M$.

We also use a fixed meshed refinement provided by Carpet [16]. This allows one to have certain fine resolutions around the black holes regions and coarser resolutions for the outside region, i.e. it is possible to evolve the above data sets, and extract gravitational waveforms by fully 3D numerical evolution.

We then analyze the dynamics of the apparent horizons and gauge-invariant waveforms as in the following section.

3 Results and Discussion

The coordinate location of horizon structures are useful for comparisons and for topology measures, but they say nothing about pure geometric measurements from which physical quantities can be derived. As shown first by Smarr [17] for a Kerr BH, the spin parameter a/m uniquely determines the geometric shape of the BH horizon. As discussed in [18, 19], this relation allows one to use the horizon shape as a tool to measure the spin of a black hole in dynamic spacetimes [18, 19, 20]. A reasonable measure of the shape of BHs that are nearly Kerr is the ratio of proper horizon circumferences measured along polar: C_p, and equatorial: C_e, geodesics [19]. The value of $C_r = C_p/C_e$ is unity for a Schwarzschild BH, and less than unity for Kerr BHs, with the precise value depending uniquely on the rotation parameter a/m as discussed below. As shown in [19], a distorted rotating BH should oscillate about its equilibrium Kerr shape. In axisymmetry, the polar circumference is uniquely defined, but in full 3D one has multiple choices. In this study, we compute the ratio C_r along circumferences in the coordinate planes (because of symmetry about the plane of the orbit, the equatorial circumference is uniquely defined).

Fig. 1 shows that three different resolutions of C_r as a function of time. The black hole is oscillating about a Kerr hole with rotation parameter $a/m = 0.7, J = 5($, M_{ADM}=2.66). We see that in order to have equilibrium with a Kerr hole for the later evolution, we need to have a certain resolution. This is important to measure for radiated angular momentum from non-axisymmetric data.

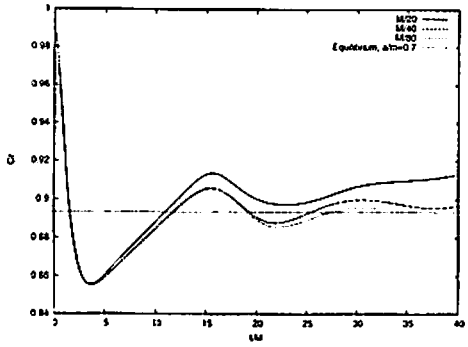


Figure 1: This figure shows C_r for three different resolutions of the inner box: 20, 40, 80 points per M respectively. The line is the offset from sphericity, determined by the fit, showing that the black hole is oscillating about a Kerr hole with rotation parameter $a/m = 0.7$. Note that $M/80$ is terminated by after 300 hours CUP time.

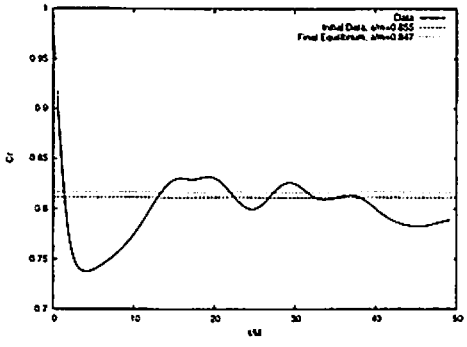


Figure 2: This figure shows C_r for the inner box has 100 points per M. The dashed line is the offset from sphericity for a Kerr hole of initial rotation parameter $a/m = 0.855$. The dotted line shows for the final Kerr hole of final rotation $a/m = 0.847$.

For the measurement of radiated angular momentum, the flux of angular momentum is defined as:

$$\frac{dJ}{dt} = \frac{r^2}{32\pi} \sum_{l=2}^{\infty} \sum_{m=-l}^{l} m\left(\frac{\psi_{lm}^{even}}{dt}\psi_{lm}^{even} + \psi_{lm}^{odd} \int \psi_{lm}^{odd} dt\right), \tag{7}$$

where ψ is the Regge-Wheeler-Zerilli function. The total radiated angular momentum is the integration of Eq. (7) over total evolution time:

$$\Delta J = \int_0^t dt \frac{dJ}{dt}. \tag{8}$$

We evolve non-axisymmetic data from Eq. (2) with $m = 2$. The initial rotation parameter is $a/m = 0.855, J = 20$ ($M_{ADM} = 4.843$). Fig. 2 shows C_r as a function of time. The dashed line shows C_r for the initial data. This means that if there is not radiated angular momentum, C_r should settle down to this equilibrium. The dotted line shows the equilibrium for the final Kerr hole which is determined from our numerical evolution. Due to gravitational radiation, the final equilibrium should be a large value as we see in Fig 2. After $40M$, deformation of 'quasi normal ringing' can be seen by numerical error. Even if we use $M/100$ for the inner box, it seems that even higher resolution is needed. Using the above Eqs. (7,8), we also calculate $\Delta J \sim 0.1\%$. This is consistent with the estimation from the horizon oscillation.

We show that in order to calculate the net angular momentum accurately, we need to have a high resolution near BHs (For all the details calculation with different parameter studies such as different rotation parameters, they will be reported in Ref [21]). Concerning the results in Ref [11], the highest resolution of the calculation was $dx = dy = dz = 0.04$ which is similar to our highest resolution. We believe that these result will be consistent with radiated gravitational waves. Even if BHs starts from the ISCO, they merge quickly with a large amount of radiated angular momentum. This indicates that the current mathematical definition of BHs ISCO may not make any circular orbits, i.e. the true location of the ISCO may be further than what we expect. As investigations of BBHs initial data is continued, it will be interesting to follow the study of Ref [22].

Acknowledgments We would like to thank Frank Herrmann for calculating the final equilibrium of Kerr holes for Fig 2, and Peter Diener, Edward Seidel for many useful discussions. We would like also thank Jason Ventrella for proof-reading the manuscript and correcting typographical errors. We use CACTUS [23], and performed in AEI.

References

[1] G. B. Cook, Phys. Rev. D **50**, 5025 (1994).

[2] T. W. Baumgarte, Phys. Rev. D **62**, 024018 (2000).

[3] E. Gourgoulhon *et al.*, Phys. Rev. D **63**, 064029 (2001).

[4] E. Gourgoulhon, P. Grandclément, and S. Bonazzola, Phys. Rev. D **65**, 044020 (2002).

[5] M. D. Hannam, C. R. Evans, G. B. Cook, and T. W. Baumgarte, Phys. Rev. **D68**, 064003 (2003).

[6] W. Tichy, B. Brügmann, and P. Laguna, Phys. Rev. D **68**, 064008 (2003).

[7] W. Tichy and B. Brügmann, Phys. Rev. D **69**, 024006 (2004).

[8] M. Alcubierre *et al.*, Phys. Rev. D **64**, 061501(R) (2001).

[9] B. Brügmann, W. Tichy, and N. Jansen, Phys. Rev. Lett. **92**, 211101 (2004).

[10] M. Koppitz *et al.*, (2003), in preparation.

[11] M. Alcubierre *et al.*, submitted to Physical Review D (2004).

[12] J. M. Bowen and J. W. York, Jr., Physical Review D **21**, 2047 (1980).

[13] S. Brandt, K. Camarda, E. Seidel, and R. Takahashi, Class. Quantum Grav. **20**, 1 (2003).

[14] M. Alcubierre *et al.*, Phys. Rev. D **67**, 084023 (2003).

[15] M. Alcubierre and B. Brügmann, Phys. Rev. D **63**, 104006 (2001).

[16] E. Schnetter, S. H. Hawley, and I. Hawke, Class. Quantum Grav. **21**, 1465 (2004).

[17] L. L. Smarr, Phys. Rev. D **7**, 289 (1973).

[18] P. Anninos *et al.*, Phys. Rev. Lett. **74**, 630 (1995).

[19] S. R. Brandt and E. Seidel, Phys. Rev. D **52**, 870 (1995).

[20] E. Seidel, Prog. Theor. Phys. Suppl. **136**, 87 (2000).

[21] P. Diener, R. Takahashi, D. Pollney, and E. Seidel, in preparation (unpublished).

[22] B. K. Sergio Dain, Jose Luis Jaramillo, (2004), gr-qc/0412061.

[23] Cactus Computational Toolkit home page: `http://www.cactuscode.org`.

KK gravitons are negative energy dust in brane cosmology

Masato Minamitsuji [1], Misao Sasaki[2], David Langlois [3]

[1] *Department of Earth and Space Science, Graduate School of Science, Osaka University, Toyonaka 560-0043, Japan*

[1,2] *Yukawa Institute for Theoretical Physics, Kyoto University, Kyoto 606-8502, Japan*

[3] *GRECO, Institut d'Astrophysique de Paris, 98bis Boulevard Arago, 75014 Paris, France and APC (Astroparticules et Cosmologie)*

Abstract

We discuss the effect of Kaluza-Klein (KK) modes of bulk metric perturbations on the second Randall-Sundrum (RS II) type brane cosmology, taking the possible back-reaction in the bulk and on the brane into account. KK gravitons may be produced via quantum fluctuations during a de Sitter (dS) inflating phase of our brane universe. The production of even a tiny amount of KK gravitons may eventually give a significant impact on the late-time brane cosmology. As a first step to quantify the effect of KK gravitons on the brane, we calculate the effective energy density and pressure for a single KK mode. We find that a KK mode behaves as cosmic dust with a *negative* energy density on the brane. We note that the bulk energy density of a KK mode is positive definite and there occurs no singular phenomenon in the bulk.

1 Introduction

The idea that our Universe might be a brane embedded in a higher dimensional bulk spacetime has attracted tremendous attention in the last few years. A particularly attractive framework, especially from a gravitational point of view, is the so-called second Randall-Sundrum (RS II) scenario, where our brane-universe is embedded in an Anti-de Sitter (AdS) five-dimensional bulk spacetime [1]. A considerable amount of work has also been devoted to the cosmological extension of the RSII model, in order to describe the cosmological behavior of a brane in this framework (See e.g., [2] for reviews.).

We study the impact of the bulk metric perturbations which are generated in the bulk (or present from the beginning) on the homogeneous evolution of the brane. The bulk metric perturbations are naturally produced via quantum fluctuations during brane inflation [3], and we will concentrate in this work mainly on a de Sitter (dS) brane. From the 4-dimensional point of view, the bulk metric perturbations can be decomposed into a massless zero mode and an infinite number of Kaluza-Klein (KK) modes with effective mass $m > 3H/2$, where H is the expansion rate of the dS brane. The time evolution of the zero mode is similar to the standard four dimensional perturbations although its amplitude, as determined by the vacuum quantum fluctuations depends on the energy scale of the dS brane expansion. In contrast, the squared-amplitude of KK modes on the brane decays as a^{-3} and thus becomes rapidly negligible during brane inflation. However, after brane inflation the background energy density in a radiation-dominated Friedmann-Lemaître-Robertson-Walker (FLRW) era decays as a^{-4}, hence the massive modes of gravitons may affect the late-time cosmological evolution of the brane. Here it should be noted that the concept of KK modes, which assumes the separation of variables with respect to the fifth dimensional coordinate, is only approximately defined in general. It is an important but longstanding problem to quantify the effect of these approximately defined KK modes on the brane evolution.

In order to discuss the cosmological impact of KK gravitons on the brane cosmology, we derive the effective stress-energy of a KK mode on a separable (e.g., a dS brane) background, taking possible backreaction in the bulk and on the brane into account.

[1] E-mail:masato@vega.ess.sci.osaka-u.ac.jp
[2] E-mail:misao@yukawa.kyoto-u.ac.jp
[3] E-mail:langlois@iap.fr

2 The backreaction of a KK mode for a bulk scalar field

Before tackling the backreaction of KK gravitons, we discuss the case of a massless, minimally coupled scalar field, because the behavior of its perturbations is quite similar to the KK gravitons [4]. We consider the five-dimensional Einstein-scalar theory with a positive tension brane. We will assume that the brane tension on the brane is tuned to its RS value so that $\kappa_5^4\sigma^2 = -6\Lambda_5$. We also take a constant bulk potential $V(\phi) = const$ (so that the scalar field is effectively massless). For $V > 0$, one has a de Sitter brane background and for $V = 0$, one has a low energy cosmological brane in general. The results for both cases are almost same. Here we treat the dS brane case explicitly.

The field equation for the bulk scalar field is linear and given by $\Box_5\,\phi = 0$. The solution of the above equation can be seen as a perturbation. This perturbation will induce a bulk energy-momentum tensor, of order $\mathcal{O}(\phi^2)$, which embodies the backreaction of the scalar field on the metric.

The backreaction-corrected gravitational equations in the bulk are given by

$$ {}^{(5)}G_{ab} + \Lambda_5 g_{ab} = -\kappa_5^2 V g_{ab} + \kappa_5^2 \mathcal{T}_{ab} - \sigma q_{ab}\delta(y - y_0) \tag{1} $$

where we have implicitly assumed a coordinate system in which the brane stays at a fixed location $y = y_0$. $\mathcal{T}^a{}_b$ is the backreaction scalar stress energy tensor, *not* including the constant potential V. It is useful to consider the projection of the gravitational equations on the brane[5]. Taking into account the bulk energy-momentum tensor, one finds

$$ {}^{(4)}G^\alpha{}_\beta = -\frac{1}{2}\kappa_5^2 V\delta^\alpha{}_\beta + \frac{1}{6}\kappa_5^4\sigma\tau^\alpha{}_\beta + \kappa_5^2 T^{(b)\alpha}{}_\beta - E^\alpha{}_\beta\,, \tag{2} $$

where

$$ T^{(b)\alpha}{}_\beta = \frac{2}{3}\Big[\phi^{,\alpha}\phi_{,\beta} + \delta^\alpha{}_\beta\Big(\frac{3}{8}\phi_{,y}^2 - \frac{5}{8}q^{\rho\sigma}\phi_{,\rho}\phi_{,\sigma}\Big)\Big]\,, \tag{3} $$

and $E_{\alpha\beta}$ is the projection on the brane of the bulk Weyl tensor and is traceless by construction. If one assumes the brane geometry to be homogeneous and isotropic then the components of $E_{\alpha\beta}$ reduce to $E^t{}_t$ and $E^i{}_j = -(1/3)\delta^i{}_j E^t{}_t$. By using the four-dimensional Bianchi identities, and assuming that the brane matter content is conserved, one is able to express the component $E^t{}_t$ in terms of the values on the brane of the bulk scalar field and its derivatives (See Ref. [4].).

We consider the case of a de Sitter brane. The bulk metric around a de Sitter brane can be expressed as

$$ ds^2 = dy^2 + b^2(y)\gamma_{\mu\nu}dx^\mu dx^\nu\,, \tag{4} $$

where the warp factor $b(y) = H\ell\sinh(y/\ell)$ and $\gamma_{\mu\nu}$ is the 4-dimensional de Sitter metric with the expansion rate H and cosmic scale factor $a(t) = e^{Ht}$. The brane is located at $y = y_0$ such that $\sinh(y_0/\ell) = (1/H\ell)$. The equations is separable and one can solve it by looking for a solution of the separable form. The separation constant m^2 corresponds to the square of the KK mass, as measured by an observer on the brane. Since there is no coupling between the brane and the bulk scalar field, the boundary condition for the scalar field at the brane location is simply $\partial_y\phi = 0$. We focus on a single KK mode, which is spatially homogeneous and sufficiently massive; $m \gg H$. One finds $\varphi(t) = a^{-3/2}\cos(mt)$. If we take a time average over a time scale much longer than the period of oscillation m^{-1}, we can ignore the oscillatory behavior and use $\langle\sin^2(mt)\rangle = \langle\cos^2(mt)\rangle = 1/2$, etc..

One finds the effective energy density and pressure on the brane

$$ \begin{aligned} \kappa_4^2\rho_{(\mathrm{eff})} &= -\Big(\kappa_5^2 T^{(b)t}{}_t - E^t{}_t\Big) = -\frac{1}{2}\kappa_5^2|f_m|^2m^2\frac{1}{a^3}\,, \\ \kappa_4^2 p_{(\mathrm{eff})} &= \frac{1}{3}\Big(\kappa_5^2 T^{(b)i}{}_i - E^i{}_i\Big) = 0\,. \end{aligned} \tag{5} $$

The above results show that the Weyl term $E_{\mu\nu}$ contributes *negatively* to the effective energy density and pressure on the brane for a massive mode. This represents the backreaction effects of the bulk scalar field, which are of order $\mathcal{O}(\phi^2)$.

We note that the bulk energy density of a KK mode on the brane remains positive as

$$ \kappa_5^2\rho_{(\mathrm{bulk})} := -\kappa_5^2 T^t{}_t = \frac{1}{4}\kappa_5^2|f_m|^2m^2\frac{1}{a^3} > 0\,. \tag{6} $$

It shows that there is no singular effect in the bulk in contrast to the peculiar behavior on the brane.

3 The backreaction of a KK mode for the gravitational perturbations

We consider the Einstein theory in the $(d+1)$-dimensional bulk bounded by a brane with positive tension. The brane tension is assumed to be larger than that of the RS value $2(d-1)/(\kappa_{d+1}^2\ell)$ because we mainly consider a dS brane background. The bulk gravitational equations in which the backreaction is taken into account are given by

$$ {}^{(d+1)}G^a{}_b + \Lambda_{d+1}\delta^a{}_b = \kappa_{d+1}^2 T^a{}_b + \bar{t}_{(\mathrm{brane})}{}^a{}_b + \delta t_{(\mathrm{brane})}{}^a{}_b \,, \tag{7} $$

where ${}^{(d+1)}G$ is the true background bulk Einstein tensor including the backreaction effects. And the stress-energy tensor due to the backreaction in the bulk is given by

$$ \kappa_{d+1}^2 T^a{}_b = -\left\langle {}^{(d+1)}\overset{(2)}{G}{}^a{}_b \right\rangle , \tag{8} $$

where ${}^{(d+1)}\overset{(2)}{G}{}^a{}_b$ is the bulk Einstein tensor at quadratic order. The tensor $\bar{t}_{(\mathrm{brane})}{}^a{}_b$ corresponds to the brane energy-momentum tensor in the background configuration defined by the background metric and thus comes from the variation of the brane action. Finally, $\delta t_{(\mathrm{brane})}{}^a{}_b$, which comes from the brane-dependent part denotes the backreaction due to the brane fluctuations. The existence of this term is the most important difference when compared to the case of the scalar field.

For the moment, we concentrate on the effective theory in the bulk. We now identify the background metric as AdS_{d+1} bulk-dS brane spacetime. Then, we consider the linear perturbation theory about it

$$ ds^2 = dy^2 + b^2(y)\left(\gamma_{\mu\nu} + h_{\mu\nu}\right)dx^\mu dx^\nu \,, \quad h^\alpha{}_\alpha = h_\alpha{}^\beta{}_{|\beta} = 0 \,, \tag{9} $$

where $b(y)$ is the warp factor (the same as in the preceding section) and $\gamma_{\mu\nu}$ is the metric of a d-dimensional dS spacetime. Note that we have adopted the so-called RS gauge for the perturbations [1, 6]. The equation of motion for the perturbations in the bulk is separable and one considers solutions of the form $h_{\alpha\beta} = f(y)\varphi_{\alpha\beta}(x^\mu)$. Similarly to the scalar case, the separation constant $m\,(> (d-1)H/2)$ represents the effective mass of a KK graviton mode. Furthermore, for simplicity, we focus on perturbations of the tensor-type with respect to the spatial $(d-1)$-geometry, namely on those with $h^t{}_t = h^t{}_i = h^i{}_t = 0$. Taking the slicing of the de Sitter space with the flat spatial $(d-1)$-geometry, they will have the form, $h^i{}_j = f_m a^{-(d-1)}\cos(mt)Q^i{}_j$, where f_m is the amplitude of the KK mode and $Q^i{}_j$ is the polarization tensor on the flat $(d-1)$-space. The amplitude f_m can be determined, for instance, by the normalization condition if one considers a quantized perturbation theory. Using these results, we can calculate the backreaction energy-momentum in the bulk $T^a{}_b$ explicitly [7].

The projected gravitational equation on the brane reads

$$ {}^{(d)}G^\alpha{}_\beta = -\Lambda_{\mathrm{eff}}\,\delta^\alpha{}_\beta + \kappa_d^2\,\tau^\alpha{}_\beta[h,h] + \kappa_{d+1}^2\,T^{(b)\alpha}{}_\beta - E^\alpha{}_\beta, \tag{10} $$

where Λ_{eff} is the effective cosmological constant on the brane, which is obtained from the bulk cosmological constant and $\bar{t}^a{}_b$.

We now concentrate on the effect of the effective energy-momentum of the bulk gravitons projected on the brane, i.e., the terms $T^{(b)\alpha}{}_\beta$ and $E^\alpha{}_\beta$. For the bulk contribution, we obtain

$$ \begin{aligned} \kappa_d^2\rho_{(\mathrm{eff})} &= -\left(\kappa_{d+1}^2 T^{(b)t}{}_t - E^t{}_t\right) = -\frac{d-2}{8}\,\frac{1}{a^{d-1}}\,m^2|f_m|^2\left\langle Q^{k\ell}Q^*_{k\ell}\right\rangle , \\ \kappa_d^2 p_{(\mathrm{eff})} &= \frac{1}{d-1}\left(\kappa_{d+1}^2 T^{(b)i}{}_i - E^i{}_i\right) = 0 \,. \end{aligned} \tag{11} $$

at late times. Thus, of course including the case of $d = 4$, the effective isotropic pressure vanishes and the effective energy density is negative. This is the same as in the case of the scalar field discussed in the previous section.

We note that the bulk energy density of a KK mode on the brane remains positive

$$ \kappa_{d+1}^2\rho_{(\mathrm{bulk})} := -\kappa_{d+1}^2 T^t{}_t = \frac{1}{8}\,\frac{1}{a^{d-1}}\,m^2|f_m|^2\left\langle Q^{k\ell}Q^*_{k\ell}\right\rangle > 0 \,. \tag{12} $$

It shows again that there is no singular effect in the bulk. The negativity of the effective energy density on the brane originates from the projected Weyl tensor $E_{\mu\nu}$.

We next consider the brane intrinsic contributions. The brane perturbations must be taken into account as well. We take the approach in which we derive the second order boundary action and regard it as the action for an effective matter on the brane. In the thin wall approximation, the second order action on the boundary has been derived in the Appendix of [6]. For an AdS-bulk configuration and with the assumption of Z_2 symmetry about the brane, this reduces to

$$\delta^2 S = \frac{3}{4(d-1)}\sigma \int_{\partial M} d^d x \sqrt{-\tilde{q}}\, h_{\rho\sigma} h^{\rho\sigma} \,. \tag{13}$$

The second order action can be regarded as an action for some effective matter induced on the brane

$$\int_{\partial M} d^d x \sqrt{-\tilde{q}}\, \mathcal{L}_m \,, \quad \mathcal{L}_m := \frac{3}{2(d-1)}\sigma h_{\rho\sigma} h^{\rho\sigma} \,. \tag{14}$$

Its variation with respect to the background metric $\tilde{q}_{\mu\nu}$ yields the induced matter energy-momentum tensor on the brane. Thus we can add this term as a part of the (effective) matter contribution in the effective equation on the brane. However, its contribution to ${}^{(d)}G^{\alpha}{}_{\beta}$ is of order

$$\kappa_{d+1}^4 \sigma \tau^{\alpha}{}_{\beta} \sim \frac{1}{\ell^2}\left(1 + (H\ell)^2\right) h^{\rho\sigma} h_{\rho\sigma} \,. \tag{15}$$

For the case $H\ell \ll 1$ and $H\ell \gg 1$, the right-handed-side of Eq. (15) is of order $\mathcal{O}(\ell^{-2}h^2)$ and $\mathcal{O}(H^2 h^2)$, respectively. Thus as long as we consider sufficiently massive KK modes, with $m \gg \max\{\ell^{-1}, H\}$, the brane perturbations can be safely neglected and only the projected bulk contributions are relevant for the effective theory on the brane.

4 Summary and discussion

We have investigated the effect of a Kaluza-Klein (KK) mode on the brane cosmology, focusing on the second Randall-Sundrum (RSII) type model, i.e., for a Z_2-symmetric brane embedded in the anti-de Sitter bulk.

We have first derived the effective energy-monemtum tensor of a KK mode in the bulk, and investigated the effect of the KK mode on the brane cosmology by projecting the effective energy-monemtum tensor onto the brane. We have found that a massive KK mode behaves as negative energy density dust. Note that the negative energy of a KK mode emerges only from the effective four-dimensional point of view on the brane. The bulk energy density for a KK mode still remains positive and thus there is no singular effect in the bulk.

To quantify this effect in realistic cosmological models, there are some more issues to be resolved. In reality, it is an integral of the KK modes that contributes to cosmology of the brane. Therefore, first we have to know the spectrum of the whole KK modes, then need an appropriate regularization scheme. In connection with this, it may be important to take into account the thickness of a brane.

In more detail, see Ref. [7].

References

[1] L. Randall and R. Sundrum, Phys. Rev. Lett. **83**, 4690 (1999) [arXiv:hep-th/9906064].

[2] R. Maartens, Living Rev. Rel. **7**, 1 (2004) [arXiv:gr-qc/0312059].

[3] D. Langlois, R. Maartens and D. Wands, Phys. Lett. B **489**, 259 (2000) [arXiv:hep-th/0006007].

[4] Y. Himemoto and M. Sasaki, Phys. Rev. D **63**, 044015 (2001) [arXiv:gr-qc/0010035].

[5] T. Shiromizu, K. i. Maeda and M. Sasaki, Phys. Rev. D **62**, 024012 (2000) [arXiv:gr-qc/9910076].

[6] U. Gen and M. Sasaki, Prog. Theor. Phys. **105**, 591 (2001) [arXiv:gr-qc/0011078].

[7] M. Minamitsuji, M. Sasaki and D. Langlois, in preparation.

Comment on Factorizable Metric Ansatz in String Cosmology

Sugumi Kanno[1], Jiro Soda[2]

Theoretical Astrophysics Group, Department of Physics, Kyoto University, Kyoto 606-8502, Japan

Abstract

The validity of a factorizable metric ansatz used in string cosmology is discussed using a toy problem in RSI model.

1 Introduction

Recent intense researches on inflationary models in string theory have stemmed from the success to construct brane inflation with moduli stabilization [1]. However, almost all studies computing potentials for moduli in type IIB string theory suppose a factorizable ansatz for the ten dimensional metric. It should be stressed that, in the presence of the moving branes, no proof for the factorizable ansatz exists even at low energy. If this ansatz is not correct, any conclusion derived using it is not reliable.

In order to examine the validity of this ansatz, as a modest step, we focus on the Randall-Sundrum (RS) I model [2]. Here, we also have a similar problem. The question is the validity of the factorizable ansatz in the context of the brane cosmology. In this paper, we derive the four dimensional low energy effective action on the brane without using this ansatz. Then, we compare the result with the effective action derived using the factorizable ansatz to examine its validity.

2 How to justify the metric ansatz?

We consider an S_1/Z_2 orbifold spacetime with the two branes as the fixed points. In the RSI model, the two flat 3-branes are embedded in the 5-dimensional asymptotically anti-deSitter (AdS) bulk with the curvature radius ℓ with brane tensions given by $\sigma_+ = 6/(\kappa^2\ell)$ and $\sigma_- = -6/(\kappa^2\ell)$. The model is described by the action

$$S = \frac{1}{2\kappa^2}\int d^5x\sqrt{-\mathcal{G}}\left[\mathcal{R}+\frac{12}{\ell^2}\right]+\frac{2}{\kappa^2}\int d^4x\sqrt{-g_+}\mathcal{K}_+ - \frac{2}{\kappa^2}\int d^4x\sqrt{-g_-}\mathcal{K}_- - \frac{6}{\kappa^2\ell}\int d^4x\sqrt{-g_+}+\frac{6}{\kappa^2\ell}\int d^4x\sqrt{-g_-}\,, \tag{1}$$

where κ^2 is the five-dimensional gravitational coupling constant and $\mathcal{R}$ is the curvature scalar. We denoted the induced metric on the positive and negative tension branes by $g^+_{\mu\nu}$ and $g^-_{\mu\nu}$, respectively. In the last line, we have taken into account the Gibbons-Hawking boundary terms instead of introducing delta-function singularities in the curvature. The factor 2 in the Gibbons-Hawking term comes from the Z_2 symmetry of this spacetime. $\mathcal{K}_\pm$ is the trace part of the extrinsic curvature of the boundary near each one of the branes.

One can assume the following factorizable metric

$$ds^2 = a^2(y)g_{\mu\nu}(x)dx^\mu dx^\nu + dy^2\,, \tag{2}$$

and the branes are moving in the above coordinates. Namely, the positive and negative tension branes are respectively placed at $y=\phi_+(x)$, $y=\phi_-(x)$, which are often referred to as the moduli fields. This is another description of the RSI cosmology and often called as moduli approximation. Although two scalar fields are introduced, one of which is the extra degree of freedom. The physical quantity is the

[1] E-mail:sugumi@tap.scphys.kyoto-u.ac.jp
[2] E-mail:jiro@tap.scphys.kyoto-u.ac.jp

difference of these moduli fields which corresponds to the radion in our previous work [3]. This ansatz leads to the action

$$S = \frac{\ell}{2\kappa^2}\int d^4x\sqrt{-g}\left[\left\{a^2(\phi_+) - a^2(\phi_-)\right\}R(g) + \frac{6}{\ell^2}\left\{a^2(\phi_+)(\partial\phi_+)^2 - a^2(\phi_-)(\partial\phi_-)^2\right\}\right] . \tag{3}$$

In this case, we do not have the result to be compared, because the gradient expansion method is not prepared for this parameterization of the model. Our aim is to examine the validity of this ansatz by conforming the gradient expansion method to the factorizable metric ansatz.

3 Revised Gradient Expansion Method

The metric we take in solving the bulk equations of motion is the one in the Gaussian normal coordinate system

$$ds^2 = \gamma_{\mu\nu}(y,x)dx^\mu dx^\nu + dy^2 , \tag{4}$$

where the factorized metric is not assumed.

Now we give the basic equations in the bulk. When solving the bulk equations of motion, it is convenient to define the extrinsic curvature on the y = constant slicing as $K_{\mu\nu} = -\frac{1}{2}\frac{\partial}{\partial y}\gamma_{\mu\nu}$. Decomposing this extrinsic curvature into the traceless part and the trace part $K_{\mu\nu} = \Sigma_{\mu\nu} + \frac{1}{4}g_{\mu\nu}K$, we obtain the basic equations which hold in the bulk;

$$\Sigma^\mu{}_{\nu,y} - K\Sigma^\mu{}_\nu = -\left[R^\mu{}_\nu(\gamma) - \frac{1}{4}\delta^\mu_\nu R(\gamma)\right] , \tag{5}$$

$$\frac{3}{4}K^2 - \Sigma^\alpha{}_\beta\Sigma^\beta{}_\alpha = R(\gamma) + \frac{12}{\ell^2} , \tag{6}$$

$$\nabla_\lambda\Sigma_\mu{}^\lambda - \frac{3}{4}\nabla_\mu K = 0 , \tag{7}$$

where ∇_μ denotes the covariant derivative with respect to the metric $\gamma_{\mu\nu}$ and $R^\mu{}_\nu(\gamma)$ is the corresponding curvature.

The effective action have to be derived by substituting the solution of Eqs. (5)~(7) into the action (1) and integrating out the result over the bulk coordinate y. In reality, it is difficult to perform this general procedure. However, what we need is the low energy effective theory. At low energy, the energy density of the matter, ρ, on a brane is smaller than the brane tension, i.e., $\rho/|\sigma| \ll 1$. In this regime, the 4-dimensional curvature can be neglected compared with the extrinsic curvature. Thus, the Anti-Newtonian or gradient expansion method used in the cosmological context is applicable to our problem.

3.1 Zeroth Order

At zeroth order, we can neglect the curvature term in Eqs. (5)~(7). Moreover, the tension term only induces the isotropic bending of the brane. Thus, an anisotropic term vanishes at this order, $\overset{(0)}{\Sigma}{}^\mu{}_\nu = 0$. As the result, we obtain $\overset{(0)}{K}{}^\mu{}_\nu = \frac{1}{\ell}\delta^\mu_\nu$. Using the definition of the extrinsic curvature, we get the zeroth order metric as

$$ds^2 = dy^2 + a^2(y)g_{\mu\nu}(x)dx^\mu dx^\nu , \quad a(y) = e^{-y/\ell} , \tag{8}$$

where the tensor $g_{\mu\nu}$ is the constant of integration which weakly depends on the brane coordinates x^μ.

3.2 First Order

Our iteration scheme is to write the metric $\gamma_{\mu\nu}$ as a sum of local tensors built out of $g_{\mu\nu}$, with the number of derivatives increasing with the order of iteration, that is, $O((\ell/L)^{2n})$, $n = 0, 1, 2, \cdots$. Here, L represents the characteristic length scale of the 4-dimensional curvature. Hence, we seek the metric as a

perturbative series $\gamma_{\mu\nu}(y,x) = a^2(y)\left[g_{\mu\nu}(x) + f_{\mu\nu}(y,x) + \cdots\right]$. The effective action can be constructed with the knowledge of the leading order metric $f_{\mu\nu}(y,x)$. Other quantities can be also expanded as

$$K = \frac{4}{\ell} + \overset{(1)}{K} + \overset{(2)}{K} + \cdots , \qquad \Sigma^{\mu}{}_{\nu} = 0 + \overset{(1)}{\Sigma}{}^{\mu}{}_{\nu} + \overset{(2)}{\Sigma}{}^{\mu}{}_{\nu} + \cdots . \tag{9}$$

The first order solutions are obtained by taking into account the terms neglected at zeroth order. Substituting the zeroth order metric into $R(\gamma)$, we can write the extrinsics curvature as

$$\overset{(1)}{K} = \frac{\ell}{6a^2}R , \quad \overset{(1)}{\Sigma}{}^{\mu}{}_{\nu} = \frac{\ell}{2a^2}(R^{\mu}{}_{\nu} - \frac{1}{4}\delta^{\mu}_{\nu}R) + \frac{\chi^{\mu}{}_{\nu}(x)}{a^4} , \tag{10}$$

where $R = R(g)$ and $\chi^{\mu}{}_{\nu}$ is the constant of integration which satisfies $\chi^{\mu}{}_{\mu} = 0$, $\chi^{\mu}{}_{\nu|\mu} = 0$. In our previous work [3] [4], we find this term corresponds to the dark radiation at this order. Due to the traceless property, $\chi^{\mu}{}_{\nu}$ is not relevant to the derivation of the effective action.

From Eqs. (10), the correction to the metric $g_{\mu\nu}$ at this order can be obtained as

$$f_{\mu\nu}(y,x^{\mu}) = -\frac{\ell^2}{2a^2}\left(R_{\mu\nu} - \frac{1}{6}h_{\mu\nu}R\right) - \frac{\ell}{2a^4}\chi_{\mu\nu} + C_{\mu\nu}(x) , \tag{11}$$

where $C_{\mu\nu}$ is the constant of integration [5].

4 Effective Action

Now, up to the first order, we have $g_{\mu\nu}(y,x) = a^2(y)\left[g_{\mu\nu}(x) + f_{\mu\nu}(y,x)\right]$. In the following, we will calculate the bulk action, $S_{\rm bulk}$, the actions for each brane, $S_{\pm}$ and the Gibbons-Hawking term, $S_{\rm GH}$, separately. After that, we collect all of them and obtain the 4-dimensional effective action.

In order to calculate the bulk action, we need the determinant of the bulk metric

$$\sqrt{-G} = a^4(y)\sqrt{-g}\sqrt{1 - \frac{\ell}{6a^2}R + C^{\mu}{}_{\mu}} \approx a^4(y)\sqrt{-g}\left(1 - \frac{\ell}{12a^2}R\right)\left(1 + \frac{C^{\mu}{}_{\mu}}{2}\right) , \tag{12}$$

where we neglected the second order quantities. Then the bulk action becomes

$$S_{\rm bulk} = -\frac{4}{\kappa^2\ell}\int d^4x\sqrt{-g}\left[\frac{\ell}{4}\left\{a^4(\phi_+) - a^4(\phi_-)\right\} - \frac{\ell^3}{24}\left\{a^2(\phi_+) - a^2(\phi_-)\right\}R\right]\left[1 + \frac{C^{\mu}{}_{\mu}}{2}\right] , \tag{13}$$

where we have used the the equation $\mathcal{R} = -20/\ell^2$ which holds in the bulk. Notice that the Ricci scalar came from ${\rm tr}f_{\mu\nu}$ in $\sqrt{-G}$.

Next, let us calculate the action for the brane tension. The induced metric on each brane is written by

$$g^{\pm}_{\mu\nu}(\phi_{\pm},x) = a^2 g_{\mu\nu}(x) + a^2 f_{\mu\nu}(\phi_{\pm},x) + \partial_{\mu}\phi_{\pm}\partial_{\nu}\phi_{\pm} . \tag{14}$$

The determinant of the induced metric can be calculated as

$$\sqrt{-g_{\pm}} \approx a^4(\phi_+)\sqrt{-g}\left(1 + \frac{1}{2a^2}(\partial\phi_{\pm})^2 - \frac{\ell}{12a^2}R\right)\left(1 + \frac{C^{\mu}{}_{\mu}}{2}\right) , \tag{15}$$

where $(\partial\phi_{\pm})^2$ means $\partial^{\alpha}\phi_{\pm}\partial_{\alpha}\phi_{\pm}$. Thus, the action for each brane becomes

$$S_{\pm} = \mp\frac{6}{\kappa^2\ell}\int d^4x\sqrt{-g}\left[a^4(\phi_{\pm}) + \frac{a^2(\phi_{\pm})}{2}(\partial\phi_{\pm})^2 - \frac{\ell^2}{12}a^2(\phi_{\pm})\ R\right]\left[1 + \frac{C^{\mu}{}_{\mu}}{2}\right] . \tag{16}$$

Note that the Ricci scalar came from ${\rm tr}f_{\mu\nu}$ in $\sqrt{-g_{\pm}}$.

In order to calculate the Gibbons-Hawking term, we need the extrinsic curvature defined by

$$\mathcal{K}_{\mu\nu} \equiv n_A\left(\frac{\partial^2 x^A}{\partial\xi^{\mu}\partial\xi^{\nu}}\right) + \Gamma^A_{BD}\frac{\partial x^B}{\partial\xi^{\mu}}\frac{\partial x^D}{\partial\xi^{\nu}} , \tag{17}$$

where x^A is the coordinate of the brane, $\xi^\mu = x^\mu$ is the one on the brane and n_A is the normal vector to the brane. Note that $K_{\mu\nu}$ is different from $K_{\mu\nu}$. The tangent basis on the brane are given by $\frac{\partial x^A}{\partial \xi^\mu} = (\delta^\alpha_\mu, \partial_\mu \phi_\pm)$. Thus, the normal vector takes the form $n_A = (-n_y \partial_\alpha \phi_\pm, n_y)$. From the normalization condition $n_A n^A = 1$, we have $n_y = \frac{1}{\sqrt{1+\frac{1}{a^2}(\partial\phi_\pm)^2}}$. Then the trace part of extrinsic curvature on each brane is calculated as

$$K_\pm = g_\pm^{\mu\nu} K^\pm_{\mu\nu} = n_y \left[\frac{4}{\ell} + \frac{1}{a^2}\Box\phi_\pm + \frac{1}{\ell a^2}(\partial\phi_\pm)^2 + \frac{\ell}{6a^2} R \right] . \tag{18}$$

Therefore, the Gibbons-Hawking term is obtained as

$$S_{\rm GH} = \frac{2}{\kappa^2}\int d^4x\sqrt{-g}\left[\frac{4}{\ell}a^4(\phi_+) + \frac{3}{\ell}a^2(\phi_+)(\partial\phi_+)^2 - \frac{\ell}{6}a^2(\phi_+)\, R\right]\left[1 + \frac{C^\mu{}_\mu}{2}\right] + (\phi_+ \to \phi_-) . \tag{19}$$

Note that the Ricci scalar came from $\mathrm{tr} f_{\mu\nu}$ in $\sqrt{-g_\pm}$ and $\mathrm{tr} f_{\mu\nu,y}$ in $K_\pm$.

Substituting the results Eqs. (13), (16) and (19) into the 5-dimensional action Eq. (1), we get the 4-dimensional effective action

$$S = \frac{\ell}{2\kappa^2}\int d^4x\sqrt{-g}\left[\left\{a^2(\phi_+) - a^2(\phi_-)\right\} R + \frac{6}{\ell^2}\left\{a^2(\phi_+)(\partial\phi_+)^2 - a^2(\phi_-)(\partial\phi_-)^2\right\}\right]\left[1 + \frac{C^\mu{}_\mu}{2}\right] . \tag{20}$$

Here, $C^\mu{}_\mu$ is the first order quantity, so we can ignore this term at leading order. We see that this effective action (20) is indistinguishable from Eq. (3) obtained by assuming the factorizable metric. Thus, we have shown that the action obtained from the factorizable ansatz is correct at the leading order.

5 Conclusion

To support the validity of the factorizable metric ansatz used in string cosmology, we investigated a toy problem in RSI model. For this purpose, we have revised the gradient expansion method to conform to the the factorizable metric ansatz. We have solved the 5-dimensional equations of motion and substituted the results into the action. Consequently, we have obtained the 4-dimensional effective action which is equivalent to that obtained by assuming the factorizable metric ansatz. Hence, our calculation supports the factorizable metric ansatz.

In the higher order analysis including Kaluza-Klein corrections, the factorizable metric ansatz cannot be correct anymore [6]. However, in string cosmology, what we want is the leading order action. Then the factorizable metric ansatz becomes useful method when discussing the cosmology without solving the bulk equations of motion at least at the leading order.

References

[1] S. Kachru, R. Kallosh, A. Linde and S. P. Trivedi, Phys. Rev. D **68**, 046005 (2003) [arXiv:hep-th/0301240]; S. Kachru, R. Kallosh, A. Linde, J. Maldacena, L. McAllister and S. P. Trivedi, JCAP **0310**, 013 (2003) [arXiv:hep-th/0308055];

[2] L. Randall and R. Sundrum, Phys. Rev. Lett. **83**, 3370 (1999) [arXiv:hep-ph/9905221];

[3] S. Kanno and J. Soda, Phys. Rev. D **66**, 083506 (2002) [arXiv:hep-th/0207029];

[4] S. Kanno and J. Soda, Phys. Rev. D **66**, 043526 (2002) [arXiv:hep-th/0205188];

[5] S. Kanno and J. Soda, arXiv:hep-th/0410061.

[6] S. Kanno and J. Soda, Phys. Lett. B 588, 203-209 (2004) [arXiv:hep-th/0312106]; S. Kanno and J. Soda, arXiv:hep-th/0407184.

Infrared divergences in the inflationary brane world

Oriol Pujolàs[1]

[2] *Yukawa Institute for Theoretical Physics, Kyoto University, Kyoto 606-8502, Japan*

Abstract

The appearance of infrared divergences in the inflationary Brane World is discussed. We show that a simple extension of the Allen Follaci vacuum does not generate a regular stress tensor -some divergences remain within the bulk. We discuss implications to the 'bulk inflaton' model.

1 introduction

It is well known that, in de Sitter space (dS), the v.e.v. of the stress tensor in the dS invariant vacuum for an effectively massless scalar is infrared divergent [1, 2, 3] (except for the massless minimally coupled case [4]). The usual procedure to tame this global divergence is to replace the dS invariant vacuum by the Allen Follaci (AF) vacuum [5]. The resulting stress tensor breaks dS symmetry but is regular everywhere.

To consider massless limit of scalar field in inflating BW is especially well motivated in the context of 'bulk inflaton' models [6, 7, 8, 9, 10], in which the dynamics of a bulk scalar drives inflation on a quasi-de Sitter brane. In this models, when the lowest lying mode becomes massless then the dS invariant vacuum also generates a globally divergent stress tensor (except for massless minimal coupling). However, the Brane World analog of the AF vacuum does not generate a regular stress tensor -some divergences remain within the bulk. We discuss implications to the 'bulk inflaton' model. This is a report based on [11].

2 Light scalar fields in the VIS model

We consider the $(n+2)$-dimensional Vilenkin-Ipser-Sikivie (VIS) model [12, 13], which corresponds to the limit the RS model [14] with large energy inflating branes. We assume a Z_2-even scalar field with generic bulk mass M, non-minimal coupling ξ, and a brane mass term, of the form $\mu\phi^2$. Since the extrinsic curvature is constant, we can introduce an *effective brane mass* as $\mu_{\rm eff} \equiv \mu + 2(n+1)\xi H$, where $H = 1/r_0$ is the Hubble constant on the brane.

We can introduce the mode decomposition $\phi = \sum\!\!\!\!\!\!\int\ \mathcal{U}_p(r)\,\mathcal{Y}_{p\ell m}(\chi,\Omega)$, where m is a multiple index and r is the Rindler radial coordinate, so one obtains a tower of modes $\mathcal{Y}_{p\ell m}$ in dS with masses $m^2_{\rm KK} = (n/2)^2 + p^2$ in units of H. The mass spectrum consists of a bound state plus a continuum of KK states with $p \geq 0$. The wave function of the bound state is $\mathcal{U}^{bs}(r) = N_d\, r^{-n/2} I_{-ip_d}(Mr)$, with $-ip_d > 0$, and in the limit $Mr_0 \ll 1$ and $\mu_{\rm eff} r_0 \ll 1$, the mass of the bound state is [11]

$$m_d^2 = nH\,\mu_{\rm eff} + \frac{n}{n+2}\,M^2 + \mathcal{O}\left(\mu_{\rm eff}^2, M^4\right), \tag{1}$$

which agrees with [8].

After some computations [11], one finds that the leading behaviour of the Green's function in the massless limit $m_d \to 0$ can be written as [11]

$$G^{(\rm ren)(1)} = \frac{2}{S_{(n+1)}}\,\frac{H^2}{m_d^2}\,\mathcal{U}_0^{bs}(r)\mathcal{U}_0^{bs}(r') + \mathcal{O}(m_d^0)\,, \tag{2}$$

where $\mathcal{U}_0^{bs}(r) = N_0 I_{n/2}(Mr)/r^{n/2}$ is the wave function of the bound state for the exactly massless case.

[1] E-mail:pujolas@yukawa.kyoto-u.ac.jp

In the same limit, the stress tensor is given by [11]

$$\begin{aligned} \langle T_{\mu\nu}\rangle^{bulk} &\simeq \frac{H^2}{S_{(n+1)}m_d^2}\,\mathcal{T}_{\mu\nu}\left[\mathcal{U}_0^{bs}(r)\mathcal{U}_0^{bs}(r')\right] \\ \langle T_{ij}\rangle^{brane} &\simeq \frac{H^2}{S_{(n+1)}m_d^2}\left[(4\xi-1)\mu_{\rm eff}-2H\xi\right]\,(\mathcal{U}_0^{bs}|_{r_0})^2\,\delta(r-r_0)\,h_{ij}\ , \end{aligned} \tag{3}$$

where $\mathcal{T}_{\mu\nu}$ is the differential operator in the point split representation [11] and h_{ij} is the induced metric on the brane. Equation (3) explicitly shows the presence of a global IR divergence in $\langle T_{\mu\nu}\rangle$ for the dS invariant vacuum whenever $M\neq 0$ or $\xi\neq 0$. For $M\neq 0$, $\mathcal{U}_0^{bs}$ is not constant, so the bulk part diverges in the $m_d\to 0$ limit. For $M=0$, the bulk part is finite. However, if $\xi\neq 0$ then the surface term in (3) diverges. Thus, in the limit $m_d=0$ we are forced to consider another state. This is the subject of Section 3.

Close to the massless minimally coupled case and in the absence of any fine tuning, the bound state mass (see (1)) is of the same order as M^2, ξH^2 and $H\mu$. Thus, only in the case when the parameters are 'fine tuned', the stress tensor (3) is large. In the bulk inflato model [6, 7], the smallness of the bound state mass appears naturally if it is due to smallness of all the bulk and brane parameters, ie without fine tuning. Therefore, we will not have to seriously worry about the backreaction in bulk inflaton models [11].

The divergence (2) appears because in the massless limit, the wave function of the homogeneous mode of the bound state in the BD vacuum broadens without bound [4]. It can be removed by considering another vacuum with finite width, which implies breaking dS symmetry [5]. We shall take the an extension of the Allen Follaci vacuum [5] involving only the bound state.

3 Exactly massless bound state

It is convenient to split the Green's function into three parts,

$$G^{(ren)(1)} = G^{(1)}_{KK} + G_{LC} + \widetilde{G}_{AF} \tag{4}$$

where $G^{(1)}_{KK}$ is the contribution from the KK modes involving only the simple poles in the integral representation. In the coincidence limit, it is regular everywhere except on the brane, and depends on the points x and x' through r, r' and $\zeta(x,x')$ (the invariant distance in dS between the projections of points x and x'), so it is dS invariant.

The second term in (4), G_{LC}, contains the contributions that potentially diverge on the light cone and take the form [11]

$$G_{LC}(x,x') = \frac{2}{nS_{(n+1)}}\,\mathcal{U}^{bs}(r)\mathcal{U}^{bs}(r')\,{\rm Re}\left[F(x)+F(x')\right] + \text{regular}, \qquad \text{with} \tag{5}$$

$$F(x) = \log r + \log\sinh\chi + \int_0^{\chi}\frac{d\chi_1}{\cosh^n\chi_1}\int_{-\frac{i\pi}{2}}^{\chi_1} d\chi_2\,\frac{\cosh^n\chi_2}{\sinh^2\chi_2}\ ,$$

where the indicated regular term depends on r and r' only and vanishes for $M=0$. The linear growth in χ is the expected behaviour from the massless bound state. On the other hand, the KK modes contribute the $\log r$ term, which cancels the light cone divergence (the double integral is bounded). The first two terms are simply $\log T$. For even dimension, in terms of the null coordinates U and V, the double integral is $\sim (V/U)^{n/2}\log(V/U)$ for $\chi\to+\infty$. So, even though the Green's function is regular at $V=0$, the stress tensor develops a singularity $\sim 1/V$ or $1/U$ on the light cone in four dimensions (and logarithmic in six dimensions) if $\xi\neq 0$.

The last term in Eq. (4) encodes the choice of vacuum for the $\ell=0$ mode. A simple is the Allen Follaci vacuum [5], which in fact is a two-parameter family of vacua. Its mode function is given by [5]

$$\widetilde{\mathcal{Y}}_{AF}(\chi) = \frac{1}{\sqrt{S_{(n)}}}\left[\frac{1}{2\alpha}+i\beta-i\alpha\int_0^{\chi}\frac{d\chi'}{\cosh^n\chi'}\right] \tag{6}$$

where $\alpha > 0$ and β are the mentioned free (real) parameters. We shall impose that the vacuum is time reversal symmetric. This translates into $\widetilde{\mathcal{Y}}_{AF}(-\chi) = \widetilde{\mathcal{Y}}^*_{AF}(\chi)$, and implies $\beta = 0$. Because of the time dependence, it breaks dS symmetry. For this vacuum, [11]

$$\widetilde{G}_{AF}(x,x') = \frac{\mathcal{U}^{bs}(r)\mathcal{U}^{bs}(r')}{S_{(n)}} \left\{ \frac{1}{2\alpha^2} + 2\alpha^2 \mathrm{Re}\left[F_{AF}(x)F^*_{AF}(x')\right] - \mathrm{Im}\left[F_{AF}(x) + F_{AF}(x')\right] \right\} \qquad (7)$$

with $F_{AF} = \int d\chi \cosh^{-n}\chi$. In order to obtain the analytic continuation of F_{AF} to the Milne region, it is better to write it as an integral over a contour with constant T. It is straightforward to see that $F_{AF}(x) = -T\int^R \frac{dR'}{R'^n}\left(R'^2 - T^2\right)^{\frac{n}{2}-1}$. It is transparent now that F_{AF} behaves like $1/R^{n-1}$ near $R = 0$. It is also clear that it is regular on the light cone and is bounded at infinity. Moreover, it gets an imaginary part in the Milne region for odd dimensions (in the Rindler region it is always real).

Let us comment now on the relation between the AF vacuum and the Garriga Kirsten (GK) vacuum mentioned in the introduction. The latter was introduced in [4] for a massless minimally coupled scalar in dS. Having a 'constant infinite' contribution to the Green's function can only be accepted in the massless minimally coupled case. The reason is that the action has the 'gauge' symmetry $\phi \to \phi +$ constant, so all the observables are constructed from derivatives of the field, and the constant contributions are irrelevant. A more precise way to introduce this vacuum is as the limit $\alpha \to 0$ of the AF vacuum. In this limit the first term in (7) is responsible for the 'infinite constant', while the second (time dependent) term vanishes. We shall note that the last term in (7) is independent of α. It is zero in dS space, because F_{AF} is real in the Rindler region. In the BW context, it picks up an imaginary part in the Milne region for odd dimensions. However, this term is irrelevant for the massless minimally coupled case since factorized terms of the form $f(x) + f(x')$ do not contribute to the stress tensor.

As for the expectation value of the stress tensor, there are three situations corresponding to the presence of $\langle\phi^2\rangle$ terms in $\langle T_{\mu\nu}\rangle$: the massless minimally coupled case, the $M = 0$ case (with $\xi \neq 0$), and the case with $M \neq 0$. In the case $M \neq 0$, $\mathcal{U}^{bs}(r)$ is not constant, and the contribution to the bulk stress tensor from $\widetilde{G}_{AF}$ contains [11]

$$\langle T_{\mu\nu}\rangle^{bulk} \supset \frac{1}{S_{(n)}} \left\{ \frac{1}{4\alpha^2}\, \mathcal{T}_{\mu\nu}\left[\mathcal{U}_{bs}\mathcal{U}'_{bs}\right] + \alpha^2\, \mathcal{T}_{\mu\nu}\left[\mathcal{U}_{bs}\mathcal{U}'_{bs}\mathrm{Re}(F_{AF}F'^*_{AF})\right] \right\} . \qquad (8)$$

The first term is analogous to (3). It diverges globally in the $\alpha \to 0$ limit, which corresponds to the GK state. Hence, this state cannot be taken and one has to content with the AF vacuum with some nonzero α. Hence, the second term is unavoidable. But this is very noticeable since it contains a singularity at $R = 0$ of the form $\sim \alpha^2/R^{2n}$, present even for minimal coupling. It corresponds to a timelike axis in the bulk passing through the center of symmetry, and in particular is dS breaking. The factorized terms in the $\widetilde{G}_{AF}$ also contribute weaker divergences at $R = 0$ of the type $1/R^n$ for $\xi = 0$ and $1/R^{n+1}$ for $\xi \neq 0$ in odd dimensions. Also, in four dimensions, the terms $\mathcal{U}_{bs}\mathcal{U}'_{bs}(F + F')$ from G_{LC} give a $1/U$ divergence on the light cone.

The main point is that in the presence of a bulk mass, $\langle T_{\mu\nu}\rangle$ contains a quite severe bulk singularity even after we get rid of the global IR divergence. There is of course the possibility that a different choice of vacua for the KK modes could cancel it out.

The case $\xi \neq 0$ with $M = 0$ is considered in [11], but one obtains the same conclusion: the dS invariant vacuum is not allowed and the AF vacuum induces a singularity in the bulk. Only for massless minimal coupling a dS invariant state (the Garriga Kirsten vacuum) generates a stress tensor free from IR divergences.

4 Conclusions

Our main results can be summarized as follows. In analogy with what happens in de Sitter (dS) space [5, 4], scalar fields with a massless bound state in the spectrum do not have a well defined dS invariant vacuum, except for the massless minimally coupled case. The Green's function and the v.e.v. of the energy momentum tensor diverge everywhere. A simple alternative from the analogy to dS case is to take the Allen Follaci vacuum for the bound state and not to modify the vacua for the KK modes, precisely

because thay are massive. However, in this vacuum, divergences in the stress tensor are not removed completely: a $\langle T_{\mu\nu} \rangle$ diverges on timelike axis within the bulk (for any coupling other than massless minimal) and on the light cone for nonminimal coupling in four and six dimensions. It remains to be clarified whether it is possible or not to avoid these singularities by choosing a vacuum for the KK modes other than the Bunch Davies.

We have also argued that these divergences do not affect the consistency of the bulk inflaton scenario as long as there is no accidental cancellations between the parameters that determine the bound state mass. This is not expected to happen in a natural model.

This report is based on [11] and summarizes a contributed talk (PRE-35) by the author at JGRG14. We are grateful to Takahiro Tanaka, Jaume Garriga, Misao Sasaki, for useful discussions. The author acknowledges support from JSPS Fellowship number P03193.

References

[1] A. Vilenkin, Nucl. Phys. B **226**, 527 (1983).

[2] A. Vilenkin and L. H. Ford, Phys. Rev. D **26**, 1231 (1982).

[3] A. D. Linde, Phys. Lett. B **116**, 335 (1982).

[4] K. Kirsten and J. Garriga, Phys. Rev. D **48**, 567 (1993) [arXiv:gr-qc/9305013].

[5] B. Allen and A. Folacci, Phys. Rev. D **35**, 3771 (1987); A. Folacci, J. Math. Phys. **32**, 2828 (1991) [Erratum-ibid. **33**, 1932 (1992)].

[6] S. Kobayashi, K. Koyama and J. Soda, Phys. Lett. B **501**, 157 (2001) [arXiv:hep-th/0009160].

[7] Y. Himemoto and M. Sasaki, Phys. Rev. D **63**, 044015 (2001) [arXiv:gr-qc/0010035].

[8] N. Sago, Y. Himemoto and M. Sasaki, Phys. Rev. D **65**, 024014 (2002) [arXiv:gr-qc/0104033].

[9] Y. Himemoto, T. Tanaka and M. Sasaki, Phys. Rev. D **65**, 104020 (2002) [arXiv:gr-qc/0112027].

[10] K. Koyama and K. Takahashi, Phys. Rev. D **67**, 103503 (2003) [arXiv:hep-th/0301165]; *ibid.* D **68**, 103512 (2003) [arXiv:hep-th/0307073].

[11] O. Pujolàs and T. Tanaka, JCAP **0412**, 009 (2004) [gr-qc/0407085].

[12] A. Vilenkin, Phys. Lett. B **133** (1983) 177.

[13] J. Ipser and P. Sikivie, Phys. Rev. D **30**, 712 (1984).

[14] L. Randall and R. Sundrum, Phys. Rev. Lett. **83**, 4690 (1999) [arXiv:hep-th/9906064].

A Possible Origin of Bimodal Distribution of Gamma-Ray Bursts

Kenji Toma[1], Ryo Yamazaki[2], and Takashi Nakamura[1]

[1] *Department of Physics, Kyoto University, Kyoto 606-8502, Japan*
[2] *Department of Earth and Space Science, Osaka University, Toyonaka 560-0043, Japan*

Abstract

We study the distribution of the durations of gamma-ray bursts (GRBs) in the unified model of short and long GRBs recently proposed by Yamazaki, Ioka, and Nakamura. Monte Carlo simulations show clear bimodal distributions, with lognormal-like shapes for both short and long GRBs, in a power-law as well as a Gaussian angular distribution of the subjets. We find that the bimodality comes from the existence of the discrete emission regions (subjets or patchy shells) in the GRB jet.

1 Introduction

The durations of gamma-ray bursts (GRBs) observed by BATSE show a bimodal distribution, which has led to a classification of GRBs into two groups: bursts with T_{90} durations < 2 s are called short GRBs, and those with durations > 2 s are called long GRBs [1, 2]. If T_{90} directly reflects the active time of the progenitor of the GRB, different origins of short and long bursts are implied, such that the former arise from the binary neutron star mergers while the latter arise from the collapse of massive stars.

The short and long bursts roughly consist of 25% and 75%, respectively, of the total BATSE GRB population. We should regard these fractions as comparable, considering possible instrumental effects on the statistics. If these two phenomena arise from essentially different origins, the similar number of events is just by chance. However, some observations have suggested that the short GRBs are similar to the long GRBs [3, 4, 5, 6, 7]. Motivated by these facts, Yamazaki, Ioka, & Nakamura (2004) ([8]; see also these proceedings) proposed a unified model of short and long GRBs, even including X-ray flashes (XRFs) and X-ray-rich GRBs (XRRs), and showed that it is possible to attribute the apparent differences of the light curves and spectra of these four kinds of events to the different viewing angles of the same GRB jet. This is a counter-argument against the current standard scenario of the origins of short and long GRBs. See also [9].

2 Unified Model of Short and Long GRBs

We briefly describe our unified model of short and long GRBs [8]. We assume that the GRB jet is not uniform but made up of multiple subjets, and that each subjet causes a spike in the observed light curve. This is an extreme case of an inhomogeneous jet model [10, 11]. Let us consider a subjet with the opening half-angle $\Delta\theta_{\rm sub}$ moving with Lorentz factor γ, observed from the viewing angle θ_v. Because of relativistic effects, the subjet emission becomes dim and soft when θ_v is larger than $\sim \Delta\theta_{\rm sub} + \gamma^{-1}$ [12]. The *effective* angular size of its emission region is $\pi(\Delta\theta_{\rm sub} - \gamma^{-1})^2$, which is larger than the geometrical size of $\pi\Delta\theta_{\rm sub}^2$. The crucial parameter in our model is the multiplicity (n_s) of the *effective* emission regions along a line of sight. Events with high n_s are long GRBs, while events with $n_s = 1$ are short GRBs.

Specifically, we suppose that 350 subjets are launched from the central engine of the GRB randomly in time and directions, being confined in the whole jet with opening half-angle 0.3 rad. The departure time of each subjet $t_{\rm dep}^{(j)}$ is assumed to be homogeneously random between $t = 0$ and $t = t_{\rm dur}$, where $t_{\rm dur}$ is the active time of the central engine measured in its own frame and is set to $t_{\rm dur} = 20$ s. The emission model for each subjet is the same as the uniform jet model in [13]. For simplicity, all the subjets are

[1] E-mail:toma@tap.scphys.kyoto-u.ac.jp

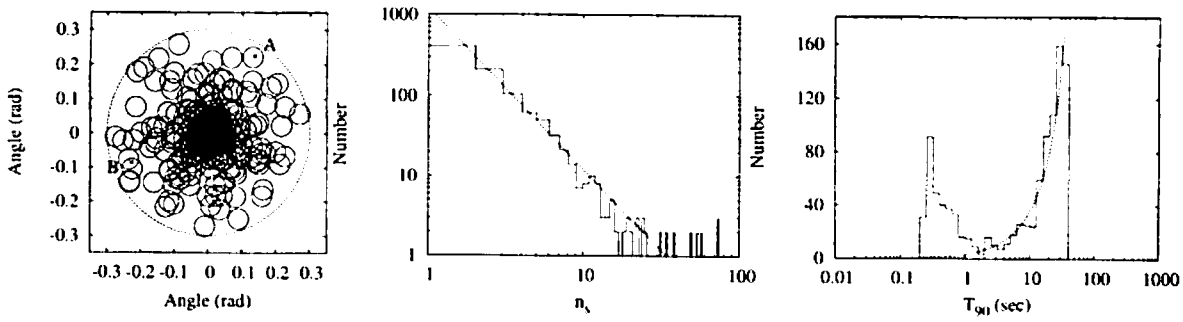


Figure 1: Left: Angular distribution of 350 subjets confined in the whole GRB jet in our simulation. The subjets are spread according to the distribution function of eq.(1). The effective angular size of the subjets are represented by the solid circles, while the whole jet is represented by the dashed circle. The examples of lines of sight A and B are shown in the figure, while C is located at $(-0.04$ rad, 0.04 rad), and D is close to the center of the whole jet. Center: Distribution of multiplicity n_s for the angular distribution of the subjets of the left panel. The dashed line represents the analytical estimate of the n_s^{-2} line (see text). Right: T_{90} duration distribution in the 50–300 keV band of hard events. All sources are located at $z = 1$. The dashed line represents the analytical formula for the long GRBs [9].

assumed to have the same intrinsic properties. We randomly spread the subjets following the angular distribution function

$$\frac{dN}{d\Omega} \equiv n(\vartheta, \varphi) = \begin{cases} n_c, & 0 < \vartheta < \vartheta_c, \\ n_c(\vartheta/\vartheta_c)^{-2}, & \vartheta_c < \vartheta < \vartheta_b, \end{cases} \tag{1}$$

where $\vartheta_b = \Delta\theta_{\rm tot} - \Delta\theta_{\rm sub}$ and $\vartheta_c = 0.02$ rad. Figure 1 (*left*) shows an example of the angular distribution of the effective emission regions of the subjets in our calculation. Most of the subjets are concentrated near the central axis. For our adopted parameters, isolated subjets exist near the edge of the whole jet, and there are some directions in which no subjet is launched.

Figure 2 (*left*) shows examples of the observed light curves in the 50–300 keV band, each of which corresponds to the lines of sight A, B, C, and D in Figure 1 (*left*). If many subjets point in the direction of the line of sight, such as in the cases of C ($n_s = 15$) and D ($n_s = 97$), we see a spiky temporal structure. In the case of B ($n_s = 2$), the event consists of the distinct emission episodes. These are identified as long GRBs. If only one subjet points toward us, like in the case of A ($n_s = 1$), the contributions to the observed light curve from the other subjets are negligible because of relativistic beaming effect, so that the observed gamma-ray fluence and duration are both about a hundredth of the typical values of long GRBs. These are quite similar to the characteristics of short GRBs.

3 Distribution of T_{90} Durations of GRBs

We perform Monte Carlo simulations to show that our unified model can explain the observed bimodal distribution of T_{90} durations of GRBs. We fix the subjets' configuration as in Figure 1 (*left*). We vary only the line of sight of the observer and calculate the T_{90} duration for each observer in the 50–300 keV band. We generate 2000 lines of sight with $0 < \vartheta_{\rm obs} < 0.35$ rad according to the probability distribution of $\sin\vartheta_{\rm obs}\, d\vartheta_{\rm obs}\, d\varphi_{\rm obs}$. We then select only hard events, whose observed hardness ratio is $S(2-30\ {\rm keV})/S(30-400\ {\rm keV}) < 10^{-0.5}$, following the definition of GRBs by the HETE team. The other soft events are classified as XRFs or XRRs, which are observed when all subjets are viewed off-axis.

Figure 1 (*center*) shows the distribution of n_s in our simulation. The multiplicity n_s is roughly proportional to $n(\vartheta_{\rm obs}, \varphi_{\rm obs})$ (eq.(1)). Then the distribution of n_s is given by $P(n_s) \propto \sin(\vartheta_{\rm obs})(d\vartheta_{\rm obs}/dn_s) \sim n_s^{-2}$ (Fig. 1 (*center*), *dashed line*). We first consider the T_{90} distribution in the case in which the redshifts of all the sources are fixed at $z = 1$ for simplicity. The result is shown in Figure 1 (*right*). One can see a bimodal distribution of T_{90} clearly. Which type of burst is observed, long or short, depends on n_s, and

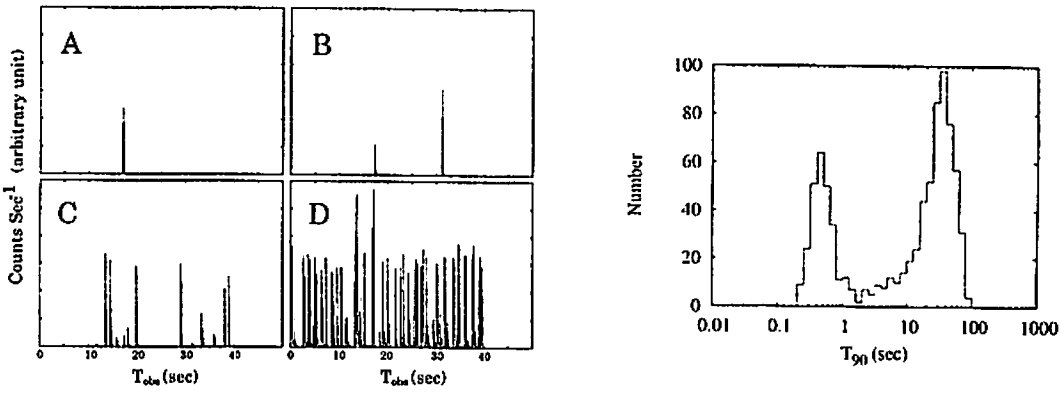


Figure 2: Left: Observed light curves in the 50–300 keV band for the lines of sight shown in Fig. 1 (*left*): A with $n_s = 1$ (*upper left*), B with $n_s = 2$ (*upper right*), C with $n_s = 15$ (*lower left*), and D with $n_s = 97$ (*lower right*). The sources are located at $z = 1$. The T_{90} durations are 0.25 s for A, 14.1 s for B, 25.4 s for C, and 37.8 s for D. Right: Same as Fig. 1 (*right*), but the source redshifts are varied according to the cosmic star formation rate (see text for details).

the distribution of n_s is unimodal. Then why does the distribution of the duration become bimodal? The reason for the scarcity of the events for $1 < T_{90} < 10$ s is as follows. Let us first consider the event with $n_s = 1$. In this case the T_{90} duration does not vary significantly around ~ 0.25 s when $\theta_v < \Delta\theta_{\rm sub}$, which is determined by the angular spreading time of a subjet. As the viewing angle increases, T_{90} increases [12]. When $\theta_v \gtrsim \Delta\theta_{\rm sub} + \gamma^{-1}$, however, the emission becomes soft and dim, so that the event will not be detected as a GRB [13]. The T_{90} takes a maximum value of ~ 0.75 s when $\theta_v \sim \Delta\theta_{\rm sub} + \gamma^{-1}$. We confirm that $n_s = 1$ for almost all $T_{90} < 1$ s events. Next let us consider the $n_s = 2$ case. The example of the light curve for this case is Figure 2 (*left*) B, and the T_{90} is 14.1 s. The T_{90} duration is roughly given by the interval between the arrival times of two pulses. Since the two pulses arrive sometime in the range $0 < T_{\rm obs} < T_{\rm dur}$, where $T_{\rm dur}$ is the active time of the central engine measured in the observer's frame, $T_{\rm dur} = (1+z)t_{\rm dur} = 40$ s, the mean interval is 40/3=13.3 s. This means that the duration of the $n_s = 2$ event is much longer than that for $n_s = 1$. For $n_s \geq 3$, the mean duration is longer than 13.3 s. The typical example is Figure 2 (*left*) C for $n_s = 15$, with $T_{90} = 25.4$ s. This is the reason we have few events for $1 < T_{90} < 10$ s. The maximum value of T_{90} is $\sim T_{\rm dur}$, which can be seen in the example D. For the long bursts, the distribution function of T_{90} durations can be derived from a simple probability argument (see [9] for details), which is represented by the dashed line in Figure 1 (*right*).

The ratio of events of the short GRBs and the long GRBs is about 2 : 5, which can be explained as follows [8]. The event rate of the long GRBs is in proportion to the effective angular size of the central core ${\vartheta_{c,eff}}^2 \sim (0.15\ {\rm rad})^2$, where $n_s \geq 2$. The event rate of the short GRBs is in proportion to $M(\Delta\theta_{\rm sub} + \gamma^{-1})^2$, where M is the number of isolated subjets in the envelope of the core and $M \sim 10$ in our present case. Then the ratio of event rates of the short and long GRBs becomes $M(\Delta\theta_{\rm sub} + \gamma^{-1})^2 : {\vartheta_{c,eff}}^2 \sim 2 : 5$.

In reality, we should take into account the source redshift distribution. We assume that the rate of GRBs is in proportion to the cosmic star formation rate. We adopt the model SF2 in [14], in which we take the standard cosmological parameters of $\Omega_M = 0.3$ and $\Omega_\Lambda = 0.7$. Figure 2 (*right*) shows the result. The distribution is again clearly bimodal, and the shapes of the short and long GRBs look like lognormal distributions. The ratio of the number of short and long GRBs is about 2 : 5 in this case as well. The dispersion of the lognormal-like distribution seems relatively small compared to the observations. This is ascribed to simple modeling in this paper. We fix the jet configuration and use the same intrinsic properties of the subjets. If we vary $t_{\rm dur}$ for each source and $\gamma^{(j)}$ for each subjet randomly, for example, the dispersion of lognormal-like T_{90} duration distribution will increase from the general argument that the dispersion of the lognormal distribution increases with the increase of the number of the associated random variables [15]. In more realistic modeling the observed dispersion will be reproduced.

4 Conclusion

We have investigated the T_{90} duration distribution of GRBs under the unified model of short and long GRBs proposed by [8], and found that the model can reproduce the bimodal distribution observed by BATSE. In our model, the crucial parameter is the multiplicity (n_s) of the subjets in the direction of the observer. The duration of an $n_s = 1$ burst is determined by the angular spreading time of one subjet emission, while that of an $n_s \geq 2$ burst is determined by the time interval between the observed first pulse and the last one. These two different time scales naturally lead to a division of the burst T_{90} durations into the short and long ones. We also performed a similar calculation for a Gaussian distribution, $n(\vartheta, \varphi) = n_c \exp\left[-(\vartheta/\vartheta_c)^2/2\right]$, and found that the T_{90} duration distribution is bimodal in the same way as for the power-law subjet model.

At present we assume that a subjet produces one pulse and all the subjets have the same intrinsic properties. In reality, there are more complicated temporal properties of short and long GRBs; distribution of ON durations of GRBs is bimodal, and according to the analysis of temporal profiles of short GRBs with 2 ms resolution, they also consist of several pulses [5] (see also [9]). We hope that in the near future more sophisticated modeling will reproduce these properties.

It has commonly been said that the observed bimodal distribution of the T_{90} durations of BATSE bursts shows the different origins of short and long GRBs. However, the bimodal distribution is also available as a natural consequence of our unified model of short and long GRBs. The clear prediction of our unified model is that short GRBs are associated with energetic supernovae (SNe), since the association of long duration GRBs with SNe is strongly suggested [16, 17, 18]. Indeed, one of the short GRBs shows possible association with a SN [3].

References

[1] Kouveliotou, C., et al. 1993, ApJ, 554, L163

[2] McBreen, B., Hurley, K. J., Long, R., & Metcalfe, L. 1994, MNRAS, 271, 662

[3] Germany, L. M., et al. 2000, ApJ, 533, 320

[4] Lazzati, D., Ramirez-Ruiz, E., & Ghisellini, G. 2001, A&A, 379, L39

[5] Nakar, E., & Piran, T. 2002, MNRAS, 330, 920

[6] Lamb, D. Q., et al. 2002, in Proc. 3rd Rome Workshop: Gamma-Ray Bursts in the Afterglow Era (astro-ph/0312503)

[7] Ghirlanda, G., Ghisellini, G., & Celotti, A. 2004, A&A, 422, L55

[8] Yamazaki, R., Ioka, K., & Nakamura, T. 2004, ApJ, 607, L103

[9] Toma, K., Yamazaki, R., & Nakamura, T. 2004, ApJ in press (astro-ph/0407012)

[10] Nakamura, T. 2000, ApJ, 534, L159

[11] Kumar, P., & Piran, T. 2000, ApJ, 535, 152

[12] Ioka, K., & Nakamura, T. 2001, ApJ, 554, L163

[13] Yamazaki, R., Ioka, K., & Nakamura, T. 2003, ApJ, 593, 941

[14] Porciani, C., & Madau, P. 2001, ApJ, 548, 522

[15] Ioka, K., & Nakamura, T. 2002, ApJ, 570, L21

[16] Galama, T. J., et al. 1998, Nature, 395, 670

[17] Hjorth, J., et al. 2003, Nature, 423, 847

[18] Stanek, K. Z., et al. 2003, ApJ, 591, L17

Reconstructing the Primordial Spectrum with CMB Temperature and Polarization

Noriyuki Kogo [1], Misao Sasaki [2], Jun'ichi Yokoyama [3]

[1,3] *Department of Earth and Space Science, Graduate School of Science, Osaka University, Toyonaka 560-0043, Japan*

[1,2] *Yukawa Institute for Theoretical Physics, Kyoto University, Kyoto 606-8502, Japan*

Abstract

We develop a new method to reconstruct the power spectrum of primordial curvature perturbations, $P(k)$, by using not only the temperature spectrum but also the polarization spectrum of the cosmic microwave background (CMB). We test this method using some mock $P(k)$ having nontrivial features. As a result, we find that $P(k)$ can be reconstructed within a few percent accuracy under the assumption that there is no observational error in the CMB data. In particular, although the previous method, which used only the temperature fluctuations, suffered from large numerical errors around nodes in a transfer function, these errors are found to disappear almost completely in the new method.

1 Introduction

The cosmic microwave background (CMB) anisotropies contain important pieces of information on physics of the early universe. The recent precise data of the Wilkinson Microwave Anisotropy Probe (WMAP) has shown that our universe is consistent with the so-called concordance model, namely, a spatially flat universe dominated by the dark energy and the dark matter with slow-roll inflation at its early stage which has generated Gaussian, adiabatic, and nearly scale-invariant primordial fluctuations [1]. However, it is reported that the observed CMB angular power spectrum may have some nontrivial features such as lack of power on large scales, running of the spectral index, and oscillatory behaviors of the spectrum on intermediate scales. And then, many possible inflation models which can produce such nontrivial features have been proposed. But, it is also important to understand the implication of these observed possible nontrivial features on the primordial power spectrum of the curvature perturbation, $P(k)$, without a theoretical prejudice. In this respect, there have been several attempts to reconstruct the primordial spectrum using the WMAP data by model-independent methods [2]. In our previous work, we developed a method to reconstruct the primordial spectrum directly from the observed CMB anisotropy, which we call the cosmic inversion method, and applied it to the WMAP first-year data [3]. Compared with other reconstruction methods such as the binning, wavelet band powers, and direct wavelet expansion method, we have shown that our method can reproduce fine features in $P(k)$. In this presentation, we derive an improved inversion formula that takes account of the CMB polarization spectrum, and test our new method for mock $P(k)$.

2 Inversion Method

Here we describe our method of the reconstruction of $P(k)$. We deal only with scalar-type perturbations and assume Gaussian and adiabatic primordial fluctuations.

The angular power spectrum of the CMB anisotropy is expressed as

$$\frac{2\ell+1}{4\pi}C_\ell^{XX} = \frac{1}{2\pi^2}\int_0^\infty \frac{dk}{k}\,\frac{k^3\langle X_\ell^*(\eta_0,k)\bar{X}_\ell(\eta_0,k)\rangle}{2\ell+1}. \tag{1}$$

[1] E-mail:kogo@yukawa.kyoto-u.ac.jp

[2] E-mail:misao@yukawa.kyoto-u.ac.jp

[3] E-mail:yokoyama@vega.ess.sci.osaka-u.ac.jp

where X and $\bar{X}$ are either Θ $(= T)$ or E. $\Theta_\ell(\eta, k)$ and $E_\ell(\eta, k)$ are the multipole moments of the temperature fluctuations and the E-mode polarization which are given by solving the Boltzmann equations. If we adopt the thin last scattering surface (LSS) approximation taking its thickness into account, we obtain the approximated TT and EE angular power spectra in a spatially flat universe,

$$\frac{2\ell+1}{4\pi}C_\ell^{TT,\mathrm{app}} = \frac{2\ell+1}{2\pi^2}\int_0^\infty \frac{dk}{k}\, k^3 P(k)\left[f(k)j_\ell(kd) + g(k)j_\ell'(kd)\right]^2, \tag{2}$$

$$\frac{2\ell+1}{4\pi}C_\ell^{EE,\mathrm{app}} = \frac{2\ell+1}{2\pi^2}\frac{(\ell+2)!}{(\ell-2)!}\int_0^\infty \frac{dk}{k}\, k^3 P(k)\left[h(k)j_\ell(kd)\right]^2, \tag{3}$$

where d is the conformal distance from the present to the LSS, and $f(k)$, $g(k)$, and $h(k)$ are the transfer functions integrated over the thickness of LSS. The primordial power spectrum of the curvature perturbation is defined as $P(k) \equiv \langle|\Phi(0,k)|^2\rangle$, where Φ is the spatial curvature perturbation in the Newton gauge.

Let us briefly review the case of the temperature fluctuations proposed in [3]. The CMB temperature fluctuations can be quantified by the angular correlation function defined as

$$C^{TT}(\theta) \equiv \langle\Theta(\hat{n}_1)\Theta(\hat{n}_2)\rangle = \sum_{\ell=0}^{\infty}\frac{2\ell+1}{4\pi}C_\ell^{TT}P_\ell(\cos\theta), \quad \cos\theta = \hat{n}_1\cdot\hat{n}_2. \tag{4}$$

Here we introduce a new variable r instead of θ defined as $r = 2d\sin(\theta/2)$ which is the conformal distance between two points on the LSS, and focus only on small scales, $r \ll d$. Because a geometrical effect is only the variation of d on small scales, we can deal with a spatially nonflat universe. Substituting Eq. (2) into Eq. (4) and applying the Fourier sine formula, we obtain a first-order differential equation for $P(k)$,

$$-k^2 f^2(k)P'(k) + \left[-2k^2 f(k)f'(k) + kg^2(k)\right]P(k) = 4\pi\int_0^\infty dr\,\frac{1}{r}\frac{\partial}{\partial r}\{r^3 C^{TT,\mathrm{app}}(r)\}\sin kr \equiv S^{TT}(k). \tag{5}$$

This is the basic equation for the inversion of the TT angular power spectrum to $P(k)$. Since $f(k)$ is an oscillatory function, the boundary conditions are given at zero points of $f(k)$, say $k = k_s$, as

$$P(k_s) = \frac{S^{TT}(k_s)}{k_s\, g^2(k_s)} \quad \text{for} \quad f(k_s) = 0, \tag{6}$$

assuming that $P'(k)$ is finite at $k = k_s$. But, the points of $f(k) = 0$ are the singularities which cause numerical errors around them.

Now we consider the case of the polarization. Like Eq. (4), we introduce the following quantity:

$$\tilde{C}^{EE}(\theta) \equiv \sum_{\ell=0}^{\infty}\frac{2\ell+1}{4\pi}\frac{(\ell-2)!}{(\ell+2)!}C_\ell^{EE}P_\ell(\cos\theta). \tag{7}$$

Note that this is not the conventional angular correlation function but just quantity that are convenient for inversion. Substituting Eq. (3) into Eq. (7) and applying the Fourier sine formula, we obtain the algebraic equation for $P(k)$,

$$kh^2(k)P(k) = 4\pi\int_0^\infty dr\, r\tilde{C}^{EE,\mathrm{app}}(r)\sin kr \equiv S^{EE}(k). \tag{8}$$

In this case, we can find $P(k)$ at the values of k where $h(k) \neq 0$ without solving a differential equation. The equations (8) is the basic inversion formulas for the EE angular power spectrum. However, the points of $h(k) = 0$ are the singularities which cause large numerical errors around them as well.

To avoid these numerical difficulties, we combine the TT formula (8) and the EE formula (5) as

$$-k^2 f^2(k)P'(k) + \left[-2k^2 f(k)f'(k) + kg^2(k) + \alpha kh^2(k)\right]P(k) = S^{TT}(k) + \alpha S^{EE}(k), \tag{9}$$

with the boundary conditions as

$$P(k_s) = \frac{S^{TT}(k_s) + \alpha S^{EE}(k_s)}{k_s\left[g^2(k_s) + \alpha h^2(k_s)\right]} \quad \text{for} \quad f(k_s) = 0, \tag{10}$$

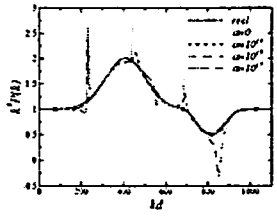


Figure 1: Dependence of the reconstructed $P(k)$ on the parameter α for $P(k)$ with a peak and a dip. The cosmological parameters are assumed to be known. The result of reconstruction is shown for $\alpha = 0$, 10^{13}, 10^{15}, and 10^{17}. The singularities $f(k) = 0$ and $h(k) = 0$ are denoted by squares and triangles, respectively.

assuming that $P'(k)$ is finite at $k = k_s$. Here, α is a free parameter which controls the contribution of EE. Since the zero points of $f(k)$ and $h(k)$ are different from each other, the solution of Eq. (9) becomes numerically stable even around the singularities if we take an appropriate value of α so that the contribution of EE is comparable to that of TT.

Since relative errors between the approximated spectrum $C_\ell^{XX,\mathrm{app}}$ and the exact one $C_\ell^{XX,\mathrm{ex}}$ ($X = T$ or E) are as large as about $20-30\%$, it is necessary to correct the errors. For this purpose, we first define the ratio, $b_\ell^{XX} \equiv C_\ell^{XX,\mathrm{ex}}/C_\ell^{XX,\mathrm{app}}$, which is found to be almost independent of $P(k)$ for EE as well as TT. We use this property of b_ℓ^{XX} to perform an iteration as previously done in the TT case [3]. First we calculate $b_\ell^{XX,(0)} = C_\ell^{XX,\mathrm{ex}(0)}/C_\ell^{XX,\mathrm{app}(0)}$, for a fiducial primordial spectrum $P^{(0)}(k)$ such as a scale-invariant one. Since $C_\ell^{XX,\mathrm{obs}}/b_\ell^{XX,(0)}$ gives a better guess to $C_\ell^{XX,\mathrm{app}}$, we use it when solving Eq. (9). Let us denote the reconstructed primordial spectrum from $C_\ell^{XX,\mathrm{obs}}/b_\ell^{XX,(0)}$ by $P^{(1)}(k)$. Repeating this procedure, we can find $P(k)$ with much better accuracy. The n-th iteration is summarized as

$$\cdots \Rightarrow P^{(n-1)}(k) \rightarrow b_\ell^{XX,(n-1)} = \frac{C_\ell^{XX,\mathrm{ex}(n-1)}}{C_\ell^{XX,\mathrm{app}(n-1)}} \rightarrow \frac{C_\ell^{XX,\mathrm{obs}}}{b_\ell^{XX,(n-1)}} \Rightarrow P^{(n)}(k) \rightarrow \cdots. \tag{11}$$

3 Numerical Tests

To test our new inversion method including the CMB polarization, we perform the reconstruction of $P(k)$ from C_ℓ^{XX} for given $P(k)$. As a first step, we assume that the CMB data contain no observational error. We assume that the cosmological parameters are $h = 0.70$, $\Omega_b = 0.050$, $\Omega_\Lambda = 0.70$, $\Omega_{\mathrm{total}} = 1$, and $\tau = 0.20$ and $P(k)$ has a peak and a dip. We calculate the CMB power spectra based on CMBFAST [4].

First we examine the dependence of the reconstructed $P(k)$ on the parameter α which controls the contribution of EE, assuming that the cosmological parameters are known and performing no iteratation. As shown in Fig. 1, we find that $P(k)$ is reconstructed well even near the singularities for $\alpha = 10^{15}$, while spurious sharp features appear near the TT singularities for $\alpha = 0$ and those appear near the EE singularities for $\alpha = 10^{17}$. This behavior is reasonable because the contribution of EE is found to be of the same order of TT for $\alpha \sim 10^{14-15}$. Then we perform the iteration for $\alpha = 10^{15}$ and the results are shown in Fig. 2. We see that the iteration converges within a few times and the relative errors are reduced to about a few percent level.

We also examine how the shape of reconstructed $P(k)$ changes if we adopt the values of the cosmological parameters different from the assumed values. Figure 3 shows how the reconstructed $P(k)$ changes depending on α for a correct and an incorrect values of the cosmological parameters. We can see that for a correct value, $P(k)$ is reconstructed rather well for both $\alpha 10^{13}$ and 10^{15} On the other hand, for an incorrect value, we obtain a deformed shape of the reconstructed $P(k)$ and the location of the deformation depends on the value of α. Thus we may obtain constraints on the cosmological parameters by minimizing the α-dependence of the reconstructed $P(k)$. An intriguing point is that no assumption on the shape of $P(k)$ is necessary to derive the constraints.

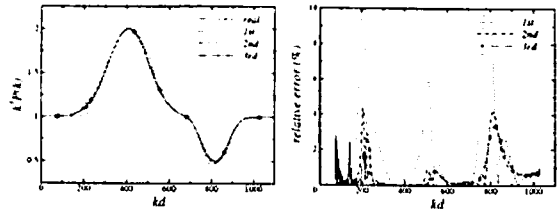


Figure 2: Reconstructed spectrum for $P(k)$ with a peak and a dip. The left panel shows the results after each round of iteration, and the right panel shows their relative errors, $|P^{(n)}(k) - P^{\rm real}(k)|/P^{\rm real}(k)$.

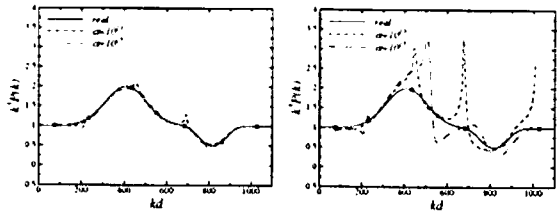


Figure 3: Dependence of the reconstructed $P(k)$ on the parameter α in the cases of $h = 0.70$ which is a correct value (left panel) and $h = 0.75$ which is an incorrect value (right panel).

4 Conclusion

We have developed a numerically stable method to reconstruct $P(k)$ by combining the CMB temperature (TT) and polarization (EE) spectra, in the form TT + αEE, where α is a constant free parameter. As a result of numerical tests, we have confirmed that the relative errors of the reconstructed $P(k)$ are reduced to a few percent level after a few steps of iteration if no observational error is assumed. And also, we have suggested that the cosmological parameters may be constrained under the condition that the reconstructed $P(k)$ has the least α-dependence. As a next step, we should discuss the effects of observational errors, constraints on the cosmological parameters, and extensions to tensor modes which are probed by the B-mode polarization.

References

[1] C. L. Bennett *et al.*, Astrophys. J. Suppl. **148**, 1 (2003); E. Komatsu *et al.*, Astrophys. J. Suppl. **148**, 119 (2003); D. N. Spergel *et al.*, Astrophys. J. Suppl. **148**, 175 (2003); H. Peiris *et al.*, Astrophys. J. Suppl. **148**, 213 (2003)

[2] P. Mukherjee and Y. Wang, Astrophys. J. **598**, 779 (2003); Astrophys. J. **599**, 1 (2003); S. L. Bridle, A. M. Lewis, J. Weller, and G. Efstathiou, Mon. Not. Roy. Astron. Soc. **342**, L72 (2003); S. Hannestad, JCAP **0404**, 002 (2004); A. Shafieloo and T. Souradeep, Phys. Rev. D **70**, 043523 (2004); D. Tocchini-Valentini, M. Douspis, and J. Silk, astro-ph/0402583

[3] M. Matsumiya, M. Sasaki, and J. Yokoyama, Phys. Rev. D **65**, 083007 (2002); JCAP **0302**, 003 (2003); N. Kogo, M. Matsumiya, M. Sasaki, and J. Yokoyama, Astrophys. J. **607**, 32 (2004)

[4] http://www.cmbfast.org/

A Unified Model of Short and Long Gamma-Ray Bursts, X-Ray Rich Gamma-Ray Bursts, and X-Ray Flashes

Ryo Yamazaki[1], Kunihito Ioka[2], Takashi Nakamura[3], Kenji Toma[4]

[1] *Department of Earth and Space Science, Graduate School of Science, Osaka University, Toyonaka, Osaka 560-0043, Japan*

[2] *Physics Department and Center for Gravitational Wave Physics, 104 Davey Laboratory, Pennsylvania State University, University Park, PA 16802, USA*

[3,4] *Theoretical Astrophysics Group, Department of Physics, Kyoto University, Kyoto 606-8502, Japan*

Abstract

We propose a possible unified model of short and long gamma-ray bursts (GRBs), X-ray rich GRBs, and X-ray flashes. The jet of a GRB is assumed to consist of multiple sub-jets or sub-shells (i.e., an inhomogeneous jet model). The multiplicity of the sub-jets along a line of sight n_s is an important parameter. If n_s is large ($\gg 1$) the event looks like a long GRB, while if $n_s = 1$, the event looks like a short GRB. Finally, when $n_s = 0$, the event looks like an X-ray flash or an X-ray rich GRB.

1 Introduction

While the association with the supernova is almost established or strongly suggested for the long gamma-ray bursts (GRBs) [1, 2], the origins of short GRBs and X-ray flashes (XRFs) remain unclear. The observed event rate of short GRBs is about a third of the long GRBs while the observed event rate of XRFs is also about a third. Although there may be a possible bias effect to these statistics, these numbers are, in an astrophysical sense, the same or comparable. If these phenomena arise from essentially different origins, the similar number of events is just by chance. On the other hand, if they are related, the similar number of events is natural and the ratio of the event rate tells us something about the geometry of the central engine. We propose a unified model in which the central engine of short GRBs, long GRBs and XRFs is the same and the apparent differences come essentially from different viewing angles. For details, see [3].

2 Unified Model

Roughly speaking, short GRBs are similar to the first 1 sec of long GRBs [4], which suggests that the difference between short and long GRBs is just the number of pulses, and each pulse is essentially the same. Thus, we may consider that each pulse is produced by essentially the same unit or the sub-jet, and the GRB jet consists of many sub-jets. If many sub-jets point to our line of sight, the event looks like the long GRB while if a single sub-jet points to us, the event looks like a short GRB. Since we can observe only the angular size of $\sim \gamma^{-1}$ within the GRB jet with the Lorentz factor γ, different observers will see different number of sub-jets depending on the distribution of sub-jets within the GRB jet.

XRFs also appear to be related to GRBs. Softer and dimmer GRBs smoothly extend to the XRFs [5, 6, 7], Other properties of the XRFs are also similar to those of the GRBs, suggesting that XRFs are in fact soft and dim GRBs. In the sub-jet model, XRFs are naturally expected when our line of sight is off-axis to any sub-jets [8, 9, 10, 11, 12, 13].

In the following, we show a numerical simulation to demonstrate how the event looks so different depending on the viewing angle in our unified model [3]. The whole jet, with an opening half-angle of $\Delta\theta_{\rm tot} \sim 0.2$ rad, consists of 350 sub-jets. All sub-jets are assumed to have the same intrinsic properties,

[1] E-mail:ryo@vega.ess.sci.osaka-u.ac.jp
[2] E-mail:kunihito@gravity.psu.edu
[3] E-mail:takashi@tap.scphys.kyoto-u.ac.jp
[4] E-mail:toma@tap.scphys.kyoto-u.ac.jp

e.g., the opening half-angle $\Delta\theta_{\rm sub}^{(j)} = 0.02$ rad, and so on. We consider the case in which the angular distribution of sub-jets is given by $P(\vartheta^{(j)}) \propto \exp[-(\vartheta^{(j)}/\vartheta_c)^2/2]$, where we adopt $\vartheta_c = 0.1$ rad [14]. In this case, sub-jets are concentrated on the central region. For our adopted parameters, isolated sub-jets exist near the edge of the whole jet with the multiplicity $n_s = 1$ and there exists a viewing angle where no sub-jets are launched. The left, middle, and right panels of Fig. 1 show the angular distributions of sub-jets and the directions of three selected lines of sight, the observed light curves in the γ-ray bands, and the observed time-integrated spectra, respectively. Note here in the left panel of Fig. 1, "A" represents the center of the whole jet and is hidden by the lines of sub-jets.

Long GRB: When we observe the source from the $\vartheta = 0$ axis (case "A"), we see spiky temporal structures (the upper-middle panel of Fig. 1) and $E_p \sim 300$ keV which are typical for the long GRBs. We may identify case "A" as long GRBs.

XRF and X-ray rich GRB: When the line of sight is away from any sub-jets (case "B"), soft and dim prompt emission, i.e. XRFs or X-ray rich GRBs are observed with $E_p = 10 \sim 20$ keV and ~ 4 orders of magnitude smaller fluence than that of case "A" (the right panel of Fig. 1). The burst duration is comparable to that in case "A". These are quite similar to the characteristics of XRFs. We may identify the case "B" as XRFs or X-ray rich GRBs.

Short GRB: If the line of sight is inside an isolated sub-jet (case "C"), its observed pulse duration is ~ 50 times smaller than case "A". Contributions to the observed light curve from the other sub-jets are negligible, so that the fluence is about a hundredth of the case "A". These are quite similar to the characteristics of short GRBs. However the hardness ratio ($= S(100-300\ {\rm keV})/S(50-100\ {\rm keV})$) is about 3 which is smaller than the mean hardness of short GRBs (~ 6). It is suggested that the hardness of short GRBs is due to the large low-energy photon index $\alpha_B \sim -0.58$ [4] so that if the central engine launches $\alpha_B \sim -0.58$ sub-jets to the periphery of the core where n_s is small, we may identify the case "C" as the short-hard GRBs. In other words, the hardness of 3 comes from $\alpha_B = -1$ in our simulation so that if $\alpha_B \sim -0.58$, the hardness will be 6 or so. We suggest here that not only the isotropic energy but also the photon index may depend on ϑ. Another possibility is that if short GRBs are the first 1 sec of the activity of the central engine, the spectrum in the early time might be $\alpha_B \sim -0.58$ for both the sub-jets in the core and the envelope. This is consistent with a high KS test probability for E_p and α_B [4]. These possibilities may have something to do with the origin of $\alpha_B \sim -1$ for the long GRBs.

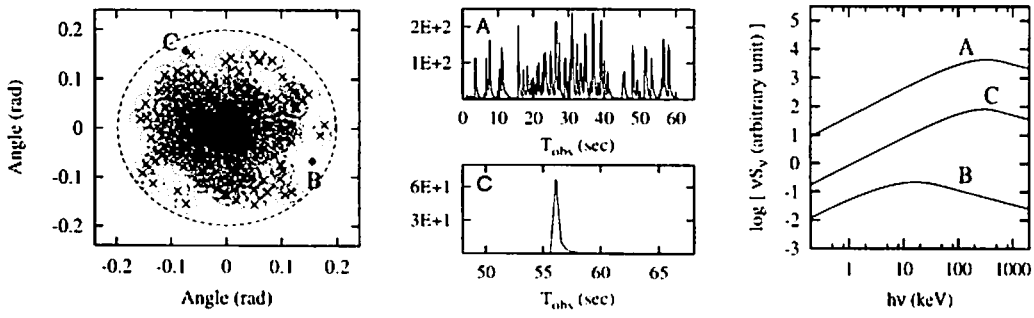


Figure 1: (Left) The angular distribution of 350 sub-jets confined in the whole GRB jet in our simulation. The whole jet has the opening half-angle of $\Delta\theta_{\rm tot} = 0.2$ rad. The sub-jets have the same properties. The axes and the angular size of sub-jets are represented by crosses and the dotted circles, respectively. "A" represents the center of the whole jet and is hidden by the lines of sub-jets. (Middle) The observed γ-ray light curves, corresponding the cases "A"and "C" in the left panel. (Right) Time-integrated energy spectrum of the emission from the multiple sub-jets for the observers denoted by "A", "B", and "C". The source is located at $z = 1$.

3 Discussions

Let $\Delta\theta_{\rm sub}$, ϑ_c and $\bar{n}_s$ be the typical opening half-angle of the sub-jet, the core size of the whole jet and the mean multiplicity in the core. Then the total number of the sub-jets ($N_{\rm tot}$) is estimated as $N_{\rm tot} = \bar{n}_s(\vartheta_c/\Delta\theta_{\rm sub})^2 \sim 10^3$, so that the total energy of each sub-jet is $\sim 10^{48}$ erg. In our model, the event rate of long GRBs is in proportion to ϑ_c^2. Let M be the number of sub-jets in the envelope of the core with a multiplicity $n_s = 1$. Then the event rate of short GRBs is in proportion to $M\Delta\theta_{\rm sub}^2$, so that $M \sim 10$ is enough to explain the event rate of short GRBs.

In this paper, we have not discussed the origin of the sub-jets, but argued the implications of the sub-jet model. The origin of sub-jets is not yet clear. They may arise from relativistically outflowing blobs generated by various fluid instabilities like Kelvin-Helmholtz, Rayleigh-Taylor instability, and so on [15, 16, 17].

Since the core may be regarded as a uniform jet, our model for the XRFs is analogous to the off-axis uniform jet model [10, 11, 13]. However the afterglow could have a different behavior between the core-envelope sub-jet model and the uniform jet model. In the uniform jet model, the afterglows of XRFs should resemble the orphan afterglows that initially have a rising light curve [18, 19]. An orphan afterglow may be actually observed in XRF 030723 [20], but the light curve may peak too early [14]. The optical afterglow of XRF 020903 is not observed initially (< 0.9 days) but may not be consistent with the orphan afterglow [21]. These problems could be overcome by introducing a Gaussian tail with a high Lorentz factor around the uniform jet [14] since the energy redistribution effects may bring the rising light curve to earlier times [14, 22]. The afterglow of a short GRB is difficult to predict since it could resemble both the orphan and normal afterglow depending on the sub-jet configuration within the envelope.

It is also found that our model can reproduce the bimodal distribution of T_{90} duration of GRBs observed by BATSE [23]. In our model, The duration of $n_s = 1$ burst is determined by the angular spreading time of one sub-jet emission, while that of $n_s \geq 2$ burst is determined by the time interval between the observed first pulse and the last one. These two different time scales naturally lead a division of the burst T_{90} durations into the short and long ones. It has commonly been said that the observed bimodal distribution of T_{90} durations of BATSE bursts shows the different origins of short and long GRBs. However, the bimodal distribution is also available as a natural consequence of our unified model of short and long GRBs. The clear prediction of our unified model is that short GRBs should be associated with energetic SNe. Indeed, one of short GRBs shows the possible association with a SN [24]. Even if the SNe are not identified with short GRBs due to some observational reasons we predict that the spatial distribution of short GRBs in host galaxies should be similar to that of the long GRBs. Another prediction is that short GRBs should have the same total kinetic energies as long GRBs, which might be confirmed by radio calorimetry.

Interestingly, our model has predicted short XRFs or short X-ray rich GRBs [3]. They are observed when isolated sub-jets are viewed slightly off-axis. The observed short XRF 040924 may be a kind of these bursts [25].

References

[1] Stanek, K. Z. Matheson, T., Garnavich, P. M. et al., 2003, ApJ, 591, L17

[2] Hjorth, J., Sollerman, J., Möller, P. et al., 2003, Nature, 423, 847

[3] Yamazaki, R., Ioka, K., & Nakamura, T., 2004b, ApJ, 607, L103

[4] Ghirlanda, G., Ghisellini, G., & Celotti, A., 2004, A&A, 422, L55

[5] Heise, J., in 't Zand, J., Kippen, R. M., & Woods, P. M., 2001, in Proc. Second Rome Workshop: Gamma-Ray Bursts in the Afterglow Era, ed. E. Costa, F. Frontera, & J. Hjorth (Berlin: Springer), 16

[6] Kippen, R. M., Woods, P. M., Heise, J. et al. 2002, AIP Conf. Proc. 662, 244 (astro-ph/0203114)

[7] Sakamoto, T., Lamb, D. Q., Graziani, C. et al., 2004, ApJ, 602, 875

[8] Nakamura, T., 2000, ApJ, 534, L159

[9] Ioka, K., & Nakamura, T., 2001, ApJ, 554, L163

[10] Yamazaki, R., Ioka, K., & Nakamura, T., 2002, ApJ, 571, L31

[11] Yamazaki, R., Ioka, K., & Nakamura, T., 2003b, ApJ, 593, 941

[12] Yamazaki, R., Yonetoku, D., & Nakamura, T., 2003c, ApJ, 594, L79

[13] Yamazaki, R., Ioka, K., & Nakamura, T., 2004a, ApJ, 606, L33

[14] Zhang, B., Dai, X., Lloyd-Ronning, N. M., & Mészáros, P., 2004, ApJ, 601, L119

[15] Aloy, M. A., Ibáñez, J.-M., Miralles, J.-A., & Urpin, V. 2002, A&A, 396, 693

[16] Zhang, W., Woosley, S. E., & Heger, A. 2003, astro-ph/0308389

[17] Gomez, E. A. & Hardee, P. E. 2003, astro-ph/0311134

[18] Yamazaki, R., Ioka, K., & Nakamura, T., 2003a, ApJ, 591, 283

[19] Granot, J., Panaitescu, A., Kumar, P., & Woosley, S. E., 2002, ApJ, 570, L61

[20] Fynbo, J. P. U., Sollerman, J., Hjorth, J. et al., 2004, ApJ. 609, 962

[21] Soderberg, A. M., Kulkarni, S. R., Berger, E. et al., 2004, ApJ, 606, 994

[22] Kumar, P., & Granot, J., 2003, ApJ, 591, 1075

[23] Toma, K., Yamazaki, R., & Nakamura, T., 2004, ApJ in press (astro-ph/0407012)

[24] Germany, L. M., Reiss, D. J., Sadler, E. M. et al., 2000, ApJ, 533, 320

[25] Fenimore, E. Ricker, G., Atteia, J-L, et al., 2004, GCN Circ. 2735

Self-force on a particle orbiting a Schwarzschild black hole
—Case of a scalar-charged particle —

Wataru Hikida[1(a,e)], Sanjay Jhingan[2(b)], Hiroyuki Nakano[3(c)], Norichika Sago[4(d)], Misao Sasaki[5(a)], Takahiro Tanaka[6(e)]

[(a)] *Yukawa Institute for Theoretical Physics, Kyoto University, Kyoto 606-8502, Japan*
[(b)] *Departamento de Física Teórica, Universidad del País Vasco, Apdo. 644, 48080, Bilbao, Spain*
[(c)] *Department of Mathematics and Physics, Graduate School of Science, Osaka City University*
[(d)] *Department of Earth and Space Science, Graduate School of Science, Osaka University*
[(e)] *Department of Physics, Graduate School of Science, Kyoto University, Kyoto 606-8502, Japan*

Abstract

Recently, we formulated a new efficient analytical method for regularizing the self-force acting on a particle of small mass μ orbiting a black hole of mass M, where $\mu \ll M$. In this paper, for simplicity, we focus on the scalar-charged particle case and calculate the self-force explicitly. The result is then examined by comparing it with those obtained in some limiting cases.

1 Introduction

One of the most promising sources of gravitational waves that can be detected by future space-based interferometric detectors such as LISA is a compact star orbiting a super-massive black hole. In order to do astronomy of such systems by gravitational waves, we have to know the precise waveforms, which can be obtained only by solving the orbital evolution accurately including the radiation backreaction.

Most of previous studies on this issue were based on the assumption of adiabatic orbital evolution, for example, by using the quadrapole formalism in the Newtonian limit [1]. For a small mass particle orbiting a black hole, the energy loss can be calculated by using the black hole perturbation theory [2]. By appealing to the conservation law, one can then solve the orbital evolution.

However, there are of course situations in which the adiabatic approximation is invalidated. In such cases, it is necessary to calculate the correction to the equation of motion explicitly. In the case of a small mass particle orbiting a black hole, the correction is given by the force due to the field generated by the particle itself, the so-called self-force. It should be also noted that the self-force not only contains a dissipative (radiative) part due to emission of gravitational waves but also a conservative part which is essentially a relativistic correction due to strong gravity.

The self-force, however, diverges at the location of the particle, and hence should be properly regularized. It is known that the properly regularized self-force is given by the tail part (or the R -part) of the self-field, obtained by subtracting the direct part (or the S-part) from the full self-field [2]. The most successful method of regularization relies on the spherical harmonic decomposition of the self-force, the so-called mode-sum regularization or mode decomposition regularization [3].

So far the regularized self-force has been calculated only for special orbits. This is primarily due to mismatch in the domain used for evaluating the full self-field and the S-part of it. The full field is calculated with either the Regge-Wheeler-Zerilli or Teukolsky formalism, which heavily relies on the Fourier decomposition of time-dependence. Thus the full field is calculated in the frequency domain. On the other hand, the S-part can be given only in the time domain. So we have to integrate the full field over the frequency ω.

[1] E-mail:hikida@yukawa.kyoto-u.ac.jp
[2] E-mail:wtpsaxxj@lg.ehu.es
[3] E-mail:denden@sci.osaka-cu.ac.jp
[4] E-mail:sago@vega.ess.sci.osaka-u.ac.jp
[5] E-mail:misao@yukawa.kyoto-u.ac.jp
[6] E-mail:tama@scphys.kyoto-u.ac.jp

Recently, we formulated a new analytical method for regularizing the self-force acting on a particle in the Schwarzschild spacetime [4]. In this new method, the frequency-domain retarded Green function can be decomposed in to what we call the $\tilde{S}$ and $\tilde{R}$-parts, in such a way that all the singular behavior is contained in the $\tilde{S}$-part and that the frequency integral of the $\tilde{S}$-part can be analytically done for a general orbit. We have then obtained an explicitly expression for the regularized $\tilde{S}$-part of the self-force, that is, the $(\tilde{S} - S)$-part for a general orbit.

In this paper, for technical simplicity, we focus on the case of a scalar charge. In Sec. 2, we present the dipole formalism, which corresponds to the quadrapole formalism for the gravitational case. In Sec. 3, first we summarize our new regularization method. Second, we calculate the self-force for an eccentric orbit. We find the energy loss rate calculated from our result agrees with the dipole formula in the nonrelativistic limit. Third, we consider the case of a circular orbit and compare it with the numerical results obtained by Detweiler and his collaborators [5, 6]. In the final section, Sec. 4, we summarize and conclude the paper.

2 Dipole radiation formula for a scalar charge

Let us consider a point particle with a scalar charge q, moving on the flat background. The scalar field ψ induced by this particle obeys wave equation:

$$\Box_{\rm flat}\psi = -\rho, \quad \rho = q\,\delta(\boldsymbol{x} - \boldsymbol{z}(\tau)) \tag{1}$$

Here $\boldsymbol{x}$ and $\boldsymbol{z}$ are a field and orbital position, respectively. If we assume $|\boldsymbol{x}| \gg |\boldsymbol{z}|$, then a solution of this equation is

$$\psi = \frac{1}{4\pi|\boldsymbol{x}|}\int\left[\rho + \frac{\boldsymbol{n}\cdot\boldsymbol{z}}{c}\partial_{t'}\rho + \cdots\right]_{t'=t_{ret}} dV = \frac{1}{4\pi|\boldsymbol{x}|}\left[q + \frac{1}{c}(\dot{\boldsymbol{d}}\cdot\boldsymbol{n}) + \cdots\right]_{t'=t_{ret}}. \tag{2}$$

Here $\boldsymbol{n} = \boldsymbol{x}/|\boldsymbol{x}|$, $\boldsymbol{d}$ is the dipole moment, the dot denotes a time derivative, and $t_{ret} = t - |\boldsymbol{x}|/c$ is the retarded time. Therefore, the energy loss can be obtained by

$$\left(\frac{dE}{dt}\right) = c\int_{|\boldsymbol{x}|\to\infty}(-T_{0i}\,n^i)|\boldsymbol{x}|^2\,d\Omega \approx \int_{|\boldsymbol{x}|\to\infty}\frac{(\ddot{\boldsymbol{d}}\cdot\boldsymbol{n})^2}{16\pi^2c^3}\,d\Omega = \frac{q^2}{4\pi c^3}\left[\frac{|\ddot{\boldsymbol{z}}|^2}{3}\right] \tag{3}$$

Here we think the particles, whose masses are M and μ ($M \gg \mu$), have coordinates $(0,0)$ and (z_x, z_y) in the xy plane, respectively. The orbital position, for eccentric orbits, is given by $z_x = d\cos\psi$ and $z_y = d\sin\psi$. We define the variables, a and e, as the semimajor axis and eccentricity, respectively. Then d and $\dot{\psi}$ can written by

$$d = \frac{a(1-e^2)}{1+e\cos\psi}, \quad \dot{\psi} = \frac{[GMa(1-e^2)]^{1/2}}{d^2}. \tag{4}$$

Therefore, the averaged value of energy loss over one period is

$$\left\langle\left(\frac{dE}{dt}\right)\right\rangle = \frac{q^2}{4\pi c^3}\frac{1}{3}\frac{a^2\Omega^4}{(1-e^2)^4}\left\langle(1+e\cos\psi)^4\right\rangle = \frac{q^2}{4\pi a^2c^3}\frac{(a\Omega)^4}{3}\frac{(2+e^2)}{2(1-e^2)^{5/2}}. \tag{5}$$

where $\Omega^2 \equiv GM/a^3$. Moreover, in order to compare with the self-force we show later, we define r_0 as $a = r_0(1 + e^2 + \cdots)$. Then

$$\left\langle\left(\frac{dE}{dt}\right)\right\rangle = \frac{q^2}{4\pi r_0^2c^3}\frac{V^4}{3}\frac{(2+e^2)}{2(1+e^2)^4(1-e^2)^{5/2}} \approx \frac{q^2}{4\pi r_0^2c^3}\frac{V^4}{3}\left(1 - e^2 + \cdots\right), \tag{6}$$

where $V^2 \equiv GM/r_0$. This means the energy loss rate starts at $1.5PN$ order.

3 Self-Force in the Schwarzschild Spacetime

Our new decomposition of the full part into the two parts, the $\tilde{S}$- and $\tilde{R}$-parts in the frequency domain, naturally arises from the analytical method developed by Mano, Suzuki and Takasugi [7]. The $\tilde{S}$-part contains all the singular terms to be subtracted, so the $\tilde{R}$-part is finite. Therefore we consider the regularization,

$$F^R = (F^{\tilde{S}} - F^S) + F^{\tilde{R}}. \tag{7}$$

The important fact is that the $\tilde{S}$-part in the frequency domain is given in the form of a simple Taylor series with respect to ω multiplied by $\exp[-i\omega(t-t')]$. Therefore, the integration over ω just produces $\delta(t-t')$ and its derivatives. Using this technique we can obtain the $\tilde{S}$-part in the time domain relatively easily. The details are given in [4, 8, 9, 10].

3.1 Eccentric Case

The solution of the geodesic equation for slightly eccentric orbits has been given by Apostolatos *et al.* [11]. Here we use the geometrized units, $G = c = 1$, and define the mean radius r_0 and eccentricity e by

$$\frac{\partial R(z^r)}{\partial z^r}(z^r = r_0) = 0, \quad R(z^r = r_0(1-e)) = 0.$$

Here R is the potential for the radial motion. From these equations, the energy $\mathcal{E}$ and the angular momentum $\mathcal{L}_z$ of the particle are expressed in terms of r_0 and e as

$$\mathcal{E}^2 = \frac{(1-2V^2)^2}{1-3V^2} + \frac{V^2(1-6V^2)}{1-3V^2}e^2 + \cdots, \quad \frac{\mathcal{L}_z}{r_0} = \frac{V}{\sqrt{1-3V^2}},$$

where $V \equiv \sqrt{M/r_0}$. Then expanding the geodesic equation in powers of e, the solution is

$$\begin{aligned} z^r(t) &= r_0[1 + e\cos\Omega_r t + \cdots], \quad \psi(t) = \Omega_\varphi t - e p_1(V)\sin\Omega_r t + \cdots, \\ \Omega_r &= \frac{V}{r_0^2}[(1-6V^2)^{1/2} + \cdots], \quad \Omega_\varphi = \frac{V}{r_0^2}[1 - f(V)e^2 + \cdots], \end{aligned}$$

where p_1 and f are functions of V.

After a long calculation, the result of regularized self-force is

$$\begin{aligned} F_t^R &= \frac{q^2 V}{4\pi r_0^2}\left[\frac{1}{3}V^3 - \frac{1}{6}V^5 + \frac{2}{3}\pi V^6 + e\left\{\left(-\frac{2}{3}V^3 - V^5 - \frac{20}{3}\pi V^6\right)\cos(\Omega_r t) + \cdots\right\}\right. \\ &\quad \left. + e^2\left\{-\frac{1}{3}V^3 + \frac{20}{3}V^5 + \pi V^6 + \left(\frac{2}{3}V^3 + \frac{1}{3}V^5 + \frac{20}{3}\pi V^6\right)\cos(\Omega_r t) + \cdots\right\} + \mathcal{O}(e^3)\right] \\ F_r^R &= \frac{q^2}{4\pi r_0^2}\left[\left(-\frac{4}{3}\gamma + \frac{7}{64}\pi^2 - \frac{4}{3}\ln(2V) - \frac{2}{9}\right)V^6\right. \\ &\quad \left. + e\left\{\left(-\frac{92}{9} - \frac{7}{32}\pi^2 + \frac{64}{3}\ln(2) + \frac{32}{3}\gamma + \frac{8}{3}\ln(V)\right)V^6\cos(\Omega_r t) + \cdots\right\} + \mathcal{O}(e^2)\right] \end{aligned}$$

Here γ is Euler's constant, $\gamma = 0.57\cdots$. The energy loss rate is consistent with that of the dipole formula.

3.2 Comparison with Detweiler et al.'s results in circular case

Detweiler and his collaborators calculated numerically the radial component of the self-force for various radii in units of $M = 1$ and $q^2 = 4\pi$ [5, 6]. So, let us compare our result with theirs in the circular case. In our case, we employed a Pade approximation for the $(\tilde{S} - S)$-force accurate to 18PN order and used the $\tilde{R}$-force which was calculated as accurately as possible including the terms up to $\ell = 19$. Their results are compared with ours for $r_0 = 6M$ (the innermost stable circular orbit: ISCO), $10M$ and $20M$ in Table 1. As clear from it, the agreement is almost perfect for $r_0 = 10M$ and $20M$, while there is a relative error of $\sim 10^{-4}$ for $r_0 = 6M$. This error may seem large, but if our result is used as a template for a LISA-type space gravitational wave detector, it turns out that the error is small enough [9]. Thus, we conclude that our new method is capable of computing the self-force with sufficient accuracy, and the result obtained to 18PN order seems accurate enough even in the limit of ISCO.

r_0	$6M$	$10M$	$20M$
Our result	$1.67620878 \times 10^{-4}$	$1.378448171 \times 10^{-5}$	$4.937905866 \times 10^{-7}$
Detweiler *et al.*	1.6772834×10^{-4}	$1.37844828 \times 10^{-5}$	4.937906×10^{-7}

Table 1: The r-component of the self-force in units of $M = 1$ and $q^2 = 4\pi$ obtained by our method (top column) and by Detweiler *et al.* [5, 6] (bottom column). The number for $r_0 = 10M$ is taken from Ref. [5] in which they estimate the error by a Monte Carlo simulation, and the numbers for $r_0 = 6M$ and $20M$ are taken from Table I of Ref. [6].

4 Summary and Discussion

So far a large number of studies have been made on regularizing the self-force. Until recently, however, the regularized self-force had only been calculated numerically. And, except for special orbits, no systematic method for computing the regularized self-force had been given.

In this paper, using the new analytical method of regularization we developed recently, we have calculated the self-force explicitly in the case of an eccentric orbit. This is the first time that the regularized self-force for eccentric orbits has been obtained, though we have focused on the scalar particle case.

To examine the validity of our result in some limiting cases, we have derived the dipole radiation formula on the flat background and compared it with ours. We found our result agrees with the dipole formula in the Newtonian (non-relativistic) limit. We have also considered the self-force in the case of a circular orbit for which some numerical results are available in the literature. We found a very good agreement between theirs and ours.

Although we have focused on the scalar-charge case, we emphasize that our method is applicable to the gravitational case as well. An extension of our method to the gravitational case is now in progress.

References

[1] P. C. Peters and J. Mathews, Phys. Rev. **131**, 435 (1963).

[2] For a review, see e.g.,
Y. Mino, M. Sasaki, M. Shibata, H. Tagoshi and T. Tanaka, Prog. Theor. Phys. Suppl. **128**, 1 (1997).
E. Poisson, Living Rev. Rel. **7** (2004) 6.

[3] L. Barack, Y. Mino, H. Nakano, A. Ori and M. Sasaki, Phys. Rev. Lett. **88**, 091101 (2002).

[4] W. Hikida, S. Jhingan, H. Nakano, N. Sago, M. Sasaki and T. Tanaka, Prog. Theor. Phys. **111** (2004) 821.

[5] S. Detweiler, E. Messaritaki and B. F. Whiting, Phys. Rev. D **67** (2003) 104016.

[6] L. M. Diaz-Rivera, E. Messaritaki, B. F. Whiting and S. Detweiler, arXiv:gr-qc/0410011.

[7] S. Mano, H. Suzuki and E. Takasugi, Prog. Theor. Phys. **95**, 1079 (1996).

[8] web page: http://www2.yukawa.kyoto-u.ac.jp/~misao/BHPC/

[9] W. Hikida, S. Jhingan, H. Nakano, N. Sago, M. Sasaki and T. Tanaka, arXiv:gr-qc/0410115.

[10] W. Hikida, H. Nakano and M. Sasaki, arXiv:gr-qc/0411150.

[11] T. Apostolatos, D. Kennefick, E. Poisson and A. Ori, Phys. Rev. D **47**, 5376 (1993).

ionizing the universe by decaying particles and CMB

Shinta Kasuya[1]

Department of Information Science, Kanagawa University, Kanagawa 259-1293, Japan

Abstract

We study the reionization scenario in which ionizing UV photons emitted from decaying particle, in addition to usual contributions from stars and quasars, ionize the universe. It is found that the scenario is consistent with both the first year data of the Wilkinson Microwave Anisotropy Probe and the fact that the universe is not fully ionized until $z \sim 6$ as observed by Sloan Digital Sky Survey. Likelihood analysis revealed that rather broad parameter space can be chosen. This scenario will be discriminated by future observations, especially by the EE polarization power spectrum of cosmic microwave background radiation.

1 Introduction

The dark age between recombination and today has begun to be revealed to be very complicated by recent observations. The first witness is the Gunn-Perterson trough observed by Sloan Digital Sky Survey (SDSS), which implies that the universe was not fully reionized until $z \sim 6$ [1]. The second shed light on the beginning of reionization history, which may have started as early as $z \sim 20$, by the spectrum of cosmic microwave background (CMB) radiation observed by Wilkinson Microwave Anisotropy Probe (WMAP) [2].

Conventionally the reionization is thought to be caused by the UV photons emitted from the early forming stars, where the ionization fraction of the universe is approximated by a step function [3]. However, it is very difficult to satisfy the above-mentioned two observations. Thus, we focus on another possibility. The idea is that the additional UV photons from decaying particles can explain the earlier reionization, while contributions from conventional stars and quasars make the ionization fraction unity at $z \sim 6$ [4, 5, 6]. Although the existence of such particles may be suspicious, the ionization history is very realistic once we admit it.

2 Ionization history

In our scenario, the sources for ionizing UV photons are decaying particles, quasars and stars. Stars (and quasars) are indeed responsible for the full reionization at $z \sim 6$. On the other hand, contribution of UV photons from the decaying particles keeps ionization fraction much smaller before $z \sim 6$ for a long period.

We follow the thermal history from $z > 10^3$ including recombination epoch, calculating the ionization fractions of hydrogen (HII) and helium (HeII and HeIII), and the electron temperature, based on the argument of Fukugita and Kawasaki [7], where the hierarchical clustering scheme of the cold dark matter scenario is used. In addition, we include the sources of ionizing UV photons from decaying particles [4]. Some different treatments of stars and QSOs from [7] can also be found in [4].

We assume that the particle ϕ emits two photons with monochromatic energy of half mass of that particle, i.e., $E_\gamma = m_\phi/2$. The number density of ϕ-particle is written as

$$n_\phi = n_\phi(0)(1+z)^3 e^{-\frac{t}{\tau_\phi}}, \tag{1}$$

where τ_ϕ is the lifetime of ϕ-particle. Notice that those emitted photons with $E_\gamma > 13.6$ eV can ionize hydrogen atoms. Then one can write a source term for the decaying particle as

$$\left(\frac{dn_\gamma}{dt}\right)_{dp} = \frac{n_\phi(t)}{\tau_\phi}. \tag{2}$$

[1]E-mail:kasuya-s@info.kanagawa-u.ac.jp

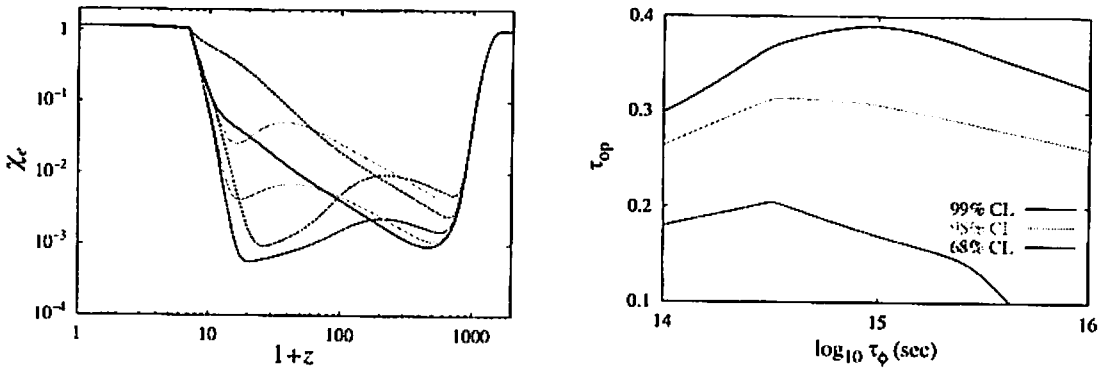


Figure 1: (Left panel) Evolution of ionization fraction. $\tau_\phi = 10^{14}$ sec (red), 10^{15} sec (green), and 10^{16} sec (blue) are plotted. For each lifetime, both $\tau_{op} = 0.1$ (solid) and 0.4 (dashed) are shown. (Right panel) Likelihood contour of the decaying particle scenario.

In order to calculate how many photons are emitted, the abundance, mass, and the lifetime of the particle should be fixed. We choose $E_\gamma = 15$ eV, since this case represents important features of decaying particle scenario. We calculate ionization histories with $\tau_\phi = 10^{14} - 10^{16}$ sec (and 10^{17} sec for some cases), adjusting the abundance Ω_ϕ to get the desired value of optical depth τ_{op}, whose range we explored is $\tau_{op} = 0.1 - 0.4$. It is defined by

$$\tau_{op} = \int_0^\infty dz \sigma_T \left(\frac{dt}{dz}\right) [n_e - n_e|_{sr}], \tag{3}$$

where σ_T is the Thomson cross section and $n_e|_{sr}$ is the electron number density for standard recombination. We subtract this term in order to estimate only the effect of reionization.

Typical ionizing histories are shown in the left panel in Fig. 1. Here ionization fraction is defined as $\chi_e = n_e/n_H$, where n_e and n_H are the number densities of electron and hydrogen atom, respectively.

As we will see later, cosmological parameters such as Hubble parameter, H_0, matter density, Ω_m, baryon density, Ω_b, and the spectral index of primordial power spectrum, n_s, are varied such that they give the minimum χ^2 for fitting both TT and TE spectrum observed by WMAP in the flat ΛCDM cosmology.

As we can see in Fig. 1, ionization due to decaying particles endures for a long period, and the ionization fraction remains very small ($10^{-3} \lesssim \chi_e \lesssim 10^{-1}$) until $z \sim 6$. Even in these cases, the optical depth becomes very large.

3 Cosmic microwave background

Now we look for how these ionization histories are consistent with CMB observation by WMAP. To this end, we calculate the power spectrum with obtained evolution of the ionization fraction and matter temperature as inputs to the code modified from CMBFAST [8], and evaluate χ^2 using the code provided by WMAP [2]. We search for the range $10^{14} - 10^{16}$ sec, for the lifetime of the decaying particle, and $\tau_{op} = 0.1 - 0.4$. For fixed lifetime and optical depth, the χ^2 minimum is estimated adjusting Ω_b, Ω_m, H_0, n_s, and the amplitude of the spectrum. As an indicator for the likelihood, we use $\Delta\chi^2 = \chi^2 - \chi^2|_{best}$ to make the contour of likelihood with grid-based analysis. Here we take $\chi^2|_{best} = 1428.6$ [9] as the six-parameter χ^2 minimum for ΛCDM model with WMAP-only data.

The likelihood contours are shown in the right panel in Fig. 1. Here, we converted $\Delta\chi^2$ into the confidence level for two degrees of freedom. One can see the decaying particle scenario is consistent with WMAP data for a broad parameter space. More precisely, it is within the 95% confidence level for $\tau_{op} \lesssim 0.3$ and $\tau_\phi = 10^{14} - 10^{16}$ sec. Roughly speaking, there is little dependence on the lifetime of

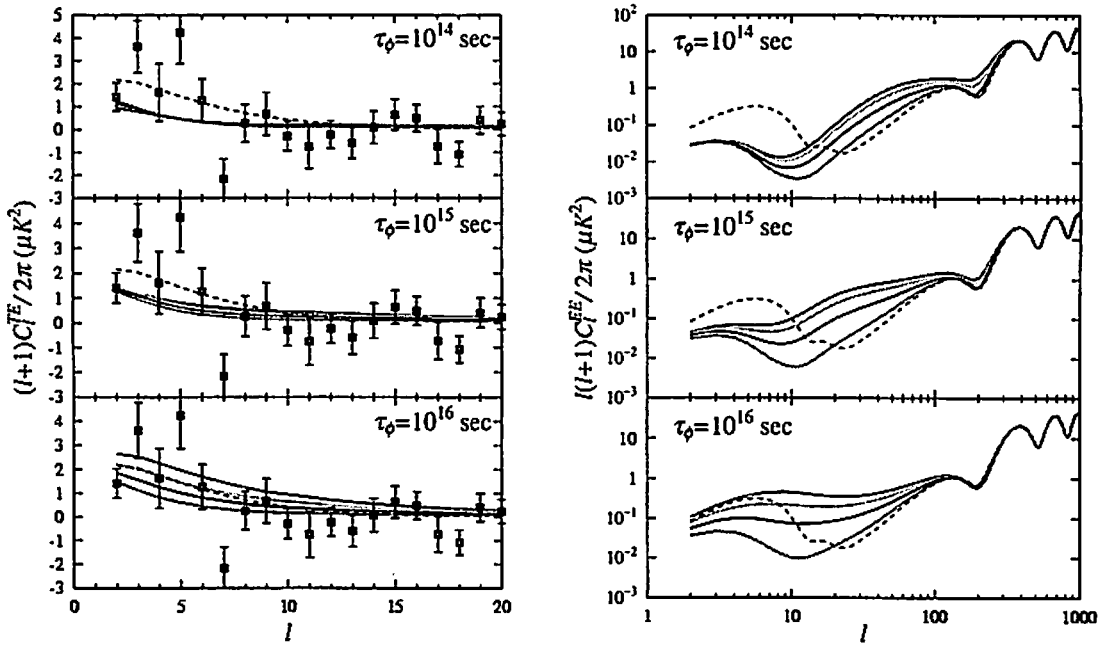


Figure 2: TE (left) and EE (right) power spectra for typical ionization histories for $\tau_\phi = 10^{14}$ sec (top), 10^{15} sec (middle), and 10^{16} sec (bottom). In each panel, the lines are for $\tau_{op} \simeq 0.4$ (red), 0.3 (green), 0.2 (blue), and 0.1 (purple). The instantaneous reionization with $\tau_{op} \simeq 0.17$ is shown in dashed black line. For TE spectrum, the WMAP data is also shown.

decaying particle, since the contours are very flat. This is because the χ^2 is more sensitive to TT power spectrum, which is determined almost by the value the optical depth, not by the actual reionization history.

We omit the lifetime longer than 10^{17} sec from the figure, because the ionization fraction becomes unity before $z \sim 6$ for $\tau_{op} \gtrsim 0.3$ even if there is no contributions of stars and quasars. Of course, if $\tau_{op} \lesssim 0.2$ and $\tau_\phi = 10^{17}$ sec, it is consistent with observations as well. For example, $\chi^2 = 1432.6$ and 1430.5 for $\tau_{op} = 0.2$ and 0.1, respectively. Notice that, for fixed optical depth, ionization histories with lifetime longer than 10^{17} sec are identical to 10^{17} sec case, since it is the value of n_ϕ/τ_ϕ that concerns with the amount of emitted photons; i.e., the abundance should be ten times larger for the ten times longer lifetime. This relation holds until the abundance reaches $\Omega_\phi \simeq \Omega_m$.

We should mention that χ^2 itself is smaller if reionization takes place instantaneously for the same optical depth. As we have mentioned several times, however, such instantaneous reionization histories do not respect the Gunn-Peterson trough at $z \sim 6$ observed by SDSS. On the other hand, optical depth becomes $\simeq 0.04$ if the ionization fraction at $z \sim 6$ is suppressed enough to meet SDSS data. (When using our code without contribution of decaying particle, we get $\tau_{op} \simeq 0.05$.)

Now let us see the CMB spectra in detail. We show TE and EE power spectra of CMB in Figs. 2. For TE spectra, we also plot the WMAP data.

In general, TE spectrum is sensitive to the ionization histories. However, for $\tau_\phi \gtrsim 10^{15}$ sec, χ^2 for TE spectrum, does not change so much through $\tau_{op} = 0.1 - 0.4$, and the total χ^2 is mostly determined by that of TT spectrum. Thus, TE power spectrum does not have much ability of determining ionization histories at the moment. For example, TE spectrum for $\tau_\phi = 10^{16}$ sec with larger optical depth seems to fit the data well, and χ^2 for TE spectrum is relatively small. But the large χ^2 for TT spectrum disfavors these cases at present. Notice that the lifetime 10^{16} sec corresponds to $z \sim 13$. If the reionization takes place instantaneously at this epoch, the model fits very well to the data [2].

Although one may discriminate among the models using TE spectrum, EE spectrum seems the most

promising tool for that purpose. Most different feature of decaying particle scenario is the larger power at $\ell \sim$(a few)$\times 10$ due to enduring UV photon emission. Moreover, we may distinguish even the lifetime of decaying particle depending on whether there is a dip around $\ell \sim 10$ and the steepness of the slope below $\ell \sim 100$. Therefore, EE spectrum expected to be seen by Planck satellite or even WMAP should (dis)prove the photons from decaying particles in the near future.

4 Conclusion

We have sought for a natural reionization history which respects both WMAP and SDSS observations. Decaying particles provide UV photons which reionize the universe from rather early period as suggested by WMAP, but keeps the ionization fraction very small until usually considered UV sources such as stars and quasars bring up the fraction to unity abruptly at $z \sim 6$ as observed by SDSS. The central concern is how well such scenario goes on. To this end, we have calculated TT and TE power spectra of CMB, and done the likelihood analysis. We have found decaying particle scenario is consistent with both observations in rather broad parameter space. Even particles with lifetime 10^{14} sec, corresponding to the redshift $z \sim 280$, which have the abundance to give $\tau_{op} \lesssim 0.3$, seems good as well.

Looking into the detail, it is the TT power spectrum that determines the value of χ^2 dominantly. This is the reason why the reionization history, whose TE spectrum does not seem to fit the data so well, can have small χ^2, such as 1429.8 for $\tau_{op} \simeq 0.1$ and $\tau_\phi = 10^{14}$ sec, for example. When the quality of TE data improves, then one may be able to tell which reionization history is preferable. As for the ability of discriminating each history, EE spectrum may be the best tool. Decaying particle scenario has a peculiar feature that there is much more excess of the power in the range $20 \lesssim \ell \lesssim 100$ compared with instantaneous reionization case. Moreover, it may be possible to observe even the lifetime of the decaying particle.

Finally, we comment on a maybe serious problem if one regards early forming stars as the whole source of ionization photons because of the less powers on smaller scales observed by, say, 2dfGRS and SDSS. Since the decaying particle scenario does not owe to early forming stars as the UV source, it is completely free from such a problem. We have checked that our model works also for the running spectral index suggested by WMAP. (Notice that the decaying particle scenario re-opens up the possibility of warm dark matter models as well.) Since all the astrophysical UV sources may suffer this problem, the decaying particle could be the better source of ionizing UV photons.

References

[1] X. Fan *et al.*, Astron. J. **123**, 1247 (2002).

[2] A. Kogut *et al.*, Astrophys. J. Suppl. **148**, 161 (2003);
D.N. Spergel *et al.*, Astrophys. J. Suppl. **148**, 175 (2003);
L. Verde *et al.*, Astrophys. J. Suppl. **148**, 195 (2003);
G. Hinshaw *et al.*, Astrophys. J. Suppl. **148**, 135 (2003).

[3] A. Loeb and R. Barkana, Ann. Rev. Astron. Astrophys. **39**, 19 (2001), and references therein.

[4] S. Kasuya, M. Kawasaki, and N. Sugiyama, Phys. Rev. D **69**, 023512 (2004);
S. Kasuya and M. Kawasaki, Phys. Rev. D **70**, 103519 (2004).

[5] S.H. Hansen and Z. Haiman, Astrophys. J. **600**, 26 (2004).

[6] X. Chen and M. Kamionkowski, Phys. Rev. D **70**, 043502 (2004);
P.P. Avelino and D. Barbosa, Phys. Rev. D **70**, 067302 (2004).

[7] M. Fukugita and M. Kawasaki, Mon. Not. R. Astron. Soc. **269**, 563 (1994).

[8] U. Seljak and M. Zaldarriaga, Astrophys. J. **496**, 437 (1996).

[9] K. Ichikawa, M. Fukugita, and M. Kawasaki, astro-ph/0409768.

Three-dimensional simulations of stellar core collapse in full general relativity: Nonaxisymmetric dynamical instabilities

Masaru Shibata and Yu-ichirou Sekiguchi

Graduate School of Arts and Sciences, University of Tokyo, Tokyo, 153-8902, Japan

We perform fully general relativistic simulations of rotating stellar core collapse in three spatial dimension. The hydrodynamic equations are solved using a high-resolution shock-capturing scheme. A parametric equation of state is adopted to model collapsing stellar cores and neutron stars following Dimmelmeier et al. The early stage of the collapse is followed by an axisymmetric code. When the stellar core becomes compact enough, we start a three-dimensional simulation adding a bar-mode nonaxisymmetric density perturbation. The axisymmetric simulations are performed for a wide variety of initial conditions changing the rotational velocity profile, parameters of the equations of state, and the total mass. It is clarified that the maximum density, the maximum value of the compactness, and the maximum value of the ratio of the kinetic energy T to the gravitational potential energy W ($\beta \equiv T/W$) achieved during the stellar collapse and bounce depend sensitively on the velocity profile and the total mass of the initial core, and equations of state. It is also found that for all the models with high degree of differential rotation, a funnel structure is formed around the rotational axis after the formation of neutron stars. For selected models in which the maximum value of β is larger than ~ 0.27, three-dimensional numerical simulations are performed. It is found that the bar-mode dynamical instability sets in for the case that the following conditions are satisfied: (i) the progenitor of the stellar core collapse should be rapidly rotating with the initial value of $0.01 \lesssim \beta \lesssim 0.02$, (ii) the degree of differential rotation for the velocity profile of the initial condition should be sufficiently high, and (iii) a depletion factor of pressure in an early stage of collapse should be large enough to induce a significant contraction to form a compact stellar core for which an efficient spin-up can be achieved surmounting the strong centrifugal force. As a result of the onset of the bar-mode dynamical instabilities, the amplitude of gravitational waves can be by a factor of ~ 10 larger than that in the axisymmetric collapse. It is found that a dynamical instability with the $m = 1$ mode is also induced for the dynamically unstable cases against the bar-mode, but the perturbation does not grow significantly and, hence, it does not contribute to an outstanding amplification of gravitational waves. No evidence for fragmentation of the protoneutron stars is found in the first a few 10 msec after the bounce. Details of this work will be published in [1].

References

[1] M. Shibata and Y. Sekiguchi, Phys. Rev. D 71 (2005) to appear.

New Numerical Methods to Evaluate Homogeneous Solutions of the Teukolsky Equation

Ryuichi Fujita[1], Hideyuki Tagoshi[2]

Department of Earth and Space Science, Graduate School of Science, Osaka University, Toyonaka 560-0043, Japan

Abstract

We investigate the formalism developed by Mano, Suzuki and Takasugi which describes the homogeneous solutions of the Teukolsky equation. In this formalism, we have to solve the continued fraction equation and determine the "renormalized angular momentum parameter". Although this parameter has been assumed to be real number, we find that it becomes complex number as the angular frequency becomes large. We check that these solutions of the continued fraction equation can be used to determine the homogeneous solution of the Teukolsky equation. We also compute the energy flux of the gravitational waves from a particle in circular orbits on the equatorial plane around a Kerr black hole by this formalism and compare our results with a direct numerical integration method. We find that both methods produce consistent results. These facts prove the validity to use the complex solutions to describe the homogeneous solutions of the Teukolsky equation.

1 Introduction

Laser Interferometer Space Antenna (LISA) is expected to be launch in 2012. LISA has the best sensitivity around mHz band and it can detect gravitational waves from inspirals of white dwarfs, neutron stars or solar mass black holes into a supermassive black hole and so on. Gair et al.[1] estimated the number of such event rates are expected to be about 600 by 3 years observation for the inspirals of $10M_\odot$ black holes into $10^6 M_\odot$ supermassive black hole. If we can detect and observe such gravitational waves, we can extract information of these systems such as distance to the source, masses of binary, spin of the star, geometry of black hole space time and so on. In the matched filtering technique, which requires theoretical waveforms to be correlated with the data, we will need very accurate theoretical waveforms to extract astrophysical information of the source although we may not need it in detection.

To predict the waveforms of the extreme mass ratio inspirals, we adopt the black hole perturbation approach. In this approach, a compact star is treated as a point particle, and the mass of the compact star is assumed to be very small compared to the mass of the black hole. In this context, the Teukolsky equation describes the evolution of a perturbation of the Kerr black hole spacetime. Solutions of the Teukolsky equation is obtained by the integration of Green's function multiplied by the source term.

In Ref.[2], we adopt a formalism, originally developed by Leaver[3] and elegantly reformulated by Mano, Suzuki and Takasugi (MST formalism)[4, 5], in which the homogeneous solutions of the Teukolsky equation are expressed in series of special functions. We calculated the gravitational wave flux induced by a particle in a circular orbit on the equatorial plane around a Kerr black hole within accuracy at least 14 significant figures. And we showed the validity to use MST formalism to solve the Teukolsky equation. However when gravitational wave frequency became large, we could not determine "renormalized angular momentum parameter", ν, which is one of the most important variable in MST's formalism.

In this paper, we investigate the solution of the continued fraction equation by which we determine ν. Although this parameter has been believed to be real number, we find that we can find it in the complex region. Using these complex ν, we compute the energy flux of the gravitational waves from a particle in circular orbits on the equatorial plane around a Kerr black hole and compare these results with a direct numerical integration method. We find that both results are consistent. These facts prove the validity to use the complex solutions to describe the homogeneous solutions of the Teukolsky equation. Throughout this paper we use units with $G = c = 1$.

[1]E-mail:draone@vega.ess.sci.osaka-u.ac.jp
[2]E-mail:tagoshi@vega.ess.sci.osaka-u.ac.jp

2 Homogeneous solution of the Teukolsky equation

The homogeneous Teukolsky equation is given by

$$\Delta^2 \frac{d}{dr}\left(\frac{1}{\Delta}\frac{dR_{\ell m\omega}}{dr}\right) - \left[-\frac{K^2+4i(r-M)K}{\Delta} + 8i\omega r + \lambda\right] R_{\ell m\omega} = 0. \tag{1}$$

Here $\Delta = r^2 - 2Mr + a^2 = (r-r_+)(r-r_-)$ with $r_\pm = M \pm \sqrt{M^2-a^2}$, $K = (r^2+a^2)\omega - ma$ and λ is the eigenvalue of the angular Teukolsky equation.

In the MST's formalism, the homogeneous solutions of the Teukolsky equation are expressed in terms of special functions [4, 5]. We consider a homogeneous solution, $R^{\rm in}_{lm\omega}$, which has purely ingoing wave property at the horizon, but has both ingoing wave property and outgoing property at infinity.

For the incoming solution $R^{\rm in}_{lm\omega}$, we define $p_{\rm in}$ by

$$\begin{cases} R^{\rm in}_{\ell m\omega} = e^{i\epsilon\kappa x}(-x)^{-s-i(\epsilon+\tau)/2}(1-x)^{i(\epsilon-\tau)/2}p_{\rm in}(x), \\ p_{\rm in}(x) = \sum_{n=-\infty}^{\infty} a_n F(n+\nu+1-i\tau, -n-\nu-i\tau; 1-s-i\epsilon-i\tau; x). \end{cases} \tag{2}$$

where $x = \omega(r_+ - r)/\epsilon\kappa$, $\epsilon = 2M\omega, \kappa = \sqrt{1-q^2}, q = \frac{a}{M}, \tau = \frac{\epsilon - mq}{\kappa}$ and $F(\alpha,\beta;\gamma;x)$ is hypergeometric function.

The expansion coefficients of the series of hypergeometric functions $\{a_n\}$ satisfy three-term recurrence relation given by

$$\alpha^\nu_n a_{n+1} + \beta^\nu_n a_n + \gamma^\nu_n a_{n-1} = 0, \tag{3}$$

where

$$\alpha^\nu_n = \frac{i\epsilon\kappa(n+\nu+1+s+i\epsilon)(n+\nu+1+s-i\epsilon)(n+\nu+1+i\tau)}{(n+\nu+1)(2n+2\nu+3)}, \tag{4}$$

$$\beta^\nu_n = -\lambda - s(s+1) + (n+\nu)(n+\nu+1) + \epsilon^2 + \epsilon(\epsilon - mq) + \frac{\epsilon(\epsilon-mq)(s^2+\epsilon^2)}{(n+\nu)(n+\nu+1)}, \tag{5}$$

$$\gamma^\nu_n = -\frac{i\epsilon\kappa(n+\nu-s+i\epsilon)(n+\nu-s-i\epsilon)(n+\nu-i\tau)}{(n+\nu)(2n+2\nu-1)}. \tag{6}$$

In MST formalism, solving the Teukolsky equation is reduced to determine a parameter ν. Dividing Eq(3) by a_n and setting $n = 0$, we obtain the following equation that determine a parameter ν,

$$g_0(\nu) \equiv \beta^\nu_0 + \alpha^\nu_0 R_1 + \gamma^\nu_0 L_{-1} = 0, \tag{7}$$

where R_1 and L_{-1} are expressed by the continued fractions,

$$R_n(\nu) = \frac{-\gamma^\nu_n}{\beta^\nu_n + \alpha^\nu_n R_{n+1}} = \cfrac{-\gamma^\nu_n}{\beta^\nu_n - \cfrac{\alpha^\nu_n\gamma^\nu_{n+1}}{\beta^\nu_{n+1} - \cfrac{\alpha^\nu_{n+1}\gamma^\nu_{n+2}}{\beta^\nu_{n+2} - \cdots}}}, \quad L_n(\nu) = \frac{-\alpha^\nu_n}{\beta^\nu_n + \gamma^\nu_n L_{n-1}} = \cfrac{-\alpha^\nu_n}{\beta^\nu_n - \cfrac{\alpha^\nu_{n-1}\gamma^\nu_n}{\beta^\nu_{n-1} - \cfrac{\alpha^\nu_{n-2}\gamma^\nu_{n-1}}{\beta^\nu_{n-2} - \cdots}}}. \tag{8}$$

3 Solutions of the continued fraction equation

As an example case, we consider $l = m = 2$, $q = 0$. As ω increases from 0, the solution ν decreases from l and approaches $l - 1/2$ at around $M\omega = 0.36$. If $M\omega$ is larger than 0.36, the real solution ν disappear. The function $g_0(x)$ is shown in Fig. 1 in the cases $M\omega \le 0.36$ and in Fig. 2 in the cases $M\omega > 0.36$. At first glance, In Fig.2, there seems to be a solution at $x = l - 1/2 = 3/2$, $x = 1$ or $x = 2$. These are solutions of $g_0(x) = 0$ mathematically, but they don't produce the homogeneous solution of the Teukolsky equation.

Next we consider the solution of $g_0(z) = 0$ in the complex plane of z in the case $M\omega$ is above the critical value and we can not find the real solution. In Fig.3, we plot a contour of $|g_0(z)|$ in the case

$M\omega = 0.5$. We find that there is a minimal around $\mathrm{Re}(z) = 3/2$ and $\mathrm{Im}(z) = 0.36$. In Fig. 4, we plot $\mathrm{Re}(g_0(z))$ and $\mathrm{Im}(g_0(z))$ as a function of $\mathrm{Im}(z)$ at $\mathrm{Re}(z) = 3/2$. It is evident that there is a solution at around $z = 3/2 + 0.36i$. The precise value of the solution is $z = 3/2 + 0.36188061539416i$. It is also suggested from Fig. 3 that there are no solutions other than this value. We find that when there are no real solutions, complex solution always exists. Further, the real part of the complex solutions are always half-integer or integer. These property is the same in the case of other parameters, s, l, m and q.

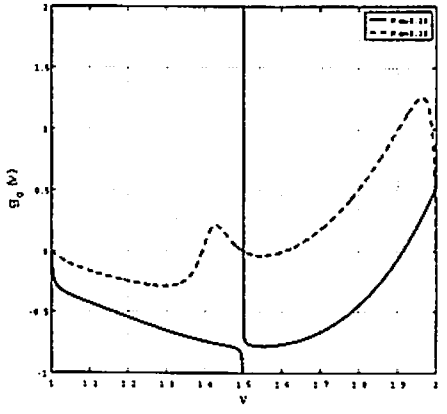


Figure 1: The function $g_0(x)$ for $M\omega = 0.20$ and 0.36. $s = -2$ and $q = 0$. There are real solutions in these cases.

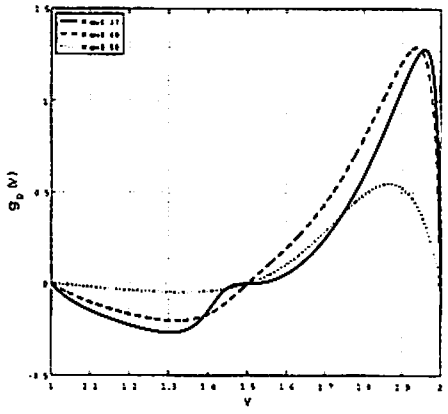


Figure 2: The function $g_0(x)$ for $M\omega = 0.37$, 0.40 and 0.50. $s = -2$ and $q = 0$. There are no real solution in these cases.

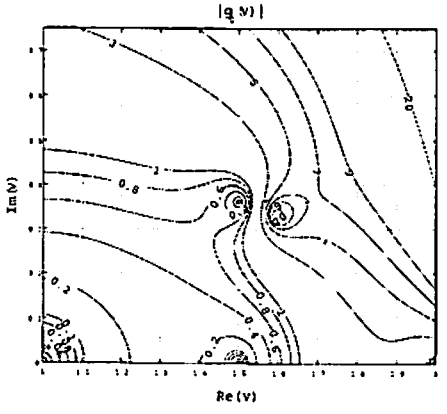


Figure 3: The $|g_0(z)|$ in the case $M\omega = 0.50$, $s = -2$, $l = m = 2$ and $q = 0$. There is a complex solution at $\nu = 1.5 + 0.36188061539416i$.

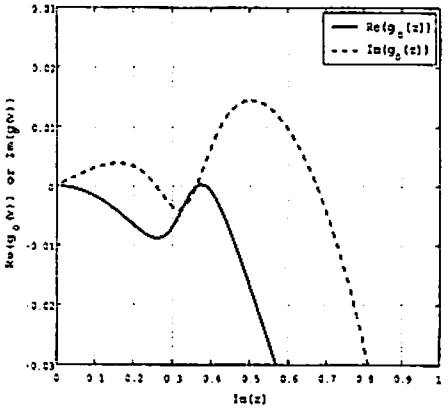


Figure 4: The real and imaginary part of the function $g_0(z)$ at $\mathrm{Re}(z) = 1.5$ in the case $M\omega = 0.50$, $s = -2$, $l = m = 2$ and $q = 0$. The real and imaginary part become 0 at $\mathrm{Im}(z) = 0.36188061539416$.

4 Numerical Results

In this section, we confirm the results of Sec.3 by computing the energy flux of the gravitational waves induced by a test particle orbiting in circular and equatorial plane around a Kerr black hole. The complete formulas are given in Appendix A of [2]. We compare our results, in the case $r_0 = 1.55M$, $q = 0.99$, and

ν is complex, with that of Kennefick[3], which are computed by numerical integration, in Table 1. We find that our numerical results agree with that of [6] for 5-7 significant figures.

Table 1: Relative error of the energy flux, up to $\ell = 7$, between Ref.[6] and our results when $r_0 = 1.55M, q = 0.99$, and ν is complex.

ℓ	$\lvert m \rvert$	Re(ν)	Im(ν)	Numerical integration	This paper	Relative error
2	2	1.5	1.1374192131794	$3.568050135 \times 10^{-2}$	$3.568033154338851 \times 10^{-2}$	4.76×10^{-6}
3	3	2.5	1.4249576682707	$2.152962111 \times 10^{-2}$	$2.152959342790158 \times 10^{-2}$	1.29×10^{-6}
4	4	3.5	1.7677955367662	$1.230541176 \times 10^{-2}$	$1.230541952573211 \times 10^{-2}$	6.31×10^{-7}
5	4	4.5	0.3735768429955	$1.933923538 \times 10^{-5}$	$1.933924400940079 \times 10^{-5}$	4.46×10^{-7}
5	5	4.5	2.1437000387424	$7.259841388 \times 10^{-3}$	$7.259849874157195 \times 10^{-3}$	1.17×10^{-6}
6	5	5.5	0.8032470628900	$1.536518877 \times 10^{-5}$	$1.536520289551414 \times 10^{-5}$	9.19×10^{-7}
6	6	5.5	2.5395166388946	$4.404590776 \times 10^{-3}$	$4.404599359654937 \times 10^{-3}$	1.95×10^{-6}
7	6	6.5	1.2521347909128	$1.148793520 \times 10^{-5}$	$1.148795883734041 \times 10^{-5}$	2.06×10^{-6}
7	7	6.5	2.9481395894691	$2.726943363 \times 10^{-3}$	$2.726949666682515 \times 10^{-3}$	2.31×10^{-6}

5 Summary and Concluding remarks

We investigated solution of the continued fraction equation and determine, ν, the "renormalized angular momentum". Although we could not find ν in real region when gravitational wave frequency becomes large, we can find it in the complex region. We compute the power radiated by gravitational waves from a particle in circular orbit in equatorial plane around a Kerr black hole using complex ν and compare our results with that of a direct numerical integration method. We find that relative errors of both methods are about 10^{-5}. Thus, the range of ω in which the MST formalism can be used for numerical analysis becomes much wider than that where ν is assumed to be real. We will apply MST's formalism using the complex solutions of ν to compute the gravitational waves from a compact star in generic orbits around a supermassive black hole in the future.

We thank D. Kennefick for kindly providing us his numerical data of the gravitational wave luminosity computed with the code developed in his work [6]. This work was supported in part by Monbukagaku-sho Grant-in-Aid for Scientific Research (Nos. 14047214, 12640269 and 16540251).

References

[1] J. R. Gair, L. Barack, T. Creighton, C. Cutler, S. L. Larson, E. S. Phinney and M. Vallisneri, Class.Quant.Grav. 21 (2004), S1595-S1606.

[2] R. Fujita and H. Tagoshi, Prog. Theor. Phys. 112 (2004), 415.

[3] Leaver, E.W., J. Math. Phys. 27, 1238 (1986).

[4] Mano, S., Suzuki, H., and Takasugi, E., Prog. Theor. Phys. 95, 1079 (1996).

[5] Mano, S., and Takasugi, E., Prog. Theor. Phys. 97, 213 (1996).

[6] K. Glampedakis and D. Kennefick, Phys. Rev. D 66 (2002) 044002.

[3]This data was calculated by D. Kennefick based on his previous work[6], and was kindly provided for us.

Supergravity Description of the open string tachyon in the D/anti D-brane system

Shinpei Kobayashi[1], Tsuguhiko Asakawa[2] and So Matsuura[3]

[1]*Research Center for the Early Universe, The University of Tokyo, 7-3-1 Hongo, Bunkyoku Tokyo 113-0033, Japan*

[2,3]*Theoretical Physics Laboratory, The Institute of Physical and Chemical Research (RIKEN), 2-1 Hirosawa, Wako, Saitama 351-0198, Japan*

Abstract

We study the tachyon condensation of the D$\bar{\text{D}}$-brane system with a constant tachyon vev in the context of classical solutions of the Type II supergravity. We find that the general solution with the symmetry $ISO(1,p) \times SO(9-p)$ (the three-parameter solution) includes the extremal black p-brane solution as an appropriate limit of the solution with fixing one of the three parameters (c_1). Furthermore, we compare the long distance behavior of the solution with the massless modes of the closed strings from the boundary state of the D$\bar{\text{D}}$-brane system with a constant tachyon vev. We find that we must fix c_1 to zero and the only two parameters are needed to express the tachyon condensation of the D$\bar{\text{D}}$-brane system. This means that the parameter c_1 does not correspond to the tachyon vev of the D$\bar{\text{D}}$-brane system. This proceeding is based on [1].

1 Introduction

This is a brief review of the paper[1] which is devoted to investigate the unstable D-brane systems and their tachyon condensation from the viewpoint of the classical solutions of the Type II supergravity[2]. Especially, we would like to understand the correspondence between the microscopic stringy objects and the classical geometry in the supergravity. It is known that the BPS D-branes and the black p-brane solutions have such correspondence. However, for unstable D-brane systems, it is not fully understood what their classical counterparts are, although there are some discussions [3].

The system we consider is that of coincident N Dp-branes and $\bar{N}$ $\bar{\text{D}}p$-branes (for simplicity we restrict ourselves to $N > \bar{N}$) and the open string tachyon excitation on them. This system is a typical example of the unstable D-brane systems. For simplicity, we assume that the tachyon profile on the world-volume is constant. In this setting, the system possesses the global symmetry $ISO(1,p) \times SO(9-p)$. Although any number of D$\bar{\text{D}}$-pairs can be annihilated by the tachyon condensation in general, we concentrate on the case where the final state is BPS saturated, that is, the system of $(N - \bar{N})$ D-branes (If we assume $(N - \bar{N}) \gg 1$, the supergravity description is valid.).

On the other hand, the general solution with the same symmetry $ISO(1,p) \times SO(9-p)$ in the Type II supergravity is known as the "three-parameter solution" [2]. Therefore, it is natural that the three parameters of the solution have a relationship to physical parameters of the D$\bar{\text{D}}$-brane system. In fact, in [3], it is argued that the three parameters correspond to microscopic quantities, that is, the number of Dp-branes N, the number of $\bar{\text{D}}p$-branes $\bar{N}$ and the tachyon vev $\langle T \rangle$, respectively. In this proceeding, we re-examine these correspondences using a new parametrization for the three-parameter solution. Since, for the extremal case, there is a direct correspondence between the boundary state for BPS Dp-brane and the black p-brane solution[4], we can apply this procedure to the non-extremal solution and can represent the parameters in the solution in terms of the string theory.

As a result, we will find that we need only two parameters to express the D$\bar{\text{D}}$-brane system. Especially, we emphasize that one of the parameters (c_1) does not correspond to $\langle T \rangle$, as opposed to the proposal which has been made so far. The physical meaning of this parameter is an open question at present, but it will be discussed in [1].

[1]E-mail:shinpei@utap.phys.s.u-tokyo.ac.jp
[2]E-mail:t.asakawa@riken.jp
[3]E-mail:matsuso@riken.jp

2 Review of the Three-parameter Solution in Ten-dimensions

In this section, we review the three-parameter solution given in [2]. We start with the ten-dimensional action,

$$S = \frac{1}{2\kappa^2}\int d^{10}x\sqrt{-g}\left[R - \frac{1}{2}(\partial\phi)^2 - \frac{1}{2(p+2)!}e^{\frac{3-p}{2}\phi}|F_{p+2}|^2\right], \tag{1}$$

where $F_{(p+2)}$ denotes the $(p+2)$-form field strength which relates to the $(p+1)$-form potential of the RR-field $\mathcal{A}^{(p+1)}$ as $F_{(p+2)} = d\mathcal{A}_{(p+1)}$. Since we consider the solution with the symmetry $ISO(1,p)\times SO(9-p)$, we impose the ansatz,

$$\begin{aligned} ds^2 &= e^{2A(r)}\eta_{\mu\nu}dx^\mu dx^\nu + e^{2B(r)}\delta_{ij}dx^i dx^j \\ &= e^{2A(r)}\eta_{\mu\nu}dx^\mu dx^\nu + e^{2B(r)}(dr^2 + r^2 d\Omega^2_{(8-p)}), \\ \phi &= \phi(r),\ \ \mathcal{A}^{(p+1)} = e^{\Lambda(r)}\, dx^0\wedge dx^1\wedge\cdots\wedge dx^p, \end{aligned} \tag{2}$$

where $\mu,\nu = 0,\cdots,p$ are indices of the longitudinal directions of the p-brane, $i,j = p+1,\cdots,9$ express the orthogonal directions, and $M = (\mu, i)$.

Authors in [2] show that the general asymptotically flat solution of the equations is given by

$$A(r) = \frac{(7-p)(3-p)c_1}{64}h(r) - \frac{7-p}{16}\ln\left[\cosh(kh(r)) - c_2\sinh(kh(r))\right], \tag{3}$$

$$\begin{aligned} B(r) = {} & \frac{1}{7-p}\ln[f_-(r)f_+(r)] \\ & - \frac{(p+1)(3-p)c_1}{64}h(r) + \frac{p+1}{16}\ln\left[\cosh(kh(r)) - c_2\sinh(kh(r))\right], \end{aligned} \tag{4}$$

$$\phi(r) = \frac{(p+1)(7-p)c_1}{16}h(r) + \frac{3-p}{4}\ln\left[\cosh(kh(r)) - c_2\sinh(kh(r))\right], \tag{5}$$

$$e^{\Lambda(r)} = -\eta(c_2^2-1)^{1/2}\,\frac{\sinh(kh(r))}{\cosh(kh(r)) - c_2\sinh(kh(r))}, \tag{6}$$

$$f_\pm(r) \equiv 1 \pm \frac{r_0^{7-p}}{r^{7-p}}, \qquad h(r) \equiv \ln\left(\frac{f_-}{f_+}\right), \qquad \eta = \pm 1, \tag{7}$$

$$k \equiv \pm\sqrt{\frac{2(8-p)}{7-p} - \frac{(p+1)(7-p)}{16}c_1^2}. \tag{8}$$

The three parameters r_0, c_1, c_2, are the integration constants that parametrize the solution. The region of the parameters is discussed in [3]. Here, for simplicity, we choose $(r_0^{7-p} \geq 0, c_2 \geq 0)$.

The RR-charge and the ADM mass of this system are, respectively,

$$Q = 2\eta N_p(c_2^2-1)^{1/2}kr_0^{7-p}, \qquad M = N_p\left(\frac{3-p}{2}c_1 + 2c_2k\right)r_0^{7-p}, \tag{9}$$

where $N_p \equiv \frac{(8-p)(7-p)\omega_{8-p}V_p}{16\kappa^2}$, and $\omega_d = \frac{2\pi^{(d+1)/2}}{\Gamma((d+1)/2)}$ is the volume of the unit sphere S^d. For convenience, we consider wrapping the spatial world-volume directions on a torus T^p of volume V_p. The RR-charge is given by an appropriate surface integral over the sphere-at-infinity in the transverse directions.

3 D/anti D-brane System in the Three-parameter Solution

In the previous section, we reviewed the ten-dimensional three-parameter solution and defined the physical quantities Q and M. In this section, we introduce another convenient parametrization for dealing with the tachyon condensation, in the sense that we can change the solution without changing the value of the RR-charge. By comparing the behavior of the solution with the boundary state corresponding to the system of N D-branes and $\bar{N}$ $\bar{\text{D}}$-branes with a constant tachyon vev, we show that we must choose $c_1 = 0$ to express the tachyon condensation of the D$\bar{\text{D}}$-brane system by the three-parameter solution.

3.1 New Parametrization

As is explained in detail in the next subsection, not the RR-charge but the mass of the D$\bar{\text{D}}$-brane system will change as the tachyon condensates. Thus, we define another parametrization by v and μ_0 to fix Q as

$$r_0^{7-p} \equiv \frac{v\mu_0}{2k}, \qquad c_2^2 - 1 \equiv \frac{1}{v^2}. \qquad (0 \le v \le \infty) \tag{10}$$

In this parametrization, the RR-charge and the ADM mass are expressed as

$$Q = \eta N_p \mu_0, \tag{11}$$

$$M = N_p \left(\sqrt{1+v^2} + \frac{3-p}{4k} c_1 v \right) \mu_0, \tag{12}$$

in which the RR-charge does not depend on v and c_1 as announced. Note that v works as the "non-extremality parameter" which denotes how much the ADM mass exceeds the RR-charge.

3.2 Comparison with the boundary state

In this subsection, we show that the D$\bar{\text{D}}$-brane system with a constant tachyon vev corresponds to the three-parameter solution of $c_1 = 0$. This means that we need only two parameters to express the D$\bar{\text{D}}$-brane system in the low-energy gravity theory. To show it, we use the correspondence between the extremal black p-brane solution and the boundary state established in [4].

The NSNS part of the ND-$\bar{N}\bar{\text{D}}$ boundary state with a constant tachyon vev is given by

$$\begin{aligned} |B_p : T\rangle_{NSNS} = \frac{T_p}{2} \left[(N-\bar{N}) + 2\mathrm{tr}\, e^{-|T|^2} \right] \delta^{(9-p)}(x^i) \\ \times \exp\left[-\sum_{n=1}^{\infty} \frac{1}{n} \alpha_{-n}^M S_{MN} \tilde{\alpha}_{-n}^N \right] \sin\left[-\sum_{r=1/2}^{\infty} b_{-r}^M S_{MN} \tilde{b}_{-r}^N \right] |0\rangle, \end{aligned} \tag{13}$$

where $S_{MN} = (\eta_{\mu\nu}, -\delta_{ij})$, $|0\rangle$ is the Fock vacuum of a closed string in the NSNS sector, and α_{-n}^M and b_{-r}^M are the creation operators of the modes of the world-sheet bosons and fermions, respectively. The trace is taken over $\bar{N} \times \bar{N}$ matrices. Note that only the difference from the BPS boundary state is the effect of the constant tachyon vev, which contributes only to the overall numerical factor $T_p[(N-\bar{N}) + 2\mathrm{tr}\, e^{-|T|^2}]$ in (13). Following [4], we obtain the behaviors of the graviton, the dilaton and the RR-potential as functions of r.

Comparing the classical solution with the result from the boundary state, first, from the results of the RR-potential, we can identify μ_0 as

$$\mu_0 = \frac{2\kappa T_p (N-\bar{N})}{(7-p)\omega_{8-p}}. \tag{14}$$

Next, from the graviton and the dilaton, we see that the parameters must satisfy the following relations simultaneously;

$$1 + \frac{2}{N-\bar{N}} \mathrm{tr}\, e^{-|T|^2} = \sqrt{1+v^2} + \frac{3-p}{4} \frac{c_1 v}{k} = \sqrt{1+v^2} - \frac{(p+1)(7-p)}{4(3-p)} \frac{c_1 v}{k}, \tag{15}$$

which are consistent only when $c_1 = 0$. From this consideration, we conclude that the three-parameter solution with

$$\begin{aligned} c_1 &= 0, \\ \mu_0 &= \frac{2\kappa T_p (N-\bar{N})}{(7-p)\omega_{8-p}}, \\ \sqrt{1+v^2} &= 1 + \frac{2}{N-\bar{N}} \mathrm{tr}\, e^{-|T|^2}, \end{aligned} \tag{16}$$

corresponds to the system of N D-branes and $\bar{N}$ $\bar{\text{D}}$-branes with a constant tachyon vev. We emphasize that the vev of the open string tachyon between the D-branes and the $\bar{\text{D}}$-branes does not correspond to c_1, but corresponds to v, in contrast to the previous expectation.

4 Conclusion and Discussion

In this review, we discussed the tachyon condensation of the system of N D-branes and $\bar{N}$ $\bar{\text{D}}$-branes with a constant tachyon vev T using the general solution of the Type II supergravity with the symmetry $ISO(1,p) \times SO(9-p)$. Since the solution is parametrized by the three parameters c_1, c_2 and r_0, it is called the "three-parameter solution".

The three-parameter solution is thought to be the low energy counterpart of the D$\bar{\text{D}}$-brane system with a constant tachyon vev. In order to clear the relation between the D$\bar{\text{D}}$-brane system and the three-parameter solution, we compared the long distance behavior of the three-parameter solution with the massless modes of the closed string from the D$\bar{\text{D}}$-brane boundary state. We discussed that we can apply the relation between the classical solution and the boundary state to our case, although the D$\bar{\text{D}}$-brane system is a non-BPS state except at the end of the tachyon condensation. In this connection, we can similarly apply this method to any other sources that are non-BPS or unstable.

When we compared the solution with the boundary state, we introduced the parametrization $\{\mu_0, v\}$ so that we can fix the RR-charge. In fact, the RR-charge is conserved during the tachyon condensation, and the parametrization $\{c_2, r_0\}$ is not suitable to such a situation. In contrast, the parametrization $\{\mu_0, v\}$ is convenient for our purpose because it makes the RR-charge depend only on μ_0, and we can change the ADM mass without changing μ_0.

By comparing the long distance behavior of the three-parameter solution with the massless mode of the closed string from the boundary state of the D$\bar{\text{D}}$-brane system, we found that we must fix c_1 to zero and the only two parameters μ_0 and v (or c_2 and r_0) are needed to express the D$\bar{\text{D}}$-brane system. This result means that we can see the tachyon vev not as an independent parameter in the supergravity solution but as a part of the ADM mass. This fact is consistent with the form of the boundary state, that is, the tachyon vev is included in the coefficient of the NSNS sector of the boundary state as shown in (13), and the coefficient is nothing but the ADM mass of the solution. So we concluded that the D$\bar{\text{D}}$-brane system corresponds to the three-parameter solution of $c_1 = 0$. If c_1 turns on, the long distance behavior of the three-parameter solution can not be reproduced by the boundary state of the D$\bar{\text{D}}$-brane system. This means that c_1 relates to another physical quantity in the string theory, which will be discussed in the paper in preparation [5].

References

[1] S. Kobayashi, T. Asakawa and S. Matsuura, "Open String Tachyon in Supergravity Solution," [arXiv:hep-th/0409044].

[2] B. Zhou and C. Zhu, "The complete black brane solutions in D-dimensional coupled gravity system," [arXiv:hep-th/9905146].

[3] P. Brax, G. Mandal and Y. Oz, "Supergravity description of non-BPS branes," Phys. Rev. D **63** (2001) 064008 [arXiv:hep-th/0005242].

[4] P. Di Vecchia, M. Frau, I. Pesando, S. Sciuto, A. Lerda and R. Russo, "Classical p-branes from boundary state," Nucl. Phys. B **507** (1997) 259 [arXiv:hep-th/9707068]; P. Di Vecchia, M. Frau, A. Lerda and A. Liccardo, "(F,Dp) bound states from the boundary state" Nucl. Phys. B **565** (2000) 397 [arXiv:hep-th/9906214];

[5] T. Asakawa, S. Kobayashi and S. Matsuura, work in progress.

The Condition of Black Hole Formation in Five-Dimensional Space-Times

Chul-Moon Yoo[1], Ken-ichi Nakao[2], Daisuke Ida[3]

[1,2]*Department of Mathematics and Physics, Graduate School of Science, Osaka City University, Osaka 558-8585, Japan*

[3]*Department of Physics, Gakushuin University, Tokyo 171-8588, Japan*

Abstract

We study the condition of black hole formation in five-dimensional space-times. We analytically solve the constraint equations of five-dimensional Einstein equations for momentarily static and conformally flat initial data sets to give a gravitational field produced by a spheroidal mass. We numerically search for apparent horizons and find both necessary and sufficient conditions for the horizon formation in terms of inequalities relating a geometric quantity and the mass.

1 Introduction

In an attempt to unify fundamental forces including gravity, the possibility that the space-time dimensions of our universe is higher than four has been much discussed. Such higher dimensional theories need mechanism to reduce the space-time dimensions down to four. The brane world scenario is an attractive idea of dimensional reduction. In this scenario, the standard model particles are confined to the boundary of higher-dimensional space-time and only gravity can propagate in the extra dimensions.

Some model of the brane world scenario suggest that small black holes are produced in accelerators, such as the CERN Large Hadron Collider [2] or in high energy cosmic ray events [3]. In order to understand physical phenomena caused by strong gravitational fields, the criterion for black hole formation is very crucial. In the case of four-dimensional Einstein gravity, such a criterion is well known as the hoop conjecture; *"Black holes with horizons form when and only when a mass M gets compacted into a region whose circumference in every direction is $\mathcal{C} \lesssim 4\pi G_4 M$."*, where G_4 is the gravitational constant in four-dimensional theory of gravity [4]. It is remarkable that no serious counterexample against the hoop conjecture has been presented.

Recently, two of the present authors, DI and KN, proposed a higher dimensional version of hoop conjecture (*the hyperhoop conjecture*) : *"Black holes with horizons form when and only when a mass M gets compacted into a region whose $(D-3)$-dimensional area V_{D-3} in every direction is*

$$V_{D-3} \lesssim G_D M\text{."}, \tag{1}$$

where G_D is the gravitational constant in D-dimensional theory of gravity, and the $(D-3)$-dimensional area means a volume of $(D-3)$-dimensional closed submanifold (*the hyperhoop*) of a spacelike hypersurface [5]. The necessity of the condition (1) was confirmed in some cases [5],[8] and consistent results with the previous ones were obtained by C. Barrabés *et al* in the case of a $(D-2)$-dimensional convex thin shell collapsing with the speed of light in D-dimensional space-time [6].

The purpose of the present paper is to study both the necessity and in particular *sufficiency* of the inequality (1) in different situations from the case treated by Barrabés *et al*. We consider the momentarily static and conformally flat four-dimensional initial hypersurfaces in which a four-dimensional homogeneous spheroid is put as a gravitational source. As will be shown later, we can solve constraint equations of five-dimensional Einstein equations and set analytically the initial data set. Then in order to investigate the validity of hyperhoop conjecture, we numerically search for apparent horizons and calculate the ratio $V_2/G_5 M$ for substantially various hyperhoops.

[1]E-mail:c_m_yoo@sci.osaka-cu.ac.jp
[2]E-mail:knakao@sci.osaka-cu.ac.jp
[3]E-mail:daisuke.ida@gakusyuin.ac.jp

This paper is organized as follows. In Sec.2, we give analytic solutions of the constraint equations. In Sec.3, we search for apparent horizons and calculate the minimal value of V_2/G_5M. Numerical results and their implication to the necessary and sufficient condition for the horizon formation are shown in this section. Finally, Sec.4 is devoted to summary.

In this paper, we adopt the unit of $c = 1$ and the conventions of metric and Riemann tensors follow Ref.[7].

2 A Momentarily static spheroid in five-dimensional space-times

Let us consider an initial data set (h_{ab}, K_{ab}) in a four-dimensional spacelike hypersurface Σ, where h_{ab} is the induced metric in Σ and K_{ab} is the extrinsic curvature. The initial data set (h_{ab}, K_{ab}) has to satisfy the Hamiltonian and momentum constraints. In this paper, we focus on momentarily static $K_{ab} = 0$ and conformally flat $h_{ab} = f^2\delta_{ab}$ initial hypersurfaces, where δ_{ab} is the metric tensor of four-dimensional Euclid space. Further we require the axial symmetry for the initial hypersurfaces. Thus the line element in the initial hypersurface Σ is written as

$$dl^2 = f^2(R,z)\left\{dR^2 + R^2\left(d\theta^2 + \sin^2\theta d\phi^2\right) + dz^2\right\}, \tag{2}$$

where $0 \leq R < +\infty$ and $-\infty < z < +\infty$ while θ and ϕ are the round coordinates. Then the momentum constraint leads to vanishing energy flux and the Hamiltonian constraint becomes

$$\frac{\partial^2 f.}{\partial R^2} + \frac{2}{R}\frac{\partial f}{\partial R} + \frac{\partial^2 f}{\partial z^2} = -4\pi^2 G_5 f^3 \rho, \tag{3}$$

where ρ is the energy density.

Let us consider the following density profile consistent with the axial symmetry,

$$f^3\rho = \begin{cases} 2M/\pi^2 a^3 b & \text{for} \quad R^2/a^2 + z^2/b^2 \leq 1, \\ 0 & \text{for} \quad \text{else where}, \end{cases} \tag{4}$$

where a, b and M are constant. Here note that by virtue of the density profile (4), the Hamiltonian constraint (3) is equivalent to the four-dimensional Poisson equation for "Newtonian" gravitational potential produced by a homogeneous spheroid.

We assume asymptotic flatness which leads to the boundary condition for the conformal factor f at spatial infinity as

$$f \to 1 \quad \text{for} \quad r \to \infty; \; r = \sqrt{R^2 + z^2}. \tag{5}$$

The regular solution is then obtained as

$$f = 1 + \frac{4G_5M\left\{b(2a+b)R^2 + 3a^2z^2 - 3ab(a^2+b^2)\right\}}{3a^3b(a+b)^2} \quad \text{for} \quad \frac{R^2}{a^2} + \frac{z^2}{b^2} \leq 1, \tag{6}$$

$$f = 1 - \frac{4G_5M}{3e^4b^4}\left[2R^2 - 6z^2 + 3e^2b^2 + \sqrt{F^2 - e^4b^4}\right.$$
$$\left. \times \left\{\frac{2e^2b^2R^2}{(F - e^2b^2)^2} - \frac{2R^2 - 3z^2 + 3e^2b^2}{F - e^2b^2} + \frac{3z^2}{F + e^2b^2}\right\}\right] \quad \text{for} \quad \frac{R^2}{a^2} + \frac{z^2}{b^2} > 1, \tag{7}$$

where e is the eccentricity defined by $e = \sqrt{1 - \frac{a^2}{b^2}}$ and F is a function of R and z defined by

$$F = F(R,z;a,b) = R^2 + z^2 + \sqrt{4b^2R^2 - 4a^2\left(b^2 - z^2\right) + \left(a^2 + b^2 - R^2 - z^2\right)^2}. \tag{8}$$

In this paper, we investigate the prolate case $a < b$ only.

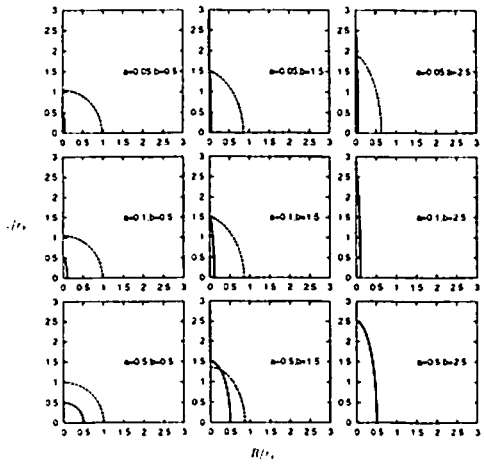


Figure 1: Apparent horizons for each shape of the four-dimensional spheroid are depicted in (R, z)-plane. The solid line shows the surface of the spheroid. The dashed line shows the apparent horizon if it is present. The coordinate value is normalized by the radius r_s of the apparent horizon which is in the case of a point source.

3 Apparent horizons and numerical results

We numerically search for apparent horizons which have same symmetry as the initial hyper surface by the relaxation method [9]. Typical examples are shown in Fig.1.

Here we should note that in general, the mass M in hyperhoop conjecture (and also in hoop conjecture) is not the total mass of the system but the mass encircled by the hyperhoop (the hoop). Therefore to check the sufficiency of this conjecture, we have to confirm that in an initial hypersurface without an apparent horizon, there is no hyperhoop satisfying $V_{D-3} \lesssim G_D M_{\rm in}$, where $M_{\rm in}$ is the mass included in the region which is encircled by this hyperhoop. In the framework of general relativity, there is no unique definition of the mass in a quasi-local manner. However, despite of this mathematical indefiniteness, hoop and hyperhoop conjectures might be useful in roughly understanding black-hole formation processes on the physical ground. In this sense, all the reasonable definitions of quasi-local mass will be meaningful in hoop and hyperhoop conjectures since these might give the results not so different from each other. Here we adopt the following simple definition for the mass $M_{\rm in}$ as

$$M_{\rm in} = 8\pi \int_0^{\pi/2} d\xi \int_0^{r_h(\xi)} dr \rho f^3 r^3 \sin^2 \xi. \tag{9}$$

In the present situation, in practice, we cannot investigate all possible hyperhoops in the initial hypersurfaces. By this reason, in this paper, we focus on axisymmetric hyperhoops which have the reflection symmetry with respect to $z = 0$. Further, since the spheroid is assumed to be prolate $a < b$, these hyperhoops are expressed in the form $r = r_h(\xi)$ and $\theta = \pi/2$, where $\xi = \arctan \frac{R}{z}$. Hereafter for notational simplicity, we introduce

$$\Gamma := \frac{V_2}{16\pi G_5 M_{\rm in}}, \tag{10}$$

where $16\pi G_5 M$ is the value of V_2 in the point source case $a = 0, b = 0$. We select the significant hyperhoops from all the possible hyperhoops expressed by $r = r_h(\xi)$ and $\theta = \pi/2$ with the reflection symmetry with respect to $z = 0$ (details are in [1]). For various a and b, numerical results of the minimal value of Γ are listed in Table1. Hereafter we denote the minimal value of Γ by $\Gamma_{\rm min}$ which is a function of a and b. We see from Table1 that $\Gamma_{\rm min}$ is not smaller than unity in the case of no apparent horizon. This means that the sufficiency of the inequality (1) is confirmed in the situations presented here.

Next, let us consider about necessity of hyperhoop conjecture. Investigating the singular spindle line source case which has a constant line density, we can find the necessary condition sugessted in [5] as

Table 1: ($\Gamma_{\rm min}$) is shown for each a and b. The existence of an apparent horizon is represented by (Yes):exist and (No):not exist.

$b\backslash a$	0.01	0.1	0.3	0.5	0.7	0.9
1.0	1.05(Yes)	1.05(Yes)	1.05(Yes)	1.04(Yes)	1.03(Yes)	1.01(Yes)
1.5	1.11(Yes)	1.11(Yes)	1.10(Yes)	1.10(Yes)	1.09(No)	1.08(No)
2.0	1.17(Yes)	1.17(Yes)	1.17(No)	1.16(No)	1.16(No)	1.17(No)
2.5	1.23(Yes)	1.23(No)	1.23(No)	1.23(No)	1.24(No)	1.26(No)
3.0	1.29(Yes)	1.29(No)	1.29(No)	1.30(No)	1.31(No)	1.35(No)
3.5	1.34(No)	1.34(No)	1.34(No)	1.35(No)	1.38(No)	1.43(No)
4.0	1.38(No)	1.38(No)	1.38(No)	1.40(No)	1.44(No)	1.51(No)

$\Gamma_{\rm min} \lesssim \frac{\pi}{2}$. The derivation of this quantity $\pi/2$ is shown in [1]. The counterexample for this condition can not be found in Table1.

4 Summary

In this paper we have investigated the condition for apparent-horizon formation in the case of momentarily static and conformally flat initial data of a spheroidal mass in the framework of five-dimensional Einstein gravity. The confirmation for hyperhoop conjecture was attempted in the case of $D = 5$, and we obtained the consistent result with this conjecture. Particularly, we confirmed the sufficiency of the inequality (1) for the present case.

Acknowledgements

We are grateful to H. Ishihara and colleagues in the astrophysics and gravity group of Osaka City University for helpful discussion and criticism. This work is supported by the Grant-in-Aid for Scientific Research (No.16540264) from JSPS.

References

[1] C. Yoo, K. Nakao and D. Ida, in preparation.

[2] P. C. Argyres, S. Dimopoulos and J. March-Russell, Phys. Lett. B 441, 96 (1998) [arXiv:hep-th/9808138] ; T. Banks and W. Fischler, arXiv:hep-th/9906038 ; S. Dimopoulos and G. Landsberg, Phys. Rev. Lett. 87, 161602 (2001) [arXiv:hep-ph/0106295] ; S. B. Giddings and S. Thomas, Phys. Rev. D 65, 056010 (2002) [arXiv:hep-ph/0106219] ; E. J. Ahn, M. Cavaglia and A. V. Olinto, Phys. Lett. B 551, 1 (2003) [arXiv:hep-th/0201042].

[3] J. L. Feng and A. D. Shapere, Phys. Rev. Lett. 88, 021303 (2002) [arXiv:hep-ph/0109106] ; R. Emparan, M. Masip and R. Rattazzi, Phys. Rev. D 65, 064023 (2002) [arXiv:hep-ph/0109287] ; L. Anchordoqui and H. Goldberg, Phys. Rev. D 65, 047502 (2002) [arXiv:hep-ph/0109242].

[4] K.S. Thorne, in *Magic Without Magic*, edited by J. Klauder (Freeman, San Francisco, 1972).

[5] D. Ida and K. i. Nakao, Phys. Rev. D 66, 064026 (2002) [arXiv:gr-qc/0204082].

[6] C. Barrabes, V. P. Frolov and E. Lesigne, Phys. Rev. D 69, 101501 (2004) [arXiv:gr-qc/0402081].

[7] R.N. Wald, *General Relativity*, (University of Chicago Press, Chicago, 1984).

[8] H. Yoshino and Y. Nambu, Phys. Rev. D 67, 024009 (2003) [arXiv:gr-qc/0209003].

[9] M. Sasaki, K. Maeda, S. Miyama and T. Nakamura, Prog. Theor. Phys. 63, 1051 (1980).

Evolution of Gravitational Waves in the High-energy Regime of Brane-world Cosmology

Takashi Hiramatsu [1], Kazuya Koyama, Atsushi Taruya

Theoretical Astrophysics Group, Department of Physics, University of Tokyo, Japan

Abstract

We discuss the evolution of gravitational waves (GWs) after inflation in a brane-world cosmology based on the Randall-Sundrum single-brane model. In this brane-world scenario, the evolution of GWs is affected by the non-standard cosmological expansion and the excitation of the Kaluza-Klein (KK) modes in high-energy regime of the universe. We numerically solve the wave equation of GWs in the Poincaré coordinates of the AdS_5 spacetime and find that these effects may compensate each other and the spectrum of the GW background mimics one predicted in 4D theory.

1 Introduction

The stochastic background of gravitational waves (SBGW) generated in the inflationary epoch can provide a direct way to probe the very early universe. In particular, information about extra-dimensions motivated by recent developments in particle physics is expected to be imprinted on the SBGW. In this paper, we focus on the brane-world cosmology based on the Randall-Sundrum single-brane model [1] in which a 3D brane is embedded in the 5D anti-de Sitter (AdS_5) bulk spacetime. According to this scenario, gravity propagates in the extra spatial dimensions, while the standard model particles are confined to the brane.

The important model parameter is the AdS_5 curvature radius $\ell < 0.1$mm. In the context of cosmology, at low-energy regime of the Universe ($H\ell < 1$), 4D general relativity is successfully recovered and the extra-dimensional effects should be fairly small. On the other hand, at high-energy regime ($H\ell > 1$), there are theoretically two main effects on the evolution of SBGW : (i) the cosmological expansion becomes slow compared with that in 4D general relativity, which enhances the amplitude of the SBGW and (ii) the excitation of Kaluza-Klein modes (KK-modes) suppresses the amplitude of the GWs on the brane. From this point of view, the critical frequency of the present spectrum of SBGW can be defined as $f_{\rm crit} = 0.2\mathrm{mHz}\,(0.1\mathrm{mm}/\ell)^{1/2}$, which is corresponding to the wavelength of the gravitational waves (GWs) that cross the horizon when $H\ell = 1$.

In this paper, we solve numerically the wave equation of GWs in the radiation-dominated (RD) epoch of the universe using the Poincaré coordinate system instead of the Gaussian normal (GN) coordinates [2] and investigate the high-energy effects.

2 Basic equations and initial conditions

We specifically consider the pure AdS_5 bulk and assume the flat Friedmann universe on the brane (the equation of state is $p = w\rho$). In the Poincaré coordinate system $(\tau, \mathbf{x}, z)$, the brane is moving in the static AdS_5 bulk. The metric is given by

$$ds^2 = \left(\frac{\ell}{z}\right)^2 \{-d\tau^2 + (\delta_{ij} + h_{ij})dx^i dx^j + dz^2\}, \tag{1}$$

where h_{ij} is the tensor perturbation satisfying the transverse and the traceless conditions. In this metric, the trajectory of the brane is described as $(\tau_b, z_b) = (T(t), \ell/a(t))$, where the variable t is the cosmic time on brane and the function $T(t)$ is given by $dT/dt = \sqrt{1 + (H\ell)^2}/a$. From the junction conditions, the Friedmann equation and the conservation law become [3]:

$$H^2(t) = \left(\frac{\dot{a}}{a}\right)^2 = \frac{\kappa_4^2}{3}\rho\left(1 + \frac{\rho}{2\lambda}\right), \qquad \dot{\rho} = -3(1+w)H\rho, \quad (\kappa_4^2 = 8\pi G). \tag{2}$$

[1] E-mail:hiramatsu-at-utap.phys.s.u-tokyo.ac.jp

where the dot denotes a derivative with respect to t. In the RD case ($w = 1/3$), the solutions for the scale factor $a(t)$ and the normalized energy density defined by $\epsilon(t) \equiv \rho(t)/\lambda$ are expressed as (e.g., [3]):

$$a(t) = a_* \left(\frac{2t^2 + t\ell}{2t_*^2 + t_*\ell} \right)^{1/4}, \quad \epsilon(t) \equiv \frac{\rho(t)}{\lambda} = \frac{\ell^2}{8t^2 + 4t\ell}. \tag{3}$$

In our numerical simulation, we set $a_* = 1$ without loss of generality. The meanings of the quantity t_* will be given in next section.

Next consider the tensor perturbation h_{ij} in the metric (1). For convenience, we decompose the quantity h_{ij} in spatial Fourier modes as $h_{ij} = h_k(\tau, z) e^{ik\cdot x} \hat{e}_{ij}$, where $\hat{e}_{ij}$ represents a transverse-traceless polarization tensor. Then the evolution equation for the perturbation $h_k(\tau, z)$ and the boundary condition at the brane determined from the junction condition become respectively

$$\frac{\partial^2 h}{\partial \tau^2} - \frac{\partial^2 h}{\partial z^2} + \frac{3}{z}\frac{\partial h}{\partial z} + k^2 h = 0, \qquad \left(\frac{\partial}{\partial \tau} - \frac{\sqrt{1 + (H\ell)^2}}{H\ell} \frac{\partial}{\partial z} \right) h \Big|_{z = z_b(t)} = 0. \tag{4}$$

Here we simply omit the subscript k.

The initial condition for the perturbed quantity h just after inflation is determined by the quantum fluctuations in the inflationary epoch. According to Ref. [4], the zero-mode solution in the GN coordinates (η, y) gives a dominant contribution to the metric fluctuation which is given by $h(\eta, y) = C(-k\eta)^{3/2} H^{(1)}_{3/2}(-k\eta)$, where C is a normalization constant and η is the conformal time. Transforming this expression into the Poincaré coordinate ($z = -\eta \sinh(y/\ell)$, $\tau = \eta \cosh(y/\ell)$), one can see that there should be mixtures of KK-modes to express the zero-mode solution even in the inflationary epoch. Nevertheless, in the long-wavelength limit $k \to 0$, both the zero-mode solutions become constant over the time and the bulk space and they coincide with each other. Since we are specifically concerned with the evolution of long-wavelength GWs after inflation, the constant mode, i.e., $h = $ const. and $dh/d\tau = 0$, seems a natural and a physically plausible initial condition for our numerical calculation in the Poincaré coordinate. In the RD epoch, however, the mode decomposition becomes generally impossible in GN coordinates due to the non-separable form of the background metric (e.g.,[3]), which is true even in the long-wavelength GWs. Thus, the validity of the initial condition $h = $ const., must be checked.

3 Results

Given the initial condition $h(t_0, z) = $ const., the remaining free parameters in our numerical simulation are the wave number k and the initial time t_0. For convenience, we set the wave number k to $k = a(t_*)H(t_*) = a_* H_*$, that is, the GW just crosses the Hubble horizon at the time $t = t_*$ (see Eq.(3)). Also, we introduce the quantity s_0 given by $s_0 \equiv a(t_0)H(t_0)/k$. Thus, the free parameters may be represented by the dimensionless energy at the horizon-crossing time, $\epsilon_* \equiv \epsilon(t_*)$ and the normalized wavelength at initial time, s_0. The following numerical results are presented for various choices of the parameters (s_0, ϵ_*).

3.1 Sensitivity to the initial condition

Let us first consider the initial condition after inflation and check the validity of the assumption $h(t_0, z) = $ const. for long-wavelength GWs.

The upper panel in Fig.1 shows the case of the de Sitter brane ($w = -1$). The lower panel shows the case of the RD brane ($w = 1/3$). In both panels, we set $\epsilon_* = 1.0$ with $s_0 = 100$. In the de Sitter case, the resultant GW amplitude remains constant not only on the brane but also in the bulk. On the other hand, in the RD case, the constancy of the GW amplitude no longer holds in the bulk even before $\tau \approx -1$, where the wavelength of GW on brane just crosses the Hubble horizon. In particular, the constancy along the z-direction is clearly broken and one can see the propagation of the GW emanating from the physical brane. This indicates that the excitation of KK-modes occurs even if the wavelength of GWs is still outside the Hubble horizon. These results show the different behaviors simply arise from the difference in the motion of the brane.

In Fig.2, the dependence of the evolution of GWs on the initial time is plotted by varying the parameter s_0. Left panels show the snapshots of the amplitude $h(\tau, z)$ in the bulk when the wavelength of GWs just becomes five times larger than the Hubble horizon, i.e., $aH/k = 5$. On the other hand, right panels show the time evolution of GWs projected on the brane. Clearly, in the bulk, the amplitude of GWs is very sensitive to the choice of the parameter s_0, or equivalently, the initial time t_0. By contrast, on the brane, the GW amplitudes tend to converge if we set the initial time t_0 early enough (or set s_0 large enough). From this fact, all results shown in the next subsection are obtained setting large $s_0(\geq 25)$.

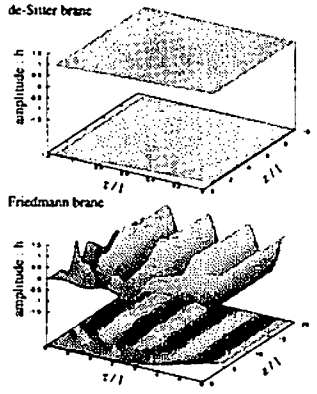


Fig. 1. The evolution of a GW in the bulk. *Upper* : a de Sitter brane, *Lower* : a Friedmann brane.

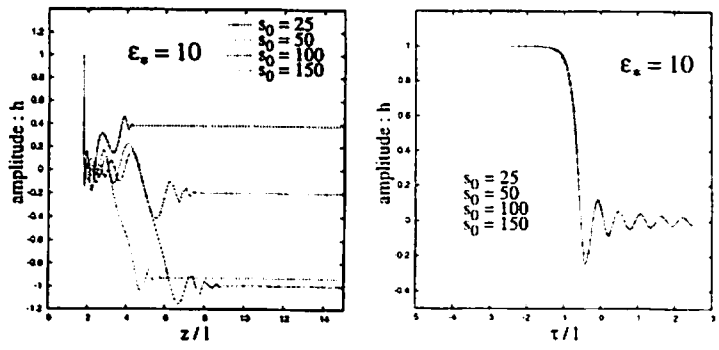


Fig. 2. *Left*: Snapshots of the GW amplitudes at $aH/k = 5$ in the bulk for various s_0. *Right* : Evolved results of GWs projected on the brane starting with the various initial times.

3.2 Influence of high-energy effects on spectrum of SBGW

We introduce the reference wave $h_{\rm ref}$, which is a solution of the 4D wave equation just replacing the scale factor and the Hubble parameter defined in the standard Friedmann equation with those defined in the modified Friedmann equation (Eqs. (2) and (3)):

$$\ddot{h}_{\rm ref} + 3H\dot{h}_{\rm ref} + \left(\frac{k}{a}\right)^2 h_{\rm ref} = 0. \tag{5}$$

Comparing numerical simulations with the solution of the wave equation (5), the effect of the excitation of KK-modes can be quantified.

Fig.3 shows the squared amplitude of the GWs, $h_{\rm 5D}^2$ and $h_{\rm ref}^2$, as functions of the scale factor a. The left and right panels show the low-energy case ($\epsilon_* = 0.1$) and high-energy case ($\epsilon_* = 10$) respectively. As we increase the energy scale at horizon crossing time, the GW amplitude $h_{\rm 5D}$ becomes significantly reduced compared to the reference wave, $h_{\rm ref}$. Since the late-time evolution of GWs simply scales as $h \propto 1/a$ in both $h_{\rm 5D}$ and $h_{\rm ref}$, the results may be interpreted as the excitation of KK-modes during crossing the horizon. Note that ϵ_* is related to the observed proper frequency $2\pi f = k/a(t_{\rm today})$ as $f/f_{\rm crit} = (\epsilon_{\rm crit}/\epsilon_*)^{1/4} H_*\ell$, where $\epsilon_{\rm crit} = \sqrt{2} - 1$ and the critical frequency $f_{\rm crit}$ is defined by $H_*\ell = 1$ which typically yields $f_{\rm crit} = 0.2{\rm mHz}\,(0.1{\rm mm}/\ell)^{1/2}$.

Based on the results in Fig.3, we estimated the ratio of the amplitude $|h_{\rm 5D}/h_{\rm ref}|$ long after the horizon crossing time for various frequencies (Fig.4). As a reference, we also show the convergence properties of the ratio $|h_{\rm 5D}/h_{\rm ref}|$ by varying the initial time; $s_0 = 25 \sim 200$. Clearly, the ratio $|h_{\rm 5D}/h_{\rm ref}|$ monotonically decreases with the frequency and the suppression of amplitude $h_{\rm 5D}$ becomes significant above the critical frequency $f_{\rm crit}$ (vertical solid line). Using the data points in the asymptotic region $\epsilon_* \geq 5$, we try to fit the ratio of amplitudes with $s_0 = 200$ to a power-law function. The result based on the least-square method becomes

$$\left|\frac{h_{\rm 5D}}{h_{\rm ref}}\right| = 0.76\left(\frac{f}{f_{\rm crit}}\right)^{-0.67} \tag{6}$$

The power-law fit (6) can be immediately translated to the spectrum of SBGW as follows. To evaluate the spectrum, we conventionally use the density parameter of SBGW $\Omega_{\rm GW}(f) \equiv \rho_c^{-1}(d\rho_{\rm GW}/d\log f) \propto f^2h^2$. where $\rho_{\rm GW}$ is the energy density of SBGW and ρ_c is the critical density. We found the blue spectrum $\Omega_{\rm GW} \propto f^{4/3}$ for the reference wave $h_{\rm ref}$. Then, combining the fitting result (6), the SBGW spectrum becomes nearly flat, i.e., $\Omega_{\rm GW} \propto f^0$ above the critical frequency.

This result seems almost indistinguishable from the standard 4D prediction and slightly contradicts with the result by Ichiki and Nakamura [5], who predict $\Omega_{\rm GW} \propto f^{-0.46}$ from the numerical simulation based on a null coordinate system. At present, the reason for this discrepancy is unclear.

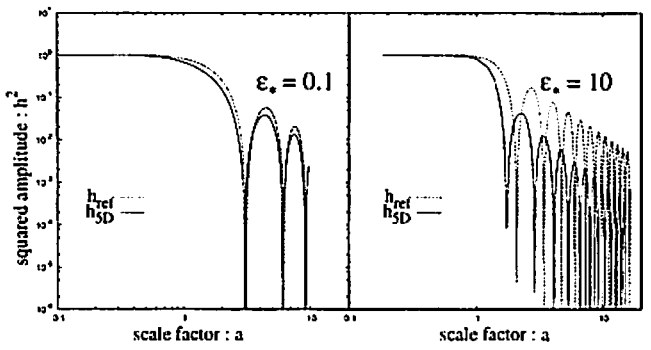


Fig. 3. Squared amplitude of GWs on the brane in low-energy (*left*) and the high-enery (*right*) regimes. *Solid line*: the numerical solutions, *Dashed line*: the amplitudes of reference wave $h_{\rm ref}$.

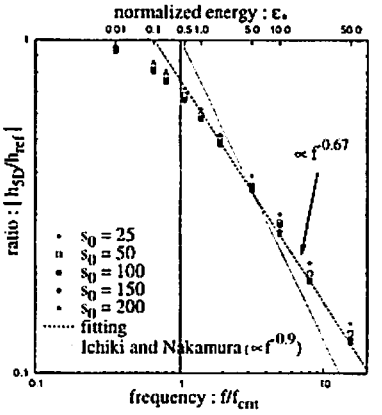


Fig. 4. Frequency dependence of the ratio of amplitudes $|h_{\rm 5D}/h_{\rm ref}|$.

4 Summary

We numerically studied the behavior of GWs in the high-energy regime of the universe in the Randall-Sundrum single-brane model with the Poincaré coordinate system.

We have confirmed that the constant mode, $h(\tau, z)$ =const., in the Poincaré coordinates just after inflation is a plausible initial condition from inflation. In the RD epoch, however, the constant mode does not hold in the bulk. Thus, in principle, we have to start our numerical calculations just after inflation. Fortunately, however, the resultant amplitude of the GWs on the brane becomes insensitive to the initial time t_0 of our numerical simulation if we set t_0 sufficiently early.

Based on these discussions, we turn to focus on the frequency dependence of the high-energy effects in order to predict the spectrum of SBGW. We found that the excitation of KK-modes compensates the effect of non-standard cosmological expansion. As a result, the density parameter of SBGW scales as $\Omega_{\rm GW} \propto f^0$ above the critical frequency $f_{\rm crit} = 0.2{\rm mHz}\,(0.1{\rm mm}/\ell)^{1/2}$.

For details, see Ref.[6].

References

[1] L.Randall and R.Sundrum, *Phys. Rev. Lett.* **83** (1999) 4690.

[2] T.Hiramatsu, K.Koyama and A.Taruya, *Phys. Lett.* **B578** (2004) 239.

[3] R.Maartens, *Living Rev. Rel.* **7** (2004) 1.

[4] D.Langlois, R.Maatens and D.Wands, *Phys. Lett.* **B489** (2000) 259.

[5] K.Ichiki and K.Nakamura, [astro-ph/0406606].

[6] T.Hiramatsu, K.Koyama and A.Taruya, *Phys. Lett. B*, in press.

Cohomogeneity One Cosmic Strings in Maximally Symmetric Spacetime

Hiroshi Kozaki[1] and Hideki Ishihara[2]

Department of Mathematics and Physics, Graduate School of Science, Osaka City University, Sugimoto, Sumiyoshi-ku, Osaka, 558-8585, Japan

Abstract

Making use of a Killing vector of the spacetime, we can reduce the equations of motion for a Nambu-Goto string to ordinary differential equations. We call this kind of string cohomogeneity one. Introducing an equivalence relation, we classify the cohomogeneity one strings in a given spacetime. We find that cohomogeneity one cosmic strings are categorized into seven classes in Minkowski spacetime.

1 Introduction

Cosmic string equations of motion are in the form of *partial* differential equations, which are so complicated that it is, in general, difficult to solve. However, when the background spacetime is symmetric, the equations of motion for a cosmic string whose world sheet is tangent to the Killing vector can be reduced to *ordinary* differential equations. In this paper, we call this type of cosmic string *cohomogeneity one*. Reduction to the ordinary differential equations helps us to solve the equations of motion. In some cases, exact solutions are available.

In a stationary spacetime, the cohomogeneity one cosmic string, which is tangent to the timelike Killing vector, is just a stationary cosmic string. The stationary strings are well investigated in some stationary spacetimes such as Minkowski spacetime and Kerr-Newmann spacetime [1, 2, 3]. In these spacetimes, there are some (as much as 10 in Minkowski spacetime) linearly independent Killing vectors. One is the generator of time translation, and the others are those of (i) spatial translations, rotations and Lorentz boosts in case of Minkowski spacetime, and (ii) rotation around the axes in case of the Kerr-Newmann spacetime. For every timelike linear combination of the Killing vectors, stationary string configurations are possible. In the Kerr-Newmann spacetime, the possible combination consists only of the generators of time translation and the rotation. The associated stationary strings, which are called rigidly rotating, are studied; especially the special configuration in which the string is confined on the equatorial plane is investigated in detail [3]. On the other hand, in Minkowski spacetime, there are so much variety of the linear combinations of the Killing vectors that all the configurations have not investigated yet. Only the rigidly rotating strings are investigated, and their exact solutions are found in general situation [3].

The aim of this paper is clarifying how much kind of cohomogeneity one strings are possible in Minkowski spacetime. For this aim, we introduce an equivalence relation for the configurations of cosmic strings. Restricted to the cohomogeneity one strings, this equivalence relation is translated to that for the Killing vectors. Classifying the Killing vectors, we find that there are only *seven* kind of cohomogeneity one strings in Minkowski spacetime.

2 Cohomogeneity One Cosmic Strings

2.1 Definition

In a symmetric spacetime, a cohomogeneity one cosmic string is defined as a timelike minimal surface which is tangent to the Killing vector. If the spacetime permits more than two linearly independent

[1]E-mail:furusaki@sci.osaka-cu.ac.jp
[2]E-mail:ishihara@sci.osaka-cu.ac.jp

Killing vectors, there are infinite number of Killing vectors which are represented as linear combinations of them. For each Killing vector, we can define cohomogeneity one strings.

An example of the cohomogeneity one cosmic string is a stationary string in a stationary spacetime, which is originally defined as a timelike minimal surface tangent to the timelike Killing vector of the spacetime [3]. In a stationary spacetime with the timelike Killing vector $\partial/\partial t$, the metric is written, in general, as:

$$ds^2 = -f(\vec{x})(dt + A_i dx^i)^2 + g_{ij}(\vec{x})dx^i dx^j, \tag{1}$$

where f, A_i and g_{ij} are the functions of x^i and do not depend on the time t. Taking the ansatz for the string as

$$\begin{cases} t(\tau,\sigma) = \tau \\ x^i(\tau,\sigma) = x^i(\sigma) \end{cases}, \tag{2}$$

where (τ,σ) is a coordinate on the worldsheet, we see that the worldsheet is tangent to the timelike Killing vector:

$$\frac{\partial}{\partial\tau} = \frac{\partial x^a}{\partial\tau}\frac{\partial}{\partial x^a} = \frac{\partial}{\partial t}. \tag{3}$$

2.2 Properties

The cohomogeneity one cosmic string has an important property; the induced metric on the worldsheet is cohomogeneity one [3]. Then, the equations of motion are reduced to ordinary differential equations. This is of great importance, since the ordinary differential equations are much more tractable than the partial differential equations. In some cases, the equations are solved analytically.

In order to examine the property, we consider the stationary string again. The induced metric is calculated as

$$\gamma_{AB} = g_{ab}\frac{\partial x^a}{\partial\zeta^A}\frac{\partial x^b}{\partial\zeta^B} = \begin{pmatrix} -f & -fA_i\dfrac{dx^i}{d\sigma} \\ -fA_i\dfrac{dx^i}{d\sigma} & (-fA_iA_j + g_{ij})\dfrac{dx^i}{d\sigma}\dfrac{dx^j}{d\sigma} \end{pmatrix}, \tag{4}$$

where the capital indices take 1 and 2, and ζ^A is the worldsheet coordinate: $\zeta^1 := \tau$, $\zeta^2 := \sigma$. Since the functions f, A_i and g_{ij} depend only on x^i and we have taken the ansatz $x^i = x^i(\sigma)$, the metric components depend only on σ. Hence, we see that the induced metric is cohomogeneity one.

Following the above settings, the Nambu-Goto action is reduced to the following form:

$$S_{NG} \propto \int \sqrt{f g_{ij}\frac{dx^i}{d\sigma}\frac{dx^i}{d\sigma}}\,d\sigma. \tag{5}$$

We see that the problem is reduced to finding a minimal curve in a 3-dimensional *space* with the metric fg_{ij}. The Euler-Lagrange equations become the geodesic equations in the 3-dimensional space. They are, of course, in the form of ordinary differential equations.

Here, we explain the meaning of the effective action (5). The point is that the minimal surface is considered as an "orbit" of a curve, i.e., a surface which appears as a result of the evolution of the curve. In case of the stationary string, the evolution is trivial in the sense that the worldsheets is generated by the timelike Killing vector. Suppose a curve set on t = const. hypersurface in the stationary spacetime, and let the curve go with the "flow" of the timelike Killing vector. There appears a 2-dimensional as an orbit of the curve. If the initial configuration of the curve minimizes the action (5), the resultant 2-dimensional surface turns out to be a timelike minimal surface, or a stationary string. Once we determine the initial configuration of the curve so as to minimize the effective action, the stationary string are automatically generated by the timelike Killing vector.

[3]Cohomogeneity one strings are named after this property.

In the above, we have used a stationary string to explain the properties. A stationary string is just a cohomogeneity one string which is generated by a *timelike* Killing vector. For general cohomogeneity one string, which is generated by timelike or spacelike Killing vectors, we can also provide the same explanations, only if the term "time" is replaced with "space" and vice versa.

We have seen that a cohomogeneity one string is generated by a Killing vector, i.e., its worldsheet is considered as an orbit which appears as a result of the evolution of the curve minimizing the effective action. Hence, the cohomogeneity one string configuration is determined not only by a generating Killing vector but also by the initial configuration of the curve. For a given Killing vector, we can obtain a family of the cohomogeneity one strings. Each member in the family is characterized by the initial configuration of the curve. We introduce a one-to-one correspondence between the Killing vectors and the families of the cohomogeneity one cosmic strings.

3 Classification of Cohomogeneity One Cosmic Strings in Minkowski Spacetime

In a spacetime with only one linearly independent Killing vector, there are only one family of cohomogeneity one cosmic strings. On the other hand, in a spacetime with more than two independent Killing vectors, there are infinite number of families; a linear combination of the Killing vectors also generate another cohomogeneity one strings. In this section, we introduce an equivalence relation, and then classify the infinite number of the families of cohomogeneity one strings into finite categories.

For general configurations of cosmic strings, we introduce an equivalence relation: worldsheets Σ_A and Σ_B are equivalent if there is an isometry φ which maps Σ_A onto Σ_B;

$$\varphi : \Sigma_A \to \Sigma_B. \tag{6}$$

Restricted to the cohomogeneity one strings, the equivalence relation is translated into that of the Killing vectors: for two cohomogeneity one strings whose worldsheets are generated by Killing vectors ξ_A and ξ_B, they are equivalent, if there is an isometry φ which pushes forward ξ_A to $\alpha\xi_B(\alpha : \text{constant})$;

$$\varphi_* : \xi_A \to \alpha\xi_B. \tag{7}$$

The scalar multiplication comes from the fact that the cohomogeneity one string generated by ξ is also considered as that generated by $\alpha\xi$.

Now that the classification of the cohomogeneity one cosmic strings is translated into that of the Killing vectors, we classify the Killing vectors in Minkowski spacetime. The strategy is as follows:

1. Start from an arbitrary linear combination of ten linearly independent Killing vectors.
2. Operate with φ_* (φ : isometry), and "contract" the Killing vector consists of n independent Killing vectors into that of $n-1$ independent Killing vectors.
3. Repeat the above process until it fails.

In the processes, there appear some cases, which result in the variety of the classes.

In Minkowski spacetime, generators of the translations P_a ($a = 0, 1, 2, 3$), the Lorentz boosts K_i ($i = 1, 2, 3$) and the rotations L_i ($i = 1, 2, 3$) are the ten linearly independent Killing vectors. An arbitrary Killing vector ξ is expressed as a linear combination of them;

$$\xi = \alpha_a P_a + \beta_i K_i + \gamma_i L_i, \tag{8}$$

where α_a, β_i and γ_i are coefficients.

Following the above strategy, an arbitrary Killing vector (8) is fallen into one of the seven subspaces

which are spanned by two basis listed below:

$$\{K_1, L_1\}, \tag{9}$$
$$\{P_0, L_1\}, \tag{10}$$
$$\{P_1, L_1\}, \tag{11}$$
$$\{P_0 + P_1, L_1\}, \tag{12}$$
$$\{P_3, K_2 + L_1\}, \tag{13}$$
$$\{P_1, K_2 + L_1\}, \tag{14}$$
$$\{P_2, K_1\}, \tag{15}$$

We have classified the Killing vectors in Minkowski spacetime. For each Killing vector, we will be able to find the associated minimal surfaces [4] However, we have to be careful about the signature of the induced metric on the surface, since the worldsheet of the cosmic string has to be timelike. Spacelike or null minimal surfaces are the results of unphysical motions of cosmic strings.

In case of a timelike Killing vector, the associated cohomogeneity one worldsheet is always timelike. Therefore, we do not have to worry about the signature. The Killing vectors of the subspaces (9), (10), (13), (14) and (15) are timelike in some regions in Minkowski spacetime. The rigidly rotating strings are generated by the Killing vectors of $\{P_0, L_1\}$ in the region where the Killing vectors are timelike. On the other hand, in case of spacelike or null Killing vector, the signature of the associated minimal surface is not definite. It depends on the initial curve, which is evolved by the Killing vector to generate the minimal surface. In order to examine the signatures, we have to investigate each case in detail.

4 Summary

We have defined a cohomogeneity one string as a timelike minimal surface which is tangent to a Killing vector. This is a generalization of the stationary string, which is defined as a timelike minimal surface tangent to a *timelike* Killing vector. As in the case of the stationary strings, cohomogeneity one string equations of motion are also reduced to ordinary differential equations.

In 4-dimensional maximally symmetric spacetime, there are ten linearly independent Killing vectors. Every linear combination of them can generate cohomogeneity one strings. We have classified the cohomogeneity one strings by introducing an equivalence relation. The equivalence relation is originally defined for the configurations of cosmic strings; worldsheets Σ_A and Σ_B are equivalent if there is an isometry which maps Σ_A onto Σ_B. In case of the cohomogeneity one strings, the equivalence relation is translated into that of the Killing vectors; worldsheets Σ_A and Σ_B which are generated by the Killing vectors ξ_A and ξ_B respectively are equivalent if there is an isometry φ which pushes forward ξ_A to $\alpha\xi_B$ (α: constant).

We have found that, in Minkowski spacetime, an arbitrary Killing vector is fallen into one of the seven subspaces (9)-(15). Every subspace is subtended by two basis, that is, 2-dimensional. However, members in each subspace are essentially characterized by one parameter, since the scalar multiplied Killing vector is equivalent to the original one: they generate the same cohomogeneity one strings. Therefore, only the elements in seven 1-parameter families of the Killing vectors generate all of the cohomogeneity one cosmic strings in Minkowski spacetime.

References

[1] V. P. Frolov, V. Skarzhinsky, A. Zelnikov and O. Heinrich, Phys. Lett. B **224**, 255 (1989).

[2] B. Carter and V. P. Frolov, Class. Quant. Grav. **6**, 569 (1989).

[3] V. P. Frolov, S. Hendy and J. P. De Villiers, Class. Quant. Grav. **14**, 1099 (1997) [arXiv:hep-th/9612199].

[4] For the Killing vectors of the subspaces (10), (11), (12) and (15), we know that the equations of motion are solved exactly.

Positivity Bounds for the Y-ADM Mass Density

Shinya Tomizawa[1], Testuya Shiromizu[2], David Kastor[3] Jennie Traschen[4]

[1,2] *Department of Physics, Tokyo Institute of Technology, Tokyo 152-8551, Japan*
[3,4] *Department of Physics, University of Massachusetts, Amherst, MA 01003, US*

Abstract

It was recently shown that Killing-Yano tensors lead to conserved gravitational charges, called Y-ADM charges. These new charges are interesting because they measure *e.g.* the mass density of a p-brane, rather than the total ADM mass which may be infinite. Here, we show that the spinorial techniques used by Witten, in his proof of the positive energy theorem, may be straightforwardly extended to study the positivity properties of the Y-ADM mass density for p-brane spacetimes. We find appropriate energy conditions for spacetimes that are conformally flat or algebraically special, and for spacetimes that have an exact Killing vector along the brane. Finally we discuss our expression for the Y-ADM mass density from the Hamiltonian point of view.

1 Introduction and Summary

The ADM mass in a p-brane spacetime, which diverges, is given by an integral over a cylinder $R^p \times S^{D-(p+2)}$ at transverse spatial infinity that encloses the entire brane - *i.e.* the integral includes directions parallel to the brane. Symmetry may be restored to the formulation of gauge and gravitational charges for p-branes by the introduction of new gravitational charges, called Y-ADM charges, associated with Killing-Yano tensors [2]. A Killing-Yano tensor is an antisymmetric tensor field of arbitrary rank that satisfies a natural generalization of Killing's equation [3]. A rank 1 Killing-Yano tensor is simply a Killing vector. It was shown in reference [2] that the Abbott-Deser (AD) construction of the ADM charge associated with an asymptotic Killing vector [4] may be generalized to give a conserved charge associated with an asymptotic Killing-Yano tensor of higher rank. The resulting Y-ADM charge is given by an integral over an $S^{D-(p+2)}$ at transverse spatial infinity.

For a p-brane spacetime, we focus on the rank $(p+1)$ asymptotic Killing-Yano tensor given by the anti-symmetric product of translations in the directions parallel to the world-volume of the brane. For a particle this is just the asymptotic time translation Killing vector and the corresponding charge is the ADM mass. For a general p-brane, we call the corresponding charge the *Y-ADM mass density*, which we will denote by M below.

One very important result [1] associated with the ADM mass is the positive energy theorem [5]. It is natural to ask if any sort of positivity result holds for the Y-ADM mass density $\mathcal{M}$? In this paper we investigate this question, making use of the spinor techniques of Witten [6] and Nester [7]. We focus on the rank 2 case corresponding to a 1-brane, or string.

Our central result [1] is a spinorial boundary integral expression for the Y-ADM mass density. Assuming that the spatial slices have no interior boundaries, *e.g.* at horizons, Stokes theorem relates this boundary integral to a volume integral, whose integrand is the sum of three terms. The first of these terms involves the stress-energy tensor; the second term is a positive definite expression quadratic in the derivative of the spinor field; the third term involves certain components of the Riemann tensor. The first two terms are similar to those that appear in Witten's proof of the positive energy theorem [6], in which an energy condition is sufficient to ensure positivity of the mass. The third term, however, cannot be written directly in terms of the stress-energy tensor and - hence - an energy condition is not sufficient to imply positivity of $\mathcal{M}$. We discuss two types of further conditions under which positivity nevertheless

[1]E-mail:tomizawa@th.phys.titech.ac.jp
[2]E-mail:shiromizu@phys.titech.ac.jp
[3]E-mail:kastor@physics.umass.edu
[4]E-mail:traschen@physics.umass.edu

holds: (i) If the spacetime is conformally flat or algebraically special and (ii) if the spacetime has an exact translational symmetry along the brane.

2 Killing-Yano tensors and Y-ADM charge

A Killing-Yano tensor [3] is a rank n rank antisymmetric tensor field $f^{a_1\cdots a_n} = f^{[a_1\cdots a_n]}$ satisfying

$$\nabla_{(a_1} f_{a_2)a_3\cdots a_{n+1}} = 0. \tag{1}$$

For rank $n = 1$ this condition reduces to Killing's equation. Flat spacetime has the maximal number of Killing-Yano tensors of each rank. In this paper we will focus on the case of rank $n = 2$. For flat spacetime in Cartesian coordinates, a basis for rank 2 Killing-Yano tensors is given by the translational tensors

$$f = dx^a \wedge dx^b, \tag{2}$$

together with the rotational tensors

$$f = x^a dx^b \wedge dx^c + x^b dx^c \wedge dx^a + x^c dx^a \wedge dx^b. \tag{3}$$

The construction is an extension of the Abbott and Deser construction of a conserved ADM charge associated with the Killing vectors of flat spacetime [4].

The construction begins by writing the metric in the form $g_{ab} = \eta_{ab} + h_{ab}$ throughout the spacetime. The difference h_{ab} between the full metric and the flat metric may be large in the interior of the spacetime, but vanishes at transverse spatial infinity. Let f^{ab} be a Yano tensor for the background metric. Using the Bianchi identities and the defining properties of Yano tensors, one can construct a rank 2 antisymmetric tensor current k^{ab} which is conserved with respect to the background derivative operator, *i.e.* $\nabla^{(0)}_a k^{ab} = 0$. This current is given by

$$k^{ab} = f^{ac} R^{L\ b}_{c} - f^{bc} R^{L\ a}_{c} - \frac{1}{2} f^{ab} R^L - \frac{1}{2} f^{cd} R^{L\ ab}_{cd}, \tag{4}$$

where $R^{L\ ab}_{cd}$, for example, is the linear term in the formal power series expansion of $R_{cd}{}^{ab}$ in h_{ab}.

Conservation of the 2-form current k can be rewritten as $d * k = 0$, where $*$ indicates the Hodge dual with respect to the background flat metric. It then follows that there locally exists a 3-form l, such that $*k = d * l$. One finds that the 3-form l is given by

$$l^{abc} = 3\delta^{[a}_k \delta^b_l \delta^{c}_m \delta^{d]}_n f^{kl} (\bar{\nabla}^m h^n{}_d) - \frac{1}{4} (\bar{\nabla}^{[a} f^{bc]}) h^n{}_d + \frac{3}{4} (\bar{\nabla}^d f^{[ab}) h^{c]}_d, \tag{5}$$

As in the previous section, let V be a spacelike, codimension two slice with normals n^a and x^a. The conserved Y-ADM charge is then defined by the integral of the $(D-3)$-form $*l$ over ∂V as $\partial V \to \infty$, *i.e.*, over a closed, codimension two, section of spatial infinity,

$$Q[f_{ab}] = \frac{1}{8\pi} \int_{\partial V} *l, \tag{6}$$

where we have used the notation $Q[f_{ab}]$ to denote the charge associated with an arbitrary asymptotic Killing-Yano tensor f_{ab}.

We now focus on the Y-ADM mass density $\mathcal{M}$, which means specifying the background Killing-Yano tensor $f^{ab} = n^a y^b - n^b x^a =: f^{(01)}$, where n^a and y^a are asymptoric timelike Killing vector and asymptotic spatial Killing vector parallel to the 1-brane,respectively. In this case, since $\bar{\nabla}_a f^{bc} = 0$, only the first term in equation (5) is nonzero. We can further specialize to Cartesian coordinates near infinity, giving the form

$$\mathcal{M} = \frac{1}{8\pi} \int_{\partial V} ds_I (\partial_J h^{IJ} - \partial^I h_J{}^J) \tag{7}$$

which is very similar to the usual formula for the ADM mass M, differing only in the higher codimension of the surface V and the correspondingly smaller range of the indices summed over - here $I, J = 2, \ldots, D-1$.

3 Spinorial method

To compute the Y-ADM mass density $\mathcal{M}$ for a 1-brane, one integrates over the boundary of a co-dimension two spatial surface transverse to the brane. This boundary has co-dimension three and we therefore need to introduce a Nester 3-form. Based on the discussion above, we take this to be

$$B^{abc} = \psi^\dagger \gamma^{\hat{0}\hat{i}} \gamma^{abcd} \nabla_d \psi. \tag{8}$$

We can show that $\mathcal{M}$ is indeed given in terms of this Nester form by

$$\mathcal{M} = \frac{1}{8\pi} \int_{\partial V} ds_a \, n_b \, y_c \, (B^{abc} + B^{abc*}), \tag{9}$$

where V is the co-dimension two surface with normals n^a and y^a, as in section (??) above, and * denotes complex conjugation.

We now focus on the volume integral form of $\mathcal{M}$ obtained from equation (9) using Stokes theorem [5]

$$\mathcal{M} = \frac{1}{8\pi} \int_V \sqrt{q} \, n_b \, y_c \, \nabla_a (B^{abc} + B^{abc*}). \tag{10}$$

It is then straightforward to show that the volume integrand above may be rewritten as the sum of two terms, as in the discsussion of the ADM mass above. The first term, which involves curvature tensors contracted with bilinears in the spinor field ψ, is given by

$$(vol)_1 = R_{ab} n^a \xi^b - R_{ab} y^a \chi^b + \frac{1}{2} R \lambda - R_{abcd} n^a y^b \xi^c y^d, \tag{11}$$

where $\lambda = \psi^\dagger \psi$, $\xi^a = -\psi^\dagger \gamma^{\hat{0}} \gamma^a \psi$ and $\chi^a = \frac{1}{2}(\psi^\dagger \gamma^{\hat{i}} \gamma^a \psi + c.c.)$. The second term, which is quadratic in derivatives of the spinor field, is given by

$$(vol)_2 = 2 \nabla_a \psi^\dagger q^{ab} \nabla_b \psi - 2(\nabla_a \psi^\dagger q^a{}_c \gamma^c)(q^b{}_d \gamma^d \nabla_b \psi) \tag{12}$$

If ψ is a solution to the Dirac-Witten equation $q^a{}_b \gamma^b \nabla_a \psi = 0$, then the second term in (12) vanishes and $(vol)_2$ is positive definite. The term $(vol)_1$ may be simplified by choosing the spinor field ψ to be an eigenfunction of $\gamma^{\hat{0}}$, which is consistent with the Dirac-Witten equation. The spinor bilinears in equation (11) are then related according to $\xi^a = -in^a \lambda$ and $\chi^a = y^a \lambda$.

4 Positivity bounds

4.1 Conditions on the Weyl Tensor

The idea here is to decompose the Reimann tensor into trace pieces, the Ricci and scalar contributions, and the rest, the Weyl tensor. When the Weyl term vanishes, the remaining terms in the volume integrand can be related to the stress-energy, which leads to an energy condition In D dimensions, $(vol)_1$ is written in terms of Weyl tensor as follows

$$(vol)_1 = [\frac{D(D-3)}{2(D-1)(D-2)} R + \frac{D-3}{D-2} R_{ab}(n^a n^b - y^a y^b) - C_{abcd} n^a y^b n^c y^d] \psi^\dagger \psi \tag{13}$$

One simple condition to consider is the vanishing of the Weyl tensor, $C_{abcd} = 0$. It is then clear that an appropriate energy condition would assure positivity of $(vol)_1$.

Another condition under which the Weyl tensor term in equation (13) vanishes is when the metric is algebraically special with all four principal null directions coinciding, and the null vector lies in the plane tangent to the brane. Explicitly, this means assuming that $p^a C_{abcd} = 0$ for a null vector $p^a = n^a \pm y^a$.

[5] We assume that there are no horizons in the spacetime so that no inner boundary terms arise in applying Stokes theorem.

If the Weyl tensor term vanishes, then $(vol)_1$ can be rewritten in terms of the stress energy tensor using Einstein's equation. If we make the definitions $\rho = T_{ab}n^a n^b$, $p_{\hat{y}} T_{ab}y^a y^b$ and similar definitions for the pressures p_i in directions transverse to the string, then the volume integral expression for $\mathcal{M}$ becomes

$$\mathcal{M} = \frac{(D-3)}{(D-1)} \int_V [(\rho - p_{\hat{y}} + \frac{1}{D-2} \sum_i p_i)\psi^\dagger \psi + 2(\nabla_a \psi^\dagger) q^{ab} \nabla_b \psi] \tag{14}$$

where the index i runs over the transverse coordinates. Therefore, we obtain $\mathcal{M} \geq 0$.

4.2 Translational Symmetry and Kaluza-Klein Reduction

We now assume that the spacetime has a spatial translation Killing field V^a that is parallel to the brane. Near infinity, the Killing vector V^a approaches $\partial/\partial x^1$, which also coincides with the unit normal vector y^a in this limit. Further assume that we extend y^a into the interior of the spacetime, such that it is parallel to the Killing field V^a, *i.e.* let $V^a = F y^a$ where $V_a V^a = F^2$. In this case, we then have the result

$$\mathcal{M} = \frac{1}{8\pi} \int_V \left(n^a n^b G^{(D-1)}_{ab}[s] \psi^\dagger \psi + 2(\nabla_a \psi^\dagger) q^{ab} \nabla_b \psi \right) \tag{15}$$

At this point one needs to know something about the dimensionally reduced theory , in order to draw a conclusion about the Y-ADM mass density $\mathcal{M}$. If the dimensionally reduced Einstein tensor is equal to a stress energy which satisfies the dominant energy condition, then $\mathcal{M}$ is positive. Therefore, the argument leading to (15) gives a consistency check on the meaning of the mass per unit length: when dimensional reduction is possible, the mass per unit length coincides with the ADM mass of the lower dimensional theory.

References

[1] David Kastor, Tetsuya Shiromizu, Shinya Tomizawa, Jennie Traschen, "Positivity Bounds for the Y-ADM Mass Density",[arXiv:hep-th/0410289]

[2] D. Kastor and J. Traschen, "Conserved gravitational charges from Yano tensors," JHEP **0408**, 045 (2004) [arXiv:hep-th/0406052].

[3] K. Yano, "Some Remarks on Tensor Fields and Curvature," Ann. Math. **55**, 328 (1952).

[4] L. F. Abbott and S. Deser, "Stability Of Gravity With A Cosmological Constant," Nucl. Phys. B **195**, 76 (1982).

[5] R. Schoen and S. T. Yau, "On The Proof Of The Positive Mass Conjecture In General Relativity," Commun. Math. Phys. **65**, 45 (1979).

[6] E. Witten, "A Simple Proof Of the Positive Energy Theorem," Commun. Math. Phys. **80**, 381 (1981).

[7] J. Nester, Phys. Lett. **83A**, 241(1981).

May gravitons be super-strong interacting particles?

Michael A. Ivanov[1]

Physics Dept.,
Belarus State University of Informatics and Radioelectronics,
6 P. Brovka Street, BY 220027, Minsk, Belarus.

Abstract

A scheme, in which gravitons are super-strong interacting, is described. The graviton background with the Planckian spectrum and a small effective temperature is considered as a reservoir of gravitons. A cross-section of interaction of a graviton with any particle is assumed to be a bilinear function of its energies. Any pair of bodies are attracting not due to an exchange with its own gravitons, but due to a pressure of external gravitons of this background. A graviton pairing is necessary to obtain classical gravity. Any divergencies are not possible in such the model because of natural smooth cut-offs of the graviton spectrum from both sides. Some cosmological consequences of this scheme are discussed, too. Also it is shown here that the main conjecture of this approach may be verified at present on the Earth.

1 Introduction

What is a quantum mechanism of gravity? To answer this question, it is necessary to keep in mind a few different circumstances. A commonly accepted hypothesis, that an exchange with gravitons, which are radiated by bodies itself, causes classical gravity, is not a single possible one - gravitons might belong to an external sea of particles which exists independently of attracting bodies. A coupling constant of quantum gravitational interaction would differ from the Newton constant and may depend on energies of interacting particles. A geometrical language for short distances may not be adequate to describe quantum gravity. Perhaps, on the present stage when we know so a little about this mechanism, it would be better to consider a problem of its searching as a separate one. Some known effects which are not usually connected with gravity may be involved in a circle of interests of researchers by considerations of possible mechanisms. At first, it concerns cosmological effects which manifest themselves only on huge distances and during big times.

There are some facts beyond cosmology, which should be taken into account in this search, too. The Pioneer 10 anomaly [1] is one of them. Another fact is an observation of discrete energy states of neutrons in the Earth's gravitational field by Nesvizhevsky et al. [2]. In this remarkable experiment we see the huge difference - about 40 orders - between observed state energies $\sim 10^{-12}$ eV and the Planck energy of $\sim 10^{19}$ GeV which is expected from dimension reasonings as a threshold of any quantum gravity effect. The long known contradiction between the general relativity and quantum mechanics in descriptions of a microparticle motion is the third fact: if in one theory all particles should move on geodesics, in another they cannot move on definite trajectories. Maybe, a cause of this contradiction is that both theories do not take into account influences of single gravitons on a microparticle; then small graviton energies in a future theory are appeared to be more appropriate than the Planchian ones. A possible compositeness [3] of the fundamental fermions - electrons, neutrinos, quarks etc - should be taken into account, too. Components of these composite fermions would be bounded with a quantum gravitational interaction which is not similar to ordinary gravity.

The main features of a quantum model of classical gravity and its cosmological consequences are described here. The model is based on the conjecture about an existence of the background of super-strong interacting gravitons.

[1]E-mail: ivanovma@gw.bsuir.unibel.by

2 A gravitational attraction due to the background

The important features of this model are the following ones (for more details, see [4, 5]).

• The graviton background has the Planckian spectrum and the same temperature T as CMB.
• The graviton background is in a state of dynamical equilibrium: it is cooled via self-interactions of gravitons and formation of virtual massive gravitons which may be dark matter particles, and is heated up via interactions with other radiations [6].
• A cross-section of interaction $\sigma(E,\epsilon)$ of a graviton with any particle is a bilinear function of its energies: $\sigma(E,\epsilon) = D \cdot E \cdot \epsilon$, where D is some new dimensional constant, E is a particle's energy, ϵ is a graviton's energy. The estimate of D is: $D \sim 10^{-27} m^2/eV^2$, i.e. gravitons are super-strong interacting particles.
• Due to a pressure of single gravitons, there act equal attractive and repulsive forces of three order greater than the Newtonian force between any two bodies, but a net force is equal to zero.
• To ensure Newtonian attraction, a pairing of single gravitons of running flux is necessary, and such pairs should be destructed by collisions with a body. A nature of this pairing remains unknown. If this pairs have spin 2, then single gravitons may have spin 1. Only two modes of spin-2 particles may exist in the model.
• Given this pairing, the Newton constant G is equal to:

$$G \equiv \frac{2}{3} \cdot \frac{D^2 c (kT)^6}{\pi^3 \hbar^3} \cdot I_2,$$

where k is the Boltzmann constant, $I_2 = 2.3184 \cdot 10^{-6}$.
• In the case of interaction of gravitons with big bodies in the aggregate, it is impossible to have Newton's law. One needs an "atomic structure" of matter to get this law.
• For proton-mass particles, the equivalence principle should be broken at distances $\sim 10^{-11}$ m, if the model is true. It means that at shorter distances gravity cannot be described alone, without other known interactions. It is also the limit to apply a geometrical language in gravity.

3 Cosmological consequences of the model

Such the mechanism of gravity should have the following cosmological consequences [7, 4]:
• A quantum interaction of photons with the graviton background would lead to redshifts of remote objects; the Hubble constant H is equal in this model to: $H = \frac{1}{2\pi} D \cdot \bar{\epsilon} \cdot (\sigma T^4)$, where $\bar{\epsilon}$ is an average graviton energy, σ is the Stephan-Boltzmann constant. Redshifts are caused by forehead collisions with gravitons.
• The Hubble constant is connected in this approach with the Newton one as:

$$H = (G \frac{45}{32\pi^5} \frac{\sigma T^4 I_4^2}{c^3 I_2})^{1/2} = 3.026 \cdot 10^{-18} s^{-1},$$

where $I_4 = 24.866$.
• Due to non-forehead collisions with gravitons, an additional relaxation of any photonic flux leads to the luminosity distance D_L :

$$D_L = a^{-1} \ln(1+z) \cdot (1+z)^{(1+b)/2},$$

where $a = H/c$, z is a redshift, and the relaxation factor b is equal to [8]: $b = 3/2 + 2/\pi = 2.137$. See a comparison of this function with observations of [9] in my paper [10].
• Any light radiation spectrum will be deformed due to the quantum nature of red-shifting process. A theory of this effect does not exist today. But it may be checked experimentally in a laser experiment (see the next section).
• Any massive objects, moving relative to the background, should be decelerated by the background. A body's acceleration w by a non-zero velocity v relative to the background is equal to: $w = -ac^2(1 - v^2/c^2)$, and has by small velocities the same order Hc as an anomalous acceleration of Pioneer 10 [1].
• An existence of black holes contradicts to Einstein's equivalence principle in a frame of this model [4].

4 How to verify the main conjecture of this approach

I would like to show here a full realizability at present time of verifying my basic conjecture about the quantum gravitational nature of redshifts in a ground-based laser experiment. Of course, many details of this precision experiment will be in full authority of experimentalists.

It was not clear in 1995 how big is a temperature of the graviton background, and my proposal [11] to verify the conjecture about the described local quantum character of redshifts turned out to be very rigid: a laser with instability of $\sim 10^{-17}$ hasn't appeared after 9 years. But if $T = 2.7K$, the satellite of main laser line of frequency ν after passing the delay line will be red-shifted at $\sim 10^{-3}$ eV/h and its position will be fixed (see Fig. 1). It will be caused by the fact that on a very small way in the delay line only a small part of photons may collide with gravitons of the background. The rest of them will have unchanged energies. The center-of-mass of laser radiation spectrum should be shifted proportionally to a photon path. Due to the quantum nature of shifting process, the ratio of satellite's intensity to main

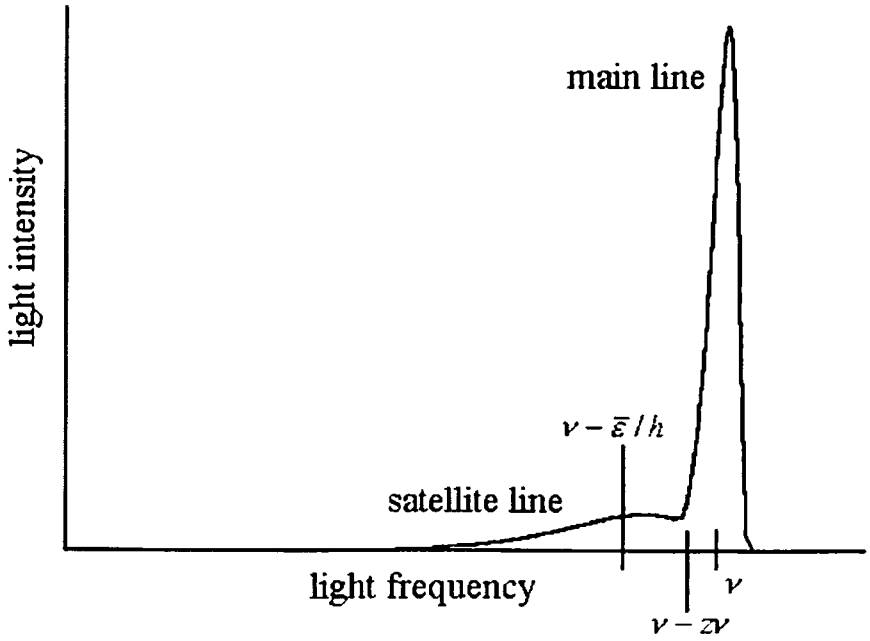


Figure 1: The main line and the expected red-shifted satellite line of a stable laser radiation spectrum after a delay line. Satellite's position should be fixed near $\nu - \bar{\epsilon}/h$, and its intensity should linear rise with a path of photons in a delay line, l. A center-of-mass of both lines is expected to be approximately near $\nu - z\nu$.

line's intensity should have the order:

$$\sim \frac{h\nu}{\bar{\epsilon}} \frac{H}{c} l,$$

where l is a path of laser photons in a vacuum tube of delay line. It gives us a possibility to plan a laser-based experiment to verify the basic conjecture of this approach with much softer demands to the equipment. An instability of a laser of a power P must be only $\ll 10^{-3}$ if a photon energy is of $\sim 1\ eV$. If one compares intensities of the red-shifted satellite at the very beginning of the path l and after it, and uses a single photon counter to measure the ones (when q is a quantum output of a cathode of the used photomultiplier, N_n is a frequency of its noise pulses, and n is a desired ratio of a signal to noise's standard deviation), then an evaluated time duration t of collecting data would have the order:

$$t = \frac{\bar{\epsilon}^2 c^2}{H^2} \frac{n^2 N_n}{q^2 P^2 l^2}.$$

Assuming $n = 10$, $N_n = 10^3\ s^{-1}$, $q = 0.3$, $P = 100\ mW$, $l = 100\ m$, we would have the estimate: $t = 100,000$ years, that is unacceptable. But given $P = 300\ W$, we get: $t \sim 4$ days, that is acceptable for the experiment of such the potential importance. Of course, one will rather choose a bigger value of l by a small laser power forcing a laser beam to whipsaw many times between mirrors in a delay line - it is a challenge for experimentalists.

5 Conclusion

The described model (my summarizing paper with its description [12] will be published soon) of Le Sage's kind has not an analogue in present-day physics of particles. If this mechanism is realized in the nature, both the general relativity and quantum mechanics should be modified. The indirectly observed objects in centers of galaxies, which are known now as black holes, should have another nature, too. Gravity at short distances, which are meantime much bigger than the Planck length, needs to be described only in some unified manner.

References

[1] J.D. Anderson et al. Phys. Rev. Lett., **81** (1998) 2858; Phys. Rev. **D65** (2002) 082004. [gr-qc/0104064 v4]

[2] V.V. Nesvizhevsky et al. Nature, **415** (2002) 297.

[3] M.A. Ivanov. Nuovo Cimento, **105A** (1992) 77. [hep-th/0207210]

[4] M.A. Ivanov. Screening the graviton background, graviton pairing, and Newtonian gravity. [gr-qc/0207006]

[5] M.A. Ivanov. In the book "Searches for a mechanism of gravity", Eds. M.A. Ivanov, L.A. Savrov, Nizhny Novgorod, Yu.A. Nikolaev Publisher, 2004, pp 275-282 (in Russian). [gr-qc/0307093]

[6] M.A. Ivanov. Model of graviton-dusty universe. [gr-qc/0107047]

[7] M.A. Ivanov, General Relativity and Gravitation, **33**, 479 (2001); Erratum: **35**, 939 (2003); [astro-ph/0005084 v2].

[8] M.A. Ivanov. Another origin of cosmological redshifts. [astro-ph/0405083].

[9] A.G. Riess et al. Type Ia Supernova Discoveries at $z > 1$ From the Hubble Space Telescope ..., [astro-ph/0402512] (to appear in ApJ, 2004).

[10] M.A. Ivanov. Another possible interpretation of SN 1a data - without kinematics: Comments on the paper astro-ph/0402512 by A. Riess et al. [astro-ph/0403130].

[11] M.A. Ivanov. Contribution to the Quantum Electronics and Laser Science Conference (QELS'95), May 21-26, 1995, Baltimore, USA; paper number: QThG1.

[12] M.A. Ivanov. Gravitons as super-strong interacting particles, and low-energy quantum gravity. Invited chapter for the volume *Progress in Quantum Gravity Research*, accepted by Nova Science Publishers, in plan of 2005 [http://ivanovma.narod.ru/nova04abstract.html].

The Accelerating Universe with Spinor Fields

Tomoki Watanabe[1]

Department of Physics, Tokai University, Kanagawa 259-1292, Japan

Abstract

We present a cosmological model based on the Einstein-Cartan theory with the Dirac fields or the Rarita-Schwinger fields. The spin correction to the energy momentum appears in the Einstein equation with the aid of the field equation which determines a relation between torsion and spin. By exactly solving the modified Friedmann equation for the scale factor, we show that the spin of the Dirac fields may cause inflation and that the initial singularity can be avoided. For the Rarita-Schwinger fields, we prove that they can also provide negative pressure. These observation might supply a hint on the riddles concerning the accelerating universe.

1 Introduction

In the Einstein-Cartan theory the intrinsic spin of matter is a crucial object as the source of torsion which brings about a natural extension of the Riemann connection within its ambiguity [1]. One of the advantages of introducing spin and torsion into a theory of gravity is to revise existing cosmology based on usual General Relativity[2]. Indeed, it was shown that the spinning matter-dominated universe causes inflation without false vacuum in the framework of the Einstein-Cartan theory[3]. Recently, Szydlowski and Krawiec concluded that the existence of the spinning matter is allowable within the constraints coming from SNIa data, although is not an alternative to the cosmological constant which is a candidate for dark energy[4].

Thus we need the motivation to propose such a new type of matter from the point of view of particle physics. We well know the spinor fields as matter which possesses non-trivial spin. In this paper we explore the possibility whether the the Dirac and the Rarita-Schwinger field can be the origin of the accelerated expansion of the Friedmann universe by investigating the contribution of thier spin within the Einstein-Cartan theory.

2 Field Equations in Einstein-Cartan Theory

In the context of the vierbein (tetrad) formalism, the vierbein $e_a{}^\mu$ and a spin connection ω_μ^{ab} can be employed instead of the metric $g_{\mu\nu}$ and the affine connection $\Gamma^\rho_{\mu\nu}$, so long as the vierbein postulate

$$\mathcal{D}_\nu e^{a\mu} = \partial_\nu e^{a\mu} + \Gamma^\mu_{\rho\nu} e^{a\rho} + \omega_\nu^{ab} e_b{}^\mu = 0, \tag{1}$$

is satisfied. It is well known that, similarly to the most general form of metric-compatible affine connection, the spin connection can be decomposed into two parts:

$$\omega_\mu^{ab} = \tilde{\omega}_\mu^{ab}(e, \partial e) + K^{ab}{}_\mu, \tag{2}$$

where $K^{ab}{}_\mu$ is a Lorentz component of contortion which is related to torsion tensor $C^\rho{}_{\mu\nu} \equiv \Gamma^\rho_{\mu\nu} - \Gamma^\rho_{\nu\mu}$ as $K^\rho{}_{\mu\nu} = (C^\rho{}_{\mu\nu} + C_{\mu\nu}{}^\rho + C_{\nu\mu}{}^\rho)/2$, and $\tilde{\omega}_\mu^{ab}$ is torsion-free part of the spin connection.

Field equations for curvature and torsion in the Einstein-Cartan theory are given by

$$G_\mu{}^a \equiv R_\mu{}^a - \frac{1}{2} e_\mu{}^a R = 8\pi G T_\mu{}^a, \tag{3}$$

$$C^\mu{}_{ab} + 2e_{[a}{}^\mu C_{b]} = -8\pi G i \frac{\partial \mathcal{L}_{\rm m}}{\partial D_\mu \phi^A} (S_{ab})^A{}_B \phi^B \equiv -16\pi G S^\mu{}_{ab}. \tag{4}$$

[1]E-mail: 2aspd004@keyaki.cc.u-tokai.ac.jp

where D_μ is the Lorentz covariant derivative with the Lorentz generator S_{ab}. Note that torsion is equivalent to the (classical) spin density $S^\mu{}_{ab}$ via the field equation (4).

Here we are interested in that the Einstein tensor as well as the energy momentum tensor can be split into the torsion-free part $\tilde{G}_{\mu\nu}$, $\tilde{T}_{\mu\nu}$ and the torsion part $G^{(t)}_{\mu\nu}$, $T^{(t)}_{\mu\nu}$ by virtue of Eq.(2). Then the torsion parts play a role of the correction to the energy momentum due to the spin:

$$\tilde{G}_{\mu\nu} = 8\pi G\, T_{\mu\nu} - G^{(t)}_{\mu\nu} \equiv 8\pi G(\tilde{T}_{(\mu\nu)} + T^{(\mathrm{spin})}_{\mu\nu}). \tag{5}$$

$T^{(\mathrm{spin})}_{\mu\nu}$ is automatically symmetric, and given by

$$\begin{aligned} T^{(\mathrm{spin})}_{\mu\nu} &= 2\bar{\nabla}_\rho S_{(\mu\nu)}{}^\rho - 8\pi G\Big[4S^{(\rho\sigma)}{}_\mu S_{(\rho\sigma)\nu} - S_\mu{}^{\rho\sigma}S_{\nu\rho\sigma} - 2S_\mu S_\nu \\ &\quad - \frac{1}{2}g_{\mu\nu}\left(4S^{(\rho\sigma)\lambda}S_{(\rho\sigma)\lambda} - S^{\lambda\rho\sigma}S_{\lambda\rho\sigma} - 2S^\rho S_\rho\right)\Big] + T^{(t)}_{(\mu\nu)}, \end{aligned} \tag{6}$$

where $\bar{\nabla}_\mu \equiv \nabla_\mu - C_\mu$ and $S_\mu \equiv S^\nu{}_{\mu\nu}$. Our purpose is just to view the effect of $T^{(\mathrm{spin})}_{\mu\nu}$ of spinor fields, say Dirac fields and Rarita-Schwinger fields, on the universe.

3 Inflation induced by Spinor Fields

The Lagrangian for the Dirac field is given by

$$\mathcal{L}_{\mathrm{D}}(e,\psi,D\psi) = \frac{i}{2}\left[\,\bar{\psi}\gamma^\mu D_\mu\psi - (\overline{D_\mu\psi})\gamma^\mu\psi\,\right] - m\bar{\psi}\psi, \tag{7}$$

which leads to

$$\tilde{G}_{\mu\nu} = 8\pi G\,\tilde{T}_{(\mu\nu)} + \frac{3}{16}g_{\mu\nu}(8\pi G\,\bar{\psi}\gamma_5\gamma_a\psi)^2. \tag{8}$$

Note that the only correction term emerged is proportional to $g_{\mu\nu}$ and hence can be expected to play the role of the effective cosmological constant.

Let us consider the flat Friedmann universe with Eq.(8). Regarding $\tilde{T}_{(\mu\nu)}$ as perfect fluid, we obtain the modified energy density and pressure:

$$\rho_{\mathrm{tot}} = \rho_{\mathrm{D}} + 2\pi G\sigma^2, \quad p_{\mathrm{tot}} = p_{\mathrm{D}} - 2\pi G\sigma^2, \tag{9}$$

where $\sigma^2 \equiv (3/4)(\bar{\psi}\gamma_5\gamma_a\psi)^2$, ρ_{D} and p_{D} indicate the energy density and the pressure of the Dirac field respectively; these are irrelevant to torsion.

In case $\sigma^2 > 0$, the spin correction yields negative contribution to the pressure. Eq.(9) implies the accelerated expansion of the universe occurs provided that

$$\rho_{\mathrm{D}} + 3p_{\mathrm{D}} < 4\pi G\sigma^2. \tag{10}$$

It can be proved that the acceleration condition (10) is fulfilled as follows. According to Ref.[5], let us assume $p_{\mathrm{D}} = k\rho_{\mathrm{D}}$ and identify σ^2 with the space-averaged spin density $\langle\sigma^2\rangle = \beta^{-2/(1+k)}\rho_{\mathrm{D}}^{2/(1+k)}$, where β is a dimensional constant. From the energy conservation law for Eq.(9), we obtain

$$\rho_{\mathrm{D}}(a) = \left(\frac{1+k}{4\pi G\beta^{-\frac{2}{1+k}}}\right)^{\frac{1+k}{1-k}}\left[W\left(\frac{4\pi G\beta^{-\frac{2}{1+k}}C^{\frac{1-k}{1+k}}}{(1+k)a^{3(1-k)}}\right)\right]^{\frac{1+k}{1-k}}, \tag{11}$$

where W is Lambert's W-function, a is the scale factor and C is an integration constant. It turns out that $\rho_{\mathrm{D}}(a)$ for $k = 0$ is a monotonic decreasing function of a as shown in Fig.1.

Moreover, the exact solution of the Friedmann equation with Eq.(11) for $k = 0$ is given by

$$t(a) = \frac{\pi\beta^{-1}}{\sqrt{3}}\left[\sqrt{1 + 2\left[W\left(\frac{4\pi G\beta^{-2}C}{a^3}\right)\right]^{-1}} - 2\sinh^{-1}\sqrt{\frac{1}{2}W\left(\frac{4\pi G\beta^{-2}C}{a^3}\right)}\right] + \mathrm{Const.} \tag{12}$$

We have shown the behavior of $a(t)$ being the inverse function of Eq.(12) in Fig.2; this remarkably exhibits that the universe has an accelerated phase and experiences a transition to deccelerated expansion. It is notable that the solution (12) allows the initial singularity of the universe to be avoided. These are the first observation of an influence of the Dirac field on the dynamics of the universe.

Next, let us consider the Rarita-Schwinger fields[6]. We take the non-Majorana Lagrangian

$$\mathcal{L}_{3/2}(e,\psi,D\psi) = -\frac{1}{2}\epsilon^{\mu\nu\rho\sigma}\left[\bar{\psi}_\mu\gamma_5\gamma_\nu D_\rho\psi_\sigma - (\overline{D_\rho\psi_\mu})\gamma_5\gamma_\nu\psi_\sigma\right] - im_{3/2}\bar{\psi}_\mu\sigma^{\mu\nu}\psi_\nu. \tag{13}$$

Consequently the spin correction due to the Rarita-Schwinger field is derived as

$$\begin{aligned} T^{(\mathrm{spin})}_{\mu\nu} &= 2\tilde{\nabla}_\rho S_{(\mu\nu)}{}^\rho + 8\pi G\Big[4J^{(\rho\sigma)}{}_\mu J_{\nu(\rho\sigma)} - 2J_\sigma{}^\rho{}_{(\mu}J^\sigma{}_{\nu)\rho} + 4J^\rho J_{(\mu\nu)\rho} \\ &\quad + 4J_\mu J_\nu + \frac{1}{2}g_{\mu\nu}\left(J^{\rho\sigma\lambda}J_{\rho\sigma\lambda} + 2J^{\rho\sigma\lambda}J_{\sigma\rho\lambda} - 4J^\rho J_\rho\right)\Big], \end{aligned} \tag{14}$$

where $J_{\mu\nu\rho} \equiv \bar{\psi}_{[\mu}\gamma_{|\nu|}\psi_{\rho]}/2$ and $J_\mu \equiv J^\nu{}_{\nu\mu}$. Eq.(14) shows that there are three types of the contribution to the pressure. One is positive, another is negative like the cosmological constant, and the other is indefinite. Defining composite fields as

$$\begin{aligned} J^{i\mu0}J_{i\mu0} &\equiv \frac{\chi^2}{4},\ J^{i\mu j}J_{i\mu j} \equiv \vartheta^2,\ J^{ij0}J_{0ij} \equiv \frac{\zeta}{4},\ J^{ikj}J_{ijk} \equiv \frac{\eta}{2}, \\ J^{ij0}J_{i0j} &\equiv \frac{\varphi}{6},\ J^{00i} \equiv \frac{\tau^i}{2},\ J^i{}_{i0} \equiv \frac{\lambda}{2\sqrt{2}},\ J^j{}_{ji} \equiv \frac{\upsilon_i}{2}, \end{aligned} \tag{15}$$

where the indices i,j,k run the spatial components, we can explicitly observe how the corrections find thier expression in the acceleration condition:

$$\rho_{\mathrm{tot}} + 3p_{\mathrm{tot}} = \rho + 3p + 8\pi G\left[\lambda^2 + (\tau_i + \upsilon_i)^2 - (\chi^2 + \vartheta^2) + \zeta - \eta - \varphi + \tau_i\upsilon^i\right]. \tag{16}$$

Therefore whether the universe becomes accelerated depends on the balance of values of the composite fields. However, it is clear that J_μ adds the positive contribution to Eq.(16) if it is time-like. Thus let us tentatively impose the irreducible condition for the Rarita-Schwinger field, i.e. $\gamma^a\psi_a = 0$ on Eq.(14). Then the acceleration condition is just simplified and relaxed:

$$\rho_{\mathrm{tot}} + 3p_{\mathrm{tot}} = \rho + 3p + 8\pi G\left[-(\chi^2 + \vartheta^2 + \tau_i^2) + \zeta - \eta - \varphi\right]. \tag{17}$$

It should be noted that the irreducible condition not only eliminates the positive contribution but also enhances the negativity for comparison with Eq.(16). Thus the possibility is not ruled out that the Rarita-Schwinger field triggers off the acceleration of the universe.

4 Summary

We definitely calculated the correction to the energy momentum due to spin of the Dirac field and the Rarita-Schwinger field in the framework of the Einstein-Cartan theory, and applied to cosmology with the interesting consequence. The results obtained imply that the spinor fields can provide negative pressure. In particular, we suggest that the Dirac field gains a position as a possible candidate to be an alternative to false vacuum or inflaton in the early stage of the universe. Our conclusions will be more important when one hopes to construct a cosmological model within realistic and promising theories, e.g. theory of supergravity, which offer a great variety of matter fields.

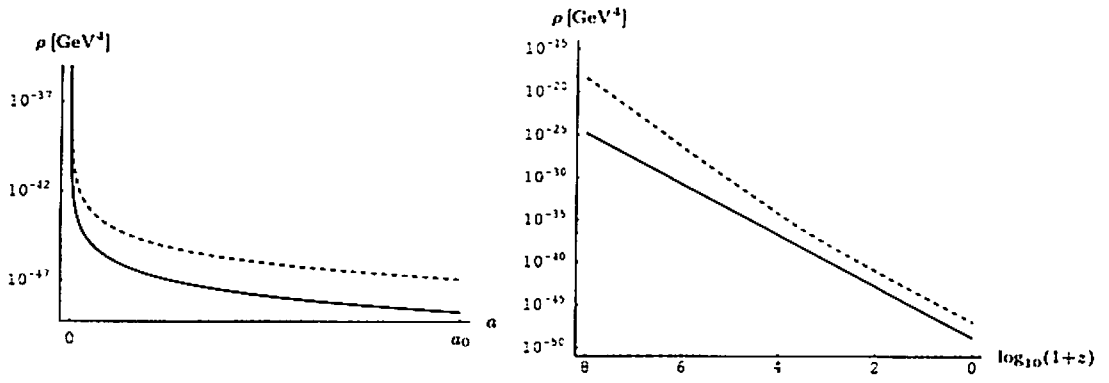


Figure 1: a-dependence of the energy density of the Dirac field. The solid line indicates $\rho_D(a)$ for $k = 0$ given by Eq(11), while the broken line represents the evolution of the energy density of matter and radiation. We choose the mass of the Dirac field to be 10^5GeV and the arbitrary constant C in order that $\rho_D(a_0)$ coincide with the present value suggested in Ref.[4] of the energy density of "spinning matter". Although that is given by Lambert's function, we can see no eccentric behavior in ρ_D.

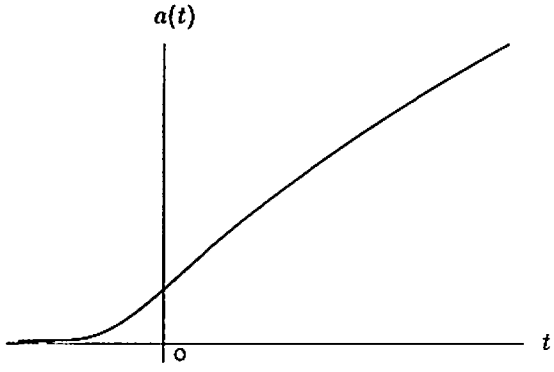


Figure 2: The time evolution of the scale factor in the Dirac field model. We set the constants to the same value as those of Fig.1 and the integration constant in Eq.(12) to zero. The function $a(t)$ is asymptotic to zero as $t \to -\infty$ owing to the term of hyperbolic sine in Eq.(12). Therefore $a \neq 0$ for any t.

References

[1] F. W. Hehl, P. von der Heyde and G. D. Kerlick, Rev. Mod. Phys. 48, 393 (1976).

[2] D. Puetzfeld, "Status of Non-Riemannian Cosmology", arXiv: gr-qc/0404119, and references therein.

[3] M. Gasperini, Phys. Rev. Lett. 56, 2873 (1986).

[4] M. Szydolowski and A. Krawiec, Phys. Rev. D70, 043510 (2004).

[5] S. Nurgaliev and V. N. Ponomariev, Phys. Lett. 130B, 378 (1983).

[6] T. Watanabe and M. J. Hayashi, "General Relativity with Torsion", arXiv: gr-qc/0409029.

Junction conditions of cosmological perturbations

Kenji Tomita[1]

Yukawa Institute for Theoretical Physics, Kyoto University, Kyoto 606-8502, Japan

Abstract

The behavior of perturbations is studied in cosmological models which consist of two different homogeneous regions connected in a spherical shell boundary. The junction conditions for the metric perturbations and the displacements of the shell boundary are analyzed and the surface densities of the perturbed energy and momentum in the shell are derived, using Mukohyama's gauge-invariant formalism and the Israel discontinuity condition. In both homogeneous regions the perturbations of scalar, vector and tensor types are expanded using the 3-dimensional harmonic functions, but the mode coupling among them is caused in the shell by the inhomogeneity. By treating the perturbations with odd and even parities separately, it is found, however, that we can have consistent displacements and surface densities for given metric perturbations.

1 Introduction and summary

In the real Universe it is known at present that there are many superclusters and void-like objects with nonlinear overdense and underdense regions which are distributed everywhere on various scales. Such objects may have complicated structures in general, but their evolution has often been studied in comparatively large-scale cases, using a simplified assumption of spherical symmetry.

In order to study the dynamical behavior of the large-scale superclusters and void-like objects and their influence on the CMB anisotropy, moreover, it is necessary to consider the gravitational instability of these models. The general gauge-invariant formalism for linear perturbations in spherical symmetric inhomogeneous models was derived by Gerlach and Sengupta [1, 2, 3, 4] in four-dimensional spacetimes. Recently the junction of perturbations in two homogeneous regions was treated by Mukohyama[5, 6] and Kodama et al.[7] in higher dimensional spacetimes on the basis of the Israel discontinuity condition [8]. In this note, we report the behavior of linear perturbations in the four-dimensional cosmological models with a single shell, using Mukohyama's formalism. Here only one of his doubly gauge-invariant variables are used, and in both homogeneous regions the perturbations are classified into scalar, vector and tensor types in three dimensional space and expanded in terms of three dimensional harmonic functions [9, 10] in order to clarify the physical image of perturbations, though he classified them in a space of the shell surface. Among them the mode coupling is caused by the inhomogeneity in the shell. By treating the perturbations with odd and even parities separately, it is found however that the consistent expressions of the shell displacement and the energy-momentum tensor in the shell can be derived for given metric perturbations in both regions.

First we describe briefly a single-shell model as the background model, in which the velocity of the shell is determined through the junction condition. Next we show the basic equations for gauge-invariant perturbations and the junction condition based on Mukohyama's formalism [5, 6]. Moreover we derive the intrinsic perturbations of metric and extrinsic curvature in the shell, and show the displacements of the shell and the intrinsic energy-momentum tensor in the shell which are derived from the junction conditions, by treating the perturbations with odd-parity and even-parity separately and imposing a localization condition on the wave-number dependence of the shell displacement. Additionally the harmonic functions in a homogeneous background model are shown, which are necessary for the analysis of the description of junction conditions, and the intrinsic energy-momentum tensor in the shell are shown.

Our results do not mean that arbitrary perturbations in both regions can always be adjusted, because it depends on the physical situation of the shell whether the obtained energy-momentum tensor in the shell is allowed or not. For instance, if we consider an expanding or collapsing star with the empty

[1] E-mail:tomita@yukawa.kyoto-u.ac.jp

external region, any energy and momentum are not expected to be stored in the boundary and only gravitational radiation is released in the external region, because there are no matter perturbations.

In the present study, though we treated the displacement of the boundary shell as spatially 3-dimensional quantities, we could recover the original local property of the shell displacement (that it has the values only in the neighborhood of the shell) by imposing the localization condition and could solve the equations for the displacements.

Our result will be useful to the analyses of CMB anisotropy observed in the nonlinear structures such as overdense regions (such as superclusters) and underdense regions (such as voids) in which we may live.

2 Background models and the junction conditions

The background universe is assumed to consist of two spatially homogeneous regions connected by a spherical shell. The four-dimensional line-elements in the inner region V^- and the outer region V^+ are described as

$$ds^2 = g^{\pm}_{\mu\nu}(dx^\mu)_\pm(dx^\nu)_\pm = [a_\pm(\eta_\pm)]^2[-(d\eta_\pm)^2 + dl^2_\pm], \tag{1}$$

$$dl^2_\pm = \gamma^\pm_{ij}(dx^i)_\pm(dx^j)_\pm = (d\chi_\pm)^2 + [\sigma_\pm(\chi_\pm)]^2 d\Omega^2, \tag{2}$$

where the suffices μ, ν and i, j run from 0 to 3 and from 1 to 3, respectively, $x^1_\pm = \chi_\pm$, $\sigma_\pm(\chi_\pm) = \sin\chi_\pm, \chi_\pm$ and $\sinh\chi_\pm$ for the spatial curvature $K_\pm = 1, 0, -1$, respectively, and $d\Omega^2 = d\theta^2 + \sin^2\theta d\varphi^2$. The shell is a time-like hypersurface Σ given as

$$x^\mu_\pm = Z^\mu_\pm(y^M), \tag{3}$$

where y^M $(M = 0, 2, 3)$ denote the intrinsic coordinates in the shell. In the following we specify the coordinates in the form

$$x^A_\pm = Z^A_\pm(y^0), \quad x^a_\pm = y^a, \tag{4}$$

where the suffices A and a take the values (0, 1) and (2, 3), respectively. When we define the tangential triads $e^\mu_{(M)\pm}$ $(M = 0, 2, 3)$ by $e^\mu_{(M)\pm} = \partial x^\mu_\pm/\partial y^M$, the intrinsic metric is given by

$$q^\pm_{MN} = e^\mu_{(M)\pm} e^\nu_{(N)\pm} g^\pm_{\mu\nu}. \tag{5}$$

If we specify y^0 as the proper time τ in the shell, the components of the triads can be expressed as

$$e^\mu_{(0)\pm} = (\partial x^0/\partial y^0, \partial x^1/\partial y^0, 0, 0) = F_\pm(1, v_\pm, 0, 0), \tag{6}$$

$e^\mu_{(2)\pm} = (0, 0, 1, 0)$ and $e^\mu_{(3)\pm} = (0, 0, 0, 1)$, where $F_\pm \equiv \gamma_\pm/a_\pm$, $v_\pm \equiv dx^1_\pm/dx^0_\pm$ $(= dx^1_\pm/d\eta_\pm)$ and $\gamma_\pm \equiv 1/\sqrt{1-(v_\pm)^2}$. Here we take the units of the light velocity $c = 1$. The unit normal vector $n^\mu_\pm$ of Σ is defined by the conditions $n_{\mu\pm} e^\mu_{(M)\pm} = 0$ $(M = 0, 2, 3)$ and $n_{\mu\pm} n^\mu_\pm = 1$, and the components can be expressed as

$$n^\mu_\pm = (-v_\pm, 1, 0, 0)\gamma_\pm/a_\pm. \tag{7}$$

The line-element in the shell in terms of the intrinsic coordinates is

$$ds^2 = q_{MN} dy^M dy^N = -d\tau^2 + R^2 d\Omega^2, \tag{8}$$

where $y^0 = \tau, y^2 = \theta, y^3 = \varphi$, and $R \equiv a_+\sigma(\chi_+) = a_-\sigma(\chi_-)$.

Since the intrinsic geometry is regular, the induced metric should be continuous and we have

$$q_{MN+} = q_{MN-} \equiv q_{MN}. \tag{9}$$

The extrinsic curvature of Σ is defined by

$$K_{MN\pm} = \frac{1}{2} e^\mu_{(M)\pm} e^\nu_{(N)\pm} \mathcal{L}_n g_{\mu\nu} = e^\mu_{(M)\pm} e^\nu_{(N)\pm} [n_{\mu;\nu} + n_{\nu;\mu}], \tag{10}$$

where $\mathcal{L}$ represents the Lie derivative, n denotes the unit normal of Σ, and a suffix $;\mu$ denotes the four-dimensional covariant derivative with respect to x^μ. For the energy-momentum tensor $T^{\mu\nu}$, the corresponding surface component $S_{\mu\nu}$ in the shell is defined using the Gaussian normal coordinates as

$$S_{\mu\nu} = \lim_{\epsilon\to 0}\int_{-\epsilon}^{\epsilon} T_{\mu\nu}d\zeta, \tag{11}$$

where ζ is the radial coordinate and $\zeta = 0$ is for the shell surface. The expression S_{MN} in the intrinsic coordinates is given by

$$S_{MN} = e^\mu_{(M)}e^\nu_{(N)}S_{\mu\nu}, \tag{12}$$

where $e^\mu_{(M)}$ is the triad in the gaussian normal coordinates. From the junction conditions derived by Israel, we obtain the relations between the jump of the extrinsic curvature and the surface energy-momentum tensor.

3 Perturbations and the junction conditions

The perturbations of $g_{\mu\nu}$ and Z^μ around the background ($\bar{g}_{\mu\nu}$ and $\bar{Z}^\mu$) are considered:

$$g_{\mu\nu} = \bar{g}_{\mu\nu} + \delta g_{\mu\nu}, \quad Z^\mu = \bar{Z}^\mu + \delta Z^\mu. \tag{13}$$

The perturbed tangent vectors are expressed as

$$e^\mu_{(M)} = \bar{e}^\mu_{(M)} - \mathcal{L}_{\delta Z}\bar{e}^\mu_{(M)}. \tag{14}$$

For the perturbations of the induced metric:

$$q_{MN} = \bar{q}_{MN} + \delta q_{MN}, \tag{15}$$

Mukohyama derived the expression

$$\delta q_{MN} = e^\mu_{(M)}e^\nu_{(N)}(\delta g_{\mu\nu} + \mathcal{L}_{\delta Z}\bar{g}_{\mu\nu}). \tag{16}$$

The perturbed normal is expressed as

$$\delta n^\mu = \frac{1}{2}\bar{n}^\mu\bar{n}^\nu\bar{n}^\lambda\delta g_{\nu\lambda} + e^\mu_{(M)}q^{MN}\bar{n}_\nu\mathcal{L}_{\delta Z}e^\nu_{(N)} \tag{17}$$

and

$$\delta K_{MN} = \frac{1}{2}e^\mu_{(M)}e^\nu_{(N)}[\mathcal{L}_{\delta Z}\bar{g}_{\mu\nu} + \mathcal{L}_{\delta Z}\mathcal{L}_n\bar{g}_{\mu\nu} - 2n^\lambda\delta\Gamma_{\lambda\mu\nu}], \tag{18}$$

where

$$\delta\Gamma_{\lambda\mu\nu} \equiv \frac{1}{2}(\delta g_{\lambda\mu;\nu} + \delta g_{\lambda\nu;\mu} - \delta g_{\mu\nu;\lambda}). \tag{19}$$

This perturbed extrinsic curvatures are reduced to

$$\delta K_{MN} = \frac{1}{2}IK_{MN} - \frac{1}{2}n^\lambda e^\mu_{(M)}e^\nu_{(N)}J_{\lambda\mu\nu}, \tag{20}$$

where

$$I \equiv n^\mu n^\nu(\delta g_{\mu\nu} + 2\delta Z_{\mu;\nu}) \tag{21}$$

and

$$J_{\lambda\mu\nu} \equiv 2\delta\Gamma_{\lambda\mu\nu} + \delta Z_{\lambda;\mu\nu} + \delta Z_{\lambda;\nu\mu} + (R_{\alpha\mu\lambda\nu} + R_{\alpha\nu\lambda\mu})\delta Z^\alpha. \tag{22}$$

Under the gauge transformation

$$x^\mu \to x'^\mu = x^\mu + \xi^\mu, \tag{23}$$

$\delta_{\mu\nu}$ and δZ^μ transform as

$$\delta g_{\mu\nu} \to \delta g_{\mu\nu} - \xi_{\mu;\nu} - \xi_{\nu;\mu}, \quad \delta Z^\mu \to \delta Z^\mu + \xi^\mu, \tag{24}$$

and it is found that δq_{MN} and δK_{MN} are invariant under this gauge transformation. The junction conditions for the perturbations of metric and extrinsic curvature which was shown by Mukohyama[6] are expressed as

$$\delta q_{MN+} = \delta q_{MN-} \tag{25}$$

and

$$[\delta \tilde{K}_{MN}]^{\pm} = -\kappa^2(\delta \tilde{S}_{MN} - \frac{1}{2}\delta \tilde{S}\, q_{MN}), \tag{26}$$

where

$$\delta \tilde{K}_{MN} \equiv \delta K_{MN} - \frac{1}{2}(K^L_M \delta q_{LN} + K^L_N \delta q_{LM}), \tag{27}$$

and

$$\delta \tilde{S}_{MN} \equiv \delta S_{MN} - \frac{1}{2}(S^L_M \delta q_{LN} + S^L_N \delta q_{LM}) \tag{28}$$

with $S = q^{MN}S_{MN}$ and $\delta \tilde{S} = q^{MN}\delta S_{MN}$. The equation (26) is consistent with a relation

$$[\delta \tilde{K}_{MN}]^{\pm} = -\kappa^2\{\delta S_{MN} - \frac{1}{2}(\delta S q_{MN} + S\delta q_{MN})\}, \tag{29}$$

so that

$$-\kappa^2 \delta S_{MN} = [\delta K_{MN} - \delta K q_{MN} - K\delta q_{MN}]^{\pm}, \tag{30}$$

where $\delta K = \delta q^{MN}K_{MN} + q^{MN}\delta K_{MN} = q^{MN}\delta K_{MN} - K^{MN}\delta q_{MN}$.

When the metric perturbations in the two regions V^+ and V^- are given, we can determine δq_{MN}, δK_{MN} and δS_{MN} using Eqs. (16), (18) and (30), and find the conditions which are imposed on the shell displacements, using Eq.(25).

Next we express first the perturbations of the induced metric and the extrinsic curvature, using the gauge-invariant variables representing metric perturbations and the shell displacement, and derive the perturbations of the energy-momentum tensors in the shell.

The complete content of this report is found in the following full paper:
K. Tomita, Phys. Rev. D70, 123502 (2004); astro-ph/0408347.

Acknowledgments

The author would like to thank S. Mukohyama and N. Sakai for valuable discussions and helpful comments.

References

[1] U. H. Gerlach and U. K. Sengupta, Phys. Rev. D19, 2268 (1979).

[2] U. H. Gerlach and U. K. Sengupta, Phys. Rev. D20, 3009 (1979).

[3] U. H. Gerlach and U. K. Sengupta, J. Math. Phys. 20, 2540 (1979).

[4] U. H. Gerlachand U. K. Sengupta, Phys. Rev. D18, 1773 (1978).

[5] S. Mukohyama, Phys. Rev. D62, 084015 (2000).

[6] S. Mukohyama, Class. Quant. Grav. 17, 4777 (2000).

[7] H. Kodama, A. Ishibashi and O. Seto, Phys. Rev. D62, 064022 (2000).

[8] W. Israel, Nuovo Cim. 44b, 1 (1966).

[9] J. M. Bardeen, Phys. Rev. D22, 1882 (1980).

[10] H. Kodama and M. Sasaki, Prog. Theor. Phys. Suppl. 78, 1 (1984).

Formula for determining parameters of an astrometric binary

Hideki Asada[1], Toshio Akasaka, Masumi Kasai

Faculty of Science and Technology, Hirosaki University, Hirosaki 036-8561, Japan

Abstract

A two-body system is simplest among self-gravitating objects. It is believed that some numerical technique must be employed for the determination of the system parameters of a visual binary or a star with a planet because the relevant equations are not only highly nonlinear but also transcendental owing to the Kepler's equation. Such a common sense however is not true; we discover an analytic inversion formula in which the original orbital parameters are expressed as elementary functions of the observable quantities such as the location of four observed points and the time interval between these points.The key thing is that we use the time interval but not the time of each observation in order to avoid treating the Kepler's equation. The present formula can be applied even in cases where the observations cover a short arc of the orbit during less than one period. Thus the formula will be useful in the future astrometric missions such as SIM, GAIA and JASMINE.

1 Introduction

In the nineteenth century, Johannes Kepler found the laws of the motion of the celestial objects based on the observations by Tycho Brahe. This led to the Newton's mechanics [1]. Since those days, one of the most fundamental problems in the astronomy is: **How to determine the orbital elements of a binary from the observed quantities of the positions projected onto the celestial sphere?**

This simple question becomes of renewed interest, because in the near future space missions such as SIM, GAIA and JASMINE will find a lot of binaries within nearly 10kpc. One is an astrometric binary which is a visible star with an unseen companion ranging from a black hole, a neutron star, a white dwarf, a brown dwarf, ... , an extrasolar planet.

By the Doppler method, one can determine a combination of a companion's mass and an inclination angle between the orbital plane and the line of sight. On the other hand, one can determine them separately in principle by using astrometric observations.

It is believed that some numerical technique must be employed for the determination of the parameters (e.g., [2, 3]). This is because the conditional equations which connect the observable quantities with the orbital parameters are not only highly nonlinear but also transcendental because of the Kepler's equation. This long-standing common sense, however, is not true: we have discovered the analytic solution to this historical inversion problem!

2 Determination of Observed Ellipse

We denote Cartesian coordinates on the celestial sphere by $(\bar{x}, \bar{y})$: A general form of the ellipse is written as

$$\alpha x^2 + \beta y^2 + 2\gamma xy + 2\delta x + 2\varepsilon y = 1. \tag{1}$$

We make five observations of a visible star, whose positions on the celestial spheres are (x_i, y_i) for $i = 1, \cdots, 5$. Henceforth, we choose (x, y) so that the observed ellipse in the standard form as

$$\frac{x^2}{a^2} + \frac{y^2}{b^2} = 1, \tag{2}$$

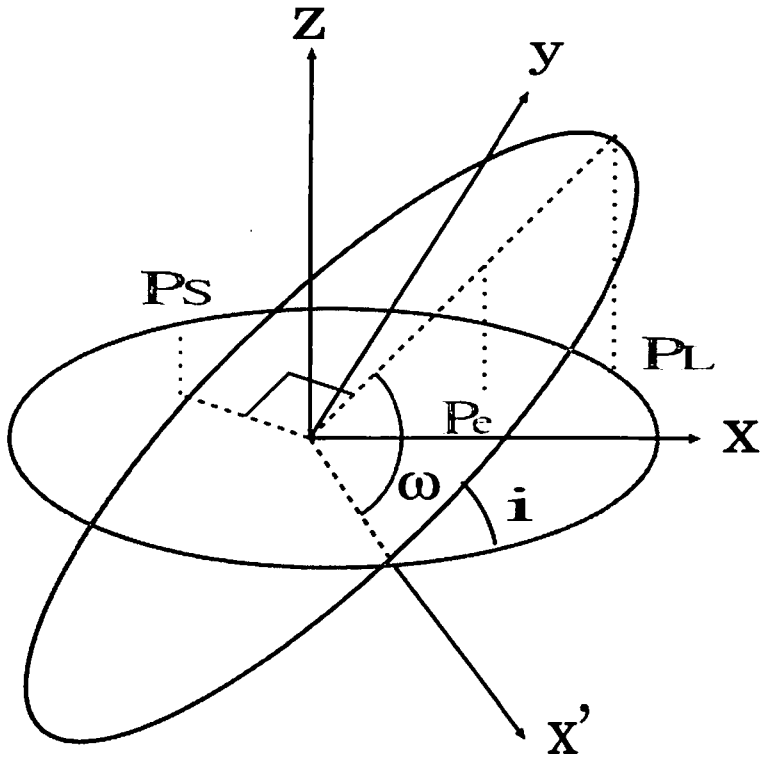
where $a \geq b$, and the ellipticity e is $\sqrt{1 - b^2/a^2}$.

[1]E-mail:asada@phys.hirosaki-u.ac.jp

3 Determination of Orbital Elements

We take four observations $\mathbf{P}_i = (x_i, y_i) = (a\cos u_i, b\sin u_i)$ at t_i $(t_4 > t_3 > t_2 > t_1)$. We use only the time interval $t_{ij} \equiv t_i - t_j$ but not the time itself.

The original Keplerian motion is characterized by the semi-major axis a_K, the ellipticity e_K, and the orbital period T. Its focus is projected onto the celestial sphere at $\mathbf{P}_e = (x_e, y_e)$, which must be determined later.



The key thing is as follows: Even after the projection, the law of the constant area velocity still holds, where the area is swept by the line interval between the projected focus and the star.

We denote the total area of the observed ellipse by $S = \pi ab$, and the area swept during the time interval t_{ij} by S_{ij}, which is given by

$$S_{ij} = \frac{1}{2}ab\Big(u_i - u_j - \frac{x_e}{a}(\sin u_i - \sin u_j) + \frac{y_e}{b}(\cos u_i - \cos u_j)\Big). \tag{3}$$

The law of the constant area velocity on the celestial sphere becomes

$$\frac{S}{T} = \frac{S_{ij}}{t_{ij}}. \tag{4}$$

This is solved as

$$x_e = -a\frac{A_2B_3 - A_3B_2}{A_1B_2 - A_2B_1},$$
$$y_e = b\frac{A_3B_1 - A_1B_3}{A_1B_2 - A_2B_1},$$

where

$$\begin{aligned} A_1 &= t_{21}\sin u_3 + t_{32}\sin u_1 - t_{31}\sin u_2, \\ A_2 &= t_{21}\cos u_3 + t_{32}\cos u_1 - t_{31}\cos u_2, \\ A_3 &= t_{21}u_3 + t_{32}u_1 - t_{31}u_2. \end{aligned}$$

B_1, B_2, B_3 are similar ($1 \to 2 \to 3 \to 4$).

The ratio of the distances from the origin to the periastron and the focus remains same even after the projection. Thus we find

$$\mathbf{P}_L = \frac{1}{e_K}\mathbf{P}_e. \tag{5}$$

The periastron is projected at $\mathbf{P}_L \equiv (x_L, y_L) = (a\cos u_L, b\sin u_L)$, located on the observed ellipse. Thus we obtain

$$e_K = \sqrt{\frac{x_e^2}{a^2} + \frac{y_e^2}{b^2}}. \tag{6}$$

By using S_{21} for instance, the orbital period is obtained as

$$T = \frac{St_{21}}{S_{21}}. \tag{7}$$

Next, the intersection of the observed ellipse and the projected minor axis, denoted by $\mathbf{P}_S$. Even after projection, the projected major and minor axes, which are not those of the observed ellipse, divide the observed ellipse in quarter areas.

It is useful to consider the invariants such as $|\mathbf{P}_L|$, $|\mathbf{P}_S|$ and $|\mathbf{P}_L \times \mathbf{P}_S|$. Now, we have exactly three unknowns as a_K, ω and i.

Finally we obtain

$$\cos i = \frac{1}{2}(\xi - \sqrt{\xi^2 - 4}), \tag{8}$$

$$a_K = \sqrt{\frac{C^2 + D^2}{1 + \cos^2 i}}, \tag{9}$$

$$\cos 2\omega = \frac{C^2 - D^2}{a_K^2 \sin^2 i}, \tag{10}$$

where

$$C = \frac{1}{e_K}\sqrt{x_e^2 + y_e^2},$$

$$D = \frac{1}{abe_K}\sqrt{\frac{a^4 y_e^2 + b^4 x_e^2}{1 - e_K^2}},$$

$$\xi = \frac{(C^2 + D^2)\sqrt{1 - e_K^2}}{ab}.$$

4 Conclusion

We have discovered the analytic solution to the long-standing inverse problem in the celestial mechanics. Our result has some advantages:

1. Numerical solvers are not needed.
   — quicker data analysis.

2. Applicable even in cases where the observations cover a short arc of the orbit during less than one period.
   — important for space missions (several years) and long orbital binaries (> 10 years).

References

[1] H. Goldstein, *Classical Mechanics* (MA: Addison-Wesley, 1980)

[2] H.K. Eichhorn and Y. Xu, ApJ, 358, 575 (1990)

[3] D. Olevic and Z. Cvetkovic, A&A, 415, 259 (2004)

[4] H. Asada, T. Akasaka and M. Kasai, PASJ, 56, L35 (2004)

Energy Extraction from Higher Dimensional Black Holes and Black Rings

Masato Nozawa[1(a)], Kei-ichi Maeda[2(a,b,c)]

[(a)] *Department of Physics, Waseda University, 3-4-1 Okubo, Shinjuku-ku, Tokyo 169-8555, Japan*
[(b)] *Advanced Research Institute for Science and Engineering, Waseda University, Shinjuku, Tokyo 169-8555, Japan*
[(c)] *Waseda Institute for Astrophysics, Waseda University, Shinjuku, Tokyo 169-8555, Japan*

Abstract

We analyze the energy extraction from higher dimensional black holes by the Penrose process. Our result shows the efficiency of the process from higher dimensional black holes and black rings can be rather productive than that in four dimensions, Kerr black hole. The thermodynamic quantities, such as the horizon area and the angular momentum, exhibit the different structure between Kerr space-time and higher dimensional counterparts. And finally we demonstrate the stability of black rings by a catastrophe theory, which indicates black rings might be unstable configuration.

1 Introduction

In recent years, a lot of studies of brane world have attracted quite a lot of interest. One characteristic feature of brane world is that mini black holes might emerge in the accelerator. If we are able to detect the production of black holes, it would be not only the direct evidence for the Hawking radiation, but also the stepping stone to the unified theory. For this reason, the basic study of higher dimensional black holes is now of great importance.

The rotating black holes in d dimensional space-times with its surface S^{d-2} were first derived by Myers and Perry [3]. The amazing discovery is the rotating black ring solution by Emparan and Reall [4], whose topology of the event horizon is $S^1 \times S^2$. This is the first counterexample that uniqueness theorem does not hold in higher dimensions. It is then important to examine the property of the black ring and black holes in detail.

We focus our attention on the energy extraction from higher dimensional black holes by the Penrose process and stability analysis via the catastrophe theory.

2 Myers-Perry and Black Ring solution

We consider a black hole with two independent rotation parameters in five dimensions. The metric is given by

$$ds^2 = -dt^2 + \frac{\rho^2 r^2}{\Delta}dr^2 + \rho^2 d\theta^2 + \frac{\mu}{\rho^2}(dt + a\sin^2\theta d\phi + b\cos^2\theta d\psi)^2 + (r^2+a^2)\sin^2\theta d\phi^2 + (r^2+b^2)\cos^2\theta d\psi^2, \tag{1}$$

$$\rho^2 = r^2 + a^2\cos^2\theta + b^2\sin^2\theta, \qquad \Delta = (r^2+a^2)(r^2+b^2) - \mu r^2. \tag{2}$$

The horizon is defined $\Delta = 0$ at $r = r_\pm$ and the condition for the existence of the event horizon is $\mu \geq (|a| + |b|)^2$.

The metric of a rotating black ring is written in the following form [4] [5]

$$ds^2 = -\frac{F(x)}{F(y)}\left(dt + R\frac{\sqrt{\lambda\nu(1+\lambda)}}{1+\nu}(1+y)d\psi\right)^2 + \frac{R^2}{(x-y)^2}\left[-F(x)\left(\frac{(1+\lambda)G(y)}{(1+\nu)^2}d\psi^2 + \frac{F(y)}{G(y)}dy^2\right) + F(y)^2\left(\frac{dx^2}{G(x)} + \frac{G(x)(1+\lambda)}{F(x)(1+\nu)^2}d\phi^2\right)\right], \tag{3}$$

[1]E-mail:tama@scphys.kyoto-u.ac.jp
[2]E-mail:misao@yukawa.kyoto-u.ac.jp

where $F(\xi) = 1 - \lambda\xi$, $G(\xi) = (1 - \xi^2)(1 - \nu\xi)$. The parameter $R > 0$ can be interpreted the radius of the ring. The parameter ν, related to the "thinness" of the ring [5], takes value in $0 < \nu < 1$. ϕ and ψ both have period $\Delta\phi = \Delta\psi = 2\pi$. x, y take the value in the range $-1 \leq x \leq 1$, $-1 \leq y^{-1} < \lambda$. $x = +1$ points into the ring, while $x = -1$ points out of the ring. The asymptotic infinity is at $x = y = -1$, the space-time singularity is located at $y = \lambda^{-1}$. And $y = \nu^{-1}$ defines the event horizon, the ergosurface $y = \pm\infty$. The parameter λ determines the topology of the objects; $\lambda = 1$ represents a black hole and $\lambda = 2\nu/(1 + \nu^2)$ a black ring. $\nu = 0$ is the static black ring with conical singularity. We define a dimensionless reduced spin parameter j such as $j^2 = 27\pi J^2/32GM^3$. There exist two black rings and a black hole with the same mass and spin in the range $27/32 < j^2 < 1$.

3 Energy Extraction

In the Penrose process, an incident particle with the momentum $p^\mu_{(1)}$ is supposed to split into two fragments in the ergoregion. One of them $p^\mu_{(2)}$ crosses the event horizon, the other $p^\mu_{(3)}$ escapes to infinity. At the point of split, the energy E, the angular momentum L_i are conserved, The momenta of three particles $p^\mu_{(I)}$, where the subscript I denotes I-th particle ($I = 1, 2, 3$), are nonspacelike and hence should lie in the local light cone. Supposed the orbit is constrained on the equatorial plane $\theta = \pi/2$. Then the t-ϕ_i and ϕ_i-ϕ_j components ($i, j \geq 2$) vanish. Defining the momenta of a particle along the geodesic γ as

$$p = \left(\frac{dx^\mu}{d\tau}\right)_\gamma \frac{\partial}{\partial x^\mu} = \dot{t}\left(\frac{\partial}{\partial t} + v\frac{\partial}{\partial r} + \Omega_1\frac{\partial}{\partial \phi_1}\right), \tag{4}$$

with $\dot{t} = dt/d\tau, v = dr/dt, \Omega = d\phi_1/dt$, where τ is an affine parameter of the test particle along γ. The relation $p_t = g_{tt}\dot{t} + g_{t\phi_1}\dot{\phi}_1$ yields $\dot{t} = -E/X, X = g_{tt} + \Omega_1 g_{t\phi_1}$. Provided the momenta p^μ has unit norm $p^\mu p_\mu = -1$, we find

$$g_{tt} + 2g_{t\phi_1}\Omega_1 + g_{\phi_1\phi_1}\Omega_1^2 + g_{rr}v^2 = -(X/E)^2 \leq 0. \tag{5}$$

Then the angular velocity for asymptotic infinity takes the value $\Omega^- \leq \Omega_1 \leq \Omega^+$;

$$\Omega^\pm = \omega_1 \pm \sqrt{\omega_1^2 - \frac{1}{g_{\phi_1\phi_1}}(g_{tt} + g_{rr}v^2)}, \tag{6}$$

where $\omega_1 = -g_{t\phi_1}/g_{\phi_1\phi_1}$ denotes the angular velocity of a locally nonrotating observer at a given r. Then the efficiency of the process is given by

$$\eta = \frac{E_3 - E_1}{E_1} = \frac{(\Omega_{1(1)} - \Omega_{1(2)})X_3}{(\Omega_{1(3)} - \Omega_{1(2)})X_1} - 1 \equiv \chi - 1. \tag{7}$$

The efficiency $\eta = \chi - 1$ is maximized when the vector $p^\mu_{(2)}$ and $p^\mu_{(3)}$ are tangent to the null cone; $\Omega_{1(2)} = \Omega^-|_{v_2=0}, \Omega_{1(3)} = \Omega^+|_{v_3=0}$. which leads m_3E_3 takes the maximum (m_2E_2 is minimum). Therefore

$$\chi_{\max} = \frac{(\Omega_{1(1)} - \Omega^-)(g_{tt} + g_{t\phi_1}\Omega^+)}{(\Omega^+ - \Omega^-)(g_{tt} + g_{t\phi_1}\Omega_{1(1)})} \leq \frac{g_{\phi_1\phi_1}(\sqrt{1 + g_{tt}} + 1) + g_{t\phi_1}^2}{2g_{\phi_1\phi_1}\sqrt{1 + g_{tt}}}, \tag{8}$$

where the equality sign holds when the split occurs at the horizon. In four dimensions, the angular momentum parameter has an upper bound $a \leq M$, then we find $\eta_{\max} = (\sqrt{2} - 1)/2 \sim 20.7\%$. The equality holds when the split occurs at the event horizon and the black hole is the extreme case $a = M$. Then we find the maximum efficiency of the Penrose process in Kerr space-time is about 20.7%. This recovers the results in [1] [2].

In five dimensions, the efficiency is maximized when the black hole is extremal $r_+^2 = ab$.

$$\eta \leq \frac{1}{2}\left(\sqrt{\frac{|a|}{|b|} + 1} - 1\right). \tag{9}$$

Hence the efficiency is determined by the ratio of the two angular parameters. Supposed $a/b \gg 1$, we can extract rather higher energy than that from Kerr black hole, albeit the angular momenta is bounded from above. The efficiency for a black ring is

$$\eta = \frac{1}{2}\left(\sqrt{1+\frac{\nu(1+\lambda)}{\lambda-\nu}}-1\right) = \frac{1}{2}\left(\sqrt{\frac{2}{1-\nu}}-1\right). \tag{10}$$

Since ν takes value in the range $0 < \nu < 1$, the efficiency is grater than that from Kerr black hole.

4 Catastrophe Theory

The surface energy, often referred to irreducible mass, for MP black hole and black ring is [3] [6]

$$M_{\rm irr} = \frac{3(2\pi^2 A^2)^{1/3}}{16\pi G} = \frac{3\pi R^2 \lambda^{1/3}(1+\lambda)^{1/3}(\lambda-\nu)}{2^{5/3}G(1+\nu)^{4/3}(1-\nu)^{2/3}}. \tag{11}$$

We find the rotational energy $\varepsilon_R \equiv E_R/M = M - M_{\rm irr}$ is

$$\varepsilon_R \equiv E_R/M = 1 - \frac{2^{1/3}\lambda^{2/3}(1+\lambda)^{2/3}(\lambda-\nu)}{(1+\nu)^{1/3}(1-\nu)^{1/3}} \tag{12}$$

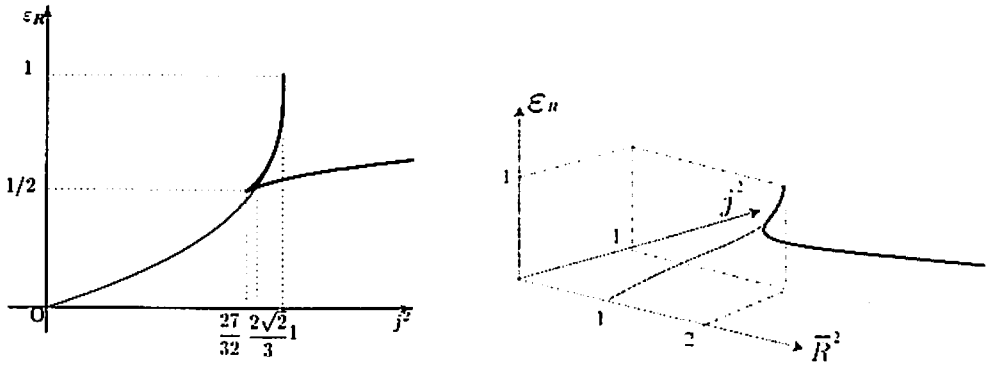


Figure 1: Plots of the rotational energy as the function of reduced spin are shown. The solid line corresponds to the black hole, the slight line to the ring. The lap $(j, E_R/M) = (1,1)$ is the naked singularity. $(0,0)$ represents the Tangherlini-Schwarzschild solution, so in this case we cannot extract energy from a black hole. The left side figure is the curve in the equilibrium space $(\bar{R}^2, j^2, \varepsilon_R)$.

Fig.1 is the plot for ε_R against j^2. The rotational energy is monotonically increasing function of j^2 for MP black holes with one angular momentum, while it has a cusp at $j^2 = 27/32$ for black rings. This point is a state of minimum angular momentum of black rings. The appearance of cusp implies the existence of a phase transition. The higher entropy branch should be relatively stable, while the lower entropy branch relatively unstable. Such behavior of the stability of black rings could be demonstrated by a catastrophe theory [7].

Catastrophe theory is a mathematical tool to explain a lot of changes of states in nature. The stability analysis via catastrophe theory has one to one correspondence to the linear perturbations.

We here assume that control parameter is the radius of a ring $\bar{R}^2 = 3\pi R^2/2GM$, state variable is the angular momentum j^2 and potential function is the rotational energy ε_R. Fig.1 is the plot of the equilibrium space M_V. The projection of the equilibrium space onto the control plane is called a catastrophe map $\chi_V : M_V \to \mathbb{R}^2$. At the point of the bifurcation $(\bar{R}^2, j^2, \varepsilon_R) = (25/12, 27/32, 1/2)$, the mapping χ_V becomes singular. If such a singular point exist, the stability of the system changes there. In this case, the lower branch of the rotational energy has higher entropy, which is thermodynamically

stable configuration. But in the limit $R \to \infty, \nu, \lambda \to 0$ [5], black ring solution approaches boosted black string solution. Since black strings are proved to be unstable against linear perturbations [9], the higher entropy branch is unstable in the dynamical sense. But this result does not lead to the conclusion that the lower entropy should be also unstable. It is not clear whether the lower branch suffers instability or settles down to other stable configuration.

5 Summary

We discussed the energy extraction from higher dimensional black holes and black rings. The result is that we can extract much more energy from higher dimensional black holes than from Kerr black hole. Although we can gain at most about 20.7% energy of incident particle in Kerr space-time, the efficiency could be rather amplified in higher dimensions.

But this results does not directly lead that higher dimensional black holes and black rings radiate at high rate. Although the efficiency of black ring is infinitely large in the limit $\nu \to 1$ (10), the effective potential becomes larger and larger in this limit. Then particles cannot escape to infinity, and energy extraction becomes unlikely. To evaluate the evolution of black ring, we have to investigate the superradiance and Hawking radiation. The evaporation and evolution mechanism of black ring would show us specific feature of them.

The stability of higher dimensional rotating black hole, of course the black ring, has not yet been fully established. An interesting thermodynamics approach to the stability shows they are unstable in special limit [5] [8]. Black ring approaches boosted black string and a rotating black hole with large angular momentum in $d \geq 6$ approaches black membrane. Black strings and membranes are shown to be unstable [9]. It would be interesting to make a stability analysis by the metric perturbations and thermodynamics viewpoint.

As we demonstrated, the appearance of cusp in Fig.1 indicates we could demonstrate the stability of the black ring by a catastrophe theory. This shows black rings becomes unstable as the angular momentum becomes large, which corresponds to the black string instability. But it is not clear whether the lower entropy branch is also unstable. This branch might settle down to other stable configuration.

References

[1] S. Chandrasekhar, *The Mathematical Theory of Black Holes* (Oxford University Press, New York, 1983)

[2] M. Bhat, S, Dhurandrhar and N. Dadhich, J. Astrophys. Astr. (1985) **6**, 85;
S.Parthasarathy, S. M. Wagh, S. V. Dhurandhar and N. Dadhich, Astrophys. J., 1986 **307**, 38

[3] R. C. Myers, M. J. Perry, Annals of Phys, **172**, 304 (1986)

[4] R. Emparan and H. S. Reall, Phys. Rev. Lett. **88** (2002), 101101

[5] H. Elvang and R. Emparan, JHEP **0311** (2003) 035

[6] L. Smarr, Phys. Rev. Lett. **30** 2 (1973)

[7] T. Torii, K. Maeda and T. Tachizawa, Phys. Rev. D. **51** 1510 (1995), T. Torii, K. Maeda and T. Tachizawa, Phys. Rev. D. **51** 4054 (1995)

[8] R. Emparan and R. C. Myers, JHEP **0309** (2003) 025

[9] R. Gregory and R. Laflamme, Phys. Rev. Lett. **70** 2837 (1993), Nucl. Phys. B **428** (1994) 399

[10] V. Frolov and D. Stojković, Phys. Rev. D. **68** 064011 (2003)

Second Order Gauge Invariant Perturbation Theory

Kouji Nakamura[1]

Department of Astronomical Science, the Graduate University for Advanced Studies, Osawa, Mitaka, Tokyo 181-8588, Japan.

Abstract

Based on the proposal of gauge invariant variables in the paper [K. Nakamura, Prog. Theor. Phys. **110** (2003), 723.], formulae of the linear and the second order perturbative curvatures are derived. These perturbative curvatures do have the same form as the definitions of gauge invariant variables for an arbitrary perturbative field which are previously proposed in the above paper. We briefly discuss physical situations to which this perturbation theory should be applied.

In many theories of physics including general relativity, the perturbative approach with an appropriate background spacetime $(\mathcal{M}_0, Q_0)$ (unperturbed spacetime) is one of the powerful techniques to investigate natural phenomena on the physical spacetime $(\mathcal{M}, Q)$ [1]. In particular, general relativity is based on the concept of general covariance which intuitively states that *there is no preferred coordinate system in nature*. Due to this general covariance, *gauge degree of freedom*, which is unphysical degree of freedom, arises in general relativistic perturbations. To obtain physically meaningful results, we have to fix this gauge degree of freedom or to extract *gauge invariant parts of perturbations*.

On the other hand, higher order multi-parameter perturbations, in which two or more small parameters are prepared, have many physical situations to be applied. One of famous applications of two-parameter perturbation technique is the perturbations of a star[2], in which we choose the gravitational field of a spherical star as the background spacetime. One of the small parameters corresponds to the rotation of the star and another is the pulsation amplitude of it. The effects due to the rotation-pulsation coupling are described in the higher order. Hence, to investigate the higher order perturbation theory from general point of view is more than to obtain quantitatively accurate results[3].

In this article, we briefly show some parts of our formulation of the second order gauge invariant perturbation theory[4]. This article is prepared for the proceedings of the workshop JGRG14 (YITP-W-04-13). Since the brief outline of our formulation is already given in the proceedings of JGRG13[5], we mainly introduce the parts of Ref.[4] which does not overlap with the ingredients of Ref.[5].

The gauge degree of freedom in linear order perturbations is usually regarded as the degree of freedom of the infinitesimal coordinate transformations. However, when we consider higher order perturbations, more deeper understanding of the "*gauge*" is required. Here, we follow the understanding of the "*gauge*" by Stewart et al.[6] and its development by Bruni et al.[7]. According to their basic understanding, the "*gauge choice*" in perturbation theories is a point identification map $\mathcal{X}$ between the background spacetime $(\mathcal{M}_0, Q_0)$ and the physical spacetime $(\mathcal{M}, Q)$. This point identification is implicitly done through the equation

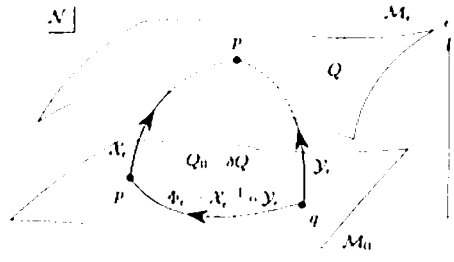


Figure 1: "Gauge choice" (one-parameter case)

$$Q(\text{“}p\text{”}) = Q_0(p) + \delta Q(p) \tag{1}$$

as depicted in Figure 1. It is important to note that this gauge choice $\mathcal{X}$ is not unique when we impose general covariance on the theory. Rather, Eq. (1) involves the degree of freedom corresponding to the choice of the map $\mathcal{X} : \mathcal{M}_0 \to \mathcal{M}$. The "*gauge transformation*" is simply regarded as the change $\mathcal{X} \to \mathcal{Y}$ $(\Phi := \mathcal{X}^{-1} \circ \mathcal{Y})$ of the gauge choice (see Figure 1.).

[1] E-mail:kouchan@th.nao.ac.jp

Though Figure 1 shows the case of the one-parameter perturbation, the extension to the multi-parameter perturbation theory is straightforward[7, 8]. Based on the above understanding of "gauge", we can derive the gauge transformation rules for the each order perturbation of an arbitrary tensor field Q in two-parameter perturbation:

$$
\begin{aligned}
{}^{(p,q)}_{\mathcal{Y}}Q - {}^{(p,q)}_{\mathcal{X}}Q &= \pounds_{\xi_{(p,q)}} Q_0 && \text{for} \quad (p,q) = (1,0),(0,1), && (2)\\
{}^{(p,q)}_{\mathcal{Y}}Q - {}^{(p,q)}_{\mathcal{X}}Q &= 2\pounds_{\xi_{(\frac{p}{2},\frac{q}{2})}} {}^{(\frac{p}{2},\frac{q}{2})}_{\mathcal{X}}Q + \left\{ \pounds_{\xi_{(p,q)}} + \pounds^2_{\xi_{(\frac{p}{2},\frac{q}{2})}} \right\} Q_0 && \text{for} \quad (p,q) = (2,0),(0,2), && (3)\\
{}^{(1,1)}_{\mathcal{Y}}Q - {}^{(1,1)}_{\mathcal{X}}Q &= \pounds_{\xi_{(1,0)}} {}^{(0,1)}_{\mathcal{X}}Q + \pounds_{\xi_{(0,1)}} {}^{(1,0)}_{\mathcal{X}}Q + \left\{ \pounds_{\xi_{(1,1)}} + \frac{1}{2}\pounds_{\xi_{(1,0)}}\pounds_{\xi_{(0,1)}} + \frac{1}{2}\pounds_{\xi_{(0,1)}}\pounds_{\xi_{(1,0)}} \right\} Q_0. && (4)
\end{aligned}
$$

In these transformation rules, the field Q on the physical spacetime $\mathcal{M}$ is pulled-back to the background spacetime $\mathcal{M}_0$ as $\mathcal{X}^*Q$ and $\mathcal{Y}^*Q$ by two different gauge choices $\mathcal{X}$ and $\mathcal{Y}$, respectively, $\mathcal{X}^*Q$ and $\mathcal{Y}^*Q$ are expanded so that

$$
\mathcal{X}^*Q = \sum_{k',k=0}^{\infty} \frac{\epsilon^k \lambda^{k'}}{k!k'!} {}^{(k,k')}_{\mathcal{X}}Q, \quad \mathcal{Y}^*Q = \sum_{k',k=0}^{\infty} \frac{\epsilon^k \lambda^{k'}}{k!k'!} {}^{(k,k')}_{\mathcal{Y}}Q, \tag{5}
$$

and $\xi^a_{(p,q)}$ are generators for gauge transformation Φ.

Inspecting gauge transformation rules (2)-(4), we define the gauge invariant variables for metric perturbations of each order[8]. First, we expand the pull-back $\mathcal{X}^*\bar{g}_{ab}$ of the metric $\bar{g}_{ab}$ on the physical spacetime $\mathcal{M}$ so that

$$
\mathcal{X}^*\bar{g}_{ab} = g_{ab} + \epsilon {}^{(1,0)}_{\mathcal{X}}h_{ab} + \lambda {}^{(0,1)}_{\mathcal{X}}h_{ab} + \frac{\epsilon^2}{2} {}^{(2,0)}_{\mathcal{X}}h_{ab} + \epsilon\lambda {}^{(1,1)}_{\mathcal{X}}h_{ab} + \frac{\lambda^2}{2} {}^{(0,2)}_{\mathcal{X}}h_{ab} + O^3(\epsilon,\lambda), \tag{6}
$$

and the each order metric perturbations is decomposed into gauge invariant part ${}^{(p,q)}\mathcal{H}_{ab}$ and gauge variant part ${}^{(p,q)}X_a$ so that

$$
\begin{aligned}
{}^{(p,q)}h_{ab} &=: {}^{(p,q)}\mathcal{H}_{ab} + \pounds_{(p,q)X} g_{ab} && \text{for} \quad (p,q) = (1,0),(0,1), && (7)\\
{}^{(p,q)}h_{ab} &=: {}^{(p,q)}\mathcal{H}_{ab} + 2\pounds_{(\frac{p}{2},\frac{q}{2})X} {}^{(\frac{p}{2},\frac{q}{2})}h_{ab} + \left(\pounds_{(p,q)X} - \pounds^2_{(\frac{p}{2},\frac{q}{2})X} \right) g_{ab} && \text{for} \quad (p,q) = (2,0),(0,2), && (8)\\
{}^{(1,1)}h_{ab} &=: {}^{(1,1)}\mathcal{H}_{ab} + \pounds_{(0,1)X} {}^{(1,0)}h_{ab} + \pounds_{(1,0)X} {}^{(0,1)}h_{ab} \\
&\quad + \left\{ \pounds_{(1,1)X} - \frac{1}{2}\pounds_{(1,0)X}\pounds_{(0,1)X} - \frac{1}{2}\pounds_{(0,1)X}\pounds_{(1,0)X} \right\} g_{ab}. && (9)
\end{aligned}
$$

Using the gauge variant part ${}^{(p,q)}X^a$ of the metric perturbation, the gauge invariant variable ${}^{(p,q)}\mathcal{Q}$ for each order perturbations ${}^{(p,q)}Q$ of an arbitrary fields Q other than metric can be defined by [8]

$$
\begin{aligned}
{}^{(p,q)}\mathcal{Q} &:= {}^{(p,q)}Q - \pounds_{(p,q)X} Q_0 && \text{for} \quad (p,q) = (1,0),(0,1), && (10)\\
{}^{(p,q)}\mathcal{Q} &:= {}^{(p,q)}Q - 2\pounds_{(\frac{p}{2},\frac{q}{2})X} {}^{(\frac{p}{2},\frac{q}{2})}Q - \left\{ \pounds_{(p,q)X} - \pounds^2_{(\frac{p}{2},\frac{q}{2})X} \right\} Q_0 && \text{for} \quad (p,q) = (2,0),(0,2), && (11)\\
{}^{(1,1)}\mathcal{Q} &:= {}^{(1,1)}Q - \pounds_{(1,0)X} {}^{(0,1)}Q - \pounds_{(0,1)X} {}^{(1,0)}Q \\
&\quad - \left\{ \pounds_{(1,1)X} - \frac{1}{2}\pounds_{(1,0)X}\pounds_{(0,1)X} - \frac{1}{2}\pounds_{(0,1)X}\pounds_{(1,0)X} \right\} Q_0. && (12)
\end{aligned}
$$

In the paper [4], we show some formulae of the second order perturbations of curvatures in terms of the gauge invariant and variant variables of the metric perturbations defined by Eqs. (7)-(9). As the results, we can see that all formulae have the same form as Eqs. (10)-(12).

To demonstrate this, we have to compare two curvatures $\bar{R}_{abc}{}^d$ on the physical spacetime $\mathcal{M}$ and $R_{abc}{}^d$ on the background spacetime $\mathcal{M}_0$ by introducing a gauge choice $\mathcal{X}$. The relation of these two curvatures is given by

$$
\bar{R}_{abc}{}^d = R_{abc}{}^d - 2\nabla_{[a}C^d{}_{b]c} + 2C^e{}_{c[a}C^d{}_{b]e}, \quad C^c{}_{ab} := \frac{1}{2}\bar{g}^{cd}\left(2\nabla_{(a}\bar{g}_{b)d} - \nabla_d\bar{g}_{ab}\right). \tag{13}
$$

In Eqs. (13), $\bar{g}^{ab}$ is defined by $\bar{g}^{ac}\bar{g}_{cb} = \delta^a{}_b$, the curvature $\bar{R}_{abc}{}^d$ and the metric $\bar{g}_{ab}$ are treated as tensor fields on the background spacetime $\mathcal{M}_0$. These are pulled back from the physical spacetime $\mathcal{M}$ to the background spacetime $\mathcal{M}_0$ by the gauge choice $\mathcal{X}$, though we do not denote it explicitly. We expand Eqs. (13) by the small parameters ϵ and λ in the form

$$\bar{R}_{abc}{}^d = \sum_{p,q=0}^{\infty} \frac{\epsilon^p \lambda^q}{p!q!} {}^{(p,q)}\bar{R}_{abc}{}^d. \tag{14}$$

Then, we obtain the expression of the perturbative Riemann curvature of each order

$$\begin{aligned}
{}^{(p,q)}\bar{R}_{abc}{}^d &= -2\nabla_{[a}H_{b]c}{}^d\left[{}^{(p,q)}\mathcal{H}\right] + \mathcal{L}_{(p,q)X}R_{abc}{}^d \qquad \text{for} \quad (p,q) = (1,0),(0,1), \qquad (15)\\
{}^{(p,q)}\bar{R}_{abc}{}^d &= -2\nabla_{[a}H_{b]c}{}^d\left[{}^{(p,q)}\mathcal{H}\right] + 4H_{[a}{}^{de}\left[{}^{(\frac{p}{2},\frac{q}{2})}\mathcal{H}\right]H_{b]ce}\left[{}^{(\frac{p}{2},\frac{q}{2})}\mathcal{H}\right] + 4{}^{(\frac{p}{2},\frac{q}{2})}\mathcal{H}_e{}^d\nabla_{[a}H_{b]c}{}^e\left[{}^{(\frac{p}{2},\frac{q}{2})}\mathcal{H}\right]\\
&\quad +2\mathcal{L}_{({}^{\frac{p}{2}},{}^{\frac{q}{2}})X}{}^{(\frac{p}{2},\frac{q}{2})}\bar{R}_{abc}{}^d + \left(\mathcal{L}_{(p,q)X} - \mathcal{L}^2_{({}^{\frac{p}{2}},{}^{\frac{q}{2}})X}\right)R_{abc}{}^d \quad \text{for} \quad (p,q) = (2,0),(0,2), \qquad (16)\\
{}^{(1,1)}\bar{R}_{abc}{}^d &= -2\nabla_{[a}H_{b]c}{}^d\left[{}^{(1,1)}\mathcal{H}\right] + 2H_{[a}{}^{de}\left[{}^{(1,0)}\mathcal{H}\right]H_{b]ce}\left[{}^{(0,1)}\mathcal{H}\right] + 2H_{[a}{}^{de}\left[{}^{(0,1)}\mathcal{H}\right]H_{b]ce}\left[{}^{(1,0)}\mathcal{H}\right]\\
&\quad +2{}^{(1,0)}\mathcal{H}_e{}^d\nabla_{[a}H_{b]c}{}^e\left[{}^{(0,1)}\mathcal{H}\right] + 2{}^{(0,1)}\mathcal{H}_e{}^d\nabla_{[a}H_{b]c}{}^e\left[{}^{(1,0)}\mathcal{H}\right]\\
&\quad +\mathcal{L}_{(0,1)X}{}^{(1,0)}\bar{R}_{abc}{}^d + \mathcal{L}_{(1,0)X}{}^{(0,1)}\bar{R}_{abc}{}^d\\
&\quad +\left(\mathcal{L}_{(1,1)X} - \frac{1}{2}\mathcal{L}_{(0,1)X}\mathcal{L}_{(1,0)X} - \frac{1}{2}\mathcal{L}_{(1,0)X}\mathcal{L}_{(0,1)X}\right)R_{abc}{}^d, \qquad (17)
\end{aligned}$$

where

$$H_{abc}\left[{}^{(p,q)}\mathcal{H}\right] := \nabla_{(a}{}^{(p,q)}\mathcal{H}_{b)c} - \frac{1}{2}\nabla_c{}^{(p,q)}\mathcal{H}_{ab}. \tag{18}$$

Equations (15)-(17) do have the same form as the definitions (10)-(12) of each order gauge invariant variable for an arbitrary field, respectively.

From these perturbative expression of the Riemann curvature (15)-(17), we can also derive the perturbative expression of the Ricci, scalar, the Einstein, and the Weyl curvature tensors. Further, we can explicitly see that all these perturbative expressions do have the same form as the definitions (10)-(12) of each order gauge invariant variable for an arbitrary field[4].

In many physical situations, it is necessary to consider the perturbation of the divergence of the energy momentum tensor of matter fields, which yields the energy conservation and the equation of motion of the matter field. In the paper [4], we also derived the second order perturbation of the equation

$$\bar{\nabla}_a\bar{T}_b{}^a = \nabla_a\bar{T}_b{}^a + C^a{}_{ca}\bar{T}_b{}^c - C^c{}_{ba}\bar{T}_c{}^a \tag{19}$$

of an arbitrary tensor field $\bar{T}_b{}^a$ of the second rank, where the derivative operator $\bar{\nabla}_a$ is regarded as the operator on the background spacetime $\mathcal{M}_0$ which is the pulled-back representation of the covariant derivative associated with the metric $\bar{g}_{ab}$ on the physical spacetime $\mathcal{M}$. These perturbative expressions also have the same form as Eqs. (10)-(12). Furthermore, using these perturbative formulae, we can also check perturbation of the Bianchi identity of each order.

Thus, in the paper [4], we derived some formulae for the second order perturbations of curvatures and explicitly show that all these formulae have the same form as Eqs. (10)-(12). This is the main result in the paper [4]. Through these derivations, we have confirmed some trivial facts. For example, the each order perturbative Weyl curvature is traceless; the each order perturbative Einstein curvature satisfies the perturbative Bianchi identity; the perturbative Einstein equations have the gauge invariant form. All of these properties are trivial from their derivations. However, these trivial results imply that the formulae derived here are mathematically correct at this level.

Further, in our framework, we do not specify anything about the background spacetime and physical meaning of the parameters for the perturbations. Our framework is based only on general covariance. Then, this framework is applicable to any theories in which general covariance is imposed and it has very many applications. Actually, we are planning to apply this to some physical problems: the radiation reaction in gravitational wave emission[9]; stationary axisymmetric ideal MHD flow around a black

hole or a star[10]; the correspondence between observables in experiment and gauge invariant variables; dynamics of gravitating membranes (for example, topological defects[11], brane world[12], ... and so on); perturbations of a compact star with its rotation and pulsation[2]; Post-Minkowski expansion alternative to post-Newtonian expansion[13]; the higher order cosmological perturbations and primordial non-Gaussianity[14]. In particular, the second order perturbative expression of the divergence of the energy momentum tensor (19) will be an useful guideline for resolving gauge problem in the radiation reaction of gravitational wave emission. We leave these as future works.

In addition to these candidates, we also note that because of little premise of our discussion, it is natural to expect that there are many applications which are not listed above and the formulae in Ref.[4] become powerful tools in applications.

The author thanks to his family and colleagues for their encouragements and taking care of his physical condition when he was writing this article.

References

[1] J. M. Bardeen, Phys. Rev. D**22** (1980), 1882; H. Kodama and M. Sasaki, Prog. Theor. Phys. Suppl. No.78 (1984), 1; V. F. Mukhanov, H. A. Feildman, and R. H. Brandenberger, Phys. Rep. **215** (1992), 203; S. Chandrasekhar, "The mathematical theory of black holes" (Oxford: Clarendon Press, 1983);

[2] Y. Kojima, Prog. Theor. Phys. Suppl. No.128 (1997), 251.
A. Passamonti, M. Bruni, L. Gualtieri, and C.F. Sopuerta, [arXiv:gr-qc/0407108].

[3] R. J. Gleiser, C. O. Nicasio, R. H. Price and J. Pullin, Phys. Rep. **325** (2000), 41.

[4] K. Nakamura, "Second order gauge invariant perturbation theory," [arXiv:gr-qc/0410024].

[5] K. Nakamura, "General framework of higher order gauge invariant perturbation theory," in *Proceedings of the thirteenth workshop on general relativity and gravitation in Japan* [arXiv:gr-qc/0402032].

[6] J. M. Stewart and M. Walker, Proc. R. Soc. London A **341** (1974), 49; J. M. Stewart, Class. Quantum Grav. **7** (1990), 1169; J. M. Stewart, *Advanced General Relativity* (Cambridge University Press, Cambridge, 1991).

[7] M. Bruni, S. Matarrese, S. Mollerach and S. Sonego, Class. Quantum Grav. **14** (1997), 2585; M. Bruni and S. Sonego, *ibid* **16** (1999), L29. M. Bruni, L. Gualtieri, and C.F. Sopuerta, *ibid* **20** (2003), 535; C.F. Sopuerta, M. Bruni, L. Gualtieri, Phys. Rev. D**70** (2004), 064002.

[8] K. Nakamura, Prog. Theor. Phys. **110**, (2003), 723.

[9] Y. Mino, M. Sasaki and T. Tanaka, Phys. Rev. D**55** (1997), 3457 ; T. C. Quinn and R. M. Wald, *ibid* D**56** (1997), 3381 ; T. C. Quinn and R. M. Wald, *ibid* D**60** (1999), 064009 ; E. Poisson, Living Rev. Rel. **7** (2004), 6 and references therein .

[10] S. Nitta, M. Takahashi and A. Tomimatsu, Phys. Rev. D**44** (1991), 2295 ; K. Ioka and M. Sasaki, *ibid* D**67** (2003), 124026; ; K. Ioka and M. Sasaki, Astrophys. J. **600** (2004), 296 ;

[11] K. Nakamura, A. Ishibashi and H. Ishihara, Phys. Rev. D**62** (2000), 101502(R); K. Nakamura and H. Ishihara, *ibid* D**63** (2001), 127501; K. Nakamura, Class. Quantum Grav. **19** (2002), 783; K. Nakamura, Phys. Rev. D**66** (2002), 084005; K. Nakamura, Prog. Theor. Phys. **110**, (2003), 201.

[12] L. Randall and R. Sundrum, Phys. Rev. Lett. **83** (1999), 4690; L. Randall and R. Sundrum, *ibid* **83** (1999), 3370; J. Garriga and T. Tanaka, *ibid* **84** (2000), 2778.

[13] S. Detweiler and L. H. Brown, Jr, Phys. Rev. D**56**, (1997), 826.

[14] K. A. Malik, D. Wands, Class. Quantum Grav. **21** (2004), L65; N. Bartolo, S. Matarrese and A. Riotto, Phys. Rev. Lett. **93** (2004), 231301 ; N. Bartolo, E. Komatsu, S. Matarrese and A. Riotto, Phys. Rep. **402** (2004), 103 ; N. Bartolo, S. Matarrese and A. Riotto, Phys. Rev. D **69** (2004), 043503 ; N. Bartolo, S. Matarrese and A. Riotto, JHEP **0404** (2004), 006 .

Spherically symmetric perfect fluid in area-radial coordinates

Hideo Iguchi[1], Tomohiro Harada[2], and Filipe C Mena[3]

[1] *Laboratory of Physics, College of Science and Technology, Nihon University, 7-24-1, Narashino-Dai, Funabashi, Chiba 274-8501, Japan*

[2] *Astronomy Unit, School of Mathematical Sciences, Queen Mary, University of London, Mile End Road, London E1 4NS, UK*

[3] *Mathematical Institute, University of Oxford, St. Giles 24-29, Oxford OX1 3LB, UK and Departamento de Matemática, Universidade do Minho, Campus de Gualtar, 4710 Braga, Portugal*

Abstract

We study the spherically symmetric collapse of a perfect fluid using area-radial coordinates. We show that analytic mass functions describe a static regular centre in these coordinates. In this case, a central singularity can not be realized without an infinite discontinuity in the central density. We construct mass functions involving fluid dynamics at the centre and investigate the relationship between those and the nature of the singularities.

1 Introduction

Recently, Giambò *et al.* gave an interesting approach to the spherically symmetric system of a perfect fluid with the barotropic equation of state $p = p(\epsilon)$ [1, 2]. They adopted the so-called area-radial coordinates and derived a second-order quasi-linear partial differential equation (PDE) for a mass function, which is identical to the Misner-Sharp quasi-local mass. Due to the presence of pressure the mass function is time dependent. A solution to this PDE gives a solution to the whole set of Einstein's field equations. Using mass functions which are analytical around the centre, they have examined the spacetime singularities resulting from the gravitational collapse. In particular, they claimed that there are always naked singularities for that class of mass functions.

In [3] we analyse the behaviour of the metric around the regular centre and show that analytic mass functions imply staticity around the centre. This means that, in this case, a central singularity can not be formed without an infinite discontinuity in the fluid density. We then present a more general analysis of the final fate of collapse in this system by (i) studying other classes of mass functions and (ii) investigating naked singularities formation within such classes.

2 GGMP equation

Here we assume a linear equation of state $p = \alpha\epsilon$. In addition, we set at a regular initial moment $R(r,0) = r$ where $R(t,r)$ is area radius. In these conditions, Giambò *et al.* [2] rewrote the Einstein equations as the following PDE for Misner-Sharp mass Ψ.

$$
\begin{aligned}
&-\frac{1}{\alpha+1}\left(\frac{2\Psi}{R}-1+(1-\alpha)Y^2\right)\frac{\Psi_{,RR}}{\Psi_{,R}}-2Y^2\frac{\Psi_{,rR}}{\Psi_{,r}}+\frac{\alpha+1}{\alpha}\frac{\Psi_{,R}}{\Psi_{,r}}Y^2\frac{\Psi_{,rr}}{\Psi_{,r}}\\
&-\frac{2\alpha}{\alpha+1}\left(\frac{2\Psi}{R}+2Y^2-1\right)\frac{1}{R}+\frac{\Psi}{R^2}+\frac{\Psi_{,R}}{\alpha R}\\
&+\frac{\alpha+1}{\alpha}\frac{\Psi_{,R}}{\Psi_{,r}}\left(\frac{Y_0'}{Y_0}-\frac{1}{\alpha+1}\frac{\Psi_0''}{\Psi_0'}-\frac{2\alpha}{(\alpha+1)r}\right)Y^2=0.
\end{aligned}
\tag{1}
$$

Notations and derivations are given in [2, 3]. In the following, we call the above quasi-linear second-order PDE Giambò-Giannoni-Magli-Piccione (GGMP) equation. Because we adopt the scaling of the comoving coordinate r, $R(r,0) = r$, the mass function must also satisfy

$$
\Psi_{,R}(r,r) = -\frac{\alpha}{\alpha+1}\Psi_{,r}(r,r) \tag{2}
$$

at the initial surface.

3 Analytic mass functions

Here we would like to investigate what type of collapse can be represented by the mass functions given by Giambò *et al.* [1, 2]. We recall that in [2] it is assumed that Ψ is an analytic function with respect to r and R which can be expanded as

$$\Psi(r, R) = \sum_{k=0}^{\infty} \sum_{i+j=3+2k} \Psi_{ij} r^i R^j. \tag{3}$$

where i and j are nonnegative integers, and it is proved that the regularity condition requires the following structure for the lowest order terms:

$$\Psi(r, R) = \frac{h}{2}\left(r^3 - \frac{\alpha}{\alpha+1}R^3\right) + \sum_{k=1}^{\infty} \sum_{i+j=3+2k} \Psi_{ij} r^i R^j. \tag{4}$$

Using this form of the mass function, it is claimed that the central singularity is naked in Theorem 3.4 of [2]. In the following, however, we show that their solution has a static centre in the regular evolution.

Let us consider that we have regular evolution after the initial moment. During the regular evolution, we can use the relation $R \approx \tau r$ $(0 < \tau < \infty)$ for small r. Then, it can be shown that the central density is

$$\lim_{r \to 0} \rho^{(1+\alpha)}(r, \tau r) = \frac{3h}{8\pi(\alpha+1)}. \tag{5}$$

by substituting equation (4) into equation (13) of [3]. We can see that the central density does not depend on τ. This means that the central density is constant in time. Therefore, the symmetric centre can not become singular without an infinite discontinuity in ρ.

To construct mass functions which can describe genuine dynamical situations, we shall include terms of negative power of R in an expansion of the mass function. In the next section we shall construct such mass functions.

4 Mass functions involving fluid dynamics

To begin with, we consider the Friedmann solution as the simplest solution of a dynamical fluid. In this case, the matter density is homogeneous and satisfies

$$\rho \propto a(t)^{-3} = \left(\frac{R}{r}\right)^{-3}, \tag{6}$$

where a is a scale factor. Substituting this relation into equation (13) of [3], we obtain,

$$\rho_0 \left(\frac{R}{r}\right)^{-3} = \left(-\frac{\Psi_{,R}}{4\pi\alpha R^2}\right)^{\frac{1}{\alpha+1}}, \tag{7}$$

where ρ_0 is a constant. After integrating equation (7) with respect to R, the mass function can be written as

$$\Psi(r, R) = \frac{4\pi\rho_0^{\alpha+1}}{3} \frac{r^{3(\alpha+1)}}{R^{3\alpha}} + f(r). \tag{8}$$

where $f(r)$ is an arbitrary function. From the assumption that $R = r$ is the initial regular slice, we get that $R = \tau r$ is also a regular slice, where $0 < \tau < 1$ is a constant. When we adopt the regularity condition for Ψ, we find $f(0) = 0$. Furthermore, from equation (2), we obtain $f' = 0$ and then

$$f(r) = 0. \tag{9}$$

Therefore, the mass function (8) of the Friedmann solution results in

$$\Psi(r, R) = \Psi_3 \frac{r^{3(\alpha+1)}}{R^{3\alpha}}, \tag{10}$$

where $\Psi_3 = 4\pi\rho_0^{\alpha+1}/3$.

Next, we would like to investigate more general situations. A physically reasonable mass function should satisfy not only the PDE (1) but also relation (2) on the initial slice as well as the regularity conditions at the regular centre on the regular slice $R = \tau r$. In addition to these conditions, we can impose condition (A) that the mass function is the same as in the Friedmann solution (10) at the lowest order around the symmetric centre. To satisfy condition (A), the generalised mass function is written as

$$\Psi(r, R) = \Psi_3 \frac{r^{3(\alpha+1)}}{R^{3\alpha}} + \Pi(r, R), \tag{11}$$

where $\Pi(r, R)$ is a higher-order term on the regular slice, related to the inhomogeneity of mass distribution. The functional form of $\Pi(r, R)$ is important for the final fate of the collapse, that is, whether it is naked or covered.

In addition to the above restrictions on the mass function, we may impose condition (B) that the mass function recovers an appropriate dust limit as $\alpha \to 0$, in which the mass function depends only on the comoving radial coordinate r. We can consider that the mass function Ψ is given by the following series:

$$\Psi = \sum_{k=1}^{\infty} \Psi_{2k+1} r^{2k+1} \left(\frac{R}{r}\right)^{\beta_{2k+1}}, \tag{12}$$

where $\{\Psi_{2k+1}; k = 1, 2, \cdots\}$ are constant coefficients and $\{\beta_{2k+1}; k = 1, 2, \cdots\}$ are constants which depend only on k and α. Equation (2) yields $\beta_{2k+1} = -(2k+1)\alpha$. This satisfies both conditions (A) and (B). From this form of expansion, we can conclude that $\Psi = \Psi(r^{\alpha+1}/R^{\alpha})$. This together with equation (12) of [3] yields $R = \tau(t)r$, where τ is an arbitrary function of t. This implies that the singularity is simultaneous and therefore covered.

A potentially more interesting form for the mass function, results from a slight generalisation of (12):

$$\Psi = \sum_{k=1}^{\infty} \sum_{i=1}^{\infty} \Psi_{2k+1,i} r^{2k+1} \left(\frac{R}{r}\right)^{\beta_{2k+1,i}}, \tag{13}$$

where $\Psi = \{\Psi_{2k+1,i}; k = 1, 2, \cdots, i = 1, 2, \cdots\}$ is a constant coefficient matrix and $\{\beta_{2k+1,i}; k = 1, 2, \cdots, i = 1, 2, \cdots\}$ are constants which depend only on α, k and i. Condition (A) yields $\beta_{31} = -3\alpha$ and $\beta_{3i} = 0$ for $i \geq 2$. Condition (B) is satisfied if and only if $\beta_{2k+1,i} \to 0$ as $\alpha \to 0$. Equation (2) yields

$$\sum_{i=1}^{\infty} \Psi_{2k+1,i} [\beta_{2k+1,i} + (2k+1)\alpha] = 0. \tag{14}$$

This implies that if the coefficient matrix Ψ is regular, $\beta_{2k+1,i} = -(2k+1)\alpha$ is obtained, which eventually results in the same situation as the simplest model. Therefore, if the mass function which admits the expansion (13) describes naked singularity formation, then the coefficient matrix Ψ must be singular, or $\det \Psi = 0$. In this case, there exists at least a set of values for k and i such that $\beta_{2k+1,i} \neq -(2k+1)\alpha$.

5 Naked singular mass functions

In this section we investigate mass functions which involve spacetimes with naked singularities. We follow a technique used by Mena and Nolan [4]. To show the existence of null geodesics emanating from the central singularity, we show the existence of the region from which future-directed outgoing null geodesics cannot get out when they are traced back to the centre. This region is between two curves $R = R_1(r)$ and $R = R_2(r)$ $(0 < R_1(r) < R_2(r))$ both emanating from the central singularity. Defining $\varphi(r, R)$ as the first-order derivative dR/dr along a future-directed outgoing radial null geodesic, i.e.

$$\varphi(r, R) \equiv -\frac{\alpha}{\alpha+1} \frac{\Psi_{,r}}{\Psi_{,R}} \left(1 - \frac{u}{Y}\right), \tag{15}$$

the curve R_1 satisfies,

$$\frac{dR_1(r)}{dr} \geq \varphi(r, R_1). \tag{16}$$

while R_2 satisfies

$$\frac{dR_2}{dr} \leq \varphi(r, R_2). \tag{17}$$

In our analysis, we assume that only one term in the expansion of $\Pi(r, R)$ in (11), say

$$\Pi_0 r^{5-m} R^m, \tag{18}$$

where m is a constant, is important to examine the existence of naked singularities. Under this assumption we will derive the conditions on Π_0 and m for the existence of radial null geodesics emanating from the singularity which forms from gravitational collapse. As we have already mentioned, to construct a solution we may need another term

$$\Pi_1 r^{5-n} R^n. \tag{19}$$

which is of the same order as the term of equation (18) on the regular slice.

In [3], we show that there are curves $R = R_1(r)$ and $R = R_2(r)$, if $m \leq -6\alpha - 1$ and $\Pi_0 < 0$. Therefore when the mass function with such parameters is a solution of the GGMP equation, for which there is a central singularity after a finite time, then we can show the existence of radial null geodesics which emanate from central singularity.

6 Concluding remarks

We have investigated the collapse of spherically symmetric perfect fluids with the equation of state $p = \alpha\epsilon$ using area-radial coordinates. In this coordinate system, the physical variables are written in terms of the mass function which obeys a second-order PDE, which we call the GGMP equation. We have found that the assumption of analyticity of the mass function has the problem of implying staticity around the regular centre. In this case, the only way to form a central singularity is to permit an infinite jump of a physical variable. Furthermore, in order to have genuine dynamics, we argued that the expansion of the mass function around the centre should have negative powers of R.

We have then constructed other forms for the mass function, starting with the Friedmann solution as the simplest dynamical solution of the GGMP equation. We have then considered classes of mass functions which represent inhomogeneous dynamical fluids. Such mass functions approach the Friedmann solution at the lowest order around the symmetric centre. We have also considered a condition for which the solution has a meaningful dust limit. We note that the power indices and the coefficients of the mass function expansions were not given a priori and should be determined, in each case, by the GGMP equation.

Using generalised forms for the mass function, we have investigated the conditions for the appearance of naked singularities resulting from collapse. We have proved that if Ψ is a solution of the GGMP equation and is given by (13) with the second-order term proportional to $r^{5-m}R^m$ with $m \leq -6\alpha - 1$, for which there is a central singularity after a finite time , then there can be naked singularities. One should be cautioned, however, that this result does not fully prove the existence of naked singularities. The work towards a complete proof of this is in progress.

References

[1] Giambò R, Giannoni F, Magli G and Piccione P 2003 *Class. Quant. Grav.* **20** 4943

[2] Giambò R, Giannoni F, Magli G and Piccione P 2004 *Gen. Rel. Grav.* **36** 1279

[3] Iguchi H, Harada T and Mena F C 2004 *preprint* gr-qc/0405026

[4] Mena F C and Nolan B C 2001 *Class. Quant. Grav.* **18** 4531

Correspondence between the adhesion model and the velocity dispersion for the cosmological fluid

Takayuki Tatekawa[1]

Department of Physics, Waseda University, 3-4-1 Okubo, Shinjuku-ku, Tokyo 169-8555, Japan

Abstract

The Lagrangian description of hydrodynamics is well-known as rather good approximation for the evolution of density fluctuation until quasi-nonlinear regime. Adhesion approximation (AA) is known as a phenomenological model that describes the nonlinear evolution of density fluctuation rather well and that does not form a caustic. However we have not clarified the origin of its modification. Recently, the relation between the isotropic velocity dispersion and effective 'pressure' or viscosity terms has been discussed. Then the Lagrangian perturbative solutions for polytropic cosmological fluid have been derived. We call this model the 'pressure model'. In this workshop, we analyze plane- and spherical-symmetric cases and compare AA with the pressure model. From our analyses, the pressure model undergoes evolution similar to that of AA until reaching a quasi-nonlinear regime. Compared with the results of a numerical calculation, the linear approximation of the pressure model seems rather good until a quasi-nonlinear regime develops. However, because of oscillation arising from the Jeans instability, we could not produce a stable nonlinear structure.

1 Introduction

The Lagrangian description for the cosmological fluid can be usefully applied to the structure formation scenario. This description provides a relatively accurate model even in a quasi-linear regime. Zel'dovich [1] proposed a linear Lagrangian approximation for dust fluid. ZA describes the evolution of density fluctuation better than the Eulerian approximation [2, 3, 4]. Although ZA gives an accurate description until a quasi-linear regime develops, ZA cannot describe the model after the formation of caustics.

In order to proceed with a hydrodynamical description in which caustics do not form, the 'adhesion approximation' [5, 6, 7, 8] (AA) was proposed based on the model equation of nonlinear diffusion (Burgers' equation). In AA, an artificial viscosity term is added to ZA. Because of the viscosity term, we can avoid caustics formation. However, the origin of the viscosity has not yet been clarified.

Buchert and Domínguez [9] showed that when the velocity dispersion is regarded as small and isotropic it produces effective 'pressure' or viscosity terms. Furthermore, they posited the relation between mass density ρ and pressure P, i.e., an 'equation of state'. Buchert *et al.* [10] showed how the viscosity term or the effective pressure of a fluid is generated, assuming that the peculiar acceleration is parallel to the peculiar velocity.

Adler and Buchert [11] have formulated the Lagrangian perturbation theory for a barotropic fluid. Morita and Tatekawa [12] and Tatekawa *et al.* [13] solved the Lagrangian perturbation equations for a polytropic fluid up to the second order. Hereafter, we call this model the 'pressure model'.

In this workshop, we examine the following questions. (a) Can we explain the origin of the viscosity term in AA with 'pressure'? (b) How long is the linear approximation of the pressure model valid? (c) Can we avoid the formation of a caustic with the pressure model?

2 The Lagrangian perturbative solutions for the cosmological fluid

Zel'dovich derived a first-order solution of the longitudinal mode for dust fluid [1]. After that, second- (PZA) and third-order (PPZA) solutions were obtained [14, 15, 16]. For the E-dS model, the solutions

[1]E-mail: tatekawa@gravity.phys.waseda.ac.jp

are written as follows:

$$\mathbf{x} = \mathbf{q} + \nabla S, \tag{1}$$

$$S^{(1)}(\mathbf{q}, t) = t^{2/3} S_+(\mathbf{q}) + t^{-1} S_-(\mathbf{q}), \tag{2}$$

$$S^{(2)}_{i,i} = \frac{3}{14}\left(S^{(1)}_{i,j} S^{(1)}_{j,i} - S^{(1)}_{i,i} S^{(1)}_{j,j}\right), \tag{3}$$

$$S^{(3)}_{i,i} = \frac{5}{9}\left(S^{(1)}_{i,j} S^{(2)}_{j,i} - S^{(1)}_{i,i} S^{(2)}_{j,j}\right) - \frac{1}{3}\det\left(S^{(1)}_{i,j}\right), \tag{4}$$

where the superscript $S^{(n)}$ means n-th order solutions. x and q mean comoving Eulerian coordinates and Lagrangian coordinates, respectively.

Adhesion approximation (AA) [5, 6, 7, 8] was proposed from a consideration based on Burgers' equation. This model is derived by the addition of an artificial viscous term to ZA.

Within the limits of a small viscous parameter ν, the analytic solution of AA is given by

$$\mathbf{u}(\mathbf{x}, t) = \sum_a \left(\frac{\mathbf{x} - \mathbf{q}_a}{a}\right) j_a \exp\left(-\frac{I_a}{2\nu}\right) \Big/ \sum_a j_a \exp\left(-\frac{I_a}{2\nu}\right), \tag{5}$$

where $\mathbf{q}_a$ means the Lagrangian points that minimize the action

$$I_a \equiv I(\mathbf{x}, a; \mathbf{q}_a) = S_0(\mathbf{q}_a) + \frac{(\mathbf{x} - \mathbf{q}_a)^2}{2a} = \min., \tag{6}$$

$$j_a \equiv \left[\det\left(\delta_{ij} + \frac{\partial^2 S_0}{\partial q_i \partial q_j}\right)\right]^{-1/2}\Bigg|_{\mathbf{q}=\mathbf{q}_a}, \tag{7}$$

$$S_0 = S(\mathbf{q}, t_0), \tag{8}$$

considered as a function of q for fixed x [8]. In AA, because of the viscosity term, the caustic does not appear and a stable nonlinear structure can exist.

Although AA seems a good model for avoiding the formation of caustics, the origin of the modification (or artificial viscosity) is not clarified. Buchert and Domínguez [9] argued that the effect of velocity dispersion becomes important beyond the caustics. They showed that when the velocity dispersion is still small and can be considered isotropic, it gives effective 'pressure' or viscosity terms. Buchert *et al.* [10] showed how the viscosity term is generated by the effective pressure of a fluid under the assumption that the peculiar acceleration is parallel to the peculiar velocity.

Adler and Buchert [11] have formulated the Lagrangian perturbation theory for a barotropic fluid. Morita and Tatekawa [12] and Tatekawa *et al.* [13] solved the Lagrangian perturbation equations for a polytropic fluid in the Friedmann Universe. Hereafter, we call this model the 'pressure model'.

When we consider the polytropic equation of state $P = \kappa\rho^\gamma$, the first-order solutions for the longitudinal mode are obtained in Lagrangian Fourier space. For $\gamma \neq 4/3$,

$$\widehat{S}(\mathbf{K}, a) \propto a^{-1/4}\, \mathcal{J}_{\pm 5/(8-6\gamma)}\left(\sqrt{\frac{2C_2}{C_1}}\frac{|\mathbf{K}|}{|4-3\gamma|}\, a^{(4-3\gamma)/2}\right), \tag{9}$$

where $\mathcal{J}_\nu$ denotes the Bessel function of order ν, and for $\gamma = 4/3$,

$$\widehat{S}(\mathbf{K}, a) \propto a^{-1/4 \pm \sqrt{25/16 - C_2|\mathbf{K}|^2/2C_1}}, \tag{10}$$

where $C_1 \equiv 4\pi G\rho_b(a_{in})\, a_{in}^3/3$ and $C_2 \equiv \kappa\gamma\rho_b(a_{in})^{\gamma-1}\, a_{in}^{3(\gamma-1)}$. ρ_b and K mean background mass density and Lagrangian wavenumber, respectively. a_{in} means scale factor when an initial condition is given. When we take the limit $\kappa \to 0$, these solutions agree with Eq. (2).

In this paper, we analyze the first-order perturbation and the full-order solution. The evolution equation for the longitudinal mode is written as follows [11, 12]:

$$\nabla_x \cdot \left(\nabla_q \ddot{\mathbf{s}} + 2\frac{\dot{a}}{a}\nabla_q \dot{\mathbf{s}} - \frac{\kappa\gamma\rho_b^{\gamma-1}}{a^2} J^{-\gamma}\nabla_x J\right) = -4\pi G\rho_b(J^{-1} - 1). \tag{11}$$

In general, it is very difficult to solve this equation for such reasons as the coordinate transformation or non-locality. Here, we imposed symmetry and avoided these difficulties.

3 Comparison between Lagrangian models

We analyze the plane- and spherical-symmetric models [17]. Here we use the pressure model with polytropic indices $\gamma = 1, 4/3, 5/3$. In the plane-symmetric case, ZA gives exact solutions for dust fluid. However, when we keep using the solutions of ZA after the appearance of caustics, the nonlinear structure diffuses and breaks. To simplify, we treat the single-wave case.

$$S_0(q) = \varepsilon \cos q \,. \tag{12}$$

The initial peculiar velocity is made equal with that given by the growing mode in ZA. The evolution of this model for ZA, AA, and N-body simulation (extrapolation of ZA) was analyzed by Nusser and Dekel [7]. In this calculation, we set up the normalization of the scale factor when first caustics appear with ZA by a=1. At a late time, the caustics will diffuse in ZA. AA remains a high-density filament and caustics do not appear.

From our results [17], when $\gamma = 4/3$, the growth of the fluctuation can be gentle. However the caustics are finally formed, the divergence of density cannot be avoided as with AA. In other words, in the plane-symmetric case, we cannot represent the behavior that resembles AA.

For the spherical-symmetric case, we consider the evolution with ZA, PZA, PPZA, the exact solution for dust fluid, AA, and the pressure models. To avoid a discontinuity of the pressure gradient, we adopt the Mexican-hat type model:

$$\delta(r) = \varepsilon(3 - r^2)\, e^{-r^2/2} \,. \tag{13}$$

For spherical collapse, when the fluctuation grew very large, we found that the behavior of AA could not be reproduced any more in the pressure model with linear approximation. In other words, it is very difficult to explain the origin of the viscosity term in AA by the pressure model. The oscillation of the fluctuation in the pressure model with linear approximation is caused by the Jeans instability.

For void evolution, although we can realize the evolution in AA with the pressure model, we cannot reproduce the existence of a stable nonlinear structure. In other words, it is very difficult to find the origin of artificial viscosity in AA with the isotropic velocity dispersion.

As for the validity of the linear approximation in the pressure model, in both the case of the plane-symmetric and the spherical-symmetric model, the approximation is rather good until a quasi-nonlinear regime develops. However, attention is necessary for extrapolation to a nonlinear stage with Lagrangian linear perturbation because it is different from the plane-symmetric case, the oscillation of the density fluctuation appearing in the spherical-symmetric case at the nonlinear regime.

4 Summary

We analyzed the corresponding relation with the viscosity term in AA and the velocity dispersion using plane- and spherical-symmetric cases. Here we evaluated the effect of isotropic velocity dispersion by linear approximation or the full-order equation. As shown by our previous papers [12, 13, 17], we derived the basic equation in Lagrangian description. The behavior of the pressure model strongly depends on the equation of state. In the case where $\gamma = 1, 4/3, 5/3$, the result seems to resemble that in AA until a quasi-nonlinear regime develops. However, in long-duration evolution, even if we consider full-order effects, the caustics will be formed. Though behavior similar to that of AA can be seen with the pressure model, more consideration is necessary for establishing the existence of stable nonlinear structure.

If we adjust the parameters of the pressure model, will it be able to obtain a result similar to the behavior of AA? According to our work, it seems quite difficult to establish the existence of a stable nonlinear structure. For example, if we choose a small γ, although we can avoid the caustics formation, the fluctuation will decay and disappear. On the other hand, if we choose a large γ, the fluctuation behaves like that of ZA. Therefore, the fluctuation forms a caustic. If the parameters are chosen carefully, we may solve the problem of caustic formation and fluctuation disappearance. However, the oscillation of the fluctuation remains, even if we can realize the tendency of the growth of the fluctuation. The oscillation also remains in full-order calculation.

Next, we consider another question. When we analyze structure formation in the fluid with pressure, can we learn whether the Lagrangian linear perturbation is valid or not? From our analyses in the plane-

and spherical-symmetric cases, until a quasi-nonlinear regime develops, the linear approximation of the pressure model seems rather good from the comparison with a full-order numerical calculation.

References

[1] Ya. B. Zel'dovich, Astron. Astrophys. **5**, 84 (1970).

[2] P. Coles and F. Lucchin, *Cosmology: The Origin and Evolution of Cosmic Structure* (John Wiley & Sons, Chichester, 1995).

[3] D. Munshi, V. Sahni, and A. A. Starobinsky, Astrophys. J. **436**, 517 (1994).

[4] V. Sahni and S. F. Shandarin, Mon. Not. R. Astron. Soc. **282**, 641 (1996).

[5] S. N. Gurbatov, A. I. Saichev, and S. F. Shandarin, Mon. Not. R. Astron. Soc. **236**, 385 (1989).

[6] D. H. Weinberg and J. E. Gunn, Mon. Not. R. Astron. Soc. **247**, 260 (1990).

[7] A. Nusser and A. Dekel, Astrophys. J. **362**, 14 (1990).

[8] L. Kofman, D. Pogosyan, S. F. Shandarin, and A. L. Melott, Astrophys. J. **393**, 437 (1992).

[9] T. Buchert and A. Domínguez, Astron. Astrophys. **335**, 395 (1998).

[10] T. Buchert, A. Domínguez, and J. Perez-Mercader, Astron. Astrophys. **349**, 343 (1999).

[11] S. Adler and T. Buchert, Astron. Astrophys. **343**, 317 (1999).

[12] M. Morita and T. Tatekawa, Mon. Not. R. Astron. Soc. **328**, 815 (2001).

[13] T. Tatekawa, M. Suda, K. Maeda, M. Morita, and H. Anzai, Phys. Rev. **D66**, 064014 (2002).

[14] F. R. Bouchet, S. Colombi, E. Hivon, and R. Juszkiewicz Astron. Astrophys., **296**, 575 (1995).

[15] P. Catelan, Mon. Not. R. Astron. Soc. **276**, 115 (1995).

[16] T. Tatekawa, astro-ph/0412025.

[17] T. Tatekawa, Phys. Rev. **D70**, 064010 (2004).

Electromagnetic radiation from naked singularity in self-similar gravitational collapse II: spectral decomposition approach

Eiji Mitsuda[1], Hirotaka Yoshino[2] and Akira Tomimatsu[3]

Department of Physics, Graduate School of Science, Nagoya University, Nagoya 464-8602, Japan

Abstract

We investigate electromagnetic radiation just before naked singularity formation during the spherically symmetric self-similar collapse of a star with electric currents. We propose an analytic method based on the spectral decomposition, where the Green's function for the wave equation is decomposed into an integral over large magnitude regime of the Fourier parameter and a sum of quasi-normal modes. The outgoing energy flux has three kinds of possible behavior depending on the parameter values of the background spacetime: it remains finite, diverges with the inverse power law of retarded time, or oscillates indefinitely increasing its amplitude. Further, the finite energy flux can be accompanied with an oscillatory behavior. The oscillatory behavior is an interesting feature found for the first time and we show that it would actually occur by approximately calculating the quasi-normal modes. How the energy flux can behave during the collapse of dust or an isothermal gas is finally discussed.

1 Introduction

Several spacetimes admitting naked singularity formation due to the gravitational collapse have been found over the past three decades. Radiation phenomena during such a collapse have important implications for the instability of the Cauchy horizon and the nature of highly energetic phenomena. It is helpful in analytic approach to this issue to adopt the spherically symmetric self-similar spacetime as a background spacetime by virtue of its mathematical simplicity that all dimensionless functions depend only on a single value $z \equiv r/t$. In addition, its realistic possibility was suggested by numerical simulations[1] showing the convergence of a more general non-self-similar spherical collapse of an isothermal gas to the self-similar solution. In fact, Scalar and semiclassical radiation during the spherically symmetric self-similar collapse to a naked singularity have been analytically investigated[2, 3].

We will be able to deepen our understanding for nature of the radiation phenomena by adding further examples to the previous studies. Here, in this paper, we purpose to analytically investigate asymptotic behaviors of outgoing energy flux carried by electromagnetic radiation just before the naked singularity formation during the spherically symmetric self-similar collapse. In particular, we focus on the flux measured by observers at the sufficiently large distance from the center. For this purpose, we derive the wave equation for the gauge invariant amplitude of the odd parity electromagnetic perturbations.

Since there exists an eigen function $\exp(i\omega \log|t|)$ for the wave equation, we can use the spectral decomposition method for the Green's function in the parameter ω space. The outgoing energy flux is expressed in a fashion reflecting each properties of the Green's function decomposed into an integral over asymptotically large magnitudes of the parameter ω and a sum of the quasi-normal modes. Such a new analytic representation for the energy flux yield a description of its features which have not been found in the previous studies.

2 Set up of the system

We express the line element of the spherically symmetric self-similar background spacetime in the comoving coordinates t and r for collapsing matter as

$$ds^2 = -e^{2\nu(z)}dt^2 + e^{2\lambda(z)}dr^2 + r^2S^2(z)(d\theta^2 + \sin^2\theta d\phi^2), \tag{1}$$

[1]E-mail:emitsuda@gravity.phys.nagoya-u.ac.jp
[2]E-mail:yoshino@gravity.phys.nagoya-u.ac.jp
[3]E-mail:atomi@gravity.phys.nagoya-u.ac.jp

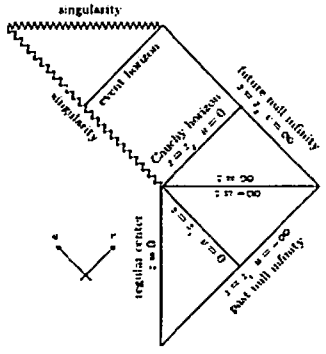


Figure 1: The spacetime structure we consider in this paper.

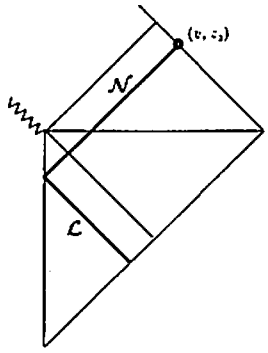


Figure 2: The diagram in the integral space.

where $z \equiv r/t$. In this spacetime, a singularity is formed at $t = 0$ and $r = 0$. The causal structure of the background spacetime is shown in Fig. 1. The characteristic lines in the diagram are represented by $z = \text{const}$ lines as shown in Fig. 1. The values z_1 and z_2 are the negative root of $V = -1$ and the largest positive root of $V = 1$, respectively, where the function $V(z)$ is defined as

$$V(z) \equiv ze^{\lambda-\nu}. \tag{2}$$

This function may be interpreted the velocity of $z = \text{const}$ surfaces relative to comoving observers.

Next, we consider electromagnetic perturbations to the self-similar spacetime, which are assumed to be generated by the axisymmetric and circular electromagnetic current $j_a = \delta^{\phi}_{a} j_1(t, r) \sin\theta(\partial P_l/\partial\theta)$. Any such currents identically satisfy the continuity equation $\nabla_a j^a = 0$ and works as a source of the wave equation for the vector potential given by

$$A_a = (0,\ 0,\ 0,\ a(t, r) \sin\theta(\partial P_l/\partial\theta)), \tag{3}$$

which is assumed not to disturb the background spacetime. The function a involved this vector potential is a gauge invariant quantity which should be solved in our analysis. The ϕ component of the Maxwell equation $\nabla_b(\partial^b A^a - \partial^a A^b) = 4\pi j^a$ gives the wave equation with the source term for the function a. It should be noted that the wave equation is expressed in $\partial/\partial(\log(-t))$ and $\partial/\partial z$ through the change of variables from t and r to t and z.

In this paper, we consider the following situation, which will play a role as the boundary conditions for the solution of the wave equation. Firstly, the vector potential is regular at the regular center (i.e., $z = 0$ and $t < 0$). Secondly, there is no ingoing wave from the past null infinity (i.e., $z = z_1$ and $t = -\infty$) because we assume the electromagnetic waves to be generated only through the gravitational collapse.

In the next section, we will consider the propagation of the waves in the regions $0 > z > -\infty$ and $\infty > z > z_2$. Then, to use null coordinates becomes helpful. The values of the null coordinates $u(t, z)$ and $v(t, z)$ on the characteristic lines are shown in Fig. 1. In particular, the retarded time u is zero on the Cauchy horizon.

3 Decomposition of the Green's function

In this section, expressing the outgoing wave part of the solution $a(t, z)$ by the notation $a_{\text{out}}(u, z)$, we examine the leading term of the function a_{out} at the future null infinity $z = z_2$ derived by the Green's function technique near $u = 0$. Then, it will be shown that there are the two distinct contributions, by decomposing the Green's function $G(t, z|s, y)$ of the wave function.

At first, the frequency-domain Green's function $\tilde{G}(z, y, \omega)$ is introduced through the Fourier transform

$$G(t, z|s, y) = \frac{1}{2\pi s} \int_{-\infty}^{\infty} \tilde{G}(z, y, \omega) e^{i\omega \log|t/s|} d\omega. \tag{4}$$

to be the Green's function of the ordinary differential equation (ODE). Note that though the parameter ω introduced in the Fourier transform has no physical meaning as a wave frequency, we will use the terminology for convenience. The frequency-domain Green's function should be constructed by the two independent homogeneous solutions $f_0(z,\omega)$ and $f_{\rm out}(z,\omega)$ of the ODE: the solution f_0 is the regular solution at $z = 0^-$, and the solution $f_{\rm out}$ is the pure outgoing mode at $z = z_1$.

We calculate the integral of Eq. (4) by considering the contour integral in the complex ω plane. We would like to emphasize that the zeros of the Wronskian of the functions f_0 and $f_{\rm out}$ are poles of the integrand of Eq. (4). Hereafter, we call the poles quasi-normal modes. Then, assuming that there is no brunch cut in the complex ω plane, we can express the Green's function as two distinct terms:

$$G(t,z|s,y) = G^{(F)}(t,z|s,y) + G^{(Q)}(t,z|s,y), \tag{5}$$

where the function $G^{(F)}$ is the integral along the large $|\omega|$ semicircle, and the function $G^{(Q)}$ is the sum of the residues at the quasi-normal modes lying in the region surrounded by the semicircle. Note that only the quasi-normal modes with negative imaginary part can contribute because the integrand of Eq. (4) converges only over the lower semicircle. By this decomposition, the function $a_{\rm out}(u,z_2) = a_{\rm out}(u)$ can be also decomposed as

$$a_{\rm out}(u) = a^{(F)}_{\rm out}(u) + a^{(Q)}_{\rm out}(u), \tag{6}$$

where the functions $a^{(F)}_{\rm out}$ and $a^{(Q)}_{\rm out}$ are the terms derived by the retarded part of the function $G^{(F)}$ and that of the function $G^{(Q)}$, respectively.

The function $a^{(F)}_{\rm out}$ can be calculated by the line integral of the source term of the wave equation along the lines $\mathcal{L}$ and $\mathcal{N}$ shown in Fig. 2. The integral over the line $\mathcal{L}$ and that over the line $\mathcal{N}$ near $u = 0$ behaves as $(-u)^{|z_1|V_1'}$ and $(-u)^{z_2V_2'}$, respectively, where $V_1' \equiv dV/dz|_{z=z_1} > 0$ and $V_2' \equiv dV/dz|_{z=z_2} > 0$. Hence, the leading term of the function $a^{(F)}_{\rm out}(u)$ near $u = 0$ is

$$a^{(F)}_{\rm out}(u) \sim (-u)^{\min(|z_1|V_1',\, z_2V_2')}. \tag{7}$$

On the other hand, the leading term of the function $a^{(Q)}_{\rm out}(u)$ near $u = 0$ becomes

$$a^{(Q)}_{\rm out}(u) \sim (-u)^{i\omega_{\rm min}}, \tag{8}$$

where $\omega_{\rm min}$ is the quasi-normal mode with the largest imaginary part in the quasi-normal modes with negative imaginary part. It should be emphasized that these behavior is independent of the detail of the current distribution j_l.

4 Energy flux just before naked singularity formation

The outgoing energy flux $\mathcal{F}$ measured by observers sufficiently far away from the center and near the Cauchy horizon can be estimated as

$$\mathcal{F}(\bar{u}) = \left(\frac{da_{\rm out}(\bar{u})}{d\bar{u}}\right)^2, \tag{9}$$

where $\bar{u}$ is the retarded time proper to the observers, which is related to u by $\bar{u} \sim -(-u)^{z_2V_2'}$.

Since which of the functions $a^{(F)}_{\rm out}(\bar{u})$ and $a^{(Q)}_{\rm out}(\bar{u})$ dominates near $\bar{u} = 0$ depends on the values of $|z_1|V_1'$, z_2V_2' and $|{\rm Im}(\omega_{\rm min})|$, there is the following three possible behaviors of the energy flux. First, when the value of z_2V_2' is the smallest in those of the three, we obtain

$$\mathcal{F}(\bar{u}) \sim {\rm const}, \tag{10}$$

by the contribution from the high frequency. This means that then the energy flux remains finite in spite of the naked singularity formation at the center. Secondly, when the value of $|z_1|V_1'$ is the smallest, also by the contribution from the high frequency, we obtain

$$\mathcal{F}(\bar{u}) \sim (-\bar{u})^{\xi_f}, \quad \text{for} \quad \xi_f = 2\left(\frac{|z_1|V_1'}{z_2V_2'} - 1\right), \tag{11}$$

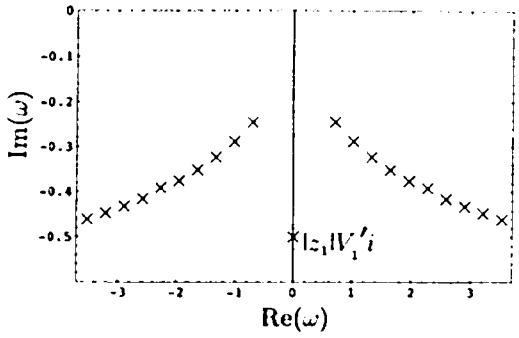


Figure 3: The quasi-normal modes approximately calculated in the complex ω plane.

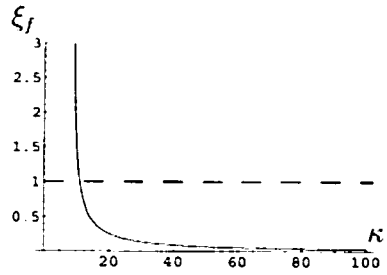


Figure 4: The plots of ξ_f for the dust self-similar spacetime.

which satisfies $-2 < \xi_f < 0$. Hence, then the energy flux diverges according to the inverse power law. Finally, when the value of $|\mathrm{Im}(\omega_{\mathrm{min}})|$ is the smallest, the contribution from the quasi-normal modes becomes dominant. Then, we obtain

$$\mathcal{F}(\bar{u}) \sim (-\bar{u})^{\xi_q}, \quad \text{for} \quad \xi_q = 2\left(\frac{i\omega_{\mathrm{min}}}{z_2 V_2'} - 1\right), \tag{12}$$

which satisfies $-2 < \mathrm{Re}(\xi_q) < 0$. This means that the energy flux diverges according to the inverse power law. In addition, if $\mathrm{Re}(\omega_{\mathrm{min}}) \neq 0$, the diverging energy flux is accompanied with an oscillatory behavior.

The last two behaviors are obviously peculiar to the naked singularity formation. However, even if the energy flux remains finite, it can exhibit behaviors peculiar to the naked singularity formation because of the contribution from the sub-dominant terms. For example, when $0 < \xi_f < 1$ or $0 < \mathrm{Re}(\xi_q) < 1$, the function $\mathcal{F}(\bar{u})$ has a cusp at $\bar{u} = 0$ because of the discontinuity of its derivative. Moreover, when $\mathrm{Re}(\omega_{\mathrm{min}}) \neq 0$ and $|\mathrm{Im}(\omega_{\mathrm{min}})| < |z_1|V_1'$, the finite energy flux is accompanied with the oscillatory behavior.

In order to confirm whether or not the oscillatory behavior is possible, we numerically calculate the quasi-normal modes by appropriately approximating the potential in the ODE. One such example is shown in Fig. 3. We can find that the conditions $\mathrm{Re}(\omega_{\mathrm{min}}) \neq 0$ and $|\mathrm{Im}(\omega_{\mathrm{min}})| < |z_1|V_1'$ are possible in a wide range of the parameter values of the approximate potential. Therefore, we expect that the oscillation would be generic behavior although whether or not the energy flux diverges depends on the value of $z_2 V_2'$.

As an example of the spacetime, we consider the collapse of dust. In this spacetime, we can exactly evaluate the values of $|z_1|V_1'$ and $z_2 V_2'$, which are parameterized by κ representing the density gradient at the center. Note that the naked singularity is formed for $\kappa \gtrsim 8.7$. We show the dependence of the power index ξ_f on the parameter κ in Fig. 4. We can find that always $z_2 V_2' < |z_1|V_1'$ and that $\xi_f < 1$ in the wide range of κ. Hence, the energy flux due to the contribution from the high frequency during the collapse of dust remains finite. In addition, there would be a cusp of the energy flux at the naked singularity formation. As an additional example, we consider the collapse of a perfect fluid with the equation of state $P = \alpha\rho$ for constant α satisfying $0 < \alpha < 1$. Also in this spacetimes, we can find from the Einstein's equation that always $z_2 V_2' < |z_1|V_1'$. Hence, the energy flux due to the contribution from the high frequency during the collapse of an isothermal gas also remains finite.

References

[1] T. Harada, and H. Maeda, Phys. Rev. **D63**, 084022 (2001).

[2] B. C. Nolan, and T. J. Waters, Phys. Rev. **D66**, 104012 (2002).

[3] U. Miyamoto, and T. Harada, Phys. Rev. **D69**, 101005 (2004).

Field Evolution of the Black Hole Bomb Model

Hironobu Furuhashi [1], Yasusada Nambu [2]

Department of Physics, Graduate School of Science, Nagoya University, Nagoya 464-8602, Japan

Abstract

We investigate the evolution of a charged scalar field in Reissner-Nordström spacetime with the wall boundary condition, and confirm the instability by dynamical simulations by using the CIP method.

1 Introduction

It is well known that if you perturb a black hole, the surrounding field will ring down, as a "quasi-normal ringing"[1], and be stable. However, is it steady in case of the super-radiance? If condition of the super-radiance are satisfied, a wave impinging on Kerr black hole can be amplified, and be scattered off the black hole[2, 3]. In this case, the bound state of a scalar field is expected to be unstable. This is so-call the "black hole bomb model"[4]. Some black hole bomb models have been studied by mode analyses [5, 6, 7, 8, 10, 11], and they implied that the growth rate of the instability is too small to confirm by dynamical simulations. However, Cardoso *et al.*[9] recently investigated a black hole bomb model in which is a wall boundary condition is imposed in Kerr spacetime, and concluded a maximum growth rate of the instability is larger than the other black hole bomb models. Motivated by this, we investigate the evolution of a charged scalar field in Reissner-Nordström (R-N) spacetime with the wall boundary condition as a simplified model by dynamical simulation by using CIP method. Especially, to compare the results of Cardoso *et.al.*[9], we search the dependence of position of the wall.

The plan of this paper is as follows. In Sec.2, we describe our physical system and numerical method. In Sec.3, we show numerical results. Finally, in Sec.4, we summarize and discuss the results.

2 Basic Equation

The Reissner-Nordström (R-N) metric is

$$ds^2 = -\frac{\Delta}{r^2}dt^2 + \frac{r^2}{\Delta}dr^2 + r^2\left(d\theta^2 + \sin^2(\theta)d\phi^2\right), \qquad (1)$$
$$\Delta = r^2 - 2Mr + Q^2,$$

where M is the mass, Q is the electric charge of the black hole. The locations of the horizons $r_\pm$ are given by the roots of the equation $\Delta = 0$. The Klein-Gordon equation for a charged scalar is

$$(\nabla^\alpha - iqA^\alpha)(\nabla_\alpha - iqA_\alpha)\Phi = 0 \qquad (2)$$
$$A_\alpha = \left(-\frac{Q}{r}, 0, 0, 0\right),$$

where ∇^α is the covariant derivative in the R-N geometry, and q is the charge of the scalar field. Equation (2) is separable in terms of the spherical harmonics Y_{lm}:

$$\Phi = \frac{u(r,t)}{r}Y_{lm}. \qquad (3)$$

[1] E-mail:hironobu@gravity.phys.nagoya-u.ac.jp
[2] E-mail:nambu@gravity.phys.nagoya-u.ac.jp

The radial function $u(r,t)$ satisfies the relation

$$\left[\partial_t^2 - \frac{2qQ}{r}\partial_t - \partial_{r_*}^2 + V_l\right] u_l(r,t) = 0, \tag{4}$$

$$V_l = \frac{\Delta}{r^2}\left(\frac{l(l+1)}{r^2} + \frac{2M}{r^3} - \frac{2Q^2}{r^4}\right) - \left(\frac{qQ}{r}\right)^2, \tag{5}$$

where l, m are integers and $|m| \leq l$, and r_* is tortoise coordinate:

$$r_* = \int dr \frac{r^2}{\Delta} = r + \frac{1}{r_+ - r_-}\left[r_+^2 \ln(r - r_+) - r_-^2 \ln(r - r_-)\right]. \tag{6}$$

To integrate the Eq.(4), we use the CIP method. This is a method of preventing a numerical diffusion of the profile by propagating not only the data of the profile but also the spatial derivative. To use the CIP method, we need to get the advection equations for the data and the spatial derivative from Eq.(4). And we can easily get the advection equations are given by Eq.(4),

$$[\partial_t \mp \partial_{r_*}] f_\pm = i\frac{qQ}{r}(f_+ + f_-) + p, \tag{7}$$

$$[\partial_t \mp \partial_{r_*}] g_\pm = \left(i\frac{qQ}{r}(f_+ + f_-) + p\right)', \tag{8}$$

where

$$\dot{u} = v' + 2i\frac{qQ}{r}u + p, \tag{9}$$

$$\dot{v} = u', \tag{10}$$

$$\dot{p} = -V_l u, \tag{11}$$

$$f_\pm = u \pm v, \tag{12}$$

$$g_\pm = f_\pm', \tag{13}$$

and the dot and the dash denote derivative with respect to t and r_* respectively.

We solve Eq.(4) using a wall boundary condition at $r = r_0$ and ingoing boundary conditions at the black hole horizon. This wall boundary condition play the role of the mirror of the black hole bomb model.

2.1 Surper-radiance

By defining $u(r,t) = \varphi(r)e^{-i\omega t}$, we can obtain the solution

$$\varphi(r) \propto e^{-i(\omega - qQ/r_+)r_*} \tag{14}$$

that consists near the horizon, and we can easily obtain the condition of the frequency:

$$0 < \omega < \frac{qQ}{r_+} \tag{15}$$

for which the super-radiance happen. In the case of this black hole bomb model, we can estimate the lowest mode is about the inverse of the distance between the horizon and the wall. This mean that the black hole bomb model have the typical distance of the wall position.

3 Numerical Results

We performed numerical calculation to confirm the instability by using the CIP method. We calculate We investigated the dependence of the location on the wall boundary. We chose the parameter values of the black hole as $Q = 0.7M$, and of the charged scalar field as $qQ = 2$, and satisfying $l = m = 1$.

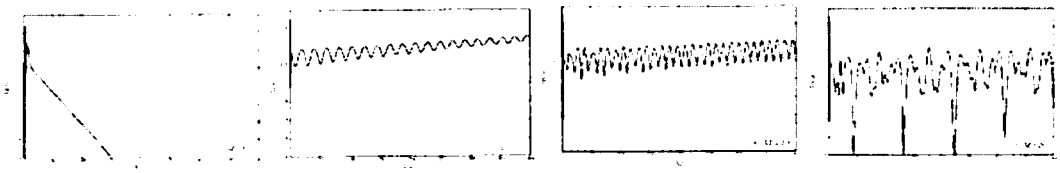


Figure 1: The dependence of the location of the wall boundary. The parameter values here are $Q = 0.7M$, $l = m = 1$, and $qQ = 2$. The solid line corresponds to $\ln|u|$ as a function of time. These figures show the case of which are $r_oM = 5, 10, 15$, and 20 from left sequentially.

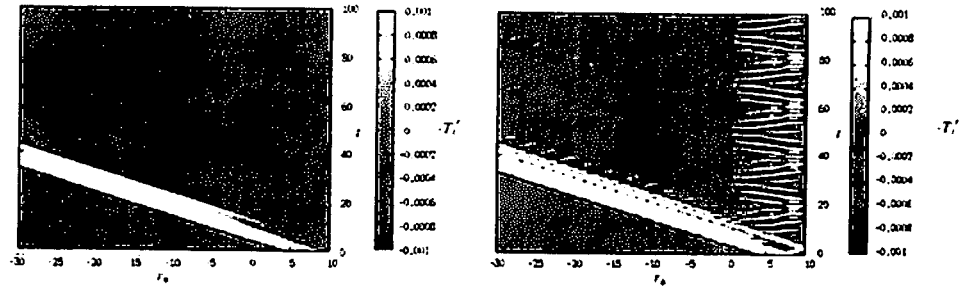


Figure 2: The dependence of the space and time on the energy-momentum flux. The left side graph is the case of which the super-radiance does not happen ($qQ = 0$), and the right side graph is the case of which the super-radiance does happen ($qQ = 2$). The parameter values here are $Q = 0.7M$, $r_oM = 10$, and $l = m = 1$.

The amplitude is plotted as a function of time in Fig.1. These figures show the case of which are $r_oM = 5, 10, 15$, and 20 from left sequentially. Comparing the amplitude in the graph of the left end with others, we can see an obviously different behavior. This result shows that the black hole bomb models have a typical distance in which it is decided whether the amplitude is unstable. From three graphs on the right side, the number of modes of the wave increase , and the growth rates of the instability decrease as the wall position r_oM increase.

Next, we check that these instabilities are due to the effect of the super-radiance. Figure.2 shows that the dependence of the space: r_* and time: t on the energy-momentum flux: $-T^r_t$. The left side graph is the case of which the super-radiance does not happen ($qQ = 0$), and the right side graph is the case of which the super-radiance does happen ($qQ = 2$), and $r_oM = 10$ together. Comparing the graphs, the left graph has out-going energy-momentum flux. It is concluded that the field is unstable due to the effect of the super-radiance.

4 Summary and Discussion

We have investigated the evolution of the charged scalar field in R-N spacetime with the wall boundary condition by dynamical simulations, and confirmed the instability. The result, that the amplitude of the wave became unstable due to the effect of the super-radiance when the position of the wall was on the outside of a certain typical place, was obtained. In this section, we discuss these results. Cardoso *et al.*[9] have investigated the mode of the scalar field in Kerr spacetime with wall boundary, and this model is not essentially different compared with our model. Our results are especially corresponding to the result of this mode analysis well. For example, the growth rate of the instability decrease, and the number of modes are increase as r_* increase, and the black hole bomb model has the typical wall position. Finally, we discuss the typical position of the wall. In this case, the parameter values here are $Q = 0.7M$ and $qQ = 2$. This means that the typical wall position may be $O(1)$. This is consistent with our results.

References

[1] K. D. Kokkotas, Living Rev. Rel. **2** (1999), 2.

[2] Y. B. Zel'dovich, Sov. Phys. JETP Lett. **14** (1971), 180.

[3] V. P. Frolov and I. D. Novikov, *Black Hole Physics* (Kluwer Academic Publishers, 1998).

[4] W. H. Press and S. A. Teukolsky, Nature **238** (1972), 211.

[5] T. Damour, N. Deruelle and R. Ruffini, Lett. Nuovo Cim. **15** (1976), 257.

[6] S. Detweiler, Phys. Rev. D **22** (1980), 2323.

[7] T. J. M. Zouros and D. M. Eardley, Ann. of Phys. **118** (1979), 139.

[8] H. Furuhashi and Y. Nambu, Prog. Theor. Phys. **112** (2004), No.6, 983.

[9] V. Cardoso, O. J. C. Dias, J. P. S. Lemos and S. Yoshida, Phys. Rev. D **70** (2004), 044039.

[10] V. Cardoso and O. J. C. Dias, Phys. Rev. D **70** (2004), 084011.

[11] E. Berti, V. Cardoso and J. P. S. Lemos, Phys. Rev. D **70** (2004), 084011.

[12] T. Yabe, F. Xiao and T. Utsumi, J. Comput. Phys. **169** (2001), 556.

[13] M. Abramowitz and I. A. Stegun, *Handbook of Mathematical Functions* (Dover, 1970).

Brane cosmology with curvature corrections

Takashi Torii[1],

Advanced Research Institute for Science and Engineering, Waseda University, Tokyo 169-8555, Japan

Abstract

We discuss the brane cosmology in the system which includes the Gauss-Bonnet terms in the bulk. The Gauss-Bonnet terms appear as the first order curvature corrections in the α' expansion in superstring theory. In the single brane model, we first derive n-dimensional bulk solutions under the static ansatz in the Einstein-Gauss-Bonnet-Maxwell-Λ system. Next examining the motion of a brane in the bulk spacetime using the generalized junction condition and Z_2-symmetry, we derive the generalized Friedmann equation on the brane. The issues of the late-time behavior, high energy limit, the fine-tuning problem and bouncing universe are investigated.

1 Introduction

Among many brane models, ones proposed by Randall and Sundrum[1] are very important. They are motivated by superstring/M-theory, i.e., the orbifold compactification of higher-dimensional string theory by the dimensional reduction of 11-D supergravity in $R^{10} \times S^1/Z_2$[2]. RSII type model[1] provides us an alternative compactification of extra dimensions. However, this model may inevitably expect a singular spacetime just as in general relativity, although they are based on a string theory[3]. One of the ways to evade this argument is adding the higher curvature corrections to the bulk Lagrangian. The higher curvature terms naturally arise as a next leading order of the α'-expansion of a superstring theory[4]. One may expect that they are described by the so-called Gauss-Bonnet combination, which is shown to be a ghost-free combination. It was shown that the graviton zero mode is localized at law energies in the Gauss-Bonnet brane system as in the RS II model[5] and that the correction of the Newton's law becomes milder by including the Gauss-Bonnet term[6].

In order to understand the higher curvature model, it may be convenient for us to extend the covariant gravitational equations on a brane[7] to the case with the Gauss-Bonnet term. When we have a system with quadratic curvature terms in a bulk spacetime, we expect terms such as $(\pounds_n K_{AB})^2$ in the field equations which could be described by the square of the δ-function. This is the breakdown is our thin-wall ansatz. In the case with the Gauss-Bonnet term, however, the basic equations show a quasi-linear property, which guarantees a thin-wall ansatz because it contains only linear terms of $\pounds_n K_{AB}$.

Although our system is not closed because of the existence of $E_{\mu\nu}$, for a cosmological setting, we recover the generalized Friedmann equation which contains one integration constant and then it gives a closed form just as in the case of Ref. [7]. With this fact, we consider Friedmann cosmology on the brane. In the present analysis we first derive n-dimensional bulk solutions under the static ansatz in the Einstein-Gauss-Bonnet-Maxwell-Λ system. They have interesting properties which can not be seen for the solutions in Einstein gravity as summarized in Sec. 2. Next examining the motion of a brane in the bulk spacetime using the generalized junction condition and Z_2-symmetry, we derive the generalized Friedmann equation on the brane. It becomes the cubic equation with respect to H^2. So there are three solutions at most, one of which can evolve to asymptotic Friedmann universe. The issues of the late-time behavior, high energy limit, the fine-tuning problem and bouncing universe are investigated.

2 Bulk solution

We start with the following n-dimensional ($n \geq 4$) action

$$S = \int d^n x \sqrt{-g} \left[\frac{1}{2\kappa_n^2} (R - 2\Lambda + \alpha L_{GB}) \right] + S_{\rm matter}, \tag{1}$$

[1] E-mail:torii@gravity.phys.waseda.ac.jp

where R and Λ are the n-dimensional Ricci scalar and the cosmological constant, respectively. $\kappa_n := \sqrt{8\pi G_n}$, where G_n is the n-dimensional gravitational constant and

$$L_{GB} = R^2 - 4R_{\mu\nu}R^{\mu\nu} + R_{\mu\nu\rho\sigma}R^{\mu\nu\rho\sigma} \tag{2}$$

is the Gauss-Bonnet Lagrangean. α is the coupling constant of the Gauss-Bonnet terms. Since the Minkowski spacetime becomes unstable for negative α, we consider only the case with $\alpha \geq 0$ in this paper. We consider the Maxwell gauge field as a matter field.

We assume the static bulk spacetime and adopt the following line element;

$$ds^2 = -f(r)e^{-2\delta(r)}dt^2 + f^{-1}(r)dr^2 + r^2 d\Omega_{n-2}^2, \tag{3}$$

where $d\Omega_{n-2}^2 = \gamma_{ij}dx^i dx^j$ is the metric of the $(n-2)$-dimensional Einstein space M^{n-2}. The (t,t) and (r,r) components of the gravitational equation give $\delta' \equiv 0$. By rescaling the time coordinate suitably, we can always set $\delta \equiv 0$ without loss of generality. The Maxwell equation is solved by using the electric field $E(r) := F_{rt}$ as $E = Q/r^{n-2}$, where the integration constant Q is the electric charge. The metric function f is obtained by solving the (t,t) component of the Einstein equations as

$$f = k + \frac{r^2}{2\tilde{\alpha}}\left\{1 \mp \sqrt{1 + 4\tilde{\alpha}\left[\frac{\tilde{M}}{r^{n-1}} - \frac{1}{\ell^2} - \frac{(n-3)\tilde{Q}^2}{2r^{2(n-2)}}\right]}\right\}, \tag{4}$$

where we have defined $\tilde{\alpha} := (n-3)(n-4)\alpha$ and $\Lambda = -(n-1)(n-2)/(2\ell^2)$. In our definition, a negative Λ gives a positive ℓ^2. k is the curvature of the $(n-2)$-dimensional Einstein space. There are two other parameters

$$\tilde{M} := \frac{16\pi G_n M}{(n-2)\Sigma_{n-2}^k}, \qquad \tilde{Q}^2 := \frac{\kappa_n^2 Q^2}{2(n-2)\pi g_c^2}. \tag{5}$$

The integration constant M is proportional to the mass of a black hole for black hole solutions. Although we will also consider solutions which do not represent black holes, we call M the mass of the solution. Σ_{n-2}^k is the volume of the unit $(n-2)$-dimensional Einstein space. There are two families of solutions which correspond to the sign in front of the square root in Eq. (4). We call the family which has minus (plus) sign the minus (plus) branch solution.

Below we list up the properties of the solution assuming $n = 5$ because that case is most important from the point of view of brane world. For the well defined theory, the following condition should be satisfied; $4\tilde{\alpha}/\ell^2 \leq 1$. From Eq. (4), the effective curvature radius is defined by $\ell_{\rm eff}^2 := \ell^2\left(1 \pm \sqrt{1 - 4\tilde{\alpha}/\ell^2}\right)/2$. The sign of the effective curvature radius $\ell_{\rm eff}^2$ is the same as ℓ^2 in the minus branch, while $\ell_{\rm eff}^2$ is always positive independently of ℓ^2 in the plus branch. Hence the spacetime approaches the adS spacetime asymptotically in the plus branch even when the pure cosmological constant is positive. By this effect, there are topological black hole solutions in the plus branch even for the positive cosmological constant case.

The spacetime structures of the solutions in the plus and minus branches are quite different. Besides the central singularity at $r = 0$, there is another singularity at $r = r_b$ called the branch singularity. r_b is determined by the condition that the inside of the square root of Eq. (4) vanishes. Around the branch singularity the Kretschemann invariant behaves as $\mathcal{I} \sim O\left[(r - r_b)^{-3}\right]$, irrespective of neutral or charged case. The spacetime has a boundary at the branch singularity for any charged solutions. For the neutral case, however, there are no positive roots when $\tilde{M} \geq 0$, while one positive root exists for $\tilde{M} < 0$. When a branch singularity exists, it is timelike if $k = 1$ or 0. When $k = -1$, it is timelike and spacelike for $r_b > \sqrt{2\tilde{\alpha}}$ and $r_b < \sqrt{2\tilde{\alpha}}$, respectively. In the special case of $k = -1$ and $r_b = \sqrt{2\tilde{\alpha}}$, the singularities are spacelike and timelike for the minus and plus branches, respectively.

For the neutral solutions with positive mass, the singularity appears only at the center. In the minus branch, the singularity is spacelike when $k = 0$ and -1. When $k = 1$, the singularity is spacelike for $\tilde{M} > \tilde{\alpha}$, null for $\tilde{M} = \tilde{\alpha}$, and timelike for $\tilde{M} < \tilde{\alpha}$. In the plus branch, the singularity is timelike when $k = 0$ and 1. When $k = -1$, the singularity is spacelike for $0 < \tilde{M} < \tilde{\alpha}$, null for $\tilde{M} = \tilde{\alpha}$, and timelike for $\tilde{M} > \tilde{\alpha}$. It is noted that the divergent behavior of the central singularity in the Gauss-Bonnet gravity is

milder than that in general relativity. It is also noted that the divergent behavior of the branch singularity is milder than that of the central singularity.

From the condition of the horizon $f(r_h) = 0$, we find

$$r_h^2 < -2\tilde{\alpha}k, \quad \text{(for the plus branch)}, \tag{6}$$

$$r_h^2 > -2\tilde{\alpha}k, \quad \text{(for the minus branch)}, \tag{7}$$

so that it is concluded that there are no horizons for $k = 1, 0$ in the plus branch. If there is a singularity in these cases, the solution is globally naked. When $k = -1$, the horizon radius is restricted as $r_h^2 < 2\tilde{\alpha}$ ($r_h^2 > 2\tilde{\alpha}$) in the plus (minus) branch. There are no such restrictions for $k = 1$ and 0.

There are three horizons at most. In general relativity, any solution with charge has inner horizon. In the Gauss-Bonnet case, however, there are charged solutions which do not have inner horizon. For these solutions the bouncing behavior of the brane is impossible as will be seen later. In the neutral case there are infinitesimally small black hole solution but has non-zero finite mass. This implies that there are maximum and minimum limitation of the abundance of the dark radiation in the brane cosmology.

3 Friedmann equation on the brane

Next let us derive the generalized Friedmann equation by the same method as the Kraus' in Einstein theory[8]. Our bulk metric has the form

$$ds^2 = -f(r)dt^2 + \frac{1}{f(r)}dr^2 + r^2 d\Omega_{n-2}^2. \tag{8}$$

We define the trajectory of the $(n-1)$-dimensional brane moves as $t = t(\tau)$ and $r = a(\tau)$, where τ is the proper time on the brane. Then the induced metric is

$$ds^2 = -d\tau^2 + a(\tau)^2 d\Omega_{n-2}^2. \tag{9}$$

The tangent vector of the brane is $u^A = (\dot{t}, 0, \cdots, 0, \dot{r})$. By the normalization condition $u_A u^A = -1$, we find $f^2\dot{t}^2 - \dot{r}^2 = f$. The unit normal vector is defined by $u^A n_A = 0$ and becomes $n_A = (-\dot{r}, 0, \cdots, 0, \dot{t})$, where we have chosen the normal vector points to the outward direction $r > r(\tau)$.

The junction condition at the brane [9] is

$$[K_{\mu\nu}]_\pm - h_{\mu\nu}[K]_\pm + 2\alpha\Big(3[J_{\mu\nu}]_\pm - h_{\mu\nu}[J]_\pm - 2P_{\mu\rho\nu\sigma}[K^{\rho\sigma}]_\pm\Big) = -\kappa_5^2\tau_{\mu\nu}, \tag{10}$$

where

$$J_{\mu\nu} = \frac{1}{3}\big(2KK_{\mu\rho}K^\rho{}_\nu + K_{\rho\sigma}K^{\rho\sigma}K_{\mu\nu} - 2K_{\mu\rho}K^{\rho\sigma}K_{\sigma\nu} - K^2K_{\mu\nu}\big), \tag{11}$$

$$P_{\mu\nu\rho\sigma} = R_{\mu\nu\rho\sigma} + 2h_{\mu[\sigma}R_{\rho]\nu} + 2h_{\nu[\rho}R_{\sigma]\mu} + Rh_{\mu[\rho}h_{\sigma]\nu}. \tag{12}$$

We have introduced $[X]_\pm \equiv X^+ - X^-$, where $X^\pm$ are X's evaluated either on the + or − side of the brane and $P_{\mu\nu\rho\sigma}$ is the divergence free part of the Riemann tensor, i.e. $D_\mu P^\mu{}_{\nu\rho\sigma} = 0$.

Now we assume the perfect fluid as a matter field on the brane, so $T_{\mu\nu} = (\rho + p)u_a u_b + p h_{ab}$. Using the (u, u) component of the junction condition, the Z_2-symmetry on the brane, and the normalization condition, the generalized Friedmann equation becomes a cubic equation with respect to H^2 as

$$\left(H^2 + \frac{f}{a^2}\right)\left[1 - \frac{2\alpha(n-1)(n-6)}{3}H^2 + \frac{4\alpha k}{a^2} - \frac{2\alpha(n-3)(n-4)}{3}\frac{f}{a^2}\right]^2 = \frac{\kappa_n^4}{4(n-3)^2}\rho^2, \tag{13}$$

for $n \neq 6$. When $n = 6$ this equation becomes linear equation w.r.t H^2 and we find

$$H^2 = -\frac{f}{a^2} + \frac{\kappa_6^4}{36}\rho^2\left[1 + \frac{4\alpha(k-f)}{a^2}\right]^{-2}. \tag{14}$$

In the late time, our universe recover the ordinary Friedmann universe. The Randall-Sundrum tuning condition is generalized as

$$1 - 2\tilde{\alpha} \mp \left(1 + \frac{2\tilde{\alpha}\Lambda_5}{3}\right)^{3/2} = \frac{\tilde{\alpha}\kappa_5^4\lambda^2}{2}. \tag{15}$$

In the plus branch, Minkowski brane can be realized even in the zero or positive cosmological constant case. Since Gauss-Bonnet term becomes dominant in the high energy regime, it can change the evolution of the universe drastically. Although the complete analysis needs numerical calculation, we can say something about the high energy behaviors by using some approximations. Around the central singularity at $r = 0$, the metric function behaves as

$$f \to \pm\sqrt{\frac{\tilde{M}}{\tilde{\alpha}}} + k. \tag{16}$$

This implies that $H^2 \propto \rho_m^{2/3}$ for $\omega > -1/3$. The gdark radiationh term behaves as if the curvature term in n=5. On the other hand, around the branch singularity at $r = r_b$, the metric function behaves as

$$f \to -1 + \frac{r^2}{\tilde{\alpha}}, \quad f' \to \infty, \tag{17}$$

which implies that $\ddot{a} \to \infty$. An infinitely accelerated universe is realized even with finite size and finite energy density.

When the bulk field is described by the Reissner-Nordström black hole, it is reported that the brane bounces inside of the inner horizon. This may be interpreted as the non-singular cosmology. It is well known, however, that the inner horizon is unstable against perturbations, i.e., mass inflation phenomenon. Considering these results, it seems difficult to realize the bouncing non-singular universe for the RN bulk field. In the Gauss-Bonnet case, the brane bounces when $H^2 = 0$. At this point, Eq. (4) becomes

$$\frac{f}{a^2}\left[1 + \frac{4\alpha k}{a^2} - \frac{2\tilde{\alpha}(n-3)(n-4)}{3}\frac{f}{a^2}\right]^2 = \frac{\kappa_n^4}{4(n-3)}\rho^2. \tag{18}$$

Hence the bounce occurs only in the untrapped region where ∂_t is timelike. Whether the the blue-shift instability occurs or not in the Gauss-Bonnet case is open problem. If not, the Gauss-Bonnet term makes the universe non-singular.

References

[1] L. Randall and R. Sundrum, Phys. Rev. Lett. **83**, 3370 (1999); Phys. Rev. Lett. **83**, 4690 (1999).

[2] P. Hořava and E. Witten, Nucl. Phys. **B475**, 94 (1996).

[3] G. W. Gibbons, *Supersymmetry. Supergravity and Related Topics* eds. F. del Aguila, et al., World Scientific, Singapore (1985); J. Maldacena and C. Nunez, Int. J. Mod. Phys. **A16**, 822 (2001).

[4] See, for example, D. J. Gross and J. H. Sloan, Nucl. Phys. **B291**, 41 (1987).

[5] Y. M. Cho and I. P. Neupane, Int. J. Mod. Phys. **A18**, 2703 (2003); Y. M. Cho, I. P. Neupane and P. S. Wesson, Nucl. Phys. **B621**, 388 (2002).

[6] N. Deruelle and M. Sasaki, Prog. Theor. Phys. **110**, 441 (2003).

[7] T. Shiromizu, K. Maeda and M. Sasaki, Phys. Rev. D **62**, 024012 (2000); K. Maeda and T. Torii, Phys. Rev. D **69**, 024002 (2004).

[8] P. Kraus, J. High Energy. Phys **12**, 011 (1999).

[9] S. C. Davis, Phys. Rev. **D67**, 024030 (2003).

Non-Gaussianity from inflation with stochastic approach

Takeshi Hattori[1] and Kazuhiro Yamamoto

Theoretical Astrophysics Group, Department of Physics, Hiroshima University, Hiroshima 739-8526, Japan

Abstract

We investigate the fluctuation generated by inflation in the frame work of the stochastic approach. Using the scaling approximation, the Fokker-Planck equation is analytically solved for the probability distribution function of the inflaton with various potentials. In order to understand the result confronting with observation, we try to obtain the probability function for the gauge invariant variable ζ from that for the inflaton. The deviation from the Gaussian statistics is investigated by evaluating the local skewness.

1 Introduction

The scalar fields during inflationary era naturally possess non-Gaussian nature. To understand the inflationary models, it is important to analyze the non-Gaussianity for the density perturbation. For such investigation the stochastic approach is useful [1,2,3,4]. The Fokker-Planck equation, which describes the evolution of the probability distribution function of the inflaton, can be analytically solved using the scaling approximation. The aim of this work is to investigate the non-Gaussian nature in an analytic manner for various inflation models confronting it with observation. In our investigation, we also investigate the effect of the generalization of the quantum state of the noise fluctuation on the probability distribution.

2 Stochastic dynamics

The equation for the scalar field operator ϕ on de-Sitter background is

$$\left[\frac{\partial^2}{\partial t^2} + 3H\frac{\partial}{\partial t} - \frac{1}{a(t)^2}\Delta\right]\phi(\boldsymbol{x},t) + \frac{\partial V}{\partial \phi}(\boldsymbol{x},t) = 0, \tag{1}$$

where H is Hubble parameter, $a(t)$ is scale factor, and V is potential. We split the scalar field operator ϕ (inflaton) into the long wavelength and the short wavelength modes as

$$\phi(\boldsymbol{x},t) = \varphi(\boldsymbol{x},t) + \varphi_s(\boldsymbol{x},t). \tag{2}$$

A coarse-grained variable ϕ is defined as the average of quantum field over Hubble volume $1/H^3$. The long-range inflaton dynamics is a Brownian motion, which is described by the Langevin equation

$$\dot{\phi} = -g(\phi) + h(\phi)\eta(t). \tag{3}$$

where

$$g(\phi) = \frac{1}{3H(\phi)}\frac{\partial V(\phi)}{\partial \phi}, \quad h(\phi) = \frac{H^{3/2}(\phi)}{\sigma^{1/2}}. \tag{4}$$

and the first term denotes the classical convective force and the second term denotes the diffusion term depending on random variable. Also, the (0,0) component of the Einstein equation gives $H(\phi) = \sqrt{V/3\sigma^2}$, where we define $\sigma = 1/\sqrt{8\pi G}$ (G is Newton's gravitational constant). The fine-grained contribution enters it through η, a Gaussian noise with

$$\langle\eta(t)\rangle = 0, \quad \langle\eta(t)\eta(t')\rangle = 2\epsilon\delta(t-t'). \tag{5}$$

[1]E-mail:tkc@hiroshima-u.ac.jp

where we define $\epsilon = \sigma/8\pi^2$. The probability distribution of the inflaton evolves according to a Fokker-Planck equation

$$\frac{\partial P(\phi,t)}{\partial t} = \frac{\partial}{\partial \phi}\left(g(\phi)P(\phi,t) + \frac{h(\phi)}{2}\frac{\partial}{\partial \phi}[h(\phi)P(\phi,t)]\right). \tag{6}$$

We here consider the following inflation potentials: The potential for the chaotic inflation

$$V(\phi) = \frac{\lambda}{2n}\sigma^4\left[\frac{\phi}{\sigma}\right]^{2n} = V_*\left[\frac{\phi}{\phi_*}\right]^{2n}, \tag{7}$$

where $(n = 1, 2, \cdots)$, and the exponential potential leading to the power-law inflation

$$V(\phi) = V_* \exp[-\lambda(\phi - \phi_*)/\sigma], \tag{8}$$

where the subscript '$*$' denotes the initial value of a given quantity.

In order to get the scaling solution of the Fokker-Planck equation, we perform two transformation. Firstly, we transform the equation from a multiplicative process (ϕ dependent noise amplitude) to an additive one (constant noise amplitude)

$$\phi \to x = 3^{3/4}\sigma^2 \int_{\phi}^{-\infty} V^{-3/4} d\phi'. \tag{9}$$

The second transformation leads to a vanishing drift term

$$x \to \xi(x,t) \equiv F^{-1}[e^{-\gamma \Delta t}F(x)], \tag{10}$$

where $\gamma = 2n\sigma(\lambda/6n)^{2/(3n-2)}[(3n-2)/2]^{(n+2)/(3n-2)}x_*^{(4-2n)/(3n-2)}$ for the chaotic inflation potential. The transformation thus leads to the non-drift Langevin equation,

$$\dot{\xi} = \left[\frac{\xi}{x}\right]^{(n+2)/(3n-2)}\eta(t). \tag{11}$$

Finally, we obtain the general scaling solution of the Fokker-Planck equation,

$$\tilde{P}_{sc}(x,t) = \frac{1}{\sqrt{2\pi\tau}}\left(\exp\left[-\frac{(\xi - x_*)^2}{2\tau}\right] + \exp\left[-\frac{(\xi + x_*)^2}{2\tau}\right]\right)\left|\frac{\partial \xi}{\partial x}\right|, \tag{12}$$

where the variance τ is

$$\tau(t) = \frac{(3n-2)\epsilon}{4\gamma}\left(1 - \left[1 + \frac{2n-4}{3n-2}\gamma\Delta t\right]^{4/(2-n)}\right) \tag{13}$$

3 α-vacuum

It is usually assumed that the quantum state of inflaton noise is in the Bunch-Davies vacuum. However, it might be possible the state is in different vacuum state. We here consider the α-vacuum [5,6], which is related with the Bunch-Davies vacuum through the Bogoliubov transformation

$$\phi_k^\alpha = N_\alpha(\phi_k^{BD} + \gamma\phi_{-k}^{BD*}), \quad N_\alpha = \frac{1}{\sqrt{1 - |e^\alpha|^2}}, \quad \gamma = e^\alpha, \tag{14}$$

where α is a complex parameter and the Bunch-Davies vacuum is reproduced in the limit $\alpha = -\infty$. In the α-vacuum case, we obtain the new Langevin equation with the α-parameter:

$$\dot{\phi} = -g(\phi) + f(\alpha)h(\phi)\eta(t), \quad f(\alpha) \equiv \frac{|1 + e^\alpha|}{\sqrt{1 - |e^\alpha|^2}} \geq 1. \tag{15}$$

and the Fokker-Planck equation is written as

$$\frac{\partial P(\phi,t)}{\partial t} = \frac{\partial}{\partial \phi}\left(g(\phi)P(\phi,t) + \frac{f(\alpha)h(\phi)}{2}\frac{\partial}{\partial \phi}[f(\alpha)h(\phi)P(\phi,t)]\right). \tag{16}$$

4 Connection with observation

The better way to understand the (scalar) perturbations during the inflation is to represent it in terms of variable connected with observation. Here we consider the gauge invariant variable ζ and assume the following relation as that in the spatially flat slicing [7].

$$\zeta = -\frac{H}{\dot{\phi}}\delta\phi = -\frac{H}{\dot{\phi}}(\phi - \phi_{cl}). \tag{17}$$

For a consistency check, the power spectrum for ζ is derived as follows. We can derive the Langevin equation

$$\dot{\zeta} = -\frac{H}{\dot{\phi}}f(\alpha)\sigma_n, \tag{18}$$

where the noise satisfies

$$\langle\sigma_n(x_1)\sigma_n(x_2)\rangle = \frac{H^3}{4\pi^2}j_0(\epsilon aH|\boldsymbol{x}_1 - \boldsymbol{x}_2|)\delta(t_1 - t_2). \tag{19}$$

Then the correlation function

$$\langle\zeta(x_1,t_1)\zeta(x_2,t_2)\rangle = \frac{1}{2\pi^2}\int_{k_0}^{k(min[t_1,t_2])} dkk^2P_\zeta(k)j_0(\epsilon aH|\boldsymbol{x}_1 - \boldsymbol{x}_2|) \tag{20}$$

leads to the standard power spectrum

$$P_\zeta(k) = \frac{f^2(\alpha)}{2k^3}\frac{H^4}{\dot{\phi}^2}\Big|_{horizon\ crossing} \tag{21}$$

5 Non-Gaussianity

Assuming equation (17), the probability function for ζ is obtained. Then we calculate the ratio of $P(\phi_{cl}+\Delta\phi(\zeta))$ to $P(\phi_{cl}-\Delta\phi(\zeta))$ as an estimator of the non-Gaussianity. It gives a very simple estimator of the local skewness in the region near ϕ_{cl} (ϕ for zero-noise).

$$\mathcal{T}_\zeta \equiv \frac{\tilde{P}_{sc}(\phi_{cl}+\Delta\phi(\zeta))}{\tilde{P}_{sc}(\phi_{cl}-\Delta\phi(\zeta))}. \tag{22}$$

Then we have

$$\mathcal{T}_\zeta = \exp\left(-\frac{f(\alpha)}{4\sqrt{2\pi}}\frac{H_*}{\sigma}\left[1-\left(\frac{\phi_{cl}}{\phi_*}\right)^4\right]^{1/2}\left[\frac{n+2}{2\sqrt{n}}+\frac{n-1}{\sqrt{n}}\left(\frac{\phi_{cl}}{\phi_*}\right)^{n-2}\right]\right), \tag{23}$$

for the chaotic inflation, and

$$\mathcal{T}_\zeta = \exp\left(-\frac{f(\alpha)}{4\sqrt{2\pi}}\frac{H_*}{\sigma}\left[\frac{2\lambda(\phi_{cl}-\phi_*)}{\sigma}\right]^{1/2}\left[\frac{1}{2}+e^{-\lambda(\phi_{cl}-\phi_*)/2\sigma)}\right]\right), \tag{24}$$

for the power-law inflation potential, respectively. If we fix the variance $\langle\zeta^2\rangle$ from observational, equation (23) can be rewritten as

$$\mathcal{T}_\zeta = \exp\left(-\frac{1}{4\sqrt{2\pi}}\left[\frac{N}{n}+\frac{1}{6}\right]^{-1/2}\langle\zeta^2\rangle^{1/2}\left[\frac{n+2}{2\sqrt{n}}+\frac{n+1}{\sqrt{n}}\left(\frac{\phi_{cl}}{\phi_*}\right)^{n-2}\right]\right), \tag{25}$$

where N is the number of e-foldings. We note that $\mathcal{T}_\zeta$ does not depend on the α-parameter. Fig. 1 shows the behavior of $\mathcal{T}_\zeta$. The non-Gaussianity is very small from the observational constraint on $\langle\zeta^2\rangle$.

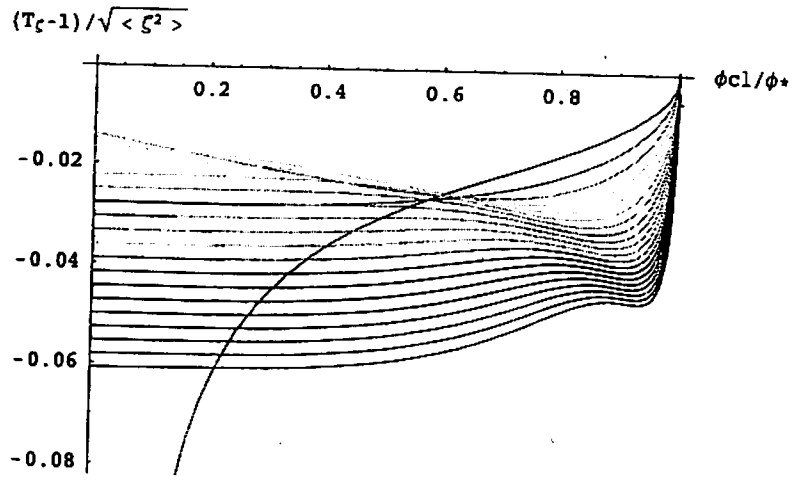


Figure 1: Non-Gaussianity $(\mathcal{T}_\zeta - 1)/\langle\zeta^2\rangle^{1/2}$ for chaotic inflation. $n = 1, \cdots, 20$ from top to bottom. Here we fixed $N = 100$.

6 Summary

We investigate the stochastic dynamics of inflaton for various potentials leading both the chaotic and the power-law inflation. The evolution of the inflaton is described by the Langevin equation, and the probability distribution function follows the Fokker-Planck equation. We solve the evolution equation adopting the scaling approximation. Also, we generalize the quantum state of inflaton, extending to the α-vacuum, and compared with Bunch-Davies vacuum which is usually used to analyze. Introducing ζ related with $\delta\phi$ by equation (17), we considered the feature of non-Gaussianity. We estimate the local skewness $\mathcal{T}$ in the region near the classical solution ϕ_{cl} for general potentials as an estimator of the non-Gaussian fluctuation. The inflaton field evolution and its non-Gaussianity significantly depend on the inflaton potential. Also, the distribution function depends on the α-parameter, which specify different vacuum state, however, the non-Gaussianity $\mathcal{T}_\zeta$ does not depend on the α-parameter if the observable $\langle\zeta^2\rangle$ is fixed. In the case of one field inflation the non-Gaussian signal is small for the observable quantity. The extension of our investigation to multiple-field inflation model is under investigation.

References

[1] A. A. Starobinsky, JETP Lett. **42**, 152 (1985)

[2] K. Nakao, Y. Nambu, M. Sasaki, Prog. of Theo. Phys. **80**, 1041 (1988)

[3] S. Matarrese, A. Ortolan, F. Lucchin, Phys. Rev. D **40**, 290 (1989)

[4] I. Yi, E. T. Vishniac, S. Mineshige, Phys. Rev. D **43**, 362 (1991)

[5] K. Goldstein, D. A. Lowe, Nucl. Phys. B **669**, 325 (2003)

[6] U. H. Danielsson, JHEP **0212**, 025 (2002)

[7] S. Dodelson, *Modern Cosmology* (Academic Pr, 2003)

Large-scale spectrums after inflation
-nonminimal coupling scalar fields case-

Yohei Araki[1] and Yasusada Nambu[2]

Department of Physics,Graduate School of Science, Nagoya University, Nagoya 464-0032, Japan

Abstract

We investigate the large-scale inhomogeneity with gradient expansion (GE) which enable us to make general relativistic and non-linear treatment. We use a nonminimal coupled two scalar fields model which has two instabilities caused by negative mass and parametric resonance. We show that GE is well accord with linear theory in linear regime and can treat the case above the linear theory.

1 Introduction

The evolution of large-scale inhomogeneity during inflation and preheating is one of the most important topics in the inflationary cosmology. Because it can be observed directly through cosmic microwave background (CMB) and we can know the information about inflationary models. Especially, the power spectrum of inhomogeneities after inflation is very important.

Many researchers had been studying such a spectrum but many of these were based on linear perturbation approach and slow rolling approximation, so the analysis has some limits to be applied. Indeed, some of inflationary models have an instability and this amplifies inhomogeneity and linear perturbation becomes invalid. In such a case, slow rolling approximation often becomes invalid too. So linear theory can't cover all of models. Of course, full numerical calculation can study such a nonlinear case, but to know the super horizon spectrum, we need the general relativistic treatment and huge numerical resolution. Therefore numerical study of large scale inhomogeneity is difficult in general and some approximation is needed.

Here, we use the first order gradient expansion (GE) instead of the linear perturbation theory. We show this approach enables us general relativistic and nonlinear study. This approximation can't involve small, sub-horizon scale structures and their contribution to large scale, but we think these are not important for super horizon scale and result will be agree with super horizon part of the nonapproximately calculation. This is because of largeness of today's cosmological scale, mega or kilo parsec scale is larger than characteristic Hubble scale during inflation or preheating which is meter scale in commoving length, so to neglect spatial differential relative to Hubble term, so-called GE is good approximation and this is also supported from viewpoint of causality. Thus as long as we are interested in super-horizon scale, GE will be valid and useful tool to investigate. And the picture of GE can be understood intuitively by the separate universe approach as we show later, so this also has an advantage to be able to image easily.

With GE, we investigate a model with two scalar fields, inflaton φ and other scalar field χ that is nonminimally coupled to gravity ($\frac{1}{2}\xi R\chi^2$). Model with multiple fields is more interesting than single one because it is known large scale curvature perturbation are more influenced on multiple fields than single one. The nonminimal coupling term are expected from quantum theory of gravity like super string theory. The model we think has two kinds of characteristic instabilities, the one is the negative mass instability and the other is the instability caused by parametric resonance on super horizon scale. χ field grows exponentially during inflation era by the negative mass instability and preheating era by the parametric resonance respectively in some parameter range. And we think the situation inflaton φ dominates initially, and usual one field inflation is occurred, but exponentially growing χ field affects on the inflaton dynamics or large scale curvature perturbation later. The dynamics of the inflaton is altered by the backreaction of χ and this means slow rolling parameter is also altered and as a result, index of spectrums of curvature perturbation and other fields are distorted by χ. Such a phenomenon is difficult

[1]E-mail:araki@gravity.phys.nagoya-u.ac.jp
[2]E-mail:nambu@gravity.phys.nagoya-u.ac.jp

to treat because this is nonlinear. Indeed, this model had already been researched by Tujikawa and Yajima with linear perturbation theory but they didn't show distortion of spectrum. We now reconsider the same situation with GE and think the distortion.

The nonminimal coupling term we think here isn't the only term expected in quantum gravitational theory. But no one knows effective collect action yet, so we think the term as a example and regard the coupling constant as model parameter. And we think the constraint from observation to the parameter. We show stronger constraint than Tujikawa and Yajima's one.

2 Model and Formalism

We think the model with following Lagrangian.

$$\mathcal{L} = \sqrt{-g}\Big(\frac{1}{2\kappa^2}R - \frac{1}{2}(\nabla\varphi)^2 - \frac{1}{2}m^2\varphi^2 - \frac{1}{2}(\nabla\chi)^2 - \frac{1}{2}\xi R\chi^2\Big) \tag{1}$$

φ is an inflaton with mass m and χ is other amplified scalar field. We put a nonminimal coupling term $\frac{1}{2}\xi R\chi^2$. This model is known to have an instability by negative mass during inflation when $\xi < 0$ and by parametric resonance during preheating when $|\xi| \ll 1$. We derive equations from this Lagrangian in following Rigopoulous and Shellard's method[2]. First, we split metric variables as follows.

$$g_{\mu\nu} = \begin{pmatrix} -N^2 + N^iN_i & N_i \\ N_i & \gamma_{ij} \end{pmatrix} \tag{2}$$

And we write extrinsic curvature as $K_{ij} \equiv \frac{1}{2N}(N_{i|j} + N_{j|i} - \dot{\gamma}_{ij})$, tracceless part of this as $K^i{}_j = \bar{K}^i{}_j + \frac{1}{3}\delta^i{}_jK$, where $X_{|i}$ means 3-dimentional covariant spatial gradient of X. Next, we neglect more than second order spatial differential, this is first order GE Hereinafter we choose synchronous slice($N^i = 0, N = 1$). Then we can see from equations that traceless part of extrinsic curvature has only decaying mode with expansion of universe so we neglect this. Finally we use more familiar notation $|\gamma_{ij}| = a^6(t,\vec{x}), K(t,\vec{x}) = -3\dot{a}/a = -3H(t,\vec{x})$ here dot denotes differential with t and so a and H are locally defined scale factor and locally defined Hubble constant.

As a result, we can get following equations.

$$3H^2 - \frac{1}{\kappa^{-2} - \xi\chi^2}(\frac{1}{2}\dot{\phi}^2 + \frac{1}{2}\dot{\chi}^2 + V + 6\xi H\chi\dot{\chi}) = 0 \tag{3}$$

$$H_{,i} + \frac{1}{2(\kappa^{-2} - \xi\chi^2)}(\dot{\phi}\phi_{,i} + (1-2\xi)\dot{\chi}\chi_{,i} - 2\xi\chi\dot{\chi}_{,i} + 2\xi H\chi\chi_{,i}) = 0 \tag{4}$$

$$\dot{H} = -\frac{1}{2(\kappa^{-2} - \xi\chi^2)}(\dot{\phi}^2 + (1-2\xi)\dot{\chi}^2 - 2\xi\chi(\ddot{\chi} - H\dot{\chi})) \tag{5}$$

$$\ddot{\phi} + 3H\dot{\phi} + V_{,\phi} = 0 \tag{6}$$

$$\ddot{\chi} + 3H\dot{\chi} + \xi R\chi = 0, R = 6\dot{H} + 12H^2 \tag{7}$$

First two equations are not evolutional equations but constraint equations same as usual ADM splitting of Einstein equations and last three equations are evolution equations of each variables. We call equation(3) Hamiltonian constraint and equation(4) momentum constraint respectively. Except for momentum constraint, each equations are same as homogeneous Friedman universe. But each variables still depend on the position, so we can treat inhomogeneous universe in these nonlinear and general relativistic equations. These are also regarded as separate universe approach of nonminimal gravity. So these show intuitively separate universe picture is valid for nonminimal gravity. From this picture, we can understand the evolution of inhomogeneity as follows. Each point of universe develops as a homogeneous Friedman universe but their evolution are different and the difference is inhomogeneity on a scale includes these patches of universe.

In this system, definition of inhomogeneity is not trivial. In this paper, we define that as follows. Homogeneous part of a variable is average over each patches, denoted as $< \phi >$, this is corresponds with volume average, and inhomogeneous part is a difference from that, $\delta\phi(\vec{x}) = \phi(\vec{x}) - < \phi >$, this depends on a position. In linear theory, Bardeen parameter ζ is often used as a measure of an inhomogeneity.

In particular this is important for super horizon scale because this is same as curvature perturbation on large scale limit. In nonminimal gravity, Bardeen parameter is also known as follows[3].

$$\zeta = -\Psi + \frac{H(1-\xi\kappa^2\chi^2)}{\dot{H}(1-\xi\kappa^2\chi^2)+2H\xi\kappa^2\chi\dot{\chi}}(\dot{\Psi}+H\Psi) = -\delta\ln a + \frac{H(1-\xi\kappa^2\chi^2)}{\dot{H}(1-\xi\kappa^2\chi^2)+2H\xi\kappa^2\chi\dot{\chi}}\delta H \tag{8}$$

where Ψ is gauge invariant metric perturbation. This is also conserved on super horizon scale like minimal coupling Einstein gravity if there is only one scalar field. We use this ζ as a measure of inhomogeneity and regard this as curvature perturbation.

3 Initial Condition

Now we introduce initial condition for numerical calculation. Initial condition of fields is determined by vacuum fluctuation during inflation and this can be known from linear theory. We solve equations with linear perturbation and slow rolling approximation, since these are reasonable for early stage of inflation. With neglecting metric perturbations, we can get a solution for inhomogeneous part of scalar fields and we choose Bunch-Davis vacuum. Then solutions in Fourier space are

$$\delta\varphi_k = \frac{\sqrt{\pi\eta}}{2a}H^{(2)}_{3/2}(k\eta), \delta\chi_k = \frac{\sqrt{\pi\eta}}{2a}H^{(2)}_{\nu}(k\eta), \nu = \frac{1}{2}\sqrt{9-48\xi}. \tag{9}$$

So large scale ($k \ll aH$) spectrum is $\Delta^2_\varphi \equiv \frac{k^3}{2\pi^2}|\delta\varphi_k|^2 = \frac{H^2}{4\pi^2}, \Delta^2_\chi = \frac{2^{2\nu}H^2\Gamma^2(\nu)}{8\pi^3}\left(\frac{k}{aH}\right)^{3-2\nu}$. We use these solutions for initial value of scalar fields and we set $\dot{\chi}=0$ at initial for simplicity. Remaining initial values of $\dot{\phi}, H$ are determined by two constraints. We solve Hamiltonian and momentum constraint for each values of parameter ξ and solve time development numerically. Homogeneous part of ϕ and χ aren't determined by quantum fluctuations and they are regarded as free parameter in this paper. But homogeneous part of inflaton ϕ is connected to e-folding number and it must be determined not to be conflict of observations.

4 Results

4.1 The $\xi > 0$ case

When $\xi > 0$, χ field isn't instable but dumping oscillates like a positive massive scalar, but for $\xi \gg 1$, preheating occur and χ is exponentially amplified. But it is seen from time development drawn in fig.1 that amplification of χ isn't large enough to exceed inflationary dumping. So we conclude that the positive ξ must not affect on the inflaton and of course observable quantity e-folding number or Bardeen parameter ζ is not altered.

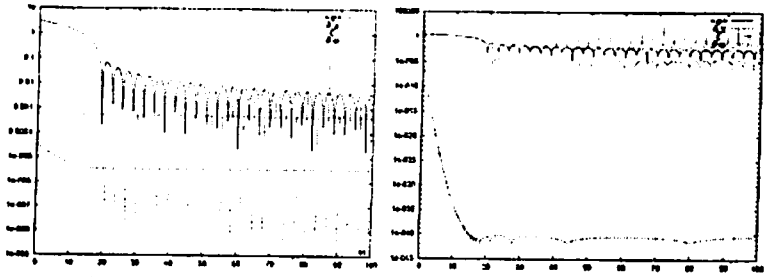


figure2:Time development of fields with negative coupling

In this figure, initial condition $<\varphi>=3m_p, <\chi>=0$ is used. Left figure is plotted with parameter $\xi = 0.1$ so the effective mass of χ is right and right one with $\xi = 100$, the heavy case. In both cases inflation continues until $mt = 20$, e-folding number is 57, so standard inflation scenario is retained. Light boson dumps slightly but be hardly amplified during preheating while heavy boson are amplified during preheating. But inflationary dumping is so strong that efficient value isn't obtained. In each case, χ field can't affect on φ so curvature perturbation is conserved.

4.2 The $\xi < 0$ case

The negative ξ case is more interesting because it shows stronger amplification during inflation. And we can see that backreaction of amplified χ field alter the inflaton dynamics and inflaton decreases rapidly. As a result, the slow rolling parameter becomes order one and de Sitter like expansion is terminated faster than single field inflation and e-folding number is reduced. Fig.2 shows the time evolution of fields with negative ξ.

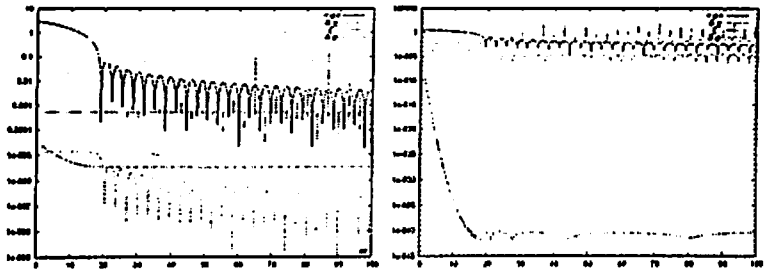


figure1:Time development of fields with positive coupling.

Left figure is plotted with $< \phi >= 3m_p, < \chi >= 0.01m_p$ and $\zeta = -0.02$. Homogeneous part of χ is amplified and it makes inflation shorter. At the same instant, first order term $< \chi > \delta\chi$ alter Bardeen parameter ζ. These result is well corresponding with the linear theory. We also calculate power spectrum of fields. And we confirm that distortion of spectrum is more significant on larger scale. This is because of initial spectrum of χ. As said in previous section, initial χ spectrum has power which index depends on ξ on super horizon scale. The index is $n \sim 0.4\xi$, so negative ξ means red spectrum. Therefore curvature perturbation is stronger altered on relative large scale.

Right one of figure2 is an example for larger $|\xi|$. If $\xi = -0.05$, χ fast grows and inflation is terminated soon. This is occurred even when homogeneous χ field is zero. Second order perturbation $\delta\chi^2$ or higher order term grows fast enough to disturb successful inflation. In this example, e-folding number become only 27, and curvature perturbation on today's cosmological scale is amplified to order one. Such a over amplification must be ruled out obviously. The important point is this is occurred in arbitrary small initial homogeneous χ field. So negative ξ is tightly constrained. To avoid the amplification of super horizon scale curvature perturbation, $\xi > -0.026$ is needed and this result doesn't depend on initial value of $< \chi >$. While positive value of ξ is hardly constrained, negative value is almost ruled out from CMB observation.

5 Summary

We investigate inflation and preheating on a model of nonminimal coupling with GE and calculate the evolution of large scale spectrum of curvature perturbation. Comparing with CMB observational data, we found negative value of ξ is strongly constrained by higher order effects while positive one is almost free. If ξ is negative, perturbations are more amplified on larger scale and this means tends to become red spectrum. The relation such a distortion and χ's backreaction to ϕ isn't clear yet and we are now researching this topic.

References

[1] S. Tujikawa and H. Yajima, Phys. Rev. **D62** 123512 (2000).

[2] G. Rigopoulos and E. Shellard astro-ph/0405185 (2004).

[3] J. Hwang, Phys. Rev. **D42**, 2601 (1990).

Approach to the Cosmological Constant Problem with a Diluting Mechanism by Extra-Dimensions

Satsuki Shimono[1], Takeshi Chiba[2]

[1] *Theoretical Astrophysics Group, Department of Physics, Kyoto University, Kyoto 606-8502, Japan*
[2] *Collage of Humanities and Sciences, Department of Physics, Nihon University, Setagaya, Tokyo 156-8850, Japan*

Abstract

The value of the cosmological constant has a gap of order 10^{-120} between observations and the standard theory. It is called the cosmological constant problem (CCP), which has been considered hard to overcome while few ten's of years. Recently a mechanism of diluting the cosmological constant by an extra dimensional effect has suggested by Dvali et al. [4]. That mechanism is that the crude cosmological constant is a Planck scale and exists in the 4 plus extra dimensional entire space, but we observe this diluted in the 4-dimensional brane embedded. Cho and Vilenkin have studied the 3-dimensional spherically symmetric extra space to examine the Dvali et al.'s diluting mechanism [5]. But out approach is observing the dependence of Hubble expansion rate H on the number of extra-dimensions n. So we have extended their model to an arbitrary $(4+n)$-dimensional one, and we have found new solutions numerically to get the relation between n and H. We have concluded that $n \geq 3$ is needed to obtain $H = 0$ if we assume the crude cosmological constant is the Planck mass.

1 Introduction

The energy density of the Universe is composed of the matter $\Omega_{M0} = 0.3$, and the cosmological constant $\Omega_{\Lambda 0} = 0.7$ [1]. The observed present value of the Hubble parameter is $H_0 \approx 10^{-33}$eV. These estimation implies the value of the cosmological constant is $\Lambda_4 \approx (10^{-3}\text{eV})^4$. On the other hand, a natural value of a constant contained in a gravitational theory is thought the Planck mass $M_p \approx 10^{18}$GeV. Both have a gap of order

$$\frac{(10^{-3}\text{eV})^4}{M_p^4} = 10^{-120}. \tag{1}$$

This inconsistency is called the cosmological constant problem (CCP) [2, 3] and still remains to be solved.

Dvali *et al.*[4] has suggested the mechanism of diluting the cosmological constant by using the extra-dimensional effect to overcome the CCP. This mechanism is that the observed effective cosmological constant becomes so small because whose energy is consumed to bend the bulk space even if the crude one is such large as the Planck scale. And they have introduced the conjecture such that

$$H = M_* \left(\frac{M_*^4}{\Lambda_4} \right)^{1/(n-2)}. \tag{2}$$

Where M_* is the $(4+n)$-dimensional Planck mass. If the number of extra dimensions n is greater than 3, Hubble parameter H is monotonically decreasing function of the cosmological constant Λ_4.

Cho and Vilenkin [5] have constructed the concrete model that has a 3-dimensional spherically symmetric extra space. In theirs model, physically acceptable solutions have features that bulk metric doesn't have a singularity at finite distance from the brane. In that paper, solutions whose asymptotic forms have the cigar ansatz and have the infinite bulk spaces were found. The relation between the scalar field's energy interpreted as the crude cosmological constant and the brane's expansion rate is calculated by

[1] E-mail:shimono@tap.scphys.kyoto-u.ac.jp
[2] E-mail:chiba@phys.chs.nihon-u.ac.jp

using these solutions. And it is concluded that both have a positive correlation and can be linear fitted against the Dvali et al.'s conjecture (2).

Our approach is to observe the relation between the number of extra-dimensions and the brane's expansion rate with the energy scale fixed near the Planck mass, and obtain the condition of vanishing the expansion rate. So we have extended Cho and Vilenkin's model to the arbitrary $(4+n)$-dimensional one. We have found new solutions under the condition that the position of the singularity becomes as far as possible and the metric doesn't have the divergence.

We have concluded that Dvali et al.'s conjecture (2) cannot be reproduced by using our new bulk solutions in any dimension n. But we have found that the brane's expansion rate is a monotonically decreasing function of the number of the extra dimensions n. And the expansion rate can vanish at the specific dimension.

2 Model

In this section, the extended $(4+n)$-dimensional model is constructed.

2.1 Space-time structure

In this model, the brane is assumed a 4-dimensional de-Sitter apace $\mathbf{dS}^4$, and the extra space is a spherically symmetric n-dimensional space $\mathbf{R} \times_{Cr} \mathbf{S}^{n-1}$. Where the number of extra dimensions n is greater than 2. The entire manifold is wrapped product of both spaces $\mathbf{R} \times_{Cr} \mathbf{S}^{n-1} \times_B \mathbf{dS}^4$, whose metric is

$$ds^2 = dr^2 + C(r)^2 r^2 d\Omega_{n-1}^2 + B(r)^2 \left(-dt^2 + e^{2Ht} \sum_{i=1}^{3} dx^{i\,2} \right). \tag{3}$$

Where the brane's coordinate is (t, x^1, x^2, x^3) and H is the positive constant expansion rate. The extra space's coordinate is $(r, \theta_1, \ldots, \theta_{n-1})$ and $d\Omega_{n-1}$ is the metric of an $n-1$ dimensional sphere $\mathbf{S}^{n-1}$. $C(r)r$, $B(r)$ are the radius of the extra space and the warp factor depending on r only. We adopt the Einstein-Hilbert action for the space-time dynamics such that

$$\mathcal{S}_{\mathrm{E-H}} = \frac{1}{2\kappa^2} \int d^{4+n}x \sqrt{-g}\mathcal{R}. \tag{4}$$

Where κ is the $(4+n)$-dimensional gravitational constant. In this paper, κ is independent of the number of extra dimensions to make clear the effect of a dilution. g and $\mathcal{R}$ are the determinant and the Ricci scalar of the metric (3).

2.2 Energy Momentum Tensor

The global defect in the n-dimensional spherically symmetric space is introduced to construct the brane, which is described by a multiplet of the scalar fields ϕ^i with a Lagrangian density,

$$\mathcal{S}_\phi = \int d^{4+n}x \sqrt{-g} \left[-\frac{1}{2} \partial^A \phi^i \partial_A \phi_i - V(\phi) \right]. \tag{5}$$

Where capital letters $(A, \ldots)$ and small letters $(i, \ldots)$ run from 1 to $4+n$ and from 1 to n respectively. Because we are thinking spherically symmetric solutions only, the scalar multiplet has been assumed to have a hedgehog configuration, $\phi^i = \phi(r) \cdot \xi^i / r$. Where $\phi(r)$ depends only on the radius coordinate r and ξ^i represent for the Cartesian coordinates of the extra space. The potential of the scalar field $V(\phi)$ has minimum at $|\phi^i| = \varphi = \eta$ such that

$$V(\phi) = \frac{\lambda}{4}(\phi^2 - \eta^2)^2. \tag{6}$$

The energy created by the scalar field is interpreted as the crude cosmological constant existed in the entire space, so ϕ's vev holds about the Planck scale $\eta \approx 1/\kappa$.

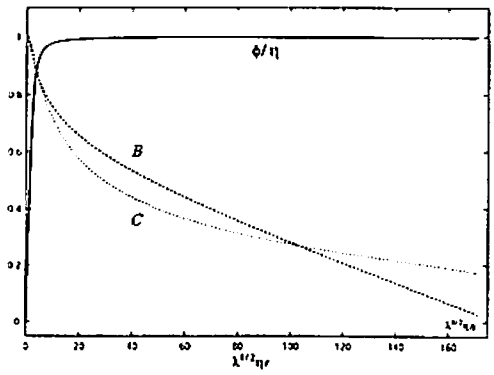


Figure 1: This graph shows the physically proper solution with the eigen value $(n, \kappa\eta, (\kappa/\lambda^{1/2})H) = (3, 1.09, 0.003786056)$. B is approaching to 0 at finite r_t.

2.3 Basic Equations

The Einstein equations and the EOM of the scalar field are obtained by the action,

$$S = S_{E-H} + S_\phi. \tag{7}$$

Independent components of the Einstein equations and EOM of the scalar field have the forms

$$B''(r) = F[n, H, \eta; B, B', C, C', \phi, \phi'], \tag{8}$$
$$C''(r) = G[n, H, \eta; B, B', C, C', \phi, \phi'], \tag{9}$$
$$\phi''(r) = H[n, H, \eta; B, B', C, C', \phi, \phi'], \tag{10}$$
$$I[n, H, \eta; B, B', C, C', \phi, \phi'] = 0. \tag{11}$$

A prime on variables denotes a differentiation about r. Eq.(11) imposes the constraint when solving eq. (8), (9) and (10) as simultaneous second differential equations for $(B(r), C(r), \phi(r))$.

3 Results

Differential equations to solve have a set of three parameters $(n, \kappa\eta, (\kappa/\lambda^{1/2})H)$. It is found by the numerical integration that the proper relation among them is obtained under the condition that the point of a singularity becomes as far as possible. We call sets of parameters this relation holds eigen values and call solutions with eigen values physically proper solutions. Solutions obtained from parameters deviated from the eigen value have a divergence of B or C. Similar situations are considered in [5] for the cigar ansatz, but we adopted our new solutions found numerically.

In the case of $(\kappa\eta)^2 \leq n - 2$, non-singular solution exists when the brane is not expanding such that $H = 0$. We have solved the Einstein equations and the EOM by an numerical method with the initial condition, $B(0) = C(0) = 1$, $B'(0) = C'(0) = 0$ and $\phi(0) = 0$. The sixth condition can be determined by the constraint (11) automatically. An example of the solution is discussed in [5]

If the case of $(\kappa\eta)^2 \geq n - 2$, arbitrary H including $H = 0$ leads to a divergence of B or C at finite distance from the origin and the singularity is formed. We call this point $r_{\rm sing}$. At the specific H, the distance of singularity becomes as far as possible and has has a local maximum, where the divergence vanishes. We call this point r_t. For example, the solution with the eigen value $(n, \kappa\eta, (\kappa/\lambda^{1/2})H) = (3, 1.09, 0.003786056)$ is shown in Fig. 1. It is noticed that the $B(r)$ vanishes at finite r but $C(r)$ doesn't diverge.

Fig. 2 shows the relations between η and H with n fixed at some values. The larger η corresponds to the larger H. This tendency can be naturally understood like the Friedmann equation. Besides, each lines approach to the point $(\kappa\eta, H) = (\sqrt{n-2}, 0)$. Fig. 3 shows the relations between n and H with

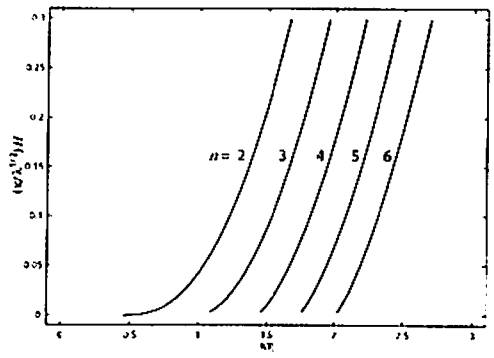


Figure 2: The relations between η and H with n fixed respectively. $H = 0$ seems to be established at $\kappa\eta = \sqrt{n-2}$.

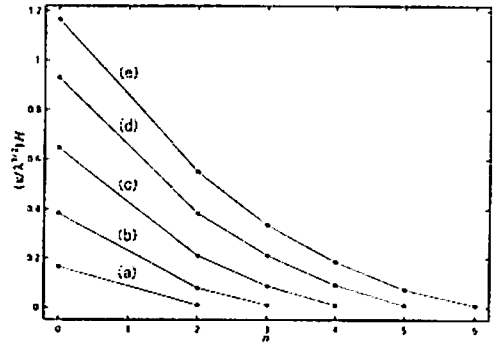


Figure 3: The relations between n and H. (a), (b), (c), (d) and (e) were given by fixing $\kappa\eta = 0.760, 1.15, 1.50, 1.80, 2.01$ respectively. Values the normal Friedmann equation holds are also indicated at $n = 0$. As a number of extra-dimensions increase, the expansion rate is suppressed. The end points of each lines are $(n, H) = (n, 0.01)$.

η fixed at some values. At $n = 0$ in this figure, the values led from the normal Friedmann equation, $H^2 = \kappa^2\rho/3$, $\rho = \lambda\eta^4/4$ are also indicated. This figure shows that the expansion rate determined normally by the Friedmann equation is suppressed as a number of extra-dimensions increases, where H vanished at specific dimension. And these lines connect to the $(\kappa\eta) \leq n - 2$ case. This effect can be considered the diluting cosmological constant.

Finally, it should be mentioned that the Dvali et al.'s conjecture (2) is not reproduced with our solutions as shown in Fig. 2.

References

[1] S. Perlmutter et al., Nature **391**, 51 (1998)

[2] S. Weinberg, Rev. Mod. Phys. **61**, 1 (1989)

[3] P. J. E. Peebles and B. Ratra, Rev. Mod. Phys. **75**, 559 (2003)

[4] G. Dvali, G. Gabadadze and M. Shifman, Phys. Rev. **D67**, 044020 (2003)

[5] I. Cho and A. Vilenkin, Phys. Rev. **D68**, 025013 (2003)

Black Hole Evaporation and Nonequilibrium Thermodynamics for a Radiation Field

Hiromi Saida[1],

Daido Institute of Technology,
Takiharu-cho 10-3, Minami-ku, Nagoya 457-8530, Japan

Abstract

When a black hole is put in an "empty" space ("zero temperature" space) on which there is no matter except the Hawking field emitted from the black hole, then an outgoing energy flow from the black hole into the empty space exists. By the way, an equilibrium between two arbitrary systems can not allow the existence of an energy (heat) flow from one system to another. Consequently, in the case of a black hole evaporation in the "empty" space, the Hawking field should be in a nonequilibrium state. Hence the total behaviour of the evaporation, for example the time evolution of the total entropy, should be analysed with a nonequilibrium thermodynamics for the Hawking field. This manuscript explains briefly the way of constructing a nonequilibrium thermodynamic theory for a radiation field, and apply it to a simplified model of a black hole evaporation to calculate the time evolution of the total entropy.

1 Introduction

The black hole evaporation due to the Hawking radiation is one of the interesting dynamical behaviours of a black hole. However, in comparison with the study on the gravitational collapse (formation of a black hole), fewer details of the black hole evaporation has been revealed so far. This manuscript aims to analyse some detail property of the black hole evaporation in four dimensions. [2] Hereafter we set the fundamental constants be unity, $h = G = c = k_B = 1$.

On the study of the black hole evaporation, the so-called generalised second law (GSL) of the black hole thermodynamics has been one of the interesting issues, and it has become a general agreement today that a black hole is a thermodynamic object whose equations of states are

$$E_g = \frac{1}{8\pi T_g} = \frac{R_g}{2} \quad , \quad S_g = \frac{1}{16\pi T_g^2} = \pi R_g^2 , \tag{1}$$

where the Schwarzschild black hole is considered for simplicity, R_g is the radius, E_g the energy, T_g the temperature and S_g is the entropy of the black hole. The GSL describes, for example, that the total entropy S_{tot} of the total system which consists of the black hole and the matter field of the Hawking radiation is given by a simple sum $S_{tot} = S_g + S_m$, where S_m is the entropy of the matter field, then S_{tot} increases monotonously, $dS_{tot_0} > 0$, during the black hole evaporation process.

When a black hole is put in an "empty" space ("zero temperature" space) on which there is no matter field except that of the Hawking radiation, then an outgoing energy flux J from the black hole into the empty space exists during the evaporation process. Since it seems to be appropriate during the evaporation process to assume that the black hole itself passes a sequence of equilibrium states characterised by the equation (1), then the flux J is given by the Stefan-Boltzmann law,

$$J = \sigma T_g^4 A_g , \tag{2}$$

where $A_g = 4\pi R_g^2$ is the area of the black hole. By the way, an equilibrium between two arbitrary systems can not allow the existence of an energy (heat) flow from one system to another. Consequently,

[1] E-mail:saida@daido-it.ac.jp

[2] The two dimensional dilatonic theory has provided an exact solution for a black hole evaporation. However in this manuscript, we are interested in the four dimensional black hole evaporation in the framework of the Einstein gravity. Hence, for simplicity, we consider the evaporation of the ordinary Schwarzschild black hole.

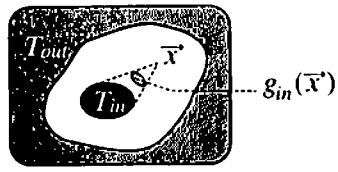


Figure 1: Pick up only the nonequilibrium effects of the Hawking radiation.

in the case of a black hole evaporation in the "empty" space, while the black hole passes a sequence of equilibrium states, the matter field of the Hawking radiation should pass a sequence of nonequilibrium states, where each nonequilibrium state in the sequence of the field's states should have the energy flux J. That is, the total behaviour of the evaporation, for example the time evolution of the total entropy S_{tot}, should be analysed with a nonequilibrium thermodynamics for the matter field of the Hawking radiation. However, because a definition of a nonequilibrium entropy has not generally been constructed in a consistent way, most of the works concerning the GSL treat an equilibrium between a black hole and a "heat bath" surrounding it, or assume the existence of a nonequilibrium entropy of matter fields.

Our main point in this manuscript is to deal with a concrete form of a nonequilibrium entropy carried and produced by the Hawking radiation. For simplicity, we consider the photons as the representative of particles of the Hawking radiation. That is, a massless free field of two helicities are used as the matter field of the Hawking radiation.

Further, in order to pick up the nonequilibrium effects of the matter field (photon field), we consider a simplified toy model: put a spherical black body satisfying the equation (1) in a Minkowski spacetime, then consider the relaxation process of the black body due to the emission of the thermal radiation. This relaxation process picks up the nonequilibrium effects of the Hawking radiation, but neglects the general relativistic effects like the lens effects on photons emitted at the event horizon in off-radial directions.

2 Steady state thermodynamics (SST) for a radiation field

As mentioned above, we want to consider a simplified model that a black body is put in an infinitely large Minkowski space. However, as a middle step before proceeding to the simple model, we consider a more simplified model shown in figure 1: make a vacuum cavity in a large black body of temperature T_{out} and put another (smaller) black body of temperature T_{in} ($\neq T_{out}$). Hereafter we set $T_{in} > T_{out}$ without loss of generality. Then, there should exist an energy flow from the inner black body to the outer black body due to the thermal radiation emitted by them, and the relaxation process leads the whole system to a total equilibrium where the two black bodies and a radiation field between them have the same temperature.

Consider the case satisfying the conditions: (C1) the thermalisation time scale of each black body is so short that each body passes a sequence of equilibrium states, and (C2) the volume of the cavity is so small that the speed of light is approximated as infinity during the relaxation process. Then the radiation field sandwiched by the two black bodies should pass a sequence of nonequilibrium states. Each nonequilibrium state in the sequence has the energy flux $J_{rad} = \sigma (T_{in} - T_{out}) A_{in}$, where A_{in} is the surface area of the inner black body. This denotes that it is enough for us to consider a set (state space) of the steady states of the radiation field whose nonequilibrium nature arises by the steady energy flow J_{rad}. [3] That is, the sequence of the nonequilibrium states of the radiation field during the relaxation process lies in the set (state space) of the steady states. Hence we search for a consistent definition of the steady state entropy of the radiation field. When such an entropy of the radiation field is obtained, the entropy during the relaxation process of the two black bodies and the radiation field can be explicitly expressed. Further, by extending the definition of the steady state entropy into the case of an infinitely large cavity with $T_{out} = 0$, it is expected that the total entropy S_{tot} of the simplified model of the black hole evaporation discussed in previous section can be analysed explicitly.

[3] The terminology "steady state" means the macro-scopically stationary nonequilibrium state.

The author H.S. has already constructed a consistent thermodynamic framework of the steady states for a radiation field [1]. The outline of the construction of the steady state thermodynamics for a radiation field is as follows:

1. Refer the Landau-Lifshitz type definition of a nonequilibrium entropy for a bosonic gas [2]

$$S_{boson} = \int \frac{dp^3}{(2\pi)^3} dx^3 \, g_{\vec{p},\vec{x}} \left[(1 + N_{\vec{p},\vec{x}}) \ln (1 + N_{\vec{p},\vec{x}}) - N_{\vec{p},\vec{x}} \ln N_{\vec{p},\vec{x}} \right] , \tag{3}$$

where $\vec{p}$ is the momentum of a photon, $\vec{x}$ is a spatial point, and $g_{\vec{p},\vec{x}}$ and $N_{\vec{p},\vec{x}}$ are respectively the number of states and the average number of (bosonic) particles at a point $(\vec{p},\vec{x})$ in the phase space of the boson gas. [4]

2. In our system, the radiation field is sandwiched by two perfect black body. Then we can determine $g_{\vec{p},\vec{x}}$ and $N_{\vec{p},\vec{x}}$ as

$$g_{\vec{p},\vec{x}} = 2 \quad , \quad N_{\vec{p},\vec{x}} = \frac{1}{\exp[\omega/T(\vec{p},\vec{x})] - 1}$$

where the frequency of a photon $\omega = p$, and $T(\vec{p},\vec{x})$ is given by

$$T(\vec{p},\vec{x}) = \begin{cases} T_{in} & \text{for } \vec{p} = \vec{p}_{in} \text{ at } \vec{x} \\ T_{out} & \text{for } \vec{p} = \vec{p}_{out} \text{ at } \vec{x} \end{cases} ,$$

where $\vec{p}_{in}$ is the photon emitted by the inner black body and $\vec{p}_{out}$ by the outer black body. The directions from which the photons of $\vec{p}_{in}$ and $\vec{p}_{out}$ can come to a point $\vec{x}$ vary from point to point. Therefor the $\vec{x}$-dependence of $T(\vec{p},\vec{x})$ arises.

3. From above two steps, we obtain the steady state entropy *density* for a radiation field as

$$\begin{aligned} S_{rad} &= \int dx^3 s_{rad}(\vec{x}) \\ s_{rad}(\vec{x}) &= \frac{16\sigma}{3} \left(g_{in}(\vec{x}) T_{in}^3 + g_{out}(\vec{x}) T_{out}^3 \right) , \end{aligned} \tag{4}$$

where $g_{in}(\vec{x})$ is the solid angle (divided by 4π) covered by the direction of $\vec{p}_{in}$ at $\vec{x}$ as shown in figure 1, and $g_{out}(\vec{x})$ is similarly defined with $\vec{p}_{out}$.

4. Further, with defining the steady state internal energy $E_{rad} = 2 \int dp^3 dx^3 \omega \, N_{\vec{p},\vec{x}}$ and the other variables like the free energy with somewhat careful discussions, it has been already checked that the 0th, 1st, 2nd and 3rd laws of the ordinary equilibrium thermodynamics are extended to include the steady states of a radiation field. That is, the steady state thermodynamics (SST) for a radiation field has already been constructed in a consistent way.

3 Time evolution of S_{tot}

We extend the SST entropy (4) to the case that the volume of the cavity is infinity, the outer temperature is zero $T_{out} = 0$ and the equations of states for the inner black body are given by (1). As mentioned in the section 1, this case corresponds to the simplified model of the black hole evaporation in an "empty" space with neglecting the gravitational effect like the lens effects on photons emitted in off-radial directions. Further the inner black body is the representative of the black hole, so we set $T_{in} = T_g$. The time evolution of T_g is given with equations (1) and (2),

$$\frac{dE_g}{dt} = -J \quad \Rightarrow \quad T_g(t) = T_0 \left(1 - 6\sigma T_0^3 t\right) , \tag{5}$$

[4] It has also been shown in reference [2] that the maximisation of S_{boson} for an isolated system gives the equilibrium Bose distribution function. This is frequently refereed in many works on nonequilibrium systems as the "H-theorem". But in reference [2], the concrete forms of $g_{\vec{p},\vec{x}}$ and $N_{\vec{p},\vec{x}}$ are not specified, since an arbitrary system is considered.

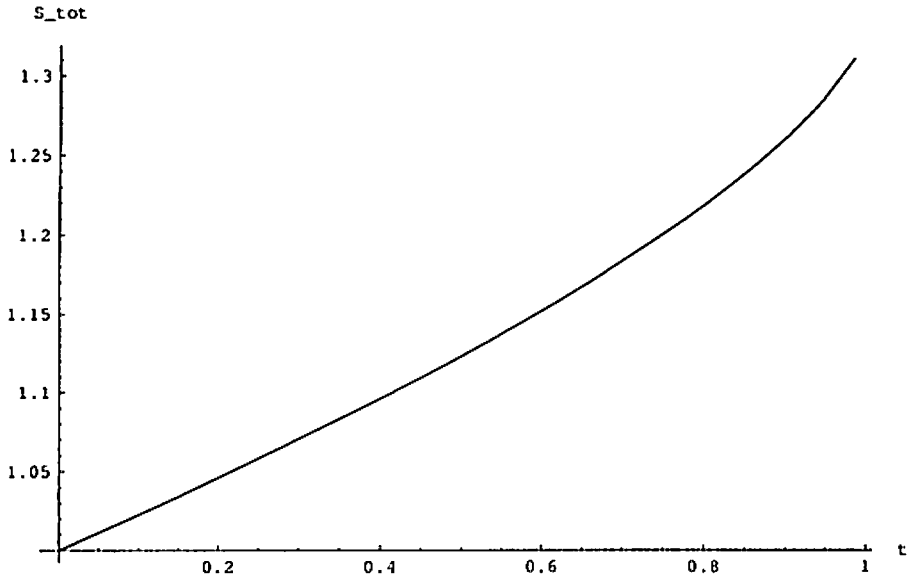


Figure 2: Time evolution of $S_{tot}(t)$.

where $T_0 = T_g(0)$ is the initial condition.

The other points we should consider are the effects of the retarded time of photons travelling in a infinitely large space, and the Doppler effects due to the "shrinkage" speed of the surface of the inner black body (the surface of the black hole). With taking the retarded time and the Doppler effects, the total entropy is obtained to be

$$S_{tot}(t) = S_g(t) + 4\pi \int_0^{r(t)} dr\, s_{rad}(r.t)\,, \tag{6}$$

where r is the areal radius, $r(t)$ is the radius of the "wave front" of emitted photons [5] and the time dependence of $S_g(t)$ and $s_{rad}(r,t)$ arise from (5).

4 Conclusion and next step

Figure 2 are the plot of S_{tot} given by (6) with setting $6\sigma T_0^3 = 1$. As far as the author knows, this is the first example to show a time evolution of the total entropy S_{tot}. And as is expected, this result support that the GSL holds. For the next step along the strategy discussed in this manuscript, it is necessary to extend our result to include the gravitational effects like the lens effects. Further, since we has just assumed that the Stefan-Boltzmann law (2) holds instead of solving the Einstein equation for the evaporating black hole, it is also searched how the background spacetime of the black hole evaporation should be described.

References

[1] H.S, to appear in *cond-mat*.

[2] §55 in, L. D. Landau, E. M. Lifshitz, *Statistical Physics. Prat I*, Pergamon, 1980

[5] Here we assume that the evaporation starts at $t = 0$. Then the photons emitted at $t = 0$ forms the boundary of the region where the radiation field exists. We call this boundary the "wave front".

Collective Quantization of a Gravitating Skyrmion

Noriko Shiiki[1], Nobuyuki Sawado[2] Shinsho Oryu[3]

Department of Physics, Tokyo University of Science, Noda, Chiba 278-8510, Japan

Abstract

Collective quantization of a $B = 1$ gravitating skyrmion is described. The rotational and isorotational modes are quantized in the same manner as the skyrmion without gravity. It is shown in this paper how the static properties of nucleons such as masses, charge densities are modified by the gravitational interaction.

1 Introduction

The Einstein-Skyrme system has been known to possess regular and black hole solutions. The first obtained solutions in this system are spherically symmetric black holes with Skyrme hair [1, 2, 3]. It was the first counter example of the no-hair conjecture for black holes discovered. Later, regular solutions for $B = 1$ [2, 3, 4] and axially symmetric black hole and regular solutions for $B = 2$ [5] were found. The extended models to $SU(3)$ and $SU(N)$ were also studied in Refs. [6].

It is, however, necessary to quantize those skyrmions to interpret as gravitating or black hole nucleons. Therefore, in this paper we shall perform collective quantization of the $B = 1$ gravitating skyrmion and compute its static properties following the work of Ref. [7]. The effects of gravity on the nucleon observables are examined. Since the skyrmion picture of a nucleon is correct within about 30% error, it is difficult to estimate the effects quantitatively. However, we believe that the results we have obtained can help us to understand qualitatively the effects of gravity on the nucleon properties.

2 Collective Quantization of a Gravitating Skyrmions

The classical regular solutions of the Einstein-Skyrme system with $B = 1$ have been already studied in Refs. [2, 3, 4]. We therefore give a short review of the model and solutions in this section.

The Skyrme model coupled with gravity can be defined by the Lagrangian

$$\mathcal{L} = \mathcal{L}_G + \mathcal{L}_S \tag{1}$$

where

$$\mathcal{L}_G = \frac{1}{16\pi G}R \tag{2}$$

$$\mathcal{L}_S = -\frac{F_\pi^2}{16}g^{\mu\nu}\mathrm{tr}(\partial_\mu U\partial_\nu U^{-1}) + \frac{1}{32e^2}g^{\mu\nu}g^{\rho\sigma}\mathrm{tr}[(\partial_\mu U)U^{-1}, (\partial_\rho U)U^{-1}][(\partial_\nu U)U^{-1}, (\partial_\sigma U)U^{-1}] \tag{3}$$

where U is an $SU(2)$-valued chiral field, F_π is the pion decay constant and e is a dimensionless free parameter. The $B = 1$ skyrmion can be obtained by imposing the hedgehog ansatz on the chiral field

$$U = \cos F(r) + i\vec{n}\cdot\vec{\tau}\sin F(r)\,. \tag{4}$$

Correspondingly we consider the static spherically symmetric metric given by

$$ds^2 = -N^2(r)C(r)dt^2 + \frac{1}{C(r)}dr^2 + r^2d\Omega^2 \tag{5}$$

[1]E-mail:norikoshiiki@mail.goo.ne.jp
[2]E-mail:sawado@ph.noda.tus.ac.jp
[3]E-mail:oryu@ph.noda.tus.ac.jp

where we have defined

$$C(r) = 1 - \frac{2m(r)}{r}.$$

Let us introduce dimensionless variables

$$x = eF_\pi r\,, \quad \mu(x) = eF_\pi m(r)\,.$$

In terms of x and μ, the static energy thus can be written by

$$E_S = 4\pi\frac{F_\pi}{e}\int\left\{\frac{1}{8}\left(CF'^2 + \frac{2\sin^2 F}{x^2}\right) + \frac{\sin^2 F}{2x^2}\left(2CF'^2 + \frac{\sin^2 F}{x^2}\right)\right\}Nx^2dx\,. \tag{6}$$

The solutions for the Einstein-Skyrme system depend on one free parameter which is the coupling constant $\alpha = 4\pi GF_\pi^2$.

To describe physical nucleon and Δ states, we need to perform quantization for the classical skyrmion. From the symmetry of the Lagrangian, one can see that if U is the soliton solution, then $U \to AUA^{-1}$ where A is an arbitrary constant $SU(2)$ matrix, is also a solution with the same finite energy. Therefore A is the collective coordinate to be quantized. Letting the matrix A time dependent $A(t)$, we replace the field U in the Lagrangian (3) as

$$U(\vec{r}, t) = A(t)U_0A(t)^{-1} \tag{7}$$

where U_0 is the hedgehog solution constructed in the previous section. For the hedgehog solution, the spin and isospin rotation are equivalent. Definite spin and isospin states are obtained by quantizing those degrees of freedom. Parameterising $A = a_0 + i\vec{\tau}\cdot\vec{a}$ with $a_0^2 + \vec{a}^2 = 1$, canonical quantization can be performed in standard manners in terms of a's. The Hamiltonian is then diagonalized as

$$H = E_S + \frac{1}{8\lambda}\sum_{i=0}^{3}\left(-\frac{\partial^2}{\partial a_i^2}\right) = E_S + \frac{I(I+2)}{8\lambda} \tag{8}$$

where

$$\lambda = \frac{2\pi}{3F_\pi e^3}\Lambda\,, \quad \Lambda = \int_0^\infty \frac{1}{NC}\left[1 + 4\left(CF'^2 + \frac{\sin^2 F}{x^2}\right)\right]x^2\sin^2 F\,dx \tag{9}$$

and $I = 2I = 2J$ with (I, J) respectively isospin and spin quantum number. The nucleon, delta mass and their mass difference are thus given by

$$M_N = E_S + \frac{1}{2\lambda}\frac{3}{4}\,, \quad M_\Delta = E_S + \frac{1}{2\lambda}\frac{15}{4}\,, \quad M_\Delta - M_N = \frac{3}{2\lambda}\,. \tag{10}$$

Hereafter we adopt the same parameter set as in Ref. [7] $F_\pi = 129$MeV and $e = 5.45$ so that for $\alpha = 0.0$, the experimental values of a nucleon and delta mass are reproduced with about 30% error. Fig. 1 shows the α dependence of the mass difference between N and Δ in units of MeV. It is seen that the mass difference increases monotonically with increasing α.

The isoscalar mean square radius of the nucleon is given by

$$\langle r^2\rangle = -\frac{1}{(eF_\pi)^2}\frac{2}{\pi}\int_0^\infty x^2F'\sin^2 F\,dx\,. \tag{11}$$

Fig. 2 shows the α dependence of the root mean square radius. It decreases with increasing α, which confirms the attractive effect of the gravity. The isoscalar and isovector charge densities per unit r are given by

$$\rho_{I=0} = \int\sqrt{-g}\,B^0 d\theta d\varphi = -eF_\pi\frac{2}{\pi}\sin^2 FF' \tag{12}$$

$$\rho_{I=1} = eF_\pi Nx^2\sin^2 F\left[1 + 4\left(CF'^2 + \frac{\sin^2 F}{r^2}\right)\right]/\Sigma\,. \tag{13}$$

where

$$\Sigma = \int N x^2 \sin^2 F \left[1 + 4 \left(C F'^2 + \frac{\sin^2 F}{x^2} \right) \right] dx . \tag{14}$$

The charge density for the proton and neutron are defined by

$$\rho_p = \frac{1}{2}(\rho_{I=0} + \rho_{I=1}) , \quad \rho_n = \frac{1}{2}(\rho_{I=0} - \rho_{I=1}) \tag{15}$$

and are shown in Fig. 3 for $\alpha = 0.0, 0.1$. For the strong gravity, the peaks of the charge densities become higher and move towards the center.

3 Conclusions

We have performed collective quantization of a $B = 1$ skyrmion in the Einstein-Skyrme system and investigated the static nucleon properties. Although the spacetime is curved, the collective space remains $SU(2)$. Therefore the quantization is rather straightforward. Modification by the gravitational interaction appears in the observables such as N-Δ mass difference, mean radius, charge densities. The results confirm the attractive feature of the gravity.

Although the Skyrme model describes a nucleon with about 30% error, the possibility that it may provide qualitatively correct description of the interaction of a nucleon with gravity can not be excluded. It is expected that in the early universe or equivalent high energy experiments, the gravitational interaction with nucleons is not negligible. We hope that our work could provide insight into the observations in such situations. It will be also interesting to quantize gravitating skyrmions with higher baryon numbers or black hole skyrmions in future.

References

[1] H. Luckock and I. G. Moss, Phys. Lett. B176 (1986) 341.

[2] H. Luckock, "String Theory, Quantum Cosmology and Quantum Gravity, Integrable and Conformal Invariant Theories", Edited by de Vega and N. Sanchez (World Scientific, Singapore, 1987).

[3] S. Droz, M. Heusler and N. Straumann, Phys. Lett. B268 (1991) 371.

[4] P. Bizon and T. Chmaj, Phys. Lett. B297 (1992) 55.

[5] N. Sawado and N. Shiiki, gr-qc/0307115; Gen. Rel. Grav. 36 (2004) 1361.

[6] B. Kleihaus, J. Kunz and A. Sood, Phys. Lett. B352 (1995) 247; Y. Brihaye, B. Hartmann, T. Ioannidou and W. Zakrzewski, Phys. Rev. D69 (2004) 124035; T. Ioannidou, B. Kleihaus and W. Zakrzewski, gr-qc/0407035.

[7] G. S. Adkins, C. R. Nappi and E. Witten, Nucl. Phys. B228 (1983) 552.

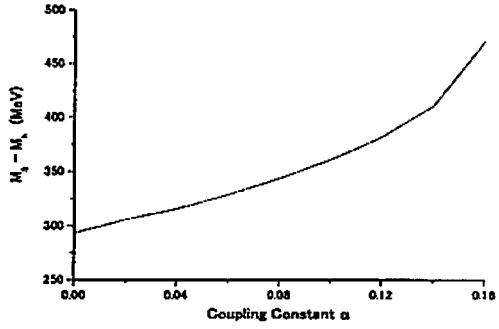


Figure 1: Coupling constant dependence of the $N - \Delta$ mass difference in units of MeV.

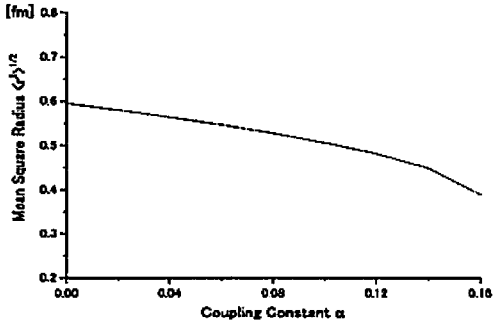


Figure 2: Coupling constant dependence of the mean square radius in units of fm.

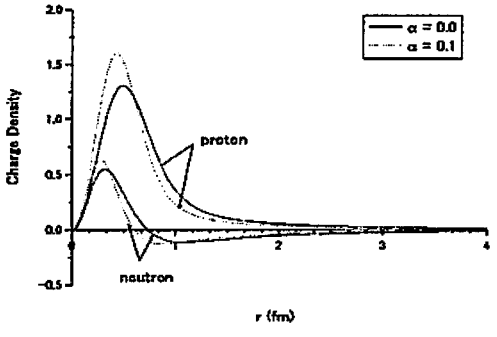


Figure 3: Radial dependence of proton and neutron charge densities as functions of the radial distance r (fm).

Quasinormal Ringing for Acoustic Black Holes in Low Temperature

Hiroyuki Nakano[1], Yasunari Kurita[2], Kouji Ogawa[3], Chul-Moon Yoo[4]

Department of Mathematics and Physics, Graduate School of Science, Osaka City University, Osaka 558-8585, Japan

Abstract

We investigate a condensed matter "black hole" analogue. In this paper, we suggest that we can know the detailed characters and corresponding geometrical information about the acoustic black hole by observing quasinormal ringdown waves.

1 Introduction

Black holes are one of the most fascinating objects for General Relativity. Strikingly, they have thermodynamic properties based on the Beckenstein-Hawking entropy formula and the Hawking's renowned effect [1]. Unfortunately, however, it seems to be impossible to detect the Hawking radiation from realistic astrophysical black holes because the Hawking temperature of astrophysical black holes is so low that its intensity is too weak to be detected. For the purpose of confirming the Hawking radiation, it will be greatly helpful to perform laboratory experiments using some kinds of analogy.

There are a lot of works about an acoustic "black hole" which has a sound horizon corresponding to an event horizon of a black hole spacetime. Unruh [2] has originally suggested a hydrodynamic analogue of an event horizon. There is a close analogy between sound propagation on a background hydrodynamic flow and field propagation in a curved spacetime. So, an analogous black hole will be experimentally powerful tool for confirming the Hawking radiation. There are some works in this direction [3].

Thanks to recent technological advances, the Bose-Einstein condensation (BEC) has been observed in 1995 in a remarkable series of experiments on vapors of rubidium [4] and sodium [5]. Garay *et al.* [6] have proposed a realistic scheme for adiabatically creating stable acoustic black/white holes. It seems to be possible to materialize an acoustic black hole in BEC system.

Astrophysical black holes will obey the uniqueness theorem for black hole spacetimes, and there will be no hair other than mass, angular momentum and electric charge. On the other hand, it will be possible to realize analogous black holes having many hairs. It means that many kinds of geometry will be realized in the analogous systems. Thus, it is necessary to identify which corresponding classical geometry is realized in the experiments. For the purpose, quasinormal modes (QNMs) of the spacetime will give the answer.

The first order perturbed Einstein equation gives a wave equation, and QNMs are complex frequency solutions of this wave equation with purely outgoing-wave boundary condition at infinity and ingoing-wave at the horizon. They have geometrical information outside the horizon and, in fact, the quasinormal ringdown waves have astrophysical significance and are searched by using the data from the gravitational wave detectors [7].

By the way, the Hawking radiation from a black hole is corrected by a gray body factor or curvature scattering of the black hole spacetime and its spectrum differs from that of a complete black body. The Hawking effects from acoustic ones would also be different from a complete black body spectrum. So, it is important to study the classical geometry and their QNMs for analogous black hole systems. Here, we consider an analogous black hole in a Bose-Einstein condensate and predict the quasinormal ringdown waves in the system for the purpose of investigating their corresponding classical geometry.

[1]E-mail:denden@sci.osaka-cu.ac.jp
[2]E-mail:kurita@sci.osaka-cu.ac.jp
[3]E-mail:kouji@sci.osaka-cu.ac.jp
[4]E-mail:c_m_yoo@sci.osaka-cu.ac.jp

2 Gross-Pitaevskii Equation and Acoustic Black Hole

In order to treat a Bose-Einstein condensate. we consider the order parameter Ψ, which is a complex function defined as the expectation value of the field operator, and written as the following form,

$$\Psi = \sqrt{n_0}\, e^{i\varphi}\,, \tag{1}$$

where n_0 and φ denote a condensate density and a phase factor of the condensed matter, respectively. The Gross-Pitaevskii (GP) equation is the equation of motion of a condensed matter;

$$i\hbar\frac{\partial\Psi}{\partial t} = -(\frac{\hbar^2}{2m}\nabla^2 + V_{\rm ext})\Psi + \frac{4\pi a\hbar^2}{m}|\Psi|^2\Psi\,. \tag{2}$$

In the above equation, m is the mass of the atoms, a is the scattering length and the atoms are trapped by an external potential $V_{\rm ext}(\mathrm{x})$. Substituting Eq. (1) into the above equation, we obtain

$$\frac{\partial n_0}{\partial t} = -\nabla(n_0\nabla\Phi)\,, \tag{3}$$

$$\frac{\partial\Phi}{\partial t} = -\frac{1}{2}(\nabla\Phi)^2 + \frac{\hbar^2}{4m^2}(\frac{\nabla^2 n_0}{n_0} - \frac{(\nabla n_0)^2}{2n_0^2}) - \frac{V_{\rm ext}}{m} - \frac{4\pi a\hbar^2}{m^2}n_0\,, \tag{4}$$

where $\Phi = \frac{\hbar}{m}\varphi$, and we introduce the velocity of a condensed matter v_0 as $\mathrm{v}_0 = \nabla\Phi$.

Next, we derive the equation for the linear perturbation of the GP equation (3) and (4).

$$\tilde{n}_0 = n_0(1+\zeta)\,, \quad \tilde{\Phi} = \Phi + \eta\,. \tag{5}$$

Here we consider n_0 and Φ as a background, and ζ and η represent small perturbations. We assume that the background is independent of time. Then, the linear perturbation equations are given by

$$\frac{\partial\zeta}{\partial t} + \mathrm{v}_0\cdot\nabla\zeta + \nabla^2\eta + \nabla\ln n_0\cdot\nabla\eta = 0\,, \tag{6}$$

$$\frac{\partial\eta}{\partial t} + \mathrm{v}_0\cdot\nabla\eta - \frac{\hbar^2}{4m^2}\frac{1}{n_0}\nabla(n_0\nabla\zeta) + \frac{4\pi a\hbar^2}{m^2}n_0\zeta = 0\,. \tag{7}$$

Now we assume that the variation of the density n_0 can be neglected for the healing length, the third term in the L.H.S. of Eq. (7) is neglected. We use this approximation in the following. Then, eliminating the density perturbation ζ, we obtain a second order differential equation for the phase perturbation;

$$\frac{1}{n_0}(\frac{\partial}{\partial t} + (\nabla\cdot\mathrm{v}_0))\frac{n_0}{c_s^2}(\frac{\partial}{\partial t} + \mathrm{v}_0\cdot\nabla)\eta - \frac{1}{n_0}\nabla(n_0\nabla\eta) = 0\,, \tag{8}$$

where c_s is the sound velocity defined by $c_s = \frac{\hbar}{m}\sqrt{4\pi a\, n_0}$.

The above wave equation corresponds to the wave propagation on the curved spacetime background;

$$\begin{aligned} ds^2 &= \frac{an_0}{c_s}\left(-(c_s^2 - v_0^2)dt^2 - 2v_0 dt dx + dx^2 + dy^2 + dz^2\right) \\ &= \frac{an_0}{c_s}\left(-\left(1-\frac{v_0^2}{c_s^2}\right)c_s^2 d\tau^2 + \left(1-\frac{v_0^2}{c_s^2}\right)^{-1}dx^2 + dy^2 + dz^2\right), \end{aligned} \tag{9}$$

where $d\tau = (dt + \frac{v_0}{c_s^2 - v_0^2}dx)$. For simplicity, we have considered the case that the background velocity has only x-component, i.e., $\{v_0^{\rm i}\} = \{v_0,\, 0,\, 0\}$ where the superscript i denotes $\{x,\, y,\, z\}$. When the superfluid velocity changes from subsonic to supersonic velocity, there is a sound horizon.

3 Quasinormal modes

In this section, we consider the background configuration of a condensed matter which has a sound horizon and then, derive the quasinormal frequencies. In order to obtain an acoustic black hole, we assume the one-dimensional background flow with the velocity in the x-direction.

Using Eq. (8), the linear perturbation equation of the system is written as

$$\left[-\partial_t^2 - \frac{2V}{n_0}\partial_t\partial_x - V\left(\partial_x\frac{1}{n_0}\right)\partial_t + C^2\partial_x\left(n_0\left(1-\frac{V^2}{C^2}\frac{1}{n_0^3}\right)\partial_x\right)\right]\eta = 0. \tag{10}$$

Here, we have rewritten the sound velocity as $c_s^2 = C^2 n_0$ and the background velocity becomes $v_0 = \frac{V}{n_0}$ because of the continuity equation (3) and the assumption that the section area of a nozzle is constant.

We assume that the background is static, so it is convenient to consider the Fourier transformation of the phase (velocity) perturbation. After simplifying the perturbation equation (for details, see [8]), we obtain the Schrödinger-type equation for the function H_ω as

$$\begin{aligned}\left[\partial_{x_*}^2 + (\sigma^2 - \mathcal{V}(x_*))\right]H_\omega &= 0, \\ \mathcal{V}(x_*) &= \frac{1}{4}\frac{\left(n_0^3-\beta^2\right)^2\left(\partial_x^2 n_0\right)}{n_0^6} - \frac{1}{16}\frac{\left(n_0^3-\beta^2\right)\left(n_0^3-13\beta^2\right)\left(\partial_x n_0\right)^2}{n_0^7},\end{aligned} \tag{11}$$

where we have defined $\beta = V/C$, $\sigma = \omega/C$, and the new coordinate $\frac{dx_*}{dx} = \frac{n_0^{5/2}}{n_0^3-\beta^2}$.

In order to calculate the quasinormal frequencies, it is necessary to choose the appropriate potential $\mathcal{V}$. For example, we consider the case that the background density n_0 has the following form:

$$n_0 = Nx^a, \tag{12}$$

where a is a constant. We find that the range of parameter a should be $0 < a < 2$ for $\mathcal{V}$ to vanish at infinity and the horizon. This condition for a also ensures the short-range character of the potential, i.e., $\int_{-\infty}^{\infty}\mathcal{V}(x_*)dx_* < \infty$ [9]. Thus, we consider the case of the parameter range $0 < a < 2$. In the following discussion, we choose $\beta = 1$ and $N = 1$.

In order to obtain the quasinormal frequencies of the background with the above potential, we use the WKB approach [10]. The quasinormal frequencies are obtained as

$$\sigma^2 = \mathcal{V}_0 - i\left(n+\frac{1}{2}\right)(-2\mathcal{V}_0'')^{1/2}. \tag{13}$$

Here n is non-negative integer for $\Re(\sigma) > 0$, n is negative integer for $\Re(\sigma) < 0$, and the prime ($'$) denotes the differentiation with respect to x_*. Here n indices the n-th quasinormal mode, and the subscript 0 on the potential denotes the value at the location where $\mathcal{V}_0' = 0$.

Now, we have a interest in the power a dependence of the quasinormal frequencies. The quasinormal frequencies in the cases of $a = 1/3$, $2/3$, 1, $4/3$ and $5/3$ are summarized in Fig. 1. The figure shows the least damped mode in each value of a differs each other, and thus, we can distinguish the power a by the quasinormal frequencies and check the realization of the corresponding geometry in the analogous black hole system, i.e., whether the wave equation on a curved spacetime is realized or not.

4 Discussion

In this paper, we have discussed the QNMs of an acoustic "black hole" in the context of the Bose-Einstein condensate. This acoustic black hole is prepared by choosing the external potential. Using the WKB method, we have derived some quasinormal frequencies in the case that the background density has a power form.

From the quasinormal frequencies shown in Fig. 1, we can identify the density of the BEC which determine the potential function (11). Thus, they are useful to check whether the system is realized to our expectations in an actual experiment and to know the potential function (11) and the corresponding geometrical information. Not only the least damped mode but the higher damped modes are useful to identify the corresponding classical geometry.

We note that "Schwarzschild like black holes" can not be obtained in the fluid configuration discussed in this paper. This is because the sound velocity c_s and the background velocity v_0 are related to the density n_0. In order to obtain a Schwarzschild black hole in the BEC, we have to consider other fluid configurations [11].

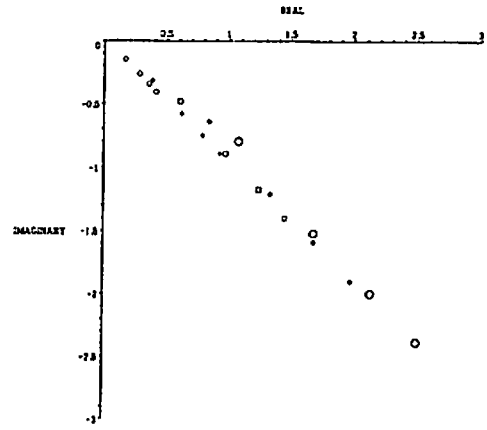


Figure 1: The quasinormal frequencies. The symbols ○, +, □, ◇, ◯ show the case of $a = \frac{1}{3}, \frac{2}{3}, 1, \frac{4}{3}, \frac{5}{3}$.

In our study, we have considered the low frequency approximation for the linearized Gross-Pitaevskii equation. This is relevant in the region where the wave length of sounds is much longer than the healing length of the system. The quasinormal ringdown waves obtained in this paper satisfy the condition and therefore, our investigation is appropriate. We leave these issues for future investigations.

Acknowledgements

We would like to thank H. Ishihara, K. Nakao and H. Kozaki for useful discussions. HN is supported by the JSPS Research Fellowships for Young Scientists, No. 5919.

References

[1] S. W. Hawking, Nature **248**, 30 (1974); Commun. Math. Phys. **43**, 199 (1975).

[2] W. G. Unruh, Phys. Rev. Lett. **46**, 1351 (1981).

[3] M. a. Sakagami and A. Ohashi, Prog. Theor. Phys. **107**, 1267 (2002).
C. Barcelo, S. Liberati and M. Visser, Int. J. Mod. Phys. A **18**, 3735 (2003).

[4] M. H. Anderson *et al.*, Science **269**, 198 (1995).

[5] K. B. Davis *et al.*, Phys. Rev. Lett. **75**, 3969 (1995).

[6] L. J. Garay, J. R. Anglin, J. I. Cirac and P. Zoller, Phys. Rev. Lett. **85**, 4643 (2000).
L. J. Garay, J. R. Anglin, J. I. Cirac and P. Zoller, Phys. Rev. A **63**, 023611 (2001).

[7] Y. Tsunesada *et al.*, arXiv:gr-qc/0410037.

[8] H. Nakano, Y. Kurita, K. Ogawa and C. M. Yoo, arXiv:gr-qc/0411041.

[9] S. Chandrasekhar and S. Detweiler, Proc. Roy. Soc. Lond. A **344**, 441 (1975).

[10] B. F. Schutz and C. M. Will, Astrophys. J. **291**, L33 (1985).

[11] OCU Gravity, in preparation.

Wavelet-based method to estimate waveforms of gravitational wave bursts

Kazuhiro Hayama[1]

[1] *National Astronomical Observatory of Japan, Mitaka 181-8588, Japan*

Abstract

This paper proposes a wavelet-based method to estimate waveforms of type II supernovae signals, which are burst-like signals that are poorly-predicted. The proposed method can approximate burst signals non-parametrically, and the estimator is nearly optimal, even if we do not use the prior information about the waveforms. It is therefore believed that this method is suitable for estimating waveforms of such burst signals after detection has occured. In order to study the performance of this method, we demonstrate detection of a supernovae signal subject to Gaussian white noise using the catalog of waveforms provided recently by Dimmelmeier et al. We compare its performance with that of the Wiener estimator. We obtain the result: Our method is superior to that of the Wiener filter on the Fourier space.

1 Introduction

Gravitational wave signals from supernovae are burst-like signals with short duration, from a few milliseconds to a few hundred milliseconds, and their waveforms have not predicted accurately, because the behavior of supernovae is too complex to be described in detail. Recently, many signal models have been computed by various groups [1], and the situation regarding them seems to have become clear: New simulations confirm the results of previous ones, and even if the computed amplitudes are spread over a large range [2]. The number of existing templates of supernovae signals is not yet sufficient, and unknown burst wave signals may exist. Therefore, to search for supernovae signals in data, methods that are robust with respect to waveform variations have been developed. For example, excess power detectors based on a quadratic form of the data [3], [4], [5]. Of course it is important to develop such methods based on a quadratic form, it is also important to develop a method to estimate waveforms of burst signals because such waveforms possess detailed information regarding the nature of spacetime. In the future, when gravitational wave astronomy is began, a method to estimate waveforms of gravitational wave signals without prior information about the waveforms will become very important, because such analysis can lead to the discovery of unknown astronomical phenomena. With this motivation, we have developed waveform estimation methods [6], [7], [8]. Here, we consider a method to estimate the waveforms of gravitational wave burst, especially from supernovae. It is not clear what kind of data analysis method is suitable for estimating waveforms of gravitational wave signals. We point out that waveforms of supernovae signals cannot be expressed in terms of parameters, and the simulated waveforms have uncertainty. Thus a data analysis method that has the following features is suitable to estimate waveforms of such signals : 1. the method estimates the signals non-parametrically; 2. the estimator is nearly optimal, even if we do not use prior information about the waveforms.

In this paper, we propose such a data analysis method to estimate waveforms of burst-like gravitational waves. In section 2, we introduce the wavelet shrinkage method. In section 3, we demonstrate our method. Finally, we give conclusions and discussion in section 4.

2 Method based on wavelet shrinkage method

We now introduce the wavelet shrinkage method [9]. We consider to estimate $f(t)$ from

$$X(t) = f(t) + W(t), \tag{1}$$

[1] E-mail:kazuhiro.hayama@nao.ac.jp

where $f(t)$ is a burst gravitational wave signal, and $W(t)$ is Gaussian white noise with variance σ^2. The dyadic wavelet translation of $X(t)$ is written as

$$X(t) = \sum_{j,k} \langle \psi_{j,k}, X \rangle \psi_{j,k}(t) \quad j,k \in Z, \tag{2}$$

where $\psi_{j,k}(t) = 2^{j/2}\psi(2^j t - k)$, with $\psi(t)$ representing a mother wavelet, and $\langle \psi_{j,k}, X \rangle = \int_{-\infty}^{\infty} X(t')\overline{\psi_{j,k}(t')}\mathrm{d}t'$. The wavelet shrinkage method is a non-parametric estimation method, and its procedure is as follows:

1. Apply the wavelet transform, obtaining the wavelet coefficients $\langle \psi_{j,k}, X \rangle$.
2. Set the threshold function as

$$\rho_T(\langle \psi_{j,k}, X \rangle) = \begin{cases} \mathrm{sgn}(\langle \psi_{j,k}, X \rangle)(|\langle \psi_{j,k}, X \rangle| - T) & \text{if } |\langle \psi_{j,k}, X \rangle| > T, \\ 0 & \text{if } |\langle \psi_{j,k}, X \rangle| \leq T. \end{cases}$$

3. Invert the wavelet transform, obtaining the estimated signal.

A thresholding estimator $\tilde{f}(t)$ is written

$$\tilde{f}(t) = \sum_{j,k} \rho_T(\langle \psi_{j,k}, X \rangle)\psi_{j,k}(t). \tag{3}$$

The threshold T is generally chosen so that there is a high probability that it is just above the maximum level of the noise coefficients. Usually $T = \sigma\sqrt{2\log_e N}$ is choosed when noise is Gaussian white noise [10]. The term $\sigma\sqrt{2\log_e N}$ comes from the fact [11] that maximum amplitude of the noise has a very high probability of being just below $T = \sigma\sqrt{2\log_e N}$.

2.1 Definition of reconstruction index

We evaluate $f(t)$. We use data that contain both a supernova signal and simulated Gaussian white noise. Here we define an evaluation parameter, reconstruction index. The reconstruction index is defined as

$$R = \frac{\sum |f_s|^2}{\sum |f_s - \tilde{f}|^2}, \tag{4}$$

where f_s is the waveform of gravitational wave signals, and $\tilde{f}$ is the estimator. By adjusting amplitude of the noise, we calculate reconstraction index as a function of the waveform amplitude and compare this estimation with the Wiener estimation.

We next compare our method with that of the Wiener estimator, $\tilde{f}_{\mathrm{wien}}(t)$. The practical Wiener filter on the Fourier space, $\hat{h}(\omega)$, can be expressed as

$$\hat{h}(\omega) = \frac{\mathsf{E}[|\hat{F}_s(\omega)|^2]}{\mathsf{E}[|\hat{F}_s(\omega)|^2] + \sigma^2}, \tag{5}$$

where $\mathsf{E}[\cdot]$ is expectation value. The Wiener estimator $\tilde{f}_{\mathrm{wien}}(t)$ can be written by:

$$\tilde{f}_{\mathrm{wien}}(t) = \mathcal{F}^{-1}[\hat{h}(\omega)\hat{X}(\omega)](t), \tag{6}$$

where $\mathcal{F}^{-1}$ is the inverse Fourier transformation.

3 Demonstration

In order to show how this method works, we carried out a simulation using the burst catalog [1]. As the mother wavelet, we use Coiflet [12]. This wavelet has a minimum size support, and therefore it is effective in treating with burst-like signals.

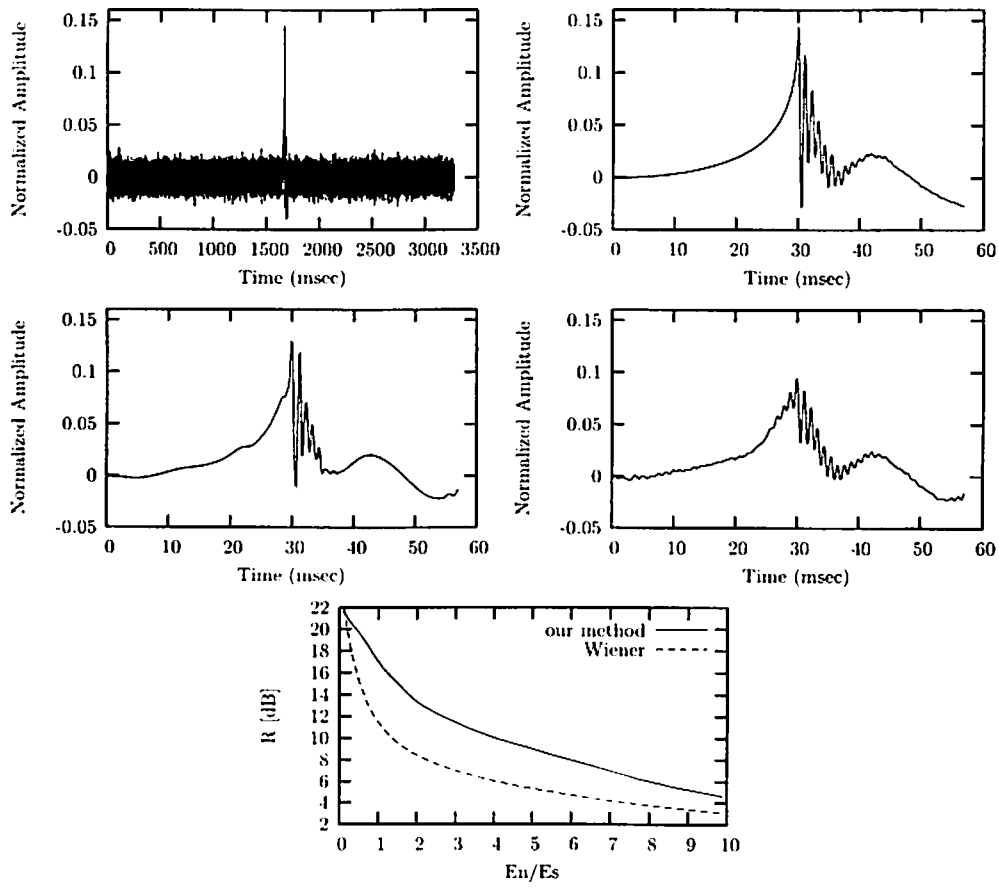


Figure 1: Demonstration to detect the supernova signal "signal_A1B3G5_R" subject to Gaussian white noise. The upper left plot displays the sample data, and the upper right plot displays a template of the supernova signal. The middle left plot displays our estimation, and the middle right plot displays the Wiener estimation. The bottom plot displays R[dB] as a function of the energy ratio of the Gaussian noise and the template, $(E_n/E_s)^{1/2}$.

The sample data contain Gaussian white noise $n(k)$, $k = 1, \ldots, 2^{16}$, and a simulated gravitational wave signal $f(k)$ provided by Dimmelmeier et al. The sampling rate is 20kHz. The energy of $n(k)$ and $f(k)$ are defined by $E_n := (\sum_{k=1}^{2^{16}} W(k))^2$, $E_s := (\sum_{k=1}^{2^{16}} f(k))^2$. The energy ratio of $W(k)$ and $f(k)$, which is defined as E_n/E_s, is set as $E_n/E_s = 1.7$. We demonstrate our method by it to a supernova signal model in relativistic gravity, signal_A1B3G5_R in the catalog.

Figure 1 displays the result. The upper left plots represent the sample data, and the upper right plots represent a template of the supernova signal. The middle left figure represents our estimator, and the middle right plots represent the Wiener estimator. These middle plots reveal that our method can detect the supernova signal with higher R than in the case of the Winer filter. Because our method expresses the supernova signal using only a few wavelet basis functions which are localized in the time domain, the noise in the plane region of the signals does not remain. By contrast, in the case of the Wiener filter, noise remains over the entire region in data. The bottom plot represents R[dB] as a function of the energy ratio of the Gaussian noise and the template, $(E_n/E_s)^{1/2}$. For $(E_n/E_s)^{1/2} \ll 1$, because the noise is negligible and the data condition is approximated to the ideal condition for the Winer estimator, our method is approximately equally effective to or inferior to the Wiener estimation. As $(E_n/E_s)^{1/2}$

becomes large, both reconstruction index decrease and converge to 0. The rate of this convergence in our method is smaller than that in the Wiener filter.

4 Summary and discussion

We proposed a waveform estimation method for gravitational wave burst signals subject to Gaussian white noise. In the wavelet space, supernovae signals can be expressed in terms of only a few large coefficients. By properly estimating the noise level and subtracting the contribution from the coefficients, we estimated the waveform of the supernovae signal. The performance of our method was studied. As the figure 1 show, our method is capable of capturing the features of locality which the supernovae signals possess. By contrast, in the signal obtained using the Wiener filter, there remains an oscillation pattern of noise as the Balian-Low Theorem asserts that it is impossible to realize a basis that has both smoothness and locality in Fourier space. The result of the demonstration also shows that our method is superior to that of the Wiener filter for estimating the sample of the supernovae signal.

We considered Gaussian white signals as noise in this paper. In reality, the noise level originating from an interferometric detector depends on the frequency. This implies that in thresholding the wavelet coefficients to subtract the components of noise, we have to determine the value of the threshold in each wavelet level j. It is known that if noise is stationary Gaussian noise, wavelet coefficients $\alpha_{j,k}$, $k \in \mathbf{Z}$ in each wavelet level j are stationary Gaussian signals, and therefore we can determine the threshold in each wavelet level j properly. For the demonstration, we use the waveform of the type III model which indicates the rapid core collapse [1]. Our method is also effective for the waveform estimation of supernovae signals of the other two types [7].

Because it allows for realization of a nearly optimal estimation without using prior information about the waveforms, our method is especially suitable to estimate waveforms of the gravitational bursts which there is little information regarding their waveforms. Thus we believe that this method will be useful to discover new features of supernovae and new astronomical phenomena through the analysis of gravitational waveforms in deatail.

References

[1] Dimmelmeier, H., Font, J. A. and Müller, E. 2002, A&A, 393, 523.

[2] Arnaud, N. et al. 2003, Astropart. Phys. 21, 201.

[3] Flanagan, É. É. and Hughes, S. A. 1998, Phys. Rev. D, 57, 4535.

[4] Anderson, W. G., Brady, P. R., Creighton, J. D. E., and Flanagan, É. É. 2001, Phys. Rev. D, 63, 042003.

[5] Viceré, A. 2002, Phys. Rev. D, 66, 062002.

[6] Hayama, K. 2004, Prog. Theor. Phys., 111 vol.1, 13.

[7] Hayama, K. 2004, Prog. Theor. Phys., 111 vol.6, 807.

[8] Hayama, K. 2005, to appear Class. Quantum Grav..

[9] Donoho, D. L. and Johnstone, I. M. 1995, J. R. Statist. Soc., B57 N2, 301.

[10] Donoho, D. L. and Johnstone, I. M. 1994, Biometrika, 81, 425.

[11] Berman, S. M. 1989, Sojourns and Extreme of Stochastic Processes (Wadsworth Reading MA).

[12] Daubechies, I 1988, Commum. on Pure and Appl. Math., 41, 909.

Quantum fluctuations in the de Sitter brane world

Wade Naylor[1] and Misao Sasaki[2]

Yukawa Institute for Theoretical Physics, Kyoto University, Kyoto 606-8502, Japan

Abstract

The vacuum expectation value of the square of the field fluctuations of a scalar field on a background consisting of *two* de Sitter branes embedded in an anti-de Sitter bulk are considered for massless, conformal fields. We find that the local behaviour of the quantum fluctuations suffers from the usual surface divergences as we approach the brane.

1 Introduction

Quantum fluctuations are of primary interest in inflationary cosmology, because they are related to the power spectrum and thus, may have an observable effect on the cosmic microwave background. In the context of the bulk inflaton model [1, 2] the quantum fluctuations of a bulk scalar field were investigated by canonical methods in [1, 3], for massless and massive fields respectively. It was argued that in the limit $H\ell \ll 1$ (where H is Hubble's constant and ℓ the AdS_5 radius) it is physically reasonable to use H as a natural cut off, even for the Kaluza-Klein modes. However, in the opposite limit the Kaluza-Klein contribution becomes significant. The work of [1, 3] looked at the difference between the Kaluza-Klein contributions and the bound state mode for field fluctuations constrained to the brane. However, because of the logarithmic divergence associated with the integral over the Kaluza-Klein tower, there was an explicit cutoff dependence in their result. Furthermore, they did not evaluate $\langle\phi^2(z)\rangle$ in the bulk.

In this talk we shall briefly discuss a different approach [4], which employs the canonical formalism to obtain a dimensionally reduced theory in terms of a de Sitter wave equation of motion with associated Kaluza-Klein masses. Then, by choosing the Euclidean vacuum state we are able to evaluate the quantum fluctuations in terms of zeta functions. For massless conformal coupling the eigenvalues are explicitly known which allows direct evaluation of $\langle\phi^2(z)\rangle$ as a function of the bulk direction z.

2 Dimensionally reduced action and zeta function

Assuming the mode decomposition

$$\phi(X) = \sum_n u_n(r)\phi_n(x) \tag{1}$$

the dimensionally reduced action is found to be

$$S = \frac{1}{2}\sum_n \int d^D x\sqrt{-g^{(D)}}\;\phi_n(x)\left(\Box_D - (m_n^2+\rho^2)H^2\right)\phi_n(x)\;. \tag{2}$$

where m_n are the KK masses and $\Box_D$ is the D-dimensional d'Alembertian for de Sitter space, for details see [4]. For convenience the eigenfunctions and normalisation condition will be defined in the conformal time frame. Then, the radial eigenfunctions, $u_n(r)$, in the proper time frame are related to those in the conformal time frame by

$$f_n(z) = H^{\rho-1/2}a^\rho(z)\,u_n(r)\,; \qquad \rho = \frac{D-1}{2} \tag{3}$$

where

$$f_n(z) = \frac{1}{\sqrt{a(z)}\,H\,N_n}\left(P^{-\nu}_{im_n-1/2}[\cosh(z_0+|z|)] + C_n\,P^{\nu}_{im_n-1/2}[\cosh(z_0+|z|)]\right) \tag{4}$$

[1] E-mail:naylor@yukawa.kyoto-u.ac.jp
[2] E-mail:misao@yukawa.kyoto-u.ac.jp

and

$$a(z) = \frac{\ell}{\sinh(z_0 + |z|)} \,. \tag{5}$$

We define $|z| = L$ as the distance between the two branes on the conformally related cylinder. The normalisation constant, N_n, is determined by the condition

$$\int_{-L}^{L} dz \; f_n(z) f_{n'}(z) = \delta_{nn'} \,, \tag{6}$$

which guarantees the dimensionally reduced action has the correct canonical form. The order, ν, of the Legendre functions in (4) is given by

$$\nu = \sqrt{\frac{D^2}{4} + \ell^2 M^2 - \xi D(D+1)} \,, \tag{7}$$

where M is the mass of the bulk scalar field and ξ is the curvature coupling. For massless conformal fields in five dimensions, $\xi_c = 3/16$ or $\nu = 1/2$, the boundary conditions are Neumann and the KK masses $m_n = n\pi/L$, see [4].

To arrive at the given set of equations above, we have assumed that the vacuum is given by the Euclidean vacuum state. In de Sitter space, this corresponds to choosing the Bunch-Davies vacuum which is de Sitter invariant. Then, the quantum fluctuations are described by fluctuations in a Euclideanised action, obtained by an analytic continuation of the Lorentzian metric, e.g., see Ref. [5]. This leads to the topology $R \times S^D$ in the conformal time frame.

In the case of $\nu = 1/2$ with Neumann boundary conditions and $m_n = n\pi/L$ the local heat kernel is given by

$$K(z,t) = \frac{2}{L} \sum_{n=0}^{\infty} \sum_{j=0}^{\infty} d_j \; e^{-(j+\rho)^2 H^2 t} e^{-m_n^2 H^2 t} \cos^2(m_n z) \tag{8}$$

where d_j is the degeneracy for the D-sphere, see [4].

It is straightforward to show that $\langle \phi^2(z) \rangle$ can be expressed in terms of a dimensionally reduced zeta function [4] and the zeta function is related to the above heat kernel by

$$\zeta(s)(z) = \frac{1}{a^{D-1}(z) V_{S^D}} \; H^2 \; \tilde{\zeta}(s)(z), \tag{9}$$

where

$$\tilde{\zeta}(s)(z) = \frac{2H^{-2s}}{L\Gamma(s)} \sum_{n=0}^{\infty} \sum_{j=0}^{\infty} d_j \int_0^{\infty} dt \; t^{s-1} \; e^{-(j+\rho)^2 t} e^{-m_n^2 t} \cos^2(m_n z) \tag{10}$$

is the associated zeta function in the conformal time frame. $\langle \phi^2(z) \rangle$ is then found by taking the limit $s \to 1$.

3 Results

Following a series of manipulations, see [4], we are able to perform the double summation in (10) leading to the result:

$$\langle \phi^2(z) \rangle_{\rm kk} = \frac{3 \sinh^3(z_0 + |z|)}{8\pi^2 \ell^3} H^2 \langle \tilde{\phi}^2(z) \rangle_{\rm kk} \tag{11}$$

$$\begin{aligned} H^2 \langle \tilde{\phi}^2(z) \rangle_{\rm kk} = \frac{1}{12} \sum_{n=1}^{\infty} \frac{1}{\sinh^3(nL)} \; + \; \frac{1}{24} \frac{1}{\sinh^3 z} \; + \; \frac{1}{24} \sum_{n=1}^{\infty} \frac{1}{\sinh^3(nL+z)} \\ + \; \frac{1}{24} \frac{1}{\sinh^3(L-z)} + \frac{1}{24} \sum_{n=2}^{\infty} \frac{1}{\sinh^3(nL-z)} \,, \end{aligned} \tag{12}$$

The second and fourth terms have been separated from the local mode sums for reasons which shall shortly become apparent. Note, if we were to consider Dirichlet boundary conditions, then the signs reverse on all but the first term in the above equation.

Straightaway we are able to obtain the result for when one of the branes is absent, $L \to \infty$,

$$H^2\langle\tilde{\phi}^2(z)\rangle_{\rm kk} \underset{L\to\infty}{\longrightarrow} \frac{1}{24}\frac{1}{\sinh^3 z}, \tag{13}$$

which is non-zero, unlike the effective action on the conformally related cylinder, see [6, 7]. By symmetry, the fourth term gives the quantum fluctuations for a single negative tension brane, located at $z = L$. Quite clearly, we have run into trouble, because, for example, in the vicinity of the positive tension brane, at $z = \varepsilon$ with $0 \le z \le L$, we find surface divergences as we approach the brane boundary, see Fig. 1,

$$H^2\langle\tilde{\phi}^2(\varepsilon)\rangle_{\rm kk} \sim \frac{1}{24\,\varepsilon^3} - \frac{1}{48\,\varepsilon} + \text{finite terms}, \tag{14}$$

with a similar result on the negative tension brane at $z = L - \varepsilon$. The first term in (14) agrees with the flat brane limit [4], while the second term is due to the curvature of the boundary.

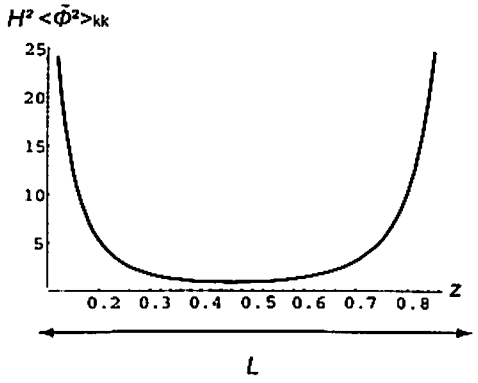


Figure 1: A plot of $H^2\langle\tilde{\phi}^2(z)\rangle_{\rm kk}$ for the brane distance, L, set to unity. The two branes are located at $z = 0$ and $z = 1$ respectively.

4 Discussion

The above method considered two branes. In the case of a single positive tension brane, there may or may not be a bound state mode, depending on the mass and curvature coupling. The existence of a bound state mode is determined from the boundary condition on the positive tension brane [2]. All the rest of the modes are unbounded, giving rise to a continuous spectrum of KK modes. However, the lowest $n = 0$ mode in the KK tower (in the large separation limit of two branes) reduces to the bound state mode if there exists a bound state in the single brane case.

Like for the stress energy tensor, quantum fluctuations also suffer from surface divergences in the vicinity of each brane/boundary. As is well known [8, 9] these surface divergences are non-integrable. Thus, for example, when integrating the $\langle T_{00}\rangle$ component of the stress energy tensor to obtain the Casimir energy between two plates, surface divergences appear in the Casimir force even after ultraviolet regularisation.[3] The point is that Neumann or Dirichlet boundary conditions are *idealised* boundary conditions, which only serve to model more realistic physical situations. There are various ways to cure these surface divergences, e.g., see [10].

[3]Evaluating the Casimir energy by the mode sum approach (which has been integrated before regularising) does not give rise to surface divergences. As discussed in [8, 9] the operations of integration and regularisation do not commute.

In the context of brane world models, one could also argue that the branes have a finite thickness which naturally cures any surface divergences. In [4] we also show another way to remove the surface divergences; by *constraining* the field point on the brane from the beginning we obtain a finite result. However, aside from surface divergences, one must take care that the back-reaction of the stress energy tensor near the brane/boundary does not ruin the self consistency of the classical model, even after curing surface divergences. This issue has been investigated in detail [11] for the Randall-Sundrum case. As is well known, e.g., [8, 9], only massless, conformal fields have a stress tensor free of surface divergences.

Finally, returning to the one brane case, a problem arises because we have employed the dimensional reduction method. If we try to discuss the one-brane case from the beginning, we find the Kaluza-Klein spectrum becomes continuous, which makes it impossible to define the lower dimensional Kaluza-Klein fields. In contrast, if we start with the two-brane case, and take the limit $L \to \infty$ in the end, we will be able to obtain a certain result. It is however totally unclear if this result is anything to do with the actual one-brane case. To resolve this issue we need to develop a different, new technique to deal with the one-brane case properly. Similar problems have been highlighted recently in [12] for the evaluation of the effective action for the one-brane case.

Acknowledgments

W.N. is supported by the 21COE program "Centre for Diversity and Universality in Physics," @ Kyoto University. M.S. is supported in part by Monbukagakusho Grant-in-Aid for Scientific Research(s) No. 14102004.

References

[1] S. Kobayashi, K. Koyama and J. Soda, Phys. Lett. B **501** (2001) 157 [arXiv:hep-th/0009160].

[2] Y. Himemoto and M. Sasaki, Phys. Rev. D **63** (2001) 044015 [arXiv:gr-qc/0010035].

[3] N. Sago, Y. Himemoto and M. Sasaki, Phys. Rev. D **65** (2002) 024014 [arXiv:gr-qc/0104033].

[4] W. Naylor and M. Sasaki, to be published in Prog. Theor. Phys. [arXiv:hep-th/0411155].

[5] J. Garriga and M. Sasaki, Phys. Rev. D **62** (2000) 043523 [arXiv:hep-th/9912118].

[6] W. Naylor and M. Sasaki, Phys. Lett. B **542** (2002) 289 [arXiv:hep-th/0205277].

[7] I. G. Moss, W. Naylor, W. Santiago-German and M. Sasaki, Phys. Rev. D **67** (2003) 125010 [arXiv:hep-th/0302143].

[8] D. Deutsch and P. Candelas, Phys. Rev. D **20** (1979) 3063.

[9] G. Kennedy, R. Critchley and J. S. Dowker, Annals Phys. **125** (1980) 346.

[10] L. H. Ford and N. F. Svaiter, Phys. Rev. D **58** (1998) 065007 [arXiv:quant-ph/9804056].

[11] A. Knapman and D. J. Toms, Phys. Rev. D **69** (2004) 044023 [arXiv:hep-th/0309176].

[12] A. Flachi, A. Knapman, W. Naylor and M. Sasaki, Phys. Rev. D **70** (2004) 124011 [arXiv:hep-th/0410083].

Wave optics in gravitational lensing of gravitational waves without thin lens approximation

Teruaki Suyama[1], Ryuichi Takahashi[2], Shugo Michikoshi[3],

[1,3] *Theoretical Astrophysics Group, Department of Physics, Kyoto University, Kyoto 606-8502, Japan*
[2] *Division of Theoretical Astrophysics, National Astronomical Observatory of Japan, Mitaka, Tokyo 181-8588,Japan*

Abstract

We must use wave optics instead of geometrical optics in gravitational lensing of gravitational waves if the wavelength is larger than the Schwarzschild radius of lens object. We develop the formulation to solve the wave equation for spherically symmetric lens potential and confirmed for the case of uniform density sphere that the error of the thin lens approximation is suppressed by the order of $\mathcal{O}(GM/R)$, where M is a lens mass and R is a radius of the sphere.

1 Introduction

Gravitational waves from coalescing compact binaries composed of neutron stars or black holes are the most promising targets for ground-based as well as space-based detectors in the near future. [1].

One possibility which alters the predicted wave forms which can be calculated with high precision is the gravitational lensing of gravitational waves. As is discussed by many authors [2], if the wavelength is larger than the Schwarzschild radius of the lens object, the diffraction effect becomes important and the magnification approaches to unity. Therefore we must use wave optics rather than the geometric optics for

$$M_L \lesssim 10^8 M_\odot \left(\frac{f}{\mathrm{mHz}}\right)^{-1}. \tag{1}$$

where M_L is a mass of the lens and f is the frequency of the gravitational wave. This is the case for LISA experiment if the lens object is a super massive black hole(SMBH). Further because the gravitational waves from compact binary are almost coherent, interference between lensed waves can be detected.

Motivated by this fact that wave effects can be detected for the gravitational lensing of gravitational waves, there are now growing interests in the wave optics in gravitational lensing [3, 4, 5, 6, 7]. However we have to solve wave equation which is generally partial differential equation between the source and the observer in order to obtain the lensed wave form at the observer. Except for a few special cases, exact solutions of wave equation are not known at present. Several authors have used thin lens approximations which reduces solving wave equation to double integral for single lens object(for multi-lens objects, integration becomes multi-integral, see [5]) and thus makes the problem easier. The thin lens approximation is to assume that the wave is scattered off by the gravitational potential which lens object produces only at the lens plane. In geometric optics which is used in the gravitational lensing of light, it is known that thin lens approximation is valid if we ignore the interference of the wave coming from different directions at the position of the observer and only focus on the trajectory of light which is obtained by solving geodesic equations.

In this paper, we develop the formulation to solve the wave equation numerically for spherically symmetric lens potential, which does not use the thin lens approximation We also apply this method to uniform density sphere and study the validity of the thin lens approximation.

[1]E-mail:suyama@tap.scphys.kyoto-u.ac.jp
[2]E-mail:takahasi@th.nao.ac.jp
[3]E-mail:shugo@tap.scphys.kyoto-u.ac.jp

2 Formulation

In this section, we formulate solving the scattering problem of gravitational wave by lensing object which is applicable to the case where lens potential is spherically symmetric. A situation we will consider throughout the paper is that plane wave is entering weak gravitational field which is spherically symmetric. When the lensing object is spherically symmetric, a scattering problem can be reduced to a problem of determining so-called phase shift which is used to probe the nature of nuclear physics and is also useful for the strong lensing by e.g. BHs where the assumption of weak gravitational field breaks down [9].

For monochromatic gravitational wave, the wave equation propagating in the weak gravitational field is [8]

$$(\Delta + \omega^2)\phi(\vec{x}) = 4\omega^2 U(\vec{x})\phi(\vec{x}), \tag{2}$$

where ω is an angular frequency of gravitational wave and U is a gravitational potential produced by the lensing object. ϕ is defined by where e_{ij} is a polarization tensor and $h_{\mu\nu}$ stands for a deviation from the background metric $g^{(0)}_{\mu\nu}$. It is Eq. (2) that we want to solve in order to evaluate quantities such as magnification factor which can be compared with the one derived under the thin lens approximation.

To solve Eq. (2), we choose a center of the lens as the origin of coordinate system. Then U becomes a function which depends only on the radius coordinate r. Now let us expand ϕ in terms of Legendre function

$$\phi(\xi,\theta) = \sum_{\ell=0}^{\infty} \frac{g_\ell(\xi)}{\xi} P_\ell(\cos\theta), \tag{3}$$

where ξ is a dimensionless variable defined by $\xi \equiv r\omega$. Then equations for $g_\ell(\xi)$ are

$$\left(\frac{d^2}{d\xi^2} + 1 - 4\tilde{U}(\xi) - \frac{\ell(\ell+1)}{\xi^2}\right) g_\ell(\xi) = 0, \tag{4}$$

where we have used $\tilde{U}$ in stead of U in order to stress that $\tilde{U}$ is a function of ξ.

For a point mass lens, i.e. $\tilde{U}(\xi) = -p/(2\xi)$, where $p \equiv 2GM\omega$ and M is a lens mass, analytic solutions of Eq. (4) are known as Coulomb wave functions [10]. The solution which is regular at $\xi = 0$ is

$$F_\ell(-p,\xi) = e^{\frac{\pi}{2}p}\frac{\Gamma(\ell+1-ip)}{\Gamma(2(\ell+1))} 2^\ell \xi^{\ell+1} e^{i\xi+i\sigma_\ell} F(\ell+1-ip; 2(\ell+1); -2i\xi),$$
$$\sigma_\ell \equiv \arg\Gamma(\ell+1+ip), \tag{5}$$

where F is the confluent hypergeometric function. The solution which is singular at $\xi = 0$ is

$$G_\ell(-p,\xi) = \xi^{\ell+1} 2^\ell e^{-\frac{\pi}{2}p}\left((-i)^{2\ell+1} e^{i\xi-i\sigma_\ell} U(\ell+1-ip; 2(\ell+1); -2i\xi) + \text{c.c.}\right), \tag{6}$$

where U is defined as

$$U(a;b;z) = \frac{1}{\Gamma(a)}\int_0^\infty dt e^{-zt} t^{a-1}(1+t)^{b-a-1}. \tag{7}$$

The asymptotic form of these functions $\xi \to \infty$ are

$$F_\ell(-p,\xi) \to \sin(\xi + p\log 2\xi - \frac{\pi}{2}\ell - \sigma_\ell), \qquad G_\ell(-p,\xi) \to \cos(\xi + p\log 2\xi - \frac{\pi}{2}\ell - \sigma_\ell). \tag{8}$$

A term $p\log 2\xi$ in the phase of trigonometric functions represents the nature of long range force which is characteristic of Coulomb force.

On the contrary, a solution of Eq. (2) that a plane wave is entering a point mass lens is well known and is given by [11]

$$\phi_0 = e^{\frac{\pi}{2}p}\Gamma(1-ip)e^{i\xi\cos\theta} F(ip; 1; i\xi(1-\cos\theta)). \tag{9}$$

Because the solution Eq. (9) is regular at $\xi = 0$, it is written as a partial wave sum of regular Coulomb wave function,

$$\phi_0 = \sum_{\ell=0}^{\infty} a_\ell \frac{F_\ell(-p,\xi)}{\xi} P_\ell(\cos\theta), \quad a_\ell = i^\ell(2\ell+1)e^{-i\sigma_\ell}. \tag{10}$$

For an extended lensing object, analytic solution of Eq. (2) does not exist in general. However if the lensing object exists only in a finite region, then the solution of Eq. (2) outside the lens can be written as a summation of partial wave which is now a linear combination of two independent Coulomb wave functions. By determining a coefficient of each Coulomb wave function, we can calculate the wave form ϕ outside the lens. In the aim of only determining the wave form far from the lensing object, we don't need to know the expression of ϕ inside the lens.

Now let us write the solution of Eq. (2) as

$$\phi = \phi_0 + \phi_s. \tag{11}$$

Thus ϕ_s represents the scattered wave which arises due to the deviation of lens from a point mass. There may be no incoming scattered wave to the lens from infinity, so we assume the asymptotic form of ϕ_s as

$$\phi_s(\xi, \theta) = \sum_{\ell=0}^{\infty} \frac{e^{i\xi + ip\log 2\xi - i\frac{\pi}{2}\ell - i\sigma_\ell}}{2i\xi} s_\ell P_\ell(\cos\theta), \tag{12}$$

where s_ℓ are undetermined complex numbers, but not arbitrary. In order that ϕ in Eq. (11) satisfy the wave equation (2), s_ℓ must be related to a_ℓ as

$$s_\ell = a_\ell(e^{2i\delta_\ell} - 1), \tag{13}$$

where δ_ℓ are real numbers. In terms of δ_ℓ, ϕ is written as

$$\phi(\xi, \theta) = \sum_{\ell=0}^{\infty} a_\ell e^{i\delta_\ell} \left(\cos\delta_\ell \frac{F_\ell(-p, \xi)}{\xi} + \sin\delta_\ell \frac{G_\ell(-p, \xi)}{\xi} \right) P_\ell(\cos\theta). \tag{14}$$

Thus we can calculate wave form outside the lens object by determining the phase shift δ_ℓ. δ_ℓ are determined by matching a solution of Eq. (4) which is obtained numerically with Eq. (14) and can be written as

$$\tan\delta_\ell = \frac{g_\ell(\xi_o)F'_\ell(-p, \xi_o) - g'_\ell(\xi_o)F_\ell(-p, \xi_o)}{g'_\ell(\xi_o)G_\ell(-p, \xi_o) - g_\ell(\xi_o)G'_\ell(-p, \xi_o)}, \tag{15}$$

where g_ℓ is a solution of Eq. (4) which is to be calculated numerically. We set the initial condition of Eq. (4) at $\xi = 0$ is that g_ℓ is regular. The range of δ_ℓ is from $-\frac{\pi}{2}$ to $\frac{\pi}{2}$.

3 Results

In this subsection, we show the results obtained by using the formulation developed in the previous subsection for the uniform density sphere and compare it with those calculated in the thin lens approximation. We focus on the amplification factor F which is defined by $F \equiv \phi/\phi_0$.

The amplification factor in the thin lens approximation Eq. (??) for the case of uniform density sphere is written as

$$F_{thin}(w, y) = -iwe^{i\frac{w}{2}y^2} \int_0^\infty dx x J_0(wxy) e^{iw(\frac{x^2}{2} - \Psi(x))}, \tag{16}$$

where

$$\Psi(x) = \begin{cases} \log\left(1 + \sqrt{1 - (\frac{D_E}{R}x)^2}\right) - \frac{1}{3}\left(4 - (\frac{D_E}{R}x)^2\right)\sqrt{1 - (\frac{D_E}{R}x)^2} & (x \le \frac{R}{D_E}) \\ \log\frac{D_E}{R}x & (x \ge \frac{R}{D_E}), \end{cases} \tag{17}$$

and $D_E \equiv \sqrt{4GM\omega}$, $w \equiv 4GM\omega$, $y \equiv \sqrt{r_\ell r_o 4GM(r_o - r_\ell)}\theta_o$. We show the difference of the amplification factor between numerical calculation and the thin lens approximation in Fig. 1. We find that the error scales as $\propto D^{-1/2}$, which suggests the analytical estimation that the error is the order of GM/R.

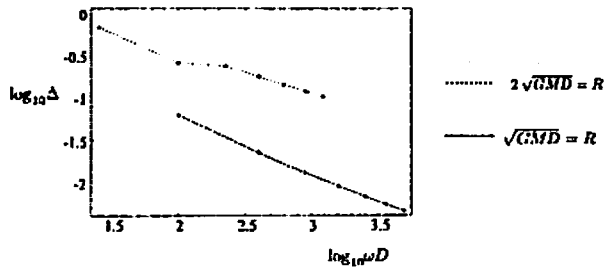


Figure 1: Error of the amplification factor for the uniform density sphere. The horizontal axis is the distance between the lens and the observer normalized in the wavelength of the gravitational wave. Lens mass M and the frequency ω is fixed.

4 Conclusion

In this paper, we discussed the validity of the thin lens approximation in the framework of wave optics.

We develop the formalism to solve wave equation numerically for the spherically symmetric potential. In this case, the partial differential equation is reduced to ordinary differential equation. The method we used is to determine the so-called phase-shift which represents the degree of difference of scattering of the partial wave between point mass lens and arbitrary spherically symmetric potential.

By numerical calculations, we found that the error of the thin lens approximation for the uniform density sphere scales as $D^{-1/2}$.

References

[1] C. Cutler and E. E. Flanagan, Phys. Rev. D **49**, 2658 (1994).

[2] H. C. Ohanian, Int. J. Theor. Phys. **9**, 425 (1974), H. C. Ohanian, Astrophys. J. **271**, 551 (1983), P. V. Bliokh and A. A. Minakov, Ap& SS. **34**, L7 (1975), R. J. Bontz and M. P. Haugan, Ap& SS. **78**, 199 (1981), K. S. Thorne, in Gravitational Radiation, ed. N. Deruell and T. Piran (Amsterdam: North-Holland), 28 S. Deguchi and W. D. Watson, Astrophys. J. **307**, 30 (1986).

[3] R. Takahashi and T. Nakamura, Astrophys. J. **595** (2003) 1039 [arXiv:astro-ph/0305055].

[4] N. Seto, Phys. Rev. D **69** (2004) 022002 [arXiv:astro-ph/0305605],
K. Yamamoto and K. Tsunoda, Phys. Rev. D **68** (2003) 041302 [arXiv:astro-ph/0309694],
F. de Paolis, G. Ingross, A. A. Nucita and A. Qadir, Astron. Astrophys. **394** (2002) 749,
T. T. Nakamura, Phys. Rev. Lett. **80**, 1138 (1998).

[5] K. Yamamoto, arXiv:astro-ph/0309696.

[6] T. T. Nakamura and S. Deguchi, Prog. Theor. Phys. Suppl. **133**, 137 (1999).

[7] C. Baraldo, A. Hosoya and T. T. Nakamura, Phys. Rev. D **59** (1999) 083001.

[8] P. C. Peters, Phys. Rev. D **9**, 2207 (1974).

[9] N. Andersson and B. P. Jensen, arXiv:gr-qc/0011025.

[10] Abramowitz, M., and Stegun, I. A. 1970, Handbook of Mathematical Functions(New York: Dover)

[11] A. Messiah, 1961, Quantum Mechanics(Ner York: Intersicence Publisher)

Gravitational Radiation from Inhomogeneous Core-Collapse

Tomoya Takiwaki[1], Kei Kotake[2], Shoichi Yamada[3], Katsuhiko Sato[4]

[1,2,4]*Department of Physics, School of Science, the University of Tokyo, 7-3-1 Hongo, Bunkyo-ku, Tokyo 113-0033, Japan*

[3]*Engineering, Waseda University, 3-4-1 Okubo, Shinjuku, Tokyo, 169-8555, Japan*

[4]*Research Center for the Early Universe, School of Science, the University of Tokyo, 7-3-1 Hongo, Bunkyo-ku, Tokyo 113-0033, Japan*

Abstract

We performed 2.5 dimensional simulations concerning gravitational core-collapse of massive star. We add perturbations of the density to consider non-spherical gravitational collapse. We found that non-spherical behaviors in the propagation of the shock and the gravitational radiations are largely depends on the profile of rotation. In case of the slow rotation the amplitudes of the gravitational wave are largely affected by the perturbations in spite of relatively small difference in hydrodynamical feature. In case of the rapid rotation on the other hand, the waveforms of gravitational radiation are almost same among the model, however the large difference are found in the propagation of the shock.

1 Introduction

The non-spherical computation is indispensable for the analysis of the explosion mechanism. On the other hand non-spherical collapse and explosion is important for the context of the gravitational wave. For more than 20 years astrophysicists struggle to compute gravitational signal produced by core-collapse supernovae. The gravitational wave (GW) astronomy will soon come true. The ground-based interferometric detectors (LIGO,VIRGO,GEO600,TAMA300) are beginning their search for GWs. A core-collapse of massive star is one of the most promising source of a gravitational radiation. An expected amplitude of the gravitational waves from the core-collapse supernova in the Milky Way is considered to be within the detection limits of the laser interferometers. If the core-collapse and/or the supernova explosion occur aspherically, gravitational wave is radiated. Such asphericities are caused by the rotation [1, 2, 3, 4, 5, 6, 7, 8, 9, 10, 11, 12, 13]. And recently magnetic effects on gravitational wave are computed [14]. Although inhomogeneity of the core is very simple source of asphericities, few works devoted to the study of inhomogeneity [15, 16]. Inhomogeneity of the core is produced by a convection prior to core-collapse [17, 18]. As a result a significant perturbation is reported in density: that is of order 5%.

The gravitational waves enable us to see the most inner part of the evolved massive star directly. We investigate an effect of this perturbation on the gravitational wave radiated at the core-collapse.

2 Setup

We employ the precollapse model of 20 solar-mass[19]. And we assume angular velocity as cylindrical differential rotation whose $T/|W|$ is 0.5%. In order to reflect the features of convective mode, we assume the form of the perturbation as follows; $\rho_{\rm initial}(r,\theta) = \rho_{\rm up}(r)\left(1+0.5\min\left(\frac{r}{r_c},1\right)\epsilon\cos l\theta\right)$ where $r_c = 1.0\times10^7$cm We change ϵ and l parametrically. In the previous works [15, 16], $l=1$ mode is only considered, however we consider wide variety of configurations now. Fig. 1 shows the density configuration of various l and constant ϵ.

[1]E-mail:takiwaki@utap.phys.s.u-tokyo.ac.jp
[2]E-mail:kkotake@utap.phys.s.u-tokyo.ac.jp
[3]E-mail:shoichi@heap.phs.waseda.ac.jp
[4]E-mail:sato@phys.s.u-tokyo.ac.jp

It should be noted that we set $r = 0$ at the center of gravity.

As for the rotation profile, we assume the cylindrical rotation: $\Omega(X,Z) = \Omega_0 \frac{X_0^4}{X^4+X_0^4} \frac{Z_0^4}{Z^4+Z_0^4}$, where X and Z denote distance from rotational axis and the equatorial plane. We adopt the value of parameters, X_0 and Z_0, as 10^7cm, 10^8cm, respectively.

3 Numerical Result

3.1 Hydrodynamical Features

Here we present final profile of our models. First of all we present the hydrodynamical features of slow rotating model whose $T/|W| \approx 0\%$. In the infall epoch, these ordinary collapse scenario; the matters fall to the center freely and bounce when the density becomes nuclear density. And the shock wave propagate outward after that. Fig. 2 shows an entropy per baryon that can show hot region where the shock goes through clearly. We found the shape of the shock is almost spherical and found the asymmetry in the odd l models. In the odd l models shock wave in south pole (initially low density) goes through more rapidly than that in north pole (initially high density). These difference is caused by the position where bounce occurs. If whole density is low, the bounce is delayed and as a result shock is formed near the center. That means falling matter collide the rigid center violently. In order to estimate these asymmetric motion quantitatively, we define asymmetric velocity, $v_{\rm asym} = \frac{\int_D \rho v_z dV}{\int_D \rho dV}$ where D is taken to the region whose density is greater than 10^{11}g/cm^3. This quantity becomes kick velocity of pulsar when the explosion succeeds. This value is oscillating with time, therefore we present maximum value of it. $|v_{\rm asym}|$ is $5.8 \times 10^7, \approx 0, 5.9 \times 10^7, 1.4 \times 10^7$cm/s at $l = 1,2,3,5$, respectively. We found asymmetry is weak in high l.

Next we present hydrodynamical features of rapid rotating models ($T/|W| = 0.5\%$). Rapid rotation prevents the matter from falling near the equatorial plane. However matters near the rotational axis can fall freely and can make violent collision. As a result the shape of the shock wave is likely to be prolate. These general features are seen in our computations. We present final profiles of these models in Fig.3. We found perturbations greatly affect the propagation of shock wave. The behavior of each models are very complicated. In these models bounce occurs relatively low density. In this case there is slight difference of the velocity of shock between north pole and south pole. However the density configuration where the shock goes through is different in each models. Consequently the velocity of shock wave is different in the direction. At this moment maximum value of asymmetric velocities, $|v_{\rm asym}|$, are $4.1 \times 10^7, \approx 6.0 \times 10^6, 5.0 \times 10^7, 1.5 \times 10^7$cm/s at $l = 1,2,3,5$, respectively. We found asymmetry is weak in high l as the slowly rotating case. In case of $l = 2$ asymmetric velocity should be 0, therefore that value indicates the order of numerical error.

3.2 Gravitational Wave

In this subsection we present gravitational wave radiated from core-collapse of our models. We use quadrupole formula in order to compute gravitational waveforms [3]. First Fig. 4 shows the waveforms of the gravitational wave in the slow rotating models. There is slight difference among the models in the hydrodynamical features however the waveforms are largely different. We found the amplitude of $l = 2$ model is the largest. We can understand that from the description of quadrupole formula, it is due to the large quadrupole moment. As for other features we found the first and second peak of $l = 1$ and $l = 3$ is similar. It means similar configuration of hydrodynamical variables.

Next Fig. 5 shows the waveforms of the gravitational wave in the rapid rotating models. Surprisingly these amplitudes at core-bounce are almost same in spite of the very various final profiles. The maximum amplitude is found in $l = 1$ mode;10% lager than others. These waveforms gave us the information of the oscillation of the central protoneutron star. These same waveforms means the configurations of hydrodynamical variables at the center is depend on rotation only. The density perturbations do not affect the property of PNS.

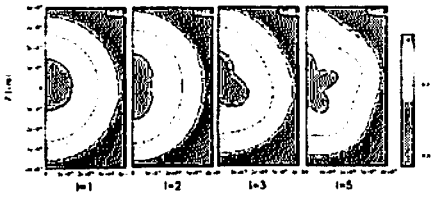


Figure 1: Initial Configurations of Density. The right figures show the log10(density) of the various models at initial state

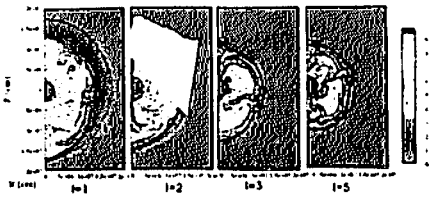


Figure 2: Final configuration of shock waves in various l in case of slow rotating models. This figures show a contour of the entropy per baryon whose time is 49ms, 26ms, 11ms, 11ms, after bounce, in $l = 1, 2, 3, 5$,respectively.

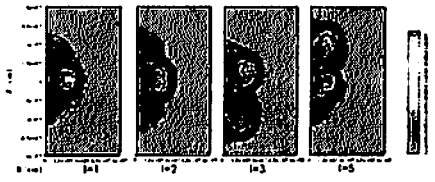


Figure 3: Final configuration of shock waves in various l in case of rapid rotating models. This figures show a contour of the entropy per baryon whose time is 27ms, 31ms, 26ms, 26ms, after bounce, in $l = 1, 2, 3, 5$,respectively.

4 Summary and Discussion

We investigate the effect of the density perturbation on the propagation of the shock and gravitational wave.

(1) We found that the density perturbations greatly affect the propagation of the shock in the rapid rotating models and do not affect that in the slow rotating models.

(2) We found that the density perturbations greatly affect the gravitational waveform in the slow rotating models and do not affect that in the rapid rotating models.

This reason can be interpreted as follows. Due to the density-configuration of the core, dynamical time scale in the central region is faster than the outer region. Therefore perturbation is likely to be leveled off before core-bounce at the central region. However the density perturbation remains still in outer region. The shock propagates in relatively thin region generated by the perturbation. In the slowly rotating cases, the shape of dense core becomes spherical and amplitudes of the gravitational wave are small. In these configurations the perturbation of outer region can affect the gravitational waves.

Finally we note the possibility that gravitational wave determine the density inhomogeneity in the core. From our result it is clear that if the core rotate rapidly, we can't determine the inhomogeneity prior to core-collapse, however we can determine that if the core rotate slowly. Particularly if $l = 2$ mode is dominant, significant difference should be found. Even if the odd mode is dominant, we can judge whether l is high or low.

References

[1] E. Mueller, A&A**114**, 53 (1982).

[2] L. S. Finn and C. R. Evans, ApJ**351**, 588 (1990).

[3] R. Moenchmeyer, G. Schaefer, E. Mueller, and R. E. Kates, A&A**246**, 417 (1991).

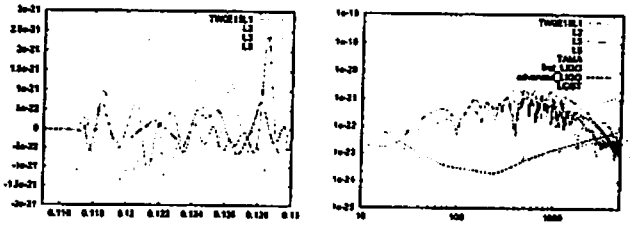


Figure 4: Gravitational waveforms of rapid rotating model. This figures shows waveform of gravitational radiation form the slow rotating ($T/|W| \approx 0\%$) inhomogeneous core.

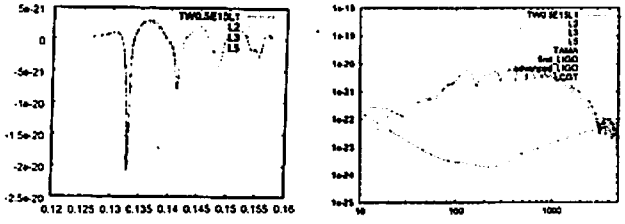


Figure 5: Left figure shows the gravitational waveforms of rapid rotating model. This figures shows waveform of gravitational radiation form the rapid rotating ($T/|W| = 0.5\%$) inhomogeneous core. The right figure is square root of energy spectrum. The differences among the models are relatively big at low frequency.

[4] S. Yamada and K. Sato, ApJ450, 245 (1995).

[5] T. Zwerger and E. Mueller, A&A320, 209 (1997).

[6] M. Rampp, E. Mueller, and M. Ruffert, A&A332, 969 (1998).

[7] H. Dimmelmeier, J. A. Font, and E. Müller, A&A393, 523 (2002).

[8] C. L. Fryer, D. E. Holz, and S. A. Hughes, ApJ565, 430 (2002).

[9] C. L. Fryer, M. S. Warren, D. E. Holz, S. A. Hughes, and R. Dupuis, Gravitational waves from core collapse, in *Gravitational-Wave Detection. Edited by Cruise, Mike; Saulson, Peter. Proceedings of the SPIE, Volume 4856, pp. 123-133 (2003).*, pp. 123-133, 2003.

[10] J. N. Imamura, B. K. Pickett, and R. H. Durisen, ApJ587, 341 (2003).

[11] C. D. Ott, A. Burrows, E. Livne, and R. Walder, ApJ600, 834 (2004).

[12] M. Shibata and Y. Sekiguchi, Phys. Rev. D68, 104020 (2003).

[13] K. Kotake, S. Yamada, and K. Sato, Phys. Rev. D68, 044023 (2003).

[14] K. Kotake *et al.*, Phys. Rev. D69, 124004 (2004).

[15] A. Burrows and J. Hayes, Physical Review Letters 76, 352 (1996).

[16] C. L. Fryer, ApJ601, L175 (2004).

[17] G. Bazan and D. Arnett, ApJ433, L41 (1994).

[18] S. M. Asida and D. Arnett, ApJ545, 435 (2000).

[19] A. Heger and N. Langer, ApJ544, 1016 (2000).

Deformed Horizon and Singularity in Five-Dimensional Charged Black Holes

Ken Matsuno[1] and Hideki Ishihara[2]

Department of Mathematics and Physics, Graduate School of Science, Osaka City University, Sumiyoshi-ku Osaka 558-8585, Japan

Abstract

We consider the internal structure of the 5-dimensional charged black hole when the spherical shape of horizon is deformed. We solve the internal region of the 5-dimensional black hole which is described by a class of spatially homogeneous anisotropic universes. When the horizon is deformed to axisymmetric, there appears a timelike singularity and a Cauchy horizon as in the case of spherically symmetric geometry. In contrast, in general non-axisymmetric case a spacelike curvature singularity appears instead.

1 Introduction

One of the most striking predictions of general relativity is the existence of spacetime singularity in black holes. All objects which fall into the Schwarzshild black hole inevitably hit on the spacelike singularity. In contrast, all free-falling objects can avoid the singularity in the case of Reissner-Nordström black hole, because the singularity is timelike in this geometry. In the case of Kerr black hole, which is the most probable fate of collapsing stars, falling objects show a similar behavior (we restrict our attention to Reissner-Nortström geometry in this paper).

The difference is related to the internal structure of the black holes: the Schwarzschild geometry has spacelike singularity inside while the Reissner-Nortstörm geometry possesses a timelike singularity with Cauchy horizon, which is a null boundary for prediction of the evolution of physical fields from initial data. It is suggested that the Cauchy horizon is unstable against small perturbations[1].

The Schwarzshild and Reissner-Nordström geometries are static and spherically symmetric outside the horizon while geometries are described as spatially homogeneous and dynamical universes with spherical symmetry inside. The inner universe start from a regular null regular hypersurface, black hole horizon, rather than the initial singularity. Then the inner universe can be extended backwards outer region beyond the black hole horizon. The future fate of the inner universe is the big-crunch, the spacelike singularity, in Schwarzschild case, while another regular null hypersurface, the inner (Cauchy) horizon, in Reissner-Nordström case. When the inner universe is extended beyond the inner (Cauchy) horizon, a timelike singularity appears.

The Schwarzshild and Reissner-Nordström black holes are asymptotically flat solutions which describe the geometries of isolated systems. However, realistic black holes in our universe may stay in their host galaxies and/or be with companions. If the black holes are not isolated system their horizon would be deformed by environment surrounding them.

Here, we consider a situation that there exists a null apparent horizon in a spacetime. If a spatially homogeneous universe starting from the apparent horizon we call the universe satisfies horizon condition (HC) initially. Such a universe is regarded as the interior of a black hole. When the inner universe with HC has spherical symmetry the shape of horizon should be a sphere but the universe has less symmetry the horizon should be deformed. Unfortunately, in 4-dimension, there is no spatially homogeneous universe satisfying HC which includes spherically symmetric geometry as a special case[2]. Then the interior of 4-dimensional black hole with deformed horizon must be inhomogeneous.

On the other hand, in 5-dimension, it is possible to consider S^3 symmetry of a black hole, SO(4), breaks to SO(3) by horizon deformation. In this case, the 4-dimensional spatial section of the inner universe is still

[1]E-mail:matsuno@sci.osaka-cu.ac.jp
[2]E-mail:ishihara@sci.osaka-cu.ac.jp

homogeneous with (space translation)×SO(3) symmetry. Investigating the (space translation)×SO(3) symmetric spatially homogeneous universe with HC we can see the non-linear structure near a singularity which might be formed inside the black hole. Then 5-dimensional black hole is a nice model to study the inner structure when the horizon is deformed. We study, here, the inner geometry of such an inner universe of 5-dimensional charged black hole with deformed horizon as an Einstein-Maxwell system.

2 Formulation

2.1 Basic equation

Let us consider 5-dimensional spatially homogeneous universe with (space translation)×SO(3) symmetry. The metric has the form

$$\begin{aligned} ds^2 &= \eta_{\mu\nu}e^\mu e^\nu, \quad (\mu,\nu = 0,4,1,2,3), \\ &= -dt^2 + f^2(t)dR^2 + a^2(t)(\sigma^1)^2 + b^2(t)(\sigma^2)^2 + c^2(t)(\sigma^3)^2, \end{aligned} \tag{1}$$

where scale factors f, a, b, and c are function of t and σ^i $(i = 1,2,3)$ satisfy the relation

$$d\sigma^i = -\frac{1}{2}C^i_{jk}\sigma^j \wedge \sigma^k, \quad C^1_{23} = C^2_{31} = C^3_{12} = 1.$$

The Maxwell equations in this metric are

$$\left[\partial_0 F_{\mu\nu} + \left(\frac{\partial_0 a_\mu}{a_\mu} + \frac{\partial_0 a_\nu}{a_\nu}\right)F_{\mu\nu}\right]\epsilon^{0\mu\nu\alpha\beta} - \frac{1}{2}\left(C^\sigma_{\rho\mu}\frac{a_\sigma}{a_\mu}F_{\sigma\nu} + C^\sigma_{\rho\nu}\frac{a_\sigma}{a_\nu}F_{\mu\sigma}\right)\epsilon^{\rho\mu\nu\alpha\beta} = 0,$$

$$\partial_0 F^{0\nu} + \sum_{\mu\neq\nu\neq\rho}\left(\frac{\partial_0 a_\rho}{a_\rho}F^{0\nu} + \frac{1}{6}C^\nu_{\mu\rho}\frac{a_\nu}{a_\rho}F^{\mu\rho} + \frac{1}{3}C^\mu_{\mu\rho}\frac{a_\mu}{a_\rho}F^{\rho\nu}\right) = 0,$$

We consider a special solution

$$F_{04} = -F^{04} = -E/(abc), \quad \text{othrwise zero},$$

where E is a constant which means the radial component of electric part of the field strength.

The Einstein equations are represented as

$$\begin{aligned} &\frac{\ddot{a}}{a} + \frac{\ddot{b}}{b} + \frac{\ddot{c}}{c} + \frac{\ddot{f}}{f} = -\frac{U^2}{(abc)^2}, \\ &\frac{(\dot{a}bcf)^\cdot}{abcf} = \frac{(b^2-c^2)^2 - a^4 + U^2}{2(abc)^2}, \\ &\frac{\left(a\dot{b}cf\right)^\cdot}{abcf} = \frac{(c^2-a^2)^2 - b^4 + U^2}{2(abc)^2}, \\ &\frac{(ab\dot{c}f)^\cdot}{abcf} = \frac{(a^2-b^2)^2 - c^4 + U^2}{2(abc)^2}, \\ &\frac{\left(abc\dot{f}\right)^\cdot}{abcf} = -\frac{U^2}{(abc)^2}, \end{aligned} \tag{2}$$

where dot denotes the derivative with respect to t and $U^2 := 4E^2/3$.

2.2 Horizon Condition

If a homogeneous universe satisfies the horizon condition initially the universe can be regarded as the interior of a black hole. Let us consider a time evolution of the scale factors with the initial condition at a moment $t = t_0$:

$$\begin{aligned} &f = 0 \quad \text{and} \quad a, b, c : \text{ finite}, \\ &\dot{a} = \dot{b} = \dot{c} = 0 \quad \text{and} \quad \dot{f} : \text{ finite}. \end{aligned} \tag{3}$$

The surface $t = t_0$ is a non singular null surface. If we extend the geometry outwards by changing the coordinates $(t, R) \to (r, T)$ suitably we can see that outgoing null bundles off the null surface have vanishing expansion. Since the null surface $t = t_0$ is the apparent horizon then the initial condition (3) is the horizon condition for the metric (1). We restrict the evolution of the universe with the initial condition (3).

3 Solutions

Introducing a new time variable $d\tau = dt/(abcf)$ we rewrite (2) in the form

$$\begin{aligned}
&\left(\frac{a'}{a}\right)' + \left(\frac{b'}{b}\right)' + \left(\frac{c'}{c}\right)' + \left(\frac{f'}{f}\right)' = 2\left(\frac{a'}{a}\frac{b'}{b} + \frac{b'}{b}\frac{c'}{c} + \frac{c'}{c}\frac{a'}{a}\right) + 2\left(\frac{a'}{a} + \frac{b'}{b} + \frac{c'}{c}\right)\frac{f'}{f} - U^2 f^2, \\
&\left(\frac{a'}{a}\right)' = [(b^2 - c^2)^2 - a^4 + U^2]f^2/2, \quad \left(\frac{b'}{b}\right)' = [(c^2 - a^2)^2 - b^4 + U^2]f^2/2, \\
&\left(\frac{c'}{c}\right)' = [(a^2 - b^2)^2 - c^4 + U^2]f^2/2, \quad \left(\frac{f'}{f}\right)' = -U^2 f^2,
\end{aligned} \tag{4}$$

where the prime denotes the derivative with respect to τ. First, we can solve for f separatory, and after for a, b, c.

3.1 Axially Symmetric Case

We can obtain analytic form of the solution for (2) which satisfies HC (3) in axisymmetric case ($a \neq b = c$):

$$\begin{aligned}
a^2(\tau) &= U\cosh(\alpha\tau)\mathrm{sech}(\alpha\tau + \beta), \\
b^2(\tau) &= c^2(\tau) = U\cosh(\alpha\tau)\cosh(\alpha\tau + \beta)\mathrm{sech}^2(\alpha\tau + \gamma), \\
f^2(\tau) &= \frac{(\alpha)^2}{U^2}\mathrm{sech}^2(\alpha\tau),
\end{aligned} \tag{5}$$

where α, β and γ are constants. It is easy to see that all of the axial symmetric solutions have two apparent horizon at $\tau \to -\infty$ and $\tau \to \infty$. The region described by the solution (5) is between the two horizons. By coordinate transformation $a^2 = r^2/4$, $T := \frac{\alpha}{U\sinh\beta}R$, the metric for (5) can be extended towards external region as

$$\begin{aligned}
ds^2 &= -\tilde{f}^2(r)dT^2 + \left[\frac{4U\sinh\beta}{\tilde{g}(r)r^2}\right]^4 \frac{dr^2}{\tilde{f}^2(r)} + \frac{r^2}{4}(\sigma^1)^2 + \left[\frac{2U\sinh\beta}{\tilde{g}(r)r}\right]^2 [(\sigma^2)^2 + (\sigma^3)^2], \\
\tilde{f}^2(r) &:= 1 - \frac{8U\cosh\beta}{r^2} + \frac{(4U)^2}{r^4}, \quad \tilde{g}(r) := \sinh(\beta - \gamma) + \frac{4U\sinh\gamma}{r^2}.
\end{aligned} \tag{6}$$

This metric reduces to the 5-dimensional Reissner-Nortström solution with spherical symmetry when $\beta = \gamma$. The axial symmetric metric has a timelike singularity at $r = 0$ as same as the spherically symmetric case. The outer and inner horizons are at $r_\pm = \sqrt{4U}e^{\pm\beta/2}$.

The solution (6) is not asymptotically flat. There is environment which causes the horizon deformation then it is impossible to describe the geometry of far region by this solution.

3.2 General Non-axisymmetric Case

In this case, f is solved as the last line in (5) but a, b, c are hardly solved analytically. When we put $A := a\sqrt{f}$, $B := b\sqrt{f}$, $C := c\sqrt{f}$, (4) are rewritten as

$$2\left(\frac{A'}{A}\right)' = (B^2 - C^2) - A^4, \quad 2\left(\frac{B'}{B}\right)' = (C^2 - A^2) - B^4, \quad 2\left(\frac{C'}{C}\right)' = (A^2 - B^2) - C^4. \tag{7}$$

This set of equations has the same form of the 4-dimensional vacuum Bianchi type IX universe[3], which has chaotic oscillations. But, the constraint equation becomes

$$\frac{A'}{A}\frac{B'}{B}+\frac{B'}{B}\frac{C'}{C}+\frac{C'}{C}\frac{A'}{A}-\frac{1}{4}[A^4+B^4+C^4-2(A^2B^2+B^2C^2+C^2A^2)]-\frac{3}{4}\alpha^2=0. \qquad (8)$$

The last term in the left hand side is additional one to 4-dimensional vacuum Bianchi type IX universe case.[4]

Because of the form of evolution equations (7) and constraint (8) it is expected that oscillatory behavior of scale factors appears, but the oscillations terminate after finite times. We solved (7) with (8) numerically. A typical behavior of scale factors is shown in Fig.nosymm.

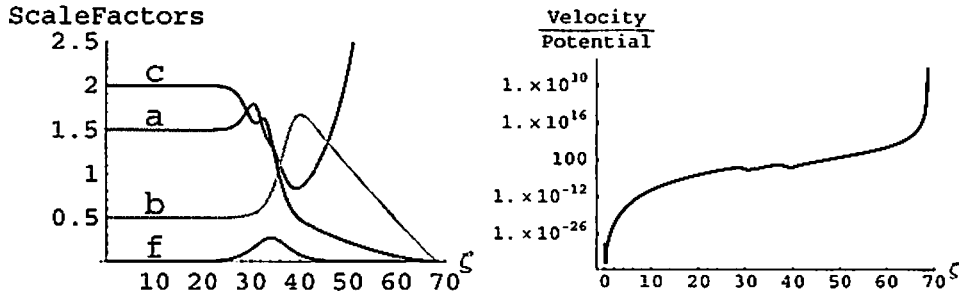


Figure 1: Time evolution of scale factors (left). Evolution of the velocity term over potential term of scale factors (right). ζ is a new time variable defined by $d\zeta := f^{1/10}(\tau)d\tau$.

In Fig.1, we see that after several oscillations two of scale factors in S^3 part collapse and one diverges in the last stage. We also see that velocity term defined by $\frac{A'}{A}\frac{B'}{B}+\frac{B'}{B}\frac{C'}{C}+\frac{C'}{C}\frac{A'}{A}$ dominates over potential term defined by $\frac{1}{4}[A^4+B^4+C^4-2(A^2B^2+B^2C^2+C^2A^2)]$ at the final epoch (see Fig.1 right). At the final stage of the inner universe since the spatial curvature terms are negligible then the evolution is described by a 5-dimensional Kasner solution. Therefore, the final singularity is spacelike.

4 Conclusion

We consider 5-dimensional spatially homogeneous universe with homogeneous electric field which satisfies horizon condition initially as the interior of a charged black hole with deformed horizon.

In axially symmetric case, the geometry has two apparent horizons and a timelike singularity appears inside the inner horizon. While, in non-axially symmetric case, the geometry has a spacelike singularity inside a horizon.

References

[1] E. Poisson and W. Israel, Phys. Rev. D 41, 1796 (1990).
A. Ori, Phys. Rev. Lett. 67, 789 (1991).
L.M. Burko, Phys. Rev. Lett. 79, 4958 (1997).

[2] K.Matsuno and H.Ishihara, in preparation.

[3] V.A. Belinskii, I.M. Khalatnikov and E.M. Lifshitz, Adv. Phys. 19, 525 (1970).

[4] J.D. Barrow and M.P. Dabrowski, Phys. Rev. D 57, 7204 (1998).
N.A. Batakis and A.A. Kehagias, Nucl. Phys. B 449, 248 (1995).

Extended Self-Similar Solutions of the Einstein-Scalar Field System

Makoto Yoshikawa[1],

[1] *Theoretical Astrophysics Group, Department of Physics, Kyoto University, Kyoto 606-8502, Japan*

Abstract

A new class of solutions for spherically symmetric Einstein-massless scalar field system is presented which contains self-similar solutions as a subclass.

1 Introduction

Self-similar solutions in general relativity have been widely studied in many literatures mainly for a technical reason. Namely, in many cases, solutions of the Einstein equations are easily obtained under the assumption of self-similarity, which simplifies the mathematical complexity of the Einstein field equations. Especially, when the system is spherically symmetric, field equations are simplified to a set of ordinary differential equations (ODEs), and we can study the properties of the solutions quite easily.

Besides the mathematical convenience, it has been suggested recently that self-similar solutions also have some physical importance. Of particular importance is *the similarity hypothesis* proposed by B. J. Carr, which asserts that, in a variety of physical situations, solutions of the Einstein equations evolve naturally to self-similar form even if the initial conditions are far from self-similar (see, e.g., [1]). Although there are many examples which support the hypothesis (see [1, 2] and references therein), it is still unclear on what condition the similarity hypothesis holds. In order to make it clear, it is necessary to find solutions of the Einstein equations which are *not* self-similar, and then observe their asymptotic behaviors. However, this is not an easy task because it requires solving the Einstein equations without assuming self-similarity, which makes testing the similarity hypothesis in general situations difficult.

In this paper, we consider the Einstein-massless scalar field system, and present a new class of solutions which contains not only self-similar solutions, but also many non-self-similar solutions. By investigating asymptotic behaviors of the non-self-similar solutions, we will be able to perform a test on the similarity hypothesis.

2 Formulation

We consider the Einstein-massless scalar field system in N (≥ 4) spacetime dimension, whose action is given by

$$S = \int d^N x \sqrt{-g} \left(R - \frac{1}{2} g^{\alpha\beta} \partial_\alpha \varphi^* \partial_\beta \varphi \right), \tag{1}$$

where φ is a complex scalar field and the asterisk represents complex conjugation. We take the scalar field to be complex because, with a real scalar field, solutions obtained from the procedure introduced below are highly restricted. The field equations are the Einstein equations $R_{ab} = \frac{1}{2}\mathrm{Re}[\partial_a \varphi^* \partial_b \varphi]$ and the wave equation $\Box \varphi = 0$.

In order to solve the field equations, we make a metric ansatz as

$$ds^2 = a^2(\eta)\{g(\zeta)(-d\eta^2 + d\zeta^2) + \rho(\zeta)^2 d\Omega^2_{N-2}\}. \tag{2}$$

where $d\Omega^2_{N-2}$ is the line element of an unit $(N-2)$-sphere. This metric form is, in fact, a generalization of those for temporally or spatially self-similar spacetimes with spherical symmetry. This can be seen by taking $a(\eta) = e^\eta$, which makes Eq. (2) a general metric form for such spacetimes.

[1] E-mail:makoto@tap.scphys.kyoto-u.ac.jp

The above metric ansatz is still insufficient for reducing the field equations to ODEs because they still contain an unknown function of two-variables, $\varphi(\eta,\zeta)$, which cannot be separated. So we make another ansatz on the functional form of $\varphi(\eta,\zeta)$ as follows:

$$\varphi(\eta,\zeta)=\sqrt{2(N-2)}\left(c_1\ln a(\eta)+c_2\int d\eta\{a(\eta)\}^{-(N-2)}+c_3\ln|g(\zeta)|+\text{const.}\right), \tag{3}$$

where c_1, c_2 and c_3 are complex constants.

Under the ansatz Eqs. (2) and (3), the field equations can be separated out into two sets of ODEs: that for the ζ-independent variable, $a(\eta)$, and that for the η-independent variables, $g(\zeta)$ and $\rho(\zeta)$.

The equation for the ζ-independent part is given by

$$\frac{\ddot{a}}{a}+(N-3)\left(\frac{\dot{a}}{a}\right)^2+(N-2)\sigma=0, \tag{4}$$

where the overdot represents the derivative with respect to η, and σ is a constant of separation normalized so that $\sigma=+1$ or 0 or -1. We can solve this equation analitically, and the solutions are classified into six types which are listed in Table 1. The value of σ is unique for each type of $a(\eta)$, which is also shown in the table. Note that type-III class is exactly the set of self-similar solutions. We excluded type-I solutions from the following discussion, because they have an additional symmetry characterized by the Killing field $\partial/\partial\eta$, which means they are contained in a class of solutions with higher symmetries.

The equations for η-independent variables, $g(\zeta)$ and $\rho(\zeta)$, can be written in the form of a two-dimensional autonomous system,

$$\begin{aligned} X' &= -(N-2)(XY+2\sigma),\\ Y' &= -\frac{\lambda^2}{4}X^2+\lambda^2XY-Y^2-(1-\lambda^2)\sigma,\\ \text{where}\quad & X\equiv\lambda^{-2}\frac{g'}{g},\qquad Y\equiv\frac{\rho'}{\rho}. \end{aligned} \tag{5}$$

together with a "constraint" equation given by

$$\mathcal{F}_C\equiv-\frac{\lambda^2}{4}X^2+\lambda^2XY+(N-3)Y^2+(N-3+\lambda^2)\sigma=(N-3)\frac{g}{\rho^2}. \tag{6}$$

which do not contain second order derivatives of $g(\zeta)$ or $\rho(\zeta)$. Here, the prime represents the derivative with respect to ζ, and λ is another constant of separation which is real-valued. We can easily see that the "constraint" is consistent with Eq. (5) in the sense that if $(g(\zeta),\rho(\zeta))$, a solution of Eq. (5), satisfies Eq. (6) initially, then it satisfies Eq. (6) for arbitrary ζ. This means that our main task is to solve Eq. (5), whereas Eq. (6) only constrains the constants of integration that appear when we integrate X and Y to obtain g and ρ.

The field equations also give some relations between the constants c_1, c_2, c_3 and λ, which are obtained in the process of deriving Eqs. (4)-(6). As a result, only λ remains to be a free parameter (although its domain is somewhat restricted), and c_1, c_2 and c_3 are expressed in terms of λ. These results are summarized in Table 1.

To summarize, the procedure of obtaining a solution is as follows: (i) Choose the type of $a(\eta)$ among II-IV. At this point, the value of σ is uniquely determined. (ii) Choose a value of λ from the interval shown in Table 1. (iii) Find a solution $(X(\zeta),Y(\zeta))$ of Eq. (5). (iv) Integrate the solution $(X(\zeta),Y(\zeta))$ to obtain $g(\zeta)$ and $\rho(\zeta)$. Here, constants of integral are taken so that Eq. (6) is satisfied.

3 Phase spaces

In this section, we focus on the autonomous system (5). Although it is difficult to solve Eq. (5) in general, we can investigate qualitative behaviors of the solutions by analyzing the phase space structure.

type	$a(\eta)$	σ	domain of λ^2	c_1	c_2	c_3
I	1	0	–	–	–	–
II	$\eta^{1/(N-2)}$	0	$(0, N-1]$	$1/\sqrt{N-2}$	0	$\frac{\lambda+i\sqrt{N-1-\lambda^2}}{2\lambda\sqrt{N-1}}$
III	e^{η}	-1	$(0, +\infty)$	λ	0	$(2\lambda)^{-1}$
IV	$\{\cosh((N-2)\eta)\}^{1/(N-2)}$	-1	$[N-1, +\infty)$	λ	$i\sqrt{\lambda^2-N+1}$	$(2\lambda)^{-1}$
V	$\{\sinh((N-2)\eta)\}^{1/(N-2)}$	-1	$(0, N-1]$	λ	$i\sqrt{N-1-\lambda^2}$	$(2\lambda)^{-1}$
VI	$\{\sin((N-2)\eta)\}^{1/(N-2)}$	$+1$	$(0, N-1]$	λ	$i\sqrt{N-1-\lambda^2}$	$(2\lambda)^{-1}$

Table 1: Functional forms of $a(\eta)$.

The phase portraits of the autonomous system (5) are shown in Fig. 1 for various values of σ and λ. In this figure, new variables (U, V) defined by

$$U \equiv \frac{X}{\sqrt{8+X^2+Y^2}}, \qquad V \equiv \frac{Y}{\sqrt{8+X^2+Y^2}}, \tag{7}$$

are used instead of (X, Y). With these variables, the whole XY-plane is mapped onto a compact region $U^2+V^2<1$, so we can observe the whole phase space including the asymptotic region $X^2+Y^2 \sim \infty$ which corresponds to $U^2+V^2 \lesssim 1$. In general, the phase space structure changes as we move the values of N, σ, λ. However, it can be proved that there are only seven patterns which are shown in Fig. 1 (for details, see [3]).

It follows from the "constraint" equation (6) that $g(\zeta)$ is positive in the region $\mathcal{F}_C > 0$, which are depicted as dark gray zones in Fig. 1, while in the region $\mathcal{F}_C < 0$, which are depicted as light gray zones, $g(\zeta)$ is negative. Therefore, $\frac{\partial}{\partial\eta}$ is temporal (resp. spatial) in dark (resp. light) gray zones. Orbits on the curves $\mathcal{F}_C = 0$, which are depicted as dashed curves, are forbidden because $g(\zeta)$ becomes 0 on them.

4 Summary and discussions

We have obtained a new class of solutions of Einstein-massless scalar field system with the action Eq. (1) by making an ansatz Eq. (2) and Eq. (3). The solutions are classified into six subclasses, type-I-VI, according to the functional forms of $a(\eta)$, where type-III class is the set of self-similar solutions. Except for type-I solutions, equations for ζ-dependent variables, $g(\zeta)$ and $\rho(\zeta)$, are reduced to an autonomous system Eq. (5) whose phase portraits are shown in Fig. 1.

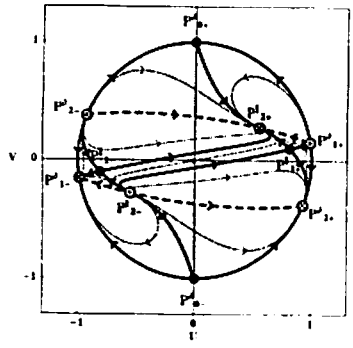
In this work, we have mainly focused on mathematical structure of the solution space, while physical properties of the solutions such as spacetime structures have been put aside. However, from a point of view of the similarity hypothesis, it is of great interest if the solutions of type-II, IV, V, VI converge to self-similar solutions as time develops. We can easily see that solutions of type-IV, V with $g > 0$ converge to self-similar solutions as time develops ($\eta \to +\infty$), which supports the similarity hypothesis. But, in other cases, it is unclear yet if the solutions are asymptotically self-similar. So we will examine asymptotic behaviors of the solutions, which will be a good test for the similarity hypothesis.

References

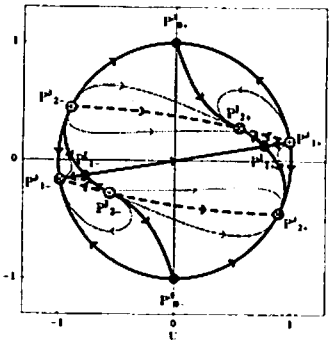
[1] B. J. Carr & A. A. Coley, Class. Quant. Grav. **16**, R31-R71 (1999).

[2] T. Harada & H. Maeda, Phys. Rev. **D 63**, 084022 (2001); J. Ibanez & S. Jhingan, Phys. Rev. **D 70**, 063507 (2004).

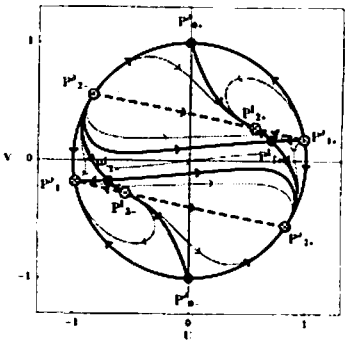
[3] M. Yoshikawa, in preparation.



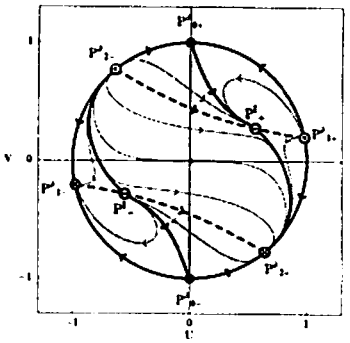
(a) $\sigma = -1$, $\lambda^2 < 1/N - 1$



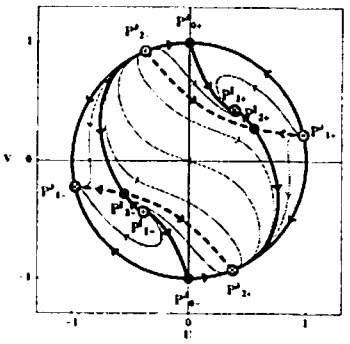
(b) $\sigma = -1$, $\lambda^2 = 1/(N-1)$



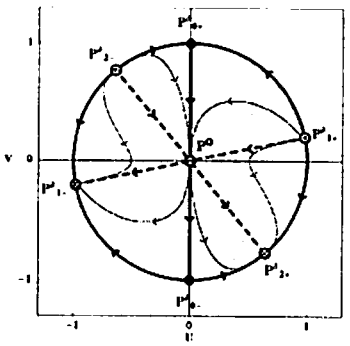
(c) $\sigma = -1$, $1 > \lambda^2 > 1/(N-1)$



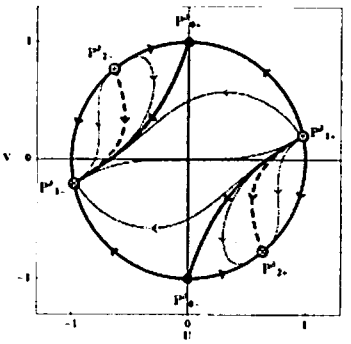
(d) $\sigma = -1$, $\lambda^2 = 1$



(e) $\sigma = -1$, $\lambda^2 > 1$



(f) $\sigma = 0$



(g) $\sigma = +1$

Figure 1: Global phase portraits of the autonomous system Eq. (5). Circle-shaped symbols represent equilibrium points; $\odot$ is a source, $\otimes$ is a sink, $\bullet$ is a saddle and $\ominus$ is a non-hyperbolic equilibrium point. Separatrices are depicted by bold curves. The metric coefficient g is positive in the dark gray regions, while it is negative in light gray regions. Orbits on dashed curves are meaningless because g becomes 0 on them.

Gravitational wave from stellar core collapse
— Odd parity perturbation of Tolman-Bondi space time —

Aya Sekido[1], Kei-ichi Maeda[2]

[1,2] *Department of Physics, Waseda University, 3-4-1 Okubo, Shinjuku-ku, Tokyo 169-8555, Japan*

Abstract

The gravitational wave from stellar core collapse is one of the most promising sources for gravitational wave detectors. We numerically study gravitational waves from dust core collapse in linearized Einstein theory. In this approach, we adopt spherically collapsing star to a black hole as the zeroth-order solution and gravitational wave are computed in the perturbation theory on the spherical background. Tolman-Bondi solution is applied to compute the gravitational wave for spherical dust collapse. The perturbation equation of odd parity is calculated for nonspherical part.

1 Introduction

Detection of gravitational waves is one of the greatest challenges in experimental and theoretical physics in this decade. Nonspherical stellar collapse is one of the most promising sources of gravitational waves for both ground-based detectors and space antennas.

We numerically study gravitational waves from slightly nonspherical stellar collapse to a black hole on the linearlized Einstein theory. In our model, we choose inhomogeneous nonspherical stellar collapse, which is a dust ball. The previous researches simulated the gravitational waves from homogeneous dust ball [1]. In our model we adopt Tolman-Bondi solution [2, 3, 4] to simulate the gravitational waves from inhomogeneous dust model. After nonspherical stellar collapse, the core will become naked singularity or Black hole which depends on initial density profile. To investigate the effects of stellar interior structures, we must proper initial mass density profile which finally becomes Black hole.

In Section 2, we induce basic equations using gauge invariant perturbation formalism. In Section 3 we overview numerical method including initial condition, and we present results. Finally in Section 4 we present conclusion.

2 Gauge Invariant Perturbation Formalism

First, we consider stellar interior. In our model we adopt Tolman-Bondi solution to simulate the gravitational waves from inhomogeneous dust model.

$$ds^2 = -d\tau^2 + A^2(\tau,\chi)d\chi^2 + R^2(\tau,\chi)(d\theta^2 + \sin^2\theta d\phi^2) \tag{1}$$

The following equations are Einstein equations.

$$A^2(\tau,\chi) = \frac{\partial_\chi R(\tau,\chi)}{\sqrt{1+f(\chi)}} \tag{2}$$

$$\rho(\tau,\chi) = \frac{1}{8\pi}\frac{1}{R^2\partial_\chi R(\tau,\chi)}\frac{dF(\chi)}{d\chi} \tag{3}$$

$$f(\chi) = (\partial_\tau R(\tau,\chi))^2 - \frac{F(\chi)}{R(\tau,\chi)} \tag{4}$$

$m(\chi)$ is Misner-Sharp mass, $F(\chi)$ and $f(\chi)$ is arbitrary functions. Giving definitions of $F(\chi)$ and $f(\chi)$ describes the motion of dust could completely.

[1] E-mail:sekido@gravity.phys.waseda.ac.jp
[2] E-mail:maeda@gravity.phys.waseda.ac.jp

Next we induce basic equations applying Gerlach-Sengupta formalism [5, ?]. For odd parity the interior perturbation equations are given by

$$\partial_\tau(Ak_0) - \partial_\chi(k_1/A) = 0 \quad (5)$$

$$\partial_\chi(R^1\psi_s) - A(l-1)(l+2)k_0 = 16\pi AR^2L_0 \quad (6)$$

$$\partial_\tau(R^1\psi_s) - \frac{1}{A}(l-1)(l+2)k_1 = 0 \quad (7)$$

L_0 is gauge invariant variable which represents matter part.

$$L_0 = \rho U(\tau,\chi), \qquad L_1 = L = 0 \quad (8)$$

U is defined in terms of fluid velocity perturbation by

$$\delta u_\mu = (0,0,0,U(\tau,\chi)\Phi^m_{lB}) \quad (9)$$

From above perturbation equations we induce interior basic equations.

$$\partial_\tau(\frac{A}{R^2}\partial_\tau(R^1\psi_s)) - \partial_\chi(\frac{1}{AR^2}\partial_\chi(R^1\psi_s)) + (l-1)(l+2)A\psi_s = -16\pi\partial_\chi(\frac{1}{AR^2}\frac{dJ}{d\chi}) \quad (10)$$

$J(\chi)$ is an arbitrary function. ψ_s is defined by

$$\psi_s = \frac{1}{A}\left[\partial_\tau(k_1/R^2) - \partial_\chi(k_0/R^2)\right] \quad (11)$$

Similarly we induce exterior equations. The exterior metric is Schwarzschild metric. The perturbation equation is Regge-Wheeler equation.

$$\partial_t(\frac{e^{2\Lambda}}{r^2}\partial_t(r^1\tilde{\psi}_s)) - \partial_r(\frac{1}{e^{2\Lambda}r^2}\partial_r(R^1\tilde{\psi}_s)) + (l-1)(l+2)e^{2\Lambda}\tilde{\psi}_s = 0 \quad (12)$$

The Figure2 is the flow diagram of the formalism.

3 Numerical Methods and Results

In 1984 Christodoulou show that the relation between initial mass density and the final stage of core collapse. If the following equations are satisfied, the final stage of core collapse becomes Black hole.

$$\rho(\chi) = c_0\chi^0 + c_2\chi^2 + c_4\chi^4 \quad (13)$$

$$d^2\rho(0)/d\chi^2 = 0 \quad (14)$$

$$\rho(\chi) = \rho_0\exp[-\frac{\chi^4}{2\sigma^2}] \quad (15)$$

The Figure3 is Penrose Diagram of the gravitational collapse. The simulation area is divided three parts. First, white background area is stellar interior. Second, colored background area is stellar exterior, it is also divided two parts. The near stellar surface area is simulated by single null coordinates, and another colored background area is computed by double null coordinates.

$$u = t - r_* \quad (16)$$

$$v = t + r_* \quad (17)$$

r_* is tortoise coordinate. From equation (12), and applying double null coordinates and tortoise coordinate, we can derive

$$4\frac{\partial^2\psi_S}{\partial u\partial v} + V\psi_S = 0 \tag{18}$$

The Figure4 shows one of interior results. Around the stellar center the metric perturbation variables grow according to time evolution. We also changed the initial mass density profile. For example, we changed the values of σ in equation(15). As a result, the significant change of the wave was not founded. After that we checked the change of initial fluid velocity perturbation. Consequently the rapid wave growth was founded.

4 Conclusion

We have investigated the behavior of the odd parity linear perturbations during gravitational stellar core collapse. We applied Gerlach-Sengupta formalism, and derived Odd parity linealized field equation for both interior and exterior region. After that we simulated these partial differential equation. The simulation area has been divided into three part. The different numerical method was adopted for each part, which was the stellar interior area, the stellar anterior area near the stellar surface, and the stellar anterior at the observation point. The area near the stellar surface was simulated by single null coordinates, and the stellar anterior at the observation point was computed by double null coordinates.

We focus on results of stellar interior, the metric perturbation variables grow according to time evolution around the stellar center. Changing of the initial mass density profile, we changed the values of σ in equation(15), have made them trivial changes. On the other hand different values of initial fluid velocity perturbation have given the rapid wave growth.

References

[1] C.T. Cunningham, R.H. Price, and V. Moncrief, Astrophys. J. 224, 643 (1978)

[2] R. C. Tolman, Proc. Natl. Acad. Sci. U.S.A. 20, 169 (1934)

[3] H. Bondi, Mon. Not. R. Astron. Soc. 107, 410 (1947)

[4] T. Harada, H. Iguchi, and K. Nakao, Prog. Theor. Phys. 107, 449 (2002).

[5] U. H. Gerlach and U. K. Sengupta, Phys. Rev. D19 2268 (1979)

[6] U. H. Gerlach and U. K. Sengupta, Phys. Rev. D22 1300 (1980)

[7] H. Iguchi, K. Nakao and T. Harada, Phys. Rev. D57 7262 (1998)

[8] H. Iguchi, T. Harada and K. Nakao, Prog. Theor. Phys. 101 1235 (1999).

[9] T.Harada, H. Iguchi, and M. Shibata,Phys. Rev. D 68 024002 (2003)

[10] Demetrios Christodoulou, Commun. Math. Phys. 93 171 (1984)

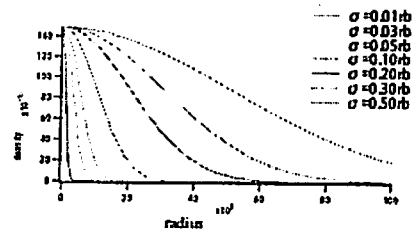


Figure 1: Initial density profile

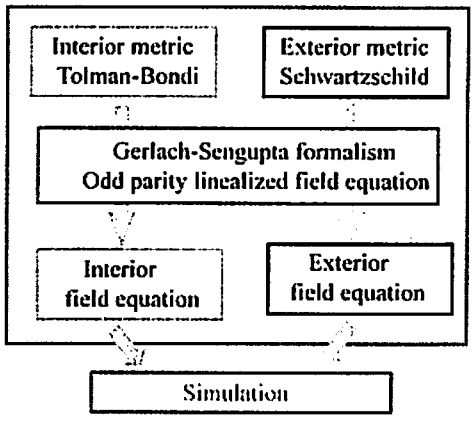


Figure 2: flow diagram

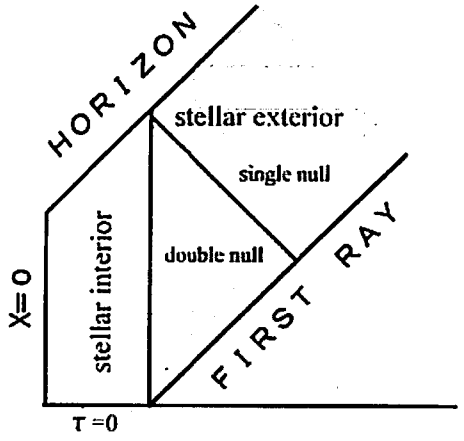


Figure 3: NumericalMethod

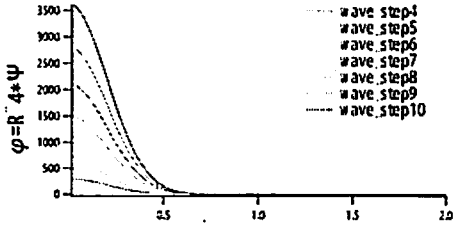


Figure 4: Stellar Interior Result

Scattering of Gravitational Waves by the Weak Gravitational Potential of Lens Objects

Ryuichi Takahashi[1], Teruaki Suyama[2], Shugo Michikoshi[3]

[1] *Division of Theoretical Astrophysics, National Astronomical Observatory of Japan, Mitaka, Tokyo 181-8588, Japan*

[2,3] *Theoretical Astrophysics Group, Department of Physics, Kyoto University, Kyoto 606-8502, Japan*

Abstract

We consider the scattering of the gravitational waves by the weak gravitational fields of lens objects. We obtain the scattered gravitational waves by treating the gravitational potential of the lens to first order, i.e. the Born approximation. We find that if the Schwartzchild radius of the lens is smaller than the wavelength of gravitational waves or if the impact parameter is larger than the Einstein radius, the Born approximation is valid. We also find that if the lens is smoothly distributed, the amplitude of the incident wave is magnified by $1 + \kappa$ where κ is convergence (or expansion), which is consistent with the result in weak gravitational lensing.

1 Introduction

Ground-based laser interferometric detectors of gravitational waves such as LIGO, VIRGO, TAMA, GEO are currently in operation to search for astrophysical sources such as neutron star binaries, black hole binaries, supernovae. The gravitational wave signals are extracted from the data by using the matched filtering with gravitational waveform template which have been calculated for many possible sources [4]. If the gravitational waves from the sources pass near massive compact objects or pass through intervening inhomogeneous mass distribution, the gravitational waveform is changed by the scattering, or gravitational lensing, by these lens objects. In this paper, we investigate this effects on incident gravitational waveform.

In the gravitational lensing of light, the scattering is discussed in the gravitational lensing under the geometrical optics approximation, which is valid because the wavelength is much smaller than the typical size of lens objects. But for the lensing of gravitational waves, the wavelength is much larger than that of light, and hence the geometrical optics is not valid in some cases. As suggested by several authors [6, 3, 5], if the wavelength is larger that the Schwartzchild radius of the lens, the wave optics should be used. Hence we use the wave optics in the limit of weak gravitational fields of lens.

We use units of $c = G = 1$.

2 Gravitational Waves Propagating through Weak Gravitational Fields

We consider the scattering of the gravitational waves by the weak gravitational fields of lens objects. We consider the scattering of scalar waves, instead of the gravitational waves, since the basic equation is the same as the scalar field wave equation (see Sect. IIC of Peters [6]). The gravitational fields of the lens objects are described by the metric $g_{\mu\nu}$ as $ds^2 = g_{\mu\nu}dx^\mu dx^\nu = -(1 + 2U)dt^2 + (1 - 2U)d\mathbf{r}^2$, where $U(\mathbf{r})$ is the gravitational potential of the lens. Since the propagation equation of the scalar wave is $\partial_\mu(\sqrt{-g}g^{\mu\nu}\partial_\nu\phi) = 0$, we have the wave equation as

$$\left(\nabla^2 + \omega^2\right)\tilde{\phi}(\mathbf{r}) = 4\omega^2 U(\mathbf{r})\tilde{\phi}(\mathbf{r}), \tag{1}$$

where ω is the frequency of the gravitational waves and we set $\phi(t, \mathbf{r}) = \tilde{\phi}(\mathbf{r})e^{i\omega t}$. We can obtain the scattered waves from Eq.(1) by treating the potential U to first order, i.e. the Born approximation.

[1] E-mail:takahasi@th.nao.ac.jp

[2] E-mail:suyama@tap.scphys.kyoto-u.ac.jp

[3] E-mail:shugo@tap.scphys.kyoto-u.ac.jp

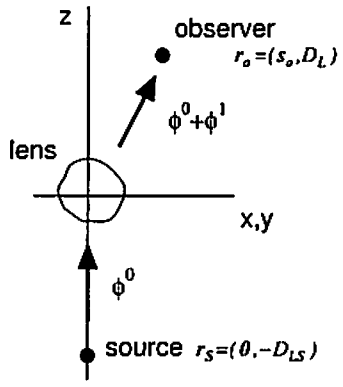


Figure 1: Gravitational lens geometry for the source, the lens and the observer. The lens is distributed around the origin. The source position is $\mathrm{r}_S = (0, -D_{LS})$, while the observer position is $\mathrm{r}_o = (\mathrm{s}_o, D_L)$ where s_o is two-dimensional vector with $|\mathrm{s}_o| \ll D_L$. D_L and D_{LS} are the distances from the lens to the observer and to the source, respectively. ϕ^0 is the incident wave, while $\phi^0 + \phi^1$ is the scattered wave.

We show the lens geometry of the source, the lens and the observer in Fig.1. The lens is distributed around the origin of the coordinate axes. The source position is $\mathrm{r}_S = (0, -D_{LS})$, while the observer position is $\mathrm{r}_o = (\mathrm{s}_o, D_L)$ where s_o is two-dimensional vector with $|\mathrm{s}_o| \ll D_L$. D_L and D_{LS} are the distances from the lens to the observer and to the source, respectively.

In the unlensed case $U = 0$ in Eq.(1), we write $\tilde{\phi}^0(\mathrm{r})$ as the solution of this equation. Including the effect of U to first order, the scattered wave at the observer is written as,

$$\tilde{\phi}(\mathrm{r}_o) = \tilde{\phi}^0(\mathrm{r}_o) + \tilde{\phi}^1(\mathrm{r}_o) \tag{2}$$

where $\tilde{\phi}^1$ represents the effect of scattering. The Green's function for the Helmholtz equation $e^{i\omega|\mathrm{r}-\mathrm{r}'|}/|\mathrm{r}-\mathrm{r}'|$ satisfies,

$$\left(\nabla^2 + \omega^2\right) \frac{e^{i\omega|\mathrm{r}-\mathrm{r}'|}}{|\mathrm{r}-\mathrm{r}'|} = -4\pi\delta^3(\mathrm{r}-\mathrm{r}'). \tag{3}$$

Inserting Eqs.(2) and (3) into Eq.(1), we obtain $\tilde{\phi}^1(\mathrm{r}_o)$ as,

$$\tilde{\phi}^1(\mathrm{r}_o) = -\frac{\omega^2}{\pi} \int d^3r' \frac{e^{i\omega|\mathrm{r}_o-\mathrm{r}'|}}{|\mathrm{r}_o-\mathrm{r}'|} U(\mathrm{r}')\tilde{\phi}^0(\mathrm{r}'). \tag{4}$$

We use the spherical wave emitted by the source as ϕ^0, then we have $\tilde{\phi}^0(\mathrm{r}) = Ae^{i\omega|\mathrm{r}-\mathrm{r}_S|}/|\mathrm{r}-\mathrm{r}_S|$. In Fig.1, ϕ^0 represents the incident wave emitted by the source, while $\phi^0 + \phi^1$ represents the scattered wave.

2.1 Geometrically thin lens

We assume that the lens objects are locally distributed at the origin. Then we have $|\mathrm{r}'| \ll D_{L,LS}$ and $|\mathrm{s}_o| \ll D_L$ in Eq.(4). Using the second order Taylor series[4] for these small quantities r' and s_o, $\tilde{\phi}^1$ is reduced to

$$\frac{\tilde{\phi}^1(\mathrm{r}_o)}{\tilde{\phi}^0(\mathrm{r}_o)} = -\frac{\omega^2}{\pi} \frac{D_S}{D_L D_{LS}} \int d^3r' U(\mathrm{s}', z') e^{i\omega t_d(\mathrm{s}', \mathrm{s}_o)} \tag{5}$$

where $D_S = D_L + D_{LS}$ and we set $\mathrm{r}' = (\mathrm{s}', z')$. t_d is the geometrical time delay which is given by,

$$t_d(\mathrm{s}', \mathrm{s}_o) = \frac{D_S}{2D_L D_{LS}} \left(\mathrm{s}' - \frac{D_{LS}}{D_S}\mathrm{s}_o\right)^2. \tag{6}$$

[4] $|\mathrm{r}-\mathrm{r}'| \simeq r - (\mathrm{r}\cdot\mathrm{r}')/r + [r'^2/r - (\mathrm{r}\cdot\mathrm{r}')^2/r^3]/2$ for $r \gg r'$

Using the two dimensional gravitational potential $\psi(\mathrm{s}') = 2\int dz' U(\mathrm{s}', z')$, the result in Eq.(5) is reduced to,

$$\frac{\tilde{\phi}^1(\mathrm{r}_o)}{\tilde{\phi}^0(\mathrm{r}_o)} = -\frac{\omega^2}{2\pi}\frac{D_S}{D_L D_{LS}}\int d^2 s' \psi(\mathrm{s}') e^{i\omega t_d(\mathrm{s}', \mathrm{s}_o)}. \tag{7}$$

The above equation is also derived by expanding ψ to first order in the diffraction integral (see Schneider *et al.* [7], Sec.7). Since the potential ψ is written by using the surface density of the lens Σ as $\psi(\mathrm{s}) = 4\int d^2 s' \Sigma(\mathrm{s}') \ln|\mathrm{s} - \mathrm{s}'|$, the result (7) is rewritten as,

$$\frac{\tilde{\phi}^1(\mathrm{r}_o)}{\tilde{\phi}^0(\mathrm{r}_o)} = 2i\omega \int d^2 s' \Sigma(\mathrm{s}') \left[E_i\left(i\omega t_d(\mathrm{s}', \mathrm{s}_o)\right) - \ln\left|\mathrm{s}' - \frac{D_{LS}}{D_S}\mathrm{s}_o\right|^2 \right]. \tag{8}$$

where E_i is the exponential integral function : $E_i(ix) = -\int_x^\infty dt e^{it}/t$ (e.g. Abramowitz and Stegun [1]). If we shift the time t by Δt, the incident wave is $\phi^0 \propto e^{i\omega(t+\Delta t)} \simeq e^{i\omega t}(1 + i\omega\Delta t)$ and Eq.(2) is rewritten as $\tilde{\phi} = \tilde{\phi}^0(1 + i\omega\Delta t) + \tilde{\phi}^1$. Hence we can choose Δt so that the second term of Eq.(8) is vanished, and we eliminate this term.

Let us discuss the validity of the Born approximation. If the scattered wave $\tilde{\phi}^0 + \tilde{\phi}^1$ is not too different from the incident wave $\tilde{\phi}^0$, this approximation is valid. We discuss the condition of $|\tilde{\phi}^1/\tilde{\phi}^0| \ll 1$ for two lens models, point mass lens and smoothly distributed lens, in following paragraphs.

Point mass lens The surface density is $\Sigma(\mathrm{s}) = M\delta^2(\mathrm{s})$ where M is the lens mass. Then, $\tilde{\phi}^1$ in Eq.(8) is rewritten as (see also Peters [6], Sect. III A),

$$\frac{\tilde{\phi}^1(\mathrm{r}_o)}{\tilde{\phi}^0(\mathrm{r}_o)} = 2iM\omega\, E_i\left(i\frac{\omega D_{LS}}{2D_L D_S}s_o^2\right) \tag{9}$$

In Fig.2, we show $Ei(ix)$ as a function of x. Solid line is the absolute value of Ei, dashed line is the real part, and dotted line is the imaginary part. From this figure, except for small $x \lesssim 1$, $|Ei|$ is smaller than 1. Thus the Born approximation is valid $|\tilde{\phi}^1/\tilde{\phi}^0| \ll 1$ in Eq.(9) if the lens mass M is smaller than the wave length of the gravitational waves $\lambda = 2\pi/\omega$ except for small impact parameter $s_o \lesssim (D_L D_S/\omega D_{LS})^{1/2}$.

Especially for large impact parameter s_o, since $Ei(ix) \sim -ie^{ix}/x$ for $x \gg 1$, Eq.(9) is reduced to

$$\frac{\tilde{\phi}^1(\mathrm{r}_o)}{\tilde{\phi}^0(\mathrm{r}_o)} = \left(\frac{s_E}{s_o}\right)^2 \exp\left(i\frac{\omega D_{LS}}{2D_L D_S}s_o^2\right), \tag{10}$$

where s_E is the Einstein radius in the observer plane : $s_E = (4MD_L D_S/D_{LS})^{1/2}$. Hence if the impact parameter s_o is larger than the Einstein radius s_E, the Born approximation is valid irrespective of the wavelength of the gravitational waves.

Smoothly distributed lens We assume that the lens is smoothly distributed in the $z = 0$ plane in Fig.1. In the unlensed case, the wave propagate through $\mathrm{s}' = (D_{LS}/D_S)\mathrm{s}_o$ in the lens plane. Expanding the lens potential $\psi(\mathrm{s}')$ around it in Eq.(7), $\tilde{\phi}^1$ is rewritten as,

$$\frac{\tilde{\phi}^1(\mathrm{r}_o)}{\tilde{\phi}^0(\mathrm{r}_o)} = -i\omega\psi + \kappa + \mathcal{O}\left(\frac{D_L D_{LS}}{\omega D_S}\nabla_s^2\kappa\right). \tag{11}$$

The first term, being $-i\omega\psi(\mathrm{s}')$ at $\mathrm{s}' = (D_{LS}/D_S)\mathrm{s}_o$, can be eliminated for the same reason as the second term in Eq.(8). In the second term, κ is the convergence field along the line of sight to the source defined as $\kappa = \Sigma(\mathrm{s}')/\Sigma_{cr}$ at $\mathrm{s}' = (D_{LS}/D_S)\mathrm{s}_o$ with $\Sigma_{cr} = D_S/(4\pi D_L D_{LS})$. If the scale of the density fluctuation $\sim |\nabla_s^2\kappa/\kappa|^{-1/2}$ is much larger than the Fresnel scale $\sim [(D_L D_{LS}/D_S)\lambda]^{1/2}$, or if the geometrical optics is valid ($\omega \to \infty$), the third term is negligible. Then, the incident wave is magnified by $1 + \kappa$, which is consistent with the result in the weak gravitational lensing (e.g. Bartelmann & Schneider [2]). If $\kappa \ll 1$, the Born approximation is valid.

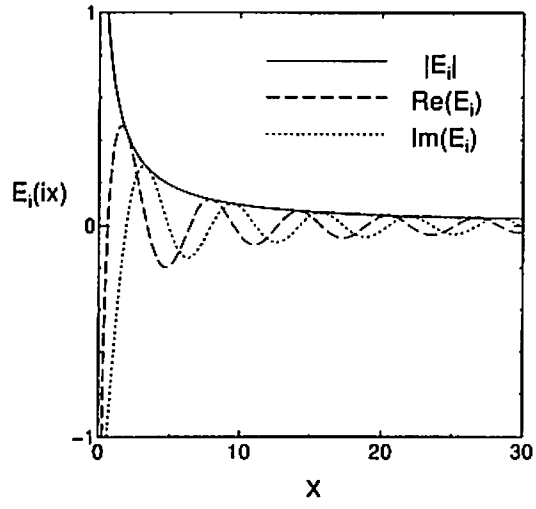


Figure 2: $Ei(ix)$ as a function of x. Solid line is the absolute value of Ei, dashed line is the real part, and dotted line is the imaginary part.

3 Conclusion

We have discussed the scattering of the gravitational waves by the weak gravitational fields of lens objects. We obtain the scattered gravitational waves by treating the gravitational potential of the lens to first order, i.e. the Born approximation. We consider the two simple lens models, the point mass lens and the smoothly distributed lens. We find that if the Schwartzchild radius of the lens is smaller than the wavelength of gravitational waves or if the impact parameter is larger than the Einstein radius, the Born approximation is valid. We also find that if the lens is smoothly distributed, the amplitude of the incident wave is magnified by $1+\kappa$ where κ is convergence, which is consistent with the result in weak gravitational lensing.

References

[1] Abramowitz, M. & Stegun, I.A., 1970, Handbook of Mathematical Functions, Dover Publications, New York

[2] Bartelmann, M. & Schneider, P., 2001, Physics Reports, 340, 291

[3] Bontz, R.J. & Haugan, M.P., 1981, Ap & SS, 78, 199

[4] Cutler, C. & Thorne, K.S., 2002, in Early Universe and Cosmological Observations: A critical Review, ed. Dunsby, P., Ellis, G.F.R., & Maartens, R., (Bristol:IOP), 72

[5] Deguchi, S. & Watson, W.D., 1986, PRD, 34, 1708

[6] Peters, P.C., 1974, PRD, 9, 2207

[7] Schneider, P., Ehlers, J. & Falco, E.E., 1992, Gravitational Lenses, Springer, New York

S-branes from multi-black holes

Kenji Sakamoto[1]

Department of Physics,
Osaka University,
Toyonaka, Osaka 560-0043, Japan

Abstract

We consider the non-singular and time-dependent solutions introduced from the multi-black holes. It is known that the solution constructed by double Wick rotation of black dihole is one of the non-singular s-brane solutions. In our study, we consider the double Wick rotation of black dihole solutions with unbalanced magnetic charges. We study the properties of these solutions and discuss the s-charge over a constant time-slice.

1 Introduction

Recently, the exact solutions of Einstein-Maxwell equation that describe the static pairs of oppositely charged extremal black holes (black diholes) have attracted much attention [1, 2]. By double Wick rotation for black diholes, the non-singular and time-dependent solution was constructed [3]. This solution is one of the s-brane type solutions. It is found that this s-brane is corresponding to the one type of s-diholes discussed in [4].

In this work, we consider the non-singular and time-dependent solutions introduced with double Wick rotating multi-black holes. Jones et al. discussed the s-brane solutions constructed from the black diholes which have the same magnitude and opposite magnetic charge [3]. In our study, we consider the double Wick rotation of the black dihole solutions with the unbalanced magnetic charge, such as the different magnitude and opposite magnetic charge. The obtained solutions contain the NUT-parameter which represents the total magnitude. For the solutions with NUT-parameter, we discuss the singularity and s-charge. Then we obtain the new s-brane solutions.

2 Black Diholes with unbalanced magnetic charges

The solutions of black diholes with unbalanced magnetic charges are discussed by Liang and Teo [5]. We consider the static, axisymmetric solution of the Einstein-Maxwell-Dilaton system. The black dihole solution is represented by

$$ds^2 = \Lambda^{\frac{2}{1+a^2}}\left(-dt^2 + \frac{\Sigma^{\frac{1}{1+a^2}}}{(\Delta+(m^2+a^2-l^2)\sin^2\theta)^{\frac{3-a^2}{1+a^2}}}\left(\frac{dr^2}{\Delta}+d\theta^2\right)\right) + \frac{\Delta\sin^2\theta}{\Lambda^{\frac{2}{1+a^2}}}d\varphi^2, \tag{1}$$

and $U(1)$ gauge field and dilaton field are following form:

$$A = -\frac{2}{\sqrt{1+a^2}}\frac{a(mr-l^2)\sin^2\theta + l\Delta\cos\theta}{\Delta + a^2\sin^2\theta}d\varphi, \tag{2}$$

$$\phi = -\frac{a}{1+a^2}ln\left(\frac{\Delta+a^2\sin^2\theta}{\Sigma}\right), \tag{3}$$

where

$$\Delta = r^2 - 2mr - a^2 + l^2, \quad \Sigma = r^2 - (a\cos\theta + l)^2, \quad \Lambda = \frac{\Delta + a^2\sin^2\theta}{\Sigma}. \tag{4}$$

[1]E-mail:sakamoto@het.phys.sci.osaka-u.ac.jp

Here, a is a measure of the distance between the two singularity (which represent two black holes) and l is the NUT-parameter, represents the monopole field strength of the solution at far field. This solution describes a pair of extremal dilatonic black holes with unbalanced charges lying on the symmetry axis. The outermost curvature singularities (black holes) are located at $r = r_+ \equiv m + \sqrt{m^2 + a^2 - l^2}$ and $\theta = 0, \pi$. From the asymptotic behavior A_φ and g_{tt}, the total mass is $M = 2m/(1 + a^2)$ and the net magnetic charge is $Q = 2l/\sqrt{1 + a^2}$. In the case of $l = 0$ and $a = 0$, this solution becomes the black magnetic diholes solution studied by Emparan [1]. The solution for $a \to \infty$ represents the extremal dilatonic black holes [6].

3 S-dihole solutions

We consider new non-singular, time-dependent solutions which arise by the double Wick rotating black dihole solutions. Depending on the way of the double Wick rotation, there are two types of spacelike brane solutions, S-dihole I and S-dihole II. The difference of two solutions are appeared in the spacetime structure [4]. Sending mass parameter $m \to im$ and NUT parameter $il \to l$ for S-dihole I produces S-dihole II solution.

3.1 S-dihole I in Weyl form

By the Weyl coordinates ρ, z and φ, we consider S-dihole solutions. The coordinate transformations between r, θ and Weyl coordinates is

$$\rho = \sqrt{r^2 - 2mr - a^2 + l^2}\sin\theta \quad = \sqrt{\Delta}\sin\theta, \tag{5}$$

$$z = (r - m)\cos\theta, \tag{6}$$

and the coordinate φ is not shifted.
One of the non-singular and time-dependent solution is constructed by double Wick rotation,

$$t \to iy\,, \quad z \to i\tau \quad l \to il. \tag{7}$$

Then, the metric is the following form:

$$ds^2 = \frac{1}{f}\left(\rho^2 d\varphi^2 + e^{2\gamma}(d\rho^2 - d\tau^2)\right) + f dy^2, \tag{8}$$

where

$$R = \sqrt{\rho^2 - (\tau + i\sqrt{m^2 + a^2 + l^2})^2}, \tag{9}$$

$$f = \left[\frac{(\mathrm{Re}R)^2 - m^2 - l^2 + \frac{a^2}{m^2+a^2+l^2}(\mathrm{Im}R)^2}{(\mathrm{Re}R + m)^2 + \{\frac{a}{\sqrt{m^2+a^2+l^2}}(\mathrm{Im}R) - l\}^2}\right]^{\frac{2}{1+a^2}}, \tag{10}$$

$$e^{2\gamma} = \left[\frac{(\mathrm{Re}R)^2 - m^2 - l^2 + \frac{a^2}{m^2+a^2+l^2}(\mathrm{Im}R)^2}{|R|^2}\right]^{\frac{1}{1+a^2}}. \tag{11}$$

$$\tag{12}$$

The gauge field and dilaton field are written by

$$A = \frac{2}{\sqrt{1+a^2}\left[-(\mathrm{Re}R)^2 + m^2 + l^2 - \frac{a^2}{m^2+a^2+l^2}(\mathrm{Im}R)^2\right]} \tag{13}$$

$$\times\left[\left\{am(\mathrm{Re}R + m) + al^2\right\}\left(1 + \frac{(\mathrm{Im}R)^2}{m^2 + a^2 + l^2}\right) + \frac{l(\mathrm{Im}R)\left\{(\mathrm{Re}R)^2 - (m^2 + a^2 + l^2)\right\}}{\sqrt{m^2 + a^2 + l^2}}\right] d\varphi, \tag{14}$$

$$\phi = -\frac{a}{1+a^2} ln\left[\frac{(\mathrm{Re}R)^2 - m^2 - l^2 + \frac{a^2}{m^2+a^2+l^2}(\mathrm{Im}R)^2}{(\mathrm{Re}R + m)^2 + \{\frac{a}{\sqrt{m^2+a^2+l^2}}(\mathrm{Im}R) - l\}^2}\right]. \tag{15}$$

In the case of $l = 0$, this solution becomes to the s-brane solution discussed by Jones et al. [3]. Our solution (8)-(15) is the expansion of their solution.

3.2 S-dihole II form

Other solution is constructed by following double Wick rotation:

$$t \to iy\,, \quad z \to i\tau \quad m \to im. \tag{16}$$

In this case, we can replace $R_- \to -R_-$ from the symmetry of equation of motion. The metric is represented by

$$ds^2 = \frac{1}{f}\left(\rho^2 d\varphi^2 + e^{2\gamma}(d\rho^2 - d\tau^2)\right) + f dy^2, \tag{17}$$

where

$$R = \sqrt{\rho^2 - (\tau + i\sqrt{a^2 - m^2 - l^2})^2}, \tag{18}$$

$$f = \left[\frac{(\mathrm{Im}R)^2 - m^2 - l^2 + \frac{a^2}{a^2-m^2-l^2}(\mathrm{Re}R)^2}{(\mathrm{Im}R + m)^2 + \{\frac{a}{\sqrt{a^2-m^2-l^2}}(\mathrm{Re}R) + l\}^2}\right]^{\frac{2}{1+\alpha^2}}, \tag{19}$$

$$e^{2\gamma} = \left[\frac{(\mathrm{Im}R)^2 - m^2 - l^2 + \frac{a^2}{a^2-m^2-l^2}(\mathrm{Re}R)^2}{|R|^2}\right]^{\frac{\alpha}{1+\alpha^2}}, \tag{20}$$

and

$$A = \frac{-2}{\sqrt{1+\alpha^2}\left[(\mathrm{Im}R)^2 - m^2 - l^2 + \frac{a^2}{a^2-m^2-l^2}(\mathrm{Re}R)^2\right]} \tag{21}$$

$$\times\Big[\left\{am(\mathrm{Im}R + m) + al^2\right\}\left(1 - \frac{(\mathrm{Re}R)^2}{a^2 - m^2 - l^2}\right) + \frac{l(\mathrm{Re}R)\left\{(\mathrm{Im}R)^2 + (a^2 - m^2 - l^2)\right\}}{\sqrt{a^2 - m^2 - l^2}}\Big]d\varphi, \tag{22}$$

$$\phi = -\frac{\alpha}{1+\alpha^2} ln\left[\frac{(\mathrm{Im}R)^2 - m^2 - l^2 + \frac{a^2}{a^2-m^2-l^2}(\mathrm{Re}R)^2}{(\mathrm{Im}R + m)^2 + \{\frac{a}{\sqrt{a^2-m^2-l^2}}(\mathrm{Re}R) + l\}^2}\right]. \tag{23}$$

The difference between S-dihole I (8)-(15) and S-dihole II (17)-(23) is appeared in the spacetime structure [4]. It is expected that the S-dihole II solution is more complicated than S-dihole I. We consider the behaviors of our solution with S-dihole I solution (8)-(15).

4 Numerical results

The behaviors of solution (8)-(15) are shown in Figure 1 for typical values of a, m, l and α. The S-dihole I solution is asymptotically flat at large radius, or in the far past or future. These components are non-singular. Outside the light cone $\rho^2 = t^2$, the fields are connected to the Minkowski space. The shape of gravitational potential g_{tt} crossing the light cone is indicating the gravitational forces which an observer feels in the case of s-brane solutions.

5 S-charge

The s-charge of S-dihole I is computed in Weyl coordinates over a constant τ slice.

$$Q_s = \frac{1}{\sqrt{1+\alpha}}\left(\frac{m}{a}\sqrt{m^2 + a^2 + l^2} + \frac{m^2}{a} + \frac{l^2}{a}\right). \tag{24}$$

This s-charge is conserved over constant τ slice. In the case of $l = 0$, (24) is equal to the s-charge obtained from the black diholes with balanced magnetic charge [3].

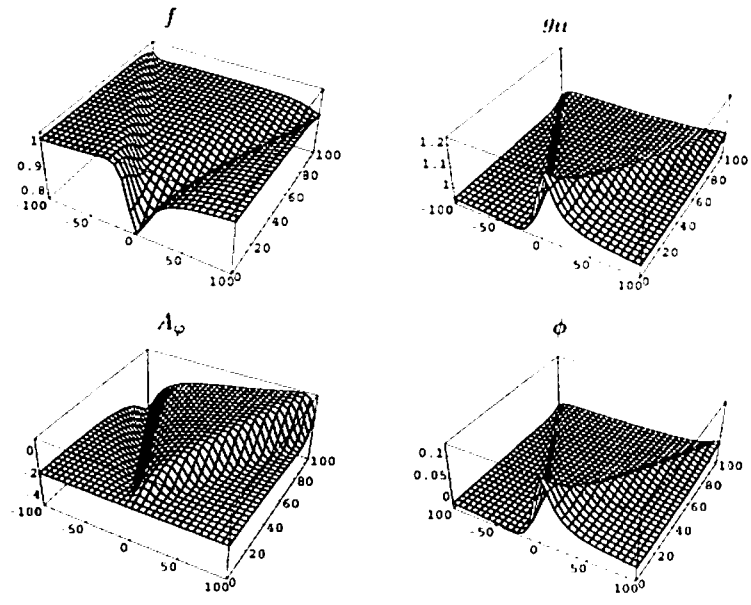


Figure 1: The behaviors of S-dihole I solution for typical values of the parameter.

6 Conclusion

We obtained the exact, non-singular and time-depending solutions. The s-charges of our solutions are conserved over constant time slice. We consider that this metric is represented one of the s-brane solutions, constructed from the black diholes with the unbalanced magnetic charges. The NUT-parameter l is represented the net magnetic charge of black diholes. In the case of no dilaton and $l = 0$, our solution is represented the s-brane solution reported by Jones et al. [4], where the s-brane solutions constructed form the black diholes. Our s-brane solutions are depending on the magnetic charge. In further study, we would like to consider the dependence of s-brane solution for the magnetic charge. Also, the double Wick rotation for static line array of alternating-charge Reissner-Nordström black holes yields s-brane solution. The relevance of these solutions to string theory is discussed in [4] (and see [7]). The extension to array solutions for our work should be discussed.

References

[1] R. Emparan, Phys. Rev. D **61**, 104009 (2000).

[2] R. Emparan and E. Teo, Nucl. Phys. B **610**, 190 (2001)

[3] G. Jones, A. Maloney and A. Strominger, Phys. Rev. D **69**, 126008 (2004)

[4] G. Jones and J. E. Wang,

[5] Y. C. Liang and E. Teo, Phys. Rev. D **64**, 024019 (2001)

[6] G. W. Gibbons and K. i. Maeda, Nucl. Phys. B **298**, 741 (1988).

[7] A. Biswas, Phys. Lett. B **600**, 157 (2004).

A New Formula for the Spectrum of Curvature Perturbations Produced from Inflation

Shuichiro Yokoyama[1], Takahiro Tanaka[2], Misao Sasaki[3], Jinn-Ouk Gong[4] and Ewan D. Stewart[5]

[1,2] *Theoretical Astrophysics Group, Department of Physics, Kyoto University, Kyoto 606-8502, Japan*
[3] *Yukawa Institute for Theoretical Physics, Kyoto University, Kyoto 606-8502, Japan*
[4,5] *Department of Physics, KAIST, Daejeon 305-701, Republic of Korea*

Abstract

We derive a new analytic hybrid formula for the spectrum of the curvature perturbations, which combines the general slow-roll approximation and the long-wavelength approximation. We assume that the general slow-roll approximation is valid until a time, η_*, shortly after the horizon crossing time, and we use the long-wavelength approximation from η_* to the time when inflation ends, $\eta_{\rm fin}$. We find it quite convenient to make use of the constancy of Wronskian to obtain a hybrid formula. This formula to evaluate the spectrum of initial curvature perturbations applies for a wider class of inflation models, and it will give a unified picture to generalization of slow roll formula.

1 Introduction

Inflation [1] provides an elegant mechanism to solve shortcomings of the standard Big Bang Model, say, flatness and horizon problems. Moreover, inflation can seed initial curvature perturbations, which are required to explain large-scale structure formation. Also, to test various models of inflation, it is important to compare theoretical prediction for the spectrum of curvature perturbations with observations. In single-field slow-roll inflation models, the spectrum of curvature perturbations evaluated on comoving hypersurfaces, $\mathcal{R}_c$, is given by

$$\mathcal{P}_{\mathcal{R}_c} \simeq \left(\frac{H^2}{\dot{\phi}}\right)^2_{t_k}, \tag{1}$$

where H is the Hubble parameter, $\dot{\phi}$ is the derivative of the inflaton ϕ with respect to the cosmological proper time, and the subscript t_k means that the expression is to be evaluated at the horizon crossing time, t_k. However, various inflation models which violate the slow-roll conditions have been proposed. Furthermore, in the context of building realistic models of particle physics based on supersymmetry and supergravity theories, it is natural to consider multi-component scalar fields. To identify conditions for viable models of inflation among various possibilities, it is useful if we know an analytic formula for the spectrum applicable to a wide class of models. There are several works aiming at generalizing the above slow-roll formula (1). Leach, Sasaki, Wands and Liddle [2] have analyzed the evolution of curvature perturbations on superhorizon scales (the long-wavelength approximation). They have found that the curvature perturbations can be enhanced when $z \equiv a\dot{\phi}/H$ decreases after the horizon crossing time t_k. This situation can happen if slow-roll conditions are violated for $t > t_k$. Stewart [3] have generalized the standard formula removing the extra assumption, necessary to obtain (1), that slow-roll parameters are approximately scale invariant (general slow-roll approximation). This generalization is motivated to explain the recently suggested running of spectral index. Under the assumptions which lead to the standard slow-roll formula (1), the running of spectrum is automatically suppressed as $dn_{\mathcal{R}_c}/d\ln k \ll |n_{\mathcal{R}_c} - 1|$, while in the general slow-roll approximation $dn_{\mathcal{R}_c}/d\ln k$ and $|n_{\mathcal{R}_c} - 1|$ can be same order. In this work, we derive a new formula for the spectrum applicable to a wider class of inflation models which

[1] E-mail:shu@tap.scphys.kyoto-u.ac.jp
[2] E-mail:tama@scphys.kyoto-u.ac.jp
[3] E-mail:misao@yukawa.kyoto-u.ac.jp
[4] E-mail:jwGong@muon.kaist.ac.kr
[5] E-mail:stewart@hep.kaist.ac.kr

takes advantage of both the long-wavelength approximation and the general slow-roll approximation. We assume that the general slow-roll approximation is valid until a time, $t_*(> t_k)$, and we use the long-wavelength approximation for the succeeding evolution until the end of inflation, $t_{\rm fin}$. We briefly explain the method to combine two different approximations. The details will be presented in a longer paper.

2 Formulation

We consider inflation model composed of a single scalar field. The background flat Friedmann metric is given by

$$ds^2 = a^2(\eta)\left(-d\eta^2 + \delta_{ij}dx^i dx^j\right). \tag{2}$$

In the following discussion we use conformal coordinate η instead of the cosmological proper time t. The equation for $\delta\phi_f$, perturbations of the inflaton field on the spatially flat hypersufaces, is given by

$$\begin{aligned} u''(\eta) + \left(k^2 - \frac{2}{\eta^2}\right)u(\eta) &= \frac{g(\eta)}{\eta^2}u(\eta)\,, \\ g(\eta) &\equiv \eta^2\frac{z''}{z} - 2, \end{aligned} \tag{3}$$

where $u \equiv a\delta\phi_f$, the prime denotes ∂_η, k is the comoving wavenumber, and $z \equiv a\dot{\phi}/H$.

Let $n(\eta)$ be a solution for Eq. (3) obtained by using the long-wavelength approximation. The solution is described in an expansion with respect to k^2 ;

$$n^{(q)} \equiv n^{(0)} + \sum_{i=1}^{q} k^{2i}\delta n^{(i)} = n^{(q-1)} + k^{2q}\delta n^{(q)}. \tag{4}$$

Each $n^{(i)}$ and $\delta n^{(j)}$ satisfies

$$\left(\partial_\eta^2 - \frac{z''}{z}\right)n^{(0)} = 0\,, \quad \left\{\partial_\eta^2 + \left(k^2 - \frac{z''}{z}\right)\right\}n^{(q)} = k^2\delta n^{(q)}\,. \tag{5}$$

A single solution is selected by imposing conditions

$$n(\eta_{\rm fin}) \equiv 0\,, \quad n'(\eta_{\rm fin}) \equiv -1/z(\eta_{\rm fin})\,, \tag{6}$$

at the end of inflation. Later we will explain the reason why we impose these conditions. To the first order in k^2, we have

$$\begin{aligned} n^{(1)} &= n^{(0)} + k^2\delta n^{(0)} \\ &= -z(\eta)\int_{\eta_{\rm fin}}^{\eta}\frac{d\eta'}{z^2(\eta')} + k^2 z(\eta)\int_{\eta_{\rm fin}}^{\eta} d\eta'\frac{I(\eta')}{z^2(\eta')}\,, \\ I(\eta) &\equiv \int_{\eta_{\rm fin}}^{\eta} d\eta' z^2(\eta')\int_{\eta_{\rm fin}}^{\eta'}\frac{d\eta''}{z^2(\eta'')}\,. \end{aligned} \tag{7}$$

Let φ be a solution for Eq. (3) obtained by using the general slow-roll approximation. Since $|g| \ll 1$ by assumption in the general slow-roll approximation, the solution will be described in an expansion with respect to g;

$$\varphi_p \equiv \varphi_0 + \sum_{j=1}^{p}\delta\varphi_j = \varphi_{p-1} + \delta\varphi_p, \tag{8}$$

where $\delta\varphi_p$ is $O(g^p)$. φ_i and $\delta\varphi_j$ respectively satisfy

$$\left(\partial_\eta^2 + k^2 - \frac{2}{\eta^2}\right)\varphi_0 = 0 \qquad \text{and} \qquad \left(\partial_\eta^2 - \frac{2}{\eta^2} + k^2 - \frac{g(\eta)}{\eta^2}\right)\varphi_p = -\frac{g(\eta)}{\eta^2}\delta\varphi_p\,. \tag{9}$$

The lowest order mode function φ_0 can be easily solved as

$$\varphi_0 = -\frac{i}{\sqrt{2k^3}}\left(ik + \frac{1}{\eta}\right)\mathrm{e}^{-ik\eta} \ . \tag{10}$$

Here we have chosen φ_0 which corresponds to the positive frequency function of the Bunch-Davies vacuum. Using the Green's function method, we obtain the solution of Eq. (3) to the linear order in g as

$$\begin{aligned}\varphi_1(\eta) &= \varphi_0(\eta) \\ &\quad + W(\varphi_0^*, \varphi_0)^{-1}\left[\varphi_0(\eta)\int_{\eta_{\rm in}}^{\eta} d\eta' \frac{g(\eta')}{\eta'^2}\varphi_0(\eta')\varphi_0^*(\eta') - \varphi_0^*(\eta)\int_{\eta_{\rm in}}^{\eta} d\eta' \frac{g(\eta')}{\eta'^2}\varphi_0(\eta')\varphi_0(\eta')\right], \end{aligned} \tag{11}$$

where $W(\varphi_0^*, \varphi_0) \equiv \varphi_0^*\varphi_0' - \varphi_0^{*\prime}\varphi_0$.

If both n and φ exactly satisfy the same equation (3), the Wronskian $W(n, \varphi)$ is constant. Evaluating this Wronskian at $\eta = \eta_{\rm fin}$, we immediately find that the conditions (6) imply $\mathcal{R}_{\rm c}(\eta_{\rm fin}) = -\varphi(\eta_{\rm fin})/z(\eta_{\rm fin}) = W(\eta_{\rm fin})$. Since both g-expansion and k^2-expansion are valid at $\eta = \eta_*$, we can evaluate $W(n, \varphi)$ there by using approximate solutions φ_p and $n^{(q)}$.

3 Results

To the first order in g and to the q-th order in k^2, we have

$$\begin{aligned}\mathcal{R}_{\rm c}(\eta_{\rm fin})_1^{(q)} = W(\eta_*)_1^{(q)} &= W(\varphi_1, n^{(q)})|_{\eta_*} \\ &= W(\varphi_0, n^{(q)})|_{\eta_*} \\ &\quad + W(\varphi_0^*, \varphi_0)^{-1}\left[W(\varphi_0, n^{(q)})|_{\eta_*}\int_{\eta_{\rm in}}^{\eta_*} d\eta' g(\eta')\varphi_0^*(\eta')\varphi_0(\eta')\right. \\ &\qquad \left. - W(\varphi_0^*, n^{(q)})|_{\eta_*}\int_{\eta_{\rm in}}^{\eta_*} d\eta' g(\eta')\varphi_0(\eta')\varphi_0(\eta')\right] , \end{aligned} \tag{12}$$

where $f^{(q)}$ means truncation of f at $\mathcal{O}(k^{2q})$ and f_1 means truncation of f at $\mathcal{O}(g)$.

To compare our formula with the standard slow-roll one (1), we want to obtain a formula in which the leading term is evaluated not at η_* but at η_k. Such a formula is found to be given by

$$\begin{aligned}\mathcal{R}_{\rm c}(\eta_{\rm fin})_1^{(q)} &\equiv W(\varphi_0, n)^{(q)}|_{\eta_k} \\ &\quad + \left[W(\varphi_0^*, \varphi_0)^{-1}\left\{W(\varphi_0, n)_{\eta_k}\int_{\eta_{\rm in}}^{\eta_*} d\eta' g(\eta')\left(\tilde{\varphi}_0^*(\eta')\tilde{\varphi}_0(\eta') - \theta(\eta' - \eta_k)\left[\varphi_0^*(\eta')\varphi_0(\eta')\right]\right)\right.\right. \\ &\qquad \left.\left. - W(\varphi_0^*, n)_{\eta_k}\int_{\eta_{\rm in}}^{\eta_*} d\eta' g(\eta')\left(\tilde{\varphi}_0(\eta')\tilde{\varphi}_0(\eta') - \theta(\eta' - \eta_k)\left[\varphi_0(\eta')\varphi_0(\eta')\right]\right)\right\}\right]^{(q)} , \end{aligned} \tag{13}$$

where the quantity with $\tilde{}$ means that it is not to be truncated even if operation "(q)" acts on it. The appearance of the additional terms proportional to step function $\theta(\eta' - \eta_k)$) is the price to pay to shift the time to evaluate the leading term to the crossing time η_k. From Eqs. (7) and (10), to the first order in g and k^2, the above formula (13) is more explicitly written as

$$\begin{aligned}\mathcal{P}_{\mathcal{R}_c} &\simeq \left[\left\{\alpha^2 + 2k^2\alpha\beta\right\}_{\eta_k}\right. \\ &\quad -\frac{2}{3}\left\{\alpha^2 + 2k^2\alpha\beta\right\}_{\eta_k}\int_{\eta_{\rm in}}^{\eta_*} d\eta' \frac{g(\eta')}{\eta'}\left(\mathrm{Re}[U(\eta')] - \theta(\eta' - \eta_k)\mathrm{Re}[U(\eta')]^{(1)}\right) \\ &\quad \left. +2\left\{\alpha\gamma + k^2(\alpha\sigma + \beta\gamma)\right\}_{\eta_k}\int_{\eta_{\rm in}}^{\eta_*} d\eta' \frac{g(\eta')}{\eta'^4}\left(\mathrm{Re}[V(\eta')] - \theta(\eta' - \eta_k)\mathrm{Re}[V(\eta')]^{(1)}\right)\right] , \end{aligned} \tag{14}$$

where

$$\begin{aligned}
\alpha(\eta) &\equiv -\frac{1}{\eta}n^{(0)\prime} - \frac{1}{\eta^2}n^{(0)}\ , \quad \beta(\eta) \equiv -\frac{\eta}{2}n^{(0)\prime} + \frac{1}{2}n^{(0)} - \frac{1}{\eta}\delta n^{(1)\prime} - \frac{1}{\eta^2}\delta n^{(1)}\ , \\
\gamma(\eta) &\equiv -\frac{\eta^2}{3}n^{(0)\prime} + \frac{2\eta}{3}n^{(0)}\ , \quad \sigma(\eta) \equiv \frac{\eta^4}{30}n^{(0)\prime} - \frac{2\eta^3}{15}n^{(0)} - \frac{\eta^2}{3}\delta n^{(1)\prime} + \frac{2\eta}{3}\delta n^{(1)}\ , \\
U(\eta) &\equiv -\frac{3i}{2\eta}\left(\varphi_0\varphi_0^* + \varphi_0\varphi_0\right) = 1 + \frac{2}{5}k^2\eta^2 + \cdots\ , \\
V(\eta) &\equiv k^3\eta^2\left(\varphi_0\varphi_0^* - \varphi_0\varphi_0\right) = 1 + k^2\eta^2 + \cdots\ .
\end{aligned} \tag{15}$$

Also, it will be worth pointing out that the general slow-roll approximation is valid under even weaker conditions than those assumed in Ref. [3]. We can rewrite $g = \eta^2 z''/z - 2$ as

$$\begin{aligned}
\eta^2 &= \frac{1}{a^2H^2}\left(1 + 2\epsilon + \mathcal{O}(\epsilon^2)\right), \\
\frac{z''}{z} &= 2a^2H^2\left(1 - \frac{V_{\phi\phi}}{2H^2} - \frac{V_\phi}{H^3}\dot{\phi} - \frac{13}{4H^2}\dot{\phi}^2 + \frac{1}{4H^4}\dot{\phi}^4\right).
\end{aligned} \tag{16}$$

and $\epsilon \equiv -\dot{H}/H^2$, $\delta \equiv \ddot{\phi}/H\dot{\phi}$ are slow-roll parameters . When the background scalar field motion stops ($\dot{\phi} \simeq 0$), a slow-roll parameter δ diverges. In such a situation, slow-roll conditions are violated. However, from Eq. (16), we can easily find that as far as $V_{\phi\phi}/H^2 \ll 1$ the condition $|g| \ll 1$ is still satisfied when $\dot{\phi} \simeq 0$.

4 Summary

We have derived a new analytic formula for the spectrum of curvature perturbations, combining the long-wavelength approximation and the general slow-roll one. We found that derivation of the formula simplifies a lot by using the constancy of the Wronskian. In Ref. [3] the general slow-roll approximation was assumed to be valid until the time when inflation ends, while here it is assumed to be valid until a time shortly after the horizon crossing time η_k. In the formula (13), integrand takes the form of $f - \theta(\eta - \eta_k)f^{(q)}$, and hence the integrand shows improved fall-off behavior in the limit $\eta \to 0$ since the leading terms up to $O(k^{2q})$ all cancel. Hence, even if fall-off of g is not very fast, we can push the evaluation time η_* to 0 for a sufficiently large q. We have also confirmed that this formula indeed includes the standard formula, the general slow-roll formula and the correction due to long-wavelength evolution. Additionally, we have found that the general slow-roll approximation is valid even when $\dot{\phi} \simeq 0$ ($\delta \to \infty$). Here, we considered only models composed of a single scalar field. However, we can extend the formula to the case of multi-components and also to the higher order in g in a parallel way. This formula will be useful to evaluate the initial power spectrum for a wider class of inflation models.

References

[1] A. H. Guth, Phys. Rev. D **23**, 347 (1981),
K. Sato, Phys. Lett. B **99** (1981) 66; Mon. Not. R. Astron. Soc. **195** (1981) 467.

[2] S. M. Leach, M. Sasaki, D. Wands and A. R. Liddle, Phys. Rev. D **64**, 023512 (2001).

[3] E. D. Stewart, Phys. Rev. D **65**, 103508 (2002),
J. Choe, J. O. Gong and E. D. Stewart, JCAP **0407**, 012 (2004) .

Gravitational Radiation from Coalescence of Binary Neutron Stars — Gauge-Invariant Wave Form Extraction —

Mari Kawamura[1] , Ken-ichi Oohara[2]

[1] *Theoretical Astrophysics Group, Department of Physics, Kyoto University, Kyoto, 606-8502, Japan*
[2] *Department of Physics, Niigata University, Niigata, 950-2181, Japan*

Abstract

We report application of a method for extracting gravitational waves to three-dimensional numerical simulation on coalescing binary neutron stars. We found the extracted wave form includes the components corresponding to the quadrupole part in the Newtonian potential of the background metric, if it is monitored at a position not far from the central stars. We present how to eliminate it.

1 Basic Equations

We are constructing computer codes on three-dimensional numerical relativity.[1, 2] At first we used the conformal slicing condition, in which the metric becomes the Schwarzschild one in the outer vacuum region so that if the three-metric is split into the Schwarzschild background and the perturbed parts, the latter can be considered as the gravitational waves at the wave zone.[3] However, it was found that this slicing involves unstable modes and long-term evolution of coalescing binary neutron star cannot be followed.[1, 4] Then we started to construct a new code using the maximal slicing condition. In this slicing, the perturbed part of the three-metric includes gauge dependent modes and therefore we need gauge-invariant wave extraction. Recently gauge-invariant wave extraction methods have been given as nonspherical perturbations of Schwarzschild geometry.[5, 6, 7, 8] In this letter, we report application of a method based on them to three-dimensional general relativistic simulation on coalescing binary neutron stars.

We use (3+1)-formalism of the Einstein equation and write the line element as $ds^2 = -\alpha^2 dt^2 + \gamma_{ij}(dx^i+\beta^i dt)(dx^j+\beta^j dt)$. Outside of the star, we split the total spacetime metric $g_{\mu\nu}$ into a Schwarzschild background and non-spherical perturbation parts: $g_{\mu\nu} = g^{(B)}_{\mu\nu} + h^{(e)}_{\mu\nu} + h^{(o)}_{\mu\nu}$, where $g^{(B)}_{\mu\nu}$ is a spherically symmetric metric given by

$$g^{(B)}_{\mu\nu}dx^\mu dx^\nu = -N^2dt^2 + A^2dr^2 + R^2(d\theta^2 + \sin^2\theta d\phi^2) \tag{1}$$

and $h^{(e)}_{\mu\nu}$ and $h^{(o)}_{\mu\nu}$ are even-parity and odd-parity metric perturbations, respectively:

$$h^{(e)}_{\mu\nu} = \sum_{lm}\begin{pmatrix} N^2H_{0lm}Y_{lm} & H_{1lm}Y_{lm} & h^{(e)}_{0lm}Y_{lm,\theta} & h^{(e)}_{0lm}Y_{lm,\phi} \\ * & A^2H_{2lm}Y_{lm} & h^{(e)}_{1lm}Y_{lm,\theta} & h^{(e)}_{1lm}Y_{lm,\phi} \\ * & * & r^2[K_{lm} + G_{lm}\frac{\partial^2}{\partial\theta^2}]Y_{lm} & r^2G_{lm}X_{lm} \\ * & * & * & h^{(e)}_{33} \end{pmatrix}, \tag{2}$$

$$h^{(e)}_{33} = r^2\sin^2\theta\left[K_{lm}Y_{lm} + G_{lm}\left(\frac{\partial^2}{\partial\theta^2}Y_{lm} - W_{lm}\right)\right] \tag{3}$$

$$h^{(o)}_{\mu\nu} = \sum_{lm}\begin{pmatrix} 0 & 0 & -h^{(o)}_{0lm}\frac{1}{\sin\theta}Y_{lm,\phi} & h^{(o)}_{0lm}\sin\theta Y_{lm,\theta} \\ 0 & 0 & -h^{(o)}_{1lm}\sin\theta Y_{lm,\phi} & h^{(o)}_{1lm}\sin\theta Y_{lm,\theta} \\ * & * & \frac{1}{2}h^{(o)}_{2lm}\frac{1}{\sin\theta}X_{lm} & -\frac{1}{2}h^{(o)}_{2lm}\sin\theta W_{lm} \\ * & * & * & -\frac{1}{2}h^{(o)}_{2lm}\sin\theta X_{lm} \end{pmatrix}. \tag{4}$$

[1] E-mail:mari@scphys.kyoto-u.ac.jp
[2] E-mail:oohara@astro.sc.niigata-u.ac.jp

where N^2, A^2, R^2, H_{1lm}, $h^{(e)}_{0lm}$, $h^{(e)}_{1lm}$, K_{lm}, G_{km}, $h^{(o)}_{0lm}$, $h^{(o)}_{1lm}$, and $h^{(o)}_{2lm}$ are the functions of t and r; Y_{lm} is the spherical harmonics and

$$X_{lm} = 2\left(\frac{\partial^2}{\partial\phi\partial\theta} - \cot\theta\frac{\partial}{\partial\phi}\right)Y_{lm}, \tag{5}$$

$$W_{lm} = \left(\frac{\partial^2}{\partial\theta^2} - \cot\theta\frac{\partial}{\partial\theta} - \frac{1}{\sin^2\theta}\frac{\partial^2}{\partial\phi^2}\right)Y_{lm}. \tag{6}$$

The symbol $*$ in Eqs.(2) and (4) indicates the symmetric components. From the linearized theory about perturbations of the Schwarzschild spacetime, the gauge invariant quantities $\Psi^{(o)}$ and $\Psi^{(e)}$ are given by

$$\Psi^{(o)}_{lm}(t,r) = \sqrt{2l(l+1)(l-1)(l+2)}N^2\frac{1}{r}\left(h^{(o)}_{1lm} + \frac{r^2}{2}\frac{\partial}{\partial r}\left(\frac{h^{(o)}_{2lm}}{r^2}\right)\right), \tag{7}$$

$$\Psi^{(e)}_{lm}(t,r) = -\sqrt{\frac{2(l-1)(l+2)}{l(l+1)}}\frac{4rN^2k_{2lm} + l(l+1)rk_{1lm}}{(l(l+1)+1-3N^2)}, \tag{8}$$

for the odd and even parity modes, respectively, where

$$k_{1lm} = K_{lm} + N^2rG_{lm,r} - 2\frac{N^2}{r}h^{(o)}_{1lm}, \tag{9}$$

$$k_{2lm} = \frac{H_{2lm}}{2N^2} - \frac{1}{\sqrt{N^2}}\frac{\partial}{\partial r}\left(\frac{r}{N^2}K_{lm}\right). \tag{10}$$

The quantities $\Psi^{(o)}$ and $\Psi^{(e)}$ satisfy the Regge-Wheeler and the Zerilli equations, respectively [10]. Two independent polarizations of gravitational waves h_+ and $h_\times$ are given by

$$h_+ - ih_\times = \frac{1}{\sqrt{2}r}\sum_{l,m}(\Psi^{(e)}_{lm}(t,r) + \Psi^{(o)}_{lm}(t,r))_{-2}Y_{lm}, \tag{11}$$

where

$$_{-2}Y_{lm} = \frac{1}{\sqrt{l(l+1)(l-1)(l+2)}}\left(W_{lm} - \frac{i}{\sin\theta}X_{lm}\right) \tag{12}$$

In numerical calculation, the functions $N^2(t,r)$, $A^2(t,r)$ and $R^2(t,r)$ of the background metric are calculated by performing the following integration over a two-sphere of radius r:

$$N^2(t,r) = -\frac{1}{4\pi}\int g_{tt}d\Omega, \tag{13}$$

$$A^2(t,r) = \frac{1}{4\pi}\int g_{rr}d\Omega, \tag{14}$$

$$R^2(t,r) = \frac{1}{8\pi}\int (g_{\theta\theta} + \frac{g_{\phi\phi}}{\sin^2\theta})d\Omega. \tag{15}$$

The components of the even parity metric perturbations are

$$H_{2lm}(t,r) = \frac{1}{A^2}\int g_{rr}Y^*_{lm}d\Omega, \tag{16}$$

$$G_{lm}(t,r) = \frac{1}{l(l-1)(l+1)(l+2)}\frac{1}{R^2}\int\left[\left(g_{\theta\theta} - \frac{g_{\phi\phi}}{\sin^2\theta}\right)W^*_{lm} + \frac{2g_{\theta\phi}}{\sin\theta}\frac{X^*_{lm}}{\sin\theta}\right]d\Omega, \tag{17}$$

$$K_{lm}(t,r) = \frac{1}{2}l(l+1)G_{lm} + \frac{1}{2R^2}\int\left(g_{\theta\theta} + \frac{g_{\phi\phi}}{\sin^2\theta}\right)Y^*_{lm})d\Omega, \tag{18}$$

$$h^{(e)}_{1lm}(t,r) = \frac{1}{l(l+1)}\int\left(g_{r\theta}Y^*_{lm,\theta} + \frac{g_{r\phi}}{\sin\theta}\frac{Y^*_{lm,\phi}}{\sin\theta}\right)d\Omega, \tag{19}$$

where $*$ denotes the complex conjugate. The components of odd parity metric perturbations are

$$h^{(o)}_{1lm}(t,r) = -\frac{1}{l(l+1)}\int\left(g_{r\theta}\frac{Y^*_{lm,\phi}}{\sin\theta} - \frac{g_{r\phi}}{\sin\theta}Y^*_{lm,\theta}\right)d\Omega, \tag{20}$$

$$h^{(o)}_{2lm}(t,r) = \frac{1}{l(l-1)(l+1)(l+2)}\int\left[\left(g_{\theta\theta} - \frac{g_{\phi\phi}}{\sin^2\theta}\right)\frac{X^*_{lm}}{\sin\theta} - \frac{2g_{\theta\phi}}{\sin\phi}W^*_{lm}\right]d\Omega. \tag{21}$$

2 Numerical results

We performed numerical simulation for a coalescing binary consisting of two identical neutron stars of mass $1.5M_\odot$ and evaluated the gravitational waves. The details of our code will be shown elsewhere[11] but it is essentially the same as Refs. [2] and [12]. The lapse function and the shift vector are determined by the maximal slicing and the pseudo-minimal distortion conditions, respectively. We used uniform $475 \times 475 \times 238$ Cartesian grid with $\Delta x = 1M_\odot$ assuming the symmetry with respect to the equatorial plane. As for an equation of state, we use the $\gamma = 2$ polytropic equation of state. The initial rotational velocity is given so that the circulation of the system vanishes. The ADM mass of the system is $2.8M_\odot$.

Figure 1 shows the gravitational wave forms rh_+ and $rh_\times$ on the z-axis evaluated at $r = 110, 120, 130$ and $140M_\odot$ as functions of the retarded time $t - r$. Here $t = 0$ is the initial time of the numerical simulation. The lines of $rh_{+,\times}(t-r)$ estimated at $r = 110 \sim 140M_\odot$ for $t - r \gtrsim 0$ coincide with each other. Then the waves proportional to r^{-1} and propagating at the speed of light are extracted. For $t - r \lesssim 0$, however, lines of $rh_{+,\times}(t-r)$ do not coincide with each other. Then we plot $r^3h_{+,\times}$ as a function of t in Fig. 2. In this figure, all the lines overlap each other for $t \lesssim 0.5$msec. It means that $h_{+,\times}$ includes a non-wave mode proportional to r^{-3}. This mode corresponds to the quadrupole part in the Newtonian potential of the background metric. It decreases fast as the merger of stars proceeds. For $t > r$, when the waves emitted at $t > 0$ in the central region arrive at the observer, the wave part dominate the none-wave part. Since this mode is proportional to r^{-3} while the wave mode is to r^{-1}, the former will be anyway negligible if the waves are monitored at a few times farther position.

By the way, h_+ and $h_\times$ include non-wave modes proportional to $O(\frac{1}{r^3})$. Therefore we eliminate non-wave modes from h_+ and $h_\times$ using fourier transformation as follows:

- Assuming that total waves are expressed as a sum of wave parts $\frac{F(t-r)}{r}$ and non-wave parts $\frac{G(t)}{r^3}$,

$$h(t,r) = \frac{F(t-r)}{r} + \frac{G(t)}{r^3}.$$

- Fourier components of $h(t,r)$ are written as

$$h_\omega(r) = \frac{\exp^{-i\omega r}}{r}F_\omega(r) + \frac{1}{r^3}G_\omega(r).$$

where

$$F_\omega \equiv \frac{1}{2\pi}\int F(t)\exp^{-i\omega t}dt,$$

$$G_\omega \equiv \frac{1}{2\pi}\int G(t)\exp^{-i\omega t}dt.$$

- From the values of $h_\omega(r)$ in different radial coodinates r_1 and r_2, F_ω can be expressed by

$$F_\omega = \frac{r_2^3h_\omega(r_2) - r_1^3h_\omega(r_1)}{r_2^2\exp^{-i\omega r_2} - r_1^2\exp^{-i\omega r_1}}.$$

- Gravitational wave's fourier components $\hat{h}_\omega(r)$ are expressed as

$$\hat{h}_\omega(r_k) \equiv \frac{\exp^{-i\omega r_k}}{r_k}F_\omega, \quad k = 1, 2.$$

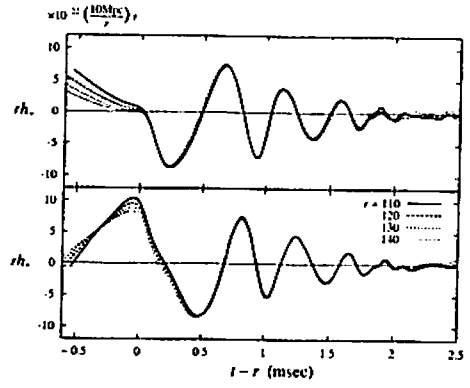


Figure 1: Plots $rh_{+,\times}$ along z-axis at $r = 110 \sim 140M_\odot$ as a function of $t - r$.

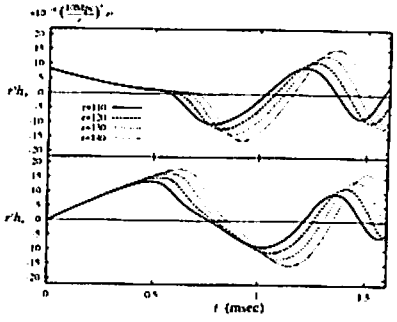


Figure 2: Plots $r^3 h_{+,\times}$ as a function of t.

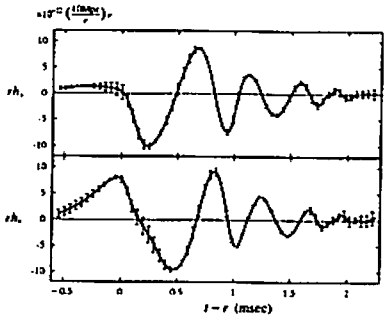


Figure 3: Wave forms $rh_{+,\times}$ along z-axis as a function of $t - r$. The curves are averages of $rh_{+,\times}$ estimated at $r = 110 \sim 200M_\odot$ and error bars denote 2σ.

- By inverse fourier transformation of $\hat{h}_\omega(r)$, we can get the gravitational waves, which are eliminated non-wave modes,

$$h_+(t,r) - ih_\times(t,r) = \int \hat{h}_\omega(r) \exp^{i\omega t} d\omega.$$

The resultant wave form is shown in Fig.3. The curves represent the average of h_+ and $h_\times$ calculated at $r = 110, 120, \cdots 200M_\odot$ and twice the dispersion 2σ is shown as error bars.

Acknowledgment

Numerical computations were carried out on SR8000/F1 at Hight Energy Accelerator Research Organization(KEK) as the Supercomputer Project and on VPP5000 at the Astronomical Data Analysis Center of the National Astronomical Observatory Japan(NAO). This work was in part supported by Grand-in-Aid 13640271 for Scientific Research from the Ministry of Education, Science and Culture of Japan.

References

[1] K. Oohara, T. Nakamura and M. Shibata, Prog. Theor. Phys. Suppl. **128** (1997), 183.

[2] K. Oohara and T. Nakamura, Prog. Theor. Phys. Suppl. **136** (1999), 270.

[3] M. Shibata and T. Nakamura, Prog. Theor. Phys. **88** (1992), 317.

[4] M. Shibata and T. Nakamura, Phys. Rev. D. **52** (1995). 5428.

[5] A. Abrahams and C. Evans, Phys. Rev. D. **36** (1988), 317.

[6] A. Abrahams and C. Evans, Phys. Rev. D. **42** (1990), 2585.

[7] A. Abrahams, D. Dernstein, D. Hobill and E. Seidel, Phys. Rev. Phys. Rev. D. **52** (1995), 5428.

[8] A. Abrahams *et al.*, Phys. Rev. Lett. **80** (1998), 1812.

[9] V. Moncrief, Ann. Phys. (N.Y.) **88** (1974), 322.

[10] F. J. Zerilli, Phys. Rev. Lett. **24** (1970), 737.

[11] M. Kawamura, K. Oohara and T. Nakamura, in preparation.

[12] K. Oohara and T. Nakamura, in proceedings of the Ninth Marcel Grossmann Meeting on General Relativity ed. by V.G. Gurzdyan, R.T. Jantzen, R. Ruffini (World Scientific, Singapore, 2002) 2295.

Probing gravitational-wave backgrounds with a space-based interferometer I

Hideaki Kudoh[1] and Atsushi Taruya[2]

[1] *Department of Physics, The University of Tokyo, Tokyo 113-0033, Japan*
[2] *Research Center for the Early Universe (RESCEU), School of Science, The University of Tokyo, Tokyo 113-0033, Japan*

Abstract

We discuss the sensitivity to anisotropies of stochastic gravitational-wave backgrounds (GWBs) observed via space-based interferometer. The anisotropies of the GWBs play a crucial role to discriminate various components of the GWBs. We study general features of antenna pattern sensitivity to the anisotropies of GWBs beyond the low-frequency approximation. We show that the sensitivity of space-based interferometer to GWBs is severely restricted by the data combinations and the symmetries of the detector configuration. The spherical harmonic analysis of the antenna pattern functions reveals that the angular power of the detector response increases with frequency. However, the cross correlation of optimal interferometric variables is blind to the monopole intensity anisotropy, and also to the dipole in some case, irrespective of the frequency band. Besides, all the self-correlated signals are shown to be blind to the odd multipole moments, independently of the frequency band.

1 Introduction

Space-based gravitational wave detectors retain many possibilities of providing access to new gravitational-wave sources that are not covered by ground-based gravitational-wave detectors. The Laser Interferometer Space Antenna (LISA) is such a planned gravitational-wave observatory aimed at detecting and studying low-frequency gravitational waves in the band 0.1 mHz $\sim$ 0.1Hz. The constellation of the LISA and the next generation detectors, e.g. DECIGO/BBO [1, 2], will consist of three spacecrafts keeping a triangle configuration.

So far most of the works aimed at probing the anisotropy of gravitational-wave background by means of space-based interferometers have been restricted to the low-frequency approximation. One reason is that a confusion gravitational-wave background formed by the superposition of many Galactic binaries comes in the low-frequency band of the LISA as the dominant source [3]. However there are many expected sources of gravitational-wave backgrounds that spread outside the low-frequency region. Thus it is an interesting problem to create maps of the gravitational-wave background in a very wide range of frequency. For that purpose we need to know the general response and properties of space-based interferometer over a wide range of frequency.

In this paper we are interesting in general features of response function for space-based detectors. The sensitivity of space-based detectors to multipole moments of a gravitational-wave distribution is in general restricted by symmetries of a response function independently of frequency. For example, symmetries of a response function tell us that a self-correlated data is blind to the odd multipole moments of anisotropy irrespective of frequency band. Other interesting features independent of frequency can be also derived based on symmetries of a detector's response and geometric configuration of the spacecrafts.

2 detection of anisotropy through the correlation analysis

We begin by discussing how one can prove the anisotropy of gravitational-wave background based on the correlation analysis. A stochastic background of gravitational waves can be expressed as a

[1] E-mail:kudoh at utap.phys.s.u-tokyo.ac.jp
[2] E-mail:ataruya at utap.phys.s.u-tokyo.ac.jp

random superposition of plane waves propagating along $\Omega = -\mathbf{n}$ direction with surfaces of constant phase $\xi(\mathbf{x}) = \mathbf{t} + \mathbf{n}\cdot\mathbf{x}$. Then the metric perturbation in transverse-traceless gauge $\mathbf{h}$ is expressed as: $\mathbf{h}(t,\mathbf{x}) = \sum_{A=+,\times}\int_{-\infty}^{\infty} df \int d\Omega\, e^{i2\pi f\xi}\tilde{h}_A(f,\Omega)\,\mathbf{e}^A(\Omega)$, where $\tilde{h}_A(-f) = \tilde{h}_A^*(f)$ are the Fourier amplitudes of the gravitational waves for each polarization mode. The Fourier amplitudes h_A is assumed to be characterized by the Gaussian random process:

$$\left\langle \tilde{h}_A(f,\Omega)\right\rangle = 0, \quad \left\langle \tilde{h}_A^*(f,\Omega)\tilde{h}_{A'}(f',\Omega')\right\rangle = \frac{1}{2}\delta(f-f')\frac{\delta^2(\Omega,\Omega')}{4\pi}\delta_{AA'}S_h(|f|,\Omega), \tag{1}$$

where $S_h(|f|,\Omega)$ is the power spectral density of gravitational waves.

The detection of a gravitational-wave background is achieved through the correlation analysis of two data streams. The output signal for the detector I denoted by $s_I(t)$ is described by a sum of the gravitational-wave signal $h_I(t)$ and the detector noise $n_I(t)$: $s_I(t) = h_I(t) + n_I(t)$. We assume that the noise $n_I(t)$ is treated as a Gaussian random process with zero mean and spectral density $S_n(f)$.

Provided the two output data sets, the correlation analysis is examined depending on the strategy of data analysis, i.e., self-correlation analysis only using the single data stream or cross-correlation analysis using the two *independent* data stream:

$$\begin{aligned} C(t) &\equiv \langle s_I(t)s_J(t)\rangle = \langle h_I(t)h_J(t)\rangle + \langle n_I(t)n_J(t)\rangle \\ &= \int_{-\infty}^{\infty}\frac{df}{2}\int\frac{d\Omega}{4\pi}S_h(|f|,\Omega)\,\mathcal{F}_{IJ}^E(f,\Omega;t) + \delta_{IJ}\int_{-\infty}^{\infty}\frac{df}{2}S_n(|f|), \end{aligned}$$

where $\mathcal{F}_{IJ}^E$ is the antenna pattern function defined in an ecliptic coordinate, which is expressed in terms of detector's response function and an optimal filter:

$$\mathcal{F}_{IJ}^E(f,\Omega;t) = e^{i2\pi f\Omega\cdot(\mathbf{x}_I-\mathbf{x}_J)/L}\sum_{A=+,\times}F_I^{A*}(\Omega,f;t)F_J^A(\Omega,f;t)\,\tilde{Q}(f) \tag{2}$$

where $F_I^A(\Omega,f;t) = \mathbf{D}_I(\Omega,f;t):\mathbf{e}^A(\Omega)$ with $\tilde{Q}(f)$ being the Fourier transform of the optimal filter. Detector response functions for several time-delay interferometric variables are given in [4].

3 Spherical harmonic analysis of antenna pattern function

The correlation analysis described in Sec. 2 reveals that the signal modulation induced by detector motion can be used to extract the information of the anisotropy of the gravitational-wave background. One important remark is that the map-making capability crucially depends on the antenna pattern and/or the detector response function in detector's rest frame. We then wish to clarify the relationship between the antenna pattern functions and the directional sensitivity to the gravitational-wave backgrounds. To investigate this issue, the spherical harmonic analysis of the antenna pattern function is employed and the general rules for multipole coefficients are derived based on the geometric properties of the antenna pattern.

The multipole coefficient $a_{\ell m}$ for (2) is

$$a_{\ell m}(\hat{f}) = \int_0^{\pi}d\theta\int_0^{2\pi}d\phi\sin\theta\,Y_{\ell m}^*(\theta,\phi)\,\mathcal{F}(\hat{f},\theta,\phi) \tag{3}$$

with $\hat{f} = 2\pi Lf/ = f/10\text{mHz}$. We are primarily concerned with how the directional sensitivity depends on the choice of the interferometric variables. Using the fact that the relations $\mathcal{F}^*(\hat{f},\Omega) = \mathcal{F}(-\hat{f},\Omega) = \mathcal{F}(\hat{f},-\Omega)$ always hold, one obtains

$$a_{\ell,m}(\hat{f},t) = (-1)^m a_{\ell,-m}^*(-\hat{f},t) = (-1)^{m+\ell}a_{\ell,-m}^*(\hat{f},t). \tag{4}$$

where we used $Y_{\ell-m}(\theta,\phi) = (-1)^m Y_{\ell m}^*(\theta,\phi)$.

While the explicit form of the multipole coefficients $a_{\ell m}$ depends on the coordinate system, a convenient quantity invariant under a Euler rotation of the coordinate system can be exploited:

$$\sigma_\ell^2(\hat{f}) = \frac{1}{2\ell+1}\sum_{m=-\ell}^{\ell}|a_{\ell m}(\hat{f})|^2, \tag{5}$$

Table 1: Symmetric properties of antenna pattern function

Combination of variables	Condition	Properties of $\sigma_\ell(f)$
All	low-frequency limit ($\hat{f} \ll 1$)	$\sigma_\ell = 0$ for $\ell \neq 0,\ 2,\ 4$
All	self-correlation	$\sigma_\ell = 0$ for $^\forall\ell$ =odd
(A,A), (E,E)		$\sigma_\ell^{\rm AA} = \sigma_\ell^{\rm EE}$
(A,E)		$\sigma_\ell = 0$ for $\ell = 0,\ 1^\dagger$
(A,T), (E,T)		$\sigma_\ell = 0$ for $\ell = 0^\dagger$, $\sigma_\ell^{\rm AT} = \sigma_\ell^{\rm ET}$

which characterizes the contribution of ℓ-th moment to the antenna pattern function. Thus, under the rigid adiabatic approximation, the angular power of the antenna pattern in the ecliptic frame is equivalent to that in detector's rest frame. We use this coordinate invariant quantity to quantify the directional sensitivity of the antenna pattern.

Apart from the low-frequency limit as simple limiting approximation, the analytical calculation of σ_ℓ becomes intractable and the perturbative expansion for $\hat{f}$ generally breaks down. In contrast to the ground-based detectors, the difficulty in the space interferometers arises from the transfer function, which explicitly exhibits both the frequency and the angular dependences. Thus, to evaluate the directional sensitivity, the numerical treatment is required for spherical harmonic analysis. Nevertheless, some important properties in the multipole coefficients of an antenna pattern can be still drawn analytically, from symmetric properties of an antenna pattern, which is closely-linked with the parity invariance of a detector response.

Let us introduce two operators, $\mathbb{Q} : \theta \to \pi - \theta$ and $\mathbb{P} : \phi \to \phi + \pi$. A composite operator $\mathbb{P}\mathbb{Q}$ represents the parity transformation. The transformation properties of the spherical harmonics $Y_{\ell m}(\theta, \phi)$ for the operators are $\mathbb{P}Y_{\ell m} = (-1)^m Y_{\ell m}$ and $\mathbb{Q}Y_{\ell m} = (-1)^{\ell+m} Y_{\ell m}$, and so the parity transformation property is $\mathbb{P}\mathbb{Q}Y_{\ell m} = (-1)^\ell Y_{\ell m}$. If the response function is parity invariant, then we see that $a_{\ell m}$ becomes vanishing for all odd multipoles (ℓ = odd) if a response function is parity invariant. A similar argument holds for the respective operators $\mathbb{P}$ and $\mathbb{Q}$. If a detector response function is invariant under the operation $\mathbb{P}$, then $a_{\ell m}$ vanishes for m =odd moment. For response function invariant under the operation $\mathbb{Q}$, the multipole coefficients $a_{\ell m}$ vanish when $\ell + m$ = odd. Here, we summarize these results.

$$a_{\ell m} = 0 \quad \text{for} \quad \mathbb{P}\mathcal{F} = \mathcal{F}, \qquad m = \text{odd}, \tag{6a}$$

$$a_{\ell m} = 0 \quad \text{for} \quad \mathbb{Q}\mathcal{F} = \mathcal{F}, \qquad \ell + m = \text{odd}, \tag{6b}$$

$$a_{\ell m} = 0 \quad \text{for} \quad \mathbb{Q}\mathbb{P}\mathcal{F} = \mathcal{F}, \qquad \ell = \text{odd}. \tag{6c}$$

Further important properties are derived based on the geometric properties of the multipole coefficients [4]. The general properties of the multipole coefficients are summarized in Table 1.

4 Angular power and directional sensitivity of space interferometer

While several important properties for directional sensitivity of the space interferometer were found in previous section, it remains still unclear how the multipole moments of the antenna pattern functions quantitatively depend on the frequency and the combinations of data streams.

To elucidate a more quantitative aspect of the directional sensitivity to the gravitational-wave background, it will need to take into account effects of detector noises. To investigate this, rather than using the Michelson and Sagnac signals, a set of optimal TDIs (A, E, T) free from the noise correlations should be applied to the correlation analysis of the gravitational-wave signals.

Figure 1 plots the quantity σ_ℓ for some combinations of the optimal TDIs. For the self-correlated signals, the amplitude σ_ℓ of $\mathcal{F}_{\rm AA}$ is quite similar to that of the self-correlated Sagnac signals $\mathcal{F}_{\rm s_1 s_1}$, while the low-frequency part of the angular power for $\mathcal{F}_{\rm TT}$ is highly suppressed. As for the cross-correlation signals, the monopole and the dipole moments for the antenna pattern function $\mathcal{F}_{\rm AE}$ are exactly canceled and the monopole moment for $\mathcal{F}_{\rm AT}$ further vanishes. Apart from these facts, the magnitude σ_ℓ at frequency $\hat{f} \gtrsim 1$ shows a rich structure with many peaks, indicating that the directional sensitivity could be

improved at $\hat{f} \gtrsim 1$. As shown in Fig. 1, the angular power of the cross-correlated signals is one order of magnitude smaller than that of the self-correlated signals, however, this does not directly imply that the self-correlated signals are more sensitive to an anisotropy of a gravitational-wave background.

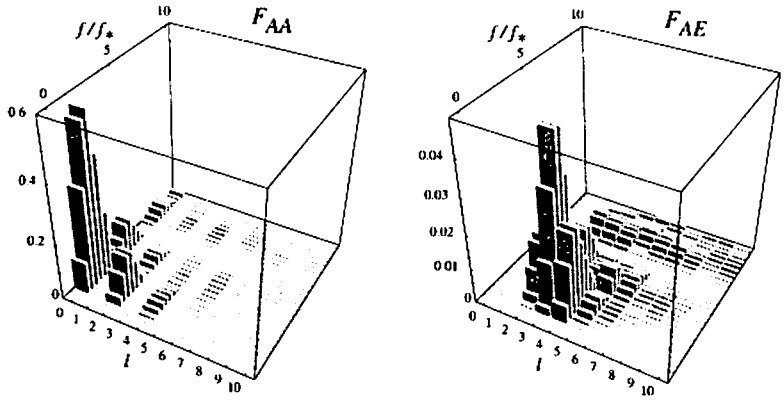


Figure 1: Angular power $\sigma_\ell(\hat{f})$ of the antenna pattern functions for the optimal TDI variables.

5 Conclusion & Discussions

In this paper, we discussed the directional sensitivity to the anisotropy of gravitational-wave background observed via space-based gravitational-wave detector. While the detection of anisotropic gravitational-wave background could be achieved utilizing the modulated signals of cross-correlated data induced by the detector motion, the directional sensitivity and the angular resolution crucially depend on the antenna pattern function and/or the detector response in detector's rest frame. In contrast to the ground based detector, the space interferometer with long baselines gives a rather complicated response to the gravitational-wave signals.

We have performed the spherical harmonic analysis of antenna pattern function for space interferometer and studied the general features of antenna pattern sensitivity beyond the low-frequency approximation. We have shown that the sensitivity to the multipole moments of an anisotropic gravitational-wave background is generally restricted by the geometry of the detector configuration and symmetries of the data combinations (see Table 1). The numerical analysis of the antenna pattern functions reveals that the angular power of the detector response increases with frequency and shows the complicated structures. (see [4] for more detailed discussion characterizing the directional sensitivity.)

References

[1] N. Seto, S. Kawamura and T. Nakamura, Phys. Rev. Lett. **87**, 221103 (2001).

[2] R. Takahashi and T. Nakamura, Astrophys. J. **596**, L231 (2003)

[3] D. Hils, P.L. Bender, and R.F. Webbink, Astrophys. J. **360**, 75 (1990)

[4] H. Kudoh and A. Taruya, Phys. Rev. D in press (gr-qc/0411017).

Probing gravitational-wave backgrounds with a space-based interferometer II

— Antenna patterns and their angular power for LISA —

Atsushi Taruya[1], Hideaki Kudoh[2]

[1] *Research Center for the Early Universe(RESCEU), School of Science, University of Tokyo, Tokyo 113-0033, Japan.*

[2] *Department of Physics, School of Science, University of Tokyo, Tokyo 113-0033, Japan,*

Abstract

We discuss the directional sensitivity to anisotropies of stochastic gravitational-wave backgrounds (GWBs) observed via space-based interferometer, LISA. Based on the geometric properties of antenna pattern functions described in part I, we show that the angular power of the detector response to the stochastic GWBs increases with frequency and the detectable multipole moments with effective sensitivity $h_{\rm eff} \sim 10^{-20}{\rm Hz}^{-1/2}$ may reach $\ell \sim 8$–10 at $f \sim f_* = 10$ mHz.

1 Introduction

Stochastic gravitational-wave backgrounds (GWBs) are promising sources for space-based gravitational-wave detector. Examples of stochastic gravitational waves are those produced by large populations of Galactic and extra-galactic binaries and primordial GWBs produced by several cosmological mechanism. Stochastic GWBs are expected to be anisotropic. It is thus important to identify unambiguously the anisotropy in order to get insights into the origin and the underlying physics of GWB.

In this article, following the part I, directional sensitivity of space-based interferometer to the stochastic GWBs is quantitatively investigated, focusing on the planned gravitational wave detector, LISA (Laser Interferometer Space Antenna).

2 Detection of anisotropic gravitational-wave backgrounds

Let us briefly summarize the detection method of anisotropic GWBs, which is achieved through the correlation analysis of two data streams obtained from the gravitational wave detectors. The output signal for the detector I denoted by $s_I(t)$ is described by a sum of the gravitational-wave signal $h_I(t)$ and the detector noise $n_I(t)$, i.e., $s_I(t) = h_I(t) + n_I(t)$. Among them, the signal $h_I(t)$ contains the time variation of the detector response caused by the detector motion. For the space interferometer LISA, which consists of three space crafts keeping a trianglur configuration, the antenna pattern sweeps over the sky as the LISA constellation orbits around the Sun with period of one sidereal year. In presence of anisotropic GWBs, this orbital motion induces the time modulation of the correlation signals, which can be used to extract the information of anisotropy of GWBs.

Provided the two output data sets, the correlation analysis is examined depending on the strategy of data analysis, i.e., self-correlation analysis only using the single data stream or cross-correlation analysis using the two *independent* data stream:

$$\begin{aligned} C(t) &\equiv \langle s_I(t) s_J(t) \rangle = \langle h_I(t) h_J(t) \rangle + \langle n_I(t) n_J(t) \rangle \\ &= \int_{-\infty}^{\infty} \frac{df}{2} \int \frac{d\Omega}{4\pi} S_h(|f|, \Omega)\, \mathcal{F}^E_{IJ}(f, \Omega; t) + \delta_{IJ} \int_{-\infty}^{\infty} \frac{df}{2} S_n(|f|), \end{aligned}$$

where $\mathcal{F}^E_{IJ}$ is the antenna pattern function for gravitational-wave detector and $S_h(|f|, \Omega)$, $S_n(|f|)$ are the spectra of GWBs and instrumental noises, respectively. The above expression implies that the time

[1] E-mail: ataruya at utap.phys.s.u-tokyo.ac.jp

[2] E-mail: kudoh at utap.phys.s.u-tokyo.ac.jp

series data $C(t)$ as observable is given by the all-sky integral of the spectral density S_h, or luminosity distribution of gravitational waves convolving with the antenna pattern function. To see this more clearly, for the moment, we neglect the noise contribution. Denoting the Fourier component of the detector output $C(t)$ by $\tilde{C}(t,f)$, we have

$$\tilde{C}(t,f) \equiv \int \frac{d\Omega}{4\pi} S_h(|f|,\Omega)\, \mathcal{F}^E_{fJ}(f,\Omega;t) = \frac{1}{4\pi} \sum_{\ell m} \left[p^E_{\ell m}(f)\right]^* a^E_{\ell m}(f,t), \tag{1}$$

where $p^E_{\ell m}(f)$ and $a^E_{\ell m}$ respectively denote the spherical harmonic coefficients of the GWB spectrum and the antenna pattern function. Note that the time-dependent multipole coefficient $a^E_{\ell m}$ appears due to the detector motion, which can be eliminated by further employing the harmonic expansion in detector's rest frame (θ,ϕ). We denote the multipole coefficients of the antenna pattern in detector's rest frame by $a_{\ell m}$. The transformation between the detector rest frame and the sky-fixed frame is described by a rotation matrix by the Euler angles (ψ,ϑ,φ), whose explicit relation is expressed in terms of the Wigner D matrices as $a^E_{\ell m}(f,t) = \sum_{n=-\ell}^{\ell} e^{-in\psi} d^\ell_{nm}(\vartheta) e^{-im\varphi} a_{\ell n}(f)$. Note that the Euler rotation conserves the multipole moment ℓ, but mixes m-th harmonics. The LISA orbital motion can be expressed by $\psi = -\omega t$, $\vartheta = -\pi/3$, $\varphi = \omega t$, where $\omega = 2\pi/T_0$ is LISA's orbital frequency (T_0 = 1 sidereal year). Using the periodicity of $\tilde{C}(t,f)$ in time, one can perform the Fourier transformation of the detector output by:

$$\tilde{C}_k(f) \equiv \frac{1}{T_0}\int_0^{T_0} dt\, e^{-ik\omega t}\, \tilde{C}(t,f) = \frac{1}{4\pi} \sum_{\ell=0}^{\infty} \sum_{m=-\ell}^{\ell-k} \left[p^E_{\ell m}(f)\right]^*\, d^\ell_{(m+k),m}(\vartheta)\, a_{\ell,(m+k)}(f). \tag{2}$$

The above equation shows how the detector output depends on the multipole coefficients $a_{\ell m}$ in detector's rest frame for a given luminosity distribution of a GWB, $p^E_{\ell m}(f)$. Given the output data $\tilde{C}_k(f)$ experimentally, the task is to solve the linear system (2) with respect to $p^E_{\ell m}(f)$ if we know the antenna pattern function. In this respect, the understanding of the angular sensitivity of antenna pattern functions is primarily important and would shed light on the problem how to reconstruct the luminosity distribution of GWBs.

3 Antenna pattern function and time-delay interferometry

To access the angular sensitivity to the stochastic GWBs, we need an explicit expression for antenna pattern function. The antenna pattern function is expressed in terms of detector's response function whose functional form generally depends on the signal processing in the space-based interferometer and/or strategy of data analysis. In this article, for practical purpose, we consider the antenna pattern function for optimal set of time-delay interferometric signals. The time-delay interferometry(TDI) is a signal processing technique to cancel the laser-frequency noise. Among various TDI signals proposed in the literature, the three Sagnac signals h_{s_i} $(i=1,2,3)$ extracted from the space crafts 1, 2 and 3 can be used to constitute an optimal data combination, which is free from the noise correlations [3]:

$$h_{\rm A} = \frac{1}{\sqrt{2}}(h_{s_3} - h_{s_1}), \quad h_{\rm E} = \frac{1}{\sqrt{6}}(h_{s_1} - 2h_{s_2} + h_{s_3}), \quad h_{\rm T} = \frac{1}{\sqrt{3}}(h_{s_1} + h_{s_2} + h_{s_3}). \tag{3}$$

The antenna pattern functions for optimal TDIs have several important properties, which can be derived from the geometric property of the LISA configuration. Define the angular power σ_ℓ of antenna pattern function, which is invariant under Euler rotation:

$$\sigma^2_\ell(f) = \frac{1}{2\ell+1} \sum_{m=-\ell}^{\ell} |a_{\ell m}(f)|^2. \tag{4}$$

We then obtain [1]:

$$\begin{aligned} &\text{(i)} \quad \sigma^{\rm AA}_\ell(f) = \sigma^{\rm EE}_\ell(f), \quad \sigma^{\rm AT}_\ell(f) = \sigma^{\rm ET}_\ell(f), \\ &\text{(ii)} \quad \sigma_0(f) = 0, \quad \sigma_1(f) = 0 \quad \text{for AE-correlation}, \\ &\text{(iii)} \quad \sigma_0(f) = 0 \qquad\qquad\quad \text{for AT-,ET-correlation}. \end{aligned} \tag{5}$$

4 Directional sensitivity for optimal TDI signals

Using a set of optimal TDIs (A, E, T), let us now investigate a more quantitative aspect of the directional sensitivity to the GWB taking account of the effects of detector noises.

Assuming that the laser frequency noise can be either canceled or sufficiently reduced by the TDI technique, the dominant noise contributions to detector's output would be the acceleration and the shot noises. According to Ref. [2], the noise spectral densities for optimal TDIs are calculated as (see also [3]):

$$\begin{aligned} S_n^{\rm AA}(f) &= S_n^{\rm EE}(f) = \sin^2(\hat{f}/2)\,\left\{8\left(2+\cos\hat{f}\right)\,S_{\rm shot}(f) + 16\left(3+2\cos\hat{f}+\cos 2\hat{f}\right)\,S_{\rm accel}(f)\right\}, \\ S_n^{\rm TT}(f) &= 2\left(1+2\cos\hat{f}\right)^2\left\{S_{\rm shot}(f) + 4\sin^2(\hat{f}/2)\,S_{\rm accel}(f)\right\} \end{aligned} \tag{6}$$

with $\hat{f}$ being the normalized frequency given by $\hat{f} \equiv f/f_* = 2\pi L f$ (L is arm-length of detector). For the LISA detector, we have $S_{\rm shot}(f) = 4.84^{-42}{\rm Hz}^{-1}$ and $S_{\rm accel}(f) = 2.31^{-40}({\rm mHz}/f)^4{\rm Hz}^{-1}$[2]. We then define the *effective sensitivity* for the multipole moment ℓ, $h_{\rm eff}^{(\ell)}(f)$, which characterizes the rms amplitude of the noise-to-angular power ratio:

$$h_{\rm eff}^{(\ell)}(f) = (4\pi)^{1/4}\,\sqrt{\frac{S_n(f)}{\sigma_\ell(f)}} \tag{7}$$

for self-correlation signals. Setting $\ell = 0$, the above definition recovers the usual meaning of sensitivity curve. Thus, the quantity $h_{\rm eff}^{(\ell)}(f)$ may be regarded as the effective power of ℓ-th moment relative to the monopole moment as a reference sensitivity. For the cross-correlated signals, on the other hand, the absence of noise correlation implies that the signal-to-noise ratio can be improved by optimally filtering the cross-correlated signals, the result of which shows the explicit dependence on the observation time T:

$$h_{\rm eff}^{(\ell)}(f) = \left(\frac{4\pi}{T\Delta f}\right)^{1/4}\,\left[\frac{S_{n,1}(f)\,S_{n,2}(f)}{\sigma_\ell^2(f)}\right]^{1/4}, \tag{8}$$

where Δf denotes the frequency resolution for actual output data.

Figure 1 shows the effective sensitivity curves for the self-correlated and cross-correlated optimal TDIs as functions of f/f_*, with characteristic frequency $f_* \simeq 10$mHz for LISA. The different lines in each panel indicate the effective strain sensitivity for each multipole moment. Clearly, the directional sensitivity to a GWB is not so good in the case of the self-correlated signals. The effective sensitivity in the low-frequency limit scales as $h_{\rm eff}^{(\ell)} \propto f^{-2}$ for $\ell = 0$, 2 and 4 of AA-correlation and $h_{\rm eff}^{(\ell)} \propto f^{-3}$ for $\ell = 0$, 4 and 6 of TT-correlation. At the frequency $f \sim f_*$, the directional sensitivities may reach at a maximal level and the higher multipole moment can be observed in both AA- and TT-correlations, however, the detectable multipole moments are still limited to ℓ =even mode with $\ell \lesssim 6$ for the sensitivity $h_{\rm eff}^{(\ell)} \sim 10^{-18}$ Hz$^{-1/2}$.

The situation might be improved if we consider the cross-correlation signals. In bottom panels of Figure 1, the observation time of $T = 1$ year and the frequency resolution with interval $\Delta f = f/10$ are assumed. In this case, the sensitivity reaches $h_{\rm eff}^{(\ell)} \sim 5 \times 10^{-21}{\rm Hz}^{-1/2}$ in both AE- and AT-correlations (and also the ET-correlation), and the detectable multipole moments become, say, $\ell \lesssim 10$ or even higher multipole moments in both ℓ =odd and even modes. At the frequency $f/f_* \sim 3$, the effective sensitivity for the higher multipole moments becomes comparable to that for the lower multipole and shows a complicated oscillatory behavior. Although the antenna pattern for cross-correlation signals is completely insensitive to the $\ell = 0$ mode, improvement of the sensitivity is noticeable, which might be useful to distinguish between the GWBs from Galactic origin and those from extragalactic origin.

5 Summary & Discussions

We discussed the directional sensitivity to the anisotropy of GWB observed via space-based gravitational-wave detector. The spherical harmonic analysis of antenna pattern function for space interferometer reveals that the angular power of the detector response increases with frequency. To characterize the

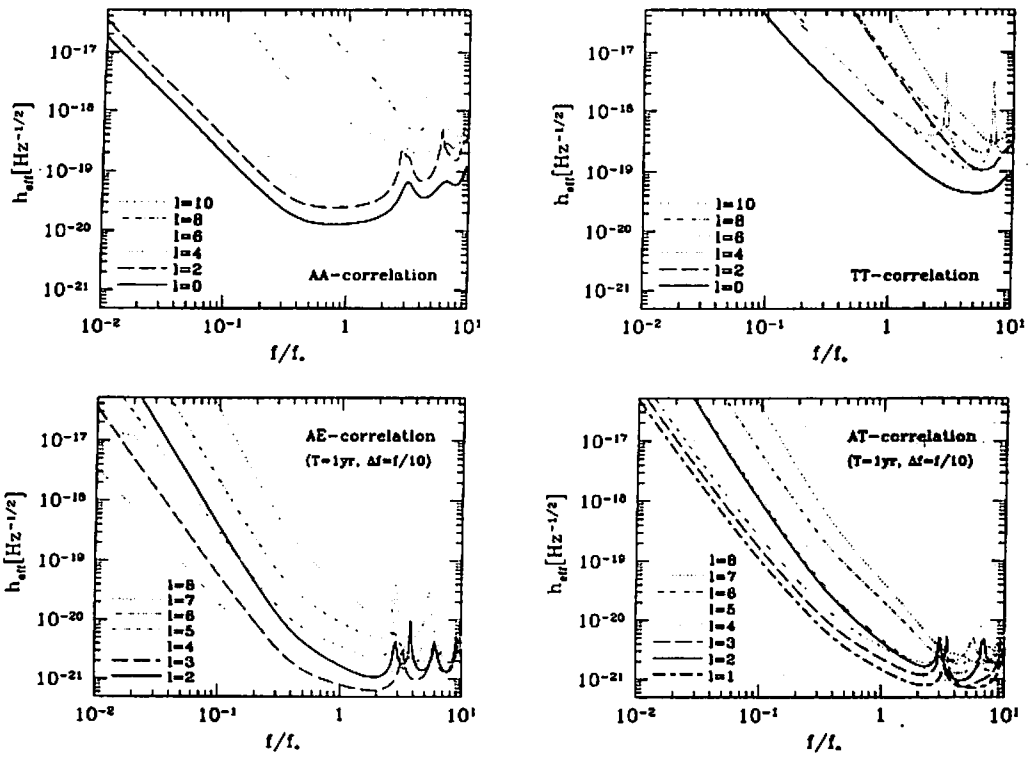


Figure 1: Effective sensitivity curves for the self-correlated and cross-correlated optimal TDI variables: AA-correlation(*top-left*); TT-correlation(*top-right*); AE-correlation(*bottom-left*); AT-correlation(*bottom-right*). In cases of the cross-correlation signals depicted in bottom panels, the observation time of $T = 1$ year and the frequency resolution $\Delta f = f/10$ are assumed. The characteristic frequency is $f_* \simeq 10$mHz.

directional sensitivity, we introduced the effective sensitivity $h_{\rm eff}^{(\ell)}(f)$ for multipole moments and found that the detectable multipole moments with effective sensitivity $h_{\rm eff}^{(\ell)} \sim 10^{-20}{\rm Hz}^{-1/2}$ may reach $\ell = 8 \sim 10$ or even higher multipoles at $f \sim f_* = 10$ mHz for cross-correlation signals of optimal TDIs.

Although the improvement of the directional sensitivity at $f \sim f_*$ is remarkable, the sensitivity of the space interferometer is still worse than the one achieved by the cosmic microwave background experiments. Further notice the important issues concerning the map-making capability of the GWB. As discussed in Sec.3, provided the time series data, the task is to solve the linear system (2) under a prior knowledge of the antenna pattern functions. The crucial remark is that the antenna pattern functions of optimal TDIs (A, E, T) are not independent. This fact implies that equations (2) are generally degenerate. Thus, one must seek a best-fit solution of $p_{lm}^E(f)$ from (2) under assuming a specific functional form of the luminosity distribution $p_{lm}^E(f)$.

References

[1] H. Kudoh, A. Taruya, Phys.Rev.D (2005) in press (gr-qc/0411017).

[2] N. Cornish, Phys.Rev.D65, 022004 (2002).

[3] T. A. Prince, M. Tinto, S. L. Larson and J. W. Armstrong, Phys.Rev.D59, 122002 (2002).

Dark Energy Reflections in the Redshift-space Quadrupole[1]

Kazuhiro Yamamoto

Department of Physical Science, Hiroshima University, Higashi-Hiroshima, 739-8526, Japan

Abstract

We derive the error estimation in a measurement of the multipole moments of the anisotropic power spectrum in the large scale distribution of galaxy redshift survey. Using the Fisher matrix approach, we then investigate how the higher multipole moments of the power spectrum contribute to the constraint on the equation of state parameter w of the dark energy in the future KAOS survey. We show that the redshift-space quadrupole will be a powerful tool for constraining dark energy even if the baryon oscillations are missing from the monopole power spectrum and bias is scale- and time-dependent. We also point out the importance of the nonlinear effects in precisely constraining w.

1 Introduction

Precise measurement of the power spectrum of high-z galaxy distribution is considered to be useful for constraining the nature of the dark energy [2, 3]. Actually, the KAOS (Kilo-Aperture Optical Spectrograph [4]) is proposed as a next-generation galaxy survey project of the large scale structure. The baryonic oscillation signature in the power spectrum, providing us with a standard ruler with which to precisely measure the extragalactic distance scale and expansion rate, plays the key role in constraining the evolution of the dark energy in such the survey (see the references in [1]). However, the bias can be a block of this technique because of its uncertainty. The bias might be scale- and time-dependent. One of the aims of this work is to investigate how the uncertainty of the bias affects the feasibility of the KAOS. On the other hand, it has been argued that the geometric distortion (Alcock-Paczynski effect) might be also useful to constrain cosmological model. The second aims of this work is to consider how the Alcock-Paczynski effect [5] is useful for the dark energy constraint.

In general the power spectrum *in redshift space* is not isotropic; the redshift-space power spectrum can be expanded as:

$$P_l(\mathbf{k}, z) = P(k, \mu, z) = \sum_{l=0,2,4\cdots} P_l(k, z)\mathcal{L}_l(\mu), \tag{1}$$

where $\mathcal{L}_l(\mu)$ is the Legendre polynomial, $\mu = \cos\theta$ and $k = |\mathbf{k}|$. The monopole $P_0(k, z)$ represents the angular averaged power spectrum and is usually what we mean by the power spectrum. $P_2(k, z)$ is the quadrupole spectrum and gives the leading anisotropic contribution. As can be seen in Fig. 1 it will be well-constrained even by just the $0.5 < z < 1.5$ sample of the total survey area 10^3 deg^2 with the mean number density $10^{-4}\ h^3\mathrm{Mp}^{-3}$, which we label KAOS1. The higher order multipoles are not well-constrained however. Crucially, the multipole moments reflect different aspects of the redshift distortions in the power spectrum which can therefore aid in breaking degeneracies between the cosmological parameters, bias and dark energy. The purpose of this work is also to consider the extent to which the anisotropic component of the power spectrum, P_ℓ, $\ell \geq 2$, gives new information about dark energy via the nonlinear effects and the geometric distortion.

2 Formalism

We have developed the optimal weighting scheme for the multipole moments of the power spectrum, as an extension of the work by Feldman, Kaiser and Peacock [6, 2]. From this result, the error in a

[1] This work is based on a collaboration with B. A Bassett and H. Nishioka in Ref.[1]

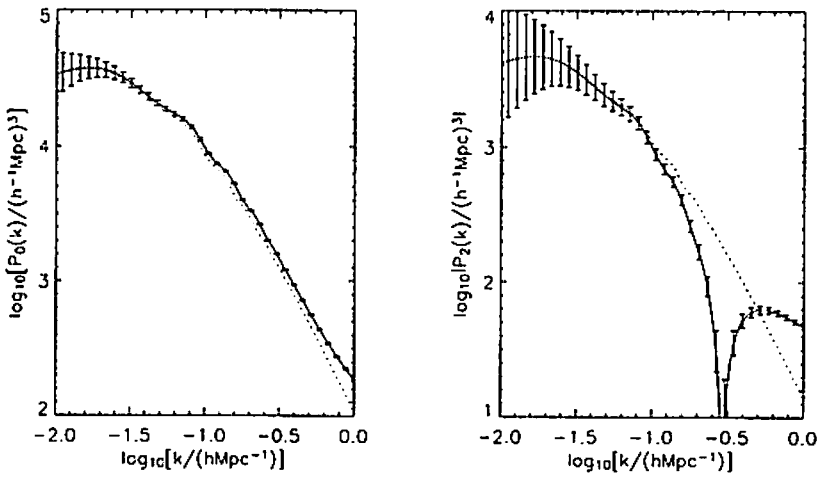


Figure 1: KAOS1 constraints ($z < 1.5$) on the multipole moments of the power spectrum, $P_0(k)$ and $P_2(k)$ for linear (dotted lines) and nonlinear (solid lines) spectra respectively. The nonlinear $P_2(k)$ prediction changes sign at large k. We have fixed $n = 1$, $h = 0.7$, $\Omega_b = 0.045$, $\Omega_m = 0.28$ and $w = -1$. For the bias we adopted $b_0 = 1.35$, $p_0 = 1$ for the linear model, $p_1 = 1$, $b_1 = 0.1$, $\nu = 1$ for the nonlinear spectrum (see eq. 4). The higher moments P_ℓ, $\ell \geq 4$ are not well-constrained, even by KAOS.

measurement of the multipole moments is evaluated as follows.

$$\Delta P_l(k)^2 \simeq \frac{(2\pi)^3}{\Delta V_k} \int_{-1}^{1} d\mu \frac{\mathcal{L}_l(\mu)^2}{\int ds \bar{n}(s)^2 [1 + \bar{n}(s) P(k, \mu, s)]^{-2}}, \tag{2}$$

where ΔV_k is the volume of the shell with the radius k in the Fourier space, and $\bar{n}$ is the mean number density. We apply this result to the Fisher matrix analysis in order to estimate the accuracy with which we can constrain the equation of state, $w \equiv p/\rho$, of the dark energy with a measurement of the power spectrum.

Next we explain our theoretical modelling of the power spectrum. we adopt a flat universe with $\Omega_m = 0.3$ as the distance-redshift relation $s = |\mathbf{s}| = s[z]$ to plot a map of objects. Here $H_0 = 100\ h$km/s/Mpc is the Hubble parameter. We consider a cosmological model with the dark energy component with constant equation of state, $w \equiv p/\rho$, then we have

$$r(z, \Omega_m, w) = \frac{1}{H_0} \int_0^z \frac{dz'}{\sqrt{\Omega_m (1+z')^3 + (1-\Omega_m)(1+z')^{-3(1+w)}}}. \tag{3}$$

Our fiducial model thus has $s(z) \equiv r(z, 0.3, -1)$. We construct the galaxy theoretical power spectrum incorporating the nonlinear effects in the quintessence model, the Alcock-Paczynski effect, the linear distortion and the Finger of God effect as well as the light-cone effect. (For details, see ref. [1])

For the nonlinear modeling, we assume a scale dependent bias model.

$$b(z, k) = \left(1 + \frac{b_0 - 1}{D_1(z)}\right) \left[1 + b_1 \left(\frac{D_1(z) p_1 q}{0.1\ h\mathrm{Mpc}^{-1}}\right)^{\nu}\right], \tag{4}$$

where b_0, b_1, p_1 and ν are constants. In the linear case the bias is taken to be scale-*independent* and given by $b(z) = 1 + (b_0 - 1) D_1(z)^{-p_0}$ where p_0 is a constant. The precise form of (4) is not crucial: our aim is to understand the impact of multiple bias parameters on dark energy reconstruction.

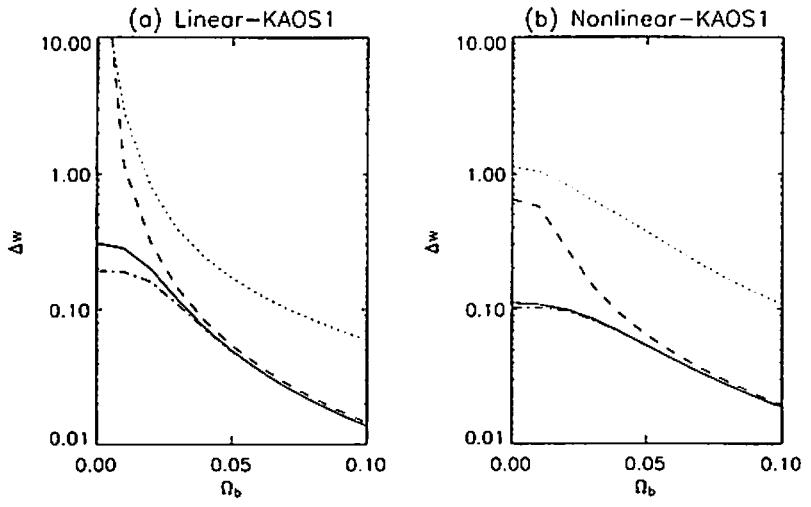


Figure 2: $1-\sigma$ error estimates for w as the baryon oscillations disappear ($\Omega_b \to 0$). The left panel (a) is the results using the linear spectrum and the right panel (b) is the nonlinear spectrum. The dashed curve is the result utilizing *only* $P_0(k)$, the dotted curve is the result with *only* $P_2(k)$, the solid curve is the result obtained using *both* $P_0(k)$ and $P_2(k)$. The target parameters here are same as those in Fig. 1. The low-redshift sample, KAOS1, is assumed. The dotted-dashed curve in (a) and (b) shows the constraint combining all $P_0(k)$ to $P_6(k)$.

3 Results

Fig. 1 shows the monopole and quadrupole power spectra $P_0(k)$ and $P_2(k)$ for the linear and nonlinear models described above, assuming the KAOS1. $P_0(k)$ is positive while the nonlinear effects cause $P_2(k)$ to change sign at large k . For $P_0(k)$, the linear power spectrum agrees well with the nonlinear power spectrum because the two nonlinear contributions to it cancel out: the finger of God effect decreases the amplitude while $P^{\rm NL}_{\rm mass}(k)$ increases the amplitude due to the nonlinearity at large k. By comparison, it is very clear that the linear theory is not good for the higher multipole moments on small scales, $k \gtrsim 0.1h{\rm Mpc}^{-1}$.

The precision with which w can be recovered is shown in Fig 2. Here Ω_m and all the bias parameters, *viz* b_0, p_0 (linear case) and b_0, p_1, b_1 and ν (nonlinear case) are marginalized over, and the other parameters are determined independently. Fig. 2 shows Δw as a function of Ω_b. The left panel is the result for the linear perturbation theory, while the right panel is the nonlinear model. In general, Δw becomes larger as the baryon fraction becomes smaller since the baryon oscillations become less and less distinct. As Ω_b becomes smaller, the contribution from P_2 becomes increasingly important. It is clear from the dashed curve that the constraint on w from P_0 is very weak around $\Omega_b = 0$ because the baryon oscillations disappear, taking with it the standard ruler. This is the same for the dotted curve which shows the constraints from P_2.

One of the main results of this work is the solid curve which shows the constraint from the combination of P_0 and P_2. It is good even in the case $\Omega_b = 0$ when the baryon oscillation are missing, implying that the geometric distortion (AP test) plays the central role in constraining w. This does not depends on the bias parameters and inclusion of a constant parameter for stochastic bias does not alter our results. It is interesting to address why the constraint on w from P_0 and P_2 combined is so much better than from either one separately. This comes from the fact that the error ellipses for P_0 and P_2 only overlap by a small amount in the full parameter space. (see Fig. 3) The power in combining P_0 and P_2 thus extends the well-known fact that P_2 gives useful information about bias.

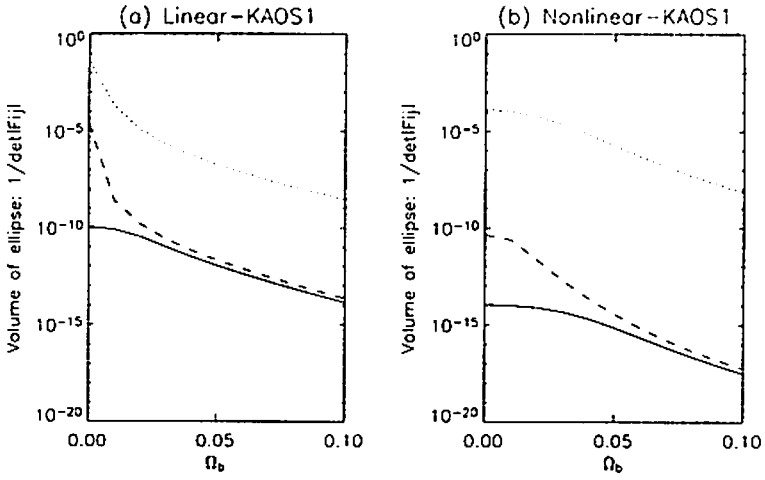


Figure 3: Volume of ellipses in the full parameter space, $1/\det F_{ij}$ as the baryon oscillations disappear ($\Omega_b \to 0$). The left panel is the result using the linear spectrum and the right panel is the nonlinear spectrum. The dashed curve is the result utilizing *only* $P_0(k)$, the dotted curve is the result with *only* $P_2(k)$, the solid curve is the result obtained using *both* $P_0(k)$ and $P_2(k)$. The target parameters here are same as those in Fig. 2.

4 Conclusions

We have investigated the accuracy with which we can expect next-generation galaxy surveys such as KAOS [4] to measure the multipole moments of the anisotropic power spectrum in redshift space and the resulting improvements in dark energy constraints. We found a number of key results: (1) the quadrupole is very useful in breaking degeneracies between bias and dark energy. (2) Nonlinear effects have a substantial influence on the quadrupole and higher multipoles at the scale $k \gtrsim 0.1h\mathrm{Mpc}^{-1}$. The inclusion of the nonlinear power spectrum enhances the precision with which the dark energy can be constrained because the nonlinear effects increase the power at small scale which is also where constraints are good. The nonlinear regime provides us with new information about the dark energy, as has been discussed in different contexts. (3) Applying these results to dark energy and the KAOS survey we have found that significant constraints arise by combining the monopole and quadrupole spectra even if there are no baryon oscillations in the monopole spectrum and even if we allow for multi-parameter scale-dependent or stochastic bias. This is a key piece of insurance for large galaxy surveys given current uncertainty about the existence of baryon oscillations and ensures that large, next-generation, galaxy surveys will make a significant contribution to the hunt for dark energy irrespective of the existence of baryon oscillations.

References

[1] K. Yamamoto, B. A. Bassett and H. Nishioka, arXiv:astro-ph/0409207, to appear in PRL

[2] K. Yamamoto, ApJ, 595, 577 (2003)

[3] K. Yamamoto, ApJ, 605, 620 (2004)

[4] http://www.noao.edu/kaos/

[5] C. Alcock, B. Paczynski, Nature, 281, 358 (1979)

[6] H. A. Feldman, N. Kaiser, J. A. Peacock ApJ, 426, 23 (1994)

Gravitational self-force effect on a particle orbiting a Schwarzschild black hole
— Third post-Newtonian force for general geodesic —

Norichika Sago[1], Hiroyuki Nakano[2], Wataru Hikida[3,4],
Sanjay Jhingan[5], Misao Sasaki[4], and Takahiro Tanaka[3]

[1] *Department of Earth and Space Science, Graduate School of Science, Osaka University, Toyonaka 560-0043, Japan*
[2] *Department of Mathematics and Physics, Graduate School of Science, Osaka City University, Osaka 558-8585, Japan*
[3] *Theoretical Astrophysics Group, Department of Physics, Kyoto University, Kyoto 606-8502, Japan*
[4] *Yukawa Institute for Theoretical Physics, Kyoto University, Kyoto 606-8502, Japan*
[5] *Departamento de Física Teórica, Universidad del País Vasco, Apdo. 644, 48080, Bilbao, Spain*

Abstract

Recently we developed a method of obtaining the gravitational self-force on a particle orbiting a Schwarzschild black hole under the Regge-Wheeler gauge condition. By using this method, we calculate the self-force exerted on a particle moving along arbitrary geodesic up to the third post-Newtonian order. In addition, we show that our results consist with the ones from the quadrupole formula in the circular orbit limit.

1 Introduction

A compact object orbiting a supermassive black hole is one of the interesting targets for the laser interferometer space antenna (LISA). To extract the information from the observed gravitational wave data, we need to predict accurate theoretical waveforms. For this purpose, we apply the black hole perturbation approach, which is an efficient approach to deal with extreme mass ratio binaries. In this approach, we consider the perturbation induced by the compact object with a small mass in the background geometry formed by a supermassive black hole. To compute the accurate waveform emitted from such a system, we have to trace the motion of the compact object. The purpose of this work is to derive the equation of motion including the effect of the self-force on the compact object.

Since we now focus on the self-force effect, we neglect the interior structure of the compact object and regard it as a point particle. Naively, the self-force on a point particle is given by the gradient of the metric perturbation. Because the perturbation diverges at the location of the particle, however, an appropriate regularization is needed to obtain the physical self-force. The formal expression of the gravitational self-force on a point particle was given in Ref.[1, 2] and then some practical method of calculating it were proposed. Most of these are based on the subtraction method. In this method, we subtract the singular part (so-called S-part), which has no effect on the particle's motion, from the bare force induced by the metric perturbation.

In the subtraction procedure, it is known that we face the '*Gauge problem*' due to the gauge dependence of the gravitational self-force. Recently some of authors proposed a prescription to solve this problem by performing the regularization in the Regge-Wheeler(RW) gauge [3]. In addition, the first post-Newtonian self-force on a particle moving along a circular orbit was derived. In this manuscript, as the next step, we calculate the third post-Newtonian force for arbitrary geodesic case. We also see the consistency of our results with the quadrupole formula in the circular orbit limit.

[1] E-mail:sago@vega.ess.sci.osaka-u.ac.jp

This manuscript is organized as follows. In Sec.2, we describe our method of calculating the gravitational self-force in the Regge-Wheeler gauge. In Sec.3, we show our third post-Newtonian results and compare them with the results of quadrupole formula. Finally, we summarize this manuscript in Sec.4.

2 Formulation

In this manuscript, we use the Regge-Wheeler-Zerilli formalism [4, 5], based on the Fourier-harmonic expansion, in order to obtain the metric perturbation on a Schwarzschild spacetime. Furthermore, when we solve the master equations in this formalism, we introduce a new technique we proposed recently to calculate the self-force efficiently. In this section, we give the brief description for these method.

2.1 Regge-Wheeler-Zerilli formalism

In the Regge-Wheeler-Zerilli formalism, it is known that the field equations can be reduced into two master equations. Since the equation for the even parity in the Zerilli's original paper is somewhat complicated, however, we simplify it by performing the Chandrasekhar transformation of the master variable. As a result, we can obtain the following equations:

$$\left[\frac{d^2}{dr_*^2}+\left(\omega^2-V_\ell^{\rm RW}(r)\right)\right]R^{\rm (odd/even)}_{\ell m\omega}(r)=S^{\rm (odd/even)}_{\ell m\omega}(r);\quad V_\ell^{\rm RW}(r)=\left(1-\frac{2M}{r}\right)\left(\frac{\ell(\ell+1)}{r^2}-\frac{6M}{r^3}\right), \tag{1}$$

where $R^{\rm (odd/even)}_{\ell m\omega}(r)$ are the master variables and $S^{\rm (odd/even)}_{\ell m\omega}(r)$ are the source terms (The explicit expressions for the source terms are given in refs.[3, 6]). Once we obtain the master variables, we can calculate the metric perturbation and the bare force in the RW gauge by applying certain differential operators.

2.2 The $(\tilde{S}+\tilde{R})$-decomposition

Recently, we developed a new decomposition of the retarded Green function into the $\tilde{S}$-part and the $\tilde{R}$-part [7]. By applying a new technique to solving the above master equations, we can calculate the self-force more efficiently.

The $\tilde{S}$-part and the $(\tilde{S}-S)$-part

By the definition, the $\tilde{S}$-part of the Green function can be expanded into the Taylor series with respect to the frequency, ω. Therefore we can perform the inverse Fourier transformation of the $\tilde{S}$-part analytically. we can calculate the $\tilde{S}$-solution for the master equations (1). After applying certain differential operators, performing the inverse Fourier transformation and the m-summation, we obtain the $\tilde{S}$-part of the bare force:

$$F_\alpha^{\tilde{S}}|_\ell = A_\alpha L + B_\alpha + C_\alpha/L + \tilde{D}_{\alpha,\ell}, \tag{2}$$

where $L=\ell+1/2$, A_α, B_α and C_α are independent of ℓ, and $\tilde{D}_{\alpha,\ell}=O(L^{-2})$. Since it is shown, in Ref.[7], that the force induced from the $\tilde{S}$-part contains all the singular terms to be removed, we expect the form of the S-part:

$$F_\alpha^{S}|_\ell = A_\alpha L + B_\alpha + C_\alpha/L + D_{\alpha,\ell};\quad D_{\alpha,\ell}=O(L^{-2}). \tag{3}$$

Assuming that the S-part of the self-force is also the standard form, $\sum_\ell D_{\alpha,\ell}=0$, under the RW gauge condition and that the $\ell=0,1$ modes have no physical contribution to the self-force, we can regularize the $\tilde{S}$-part by removing the A, B and C terms from it:

$$F_\alpha^{(\tilde{S}-S)}|_\ell = \sum_{\ell=2}^{\infty}\tilde{D}_{\alpha,\ell}. \tag{4}$$

The $\tilde{R}$-part

In general, we cannot perform the inverse Fourier transformation of the $\tilde{R}$-part analytically due to the appearance of the $\ln\omega$ terms up to the fourth and more than post-Newtonian order. However, since we consider here up to the third post-Newtonian order and there is no logarithmic term, we can also calculate the $\tilde{R}$-force analytically. In addition, from the analysis of the Green function, we can find that the ℓ mode of the $\tilde{R}$-force has $(\ell-1)$ post-Newtonian contribution. Therefore it is sufficient to consider only $\ell \leq 4$ modes in this case:

$$F_\alpha^{\tilde{R}} = \sum_{\ell=2}^{4} F_\alpha^{\tilde{R}}|_\ell, \quad \text{(at the 3PN order)}. \tag{5}$$

Calculation of The R-part

We can obtain the regularized self-force, the R-part, from the $(\tilde{S}-S)$-part and the $\tilde{R}$-part:

$$F_\alpha^R = F_\alpha^{(\tilde{S}-S)} + F_\alpha^{\tilde{R}}. \tag{6}$$

Here, from the normalization of the four velocity, $u^\alpha u_\alpha = -1$, we can find the following condition:

$$\frac{E}{1-2M/r_0}F_t + u^r F_r + \frac{L_z}{r_0^2}F_\phi = 0, \tag{7}$$

where r_0 is the orbital radius, u^μ is the four velocity of the particle, $E = -u_t$ and $L_z = u_\phi$.

3 Results

The explicit expressions of the regularized self-force are given as follows:

$$\begin{aligned}
F_t^R &= \frac{\mu^2}{r_0^2}\left[-\frac{160\,L_z^2\,M^2}{3\,r_0^4} - \frac{256\,M^2\,\delta}{15\,r_0^2} - \frac{136\,L_z^2\,M\,\delta}{5\,r_0^3} - \frac{16\,\delta^2\,M}{5\,r_0} - \frac{64\,M^3}{3\,r_0^3} + \frac{40\,L_z^4\,M}{r_0^5}\right] \\
&+ \frac{\mu^2 u^r}{r_0^2}\left[-\frac{232\,L_z^2\,M\,\delta}{5\,r_0^3} - \frac{196\,M^2\,\delta}{3\,r_0^2} + \frac{123\,M^2\,\delta\,\pi^2}{32\,r_0^2} - \frac{490\,M^3}{3\,r_0^3} + \frac{41\,M^3\,\pi^2}{4\,r_0^3} + \frac{224\,L_z^2\,M^2}{3\,r_0^4}\right. \\
&- \frac{615\,M^2\,L_z^2\,\pi^2}{64\,r_0^4} - \frac{2695\,L_z^4\,\delta}{128\,r_0^4} + \frac{424\,L_z^4\,M}{5\,r_0^5} + \frac{5\,\delta^3}{16} + \frac{9835\,L_z^6}{256\,r_0^6} + \frac{201\,L_z^2\,\delta^2}{32\,r_0^2} \\
&\left.+ \frac{4\,M\,L_z^2}{r_0^3} + \frac{3\,\delta^2}{8} - \frac{1095\,L_z^4}{64\,r_0^4} + \frac{51\,\delta\,L_z^2}{8\,r_0^2} + \frac{2\,M}{r_0} + \frac{\delta}{2} + \frac{3\,L_z^2}{4\,r_0^2}\right],
\end{aligned} \tag{8}$$

$$\begin{aligned}
F_\phi^R &= \frac{\mu^2}{r_0}\left[\frac{32\,M^2\,L_z}{r_0^3} + \frac{72\,M\,L_z\,\delta}{5\,r_0^2} - \frac{24\,M\,L_z^3}{r_0^4}\right] \\
&+ \frac{\mu^2 u^r}{r_0}\left[-\frac{608\,M\,L_z^3}{15\,r_0^4} + \frac{36\,M\,L_z\,\delta}{5\,r_0^2} + \frac{3\,L_z^3\,\delta}{r_0^3} + \frac{123\,L_z\,M^2\,\pi^2}{32\,r_0^3} - \frac{812\,M^2\,L_z}{15\,r_0^3} - \frac{1385\,L_z^5}{128\,r_0^5}\right. \\
&\left.+ \frac{8\,L_z\,M}{r_0^2} + \frac{111\,L_z^3}{16\,r_0^3} - \frac{3\,L_z}{2\,r_0}\right],
\end{aligned} \tag{9}$$

where $\delta = 1 - 1/E^2$. Taking the circular limit, we obtain:

$$F_t^R = \frac{32\,\mu^2\,M^3}{5\,r_0^5}, \quad F_\phi^R = -\frac{32}{5}\frac{M^2}{r_0^3}\sqrt{\frac{M}{r_0}} = -\frac{1}{\Omega}F_t^R, \tag{10}$$

where $\Omega = \sqrt{M/r_0^3}$. The loss of energy and angular momentum derived from these results agree with the ones from the quadrupole formula.

4 Summary and future works

In this manuscript, we calculated the gravitational self-force on a particle moving along arbitrary geodesic up to the third post-Newtonian order. In addition, we checked the consistency of our results with the ones from the quadrupole formula. The extension of our calculation to the higher post-Newtonian order requires the numerical calculation of the $\tilde{R}$-part due to its non-analytic terms with respect to ω (say, $\ln\omega$ term). Nevertheless, our method is still useful because we can deal with the $\tilde{S}$-part and therefore can perform the regularization analytically.

We calculated the self-force on the following assumptions: (1) the S-part of the self-force takes the standard form under the RW gauge condition, and (2) the $\ell = 0, 1$ modes have no contribution of the self-force. As for the first assumption, we found that it is valid up to the first post-Newtonian order by transforming the S-part in the harmonic gauge to the RW gauge. But, it is not trivial if this assumption is also the case at the higher post-Newtonian order. To prove the second assumption, we have to evaluate the $\ell = 0, 1$ modes which need the different treatment from the $\ell \leq 2$ modes. The $\ell = 0$ modes corresponds to a shift of the black hole mass and the $\ell = 1$ odd mode to adding a small angular momentum to the black hole, both of which should vanish in the limit, $\mu \to 0$. On the other hand, the $\ell = 1$ even mode is a pure gauge mode that corresponds to a dipolar shift of the coordinate. This fact makes the treatment of $\ell = 1$ even mode nontrivial.

The comparison with the standard post-Newtonian results for the same system may give us the clue to solving the above problems. And the second order perturbation should be considered to solve the problem in the low ℓ modes containing the gauge mode. In addition, the analysis of the second order perturbation is also needed to calculate the theoretical waveforms for the actual observation with LISA. These problems are left as the future works.

In this manuscript, our calculation was limited in the Schwarzschild background case. However, it is believed that most of actual black holes are rotating, so the extension of our calculation to the Kerr geometry should be discussed. This is also our important future work.

References

[1] Y. Mino, M. Sasaki and T. Tanaka, Prog. Theor. Phys. Suppl. **128**, 373 (1997)

[2] T. C. Quinn and R. M. Wald, n of particles in curved spacetime," Phys. Rev. D **56**, 3381 (1997)

[3] H. Nakano, N. Sago and M. Sasaki, er Regge-Wheeler gauge," Phys. Rev. D **68**, 124003 (2003).

[4] T. Regge and J. A. Wheeler, Phys. Rev. **108**, 1063 (1957).

[5] F. Zerilli, Phys. Rev. D **2**, 2141 (1970).

[6] S. Jhingan and T. Tanaka, Phys. Rev. D **67**, 104018 (2003)

[7] W. Hikida, S. Jhingan, H. Nakano, N. Sago, M. Sasaki and T. Tanaka, Prog. Theor. Phys. **111**, 821 (2004)

Asymptotically AdS spacetimes and conserved quantities in higher curvature gravitational theories

Naoya Okuyama[1], Jun-ichirou Koga[2]

[1]*Department of Physics, Waseda University, Okubo 3-4-1, Shinjuku, Tokyo 169-8555, Japan*
[2]*Advanced Research Institute for Science and Engineering, Waseda University, Okubo 3-4-1, Shinjuku, Tokyo 169-8555, Japan*

Abstract

We consider asymptotically AdS spacetimes in higher curvature gravitational theories. We first propose an alternative definition of an n-dimensional asymptotically AdS spacetime in higher curvature gravitational theories with $n \geq 4$, by employing the conformal completion technique, where a condition on the Ricci tensor is supplemented. Based on the definition, we also construct conserved quantities in two classes of higher curvature gravitational theories.

1 Introduction

Recently, higher dimensional asymptotically AdS spacetimes have been attracting much attention in the contexts of the AdS/CFT correspondence and the brane world cosmology. In order to analyze asymptotic structure of these spacetimes, a precise definition of *an asymptotically AdS spacetime* is required. In Einstein gravity, it has been established by employing the conformal completion technique [1], which has the advantage that asymptotic behavior of physical fields can be analyzed in well-defined manner.

On the other hand, higher curvature corrections to the standard Einstein gravity naturally arise in high energy physics. It is thus interesting to analyze asymptotically AdS spacetimes in higher curvature gravitational theories, but a precise definition in these theories has not been established yet. Therefore, we here propose a precise definition of an asymptotically AdS spacetime in higher curvature gravitational theories, by employing the conformal completion technique as in the case of Einstein gravity. We consider the higher curvature gravitational theories whose action is written as

$$S = \int d^n x \sqrt{-g} \left[\frac{\mathcal{L}(g^{ab}, R_{abcd})}{16\pi G_{(n)}} + \mathcal{L}_{\rm matter} \right], \tag{1}$$

where $\mathcal{L}(g^{ab}, R_{abcd})$ is the Lagrangian of the gravitational field that is assumed to be a scalar function of the physical metric g^{ab} and the Riemann tensor R_{abcd}, $\mathcal{L}_{\rm matter}$ is the Lagrangian of ordinary matter fields, and $G_{(n)}$ is the n-dimensional gravitational constant.

The conformal completion technique provides an intrinsic and background-independent definition of conserved quantities in an asymptotically AdS spacetime in Einstein gravity. Then we also construct conserved quantities in higher curvature gravitational theories in the same manner. Details of our analysis are presented in Ref. [2].

2 Asymptotically AdS Spacetime

In Einstein gravity, an asymptotically AdS spacetime is defined by conformal completion technique [1], where we conformally transform a physical spacetime (M, g_{ab}) into an unphysical spacetime $(\tilde{M}, \tilde{g}_{ab})$. $\tilde{M}$ includes its boundary $\mathcal{I}$ and the unphysical metric $\tilde{g}_{ab}$ is related with the physical metric g_{ab} by a conformal transformation $\tilde{g}_{ab} = \Omega^2 g_{ab}$ where Ω is the conformal factor. The boundary $\mathcal{I}$ is located at $\Omega = 0$ and represents the asymptotic infinity of the physical spacetime (M, g_{ab}), where we can apply the

[1]E-mail:okuyama@gravity.phys.waseda.ac.jp
[2]E-mail:koga@gravity.phys.waseda.ac.jp

standard method of differential geometry. Also in higher curvature gravitational theories, we apply the same technique in the definition of an asymptotically AdS spacetime.

In Einstein gravity, the fall-off conditions of the energy-momentum tensor of matter fields and the Weyl tensor are imposed. The condition on the energy-momentum tensor determines the asymptotic form of the Ricci tensor through the Einstein equation. However, when higher curvature corrections are included, the gravitational equation does not determine the asymptotic form of the Ricci tensor, because it is nonlinear in the curvature tensors and includes derivatives of the curvature tensors. It is therefore obvious that one needs to supplement a condition that ensures the desired asymptotic form of the Ricci tensor as well as the Weyl tensor in the case of generic higher curvature gravitational theories. In addition, both of the Ricci tensor and the Weyl tensor enter the gravitational field equation in general. Thus, combining the condition on the Ricci tensor with that on the Weyl tensor, we impose a condition on the Riemann tensor, instead of the Weyl tensor.

Thus, we now propose a definition of an asymptotically AdS spacetime compatible with higher curvature corrections, as follows.

Definition 1 *An n-dimensional spacetime (M, g_{ab}) is said to be an asymptotically AdS spacetime if there exists a spacetime $(\hat{M}, \hat{g}_{ab})$ equipped with the smooth metric $\hat{g}_{ab}$ and the boundary $\mathcal{I}$, which satisfies following conditions:*

1. *$\hat{M} \setminus \mathcal{I} \cong M$ and $\mathcal{I} \cong S^{n-2} \times \mathbf{R}$.*

2. *There exists a smooth scalar Ω on $\hat{M}$ such that*

$$\hat{g}_{ab} = \Omega^2 g_{ab} \quad \text{on} \quad M, \tag{2}$$

$$\Omega = 0 \quad \text{on} \quad \mathcal{I}, \tag{3}$$

$$\hat{\nabla}_a \Omega \neq 0 \quad \text{on} \quad \mathcal{I}. \tag{4}$$

3. *The physical metric g_{ab} satisfies the gravitational equation on M, and there exists a smooth tensor τ_{ab} such that the energy-momentum tensor T_{ab} in a neighborhood of $\mathcal{I}$ is given by*

$$T_{ab} = \Omega^{n-2} \tau_{ab}. \tag{5}$$

4. *There exist a smooth tensor H_{abcd} and a real constant ℓ such that the Riemann tensor R_{abcd} associated with the physical metric g_{ab} in a neighborhood of $\mathcal{I}$ is given by*

$$R_{abcd} + \frac{2}{\ell^2} g_{c[a} g_{b]d} = \Omega^{n-5} H_{abcd}. \tag{6}$$

In the above definition, the first three conditions remain the same as in the case of Einstein gravity [1]. On the other hand, the condition on the Weyl tensor in the case of Einstein gravity is now replaced by the fourth condition on the Riemann tensor. Eq. (6) can be decomposed into conditions on the Weyl tensor and the Ricci tensor. The fall-off condition of the Weyl tensor required by the above definition is same as that required by the definition in Einstein gravity. On the other hand, the asymptotic condition on the Ricci tensor required by the above definition is weaker than that required by the definition in Einstein gravity.

From Eq. (6) and the conformal relation between the curvature tensors of physical spacetime and those of unphysical spacetime, we can show that $\hat{n}_a \equiv \hat{\nabla}_a \Omega$ is spacelike at $\mathcal{I}$ as $\hat{n}^a \hat{n}_a = \ell^{-2}$, and hence that $\mathcal{I}$ is a timelike hypersurface. Furthermore, it can be shown that $\mathcal{I}$ is conformally flat. Hence we see, without using the field equation, that the asymptotic symmetry group is the n-dimensional AdS group $O(n-1,2)$, as in the case of Einstein gravity. The generators of the asymptotic symmetry group are shown to be described by the conformal Killing vectors ξ^a associated with induced metric $\hat{h}_{ab} \equiv \hat{g}_{ab} - \ell^2 \hat{n}_a \hat{n}_b$ at $\mathcal{I}$.

3 Conserved Quantities

In the case of Einstein gravity, a conservation law of the gravitational field associated with the conformal Killing vectors ξ^a can be derived from the Einstein equation [1]. In the case of higher curvature gravitational theories, a conservation law can be also derived in the same method. In contrast to Einstein gravity, however, here we impose the asymptotic condition (6) on the curvature tensors to derive the conservation law.

The derivation of the conservation law strongly depends on the Lagrangian under consideration. Therefore, we here focus on two classes of higher curvature gravitational theories, $f(R)$-gravity and quadratic curvature gravity. In the case of $f(R)$-gravity, whose Lagrangian is given by a smooth function $f(R)$ of the Ricci scalar R alone as $\mathcal{L}(g^{ab}, R_{abcd}) = f(R)$, the conservation law of the gravitational field at $\mathcal{I}$ associated with ξ^a is described as

$$f'(R_0)\hat{D}^c(\hat{\mathcal{E}}_{cd}\xi^d) = -8\pi G_{(n)}(n-3)\tau_{ab}\hat{n}^a\xi^b, \tag{7}$$

where $R_0 \equiv -n(n-1)/\ell^2$, $\hat{D}_a$ is the covariant derivative associated with induced metric $\hat{h}_{ab}$ at $\mathcal{I}$, and $\hat{\mathcal{E}}_{ab}$ is the "electric part" of the Weyl tensor defined by $\hat{\mathcal{E}}_{ab} \equiv \Omega^{-(n-5)}\ell^2 C_{acbd}\hat{n}^c\hat{n}^d$. On the other hand, in the case of quadratic curvature gravity, the Lagrangian is given by $\mathcal{L}(g^{ab}, R_{abcd}) = -2\Lambda + R + \alpha\mathcal{L}_{\rm GB} + \beta R^2 + \gamma R_{ab}R^{ab}$, where Λ is cosmological constant, α, β, and γ are coupling constants of higher curvature corrections, and $\mathcal{L}_{\rm GB}$ is the Gauss-Bonnet combination of the curvature tensors defined by $\mathcal{L}_{\rm GB} = R^2 - 4R_{ab}R^{ab} + R_{abcd}R^{abcd}$. The conservation law of the gravitational field at $\mathcal{I}$ associated with ξ^a in this case is described as

$$\Xi_q\hat{D}^c(\hat{\mathcal{E}}_{cd}\xi^d) = -8\pi G_{(n)}(n-3)\tau_{ab}\hat{n}^a\xi^b, \tag{8}$$

where Ξ_q is given as

$$\Xi_q = 1 + R_0\left[2\alpha\frac{(n-3)(n-4)}{n(n-1)} + 2\beta + 4\gamma\frac{(n-2)}{n(n-1)}\right]. \tag{9}$$

Eqs. (7) and (8) enable to define conserved quantities associated with the conformal Killing vectors ξ^a at $\mathcal{I}$. These conserved quantities $Q_\xi[C]$ are defined on an $(n-2)$-dimensional spacelike cross section C of $\mathcal{I}$ as

$$Q_\xi[C] = -\frac{\Xi\,\ell}{8\pi G_{(n)}(n-3)}\int_C dx^{n-2}\sqrt{\hat{\sigma}}\hat{\mathcal{E}}_{ab}\xi^a\hat{N}^b, \tag{10}$$

in both $f(R)$-gravity and quadratic curvature gravity, where Ξ is given by $f'(R_0)$ in $f(R)$-gravity and by Ξ_q in quadratic curvature gravity. $\hat{N}^b$ is the timelike unit normal to C and $\hat{\sigma}$ is the determinant of the induced metric on C. From the conservation law, these quantities $Q_\xi[C]$ are found to satisfy the balance equation of the form

$$Q_\xi[C_2] - Q_\xi[C_1] = \ell\int_{\Delta\mathcal{I}} dx^{n-1}\sqrt{-\hat{h}}\tau_{ab}\xi^a\hat{n}^b, \tag{11}$$

where $\Delta\mathcal{I}$ is a portion of $\mathcal{I}$, C_1 and C_2 are the past and future boundaries of $\Delta\mathcal{I}$, respectively. The balance equation (11) indicates that decrease of a conserved quantity coincides with the corresponding flux of matter fields carried away across $\mathcal{I}$, and hence there is no unphysical increase or decrease of these conserved quantities, as in the case of Einstein gravity. We also see that, in the both cases of $f(R)$-gravity and quadratic curvature gravity, the conserved quantities $Q_\xi[C]$ are expressed as an integral of the electric part of the Weyl tensor alone, while the proportion factor Ξ depends on the Lagrangian.

In Einstein-Gauss-Bonnet gravity (quadratic curvature gravity with $\beta = \gamma = 0$), the exact black hole solution has been found [3]. In addition, it has been shown that the Kerr-AdS spacetime is an asymptotic solution near infinity in Einstein-Gauss-Bonnet gravity. We can show that our expression Eq. (10) of the conserved quantities $Q_\xi[C]$ correctly reproduces the results for these solutions in Ref. [3, 4], when we set ξ^a in Eq. (10) equal to an appropriate timelike Killing vector [5].

4 Summary and Discussion

We proposed the definition of an n-dimensional AdS spacetime in higher curvature gravitational theories, by using the conformal completion technique, where we imposed the condition on the Riemann tensor

instead of the Weyl tensor. By noticing that the asymptotic symmetry group is unaffected by higher curvature corrections, we explicitly showed for $f(R)$-gravity and quadratic curvature gravity that the proposed definition ensures well-defined conserved quantities which satisfy the balance equation (11) as in the case of Einstein gravity. They were shown to be expressed as an integral of the electric part of the Weyl tensor alone, while it is multiplied by the proportion factor Ξ, which depends on the gravitational Lagrangian, as described in Eq. (10).

The Lagrangian of $f(R)$-gravity is an arbitrary function of the Ricci scalar R alone, while the Lagrangian of quadratic curvature gravity includes all components of the curvature tensors but should be quadratic at most. These results complement each other, based on which we can speculate on the behavior of conserved quantities in more general classes of gravitational theories. Actually, it is not difficult to expect that conserved quantities in an asymptotically AdS spacetime in an arbitrary gravitational theory are expressed as an integral of the electric part of the Weyl tensor alone. We have not proven whether it is indeed the case in general. It will be interesting to investigate this issue further, since if this expectation is true, all of the conserved quantities identically vanish in the pure AdS spacetime, as in the case of Einstein gravity.

Although the asymptotic condition we impose is sufficient for the conserved quantities to be well-defined, we have not shown that it is necessary. Since the conserved quantities depend only on the electric part of the Weyl tensor, it looks reasonable to impose the condition on the electric part of the Weyl tensor. However, it is not straightforward to extrapolate it to the magnetic part of the Weyl tensor and even to the Ricci tensor. Actually, we can show that Eqs. (7) and (8) remain valid even when the asymptotic conditions on the curvature tensors are weakened further, which implies that the conserved quantities are still well-defined under weaker asymptotic conditions. Then, although we can argue that the asymptotic condition we imposed is reasonable when we respect the definition in Ref. [1], refined analysis on this issue will be required in future investigations.

Acknowledgments

We are grateful to N. Deruelle and Y. Morisawa for useful discussion and comments. We are also grateful to K. Maeda for his continuous encouragement. This work was partially supported by a Grant for The 21st Century COE Program (Holistic Research and Education Center for Physics Self-Organization Systems) at Waseda University.

References

[1] A. Ashtekar and A. Magnon, Class. Quantum Grav. **1**, L39 (1984); A. Ashtekar and S. Das, Class. Quantum Grav. **17**, L17 (2000).

[2] N. Okuyama and J. Koga, hep-th/0501044.

[3] D. G. Boulware, and S. Deser, Phys. Rev. Lett. **55**, 2656 (1985); R. G. Cai, Phys. Rev. D **65**, 084014 (2002).

[4] N. Deruelle, J. Katz, and S. Ogushi, Class. Quantum Grav. **21**, 1971 (2004); N. Deruelle and Y. Morisawa, hep-th/0411135.

[5] G. W. Gibbons, M. J. Perry, and C. N. Pope, hep-th/0408217.

Scalar field perturbation on six-dimensional ultra-spinning black holes

Yoshiyuki Morisawa[1] and Daisuke Ida[2]

[1] *Yukawa Institute for Theoretical Physics, Kyoto University, Kyoto 606-8502, Japan*
[2] *Department of Physics, Gakushuin University, Tokyo 171-8588, Japan*

Abstract

We have studied the scalar field perturbations on six-dimensional ultra-spinning black holes. We have numerically calculated the quasinormal modes of rotating black holes. Our results suggest that such perturbations are stable.

1 Introduction

The production of higher-dimensional black holes in collider [1, 2, 3] is the important prediction arising from the large extra dimension scenario [4, 5] or the warped compactification (RS1) scenario [6], where the fundamental (higher-dimensional) scale of gravitation can be set to the order of TeV. Such phenomena would strongly suggest the presence of the extra dimensions, and we would also obtain the experimental method to seek for the quantum gravity. Hence, it is important to investigate the fundamental properties of higher-dimensional black holes such as stability, which is the subject of the present work.

Concerning the static black objects, Gregory and Laflamme [7] have found that the black branes are unstable under linear gravitational perturbations when the compactification scales are large compared with the Schwarzschild radius. On the other hand, Ishibashi and Kodama [8] have shown that the higher-dimensional Schwarzschild black holes in the spherically symmetric space-times are gravitationally stable as in the case with the four space-time dimensions.

It is also important to consider the stability of the rotating black holes, since black holes produced in the collider generically have angular momenta and the production cross section is larger for more rapidly rotating black holes [9]. In contrast to the Kerr-bound on four-dimensional rotating black holes, there are black hole solutions with an arbitrary large angular momentum for a fixed mass in higher-dimensional general relativity. Recently, the existence of the effective Kerr-bound on such rapidly rotating black holes in higher dimension has been conjectured by Emparan and Myers [10]. They showed that the geometry of the event horizon of such rapidly rotating black holes in six or higher dimension behaves like the black membranes and argued that such rapidly rotating black holes therefore become unstable.

Although we should analyze the gravitational perturbations of rotating black holes to confirm such instability, any formalism where the perturbative equations are separable is yet unknown. Here we just consider the perturbation of the massless scalar field propagating on the rotating black hole space-times. Even if we restrict ourselves to field perturbation on fixed background space-time, there exists an instability of massless field perturbation on rotating black branes and strings discovered by Cardoso and Lemos [11]. The equation of motion for the massless scalar field perturbation on the rotating black holes is known to be separable in any dimension [12, 13], and authors examined the stability of this system in five-dimension as the simplest case in the previous work [13]. The present work is the complementary one on the renewed interest in the instability (or stability) of the rapidly rotating black holes in six dimensions.

2 Myers-Perry black hole and its membrane limit

The $(4+n)$-dimensional Myers-Perry metric [14] with only one nonzero angular momentum is given by

$$g = -\frac{\Delta - a^2 \sin^2\vartheta}{\Sigma} dt^2 - \frac{2a(r^2 + a^2 - \Delta)}{\Sigma} \sin^2\vartheta dt d\varphi$$

[1] E-mail:morisawa@yukawa.kyoto-u.ac.jp
[2] E-mail:daisuke.ida@gakushuin.ac.jp

$$+\frac{(r^2+a^2)^2-\Delta a^2\sin^2\vartheta}{\Sigma}\sin^2\vartheta d\varphi^2+\frac{\Sigma}{\Delta}dr^2+\Sigma d\vartheta^2+r^2\cos^2\vartheta d\Omega_n^2, \tag{1}$$

where

$$\Sigma = r^2+a^2\cos^2\vartheta, \tag{2}$$
$$\Delta = r^2+a^2-\mu r^{1-n}, \tag{3}$$

and $d\Omega_n^2$ denotes the standard metric of the unit n-sphere. This metric describes a rotating black hole in asymptotically flat, vacuum space-time with the mass and angular momentum proportional to μ and μa, respectively. Hereafter, $\mu, a > 0$ are assumed. The event horizon is located at $r = r_H$, such that $\Delta|_{r=r_H} = 0$, which is homeomorphic to S^{n+2}. For $n \geq 2$, Δ always has a positive root for arbitrary a, namely regular black hole solutions exist with arbitrarily large angular momentum per unit mass.

In the limit where $a \to \infty$, the coordinate radius of the horizon is approximated by $r_H \approx (\mu/a^2)^{1/(n-1)}$. Hence, the horizon radius r_H shrinks to zero when one take the limit where $a \to \infty$ with fixed μ. To avoid a vanishing horizon radius, Emparan and Myers introduced the black membrane limit where $a \to \infty$ and $\mu \to \infty$ with fixed $\hat{\mu} := \mu/a^2$. In this limit, the Myers-Perry metric behaves like a black membrane metric near the pole $\vartheta = 0$:

$$g = -\left(1-\frac{\hat{\mu}}{r^{n-1}}\right)dt^2+\frac{dr^2}{1-\hat{\mu}/r^{n-1}}+r^2d\Omega_n^2+d\varsigma^2+\varsigma^2d\varphi^2, \tag{4}$$

where the new coordinate is defined by $\varsigma := a\sin\vartheta$. In this paper, we are concerned with the dimensionless Kerr parameter $a_* := a/r_H$. The limit where $a_* \to \infty$ with fixed r_H is consistent to the membrane limit.

3 Basic equations and numerical method

Here we consider the perturbation of the massless scalar field on the background Myers-Perry metric (1). We put the scalar field configuration as

$$\phi = e^{i\omega t-im\varphi}R(r)S(\vartheta)Y(\Omega), \tag{5}$$

where $Y(\Omega)$ is the hyperspherical harmonics on the n-sphere with the eigenvalue $j(j+n-1)$, $(j = 0,1,2,\cdots)$. Then we obtain the field equations with separated variables:

$$\frac{1}{\sin\vartheta\cos^n\vartheta}\left(\frac{d}{d\vartheta}\sin\vartheta\cos^n\vartheta\frac{dS}{d\vartheta}\right)+[\omega^2a^2\cos^2\vartheta-m^2\csc^2\vartheta-j(j+n-1)\sec^2\vartheta+A]S = 0, \tag{6}$$

and

$$\frac{1}{r^n}\frac{d}{dr}\left(r^n\Delta\frac{dR}{dr}\right)+\left\{\frac{[\omega(r^2+a^2)-ma]^2}{\Delta}-\frac{j(j+n-1)a^2}{r^2}-\lambda\right\}R = 0, \tag{7}$$

where $\lambda := A-2m\omega a+\omega^2a^2$.

We will solve the eigenvalue problem under the quasinormal boundary condition:

$$R\sim\begin{cases}(r-r_H)^{i\sigma} & (r\to r_H),\\ r^{-(n+2)/2}e^{-i\omega r} & (r\to+\infty),\end{cases} \tag{8}$$

where

$$\sigma := \frac{(r_H^2+a^2)\omega-ma}{(n-1)(r_H^2+a^2)+2r_H^2}r_H. \tag{9}$$

We use the continued fraction method to determine the resonant frequency ω and the separation constant A. We assume the following series expansion for S:

$$S = (\sin\vartheta)^{|m|}(\cos\vartheta)^j\sum_{k=0}^{\infty}a_k(\cos^2\vartheta)^k, \tag{10}$$

which automatically satisfies the regular boundary conditions at $\vartheta = 0, \pi/2$ and converges at any time. Substituting this expansion into the angular equation (6), we obtain the three-term recurrence relations:

$$\bar{\alpha}_k a_k + \bar{\beta}_k a_{k-1} + \bar{\gamma}_k a_{k-2} = 0, \ (k = 1, 2, \cdots), \tag{11}$$

where $a_{-1} = 0$ and the coefficients are given by

$$\bar{\alpha}_k = -8k(2j + 2k + n - 1), \tag{12}$$

$$\bar{\beta}_k = 2[(j + |m| + 2k - 2)(j + |m| + 2k + n - 1) - A], \tag{13}$$

$$\bar{\gamma}_k = -a_*^2 \omega_*^2. \tag{14}$$

Here $a_* := a/r_H$ and $\omega_* := \omega r_H$ are the dimensionless quantities. The limit where $a_* \to \infty$ corresponds to the membrane limit as mentioned above.

We expand the radial function R as

$$R = e^{-i\omega_* r/r_H} \left(\frac{r - r_H}{r_H}\right)^{i\sigma} \left(\frac{r + r_H}{r_H}\right)^{-(n+2)/2 - i\sigma} \sum_{k=0}^{\infty} b_k \left(\frac{r - r_H}{r + r_H}\right)^k, \tag{15}$$

which automatically satisfies the quasinormal boundary conditions and converges at any time. When $n = 2$, substituting Eq. (15) into the radial equation (7), we obtain the eight-term recurrence relations

$$\alpha_k b_k + \beta_k b_{k-1} + \gamma_k b_{k-2} + \delta_k b_{k-3} + \epsilon_k b_{k-4} + \zeta_k b_{k-5} + \eta_k b_{k-6} + \theta_k b_{k-7} = 0, \ (k = 1, 2, \cdots), \tag{16}$$

where $b_{-1} = b_{-2} = \cdots = 0$ and the coefficients $\alpha_k, \cdots, \theta_k$ are given in the full version of this paper [15]. After we repeatedly use the Gaussian elimination, the eight-term recurrence relations (16) are reduced to the three-term ones

$$\alpha_k'''' b_k + \beta_k'''' b_{k-1} + \gamma_k'''' b_{k-2} = 0, \quad (k = 1, 2, \cdots). \tag{17}$$

For given the three-term recurrence relations (11), the successive coefficients are obtained in two ways, the finite and infinite continued-fraction representations:

$$\begin{aligned} \frac{a_k}{a_{k-1}} &= -\frac{\bar{\beta}_k}{\bar{\alpha}_k} - \frac{1}{\bar{\alpha}_k} \frac{-\bar{\gamma}_k \bar{\alpha}_{k-1}}{\bar{\beta}_{k-1}+} \cdots \frac{-\bar{\gamma}_3 \bar{\alpha}_2}{\bar{\beta}_2+} \frac{-\bar{\gamma}_2 \bar{\alpha}_1}{\bar{\beta}_1} \\ &= -\frac{\bar{\gamma}_{k+1}}{\bar{\beta}_{k+1}+} \frac{-\bar{\alpha}_{k+1}\bar{\gamma}_{k+2}}{\bar{\beta}_{k+2}+} \frac{-\bar{\alpha}_{k+2}\bar{\gamma}_{k+3}}{\bar{\beta}_{k+3}+} \cdots, \end{aligned} \tag{18}$$

where $(1/x+)(y/z)$ is an abbreviation for $1/[x + (y/z)]$. Similarly for Eq. (17), we obtain

$$\begin{aligned} \frac{b_{k'}}{b_{k'-1}} &= -\frac{\beta_{k'}''''}{\alpha_{k'}''''} - \frac{1}{\alpha_{k'}''''} \frac{-\gamma_{k'}'''' \alpha_{k'-1}''''}{\beta_{k'-1}''''+} \cdots \frac{-\gamma_3'''' \alpha_2''''}{\beta_2''''+} \frac{-\gamma_2'''' \alpha_1''''}{\beta_1''''} \\ &= -\frac{\gamma_{k'+1}''''}{\beta_{k'+1}''''+} \frac{-\alpha_{k'+1}''''\gamma_{k'+2}''''}{\beta_{k'+2}''''+} \frac{-\alpha_{k'+2}''''\gamma_{k'+3}''''}{\beta_{k'+3}''''+} \cdots. \end{aligned} \tag{19}$$

For fixed k and k', we obtain nonlinear algebraic equations (18) and (19) for two unknown complex numbers ω_* and A. We use a standard nonlinear root search algorithm provided by the MINPACK subroutine package to evaluate the numerical solutions of these equations. The equations for different sets of (k, k') are used as numerical check.

4 Results

We have calculated typical quasinormal modes of the six-dimensional Myers-Perry black holes. Although the Kerr parameter a_* is taken to have a sufficiently large value, each mode does not seem to have negative imaginary part in any case. Thus they do not show any evidence for instability. Fig. 1 shows the QNM for $(j, m, \ell) = 0$. Here the real and imaginary parts of the resonant frequencies ω_* as function of the parameter $a_*/\sqrt{1 + a_*^2}$ is plotted.

Recently, Cardoso, Siopsis and Yoshida [16] investigated the stability of the same system. Several quasinormal modes within our present work are also calculated by them in different way to expand the radial function and their results are consistent to our present results. They also conclude that the stability of scalar field perturbations on Myers-Perry black holes are suggested.

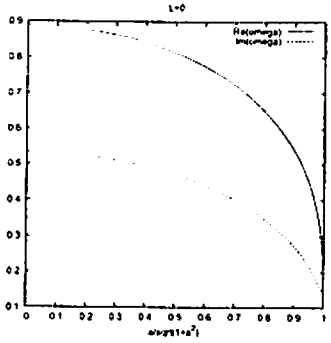


Figure 1: The quasinormal modes for $(j, m, \ell) = (0, 0, 0)$.

References

[1] T. Banks and W. Fischler, arXiv:hep-th/9906038.

[2] S. B. Giddings and S. Thomas, Phys. Rev. D **65**, 056010 (2002) [arXiv:hep-ph/0106219].

[3] S. Dimopoulos and G. Landsberg, Phys. Rev. Lett. **87**, 161602 (2001) [arXiv:hep-ph/0106295].

[4] N. Arkani-Hamed, S. Dimopoulos and G. R. Dvali, Phys. Lett. B **429**, 263 (1998) [arXiv:hep-ph/9803315].

[5] I. Antoniadis, N. Arkani-Hamed, S. Dimopoulos and G. R. Dvali, Phys. Lett. B **436**, 257 (1998) [arXiv:hep-ph/9804398].

[6] L. Randall and R. Sundrum, Phys. Rev. Lett. **83**, 3370 (1999) [arXiv:hep-ph/9905221].

[7] R. Gregory and R. Laflamme, Phys. Rev. Lett. **70**, 2837 (1993) [arXiv:hep-th/9301052].

[8] A. Ishibashi and H. Kodama, Prog. Theor. Phys. **110**, 901 (2003) [arXiv:hep-th/0305185].

[9] D. Ida, K.-y. Oda and S. C. Park, Phys. Rev. D **67**, 064025 (2003) [arXiv:hep-th/0212108].

[10] R. Emparan and R. C. Myers, JHEP **0309**, 025 (2003) [arXiv:hep-th/0308056].

[11] V. Cardoso and J. P. S. Lemos, arXiv:hep-th/0412078.

[12] V. P. Frolov and D. Stojkovic, Phys. Rev. D **67**, 084004 (2003) [arXiv:gr-qc/0211055].

[13] D. Ida, Y. Uchida and Y. Morisawa, Phys. Rev. D **67**, 084019 (2003) [arXiv:gr-qc/0212035].

[14] R. C. Myers and M. J. Perry, Annals Phys. **172**, 304 (1986).

[15] Y. Morisawa and D. Ida, arXiv:gr-qc/0412070.

[16] V. Cardoso, G. Siopsis and S. Yoshida, arXiv:hep-th/0412138.

Improved analysis of black hole formation in high-energy particle collision

Hirotaka Yoshino[1], Vyacheslav S. Rychkov[2]

[1] *Department of Physics, Graduate School of Science, Nagoya University, Chikusa, Nagoya 464-8602, Japan*
[2] *Instituut voor Theoretische Fysica, Universiteit van Amsterdam, Valckenierstraat 65, 1018XE Amsterdam, The Netherlands*

Abstract

In the brane world scenario, there is a possibility that we can produce black holes in future-planned accelerators. One of the author and Nambu investigated the system of colliding high-energy particles and numerically calculated the apparent horizon (AH) on the past light cone of the collision. In this article, we improve this analysis by taking another slice which is at the future of the previous one. The maximal impact parameter of the AH formation increases by 5% and 18% in four and five dimensional cases, respectively.

1 Introduction

The brane world scenario has been paid much attention. In this scenario, our space is the 3-brane with large extra dimensions on which gauge particles and interactions are confined and the fundamental Planck energy could be at the O(TeV) [1]. If this is true, the black hole smaller than the extra-dimension scale is well-described as a D-dimensional black hole centered on the brane. Further, its gravitational radius is far larger than that of the usual black hole with the same mass. This brings about the expectation that we might be able to produce black holes using future planned accelerators, because the gravitational interaction would become dominant in the particle collisions above the TeV scale and the black hole production cross section $\sigma_{\rm BH} \sim \pi [r_h(2\mu)]^2$ becomes sufficiently large, where μ is the energy of each incoming particle and $r_h(2\mu)$ denotes the gravitational radius of the system. The phenomenology of the black holes in accelerators has been discussed by several authors [2].

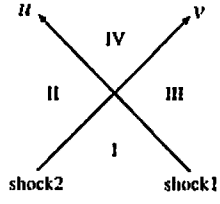


Figure 1: Schematic picture of the spacetime of colliding high-energy particles.

One of the necessary investigations for improving the experimental predictions is to analyze the process of the black hole formation in the particle collision using the general relativity. This is because the precise predictions are required for testing the validity of the higher-dimensional general relativity and the quantum gravity effects are understood by the difference from the semi-classical signals. A schematic picture of the spacetime with two high-energy particles are shown in Fig. 1. Two particles collide almost at the speed of light. The gravitational field of each incoming particle is infinitely Lorentz-contracted and forms a shock wave. Except at the shock wave, the spacetime is flat before the collision (i.e., the regions I, II, and III). After the collision, two shocks nonlinearly interact each other and the spacetime

[1] E-mail:yoshino@gravity.phys.nagoya-u.ac.jp
[2] E-mail:rychkov@science.uva.nl

within the future lightcone of the collision becomes highly curved one (i.e., the region IV). The final goal of our analysis is to clarify the structure of the region IV. If this is possible, the cross section of the black hole production and the gravitational wave emitted in the relaxation process would become clear. But this analysis is difficult because of the quite complicated structure of the gravitational field and no one has succeeded in deriving the metric of the region IV.

Nonetheless, one can estimate the lower bound of the cross section of the black hole production, which is one of the interesting quantities in this process, only with the knowledge of the regions I, II, and III. This becomes possible by the analysis of the apparent horizon (AH), because the AH existence is the sufficient condition of the black hole formation assuming the cosmic censorship. Eardley and Giddings [3] analytically investigated the AH formation in the four-dimensional spacetime. Subsequently, one of the present authors and Nambu [4] extended this analysis for the D-dimensional spacetimes numerically. Our results have shown that the maximal impact parameter of the AH formation is given by $b_{max} \simeq 1.5 \times 2^{-1/(D-3)} r_h(2\mu)$. In this analysis, we constructed the AH on the slice which is the union of two incoming shocks, $u = 0, v < 0$ and $v = 0, u < 0$. Here, we would like to point out that we can take another slice which includes the instant of the collision $u = v = 0$. Obviously, the maximal impact parameter of the AH formation would become larger if one can take the slice at the future. Motivated by this observation, we proceed the AH analysis on the slice $u = 0, v > 0$ and $v = 0, u > 0$. This is the future-most slice that we can take without the knowledge of the region IV. By this analysis, we improve the lower bound of the cross section of the black hole production. In addition, such analysis would be the necessary step for investigating the spacetime structure of the region IV.

2 Finding apparent horizons

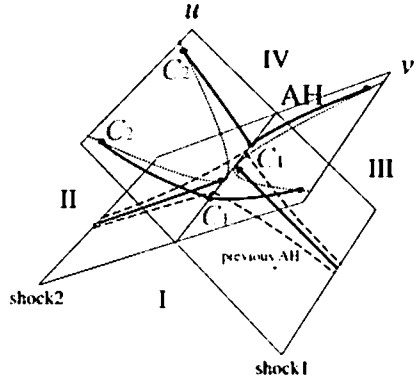


Figure 2: Schematic picture of the spacetime of colliding high-energy particles with $(D-3)$ dimensions suppressed. The shape of AH on the slice $u > 0, v = 0$ and $v > 0, u = 0$ is shown.

We adopt $r_0 = (8\pi G_D \mu/\Omega_{D-3})^{1/(D-3)}$ as the length unit, which is close to $r_h(2\mu)$. Here, G_D is the gravitational constant and Ω_{D-3} denotes the area of the unit $(D-3)$-sphere. We show in Fig. 2 the schematic spacetime structure adding one dimension to Fig. 1. The metric of the regions I and II is written as

$$ds^2 = -dudv + \left(1 + (D-3)\frac{u}{r^{D-2}}\theta(u)\right)^2 dr^2 + r^2\left(1 - \frac{u}{r^{D-2}}\theta(u)\right)^2 \left(d\phi^2 + \sin^2\phi d\Omega_{D-4}^2\right). \qquad (1)$$

In this coordinate, the incoming particle 1(2) is located at $r = 0$ $(r = b, \phi = 0)$. The schematic shape of the AH on the slice $u = 0, v > 0$ and $v = 0, u > 0$ which we would like to construct is also drawn in Fig. 2. Because $u = r^{D-2}$ is the coordinate singularity, we have two boundaries in this analysis: C_1 at $u = v = 0$ and C_2 at $u = r^{D-2}, v = 0$. We assume that the AH is specified by $u = h(r, \phi)$ at $v = 0$, $u > 0$. The equation of the AH is derived by imposing that the surface has zero expansion. It becomes

as follows:

$$\left(r^{D-2}-h\right)^2\left\{h_{,rr}+(D-3)\frac{h_{,r}}{r}\left[1+\frac{(D-2)h-(3/2)rh_{,r}}{r^{D-2}+(D-3)h}+\frac{(D-2)h-(1/2)rh_{,r}}{r^{D-2}-h}\right]\right\}$$
$$+r^{-2}\left(r^{D-2}+(D-3)h\right)^2\left\{h_{,\phi\phi}+(D-4)\cot\phi h_{,\phi}+\frac{h_{,\phi}^2}{2}\left[\frac{(D-3)}{r^{D-2}+(D-3)h}-\frac{(D-7)}{r^{D-2}-h}\right]\right\}=0. \quad (2)$$

Two boundary conditions are obtained for each boundary by imposing the continuity of the surface and of the null normal. The boundary conditions at C_1 are

$$h(r,\phi)=0, \quad (3)$$
$$\left(h_{,r}^2+r^{-2}h_{,\phi}^2\right)\Big|_x\left(h_{,r}^2+r^{-2}h_{,\phi}^2\right)\Big|_{x^*}=16, \quad (4)$$

where x^* denotes the point symmetric to x concerning the central point of C_1. Simple analysis shows that C_2 should be given by $r=r_{max}$ and the boundary conditions become

$$h=r_{max}^{D-2}, \quad (5)$$
$$h_{,r}=(D-2)r_{max}^{D-3}\left(1+\frac{1-B^2}{1+B^2+2B\cos\phi}\right). \quad (6)$$

Note that the shape of C_1 and the values of r_{max} and B as well as h should be determined so as to be consistent with all these boundary conditions.

We solved numerically the AH and the boundaries C_1 and C_2 as follows. First we solve h giving some boundaries under the boundary conditions (3) and (5). If h converges, we calculate the difference from the boundary conditions (4) and (6). Using these values, we modify the boundaries properly. We iterate these steps until h and the boundaries converge.

3 Numerical results for $D=4$ and 5

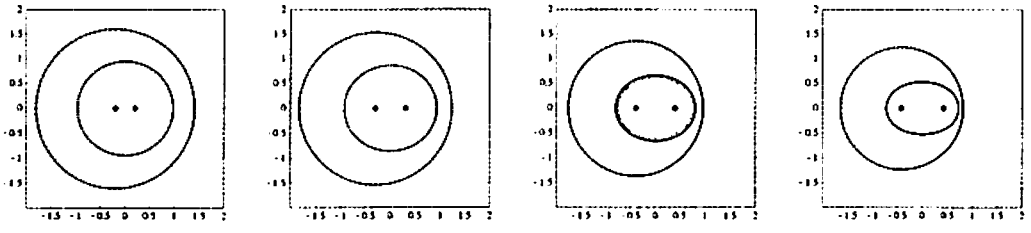


Figure 3: The shape of C_1 and C_2 for $b=0.4, 0.6, 0.8, 0.837$ in the $D=4$ case. Two dots in each figure indicate the location of incoming particles.

Figure 3 shows the shape of C_1 and C_2 for various values of b in the four-dimensional case. The previous AHs of Eardley and Giddings [3] are also shown. For small b, C_1 and the previous AH almost coincide, which indicates the correctness of our numerical program. For large b, C_1 exists outside of the previous AH and b_{max} becomes 5% larger than the previous result.

Figure 4 shows the shape of the C_1 and C_2 in the five-dimensional case. In this case, the shape of C_1 becomes non-convex for large b. The value of b_{max} is 18% larger than the previous result, which would be quite impressive. The cross section of the AH formation becomes 40% larger and its value is $\sigma_{AH}\simeq 1.5\pi\left[r_h(2\mu)\right]^2$. This result indicates that the black hole production rate is somewhat larger compared to the previous estimates.

Finally we show in Fig. 5 the behavior of the indicater of the trapped energy

$$M_{AH}=\frac{(D-2)\Omega_{D-2}}{16\pi G_D}\left(\frac{A_{D-2}}{\Omega_{D-2}}\right)^{(D-3)/(D-2)}, \quad (7)$$

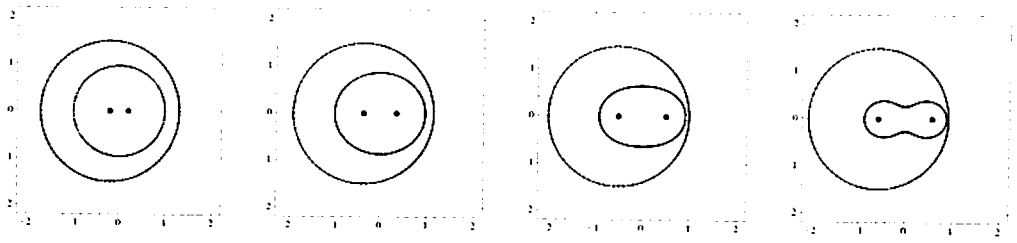


Figure 4: The shape of C_1 and C_2 for $b = 0.4, 0.7, 1.0, 1.147$ in the $D = 5$ case. Two dots in each figure indicate the location of the incoming particles.

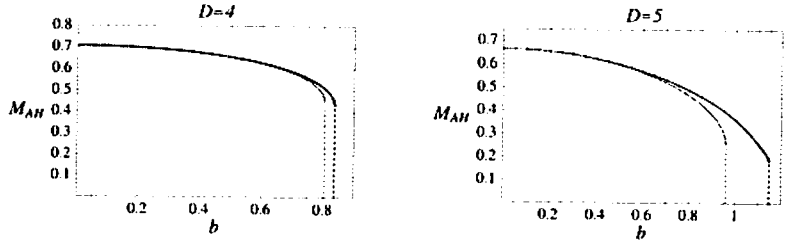


Figure 5: The relation between the impact parameter b and the indicator of the trapped energy M_{AH} in the $D = 4$ case (left) and in the $D = 5$ case (right).

which is determined by the AH area A_{D-2}. The previous results are also shown. Although the value of M_{AH} is very similar as the previous one for small b, it becomes quite larger near the maximal impact parameter especially in the five-dimensional case.

4 Summary

We have improved Yoshino and Nambu's previous analysis of the AH formation in the high-energy particle collision by taking a slice which exists at the future of the previous one. The maximal impact parameter of the AH formation increases by 5% for $D = 4$ and by 18% for $D = 5$. The result of the five-dimensional case is quite impressive, because the cross section becomes 40% larger.

We have also completed the preliminary analysis in the $D \geq 6$ cases. Our results indicate that the maximal impact parameter of the AH formation becomes larger by 25-30% for $6 \leq D \leq 11$ compared to Yoshino and Nambu's previous results. For large D, the cross section of the AH formation becomes $\sigma_{\rm AH} \simeq 3\pi \left[r_h(2\mu)\right]^2$, which is quite larger than the value used in the previous discussions. The black hole production rate in accelerators is much larger than we had expected, although there would be correction of the quantum gravity effects.

Our remaining problem is to decrease the error because there remains somewhat large error at this point. Our work will be completed and submitted soon.

References

[1] N. Arkani-Hamed, S. Dimopoulos and G. R. Dvali, Phys. Lett. B **429**, 263 (1998); I. Antoniadis, N. Arkani-Hamed, S. Dimopoulos and G. R. Dvali, Phys. Lett. B **436**, 257 (1998).

[2] S. Dimopoulos and G. Landsberg, Phys. Rev. Lett. **87** 161602 (2001); S. B. Giddings and S. Thomas, Phys. Rev. D **65** 056010 (2001).

[3] D.M. Eardley and S.B. Giddings, Phys. Rev. D **66**, 044011 (2002).

[4] H. Yoshino and Y. Nambu, Phys. Rev. D **67**, 024009 (2003).

Kink instability and stabilization of the Friedmann universe

Hideki Maeda[1], Tomohiro Harada[2]

[1]*Advanced Research Institute for Science and Engineering, Waseda University, Okubo 3-4-1, Shinjuku, Tokyo, 169-8555, Japan*

[2]*Astronomy Unit, School of Mathematical Sciences, Queen Mary, University of London, Mile End Road, London E1 4NS, UK*

Abstract

The evolution of weak discontinuity is investigated in the flat FRW universe with a single scalar field and with multiple scalar fields. We consider both massless scalar fields and scalar fields with exponential potentials. Then we find a new type of instability, which we call the kink instability, of the flat FRW universe with massless scalar fields. The kink instability develops with scalar fields with considerably steep exponential potentials, while less steep exponential potentials do not suffer from kink instability. In particular, assisted inflation with multiple scalar fields does not suffer from kink instability.

1 Introduction

The data of WMAP for the cosmic microwave background radiation tell us that the universe at the last scattering surface is well approximated by the Friedmann-Robertson-Walker (FRW) universe so that understanding of the detailed properties of the FRW universe is an important step in cosmology [1]. One of the most important problems is how cosmological structures on various scales formed from the very homogeneous and isotropic universe at early times.

Recently, a new kind of instability has been found in the studies of self-similar solutions, which include a class of the flat FRW solutions. (See [2] for the review of self-similar solutions.) The instability concerns weak discontinuity. If the perturbations with weak discontinuity are inserted into a self-similar solution which is unstable against this mode, the discontinuity grows as time proceeds. This instability has been called *kink instability*. Kink instability of self-similar solutions was originally found by Ori and Piran in spherically symmetric isothermal gas systems in Newtonian gravity [3]. In general relativity, Harada investigated the kink instability of self-similar solutions for the spherical system of a perfect fluid with the equation of state $p = k\mu$ [4]. The present authors investigated the kink instability of self-similar solutions for the spherical system of a stiff ($k = 1$) fluid and those of a massless scalar field [5]. These works have shown that the kink instability can occur in a large class of self-similar solutions. In particular, the work in general relativity showed that the flat FRW universe is unstable for a perfect fluid for $1/3 \leq k \leq 1$ and for a massless scalar field.

This article is based on [6]. In this article we derive a stability criterion against kink mode perturbations for the power-law flat FRW universe with a single scalar field and with multiple scalar fields with and without exponential potentials, which arise in supergravity or theories obtained through dimensional reduction to effective four dimensional theories. We adopt the units such that $c = G = 1$.

2 Stability criterion for the flat FRW universe

2.1 power-law flat FRW solution with and without exponential potentials

We begin with the action which describes the self-gravitating system of scalar fields with and without exponential potentials.

$$S = \int d^4x\sqrt{-g}\left\{\frac{1}{8\pi}R - \sum_{i=1}^{n}\left[\frac{1}{2}(\nabla\phi_i)^2 + V_i e^{-\sqrt{8\pi}\lambda_i\phi_i}\right]\right\}, \tag{1}$$

[1]E-mail:hideki@gravity.phys.waseda.ac.jp

[2]E-mail:T.Harada@qmul.ac.uk

where $\{V_i|i=1,\cdots,n\}$ and $\{\lambda_i|i=1,\cdots,n\}$ are n real non-negative and positive constants, respectively. In this model we currently have n real scalar fields $\{\phi_j|j=1,\cdots,n\}$. If $V_j=0$, then ϕ_j is massless and λ_j is meaningless. This action has been considered in the context of assisted inflation [7, 8].

We consider the power-law flat FRW solution in the self-similar form [2];

$$ds^2 = -dt^2 + z^{2\alpha}(d\bar{r}^2 + (1-\alpha)^{-2}\bar{r}^2 d\Omega^2), \tag{2}$$

$$\phi_j = -\kappa_j \ln t, \tag{3}$$

where $\{\kappa_j|j=1,\cdots,n\}$ and t_0 are constants, α is the power index of the scale factor, $z \equiv t/\bar{r}$ is the self-similarity coordinate and $d\Omega^2 \equiv d\theta^2 + \sin^2\theta d\varphi^2$. $\{\kappa_j\}$ satisfy $4\pi\sum_{i=1}^n \kappa_i^2 = \alpha$. This form is obtained with a coordinate transformation $r = |1-\alpha|^{-1}\bar{r}^{1-\alpha}$ from the usual coordinate r. We consider only the case with $\alpha \neq 1$, which is exceptional [2]. It is shown that there are no self-similar flat FRW solutions if there exist both nontrivial massless scalar fields and those with exponential potentials [6].

Governing equations give $\alpha = 1/3$ for massless scalar fields, while $\kappa_j = -2/(\sqrt{8\pi}\lambda_j)$, $\alpha = \sum_{i=1}^n (2/\lambda_i^2)$ and

$$V_j = \frac{1}{4\pi\lambda_j^2}\left(\sum_{i=1}^n \frac{6}{\lambda_i^2} - 1\right), \tag{4}$$

for those with exponential potentials. The last equation gives a condition $\sum_{i=1}^n \lambda_i^{-2} > 1/6$ for $V_j > 0$. Setting $n=1$ in both cases, we can obtain the results for a single scalar-field case.

The particle horizon $z=1$ plays an important role in the following analysis. This is because it is a *similarity horizon*, which is given by a radial null ray on which z is constant.

2.2 kink instability

We consider general full-order spherically symmetric perturbations with scalar fields such as

$$ds^2 = -e^{2\bar{\sigma}(t,r)}dt^2 + z^{2\alpha}e^{2\bar{\omega}(t,\bar{r})}d\bar{r}^2 + (1-\alpha)^{-2}z^{2\alpha}\bar{r}^2 e^{2\bar{\eta}(t,\bar{r})}d\Omega^2, \tag{5}$$

$$\phi_j = -\kappa_j \ln t + \bar{\psi}_j(t,\bar{r}). \tag{6}$$

Hereafter we adopt the isotropic coordinates, in which $\bar{\omega} = \bar{\eta}$. We define the coordinates $Z \equiv \ln z$ and $T \equiv \ln t$, in which Eqs. (5) and (6) are represented by

$$\begin{aligned} ds^2 = &-(e^{2\sigma(T,Z)} - e^{2(\alpha-1)Z+2\omega(T,Z)})e^{2T}dT^2 - 2e^{2(\alpha-1)Z+2T+2\omega}dTdZ \\ &+e^{2(\alpha-1)Z+2T+2\omega}dZ^2 + (1-\alpha)^{-2}e^{2(\alpha-1)Z+2T+2\omega}d\Omega^2, \end{aligned} \tag{7}$$

$$\phi_j = -\kappa_j T + \psi_j(T,Z), \tag{8}$$

where $\sigma(T,Z) \equiv \bar{\sigma}(t(T),\bar{r}(T,Z))$, $\omega(T,Z) \equiv \bar{\omega}(t(T),\bar{r}(T,Z))$ and $\psi_j(T,Z) \equiv \bar{\psi}_j(t(T),\bar{r}(T,Z))$.

We consider perturbations σ, ω and $\{\psi_j\}$ which satisfy the following conditions:

(1) The initial perturbations vanish outside the similarity horizon.

(2) σ, ω, $\{\psi_j\}$ and $\{\psi_j'\}$ are continuous, in particular at the similarity horizon $Z=0$, where a prime denotes the derivative with respect to Z.

(3) $\{\dot{\psi}_j''\}$ and $\{\psi_j''\}$ are discontinuous at the similarity horizon, although they have finite one-sided limit values as $Z \to -0$ and $Z \to +0$, where a dot denotes the derivative with respect to T.

(4) The quasi-local mass is continuous, i.e., there are no singular hypersurfaces in the spacetime.

Now we consider the behavior of the perturbations at the similarity horizon. The perturbations satisfy $\dot{\psi}_j = \psi_j' = 0$ for all j and $\psi_j'' \neq 0$ for some j at the similarity horizon at the initial moment $T = T_0$ due to condition (2). The evolution of the initially unperturbed region is completely described by the background flat FRW solution because information from the perturbed side cannot penetrate the unperturbed side due to condition (1). Then, we find $\sigma = \omega = 0$, $\dot{\psi}_j = \psi_j' = 0$ for all j and $\psi_j'' \neq 0$ for some j at the similarity horizon for $T \geq T_0$ due to conditions (2) and (3). Due to condition (4), $\omega' = 0$ is satisfied at the similarity horizon. Then we find $\sigma' = 0$ from the equation of motion for scalar fields. From the Einstein equations, $\omega'' = 0$ and $\sigma'' = 0$ are obtained, respectively. Differentiating the equation of motion for scalar fields with respect to Z and estimating both sides at the similarity horizon, we obtain

$$\dot{\psi}_j''' - (1-2\alpha)\dot{\psi}_j'' = \frac{1}{2}\lim_{Z\to 0}\left(1 - e^{2(\alpha-1)Z}\right)\psi_j''', \tag{9}$$

for each j. We can show that the right-hand side vanishes [5]. Finally, the full-order perturbation equation for ψ_j'' at the similarity horizon is obtained as

$$\dot{\psi}_j'' = (1 - 2\alpha)\,\psi_j''. \tag{10}$$

It should be noted that the perturbations are those of full-order although this equation is linear. This equation can be integrated to obtain

$$\psi_j'' \propto e^{(1-2\alpha)T}. \tag{11}$$

Therefore, it is found that the perturbation decays exponentially for $\alpha > 1/2$, it is constant for $\alpha = 1/2$ and it grows exponentially for $\alpha < 1/2$.

It is noted that these perturbations are gauge-independent. Here we define instability by the exponential growth of discontinuity. Then we find the following criterion: the flat FRW universe with $\alpha > 1/2$ are stable against the kink mode, while those with $\alpha < 1/2$ are unstable. Solutions with $\alpha = 1/2$ are marginally stable against this mode.

3 Discussions

We have derived the stability criterion for the flat FRW universe with scalar fields with independent exponential potentials to suffer from kink instability. It was also obtained in general relativity for a perfect fluid with an equation of state $p = k\mu$ [4, 5] and for a massless scalar field [5]. The results are summarized in Tables 1 and 2. This is a new kind of instability of the FRW universe. We first discuss the relations of our result to other studies in the literature on the system with scalar fields with or without exponential potentials. After that, we discuss astrophysical or cosmological implications of the kink instability of the flat FRW universe.

Let us see the flat FRW universe filled with a single matter field. The FRW universe is unstable for a perfect fluid with $1/3 \leq k \leq 1$, for a massless scalar field and for a scalar field with an exponential potential for $4 < \lambda^2 < 6$. These results suggest that if there exists a phase in the flat FRW universe in which a scalar field dominates other matter fields, the scalar field with an exponential potential for $0 < \lambda^2 < 4$ is preferred rather than a massless scalar field.

Kitada and Maeda [9] showed the cosmic no-hair theorem, which states that all ever-expanding homogeneous models which contain a scalar field with an exponential potential together with a matter field satisfying the dominant energy condition asymptote to the inflationary flat FRW solution for $0 < \lambda^2 < 2$. According to the criterion obtained in this letter, the flat FRW solution with $4 < \lambda^2 < 6$ suffers from kink mode perturbations so that our result does not affect the cosmic no-hair theorem.

Next let us move on to the case with multiple scalar fields. In such a situation, assisted inflation was proposed, in which an arbitrary number of scalar fields with independent exponential potentials evolve to the inflationary flat FRW solution even if each individual potential is too steep to support inflation by its own [7]. Together with the result on the spatially homogeneous scalar-field cosmological models [10], Coley and van den Hoogen concluded that the assisted inflationary solution is a global attractor for all ever-expanding spatially homogeneous cosmological models with multiple scalar fields with exponential potentials provided $\sum_{i=1}^{n} \lambda_i^{-2} > 1/2$ [8]. According to the criterion obtained in this letter, the expanding flat FRW solution with $\sum_{i=1}^{n} \lambda_i^{-2} > 1/4$ does not suffer from kink instability, so that our result does not affect the genericity of assisted inflation.

For any case of the flat FRW universes we have seen in this letter, we find that the stability of the flat FRW universe against kink mode perturbation changes from stability to instability as the power index α of the scale factor increases through $1/2$, which is clear from Tables 1 and 2. This suggests that the cosmological kink instability is related to the expansion-law of the universe rather than the characteristics of the matter fields.

The kink instability is particularly important for the flat FRW universe in the radiation ($k = 1/3$) dominated era. It is critical for some cosmological models which assume a stage when the effective equation of state is "harder" than the radiation fluid. Because the flat FRW solution is homogeneous, we can choose any point as a symmetric centre in the present analysis. This implies that a bubble-like structure will develop and the bubble walls collide with each other. This consideration suggests that

density perturbations can arise in different scales as a result of multiple bubble wall collisions. Although the product of kink instability has not been clear yet, it is plausible that it will bring shock-wave formation, which could be important for the cosmological structure formation. Actually, the shock-wave formation has been observed in the numerical simulations of the gravitational collapse of the density fluctuations in the radiation-dominated flat FRW universe [11]. The outcome of the instability and the effect on the structure formation should be comprehensively investigated.

Parameter	Power index α	Stability
$0 < k < 1/3$	$1/2 < \alpha < 2/3$	Stable
$k = 1/3$	$\alpha = 1/2$	Unstable
$1/3 < k \leq 1$	$1/3 \leq \alpha < 1/2$	Unstable

Table 1: Stability of kink mode perturbation in the flat FRW universe with a perfect fluid with the equation of state $p = k\mu$. The index α of the scale factor is given by $\alpha = 2/[3(1+k)]$. See [4] for details.

Potential	Parameters	Power index α	Stability
Massless	—	$\alpha = 1/3$	Unstable
Exp	$\sum_i \lambda_i^{-2} > 1/4$	$\alpha > 1/2$	Stable
	$\sum_i \lambda_i^{-2} = 1/4$	$\alpha = 1/2$	Marginal
	$1/6 < \sum_i \lambda_i^{-2} < 1/4$	$1/3 < \alpha < 1/2$	Unstable

Table 2: Stability of kink mode perturbation in the flat FRW universe with scalar fields. For exponential potentials, we consider the sum of independent potentials, $V_{\rm tot} = \sum_i V_i \exp(-\sqrt{8\pi}\lambda_i\phi_i)$, for scalar fields $\{\phi_i\}$, where the power index α of the scale factor is given by $\alpha = 2\sum_i \lambda_i^{-2}$.

References

[1] WMAP website: http//map.gsfc.nasa.gov; C.L. Bennett, et al., Astrophys. J. Suppl. **148**, 1 (2003); D.N. Spergel, et al., Astrophys. J. Suppl. **148**, 175 (2003); H.V. Peiris, et al., Astrophys. J. Suppl. **148**, 213 (2003).

[2] H. Maeda and T. Harada, to appear in *"Progress in General Relativity and Quantum Cosmology Research"*, (Nova Science Publishers, New York, USA, 2005), gr-qc/0405113.

[3] A. Ori and T. Piran, Mon. Not. R. Astron. Soc. **234**, 821 (1988).

[4] T. Harada, Class. Quantum Grav. **18**, 4549 (2001).

[5] T. Harada and H. Maeda, Class. Quantum Grav. **21**, 371 (2004).

[6] H. Maeda and T. Harada, Phys. Lett. B, in press, gr-qc/0412040.

[7] A.R. Liddle, A. Mazumdar and F.E. Schunck, Phys. Rev. D **58**, 061301 (1998).

[8] A.A. Coley and R.J. van den Hoogen, Phys. Rev. D **62**, 023517 (2000).

[9] Y. Kitada and K. Maeda, Phys. Rev. D **45**, 1416 (1992); Class. Quantum Grav. **10**, 703 (1993).

[10] A.P. Billyard, A.A. Coley, R.J. van den Hoogen, J. Ibáñez and I. Olasagasti, Class. Quantum Grav. **16**, 4035 (1999).

[11] I. Hawke and J.M. Stewart, Class. Quantum Grav. **19**, 3687 (2002).

Geometrical Pinning in Superconductor

Izumi Tanaka[1]

Department of Mathematics and Physics, Graduate School of Science, Osaka City University, Osaka 558-8585, Japan

Abstract

Deformed superconductor with dislocation or disclination is considered. By tight-binding approximation, electron moves in the superconductor described as the space with metric of spatial part of Gal'tsov-Letelier-Tod "GLT" metric in the continum limit. The boundary condition for singular point is determined to realiaze quantum mechanics.

1 Introduction

Deformed medium with dislocation or disclination is expressed in curved geometry. [1] . These distortions can be characterized by Volterra process, cutting and welding process using the $SO(3)\otimes T(3)$ [2] symmetry to classify the distortions of flat space.

It directly describes the atomic arrangement and plastic deformed medium corresponds to the curved space. Typical geometry as spacetime with disclination and dislocations has been discussed by Gal'tsov and Letelier. [3, 4] Spatial part of Gal'tsov-Letelier-Tod "GLT" metric is given as follows:

$$ds^2 = dr^2 + \beta^2 r^2 d\theta^2 + (dz + \gamma d\theta)^2 \tag{1}$$

In fact, this metric is flat except for $r = 0$. There are distributional curvature and torsion at $r = 0$.

2 Tight-Binding Approximation

The electron in lattice can be described by tight-binding approximated decription in certain situation. In the tight-binding approximation, electron's wave funcion on atom at some cite is determined by nearest neighbouring cite's amplitude. Tight-binding approximation of one-dimensional case is described below: [6, 5]

$$i\hbar\frac{dC(x_n)}{dt} = EC(x_n) - TC(x_n + b) - TC(x_n - b) \tag{2}$$

$$= (E - 2T)C(x_n) + T\{2C(x_n) - C(x_n + b) - C(x_n - b)\} \tag{3}$$

Hopping amplitude T is assumed to be constant between nearest neighbours and zero for more distant neighbours.

$C(x_n)$ shows probability amplitude for finding an electron on the atom at n sites.

$$C(x_n) = \langle x_n | \psi \rangle \tag{4}$$

where $|x_n\rangle$ is the base electron's state at n sites. Probability amplitude $C(x_n)$ is determined by nearest neighbour's amplitude.

To achieve the continuum limit, $C(x_n)$ is assumed to vary slowly in the sense that only small changes in $C(x_n)$ occur over distances of order b so as to define a function $C(x)$ of continuous variable x.

With the limit

$$\lim_{b\to 0} b^2 T = \hbar^2/2m_{eff}, \tag{5}$$

[1]E-mail:itanaka@sci.osaka-cu.ac.jp

and

$$C(x) - C(x-b) - C(x+b) \approx \frac{\partial^2 C(x)}{\partial x^2}, \tag{6}$$

we have

$$i\hbar\frac{dC(x)}{dt} = (E-2T)C(x) - \frac{\hbar^2}{2m_{eff}}\frac{\partial^2 C(x)}{\partial x^2}. \tag{7}$$

When tight-binding approximation can be adopted, the perfect lattice just corresponds to the flat space for electron.

Next tight-binding approximation for disclinated or dislocated medium is considered. In disclinated medium, each lattice is distorted different way. [7] As electron experiences more complex curved space as described in metric [8], we can not use the metric for electron's playground. In dislocated medium, we particularly think screw-dislocated simple cubic lattice. In screw dislocated medium, perfect lattice spirally arranged along the dislocation line. It is generally known that as the trace of strain tensor is zero for dislocated medium, electrons are not scattered by dislocation. [9, 10] This also suggests that electrons feel flat in the dislocated medium. Through tight-binding approximation, electrons feel flat except for the dislocation line. This space is shown as $\beta^2 = 1, \gamma \neq 0$ in the metric of Eq.(1).

3 Bogolibov-de Genne Equation

Bardeen, Cooper and Schrieffer devoloped the BCS theory, based on the fact the interaction between electrons resulting from virtual exchange of phonon is attractive when the energy difference between the electron states involved is less than the phonon energy.

Superconductor is classified in two types. If a type I superconductor is cooled in a magnetic field below the transition temperature Tc, then at the transition the lines of induction B are pushed out. In type II superconductor, magnetic flux starts to penetrate at the critical value, and moves in the superconductor. i.e. superconducting state and normal state are coexist. Quantized magnetic flux can be captured, or "pinned" by impurities, etc..

To investigate the influence of disclination and dislocations to superconductor, Bogolibov-de Genne equation can be used. [11] Bogolibov-de Genne equation is solved self-consistently and suited to treat the case where the electrons experience an arbitrary external potential. The BCS Hamiltonan is given as: [12]

$$H_{mf} = \int d\vec{r} \sum_{\alpha} \Psi^+(\vec{r}\alpha)\left[\frac{(\vec{p} - \frac{e}{c}\vec{A})^2}{2m} + U_0(r)\right]\Psi(\vec{r}) \tag{8}$$

$$-\frac{1}{2}\int d\vec{r}\ (\ \Psi^+(\vec{r}\alpha)\Psi^+(\vec{r}\beta)\Delta(\vec{r}) + \Delta^*(r)\Psi(\vec{r}\alpha)\Psi(\vec{r}\beta)\ ) \tag{9}$$

where

$$\Delta(r) = \langle\Psi_\uparrow(\vec{r})\Psi_\downarrow(\vec{r})\rangle \tag{10}$$

$$H = \left[\frac{(\vec{p} - \frac{e}{c}\vec{A})^2}{2m} + U_0(r)\right] \tag{11}$$

From this we have

$$i\frac{\partial\psi_\uparrow}{\partial t} = [H+U]\psi_\uparrow - \Delta(x)\psi_\downarrow^+ \tag{12}$$

$$i\frac{\partial\psi_\downarrow^+}{\partial t} = [H^*+U]\psi_\downarrow^+ - \Delta^*(x)\psi_\uparrow \tag{13}$$

We can diagonalize this Hamilonian by Bogolibov transformation:

$$\begin{pmatrix} \psi_\uparrow \\ \psi_\downarrow^+ \end{pmatrix} = \sum_n \begin{pmatrix} u_n(x) & v_n(x) \\ -v_n^*(x) & u_n(x) \end{pmatrix} \begin{pmatrix} \gamma_{n\uparrow} \\ \gamma_{n\downarrow}^+ \end{pmatrix} \tag{14}$$

Bogolibov-de Genne equation is given as follows:

$$\begin{pmatrix} H + U(x) - \varepsilon_n & \Delta(x) \\ -\Delta^*(x) & H^* + U(x) + \varepsilon_n \end{pmatrix} \begin{pmatrix} u_n(x) \\ v_n^*(x) \end{pmatrix} = 0 \tag{15}$$

$u_n(x)$ and $v_n(x)$ show the effect of the configuration of deformation.

4 Boundary Condition for Deformed Superconductor

We investigate a crystal of simple cubic strucure with screw dislocation and assume the tight-binding approximation to solve Bogolibov-de Genne equation.

Using tight-binding approximation, Laplacian of $H+U(x)-\varepsilon_n$ in Eq.(15) can be expressed as following,

$$-\frac{1}{2m}\nabla^2 + \frac{e}{2mi}(\nabla \cdot \mathrm{A} + \mathrm{A} \cdot \nabla) + \frac{e^2}{c^2}\mathrm{A}^2 - \mu - \varepsilon_n \tag{16}$$

where

$$\nabla^2 = \frac{\partial^2}{\partial r^2} + \frac{1}{r}\frac{\partial}{\partial r} + \frac{1}{\beta^2 r^2}\left(\frac{\partial^2}{\partial \theta^2} - 2\gamma\frac{\partial^2}{\partial \theta \partial z} + [\gamma^2 + \beta^2 r^2]\frac{\partial^2}{\partial z^2}\right) \tag{17}$$

is corresponding to the geometry of deformed type II superconductor shown as Eq.(1), with $\beta^2 = 1$ and $\gamma \neq 0$. Further constant z-directioned electromagnetic field is assumed:

$$\mathrm{A} = \frac{1}{2}\mathrm{H} \times \mathrm{r}, \mathrm{H} = (0, 0, H_z) \tag{18}$$

The operator ∇^2 is not essentially self-adjoint and has a self-adjoint extensions. [13, 14, 15, 16]

The differentiation of electromagnetic field is done not on the space of superconductor but on the Euclid space.

Further from the Theorem X.28 in [17], $H + U(x) - \varepsilon_n$ has a self-adjoint extensions with specified boundary conditions.

Separation of variable in the Eq.(15) yields

$$u(r, \theta, z), v(r, \theta, z) \sim f_{m,k}(r)e^{im\theta}e^{ikz} \tag{19}$$

To determine boundary condition at $r = 0$, variable separated simultaneous differential equations (15) are expand in series. The self-adjointness and normalisability require $f_{m,k}(r) = 0$ for $u(r, \theta, z)$ and $v(r, \theta, z)$ at $r = 0$. This directly suggests that macroscopic wave function $\Delta(r)$ becomes zero at $r = 0$, and magnetic flux can penetrate the superconductor at r=0.

5 Discussion

Geometrical pinning in type II superconductor is given by specifying boundary condition at singular point $r = 0$ of Bogolibov-de Genne eqation. This is because

1.By tight-binding approximation, perfect lattice becames flat space for electron. Considering screw dislocated superconductor, we can determined the boundary condition of macroscopic wave function from self-adjontness and normalisability genuinely originated in geometrical property of superconductor.

2.Since macroscopic wave function becomes zero at singular point $r = 0$, quantized magnetic flux can penetrate the singular point. Except for $r = 0$, macroscopic wave function is not vanishing, and becomes *rigid*, therefore is not influenced by the electromagnetic field.

References

[1] M. O. Katanaev and I. V. Volovich, Ann. Phys. **216**, 1 (1992).

[2] R. A. Puntigam and H. H. Soleng, Class. Quantum. Grav. **14**, 1129 (1997).

[3] D. V. Gal'tsov and P. S. Letelier, Phys. Rev. D. **47**, 4273 (1993).

[4] K. P. Tod, Class. Quantum. Grav. **11**, 1331 (1994).

[5] R. P. Feynman, R. B. Leighton and M. Sands, *The Feynman lectures on Physics vol III*, (Reading Massahusetts: Addison-Wesley 1965)

[6] K. Kawamura, Z. Phys. Rev. B. **29**, 101 (1978).

[7] H. Kleinert, *Gauge Fields in Condensed Matter* (World Scientific, Singapore, 1989).

[8] R. Bausch and R. Schmitz, Phys. Rev. Lett. **80**, 2257 (1998).

[9] S. C. Hunter and F. R. N. Nabarro, Proc. R. Soc. London. A. **220**, 542 (1953).

[10] D. L. Dexter, Phys. Rev. **86**, 770 (1952).

[11] P. G. De Gennes, *Superconductivity of metals and alloys* Perseus Books 1966)

[12] T. Tsuneto, *Superconductivity and superfluidity* (Cambridge University Press 1998).

[13] B. S. Kay and U. M. Studer, Commun. Math. Phys. **139**, 103 (1991).

[14] D. A. Konkowski and T. M. Helliwell, Gen. Rel. Grav. **33**, 1131 (2001).

[15] T. M. Helliwell, D. A. Konkowski and V. Arndt, Gen. Rel. Grav. **35**, 79 (1999).

[16] A. Ishibahi and A. Hosoya, Phys. Rev. D. **60**, 104028 (1999).

[17] M. Reed and B. Simon, *Fourier Analysis and Self-Adjointness* (Academic Press, New York, 1975).

CMB temperature and polarization anisotropies produced by the primordial magnetic fields

Hiroyuki Tashiro[1], Naoshi Sugiyama[2]

[1] *Theoretical Astrophysics Group, Department of Physics, Kyoto University, Kyoto 606-8502, Japan*
[2] *Division of Theoretical Astrophysics, National Astronomical Observatory, Tokyo 181-8588, Japan*

Abstract

Primordial magnetic fields produce the Alfven mode. This mode can survive the Silk damping and can leave the trace on the cosmic microwave background radiation in the small scales. We calculate the anisotropies of the temperature and the B-mode polarization. We find that these anisotropies can dominate the anisotropies produced by other origins and we obtain the constraint of the primordial magnetic fields.

1 Introduction

Magnetic fields are observed in many galaxies and galaxy clusters. These magnetic fields have a few μG strengths and large coherent scales. The standard origin of such magnetic fields is following. The small seeds of the magnetic fields are produced in astronomical objects and those are amplified by the dynamo process (for a comprehensive review see [1]). But the facts that the magnetic fields with the very large coherent scales are observed in galaxy clusters or that the magnetic fields are observed in high redshift galaxies with a few μG strength cast some questions on standard dynamo scenario. It may be difficult to produce these magnetic fields in the dynamo process because host galaxy clusters and galaxies are dynamically young. These things motivate to consider alternative scenarios that the magnetic fields are produced in the early universe. Many authors suggested the generation of the primordial magnetic fields in the early universe, e.g. during an inflation or at cosmological phase transitions (QCD or electroweak phase transition) (for a detail discussion see [2]).

The primordial magnetic fields have been constrained by their effect on the CMB. In this paper we investigate the CMB temperature and polarization anisotropies which are produced by the Alfven mode. Particularly we are interested in the anisotropies at the small scales and we do not use the tight coupling approximation in the anisotropy calculation. In considering the growth of the Alfven mode, we count not only the cosmological viscosity but also the nonlinear effect. To be more precise, we use the numerical simulation results of Banerjee and Jedamzik as the evolution of the Alfven mode in order to calculate the CMB temperature and polarization anisotropies [3, 4].

2 Magnetic field evolution

The pressure gradient of the magnetic fields produces the vorticity called "Alfven mode" in the MHD. This Alfven mode generates the temperature anisotropies by the Doppler shift. Therefore, to calculate the CMB anisotropies we need to know the evolution of Alfven mode. The evolution of the Alfven mode and the magnetic fields with considering the nonlinear effect [3, 4] are different from the result of the linear perturbations.

Considering the cosmological expansion and the viscosity, we can describe the non-linear MHD equations as [4]

$$\frac{\partial \mathbf{v}}{\partial t} + \frac{1}{a}(\mathbf{v}\cdot\nabla)\mathbf{v} + \frac{\rho_b}{\rho_t + p_t} H\mathbf{v} + \frac{1}{a}\left(\frac{\mathbf{B}\times(\nabla\times\mathbf{B})}{4\pi(\rho_t + p_t)}\right) = \mathbf{f}, \tag{1}$$

$$\frac{\partial \mathbf{B}}{\partial t} + 2H\mathbf{B} = \frac{1}{a}\nabla\times(\mathbf{v}\times\mathbf{B}), \tag{2}$$

[1] E-mail:htashiro@tap.scphys.kyoto-u.ac.jp
[2] E-mail:naoshi@th.nao.ac.jp

where ρ_b is the baryon density, ρ_t and p_t denote the total density and pressure of the photons and the baryons, H is the Hubble parameter and f is the dissipation term which is produced by the photons. The fluid velocity v is the Alfven mode so that v satisfies $\nabla \cdot \mathrm{v} = 0$. The dissipation term, f, is written as

$$\mathrm{f} = a^{-2}\nu(\rho + p)^{-1}(\nabla^2 \mathrm{v}), \tag{3}$$

where the shear viscosity by the photons ν is given by

$$\nu = \frac{4}{15}\rho_\gamma L_{\mathrm{mfp}}. \tag{4}$$

Here ρ_γ is the radiation energy density and L_{mfp} is the photon mean free path, $L_{\mathrm{mfp}} = (\sigma_T n_e)^{-1}$ where σ_T is the Thomson cross section and n_e is the free electron density.

This viscous description is no longer valid in the scale which satisfies $a/k \ll L_{\mathrm{mfp}}$. We must treat the baryons and the photons separately. The baryon fluids are dissipated due to a photon background and photons start free streaming. For the baryon fluid the dissipation term is must described as the drag force term by using the drag coefficients α. The drag coefficient α by the photons is given by

$$\alpha = \frac{4}{3}\frac{\rho_\gamma}{\rho_b}L_{\mathrm{mfp}}^{-1}. \tag{5}$$

The Euler equation for the baryon fluids when photons are free streaming is written as

$$\frac{\partial \mathrm{v}}{\partial t} + \frac{1}{a}(\mathrm{v}\cdot\nabla)\mathrm{v} + H\mathrm{v} - \frac{1}{a}\left(\frac{\rho_t + p_t}{\rho_b}\right)(\mathrm{v}_A \cdot \nabla)\mathrm{v}_A = -\alpha \mathrm{v}. \tag{6}$$

where v_A is the Alfven velocity, $\mathrm{v}_A = \mathrm{B}/\sqrt{4\pi(\rho_t + p_t)}$.

As the characteristic scale of the magnetic fields we use the integral scale, $L_{\mathrm{int}} = a/k_{\mathrm{int}}$. The integral scale have the most of the magnetic energy and the kinetic energy. From the MHD nonlinear simulation, it is important that the nonlinear effect at the integral scale occurs or does not. The time scale of the nonlinearity is represented as the eddy time scale,

$$t_{\mathrm{eddy}} = L/v. \tag{7}$$

Comparison of this time scale on the integral scale and the cosmological time scale (i.e. H^{-1}) tells us the existence of the nonlinear effect on the integral scale. The nonlinear effect arise when $t_{\mathrm{eddy}} < H^{-1}$ and vice versa. From the numerical results we can classify the evolution of the MHD nonlinear Alfven mode into three regimes. These regimes depend on the nonlinear effect arising (which is longer at the integral scale, the eddy time scale or the cosmological time scale) and the scale of the photon mean free path (which is longer, the integral scale or the photon mean free path).

The first regime is named the "turbulent regime". In this regime the inertial term dominates the dissipation term at the integral scale in Eq. (1). The nonlinear effect works well in this regime. The nonlinearity causes that the magnetic fields energy and the fluid kinetic energy reaches the equipartition (i.e. $v = v_A$) and the turbulence of the fluids transports the kinetic energy from large scales to small scales. Due to this effect, the integral scale grows up. This regime exists in the early universe because the viscosity, Eq. (4), is very small in the early universe.

As the universe evolves, the photon mean free path becomes longer. The dissipation due to the viscosity becomes effective and the velocity ends up declining. Accordingly the dissipation term dominates the inertial term at the integral scale in Eq. (1). This is the second regime and we called this regime the "viscous regime". The eddy time scale at the integral scale is larger than the cosmological time scale. The nonlinear effect does not affect the evolution of the magnetic fields.

The third regime is the regime during which the photon mean free path is longer than the integral scale. We call this regime "free streaming regime". We must acquire the fluid velocity at the integral scale by Eq. (6). Typically, the eddy time scale at the smaller scales than the integral scale is smaller than the cosmological time scale and that at the larger scales becomes larger than the cosmological time scale during this regime.

We can also classify the evolution types of the magnetic fields into the three types. Fig. 1 is the illustration of the magnetic field evolution types. The dotted line is the magnetic fields with $k_{\mathrm{int}} <$

$1.2\mathrm{Mpc}^{-1}$ at the LSS. The solid line is the magnetic fields with $1.2\mathrm{Mpc}^{-1} < k_{\rm int} < 9.8\mathrm{Mpc}^{-1}$ at the LSS. The dashed line is the magnetic fields with $k_{\rm int} > 9.8\mathrm{Mpc}^{-1}$ at the LSS. We also find the relation between the magnetic field strength and the integral scale,

$$B_{-9} \approx 33 \left(\frac{k_{\rm int}}{1\mathrm{Mpc}^{-1}} \right)^{-1/3}, \tag{8}$$

where B_{-9} is normalized by the comoving magnetic field 10^{-9}Gauss.

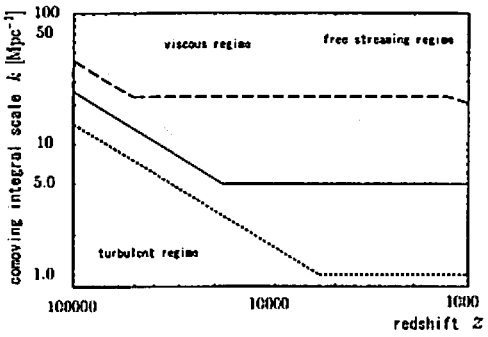


Figure 1: The evolutions of the comoving integral scale of the magnetic fields. The dotted line undergoes the turbulent regime and the viscous regime until the LSS. The solid line and the dashed line pass through the turbulent, the viscous and the free streaming regime. But, there is not the growing of the integral scale during the free streaming regime in the magnetic fields represented as the solid line. The thin solid line is the transition line from the turbulent regime to the viscous regime. The thin dotted line is the transition line from the viscous regime to the free streaming regime. The thin dashed line represents the start of the direct cascade in the free streaming regime.

3 CMB anisotropies

The Alfven mode produced by the primordial magnetic fields generates the CMB temperature fluctuations by the Doppler sift. The quadrupole component of the generated temperature anisotropies produces the polarization by the Thomson scattering. The polarization is decomposed into the E-mode polarization and the B-mode polarization. In particular, the B-mode is not primary produced by the scalar type perturbation which provides dominant contribution in the temperature anisotropies. The B-mode is a good observation for the detection of the other type components than the scalar type.

We calculate the CMB anisotropies produced by the Alfven mode through the total angular method [5]. We plot these temperature anisotoropies and the B-mode polarization anisotoropies in Fig. 2. The plotted anisotropies are produced by the magnetic fields whose integral scales at the LSS are $10\mathrm{Mpc}^{-1}$, $1.5\mathrm{Mpc}^{-1}$ and $1.0\mathrm{Mpc}^{-1}$. The magnetic fields with the integral scale $10\mathrm{Mpc}^{-1}$ which is dotted line in Fig. 2 is corresponding to the type which illustrated as the dashed line in Fig. 1. The magnetic fields with the integral scale $1.5\mathrm{Mpc}^{-1}$ which is solid line in Fig. 2 is corresponding to the type which illustrated as the dotted line in Fig. 1. The magnetic fields with the integral scale $1.0\mathrm{Mpc}^{-1}$ which is dashed line in Fig. 2 is corresponding to the type which illustrated as the solid line in Fig. 1.

The difference between the linear case [6] and our nonlinear case is at the point of the cut-off scale. The cut-off scale in the nonlinear case is corresponding to the integral scale. This scale is obtained by equating the eddy time scale in the turbulent regime to the cosmological time. In the linear theory the cut-off scale in the case of the blue spectrum is given as the scale where the amplitude is damped by one e-folding at physical time t

$$k_{\rm cut}^{-1} \approx \sqrt{\frac{3}{5}} \frac{v_A L_S}{a}. \tag{9}$$

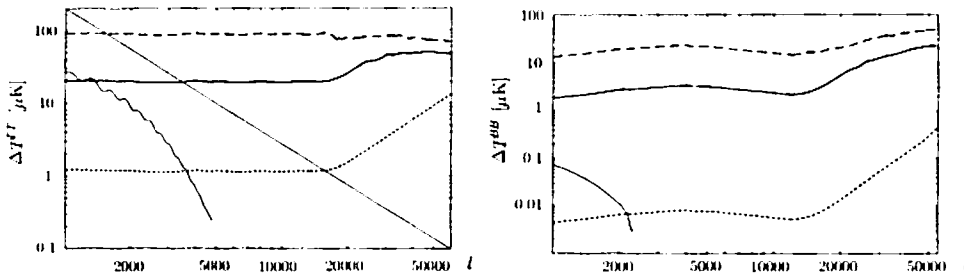


Figure 2: The temperature anisotropies. The left panel shows the temperature anisotropies and the right panel is the B-mode polarization. The solid line is the case of the magnetic fields with the comoving integral scale $k_{\rm int} = 1.5{\rm Mpc}^{-1}$ The dashed line is the case of $k_{\rm int} = 1.0{\rm Mpc}^{-1}$ and the dotted line is the case of $k_{\rm int} = 10{\rm Mpc}^{-1}$. The comoving integral scale is related with the magnetic field strength by Eq. (8). The gray line is the linear result of the magnetic field strength 28nG at 1Mpc with spectral index $n = 4$ [6]. For purpose of comparison, we plot the temperature anisotropies in the standard ΛCDM model (a narrow line), computed using CAMB with the same cosmological parameters [7].

where L_s is the Silk scale. This is corresponding to the relation between the integral scale and the magnetic field strengths at the free streaming regime. If the integral scale is satisfied with $1.2{\rm Mpc}^{-1} < k < 9.87{\rm Mpc}^{-1}$ at the LSS, the integral scale as the damping scale is different from the damping scale obtained from Eq. (9). This is because such magnetic fields are already damped at the turbulent regime. In this case, the equation corresponding to the Eq. (9) is Eq. (8). The integral scale is larger than the damping scale in the linear analysis. In the case of the magnetic fields in the viscous regime at the LSS for the same reason, the integral scale is larger than the damping scale in the linear analysis.

We get the anisotropy spectrum below the cut-off scale (the integral scale) from the nonlinear simulation. It is difficult to obtain the linear results in the scale below the cut-off scale. The obtained anisotropy spectra are classified into two types. These types are the type caused by the nonlinear effect and the frozen-in type. The property of the spectrum depends on the integral scale at the LSS.

The lower-multipole branch continues to the low multipole $l \sim 100$ where the anisotropies are observed accurately by the satellite (e.g. COBE or WMAP). Therefore, we conclude from the observations that there are not the magnetic fields with the integral scale 1Mpc which are in the viscous regime at the LSS.

The details will be published elsewhere [8].

References

[1] L. M. Widrow, Rev. Mod. Phys. 74, 775 (2003).

[2] D. Grasso and H. R. Rubinstein, Phys. Rept. 348, 163 (2001);
M. Giovannini, Int. J. Mod. Phys. D13, 391 (2004).

[3] R. Banerjee and K. Jedamzik, Phys. Rev. Lett. **91**, 251301 (2003).

[4] R. Banerjee and K. Jedamzik, astro-ph/0410032 (2004).

[5] W. Hu and M. White, Phys. Rev. D **56**, 596 (1997).

[6] K. Subramanian and J. D. Barrow, Phys. Rev. Lett. **81**, 3575 (1998);
K. Subramanian and J. D. Barrow, Mon. Not. R. Astron. Soc, **335**, L57 (2002);
A. Mack, T. Kahniashvili and A. Kosowsky, Phys. Rev. D **65**, 123004 (2002);
K. Subramanian, T. R. Seshadri and J. D. Barrow, Mon. Not. R. Astron. Soc, **344**, L31 (2003).

[7] A. Lewis, L. Challior and A. Lasnby, Astrophys.J. **538**, 473, (2000).

[8] H. Tashiro, N. Sugiyama, R. Banerjee and K. Jedamzik, in preparation.

Dynamical bar instability in collapsing stars

Motoyuki Saijo [1]

Department of Physics, Kyoto University, Kyoto 606-8502, Japan

Abstract

We investigate the rotational core collapse of a rapidly rotating relativistic star by means of a 3+1 hydrodynamic simulations in conformally flat spacetime of general relativity. The dynamics is started from a differentially rotating equilibrium star of $T/W \sim 0.16$ (T is the rotational kinetic energy and W is the gravitational binding energy of the equilibrium star), depleting the pressure to initiate the collapse and to exceed the threshold of dynamical bar instability. Our finding is that the collapsing star potentially forms a bar when we collapse the toroidal star due to the redistribution of the angular momentum at the core bounce. On the other hand, the collapsing star weakly forms a bar when we collapse the spheroidal star. We also find that the bar structure is destroyed when the torus is destroyed in the rotational core collapse. Since the collapse of a toroidal star has a potential to form a bar if it exceeds the threshold of dynamical instability, it can become a promising source of gravitational waves which will be detected in advanced LIGO.

Rotational core collapse occurs in the first phase of the collapse-driven supernova explosion. The collapse takes place in a dynamical timescale and the bounce occurs when the central part of the star collapses into a nuclear density and then stiffens its equation of state. The final outcome of the collapse forms a compact object, such as a neutron star or a black hole, which is a candidate for sources of gravitational waves. There are two different approaches to investigate the rotational core collapse. One is to take into account the realistic picture of the rotational collapse such as realistic equation of state of the neutron star and/or neutrino effect in Newtonian gravity. The other is to illustrate simplified physics in relativistic gravitation. Since one of our aims in this paper is to investigate a possibility of gravitational wave sources in rotational core collapse, we should at least take into account relativistic gravitation, which significantly affects the quantitative behavior of gravitational waves from rotational core collapse. [1]

Dynamical bar instability in a rotating equilibrium star takes place when the ratio between rotational kinetic energy and the gravitational binding energy exceeds the critical value. In the Newtonian incompressible star, the critical onset of dynamical instability is $T/W \approx 0.27$, and the relativistic gravitation decreases that value to $T/W \approx 0.24 - 0.26$, depending on the compaction of the star. It potentially occurs during the collapse since the nondimensional value T/W, where T is a rotational kinetic energy and W is the gravitational binding energy, scales as R^{-1} in the dimensional analysis where R is the radius of the star. Let us briefly discuss a picture of core bounce. During the collapse phase, when the star exceeds the critical value of dynamical instability, the star starts to deform its shape to bar. During the bounce phase, T/W could fall below the threshold of dynamical instability, and the star cannot deform furthermore. In such a situation, what happens to the nonaxisymmetric deformation?

Our purpose in this paper is the following twofold. One is that we investigate a necessary condition and mechanism to enhance the dynamical bar instability in a collapsing star. Brown [2] performed long time integration of the rotational core collapse to investigate whether a dynamical bar can significantly form during the evolution. He found that the dynamical bar instability sets in at $T/W \approx 0.23$, which is far below the standard value $T/W \approx 0.27$. He found that the role of dynamical bar in rotational core collapse may be quite different from that in the equilibrium star. He also found that the bar instability grows slowly in core bounce. His finding can be interpreted that bar instability is initiated by the interaction between the core part and the surrounding part of the star. Therefore the "dynamical" bar instability in the collapsing star is quite different from that in the equilibrium state.

[1] E-mail: saijo@tap.scphys.kyoto-u.ac.jp

Table 1: Relativistic Rotating Equilibrium stars

Model	n^a	$\hat{A}^b$	$R_p/R_e{}^c$	$\rho_0^{\max d}$	T/W^e	R_e/M^f	$P_{\rm dep}{}^g$
I-a	1.5	0.5	0.467	8.26×10^{-4}	1.59×10^{-1}	3.99×10^{1}	70%
I-b	1.5	0.8	0.467	1.36×10^{-3}	1.59×10^{-1}	4.04×10^{1}	70%
II-a	2.0	0.5	0.450	1.10×10^{-4}	1.63×10^{-1}	4.03×10^{1}	60%
II-b	2.0	0.6	0.417	2.19×10^{-4}	1.62×10^{-1}	3.98×10^{1}	60%
III-a	2.5	0.3	0.417	1.05×10^{-5}	1.59×10^{-1}	3.99×10^{1}	50%
III-b	2.5	0.42	0.417	2.24×10^{-5}	1.60×10^{-1}	4.00×10^{1}	50%

(a): Polytropic index
(b): Parameter of the degree of differential rotation
(c): Ratio of the polar proper radius to the equatorial proper radius
(d): Maximum rest-mass density
(e): T: Rotational kinetic energy; W: Gravitational binding energy
(f): R_e: Circumferential radius; M: Gravitational mass
(g): $P_{\rm dep}$: Ratio of pressure depletion to the equilibrium star

The other is that, it is important to probe whether the rotational core collapse becomes a promising source of gravitational waves. Direct detection of gravitational waves by ground based and space based interferometers is of great importance in general relativity, in astrophysics, and in cosmology. Once a bar has formed in the neutron star, we may expect quasi-periodic gravitational waves in the kHz band, which may be detectable in advanced LIGO. Rampp, Müller, and Ruffert (1998) [3] investigated the rotational core collapse of $n = 3$ polytropic star in Newtonian gravity. They also used a mimic equation of state including the thermal pressure and the nuclear matter. They found that although the rotating star has a nonaxisymmetric deformation, the amplitude of gravitational waves does not significantly grow during the deformation. In fact, they compared the gravitational waveform computed in their simulation with that in the previous 2D calculation [4] and found that it is quite similar with each other. Therefore, even if the nonaxisymmetric instability takes place during the collapse, the bar does not significantly grow at the core bounce. What else do we need to enhance the bar formation in the rotational core collapse?

Our interest is to focus on the core bounce of the rotational core collapse in order to investigate the angular momentum redistribution at that time and to investigate the possibility of gravitational wave sources. Accordingly we construct a mimic model to investigate the above two marks. We deplete the

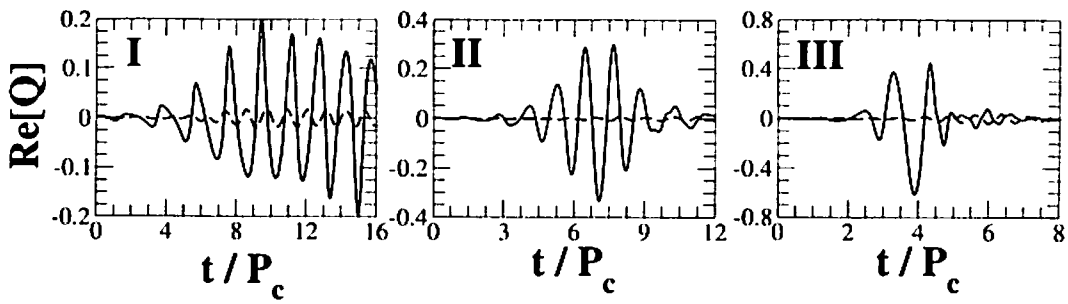


Figure 1: Diagnostics Q (represented as $m = 2$ mode) as a function of t/P_c for our 6 different models (see Table 1). Note that P_c is the central orbital period of the equilibrium star. Solid and dash lines represent toroidal and spheroidal stars, respectively.

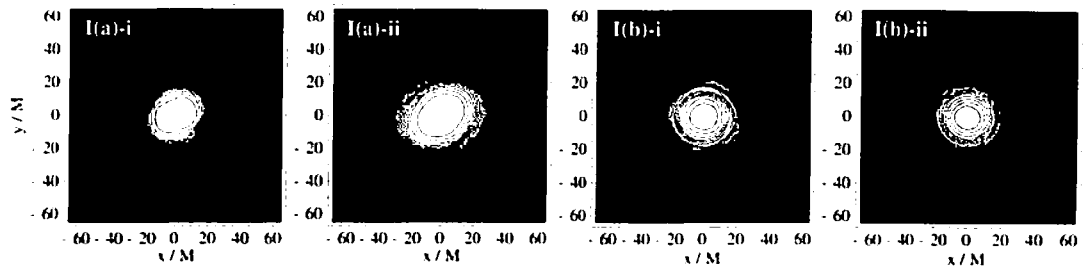


Figure 2: Density contour in the equatorial plane of 2 different collapsing stars with a polytropic index $n = 1.5$. Model I(a), I(b) (see Table. 1) is plotted at the parameter $(t/t_{\rm dyn}, \rho^*_{\rm max})$ = I(a)-i (9.61, 9.13×10^{-3}), I(a)-ii (16.0, 6.04×10^{-3}), I(b)-i (9.67, 1.33×10^{-2}), I(b)-ii (15.3, 1.57×10^{-2}), respectively. The contour lines denote coordinate densities $\rho^* = \rho^*_{\rm max} \times 10^{-0.220(16-i)} (i = 1, \cdots, 15)$.

pressure of the equilibrium star to initiate collapse and bounce. We also use polytropic equation of state in the equilibrium state, and use Γ-law equation of state ($\Gamma \approx 1.40, 1.50, 1.67$) in the evolution to focus on the dependence of equation of state. We furthermore concentrate on the structure of the star, spheroidal and toroidal, to investigate the dynamical bar instability in a collapsing star.

We investigate the role of dynamical bar instability in rotational core collapse by means of hydrodynamic simulations in conformally flat approximation in general relativity. We specifically focus on the structure of the star to see whether it takes a significant role to enhance dynamical bar instability. A more detailed discussion will be presented in Ref. [5].

We find that the structure of the star takes a significant role in enhancing the dynamical bar instability at core bounce (See Figs. 1, 2). The angular velocity of the collapsing star has already reached the "Keplarian" to produce a toroidal structure. Therefore the angular momentum can only shift outwards at the bounce. On the other hand, for a spheroidal star, the angular momentum can shift both inwards and outwards at bounce since it does not reach the "Keplarian". That means rotational core collapse cannot significantly break the central core of the star. Consequently, a bar structure can be easily constructed in case of a toroidal star during the evolution. We show the profile of the coordinate density along x-axes in the intermediate stage and in the termination stage of the integration in Fig. 4. Note that for a soft equation of state ($n = 2.0, 2.5$) as the torus is destroyed in the rotational core collapse, the amplitude of gravitational waves is also decreased. The torus is the key issue to trigger the bar formation.

Once a bar has formed, the amplitude of gravitational waves has been significantly increased due to the nonaxisymmetric deformation of the star (See Fig. 3). The previous 2D calculation shows that a peak amplitude of gravitational waves comes from the core bounce of the star, and the behavior of it also

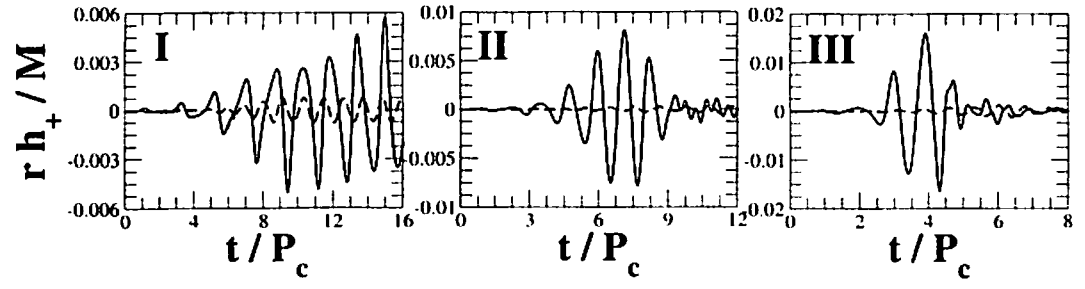


Figure 3: Gravitational waveforms from a distant observer along the rotational axes of 6 different stars using quadrupole formula (See Table. 1). Solid and dash lines represent toroidal and spheroidal stars, respectively.

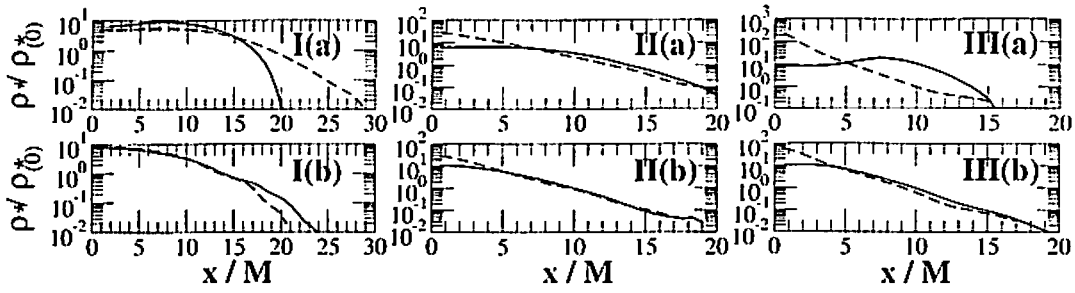


Figure 4: Snapshot of the coordinate density along the x-axes for 6 different stars (see Table. 1). Solid and dash line represents t/P_c = I(a) (9.61, 16.0), I(b) (9.67, 15.3), II(a) (2.39, 12.0), II(b) (3.25, 12.0), III(a) (3.19, 7.77), III(b) (3.20, 7.77), respectively.

coincides with that of 3D calculation. In our results, gravitational radiation is dominantly generated in the bar formation process. The amplitude of bar formation is about 20 times larger than that of core bounce. The characteristic amplitude and frequency of gravitational waves in the collapsing star can be written as

$$f_{\rm gw} \approx \frac{1}{2\pi t_{\rm dyn}} = 100\ [{\rm Hz}] \left(\frac{M_\odot}{M}\right)\left(\frac{40M}{R}\right)^{3/2}, \quad (1)$$

$$h_{\rm gw} \approx 4.8\times 10^{-23}\left(\frac{M}{M_\odot}\right)\left(\frac{10{\rm Mpc}}{d}\right)\left(\frac{rh/M}{0.01}\right). \quad (2)$$

Therefore, gravitational waves from a dynamical bar in a collapsing neutron star could be detected in advanced LIGO.

References

[1] P. Cerdá-Durán, G. Faye, H. Dimmelmeier, J. A. Font, J. M. Ibáñez, E. Müller, and G. Schäfer, submitted to Astron. Astrophys. (astro-ph/0412611).

[2] J. D. Brown, in *Astrophysical Sources for Ground-based Gravitational Wave Detectors*, edited by J. M. Centrella (American Institute of Physics, New York, 2001), 234.

[3] M. Rampp, E. Müller, and M. Ruffert, Astron. Astrophys. **332**, 969 (1998).

[4] T. Zwerger and E. Müller, Astron. Astrophys. **320**, 209 (1997).

[5] M. Saijo, in preparation (2005).

Stochastic Gravitational Wave Background in Brane World Cosmology

Kiyotomo Ichiki[a,b,1], Kouji Nakamura[c,2]

[a] *Department of Astronomy, University of Tokyo, 7-3-1 Hongo, Bunkyo-ku, Tokyo 113-0033, Japan*
[b] *Division of Theoretical Astrophysics, National Astronomical Observatory, 2-21-1, Osawa, Mitaka, Tokyo 181-8588, Japan*
[c] *Department of Astronomical Science, the Graduate University for Advanced Studies, 2-21-1, Osawa, Mitaka, Tokyo 181-8588, Japan*

Abstract

We investigate cosmological evolution of gravitational waves in Friedman-Robertson-Walker brane world model embedded in a five dimensional anti de-Sitter spacetime. To predict the spectrum of stochastic gravitational background at present generated in the inflationary phase, we numerically calculate the evolution of gravitational waves according to the method developed in our recent paper [K. Ichiki and K. Nakamura, Phys. Rev. D70, 064017, (2004)]. The behavior of time evolution of gravitational waves in brane world model is significantly altered from that of the standard four dimensional one in the frequency range $f \gtrsim f_{\rm AdS} \approx 10^{-4}$ Hz, which corresponds to the curvature scale we set of anti de-Sitter spacetime, $l \approx 1$mm.

1 Introduction

In recent years much attention has been paid to interesting models of spacetimes in which fields of the standard model are confined to a "brane", while only the gravitational field propagates in all the dimensions called the "bulk". Since the proposal of a brane world model of our spacetime by Randall and Sundrum [1] (RS II model), the phenomenology of brane world cosmological models has been the subject of intensive investigations [2]. In their models our four dimensional spacetime is embedded in the five dimensional anti de-Sitter (AdS5) spacetime with curvature scale l, and the four-dimensional gravity is effectively recovered in larger scales than l. The current direct bound of the experimental gravitational probe allows the scale of extra dimensions or curvature scale l to be as large as a (sub)millimeter [3].

In addition to the direct experimental probe of the Newton potential, if our universe is really the RS II type brane universe, there is a possibility that the evolution history of the universe is significantly altered when the Hubble scale H^{-1} is smaller than l in the early universe. The stochastic gravitational waves will be a promising candidate which provides direct and deep probes of such early universe (for example, see [4]). Though some authors have investigated the evolution of gravitational waves in brane world cosmology based on the Gaussian normal coordinate system in the neighborhood of the brane [5], this coordinate system includes a coordinate singularity in the bulk, where the metric function vanishes [6], and the treatment of the wave equation near the singularity becomes delicate. However, these delicate problems are removed by the introduction of the coordinate system proposed in Ref.[7]. In this work, we solve the evolution of gravitational waves in the brane world model and predict the present energy spectrum, following the previous proposal[7]. We have concentrated on the brane world model of the flat Friedmann-Robertson-Walker (FRW) universe which is supported by recent precise measurements of the cosmic microwave background (CMB) anisotropies [8], without "dark radiation" following discussions in Ref.[9].

2 The Basic Equations

In terms of the single null coordinate system, the metric on the AdS_5 is given by

$$ds^2 = -F(\tau,\overline{w})du^2 - 2F(\tau,\overline{w})du d\overline{w} + r^2(\tau,\overline{w})d\Sigma_0^2 \,. \tag{1}$$

[1] E-mail:ichiki@th.nao.ac.jp
[2] E-mail:kouchan@th.nao.ac.jp

Here the metric functions $F(\tau, \overline{w})$ and $r(\tau, \overline{w})$ are given by

$$F(\tau(u,\overline{w}),\overline{w}) = \frac{r^2/l^2}{\sqrt{r^2/l^2+\dot{a}^2}+\dot{a}}\ , \tag{2}$$

$$r(\tau(u,\overline{w}),\overline{w}) = \frac{a(\tau)}{2}\times\left[(1-A)e^{\overline{w}/l}+(1+A)e^{-\overline{w}/l}\right]\ ,$$

respectively, where $A \equiv \sqrt{1+l^2H^2}$. Here $a(\tau)$ is the scale factor of the FRW brane whose time evolution is given by the generalized Friedmann equation [2], $H^2 = \left(\frac{\dot{a}}{a}\right)^2 = \frac{8\pi G_N}{3}\rho + \frac{\Lambda_4}{3} + \frac{\kappa_5^4}{36}\rho^2$, where $\dot{a} = da/d\tau$, τ is the comoving time on the FRW brane, ρ is the energy density on the brane, $\Lambda_4 = \kappa_5^4\lambda^2/12 + 3\Lambda_5/4$ is the cosmological constant induced on the brane, $G_N = \kappa_5^4\lambda/48\pi$ and κ_5 are the four-dimensional and five-dimensional gravitational constants, respectively. We also assume Z_2 symmetry across the brane following to the original RS II model. Hereafter we set $l = 1$ mm for the purpose of numerical calculations.

Apart from the polarization tensor, the equation of gravitational waves in the bulk is simply given by that of the five dimensional massless scalar field, $\Box_5 h = 0$. As derived in Ref.[7], this equation is equivalent to:

$$\partial_u h = r^{-3/2}\left[g\partial_{\overline{w}}h\right]_0^{\overline{w}} + r^{-3/2} \times \left\{\int_0^{\overline{w}}\left(\partial_{\overline{w}}h\left(J-\frac{\partial g}{\partial\overline{w}}\right)-g\frac{k^2}{r^2}h\right)dw + C(u)\right\}\ , \tag{3}$$

where $-k^2$ is the eigen value of the Laplacian of Σ_0, and

$$g := \frac{F}{2}r^{3/2}\ , \tag{4}$$

$$J := \left(\frac{1}{2}\frac{\partial F}{\partial\overline{w}}+\frac{3F}{2}\frac{\partial\ln r}{\partial\overline{w}}-\frac{3}{2}\frac{\partial\ln r}{\partial u}\right)r^{3/2}\ . \tag{5}$$

$C(u)$ is determined by the boundary conditions of the Neumann type on the brane at each time step

$$C(u) = a^{3/2}F(\tau,w)\times\partial_{\overline{w}}h(u,\overline{w})|_{\overline{w}=0}\ . \tag{6}$$

As an initial condition of numerical examples, we follow the inflationary scenario and start the numerical calculation by setting $h = const.$ on an initial null hypersurface. This initial value is a solution to the wave equation in the long wavelength limit $k/aH \to 0$ [10]. We should note, however, that $h = const.$ is not an exact solution to the wave equation for $k \neq 0$ mode, but an approximate one in the situation $k/aH \ll 1$. Further, as the universe expands and decelerates, the approximation $k/aH \ll 1$ becomes violated. Conversely, this also implies that $h = const.$ is an appropriate initial condition in the long wavelength approximation, if we start the calculation from the much earlier time than that of the horizon crossing of each mode on the brane. For this reason, we start the calculation when the wave is far enough outside the horizon with the initial condition $h = const.$ to keep the validity of the long wavelength approximation $k/aH \to 0$.

3 Numerical Results and Discussion

We show the examples of the evolution of gravitational waves h_{5d} in Fig.1, In these figures we also show "four dimensional gravitational waves" h_{4d} for comparison, which is a solution of the four dimensional equation $\ddot{h}_{4d} + 3H\dot{h}_{4d} + \left(k^2/a^2\right)h_{4d} = 0$. The solution is expressed by using the spherical Bessel function and the amplitude simply falls as a^{-1}.

The feature of the evolutions of gravitational waves, which one can easily see from Fig.1, is that the amplitudes of them are constant in time at first, and then start damping with oscillation. In the standard four-dimensional cosmology, it is well known that the amplitude of gravitational waves is "frozen" when the modes are outside the horizon ($k/aH \ll 1$), and then starts to oscillate after the modes enter the horizon ($k/aH \gg 1$). As shown in Fig.1, it turns out that this behavior is also seen in the evolution of gravitational waves in the brane world model considered here.

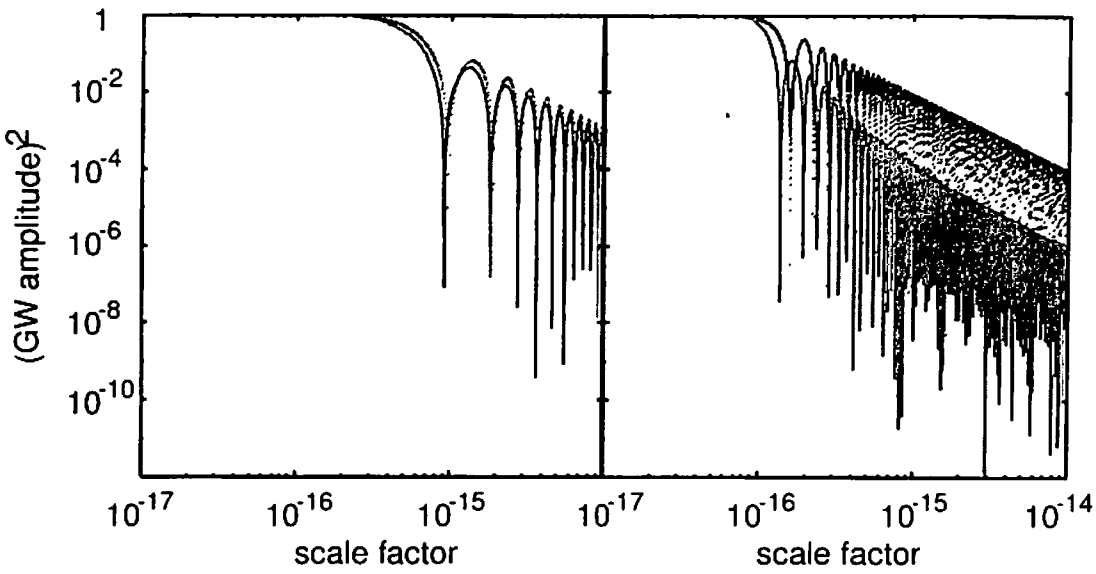


Figure 1: The time evolution of gravitational waves with comoving frequency, $f = 7.1 \times 10^{-5}$[Hz] (left panel) and $f = 1.4 \times 10^{-3}$ [Hz] (right panel). Solid and dotted lines correspond to the evolutions of gravitational waves in brane world model and standard four dimensional one, respectively. The time evolution of gravitational wave with lower frequency is almost "four dimensional" one, in which the amplitude of gravitational waves falls as a^{-1}. On the other hand, the amplitude of gravitational wave with higher frequency in the brane world model decays faster than a^{-1} first, and its evolution asymptotically becomes similar to that of the standard model.

The other important feature is that the amplitude of five-dimensional gravitational waves (h_{5d}) decays faster than that of standard four-dimensional gravitational waves (h_{4d}) in higher frequency modes (the right panel in Fig.1). This is an essential feature of the five-dimensional evolution of gravitational waves. As we mentioned above, the gravitational waves with wavelength smaller than the curvature scale of AdS_5 ($\lambda_{\rm phy} \equiv 2\pi a/k \lesssim l$) would *feel* the universe to be five dimensional, and thus the evolution of gravitational waves with such wavelength can be significantly altered. Even though the decomposition of independent Kaluza-Klein (KK) modes is quite non-trivial in FRW brane universe, the strongly decelerating brane motion and Doppler effects by the moving brane cause a mode mixing of gravitational waves, and do generate the effective "KK modes" which propagate into the bulk [5]. This is the reason for the damping in the amplitude of five-dimensional gravitational waves relative to that of four-dimensional gravitational waves.

In order to predict the spectrum of stochastic gravitational waves at present, we have to know how much amplitude of gravitational waves in five dimensional model has escaped from the brane compared to that in four dimensional model. To accomplish this, we draw two envelope curves of the evolution of gravitational waves for h_{5d} and h_{4d}, and numerically observe the ratio h_{5d}/h_{4d} after the evolution of gravitational waves in five dimensional model exhibits asymptotic behavior, i.e., h_{5d} falls as a^{-1}. We find that the ratio can be well fitted by a simple power law above some critical frequency:

$$\frac{h_{5d}}{h_{4d}} = \begin{cases} 1 & \text{for } f < f_{\rm AdS} \\ \left(\frac{f}{f_{\rm AdS}}\right)^{-\alpha} & \text{for } f > f_{\rm AdS} \end{cases} \tag{7}$$

where we numerically obtain that $f_{\rm AdS} \approx 10^{-4}$ Hz and α is roughly about 0.8. This leads $\Omega_{\rm GW}(f)h_0^2 \propto f^{-0.28}$, where $\Omega_{\rm GW}(f) \propto k^2h^2$ is the energy density of gravitational waves per logarithmic frequency interval in critical density units, and h_0 is Hubble parameter today in units of 100 km/s/Mpc. We should caution, however, that although we have corrected an numerical error found in our previous paper [11], our results have not yet been fully consistent with those obtained in a recent study [12]. The reason

is still unclear, though this might caused by an different choice of initial conditions due to that of bulk coordinate system. We still need further investigation.

Finally let us briefly mention the observational aspects in the case where our results would be correct. In standard models with CMB quadrupole anisotropies measured by COBE, the energy density of gravitational waves is constrained to $\Omega_{GW} \lesssim 10^{-15}$ at $f \sim 0.1$ Hz. If future CMB experiments could directly measure the tensor amplitude and its spectral tilt (n_T) through temperature and polarization anisotropies [13], one can in principle extrapolate and expect the amplitude of gravitational waves to much higher frequency range, even up to 10^{15} Hz [14]. On the other hand, in the brane world model considered in this paper, it is derived from our results that the spectral energy density will be much smaller than expected above some critical frequency $f_{AdS} \approx 10^{-4}$ Hz. Unfortunately, stochastic radiation from white dwarf binaries prevents us from detecting primordial gravitational waves in the frequency range $10^{-5} \lesssim f \lesssim 10^{-2}$ Hz. However, the sky would be "transparent" to a primordial signal above the frequency $f \sim 0.1$ Hz by one year observation, if the neutron star - neutron star merger rate is around $R \sim 10^{-5}$/yr/galaxy [15]. In these bands, the decihertz ($10^{-2} - 10$ Hz) interferometer gravitational wave detectors, such as DECIGO [16] and BBO , have been proposed aiming to detect the primordial gravitational waves as one of their important goals. Therefore, the signal of the brane world cosmological model might be detected as a "lack" of gravitational waves in such higher frequencies.

References

[1] L. Randall and R. Sundrum, Phys. Rev. Lett. **83**, 4690 (1999)

[2] P. Binetruy, C. Deffayet, U. Ellwanger and D. Langlois, Phys. Lett. B **477**, 285 (2000) P. Kraus, JHEP **9912**, 011 (1999) S. Mukohyama, Phys. Lett. B **473**, 241 (2000)

[3] J. Chiaverini, S. J. Smullin, A. A. Geraci, D. M. Weld and A. Kapitulnik, Phys. Rev. Lett. **90**, 151101 (2003)

[4] M. Maggiore, Phys. Rept. **331**, 283 (2000)

[5] T. Hiramatsu, K. Koyama and A. Taruya, Phys. Lett. B **578**, 269 (2004) R. A. Battye, C. Van de Bruck and A. Mennim, Phys. Rev. D **69**, 064040 (2004) T. Kobayashi, H. Kudoh and T. Tanaka, Phys. Rev. D **68**, 044025 (2003) R. Easther, D. Langlois, R. Maartens and D. Wands, JCAP **0310**, 014 (2003)

[6] H. Ishihara, Phys. Rev. D **66**, 023513 (2002)

[7] K. Ichiki and K. Nakamura, arXiv:hep-th/0310282.

[8] D. N. Spergel *et al.*, Astrophys. J. Suppl. **148**, 175 (2003)

[9] K. Ichiki, M. Yahiro, T. Kajino, M. Orito and G. J. Mathews, Phys. Rev. D **66**, 043521 (2002)

[10] D. Langlois, R. Maartens and D. Wands, Phys. Lett. B **489**, 259 (2000)

[11] K. Ichiki and K. Nakamura, arXiv:astro-ph/0406606.

[12] T. Hiramatsu, K. Koyama and A. Taruya, arXiv:hep-th/0410247.

[13] D. J. Eisenstein, W. Hu and M. Tegmark, Astrophys. J. **518**, 2 (1998)

[14] M. S. Turner, Phys. Rev. D **55**, 435 (1997)

[15] C. Ungarelli and A. Vecchio, Phys. Rev. D **63**, 064030 (2001)

[16] N. Seto, S. Kawamura and T. Nakamura, Phys. Rev. Lett. **87**, 221103 (2001)